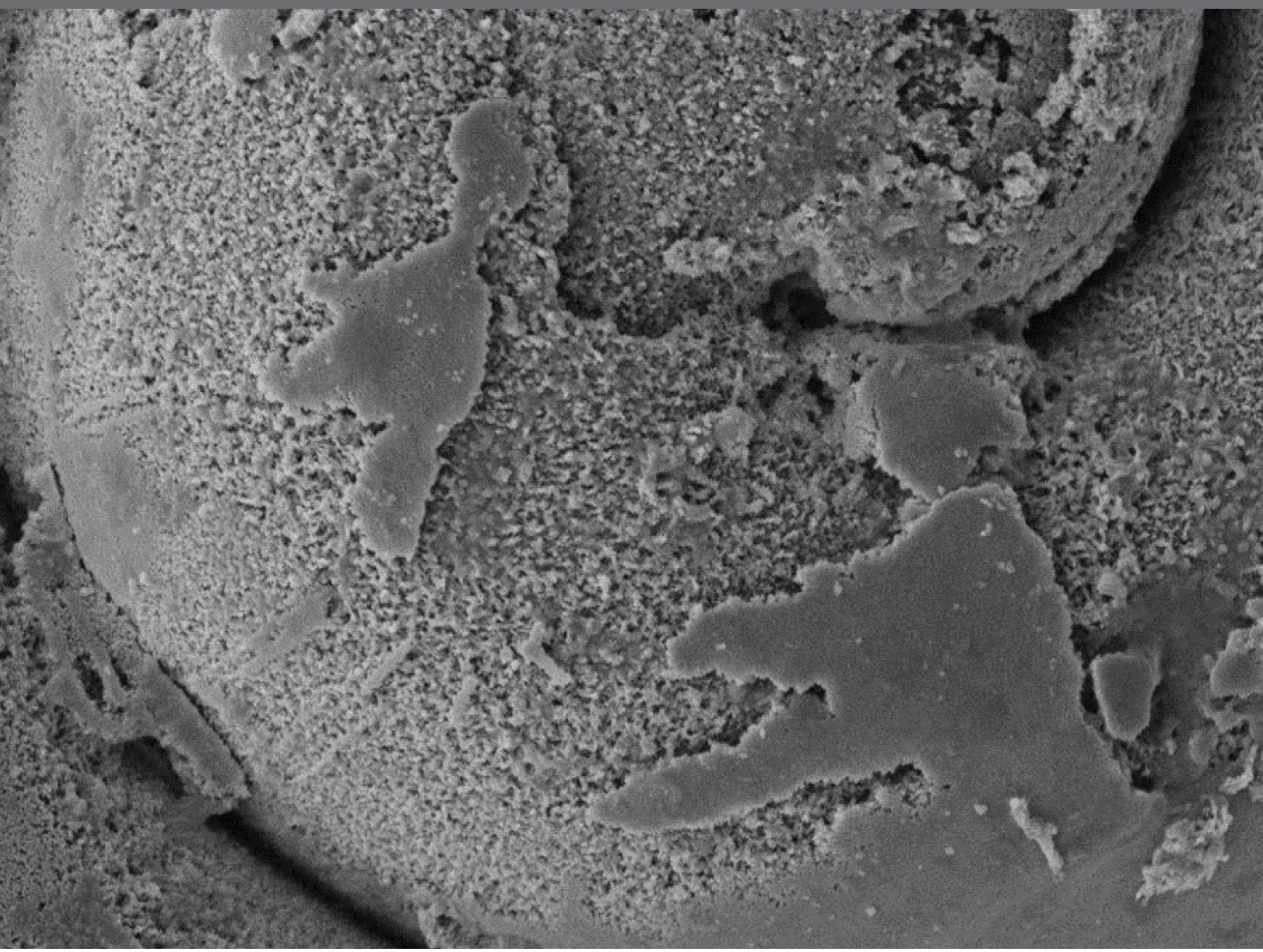
ACIDIFICATION AND HYPOXIA IN MARGINAL SEAS

EDITED BY: Xianghui Guo, Hongjie Wang, Richard Alan Feely, Arnaud Laurent and Nina Bednarsek

PUBLISHED IN: Frontiers in Marine Science



frontiers Research Topics

Frontiers eBook Copyright Statement

The copyright in the text of individual articles in this eBook is the property of their respective authors or their respective institutions or funders. The copyright in graphics and images within each article may be subject to copyright of other parties. In both cases this is subject to a license granted to Frontiers.

The compilation of articles constituting this eBook is the property of Frontiers.

Each article within this eBook, and the eBook itself, are published under the most recent version of the Creative Commons CC-BY licence. The version current at the date of publication of this eBook is CC-BY 4.0. If the CC-BY licence is updated, the licence granted by Frontiers is automatically updated to the new version.

When exercising any right under the CC-BY licence, Frontiers must be attributed as the original publisher of the article or eBook, as applicable.

Authors have the responsibility of ensuring that any graphics or other materials which are the property of others may be included in the CC-BY licence, but this should be checked before relying on the CC-BY licence to reproduce those materials. Any copyright notices relating to those materials must be complied with.

Copyright and source acknowledgement notices may not be removed and must be displayed in any copy, derivative work or partial copy which includes the elements in question.

All copyright, and all rights therein, are protected by national and international copyright laws. The above represents a summary only. For further information please read Frontiers' Conditions for Website Use and Copyright Statement, and the applicable CC-BY licence.

ISSN 1664-8714
ISBN 978-2-88976-253-8
DOI 10.3389/978-2-88976-253-8

About Frontiers

Frontiers is more than just an open-access publisher of scholarly articles: it is a pioneering approach to the world of academia, radically improving the way scholarly research is managed. The grand vision of Frontiers is a world where all people have an equal opportunity to seek, share and generate knowledge. Frontiers provides immediate and permanent online open access to all its publications, but this alone is not enough to realize our grand goals.

Frontiers Journal Series

The Frontiers Journal Series is a multi-tier and interdisciplinary set of open-access, online journals, promising a paradigm shift from the current review, selection and dissemination processes in academic publishing. All Frontiers journals are driven by researchers for researchers; therefore, they constitute a service to the scholarly community. At the same time, the Frontiers Journal Series operates on a revolutionary invention, the tiered publishing system, initially addressing specific communities of scholars, and gradually climbing up to broader public understanding, thus serving the interests of the lay society, too.

Dedication to Quality

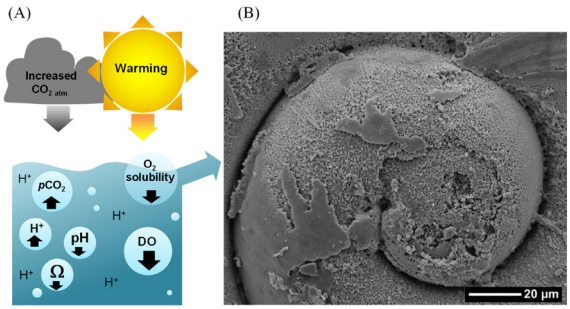
Each Frontiers article is a landmark of the highest quality, thanks to genuinely collaborative interactions between authors and review editors, who include some of the world's best academicians. Research must be certified by peers before entering a stream of knowledge that may eventually reach the public - and shape society; therefore, Frontiers only applies the most rigorous and unbiased reviews.
Frontiers revolutionizes research publishing by freely delivering the most outstanding research, evaluated with no bias from both the academic and social point of view. By applying the most advanced information technologies, Frontiers is catapulting scholarly publishing into a new generation.

What are Frontiers Research Topics?

Frontiers Research Topics are very popular trademarks of the Frontiers Journals Series: they are collections of at least ten articles, all centered on a particular subject. With their unique mix of varied contributions from Original Research to Review Articles, Frontiers Research Topics unify the most influential researchers, the latest key findings and historical advances in a hot research area! Find out more on how to host your own Frontiers Research Topic or contribute to one as an author by contacting the Frontiers Editorial Office: frontiersin.org/about/contact

ACIDIFICATION AND HYPOXIA IN MARGINAL SEAS

Topic Editors:
Xianghui Guo, Xiamen University, China
Hongjie Wang, University of Rhode Island, United States
Richard Alan Feely, Pacific Marine Environmental Laboratory, National Oceanic and Atmospheric Administration (NOAA), United States
Arnaud Laurent, Dalhousie University, Canada
Nina Bednarsek, National Institute of Biology (NIB), Slovenia



The image is modified based on Figure 1a of Lucey *et al*. (this Research Topic) and Figure 7b of Niemi *et al*. (this Research Topic). (A) Graphical depiction of atmospheric warming and increasing atmospheric carbon dioxide (CO_{2atm}), which drives ocean warming, contribute to the decreases in dissolved oxygen (DO), and lowers pH and saturation state index of calcium carbonate (Ω). The partial pressure of CO_2 (pCO_2) increases due to increasing atmospheric CO_2 that is absorbed into the seawater (i.e., ocean acidification), along with other biological processes in the marine environment. (B) Scanning Electron Microscope (SEM) image showing dissolution on pteropod shells collected in the Amundsen Gulf in the Canadian Arctic, in 2017.

Lucey N, Haskett E and Collin R (2020) Multi-stressor Extremes Found on a Tropical Coral Reef Impair Performance. *Front. Mar. Sci.* 7:588764. doi: 10.3389/fmars.2020.588764

Niemi A, Bednaršek N, Michel C, Feely RA, Williams W, Azetsu-Scott K, Walkusz W and Reist JD (2021) Biological Impact of Ocean Acidification in the Canadian Arctic: Widespread Severe Pteropod Shell Dissolution in Amundsen Gulf. *Front. Mar. Sci.* 8:600184. doi: 10.3389/fmars.2021.600184

Citation: Guo, X., Wang, H., Feely, R. A., Laurent, A., Bednarsek, N., eds. (2022). Acidification and Hypoxia in Marginal Seas. Lausanne: Frontiers Media SA. doi: 10.3389/978-2-88976-253-8

Table of Contents

07 ***Editorial: Acidification and Hypoxia in Marginal Seas***
Xianghui Guo, Nina Bednaršek, Hongjie Wang, Richard A. Feely and Arnaud Laurent

CHAPTER 1
OCEAN ACIDIFICATION AND DEOXYGENATION IN MARGINAL SEAS RIVER DOMINATED MARGINS

12 ***Comparing Subsurface Seasonal Deoxygenation and Acidification in the Yellow Sea and Northern East China Sea Along the North-to-South Latitude Gradient***
Tian-qi Xiong, Qin-sheng Wei, Wei-dong Zhai, Cheng-long Li, Song-yin Wang, Yi-xing Zhang, Shuo-jiang Liu and Si-qing Yu

33 ***Clarifying Water Column Respiration and Sedimentary Oxygen Respiration Under Oxygen Depletion Off the Changjiang Estuary and Adjacent East China Sea***
Jun Zhou, Zhuo-Yi Zhu, Huan-Ting Hu, Gui-Ling Zhang and Qian-Qian Wang

49 ***Intrusion of Kuroshio Helps to Diminish Coastal Hypoxia in the Coast of Northern South China Sea***
Hon-Kit Lui, Chen-Tung Arthur Chen, Wei-Ping Hou, Jian-Ming Liau, Wen-Chen Chou, You-Lin Wang, Chau-Ron Wu, Jay Lee, Yi-Chia Hsin and Yan-Yu Choi

62 ***Advances on Coastal and Estuarine Circulations Around the Changjiang Estuary in the Recent Decades (2000–2020)***
Zhiqiang Liu, Jianping Gan, Hui Wu, Jianyu Hu, Zhongya Cai and Yongfei Deng

81 ***Temporal and Spatial Variability of the CO_2 System in a Riverine Influenced Area of the Mediterranean Sea, the Northern Adriatic***
Lidia Urbini, Gianmarco Ingrosso, Tamara Djakovac, Salvatore Piacentino and Michele Giani

102 ***Effects of Wind-Driven Lateral Upwelling on Estuarine Carbonate Chemistry***
Ming Li, Renjian Li, Wei-Jun Cai, Jeremy M. Testa and Chunqi Shen

121 ***Inter-annual Variability of the Carbonate System in the Hypoxic Upper Pearl River Estuary in Winter***
Xianghui Guo, Xue Song, Ying Gao, Yaohua Luo, Yi Xu, Tao Huang and Lifang Wang

136 ***Seasonal Mixing and Biological Controls of the Carbonate System in a River-Dominated Continental Shelf Subject to Eutrophication and Hypoxia in the Northern Gulf of Mexico***
Wei-Jen Huang, Wei-Jun Cai and Xinping Hu

NON-RIVER DOMINATED MARGINS

155 ***Summertime Oxygen Depletion and Acidification in Bohai Sea, China***
Guisheng Song, Liang Zhao, Fei Chai, Fangfang Liu, Mengting Li and Huixiang Xie

166 ***Ocean Acidification State in the Highly Eutrophic Tokyo Bay, Japan: Controls on Seasonal and Interannual Variability***
Michiyo Yamamoto-Kawai, Soichiro Ito, Haruko Kurihara and Jota Kanda

179 ***Continuous Monitoring and Future Projection of Ocean Warming, Acidification, and Deoxygenation on the Subarctic Coast of Hokkaido, Japan***
Masahiko Fujii, Shintaro Takao, Takuto Yamaka, Tomoo Akamatsu, Yamato Fujita, Masahide Wakita, Akitomo Yamamoto and Tsuneo Ono

191 ***High-Resolution Carbonate System Dynamics of Netarts Bay, OR From 2014 to 2019***
William Fairchild and Burke Hales

207 ***The Mid-Atlantic Bight Dissolved Inorganic Carbon System Observed in the March 1996 DOE Ocean Margins Program (OMP)—A Baseline Study***
Ting-Hsuan Huang, Wei-Jun Cai, Penny Vlahos, Douglas W. R. Wallace, Ernie R. Lewis and Chen-Tung Arthur Chen

223 ***Ecosystem Metabolism Modulates the Dynamics of Hypoxia and Acidification Across Temperate Coastal Habitat Types***
Ryan B. Wallace, Bradley J. Peterson and Christopher J. Gobler

CHAPTER 2
OCEAN ACIDIFICATION AND HYPOXIA AT THE CHEMICAL-BIOLOGICAL INTERFACE

243 ***Early Diagenesis in the Hypoxic and Acidified Zone of the Northern Gulf of Mexico: Is Organic Matter Recycling in Sediments Disconnected From the Water Column?***
Christophe Rabouille, Bruno Lansard, Shannon M. Owings, Nancy N. Rabalais, Bruno Bombled, Edouard Metzger, Julien Richirt, Eryn M. Eitel, Anthony D. Boever, Jordon S. Beckler and Martial Taillefert

261 ***Massive Methane Loss During Seasonal Hypoxia/Anoxia in the Nearshore Waters of Southeastern Arabian Sea***
V. Sudheesh, G. V. M. Gupta and S. W. A. Naqvi

274 ***Massive Nitrogen Loss Over the Western Indian Continental Shelf During Seasonal Anoxia: Evidence From Isotope Pairing Technique***
Amit Sarkar, Syed Wajih Ahmad Naqvi, Gaute Lavik, Anil Pratihary, Hema Naik, Gayatri Shirodkar and Marcel M. M. Kuypers

288 ***Early Diagenesis in Sediments of the Venice Lagoon (Italy) and Its Relationship to Hypoxia***
Daniele Brigolin, Christophe Rabouille, Clément Demasy, Bruno Bombled, Gaël Monvoisin and Roberto Pastres

CHAPTER 3
IMPACTS OF OCEAN ACIDIFICATION AND HYPOXIA ON MARINE ORGANISMS AND ECOSYSTEMS

303 ***Interactive Effects of Elevated CO_2 Concentration and Light on the Picophytoplankton* Synechococcus**
Nanou Bao and Kunshan Gao

310 ***Response of Phytoplankton Assemblages From Naturally Acidic Coastal Ecosystems to Elevated* pCO_2**
Natalia Osma, Laura Latorre-Melín, Bárbara Jacob, Paulina Y. Contreras, Peter von Dassow and Cristian A. Vargas

331 ***Elevated* pCO_2 *Impedes Succession of Phytoplankton Community From Diatoms to Dinoflagellates Along With Increased Abundance of Viruses and Bacteria***
Ruiping Huang, Jiazhen Sun, Yunlan Yang, Xiaowen Jiang, Zhen Wang, Xue Song, Tifeng Wang, Di Zhang, He Li, Xiangqi Yi, Shouchang Chen, Nanou Bao, Liming Qu, Rui Zhang, Nianzhi Jiao, Yahui Gao, Bangqin Huang, Xin Lin, Guang Gao and Kunshan Gao

345 ***The Combined Effects of Increased* pCO_2 *and Warming on a Coastal Phytoplankton Assemblage: From Species Composition to Sinking Rate***
Yuanyuan Feng, Fei Chai, Mark L. Wells, Yan Liao, Pengfei Li, Ting Cai, Ting Zhao, Feixue Fu and David A. Hutchins

360 ***Multi-stressor Extremes Found on a Tropical Coral Reef Impair Performance***
Noelle Lucey, Eileen Haskett and Rachel Collin

374 ***Marine Heatwaves, Sewage and Eutrophication Combine to Trigger Deoxygenation and Biodiversity Loss: A SW Atlantic Case Study***
Kalina M. Brauko, Alex Cabral, Natasha V. Costa, Juliana Hayden, Carlos E. P. Dias, Edilene S. Leite, Renan D. Westphal, Carolina M. Mueller, Jason M. Hall-Spencer, Regina R. Rodrigues, Leonardo R. Rörig, Paulo R. Pagliosa, Alessandra L. Fonseca, Orestes E. Alarcon and Paulo A. Horta

385 ***Ocean Acidification Amplifies Multi-Stressor Impacts on Global Marine Invertebrate Fisheries***
Travis C. Tai, U. Rashid Sumaila and William W. L. Cheung

397 ***Synthesis of Thresholds of Ocean Acidification Impacts on Echinoderms***
Nina Bednaršek, Piero Calosi, Richard A. Feely, Richard Ambrose, Maria Byrne, Kit Yu Karen Chan, Sam Dupont, Jacqueline L. Padilla-Gamiño, John I. Spicer, Faycal Kessouri, Miranda Roethler, Martha Sutula and Stephen B. Weisberg

412 ***Molecular Biomarkers of the Mitochondrial Quality Control are Differently Affected by Hypoxia-Reoxygenation Stress in Marine Bivalves* Crassostrea gigas *and* Mytilus edulis**
Jennifer B. M. Steffen, Halina I. Falfushynska, Helen Piontkivska and Inna M. Sokolova

431 ***Biological Impact of Ocean Acidification in the Canadian Arctic: Widespread Severe Pteropod Shell Dissolution in Amundsen Gulf***
Andrea Niemi, Nina Bednaršek, Christine Michel, Richard A. Feely, William Williams, Kumiko Azetsu-Scott, Wojciech Walkusz and James D. Reist

447 ***Comparative Sensitivities of Zooplankton to Ocean Acidification Conditions in Experimental and Natural Settings***
Katherine E. Keil, Terrie Klinger, Julie E. Keister and Anna K. McLaskey

455 ***Integrated Assessment of Ocean Acidification Risks to Pteropods in the Northern High Latitudes: Regional Comparison of Exposure, Sensitivity and Adaptive Capacity***
Nina Bednaršek, Kerry-Ann Naish, Richard A. Feely, Claudine Hauri, Katsunori Kimoto, Albert J. Hermann, Christine Michel, Andrea Niemi and Darren Pilcher

478 ***Distribution and Activity of Ammonia-Oxidizers on the Size-Fractionated Particles in the Pearl River Estuary***
Li Ma, Shangjin Tan, Hongbin Liu, Shuh-Ji Kao, Minhan Dai and Jin-Yu Terence Yang

CHAPTER 4
LONG-TERM VARIABILITY IN OCEAN ACIDIFICATION AND HYPOXIA IN MARGINAL SEAS

489 ***Deoxygenation in Marginal Seas of the Indian Ocean***
S. Wajih A. Naqvi

505 ***Decadal Dynamics of the CO_2 System and Associated Ocean Acidification in Coastal Ecosystems of the North East Atlantic Ocean***
Jean-Philippe Gac, Pierre Marrec, Thierry Cariou, Emilie Grosstefan, Éric Macé, Peggy Rimmelin-Maury, Marc Vernet and Yann Bozec

531 ***Climate and Human-Driven Variability of Summer Hypoxia on a Large River-Dominated Shelf as Revealed by a Hypoxia Index***
Kui Wang, Wei-Jun Cai, Jianfang Chen, David Kirchman, Bin Wang, Wei Fan and Daji Huang

frontiers in Marine Science

EDITORIAL
published: 31 March 2022
doi: 10.3389/fmars.2022.861850

Editorial: Acidification and Hypoxia in Marginal Seas

Xianghui Guo[1]*, *Nina Bednaršek*[2], *Hongjie Wang*[3], *Richard A. Feely*[4] and *Arnaud Laurent*[5]

[1] State Key Laboratory of Marine Environmental Science, College of Ocean and Earth Sciences, Xiamen University, Xiamen, China, [2] National Institute of Biology, Marine Biology Station Piran, Piran, Slovenia, [3] Graduate School of Oceanography, University of Rhode Island, Narragansett, RI, United States, [4] National Oceanic and Atmospheric Administration (NOAA) Pacific Marine Environmental Laboratory, Seattle, WA, United States, [5] Department of Oceanography, Dalhousie University, Halifax, NS, Canada

Keywords: ocean acidification, hypoxia, marginal seas, biological impacts, long-term variation

Editorial on the Research Topic

Acidification and Hypoxia in Marginal Seas

ACIDIFICATION AND DEOXYGENATION IN MARGINAL SEAS

Ocean acidification and hypoxia (dissolved oxygen <2 mg L^{-1} or $<62\,\mu$mol L^{-1}) are universal environmental concerns that can impact ecological and biogeochemical processes, including element cycling, carbon sequestration, community shifts, contributing to biodiversity reduction, and reducing marine ecosystem services (Riebesell et al., 2000; Feely et al., 2004, 2009; Andersson et al., 2005; Doney, 2006; Cohen and Holcomb, 2009; Doney et al., 2009, 2020; Kleypas and Yates, 2009; Ekstrom et al., 2015; Gattuso et al., 2015). While the stressors are global in their occurrence, local and regional impacts might be enhanced and even more accelerated, thus requiring even greater and faster consideration (Doney et al., 2020).

The driving mechanisms of acidification and hypoxia are inextricably linked in near-shore and coastal habitats. Along coastal shelf and its adjacent marginal seas, where the natural variability of multiple stressors is high, human-induced eutrophication is additionally enhancing both local acidification and hypoxia. For example, the well-known eutrophication of surface waters in the northern Gulf of Mexico caused hypoxic conditions that result in a pH decrease by 0.34 in the oxygen-depleted bottom water, which is significantly more than the pH decrease via atmospheric CO_2 sequestration alone (pH decrease by 0.11; Cai et al., 2011). Similar changes in coastal conditions involving biological respiration and atmospheric CO_2 invasion have also been observed in other marginal seas, urbanized estuaries, salt marshes and mangroves (Feely et al., 2008, 2010, 2018; Cai et al., 2011; Howarth et al., 2011). Other natural and anthropogenic processes, such as increased wind intensity and coastal upwelling, enhanced stratification due to global warming, along with more intense benthic respiration, more frequent extreme events, oscillation of water circulations, and variations in the terrestrial carbon and/or alkalinity fluxes, etc., all influence the onset and maintenance of acidification and/or hypoxia. For example, coastal upwelling brings both low pH and hypoxic water from below and enhances acidification and hypoxia in the coastal regions (Feely et al., 2008). Although acidification and hypoxia in the open oceans have received considerable attention already, the advances in our understanding of the driving mechanisms and the temporal evolution under global climate change is still poorly understood, particularly with respect to the region-specific differences, various scales of temporal and spatial variability, predictability patterns, and interactive multiple stressor impacts. Therefore, coastal ecosystems have a much broader range of rates of change in pH than the open ocean does (Carstensen and Duarte, 2019). The importance of understanding acidification and hypoxia for the biogeochemical and ecosystem implications in marginal seas is essential for climate change mitigation and adaptation strategy implementations in the future.

OPEN ACCESS

Edited and reviewed by:
Marta Marcos, University of the Balearic Islands, Spain

***Correspondence:**
Xianghui Guo
xhguo@xmu.edu.cn

Specialty section:
This article was submitted to Coastal Ocean Processes, a section of the journal Frontiers in Marine Science

Received: *25 January 2022*
Accepted: *25 February 2022*
Published: *31 March 2022*

Citation:
Guo X, Bednaršek N, Wang H, Feely RA and Laurent A (2022) Editorial: Acidification and Hypoxia in Marginal Seas. Front. Mar. Sci. 9:861850. doi: 10.3389/fmars.2022.861850

The scope of this Research Topic is to cover the most recent advances related to the status of acidification and hypoxia in marginal seas, the coupling mechanisms of multi-drivers and human impacts, ecosystem responses, prediction of their evolution over space and time, and under future climate change scenarios. The authors of this Research Topic contributed a total of 35 papers covering a wide variety of subjects spanning from acidification and/or hypoxia (OAH) status, the carbonate chemistry baseline and trends, the impacts of OAH on the habitat suitability and ecosystem implications, and the long-term changes and variability of OAH in marginal seas.

Across many different temporal and spatial scales, the contributed papers highlighted the presence of acidification and hypoxia with their major controls in the marginal seas of the North Pacific, including the subpolar Bering Sea, the temperate China Seas of Bohai Sea, Yellow Sea and the East China Sea, Japanese coasts (Tokyo Bay and the coast of Hokkaido); the Atlantic, including the northern Gulf of Mexico, the Chesapeake Bay, and the Mediterranean Sea; the Arctic, including the Amundsen Gulf; the Indian Ocean, including the Arabian Sea, the Red Sea, etc.

In the large river dominated East China Sea shelf, hypoxia occurs in bottom waters in summer (Li et al., 2002; Zhu et al., 2017). Circulation plays an important role in the biogeochemical processes including redistribution of nutrients, changes in stratification, water residence time and ventilation of the shelf water (Liu et al.). Furthermore, the impact of typhoons results in hypoxia demise with immediate extensive vertical mixing. However, the excess freshwater and nutrient loading during the typhoon period would boost the hypoxia restoration later on when the shelf waters are re-stratified (Liu et al.). With respect to coastal oxygen consumption, water, and sediment interactions contribute dynamically, and water-column respiration processes contribute to as much as 24–69% of total oxygen consumption beneath the pycnocline (Zhou et al.). Deconvolving the water column vs. sedimentary oxygen respiration in the oxygen depletion off the Changjiang estuary and East China Sea is an important advancement of our understanding of oxygen sinks.

From the perspective of a comparison between the northern East China Sea and the adjacent southern Yellow Sea, higher CO_2 solubility together with the biogeochemical CO_2 additions caused the colder Yellow Sea water generally to have lower aragonite saturation state index (Ω_{Ar}) than the warmer northern East China Sea water (Xiong et al.). Although marine organic matter is the major source of the oxygen-consuming carbon in the large river-dominated margins (Green et al., 2006; Wang et al., 2016), the maximum of hypoxia may come at a significant lag from the time of peak productivity. For example, bottom water hypoxia and acidification has a 2-month delay when compared with the maximum primary production in surface waters of the northern Gulf of Mexico (Huang W-J. et al.).

In addition to biogeochemical processes, upwelling also plays an important role in the status and distribution of hypoxia/acidification occurrence, such as in the well-known upwelling region off the California coast (Feely et al., 2008, 2016). The Chesapeake Bay is also impacted by upwelling-induced acidification, which will intensify with the wind-driven upwelling to cause low pH and "corrosive" water in the shallow shoals of the estuaries, enhancing large temporal pH and Ω_{Ar} seasonal fluctuations (Li et al.). Furthermore, non-local mechanisms may also be important in regulating the occurrence of hypoxia. For example, the Kuroshio intrusion into the northern South China Sea relieves the occurrence of hypoxia in the coastal zone (Lui et al.).

In the coastal seas without large river influence, OAH also occurs as a consequence of seasonal productivity and large-scale circulation processes. Along the Hokkaido coast, the highly euphotic Tokyo Bay, the Netarts Bay off Oregon, and the coastal habitat types on eastern Long Island, time series observations show the progression of seasonal OA and deoxygenation, often resulting in hypoxic conditions. In addition, high frequency pH and dissolved oxygen (DO) observations across sub-diel, diel and seasonal time scales across various habitat types (salt marsh, macroalgae, seagrass, open water) in the northeast US show the impact of ecosystem metabolism to modulate OAH (Wallace et al.). Comprehensive analysis of coastal observations suggests that pH and Ω_{Ar} decreased by 0.2-0.6 and 1–2, respectively, via circulation and biogeochemical processes, where Ω_{Ar} decreases can occur in the summer bottom waters and will be a common phenomenon in the near future in the eutrophic Tokyo Bay (Yamamoto-Kawai et al.). Fujii et al. and Fairchild and Hales separately showed that along the Hokkaido coast and in Netarts Bay along the Oregon coast, Ω_{Ar} sometimes decreases to values below the threshold for significant negative impacts on some calcifiers (e.g., 1.1–1.5 for bivalve larvae, 1–1.5 for pteropods, and pH values of 7.6-7.8 for echinoderms and decapods; Bednaršek, Ambrose et al.; Bednaršek, Calosi, et al.; Bednaršek, Naish, et al.; Bednaršek et al., 2019). Continued oceanic uptake of carbon dioxide will continue to decrease pH and Ω_{Ar}, with high-latitude surface waters expected to be fully undersaturated by the end of this century because of the natural low buffer capacity there (Feely et al., 2009; Steinacher et al., 2009).

Crossing these pH thresholds consistently occurs in salt marsh and seagrass habitats along with hypoxic conditions (Wallace et al.). Under the IPCC global warming and acidification scenarios, Ω_{Ar} in some coastal environments will drop below these thresholds by 2090, indicating that critical thresholds may be crossed more frequently in the future and severely damage calcifiers and impact overall fisheries production (Tai et al.).

OCEAN ACIDIFICATION AND HYPOXIA AT THE CHEMICAL-BIOLOGICAL INTERFACE

Under continuously decreasing pH and low dissolved oxygen conditions, there is a general concern that the local bottom waters and the underlying sediments could switch from hypoxic to anoxic conditions. For example, in the hypoxic northern Gulf of Mexico, low DO conditions in sediment did not promote anoxic diagenesis as anticipated, possibly linked to the reduction of bioturbation during the hypoxic spring and summer months (Rabouille et al.). In the hypoxic area of the Eastern Arabian Sea, strong denitrification results in large nitrogen loss, accounting for as much as 20–60% of the total annual fixed nitrogen loss in oxygen minimum zone of the Arabian Sea (Sarkar et al.). Methane emissions in coastal regions can also be very large,

accounting for as much as 15% of the methane emission from the Arabian Sea (Sudheesh et al.). Moreover, sediment diagenesis plays a critical role in triggering and maintaining hypoxia of lagoon waters, and it may be enhanced by changes in regional climate conditions, such as the increase in frequency of summer heat waves (Brigolin et al.).

IMPACTS OF OCEAN ACIDIFICATION AND HYPOXIA ON MARINE ORGANISMS AND ECOSYSTEMS

OA and hypoxia are significant stressors for marine species, communities, ecosystems, especially when they act interactively and cumulatively. Studies show that harmful effects of OA on the marine calcifiers have already been observed. In the Arctic and subpolar Beaufort Sea, Bering Sea, and the Amundsen Gulf, corrosive water for aragonite induced extensive shell dissolution in ecologically important zooplankton, i.e., pteropods (Niemi et al.). Conducting a more comprehensive OA risk assessment, Bednaršek, Naish, et al. elucidated high exposure OA risk in combination with high sensitivity and low adaptive capacity for pteropods in the polar habitats of the Northern Hemisphere.

Thresholds are very useful tools to determine when the OA exposure can start causing negative physiological and organismal impairments. With the echinoderms and decapods being one of the most dominant as well as ecologically and economically important species, the application of the thresholds for these two groups can have important regional and global implications (Bednaršek, Ambrose, et al.; Bednaršek, Calosi, et al.). These thresholds provide the foundation for consistent interpretation of OA monitoring data or numerical ocean model simulations to support climate change marine vulnerability assessments and evaluation of ocean management strategies.

On longer time scales, model results indicate that OA amplifies multi-stressor impacts on global marine invertebrate fisheries, with the fish catch potential to decrease by 12%, with 3.4% being attributed to OA by the end of this century (Tai et al.). A comprehensive understanding of OA effects based on the thresholds and predictive sensitives allows for improved predictions of ecosystem change relevant to effective fisheries resource management, as well as providing a more robust foundation for ecosystem health monitoring of the negative OA impacts in the most sensitive OAH habitats. While OA can also significantly affect the range of responses in different zooplankton taxa, the study by Keil et al. found little association between empirical measures of *in situ* pH and the abundance of sensitive taxa as revealed by meta-analysis. The authors concluded that the mismatch between experimental studies and field observations should have some important ramifications for the design of long-term monitoring programs and interpretation and use of the data produced.

On the community level, the results of mesocosms-based experiments across various marginal seas, from the coastal East China Sea, Bohai Sea, coastal upwelling and riverine ecosystems in Chile, all agree that increasing partial pressure of CO_2 (pCO_2) can modulate plankton structure, composition and abundance, leading to altered biogeochemical cycles of carbon and nutrients, and carbon fluxes. Elevated pCO_2 mesocosm experiments in the East China Sea boosted biomass of diatoms, while impeding the succession of diatoms to dinoflagellates, and corresponds with increased abundance of virus and bacteria (Huang R. et al.). Such results appear to be region specific, because a different community response was demonstrated in the Bohai Sea, where high pCO_2 resulted in the decreased total diatom abundance, favoring the ratio of central to pennate diatoms. In addition, combined warming and OA significantly decreased the proportion of diatoms to dinoflagellates and caused the shifts in phytoplankton composition due to interactive and cumulative effect, ultimately resulting in carbon flux and sinking rate changes (Feng et al.). Another study in the coastal area off Chile, characterized by high natural variability, showed no response to high pCO_2 treatments; instead the changes during the incubations were related to other factors, such as competition and growth phase (Osma et al.). The study suggests that the pre-exposure to variable coastal gradients that structure local adaptation patterns could play an important role in determining responses of coastal phytoplankton communities to increased impact of OA. In the experiments combining various OA and light treatments conducted on 15 laboratory experimental generations of picophytoplankton, Bao and Gao showed that *Synechococcus* grew faster under the OA treatment with inhibiting light level only, suggesting differential picophytoplankton responses that are light dependent under various depth conditions.

Hypoxia is another stressor present mostly in the tropical and temperate marine ecosystems. In a tropical Caribbean reef, hypoxia had largest negative impact on the performance of a key reef herbivore. The interactive temperature and DO extremes with low pH led to impaired performance of the reef echinoderms (Lucey et al.).

The studies investigating the impact of carbonate chemistry variability in coastal regions demonstrate the importance on both biological and biogeochemical responses. Coastal and estuarine habitats are characterized by distinct temporal fluctuations in carbonate chemistry, ranging from sub-diel to diel to seasonal, which are expected to increase under projected scenarios even in the highly buffered systems (Urbini et al.). Extreme variability in hypoxia/reoxygenation seem to change the expression of the mitochondrial quality control pathways only of the species with high DO sensitivity, such as Pacific oysters *Crassostrea gigas*, but not blue mussels *Mytilus edulis*, elucidating the mechanisms of mitochondrial protection against hypoxia-reoxygenation-induced damage that might contribute to hypoxia tolerance in marine bivalves (Steffen et al.). In addition to eutrophication, marine heatwave might also contribute to triggering deoxygenation and biodiversity loss in the marginal seas. In a southwestern Atlantic coast, marine heatwaves, sewage and eutrophication combined to trigger deoxygenation and biodiversity loss (Brauko et al.).

LONG-TERM VARIABILITY IN OCEAN ACIDIFICATION AND HYPOXIA IN MARGINAL SEAS

In the marginal seas of the Indian Ocean (Persian Gulf, Red Sea and Andaman Sea), deoxygenation has been observed numerous

times over the last few decades (Naqvi). Hypoxia in the East China Sea has become more severe since the 1960s mainly due to eutrophication, stronger stratification, and longer water residence times (Wang et al.). ENSO and global warming may also have indirect effects by regulating river discharge, stratification, and water residence time, etc. (Wang et al.). In the southwestern English Channel within the Northeastern Atlantic Ocean, time-series observations show that average pCO_2 increases at rate of 2.95–3.52 μatm yr^{-1}, with a corresponding decrease in mean pH of 0.0028 yr^{-1} (Gac et al.), an acidification rate faster than the open ocean (∼1.5 μatm yr^{-1} for pCO_2 and $-0.0016 \sim -0.0017$ yr^{-1} for pH; Bates et al., 2014), and consistent with some other marginal seas, including the Mediterranean (Hassoun et al., 2015). Both atmospheric CO_2 absorption and climatic indices (i.e., North Atlantic Oscillation and Atlantic Multidecadal Variability) are responsible for this fast OA rate in the northern East Atlantic Ocean (Gac et al.).

CONCLUSIONS AND PERSPECTIVES

OA and hypoxia often occur more severely in the marginal seas than in the open ocean globally, making the marginal seas species and ecosystems more vulnerable to future climate change related changes. Ω_{Ar} and pH conditions in some marginal seas are already below the thresholds that can induce negative biological responses for many marine calcifiers, especially in the rapidly changing polar/subpolar marginal seas or in coastal upwelling regions. In temperate marginal seas, subsurface water can be corrosive, which may be having an impact on fisheries and the ecosystem services they provide. For large river-dominated margins, there might be significant time lags of the bottom water hypoxia/acidification after the peak of the primary production. For coastal ecosystems in the margin systems characterized by the OA/hypoxia, we can expect differential effects and evolution across regional habitats, depending on the baseline and the physical and biogeochemical dynamics of local conditions. Understanding of such spatial and temporal variability is thus essential to start recognizing more sensitive habitats and conduct appropriate monitoring or management practices to protect and preserve ecologically and economically important ecosystems.

Marginal seas are productive areas essential for the human wellbeing and economic dependence, but insufficient awareness of biological and ecosystem responses and potential management strategies might be detrimental, especially in the developing countries. Although this Research Topic contributed to advance understanding of the chemical changes, the interpretation of biological responses in the marginal seas is still in need of more research. Such responses are complex, thus requiring a tight integration with the chemical and biogeochemical multi-scale parameters that can induce stress, community reorganization and shifts, biological interactions and others impacts.

An immediate need for enhanced understanding of multiple stressor effects as well as the effects of increased variability and unpredictability in the marginal seas systems is critical for developing better management strategies. While a single study indicates that multiple stressor extremes in the tropics lead to the physiological impairments, systematic studies are needed to reveal multiple stressor impacts on the marginal seas marine ecosystems. Equally, the projections of future conditions in dynamic coastal systems show enhanced variability and extreme values related to OA, which can be habitat specific and thus extremely variable, yet biological and biogeochemical implications of these impacts are largely unknown. In particular, a better understanding of increased amplitude variability and prolonged duration below thresholds for organisms and ecosystems is needed for the coastal-estuarine habitat. Various temporal scales of variability (from sub-diel to diel to seasonal) needs to be further examined to understand where and when the biological bottlenecks will first occur. The comparison of sensitivity and resilience of various marginal seas systems should be examined through the natural variability baseline to understand the extent of species plasticity and adaptation. Moreover, attention needs to be given to the temporal variation (autocorrelation and cross-correlations) that represents the framework of the "predictability" in the habitats (Bernhardt et al., 2020), which can also significantly structure biological responses. Extensive theoretical and empirical work shows that the predictability might in fact be a primary driver determining the biological responses compared to the variability, thus both, predictability and variability require more attention to assess their impact and trade-offs in the marginal seas.

The integrated results of this Research Topic carry important implications for variety of ecosystems and ecosystem services, including aquaculture practices, fisheries management, human wellbeing carbon sequestration, etc. Given enormous potential of ecosystems services in the marginal seas systems, much more comprehensive approaches are needed to assess the impacts and economic evaluation of their losses. The approach needs to be based on the integration of the chemical, biological and biogeochemical data, allowing to monitor changes over time, and developing management approaches to preserve the health and the biodiversity within the marginal seas in the face of the global climate change, including habitat restoration, protection of biogenic habitats, removal of anthropogenic nutrients, potential development of OAH habitat refugia, marine spatial planning, fishing practices and capacity of adaptation and resilience of the changing socio-ecological system. Special attention needs to be given to the "blue carbon" ecosystems given their role related to sequestering carbon and potentially slowing down the long-term changes at the local level while also exacerbating short-term variability. To this end, a spatially targeted evaluation related to different causes of OAH involving comprehensive interactions with local stakeholders is needed maximize the utility of smaller-scale policy recommendations.

AUTHOR CONTRIBUTIONS

All authors listed have made a substantial, direct, and intellectual contribution to the work and approved it for publication.

FUNDING

This Research Topic was supported by the National Natural Science Foundation of China (41876080), the Strategic Priority Research Program of the Chinese Academy of Sciences (XDB42000000), and the NOAA Ocean Acidification Program. This is contribution number 5332 from the NOAA Pacific Marine Environmental Laboratory. NB was supported by the Slovene Research Agency (J12468).

ACKNOWLEDGMENTS

We thank the Frontiers in Marine Sciences editorial staff for their professional support. The peer-review team are appreciated for their insightful comments and suggestions.

REFERENCES

Andersson, A. J., Mackenzie, F. T., and Lerman, A. (2005). Coastal ocean and carbonate systems in the high CO_2 world of the anthropocene. *Am. J. Sci.* 305, 875–918. doi: 10.2475/ajs.305.9.875

Bates, N. R., Astor, Y. M., Church, M. J., Currie, K., Dore, J. E., Gonzalez-Davila, M., et al. (2014). A time-series view of changing surface ocean chemistry due to ocean uptake of anthropogenic CO_2 and ocean acidification. *Oceanography* 27, 126–141. doi: 10.5670/oceanog.2014.16

Bednaršek, N., Feely, R. A., Howes, E. L., Hunt, B. P. V., Kessouri, F., Leon, P., et al. (2019). Systematic review and meta-analysis toward synthesis of thresholds of ocean acidification impacts on calcifying pteropods and interactions with warming. *Front. Mar. Sci.* 6, 227. doi: 10.3389/fmars.2019.00227

Bernhardt, J. R., O'Connor, M. I., Sunday, J. M., and Gonzalez, A. (2020). Life in fluctuating environments. *Philos. Trans. R. Sock. B Biol. Sci.* 375, 20190454. doi: 10.1098/rstb.2019.0454

Cai, W.-J., Hu, X., Huang, W.-J., Murrell, M. C., Lehrter, J. C., Lohrenz, S. E., et al. (2011). Acidification of subsurface coastal waters enhanced by eutrophication. *Nat. Geosci.* 4, 766–770. doi: 10.1038/ngeo1297

Carstensen, J., and Duarte, C. M. (2019). Drivers of pH variability in coastal ecosystems. *Environ. Sci. Technol.* 53, 4020–4029. doi: 10.1021/acs.est.8b03655

Cohen, A. L., and Holcomb, M. (2009). Why corals care about ocean acidification: Uncovering the mechanism. *Oceanography* 22, 118–127. doi: 10.5670/oceanog.2009.102

Doney, S. C. (2006). The dangers of ocean acidification. *Sci. Am.* 294, 58–65. doi: 10.1038/scientificamerican0306-58

Doney, S. C., Busch, D. S., Cooley, S. R., and Kroeker, K. J. (2020). The impacts of ocean acidification on marine ecosystems and reliant human communities. *Annu. Rev. Environ. Resour.* 45, 83–112. doi: 10.1146/annurev-environ-012320-083019

Doney, S. C., Fabry, V. J., Feely, R. A., and Kleypas, J. A. (2009). Ocean acidification: The other CO_2 problem. *Ann. Rev. Mar. Sci.* 1, 169–192. doi: 10.1146/annurev.marine.010908.163834

Ekstrom, J. A., Suatoni, L., Cooley, S. R., Pendleton, L. H., Waldbusser, G. G., Cinner, J. E., et al. (2015). Vulnerability and adaptation of US shellfisheries to ocean acidification. *Nat. Clim. Chang.* 5, 207–214. doi: 10.1038/nclimate2508

Feely, R. A., Alin, S. R., Carter, B., Bednaršek, N., Hales, B., Chan, F., et al. (2016). Chemical and biological impacts of ocean acidification along the west coast of North America. *Estuar. Coast. Shelf Sci.* 183, 260–270. doi: 10.1016/j.ecss.2016.08.043

Feely, R. A., Alin, S. R., Newton, J., Sabine, C. L., Warner, M., Devol, A., et al. (2010). The combined effects of ocean acidification, mixing, and respiration on pH and carbonate saturation in an urbanized estuary. *Estuar. Coast. Shelf Sci.* 88, 442–449. doi: 10.1016/j.ecss.2010.05.004

Feely, R. A., Doney, S. C., and Cooley, S. R. (2009). Ocean acidification: Present conditions and future changes in a high-CO_2 world. *Oceanography* 22, 36–47. doi: 10.5670/oceanog.2009.95

Feely, R. A., Okazaki, R. R., Cai, W.-J., Bednaršek, N., Alin, S. R., Byrne, R. H., et al. (2018). The combined effects of acidification and hypoxia on pH and aragonite saturation in the coastal waters of the California current ecosystem and the northern Gulf of Mexico. *Cont. Shelf Res.* 152, 50–60. doi: 10.1016/j.csr.2017.11.002

Feely, R. A., Sabine, C. L., Hernandez-Ayon, J. M., Ianson, D., and Hales, B. (2008). Evidence for upwelling of corrosive "acidified" water onto the continental shelf. *Science* 320, 1490–1492. doi: 10.1126/science.1155676

Feely, R. A., Sabine, C. L., Lee, K., Berelson, W., Kleypas, J., Fabry, V. J., et al. (2004). Impact of anthropogenic CO_2 on the $CaCO_3$ system in the oceans. *Science* 305, 362–366. doi: 10.1126/science.1097329

Gattuso, J. P., Magnan, A., Bille, R., Cheung, W. W. L., Howes, E. L., Joos, F., et al. (2015). Contrasting futures for ocean and society from different anthropogenic CO_2 emissions scenarios. *Science* 349, aac4722. doi: 10.1126/science.aac4722

Green, R. E., Bianchi, T. S., Dagg, M. J., Walker, N. D., and Breed, G. A. (2006). An organic carbon budget for the Mississippi River turbidity plume and plume contributions to air-sea CO_2 fluxes and bottom water hypoxia. *Estuar. Coasts* 29, 579–597. doi: 10.1007/BF02784284

Hassoun, A. E. R., Gemayel, E., Krasakopoulou, E., Goyet, C., M., Saab, A.-A., et al. (2015). Acidification of the Mediterranean Sea from anthropogenic carbon penetration. *Deep Sea Res. Part I Oceanogr. Res. Pap.* 102, 1–15. doi: 10.1016/j.dsr.2015.04.005

Howarth, R., Chan, F., Conley, D. J., Garnier, J., Doney, S. C., Marino, R., et al. (2011). Coupled biogeochemical cycles: Eutrophication and hypoxia in temperate estuaries and coastal marine ecosystems. *Front. Ecol. Environ.* 9, 18–26. doi: 10.1890/100008

Kleypas, J. A., and Yates, K. K. (2009). Coral reefs and ocean acidification. *Oceanography* 22, 108–117. doi: 10.5670/oceanog.2009.101

Li, D. J., Zhang, J., Huang, D. J., Wu, Y., and Liang, J. (2002). Oxygen depletion off the Changjiang (Yangtze River) estuary. *Sci. China Ser. D Earth Sci.* 45, 1137–1146. doi: 10.1360/02yd9110

Riebesell, U., Zondervan, I., Rost, B., Tortell, P. D., Zeebe, R. E., and Morel, F. M. M. (2000). Reduced calcification of marine plankton in response to increased atmospheric CO_2. *Nature* 407, 364–367. doi: 10.1038/35030078

Steinacher, M., Joos, F., Froelicher, T. L., Plattner, G. K., and Doney, S. C. (2009). Imminent ocean acidification in the Arctic projected with the NCAR global coupled carbon cycle-climate model. *Biogeosciences* 6, 515–533. doi: 10.5194/bg-6-515-2009

Wang, H., Dai, M., Liu, J., Kao, S.-J., Zhang, C., Cai, W.-J., et al. (2016). Eutrophication-driven hypoxia in the East China Sea off the Changjiang estuary. *Environ. Sci. Technol.* 50, 2255–2263. doi: 10.1021/acs.est.5b06211

Zhu, Z.-Y., Wu, H., Liu, S.-M., Wu, Y., Huang, D.-J., Zhang, J., et al. (2017). Hypoxia off the Changjiang (Yangtze River) estuary and in the adjacent East China Sea: quantitative approaches to estimating the tidal impact and nutrient regeneration. *Mar. Pollut. Bull.* 125, 103–114. doi: 10.1016/j.marpolbul.2017.07.029

Conflict of Interest: The authors declare that the research was conducted in the absence of any commercial or financial relationships that could be construed as a potential conflict of interest.

Publisher's Note: All claims expressed in this article are solely those of the authors and do not necessarily represent those of their affiliated organizations, or those of the publisher, the editors and the reviewers. Any product that may be evaluated in this article, or claim that may be made by its manufacturer, is not guaranteed or endorsed by the publisher.

Copyright © 2022 Guo, Bednaršek, Wang, Feely and Laurent. This is an open-access article distributed under the terms of the Creative Commons Attribution License (CC BY). The use, distribution or reproduction in other forums is permitted, provided the original author(s) and the copyright owner(s) are credited and that the original publication in this journal is cited, in accordance with accepted academic practice. No use, distribution or reproduction is permitted which does not comply with these terms.

frontiers in Marine Science

ORIGINAL RESEARCH
published: 18 August 2020
doi: 10.3389/fmars.2020.00686

Comparing Subsurface Seasonal Deoxygenation and Acidification in the Yellow Sea and Northern East China Sea Along the North-to-South Latitude Gradient

Tian-qi Xiong[1], Qin-sheng Wei[2,3], Wei-dong Zhai[1], Cheng-long Li[1], Song-yin Wang[1], Yi-xing Zhang[1], Shuo-jiang Liu[1] and Si-qing Yu[1]*

[1] Institute of Marine Science and Technology, Shandong University, Qingdao, China, [2] First Institute of Oceanography, Ministry of Natural Resources, Qingdao, China, [3] Laboratory for Marine Ecology and Environmental Science, Qingdao National Laboratory for Marine Science and Technology, Qingdao, China

OPEN ACCESS

Edited by:
Nina Bednarsek, Southern California Coastal Water Research Project, United States

Reviewed by:
Stephen F. Gonski, University of Delaware, United States
Wen-Chen Chou, National Taiwan Ocean University, Taiwan
Jianzhong Su, Xiamen University, China

***Correspondence:**
Wei-dong Zhai
wdzhai@126.com

Specialty section:
This article was submitted to Coastal Ocean Processes, a section of the journal Frontiers in Marine Science

Received: *28 May 2020*
Accepted: *28 July 2020*
Published: *18 August 2020*

Citation:
Xiong T, Wei Q, Zhai W, Li C, Wang S, Zhang Y, Liu S and Yu S (2020) Comparing Subsurface Seasonal Deoxygenation and Acidification in the Yellow Sea and Northern East China Sea Along the North-to-South Latitude Gradient. Front. Mar. Sci. 7:686. doi: 10.3389/fmars.2020.00686

To better understand the relationship between subsurface seasonal deoxygenation and acidification in the Yellow Sea and northern East China Sea (ECS), we examined carbonate system parameters and dissolved oxygen (DO) of seven field surveys conducted in 2017–2018, spanning all four seasons. Low pH_T values of 7.71–7.80 and critically low aragonite saturation state (Ω_{arag}) values of 1.07–1.40 along with undersaturated DO of mostly higher than 150 μmol O_2 kg^{-1} occurred in the Yellow Sea Cold Water Mass area in summer and autumn, while hypoxic DO values of 49–63 μmol O_2 kg^{-1} and extremely low pH_T values of 7.68–7.74 as well as critically low Ω_{arag} values of 1.21–1.39 were observed in the northern ECS in July 2018. At the beginning of warm-season stratification formation, the cold Yellow Sea waters had much higher DO but lower Ω_{arag} values than those in relatively warmer ECS waters, while yearly initial pH_T values rarely exhibited differences between the two coastal seas. During warm seasons, the central Yellow Sea accumulated respiration products beneath the thermocline in summer and autumn, while the northern ECS bottom waters preserved them only in summer. This study highlights fundamental roles of wintertime carbon dioxide (CO_2) solubility along a north-to-south latitude gradient in the coastal acidification development. In comparison with the relatively low-latitude northern ECS subject to seasonal hypoxia, relatively high-latitude Yellow Sea exhibits higher CO_2 solubility in winter and longer respiration-product accumulations in warm seasons, leading to lower Ω_{arag} in the central Yellow Sea than those in the northern ECS. However, the present-day central Yellow Sea is free from hypoxia.

Keywords: coastal acidification, hypoxia, carbon dioxide solubility, community respiration, Yellow Sea, northern East China Sea

KEY POINTS

- Wintertime air-sea re-equilibration, summertime respiration and autumnal upset dominate subsurface carbonate chemistry in coastal seas.
- High CO_2 solubility together with respiration leads to high DIC:TAlk ratios and low aragonite saturation state in the central Yellow Sea.
- The northern East China Sea is subject to concurrent hypoxia and CO_2 acidification in summer, while the Yellow Sea is free from hypoxia.

INTRODUCTION

The oceanic absorption of anthropogenic carbon dioxide (CO_2) has lowered sea surface pH and calcium carbonate ($CaCO_3$) mineral saturation state (Ω) as compared with the preindustrial era, known as ocean acidification (Caldeira and Wickett, 2003; Orr et al., 2005; Doney et al., 2009). Here pH is the negative logarithm of the sum of the concentrations of hydrogen (H^+) and bisulfate (HSO_4^-) ions, i.e., total hydrogen ion concentration scale, $pH_T = -\log_{10}[H^+]_T$, where $[H^+]_T = [H^+] + [HSO_4^-]$. It affects chemical/biochemical properties of seawater, including chemical reactions, equilibrium conditions, and biological toxicity. Ω is defined as $[Ca^{2+}] \times [CO_3^{2-}]/K_{sp}^*$, where $[Ca^{2+}]$ and $[CO_3^{2-}]$ are the concentrations of calcium and carbonate ions, respectively, and K_{sp}^* is the apparent solubility product for either calcite or aragonite. The declines in pH and Ω could lead to $CaCO_3$-undersaturated corrosive seawater conditions, affecting marine calcifying organisms and even the whole marine ecosystem (Fabry, 2008; Jin et al., 2015; Ravaglioli et al., 2020).

The anthropogenic CO_2 invasion has resulted in a decrease in pH by 0.1 unit (Orr et al., 2005) and a decline in $[CO_3^{2-}]$ by 30% (Sabine et al., 2004) in the upper ocean since the industrial revolution. The present-day open ocean pH_T was detected at 8.023 ± 0.004 in the tropical Central Pacific (6.4°N 162.4°W), at 8.074 ± 0.004 in the subtropical Eastern Pacific (33.5°N 122.5°W), and at 8.020 ± 0.008 at an Antarctic site (77.6°S 166.4°W) (Hofmann et al., 2011). In the Pacific Ocean, the present surface Ω_{arag} values are 3–4.5 in low-latitude regions while only 1–2 in high-latitude regions (Feely et al., 2012). This latitude gradient of Ω_{arag} is largely attributed to higher solubility of CO_2 in colder seawaters of high-latitude regions. Moreover, seasonal aragonite undersaturation (i.e., $\Omega_{arag} < 1$) has already been observed in surface and shallow subsurface waters of some northern polar seas (Bates et al., 2009; Fabry et al., 2009; Qi et al., 2017).

Chemically, $\Omega_{arag} > 1$ indicates that the $CaCO_3$ mineral of aragonite is stable in the seawater, while $\Omega_{arag} < 1$ indicates that the mineral is unstable. Although corals usually require much higher Ω_{arag} of > 3.0 for optimal growth (Eyre et al., 2018; Yamamoto A. et al., 2012), many researchers regarded an Ω_{arag} value of 1.5 as a critical threshold for marine shellfish development (Gruber et al., 2012; Ekstrom et al., 2015; Waldbusser et al., 2015), below which marine calcifying organisms may be under threat of acidified seawaters. On the Chinese side of the North Yellow Sea, the net community calcification rate in subsurface waters declined to zero when the Ω_{arag} value reached the critical level of 1.5–1.6 (Li, 2019; Li and Zhai, 2019).

In productive coastal zones, algae and other biogenic particles decompose in subsurface waters. Their respiration and/or remineralization processes consume dissolved oxygen (DO) and release a great deal of CO_2 into subsurface waters, leading to more rapid seawater acidification in coastal seas, compared with the open ocean (Feely et al., 2010; Cai et al., 2011; Melzner et al., 2013; Jiang et al., 2019). Moreover, the respiration-induced seasonal acidification is subject to uneven distributions of seawater temperature, salinity and alkalinity in coastal seas. For example, transregional carbonate studies along the U.S. East Coast have indicated that its northeast shelf region is more susceptible to CO_2 acidification than the southern region, along with a north-to-south increasing gradient in total alkalinity (TAlk) and limited geographical variation in dissolved inorganic carbon (DIC) (Wang et al., 2013; Wanninkhof et al., 2015). Exposure, sensitivity and adaptive capacity to the acidification driven by atmospheric CO_2 absorption and local amplifiers (i.e., eutrophication, upwelling of CO_2-riched waters and input of river water with low $[Ca^{2+}]$ and subsequently Ω_{arag}) were also assessed and compared throughout the U.S. coastal regions (Ekstrom et al., 2015). Along China's coasts, so far, the latitude gradient of coastal acidification and its controlling mechanisms are unclear because previous studies have been primarily confined to individual coastal seas (e.g., Cao et al., 2011; Chou et al., 2013a; Zhai, 2018). Ocean environments along China's coasts also exhibit complex local geological and hydrological characteristics, such as contrasting bottom topography, residence time and monsoon-driven coastal currents (e.g., Su and Yuan, 2005; Chen, 2009; Men and Liu, 2015).

In this study, we examined carbonate system parameters in the Yellow Sea and northern East China Sea (ECS) during 2017–2018, spanning all four seasons. For the first time, a north-to-south gradient of carbonate system parameters in contrasting coastal seas along China's east coast was revealed. Together with hydrological data and DO measurements, the regional differentiation of the respiration-induced coastal acidification in the two coastal seas were investigated. This study provides the best understanding so far of the relationship between subsurface seasonal deoxygenation and acidification in the two coastal seas of both ecological and economic importance, which will assist future predictions of marine environmental changes under ocean acidification in the coming decades.

MATERIALS AND METHODS

Study Area

The Yellow Sea and ECS, located on the China eastern shelf, are two major marginal seas of the western North Pacific. The boundary of the two coastal seas lies between the northern corner of the Changjiang Estuary and Jeju Island (**Figure 1A**). The Yellow Sea is surrounded by mainland China to the west and the

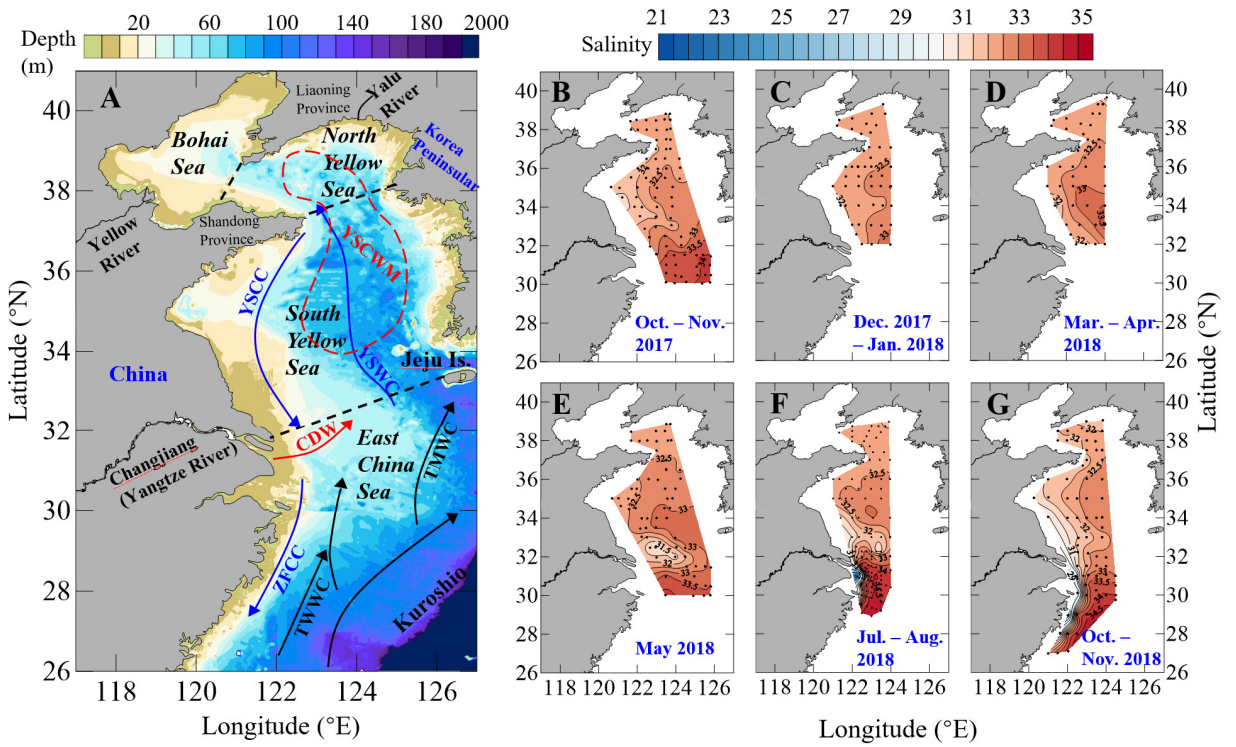


FIGURE 1 | Maps showing **(A)** the circulation and depth contour in the Yellow Sea and East China Sea, and **(B–G)** sampling sites together with our bottom-water salinity data during our seasonal mapping cruises in 2017–2018. In **(A)**, boundaries among the Bohai Sea, North Yellow Sea, South Yellow Sea and East China Sea are shown as dashed black lines. The year-round Kuroshio, TsushiMa Warm Current (TMWC) and TaiWan Warm Current (TWWC) are sketched with black arrows. The wintertime Yellow Sea Coastal Current (YSCC), Yellow Sea Warm Current (YSWC) and Zhejiang-Fujian Coastal Current (ZFCC) are sketched with blue arrows. The summertime Changjiang Dilute Water (CDW) and Yellow Sea Cold Water Mass (YSCWM) are sketched with the red arrow and the dashed red circle, respectively.

Korea Peninsula to the east. It is geographically divided into two basins, i.e., the North Yellow Sea and the South Yellow Sea. The former is connected to the Bohai Sea to the west, and the latter to the ECS to the south. The North Yellow Sea has an area of $\sim 7 \times 10^4$ km^2 with an average water depth of ~38 m, while the South Yellow Sea has an area of $\sim 30 \times 10^4$ km^2 with an average water depth of ~44 m. The more open ECS has a larger area of $\sim 77 \times 10^4$ km^2 with an average water depth of ~370 m. The ECS inner shelf within the 50 m isobaths is quite broad. The climatic variations are primarily dominated by the East Asian Monsoon, with the rain-bearing southwest monsoon prevailing in summer (from June to early September) and a strong northeast monsoon lasting in winter (from December to early March of the next year, Chen, 2009).

Both of the ECS and the Yellow Sea are connected to the North Pacific via the Kuroshio intrusion, including those Kuroshio-derived currents such as the TaiWan Warm Current (TWWC), the TsushiMa Warm Current (TMWC), and the Yellow Sea Warm Current (YSWC). Moreover, they are subject to freshwater discharges from the Changjiang and Yalu Rivers (**Figure 1A**), as well as several monsoon-driving coastal currents, including the northeastward-moving Changjiang Diluted Water (CDW) from late spring to early autumn, and the southward-moving Yellow Sea Coastal Current (YSCC) and Zhejiang-Fujian Coastal Current (ZFCC) in winter and early spring.

The Yellow Sea is semi-enclosed. Its summertime hydrography is characterized by a pronounced stratification in its deeper regions. A cold pool with water temperatures of 5–11°C, the Yellow Sea Cold Water Mass (YSCWM), develops under the thermocline from late spring to autumn as the remnant of the previous winter cooling (Miao et al., 1990; Zhai et al., 2014b). The wintertime hydrography in the Yellow Sea is characterized by the southward-moving YSCC and the northward-moving YSWC (**Figure 1A**). The YSWC is considered to be a compensating current to the monsoon-driven coastal current (Yuan et al., 2008), transporting warm and saline waters into the Yellow Sea. Based on ^{228}Ra/^{226}Ra measurements, the Yellow Sea hydraulic residence time has been estimated to be 5–6 years, while the residence time may only be 2–3 years or shorter on the ECS shelf (Nozaki et al., 1991; Men and Liu, 2015).

TAlk in the Yalu River is only 320–800 μmol kg^{-1} (Zhai et al., 2014b, 2015), approximately 1000 μmol kg^{-1} lower than the Changjiang TAlk value (1500–1900 μmol kg^{-1}, Xiong et al., 2019). As illustrated by Chen and Wang (1999) and Zhai et al. (2014a), the ECS offshore waters originate from the Kuroshio tropical water. The latter has a typical TAlk value of 2293 μmol kg^{-1} and the DIC value of 1994 μmol kg^{-1} (with the DIC:TAlk ratio of < 0.9) at a salinity of 34.9 (Chen and Wang, 1999). By comparison, the TAlk values in the semi-enclosed Yellow Sea were usually detected in a compact range of 2290 ± 25 μmol kg^{-1}

(Zhai, 2018). In the North Yellow Sea, a usual water mixing model has been reported by Zhai et al. (2014b), i.e.,

$$TAlk^{North_Yellow_Sea} = 61.745 \times Salinity + 320 \quad (1)$$

where 320 (μmol kg^{-1}) represents the low TAlk feature of the mixture of rainwater and freshwater discharged from the Yalu River.

Sampling and Analyses

In this study, seven field surveys were conducted on the Chinese side of the Yellow Sea and the northern ECS during 2017–2018 (**Supplementary Table S1**), spanning a wet summer (July–August 2018) and a dry winter (December 2017–January 2018), as well as those transitional seasons of spring (March–May 2018) and autumn (October–November 2017 and October–November 2018) (**Figures 1B–G** and **Supplementary Figure S1A**).

Water samples were collected at two to seven different depths (including sea surface and the bottom water) using a rosette of 10 or 12 Niskin bottles, integrated with Conductivity-Temperature-Depth/Pressure (CTD) sensor packages. The ancillary data of *in situ* temperature (after the International Temperature Scale of 1990) and salinity (after the Practical Salinity Scale of 1978) were obtained primarily using the calibrated CTD sensor packages (SBE-19 plus in our October–November 2017 and May 2018 cruises, and SBE-911 plus during the other cruises, Sea-Bird Scientific, Bellevue, WA, United States). During the summertime estuarine survey conducted in July 2018, salinity values of discrete samples were also measured using a calibrated WTW's TetrCon925 probe.

DO samples were collected, fixed and titrated aboard following the Winkler procedure at an overall uncertainty level of <0.5%. A small quantity of sodium azide (NaN_3) was added during subsample fixation to remove possible interferences from nitrites (Wong, 2012). The DO saturation (DO%) was calculated from field-measured DO concentration divided by the DO concentration at equilibrium with the atmosphere which was calculated from temperature, salinity and local air pressure, as per the Benson and Krause (1984) equation. To quantify the effect of net community metabolism, apparent oxygen utilization (AOU) was also calculated by subtracting the field-measured DO concentration from the air-equilibrated DO. Assuming the water starts with a fully saturated state, and ignoring effects of air-sea exchange and water mixing, an AOU > 0 implies net community respiration, while an AOU < 0 implies net community production.

Water samples for DIC and TAlk analyses were also collected aboard. As recommended by Huang et al. (2012), water samples for DIC and TAlk were stored in 60 mL borosilicate glass bottles (for DIC, bubble free) and 140 mL high-density polyethylene bottles (for TAlk). There were no statistical differences between the measuring results from the above-mentioned sample storing procedure and from those procedure suggested by Dickson et al. (2007). Following filling procedure in Dickson et al. (2007), we filled these triple-rinsed sample bottles of DIC and TAlk smoothly from the bottom, and then immediately added 50 μL of saturated mercuric chloride ($HgCl_2$). Finally, water samples for DIC and TAlk were sealed and preserved at room temperature until determination. Note that the volume of saturated $HgCl_2$ added to the DIC samples exceeded the upper limit of recommended range (0.02–0.05% by volume), but was still below the maximum amount, i.e., 0.1% by volume (Dickson et al., 2007). Both DIC and TAlk samples were unfiltered but allowed to settle before measurement, although filtration techniques suitable for these samples were reported earlier by Bockmon and Dickson (2014). DIC was measured by an infrared CO_2 detector-based DIC analyzer (AS-C3, Apollo SciTech Inc., United States), and TAlk was determined at 25°C by the Gran acidimetric titration using a semi-automated titrator (AS-ALK2, Apollo SciTech Inc., United States). DIC and TAlk determinations were referred to Certificated Reference Materials (CRM) from Andrew G. Dickson's lab at Scripps Institution of Oceanography at a precision of $\pm$ 2 μmol kg^{-1} (Dickson et al., 2007; Zhai et al., 2014b).

Calculation of Other Carbonate System Parameters

Seawater fugacity of CO_2 (fCO_2), pH_T and Ω_{arag} were calculated from seawater temperature, salinity, and measured DIC and TAlk using the software CO2SYS.XLS (Version 24) (Pelletier et al., 2015), which is an updated version of the original CO2SYS.EXE (Lewis and Wallace, 1998). This program has been favorably evaluated by Orr et al. (2015) in a study comparing 10 packages of carbonate calculation program. The Millero et al. (2006) dissociation constants of carbonic acid were used in the calculation because they cover much broader applicable ranges of temperature (0–50°C) and salinity (0–50). The Dickson (1990) dissociation constant was used for HSO_4^- ion. The phosphate and silicate values required by the program were usually unavailable and replaced by zero. The Ca^{2+} concentrations were assumed to be proportional to salinity as presented in Millero (1979) and the values of apparent solubility product for aragonite ($K_{sp}{}^*{}_{arag}$) were taken from Mucci (1983).

To assess the quality of the carbonate system data, we calculated pH data using the National Bureau of Standards scale (pH_{NBS}) based on field-measured DIC and TAlk values. These data were compared with field-measured pH_{NBS} data (see collection and analysis of pH_{NBS} samples in **Supplementary Material**). Most measured and calculated values were consistent at a deviation level of $\pm$ 0.05 pH (**Supplementary Figure S2A**). To examine the possible existences of organic alkalinity in coastal waters within our study area, we also calculated TAlk values from field-measured DIC and pH_{NBS} data. Most measured TAlk data and calculated results were consistent with each other at a deviation level of $\pm$ 20 μmol kg^{-1} (**Supplementary Figure S2B**). This deviation level was reasonably higher than the precision of TAlk determination ($\pm$ 2 μmol kg^{-1}). These comparisons suggested that the measured and calculated results of the carbonate system parameters were reliable. Due to accidentally insufficient addition of $HgCl_2$, the North Yellow Sea DIC samples collected in April 2018 were damaged before determination. The

relevant DIC data were calculated from field-measured TAlk and pH_{NBS}.

To quantify the effect of net community metabolism on DIC, we calculated the air-equilibrated DIC (corresponding to a mean air-equilibrated fCO_2 value of 415 ± 5 μatm during our seasonal cruises conducted in 2017–2018) from corresponding field-measured seawater temperature, salinity and TAlk (Zhai, 2018). The air-equilibrated fCO_2 was calculated from the flask analysis data of atmospheric CO_2 mole fraction at the adjacent Tae-ahn Peninsula (TAP) site (36°44'N 126°08'E), which varied from 406 ppm (ppm = parts of CO_2 per million dry air) in August to 419–421 ppm during January to May in 2017–2018 (**Supplementary Figure S1B**, data from NOAA/ESRL's Global Monitoring Division)[1], and corrected to the survey-based barometric pressure and 100% humidity at water temperature and salinity (Zhai et al., 2019). Similar to the definition of AOU (section "Sampling and Analyses"), the DIC departure from the air-equilibrated DIC was defined as the excess DIC (ExcessDIC). Assuming water starts with a fully saturated state, and ignoring effects of air-sea exchange, water mixing and $CaCO_3$ precipitation/dissolution, an ExcessDIC > 0 means net community respiration, while an ExcessDIC < 0 implies net community production.

RESULTS

Hydrological Settings

Generally, water temperature exhibited a north-to-south-increasing gradient from the North Yellow Sea, to the South Yellow Sea, and to the northern ECS in winter, spring and autumn (**Supplementary Figures S3–S5**). The only exception was sea surface temperature in summer, showing no latitude gradient in these sea areas. However, summertime temperature in subsurface and bottom waters exhibited a north-to-south-increasing gradient (**Supplementary Figures S4, S5**). During our winter and spring cruises, regionally survey-averaged temperatures were 4.8–7.8°C in the North Yellow Sea, 7.2–11.7°C in the South Yellow Sea and 9.6–16.7°C in the northern ECS (**Table 1**).

Salinity also exhibited the north-to-south-increasing gradient, with annual mean values of 32.1 ± 0.3 in the North Yellow Sea, 32.2 ± 0.7 in the South Yellow Sea and 32.6 ± 1.9 in the northern ECS, based on data obtained from our seasonal cruises in 2017–2018. The Yellow Sea had relatively low salinity values and small salinity variations as compared with the northern ECS (**Figures 1B–G**, **2A–C**). In the Yellow Sea, relatively high salinity values of > 32 dominated the whole study area in winter and spring (**Figures 1C–E**). In summer and autumn, the relatively high salinity values of > 32 still dominated bottom waters in the central Yellow Sea (**Figures 1B,F–G**), i.e., the summertime YSCWM area (**Figure 1A**). In the connection between the northern ECS and South Yellow Sea, several low salinity values of 29.7–31.5 were observed in late spring (**Figure 1E**), likely due to the offshore transport of the CDW. In summer, the CDW-affected sampling sites considerably increased, covering the northwestern ECS and the southern part of the South Yellow Sea (**Figure 1F** and **Supplementary Figure S1A**). In autumn, low salinity values of 26.1–30.5 were observed at nearshore stations in the ECS (**Figure 1G**), indicating the effect of the southward-moving ZFCC during this northeast monsoon-driven season (**Figure 1A**).

In the Yellow Sea, significant thermoclines and stratification occurred in summer and autumn (**Figures 3A–C**), with mean surface temperatures of 26.7 ± 2.3°C and 19.2 ± 1.7°C in summer and autumn, respectively, and with mean bottom-water temperatures of 12.5 ± 6.2°C and 13.9 ± 4.7°C in summer and in autumn, respectively (**Supplementary Figure S6**). In the central Yellow Sea, subsurface water had quite low temperature of ∼9°C in warm seasons (**Figures 2A,B**), shaping the YSCWM area with large density difference between bottom and surface waters (ΔDensity) of ∼5 kg m^{-3} in summer and ∼2 kg m^{-3} in autumn (**Figures 3A–C**). Compared with the Yellow Sea, the northern ECS had relatively small bottom-surface temperature differences (26.1 ± 1.8°C versus 20.9 ± 1.7°C) and ΔDensity (3.7 ± 1.8 kg m^{-3}) in summer, and nearly homogenous vertical profiles in autumn, except for several southeastern stations with bottom-water temperatures of 19.9–23.7°C and ΔDensity of 0.4–2.1 kg m^{-3} in October 2018 (**Figures 3A–C** and **Supplementary Figure S6**).

DO and Carbonate System Parameters

DO, fCO_2, and Apparent DO Depletion Rate

During our winter and spring cruises, most DO values were at ∼100% saturations, while fCO_2 were close to the present-day air-equilibrated fCO_2 of 415 μatm in the Yellow Sea and northern ECS (**Table 1** and **Figures 2D–F**), suggesting a vertically well-mixed situation during cold seasons. Exceptions to this were observed in the central part of the South Yellow Sea in winter, where relatively low DO% of 65–72% and supersaturated fCO_2 of 672–806 μatm occurred in bottom waters at four deep stations (**Supplementary Figure S5**). From late spring to autumn, the YSCWM bottom waters exhibited DO declines (from 97% or 285 μmol O_2 kg^{-1} in late spring to 87% or 248 μmol O_2 kg^{-1} in summer and 68% or 195 μmol O_2 kg^{-1} in autumn) and fCO_2 increases (from 440 μatm in late spring to 505 μatm in summer and 680 μatm in autumn) (**Figures 2D,E**, **3D–F**). These low DO values in the YSCWM (mostly higher than 150 μmol O_2 kg^{-1}) were still above the threshold of hypoxia (i.e., <63 μmol O_2 kg^{-1}). The regional averaged apparent DO depletion rate in the YSCWM bottom waters was estimated to be 0.6 μmol O_2 kg^{-1} d^{-1} from late spring to autumn (∼150 days).

In the northern ECS, summertime bottom-water DO% values were averaged at only 56 ± 13% (with a range of 21–84%, having the DO concentrations of 49–185 μmol O_2 kg^{-1}), while the autumnal bottom-water DO% increased to the air-equilibrated level (**Figures 2F**, **3D–F**). The three summertime hypoxic stations (with DO values of 49–63 μmol O_2 kg^{-1}) off the Changjiang Estuary had extremely high fCO_2 values of ∼1000 μatm (**Supplementary Figure S5**). Since water stratification in the northern ECS was intensified from late spring to summer

[1]http://www.esrl.noaa.gov/gmd/

TABLE 1 | Summary of field data of water temperature, salinity, DO saturation (DO%) and carbonate system parameters[a].

Season	Region	Sampling period	Temperature (°C)	Salinity	DO%	TAlk (μmol kg^{-1})	DIC (μmol kg^{-1})	DIC:TAlk ratio	pH_T (*in situ*)	Ω_{arag}
Autumn	North Yellow Sea	13–16 Oct. 2017[b]	16.6 ± 3.4	32.0 ± 0.1	89 ± 13%	2300 ± 10	2119 ± 54	0.921 ± 0.023	7.97 ± 0.09	2.16 ± 0.53
	South Yellow Sea	13, 18–27 Oct. 2017	17.5 ± 4.2	32.0 ± 0.3	92 ± 12%	2295 ± 21	2089 ± 70	0.910 ± 0.027	8.01 ± 0.10	2.41 ± 0.63
	northern ECS	31 Oct.–7 Nov. 2017	21.9 ± 1.1	33.6 ± 0.6	98 ± 3%	2242 ± 8	2001 ± 26	0.892 ± 0.011	8.02 ± 0.03	2.73 ± 0.23
Early winter	North Yellow Sea	30 Dec. 2017–8 Jan. 2018[b]	7.8 ± 0.9	32.3 ± 0.1	97 ± 1%	2324 ± 11	2169 ± 14	0.933 ± 0.005	8.04 ± 0.03	1.81 ± 0.12
	South Yellow Sea	18–30 Dec. 2017	10.6 ± 1.2	32.3 ± 0.2	96 ± 6%	2320 ± 22	2146 ± 25	0.925 ± 0.011	8.04 ± 0.06	2.00 ± 0.24
	northern ECS	19–20 Dec. 2017	13.0 ± 0.9	32.8 ± 0.4	98 ± 1%	2283 ± 23	2101 ± 24	0.920 ± 0.003	8.03 ± 0.02	2.08 ± 0.07
Early spring	North Yellow Sea	8–16 Apr. 2018	4.8 ± 0.8	32.3 ± 0.3	107 ± 3%	2330 ± 23	2167 ± 25[c]	0.930 ± 0.006[c]	8.11 ± 0.04[c]	1.85 ± 0.13[c]
	South Yellow Sea	28 Mar.–8 Apr. 2018	7.2 ± 1.6	32.5 ± 0.4	105 ± 4%	2324 ± 26	2161 ± 33	0.930 ± 0.009	8.07 ± 0.05	1.87 ± 0.19
	northern ECS	1–2 Apr. 2018	9.6 ± 0.6	32.5 ± 0.6	104 ± 3%	2300 ± 16	2137 ± 24	0.930 ± 0.006	8.03 ± 0.02	1.85 ± 0.12
Late spring	North Yellow Sea	9–11 May 2018	7.6 ± 2.6	32.4 ± 0.1	104 ± 5%	2332 ± 17	2169 ± 28	0.930 ± 0.009	8.06 ± 0.03	1.89 ± 0.22
	South Yellow Sea	12–19 and 29–30 May 2018	11.7 ± 3.4	32.5 ± 0.4	102 ± 9%	2306 ± 22	2130 ± 43	0.924 ± 0.015	8.03 ± 0.07	2.02 ± 0.35
	northern ECS	23–28 May 2018	16.7 ± 3.0	32.3 ± 0.9	99 ± 14%	2261 ± 19	2053 ± 59	0.908 ± 0.022	8.03 ± 0.08	2.38 ± 0.51
Summer	North Yellow Sea	2–5 Aug. 2018	16.7 ± 8.4	31.9 ± 0.3	104 ± 10%	2318 ± 19	2127 ± 56	0.918 ± 0.019	7.99 ± 0.05	2.26 ± 0.53
	South Yellow Sea	24 Jul.–2 Aug. 2018	19.3 ± 7.3	31.8 ± 1.1	96 ± 19%	2296 ± 43	2104 ± 77	0.916 ± 0.025	7.96 ± 0.08	2.32 ± 0.65
	northern ECS	12–20 Jul. 2018	23.0 ± 2.9	32.2 ± 2.6	74 ± 29%	2234 ± 31	2042 ± 80	0.914 ± 0.033	7.90 ± 0.13	2.33 ± 0.81
Autumn	North Yellow Sea	24 Oct.–4 Nov. 2018	14.7 ± 2.3	31.9 ± 0.2	88 ± 12%	2307 ± 12	2143 ± 45	0.929 ± 0.017	7.96 ± 0.07	1.96 ± 0.40
	South Yellow Sea	14–24 Oct. 2018	17.7 ± 4.9	32.0 ± 0.5	89 ± 13%	2302 ± 25	2106 ± 74	0.915 ± 0.026	7.98 ± 0.08	2.32 ± 0.62
	northern ECS	8–14 Oct. 2018	23.8 ± 1.0	32.6 ± 1.6	91 ± 10%	2233 ± 18	2002 ± 32	0.896 ± 0.015	7.98 ± 0.04	2.69 ± 0.32

[a]Data were summarized by mean ± standard deviation across all stations and samples. TAlk, total alkalinity; DIC, dissolved inorganic carbon. [b]Some of the data collected from these surveys have been partially reported by Li (2019). [c]Calculated from field-measured TAlk and pH_{NBS} data, since DIC samples collected during this survey were accidentally damaged before determination.

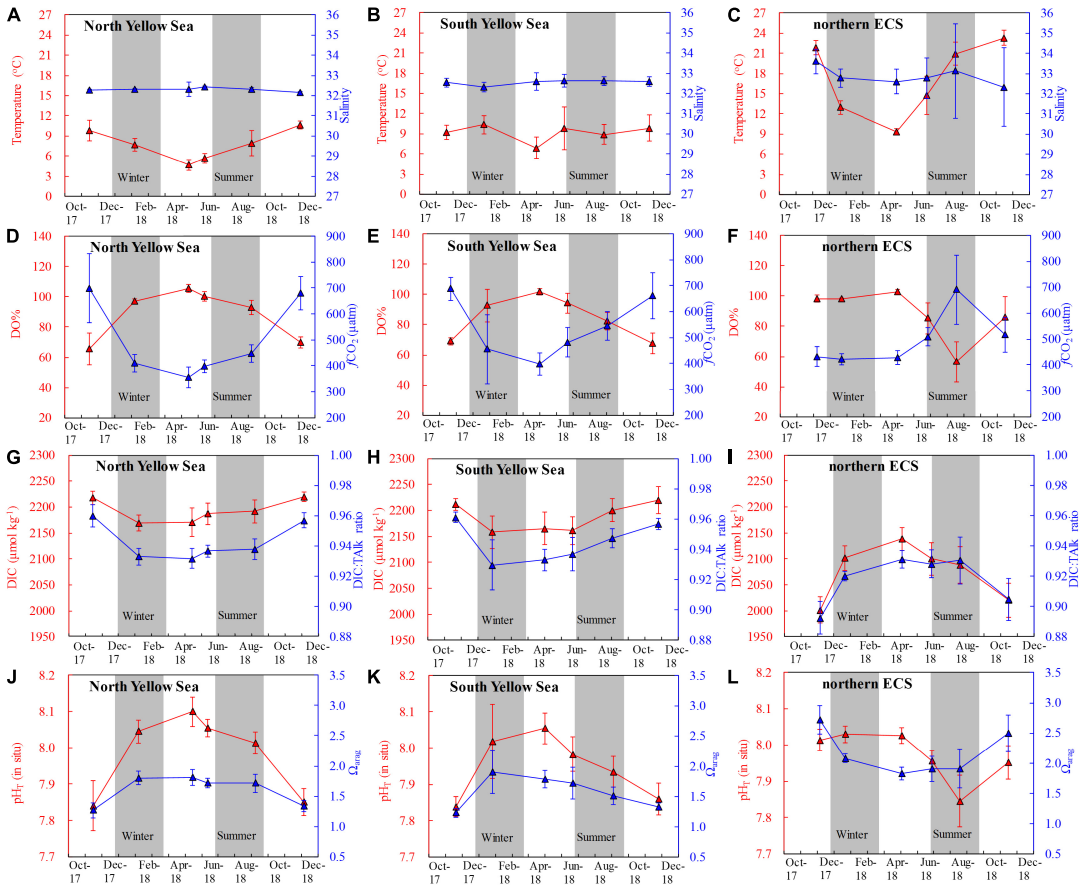


FIGURE 2 | Time series of survey-averaged values of bottom-water **(A–C)** temperature and salinity, **(D–F)** DO saturation (DO%) and fugacity of CO_2 (fCO_2), **(G–I)** dissolved inorganic carbon (DIC) and DIC:TAlk ratio, and **(J–L)** pH_T (*in situ*) and aragonite saturation state (Ω_{arag}). TAlk = Total alkalinity. Data points in the Yellow Sea during summer to autumn are within the YSCWM. Error bars denote standard deviations.

(∼50 days), its bottom-water averaged apparent DO depletion rate (from 85% or 215 μmol O_2 kg^{-1} in late spring to 56% or 126 μmol O_2 kg^{-1} in summer) was estimated to be 1.8 μmol O_2 kg^{-1} d^{-1}.

In addition, moderately low bottom-water DO values of ∼140 μmol O_2 kg^{-1} were also observed in autumn at several southeastern stations (**Figure 3F**), where water temperature was moderately low (∼22°C) (**Supplementary Figure S6F**), and salinity was quite high (∼34) (**Figure 1G**), likely resulted from the TWWC that intruded into the northern ECS (**Figure 1A**).

TAlk

Survey-averaged TAlk in the North Yellow Sea ranged between 2300 ± 10 μmol kg^{-1} and 2332 ± 17 μmol kg^{-1} (**Table 1**, with the annual mean of 2316 ± 19 μmol kg^{-1}), while survey-averaged TAlk in the South Yellow Sea ranged between 2295 ± 21 μmol kg^{-1} and 2324 ± 26 μmol kg^{-1} (**Table 1**, with the annual mean of 2305 ± 31 μmol kg^{-1}). In the northern ECS, however, relatively low TAlk values were observed, ranging from 2233 ± 18 μmol kg^{-1} to 2300 ± 16 μmol kg^{-1} (**Table 1**, with the annual mean of 2243 ± 28 μmol kg^{-1}).

TAlk versus salinity showed different relationships in the three regions (**Figures 4A**–C). In the North Yellow Sea, TAlk versus salinity roughly followed Eq. (1), although TAlk data obtained from our five cruises in 2018 were 10–30 μmol kg^{-1} higher than those values predicted by salinity and Eq. (1). In the South Yellow Sea, however, quite complicated water mixing behaviors were involved (**Figure 4B**). In the northern ECS, many data points of TAlk versus salinity fairly followed a linear relationship (**Figure 4C**), i.e.,

$$TAlk^{northern_ECS} = 11.922 \times Salinity + 1850 (R^2 = 0.94, n = 172) \quad (2)$$

Equation (2) indicated a two-endmember water mixing between the Changjiang freshwater (S = 0, TAlk = 1850 μmol kg^{-1}) and the ECS offshore waters (S = 34.9, TAlk = 2266 μmol kg^{-1}), as derived from our July 2018 cruise conducted off the Changjiang Estuary (**Figure 1**). This linear relationship also roughly characterized several ECS nearshore stations (along the China's east coast) sampled during

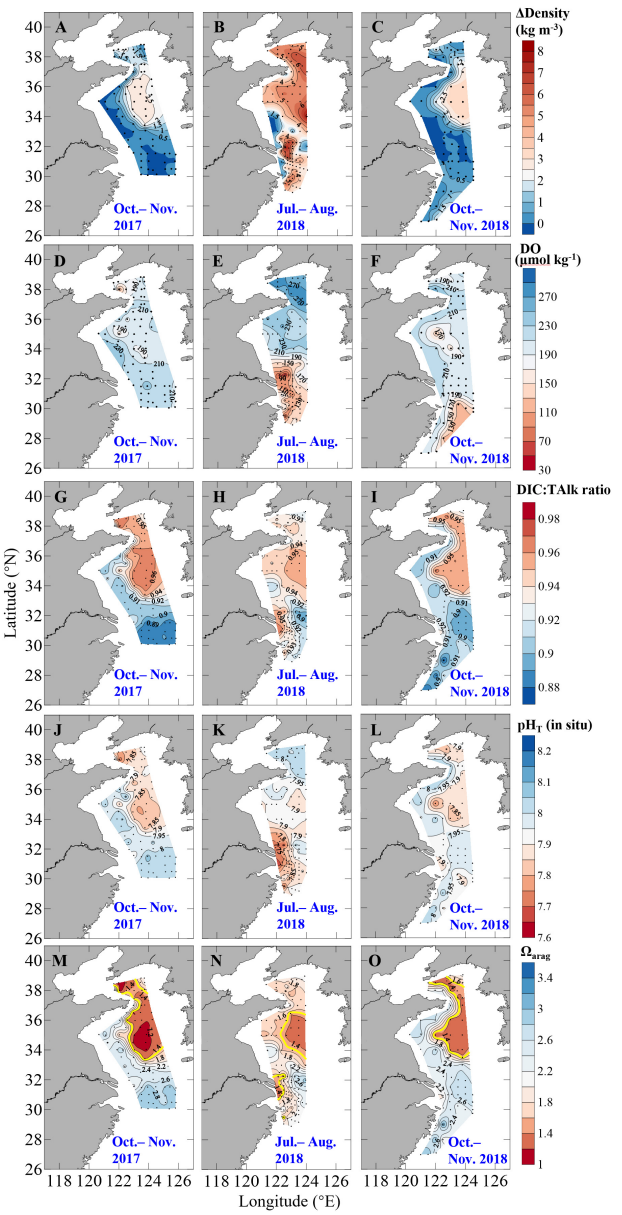


FIGURE 3 | Distributions of **(A–C)** density difference between bottom and surface waters (ΔDensity), bottom-water **(D–F)** dissolved oxygen (DO), **(G–I)** DIC:TAlk ratio, **(J–L)** pH_T (*in situ*), and **(M–O)** aragonite saturation state (Ω_{arag}) in autumn 2017, summer 2018 and autumn 2018. In panels **(M–O)**, contours of bottom-water critical Ω_{arag} level of 1.5 are plotted as thick yellow lines.

our autumn 2018 cruise, with quite low salinity values of 26.0–30.5 (**Figure 1G**) and TAlk values of 2138–2229 μmol kg^{-1} (**Figure 4C**), indicating that the southward-moving ZFCC was closely coupled with the CDW (**Figure 1A**). In winter and spring, however, quite high TAlk values of 2283–2333 μmol kg^{-1} at moderate salinity values of 31.3–32.8 were observed in the northern ECS (**Figure 4C**), showing the intrusion of the northeast monsoon−driven YSCC (**Figure 1A**).

DIC and DIC:TAlk Ratio

The Yellow Sea exhibited higher DIC values than the northern ECS (**Figures 2G,H** versus **Figure 2I**). Annual mean DIC values were 2145 ± 47 μmol kg^{-1} in the North Yellow Sea, 2119 ± 65 μmol kg^{-1} in the South Yellow Sea, and 2031 ± 65 μmol kg^{-1} in the northern ECS. Wintertime and springtime DIC values in the North Yellow Sea were averaged at 2168 ± 22 μmol kg^{-1} (**Figure 4D**), while wintertime and springtime DIC values in the South Yellow Sea were averaged at 2144 ± 36 μmol kg^{-1} (**Figure 4E**). In the Yellow Sea, DIC data showed greater vertical variations in summer and autumn than in winter and spring (**Supplementary Figures S3–S5**), and the YSCWM had relatively high DIC values of 2150–2270 μmol kg^{-1} in summer and autumn (**Figures 4D,E**). In the northern ECS, the low DIC values of this study of 1650–1950 μmol kg^{-1} were observed in the summertime ECS surface waters (**Supplementary Figure S7F**), while the ECS bottom-water DIC values were mostly 2050–2150 μmol kg^{-1} in summer (**Figure 4F**).

The Yellow Sea usually had higher DIC:TAlk ratios than the northern ECS (**Figures 2G–I**). From early winter to late spring, survey-averaged DIC:TAlk ratio in the North Yellow Sea ranged between 0.930 ± 0.009 and 0.933 ± 0.005 (**Table 1**), usually at 0.930 ± 0.010 (**Figure 4G**), while survey-averaged DIC:TAlk ratio in the South Yellow Sea varied from 0.924 ± 0.016 to 0.930 ± 0.009 (**Table 1**), usually at 0.925 ± 0.010 (**Figure 4H**). In the YSCWM (with salinity of > 32 and temperature of < 12°C), bottom-water DIC:TAlk ratios increased to 0.944 ± 0.008 in summer and 0.959 ± 0.005 in autumn (**Figures 3G–I**, **4G,H**). In early winter, several very high bottom-water DIC:TAlk ratio values of 0.958–0.967 (**Figure 4H**) were observed at the four deep stations in the central South Yellow Sea, together with DO% of 65–72% and fCO_2 of 672–806 μatm (**Supplementary Figure S5**).

In the northern ECS, survey-averaged DIC:TAlk ratio values in early winter (0.920 ± 0.003) and early spring (0.930 ± 0.006) were much higher than the usual ratio of ∼0.9 in the ECS offshore waters (**Table 1**), but quite close to the usual DIC:TAlk ratio of wintertime and springtime Yellow Sea waters (**Figures 2G–I**). This was likely because the YSCC transported the Yellow Sea waters into the northern ECS during the northeast monsoon season (**Figure 1A**). In late spring, the ECS DIC:TAlk ratio tended to show limited vertical gradient, with surface values of 0.891 ± 0.013 (**Supplementary Figure S7I**) and bottom-water values of 0.928 ± 0.009 (**Figure 4I**). In general, the ECS bottom waters increased their DIC:TAlk ratio values to 0.930–0.970 in summer, and then declined to < 0.9 in autumn (**Figures 3G–I**). At several nearshore stations affected by the ZFCC and those southeastern stations likely affected by the TWWC intrusion, relatively high bottom-water DIC:TAlk ratio values of 0.920–0.930 were also revealed during our autumn 2018 cruise (**Figures 3I**, **4I**).

Bottom-Water AOU and Excess DIC From Late Spring to Autumn

In late spring, both bottom-water AOU and ExcessDIC varied around 0 in the North Yellow Sea (**Figure 5A**), while the South Yellow Sea bottom-water AOU and ExcessDIC

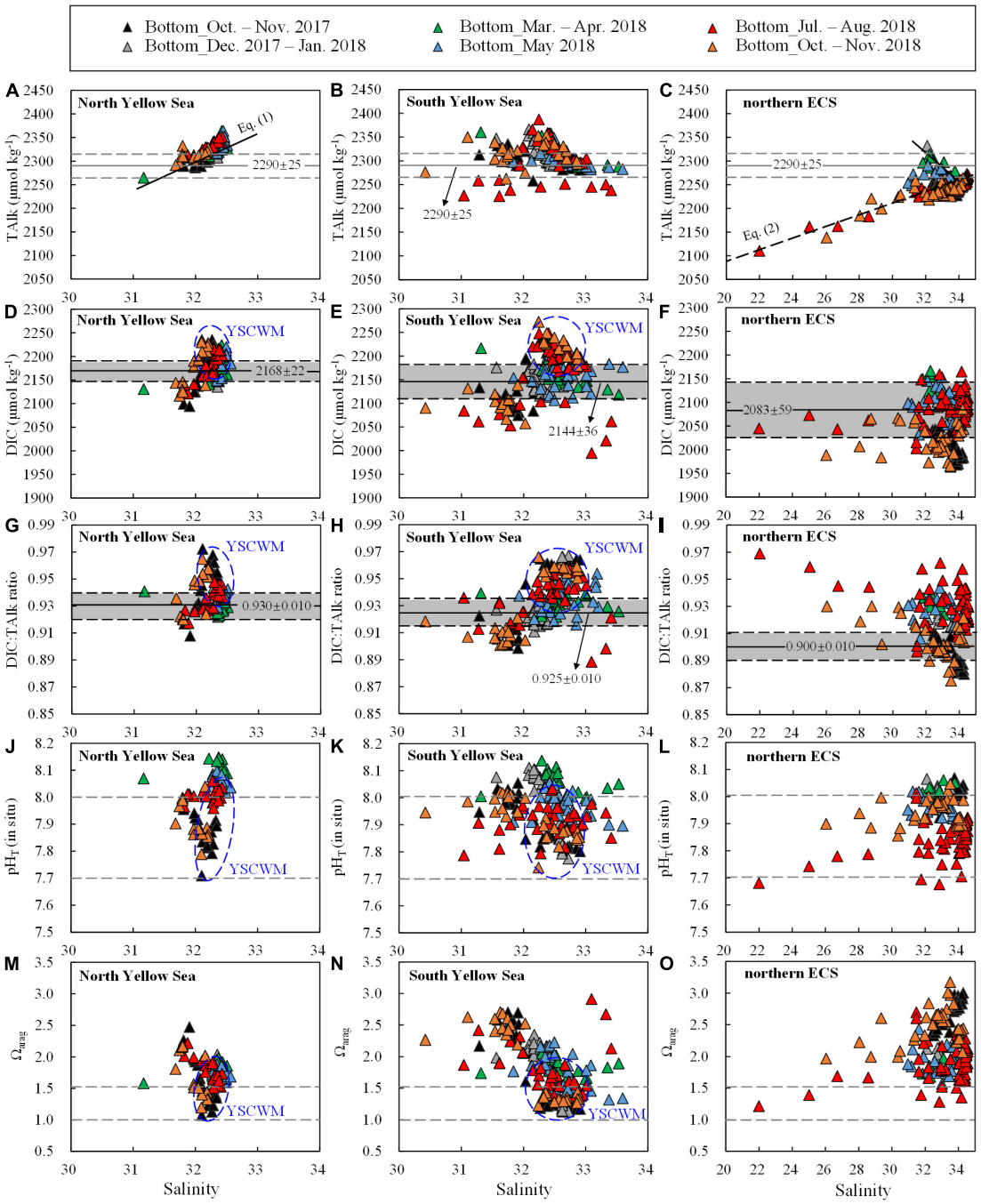


FIGURE 4 | Bottom-water **(A–C)** TAlk, **(D–F)** DIC, **(G–I)** DIC:TAlk ratio, **(J–L)** pH_T (*in situ*) and (m–o) Ω_{arag} versus salinity. Data for the YSCWM are enclosed within blue ellipses. In **(A–C)**, 2290 ± 25 μmol kg^{-1} was the earlier usual value of TAlk in the Yellow Sea (Zhai et al., 2014b; Zhai, 2018). In **(D–I)**, gray shaded areas represent mean ± SD of wintertime/springtime DIC or DIC:TAlk ratios in individual regions. In **(J–L)**, the pH_T of 8.0 is comparable with the present-day air-equilibrated pH_T (corresponding to a mean air-equilibrated fCO_2 value of 415 ± 5 μatm during our seasonal cruises in 2017–2018), while the pH_T of 7.7 shows the doubled concentration of total hydrogen ions. In **(M–O)**, the Ω_{arag} of 1.5 shows a critical value that the net community $CaCO_3$ dissolution occurs in the North Yellow Sea (Li, 2019; Li and Zhai, 2019), while the Ω_{arag} of 1.0 indicates the critical value for the ideal aragonite dissolution.

were 17 ± 18 μmol kg^{-1} and 22 ± 18 μmol kg^{-1}, respectively (**Figure 5B**). In summer and autumn, the YSCWM AOU increased to summertime 38 ± 21 μmol kg^{-1} and autumnal 91 ± 15 μmol kg^{-1}, while the YSCWM ExcessDIC increased to summertime 28 ± 20 μmol kg^{-1} and autumnal 71 ± 16 μmol kg^{-1} (**Figures 5A,B**). It is worthwhile to note that the AOU values in the YSCWM area were rarely higher than 110 μmol kg^{-1}.

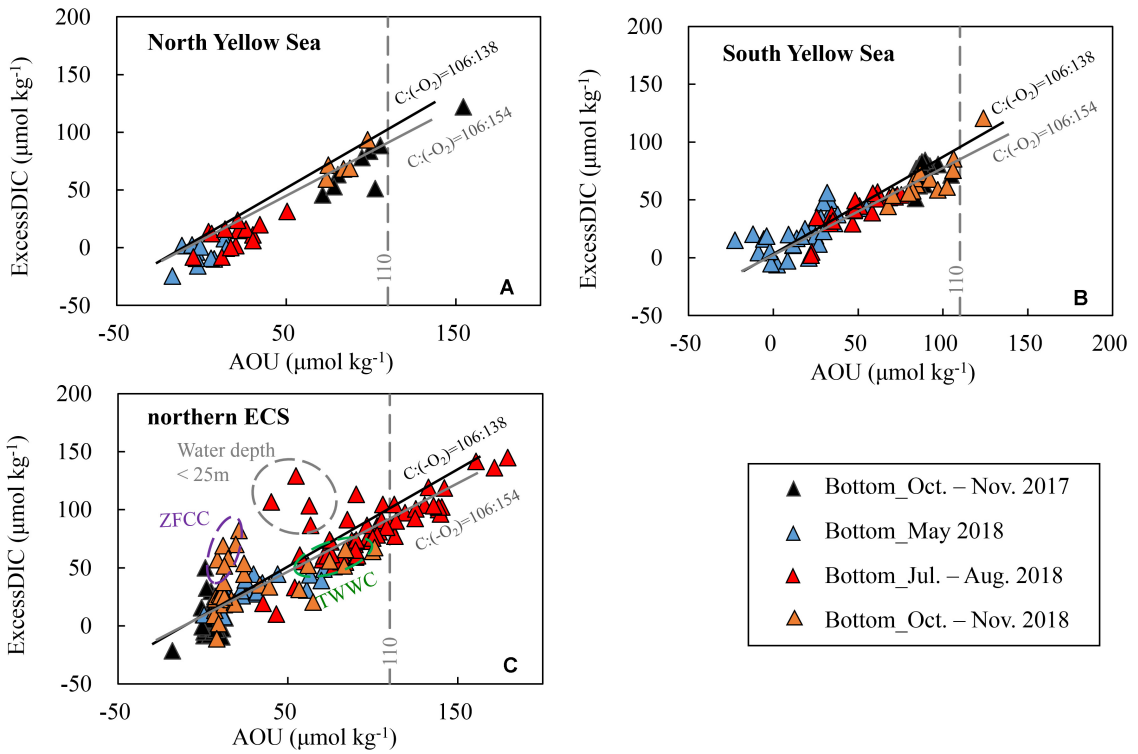


FIGURE 5 | Bottom-water excess dissolved inorganic carbon (ExcessDIC) versus apparent oxygen utilization (AOU) in late spring, summer and autumn. ExcessDIC was defined as the departure from the air-equilibrated DIC (corresponding to a mean atmospheric fCO_2 level of 415 ± 5 μatm during our seasonal cruises in 2017–2018). The solid black line exhibits the traditional Redfield ratio, i.e., $\Delta C{:}\Delta(-O_2)$ = 106:138 (Redfield et al., 1963), and the solid gray line indicates the more recent estimation of $\Delta C{:}\Delta(-O_2)$ = 106:154 (Hedges et al., 2002). Plots of **(A)** the North Yellow Sea and **(B)** South Yellow Sea during summer and autumn are within the YSCWM. In panel **(C)**, several summer plots in the northern East China Sea (ECS) deviated from the Redfield line, as enclosed by gray dashed ellipse, are at shallow sampling sites with water depth of < 25 m. ZFCC = Zhejiang-Fujian Coastal Current in winter and early spring, while TWWC = TaiWan Warm Current.

In the northern ECS, bottom-water AOU and ExcessDIC increased from moderate levels (AOU = 36 ± 23 μmol kg^{-1}, ExcessDIC = 33 ± 12 μmol kg^{-1}) in late spring to very high levels (AOU = 98 ± 31 μmol kg^{-1}, ExcessDIC = 83 ± 27 μmol kg^{-1}) in summer, and declined to relatively low levels (AOU = 11 ± 16 μmol kg^{-1}, ExcessDIC = 20 ± 24 μmol kg^{-1}) in autumn (**Figure 5C**). Different from the Yellow Sea situation that only a few sampling sites had extremely high AOU values of more than 110 μmol kg^{-1}, nearly one third of our ECS sampling sites were occupied with the extremely high AOU values of 110–179 μmol kg^{-1} in summer (**Figure 5C**). The southward-moving ZFCC (observed at nearshore stations with low salinity of < 31) was characterized by AOU of nearly 0 but high ExcessDIC of 40–80 μmol kg^{-1}, while the northward-upwelling TWWC (observed at southeastern offshore stations with high salinity of > 34) was characterized by both high AOU (60–100 μmol kg^{-1}) and high ExcessDIC (50–65 μmol kg^{-1}) (**Figure 5C**).

Seasonal Variations in pH_T and Ω_{arag}

In the Yellow Sea, wintertime and springtime pH_T and Ω_{arag} were generally homogenous, while pH_T and Ω_{arag} displayed vertical gradient in summer and autumn. Its early-winter pH_T and Ω_{arag} were 8.04 ± 0.05 and 1.94 ± 0.22, respectively, while its early-spring pH_T and Ω_{arag} were 8.08 ± 0.05 and 1.86 ± 0.16, and the late-spring pH_T and Ω_{arag} were 8.04 ± 0.06 and 1.98 ± 0.34 (**Table 1**). During our summer and autumn cruises, surface pH_T ranged between 7.98 ± 0.07 and 8.04 ± 0.05 (**Supplementary Figures S7M,N**), while surface Ω_{arag} varied from 2.58 ± 0.30 to 3.00 ± 0.36 (**Supplementary Figures S7P,Q**). The YSCWM pH_T decreased to 7.97 ± 0.05 in summer (mostly lower than the present-day air-equilibrated level of 8.0–8.1) and 7.85 ± 0.04 in autumn. Note that very low pH_T values of 7.71–7.80 occurred in the YSCWM in autumn (**Figures 4J,K**), suggesting that the concentration of total hydrogen ions should be twice the present-day air-equilibrated level of 8.0–8.1. The YSCWM Ω_{arag} declined to 1.59 ± 0.18 in summer and 1.28 ± 0.09 in autumn (**Figures 2J,K**). Its autumnal lowest Ω_{arag} value of 1.07 was detected in the northern area of the YSCWM (**Figure 4M**), which was even close to the critical value for the ideal aragonite dissolution. Even in early winter, very low bottom-water pH_T values of 7.77–7.85 (**Figure 4K**) and Ω_{arag} values of 1.13–1.29 (**Figure 4N**) were also observed at the four deep stations (in the central South Yellow Sea) mentioned in section "DIC and DIC:TAlk Ratio."

In the northern ECS, the early-winter pH_T and Ω_{arag} were averaged at 8.03 ± 0.02 and 2.08 ± 0.07, respectively, and the early-spring pH_T and Ω_{arag} were averaged at 8.03 ± 0.02 and 1.85 ± 0.12, respectively (**Table 1**). In late spring, the ECS

bottom-water pH_T and Ω_{arag} were averaged at 7.96 ± 0.03 and 1.90 ± 0.21, respectively (**Figure 2L**), while its surface pH_T and Ω_{arag} were averaged at 8.09 ± 0.05 (**Supplementary Figure S7O**) and 2.80 ± 0.30 (**Supplementary Figure S7R**), respectively. In summer, the ECS bottom-water pH_T and Ω_{arag} were averaged at 7.85 ± 0.07 and 1.91 ± 0.32, respectively (**Figure 2L**), while the surface pH_T and Ω_{arag} were averaged at 7.99 ± 0.16 (**Supplementary Figure S7O**) and 2.99 ± 0.99 (**Supplementary Figure S7R**), respectively. Near the riverine mouth of Changjiang, quite low summertime bottom-water pH_T values of 7.68–7.74 and Ω_{arag} values of 1.21–1.39 were observed at five stations (**Figures 3K,N**, **4L,O**). Three of these seriously acidified stations (pH_T 7.68–7.71; Ω_{arag} 1.28–1.39) suffered from summertime hypoxia (with DO values of 49–63 μmol O_2 kg^{-1}), while the other two stations (pH_T 7.68 and 7.74; Ω_{arag} 1.21 and 1.39) were very shallow (with water depth of ∼10 m) and vertically well-mixed. In autumn, most pH_T and Ω_{arag} in the northern ECS increased to nearly air-equilibrated values of ∼8.00 and ∼2.60 (**Figures 2–3**), except for several stations likely affected by the ZFCC and the TWWC intrusion, where low pH_T values of 7.86–7.99 and low Ω_{arag} values of 1.97–2.60 were detected (**Figures 4L,O**).

DISCUSSION

Processes Driving Seasonal Variations of Bottom-Water DIC, pH_T, and Ω_{arag}

Dynamics of DIC, pH_T, and Ω_{arag} in coastal zones are subject to multi-drivers, including coastal upwelling (Feely et al., 2008), riverine freshwater inputs (Salisbury et al., 2008; Rheuban et al., 2019; Xiong et al., 2019), vertical and lateral water mixing (Wang et al., 2013; Wanninkhof et al., 2015), and metabolic processes (Feely et al., 2010). In addition to these drivers, the seasonal temperature variability also affects the carbonate chemistry (Zhai et al., 2014b). In an open system, the temperature effect on carbonate system parameters includes the internal thermodynamic equilibrium shift and the air-sea CO_2 exchange caused by the solubility change (Xue et al., 2017; Cai et al., 2020). These two temperature effects tend to cancel each other out for pH_T, but to enhance each other for Ω_{arag} because of the dominant role of gas equilibrium (Cai et al., 2020).

To illuminate the temperature effect on seasonal changes of carbonate system parameters, air-equilibrated DIC, DIC:TAlk ratio, pH_T and Ω_{arag} values (corresponding to a mean air-equilibrated fCO_2 value of 415 ± 5 μatm in 2017–2018) in the Yellow Sea and northern ECS were plotted against the seawater temperature. Both of air-equilibrated DIC and DIC:TAlk ratio increased as temperature decreased (**Figures 6A–C,E–G**). However, air-equilibrated pH_T varied limitedly with temperature change (**Figures 6I–K**), whereas air-equilibrated Ω_{arag} decreased as temperature decreased (**Figures 6M–O**).

Wintertime Re-equilibration

In shallow waters away from upwelling systems, the carbonate system within the water column re-equilibrated with atmospheric CO_2 every year between winter and spring (**Figures 2D–F**). Comparing field-measured carbonate system parameters in the two coastal seas with their air-equilibrated levels, wintertime and springtime carbonate system parameters mostly varied around the corresponding air-equilibrated levels (**Figure 6**), showing the dominant role of air-sea re-equilibration at the beginning of warm-season stratification formation. At the four deep stations within the central South Yellow Sea, however, the early-winter DIC and DIC:TAlk ratio were much higher than their air-equilibrated values (**Figures 6B,F**), while the early-winter pH_T and Ω_{arag} were substantially lower than their air-equilibrated values (**Figures 6J,N**). Supersaturated bottom-water fCO_2 values of 672–806 μatm were also detected at these four stations, despite their vertical profiles of temperature and salinity were nearly homogenous (**Supplementary Figures S3–S5**). This is because that a longer period of time of 25–100 days was needed for the CO_2-rich waters to equilibrate with the atmosphere (Zhai et al., 2014b; Li and Zhai, 2019). In the North Yellow Sea, the early-spring pH_T (8.10 ± 0.04) and Ω_{arag} (1.81 ± 0.13) were slightly higher than those air-equilibrated levels estimated at a low temperature of 5°C (**Figures 6I,M**). This was likely because water-cooling lowered fCO_2 to form an undersaturated level of ∼350 μatm in April 2018 (**Figure 2D**). The similarly springtime undersaturated fCO_2 has been observed earlier in the North Yellow Sea in May 2011 and May 2012 (Zhai et al., 2014b).

Summertime Respiration Beneath Thermoclines

In summer, most bottom-water DIC and DIC:TAlk ratio in the Yellow Sea and northern ECS were higher than their air-equilibrated levels (**Figures 6A–C,E–G**). In the YSCWM waters, summertime DIC addition and DIC:TAlk ratio increase relative to the corresponding air-equilibrated values were 10–50 μmol kg^{-1} and 0.1–0.2, respectively (**Figures 6A,B,E,F**). In comparison, the northern ECS showed much greater summertime increases in bottom-water DIC and DIC:TAlk ratio, which were 50–100 μmol kg^{-1} and 0.2–0.7 over the air-equilibrated values (**Figures 6C,G**). An abundant supply of sinking organic matter induced by the eutrophic Changjiang plume and summertime strong stratification were key factors forming and maintaining very high bottom-water DIC and pCO_2 in the ECS shelf waters in summer (Chou et al., 2009, 2013b). It is worthwhile to note that several warm southern stations in the South Yellow Sea also exhibited very high DIC:TAlk ratio (∼0.93) relative to their air-equilibrated levels (∼0.89) at seawater temperature of >20°C (**Figure 6F**), likely due to the northeastward-flowing CDW in summer (Xu et al., 2016; Zhai, 2018).

To reveal the possible source processes dominating these DIC additions, we plotted bottom-water DIC additions relative to the corresponding air-equilibrated levels (i.e., ExcessDIC) against AOU (**Figure 5**). In both of the YSCWM and the northern ECS, ExcessDIC versus AOU was reasonably in agreement with the stoichiometry of marine phytoplankton organic matter oxidation, including the traditional Redfield ratio, i.e., $\Delta C{:}\Delta(-O_2)$ = 106:138, and the more recent estimation of $\Delta C{:}\Delta(-O_2)$ = 106:154 (Hedges et al., 2002). The $\Delta C{:}\Delta(-O_2)$ ratio of 106/154 falls in the range of marine phytoplankton respiration quotients of 106/140 and 106/160 recommended

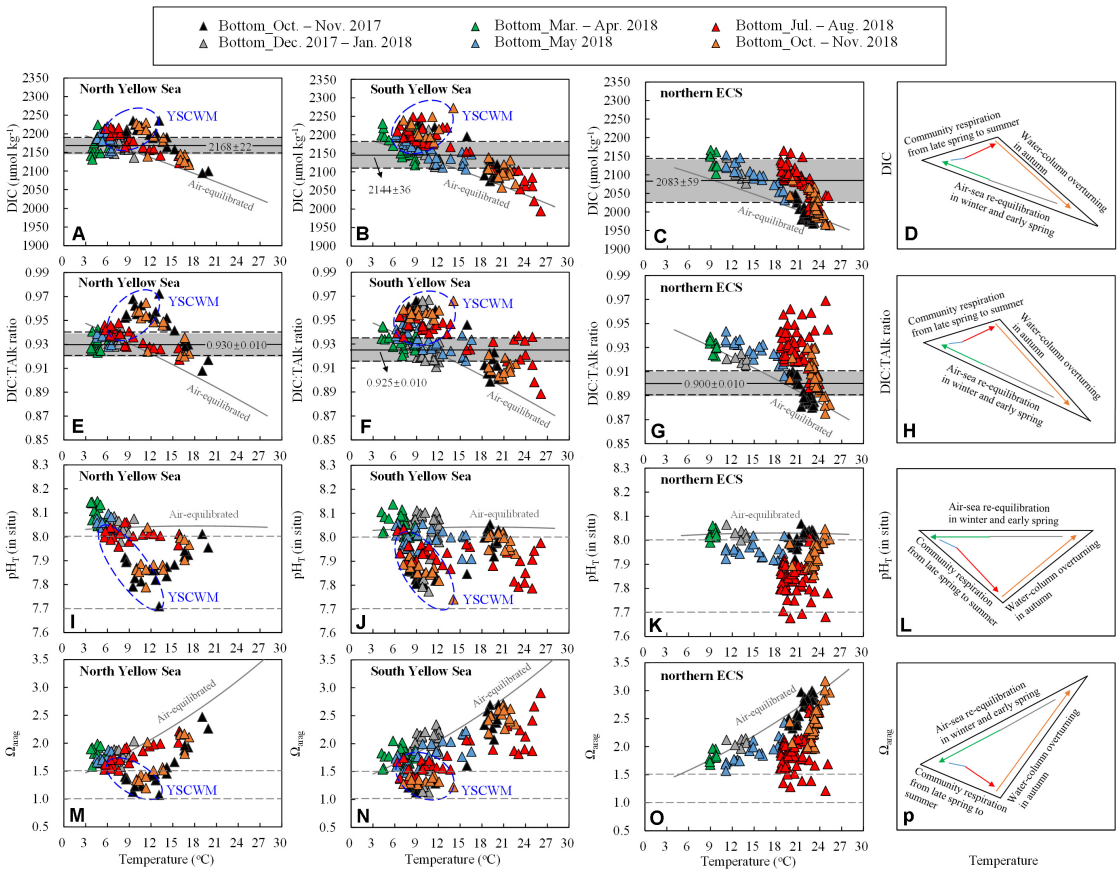


FIGURE 6 | Bottom-water **(A–C)** DIC, **(E–G)** DIC:TAlk ratio, **(I–K)** pH_T (*in situ*), and **(M–O)** Ω_{arag} versus temperature. Solid gray curves are air-equilibrated levels of bottom-water DIC, DIC:TAlk ratio, pH_T and Ω_{arag} (corresponding to a mean air-equilibrated fCO_2 value of 415 ± 5 μatm during our seasonal cruises in 2017–2018) at mean salinity and TAlk in the North Yellow Sea (salinity = 32.1, TAlk = 2316 μmol kg^{-1}), South Yellow Sea (salinity = 32.2, TAlk = 2305 μmol kg^{-1}) and northern ECS (salinity = 33.0, TAlk = 2243 μmol kg^{-1}). Data for the YSCWM are enclosed within a blue ellipse. In **(A–C)** and **(E–G)**, gray shaded areas represent mean ± SD of wintertime/springtime DIC and DIC:TAlk ratios in the North Yellow Sea, in the South Yellow Sea, and in the northern ECS. Major processes controlling seasonal variations of bottom-water **(D)** DIC, **(H)** DIC:TAlk ratio, **(L)** pH_T (*in situ*) and **(P)** Ω_{arag} are also sketched.

by Anderson (1995) and Sarmiento and Gruber (2006). These facts indicate that both bottom-water DIC additions and DO depletions were dominated by the community respiration beneath thermoclines.

In the ECS shallow areas where wind-driven collapse of water stratification occasionally occurred (**Figure 3B**), the bottom-water ventilation might bias the relationship of ExcessDIC and AOU (**Figure 5C**) due to the slower re-equilibration of CO_2 than O_2 (Zeebe and Wolf-Gladrow, 2001). In the South Yellow Sea and northern ECS, some late-spring plots also followed the Redfield line (**Figures 5B,C**), likely due to an earlier start of metabolic processes in warm southern waters, as supported by those sinking biogenic particles induced by frequent springtime blooms in the outer Changjiang Estuary and the South Yellow Sea (He et al., 2013).

The summertime increases in bottom-water DIC and DIC:TAlk ratio suppressed the Ω_{arag} (**Figure 8**), while the bottom-water pH_T declines in summer and/or autumn (**Figures 6I–K**) also mirrored the seasonal increases in bottom-water DIC (**Figures 6A–C**) and DIC:TAlk ratio (**Figures 6E–G**). Therefore, the community respiration under thermoclines was mainly responsible for summertime and/or autumnal low pH_T and Ω_{arag} in these regions.

In comparison to the Yellow Sea, the northern ECS exhibited greater increases in bottom-water DIC and DIC:TAlk ratio in summer, thereby leading to larger decreases in the bottom-water pH_T and Ω_{arag} (**Figure 6**). It is worthwhile to note that summertime bottom-water pH_T values in the northern ECS were lower than those in the Yellow Sea (**Figures 6I–K**), while summertime bottom-water Ω_{arag} values were roughly comparable in the two coastal seas (**Figures 6M–O**). The latter was partially caused by the lower yearly initial Ω_{arag} in the colder Yellow Sea waters in winter and spring (section "Wintertime Re-equilibration Naturally Preconditions the Water Column").

Autumnal Collapse of Thermoclines and the Water-Column Overturning

In typical autumn months (October and November), the seasonal stratification was usually weakened and even collapsed, except for the central Yellow Sea and a small ECS region affected by the

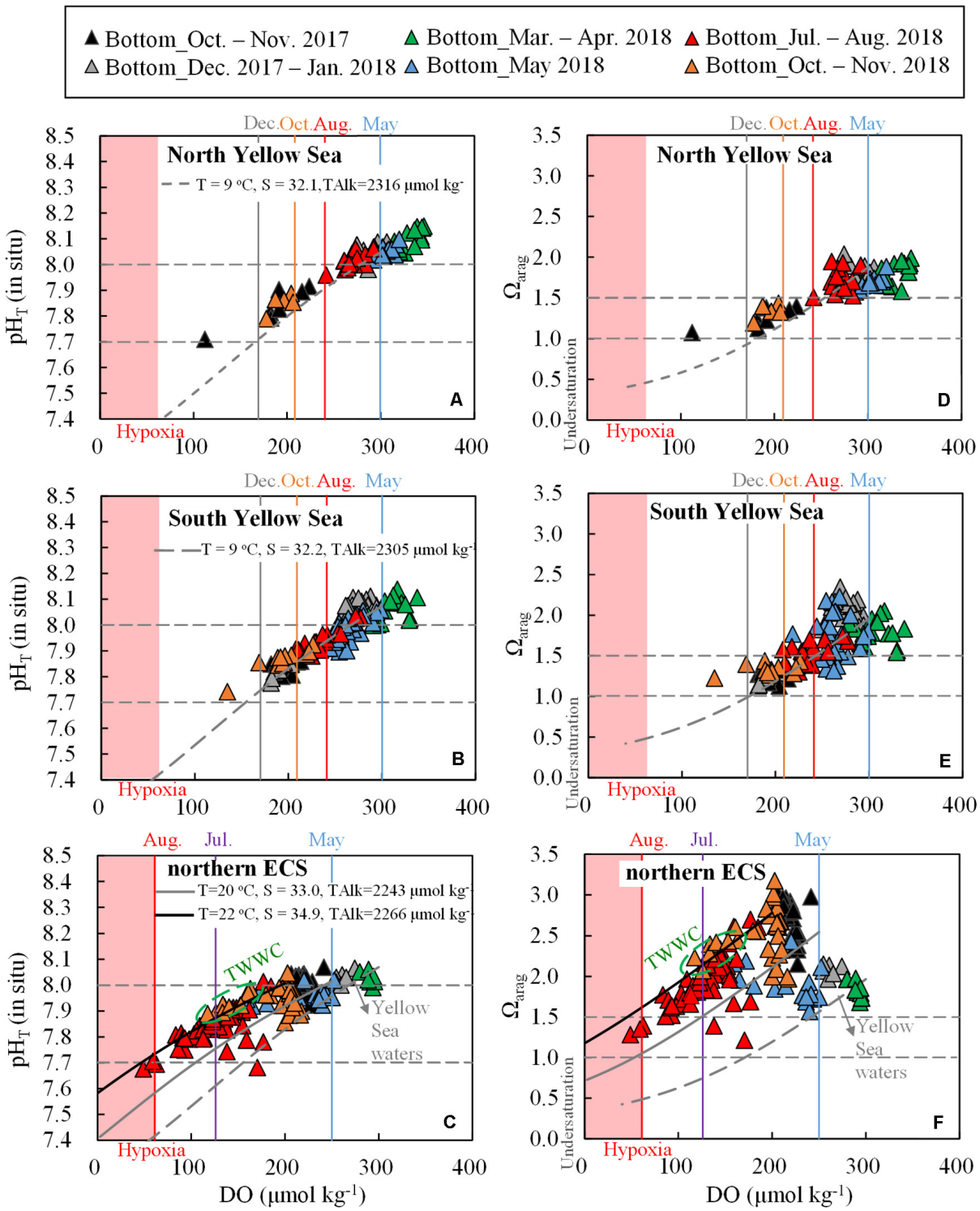


FIGURE 7 | (A–C) Bottom-water pH_T (*in situ*) versus DO and **(D–F)** Ω_{arag} versus DO. Shaded pink areas represent hypoxia (DO < 63 μmol O_2 kg^{-1}). Data points in the Yellow Sea during summer to autumn are within the YSCWM. Black and gray curves represent respiration-induced pH_T and Ω_{arag} changes, based on the Redfield equation and the corresponding net DO consumption rates in the Yellow Sea (0.6 μmol O_2 kg^{-1} d^{-1}) and northern ECS (2 μmol O_2 kg^{-1} d^{-1}). During calculation, starting conditions for the North Yellow Sea were DO = 300 μmol kg^{-1}, DIC:TAlk ratio = 0.930; starting conditions for the South Yellow Sea were DO = 300 μmol kg^{-1}, DIC:TAlk ratio = 0.925; starting conditions for the northern ECS were DO = 250 μmol kg^{-1}, DIC:TAlk ratio = 0.900, while for the ECS offshore waters (affected by the TWWC) were DO = 200 μmol kg^{-1}, DIC:TAlk ratio = 0.890. The impact of respiration on TAlk (ΔTAlk:ΔDIC = −17/106) was also included.

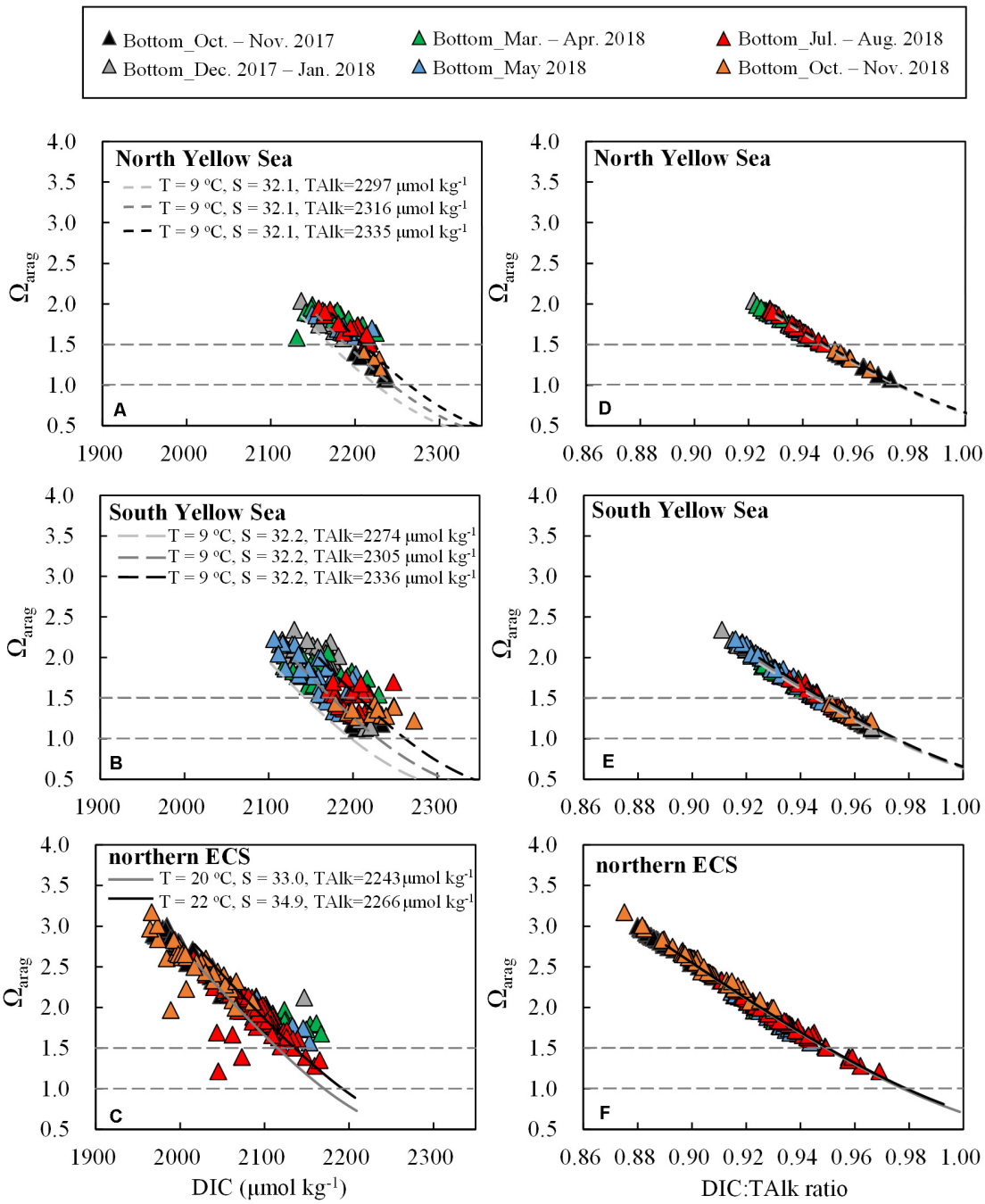


FIGURE 8 | Plots of bottom-water Ω_{arag} versus **(A–C)** DIC and **(D–F)** DIC:TAlk ratio. Black and gray curves represent ideal relationships between Ω_{arag} versus DIC and DIC:TAlk ratio using CO2SYS.XLS. During calculation, starting condition for the North Yellow Sea was DIC:TAlk ratio = 0.930; starting condition for the South Yellow Sea was DIC:TAlk ratio = 0.925; starting condition for the northern ECS was DIC:TAlk ratio = 0.900, while for the ECS offshore waters was DIC:TAlk ratio = 0.890. The impact of respiration on TAlk (ΔTAlk:ΔDIC = −17/106) was included.

TWWC intrusion (**Figures 3A,C**). Correspondingly, the earlier CO_2-rich and DO-depleted subsurface and/or bottom waters tended to approach their air-equilibrated levels (**Figure 6**). The similar autumn CO_2-releasing process has been reported earlier in the northern ECS (Shim et al., 2007; Zhai and Dai, 2009; Guo et al., 2015).

In summary, three primary processes controlled seasonal variations of bottom-water DIC, DIC:TAlk ratio, pH_T and Ω_{arag} in the Yellow Sea and northern ECS (**Figures 6D,H,L,P**). The air-sea re-equilibration played a fundamental role in wintertime carbonate system parameters. In summer, the community respiration beneath thermoclines dominated the

increases in bottom-water DIC and DIC:TAlk ratio and the declines in bottom-water pH_T and Ω_{arag}. Moreover, the autumnal collapse of thermoclines driven by cooling-induced water-column overturning or episodic wind-driven mixing events led to bottom-water ventilation, causing these carbonate system parameters to approach their air-equilibrated levels.

Comparison With Other Studies Relating to Seasonal Acidification in the Yellow Sea and the Northern East China Sea

In the Yellow Sea, respiration-induced declines in subsurface pH_T, Ω_{arag} and DO from spring to autumn were first reported by Zhai et al. (2014b). Low pH_T values of 7.79–7.90, low Ω_{arag} values of 1.13–1.40 and low DO% of 57–66% dominated subsurface waters of the central North Yellow Sea in autumn 2011 (Zhai et al., 2014b). During a summer flood in 2013, the community respiration coupled with freshwater dilution contributed to the occurrence of corrosive waters ($\Omega_{arag} < 1$) along the north coast of the North Yellow Sea, near the Yalu River estuary (Zhai et al., 2015). Stratification was an important factor affecting the accumulation of respiration-induced CO_2 in the Yellow Sea, especially in the YSCWM (Xu et al., 2018). The respiration-induced CO_2 was accumulated during summer and autumn in the YSCWM-dominated area, leading to one third of the surveyed areas in the Yellow Sea to have $pH_T < 7.9$ and $\Omega_{arag} < 1.5$ in subsurface and bottom waters (Zhai, 2018). Also, a significant DO depletion occurred in the summertime and autumnal YSCWM, with the lowest DO% of 45% observed in autumn (Xu et al., 2016; Zhai, 2018). In addition, the bottom water on the Korean side of the South Yellow Sea was already undersaturated with aragonite (with DO% of ∼60%) in autumn (Choi et al., 2020), presumably due to ocean dumping of organic materials in the central Yellow Sea (Choi et al., 2020).

In the northern ECS off the Changjiang Estuary, low pH_T values of ∼7.8 and low Ω_{arag} values of ∼1.5 have been reported earlier in its summertime hypoxic zone (Cai et al., 2011; Wang B. et al., 2017). The term hypoxia refers to a DO threshold of lower than 2 mg L^{-1}, that is, 63 μmol O_2 L^{-1} or approximately 30% saturation (Dauer et al., 1992; Rabalais et al., 2010). The summertime hypoxic area in the ECS was estimated at greater than 12,000 km^2 (or 432 km^3 volume, Chen et al., 2007), which was comparable to the largest coastal hypoxic zones observed in the world (Diaz, 2001; Fennel and Testa, 2019). To date, aragonite undersaturation has not been observed in the northern ECS, although the lowest summertime bottom-water Ω_{arag} value in the outer Changjiang Estuary has showed an alarming decline in recent years from 1.70 in July 2009 (Chou et al., 2013a) to 1.52 in July 2016 and to 1.39 in July 2017 (Xiong et al., 2019). Chou et al. (2013a) predicted that the combination of intensifying eutrophication and increasing atmospheric CO_2 would push the bottom water of the Changjiang plume area toward undersaturated with respect to aragonite (Ω_{arag} ∼0.8) by the end of this century.

The integrated results of these fragmented studies have suggested that the present-day lowest bottom-water Ω_{arag} in the Yellow Sea was usually lower than that in the northern ECS. The Yellow Sea might be more vulnerable than the adjacent ECS shelf to the potentially negative effects of CO_2 acidification (Zhai et al., 2014b). However, the difference in behaviors of bottom-water DO depletion and CO_2 acidification between the two coastal seas was not investigated in previous studies.

In this new research, the lowest regional bottom-water Ω_{arag} values were detected at 1.07 in the Yellow Sea and 1.21 in the northern ECS (**Figures 6M–O**), which were generally in agreement with the previous results. However, the lowest bottom-water pH_T and Ω_{arag} in the northern ECS observed in this study (7.68 and 1.21 in July 2018) were lower than those reported in previous studies. This might suggest that the respiration-induced CO_2 acidification was developing rapidly in the northern ECS bottom waters off the Changjiang Estuary. Note that our results of this study were based on a latest transregional investigation, spanning all four seasons. Seasonal evolutions and controls of bottom-water DO and carbonate system parameters in both the Yellow Sea and northern ECS were detailed in this study (**Figures 2**, **6**). Moreover, the different behaviors of bottom-water DO depletion and CO_2 acidification in the two coastal seas will be discussed in section "Different Behaviors of Bottom-Water DO Depletion and CO_2 Acidification in the Two Contrasting Coastal Seas."

Different Behaviors of Bottom-Water DO Depletion and CO_2 Acidification in the Two Contrasting Coastal Seas

The community respiration beneath thermoclines induces both DO depletions and CO_2 accumulations, thus depressing bottom-water pH_T and Ω_{arag}. The following stoichiometric relationships (assuming the usual Redfield ratio) were used to characterize this respiration-driven process:

$$(CH_2O)_{106}(NH_3)_{16}H_3PO_4 + 138O_2 + 18HCO_3^- \rightarrow 124CO_2 + 16NO_3^- + HPO_4^{2-} + 140H_2O \quad (3)$$

All acid-base conversions were based on the dominant species in the saline aquatic environment at a pH of ∼8.

The coastal hypoxia is usually associated with the respiration-induced CO_2 acidification (Cai et al., 2011; Melzner et al., 2013). However, the Yellow Sea bottom-water DO values were always much higher than the threshold for hypoxia, despite the occurrence of seasonal acidification (**Figures 7A,B,D,E**). In contrast, the northern ECS off the Changjiang Estuary is a well-documented summertime hypoxic zone (e.g., Li et al., 2002; Zhu et al., 2011). In the ECS hypoxic zone, quite low pH_T values of ∼7.7 and critically low Ω_{arag} values of < 1.5 were observed in summer (**Figures 7C,F**).

To investigate the different behaviors of bottom-water DO depletion and CO_2 acidification in the Yellow Sea and the northern ECS, we compared their yearly initial conditions and respiration processes, and then modeled seasonal changes in bottom-water DO, pH_T and Ω_{arag} in the two contrasting coastal seas.

Wintertime Re-equilibration Naturally Preconditions the Water Column

At the beginning of the warm-season stratification formation, yearly initial DO values (i.e., air-equilibrated wintertime/springtime values) in cold Yellow Sea waters (∼300 μmol kg^{-1} at 9°C) were higher than those in the warmer northern ECS waters (∼250 μmol kg^{-1} at 20°C) (**Figure 7**). The yearly initial pH_T values in the two coastal seas were similar (8.0–8.1, **Figures 7A–C**), whereas yearly initial DIC:TAlk ratio and Ω_{arag} values were quite different. The Yellow Sea had higher yearly initial DIC:TAlk ratio (0.925–0.930) and lower yearly initial Ω_{arag} values (1.8–1.9) than those in the northern ECS (DIC:TAlk ratio ∼0.9 and Ω_{arag} ∼2.5) (**Figures 6E–G**, **7D–F**).

In these cold seasons that were free from community respiration, the north-to-south decreasing gradient of yearly initial DIC:TAlk ratio was dominated by the CO_2 solubility. Seawater CO_2 solubility increased with the decrease of temperature (Weiss, 1974), resulting in lower [CO_3^{2-}] and Ω_{arag} in colder waters compared with warmer waters. Note that the internal temperature effect only accounts for < 5% of the variations in Ω_{arag} (Zhai et al., 2014b). With respect to pH_T, however, the CO_2-dissolving induced [H^+] increase in cold waters was greatly canceled out by the [H^+] decrease due to the internal temperature effect of pH (Yamamoto S. et al., 2012; Cai et al., 2020). Therefore, the yearly initial pH_T varied minimally along the north-to-south latitude gradient. Even over diverse ecosystems found between the poles and tropics, the air-equilibrated pH_T values changed limitedly in a narrow range of 8.020–8.074 (Hofmann et al., 2011). In a word, the air-equilibrated Ω_{arag} was much more sensitive to seawater temperature than the air-equilibrated pH_T. Wintertime re-equilibration naturally preconditioned the water column to have different yearly initial values of DO, pH_T, Ω_{arag} and DIC:TAlk ratio.

Different Respiration Rates and Duration

Not only yearly initial values of DO and carbonate system parameters, but also respiration rates and duration were quite different between the two coastal seas. The Yellow Sea (especially within the YSCWM) showed higher bottom-water AOU in autumn than in summer (**Figures 5A,B**). In the northern ECS, bottom-water AOU reached the maximum value in summer and then sharply declined in autumn (**Figure 5C**). Although the respiration duration beneath thermoclines in the northern ECS was shorter than the Yellow Sea, nearly one third of summertime bottom-water AOU values (with a range of 113–179 μmol kg^{-1}) in northern ECS was about 24–97% higher than autumnal bottom-water AOU values in the Yellow Sea (91 ± 15 μmol kg^{-1}). Also, the bottom-water averaged apparent DO depletion rate in the northern ECS (1.8 μmol O_2 kg^{-1} d^{-1}) were about three times higher than that in the Yellow Sea (0.6 μmol O_2 kg^{-1} d^{-1}), indicating a much higher net community respiration rate in the northern ECS as compared to the Yellow Sea.

In the Yellow Sea, the low bottom-water averaged apparent DO depletion rate of 0.6 μmol O_2 kg^{-1} d^{-1} was comparable to the net community respiration rate previously observed in the northern area of the YSCWM (Zhai et al., 2014b; Li and Zhai, 2019). In the northern ECS, however, its bottom-water averaged apparent DO depletion rate of 1.8 μmol O_2 kg^{-1} d^{-1} was lower than the lower limit of field-measured community respiration rates (∼3 μmol O_2 kg^{-1} d^{-1}) on the basis of DO decreasing in dark incubation experiments (Chen et al., 2006; Zhu et al., 2016). A quick formation of bottom-water hypoxia was observed off the Changjiang Estuary within only 6 days after a typhoon disturbance (Wang B. et al., 2017), equivalent to an extremely high DO drawdown rate of 22 μmol O_2 kg^{-1} d^{-1}. Both bottle incubation results and the field data deduction suggest that the northern ECS should have relatively high net community respiration rates in its summertime oxygen-depleted bottom waters. However, the central Yellow Sea accumulated respiration products beneath the thermocline in summer and autumn, while the northern ECS bottom waters preserved them only in summer.

Coupling of Bottom-Water DO Depletion and CO_2 Acidification

To further explore the differentiation of bottom-water DO depletion and CO_2 acidification in the Yellow Sea and northern ECS, seasonal changes in bottom-water DO, pH_T and Ω_{arag} were modeled based on Eq. (3) and different yearly initial values and respiration rates in the two coastal seas. When the respiration-induced DO depletion process started, DIC changed according the traditional Redfield ratio, i.e., ΔDIC:ΔAOU = 106:138, and the impact of respiration on TAlk (ΔTAlk:ΔDIC = −17/106) was also considered. During calculation, as detailed above, yearly initial conditions in the North Yellow Sea were DO = 300 μmol O_2 kg^{-1}, DIC:TAlk ratio = 0.930; in the South Yellow Sea, yearly initial DO = 300 μmol O_2 kg^{-1}, yearly initial DIC:TAlk ratio = 0.925; in the northern ECS, yearly initial DO = 250 μmol O_2 kg^{-1}, yearly initial DIC:TAlk ratio = 0.900. The net community respiration rates were assumed to be 0.6 μmol O_2 kg^{-1} d^{-1} in the Yellow Sea and 2 μmol O_2 kg^{-1} d^{-1} in the northern ECS. Temperature, salinity and TAlk were set to the mean value in bottom waters in the given region: T = 9°C, S = 32.1, and TAlk = 2316 μmol kg^{-1} in the North Yellow Sea; T = 9°C, S = 32.1, and TAlk = 2305 μmol kg^{-1} in the South Yellow Sea; T = 20°C, S = 33.0, and TAlk = 2243 μmol kg^{-1} in the northern ECS. The effect of mixing with the northeast-monsoon-driven ZFCC was not included (affected only several nearshore stations, **Figure 1G**), while the effect of the year-round TWWC intrusion was included. Starting conditions for the TWWC-affected offshore waters were DO = 200 μmol kg^{-1} and DIC:TAlk ratio = 0.890.

Field-measured bottom-water pH_T versus DO and Ω_{arag} versus DO reasonably followed those Redfield lines in both the Yellow Sea and northern ECS (**Figure 7**). The Redfield-based coupling of DO depletion and CO_2 acidification suggested again that both pH_T and Ω_{arag} declines in the two coastal seas were controlled by the community respiration beneath thermoclines. At those low-oxygen levels, the Yellow Sea data showed consistently lower bottom-water pH_T and Ω_{arag} values than those in the northern ECS (**Figure 7**). It is worthwhile to note that field-measured observations in the northern ECS fell between the local reaction in the northern ECS (solid gray curves) and the TWWC-affected reaction (solid black curves,

Figures 7C,F), suggesting the both the local respiration and the TWWC intrusion influenced DO and carbonate system parameters in the northern ECS.

In summary, the Yellow Sea had higher yearly initial DO values, higher yearly initial DIC:TAlk ratio but lower yearly initial Ω_{arag} values than those in the northern ECS. However, yearly initial pH_T values exhibited only a few differences between the two coastal seas. The different behaviors of yearly initial pH_T and Ω_{arag} were consistent with their different responses to the temperature variability. Moreover, higher CO_2 solubility together with the respiration-induced CO_2 additions resulted in the colder Yellow Sea waters to have higher DIC:TAlk ratio and thus lower Ω_{arag} as compared with those in warm northern ECS waters. Assuming that the DIC:TAlk ratio difference (0.025) between 0.925 in wintertime/springtime Yellow Sea waters (**Figure 6F**) and a typical open-ocean seawater DIC:TAlk ratio of 0.900 (**Figure 6G**) was only induced by CO_2 solubility difference, and considering the excellent linear relationship between bottom-water Ω_{arag} and DIC:TAlk ratio, the contribution of the yearly initial high CO_2 solubility to summertime low Ω_{arag} in the Yellow Sea (with the averaged DIC:TAlk ratio of 0.944 in summer, section "DIC and DIC:TAlk Ratio") was estimated to be $0.025/0.044 \times 100\% = 57\%$. Similarly, the contribution of the yearly initial high CO_2 solubility to autumnal low Ω_{arag} in the Yellow Sea (with the averaged DIC:TAlk ratio of 0.959 in autumn, section "DIC and DIC:TAlk Ratio") was estimated to be $0.025/0.059 \times 100\% = 42\%$.

Concurrent Hypoxia and CO_2 Acidification in the Northern ECS off Changjiang Estuary

In 2018, we observed concurrent hypoxia (DO 49–63 μmol O_2 kg^{-1}) and CO_2 acidification (pH_T 7.68–7.71, Ω_{arag} 1.28–1.39) at three sampling sites in the northern ECS off the Changjiang Estuary in the middle of July, although the modeling prediction suggested that the bottom-water hypoxia (DO 61 μmol O_2 kg^{-1}) and CO_2 acidification (pH_T 7.59, Ω_{arag} 1.05) should concurrently occur in early August (**Figures 7C,F**). Apart from the intensive respiration rates (section "Different Respiration Rates and Duration"), the excess DO decline was likely attributed to those non-local drivers of summertime hypoxia in the northern ECS bottom waters, such as the TWWC intrusion (**Figures 7C,F**, Wei et al., 2015; Wang B. et al., 2017) and the nearshore upwelling of the Kuroshio branch (Yang et al., 2011, 2012, 2013; Qian et al., 2017). Sediment oxygen consumption may also contribute to the hypoxia formation in the northern ECS (Zhang et al., 2017; Zhou et al., 2017).

In the Yellow Sea, declines in DO, pH_T, and Ω_{arag} in the Yellow Sea were much less than those in the northern ECS (**Figure 7**). Especially the modeled October DO in Yellow Sea was ∼150 μmol O_2 kg^{-1} higher than the modeled August DO in the northern ECS. Even if the water stratification could have lasted in the central Yellow Sea (maintaining the YSCWM) until December, the modeling prediction of bottom-water DO in December (170 μmol O_2 kg^{-1}) would be still quite high, despite that extremely low pH_T and Ω_{arag} values (7.73 and 0.96, respectively) would dominate the YSCWM in this early winter month. The modeled results in December were comparable with those field-measured values at the four deep stations (in the central South Yellow Sea) during our early winter survey (**Figures 7B,E**). Therefore, the seasonal hypoxia that usually associated with the respiration-induced coastal CO_2 acidification did not occur in the present-day central Yellow Sea.

Recently, studies relating the concurrency of bottom hypoxia and CO_2 acidification were conducted in many other coastal zones. For example, summertime hypoxia and acidification (pH < 7.7) covered almost one-third of an aquaculture area in southern nearshore waters of the North Yellow Sea (Zhang et al., 2018). In the central Bohai Sea, the near-hypoxic (DO < 90 μmol O_2 kg^{-1}) and concurrent low pH_T (∼7.7) and Ω_{arag} (∼1.3) were observed in late summer (Zhai et al., 2019; Song et al., 2020). In the northern South China Sea shelf, summertime low pH values were mainly measured nearshore in the hypoxic zone, along with relatively high DIC concentrations (Zhao et al., 2020). In the hypoxic zone of the northern Gulf of Mexico, the lowest bottom DO value obtained in summer 2010 (only at 11 μmol O_2 kg^{-1}) matched with the lowest pH_T (7.60) and Ω_{arag} (1.63) values (Hu et al., 2017). Even in the Chesapeake Bay, both anoxia and the production of hydrogen sulfide (H_2S) were observed in summertime subsurface waters (with pH_T < 7.6, Cai et al., 2017). Diverging from all the above-mentioned situations, in the well-buffered Corpus Christi Bay located along the Texas coast, relatively high pH_T (>7.8) and Ω_{arag} (>2.6) values were revealed in its summertime hypoxia zone (McCutcheon et al., 2019). The high buffering capacity in the Corpus Christi Bay was attributed to abundant seagrass meadows and the strong evaporation that introduced low pCO_2, high pH_T and Ω_{arag} waters (McCutcheon et al., 2019). Hence, the concurrent occurrence of coastal hypoxia and CO_2 acidification does not always hold true in all situations. Such issues are worthy of further investigation in order to be better understood.

Correlations Between Bottom-Water Ω_{arag} Versus DIC and DIC:TAlk Ratio

We also found that bottom-water Ω_{arag} was negatively correlated with DIC (**Figures 8A–C**). The correlations in the Yellow Sea and northern ECS roughly fit in with several ideal relationships between Ω_{arag} and DIC that were estimated using CO2SYS.XLS. During simulation, regional mean TAlk with standard deviation (**Table 1** and **Figures 4A–C**) and typical wintertime and springtime DIC:TAlk ratio (**Table 1** and **Figures 6E–G**) were set for starting conditions, while fixed regional mean salinity and temperature were used (**Figures 2A–C**). At a given DIC, Ω_{arag} decreased along with TAlk decrease. An early-spring plot near the Yalu river estuary with moderately low TAlk value of 2265 μmol kg^{-1} deviated from the three ideal relationships in the North Yellow Sea (**Figure 8A**). Also, several summertime plots affected by the CDW with low TAlk values of 2110–2183 μmol kg^{-1} and autumnal plots affected by the ZFCC with low TAlk values of 2138–2185 μmol kg^{-1}

deviated from the two ideal relationships in the northern ECS (**Figure 8C**).

By comparison, the correlation between Ω_{arag} and DIC:TAlk ratio (**Figures 8D–F**) was much tighter than that between Ω_{arag} and DIC. This was because that DIC and TAlk were inversely related to Ω_{arag} with higher DIC decreasing Ω_{arag} and higher TAlk increasing Ω_{arag} in seawater (Wanninkhof et al., 2015). Seawater DIC:TAlk ratio, by definition, could reflect the fraction of free CO_2 in the DIC pool (Cai et al., 2020), which essentially determined Ω_{arag}. When more CO_2 was dissolved in seawater (solubility and/or respiration induced CO_2 additions) as indicated by higher DIC:TAlk ratio, more CO_3^{2-} ions were titrated, resulting in lower Ω_{arag} values. On condition that the DIC:TAlk ratio varied between 0.83 and 0.95, the correlation was expressed linearly as $\Omega_{arag} = -24.08 \times (\text{DIC:TAlk}) + 24.3$ ($r = 0.992$, $n = 832$), exhibiting little differences among those diverse waters involved in this study (**Supplementary Figure S8**). It might suggest that DIC:TAlk ratio was a qualified indicator of Ω_{arag} in seawater, even in contrasting coastal waters.

SUMMARY AND IMPLICATIONS

Seasonal variations and the controls of bottom-water carbonate system parameters and DO in the Yellow Sea and northern ECS were examined in this study. Wintertime air-sea re-equilibration, summertime respiration under thermoclines and autumnal water-column overturning are three primary processes controlling seasonal variations in these parameters. At the beginning of warm-season stratification formation, the colder Yellow Sea waters had higher DO values but lower Ω_{arag} values than those in the relatively warmer northern ECS waters, while yearly initial pH_T values were similar in the two coastal seas. During warm seasons, the Yellow Sea accumulated respiration products under the thermocline in summer and autumn, while the northern ECS bottom waters preserved them only in summer. Higher CO_2 solubility together with the respiration-induced CO_2 additions caused the colder Yellow Sea waters to have higher DIC:TAlk ratio and thus lower Ω_{arag} as compared with those in warm northern ECS waters. The seasonal hypoxia that usually associated with the respiration-induced coastal CO_2 acidification did not occur in the central Yellow Sea. In contrast, the summertime hypoxia and CO_2 acidification concurrently occurred in the northern ECS.

We could also evaluate how seawater acidity ($[H^+]$) in the Yellow Sea and northern ECS along the north-to-south latitude gradient respond to coastal acidification, considering starting conditions for the North Yellow Sea (T = 6°C, S = 32.1, TAlk = 2316 μmol kg^{-1}, DIC:TAlk = 0.930), for the South Yellow Sea (T = 9°C, S = 32.1, TAlk = 2305 μmol kg^{-1}, DIC:TAlk = 0.925), and for the northern ECS (T = 17°C, S = 33.0, TAlk = 2243 μmol kg^{-1}, DIC:TAlk = 0.900). These starting conditions were those late spring levels in the given regions when water stratification was just formed. For an increase of seawater fCO_2 of 1 μatm, $[H^+]$ increased by 1.97×10^{-5} μmol kg^{-1} in the North Yellow Sea, by 1.94×10^{-5} μmol kg^{-1} in the South Yellow Sea and by 1.90×10^{-5} μmol kg^{-1} in the northern ECS, indicating a north-to-south decline in the sensitivity to coastal acidification stresses, related to atmospheric CO_2 intrusion and/or community respiration induced CO_2 addition. A similar north-to-south-decreasing gradient along the U.S. East Coast and Gulf of Mexico has been reported by Wang et al. (2013) based on a summertime cross-shelf observation. The $[H^+]$ increase related to an increase of seawater fCO_2 of 1 μatm has been estimated to be 2.0×10^{-5} μmol kg^{-1} in the Gulf of Maine, 11% greater than that in the Gulf of Mexico (1.8×10^{-5} μmol kg^{-1}). The northeastern U.S. shelf waters appear more susceptible to CO_2 acidification than their southern counterparts, likely due to relatively low temperature and thus high CO_2 solubility in the northeastern regions. Recent studies have predicted that waters unfavorable to calcification will exist year round in the subsurface waters within northern shelf waters along China's and U.S. eastern coasts, i.e., the North Yellow Sea (Li and Zhai, 2019) and Gulf of Maine (Wang Z. A. et al., 2017), by the middle of the century under the future ocean acidification. Consequently, cold northern shelf waters appear to be more vulnerable to the potentially negative effects of ocean acidification. In the future, more studies are needed to quantify ecological responses of different coastal zones to those acidification pressures, particularly in the relatively colder northern shelf waters.

DATA AVAILABILITY STATEMENT

The mapping dataset of dissolved oxygen and carbonate system parameters reported in this study is available at figshare.com via doi: 10.6084/m9.figshare.12630335.

AUTHOR CONTRIBUTIONS

WZ designed the research and performed one of the field surveys. TX performed three field surveys and analyzed the data set and drafted an early version of the manuscript. QW, CL, and YZ separately performed the other field surveys. SW, SL, SY, TX, and CL contributed to the data collection. All authors contributed to discussion and revision of the manuscript.

FUNDING

This research was jointly supported by the State Key R&D project of China (Grant No. 2016YFA0601103), the National Natural Science Foundation of China (Grant Nos. 91751207 and 41876085) and the Basic Scientific Fund of the National Public Research Institutes of China (Grant No. GY0219JH01). Sampling surveys were separately supported by the National Natural Science Foundation of China (via Ship−time Sharing Projects during the Open Research Cruises conducted in the Bohai and Yellow Seas in 2017 and 2018 onboard R/V *Dongfanghong 2* with Cruise Numbers of NORC2017-01 and NORC2018-01, and in the

Changjiang Estuary in 2018 onboard R/V *Kexue 3* with the Cruise Number of NORC2018-03), the Yellow Sea Fisheries Research Institute of Chinese Academy of Fishery Sciences (onboard R/V *Beidou*), and the First Institute of Oceanography, Ministry of Natural Resources, China (onboard R/V *Xiangyanghong 18*).

SUPPLEMENTARY MATERIAL

The Supplementary Material for this article can be found online at: https://www.frontiersin.org/articles/10.3389/fmars.2020.00686/full#supplementary-material

REFERENCES

Anderson, L. A. (1995). On the hydrogen and oxygen content of marine phytoplankton. *Deep Sea Res. Part I Oceanogr. Res. Pap.* 42, 1675–1680. doi: 10.1016/0967-0637(95)00072-E

Bates, N. R., Mathis, J. T., and Cooper, L. W. (2009). Ocean acidification and biologically induced seasonality of carbonate mineral saturation states in the western Arctic Ocean. *J. Geophys. Res.* 114:C11007. doi: 10.1029/2008JC004862

Benson, B. B., and Krause, D. (1984). The concentration and isotopic fractionation of oxygen dissolved in fresh water and seawater in equilibrium with the atmosphere. *Limnol. Oceanogr.* 29, 620–632. doi: 10.4319/lo.1984.29.3.0620

Bockmon, E. E., and Dickson, A. G. (2014). A seawater filtration method suitable for total dissolved inorganic carbon and pH analyses. *Limnol. Oceanogr. Methods* 12, 191–195. doi: 10.4319/lom.2014.12.191

Cai, W.-J., Hu, X.-P., Huang, W.-J., Murrell, M. C., Lehrter, J. C., Lohrenz, S. E., et al. (2011). Acidification of subsurface coastal waters enhanced by eutrophication. *Nat. Geosci.* 4, 766–770. doi: 10.1038/ngeo1297

Cai, W.-J., Huang, W.-J., Lutherlll, G. W., Pierrot, D., Li, M., Testa, J., et al. (2017). Redox reactions and weak buffering capacity lead to acidification in the Chesapeake Bay. *Nat. Commun.* 8:369.

Cai, W.-J., Xu, Y.-Y., Feely, R. A., Wanninkhof, R., Jönsson, B., Alin, S. R., et al. (2020). Controls on surface water carbonate chemistry along North American ocean margins. *Nat. Commun.* 11:2691. doi: 10.1038/s41467-020-16530-z

Caldeira, K., and Wickett, M. E. (2003). Oceanography: anthropogenic carbon and ocean pH. *Nature* 425:365. doi: 10.1038/425365a

Cao, Z. M., Dai, M. H., Zheng, N., Wang, D. L., Li, Q., Zhai, W. D., et al. (2011). Dynamics of the carbonate system in a large continental shelf system under the influence of both a river plume and coastal upwelling. *J. Geophys. Res.* 116:G02010. doi: 10.1029/2010JG001596

Chen, C.-C., Chiang, K. P., Gong, G. C., Shiah, F. K., Tseng, C. M., and Liu, K. K. (2006). Importance of planktonic community respiration on the carbon balance of the East China Sea in summer. *Glob. Biogeochem. Cycles* 20:GB4001. doi: 10.1029/2005GB002647

Chen, C.-C., Gong, G.-C., and Shiah, F.-K. (2007). Hypoxia in the East China Sea: one of the largest coastal low-oxygen areas in the world. *Mar. Environ. Res.* 64, 399–408. doi: 10.1016/j.marenvres.2007.01.007

Chen, C. T. A. (2009). Chemical and physical fronts in the Bohai, Yellow and East China seas. *J. Mar. Syst.* 78, 394–410. doi: 10.1016/j.jmarsys.2008.11.016

Chen, C. T. A., and Wang, S. L. (1999). Carbon, alkalinity and nutrient budget on the East China Sea continental shelf. *J. Geophys. Res.* 104, 20675–20686. doi: 10.1029/1999JC900055

Choi, Y., Cho, S., and Kim, D. (2020). Seasonal variation in aragonite saturation states and the controlling factors in the southeastern Yellow Sea. *Mar. Pollut. Bull.* 150:110695. doi: 10.1016/j.marpolbul.2019.110695

Chou, W.-C., Gong, G.-C., Hung, C. C., and Wu, Y. H. (2013a). Carbonate mineral saturation states in the East China Sea: present conditions and future scenarios. *Biogeosciences* 10, 6453–6467. doi: 10.5194/bg-10-6453-2013

Chou, W.-C., Gong, G.-C., Cai, W.-J., and Tseng, C.-M. (2013b). Seasonality of CO_2 in coastal oceans altered by increasing anthropogenic nutrient delivery from large rivers: evidence from the Changjiang-East China Sea system. *Biogeosciences* 10, 3889–3899. doi: 10.5194/bg-10-3889-2013

Chou, W.-C., Gong, G.-C., Sheu, D. D., Jan, S., Hung, C.-C., and Chen, C.-C. (2009). Reconciling the paradox that the heterotrophic waters of the East China Sea shelf act as a significant CO_2 sink during the summertime: evidence and implications. *Geophys. Res. Lett.* 36:L15607. doi: 10.1029/2009GL038475

Dauer, D. M., Rodi, A. J., and Ranasinghe, J. A. (1992). Effects of low dissolved oxygen events on the macrobenthos of the lower Chesapeake Bay. *Estuaries* 15, 384–391. doi: 10.2307/1352785

Diaz, R. J. (2001). Overview of hypoxia around the world. *J. Environ. Qual.* 30, 275–281. doi: 10.2134/jeq2001.302275x

Dickson, A. G. (1990). Standard potential of the reaction: AgCl(s) + 1/2H2(g) = Ag(s) + HCl(aq), and the standard acidity constant of the ion HSO4- in synthetic sea water from 273.15 to 318.15 K. *J. Chem. Thermodyn.* 22, 113–127. doi: 10.1016/0021-9614(90)90074-Z

Dickson, A. G., Sabine, C. L., and Christian, J. R. (2007). *Guide to Best Practices for Ocean CO_2 Measurements PICES*. (Sidney: North Pacific Marine Science Organization), 1–191.

Doney, S. C., Fabry, V. J., Feely, R. A., and Kleypas, J. A. (2009). Ocean acidification: the other CO_2 problem. *Annu. Rev. Mar. Sci.* 1, 169–192. doi: 10.1146/annurev.marine.010908.163834

Ekstrom, J. A., Suatoni, L., Cooley, S. R., Pendleton, L. H., Waldbusser, G. G., Cinner, J. E., et al. (2015). Vulnerability and adaptation of US shellfisheries to ocean acidification. *Nat. Clim. Change* 5, 207–214. doi: 10.1038/nclimate2508

Eyre, B. D., Cyronak, T., Drupp, P., De Carlo, E. H., Sachs, J. P., and Andersson, A. J. (2018). Coral reefs will transition to net dissolving before end of century. *Science* 359, 908–911. doi: 10.1126/science.aao1118

Fabry, V. J. (2008). Marine calcifiers in a high-CO_2 ocean. *Science* 320, 1020–1022. doi: 10.1126/science.1157130

Fabry, V. J., McClintock, J. B., Mathis, J. T., and Grebmeier, J. M. (2009). Ocean acidification at high latitudes: the bellwether. *Oceanography* 22, 160–171. doi: 10.5670/oceanog.2009.105

Feely, R. A., Alin, S. R., Newton, J., Sabine, C. L., Warner, M., Devol, A., et al. (2010). The combined effects of ocean acidification, mixing, and respiration on pH and carbonate saturation in an urbanized estuary. *Estuar. Coast. Shelf Sci.* 88, 442–449. doi: 10.1016/j.ecss.2010.05.004

Feely, R. A., Sabine, C. L., Byrne, R. H., Millero, F. J., Dickson, A. G., Wanninkhof, R., et al. (2012). Decadal changes in the aragonite and calcite saturation state of the Pacific Ocean. *Glob. Biogeochem. Cycles* 26:GB3001. doi: 10.1029/2011GB00415

Feely, R. A., Sabine, C. L., Hernandez-Ayon, J. M., Ianson, D., and Hales, B. (2008). Evidence for upwelling of corrosive "acidified" water onto the continental shelf. *Science* 320, 1490–1492. doi: 10.1126/science.1155676

Fennel, K., and Testa, J. M. (2019). Biogeochemical controls on coastal hypoxia. *Annu. Rev. Mar. Sci.* 11, 105–130. doi: 10.1146/annurev-marine-010318-095138

Gruber, N., Hauri, C., Lachkar, Z., Loher, D., Frölicher, T. L., and Plattner, G. K. (2012). Rapid progression of ocean acidification in the California current system. *Science* 337, 220–223. doi: 10.1126/science.1216773

Guo, X. H., Zhai, W. D., Dai, M. H., Zhang, C., Bai, Y., Xu, Y., et al. (2015). Air-sea CO_2 fluxes in the East China Sea based on multiple-year underway observations. *Biogeosciences* 12, 5495–5514. doi: 10.5194/bg-12-5495-2015

He, X. Q., Bai, Y., Pan, D. L., Chen, C. T. A., Cheng, Q., Wang, D. F., et al. (2013). Satellite views of the seasonal and interannual variability of phytoplankton blooms in the eastern China seas over the past 14 yr (1998–2011). *Biogeosciences* 10, 4721–4739. doi: 10.5194/bg-10-4721-2013

Hedges, J. I., Baldock, J. A., Gélinas, Y., Lee, C., Peterson, M. L., and Wakeham, S. G. (2002). The biochemical and elemental compositions of marine plankton: a NMR perspective. *Mar. Chem.* 78, 47–63. doi: 10.1016/S0304-4203(02)00009-9

Hofmann, G. E., Smith, J. E., Johnson, K. S., Send, U., Levin, L. A., Micheli, F., et al. (2011). High-frequency dynamics of ocean pH: a multi-ecosystem comparison. *PLoS One* 6:e28983. doi: 10.1371/journal.pone.0028983

Hu, X. P., Li, Q., Huang, W. J., Chen, B. S., Cai, W. J., Rabalais, N. N., et al. (2017). Effects of eutrophication and benthic respiration on water column carbonate chemistry in a traditional hypoxic zone in the Northern Gulf of Mexico. *Mar. Chem.* 194, 33–42. doi: 10.1016/j.marchem.2017.04.004

Huang, W. J., Wang, Y. C., and Cai, W. J. (2012). Assessment of sample storage techniques for total alkalinity and dissolved inorganic carbon in seawater. *Limnol. Oceanogr. Methods* 10, 711–717. doi: 10.4319/lom.2012.10.711

Jiang, Z. P., Cai, W. J., Chen, B. S., Wang, K., Han, C. H., Roberts, B. J., et al. (2019). Physical and biogeochemical controls on pH dynamics in the Northern Gulf

of Mexico during summer hypoxia. *J. Geophys. Res. Oceans* 124, 5979–5998. doi: 10.1029/2019JC015140

Jin, P., Wang, T. F., Liu, N. N., Dupont, S., Beardall, J., Boyd, P. W., et al. (2015). Ocean acidification increases the accumulation of toxic phenolic compounds across trophic levels. *Nat. Commun.* 6:8714. doi: 10.1038/ncomms9714

Lewis, E., and Wallace, D. W. R. (1998). *Program devEloped for CO_2 System Calculations, ORNL/CDIAC-105*. Oak Ridge, TN: Oak Ridge National Laboratory.

Li, C. L. (2019). *A Comparative Study of Seasonal Acidification in Southern Nearshore and Central Offshore Waters of the North Yellow Sea (in Chinese)*. Master's thesis, Shandong University, Jinan.

Li, C. L., and Zhai, W. D. (2019). Decomposing monthly declines in subsurface-water pH and aragonite saturation state from spring to autumn in the North Yellow Sea. *Cont. Shelf. Res.* 185, 37–50. doi: 10.1016/j.csr.2018.11.003

Li, D. J., Zhang, J., Huang, D. J., Wu, Y., and Liang, J. (2002). Oxygen depletion off the Changjiang (Yangtze River) Estuary. *Sci. China Ser. D* 45, 1137–1146. doi: 10.1360/02yd9110

McCutcheon, M. R., Staryk, C. J., and Hu, X. P. (2019). Characteristics of the carbonate system in a semiarid estuary that experiences summertime hypoxia. *Estuar. Coast.* 42, 1509–1523. doi: 10.1007/s12237-019-00588-0

Melzner, F., Thomsen, J., Koeve, W., Oschlies, A., Gutowska, M. A., Bange, H. W., et al. (2013). Future ocean acidification will be amplified by hypoxia in coastal habitats. *Mar. Biol.* 160, 1875–1888. doi: 10.1007/s00227-012-1954-1

Men, W., and Liu, G. S. (2015). Distribution of ^{226}Ra and the residence time of the shelf water in the Yellow Sea and the East China Sea. *J. Radioanal. Nucl. Chem.* 303, 2333–2344. doi: 10.1007/s10967-014-3749-y

Miao, J. B., Liu, X. Q., and Xue, Y. (1990). Study on the formational mechanism of the Northern Yellow (Huanghai) Sea Cold Water Mass (I)–Solution of the model (in Chinese). *Sci. China Ser. B* 12, 1311–1321.

Millero, F. J. (1979). The thermodynamics of the carbonate system in seawater. *Geochim. Cosmochim. Acta* 43, 1651–1661. doi: 10.1016/0016-7037(79)90184-4

Millero, F. J., Graham, T. B., Huang, F., Bustos-Serrano, H., and Pierrot, D. (2006). Dissociation constants of carbonic acid in sea water as a function of salinity and temperature. *Mar. Chem.* 100, 80–94. doi: 10.1016/j.marchem.2005.12.001

Mucci, A. (1983). The solubility of calcite and aragonite in seawater at various salinities, temperatures, and one atmosphere total pressure. *Am. J. Sci.* 283, 780–799. doi: 10.2475/ajs.283.7.780

Nozaki, Y., Tsubota, H., Kasemsupaya, V., Yashima, M., and Ikuta, N. (1991). Residence times of surface water and particle-reactive 210Pb and 210Po in the East China and Yellow seas. *Geochim. Cosmochim. Acta* 55, 1265–1272. doi: 10.1016/0016-7037(91)90305-O

Orr, J. C., Epitalon, J. M., and Gattuso, J. P. (2015). Comparison of ten packages that compute ocean carbonate chemistry. *Biogeosciences* 12, 1483–1510. doi: 10.5194/bg-12-1483-2015

Orr, J. C., Fabry, V. J., Aumont, O., Bopp, L., Doney, S. C., Feely, R. A., et al. (2005). Anthropogenic ocean acidification over the twenty-first century and its impacts on calcifying organisms. *Nature* 437, 681–686. doi: 10.1038/nature04095

Pelletier, G. J., Lewis, E., and Wallace, D. W. R. (2015). *CO_2SYS.XLS: A Calculator for the CO_2 System in Seawater for Microsoft Excel/VBA, Version 24*. Olympia, WA: Washington State Department of Ecology.

Qi, D., Chen, L. Q., Chen, B. S., Gao, Z. Y., Zhong, W. L., Feely, R. A., et al. (2017). Increase in acidifying water in the western Arctic Ocean. *Nat. Clim. Change* 7, 195–199. doi: 10.1038/nclimate3228

Qian, W., Dai, M. H., Xu, M., Kao, S. J., Du, C. J., Liu, J. W., et al. (2017). Non-local drivers of the summer hypoxia in the East China Sea off the Changjiang Estuary. *Estuar. Coast. Shelf Sci.* 198, 393–399. doi: 10.1016/j.ecss.2016.08.032

Rabalais, N. N., Díaz, R. J., Levin, L. A., Turner, R. E., Gilbert, D., and Zhang, J. (2010). Dynamics and distribution of natural and human-caused hypoxia. *Biogeosciences* 7, 585–619. doi: 10.5194/bg-7-585-2010

Ravaglioli, C., Lardicci, C., Pusceddu, A., Arpe, E., Bianchelli, S., Buschi, E., et al. (2020). Ocean acidification alters meiobenthic assemblage composition and organic matter degradation rates in seagrass sediments. *Limnol. Oceanogr.* 65, 37–50. doi: 10.1002/lno.11246

Redfield, A. C., Ketchum, B. H., and Richards, F. A. (1963). "The influence of organisms on the composition of sea-water," in *The Sea: ideas and Observations on Progress in the Study of the Seas,* 2nd Edn, ed. M. N. Hill (New York, NY: Interscience Publishers), 26–77.

Rheuban, J. E., Doney, S. C., McCorkle, D. C., and Jakuba, R. W. (2019). Quantifying the effects of nutrient enrichment and freshwater mixing on coastal ocean acidification. *J. Geophys. Res. Oceans* 124, 9085–9100. doi: 10.1029/2019JC015556

Sabine, C. L., Feely, R. A., Gruber, N., Key, R. M., Lee, K., Bullister, J. L., et al. (2004). The oceanic sink for anthropogenic CO_2. *Science* 305, 367–371. doi: 10.1126/science.1097403

Salisbury, J., Green, M., Hunt, C., and Campbell, J. (2008). Coastal acidification by rivers: a threat to shellfish– *EOS Trans. Am. Geophys. Union* 89, 513–528. doi: 10.1029/2008EO500001

Sarmiento, J. L., and Gruber, N. (2006). *Ocean Biogeochemical Dynamics*. Princeton, NJ: Princeton University Press, 116.

Shim, J., Kim, D., Kang, Y. C., Lee, J. H., Jang, S.-T., and Kim, C.-H. (2007). Seasonal variations in pCO_2 and its controlling factors in surface seawater of the northern East China Sea. *Cont. Shelf Res.* 27, 2623–2636. doi: 10.1016/j.csr.2007.07.005

Song, G. S., Zhao, L., Chai, F., Liu, F. F., Li, M. T., and Xie, H. X. (2020). Summertime oxygen depletion and acidification in Bohai Sea, China. *Front. Mar. Sci.* 7:252. doi: 10.3389/fmars.2020.00252

Su, J. L., and Yuan, Y. L. (2005). *Hydrology of Chinese Coastal Waters*. Beijing: China Ocean Press, 367.

Waldbusser, G. G., Hales, B., Langdon, C. J., Haley, B. A., Schrader, P., Brunner, E. L., et al. (2015). Saturation-state sensitivity of marine bivalve larvae to ocean acidification. *Nat. Clim. Change* 5, 273–280. doi: 10.1038/NCLIMATE2479

Wang, B., Chen, J. F., Jin, H. Y., Li, H. L., Huang, D. J., and Cai, W. J. (2017). Diatom bloom-derived bottom water hypoxia off the Changjiang estuary, with and without typhoon influence. *Limnol. Oceanogr.* 62, 1552–1569. doi: 10.1002/lno.10517

Wang, Z. A., Lawson, G. L., Pilskaln, C. H., and Maas, A. E. (2017). Seasonal controls of aragonite saturation states in the Gulf of Maine. *J. Geophys. Res. Oceans* 122, 372–389. doi: 10.1002/2016JC012373

Wang, Z. A., Wanninkhof, R., Cai, W. J., Byrne, R. H., Hu, X. P., Peng, T. H., et al. (2013). The marine inorganic carbon system along the Gulf of Mexico and Atlantic coasts of the United States: insights from a transregional coastal carbon study. *Limnol. Oceanogr.* 58, 325–342. doi: 10.4319/lo.2013.58.1.0325

Wanninkhof, R., Barbero, L., Byrne, R., Cai, W. J., Huang, W. J., Zhang, J. Z., et al. (2015). Ocean acidification along the Gulf Coast and East Coast of the USA. *Cont. Shelf. Res.* 98, 54–71. doi: 10.1016/j.csr.2015.02.008

Wei, Q. S., Wang, B. D., Chen, J. F., Xia, C. S., Qu, D. P., and Xie, L. P. (2015). Recognition on the forming-vanishing process and underlying mechanisms of the hypoxia off the Yangtze River estuary. *Sci. China Earth Sci.* 58, 628–648. doi: 10.1007/s11430-014-5007-0

Weiss, R. F. (1974). Carbon dioxide in water and seawater: the solubility of a non-ideal gas. *Mar. Chem.* 2, 203–215. doi: 10.1016/0304-4203(74)90015-2

Wong, G. T. F. (2012). Removal of nitrite interference in the Winkler determination of dissolved oxygen in seawater. *Mar. Chem.* 130, 28–32. doi: 10.1016/j.marchem.2011.11.003

Xiong, T. Q., Liu, P. F., Zhai, W. D., Bai, Y., Liu, D., Qi, D., et al. (2019). Export flux, biogeochemical effects, and the fate of a terrestrial carbonate system: from Changjiang (Yangtze River) Estuary to the East China Sea. *Earth Space Sci.* 6, 2115–2141. doi: 10.1029/2019EA000679

Xu, X. M., Zang, K. P., Huo, C., Zheng, N., Zhao, H. D., Wang, J. Y., et al. (2016). Aragonite saturation state and dynamic mechanism in the southern Yellow Sea, China. *Mar. Pollut. Bull.* 109, 142–150. doi: 10.1016/j.marpolbul.2016.06.009

Xu, X. M., Zheng, N., Zang, K. P., Huo, C., Zhao, H. D., Mu, J. L., et al. (2018). Aragonite saturation state variation and control in the river-dominated marginal BoHai and Yellow seas of China during summer. *Mar. Pollut. Bull.* 135, 540–550. doi: 10.1016/j.marpolbul.2018.07.032

Xue, L., Cai, W. J., Sutton, A. J., and Sabine, C. (2017). Sea surface aragonite saturation state variations and control mechanisms at the Gray's Reef time-series site off Georgia, USA (2006–2007). *Mar. Chem.* 195, 27–40. doi: 10.1016/j.marchem.2017.05.009

Yamamoto, A., Kawamiya, M., Ishida, A., Yamanaka, Y., and Watanabe, S. (2012). Impact of rapid sea-ice reduction in the Arctic Ocean on the rate of ocean acidification. *Biogeosciences* 9, 2365–2375. doi: 10.5194/bg-9-2365-2012

Yamamoto, S., Kayanne, H., Terai, M., Watanabe, A., Kato, K., Negishi, A., et al. (2012). Threshold of carbonate saturation state determined by CO_2 control experiment. *Biogeosciences* 9, 1441–1450. doi: 10.5194/bg-9-1441-2012

Yang, D. Z., Yin, B. S., Liu, Z. L., Bai, T., Qi, J. F., and Chen, H. Y. (2012). Numerical study on the pattern and origins of Kuroshio branches in the bottom water of southern East China Sea in summer. *J. Geophys. Res.* 117:C02014. doi: 10.1029/2011JC007528

Yang, D. Z., Yin, B. S., Liu, Z. L., and Feng, X. R. (2011). Numerical study of the ocean circulation on the East China Sea shelf and a Kuroshio bottom branch northeast of Taiwan in summer. *J. Geophys. Res.* 116:C05015. doi: 10.1029/2010JC006777

Yang, D. Z., Yin, B. S., Sun, J. C., and Zhang, Y. (2013). Numerical study on the origins and the forcing mechanism of the phosphate in upwelling areas off the coast of Zhejiang province, China in summer. *J. Mar. Syst.* 123-124, 1–18. doi: 10.1016/j.jmarsys.2013.04.002

Yuan, D. L., Zhu, J. R., Li, C. Y., and Hu, D. X. (2008). Cross-shelf circulation in the Yellow and East China Seas indicated by MODIS satellite observations. *J. Marine Syst.* 70, 134–149. doi: 10.1016/j.jmarsys.2007.04.002

Zeebe, R. E., and Wolf-Gladrow, D. (2001). *CO_2 in Seawater: Equilibrium, Kinetics, Isotopes*, Vol. 65. (Amsterdam: Elsevier), 1–346.

Zhai, W. D. (2018). Exploring seasonal acidification in the Yellow Sea. *Sci. China Earth Sci.* 61, 647–658. doi: 10.1007/s11430-017-9151-4

Zhai, W.-D., and Dai, M.-H. (2009). On the seasonal variation of air-sea CO_2 fluxes in the outer Changjiang (Yangtze River) Estuary, East China Sea. *Mar. Chem.* 117, 2–10. doi: 10.1016/j.marchem.2009.02.008

Zhai, W. D., Zang, K. P., Huo, C., Zheng, N., and Xu, X. M. (2015). Occurrence of aragonite corrosive water in the North Yellow Sea, near the Yalu River estuary, during a summer flood. *Estuar. Coast. Shelf Sci.* 166, 199–208. doi: 10.1016/j.ecss.2015.02.010

Zhai, W. D., Zhao, H. D., Su, J. L., Liu, P. F., Li, Y. W., and Zheng, N. (2019). Emergence of summertime hypoxia and concurrent carbonate mineral suppression in the central Bohai Sea, China. *J. Geophys. Res. Biogeosci.* 124, 2768–2785. doi: 10.1029/2019JG005120

Zhai, W. D., Chen, J. F., Jin, H. Y., Li, H. L., Liu, J. W., He, X. Q., et al. (2014a). Spring carbonate chemistry dynamics of surface waters in the northern East China Sea: water mixing, biological uptake of CO_2, and chemical buffering capacity. *J. Geophys. Res. Oceans* 119, 5638–5653. doi: 10.1002/2014JC009856

Zhai, W. D., Zheng, N., Huo, C., Xu, Y., Zhao, H. D., Li, Y. W., et al. (2014b). Subsurface pH and carbonate saturation state of aragonite on the Chinese side of the North Yellow Sea: seasonal variations and controls. *Biogeosciences* 11, 1103–1123. doi: 10.5194/bg-11-1103-2014

Zhang, H. Y., Zhao, L., Sun, Y., Wang, J. N., and Wei, H. (2017). Contribution of sediment oxygen demand to hypoxia development off the Changjiang Estuary. *Estuar. Coast. Shelf Sci.* 192, 149–157. doi: 10.1016/j.ecss.2017.05.006

Zhang, Y., Gao, X. L., Guo, W. D., Zhao, J. M., and Li, Y. F. (2018). Origin and dynamics of dissolved organic matter in a mariculture area suffering from summertime hypoxia and acidification. *Front. Mar. Sci.* 5:325. doi: 10.3389/fmars.2018.00325

Zhao, Y. Y., Liu, J., Uthaipan, K., Song, X., Xu, Y., He, B. Y., et al. (2020). Dynamics of inorganic carbon and pH in a large subtropical continental shelf system: interaction between eutrophication, hypoxia, and ocean acidification. *Limnol. Oceanogr.* 65, 1359–1379. doi: 10.1002/lno.11393

Zhou, F., Chai, F., Huang, D. J., Xue, H. J., Chen, J. F., Xiu, P., et al. (2017). Investigation of hypoxia off the Changjiang Estuary using a coupled model of ROMS-CoSiNE. *Prog. Oceanogr.* 159, 237–254. doi: 10.1016/j.pocean.2017.10.008

Zhu, Z. Y., Hu, J., Song, G. D., Wu, Y., Zhang, J., and Liu, S. M. (2016). Phytoplankton-driven dark plankton respiration in the hypoxic zone off the Changjiang Estuary, revealed by in vitro incubations. *J. Mar. Syst.* 154, 50–56. doi: 10.1016/j.jmarsys.2015.04.009

Zhu, Z. Y., Zhang, J., Wu, Y., Zhang, Y. Y., Lin, J., and Liu, S. M. (2011). Hypoxia off the Changjiang (Yangtze River) Estuary: oxygen depletion and organic matter decomposition. *Mar. Chem.* 125, 108–116. doi: 10.1016/j.marchem.2011.03.005

Conflict of Interest: The authors declare that the research was conducted in the absence of any commercial or financial relationships that could be construed as a potential conflict of interest.

Copyright © 2020 Xiong, Wei, Zhai, Li, Wang, Zhang, Liu and Yu. This is an open-access article distributed under the terms of the Creative Commons Attribution License (CC BY). The use, distribution or reproduction in other forums is permitted, provided the original author(s) and the copyright owner(s) are credited and that the original publication in this journal is cited, in accordance with accepted academic practice. No use, distribution or reproduction is permitted which does not comply with these terms.

frontiers in Marine Science

ORIGINAL RESEARCH
published: 09 February 2021
doi: 10.3389/fmars.2020.623581

Clarifying Water Column Respiration and Sedimentary Oxygen Respiration Under Oxygen Depletion Off the Changjiang Estuary and Adjacent East China Sea

Jun Zhou[1], *Zhuo-Yi Zhu*[1,2]*, *Huan-Ting Hu*[2]*, *Gui-Ling Zhang*[3] and *Qian-Qian Wang*[2]

[1] State Key Laboratory of Estuarine and Coastal Research, East China Normal University, Shanghai, China, [2] School of Oceanography, Shanghai Jiao Tong University, Shanghai, China, [3] Key Laboratory of Marine Chemistry Theory and Technology, Ministry of Education/Institute for Advanced Ocean Study, Ocean University of China, Qingdao, China

OPEN ACCESS

Edited by:
Hongjie Wang,
Pacific Marine Environmental Laboratory (NOAA), United States

Reviewed by:
Neha Ghaisas,
Louisiana State University, United States
Baodong Wang,
Ministry of Natural Resources, China

***Correspondence:**
Zhuo-Yi Zhu
zhu.zhuoyi@sjtu.edu.cn
Huan-Ting Hu
huanting.hu@sjtu.edu.cn

Specialty section:
This article was submitted to Coastal Ocean Processes, a section of the journal Frontiers in Marine Science

Received: *30 October 2020*
Accepted: *22 December 2020*
Published: *09 February 2021*

Citation:
Zhou J, Zhu Z-Y, Hu H-T, Zhang G-L and Wang Q-Q (2021) Clarifying Water Column Respiration and Sedimentary Oxygen Respiration Under Oxygen Depletion Off the Changjiang Estuary and Adjacent East China Sea. Front. Mar. Sci. 7:623581. doi: 10.3389/fmars.2020.623581

The Changjiang Estuary and its adjacent East China Sea are among the largest coastal hypoxic sites in the world. The oxygen depletion in the near-bottom waters (e.g., meters above the seabed) off the Changjiang Estuary is caused by water column respiration (WCR) and sedimentary oxygen respiration (SOR). It is essential to quantify the contributions of WCR and SOR to total apparent oxygen utilization (AOU) to understand the occurrence of hypoxia off the Changjiang Estuary. In this work, we analyzed the $\delta^{18}O$ and O_2/Ar values of marine dissolved gas samples collected during a field investigation in July 2018. We observed that the $\delta^{18}O$ values of dissolved oxygen in near-bottom waters ranged from 1.039 to 8.457‰ (vs. air), generally higher than those of surface waters (−5.366 to 2.336‰). For all the sub-pycnocline samples, the $\delta^{18}O$ values were negatively related to O_2 concentrations ($r^2 = 0.97$), indicating apparent fractionation of $\delta^{18}O$ during oxygen depletion in the water column. Based on two independent isotope fractionation models that quantified the isotopic distillation of dissolved oxygen concentration and its $\delta^{18}O$, the mean contributions of WCR and SOR to total near-bottom AOU were calculated as 53 and 47%, respectively. Beneath the pycnocline, the WCR contribution to the total AOU varied from 24 to 69%, and the SOR contribution varied from 31 to 76%. The pooled samples beneath both the pycnocline and upper mixed layer indicated that WCR contributions (%) to total AOU increased with increasing AOU (μmol/L), whereas SOR% – AOU had the reverse trend. We propose that the WCR% and SOR% contributions to the total AOU of the sub-pycnocline waters are dynamic, not stationary, with changes in ambient environmental factors. Under hypoxic conditions, we observed that up to 70% of the total AOU was contributed by WCR, indicating that WCR is the major oxygen consumption mechanism under hypoxia; that is, WCR plays a vital role in driving the dissolved oxygen to become hypoxic off the Changjiang Estuary.

Keywords: hypoxia, $\delta^{18}O$, Changjiang estuary, sediment oxygen respiration, water column respiration

INTRODUCTION

Dissolved oxygen is essential and of great importance for most marine habitats. Dissolved oxygen depletion in estuarine and coastal near-bottom waters is worsening worldwide (2001), causing negative effects on the structure of marine ecosystems and their biodiversity (Nilsson and Rosenberg, 1994; Crain, 2007). Severe oxygen depletion, or hypoxia, destroys fishery resources and brings economic losses (Sindermann and Swanson, 1979; Naqvi et al., 2000). In addition, the change in the oxygen concentration changes the redox potential of the water environment, alters the balance of oxygen, carbon and nitrogen cycles, and hence produces feedback to global climate change. Therefore, hypoxia has recently attracted much attention in marine research (Diaz, 2001; Keeling et al., 2010).

The Changjiang Estuary and its adjacent offshore areas are typical estuarine and coastal sea environments that are affected by one of the largest rivers worldwide. In recent decades, Changjiang fluvial nutrients have increased more than ten times, and such eutrophication trends are expected to continue (Zhang et al., 1999; Yan et al., 2003; Daoji and Daler, 2004). Under the eutrophication background, estuarine and coastal summer algal blooms have increased dramatically in recent decades (Liu et al., 2013; Li et al., 2014). As the water depth is only tens of meters, excess organic matter generated in surface waters can quickly settle and reach near-bottom waters, which fuels oxygen consumption at the bottom of the water column. Furthermore, the water column is usually well stratified in summer, with high-temperature and low-salinity Changjiang diluted water at the surface and high-salinity Kuroshio-originated water prevailing at the bottom (Su, 1998). The degradation of this excess organic matter in the near-bottom waters has a strong influence on dissolved oxygen off the Changjiang Estuary.

Hypoxia off the Changjiang Estuary is unstable, in contrast to other marginal sea hypoxic conditions, such as the Gulf of Mexico (Turner et al., 2005) and the Baltic Sea (Carstensen et al., 2014). The earliest recorded hypoxia (1900 km^2) off the Changjiang Estuary was in August 1959, with a minimum dissolved oxygen concentration ($[O_2]$) as low as 0.34 mg/L (Office of Integrated Oceanographic Survey of China, 1961). Hypoxic areas have increased significantly in the last 20 years relative to earlier times. In August 1999, 2006, and 2013, hypoxic areas were 13,700 km^2, 15,400 km^2, and 11,150 km^2, respectively (Li et al., 2002; Zhu et al., 2011, 2017). To the best of our knowledge, another hypoxic event, with an area likely over 10,000 km^2, occurred off the Changjiang Estuary in the summer of 2016 (WD Zhai, personal communication). Although hypoxia is unstable and can disappear for several years before the next occurrence of a severe hypoxic event (Zhu et al., 2017), in the 21st century, the Changjiang Estuary and adjacent East China Sea (ECS) became another coastal sea region with a hypoxic area exceeding 10,000 km^2, similar to the Baltic Sea (Carstensen et al., 2014), the Gulf of Mexico (Wendel, 2015), and the northwestern shelf of the Black Sea (Capet et al., 2013).

The occurrence of hypoxia in near-bottom waters is primarily due to the stratification of the water column and the degradation of excess organic matter (Diaz, 2001). This also applies to the case off the Changjiang Estuary (Li et al., 2002; Wei et al., 2007, 2017; Chi et al., 2020). With hypoxic mechanism studies in recent years, it has been revealed that wind (Ni et al., 2016; Zhang et al., 2019), tides (Zhu et al., 2017), topography (Wang, 2009), and $[O_2]$ in Kuroshio waters (Qian et al., 2017) also have an important influence on the occurrence, development, and/or severity of hypoxia.

Despite the above hypoxic mechanism studies, integrated research that quantified both sediment oxygen respiration (SOR) and water column respiration (WCR) contributions is still sparse. On the one hand, the locations of hypoxia vary from year to year (Zhu et al., 2011), indicating that the floating and sinking of organic matter (i.e., WCR), rather than stationary sediment (i.e., SOR), play a more important role in the formation of hypoxia. Studies that focused on water column processes provide additional evidence that WCR dominates hypoxia. For example, hypoxia tends to correlate with sites with high chlorophyll concentrations and high sinking rates in the water column (Li et al., 2018), and the degraded organic matter that fuels hypoxia is of marine origin (Wang et al., 2016, 2017). In addition, a significant relationship between a high chlorophyll concentration in the surface waters and low $[O_2]$ in the near-bottom waters was observed (Chen et al., 2017). However, some work that focused on sediments highlighted the contribution of SOR to the occurrence of hypoxia. For example, a study based on the radium-thorium imbalance method indicated that the SOR contribution ranged from 6 to 61% of the total oxygen depletion in the near-bottom waters (Cai et al., 2014). Furthermore, in situ SOR incubations conducted on the deck suggested that the contribution of SOR ranged from 15% (Song et al., 2016) to 100% (Zhang et al., 2017). The reported SOR contribution range varied greatly (15–100%) (Song et al., 2016; Zhang et al., 2017), indicating that the contribution of SOR may have a dynamic spatial and/or temporal distribution gradient. Due to the lack of integrated WCR and SOR studies, WCR% (the WCR contribution to total apparent oxygen utilization (AOU) in percent) and SOR% (the SOR contribution to total AOU in percent) in the total oxygen depletion of near-bottom waters remain unclear. This uncertainty hinders the comprehensive understanding of the occurrence of hypoxia, preventing accurate hypoxia prediction (e.g., by modeling), and hence interferes with the formulation of environmental protection policies in the future.

Oxygen has three natural stable isotopes (^{16}O-99.76, ^{17}O-0.04, and ^{18}O-0.20%). Fractionation of oxygen usually follows a mass-dependent law; for example, ^{18}O is less preferred in aerobic respiration than ^{16}O (Lane and Dole, 1956). In the water column, $[O_2]$ is consumed by various processes but seldom reaches zero (Zhu et al., 2011; Wang et al., 2017), resulting in enriched ^{18}O in residual O_2 due to isotopic fractionation caused by respiration. However, the oxygenated depth in sediments is usually only a few millimeters, beneath which $[O_2]$ could be totally consumed. Previous studies reported that fractionation factors (ε) of WCR range from −12 to −25‰ (Bender and Grande, 1987) and SOR ranges from 0 to 3‰ (Brandes and Devol, 1997). Because of the significant differences between WCR and SOR fractionation factors, it is possible to distinguish the different isotopic effects of

WCR and SOR on dissolved oxygen ^{18}O and hence evaluate the WCR% and SOR% contribution to total AOU in the near-bottom waters. In the Gulf of Mexico, SOR contributed an average of 73% to the total bottom AOU under nonhypoxic circumstances, but the contribution of WCR was larger when hypoxia occurred (Quinones-Rivera et al., 2007). Later, it was found that there may be a lack of a relationship between declining O_2 and $\delta^{18}O$ in the water column (Ostrom et al., 2014). However, to the best of our knowledge, the dissolved gas ^{18}O approach has never been applied to hypoxia off the Changjiang Estuary, and the contributions of WCR and SOR remain largely unclear (Cai et al., 2014; Song et al., 2016).

Therefore, we bring up the question of the spatial features of WCR and SOR% regarding the near-bottom AOU off the Changjiang Estuary and adjacent ECS and the implications for the occurrence of hypoxia. To address this question, we conducted a cruise off the Changjiang Estuary and adjacent ECS in July 2018. Dissolved gas samples for $\delta^{18}O$ analyses were collected onboard into a pre-vacuumed bottle and analyzed in the laboratory. Then, we interpreted the $\delta^{18}O$ data via a self-developed isotopic model and via a reported model (Fry, 2006; Quinones-Rivera et al., 2007). We also applied sensitivity tests for the modeled WCR% and SOR% using different WCR fractionation factors. We discussed the potential controlling factors of the WCR% and SOR%, especially for the sub-pycnocline [O_2]. Finally, we proposed a schematic oxygen consumption mechanism behind the occurrence of hypoxia off the Changjiang Estuary.

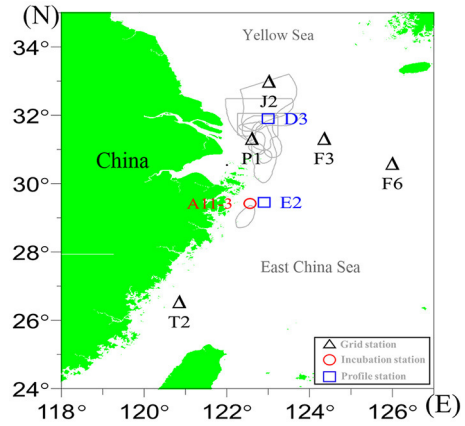


FIGURE 1 | The study area and sampling stations. Gray lines indicate the observed hypoxia in previous studies derived from Zhu et al. (2011).

MATERIALS AND METHODS

Field Sampling

The field investigation was conducted in July 2018, covering the Changjiang Estuary and its adjacent coastal sea (**Figure 1**). Discrete water samples for dissolved gas analyses were collected by Niskin samplers attached to a CTD (Seabird 911), which also measured the temperature and salinity profile. Surface samples were collected 3 m beneath the surface, and near-bottom waters were collected ∼2 m above the sea bed. At stations D3 and E2, water samples at the middle layers (but beneath the pycnocline) were also collected (**Figure 1**).

On board the ship, water samples were collected following the same protocol as that used by Reuer et al. (2007). Briefly, homemade glass flasks (500 mL) with Louwers-Hanique valves on top (**Supplementary Figure 1**) were thoroughly rinsed with deionized water. All internal valves were cleaned, and all O-rings were greased for better sealing. Sample flasks were poisoned with saturated $HgCl_2$ (∼75 μL), dried at 40°C, and then evacuated to 10^{-5} mbar. We usually collected ∼200 ml (at most 250 ml of water) of seawater from the Niskin sampler. Bubble-free seawater entered the pre-evacuated sample flask through the side arm of a Louwers-Hanique valve, while dripping water maintained a good seal during the whole collection period. Collected seawater samples had a final $HgCl_2$ concentration higher than 21 μg/mL, higher than the 20 μg/mL concentration recommended by Kirkwood (1992), ensuring that the dissolved gases preserved the *in situ* isotopic compositions. Flasks were stored at room temperature until analyses were conducted in the laboratory.

Dark Incubation

We also performed a dark incubation experiment using surface seawater to determine the respiration fractionation factor for living organisms off the Changjiang Estuary. Basically, the surface water of station A11-3 (**Figure 1**) was collected into a few independent BOD bottles, incubated for 0, 300, 450, and 760 h, collected into the same pre-evacuated sample flasks, and then analyzed for $\delta^{18}O$ values.

Laboratory Measurements

In the laboratory, headspace dissolved gases were equilibrated with underneath seawater in the sample flasks at room temperature (22°C) for at least 48 h. The equilibrated dissolved gases were then extracted (**Supplementary Figure 2**) and purified through a vacuum line (**Supplementary Figure 3**) to remove the CO_2 and water vapor in the gas mixture. The final gas mixture containing O_2, Ar, and N_2 was collected onto a sample finger filled with silica gel at liquid nitrogen temperature. A detailed description and schematics of the sampling and processing of dissolved gas samples can be found in **Supplementary Materials**.

The sample finger was heated at 100°C for 15 min to mix all gases well before introduction into the mass spectrometer, a Delta V plus with a dual inlet system, for isotopic analysis. For every sample, we ran 3 blocks of 15 cycles in total, with a pre-delay time of 20 s. The integration time for every cycle was 10 s. The instrument was equipped with Faraday cups with masses of 28, 32, 34, and 40, so $\delta^{18}O$ and $\delta O_2/Ar$ could be simultaneously analyzed in this study; $\delta^{18}O$ and $\delta O_2/Ar$ were

TABLE 1 | Temperature, salinity, and O_2 results, and estimated WCR% and SOR% in this study.

Station	Layer	Mixed layer depth	Depth	T	Salinity	$\delta^{18}O$	$\delta O_2/Ar$	AOU	WCR	SOR	WCR	SOR
	m	m	m	°C		‰	‰	μmol/L	AS model		IR model	
D3	3	4	38	24.2	25.183	−5.366	113.4	−47				
	10			20.4	32.949	9.263	−614.4	138	48%	52%	58%	42%
	36			20.2	32.932	7.835	−594.0	133	39%	61%	52%	48%
E2	3	5	60	27.5	31.223	−1.756	−22.5	−11				
	10			26.7	32.788	15.416	−756.4	156	54%	46%	69%	31%
	30			19.6	34.500	5.497	−434.9	93	48%	52%	54%	46%
	58			18.5	34.527	6.028	−457.0	100	51%	49%	56%	44%
F3	3	6	54	26.3	31.676	−0.324	−63.4	−2				
	52			21.6	31.307	3.710	−370.7	75	40%	60%	44%	56%
F6	3	9	81	25.4	31.925	0.424	−17.5	−13				
	79			14.6	32.947	6.834	−435.6	104	62%	38%	67%	33%
J2	3	2.5	35	26.1	27.986	0.030	−123.2	12				
	33			18.6	31.518	4.176	−368.0	79	46%	54%	50%	50%
P1	3	3	38	23.3	26.514	−3.956	−16.4	−14				
	36			20.2	34.158	8.457	−571.7	127	49%	51%	59%	41%
T2	3	11.5	64	27.1	34.067	2.336	−190.2	26				
	62			25.9	34.125	1.039	−151.2	18	24%	76%	24%	76%

calculated as follows:

$$\delta^{18}O = \left[\left(\frac{\frac{^{18}O}{^{16}O_{sample}}}{\frac{^{18}O}{^{16}O_{standard}}} - 1 \right) \times 1000 \right] \quad (1)$$

$$\delta \frac{O_2}{Ar} = \left[\left(\frac{\frac{^{16}O}{^{40}Ar_{sample}}}{\frac{^{16}O}{^{40}Ar_{standard}}} - 1 \right) \times 1000 \right] \quad (2)$$

During the period of measurement, the result of the reference gas vs. reference gas (so-called zero enrichment) was −0.018‰ (±0.022 SD, 1σ) and 0.1‰ (±0.2 SD, 1σ) for $\delta^{18}O$ and $\delta O_2/Ar$, respectively. For all sample data, a chemical slope calibration was conducted to correct the isotopic interference of $\delta^{18}O$ values caused by the differences in elemental ratios (N_2/O_2/Ar ratios) between sample gases and the reference gas. We applied two calibration curves of $\delta N_2/O_2$ vs. $\delta^{18}O$ and $\delta Ar/O_2$ vs. $\delta^{18}O$ to correct the $\delta^{18}O$ values of all samples.

Then, all data were normalized to concurrent analyses of air ($\delta^{18}O \equiv 0‰$, $\delta O_2/Ar \equiv 0‰$) collected in the back yard of the laboratory, Shanghai, China. During the course of this study, we observed analytical precisions for $\delta^{18}O$ and $\delta O_2/Ar$ of 0.057‰ and 0.4‰ ($n = 11$), respectively. Equilibrated dissolved gases in water at 22°C (deionized water poisoned with $HgCl_2$) were also repeatedly collected and measured in the laboratory, and we observed mean values of $\delta^{18}O = 0.706 \pm 0.051‰$ and $\delta O_2/Ar = -95.0 \pm 0.7‰$, which were within the accepted error threshold compared to their theoretical values. All data running on the same filament were finally converted to values relative to air after the chemical slope corrections.

The sampling flasks were prepared and evacuated by a vacuum line at East China Normal University. Dissolved gas extractions and analyses were conducted at the Stable Isotope Climate Lab at Shanghai Jiao Tong University, Shanghai, China.

The temperature and salinity data of all stations and the analyzed $\delta^{18}O$ and $\delta O_2/Ar$ data of all samples are listed in **Table 1**. AOU and modeled WCR% and SOR% in the following sections are also listed in **Table 1**.

RESULTS

In July 2018, warm and fresh water prevailed in the surface layer, whereas waters of lower temperature and higher salinity were commonly found in the near-bottom layers (**Figure 2** and **Table 1**). The temperature of the surface waters varied between 23.3°C and 27.5°C and 14.6°C to 25.9°C for the near-bottom layers. The surface and near-bottom salinities ranged between 25.183 and 34.067 and 31.307 and 34.527, respectively. Waters with low temperature and low salinity were identified in the surface layer of station P1, indicating the presence of Changjiang diluted water, and a gradual eastward increase in both temperature and salinity was observed (**Figures 2A,B**). In the near-bottom waters, temperature and salinity gradually decreased from south to north (**Figures 2C,D**).

The water column was well stratified in our observations for all the stations we covered, namely, the density of near-bottom waters was higher than that of the surface waters. The density differences between near-bottom waters and surface waters ranged from 0.58 to 8.39 kg/m^3, with the maximum value (8.39 kg/m^3) occurring at station D3. Based on the temperature and salinity profile and a 0.125 kg/m^3 threshold, the upper mixed layer depth ranged from 2.5 m (J2) to 11.5 m (T2) during our observations, with a mean depth

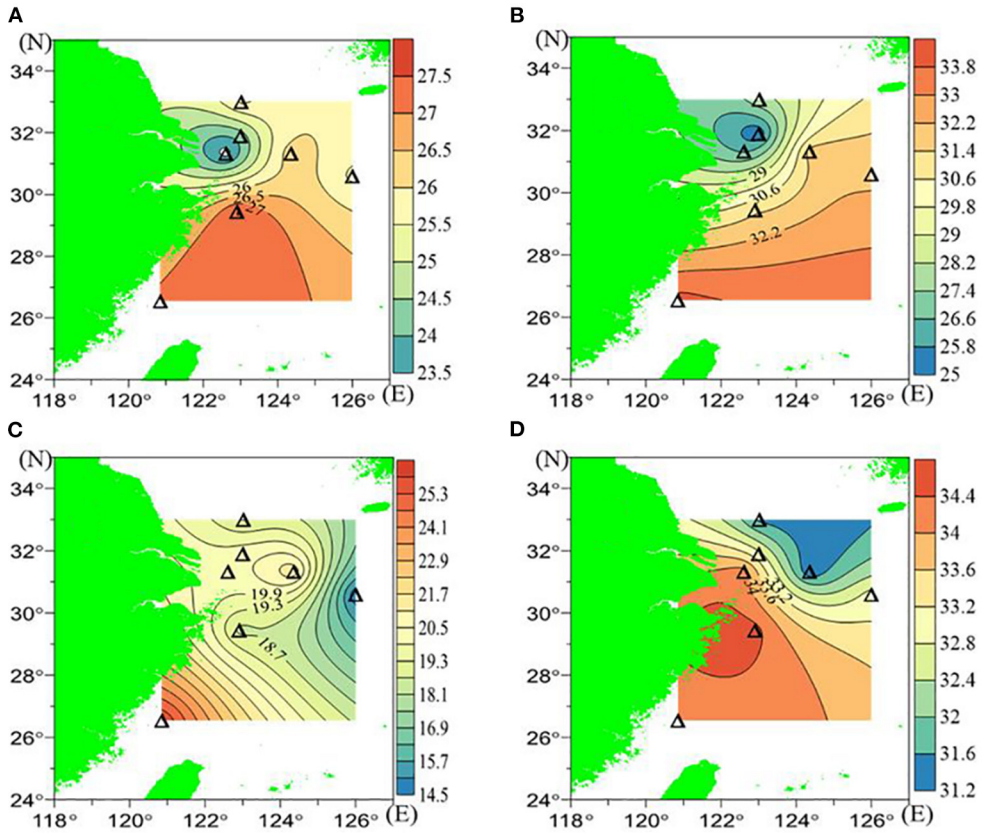


FIGURE 2 | The hydrological background in July 2018: **(A)** Surface temperature (°C), **(B)** surface salinity, **(C)** bottom temperature (°C), and **(D)** bottom salinity.

of 4.9 m. The upper mixed layer was shallower than the corresponding pycnocline.

The $\delta O_2/Ar$ values at the surface varied from −190.2 to 113.4‰, and in the near-bottom waters, they varied from −594.0 to −151.2‰. The lowest $\delta O_2/Ar$ value in the near-bottom waters occurred at station D3 (−594.0‰), and it gradually increased both southwards and eastwards (**Figure 3B** and **Table 1**). The distribution of $\delta O_2/Ar$ in the near-bottom water was opposite to that in the surface water (**Figures 3A,B**); that is, higher $\delta O_2/Ar$ values in surface waters usually corresponded to lower $\delta O_2/Ar$ values in the corresponding near-bottom waters. The $[O_2]$ was calculated from the observed $\delta O_2/Ar$, assuming that Ar was saturated in all layers. Accordingly, the $[O_2]$ ranged from 182 μmol/L to 279 μmol/L in the surface waters and from 104 μmol/L to 195 μmol/L in the near-bottom waters (**Figures 3C,D**).

AOU was calculated by subtracting the observed $[O_2]$ from the equilibrated $[O_2]$, which ranged from −47 to 26 μmol/L for the surface waters and from 18 to 133 μmol/L for the near-bottom waters. In the near-bottom waters, elevated AOU and $\delta^{18}O$ (133 μmol/L and 7.835‰, respectively) were found at station D3. By contrast, minimum values in the near-bottom waters were found at station T2, which were 18 μmol/L and 1.039‰ (**Figures 4C,D**). A similar mirrored distribution pattern between AOU and $\delta^{18}O$ was found in the surface waters (**Figures 4A,B** and **Table 1**).

Vertically, obvious water stratification was identified by the temperature and salinity profile. $\delta O_2/Ar$ (or $[O_2]$) gradually decreased from the surface to near the bottom waters, but the $\delta O_2/Ar$ minimum (or $[O_2]$ minimum) occurred in the intermediate layers beneath the pycnocline (10 m; **Figure 5**), indicating that most oxygen consumption occurred in the middle layer instead of near-bottom waters. The $[O_2]$ at 10 m at station E2 (56 μmol/L) was the minimum observed $[O_2]$, even lower than the corresponding near-bottom $[O_2]$. Horizontally, the $\delta^{18}O$ values showed a good relationship with declining $[O_2]$ (**Figure 3D** vs. **Figure 4D**). Vertically, although discrete samples were limited in number, the $\delta^{18}O$ values were also well related to declining $[O_2]$ (**Figure 5**). Indeed, among all sub-pycnocline samples, the relationship between $\delta^{18}O$ and declining $[O_2]$ (as $[O_2]/[O_2]_0$) was significant ($r^2 = 0.97$; **Supplementary Figure 4**), indicating apparent isotope fractionation during O_2 consumption in the water column.

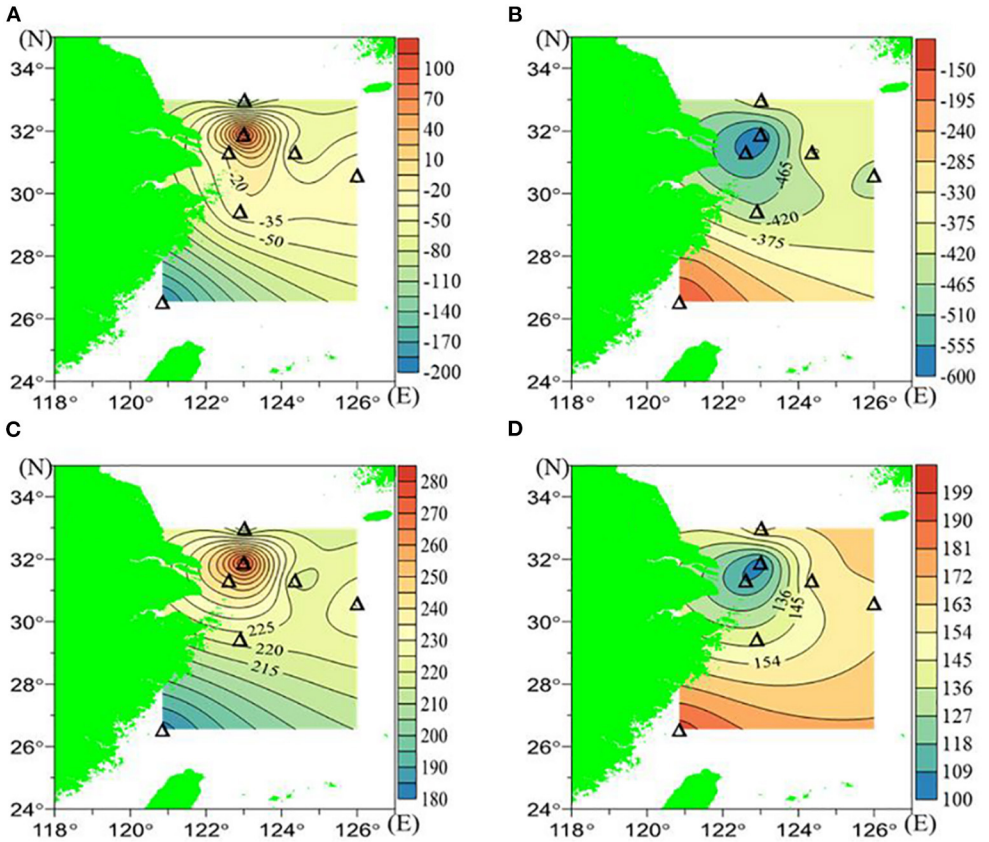


FIGURE 3 | The $\delta O_2/Ar$ (‰) and $[O_2]$ (μmol/L) calculated based on $\delta O_2/Ar$ in July 2018: **(A)** surface $\delta O_2/Ar$, **(B)** bottom $\delta O_2/Ar$, **(C)** calculated surface $[O_2]$, and **(D)** calculated bottom $[O_2]$.

MODEL

Under the simplest condition, we assume that the near-bottom waters are in the dark and beneath the upper mixed layer. There is no diapycnal gas exchange between the upper mixed layer and near-bottom waters. Photosynthesis in near-bottom waters can be ignored, and the vertical mixing process is strongly prohibited by stratification over one to a few weeks. The oxygen budget is controlled only by WCR and SOR. In addition, the fractionation factors for WCR and SOR are constant during oxygen consumption. Based on these assumptions, we used two separate one-dimensional models to quantify the contributions of WCR and SOR to total AOU. In the following section, we first describe the principle of the two models and then use the models to calculate WCR and SOR%. Further discussions of the model results and their implications for the local environment are presented in section 5.1.

Model Description

Oxygen Isotope Rayleigh Fractionation Model (IR Model)

Visualizing the entire fate of O_2 in the water column: initially, O_2 is first dissolved (or generated) in the water column in surface layers via air-sea gas exchange or photosynthesis. Then, O_2 consumption caused by WCR occurs in the surface layers, and SOR will also influence O_2 when sediments get involved in the water column. The impacts of both SOR and WCR on O_2 are recorded in the O_2 properties, including the O_2 concentration and $\delta^{18}O$ values. Finally, in the current case, large amounts of O_2 are consumed in the layers beneath the pycnocline, with certain WCR and SOR proportions relative to the total AOU until our observations.

The IR model is built using the isotope ratio R ($R = {}^{18}O/{}^{16}O$) and $[O_2]$. The initial dissolved O_2 in the water column is assumed to be at equilibrium with air at the air-sea interference before any oxygen consumption takes place. Beneath the pycnocline, there are no air-sea gas exchange and no O_2 production, only oxygen consumption occurs, and the O_2 budget is:

$$[O_2]_{obs} = [O_2]_0 - [O_2]_{WCR} - [O_2]_{SOR} \quad (3)$$

where $[O_2]_{obs}$ is the observed $[O_2]$. $[O_2]_0$ is the initial oxygen concentration, which is assumed at saturation. $[O_2]_{WCR}$ is the oxygen consumed by water column respiration; $[O_2]_{SOR}$ is the oxygen consumed by sediment oxygen respiration.

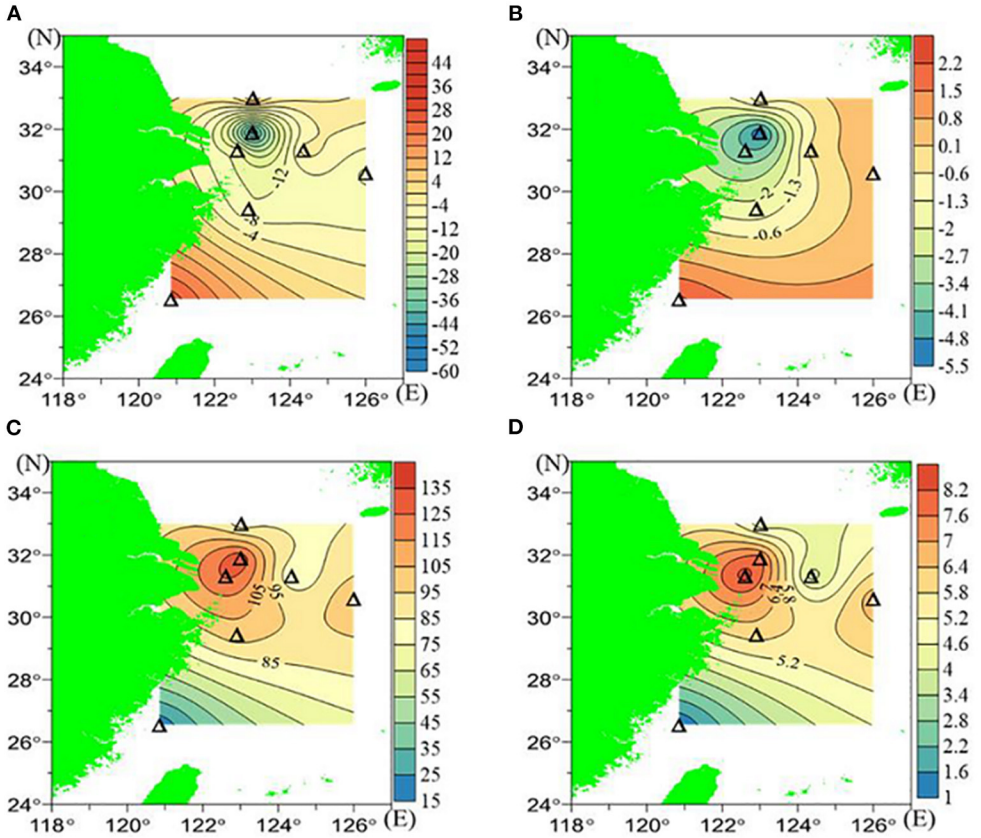


FIGURE 4 | The AOU and $\delta^{18}O$ in July 2018: **(A)** surface AOU (μmol/L), **(B)** surface $\delta^{18}O$ (‰), **(C)** bottom AOU (μmol/L), and **(D)** bottom $\delta^{18}O$ (‰).

Respiration is a Rayleigh fractionation process, that is,

$$\frac{R_{WCR}}{R_0} = f^{(\alpha_{WCR}\,-\,1)} \tag{4}$$

where α_{WCR} ($= R_{respired}/R_{residual}$) is the respiration fractionation factor for the WCR process. R_{WCR} is the $^{18}O/^{16}O$ value of residual O_2 after WCR consumption, which can be measured from our collected samples. R_0 is the $^{18}O/^{16}O$ value of $[O_2]_0$, and f is the fraction of residual $[O_2]$ relative to the initial $[O_2]_0$ (ranging between 0 and 1). As WCR occurs in all layers and at all times in the water column, the fraction of residual O_2 after WCR consumption can be written as $f = \frac{[O_2]_0 - [O_2]_{WCR}}{[O_2]_0}$.

Therefore, from equation 4 we obtain

$$R_{WCR} = R_0 \times \left(\frac{[O_2]_0 - [O_2]_{WCR}}{[O_2]_0}\right)^{(\alpha_{WCR}\,-\,1)} \tag{5}$$

In addition to WCR processes, SOR would also consume O_2. However, the fractionation factor of SOR processes, α_{SOR}, is very close to 1 (Brandes and Devol, 1997), and oxygen will be mostly and totally consumed once it interacts with sediments. In other words, the SOR processes will cause no or negligible isotopic fractionation of the R values of dissolved O_2 and will only influence the O_2 concentrations. Therefore,

$$R_{obs} = R_{WCR} = R_0 \times \left(\frac{[O_2]_0 - [O_2]_{WCR}}{[O_2]_0}\right)^{(\alpha_{WCR}\,-\,1)} \tag{6}$$

where R_{obs} is the observed isotopic composition of O_2 from the near-bottom water samples. Based on equation 6, $[O_2]_{WCR}$ can be calculated with known R_{obs}, R_0, $[O_2]_0$, and α_{WCR}. $[O_2]_0$ is the saturated concentration of O_2 at the known temperature and salinity for each station, and R_0 is calculated from the isotopic composition, $\delta^{18}O = 0.7\%0$, of saturated O_2 at the sea surface.

Then, the fraction of oxygen consumed by WCR (WCR%) is calculated as:

$$WCR\% = \frac{[O_2]_{WCR}}{[O_2]_0 - [O_2]_{obs}} \tag{7}$$

Additionally, SOR% = 1 – WCR%, which is the fraction of oxygen consumed by SOR.

Apparent Fractionation Factor-Based and Step-By-Step Model (AS Model)

In principle, this model is similar to the model presented by Bender and Grande (1987) and the model with sequential

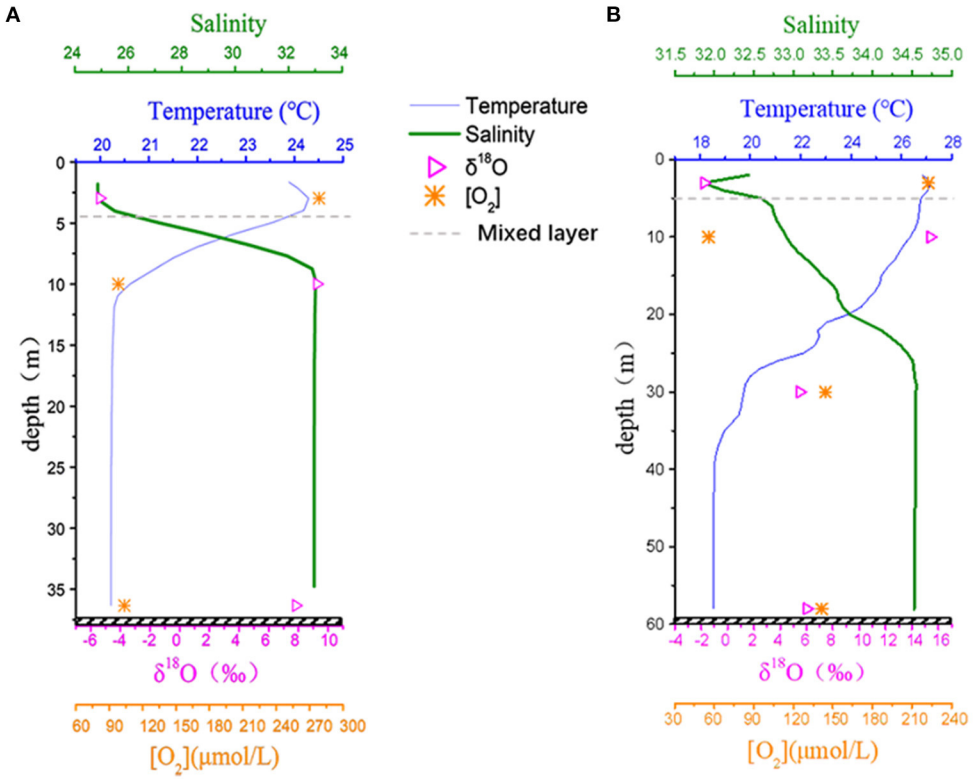


FIGURE 5 | Vertical profile of salinity, temperature (°C), and [O_2] (μmol/L) calculated using δO_2/Ar, and $\delta^{18}O$ (‰) for **(A)** station D3 and **(B)** station E2. The gray dashed lines indicate the depth of the upper mixed layer.

steps reported by Fry (2006). It has been used in the Gulf of Mexico (Quinones-Rivera et al., 2007). As we focused on the oxygen budget in the near-bottom waters in this work, where no photosynthesis is present, only respiration processes are considered.

At the initial given O_2 concentrations and $\delta^{18}O$ values, the depletion of O_2 was calculated at a given respiration rate. In every step, we decreased the initial O_2 (i.e., caused by WCR and SOR, simultaneously) with a step size of ∼1 μmol/L. The corresponding increase in $\delta^{18}O$ (in ‰) was quantified by logarithmic distillation equations (exact expression; Mariotti et al., 1981). Through a repeated step-by-step calculation, the O_2 concentration will finally decrease to nearly zero, with very high corresponding $\delta^{18}O$ values. By doing this, a curve can be made, with the x-axis as the modeled O_2 concentration and the y-axis as the modeled $\delta^{18}O$. The fractionation factor for all steps was fixed; changing the fractionation factor would change the shape (curvature) of the curve. By tuning the model fractionation factor, we found the best fit of the modeled curve and our observed [O_2] – $\delta^{18}O$ pairs for every near-bottom water sample. Then, the best-fit model fractionation factor was recorded for that sample, termed the apparent fractionation factor (ε_{app}) (Quinones-Rivera et al., 2007). Similarly, the initial O_2 properties for modeling were set as the theoretical equilibrium value (100% solubility and 0.7‰ $\delta^{18}O$ for dissolved O_2). The respiration rate was set as 0.03 mg O_2/L/h.

The apparent fractionation factor was then used to calculate the relative contributions from WCR and SOR using a previously reported equation (Quinones-Rivera et al., 2007):

$$SOR\% = \left(\varepsilon_{app} - \varepsilon_{WCR}\right) / \left(\varepsilon_{SOR} - \varepsilon_{WCR}\right) \times 100 \quad (8)$$

where ε_{app} is the apparent fractionation factor, ε_{WCR} is the water column respiration fractionation factor, and ε_{SOR} is the sedimentary oxygen respiration fractionation factor.

MODEL RESULTS

A previous study suggested a value of −22‰ for the WCR fractionation factor ε_{WCR} in coastal waters such as the Gulf of Mexico (Quinones-Rivera et al., 2007). In this work, ε_{WCR} was regarded as −20.8‰ (α_{WCR} = 0.9792) based on incubation experiments using in situ surface seawater (**Supplementary Figure 5**). For the SOR processes, during which O_2 is totally consumed, the fractionation factor ε_{SOR} is regarded as 0 (α_{SOR} = 1, namely, no isotopic fractionation of residual O_2) (Brandes and Devol, 1997).

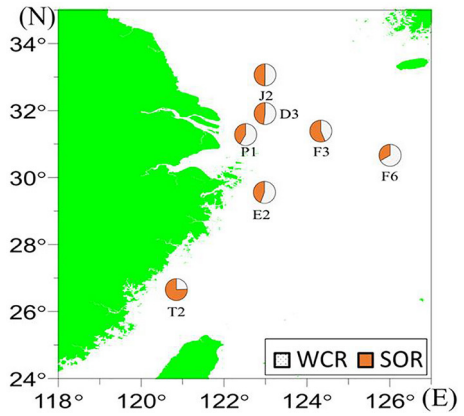


FIGURE 6 | The WCR and SOR% contributions to total AOU in the near-bottom waters in July 2018 as revealed by the IR model.

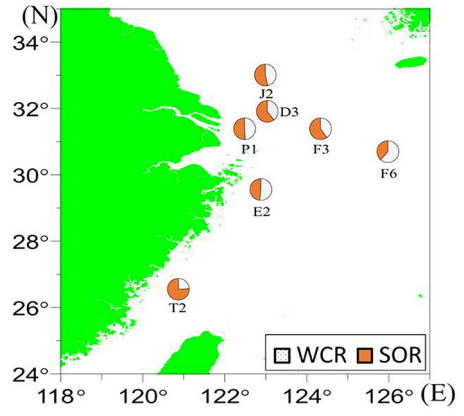


FIGURE 7 | The WCR% and SOR% contributions to total AOU in the near-bottom waters in July 2018, as revealed by the AS model.

Results of the IR Model

The mean WCR% that contributed to the total AOU beneath the pycnocline was 53%, and the remaining 47% was contributed by SOR. Except for a few stations (T2, F3, J2), the WCR% was usually higher than the SOR (**Figure 6**). The maximum WCR% occurred in the 10 m layer (not near the bottom layer) of E2 (69%). Among all the near-bottom samples, the minimum value occurred at the southernmost station T2 (WCR% = 24%) (**Figure 6** and **Table 1**).

Results of the AS Model

The mean SOR% relative to the total AOU beneath the pycnocline was 54%, and the WCR% contributed the remaining 46% (**Figure 7** and **Table 1**). The minimum SOR% (and hence maximum WCR%) was found at station F6 (SOR=38%, WCR=62%), and the maximum SOR% (and the minimum WCR%) occurred at station T2 (SOR=76%, WCR=24%).

We observed good consistencies and correlations of the results between the IR model and the AS model (slope = 1.18, $r^2 = 0.89$, **Figure 8**).

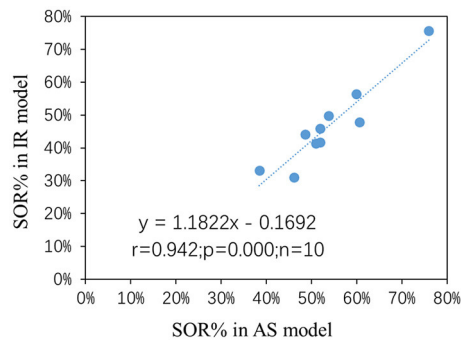


FIGURE 8 | The SOR% contribution to the total AOU based on both models: AS model result vs. IR model result.

DISCUSSION

Caveats and Limitations of the Models

For both the IR and AS models, we assumed equilibrium of the initial O_2 (concentration and $\delta^{18}O$) at the sea surface. However, photosynthetic O_2 and fresh water input might influence the initial conditions of O_2. Here, we propose that these influences are not significant because of the limited fractions of photosynthetic O_2 relative to dissolved atmospheric O_2 and the small isotopic effects of fresh water input.

In the vicinity of Changjiang, the terrestrial impact is very clear. Changjiang water has a $\delta^{18}O$-H_2O value of −31.6‰ (vs. air, converted from the VSMOW scale) (Li et al., 2010), which is 8.3‰ lower than that of seawater (−23.3‰ vs. air). Photosynthesis generates O_2 by splitting the H-O bond in water, and hence, photosynthetic O_2 has the same $\delta^{18}O$ as its source water, which usually has much lower $\delta^{18}O$ values than dissolved O_2 from the atmosphere. However, we believe the terrestrial impact on $\delta^{18}O$-O_2 was limited for our samples. We will use the surface waters of D3, where the lowest surface salinity (25.183) was observed, as an example for the following discussion. Given a typical marine water salinity of 34.500 and a salinity of 25.183 for the surface waters at D3, the freshwater contribution in the surface waters of D3 was expected to be 27%, with the remaining 73% as marine water based on a mass-balance calculation. If the $\delta^{18}O$-H_2O of Changjiang water is linearly diluted by marine water along with increasing salinity, the presence of 27% freshwater would then reduce the bulk surface water $\delta^{18}O$-H_2O from the original −23.3to −25.5‰ (vs. air). Therefore, photosynthetic O_2 would have a $\delta^{18}O$-O_2 of −25.5‰ instead of −23.3‰, assuming that there is trace fractionation of oxygen isotopes during the assimilation process in photosynthesis (Hopkinson and Smith, 2005). Therefore, the freshwater input would only change the $\delta^{18}O$ of photosynthetic O_2 by 2.2‰ (i.e., 23.3–25.5) or by 9.5% for all photosynthetic O_2 at station D3. This estimation of freshwater influence is expected to be the maximum, as all the remaining stations had salinities much higher than 25.183 (**Figure 2**).

The coupling of $\delta^{18}O$ and $[O_2]$ is impacted by various processes off the Changjiang Estuary and adjacent ECS, such as mixing with other water masses and additional freshwater input. However, there is barely an effect of these two processes from previous years because the residence time of the ECS shelf water is only one year (Tsunogai et al., 1997). Instead, the impact from mixing or freshwater input on $\delta^{18}O$ and $[O_2]$ coupling is expected to be reset every year. However, more work is still needed to clarify the mixing process effect on $\delta^{18}O$ and $[O_2]$ coupling over short time scales.

Another point is the euphotic zone depth and its relationships with the upper mixed layer depth. In the flood season (i.e., July), Changjiang water is very turbid and exerts a great impact on the estuary and adjacent coastal sea, as indicated by the salinity distribution pattern at the surface (**Figure 2B**). Under this background, the euphotic zone and upper mixed layer are very shallow (Zhu et al., 2009). For the near-bottom water samples, the sampling depths were all deeper than the euphotic zone and upper mixed layer depth. For the profile stations (D3 and E2), the middle layer samples were also all below the upper mixed layer, indicated by the density differences (density difference was > 1.5 kg/m^3 or even > 7.4 kg/m^3, far higher than 0.125 kg/m^3).

Previously, while $\delta^{18}O$ basically showed a good relationship with declining $[O_2]$, at times, sub-pycnocline samples showed a lack of such a relationship at certain sites in the Gulf of Mexico (Ostrom et al., 2014). This was suggested to be due to the fast oxygen consumption rate and hence an SOR-like process in the microenvironment in the water column (Ostrom et al., 2014). In our case, all sub-pycnocline $\delta^{18}O$ and O_2 were negatively coupled (r^2 = 0.97; **Supplementary Figure 4**), indicating apparent isotope fractionation in the water column. Critically, we again claim that SOR in this work was related to any process in which $[O_2]$ was totally consumed in the depletion process, regardless of whether it occurred in the sediment, at the sediment-water interface or in the water column. However, given the good relationship between $\delta^{18}O$ and $[O_2]$ (**Supplementary Figure 4**), it is unlikely that the SOR process (or diffusion-controlled process) significantly took place in the water column during our observation. Further work is needed to explore and confirm this.

Finally, the WCR endmember fractionation factor impacts the final output. The reported aerobic respiration fractionation factor has a large range, varying from −12 to −25‰ (Bender and Grande, 1987). Our in situ incubation indicated that the fractionation factor off the Changjiang Estuary was −20.8‰ (ε = −20.8‰ or α = 0.9792; **Supplementary Figure 5**). Previously, a WCR endmember fractionation factor of −22‰ was reported based on incubations in the Gulf of Mexico (Quinones-Rivera et al., 2007). Additionally, Hendricks et al. (2005) reported a respiration fractionation factor ranging between −21 and −22‰ (Hendricks et al., 2005), both of which are very close to our incubated value of −20.8‰ for Changjiang Estuary surface waters. Nevertheless, we also ran a sensitivity test showing that changing the WCR endmember fractionation factor from the current value (−20.8‰) to either −16 or −25‰ indeed introduced some changes in the estimated WCR% and SOR%, but the overall distribution pattern and relationships remained unchanged (see **Supplementary Figures 6**, **7**).

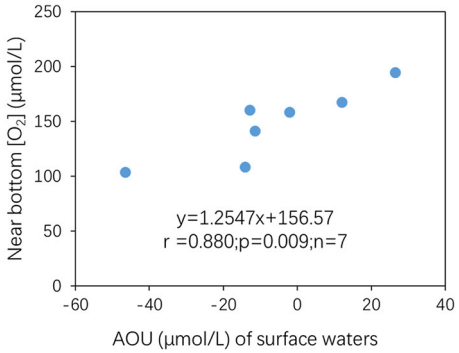


FIGURE 9 | Near-bottom $[O_2]$ (μmol/L) plotted against AOU (μmol/L) in the surface waters.

Implications of the Oxygen Depletion Mechanisms off the Changjiang Estuary

The main controlling factor for WCR is organic matter (OM) degradation driven by microbial respiration (Diaz, 2001). As organic matter sinking from the upper waters is much more abundant (in % of total suspended matter) and more labile relative to the sediment, the WCR of the near-bottom waters is greatly contributed to and controlled by sinking organic matter from the surface waters instead of by resuspended sediment OM, in which the organic matter is more depleted and refractory. Off the Changjiang Estuary, there are two sources of OM in the surface waters, namely, OM from rivers and OM from in situ production. Previous studies have shown that the OM that degrades in near-bottom waters and drives hypoxia is mainly of marine origin (Wang et al., 2016, 2017). Although surface productivity data are lacking, such a rate can be inferred by the negative AOU of surface waters. AOU in the surface waters ranged from −47 to 26 μmol/L (**Figure 4A** and **Table 1**), with the minimum AOU (−47 μmol/L) occurring at station D3 and gradually increasing southwards and outwards (**Figure 4A**). This trend was similar to the $[O_2]$ distribution pattern in the near-bottom waters (**Figure 3D**); that is, higher O_2 production (lower AOU values) at the surface correlated with lower $[O_2]$ in the near-bottom waters (**Figure 9**), which also suggests a coupling between excess organic matter production at the surface and stronger O_2 consumption beneath. Furthermore, although there was an outlier (a sample from station D3), near-bottom water WCR% showed a good negative relationship with surface AOU in both models (**Figures 10A,B**). In other words, lower surface water AOU (higher O_2 productivity at the surface) corresponded to a higher WCR% contribution to AOU in the near-bottom waters (**Figures 10A,B**), which is consistent with the mechanism by

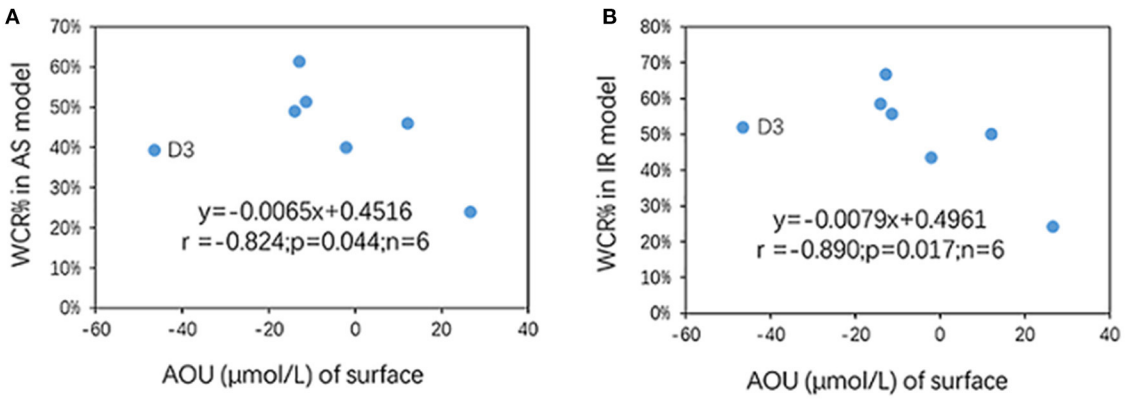


FIGURE 10 | The WCR% contribution to the total AOU of the near-bottom waters and its relationship with AOU of the surface waters: **(A)** AS model and **(B)** IR model. Note that only near-bottom water samples are shown; r, p, n in the plot were derived without data from D3.

which the generation of excess organic matter fuels near-bottom water O_2 consumption (Diaz, 2001).

With respect to SOR, the influential factors have been adequately reviewed (Glud, 2008), including sedimentation rates, near-bottom $[O_2]$, diffusive boundary layers, faunal activity, light, temperature, and sediment permeability. Because these influential factors vary greatly and the SOR is usually determined by these factors simultaneously, the dynamics of near-bottom $[O_2]$ are complicated but of great interest.

From the aspect of direct diffusion, the depth of O_2 penetration into sediment (L) and the diffusive oxygen utilization (DOU) between sediment and near-bottom waters can be described using equation 9 (Cai and Sayles, 1996) and equation 10 (Rasmussen and Jorgensen, 1992), respectively:

$$L = 2 \times \emptyset \times D_S \times \frac{[O_2]_{BW}}{F^0_{O_2}} \quad (9)$$

$$DOU = D_0 \times (dC_{(z)}/dz) \quad (10)$$

where in Equation 9, $\emptyset$ and D_S are the respective porosity and diffusivity of O_2 in the sediment, $[O_2]_{BW}$ is the near-bottom $[O_2]$, and $F^0_{O_2}$ is the benthic oxygen flux. In equation 10, D_0 is the diffusion coefficient of oxygen in water at a certain temperature and salinity, and $dC_{(z)}/dz$ is the oxygen content decreasing gradient (rate, or slope) along the diffusive boundary layer. Both equations 9 and 10 indicate that a higher SOR rate is expected under a higher near-bottom $[O_2]$. Although positive cases can be found to support such expectations (Rowe et al., 2002; Murrell and Lehrter, 2011; Lehrter et al., 2012), a few contrary examples have also been reported (Mccarthy et al., 2013).

The SOR% contribution to the total AOU beneath the pycnocline was positively related to near-bottom $[O_2]$ (**Figures 11A,C**) for the results from both models, supporting the expectation that higher bottom $[O_2]$ is accompanied by a higher SOR rate (Murrell and Lehrter, 2011; Song et al., 2020). The latest incubation work carried out on deck suggested that the SOR rate (mmol O_2/m^2/day) was positively related to near-bottom $[O_2]$ in summer (Song et al., 2020), which is consistent with our suggested SOR% pattern with bottom $[O_2]$ (**Figure 11**). As a comparison, lower near-bottom $[O_2]$ corresponded to a greater WCR contribution (**Figures 11B,D**). Furthermore, sensitivity analysis indicated that the pattern in **Figure 12** held even when the WCR endmember fractionation factor varied from −16 to −25‰ (**Supplementary Figures 5**, **6**), suggesting that our findings (**Figure 11**) are robust under a wide range of scenarios.

In addition to the horizontal distribution pattern (**Figures 11A,C**), the vertical distribution was investigated. A higher WCR% (lower SOR%) was usually expected at shallower depths, whereas in deeper layers (e.g., in the near-bottom waters), the SOR% could be higher than that in the corresponding shallower layers (**Figure 12**). At station E2, however, a reverse trend was found, where SOR% in deeper layers was generally lower than that at the shallower depth (i.e., SOR% at 60 m < SOR% at 30 m; **Figure 12B**). Oxygen depletion at 60 m was more severe than that at 30 m, with AOU values at 30 m and 60 m of 93 and 100 μmol/L, respectively. The SOR% and AOU relationship between 30 m and 60 m indicated that WCR tended to play a larger role in the more severe oxygen depletion scenario beneath the pycnocline, regardless of the depth (**Figure 12**).

Given the horizontal (**Figure 11**) and vertical patterns (**Figure 12**) of WCR% and SOR%, we propose dynamic, instead of fixed, oxygen consumption mechanisms of WCR and SOR in the near-bottom waters beneath the pycnocline (**Figures 10A,B**, **11**) that finally cause hypoxia off the Changjiang Estuary and adjacent ECS (**Figure 13**): In the stratified water column, the SOR contribution to the total bottom AOU is a background-like, chronic process that exists at all times. The WCR contribution to the total AOU can be very limited in near-bottom waters relative to SOR when no extra organic matter is abruptly introduced (e.g., via particle sinking). During the productive season (summer), however, excess organic matter assimilates in the surface waters, intensively sinks to the near-bottom waters within a very short time period, and hence stimulates WCR in the near-bottom waters. Compared to the background-like, chronic

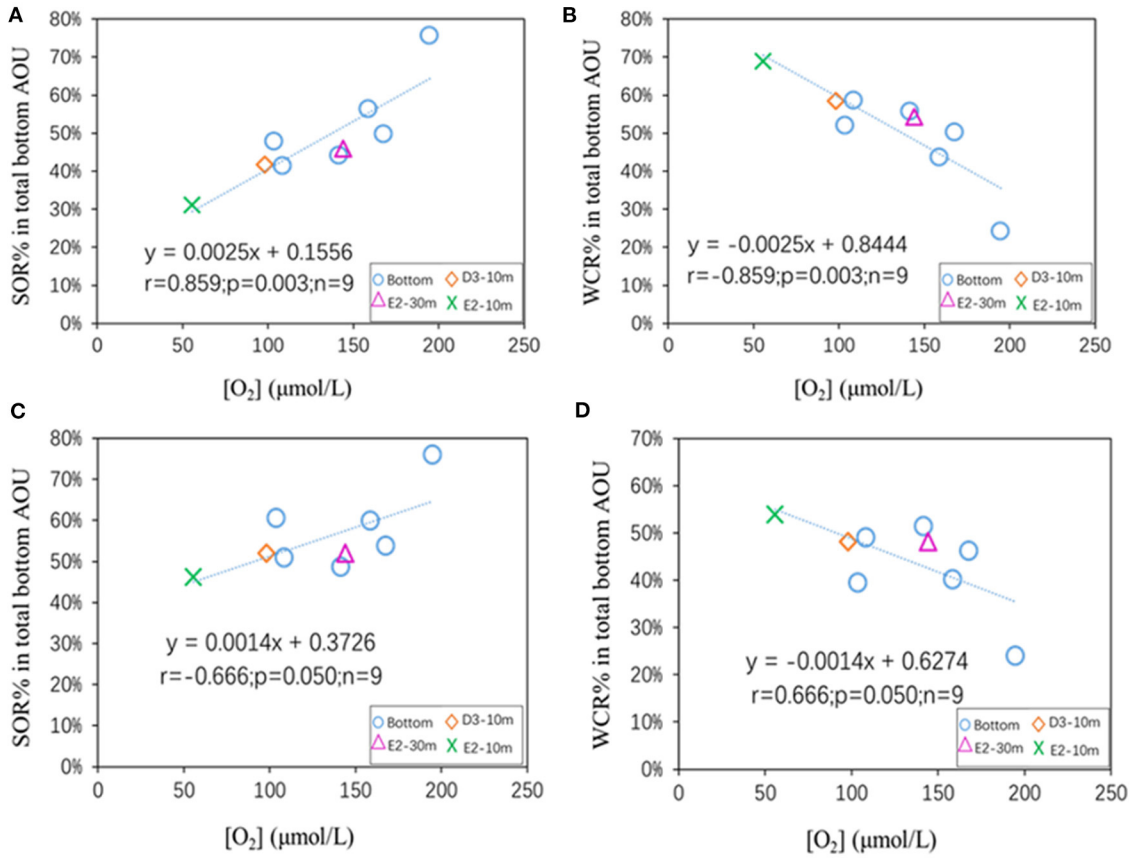


FIGURE 11 | The relationship between [O_2] (μmol/L) and the SOR% and WCR% contributions to total AOU for all sub-pycnocline samples shallower than 70 m: **(A,B)** Calculated from the IR model, **(C,D)** calculated from the AS model.

SOR, a sudden increase in WCR is a pulse-like and acute event (**Figures 10A,B**). If stratification prevails and prevents additional O_2 supply, hypoxia occurs. With decreasing [O_2], the O_2 penetration depth, as well as the diffusion rate of oxygen into the sediment, is expected to be increasingly restricted (Equations 9, 10), which in turn would further reduce the SOR contributions in the bottom AOU at that site during our observation. Therefore, the dominating oxygen consumption mechanisms would shift from SOR to WCR under such circumstances. Similar dynamics of the oxygen consumption shift between SOR and WCR can be inferred in the case of hypoxia in the Gulf of Mexico (Quinones-Rivera et al., 2007).

If the oxygen consumption scenario in **Figure 11** is valid for our observations, bloom management, instead of sediment management, would reduce organic matter that sinks into the near-bottom waters and hence would be more effective and instant in reducing hypoxia. Unfortunately, even if blooms in surface waters are controlled, near the bottom, [O_2] is unlikely to recover promptly. This is because of the presence of background-like, chronic SOR. In the worst condition, with controlled blooms in the surface waters, the reduced WCR and alleviated sub-pycnocline [O_2] will in turn promote increasing SOR contributions to oxygen depletion. Our work suggests that hypoxia management would be a comprehensive and long-term mission.

It should be pointed out that such a schematic (**Figure 13**) is at least partly based on an assumption that sediments in the whole study area are homogeneous in nature. Instead, the sediment grain size, porosity, and organic carbon content show clear spatial patterns (Niino and Emery, 1961; Song et al., 2016; Yang et al., 2016; Zhang et al., 2020). Although the sediment total organic carbon and total nitrogen contents showed no clear relationship with the SOR rate, the grain size effect has been suspected in the ECS (Song et al., 2016), with coarser surface sediment having stronger sediment-water exchange efficiency and hence playing an equally important role in SOR relative to organic matter-abundant fine sediment (De Beer et al., 2005).

Based on the radium-thorium imbalance method, SOR contributed 6–61% of the total bottom AOU (Cai et al., 2014), whereas sediment incubations carried out on deck on the ship showed that the SOR contribution could reach 100% (Zhang et al., 2017). While previous work showed a large variation range for SOR%, our result, which is based on an oxygen isotope and O_2 budget approach, also showed some fluctuations (**Figures 11A,C**). The fluctuation may result from the uncertainties of our approach, or more likely, from the heterogeneous sediment nature, which led to the SOR rate

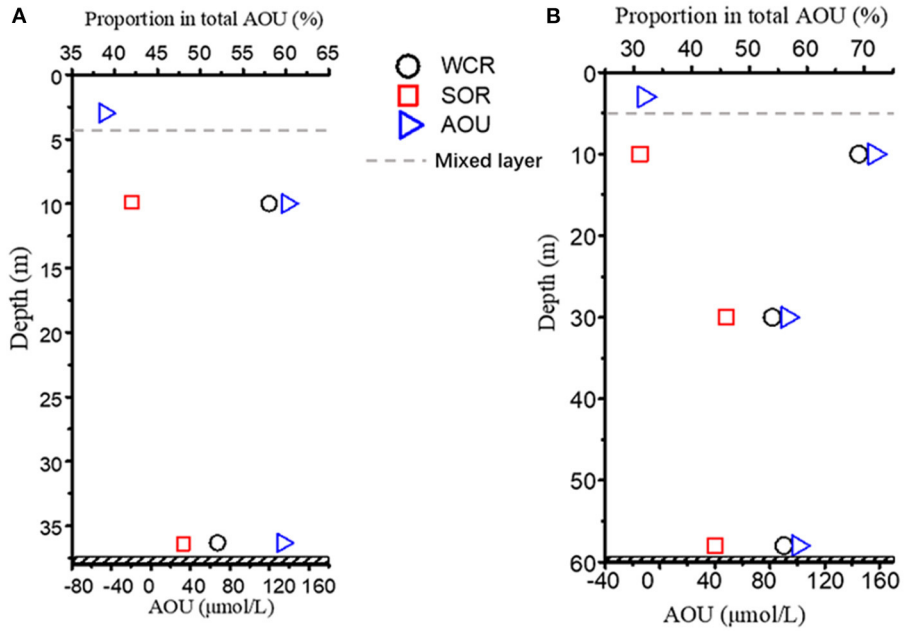


FIGURE 12 | The vertical distribution of the SOR% and WCR% contributions to total AOU at **(A)** station D3 and **(B)** station E2.

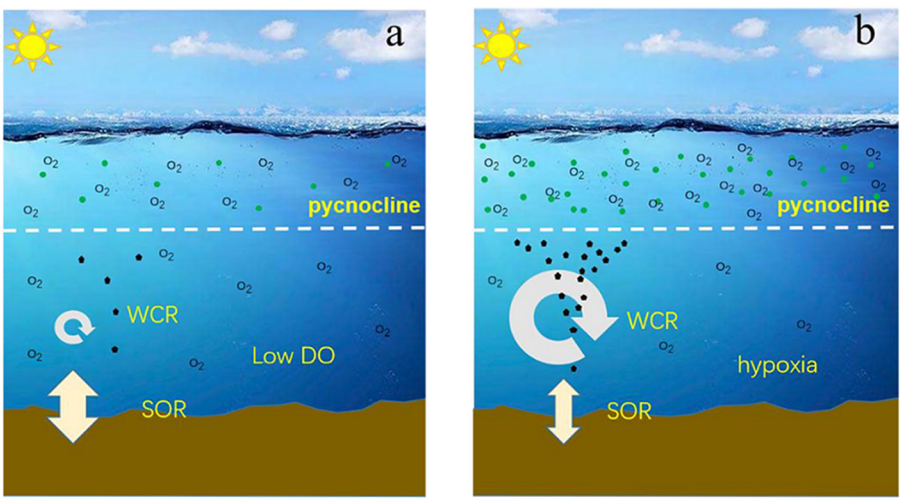


FIGURE 13 | Schematic of the dynamic WCR and SOR contributions to the total AOU at a fixed depth: **(a)** low DO ([O_2]>2 mg/L) scenario when there is no excess organic matter exported into the near-bottom waters and SOR dominates the bottom AOU; **(b)** hypoxia scenario when there is excess organic matter exported into the near-bottom waters and WCR drives [O_2] to a hypoxic level.

and further SOR% difference. We are also aware that O_2 diffusion-controlled fractionation may play a role in such a $\delta^{18}O$-based approach (Ostrom et al., 2014). But off the Changjiang Estuary, at least during our observation, similar decoupling between [O_2] and $\delta^{18}O$ was not observed. Nevertheless, more observation-based integrated studies (i.e., covering both SOR and WCR contributions) are needed to clarify the shift in SOR and WCR contributions to bottom hypoxia off the Changjiang Estuary and adjacent ECS.

CONCLUSION

In addition to respiration incubation experiments using sediments and water column organic matter, the oxygen isotope budget provides another approach to quantify both WCR and SOR under oxygen depletion. In the near-bottom waters off the Changjiang Estuary and adjacent ECS, the $\delta^{18}O$ of dissolved oxygen ranged from 1.039 to 8.457‰, indicating a significant fractionation effect during oxygen consumption.

To clarify the WCR and SOR contributions to the total AOU, respiration models are used to quantify the coupling between $[O_2]$ and the corresponding $\delta^{18}O$. In addition to a model published by Quinones-Rivera (AS model) (Quinones-Rivera et al., 2007), we also developed an IR model to evaluate the WCR and SOR% in the sub-pycnocline waters. The results from the two models basically agreed with each other, but the pattern of decreasing SOR% contribution to the total AOU with decreasing $[O_2]$ was clearer in the IR model than in the AS model (**Figure 11A**).

Our results indicated that the WCR and SOR% contributions to the total AOU of the near-bottom waters were dynamic, not stationary, and were likely affected by ambient environmental factors (e.g., $[O_2]$; **Figure 11**). Accordingly, we propose that SOR is the main factor that determines the background AOU of the near-bottom waters off the Changjiang Estuary, but the WCR drives the dissolved oxygen level to hypoxia. In July 2018, WCR contributed ∼70% of the total AOU when hypoxia occurred ($[O_2]$ ∼50 μmol/L).

As primary research, there are still some other factors that are not well addressed in the oxygen isotope budget. Although the terrestrial input from the Changjiang River is expected to play a limited role in increasing bias in the expected coupling between $[O_2]$ and $\delta^{18}O$, the mixing effect of various water masses in the study area and its impact on the oxygen isotope budget (Bender, 1990) should still be considered in the future.

DATA AVAILABILITY STATEMENT

The original contributions presented in the study are included in the article/**Supplementary Materials**, further inquiries can be directed to the corresponding authors.

AUTHOR CONTRIBUTIONS

G-LZ participated field sampling and revised the manuscript. H-TH provided the IR model, helped and funded the sample measurements, and revised the manuscript. Z-YZ composed the idea and scientific question, revised the manuscript, and funded the project. JZ wrote the original manuscript and measured the samples. Q-QW conducted the incubation experiment. All authors contributed to the article and approved the submitted version.

FUNDING

This work was funded by the Ministry of Science and Technology in China (via the National Key Research and Development Program of China, No. 2020YFA0608301), by the Shanghai Sailing Program under grant 19YF1422500, and by the National Natural Science Foundation of China (No. 41976042, 41776122, and 41530960).

ACKNOWLEDGMENTS

We are grateful to the captain and crew of R/V *Dongfanghong 2* and R/V *Runjiang* for their assistance in the field. We thank Chuan Qin from OUC for collecting water samples in July 2018. Z-YZ thanks Michael L. Bender for his help and inspiration during the early period of the dissolved gas isotope study.

SUPPLEMENTARY MATERIAL

The Supplementary Material for this article can be found online at: https://www.frontiersin.org/articles/10.3389/fmars.2020.623581/full#supplementary-material

REFERENCES

Bender, M. L. (1990). The δ18O of dissolved O2 in seawater: a unique tracer of circulation and respiration in the deep sea. *J. Geophys. Res.* 95, 22243–22252. doi: 10.1029/JC095iC12p22243

Bender, M. L., and Grande, K. D. (1987). Production, respiration, and the isotope geochemistry of O2in the upper water column. *Glob. Biogeochem. Cycles* 1, 49–59. doi: 10.1029/GB001i001p00049

Brandes, J. A., and Devol, A. H. (1997). Isotopic fractionation of oxygen and nitrogen in coastal marine sediments. *Geochim. Cosmochim. Acta* 61, 1793–1801. doi: 10.1016/S0016-7037(97)00041-0

Cai, P. H., Shi, X. M., Moore, W. S., Peng, S. Y., Wang, G. Z., and Dai, M. H. (2014). 224Ra:228Th disequilibrium in coastal sediments: implications for solute transfer across the sediment–water interface. *Geochim. Cosmochim. Acta* 125, 68–84. doi: 10.1016/j.gca.2013.09.029

Cai, W.-J., and Sayles, F. L. (1996). Oxygen penetration depths and fluxes in marine sediments. *Marine Chem.* 52, 123–131. doi: 10.1016/0304-4203(95)00081-X

Capet, A., Beckers, J. M., and Grégoire, M. (2013). Drivers, mechanisms and long-term variability of seasonal hypoxia on the Black Sea northwestern shelf – is there any recovery after eutrophication? *Biogeosciences* 10, 3943–3962. doi: 10.5194/bg-10-3943-2013

Carstensen, J., Andersen, J. H., Gustafsson, B. G., and Conley, D. J. (2014). Deoxygenation of the Baltic Sea during the last century. *Proc. Natl. Acad. Sci. U.S.A.* 111, 5628–5633. doi: 10.1073/pnas.1323156111

Chen, J. Y., Pan, D. L., Liu, M. L., Mao, Z. H., Zhu, Q. K., Chen, N. H., Zhang, X. Y., and Tao, B. Y. (2017). Relationships between long-term trend of satellite-derived chlorophyll-a and hypoxia off the changjiang Estuary. *Estuaries Coasts* 40, 1055–1065. doi: 10.1007/s12237-016-0203-0

Chi, L., Song, X., Yuan, Y., Wang, W., Cao, X., Wu, Z., and Yu, Z. (2020). Main factors dominating the development, formation and dissipation of hypoxia off the Changjiang Estuary (CE) and its adjacent waters, China. *Environ. Pollution* 265:115066. doi: 10.1016/j.envpol.2020.115066

Crain, C. M. (2007). Shifting nutrient limitation and eutrophication effects in marsh vegetation across estuarine salinity gradients. *Estuaries Coasts* 30, 26–34. doi: 10.1007/BF02782964

Daoji, L., and Daler, D. (2004). Ocean Pollution from Land-based Sources: East China Sea, China. *AMBIO* 33, 107–113. doi: 10.1579/0044-7447-33.1.107

De Beer, D., Wenzhöfer, F., Ferdelman, T. G., Boehme, S. E., Huettel, M., Van Beusekom, J. E. E., Böttcher, M. E., et al. (2005). Transport and mineralization rates in North Sea sandy intertidal sediments, Sylt-Rømø Basin, Wadden Sea. *Limnol. Oceanogr.* 50, 113–127. doi: 10.4319/lo.2005.50.1.0113

Diaz, R. J. (2001). Overview of hypoxia around the world. *J. Environ. Qual.* 30, 275–281. doi: 10.2134/jeq2001.302275x

Fry, B. (2006). *Stable Isotope Ecology*. New York, NY: Springer. doi: 10.1007/0-387-33745-8

Glud, R. N. (2008). Oxygen dynamics of marine sediments. *Marine Biol. Res.* 4, 243–289. doi: 10.1080/17451000801888726

Hendricks, M. B., Bender, M. L., and Barnett, B. A. (2005). Triple oxygen isotope composition of dissolved O_2 in the equatorial Pacific: A tracer of mixing, production, and respiration. *J. Geophys. Res.* 110:C12021. doi: 10.1029/2004JC002735

Hopkinson, C. S., and Smith, E. M. (2005). "Estuarine respiration: an overview of benthic, pelagic, and whole system respiration," in *Respiration in Aquatic Ecosystems*, eds P. Giorgio, A. Del, and P. J. L. B. Williams (New York, NY: Oxford University Press), 123–146. doi: 10.1093/acprof:oso/9780198527084.003.0008

Keeling, R. F., Körtzinger, A., and Gruber, N. (2010). Ocean deoxygenation in a warming world. *Annual Rev. Marine Sci.* 2, 199–229. doi: 10.1146/annurev.marine.010908.163855

Kirkwood, D. S. (1992). Stability of solutions of nutrient salts during storage. *Marine Chem.* 38, 151–164. doi: 10.1016/0304-4203(92)90032-6

Lane, G. A., and Dole, M. (1956). Fractionation of oxygen isotopes during respiration. *Science* 123, 574–576. doi: 10.1126/science.123.3197.574

Lehrter, J. C., Beddick, D. L., Devereux, R., Yates, D. F., and Murrell, M. C. (2012). Sediment-water fluxes of dissolved inorganic carbon, O2, nutrients, and N2 from the hypoxic region of the Louisiana continental shelf. *Biogeochemistry* 109, 233–252. doi: 10.1007/s10533-011-9623-x

Li, D. J., Zhang, J., Huang, D. J., Wu, Y., and Liang, J. (2002). Oxygen depletion off the Changjiang (Yangtze River) Estuary. *Sci. China Seri. D* 45, 1137–1146. doi: 10.1360/02yd9110

Li, H.-M., Tang, H.-J., Shi, X.-Y., Zhang, C.-S., and Wang, X.-L. (2014). Increased nutrient loads from the Changjiang (Yangtze) River have led to increased Harmful Algal Blooms. *Harmful Algae* 39, 92–101. doi: 10.1016/j.hal.2014.07.002

Li, S. L., Liu, C. Q., Li, J., Liu, X. L., Chetelat, B., Wang, B. L., and Wang, F. S. (2010). Assessment of the sources of nitrate in the changjiang river, China using a nitrogen and oxygen isotopic approach. *Environ. Sci. Technol.* 44, 1573–1578. doi: 10.1021/es902670n

Li, Z., Song, S. Q., Li, C. W., and Yu, Z. M. (2018). The sinking of the phytoplankton community and its contribution to seasonal hypoxia in the Changjiang (Yangtze River) estuary and its adjacent waters. *Estuarine Coastal Shelf Sci.* 208, 170–179. doi: 10.1016/j.ecss.2018.05.007

Liu, L., Zhou, J., Zheng, B., Cai, W., Lin, K., and Tang, J. (2013). Temporal and spatial distribution of red tide outbreaks in the Yangtze River Estuary and adjacent waters, China. *Marine Pollut. Bull.* 72, 213–221. doi: 10.1016/j.marpolbul.2013.04.002

Mariotti, A., Germon, J. C., Hubert, P., Kaiser, P., Letolle, R., Tardieux, A., and Tardieux, P. (1981). Experimental determination of nitrogen kinetic isotope fractionation: some principles; illustration for the denitrification and nitrification processes. *Plant Soil* 62, 413–430. doi: 10.1007/BF02374138

Mccarthy, M. J., Carini, S. A., Liu, Z., Ostrom, N. E., and Gardner, W. S. (2013). Oxygen consumption in the water column and sediments of the northern Gulf of Mexico hypoxic zone. *Estuarine Coastal Shelf Sci.* 123, 46–53. doi: 10.1016/j.ecss.2013.02.019

Murrell, M. C., and Lehrter, J. C. (2011). Sediment and lower water column oxygen consumption in the seasonally hypoxic region of the louisiana continental shelf. *Estuar. Coasts* 34, 912–924. doi: 10.1007/s12237-010-9351-9

Naqvi, S. W. A., Jayakumar, D. A., Narvekar, P. V., Naik, H., Sarma, V. V., D'souza, S. S., et al. (2000). Increased marine production of N2O due to intensifying anoxia on the Indian continental shelf. *Nature* 408, 346–349. doi: 10.1038/35042551

Ni, X. B., Huang, D. J., Zeng, D. Y., Zhang, T., Li, H. L., and Chen, J. F. (2016). The impact of wind mixing on the variation of bottom dissolved oxygen off the Changjiang Estuary during summer. *J. Marine Syst.* 154, 122–130. doi: 10.1016/j.jmarsys.2014.11.010

Niino, H., and Emery, K. O. (1961). Sediments of shallow portions of east China Sea and South China Sea. *Geol. Soc. Am. Bull.* 72:731. doi: 10.1130/0016-7606(1961)72[731:SOSPOE]2.0.CO;2

Nilsson, H. C., and Rosenberg, R. (1994). Hypoxic response of two marine benthic communities. *Marine Ecol. Progr. Seri.* 115, 209–217. doi: 10.3354/meps115209

Office of Integrated Oceanographic Survey of China (1961). *Dataset of the National Integrated Oceanographyic Survey*. vol 1. Survey data of hydrometeorological and chemical elements in the bohai, Huanghai and East China Seas (Beijing).

Ostrom, N. E., Gandhi, H., Kamphuis, B., Decamp, S., Liu, Z., Mccarthy, M. J., and Gardner, W. S. (2014). Oxygen metabolism and water mass mixing in the northern Gulf of Mexico hypoxic zone in 2010. *Geochim. Cosmochim. Acta* 140, 39–49. doi: 10.1016/j.gca.2014.05.020

Qian, W., Dai, M., Xu, M., Kao, S.-J., Du, C., Liu, J., Wang, H., Guo, L., and Wang, L. (2017). Non-local drivers of the summer hypoxia in the East China Sea off the Changjiang Estuary. *Estuarine Coastal Shelf Sci.* 198, 393–399. doi: 10.1016/j.ecss.2016.08.032

Quinones-Rivera, Z. J., Wissel, B., Justic, D., and Fry, B. J. M. (2007). Partitioning oxygen sources and sinks in a stratified, eutrophic coastal ecosystem using stable oxygen isotopes. *Mar. Ecol. Progr.* 342, 69–83. doi: 10.3354/meps342069

Rasmussen, H., and Jorgensen, B. B. (1992). Microelectrode studies of seasonal oxygen uptake in a coastal sediment: role of molecular diffusion. *Marine Ecol. Progr. Seri.* 81, 289–303. doi: 10.3354/meps081289

Reuer, M. K., Barnett, B. A., Bender, M. L., Falkowski, P. G., and Hendricks, M. B. (2007). New estimates of Southern Ocean biological production rates from O2/Ar ratios and the triple isotope composition of O2. *Deep Sea Res. Part I* 54, 951–974. doi: 10.1016/j.dsr.2007.02.007

Rowe, G. T., Kaegi, M. E. C., Morse, J. W., Boland, G. S., and Escobar Briones, E. G. (2002). Sediment community metabolism associated with continental shelf hypoxia, Northern Gulf of Mexico. *Estuaries* 25, 1097–1106. doi: 10.1007/BF02692207

Sindermann, C. J., and Swanson, R. L. (1979). *Oxygen depletion and associated benthic mortalities in New York Bight, 1976/editors*, R. Lawrence Swanson, Carl J. Sindermann. National Oceanic and Atmospheric Administration. doi: 10.5962/bhl.title.4193

Song, G.-D., Liu, S.-M., Zhang, J., Zhu, Z.-Y., Zhang, G.-L., Marchant, H. K., Kuypers, M. M. M., and Lavik, G. (2020). Response of benthic nitrogen cycling to estuarine hypoxia. *Limnol. Oceanogr.* 9999, 1–15. doi: 10.1002/lno.11630

Song, G.-D., Liu, S.-M., Zhu, Z.-Y., Zhai, W.-D., Zhu, C.-J., and Zhang, J. (2016). Sediment oxygen consumption and benthic organic carbon mineralization on the continental shelves of the East China Sea and the Yellow Sea. *Deep Sea Res. Part II* 124, 53–63. doi: 10.1016/j.dsr2.2015.04.012

Su, J. L. (1998). "Circulation dynamics of the China Sea north of 18°N," in *The Sea* eds A. R. Robinson and K. H. Brink (New York, NY: John Wiley and Sons Inc.), 483–505.

Tsunogai, S., Shuichi, W., Yunya, N., Tsuneo, O., and Tetsuro, S. (1997). A preliminary study of carbon system in the East China Sea. *J. Oceanogr.* 53, 9–17. doi: 10.1007/BF02700744

Turner, R. E., Rabalais, N. N., Swenson, E. M., Kasprzak, M., and Romaire, T. (2005). Summer hypoxia in the northern Gulf of Mexico and its prediction from 1978 to 1995. *Marine Environ. Res.* 59, 65–77. doi: 10.1016/j.marenvres.2003.09.002

Wang, B., Chen, J. F., Jin, H. Y., Li, H. L., Huang, D. J., and Cai, W. J. (2017). Diatom bloom-derived bottom water hypoxia off the Changjiang estuary, with and without typhoon influence. *Limnol. Oceanogr.* 62, 1552–1569. doi: 10.1002/lno.10517

Wang, B. D. (2009). Hydromorphological mechanisms leading to hypoxia off the Changjiang estuary. *Marine Environ. Res.* 67, 53–58. doi: 10.1016/j.marenvres.2008.11.001

Wang, H. J., Dai, M. H., Liu, J. W., Kao, S.-J., Zhang, C., Cai, W.-J., et al. (2016). Eutrophication-driven hypoxia in the east China Sea off the changjiang estuary. *Environ. Sci. Technol.* 50, 2255–2263. doi: 10.1021/acs.est.5b06211

Wei, H., He, Y., Li, Q., Liu, Z., and Wang, H. (2007). Summer hypoxia adjacent to the Changjiang Estuary. *J. Marine Syst.* 67, 292–303. doi: 10.1016/j.jmarsys.2006.04.014

Wei, Q. S., Wang, B. D., Yu, Z. G., Chen, J. F., and Xue, L. (2017). Mechanisms leading to the frequent occurrences of hypoxia and a preliminary analysis of the associated acidification off the Changjiang Estuary in summer. *Sci. China Earth Sci.* 60, 360–381. doi: 10.1007/s11430-015-5542-8

Wendel, J. (2015). Gulf of Mexico dead zone largest since 2002. *Mar. Ecol. Progr.* Series 96. doi: 10.1029/2015EO033929

Yan, W., Zhang, S., Sun, P., and Seitzinger, S. P. (2003). How do nitrogen inputs to the Changjiang basin impact the Changjiang River nitrate: a temporal analysis for 1968-1997. *Glob. Biogeochem. Cycles* 17. doi: 10.1029/2002GB002029

Yang, Y.-P., Zhang, M.-J., Li, Y.-T., and Fan, Y.-Y. (2016). Trend and dynamic cause of sediment particle size on the adjacent continental shelf of the Yangtze Estuary. *China Ocean Eng.* 30, 992–1003. doi: 10.1007/s13344-016-0065-z

Zhang, H. Y., Zhao, L., Sun, Y., Wang, J. N., and Wei, H. (2017). Contribution of sediment oxygen demand to hypoxia development off the Changjiang Estuary. *Estuarine Coastal Shelf Sci.* 192, 149–157. doi: 10.1016/j.ecss.2017.05.006

Zhang, J., Zhang, Z. F., Liu, S. M., Wu, Y., Xiong, H., and Chen, H. T. (1999). Human impacts on the large world rivers: Would the Changjiang (Yangtze River) be an illustration? *Glob. Biogeochem. Cycles* 13, 1099–1105. doi: 10.1029/1999GB900044

Zhang, S., Liang, C., and Xian, W. (2020). Spatial and temporal distributions of terrestrial and marine organic matter in the surface sediments of the Yangtze River estuary. *Continental Shelf Res.* 203:104158. doi: 10.1016/j.csr.2020.104158

Zhang, W.-X., Wu, H., Hetland, R. D., and Zhu, Z.-Y. (2019). On mechanisms controlling the seasonal hypoxia hot spots off the changjiang river estuary. *J. Geophys. Res.* 124, 8683–8700. doi: 10.1029/2019JC015322

Zhu, Z.-Y., Wu, H., Liu, S.-M., Wu, Y., Huang, D.-J., Zhang, J., and Zhang, G.-S. (2017). Hypoxia off the Changjiang (Yangtze River) estuary and in the adjacent East China Sea: quantitative approaches to estimating the tidal impact and nutrient regeneration. *Marine Pollution Bull.* 125, 103–114. doi: 10.1016/j.marpolbul.2017.07.029

Zhu, Z.-Y., Zhang, J., Wu, Y., Zhang, Y.-Y., Lin, J., and Liu, S.-M. (2011). Hypoxia off the Changjiang (Yangtze River) Estuary: Oxygen depletion and organic matter decomposition. *Marine Chem.* 125, 108–116. doi: 10.1016/j.marchem.2011.03.005

Zhu, Z. Y., Ng, W. M., Liu, S. M., Zhang, J., Chen, J. C., and Wu, Y. (2009). Estuarine phytoplankton dynamics and shift of limiting factors: A study in the Changjiang (Yangtze River) Estuary and adjacent area. *Estuarine Coastal Shelf Sci.* 84, 393–401. doi: 10.1016/j.ecss.2009.07.005

Conflict of Interest: The authors declare that the research was conducted in the absence of any commercial or financial relationships that could be construed as a potential conflict of interest.

Copyright © 2021 Zhou, Zhu, Hu, Zhang and Wang. This is an open-access article distributed under the terms of the Creative Commons Attribution License (CC BY). The use, distribution or reproduction in other forums is permitted, provided the original author(s) and the copyright owner(s) are credited and that the original publication in this journal is cited, in accordance with accepted academic practice. No use, distribution or reproduction is permitted which does not comply with these terms.

frontiers in Marine Science

ORIGINAL RESEARCH
published: 08 October 2020
doi: 10.3389/fmars.2020.565952

Intrusion of Kuroshio Helps to Diminish Coastal Hypoxia in the Coast of Northern South China Sea

Hon-Kit Lui[1], Chen-Tung Arthur Chen[1,2]*, Wei-Ping Hou[3], Jian-Ming Liau[4], Wen-Chen Chou[5,6], You-Lin Wang[7], Chau-Ron Wu[7], Jay Lee[1,3], Yi-Chia Hsin[8] and Yan-Yu Choi[9]*

[1] Department of Oceanography, National Sun Yat-sen University, Kaohsiung, Taiwan, [2] Institute of Marine Environment and Chemistry, Zhejiang University, Zhoushan, China, [3] Taiwan Ocean Research Institute, National Applied Research Laboratories, Kaohsiung, Taiwan, [4] National Academy of Marine Research, Kaohsiung, Taiwan, [5] Institute of Marine Environmental and Ecology, National Taiwan Ocean University, Keelung, Taiwan, [6] Center of Excellence for the Oceans, National Taiwan Ocean University, Keelung, Taiwan, [7] Department of Earth Sciences, National Taiwan Normal University, Taipei, Taiwan, [8] Research Center for Environmental Changes, Academia Sinica, Taipei, Taiwan, [9] Department of Mathematics, The University of Hong Kong, Pokfulam, Hong Kong

Since half a century ago, the number and area of dead zones (dissolved oxygen (DO) < 2 mg L^{-1} or 30% saturation) in the coastal oceans has increased dramatically. As widely recognized, the increased terrestrial nutrient and organic matter inputs are the two main factors causing the eutrophication of many coastal oceans. Here we show with decadal observed time series data from stations off the Pearl River Estuary and in the northern South China Sea (nSCS) that a strong intrusion into the nSCS of the West Philippine Sea (WPS) seawater in the form of Kuroshio branch occurred during the warm phase of the Pacific Decadal Oscillation (PDO) around 2003–2004 and 2015–2016 (also a strong El Niño event). Consequently, the DO concentration increased but NO_3^- and PO_4^{3-} concentrations decreased in the subsurface layers of the nSCS. The WPS seawater was observed to reach the hypoxic area off the Pearl River Estuary in 2003–2004. Likely, due to the oxygen supply carried by the Kuroshio, little hypoxia developed. Yet, anoxic condition developed in the cold phase of PDO or strong La Niña years with weak Kuroshio intrusions.

Keywords: hypoxia, Kuroshio, intrusion, Pearl River Estuary, South China Sea, El Niño, PDO

OPEN ACCESS

Edited by:
Xianghui Guo, Xiamen University, China

Reviewed by:
Zhiqiang Liu, Southern University of Science and Technology, China
Sabine Schmidt, Centre National de la Recherche Scientifique (CNRS), France

****Correspondence:***
Hon-Kit Lui
hklui@mail.nsysu.edu.tw
Chen-Tung Arthur Chen
ctchen@mail.nsysu.edu.tw

Specialty section:
This article was submitted to Coastal Ocean Processes, a section of the journal Frontiers in Marine Science

Received: *26 May 2020*
Accepted: *28 August 2020*
Published: *08 October 2020*

Citation:
Lui HK, Chen CTA, Hou WP, Liau JM, Chou WC, Wang YL, Wu CR, Lee J, Hsin YC and Choi YY (2020) Intrusion of Kuroshio Helps to Diminish Coastal Hypoxia in the Coast of Northern South China Sea. Front. Mar. Sci. 7:565952. doi: 10.3389/fmars.2020.565952

INTRODUCTION

Coastal oceans are important habitats and spawning grounds for many marine organisms, which need dissolved oxygen (DO) to live. However, the number and size of hypoxic regions (DO < 2 mg L^{-1}), the so-called dead zone, has risen significantly in recent decades, adversely impacting the sustainability of the coastal ecosystems (Diaz and Rosenberg, 2008; Howarth et al., 2011; Rabalais et al., 2014; Breitburg et al., 2018). Eutrophication due to the increasing terrestrial nutrient flux is one of the main factors that causes hypoxia, although hypoxia can also form naturally, for instance by the intrusion of upwelled low DO water into coastal oceans (Feely et al., 2008; Rabalais et al., 2010; Howarth et al., 2011; Breitburg et al., 2018). Dead zones mostly exist off river mouths. This is because the excess nutrients from riverine inputs enhance biological productivity in the surface ocean. Yet, dead phytoplankton sink to the bottom of the coastal zone, where they decompose and consume oxygen. The stratification of seawater in coastal oceans in summer reduces bottom

water ventilation. The incoming, subsurface, offshore seawater thus becomes the dominant source of DO for the bottom water. If the oxygen consumption rate due to organic matter decomposition exceeds the supply rate due to the inflow of offshore seawater, then hypoxia or even anoxia may develop, leading to so-called dead zones. Global warming makes the situation worse by increasing stratification and reducing DO solubility in seawater (Schmidtko et al., 2017; Breitburg et al., 2018).

River delivered organic matter and the inorganic nutrients are two of the main factors causing hypoxia in many estuaries (Diaz and Rosenberg, 2008; Conley et al., 2009; Lui and Chen, 2012; Rabalais et al., 2014; Breitburg et al., 2018). In the East China Sea off the Changjiang Estuary for instance, the $\delta^{13}C$ of the remineralized organic carbon in the hypoxic zone was $-18.5 \pm 1.0\%$, matching well with the $\delta^{13}C$ of the *in situ* produced marine particulate organic carbon ($-18.5 \pm 0.3\%$), while the terrestrial source was about $-24.4 \pm 0.2\%$ (Wang et al., 2016). Such a result indicates that the riverine nutrient-induced productivity, and not the river-delivered terrestrial organic matter, was the dominant oxygen consumer in the hypoxic zone off the Changjiang Estuary. Pearl River, also known as Zhujiang by its Chinses name, is the second largest in terms of outflow among the rivers in China and discharges directly into the northern South China Sea (nSCS). Largely due to the riverine inputs of both nutrients and organic matter, hypoxic conditions have appeared in and off the Pearl River estuary in summer (Cai et al., 2004; Lu et al., 2018; Qian et al., 2018). In the hypoxic area off the Pearl River Estuary, the $\delta^{13}C$ of the remineralized organic carbon was $-23.2 \pm 1.1\%$, resulting from the combination of organic matter decomposition from mainly the marine source (produced locally, $65 \pm 16\%$) and partly the terrestrial source ($35 \pm 16\%$) (Su et al., 2017). Such a result reveals that both river-delivered nutrients and terrestrial organic matter played important roles in consuming the DO of the bottom water of the hypoxic zone in the Pearl River Estuary.

Another fact is that, the nSCS is influenced frequently by the intrusion of the West Philippine Sea (WPS) seawater in the form of Kuroshio branch through the Luzon Strait (**Figure 1**). The WPS and South China Sea (SCS) seawaters have distinctive vertical salinity, DO, and nutrient distributions (Chen et al., 2001). The intruded Kuroshio exerts inter-annual influences on the biogeochemical cycles in the nSCS (Lui et al., 2018), and possibly the hypoxic condition in the coastal regions therein. A related incidence occurred in the almost enclosed Baltic Sea, where the strong inflow of the DO-rich North Sea seawater in 2014 turned the Baltic deep water from anoxic to oxic conditions (Mohrholz et al., 2015). Namely, in addition to eutrophication, the amount of offshore water intrusion could play a significant role in coastal hypoxia. Moreover, the intrusion patterns in some marginal seas follow that of natural climatic oscillations, such as Pacific Decadal Oscillation (PDO) or El Niño/Southern Oscillation (ENSO) (Wu et al., 2014, 2017; Chen et al., 2016). Generally speaking, the PDO and ENSO refer to periodic variations in the sea surface temperature (SST) of the Pacific Ocean north of 20°N and in tropical region, respectively (Mantua et al., 1997). The PDO index or Oceanic Nino Index (ONI) is commonly used to quantify the strength of the PDO or ENSO, respectively. A PDO warm (cold) phase, positive (negative) PDO index, corresponds with positive (negative) SST anomalies in the eastern North Pacific Ocean north 20°N (Mantua et al., 1997). An ENSO warm (cold) phase, positive (negative) ONI, corresponds with positive (negative) SST anomalies in the eastern tropical Pacific Ocean (Banholzer and Donner, 2014). An El Niño or La Niña event occurs when the 3-month-running-average SST anomalies in the Nino 3.4 region (about 5°S–5°N, 120–170°W) reaches 0.5 or −0.5°C, respectively, for at least five consecutive overlapping months (Banholzer and Donner, 2014). Therefore, an ENSO warm (cold) phase usually is known as El Niño (La Niña) event.

To examine the influence of offshore water intrusion on coastal hypoxic condition, we start by looking at the lower Pearl River Estuary near Hong Kong. Located at the southeastern Pearl River Estuary in the nSCS, Hong Kong has a coastal area of 1,651 km^2 which supports a variety of marine lives and ecosystems (Hong Kong Environmental Protection Department, 2015). Since 1986, the Hong Kong Environmental Protection Department (HKEPD) has a water quality monitoring program. The bottom water data of the station SM18 (22.15°N, 114.08°E, 21 m depth) used here are located off the southern coast of Hong Kong, where seawater is stratified well in summer (Lui and Chen, 2012). Meanwhile, we also look at the data from the South East Asia Time-Series Study (SEATS, 18°N, 116°E, with bottom depth > 3700 m) station located in the nSCS and from the station 21 located in the WPS (**Figure 1**). Generally speaking, SEATS was initially established as a part of the Joint Global Ocean Flux Study (JGOFS, 1987–2003), whereas station 21 was one of the stations of the World Ocean Circulation Experiment (WOCE, 1990–2002) Pacific Repeated Line 20 (PR20) across 21°45′ N from the southern tip of Taiwan eastward to about 130°E.

MATERIALS AND METHODS

Data at SM18 were taken from the HKEPD. Samples were taken bimonthly between 1990 and 1998, and monthly after 1999. The surface and bottom water samples were taken from 1 m below the surface and 1 m above the seabed, respectively. The reporting limits are 0.1 for salinity, 0.1 mg/L for DO, 0.01 mg N/L (equivalent to 0.7 μM) for dissolved inorganic nitrogen (DIN = $NO_3 + NO_2 + NH_4$), and 0.2 μg/L for chlorophyll-a concentrations (Hong Kong Environmental Protection Department, 2015). Detailed sampling methods and measurements were presented in the 2015 Annual Marine Water Quality Report, published by the HKEPD (Hong Kong Environmental Protection Department, 2015). One DO datum in 1992/12 was not considered in our analysis due to its abnormally low value of only 1% saturation. The Pearl River has three major tributaries which are the West River, North River, and the East River (Chen et al., 2008). The annual water discharge and sediment loading data, estimated by summing up the water discharges and sediment loadings at the Gaoyao gauging station on the West River, Shijiao gauging station on the North River,

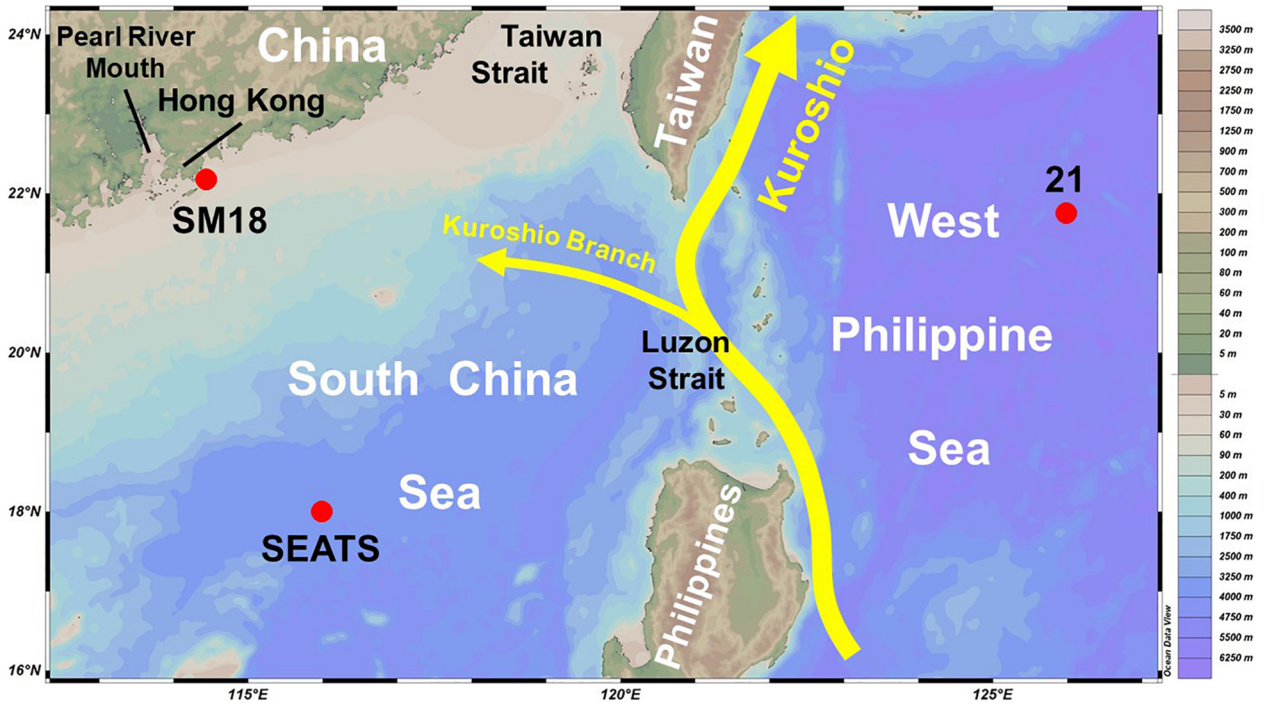


FIGURE 1 | Study areas and basic hydrology. Red solid circles indicate the station locations. The yellow curves and arrows show the typical Kuroshio current, as well as its branch. The map was generated using Ocean Data View 5.0.0. Schlitzer, R., Ocean Data View, https://odv.awi.de, 2018.

and the Boluo gauging station on the East River, were taken from the China River Sediment Bulletin 2002–2018 (Ministry of Water Resources of the People's Republic of China, (2002–2018)).

At the SEATS station, data from 73 cruises were provided by the Ocean Data Bank of Taiwan (ODB)[1]. Sampling dates and the cruise information are listed in the website of the OBD. This study collected data from another seven cruises on 1997/11/18, 1999/4/10, 2013/9/14, 2014/5/25, 2018/7/7, 2019/8/18, and 2019/11/3. Data since 2013/9/14 can be applied through the Taiwan Ocean Research Institute, National Applied Research Laboratories. The salinity data used were measured by the conductivity, temperature, and pressure unit (the so-called CTD unit). Salinity of discrete seawaters were sampled and measured by the AUTOSAL salinometer which was calibrated according to the seawater standard produced by the International Association for the Physical Sciences of the Oceans with a precision of 0.003. The CTD-measured salinity agrees well with those from the salinometer (**Figure 2**) with an average difference (salinometer-measured salinity minus CTD-measured salinity) of just 0.012 ± 0.024 (n = 14), confirming the validity of the CTD-measured salinity. At station 21, and to our best information for most of the data at SEATS, DO was measured by spectrophotometry with a detection limit and precision of about 0.5 μM and 0.3%, respectively (Pai et al., 1993). Nitrate concentration was determined using the pink azo dye method by a flow injection analyzer with a detection limit and precision of about 0.01 μM and 1–3%, respectively (Strickland and Parsons, 1972). Phosphate was measured using the molybdenum blue method by a flow injection analyzer with a detection limit and precision of about 0.03 μM and 0.5%, respectively (Murphy and Riley, 1962; Pai et al., 1990). Further details including the precisions of the measurements can be found in Chen and Wang (2006).

The Princeton Ocean Model[2] was applied to model the water flux along 120.75°E in the Luzon Strait. The computational domain covered an area from 117° to 124.5°E and 18° to 26.5°N in latitude with a 0.02° horizontal resolution and 41 vertical layers. The initial values for salinity and temperature were based on the World Ocean Atlas 2013 climatology fields[3]. The sea surface conditions used, including 10 m wind field, sea level pressure, 2 m air temperature, 2 m specific humidity, longwave radiation flux, shortwave radiation flux, latent heat flux, and surface sensible heat flux and precipitation rate were driven by the 6-hourly sea surface flux of the National Centers for Environmental Prediction (NCEP)/National Center for Atmospheric Research reanalysis dataset (Kalnay et al., 1996) from 1980 to 2009, and the NCEP Global Data Assimilation System/Final dataset from 2010 to 2017. The simulation runs were spun up from 1980. The data assimilation was also implemented in this simulation starting from 1993 by using the Ssalto/Duacs sea level anomalies dataset (AVISO)[4]. The monthly mean of the Luzon Strait transport was integrated from

[1]http://www.odb.ntu.edu.tw/

[2]http://www.ccpo.odu.edu/POMWEB/

[3]https://www.nodc.noaa.gov/OC5/woa13/

[4]https://www.aviso.altimetry.fr/

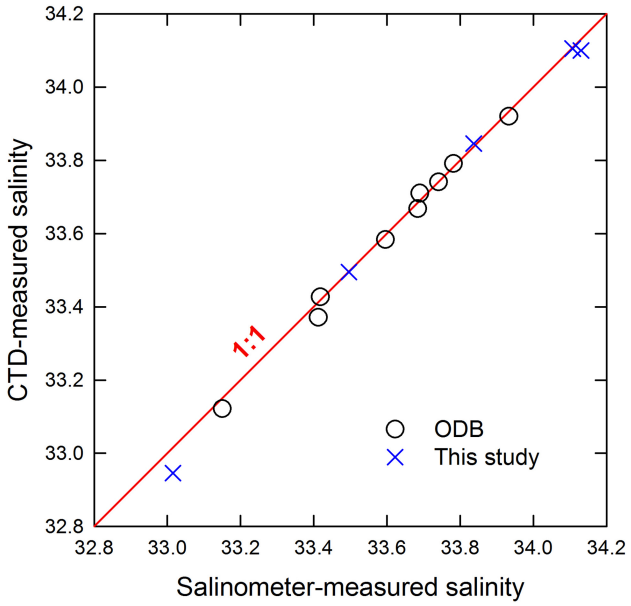


FIGURE 2 | AUTOSAL salinometer-measured salinity vs. CTD-measured salinity plot at SEATS. The solid line in red shows the 1:1 ratio.

the surface down to 300 m along 120.75°E from the model results. No observable difference was detected when integration was performed down to 500 m depth. The anomaly value was calculated as the monthly data minus the average.

PDO index was taken from the Joint Institute for the Study of the Atmosphere and Ocean[5]. The ONI data were taken from the Climate Prediction Center of the National Oceanic and Atmospheric Administration (NOAA). Twelve-month smoothing was applied to remove the seasonal signals of the PDO index and the ONI and used in this study. The average currents at 15 m depth from 1993 to 2019 were determined using two datasets, which were the Global Drifter Program (GDP) database of the NOAA[6], and the reanalysis using the 1/12° global Hybrid Coordinate Ocean Model (HYCOM) and the Navy Coupled Ocean Data Assimilation (NCODA) scheme[7]. The 15 m depth was chosen due to the fact that the drogue of the drifter was centered at a depth of 15 m.

RESULTS

Figure 3 shows the salinity and chlorophyll-a and DO concentration time series for both surface and bottom waters at SM18. The salinity and chlorophyll-a of the surface water and the DO of the surface and bottom waters had strong seasonal variations. In summer, the Pearl River discharge reaches SM18 and enhances productivity, resulting in low salinity but high concentrations of chlorophyll-a and DO of the surface water. Meanwhile, the bottom water with high salinity had low DO concentrations, reflecting the summer stratification and decomposition of organic matter settled from the surface water. To simplify, the lowest monthly DO concentrations of the bottom water in each year (DO_{min}) at SM18 were selected (indicated by the solid black line in **Figures 3**, **4A**) and examined herein.

On the whole, the DO_{min} at SM18 all occurred in summer [18 years (62%) in August, 6 years (21%) in July, and 5 years (17%) in June] and had a rate of change of -0.067 ± 0.019 mg L^{-1} yr^{-1} (equivalent to about -1% of DO saturation yr^{-1}) between 1990 and 2018 (**Figure 4A**). Notably, the hypoxic condition diminished between 2003 and 2004 (highlighted in yellow), reaching a maximum DO_{min} 5.2 mg L^{-1} in 2004. In addition, 2002 was an El Niño year (Santoso et al., 2017) and the ONI was positive between 2002 and 2004 (**Figure 4E**). The DO_{min} then fell rapidly to 1.6 mg L^{-1} in 2007 (a strong La Niña year), and reached the lowest of just 0.4 mg L^{-1} in 2011 which was a weak La Niña year. Worth mentioning, 2007 and 2010 were strong La Niña years, whereas 2005 and 2008 were weak La Niña years (Santoso et al., 2017).

Correspondingly, the DIN mirrored that of the DO_{min}, reflecting the rise in DIN but fall in DO due to the organic matter decomposition (**Figure 4A**). The linearity between DO and DIN had a slope −20.9 (by mass, unitless) (**Figure 5**). Such a value matched well the classic Redfield ratio −19.7, assuming that O_2:DIN molar ratio is equal to −138:16 (Chen et al., 2017). Notably, unlike the other years when the DO concentration of the bottom water remained low for about 3–4 months in summer, the monthly DO concentrations of the bottom water in the summer months of 2004 all remained high (**Figure 3**), indicating that the highest DO_{min} 5.2 mg L^{-1} in 2004 was not a bias of measurement. The factor at play to keep the bottom DO high in the summer in 2004 is discussed as follows.

DISCUSSION

Intrusion of Offshore Water Raises DO of Subsurface Water in nSCS and Its Coastal Region

In 2004, the Pearl River water discharge of 214×10^9 m^3 yr^{-1} was just slightly lower than the average of $271 \pm 51\times10^9$ m^3 yr^{-1} between 2002 and 2018 (**Figure 4F**). The sediment loading of 27×10^6 ton yr^{-1} was the same as the average of $27 \pm 13 \times 10^6$ ton yr^{-1} (**Figure 4F**), suggesting no significant difference in water discharge and sediment loading in 2014. Unexpectedly, the DO_{min} was the highest in SM18 in that year (**Figure 4A**). Notably, the Pearl River discharge (177×10^9 m^3 yr^{-1}) and sediment loading (13×10^6 ton yr^{-1}) were the lowest in 2011 since as early as 2002 (**Figure 4F**). Reducing terrestrial inputs were expected to reduce the hypoxic condition. Yet, the DO_{min} reached its lowest level in that year, showing that besides the influence from the terrestrial inputs, other factors were also affecting the DO level of the bottom water.

Interestingly, at SM18, the highest monthly salinity of the bottom water in each year (S_{max}, referring to the condition that

[5]http://research.jisao.washington.edu/pdo/PDO.latest.txt

[6]https://www.aoml.noaa.gov/phod/gdp/

[7]https://www.hycom.org/dataserver/gofs-3pt0/reanalysis

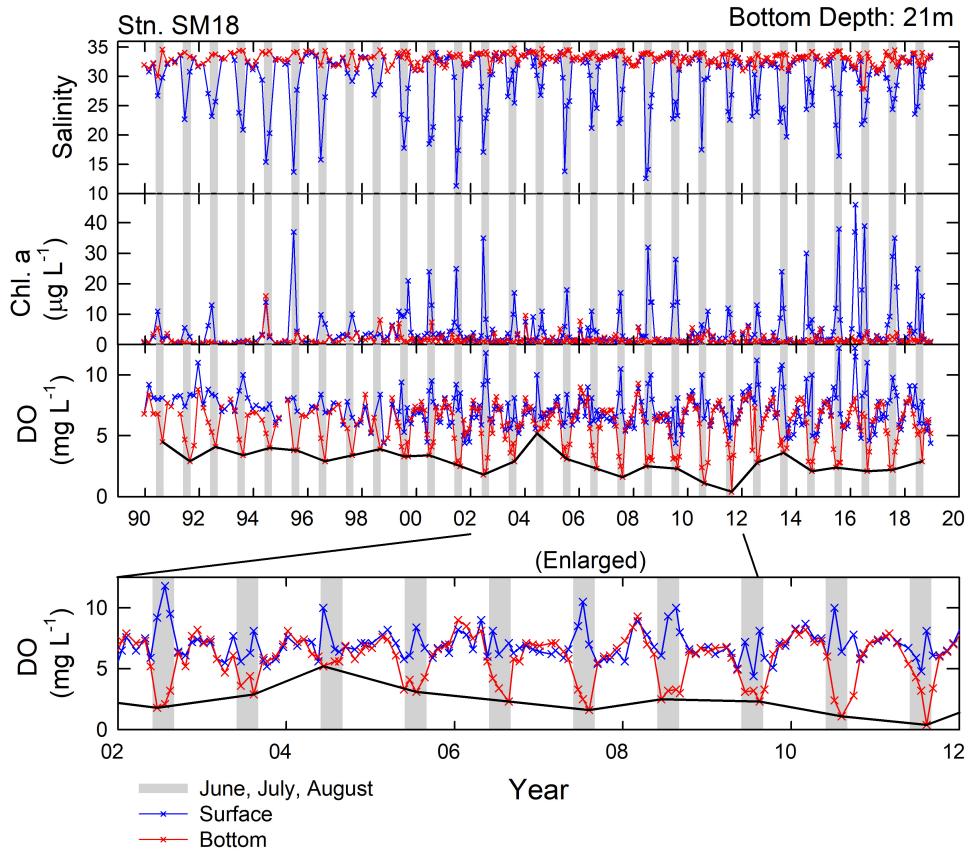


FIGURE 3 | Time series of salinity and chlorophyll-a and DO concentrations in surface and bottom waters at SM18 between 1989 and 2018. The solid black line shows the DO_{min}. Gray bars indicate the periods of June to August.

the bottom seawater is influenced the least by the Pearl River water) showed similar patterns of changes as that of DO_{min} between 2002 and 2011 (**Figure 4B**). Additionally, all S_{max} were found in summer, having 16 years in August (55%), 11 years in July (38%), and 2 years in June (7%). Changing atmospheric forcing could be a critical factor for changing the DO and salinity of the bottom water at SM18. For instance, increasing atmospheric forcing (e.g., typhoon events) could increase the DO of bottom water through enhanced vertical mixing. Changes in the distribution of the Pearl River plume could change the hypoxic condition at SM18 as well. **Figure 6** plots the S_{max} and the corresponding salinity of the surface water, as well as the seawater temperature and density of the surface and bottom waters. Obviously, these parameters have distinguishable differences between the surface and bottom waters, suggesting good stratification of the water column. Implications are that the influence of enhanced atmospheric forcing on the bottom water DO at SM18 during the sampling period likely was either insignificant or not lasting.

Notably, about 500 km away from the SM18, the measured surface seawater salinity (SSS) at the SEATS station had similar patterns of changes as well (**Figure 4B**), suggesting that the changes in S_{max} at SM18 and SSS at SEATS were due to large scale changes in seawater chemistry rather than local fluctuations. Having a minimum S_{max} of 34.0 in 2001/3 at SM18, the S_{max} increased to the highest of 34.8 in 2003/8 and to the second highest, 34.7, in 2004/8. The S_{max} then gradually decreased to the second lowest of 33.9 in 2012/7 (the lowest value was 33.8 in 1992/8). Similarly, at SEATS, the second lowest salinity of 33.05 was found in 2000/5. Afterward, the salinity increased rapidly to the highest of 34.69 in 2004/5, and then gradually decreased to the lowest of 32.95 in 2012/8. Such large changes in salinity at SM18 and at SEATS were unlikely due to evaporation or precipitation. Indeed, evaporation or precipitation may only contribute a several percentage to the interannual changes in salinity in the nSCS (Nan et al., 2016). In fact, the surface and subsurface WPS seawaters have salinities significantly higher than that of the SCS (Chen et al., 2016). Any intrusion of the WPS seawater would then increase the salinity in the SCS.

Offshore Seawater Intrusion Increases DO but Reduces Nutrients Inventories and Eutrophication

Using the GDP and 1/12° global reanalysis databases, the average surface currents (15 m depth) in winter and summer of our study area were determined (**Figure 7**). Our result agrees with previous studies that the northward-flowing Kuroshio

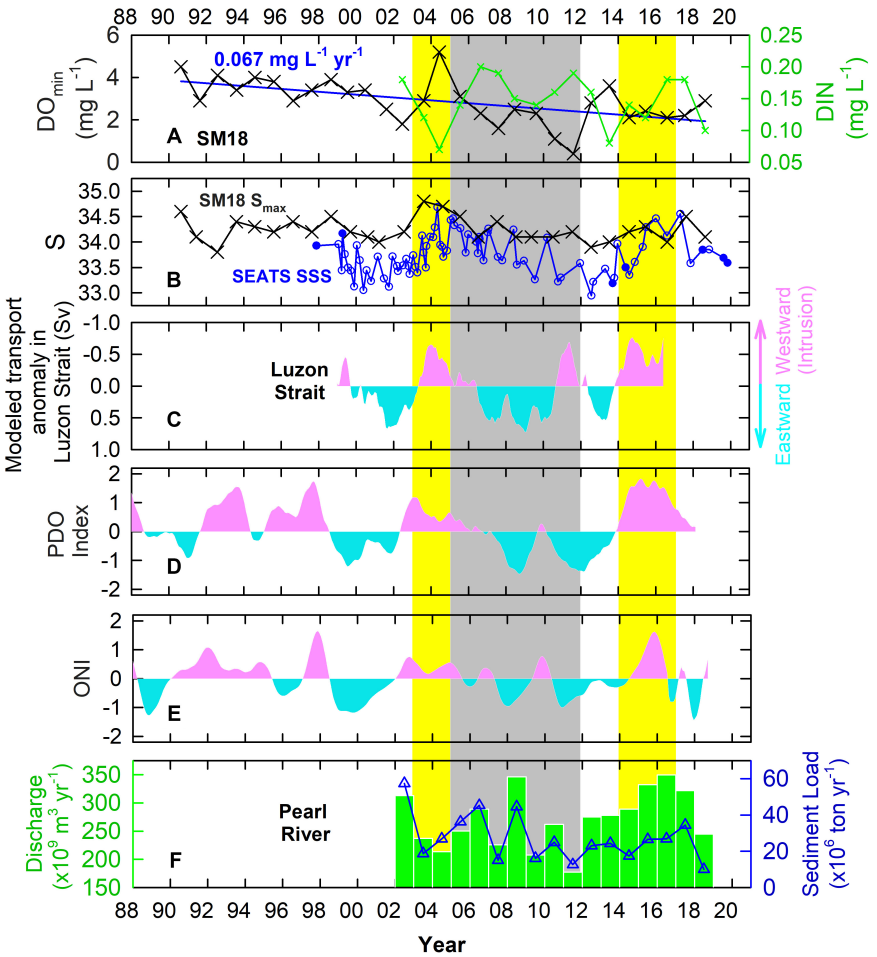


FIGURE 4 | Time series of **(A)** bottom water DO_{min} (black cross) and DIN (green cross) at SM18, **(B)** bottom water S_{max} at SM18 (black cross) and SSS at SEATS (taken from ODB: blue open circles, from this study: blue solid circles), **(C)** anomaly of water flux (0–300 m) through the Luzon Strait (vertical red and blue bands refer to positive and negative values, respectively), **(D,E)** deseasoned PDO index and ONI (vertical red and blue bands refer to positive and negative values, respectively), and **(F)** the annual average water discharge (green bar) and sediment load (blue open triangle) of the Pearl River.

intrudes into the SCS through the Luzon Strait mainly in winter (Nan et al., 2011, 2013, 2015; Wu and Hsin, 2012; Wu et al., 2017). Besides the main branch of the intrusion that centers along 20°N east of 115°E, two intrusion paths, indicated by the dashed blue lines in **Figure 7**, show that part of the Kuroshio intrusion could reach directly the coastal regions of the nSCS, such as the SM18 station. To examine whether the changes in salinity were due to the changes in the mixing proportion between the SCS and the WPS seawaters, we firstly modeled the amount of Kuroshio intrusion using the Princeton Ocean Model along 120.75°E in the Luzon Strait, which connects the nSCS and the WPS (**Figure 4C**). Our result showed that the 12-month smoothed model flux anomaly agreed with the observations (e.g., SSS at SEATS, and S_{max} and DO_{min} at SM18), suggesting that the fluctuation in DO_{min} at SM18 was due to enhanced and then diminished the amounts of intrusions of the WPS seawater into the SCS through the Luzon Strait in the form of the Kuroshio branch (**Figure 4C**).

Integrating the water flux anomaly between 2013/5 and 2015/3 (enhanced westward intrusion indicated by the first yellow bar shown in **Figure 4**) gives an enhanced westward water flux of 22.3×10^3 km^3. The SCS has an area of about 3.5×10^6 km^2. Wong et al. (2015) estimated that the area and volume of the nSCS shelves are 514.4×10^3 km^2 and 16.15×10^3 km^3. We assume that the nSCS off the shelves influenced by the intruded Kuroshio has the same area as that of the shelves (in total about 30% of the total SCS area). Based on that, we estimate that the volume of the nSCS from the surface down to 200 m depth is about (16.15×10^3 km^3 + 514.4×10^3 km^2 × 0.2 km) = 119.03×10^3 km^3. The amount of the westward flux between 2013/5 and 2015/3 is considerable, at about 19% of the volume of the nSCS. But, the intruded Kuroshio is not distributed evenly in the nSCS, as shown in **Figure 7**. The regions close to the main streams of the intruded Kuroshio, such as at SEATS or at SM18, must have higher proportions of the intruded Kuroshio. Indeed, the potential temperature (θ) vs. salinity plot provides information on such proportions.

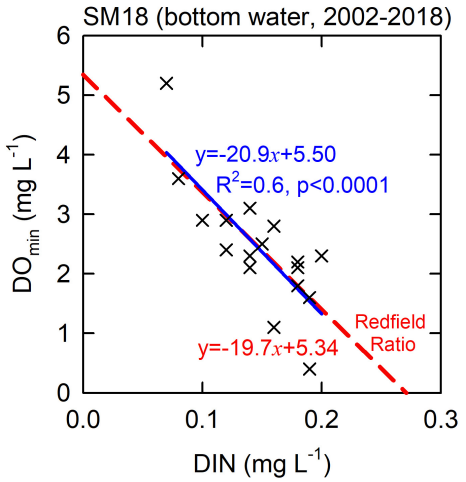


FIGURE 5 | DO_{min} vs. DIN plot at SM18 with linear regression line and equation in blue. The dash line and equation in red show the classic Redfield DO vs. DIN correlation by passing the center of the regression line.

We differentiated the WPS and SCS seawaters using θ and salinity, as the WPS and SCS seawaters have distinctive θ and salinity distributions from the surface to the bottom (Chen et al., 2016; Lui et al., 2018). Generally speaking, the surface and subsurface waters of the WPS are notably saltier than that of the SCS. The measured θ and salinity at the SEATS site clearly indicated a gradual increase in the WPS proportion above about 200 m (θ at ∼17°C) between 2003 and 2004, suggesting enhanced amounts of intrusions of the WPS water to the SCS (**Figure 8A**). At SM18, the S_{max} and its corresponding temperature showed the same result, where a gradual increase in DO_{min} corresponded to a gradual increase in the WPS seawater proportions in 2003–2004, and *vice versa* in 2005–2011 (**Figure 8B**).

Lui et al. (2018) showed that, similar to that in 2003–2004, there was a strong interannual WPS seawater intrusion between 2014 and 2016 (**Figure 8C**). Consequently, the SSS at SEATS gradually increased from 33.19 in 2013/9 to the third highest of 34.46 in 2016/1 (**Figure 4B**). Unexpectedly, the DO_{min} at SM18 did not follow the trend of SEATS SSS. This is because, as shown in **Figure 8D**, the intruded WPS did not reach the SM18 site in 2016. The temperature *vs.* S_{max} correlation of SM18 shows with no observable signal of WPS intrusion between 2012 and 2018 (**Figure 8D**). Such a result revealed a fact that a large scale intrusion of WPS into the SCS does not mean to increase the DO concentration of the coastal bottom water until the intruded offshore seawater reaches and replenishes the low-DO coastal bottom water. Worth mentioning, the SM18 bottom water had the highest WPS seawater proportion in 2003 (**Figure 8B**), but it had the highest DO_{min} in 2014 (**Figure 4A**). Our modeled intrusion anomaly suggested that the intrusion was the strongest between the end of 2013 and the beginning of 2014 (**Figure 4C**). Such results implied that not only the proportion, but also the amount of offshore water intrusion plays an important role in controlling the summer hypoxic condition.

Additionally, the DO concentration in the WPS is significantly higher than that of the SCS from the mixed layer to several

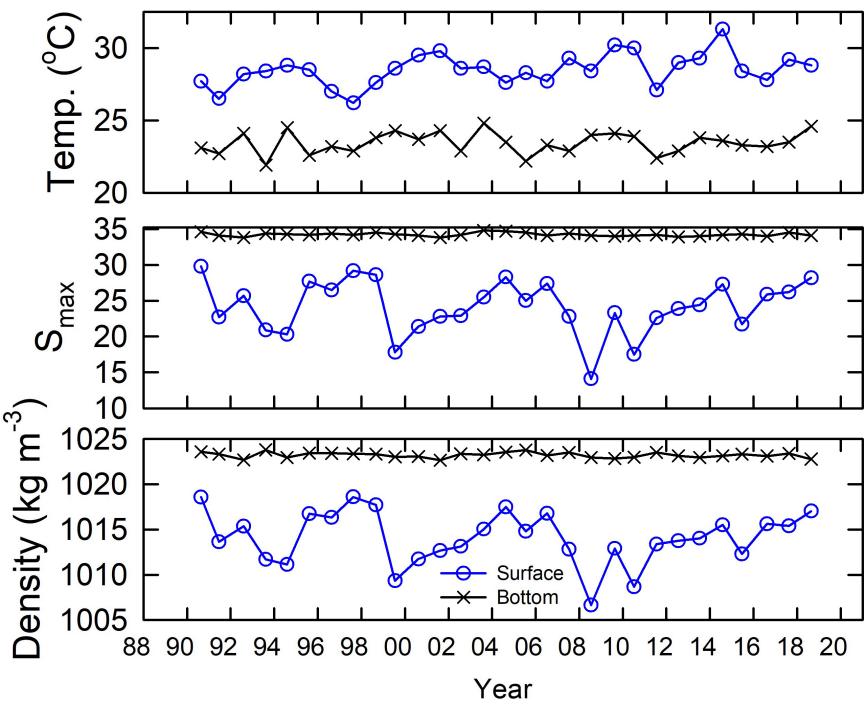


FIGURE 6 | The corresponding temperature, salinity, and density of surface and bottom seawaters when the bottom water S reaches its highest value each year (S_{max}).

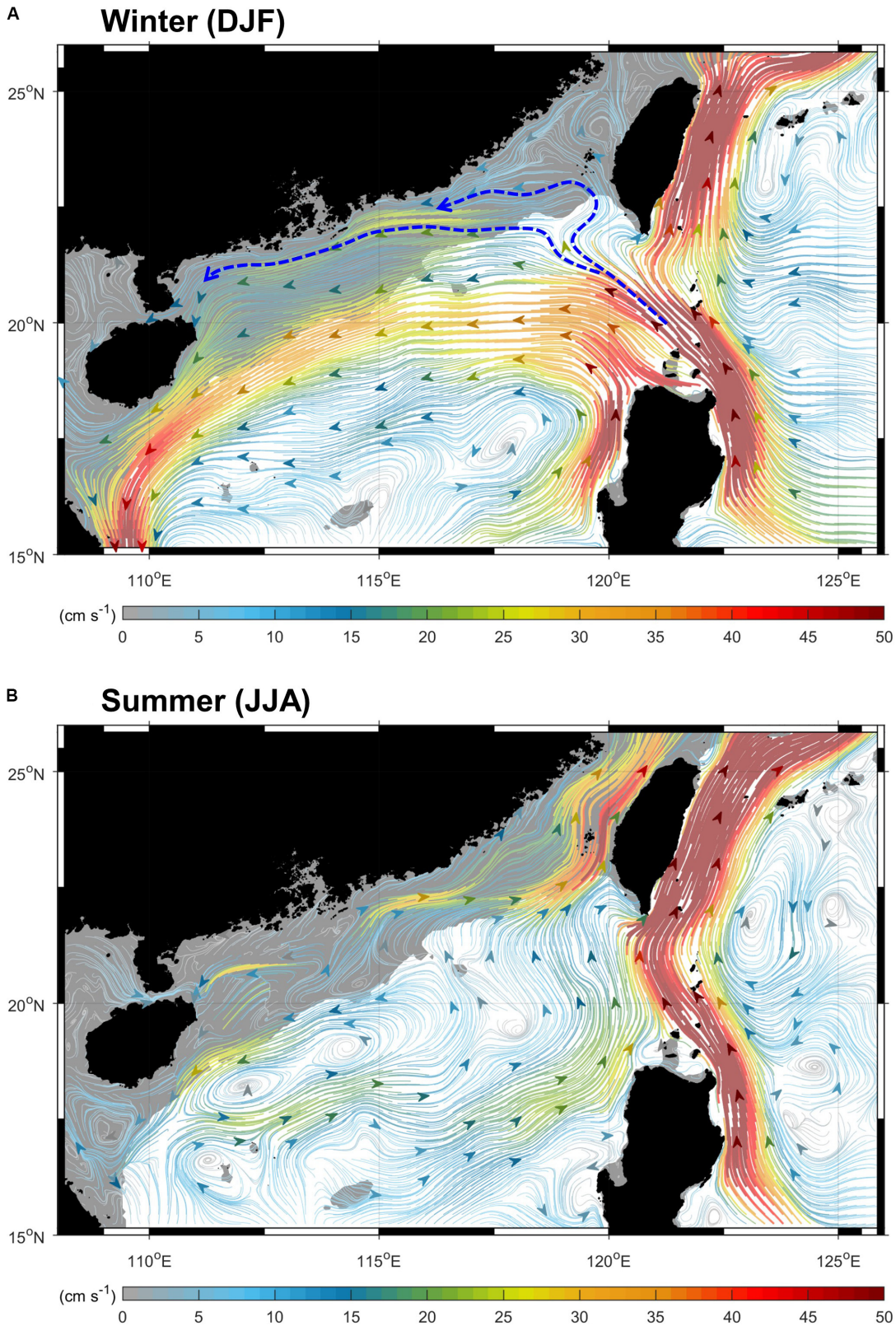


FIGURE 7 | Mean surface currents (15 m depth) of **(A)** winter and **(B)** summer in the study area over 1993–2019, obtained from the GDP and 1/12° global reanalysis databases. The color shows the speed, and the shaded areas refer to the regions of continental shelves (depth < 200 m). Two dashed lines and arrows indicate two pathways that the intruded Kuroshio could directly reach the nSCS and SM18.

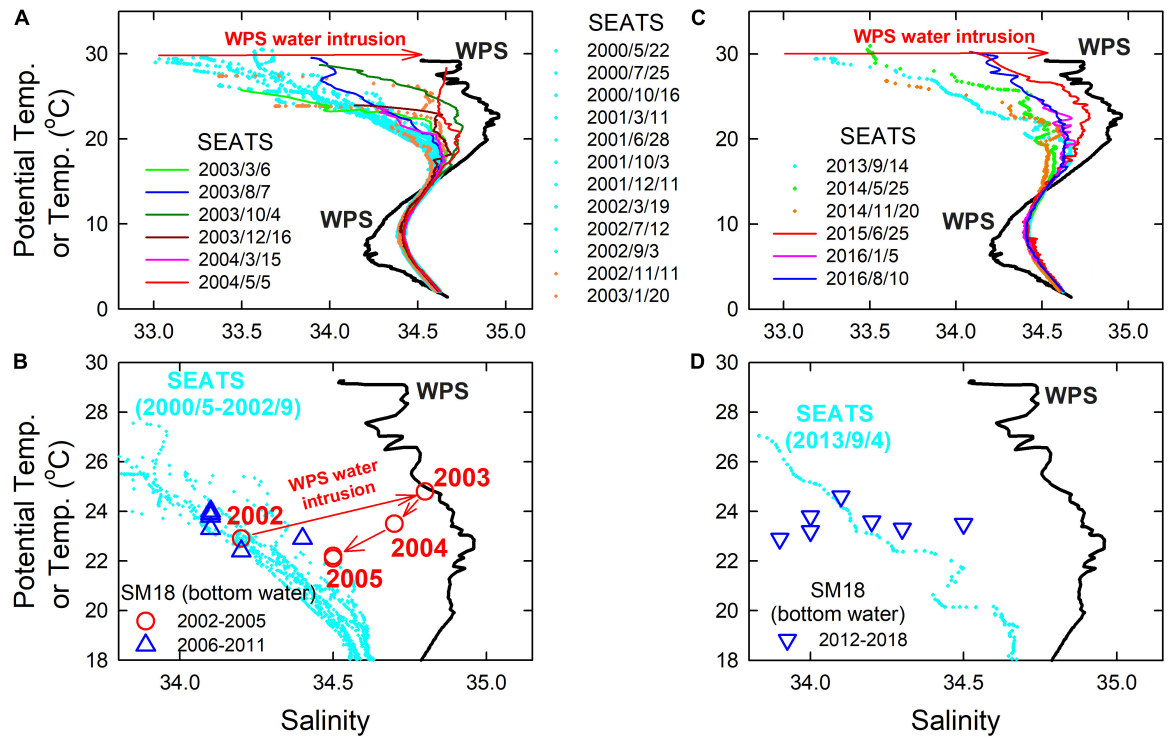


FIGURE 8 | θ-salinity diagram of the water column at SEATS in **(A)** 2000–2004 and **(C)** 2013–2016. Temperature—S_{max} of the bottom water at SM18 in **(B)** 2002–2011 and **(D)** 2012–2018. The typical plot for WPS water collected at station 21 in the WPS in 1991/6 (black solid line), as well as the θ and salinity values at SEATS between 2000/5/22 and 2002/9/3 [cyan dot in **(A)**] and 2013/9/4 [cyan dot in **(C)**] are shown in **(B,D)**, respectively, for reference. The numbers in **(B)** show the years of the data at SM18.

hundred meters in depth. For instance, at a depth of about 100 m, the DO concentration in the WPS is 1 mg L^{-1} higher than that of the SCS (Chen et al., 2001). Notably, the WPS seawater kept its original chemical properties after moving 800 km from the western boundary of the WPS to SM18 in 2003 (**Figure 8B**), when the Pearl River influence was minimal. Thus, simply replacing the SCS seawater by the WPS seawater by keeping everything else (e.g., terrestrial inputs, strength of stratification, productivity, amount of DO consumption, etc.) unchanged would increase the DO by 1 mg L^{-1}. The enhanced lateral transport of the bottom water would have a large influence on the bottom water DO. For instance, replacing a low-DO bottom water, such as 0 mg L^{-1}, by an offshore seawater with DO concentration 6 mg L^{-1} would lead the bottom water DO to have a 6 mg L^{-1} increment. That is, the amount and the pattern of offshore seawater intrusion are two critical factors governing the DO of the bottom water in the hypoxic zone.

Indeed, the WPS seawater intrusion increases the DO inventory but reduces the nutrients inventories and productivity in the nSCS, as the DO and nutrients are significantly higher and lower, respectively, than that of the nSCS in the subsurface layer. For instance, at depths between 125 and 150 m, the WPS (Stn. 21) and SCS (2000–2002 at SEATS) seawaters have distinct differences in DO of about 6.72 mg L^{-1} (or 210 μmol L^{-1}) and 4.51 mg L^{-1} (or 141 μmol L^{-1}), respectively (**Figures 9A,B**). The difference in NO_3^- are about 2 and 13 μmol L^{-1} (**Figures 9C,D**), respectively, and for PO_4^{3-} they are about 0.1 and 0.9 μmol L^{-1} (**Figures 9E,F**), respectively. Influenced by the WPS seawater under a large scale Kuroshio intrusion, the DO, NO_3^-, and PO_4^{3-} concentrations at SEATS in 2003–2004 were between those of the WPS and SCS, depending on the mixing proportions. Taking DO as an example, the DO concentration could be as low as 4.03 mg L^{-1} (or 126 μmol L^{-1}) at 150 m depth between 2000 and 2002 when the intrusion was weak. In 2004/5/5 while the intrusion was strong, DO increased to as high as 5.66–6.30 mg L^{-1} (or 177–197 μmol L^{-1}) at 150 m, having a 1.63–2.27 mg L^{-1} (or 51–71 μmol L^{-1}) increment. The θ vs. salinity plot shows that the SCS:WPS seawater mixing ratio is about 0.6:0.4 at 150 m depth. The DO concentration based on this mixing ratio is about 5.11 mg L^{-1} (160 μmol L^{-1}), agreeing with the observations. The NO_3^- and PO_4^{3-} have similar but opposite changes as that of the DO concentration. That is, the degree of intrusion of the surface layer of the WPS seawater as a Kuroshio branch is one of the main factors governing the changes in nutrient inventories and, hence, productivity in the euphotic zone of the SCS (Du et al., 2013; Lui et al., 2018). Lui et al. (2018) showed that the increase in the WPS seawater proportions at the SEATS station between 2014 and 2016 reflects the Kuroshio intrusion into the SCS. Consequently, the satellite-derived Chl.-a concentration and the fluxes of sinking particles collected at 2000 and 3500 m depths decreased significantly.

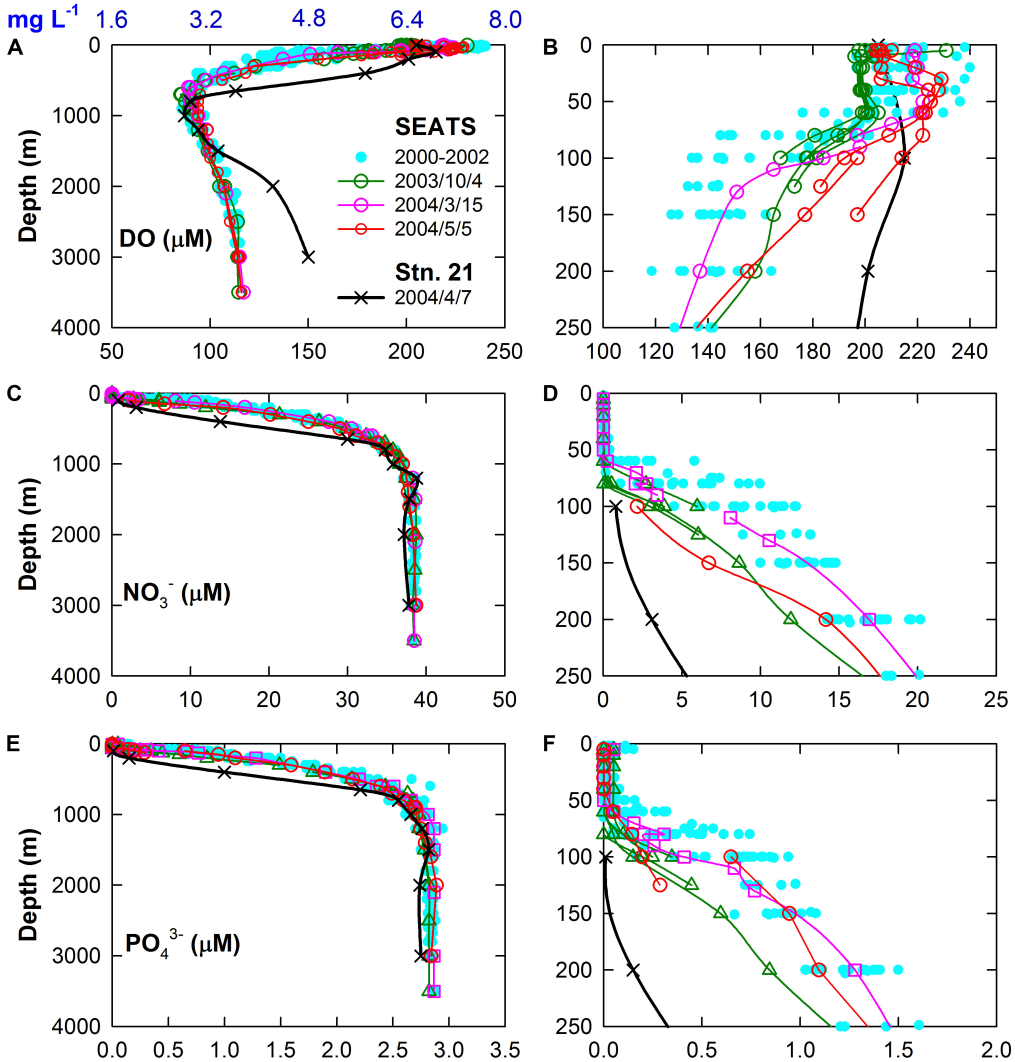


FIGURE 9 | Plots of **(A)** DO, **(C)** NO_3^-, **(E)** PO_4^{3-} vs. depths at SEATS in 2000–2004 (taken from the ODB) and at station 21 in 2004/7/27 (from this study). The **(B,D,F)** panels show the enlarged plots. The numbers show the sampling dates.

Expectably, the intrusion of offshore water to the coastal regions reduces the degree of eutrophication as well as the bottom hypoxic condition.

Climatic Oscillation of Intrusion Patterns and Its Implications

The intrusion patterns of the WPS water into the nSCS were reported to be driven by natural climate oscillations, namely, the ENSO and the PDO, which also influence the weather and hydrology worldwide (Jungclaus et al., 2006; Wu and Hsin, 2012; Wu, 2013; Wu et al., 2016, 2017). Largely due to changes in the wind stress curl, the Kuroshio intrudes more readily into the SCS during El Niño years or PDO warm phases, and the least during the La Niña or PDO cold phase years (Wu, 2013). The modeled fluxes at the Luzon Strait and the observed seawater chemistry parameters matched well with the patterns of changes of the ONI and PDO index (**Figures 4A–E**). For instance, the two large scale intrusions of the WPS seawater to the nSCS occurred in 2003–2004 and 2014–2016, when the PDO was in the warm phases (**Figure 4**, highlighted in yellow). Additionally, 2002 (weak) and 2015 (very strong) are El Niño years (Santoso et al., 2017). The gradually decreased DO_{min} at SM18 between 2005 and 2011 happened while PDO was in its cold phases. Meanwhile, 2005 (weak), 2007 (strong), 2008 (weak), 2010 (strong), and 2011 (weak) were La Niña years (Santoso et al., 2017). The S_{max} at SM18 and the SSS at SEATS show positive correlations with the PDO Index, and the transport anomaly in the Luzon Strait shows a negative correlation with the PDO Index (**Figures 10A,C,E**). Such results agree with the previous studies that the Kuroshio intrudes more into the SCS when the PDO is in a warm phase, and less in a cold phase (Wu, 2013; Wu et al., 2017). Interestingly, the correlation coefficient (R) reaches the highest when the time series of S_{max} at SM18, SSS at SEATS, and the transport anomaly

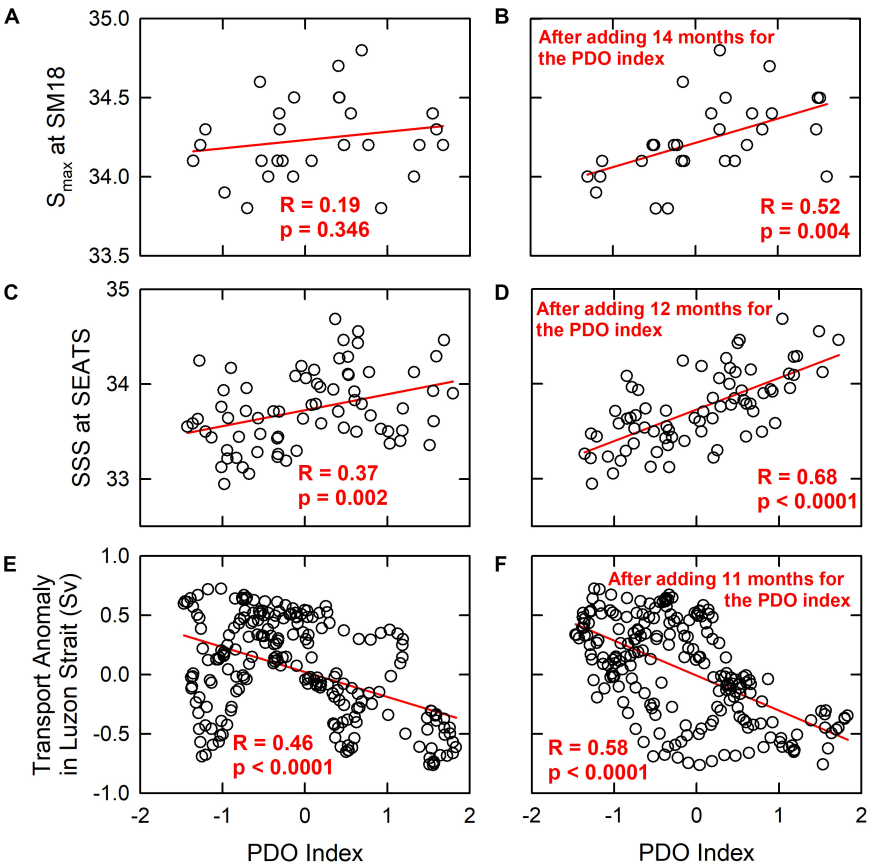


FIGURE 10 | (A,C,E) The S_{max} at SM18, the SSS at SEATS and the transport anomaly in the Luzon Strait vs. the PDO index. **(B,D,F)** The best fitted correlations (the correlation coefficient, R, reaches the highest value) when the time series of S_{max} at SM18, the SSS at SEATS, and the transport anomaly in the Luzon Strait are ahead by 14, 12, and 11 months, respectively. The red lines show the linear regression, and the numbers refer to the *R*- and *p*-values of the regression.

in Luzon Strait are ahead by 14, 12, and 11 months, respectively (**Figures 10B,D,F**). These values reflect the lag of the changes in these parameters behind the PDO. The numbers are in line with those of Huang et al. (2015) in that the signals of seawater chemistry change in the Taiwan Strait was 7 months behind the Nino 3.4 Index.

Importantly, the influence of intruded Kuroshio on the seawater chemistry in the nSCS can sustain for years. Liu and Gan (2017) indicated that the intruded Kuroshio in the upper layer had a residence time of about 3 years before subducting into deeper layers or flowing out of the SCS. Restated, the intruded Kuroshio could have inter-annual influences on the biogeochemical cycles in the SCS. Indeed, the Kuroshio intrusion into the SCS was reported to be weakened between 1993 and 2010 (Nan et al., 2013), while the salinity decreased (Nan et al., 2016). However, how decadal decrease in Kuroshio intrusion affects the long-term decrease in DO_{min} is unclear and requires further investigation. Previous studies indicated that the natural climatic oscillations may enhance under global warming (Wang et al., 2017), possibly adjusting the intrusion pattern of offshore seawaters in many coastal areas. To conclude, most hypoxic zones are located in regions linked directly to the open oceans. With reference to the decadal records from SM18 and SEATS stations, this study illustrates the importance of increasing offshore water intrusion in diminishing the coastal hypoxic condition. Changing the amount of offshore water intrusion under changing climate needs to be considered to increase the accuracy of forecasting hypoxic conditions in many coastal regions.

CONCLUSION

Using decadal time series data off the Pearl River Estuary (SM18) and in the deep basin of the SCS (SEATS), this study shows that two strong Kuroshio intrusions occurred in the SCS around 2003–2004 and 2015–2016. Consequently, the nutrient concentrations at the SEATS site decreased about 200 m in depth. Likely, due to the oxygen supply carried by the enhanced Kuroshio intrusion, little hypoxia developed at SM18 in 2004. This provides a possible mechanism that enhanced amount of offshore water intrusion to the coastal region could diminish its degree of hypoxia.

DATA AVAILABILITY STATEMENT

Publicly available datasets were analyzed in this study. This data can be found here: https://cd.epic.epd.gov.hk/EPICRIVER/marine.

AUTHOR CONTRIBUTIONS

HKL designed the manuscript. HKL and CTC wrote the manuscript. WCC and WPH provided the information and participated in discussions on the SEATS data. JML provided the modeled data of the water flux. WPH and JL participated in part in the data analysis. YLW and CRW provided the surface current data. YLW, CRW, YCH, and YYC examined the mechanisms of the open ocean intrusions into the marginal seas. All authors read and commented on the final version of the manuscript.

FUNDING

This research was funded by the Ministry of Science and Technology of Taiwan (MOST 107-2611-M-110-026-, MOST 108-2611-M-110-025, MOST 108-2611-M-110-016, and MOST 109-2611-M-110-010).

ACKNOWLEDGMENTS

We would like to thank the Hong Kong Environmental Protection Department, the Taiwan Ocean Data Bank, and the principal investigators of the studied time series for providing the invaluable data. We also thank the captain and crew of R/V Ocean Researchers I, II, III, and Legend. Two reviewers provided detailed and constructive comments which helped strengthen the manuscript.

REFERENCES

Banholzer, S., and Donner, S. (2014). The influence of different El Niño types on global average temperature. *Geophys. Res. Lett.* 41, 2093–2099. doi: 10.1002/2014gl059520

Breitburg, D., Levin, L. A., Oschlies, A., Grégoire, M., Chavez, F. P., Conley, D. J., et al. (2018). Declining oxygen in the global ocean and coastal waters. *Science* 359:eaam7240.

Cai, W. J., Dai, M. H., Wang, Y. C., Zhai, W. D., Huang, T., Chen, S. T., et al. (2004). The biogeochemistry of inorganic carbon and nutrients in the Pearl River estuary and the adjacent Northern South China Sea. *Continent. Shelf Res.* 24, 1301–1319. doi: 10.1016/j.csr.2004.04.005

Chen, C. T. A., Lui, H. K., Hsieh, C. H., Yanagi, T., Kosugi, N., Ishii, M., et al. (2017). Deep oceans may acidify faster than anticipated due to global warming. *Nat. Clim. Change* 7, 890–899. doi: 10.1038/s41558-017-0003-y

Chen, C. T. A., and Wang, S. L. (2006). A salinity front in the southern East China Sea separating the Chinese coastal and Taiwan Strait waters from Kuroshio waters. *Continent. Shelf Res.* 26, 1636–1653. doi: 10.1016/j.csr.2006.05.003

Chen, C. T. A., Wang, S. L., Lu, X. X., Zhang, S. R., Lui, H. K., Tseng, H. C., et al. (2008). Hydrogeochemistry and greenhouse gases of the Pearl River, its estuary and beyond. *Quatern. Int.* 186, 79–90. doi: 10.1016/j.quaint.2007.08.024

Chen, C. T. A., Wang, S. L., Wang, B. J., and Pai, S. C. (2001). Nutrient budgets for the South China Sea basin. *Mar. Chem.* 75, 281–300. doi: 10.1016/s0304-4203(01)00041-x

Chen, C. T. A., Yeh, Y. T., Yanagi, T., Bai, Y., He, X., and Huang, T. H. (2016). The tug-of-war between the West Philippine Sea and South China Sea tropical waters and intermediate waters in the Okinawa trough. *J. Geophys. Res.* 121, 1736–1754. doi: 10.1002/2015jc011274

Conley, D. J., Paerl, H. W., Howarth, R. W., Boesch, D. F., Seitzinger, S. P., Havens, K. E., et al. (2009). Controlling eutrophication: nitrogen and phosphorus. *Science* 323, 1014–1015. doi: 10.1126/science.1167755

Diaz, R. J., and Rosenberg, R. (2008). Spreading dead zones and consequences for marine ecosystems. *Science* 321, 926–929. doi: 10.1126/science.1156401

Du, C., Liu, Z., Dai, M., Kao, S. J., Cao, Z., Zhang, Y., et al. (2013). Impact of the Kuroshio intrusion on the nutrient inventory in the upper northern South China Sea: insights from an isopycnal mixing model. *Biogeosciences* 10, 6419–6432. doi: 10.5194/bg-10-6419-2013

Feely, R. A., Sabine, C. L., Hernandez-Ayon, J. M., Ianson, D., and Hales, B. (2008). Evidence for upwelling of corrosive "acidified" water onto the continental shelf. *Science* 320, 1490–1492. doi: 10.1126/science.1155676

Hong Kong Environmental Protection Department (2015). *Marine Water Quality in Hong Kong*. Hong Kong: Hong Hong Kong Environmental Protection Department.

Howarth, R., Chan, F., Conley, D. J., Garnier, J., Doney, S. C., Marino, R., et al. (2011). Coupled biogeochemical cycles: eutrophication and hypoxia in temperate estuaries and coastal marine ecosystems. *Front. Ecol. Environ.* 9, 18–26. doi: 10.1890/100008

Huang, T. H., Chen, C. T. A., Zhang, W. Z., and Zhuang, X. F. (2015). Varying intensity of Kuroshio intrusion into Southeast Taiwan Strait during ENSO events. *Continent. Shelf Res.* 103, 79–87. doi: 10.1016/j.csr.2015.04.021

Jungclaus, J. H., Keenlyside, N., Botzet, M., Haak, H., Luo, J. J., Latif, M., et al. (2006). Ocean circulation and tropical variability in the coupled model ECHAM5/MPI-OM. *J. Clim.* 19, 3952–3972. doi: 10.1175/jcli3827.1

Kalnay, E., Kanamitsu, M., Kistler, R., Collins, W., Deaven, D., Gandin, L., et al. (1996). The NCEP/NCAR 40-year reanalysis project. *Bull. Am. Meteorol. Soc.* 77, 437–472.

Liu, Z., and Gan, J. (2017). Three-dimensional pathways of water masses in the South China Sea: a modeling study. *J. Geophys. Res. Oceans* 122, 6039–6054. doi: 10.1002/2016jc012511

Lu, Z. M., Gan, J. P., Dai, M. H., Liu, H. B., and Zhao, X. Z. (2018). Joint effects of extrinsic biophysical fluxes and intrinsic hydrodynamics on the formation of hypoxia west off the Pearl River Estuary. *J. Geophys. Res. Oceans* 123, 6241–6259. doi: 10.1029/2018jc014199

Lui, H. K., and Chen, C. T. A. (2012). The nonlinear relationship between nutrient ratios and salinity in estuarine ecosystems: implications for management. *Curr. Opin. Environ. Sustainabil.* 4, 227–232. doi: 10.1016/j.cosust.2012.03.002

Lui, H. K., Chen, K. Y., Chen, C. T., Wang, B. S., Lin, H. L., Ho, S. H., et al. (2018). Physical forcing-driven productivity and sediment flux to the deep basin of northern South China Sea: a decadal time series study. *Sustainability* 10:971. doi: 10.3390/su10040971

Mantua, N. J., Hare, S. R., Zhang, Y., Wallace, J. M., and Francis, R. C. (1997). A Pacific interdecadal climate oscillation with impacts on salmon production. *Bull. Am. Meteorol. Soc.* 78, 1069–1080. doi: 10.1175/1520-0477(1997)078<1069:apicow>2.0.co;2

Ministry of Water Resources of the People's Republic of China (2002–2018). *China River Sediment Bulletin, China Water and Power Press*. Ministry of Water Resources, China.

Mohrholz, V., Naumann, M., Nausch, G., Krüger, S., and Gräwe, U. (2015). Fresh oxygen for the Baltic Sea — An exceptional saline inflow after a decade of stagnation. *J. Mar. Syst.* 148, 152–166. doi: 10.1016/j.jmarsys.2015.03.005

Murphy, J., and Riley, J. P. (1962). A modified single solution method for the determination of phosphate in natural waters. *Anal. Chim. Acta* 27, 31–36. doi: 10.1016/S0003-2670(00)88444-5

Nan, F., Xue, H., Chai, F., Wang, D., Yu, F., Shi, M., et al. (2013). Weakening of the Kuroshio intrusion into the South China Sea over the past two decades. *J. Clim.* 26, 8097–8110. doi: 10.1175/jcli-d-12-00315.1

Nan, F., Xue, H., and Yu, F. (2015). Kuroshio intrusion into the South China Sea: a review. *Prog. Oceanogr.* 137, 314–333. doi: 10.1016/j.pocean.2014.05.012

Nan, F., Xue, H. J., Chai, F., Shi, L., Shi, M. C., and Guo, P. F. (2011). Identification of different types of Kuroshio intrusion into the South China Sea. *Ocean Dyn.* 61, 1291–1304. doi: 10.1007/s10236-011-0426-3

Nan, F., Yu, F., Xue, H., Zeng, L., Wang, D., Yang, S., et al. (2016). Freshening of the upper ocean in the South China Sea since the early 1990s. *Deep Sea Res. I Oceanogr. Res. Pap.* 118, 20–29. doi: 10.1016/j.dsr.2016.10.010

Pai, S.-C., Gong, G.-C., and Liu, K.-K. (1993). Determination of dissolved oxygen in seawater by direct spectrophotometry of total iodine. *Mar. Chem.* 41, 343–351. doi: 10.1016/0304-4203(93)90266-Q

Pai, S.-C., Yang, C.-C., and Riley, J. P. (1990). Effects of acidity and molybdate concentration on the kinetics of the formation of the phosphoantimonylmolybdenum blue complex. *Anal. Chim. Acta* 229, 115–120. doi: 10.1016/S0003-2670(00)85116-8

Qian, W., Gan, J., Liu, J., He, B., Lu, Z., Guo, X., et al. (2018). Current status of emerging hypoxia in a eutrophic estuary: the lower reach of the Pearl River Estuary, China. *Estuar. Coast. Shelf Sci.* 205, 58–67. doi: 10.1016/j.ecss.2018.03.004

Rabalais, N., Cai, W.-J., Carstensen, J., Conley, D., Fry, B., Hu, X., et al. (2014). Eutrophication-driven deoxygenation in the coastal ocean. *Oceanography* 27, 172–183. doi: 10.5670/oceanog.2014.21

Rabalais, N. N., Diaz, R. J., Levin, L. A., Turner, R. E., Gilbert, D., and Zhang, J. (2010). Dynamics and distribution of natural and human-caused hypoxia. *Biogeosciences* 7, 585–619. doi: 10.5194/bg-7-585-2010

Santoso, A., McPhaden, M. J., and Cai, W. J. (2017). The defining characteristics of ENSO extremes and the strong 2015/2016 El Niño. *Rev. Geophys.* 55, 1079–1129. doi: 10.1002/2017rg000560

Schmidtko, S., Stramma, L., and Visbeck, M. (2017). Decline in global oceanic oxygen content during the past five decades. *Nature* 542, 335–339. doi: 10.1038/nature21399

Strickland, J. D. H., and Parsons, T. R. (1972). *A Practical Handbook of Seawater Analysis*. Ottawa: Fisheries Research Board of Canada.

Su, J., Dai, M., He, B., Wang, L., Gan, J., Guo, X., et al. (2017). Tracing the origin of the oxygen-consuming organic matter in the hypoxic zone in a large eutrophic estuary: the lower reach of the Pearl River Estuary, China. *Biogeosciences* 14, 4085–4099. doi: 10.5194/bg-14-4085-2017

Wang, G., Cai, W., Gan, B., Wu, L., Santoso, A., Lin, X., et al. (2017). Continued increase of extreme El Niño frequency long after 1.5 °C warming stabilization. *Nat. Clim. Change* 7, 568–572. doi: 10.1038/nclimate3351

Wang, H., Dai, M., Liu, J., Kao, S.-J., Zhang, C., Cai, W.-J., et al. (2016). Eutrophication-driven hypoxia in the East China Sea off the Changjiang Estuary. *Environ. Sci. Technol.* 50, 2255–2263. doi: 10.1021/acs.est.5b06211

Wong, G. T. F., Pan, X., Li, K.-Y., Shiah, F.-K., Ho, T.-Y., and Guo, X. (2015). Hydrography and nutrient dynamics in the Northern South China Sea Shelf-sea (NoSoCS). *Deep Sea Res. II Top. Stud. Oceanogr.* 117, 23–40. doi: 10.1016/j.dsr2.2015.02.023

Wu, C. R. (2013). Interannual modulation of the Pacific Decadal Oscillation (PDO) on the low-latitude western North Pacific. *Prog. Oceanogr.* 110, 49–58. doi: 10.1016/j.pocean.2012.12.001

Wu, C. R., and Hsin, Y. C. (2012). The forcing mechanism leading to the Kuroshio intrusion into the South China Sea. *J. Geophys. Res. Oceans* 117:7015. doi: 10.1029/2012jc007968

Wu, C. R., Hsin, Y. C., Chiang, T. L., and Lin, Y. F. (2014). Seasonal and interannual changes of the Kuroshio intrusion onto the East China Sea Shelf. *J. Geophys. Res.* 119, 5039–5051. doi: 10.1002/2013jc009748

Wu, C. R., Wang, Y. L., Lin, Y. F., and Chao, S. Y. (2017). Intrusion of the Kuroshio into the South and East China Seas. *Sci. Rep.* 7:7895. doi: 10.1038/s41598-017-08206-4

Wu, C. R., Wang, Y. L., Lin, Y. F., Chiang, T. L., and Wu, C. C. (2016). Weakening of the Kuroshio intrusion into the South China Sea under the global warming hiatus. *IEEE J. Select. Top. Appl. Earth Observ. Remote Sens.* 9, 5064–5070. doi: 10.1109/jstars.2016.2574941

Conflict of Interest: The authors declare that the research was conducted in the absence of any commercial or financial relationships that could be construed as a potential conflict of interest.

Copyright © 2020 Lui, Chen, Hou, Liau, Chou, Wang, Wu, Lee, Hsin and Choi. This is an open-access article distributed under the terms of the Creative Commons Attribution License (CC BY). The use, distribution or reproduction in other forums is permitted, provided the original author(s) and the copyright owner(s) are credited and that the original publication in this journal is cited, in accordance with accepted academic practice. No use, distribution or reproduction is permitted which does not comply with these terms.

frontiers in Marine Science

REVIEW
published: 03 February 2021
doi: 10.3389/fmars.2021.615929

Advances on Coastal and Estuarine Circulations Around the Changjiang Estuary in the Recent Decades (2000–2020)

Zhiqiang Liu[1,2]*, *Jianping Gan*[3,4], *Hui Wu*[5], *Jianyu Hu*[6], *Zhongya Cai*[7] *and Yongfei Deng*[1]

[1] *Department of Ocean Science and Engineering, Southern University of Science and Technology, Shenzhen, China,* [2] *Southern Marine Science and Engineering Guangdong Laboratory, Guangzhou, China,* [3] *Department of Ocean Science, Hong Kong University of Science and Technology, Hong Kong, China,* [4] *Department of Mathematics, Hong Kong University of Science and Technology, Hong Kong, China,* [5] *State Key Laboratory of Estuarine and Coastal Research, East China Normal University, Shanghai, China,* [6] *State Key Laboratory of Marine Environmental Science, Xiamen University, Xiamen, China,* [7] *State Key Laboratory of Internet of Things for Smart City, Department of Civil and Environmental Engineering, University of Macau, Macau, China*

Advances on the circulation in the Changjiang Estuary and adjacent East China Sea (ECS) and Yellow Sea (YS) coastal waters in the recent decades (2000–2020) are synthesized in this review. The circulation over the complicated bathymetry in the region is locally driven by winds, tides, as well as riverine discharge, and is remotely influenced by shelf currents between the 50 and 100-m isobaths through the cross-shelf exchanges. The interchange of the momentum and the freshwater pathway inside the Changjiang Estuary are jointly determined by tides and seasonally varying discharge and winds over the shelf. The buoyant waters are trapped inside the bulge that forms and expands over the shelf to the west of the 30-m isobath in the vicinity of Hangzhou Bay and the Changjiang Estuary. These buoyant waters are exported offshore by the shelf current, tidal mixing, and variations of wind patterns, forming the Changjiang River plume, which shows notable seasonality due to the reversal of both winds and shelf currents in the ECS and YS. Extensive spatial irregularities in the form of freshwater patches are present along its pathway to the Tsushima Strait in summer and to the Taiwan Strait in winter, respectively. Tides and the bathymetry irregularity have recently been found to play critical roles in determining the cross-shelf exchanges of water mass and momentum along the pathway of the ECS coastal current, and along this pathway, a year-round upslope intrusion of shelf waters appears in both summer and winter. Tides also play an important role in altering the expansion of the Changjiang River plume, cross-shelf extrusion of waters, and variation in the Yellow Sea Coastal Current over the shallow Subei Shoal.

Keywords: Changjiang (Yangtze river) estuary, coastal circulation, East China Sea, river plume, bulge

OPEN ACCESS

Edited by:
Hongjie Wang,
Pacific Marine Environmental Laboratory (NOAA), United States

Reviewed by:
Dz Yang,
Institute of Oceanology (CAS), China
Jae Hak Lee,
Korea Institute of Ocean Science and Technology (KIOST), South Korea

***Correspondence:**
Zhiqiang Liu
liuzq@sustech.edu.cn

Specialty section:
This article was submitted to Coastal Ocean Processes, a section of the journal Frontiers in Marine Science

Received: *10 October 2020*
Accepted: *11 January 2021*
Published: *03 February 2021*

Citation:
Liu Z, Gan J, Wu H, Hu J, Cai Z and Deng Y (2021) Advances on Coastal and Estuarine Circulations Around the Changjiang Estuary in the Recent Decades (2000–2020). Front. Mar. Sci. 8:615929. doi: 10.3389/fmars.2021.615929

INTRODUCTION

The coastal waters in the East China Sea (ECS) and southern Yellow Sea (YS) are found over their respective shelves to the west of the 50-m isobath, which extends northward from ∼25°N to ∼37°N (**Figure 1A**). These coastal waters are bordered by the southern coast of the Shandong and the coastlines of the Jiangsu, Shanghai, Zhejiang, and Fujian. In the southern ECS, the interlinked

coastal waters mainly extend southwestward, running parallel to the Fujian and Zhejiang coasts to the south of the Changjiang Estuary. The complicated coastlines are composed by many islands, bays, and channels, such as those in the vicinity of the Zhoushan Islands and Changjiang Estuary. Coastal waters in the southern ECS are generally shallower than 50 m, except in some deep channels with depths >100 m among the Zhoushan Islands. The Hangzhou Bay and the Changjiang Estuary widen toward the east and the ECS. The bathymetry of the coastal waters in the southwestern YS is generally characterized by the Subei Shoal (a.k.a. the Yangtze Bank), which extends to the southeast and over which the nearshore waters are generally shallower than 10 m. A northwestward incising submerged valley is surrounded by the 50-m isobath in the northwestern ECS to the southwest of the Subei Shoal. The northwestward extending YS Trough characterizes the bathymetry of the southern YS.

The Changjiang River is the largest river in the East Asia and exports buoyant waters with an averaged discharge rate of ∼26,400 m^3/s into the ECS and YS (Mei et al., 2015). The water depth in this long estuary is generally shallower than 20 m, and riverine waters rush into the ECS shelf through its complicated passages and channels (**Figure 1B**). The Changjiang Estuary is divided into the North and South Branches by the Chongming Island. In the mid-estuary, the Changxing Island separates the South Branch into the North and South Channels. The anthropogenic underwater infrastructure and the navigation channel in the vicinity of Hengsha Island further divide the South Channel into the North and South Passages. This complicated bathymetry, which will be explored in the following sections, greatly alters the characteristics of the circulation and freshwater as well as the interaction between the estuarine circulation and the coastal circulation at the mouth of the Changjiang Estuary. Coastal circulations over the complicated nearshore bathymetry to the west of the 50-m isobath in the ECS and southern YS are jointly forced by variable multiscale local forcing, including tides, winds, and river discharge. Coastal and estuarine circulations also interact with shelf circulations, for example, the Taiwan Warm Current (TWWC), Yellow Sea Warm Current (YSWC, in winter), and Yellow Sea Cold Water Mass (YSCM, in summer) as well as the Kuroshio in the Okinawa Trough and the Taiwan Strait Current (TSC).

The Kuroshio and the intrinsic characteristics of the ECS shelf current act as the major external factors that influence coastal and estuarine circulation. The annually average volume transport of the Kuroshio is ∼24.37 Sv in the central ECS (Liu et al., 2021), and a stronger/weaker Kuroshio is usually present in the warm/cold half of the year in the northern hemisphere (Yang et al., 2018). Observations based on the conservation of the total water volume over the shelf reveal that the integrated volume transport by the Kuroshio intrusion into the ECS is ∼1.3–1.4 Sv (Isobe, 2008). The shelf currents, which originate from the southern ECS, interact with the circulation between the 100 and 200-m isobaths and flow into the Tsushima Strait, exiting into the southern Japan Sea further north (Gan et al., 2016; Lie and Cho, 2016; Li et al., 2016). The northward penetrating warm waters in the ECS are from the TSC and those that originated from the Kuroshio intrusion over the shelf to the northeast of Taiwan [synthesized by Hu and Wang (2016) and simulated by Yang et al. (2013), among others]. They form the northward flowing TWWC, which greatly modulates the shoreward intrusion of shelf waters toward the coastal seas off the Zhejiang and Fujian coasts in summer. This northward current has also been found to be largely regulated by the southwestward flowing Zhe-Min Coastal Current (ZMCC), which carries buoyant waters from the Changjiang River to the Taiwan Strait in winter. The TSC and the interactions between the TWWC and ZMCC are also greatly regulated by synoptic wind variability, which establishes downshelf propagating coastally trapped waves that alter the respective intensity of these currents (Li and Huang, 2019).

In the southern YS, a notable northward penetration of warm waters, indicative of YSWC, is observed in the Yellow Sea Trough in winter. Previous studies have recognized that the YSWC mainstream shifts westward toward the eastern flank of the shallower Subei Shoal (Lin and Yang, 2011; Lin et al., 2011), where tides have been suggested to play important roles in regulating the regional circulation. The circulation in summer is mainly governed by the monsoonal winds, tides, Changjiang River Plume and the YSCM, which resides from the YSWC in winter and is sealed in the lower layers of the Yellow Sea Trough in summer. The expansion of the Changjiang River Plume, whose underlying dynamics will be further explored in the following sections, shows notable spatial variations in its pathways in the ECS and southern YS.

We revisit recent understandings on estuarine circulation in the Changjiang River Estuary and coastal circulations in the ECS and southern YS, and pay more attention on the circulation dynamics than the recent comparative reviews, which focus more on the seasonal (Guan and Fang, 2006; Lie and Cho, 2016) and interannual (Matsuno, 2020) variabilities of the shelf waters and biogeochemical processes (Chen J. et al., 2020) to the further seaward of the studied area. The rest of this manuscript is arranged as follow. In Section Changjiang estuarine circulation, we synthesize the characteristics of the circulation in the Changjiang Estuary. The expansion of the Changjiang river plume is synthesized in Section Changjiang River plume. Section Coastal Currents in the ECS and southern YS summarizes recent advances on the coastal currents in the ECS and southern YS, and the impact of circulation dynamics on hypoxia off the Changjiang Estuary is synthesized in Section Impacts of Circulation on Hypoxia off the Changjiang Estuary. The summary and prospects are given in Section Summary and Prospects.

CHANGJIANG ESTUARINE CIRCULATION

The Changjiang River is the largest river in the East Asia and the fifth largest river worldwide in terms of riverine discharge. The maximum/minimum discharge rate of Changjiang River appears in summer/winter (∼40,000/∼13,000 m^3/s) (Luan et al., 2016). The buoyant waters that flow through the complicated passages and channels of the Changjiang Estuary (**Figure 1B**) form the interactive estuarine circulation, and its underlying mechanisms have often been investigated in studies of the general flow pattern [e.g., Xue et al. (2009) and the references therein]. Majority of the

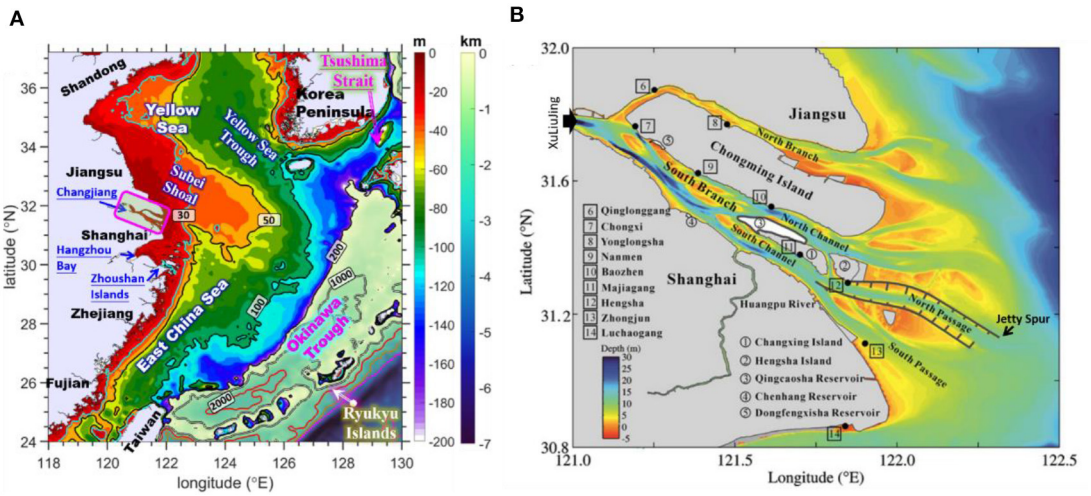


FIGURE 1 | (A) Water depth (m) of ECS and YS. The waters deeper and shallower than 200 m in this figure are illustrated by different colormaps. The 30, 50, 100, and 200 m isobaths over the shelf, and 1,000, 2,000, 3,000, 4,000 m isobaths in the deeper oceans are also shown. The bathymetry is composed from the digitalized navigation map in the coastal areas and the ETOPO1 global relief model. **(B)** Water depth (m) in Changjiang Estuary with name of the branches, channels, passages, and islands (Zhu et al., 2019). The underwater jetty spur bordering the North Passage is shown in **(B)**.

riverine runoff rushes into the ECS through the South Branch, which, in winter, counts for over 95% of the discharges (Li et al., 2010). The partitioning of buoyant waters toward the North Branch (<5%) oscillates with flood and ebb tides and varies in the spring and neap tidal cycles. The main features of Changjiang estuarine circulation are an onshore intrusion of shelf waters and the extrusion of buoyant waters, which are also modulated by anthropogenic activities. It should be noted that although we, respectively, reviewed the characteristics of the intrusion of shelf waters and the extrusion of riverine waters, the exchange flow in the Changjiang Estuary is composition of these bidirectional circulations with the general circulation pattern is shown in the **Figure 2**, and the underlying dynamics are synthesized in the follow contents.

Intrusion of Shelf Waters

The Changjiang estuarine circulation is generally stronger in summer (**Figure 2A**) than that in winter (**Figure 2B**). In addition to the intrusion of the shelf waters from the lower layer at the mouth of the estuary (**Figure 2C**), there is a long-distance intrusion of saltwater from the North Branch to the South Branch (white arrows in North Branch and the black arrows in South Branch in **Figure 2C**). This intrusion, due to its notable threat on freshwater supply of the neighboring cities, is the focus of the previous studies in the recent decades and it is reported to occasionally inject saltwater into the mainstream freshwater of the South Branch (Xu et al., 2018). This intrusion is regulated by the intensity of upstream riverine runoff and the tidal range over the shelf neighboring the North Branch in the lower estuary (Wu et al., 2006), as well as winds over the shelf off the Changjiang Estuary (Zhang et al., 2017; Lyu and Zhu, 2018; Zhu et al., 2018a; Zhu et al., 2019). The respective responses of the estuarine circulation in those complicated branches and channels to those forces will be further synthesized in the following contents.

The intrusion of salt waters from the North Branch to the South Branch is greatly altered by the tidal and wind forcings. The non-linearity of the tidally induced momentum flux and bottom friction over the abrupt topography induce tidal rectification (Xue et al., 2009). The invasion of shelf waters through the North Branch then occurs when the intensity of the freshwater flow in this branch is weaker than that of the tidally rectified current. The influence of non-linear tidal rectification in modulating the exchanges among the channels and passages in the Changjiang Estuary network was also described in detail by Alebregtse and de Swart (2016), which further emphasized the attenuation of the semi-diurnal tide by extensive riverine discharge in summer. The associated non-linear river-tide interactions diminish the semi-diurnal variation of the surface-elevation amplitude and thus have minimal effects on the tidal velocity amplitude and phase of tidal waves. The numerical experiments in Qiu et al. (2012) showed that the water exchanges between the North Branch and South Branch are much stronger during spring tides than during neap tides. The intrusion of shelf waters from the North Branch toward the South Branch also shows notable seasonality. In winter, the tidally rectified current is intensified to strengthen the intrusion of shelf waters from the North Branch toward the South Branch, when the seaward surface elevation gradient (i.e., barotropic pressure gradient) is reduced by northerly winds (Xue et al., 2009). The estuary-ward Ekman transport by the northerly winds strengthens the intrusion of saltwater toward the South Branch (Li et al., 2010, 2012), and this intrusion is greatly intensified since 1999, possibly due to the more frequent

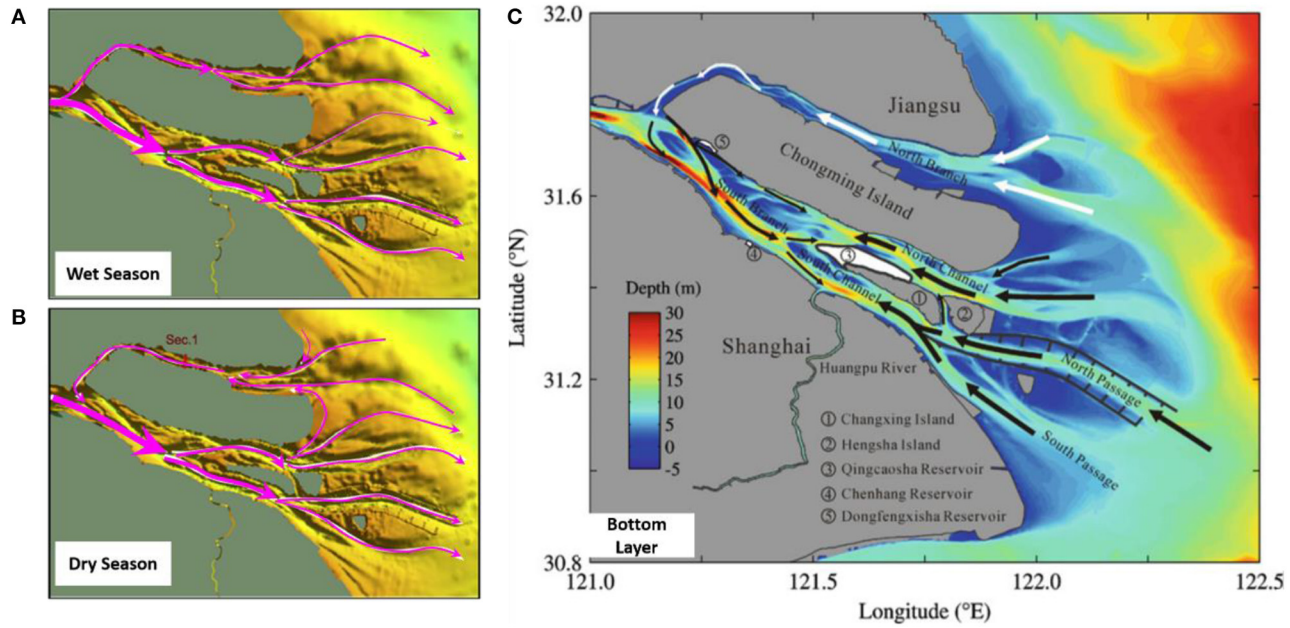


FIGURE 2 | Schematics of the subtidal flow patterns (Xue et al., 2009) during **(A)** wet and **(B)** dry seasons, and **(C)** pathways for saltwater intrusion (arrows) (Zhu et al., 2015), with the white and black arrows in **(C)** denoting pathway of the onshore invading shelf waters.

outbreaks of northerly and northeasterly wind event (Zhang et al., 2019a). Water exchange between the South Channel and North Channel is greatly affected by the variation in wind direction (Li et al., 2012). When the northeasterly wind prevails, saltwater intrusions in the North Channel have been found to be weaker than those imposed by the northerly winds. Li L. et al. (2014) found that the shelf water intrusions in the North Channel are amplified due to the deepening topography mid-channel and to the east of Chongming Island.

In the further downstream, circulations in the South Passage and North Passage are also greatly influenced by tides and winds. The numerical simulations by Wu and Zhu (2010) and Wu et al. (2010) suggested that tidally induced subtidal circulation plays an important role, and Stokes transport due to the propagation of tidal waves has been found to amplify the onshore invasion of shelf waters in the South Passage. This process makes the South Passage the most saline outlet besides the North Branch. The circulation in the North Channel and North Passage is primarily dominated by the extensive seaward export of riverine buoyant waters. Passive tracers deployed in a simulation have further revealed a significant intrusion of saltwater in the South Passage toward the North Passage, and this intrusion has been found to be diminished by northerly winds.

Extrusion of Riverine Waters

The riverine waters mainly extrude out of the Changjiang Estuary through the South Branch. The transport time required for the buoyant waters to travel from the river entrance (XuLiuJing in **Figure 1B**) to the estuary exit (∼122.5°E) is approximately 23 and 35 days for high and low discharge conditions, respectively (Wang et al., 2010). The time required for the buoyant waters to exit the estuary increases from the North Channel to the South Channel and from the North Passage to the South Passage due to the diversion of freshwater discharge and the increase in bottom friction. The gravitational exchange flow at the exit of the estuary accelerates the seaward export of the buoyant waters from the river entrance further downstream.

This transport time experiences notable seasonality and spring-neap variation (Wang Y. et al., 2015). It is greater in winter compared to that in summer, and the seaward export of freshwater is stronger during the neap-tide period than during the spring-tide period. Similarly, field observations have shown that the residual current in the North Passage is stronger in summer than that in winter, and it is more influential during spring tides than during neap tides (Pu et al., 2015). Tidal stirring, longitudinal and lateral depth-mean straining act as the principal mechanism determining the contrasting mixing intensity observed during spring and neap tides (Pu et al., 2016). The tidal effect is more important in winter, when the discharge rate is greatly reduced, compared to that in summer (Zhang et al., 2017). Tidal waves invade further upstream toward the South Branch in winter (Zhang et al., 2018a). Surface elevation at the upstream of the South Branch is higher in summer than that in winter, while variations of surface elevation is minimal at the estuary exit. In the down-estuary section, a higher barotropic pressure gradient is thereafter established in summer. The lateral circulation in the cross-branch direction is generated by the

barotropic pressure gradient to enhance the intrusion of shelf waters in the North Channel (Zhu et al., 2018b).

Anthropogenic Impacts

Anthropogenic impacts on the Changjiang estuarine circulation are represented by the Three Gorges Dam in the further upstream of the river (not shown), the progressive narrowing of the North Branch and the underwater infrastructure in the North Passage (**Figure 2B**). The impoundment of Three Gorges Dam was considered to greatly alter the streamflow (Zhang et al., 2019b; Wang et al., 2020; Yu et al., 2020a) and nutrient discharges of Changjiang river and thereby have a great potential in altering the hydrographic properties (Yan et al., 2008), sediments (Dai et al., 2016) and biogeochemical processes (Chai et al., 2009) in the estuary and thereafter the coastal seas. The increased discharge rate in the dry season, due to impoundment of Three Gorges Dam could be favorable for ensuring the freshwater supplement (Cai et al., 2019) and has potentials to suppress the injection of saltwater from the North Branch to the South Branch. The incremental anthropogenic impacts, such as the narrowing and shallowing of the North Branch, also progressively reduced the saltwater intrusions from the North Branch to the South Branch, and the topographic changes in the North Channel from 2007 to 2017 strengthened/weakened the intrusion of shelf waters during spring/neap tides (Chen et al., 2019). However, the role of Three Gorges Dam in changing the estuarine and coastal circulations is considered to be secondary referring to the underwater infrastructure in the North Passage (Wu et al., 2018c). The large-scale underwater construction (**Figure 1B**) in the vicinity of Hengsha Island greatly strengthens the tidal current (Zhang et al., 2018a), direction of rotation and vertical structure of the tidal ellipse (Pu et al., 2017) and thereby stability of the inside waters (Wan and Zhao, 2017), thus altering the stratification in the North Passage (Ma et al., 2011; Wan et al., 2014; Chen et al., 2020b). This underwater construction diminishes the freshwater partition in the South Channel while amplifies the onshore intrusion of saltwater in the South and North Passages, and alleviates the invasion of shelf waters in the North Channel by reducing/increasing the partition of riverine waters in the South/North Channel (Zhu et al., 2018a; Zhu et al., 2019). From the North to the South Channel, an anticlockwise circulation anomaly is thereby established (Li et al., 2020). The built underwater jetty spur (**Figure 1B**) has greatly increased the transport time by 50% (Wang et al., 2010). This underwater infrastructure has also been observed to strengthen the southward motion of the Changjiang River plume over the shelf by eliminating the lateral circulation at the estuary exit, where the northeastward extension of the buoyant plume begins (Wu et al., 2018c).

CHANGJIANG RIVER PLUME

The Changjiang River plume is formed by the massive amount of freshwater extruding through the Changjiang Estuary and plays a critical role in determining the regional circulation in the coastal seas. For example, the recent synthesis of previous observations and numerical simulations showed the seasonality of the coastal circulation over the shelf to the west of the 50-m isobath (Wu and Wu, 2018), and a year-round persisting bottom-trapped plume off the Zhejiang and Fujian coasts is proposed (Zhang et al., 2020). This bottom-trapped plume is critically sustained by extensive tidal mixing, and it imposes an unexpected counter-wind southwestward coastal current off Zhejiang in the summers of 2006 and 2009 (Li et al., 2014b).

The Changjiang River Plume also interacts with the TWWC in the central ECS shelf, the TSWC in the Tsushima Strait (Isobe et al., 2002), and TSC in the Taiwan Strait (Lie and Cho, 2016), and shows notable seasonality and remarkable spatial variation, which is characterized by distinct flow patterns over the shelf of the coastal sea off the Changjiang Estuary. These freshwaters can also greatly impact the connectivity between the Japan Sea and the northern ECS by altering the baroclinicity of the water in the Tsushima Strait in summer (Isobe et al., 2002; Senjyu et al., 2006). For example, the numerical tracer experiments conducted by Chang and Isobe (2003) showed that 68% of the Changjiang River plume is transported into the Tsushima Strait and the extension of these buoyant waters is strongly constrained by the TWWC. In the following contents, we will further synthesize the spatial characteristics and driving mechanisms of the Changjiang River plume in summer and winter, respectively.

Changjiang River Plume in Summer

The freshwater that rushes out of the Changjiang estuary is arrested by the northward coastal current and northeastward flowing TWWC and widely broadened to the southeast, east, and northeast over the shelf region in the surface layer (Hwang et al., 2014). There is weak bidirectional southwestward and northwestward extrusion of these buoyant waters observed over the coastal seas off Zhejiang and over the Subei Shoal (Kim et al., 2009; Bai et al., 2013; Zhu et al., 2015; Zhang et al., 2020). However, this southwestward branch of the plume cannot travel further southward into the Taiwan Strait (Wu et al., 2018b). The entirety of the plume, which widely spreads over the central and northern ECS and southern YS shelves (Lie et al., 2003), turns northeastward over the shelf to the east of the 50-m isobath and flows toward Cheju Island (Chen et al., 2008). The behavior of the plume in the coastal seas to the west of the 50-m isobath is different from that over the shelf in depths >50 m since the coastal waters are better mixed than those offshore, which is further described below.

Bulge Circulation

Numerous numerical simulations and observations have clearly shown that the buoyant waters from the Changjiang River plume are partially mixed with the saltwater being stored in a bulge over the shelf to the west of the 50-m isobath (Chang and Isobe, 2003; Shan et al., 2009). This bulge, which is enveloped by sharp density fronts (Lu and Shi, 2007), usually bifurcates at the head of the submerged valley that is delineated by the 50-m isobath over the shelf to the southeast of the Changjiang Estuary and then extends northward into the Subei Shoal, southwestward to Hangzhou Bay and then the coastal seas off Zhejiang (Du et al., 2011) (**Figure 3**).

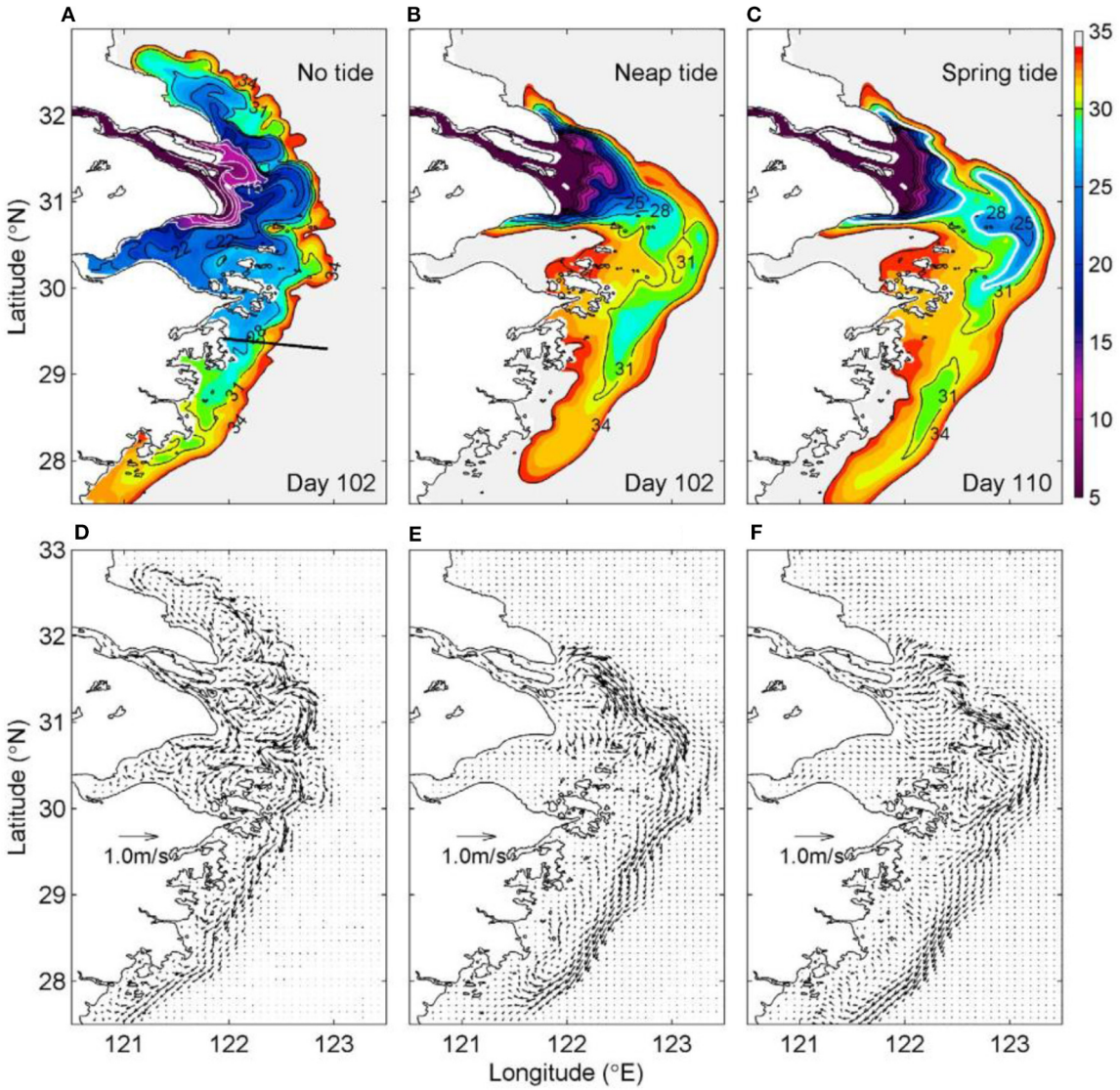


FIGURE 3 | Distributions of **(A–C)** surface salinity and **(D–F)** surface currents, respectively, under the condition with **(A,D)** low discharge without tides, and low discharge with tides during **(B,E)** neap and **(C,F)** spring tide periods. The contour interval for surface salinity distributions in **(A–C)** is 3 psu. This figure is adapted from Li and Rong (2012).

The majority of these plume waters then extend northeastward toward the central ECS shelf and interact with the TWWC.

The characteristics of the circulation of this bidirectional extruding bulge is critically determined by tides (Wu et al., 2018b). The Changjiang River plume in the coastal areas off the estuary disperses eastward and southeastward in the form of "cloudy patches" and that the dispersion direction varies coherently with tides, when steady winds force estuarine and coastal circulations (Shi and Lu, 2011). The strong tidal mixing over the shallow Subei Shoal suppressed the northward extrusion of Changjiang River plume (Wu et al., 2011). The bulge also considerably varies with the spring-neap tide transition (**Figure 3**), and is mainly limited in the coastal seas to the west of the 30-m isobath during spring tides and extends further eastward during neap tides when tidal rectification and tidal asymmetry are weak. Tidal asymmetry has been found to establish high pressure at the head of the submerged valley, and the plume is thus guided to extend northeastward at ∼122.5° E. Although its magnitude is much weaker than that in the southward and northeastward branches, tidally induced Stokes drift transports a small portion of the shallow Subei Shoal in winter (Wu et al., 2014), and the wind can only affect this northward extrusion during the neap-tide period.

Tides also increase the amount of freshwater trapped by the bulge (**Figure 3**; Li and Rong, 2012; Rong and Li, 2012). The bulge circulation is stabilized and its ballooning is suppressed with time (**Figures 3B,C,E,F**). Detachment of buoyant waters from the plume occurs during the transition period from

neap to spring tides, when the stratification of the partially mixed plume waters is destroyed and buoyant water patches form, while variation of the Changjiang River discharge rate cannot greatly influence this process of detachment. However, the numerical simulation by Yuan et al. (2016) showed that although the buoyant plume neighboring the Changjiang Estuary instantly (within 1 day) responds to variation in Changjiang River discharge, it takes ∼15 days for the offshore branches of this plume to respond in summer. Thereby, the response of the detachment of buoyant plume to the changing discharge rate should be further investigated.

Winds may also play a crucial role in detaching buoyant waters during the growth of the bulge (Xuan et al., 2012). Wind-induced mixing and upwelling along the edge of the bulge causes saltwater to detach the buoyant waters over the 30-m isobath. This detachment mainly occurs during the period when the speed of southwesterly winds exceeds 8 m s^{-1}. Thus, the characteristics of the complicated bulge circulation and its dynamics also necessitate further study (Wu et al., 2018b).

Far-Field Plume

Over the ECS shelf to the east of the 50-m isobath, the interaction between the Changjiang River plume and shelf currents is associated with the complicated wind and tidal patterns and the remote influence of previously introduced shelf currents, which alter the pathway of the plume (**Figure 4**). For example, the long-term satellite observations (Kim et al., 2009, 2014) of Chlorophyll-*a* indicated that the eastward motion of the Changjiang River plume lags behind the variations in river discharge by about 1 to 2 months. Bai et al. (2015) adapted and validated the advanced satellite-derived salinity algorithm in Bai et al. (2013) and reported strong interannual variability in the distribution of the Changjiang River plume (**Figure 4**), which was partially identified in some earlier satellite observations (Ahn et al., 2008). In addition to the most frequently observed northward and northeastward pathways, Bai et al. (2015) identified two unusual pathways of the Changjiang River plume, which flows into the Cheju and Tsushima Straits without residing over the shelf and flows southeastward in the central ECS (Types 2 and 3 in **Figure 4**). The plume area estimated in that study is regulated by the intensity of river discharge and winds over the shelf. The arrival of typhoons may also play an important role in altering the variability of the pathways of this plume. For example, Oh et al. (2014) and Hong et al. (2016) proposed an extensive northward extrusion of the Changjiang River plume into the YS in 2012. The velocity records of July 2015 further showed that typhoons could even bend the Changjiang River plume to flow southwestward along the Zhejiang coast (Zhang et al., 2018c).

Changjiang River plume extends eastward in the form of patches of low-salinity water instead of as a tongue-shaped plume extending toward Cheju Island (Lie et al., 2003), and it intensifies the TWWC and TSWC (Chen et al., 2008). The baroclinic instability associated with the extensive density fronts enveloping these massive buoyant waters facilitates the eastward transmission of the Changjiang River plume through buoyant eddies that detach from its edge, while the southerly summer monsoon enhances this detachment. The strong tides over the ECS shelf suppress this baroclinic instability, while the detachments of low-salinity water patches are primarily caused by the spatially non-uniform southeasterly wind (Ge et al., 2015). However, the extensive tide-induced vertical mixing in the northern ECS shelf tends to enhance the meandering of buoyant waters off the Subei Shoal and displaces the plume to the north toward the YS (Type 2 in **Figure 4**). The formation of low-salinity water patches of the plume is induced by increased vertical mixing, especially during the spring-tide period (Moon et al., 2010). The freshwater content of these patches is highly dependent on the intensity of winds, which contributes to the variation of the motion of the plume by altering wind-driven Ekman transport, and a synoptically weakened southerly summer monsoon facilitates the southeastward displacement of the buoyant plume (Moon et al., 2012; Chang et al., 2014). There is not close correlation between the changes in the Changjiang River discharge and the pathway of the Changjiang River plume in the central ECS, although the area of the buoyant plume in the central ECS has been observed to vary closely with the discharge rate (Bai et al., 2015).

Changjiang River Plume in Winter

When flushing out of the estuary, the cold and buoyant waters from the Changjiang estuary are constrained in the coastal seas to the west of the 30-m isobath and advected southwestward in form of the Zhe-Mini Coastal Current (ZMCC) toward the Taiwan Strait (Guan and Fang, 2006). This extensive coastal current, which may be identified by surface temperature and salinity (Gao et al., 2009; Wu et al., 2018b), and the mud belt (Bian et al., 2013; Li et al., 2013) off Zhejiang and Fujian coasts, can be seen in winter. The intensity of the ZMCC in February 2012 was quantified to be ∼0.215 Sv by Wu et al. (2013) using phase-averaging technology. The tidally induced residual current roughly contributes ∼0.12 Sv to the transport of ZMCC (Li and Rong, 2012).

Along its path to the Taiwan Strait, the baroclinicity induced by this extensive buoyant plume stimulates the upshelf motion of shelf waters beneath the TWWC and alters the connectivity between the northern SCS and southern ECS (Hu et al., 2010). The baroclinicity from this plume facilitates the formation of the upshelf motion of waters beneath the TWWC, even when downwelling-favorable winter monsoon prevails (Qiao et al., 2006). It has also been reported that a portion of these buoyant waters extrudes northwestward along the coastline of the Subei Shoal in the southern YS to form Subei Coastal Waters (Wu et al., 2018a), whose underlying dynamics will be synthesized below.

Although the buoyant waters from the Changjiang River can be seen off the Zhejiang and Fujian coasts, its southward pathway with the ZMCC showed an extensive meandering that excites synoptic cross-shelf water exchanges (Yuan et al., 2008; He et al., 2010; Bai et al., 2013). The concurrent transport of the northward Kuroshio intrusion from the shelf to the northeast of Taiwan and the TWWC establish water-column stratification over the shelf to the east of the 50-m isobath off the Zhejiang and Fujian coasts, where the tidal wave diverges (Wu, 2015). The tidal current and associated mixing are minimized in the coastal

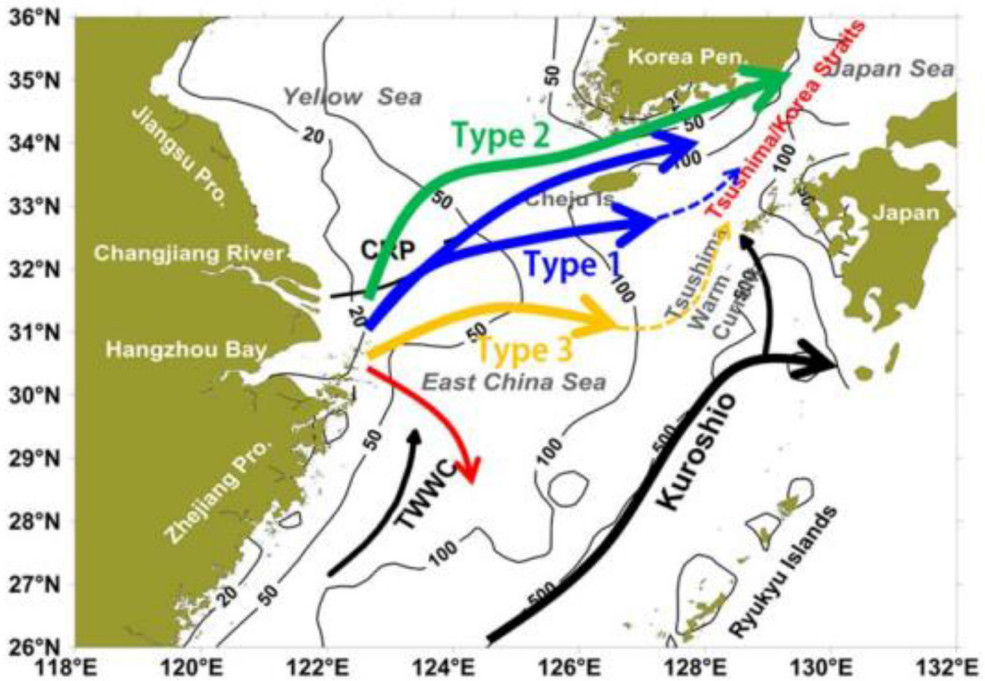


FIGURE 4 | Schematic pathways (colored arrows) of the three types of Changjiang River Plume identified from the 31 psu isohalines. The dashed arrows in blue and yellow signify plume water higher than the 31 psu would have advected by the Tsushima Warm Current to the Tsushima-Korea Straits. The red arrow shows the occasional movement triggered by typhoons. This figure is adapted from Bai et al. (2015), and Type 1 stands for the most frequently observed pathway of the plume, while Type 2 shows the pathway of buoyant waters when the buoyant waters are extensively advected toward Tsushima Strait, without residing over the shelf. Type 3 is rarely observed southeastward motion of the buoyant plume.

areas where a divergence occurs, which stimulates the cross-shelf penetration of two cold-water tongues. The penetration of these shelf waters then induces the offshore export of coastal waters carried by the ZMCC through the joint effect of baroclinicity and relief (JEBAR). This scheme explains the quasi-stationary or less-propagational cross-shelf water exchanges along the Zhejiang and Fujian coasts (Yuan et al., 2010). This cross-shelf meandering of the coastal current seems not to be governed by frontal instability, and interestingly, fluctuations in temperature but not salinity are a prerequisite for extensive cross-shelf water exchanges, although the appearance of the buoyant plume was found to play an essential role in maintaining the extensive southwestward flow of the ZMCC (Wu et al., 2013).

COASTAL CURRENTS IN THE ECS AND SOUTHERN YS

East China Sea Coastal Current (ECSCC)

The variations of coastal circulation in the ECS are jointly driven by monsoons, tides, and the buoyancy forcing from the extensive Changjiang River discharge (Lie and Cho, 2016; Wu et al., 2018b). In general, coastal circulation over the shelf shallower than 50 m generally flows northeastward in summer and southwestward in winter (Lee and Chao, 2003; Ge et al., 2013; Gan et al., 2016), although extensive synoptic variation has also been observed (Xuan et al., 2016a). The instabilities associated with this current may stimulate notable cross-shelf water exchange in both seasons (Yuan et al., 2005, 2008; He et al., 2010).

The northeastward coastal circulation has been found to generate the upshelf intrusion of shelf waters from the bottom layers of the TWWC, forming a distinct and extensive cold water belt off the Zhejiang and Fujian coasts in summer (Hu and Wang, 2016). In winter, the ZMCC carries ∼90% of the Changjiang River discharge (Wu et al., 2013) into the Taiwan Strait (Shen et al., 2017), which modulate the intensity of the TSC through the formation of a zonal density front in the strait (Chen and Sheu, 2006). Along its path, these cold and buoyant waters are vertically well mixed and form a sharp density front with the northeastward flowing TWWC over the outer shelf in winter (Huang et al., 2010).

The characteristics of coastal currents in the ECS are partially synthesized in Guan and Fang (2006) and Hu and Wang (2016), which were important references in our review, especially for studies prior to 2010. In this section, we focus more on the detailed dynamics that govern the cross-isobath transport, and pay more attention on the coastal circulations specifically in the ECS, instead of the entire China Seas.

It has long been recognized in 1990s (Liu and Su, 1991) that the possible forcing mechanisms driving the summer upwelling off the Zhejiang coast include the upwelling favorable southerly monsoon, upward lifting of the shoreward intrusion of the Kuroshio Current from the shelf to the northeast of Taiwan,

shoreward and upward movements of the TWWC induced by bottom friction, and the response of the TWWC to the regionally diverging isobaths. It was also suggested that upwelling could be divided into inshore and offshore segments (roughly divided by the 70-m isobath), with wind forcing dominating the upwelling process of the inshore area and the TWWC driving the upwelling in the offshore region. Subsequent numerical simulations and observations in the 2000s further confirmed the importance of winds and TWWC in generating the upwelling along the ECS coast (Jing et al., 2007; Wei et al., 2007).

These previous studies have proposed that upwelling does not uniformly occur along the ECS coast, and the detailed dynamics underlying this upwelling circulation are progressively revealed in the recent decades. The upshelf intrusion of shelf waters is intensified on the lee side of coastal promontories along the Zhejiang and Fujian coasts (Chen et al., 2014; Liu and Gan, 2014) as well as at the head of the submerged valley in the central ECS shelf and to the southeast of the Changjiang Estuary (Liu and Gan, 2015; Yuan et al., 2017), where a cold water center with high primary productivity is frequently observed (Shi and Wang, 2012). That upwelling in that submerged valley is strengthened by the baroclinicity of waters imposed by the extensive presence of buoyant waters from the Changjiang River discharge (Zhu, 2003), and it is considered to be the onshore branch of the TWWC over the shelf to the east of the 50 m isobath (Wang et al., 2019a). This spatially irregular distribution of upwelling circulation has been frequently reported in recent decades, and we have now recognized the importance of topography as well as tidally induced mixing in generating upwelling in the ECS. For example, field observations and numerical simulations by Lü et al. (2006) have shown that the upslope intrusion of shelf waters in the vicinity of the Changjiang Estuary is mainly induced by a cross-frontal density gradient that is compensated by extensive tidal mixing. Liu and Gan (2014, 2015) proposed that the onshore intrusion of shelf waters on the lee-side of Zhoushan Islands and at the head of the submerged valley is not merely induced by bottom Ekman transport but is generated by the along-shore variation of the meridional pressure gradient, which is exerted by the response of the coastal current to the variation in bottom topography.

Interestingly, although we have recognized that it is mainly the northeasterly wind that prevails in the ECS and that a strong southwestward flowing ZMCC characterizes the coastal circulation in winter (Wu et al., 2013), the downslope export of coastal waters due to coastal Ekman dynamics has rarely been reported. For example, previous studies like those of Qiao et al. (2006), Jing et al. (2007), and references therein have suggested that although both the wind and ZMCC favor the downwelling of shelf waters, it is mainly the upshelf intrusion of shelf waters due to the northeastward flowing TWWC that is observed (Hu, 1994).

Some previous studies have focused on the dynamics governing the formation of this upwelling circulation in winter, and tides, as well as the buoyant nature of the coastal currents, have been found to play predominant roles. For example, the numerical simulation and field observations by Qiao et al. (2006) revealed that the sharp density front between the ZMCC and TWWC, due to extensive buoyant discharge from the Changjiang Estuary, facilitates the formation of an extensive cross-front baroclinic pressure gradient that drove upwelling off the Zhejiang coast. Tidal currents extend the river plume further to the southwest and contribute to the formation of upwelling. The northeastward flowing TWWC obstructs the pathway of the ZMCC, the associated density front, and the upwelling of deep shelf waters. Upwelling in the coastal area of the ECS is thereby a year-round phenomenon, with maximum and minimum upward velocities in summer ($\sim 10^{-2}$ ms^{-1}) and winter ($\sim 10^{-3}$ ms^{-1}), respectively (Jing et al., 2007). The recent long-term observations by Huang et al. (2016) over the shelf to the east of Zhejiang in the central ECS have clearly shown that the cross-isobath transport of shelf waters varies coherently with the along-shore velocities of the ZMCC. More importantly, that study proposed that shelf velocities also present extensive synoptic and intra-seasonal variability and suggested that the along-shore geostrophic current may play a more important role in generating the cross-shore water exchange than the role of bottom friction.

Yellow Sea Coastal Current (YSCC)

The coastal current in the southwestern YS over the shallow Subei Shoal was named as the Yellow Sea Coastal Current (YSCC), which, together with the ECSCC, comprises the China Coastal Current system (Guan and Fang, 2006). In the water column, it is recently proposed that the observed current profiles demonstrate a clockwise rotation, probably due to the "horizontal diffusion of geostrophic vortex stretching" (Song et al., 2019). The YSCC was considered to be a year-round southward flow (Lie and Cho, 1994), and the southward YSCC in winter is generated by the baroclinicity of the fresher waters carried by the Lubei Coastal Current (Wei et al., 2016) or Bohai Sea Coastal Current (Sun et al., 2018) from further north of the Shandong Peninsula. In summer, it is formed by the baroclinicity from the YSCM in the Yellow Sea Trough (Xia et al., 2006) to flow southeastward along the eastern flank of the Subei Shoal (Lie and Cho, 2016).

Yuan et al. (2008) questioned the conclusions of the flow pattern of the YSCC and suggested that the YSCC could be reversed to flow northwestward along the coastline of the Subei Shoal in summer, as also revealed by some simulations in the recent decades (Qiao et al., 2011; Wang et al., 2013b; Shi et al., 2016). A northward extending buoyant plume associated with upwelling in the summers of 2008 and 2009 was observed over the Subei Shoal (Yuan et al., 2017). This northwestward YSCC in summer, accompanied with the southeastward flow in winter, indicates a seasonal reversal of the flow direction, and this seasonal reversal is proven by the *in-situ* hydrography observations (Wei et al., 2016) and some recent numerical simulations (Gan et al., 2016).

Tides have recently been considered to be another important driving force that alters the circulation over the Subei Shoal. The density front, which is established by extensive tidal mixing over the shelf surrounding the shallow Subei Shoal, generates upwelling of shelf waters along its eastern flank in summer (Lü et al., 2010; Liu and Gan, 2016). This upwelling may result in cold surface waters that are most frequently observed when southerly

winds prevail (Zhu et al., 2018c). The formation of these cold surface waters is also impacted by the spring-neap tides (Liang et al., 2018). The water column is stratified during neap tides, while during the spring tides, sea surface temperature is at a minimum, which implies strong vertical mixing. YSCC along the eastern flank of the Subei shoal flows southeastward along the 30-m isobath (Xia et al., 2006; Wang et al., 2013a). However, the Lagrangian drifters released over the Subei Shoal clearly showed a northeastward floating trajectory, which is generally perpendicular to the southeastward Eulerian residual current, given that the impact of the southerly summer monsoon exceeds that of the residual current due to increased bottom friction from the extensive tidal currents.

The high-resolution numerical simulation by Xuan et al. (2016b) showed that the tidally induced residual current flows northwestward along the coastline of the Subei Shoal and reverses to the southeastward along the 50-m isobath over the eastern flank of the Subei Shoal (**Figure 5A**). The authors considered the offshore branch of this current as the YSCC, which exhibits clear seasonal variability. The inshore branch is named as the Tide-Induced Coastal Current (TICC), and it was considered to be a year-round northwestward current. The observations and numerical simulation (Wu et al., 2018a) for the circulation in December 2016 and January 2017 also clearly showed a northwestward current flowing against the northerly wind along the coastline of the Subei Shoal (**Figure 5B**). The tidal stress induced by the propagation of a Poincaré wave, together with the rotation of the earth, forces the northwestward current along the coastline of Jiangsu, while tidally strengthened bottom friction suppresses the wind-forced current. The standing wave imposed by the collapsing of tidal waves from the YS and ECS modulate this coastal current, resulting in an eastward flow in the cross-shore direction. This northward current is generated by the Stokes drift due to the propagation of tidal waves (Wu et al., 2014).

The numerical simulation by Wang et al. (2017b) exhibited a different winter flow pattern from that of Xuan et al. (2016b) and Wu et al. (2018a) by taking those buoyant waters from the minor rivers along the coastline of Jiangsu. Although the tidally induced residual current was still suggested to play a critical role in modulating the interactions between the YSWC and YSCC in winter, Wang et al. (2017b) considered that the currents over the Subei Shoal mainly flow southeastward in winter and that these freshwaters are merely from the rivers with minimal discharge along the Subei coast, instead of the Changjiang River plume, since the variations of salinity is insensitive to the discharges of Changjiang River. This finding contradicts those of Wu et al. (2014), Oh et al. (2014), and Xuan et al. (2016b), in which the Changjiang River plume was considered to be the major source of these freshwaters. The recent numerical simulation using water ages indicated that the minimum salinity of these fresher coastal waters lags behind the peak in Changjiang river discharge by about 2 months in summer, and these waters reside over the shallow Subei Shoal in winter (Zhu and Wu, 2018). Taking this lagged response of the circulations over the Subei Shoal to the river discharge from Changjiang river into consideration, the roles of buoyancy forcing in altering the YSCC are worth to be further explored.

It can be summarized that the flow pattern of the YSCC, which is the result of complicated forcing conditions associated with the shallow shelf of the Subei Shoal, should be further investigated. According to the contrasting flow patterns of the shallow coastal waters in the vicinity of its eastern flank and the submerged valley to the south, it becomes necessary to further evaluate the YSCC by examining its coastal and offshore branches (Wei et al., 2016; Xuan et al., 2016b; Wu et al., 2018a). The former branch is characterized as Subei Coastal Water (SCW), while the latter is characterized as the YSCC in Xuan et al. (2016b), which interacts with the YSWC/YSCM and the offshore branch of TWWC to the east of the 50-m isobath.

IMPACTS OF CIRCULATION ON HYPOXIA OFF THE CHANGJIANG ESTUARY

The buoyant plume from Changjiang exports huge amounts of dissolved inorganic nitrogen (∼5,896 Gg N/yr), phosphate (∼381 Gg P/yr) (Gao et al., 2008, 2012; Tong et al., 2017; Liu et al., 2018) and sediments (∼250 million tons/year) (Yang et al., 2006, 2015) into the ECS. As shown in **Figure 6**, the nutrients from Changjiang discharge, together with those intruding into the ECS through the Taiwan Strait (Huang et al., 2019) and from the Kuroshio (Chen et al., 1995; Chen, 1996; Lui et al., 2015; Qian et al., 2017; Zhang et al., 2019c; Zuo et al., 2019), played critical roles in stimulating the phytoplankton bloom (Li et al., 2014a; Yu et al., 2018), eutrophication and hypoxia in the coastal water. Chen et al. (2017) proposed that hypoxia usually occurs in the bottom waters in the eutrophication area with the concentration of surface chlorophyll-*a* exceeds 3.0 mg L^{-1}. The formed hypoxia are destructive to the marine ecosystem (Xu et al., 2015; Zhu et al., 2016b) in ECS (Chen et al., 2003; Wang et al., 2012; Qian et al., 2017; Wei et al., 2017a; Zhou et al., 2017; Zhang et al., 2018b; Wang et al., 2019c; Wang et al., 2019b; Zhang et al., 2019c; Chen et al., 2020a) and the YS (Zhai et al., 2020). It is generally considered that during the recent decades from 1980s to 2010s, there is an accelerated anthropogenic nutrient loading, and occurrence of eutrophication (Wang J. et al., 2015; Wang et al., 2016, 2018) and hypoxia (Wu et al., 2020) in the coastal waters (Liu et al., 2018; Chen J. et al., 2020). The recent overview by Chen J. et al. (2020) is recommended as an important reference that comprehensively synthesized the nutrient dynamics and biogeochemical processes, and here we focus on the impact of circulation dynamics to the changing hypoxia condition in the coastal seas of the ECS. The impact of circulation on the biogeochemical processes, not only revealed by its redistribution (Wang et al., 2019b; Wei et al., 2020) of nutrients and the elevated Redfield ratio (Wang J. et al., 2015; Chen et al., 2017; Liu et al., 2018), but also its changes on the stratification, residence time and ventilation of the shelf waters (Rabouille et al., 2008; Zhu et al., 2016a; Luo et al., 2018; Zhang et al., 2019c) will be overviewed in this section.

Hypoxia, usually with acidification of the seawaters (Wei et al., 2017b, 2020), generally occurs in the coastal seas neighboring

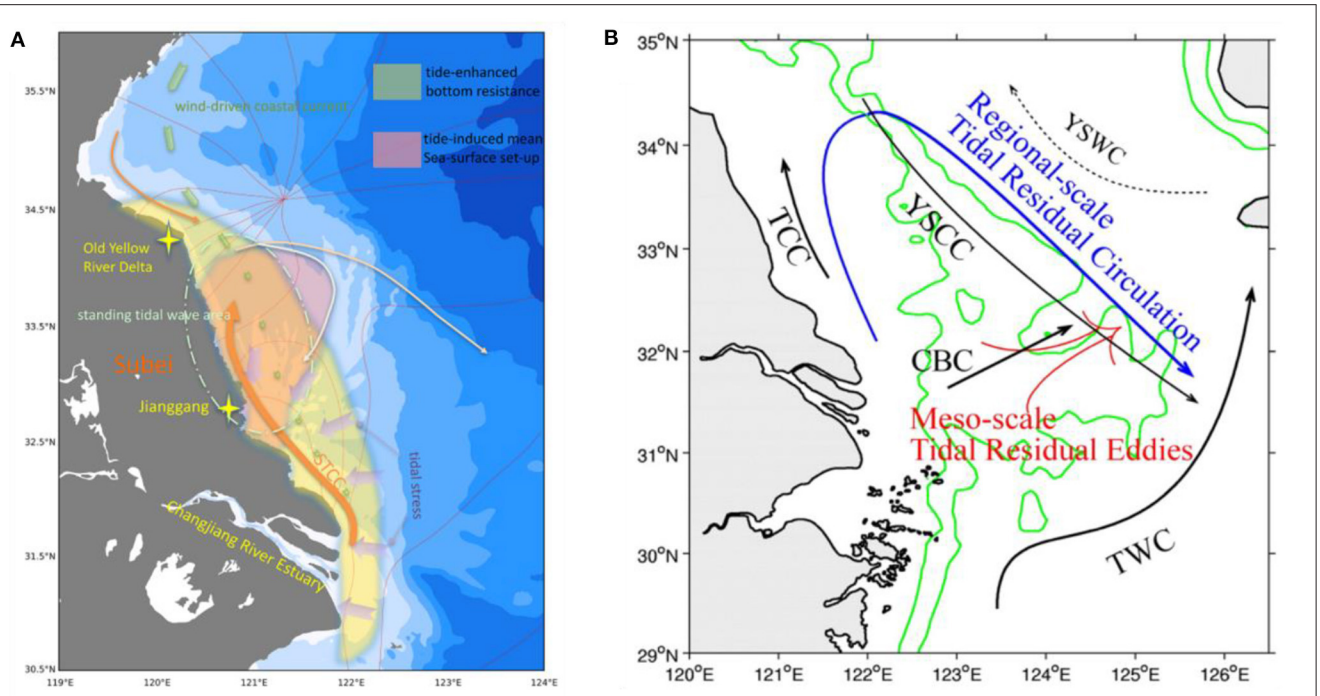


FIGURE 5 | (A) Sketch map of residual transport over the Subei Shoal and its controlling mechanisms by the Subei tide-induced coastal current (STCC), which is raised from tidal stress (pink arrows) in the coastal seas to the north of Changjiang Estuary. The thin red lines indicate co-phase lines for the M_2 tide with an interval of 30°. The wind driven coastal current in winter is indicated by the green arrows, and the circulations over the eastern flank of Subei Shoal is indicated by the yellow thin lines. This figure is adapted from Wu et al. (2018a). **(B)** Tidal residual current and mean flow over the Subei Shoal. Meso-scale tidal residual eddies (red arrow) and regional-scale tidal residual circulation (blue arrow) show the patterns of the tidal residual current across and around the Subei Shoal. The structure of mean flows (five black arrows) is composed by Taiwan Warm Current (TWC), YSCC, Changjiang Bank Current (CBC), Tidal-induced Coastal Current (TCC), and YSWC. This figure is adapted from Xuan et al. (2016b).

the 30 m isobath over the shelf. It strengthens from the late spring to summer (Zuo et al., 2019) and peaks in August (Zhu et al., 2011, 2017). There are also observations showing that the hypoxia can occasionally last longer to the mid-autumn (Wang et al., 2012; Chen C. C. et al., 2020). In winter, the buoyant waters are well-ventilated and hypoxia is thereby prevented (Zheng et al., 2016; Liblik et al., 2020). It is considered that the physical environment favors the development of hypoxia in summer, when the Changjiang river discharge maximizes (section Changjiang estuarine circulation), an intensified northeastward TWWC appears (Wang et al., 2012), upwelling of the shelf waters is established and the coastal waters are more stratified (Zheng et al., 2016; Chen et al., 2017). From June to August, the hypoxic waters mainly expand northeastward from the coastal seas to the east of Zhejiang and where mud-belt is observed (Zhang et al., 2019c). This hypoxia is mainly established by the Changjiang buoyant plume and intrusion of Kuroshio subsurface water (Zhang et al., 2019c), while the northeastward expansion is largely related to the strengthening of the northeastward TWWC and advances of upwelling circulation (Wei et al., 2011). Stratification of the coastal waters responses to circulation/discharges within ∼35 hr (Ni et al., 2016), followed by an response of the bottom dissolved oxygen to changes of stratification is generally ∼6 to ∼50 h (Zhang et al., 2018b). The stratification is also sensitive to changes in the wind intensity and direction (Chen et al., 2015; Zheng et al., 2016; Zhou et al., 2017), which jointly regulate the stratification, coastal current and pathway of the buoyant plume.

Kuroshio intrusion mainly regulates the hypoxia by increasing the residence time of the bottom coastal waters (from ∼11 to ∼40 days) in summer (Zhang et al., 2019c). However, the intrusion also alleviates the hypoxia through carrying shelf waters with a higher concentration of dissolved oxygen (Luo et al., 2018; Zuo et al., 2019). It is also found that the incoming Kuroshio waters is deoxygenating and acidifying (Lui et al., 2015). The overall effect of the Kuroshio intrusion is to increase the intrusion of nutrients and strengthen the stratification intensity over the shelf. Thus, the summer hypoxia have a tendency of being worsened under the influence of the Kuroshio intrusion (Lui et al., 2014).

In the synoptic timescale, the increment of Changjiang river discharge is believed to stimulate the expansion of hypoxia (Zheng et al., 2016; Zhou et al., 2017), although there are also studies suggested that the changes in hypoxia are not response to the changes in the river discharge instantly (Chen et al., 2015). The offshore detachment of buoyant waters in form of "cloudy patches" synthesized in the section 3.1, played critical roles in regulating the hypoxia condition (Liblik et al., 2020;

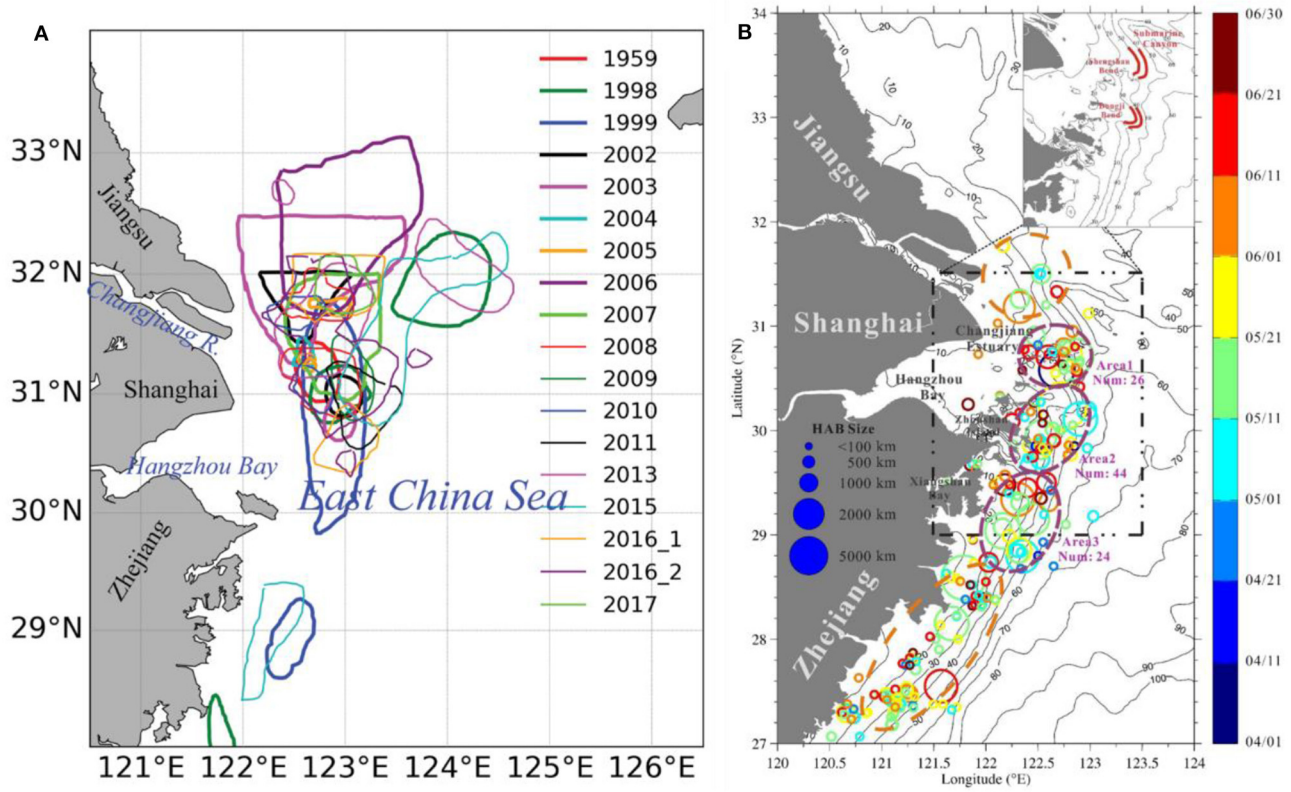


FIGURE 6 | Maps for **(A)** the observed distributions of bottom hypoxic waters (Zhang et al., 2019c) and **(B)** events of harmful algae bloom (HAB) between 2000 and 2014 (Wang Y. H. et al., 2019). "The color and size of the solid circle represent the date and affected area of each event. The black lines are the isobaths. Three HAB hotspots and two scattered HAB areas are marked with purple and orange dashed circles, respectively. The event occurrence numbers in HAB hotspots are also labeled" in **(B)** (Wang Y. H. et al., 2019).

Wei et al., 2020). The phytoplankton bloom sealed inside these patches with relatively stable environment and the organic debris favor the formation of hypoxia. This offshore detachment of buoyant plume is also found to play critical roles in regulating the algal bloom and formation of high chlorophyll-*a* centers (**Figure 6B**) in the coastal seas (Wang Y. H. et al., 2019). In summer, the hypoxia off the Changjiang Estuary is dissipated by the arriving typhoon (Wu et al., 2005), which greatly alters the pathway of buoyant plume from Changjiang and strengthens vertical mixing (Zhu et al., 2016a). However, the extensive vertical mixing and the excessive nutrient loading due to the increased river discharge during the typhoon period greatly stimulate the establishment of phytoplankton bloom after typhoon. This process boosts the restoration of hypoxia within several days after typhoon landing and the waters are re-stratified (Wang et al., 2017a). This timescale is shorter than the formation of hypoxia due to moderate changes in winds (Ni et al., 2016). The changes of hypoxia condition, in a shorter timescale, is also found to vary in a semi-diurnal tidal period, e.g., ∼12 h, due to the combined effect of the bottom topography and spatial irregularity of the tidal extrusion distance off the Changjiang estuary (Zhu et al., 2017; Zhang et al., 2019c).

SUMMARY AND PROSPECTS

Summary

This manuscript synthesizes the recent studies on the circulation in the Changjiang Estuary and the neighboring circulation in the coastal East China Sea and southern Yellow Sea (**Figure 7**). The exchange flows among the branches, channels, and passages in the Changjiang Estuary have been found to be greatly influenced by seasonal variation in riverine discharge while also being regulated by the tides. It has been found that over 95% of the riverine runoff rushes into the East China Sea through the South Branch, while the greatly diminished discharge rate in winter (i.e., dry season) facilitates the extrusion of saltwater and the injection of saltwater from the North Branch to the South Branch. This upstream extrusion oscillates with the flood and ebb tides and its amplitude increases during the spring-tide period, while the byproducts of these propagating tidal waves have been recently recognized to play important roles in regulating the estuary-ward extrusion of shelf waters. The northerly wind facilitates the injection of saltwater from the North Branch to the South Branch.

The buoyant waters from the South Branch have been found to be evenly partitioned toward the South and North Channels. Gravitational circulation, forced by the density gradient between

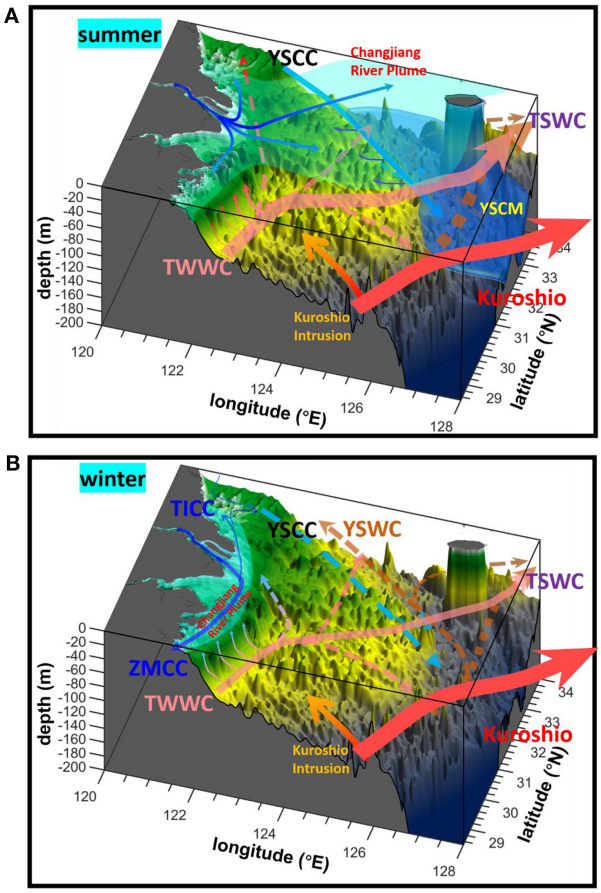


FIGURE 7 | Schematic of general circulations around the Changjiang Estuary in **(A)** summer and **(B)** winter. The shelf currents over the ECS are indicated by the vectors with warm colors, and the buoyant plume, TICC and YSCC are shown by the cold colors. The dashed lines indicate uncertainty in observed pathway of circulations in the ECS and southern YS.

the buoyant waters from riverine discharge and the denser shelf waters, intensifies the exchange of these flows. The jetty spur that borders the North Passage acts to extensively redistribute the freshwaters in the lower estuary, resulting in great circulation complexity. It is generally understood that this construction substantially increases the transport time required for the buoyant waters to travel from the river entrance to the estuary mouth.

In the coastal waters off the estuary, bulge circulation delineated by an extensive density front traps a considerable portion of riverine buoyant waters and mixes them with the waters from the ECS shelf. This bulge broadly expands southwestward toward Hangzhou Bay, southeastward toward the submerged valley, eastward, and northeastward toward the central ECS shelf, and northwestward toward the shallow waters over the Subei Shoal. Thus, the Changjiang River plume plays an important role in regulating the general circulation in the ECS and southern YS. Tides also play important roles in regulating the formation of this bulge. It has been shown that along the edge of the bulge, buoyant waters are shed in the form of "cloudy patches" in response to the variability in tidal and wind forcing and variations in the TWWC. The baroclinicity associated with these shed buoyant waters and the spatial variations of the tides facilitate the cross-shelf export of freshwaters in the coastal seas to the southwest of the Changjiang Estuary.

When southerly winds prevail, the Changjiang River plume generally travels to the northeast and is exported toward the southern YS and Tsushima Strait further to the north. This northward and northeastward motion of the buoyant plume shows extensive spatial variability in the form of notable patches of buoyant waters. The southward motion of the Changjiang River plume is diminished by the northeastward coastal current, which facilitates the formation of the extensive upwelling in the coastal seas off the Fujian and Zhejiang coasts, where the upslope intrusion of colder shelf waters is regulated by the along-shore irregularity of the bathymetry. A northwestward extrusion of buoyant waters from the Changjiang River plume is also observed in the nearshore regions of the shallow Subei Shoal.

In winter, the Changjiang River plume is carried by the ZMCC to flow southwestward in the coastal seas off the Zhejiang and Fujian coasts. Along its pathway, the cold water from the bottom-advected buoyant plume exerts an extensive shoreward pressure gradient, which is balanced by extensive tidal mixing, and stimulates upwelling in the coastal seas off the Zhejiang and Fujian coasts. A minimal portion of these buoyant waters (∼10%) also extrude northwestward toward the nearshore regions of the shallow Subei Shoal and alter the YSCC, which was recently found to be regulated by the southeastward coastal current from the Shandong Peninsula, the intrusion of the YSWC, and tidal mixing along the eastern flank of the Subei Shoal.

The general circulation associated with the YSCC to the west of the 50-m isobath in the southern YS has been frequently debated in recent decades. A year-round southeastward current over the shallow Subei Shoal has been observed, and the details of its flow pattern have been progressively evaluated, although the underlying dynamics remain unclear. A series of recent observations and high-resolution numerical simulations have suggested that tides play important roles in regulating the YSCC by increasing turbulent mixing and establishing a cross-isobath pressure gradient that facilitates the seasonal reversal of its mainstream flow, and the cross-shore exchanges between the waters in the Subei Shoal and Yellow Sea Trough.

It is considered that the physical environment favors the development of hypoxia, particularly in summer, when the river discharge maximizes, an intensified northeastward TWWC appears (Wang et al., 2012), upwelling of the shelf waters is established and the coastal waters are more stratified. Those physical processes redistribute nutrients, elevate Redfield ratio (Wang J. et al., 2015; Chen et al., 2017; Liu et al., 2018), and further affect the stratification, residence time and ventilation of the shelf waters. Thus, could largely modulate the biogeochemical processes and hypoxia off the Changjiang Estuary.

Prospects

Although the recent observations and numerical simulations have greatly enriched our understanding of the details of the

coastal circulation in the ECS and YS as well as circulation in the Changjiang Estuary, it should be noted that the interactions and circulation dynamics governing the estuarine-coastal-shelf-slope-Kuroshio current system are still not thoroughly understood due to the complex bathymetry, regional and remote forcing factors, and the wide-spectrum temporal variabilities in this circulation system. These wide-spectrum variabilities are transmitted to the current system over the ECS and southern YS through cross-scale interactive exchange flows, which should be further investigated. Our prospects of future studies on the coastal and estuarine circulations around of the Changjiang Estuary are as follow:

- The detailed mechanisms of, for example, tides in determining the exchange flows in the branches and channels in the Changjiang Estuary are worthy to be further investigated to better reveal the cross-scale interactions (Lu et al., 2015) of the wind-driven shelf circulation and the tidally-modulated estuarine circulations. The roles of tidal-straining, asymmetric tidal mixing (Lu et al., 2019), wind-straining and buoyancy run-offs could be investigated in details (Zhu et al., 2018b) to complete the mechanisms governing this multichannel estuary. The coastal, shelf and estuarine circulations must be systematically coupled in a quasi-seamless way, instead of, respectively, taking the coastal and estuarine circulations as the lateral boundary of each other. The synoptic fluctuations in not only the winds around the estuary, but also their remote impacts arriving with the downshelf propagating of, for example, coastally trapped waves (Ding et al., 2018), should be included.
- Given the nutrients carried by the buoyant waters from Changjiang are largely trapped inside the bulge off the estuary, we should further investigate its behavior, includes the residence time of the sealed waters, the processes governing its growth, as well as the dynamical role of bulge in communicating the circulations in Hangzhou Bay and Changjiang Estuarine. The synoptic fluctuation and fate of the far-field plume should be better investigated through measuring the surface salinity in fine-scales by satellite remote sensing and high-frequency profiles by the moored buoy array observations.
- The dynamical role of the TWWC, including the variations of its intensity and meanders in the mainstream should be better observed by a series of multi-functional buoys or regularly performing field cruises by using the phase-averaged method. We should also further clarify the general flow pattern of the YSCC and TICC/SCW, and investigate the impact of the diurnal variations of forces, including not only heat flux but also land-sea breeze, which is recently considered to non-negligibly modulate the long-term variation of ECS circulation (Yu et al., 2020b).
- The contribution of the various physical processes to the biogeochemical process like hypoxia need to be further clarified and quantified. The interactive multi-scale physical processes should be considered to provide comprehensive understanding on the marine environmental issues in the region.

The accumulation of information based on multiple long-term observations from bottom- or surface-moored instruments, as well as high-resolution numerical simulations, is essential. These high-resolution numerical simulations and accompanying field observations will facilitate the formation of a comprehensive understanding of the exchange flows and their underlying dynamics and mechanisms. Moreover, cautious is required to interpretate the interannual or decadal variabilities of estuarine and coastal circulations over this shallow shelf sea. The rapid changes of forces, including, for example, strong winds (Chai et al., 2020), and the associated near inertial oscillation (Meng et al., 2020) or riverine discharges (Lee et al., 2017; Moon et al., 2019), potentially have the long-lasting influences to overtake the responses of the coastal and estuarine circulations in the lower-frequency.

AUTHOR CONTRIBUTIONS

ZL writes the manuscript by integrating the comments and suggestions from JH, HW, JG, ZC, and YD. All authors contributed to the article and approved the submitted version.

FUNDING

This study was supported by the National Natural Science Foundation of China (41906016 and 41942034), the National Key R&D Program of China (2018YFC1406302 and 2016YFA0601903), and Science, Technology, and Innovation Commission of Shenzhen Municipality (JCYJ20190809144411368), and the Science and Technology Development Fund, Macau SAR (SKL-IOTSC2018-2020).

REFERENCES

Ahn, Y. H., Shanmugam, P., Moon, J. E., and Ryu, J. H. (2008). Satellite remote sensing of a low-salinity water plume in the East China Sea. *Ann. Geophys.* 26, 2019–2035. doi: 10.5194/angeo-26-2019-2008

Alebregtse, N. C., and de Swart, H. E. (2016). Effect of river discharge and geometry on tides and net water transport in an estuarine network, an idealized model applied to the yangtze estuary. *Cont. Shelf Res.* 123, 29–49. doi: 10.1016/j.csr.2016.03.028

Bai, Y., He, X., Pan, D., Chen, C.-T. A., Kang, Y., Chen, X., et al. (2015). Summertime Changjiang River plume variation during 1998-2010. *J. Geophys. Res. Oceans* 119, 6238–6257. doi: 10.1002/2014JC009866

Bai, Y., Pan, D. L., Cai, W. J., He, X. Q., Wang, D. F., Tao, B. Y., et al. (2013). Remote sensing of salinity from satellite-derived CDOM in the Changjiang river dominated East China sea. *J. Geophys. Res. Oceans* 118, 227–243. doi: 10.1029/2012JC008467

Bian, C. W., Jiang, W. S., and Greatbatch, R. J. (2013). An exploratory model study of sediment transport sources and deposits in the Bohai sea,

Yellow sea, and East China sea. *J. Geophys. Res. Oceans* 118, 5908–5923. doi: 10.1002/2013JC009116

Cai, H. Y., Zhang, X. Y., Zhang, M., Guo, L. C., Liu, F., and Yang, Q. S. (2019). Impacts of Three Gorges Dam's operation on spatial-temporal patterns of tide-river dynamics in the Yangtze River estuary, China. *Ocean Science* 15, 583–599. doi: 10.5194/os-15-583-2019

Chai, C., Yu, Z., Shen, Z., Song, X., Cao, X., and Yao, Y. (2009). Nutrient characteristics in the Yangtze river estuary and the adjacent East China sea before and after impoundment of the Three Gorges dam. *Sci. Total Environ.* 407, 4687–4695. doi: 10.1016/j.scitotenv.2009.05.011

Chai, X., Liang, X., Zhao, Y., Wu, H., and Wang, Y. (2020). An abnormal sea surface warming event as typhoon bolaven passes the Yellow sea. *Acta Oceanol. Sin.* 42, 41–50.

Chang, P. H., and Isobe, A. (2003). A numerical study on the Changjiang diluted water in the Yellow and East China seas. *J. Geophys. Res. Oceans* 108, 1–17. doi: 10.1029/2002JC001749

Chang, P. H., Isobe, A., Kang, K. R., Ryoo, S. B., Kang, H. S., and Kim, Y. H. (2014). Summer behavior of the Changjiang diluted water to the East/Japan sea: a modeling study in 2003. *Cont. Shelf Res.* 81, 7–18. doi: 10.1016/j.csr.2014.03.007

Chen, C., Zhu, J., Beardsley, R. C., and Franks, P. J. S. (2003). Physical-biological sources for dense algal blooms near the Changjiang river. *Geophys. Res. Lett.* 30:1515. doi: 10.1029/2002GL016391

Chen, C.-C., Gong, G.-C., Chou, W.-C., and Shiah, F.-K. (2020a). Hypoxia in autumn of the East China Sea. *Mar. Pollut. Bull.* 152:110875. doi: 10.1016/j.marpolbul.2019.110875

Chen, C.-T. A. (1996). The kuroshio intermediate water is the major source of nutrients on the East China sea continental shelf. *Oceanol. Acta* 19, 523–527.

Chen, C.-T. A., and Sheu, D. D. (2006). Does the Taiwan warm current originate in the Taiwan strait in wintertime? *J. Geophys. Res.* 111:C04005. doi: 10.1029/2005JC003281

Chen, C. S., Xue, P. F., Ding, P. X., Beardsley, R. C., Xu, Q. C., Mao, X. M., et al. (2008). Physical mechanisms for the offshore detachment of the Changjiang diluted water in the East China sea. *J. Geophys. Res. Oceans* 113:C02002. doi: 10.1029/2006JC003994

Chen, C. T. A., Ruo, R., Pai, S. C., Liu, C. T., and Wong, G. T. F. (1995). Exchange of water masses between the East-China-sea and the Kuroshio off Northeastern Taiwan. *Cont. Shelf Res.* 15, 19–39. doi: 10.1016/0278-4343(93)E0001-O

Chen, J., Li, D., Jin, H., Jiang, Z., Wang, B., Wu, B., et al. (2020). "Changing nutrients, oxygen and phytoplankton in the East China sea," in *Changing Asia-Pacific Marginal Seas,* eds C. T. A. Chen and X. Guo (Singapore: Springer Singapore), 155–178.

Chen, J., Pan, D., Liu, M., Mao, Z., Zhu, Q., Chen, N., et al. (2017). Relationships between long-term trend of satellite-derived chlorophyll-a and hypoxia off the changjiang estuary. *Estuar. Coasts* 40, 1055–1065. doi: 10.1007/s12237-016-0203-0

Chen, Q., Zhu, J. R., Lyu, H. H., Pan, S. Q., and Chen, S. L. (2019). Impacts of topography change on saltwater intrusion over the past decade in the Changjiang estuary. *Estuar. Coast. Shelf Sci.* 231:106469. doi: 10.1016/j.ecss.2019.106469

Chen, X., Shen, Z., Li, Y., and Yang, Y. (2015). Physical controls of hypoxia in waters adjacent to the yangtze estuary: a numerical modeling study. *Mar. Pollut. Bull.* 97, 349–364. doi: 10.1016/j.marpolbul.2015.05.067

Chen, Y., He, Q., Shen, J., and Du, J. B. (2020b). The alteration of lateral circulation under the influence of human activities in a multiple channel system, Changjiang estuary. *Estuar. Coast. Shelf Sci.* 242:106823. doi: 10.1016/j.ecss.2020.106823

Chen, Z. Y., Yan, X. H., and Jiang, Y. W. (2014). Coastal cape and canyon effects on wind-driven upwelling in northern Taiwan strait. *J. Geophys. Res. Oceans* 119, 4605–4625. doi: 10.1002/2014JC009831

Dai, Z. J., Fagherazzi, S., Mei, X. F., and Gao, J. J. (2016). Decline in suspended sediment concentration delivered by the Changjiang (yangtze) River into the East China sea between 1956 and 2013. *Geomorphology* 268, 123–132. doi: 10.1016/j.geomorph.2016.06.009

Ding, Y., Bao, X. W., Yao, Z. G., Song, D. H., Song, J., Gao, J., et al. (2018). Effect of coastal-trapped waves on the synoptic variations of the Yellow sea warm current during winter. *Cont. Shelf Res.* 167, 14–31. doi: 10.1016/j.csr.2018.08.003

Du, P. J., Zhang, H., Xiao, W. J., Kang, X., and Guan, Q. L. (2011). Analysis of thermohaline and current distribution characteristics of Zhejiang and Fujian waters in summer. *Acta Oceanol. Sin.* 30, 71–83. doi: 10.1007/s13131-011-0149-9

Gan, J. P., Liu, Z. Q., and Liang, L. L. (2016). Numerical modeling of intrinsically and extrinsically forced seasonal circulation in the China seas: a kinematic study. *J. Geophys. Res. Oceans* 121, 4697–4715. doi: 10.1002/2016JC011800

Gao, L., Li, D., and Zhang, Y. (2012). Nutrients and particulate organic matter discharged by the Changjiang (Yangtze river): seasonal variations and temporal trends. *J. Geophys. Res* 117:G04001. doi: 10.1029/2012JG001952

Gao, L., Li, D. J., and Ding, P. X. (2008). Nutrient budgets averaged over tidal cycles off the Changjiang (Yangtze river) estuary. *Estuar. Coast. Shelf Sci.* 77, 331–336. doi: 10.1016/j.ecss.2007.09.018

Gao, L., Li, D. J., and Ding, P. X. (2009). Quasi-simultaneous observation of currents, salinity and nutrients in the Changjiang (Yangtze river) plume on the tidal timescale. *J. Mar. Syst.* 75, 265–279. doi: 10.1016/j.jmarsys.2008.10.006

Ge, J. Z., Ding, P. X., and Chen, C. S. (2015). Low-salinity plume detachment under non-uniform summer wind off the Changjiang estuary. *Estuar. Coast. Shelf Sci.* 156, 61–70. doi: 10.1016/j.ecss.2014.10.012

Ge, J. Z., Ding, P. X., Chen, C. S., Hu, S., Fu, G., and Wu, L. Y. (2013). An integrated East China Sea-Changjiang Estuary model system with aim at resolving multi-scale regional-shelf-estuarine dynamics. *Ocean Dynamics* 63, 881–900. doi: 10.1007/s10236-013-0631-3

Guan, B. X., and Fang, G. H. (2006). Winter counter-wind currents off the southeastern China coast: a review. *J. Oceanogr.* 62, 1–24. doi: 10.1007/s10872-006-0028-8

He, L., Li, Y., Zhou, H., and Yuan, D. L. (2010). Variability of cross-shelf penetrating fronts in the East China sea. *Deep Sea Res. Part II Top. Stud. Oceanogr.* 57, 1820–1826. doi: 10.1016/j.dsr2.2010.04.008

Hong, J. S., Moon, J. H., Lee, J. H., and Pang, I. C. (2016). Modeling the largest inflow of Changjiang freshwater into the Yellow sea in 2012 with particle-tracking experiment. *Ocean Sci. J.* 51, 549–562. doi: 10.1007/s12601-016-0057-1

Hu, D. X. (1994). "Some striking features of circulation in Huanghai sea and East China sea," in *Oceanology of China Seas,* eds Z. Di, L. Yuan-Bo, and Z. Cheng-Kui (Dordrecht: Springer Netherlands), 27–38.

Hu, J., and Wang, X. H. (2016). Progress on upwelling studies in the China seas. *Rev. Geophys.* 54, 653–673. doi: 10.1002/2015RG000505

Hu, J. Y., Kawamura, H., Li, C. Y., Hong, H. S., and Jiang, Y. W. (2010). Review on current and seawater volume transport through the taiwan strait. *J. Oceanogr.* 66, 591–610. doi: 10.1007/s10872-010-0049-1

Huang, D. J., Zeng, D. Y., Ni, X. B., Zhang, T., Xuan, J. L., Zhou, F., et al. (2016). Alongshore and cross-shore circulations and their response to winter monsoon in the western East China sea. *Deep Sea Res. Part II Top. Stud. Oceanogr.* 124, 6–18. doi: 10.1016/j.dsr2.2015.01.001

Huang, D. J., Zhang, T., and Zhou, F. (2010). Sea-surface temperature fronts in the yellow and East China seas from TRMM microwave imager data. *Deep Sea Res. Part II Top. Stud. Oceanogr.* 57, 1017–1024. doi: 10.1016/j.dsr2.2010.02.003

Huang, T.-H., Chen, C.-T. A., Lee, J., Wu, C.-R., Wang, Y.-L., Bai, Y., et al. (2019). East China Sea increasingly gains limiting nutrient P from South China Sea. *Sci. Rep.* 9:5648. doi: 10.1038/s41598-019-42020-4

Hwang, J. H., Van, S. P., Choi, B. J., Chang, Y. S., and Kim, Y. H. (2014). The physical processes in the Yellow sea. *Ocean Coast. Manag.* 102, 449–457. doi: 10.1016/j.ocecoaman.2014.03.026

Isobe, A. (2008). Recent advances in ocean-circulation research on the Yellow sea and East China sea shelves. *J. Oceanogr.* 64, 569–584. doi: 10.1007/s10872-008-0048-7

Isobe, A., Ando, M., Watanabe, T., Senjyu, T., Sugihara, S., and Manda, A. (2002). Freshwater and temperature transports through the Tsushima-Korea straits. *J. Geophys. Res. Oceans* 107, 2–1–2–20. doi: 10.1029/2000JC000702

Jing, Z. Y., Hua, Z. L., Qi, Y. Q., and Cheng, X. H. (2007). Numerical study on the coastal upwelling and its seasonal variation in the East China sea. *J. Coast. Res.* 50, 555–563.

Kim, H. C., Yamaguchi, H., Yoo, S., Zhu, J., Okamura, K., Kiyomoto, Y., et al. (2009). Distribution of Changjiang diluted water detected by satellite chlorophyll-a and its interannual variation during 1998-2007. *J. Oceanogr.* 65, 129–135. doi: 10.1007/s10872-009-0013-0

Kim, S. B., Lee, J. H., De Matthaeis, P., Yueh, S., Hong, C. S., Lee, J. H., et al. (2014). Sea surface salinity variability in the East China sea

observed by the aquarius instrument. *J. Geophys. Res. Oceans* 119, 7016–7028. doi: 10.1002/2014JC009983

Lee, H. J., and Chao, S. Y. (2003). A climatological description of circulation in and around the East China sea. *Deep Sea Res. Part II Top. Stud. Oceanogr.* 50, 1065–1084. doi: 10.1016/S0967-0645(03)00010-9

Lee, J. H., Moon, I. J., Moon, J. H., Kim, S. H., Jeong, Y. Y., and Koo, J. H. (2017). Impact of typhoons on the Changjiang plume extension in the Yellow and East China seas. *J. Geophy. Res. Oceans* 122, 4962–4973. doi: 10.1002/2017JC012754

Li, G. X., Qiao, L. L., Dong, P., Ma, Y. Y., Xu, J. S., Liu, S. D., et al. (2016). Hydrodynamic condition and suspended sediment diffusion in the Yellow sea and East China sea. *J. Geophys. Res. Oceans* 121, 6204–6222. doi: 10.1002/2015JC011442

Li, H. M., Tang, H. J., Shi, X. Y., Zhang, C. S., and Wang, X. L. (2014a). Increased nutrient loads from the Changjiang (Yangtze) river have led to increased harmful algal blooms. *Harmful Algae* 39, 92–101. doi: 10.1016/j.hal.2014.07.002

Li, L., Zhu, J. R., and Wu, H. (2012). Impacts of wind stress on saltwater intrusion in the Yangtze estuary. *Sci. China Earth Sci.* 55, 1178–1192. doi: 10.1007/s11430-011-4311-1

Li, L., Zhu, J. R., Wu, H., and Guo, Z. G. (2014). Lateral saltwater intrusion in the north channel of the Changjiang estuary. *Estuar. Coasts* 37, 36–55. doi: 10.1007/s12237-013-9669-1

Li, L., Zhu, J. R., Wu, H., and Wang, B. (2010). A numerical study on water diversion ratio of the Changjiang (Yangtze) estuary in dry season. *Chin. J. Oceanol. Limnol.* 28, 700–712. doi: 10.1007/s00343-010-9114-2

Li, L. J., Zhu, J. R., Chant, R. J., Wang, C. N., and Pareja-Roman, L. F. (2020). Effect of dikes on saltwater intrusion under various wind conditions in the Changjiang estuary. *J. Geophys. Res. Oceans* 125:e2019JC015685. doi: 10.1029/2019JC015685

Li, M., and Rong, Z. R. (2012). Effects of tides on freshwater and volume transports in the Changjiang river plume. *J. Geophys. Res. Oceans* 117:C06027. doi: 10.1029/2011JC007716

Li, P., Wang, S. J., Li, Y. G., and Qin, W. H. (2014b). Current conditions in summer in the Zhejiang offshore. *J. Mar. Sic.* 32, 16–25. doi: 10.3969/j.issn.1001-909X.2014.03.003

Li, Y. H., Qiao, L., Wang, A. J., Zhang, Y., Fang, J. Y., and Chen, J. (2013). Seasonal variation of water column structure and sediment transport in a mud depo-center off the Zhejiang-Fujian coast in China. *Ocean Dyn.* 63, 679–690. doi: 10.1007/s10236-013-0620-6

Li, Z. Y., and Huang, D. J. (2019). Sea surface height and current responses to synoptic winter wind in the Bohai, Yellow, and East China seas: two leading coastal trapped waves. *J. Geophys. Res. Oceans* 124, 2289–2312. doi: 10.1029/2018JC014120

Liang, X. S., Huang, M., Wu, H., and Wang, Y. (2018). "The Yellow sea surface cold patches in warm seasons," in *Coastal Environment, Disaster, and Infrastructure - A Case Study of China's Coastline*, eds X. S. Liang and Y. Zhang (London: IntechOpen). doi: 10.5772/intechopen.80732

Liblik, T., Wu, Y. J., Fan, D. D., and Shang, D. H. (2020). Wind-driven stratification patterns and dissolved oxygen depletion off the Changjiang (Yangtze) estuary. *Biogeosciences* 17, 2875–2895. doi: 10.5194/bg-17-2875-2020

Lie, H. J., and Cho, C. H. (1994). On the origin of the tsushima warm current. *J. Geophys. Res Oceans* 99, 25081–25091. doi: 10.1029/94JC02425

Lie, H. J., and Cho, C. H. (2016). Seasonal circulation patterns of the Yellow and East China seas derived from satellite-tracked drifter trajectories and hydrographic observations. *Prog. Oceanogr.* 146, 121–141. doi: 10.1016/j.pocean.2016.06.004

Lie, H. J., Cho, C. H., Lee, J. H., and Lee, S. (2003). Structure and eastward extension of the Changjiang River plume in the East China sea. *J. Geophys. Res. Oceans* 108:3077. doi: 10.1029/2001JC001194

Lin, X. P., and Yang, J. Y. (2011). An asymmetric upwind flow, Yellow Sea Warm Current: 2. Arrested topographic waves in response to the northwesterly wind. *J. Geophys. Res. Oceans* 116:C04027. doi: 10.1029/2010JC006514

Lin, X. P., Yang, J. Y., Guo, J. S., Zhang, Z. X., Yin, Y. Q., Song, X. Z., et al. (2011). An asymmetric upwind flow, Yellow sea warm current: 1. New observations in the western Yellow sea. *J. Geophys. Res. Oceans* 116:C04026. doi: 10.1029/2010JC006513

Liu, X., Beusen, A. H. W., Beek, L. P. H. V., Mogollón, J. M., Ran, X., and Bouwman, A. F. (2018). Exploring spatiotemporal changes of the Yangtze river (Changjiang) nitrogen and phosphorus sources, retention and export to the East China sea and Yellow sea. *Water Res.* 142, 246–255. doi: 10.1016/j.watres.2018.06.006

Liu, X. B., and Su, J. L. (1991). Numerical study of coastal upwelling and jet along Zhejiang. *Acta Oceanol. Sin.* 13, 305–314.

Liu, Z. Q., and Gan, J. P. (2014). Modeling study of variable upwelling circulation in the east China sea: response to a coastal promontory. *J. Phys. Oceanogr.* 44, 1078–1094. doi: 10.1175/JPO-D-13-0170.1

Liu, Z. Q., and Gan, J. P. (2015). Upwelling induced by the frictional stress curl and vertical squeezing of the vortex tube over a submerged valley in the East China sea. *J. Geophys. Res. Oceans* 120, 2571–2587. doi: 10.1002/2015JC010715

Liu, Z. Q., and Gan, J. P. (2016). Open boundary conditions for tidally and subtidally forced circulation in a limited-area coastal model using the regional ocean modeling system (ROMS). *J. Geophys. Res. Oceans* 121, 6184–6203. doi: 10.1002/2016JC011975

Liu, Z. Q., Gan, J. P., Hu, J. Y., Wu, H., Cai, Z. Y., and Deng, Y. F. (2021). Progress of studies on circulation dynamics in the East China sea: the kuroshio exchanges with the shelf currents. *Front. Mar. Sci.* doi: 10.3389/fmars.2021.620910

Lu, H. F., Gu, F. F., Qi, D. M., Chen, X. E., and Wang, Y. Y. (2019). Investigating near-bottom hydrodynamic processes in the yangtze river estuary using *in situ* measurements. *J. Coast. Res.* 35, 805–813. doi: 10.2112/JCOASTRES-D-18-00131.1

Lu, L. F., and Shi, J. Z. (2007). The dispersal processes within the tide-modulated Changjiang river plume, China. *Int. J. Num. Methods Fluids* 55, 1143–1155. doi: 10.1002/fld.1520

Lu, S., Tong, C. F., Lee, D. Y., Zheng, J. H., Shen, J., Zhang, W., et al. (2015). Propagation of tidal waves up in Yangtze estuary during the dry season. *J. Geophys. Res. Oceans* 120, 6445–6473. doi: 10.1002/2014J. C.010414

Lü, X., Qiao, F., Xia, C., Wang, G., and Yuan, Y. (2010). Upwelling and surface cold patches in the Yellow sea in summer: effects of tidal mixing on the vertical circulation. *Cont. Shelf Res.* 30, 620–632. doi: 10.1016/j.csr.2009.09.002

Lü, X. G., Qiao, F., Xia, C., Zhu, J., and Yuan, Y. (2006). Upwelling off Yangtze river estuary in summer. *J. Geophys. Res.* 111:C11S08. doi: 10.1029/2005JC003250

Luan, H. L., Ding, P. X., Wang, Z. B., Ge, J. Z., and Yang, S. L. (2016). Decadal morphological evolution of the Yangtze estuary in response to river input changes and estuarine engineering projects. *Geomorphology* 265, 12–23. doi: 10.1016/j.geomorph.2016.04.022

Lui, H.-K., Chen, C.-T. A., Lee, J., Bai, Y., and He, X. (2014). Looming hypoxia on outer shelves caused by reduced ventilation in the open oceans: case study of the East China sea. *Estuar. Coast. Shelf Sic.* 151, 355–360. doi: 10.1016/j.ecss.2014.08.010

Lui, H.-K., Chen, C.-T. A., Lee, J., Wang, S.-L., Gong, G.-C., Bai, Y., et al. (2015). Acidifying intermediate water accelerates the acidification of seawater on shelves: an example of the East China sea. *Cont. Shelf Res.* 111, 223–233. doi: 10.1016/j.csr.2015.08.014

Luo, X., Wei, H., Fan, R., Liu, Z., Zhao, L., and Lu, Y. (2018). On influencing factors of hypoxia in waters adjacent to the Changjiang estuary. *Cont. Shelf Res.* 152, 1–13. doi: 10.1016/j.csr.2017.10.004

Lyu, H. H., and Zhu, J. R. (2018). Impact of the bottom drag coefficient on saltwater intrusion in the extremely shallow estuary. *J. Hydrol.* 557, 838–850. doi: 10.1016/j.jhydrol.2018.01.010

Ma, G. F., Shi, F. Y., Liu, S. G., and Qi, D. M. (2011). Hydrodynamic modeling of Changjiang estuary: model skill assessment and large-scale structure impacts. *Appl. Ocean Res.* 33, 69–78. doi: 10.1016/j.apor.2010.10.004

Matsuno, T. (2020). "The changing east China sea—a physical view," in *Changing Asia-Pacific Marginal Seas,* eds C. T.A. Chen and X. Guo. (Singapore: Springer Singapore), 139–153.

Mei, X. F., Dai, Z. J., Van Gelder, P. H.,a,J. M., and Gao, J.J. (2015). Linking three gorges dam and downstream hydrological regimes along the Yangtze river, China. *Earth and Space Sci.* 2, 94–106. doi: 10.1002/2014EA000052

Meng, Q. J., Li, P. L., Zhai, F. G., and Gu, Y. Z. (2020). The vertical mixing induced by winds and tides over the Yellow sea in summer: a numerical study in 2012. *Ocean Dyn.* 70, 847–861. doi: 10.1007/s10236-020-01368-2

Moon, J. H., Hirose, N., Pang, I. C., and Hyun, K. H. (2012). Modeling offshore freshwater dispersal from the Changjiang river and controlling factors during summer. *Terr. Atmos. Ocean. Sci.* 23, 247–260. doi: 10.3319/TAO.2012.01.10.01(Oc)

Moon, J. H., Hirose, N., Yoon, J. H., and Pang, I. C. (2010). Offshore detachment process of the low-salinity water around Changjiang bank in the East China sea. *J. Phys. Oceanogr.* 40, 1035–1053. doi: 10.1175/2010JPO4167.1

Moon, J. H., Kim, T., Son, Y. B., Hong, J. S., Lee, J. H., Chang, P. H., et al. (2019). Contribution of low-salinity water to sea surface warming of the East China sea in the summer of 2016. *Prog. Oceanogr.* 175, 68–80. doi: 10.1016/j.pocean.2019.03.012

Ni, X., Huang, D., Zeng, D., Zhang, T., Li, H., and Chen, J. (2016). The impact of wind mixing on the variation of bottom dissolved oxygen off the Changjiang estuary during summer. *J. Mar. Syst.* 154, 122–130. doi: 10.1016/j.jmarsys.2014.11.010

Oh, K. H., Lee, J. H., Lee, S., and Pang, I. C. (2014). Intrusion of low-salinity water into the Yellow sea interior in 2012. *Ocean Sci. J.* 49, 343–356. doi: 10.1007/s12601-014-0032-7

Pu, X., Shi, J. Z., and Hu, G. (2017). The effect of stratification on the vertical structure of the tidal ellipse in the Changjiang river estuary, China. *J. Hydro Environ. Res.* 15, 75–94. doi: 10.1016/j.jher.2017.03.004

Pu, X., Shi, J. Z., and Hu, G. D. (2016). Analyses of intermittent mixing and stratification within the north passage of the Changjiang (Yangtze) river estuary, China: a three-dimensional model study. *J. Mar. Syst.* 158, 140–164. doi: 10.1016/j.jmarsys.2016.02.004

Pu, X., Shi, J. Z., Hu, G. D., and Xiong, L. B. (2015). Circulation and mixing along the north passage in the Changjiang river estuary, China. *J. Mar. Syst.* 148, 213–235. doi: 10.1016/j.jmarsys.2015.03.009

Qian, W., Dai, M. H., Xu, M., Kao, S. J., Du, C. J., Liu, J. W., et al. (2017). Non-local drivers of the summer hypoxia in the East China sea off the Changjiang estuary. *Estuar. Coast. Shelf Sci.* 198, 393–399. doi: 10.1016/j.ecss.2016.08.032

Qiao, F. L., Wang, G. S., Lu, X. G., and Dai, D. J. (2011). Drift characteristics of green macroalgae in the Yellow sea in 2008 and 2010. *Chin. Sci. Bull.* 56, 2236–2242. doi: 10.1007/s11434-011-4551-7

Qiao, F. L., Yang, Y. Z., Lv, X. G., Xia, C. S., Chen, X. Y., Wang, B. D., et al. (2006). Coastal upwelling in the East China sea in winter. *J. Geophys. Res. Oceans* 111:C11S06. doi: 10.1029/2005JC003264

Qiu, C., Zhu, J., and Gu, Y. (2012). Impact of seasonal tide variation on saltwater intrusion in the Changjiang river estuary. *Chin. J. Oceanol. Limnol.* 30, 342–351. doi: 10.1007/s00343-012-1115-x

Rabouille, C., Conley, D. J., Dai, M. H., Cai, W. J., Chen, C. T. A., Lansard, B., et al. (2008). Comparison of hypoxia among four river-dominated ocean margins: the Changjiang (Yangtze), Mississippi, Pearl, and Rhone rivers. *Cont. Shelf Res.* 28, 1527–1537. doi: 10.1016/j.csr.2008.01.020

Rong, Z., and Li, M. (2012). Tidal effects on the bulge region of Changjiang river plume. *Estuar. Coast. Shelf Sic.* 97, 149–160. doi: 10.1016/j.ecss.2011.11.035

Senjyu, T., Enomoto, H., Matsuno, T., and Matsui, S. (2006). Interannual salinity variations in the tsushima strait and its relation to the Changjiang discharge. *J. Oceanogr.* 62, 681–692. doi: 10.1007/s10872-006-0086-y

Shan, F., Qiao, F. L., and Xia, C. S. (2009). A numerical study of summertime expansion pattern of Changjiang (Yangtze) river diluted water. *Acta Oceanol. Sin.* 28, 11–16.

Shen, J. Q., Qiu, Y., Guo, X. G., Pan, A. J., and Zhou, X. W. (2017). The spatio-temporal variation of wintertime subtidal currents in the western Taiwan strait. *Acta Oceanol. Sin.* 36, 4–13. doi: 10.1007/s13131-017-1120-1

Shi, F., Luo, Y. Y., and Rong, Z. R. (2016). A numerical study of the summer circulation in the southwestern Yellow sea. *Acta Oceanol. Sin.* 35, 1–8. doi: 10.1007/s13131-016-0943-5

Shi, J. Z., and Lu, L. F. (2011). A short note on the dispersion, mixing, stratification and circulation within the plume of the partially-mixed Changjiang river estuary, China. *J. Hydro Environ. Res.* 5, 111–126. doi: 10.1016/j.jher.2010.06.002

Shi, W., and Wang, M. H. (2012). Satellite views of the Bohai sea, Yellow sea, and East China sea. *Prog. Oceanogr.* 104, 30–45. doi: 10.1016/j.pocean.2012.05.001

Song, X. Z., Huang, R. X., Wu, D. X., Qiao, F. L., and Wang, G. S. (2019). Geostrophic spirals generated by the horizontal diffusion of vortex stretching in the Yellow sea. *Adv. Atmosph. Sci.* 36, 219–230. doi: 10.1007/s00376-018-8091-9

Sun, J., Yang, D., Yin, B., Chen, H., and Feng, X. (2018). Onshore warm tongue and offshore cold tongue in the western Yellow sea in winter: the evidence. *J. Oceanol. Limnol.* 36, 1475–1483. doi: 10.1007/s00343-018-7021-0

Tong, Y., Bu, X., Chen, J., Zhou, F., Chen, L., Liu, M., et al. (2017). Estimation of nutrient discharge from the Yangtze river to the East China sea and the identification of nutrient sources. *J. Hazard. Mater.* 321, 728–736. doi: 10.1016/j.jhazmat.2016.09.011

Wan, Y., Gu, F., Wu, H., and Roelvink, D. (2014). Hydrodynamic evolutions at the Yangtze estuary from 1998 to 2009. *Appl. Ocean Res.* 47, 291–302. doi: 10.1016/j.apor.2014.06.009

Wan, Y., and Zhao, D. (2017). Observation of saltwater intrusion and ETM dynamics in a stably stratified estuary: the Yangtze estuary, China. *Environ. Monit. Assess.* 189:89. doi: 10.1007/s10661-017-5797-6

Wang, B., Chen, J., Jin, H., Li, H., Huang, D., and Cai, W.-J. (2017a). Diatom bloom-derived bottom water hypoxia off the Changjiang estuary, with and without typhoon influence. *Limnol. Oceanogr.* 62, 1552–1569. doi: 10.1002/lno.10517

Wang, B., Hirose, N., Moon, J. H., and Yuan, D. L. (2013a). Difference between the Lagrangian trajectories and eulerian residual velocity fields in the southwestern Yellow sea. *Ocean Dynam.* 63, 565–576. doi: 10.1007/s10236-013-0607-3

Wang, B., Hirose, N., Yuan, D. L., Moon, J. H., and Pan, X. S. (2017b). Effects of tides on the cross-isobath movement of the low-salinity plume in the western Yellow and East China seas in winter. *Cont. Shelf Res.* 143, 228–239. doi: 10.1016/j.csr.2016.06.011

Wang, B., Li, Y., and Yuan, D. L. (2013b). Effects of topography on the sub-tidal circulation in the southwestern Huanghai sea (Yellow sea) in summer. *Acta Oceanol. Sin.* 32, 1–9. doi: 10.1007/s13131-013-0282-8

Wang, B., Wei, Q., Chen, J., and Xie, L. (2012). Annual cycle of hypoxia off the Changjiang (Yangtze river) estuary. *Mar. Environ. Res.* 77, 1–5. doi: 10.1016/j.marenvres.2011.12.007

Wang, B., Xin, M., Wei, Q., and Xie, L. (2018). A historical overview of coastal eutrophication in the China seas. *Mar. Pollut. Bull.* 136, 394–400. doi: 10.1016/j.marpolbul.2018.09.044

Wang, H., Dai, M., Liu, J., Kao, S. J., Zhang, C., Cai, W. J., et al. (2016). Eutrophication-driven hypoxia in the East China sea off the Changjiang estuary. *Environ. Sci. Technol.* 50, 2255–2263. doi: 10.1021/acs.est.5b06211

Wang, H., Sun, F. B., and Liu, W. B. (2020). Characteristics of streamflow in the main stream of Changjiang river and the impact of the three gorges dam. *Catena* 189:104498. doi: 10.1016/j.catena.2020.104498

Wang, J., Yan, W., Chen, N., Li, X., and Liu, L. (2015). Modeled long-term changes of DIN:DIP ratio in the Changjiang river in relation to Chl-α and DO concentrations in adjacent estuary. *Estuar. Coast. Shelf Sic.* 166, 153–160. doi: 10.1016/j.ecss.2014.11.028

Wang, J. F., Yu, F., Ren, Q., Si, G. C., and Wei, C. J. (2019a). The observed variations of the north intrusion of the bottom Taiwan warm current inshore branch and its response to wind. *Reg. Stud. Mar. Sci.* 30:17. doi: 10.1016/j.rsma.2019.100690

Wang, Y., Shen, J., He, Q., Zhu, L., and Zhang, D. (2015). Seasonal variations of transport time of freshwater exchanges between Changjiang estuary and its adjacent regions. *Estuar. Coast. Shelf Sci.* 157, 109–119. doi: 10.1016/j.ecss.2015.03.008

Wang, Y., Shen, J. A., and He, Q. (2010). A numerical model study of the transport timescale and change of estuarine circulation due to waterway constructions in the Changjiang estuary, China. *J. Mar. Syst.* 82, 154–170. doi: 10.1016/j.jmarsys.2010.04.012

Wang, Y., Wu, H., Lin, J., Zhu, J., Zhang, W., and Li, C. (2019c). Phytoplankton blooms off a high turbidity estuary: a case study in the Changjiang river estuary. *J. Geophys. Res. Oceans* 124, 8036–8059. doi: 10.1029/2019JC015343

Wang, Y. H., Wu, H., Gao, L., Shen, F., and Liang, X. S. (2019b). Spatial distribution and physical controls of the spring algal blooming off the Changjiang river estuary. *Estuar. Coasts* 42, 1066–1083. doi: 10.1007/s12237-019-00545-x

Wei, H., He, Y. C., Li, Q. J., Liu, Z. Y., and Wang, H. T. (2007). Summer hypoxia adjacent to the Changjiang estuary. *J. Mar. Syst.* 67, 292–303. doi: 10.1016/j.jmarsys.2006.04.014

Wei, Q., Wang, B., Yu, Z., Chen, J., and Xue, L. (2017b). Mechanisms leading to the frequent occurrences of hypoxia and a preliminary analysis of the associated acidification off the Changjiang estuary in summer. *Sci. China Earth Sci.* 60, 360–381. doi: 10.1007/s11430-015-5542-8

Wei, Q., Wang, B., Zhang, X., Ran, X., Fu, M., Sun, X., et al. (2020). Contribution of the offshore detached Changjiang (Yangtze river) diluted water to the formation of hypoxia in summer. *Sci. Total Environ.* doi: 10.1016/j.scitotenv.2020.142838

Wei, Q. S., Yu, Z. G., Wang, B. D., Fu, M. Z., Xia, C. S., Liu, L., et al. (2016). Coupling of the spatial-temporal distributions of nutrients and physical conditions in the southern Yellow sea. *J. Mar. Syst.* 156, 30–45. doi: 10.1016/j.jmarsys.2015.12.001

Wei, Q. S., Yu, Z. G., Wang, B. D., Wu, H., Sun, J. C., Zhang, X. L., et al. (2017a). Offshore detachment of the Changjiang River plume and its ecological impacts in summer. *J. Oceanogr.* 73, 277–294. doi: 10.1007/s10872-016-0402-0

Wei, Q. S., Yu, Z. G., Xia, C. S., Zang, J. Y., and Zhang, X. L. (2011). A preliminary analysis on the dynamic characteristics of the hypoxic zone adjacent to the Changjiang estuary in summer. *Acta Oceanol. Sin.* 33, 100–109.

Wu, H. (2015). Cross-shelf penetrating fronts: a response of buoyant coastal water to ambient pycnocline undulation. *J. Geophys. Res. Oceans* 120, 5101–5119. doi: 10.1002/2014JC010686

Wu, H., Deng, B., Yuan, R., Hu, J., Gu, J. H., Shen, F., Zhu, J. R., and Zhang, J. (2013). Detiding measurement on transport of the changjiang-derived buoyant coastal current. *J. Phys. Oceanogr.* 43. 2388–2399. doi: 10.1175/Jpo-D-12-0158.1

Wu, H., Gu, J. H., and Zhu, P. (2018a). Winter counter-wind transport in the inner southwestern yellow sea. *J. Geophys. Res. Oceans* 123, 411–436. doi: 10.1002/2017JC013403

Wu, H., Shen, J., Zhu, J. R., Zhang, J., and Li, L. (2014). Characteristics of the Changjiang plume and its extension along the Jiangsu Coast. *Conti. Shelf Res.* 76, 108–123. doi: 10.1016/j.csr.2014.01.007

Wu, H., Wu, T., Shen, J., and Zhu, J. (2018b). "Dynamics of the Changjiang river plume," in *Coastal Environment, Disaster, and Infrastructure - A Case Study of China's Coastline*, eds X. S. Liang and Y. Zhang (London: IntechOpen). doi: 10.5772/intechopen.80734

Wu, H., Wu, T. N., and Bai, M. (2018c). Mega estuarine constructions modulate the Changjiang river plume extension in adjacent seas. *Estuar. Coasts* 41, 1234–1252. doi: 10.1007/s12237-017-0357-4

Wu, H., and Zhu, J. R. (2010). Advection scheme with 3rd high-order spatial interpolation at the middle temporal level and its application to saltwater intrusion in the Changjiang estuary. *Ocean Model.* 33, 33–51. doi: 10.1016/j.ocemod.2009.12.001

Wu, H., Zhu, J. R., Chen, B. R., and Chen, Y. Z. (2006). Quantitative relationship of runoff and tide to saltwater spilling over from the north branch in the Changjiang estuary: a numerical study. *Estuar. Coast. Shelf Sci.* 69, 125–132. doi: 10.1016/j.ecss.2006.04.009

Wu, H., Zhu, J. R., and Choi, B. H. (2010). Links between saltwater intrusion and subtidal circulation in the Changjiang estuary: a model-guided study. *Conti. Shelf Res.* 30, 1891–1905. doi: 10.1016/j.csr.2010.09.001

Wu, H., Zhu, J. R., Shen, J., and Wang, H. (2011). Tidal modulation on the Changjiang river plume in summer. *J. Geophys. Res. Oceans* 116:C08017. doi: 10.1029/2011JC007209

Wu, L. G., Wang, B., and Geng, S. Q. (2005). Growing typhoon influence on east Asia. *Geophys. Res. Lett.* 32:L18703. doi: 10.1029/2005GL022937

Wu, T. N., and Wu, H. (2018). Tidal mixing sustains a bottom-trapped river plume and buoyant coastal current on an energetic continental shelf. *J. Geophys. Res. Oceans* 123, 8026–8051. doi: 10.1029/2018JC014105

Wu, Y., Fan, D., Wang, D., and Yin, P. (2020). Increasing hypoxia in the Changjiang estuary during the last three decades deciphered from sedimentary redox-sensitive elements. *Mar. Geol.* 419:106044. doi: 10.1016/j.margeo.2019.106044

Xia, C. S., Qiao, F. L., Yang, Y. Z., Ma, J., and Yuan, Y. L. (2006). Three-dimensional structure of the summertime circulation in the Yellow sea from a wave-tide-circulation coupled model. *J. Geophys. Res. Oceans* 111:C11S03. doi: 10.1029/2005JC003218

Xu, Z., Ma, J., Wang, H., Hu, Y. J., Yang, G. Y., and Deng, W. (2018). River discharge and saltwater intrusion level study of Yangtze river estuary, China. *Water* 10:683. doi: 10.3390/w10060683

Xu, Z. L., Shen, X. M., and Gao, Q. (2015). "Marine biology of the Changjiang (Yangtze river) estuary and adjacent East China sea shelf," in *Ecological Continuum from the Changjiang (Yangtze River) Watersheds to the East China Sea Continental Margin,* ed J. Zhang (Cham: Springer International Publishing), 161–180.

Xuan, J. L., Huang, D. J., Pohlmann, T., Su, J., Mayer, B., Ding, R. B., et al. (2016a). Synoptic fluctuation of the taiwan warm current in winter on the East China sea shelf. *Ocean Sci.* 13, 105–122. doi: 10.5194/os-13-105-2017

Xuan, J. L., Huang, D. J., Zhou, F., Zhu, X. H., and Fan, X. P. (2012). The role of wind on the detachment of low salinity water in the Changjiang estuary in summer. *J. Geophys. Res. Oceans* 117:C10004. doi: 10.1029/2012JC008121

Xuan, J. L., Yang, Z. Q., Huang, D. J., Wang, T. P., and Zhou, F. (2016b). Tidal residual current and its role in the mean flow on the Changjiang bank. *J. Mar. Syst.* 154, 66–81. doi: 10.1016/j.jmarsys.2015.04.005

Xue, P. F., Chen, C. S., Ding, P. X., Beardsley, R. C., Lin, H. C., Ge, J. Z., et al. (2009). Saltwater intrusion into the Changjiang river: a model-guided mechanism study. *J. Geophys. Res. Oceans* 114:C02006. doi: 10.1029/2008JC004831

Yan, X. H., Jo, Y. H., Jiang, L., Wan, Z. W., Liu, W. T., Li, Y., et al. (2008). Impact of the three gorges dam water storage on the Yangtze river outflow into the East China sea. *Geophys. Res. Lett.* 35:L05610. doi: 10.1029/2007GL032908

Yang, D., Yin, B., Chai, F., Feng, X., Xue, H., Gao, G., et al. (2018). The onshore intrusion of Kuroshio subsurface water from February to July and a mechanism for the intrusion variation. *Prog. Oceanog.* 167, 97–115. doi: 10.1016/j.pocean.2018.08.004

Yang, D. Z., Yin, B. S., Sun, J. C., and Zhang, Y. (2013). Numerical study on the origins and the forcing mechanism of the phosphate in upwelling areas off the coast of Zhejiang province, China in summer. *J. Mar. Syst.* 123, 1–18. doi: 10.1016/j.jmarsys.2013.04.002

Yang, S. L., Xu, K. H., Milliman, J. D., Yang, H. F., and Wu, C. S. (2015). Decline of Yangtze River water and sediment discharge: impact from natural and anthropogenic changes. *Sci. Rep.* 5, 12581–12581. doi: 10.1038/srep12581

Yang, Z., Wang, H., Saito, Y., Milliman, J. D., Xu, K., Qiao, S., et al. (2006). Dam impacts on the Changjiang (Yangtze) river sediment discharge to the sea: the past 55 years and after the three gorges dam. *Water Res. Res.* 42:W04407. doi: 10.1029/2005WR003970

Yu, R.-C., Lü, S.-H., and Liang, Y.-B. (2018). "Harmful algal blooms in the coastal waters of China," in *Global Ecology and Oceanography of Harmful Algal Blooms,* eds P. M. Glibert, E. Berdalet, M. A. Burford, G. C. Pitcher & M. Zhou (Cham: Springer International Publishing), 309–316.

Yu, X., Zhang, W., and Hoitink, A. J. F. (2020a). Impact of river discharge seasonality change on tidal duration asymmetry in the Yangtze river estuary. *Sci. Rep.* 10:6304. doi: 10.1038/s41598-020-62432-x

Yu, Y., Chen, S. H., Tseng, Y. H., Guo, X. Y., Shi, J., Liu, G. L., et al. (2020b). Importance of diurnal forcing on the summer salinity variability in the East China sea. *J. Phys. Oceanogr.* 50, 633–653. doi: 10.1175/JPO-D-19-0200.1

Yuan, D. L., Li, Y., He, L., Zhou, H., Li, R. X., Wang, F., et al. (2010). An observation of the three-dimensional structure of a cross-shelf penetrating front off the Changjiang mouth. *Deep Sea Res. Part II Top. Stud. Oceanogr.* 57, 1827–1834. doi: 10.1016/j.dsr2.2010.04.009

Yuan, D. L., Li, Y., Wang, B., He, L., and Hirose, N. (2017). Coastal circulation in the southwestern Yellow sea in the summers of 2008 and 2009. *Conti. Shelf Res.* 143, 101–117. doi: 10.1016/j.csr.2017.01.022

Yuan, D. L., Qiao, F. L., and Su, J. (2005). Cross-shelf penetrating fronts off the southeast coast of China observed by MODIS. *Geophys. Res. Lett.* 32:L19603. doi: 10.1029/2005GL023815

Yuan, D. L., Zhu, J. R., Li, C. Y., and Hu, D. X. (2008). Cross-shelf circulation in the Yellow and East China seas indicated by MODIS satellite observations. *J. Mar. Syst.* 70, 134–149. doi: 10.1016/j.jmarsys.2007.04.002

Yuan, R., Wu, H., Zhu, J. R., and Li, L. (2016). The response time of the Changjiang plume to river discharge in summer. *J. Mar. Syst.* 154, 82–92. doi: 10.1016/j.jmarsys.2015.04.001

Zhai, W.-D., Zheng, L.-W., Li, C.-L., Xiong, T.-Q., and Wang, S.-Y. (2020). "Changing nutrients, dissolved oxygen and carbonate system in the bohai and yellow seas, China," in *Changing Asia-Pacific Marginal Seas,* eds C. T.A. Chen & X. Guo (Singapore: Springer Singapore), 121–137.

Zhang, E. F., Gao, S., Savenije, H. H. G., Si, C. Y., and Cao, S. (2019a). Saline water intrusion in relation to strong winds during winter cold outbreaks: north branch of the Yangtze estuary. *J. Hydrol.* 574, 1099–1109. doi: 10.1016/j.jhydrol.2019.04.096

Zhang, F. Y., Lin, B. L., and Sun, J. (2019b). Current reversals in a large tidal river. *Estuar. Coast. Shelf Sci.* 223, 74–84. doi: 10.1016/j.ecss.2019.04.017

Zhang, F. Y., Sun, J., Lin, B. L., and Huang, G. X. (2018a). Seasonal hydrodynamic interactions between tidal waves and river flows in the Yangtze estuary. *J. Mar. Syst.* 186, 17–28. doi: 10.1016/j.jmarsys.2018.05.005

Zhang, W., Feng, H. C., Hoitink, A. J. F., Zhu, Y. L., Gong, F., and Zheng, J. H. (2017). Tidal impacts on the subtidal flow division at the main

bifurcation in the Yangtze river delta. *Estuar. Coast. Shelf Sci.* 196, 301–314. doi: 10.1016/j.ecss.2017.07.008

Zhang, W., Wu, H., Hetland, R. D., and Zhu, Z. (2019c). On mechanisms controlling the seasonal hypoxia hot spots off the changjiang river estuary. *J. Geophys. Res. Oceans* 124, 8683–8700. doi: 10.1029/2019JC015322

Zhang, W. X., Wu, H., and Zhu, Z. Y. (2018b). Transient hypoxia extent off changjiang river estuary due to mobile changjiang river plume. *J. Geophys. Res. Oceans* 123, 9196–9211. doi: 10.1029/2018JC014596

Zhang, Y., Fan, D. D., and Qin, R. F. (2020). Estuary-shelf interactions off the Changjiang delta during a dry-wet seasonal transition. *Mar. Geol.* 426:13. doi: 10.1016/j.margeo.2020.106211

Zhang, Z. W., Wu, H., Yin, X. Q., and Qiao, F. L. (2018c). Dynamical response of Changjiang river plume to a severe typhoon with the surface wave-induced mixing. *J. Geophys. Res. Oceans* 123, 9369–9388. doi: 10.1029/2018JC014266

Zheng, J., Gao, S., Liu, G., Wang, H., and Zhu, X. (2016). Modeling the impact of river discharge and wind on the hypoxia off Yangtze estuary. *Nat. Hazards Earth Syst. Sci.* 16, 2559–2576. doi: 10.5194/nhess-16-2559-2016

Zhou, F., Chai, F., Huang, D. J., Xue, H. J., Chen, J. F., Xiu, P., et al. (2017). Investigation of hypoxia off the Changjiang estuary using a coupled model of ROMS-CoSiNE. *Progr. Oceanogr.* 159, 237–254. doi: 10.1016/j.pocean.2017.10.008

Zhu, J., Wu, H., and Li, L. (2015). "Hydrodynamics of the Changjiang estuary and adjacent seas," in *Ecological Continuum from the Changjiang (Yangtze River) Watersheds to the East China Sea Continental Margin*, ed. J. Zhang (Cham: Springer International Publishing), 19–45.

Zhu, J., Wu, H., Li, L., and Qiu, C. (2019). "Changjiang estuary," in *Sediment Dynamics of Chinese Muddy Coasts and Estuaries,* ed X. H. Wang (Academic Press), 51–75.

Zhu, J. R. (2003). Dynamic mechanism of the upwelling on the west side of the submerged river valley off the Changjiang mouth in summertime. *Chin. Sci. Bull.* 48, 2754–2758. doi: 10.1007/BF02901770

Zhu, J. R., Wu, H., Li, L., and Qiu, C. (2018a). "Saltwater Intrusion in the Changjiang Estuary," in *Coastal Environment, Disaster, and Infrastructure, A Case Study of China's Coastline,* eds X. San Liang and Y. Zhang (London: IntechOpen). doi: 10.5772/intechopen.80903

Zhu, J. R., Zhu, Z. Y., Lin, J., Wu, H., and Zhang, J. (2016a). Distribution of hypoxia and pycnocline off the Changjiang estuary, China. *J. Mar. Syst.* 154, 28–40. doi: 10.1016/j.jmarsys.2015.05.002

Zhu, L., He, Q., and Shen, J. (2018b). Modeling lateral circulation and its influence on the along-channel flow in a branched estuary. *Ocean Dyn.* 68, 177–191. doi: 10.1007/s10236-017-1114-8

Zhu, P., and Wu, H. (2018). Origins and transports of the low-salinity coastal water in the southwestern Yellow sea. *Acta Oceanol. Sin.* 37, 1–11. doi: 10.1007/s13131-018-1200-x

Zhu, S. X., He, Z. Y., Zhang, W. J., Xie, S. J., and Xu, Y. C. (2018c). Characteristics analysis for cold water patches off the Jiangsu coast in the last 35 a. *Acta Oceanol. Sin.* 37, 19–25. doi: 10.1007/s13131-018-1293-2

Zhu, Z.-Y., Hu, J., Song, G.-D., Wu, Y., Zhang, J., and Liu, S.-M. (2016b). Phytoplankton-driven dark plankton respiration in the hypoxic zone off the Changjiang estuary, revealed by *in vitro* incubations. *J. Mar. Syst.* 154, 50–56. doi: 10.1016/j.jmarsys.2015.04.009

Zhu, Z.-Y., Wu, H., Liu, S.-M., Wu, Y., Huang, D.-J., Zhang, J., et al. (2017). Hypoxia off the Changjiang (Yangtze River) estuary and in the adjacent East China sea: quantitative approaches to estimating the tidal impact and nutrient regeneration. *Mar. Pollut. Bull.* 125, 103–114. doi: 10.1016/j.marpolbul.2017.07.029

Zhu, Z. Y., Zhang, J., Wu, Y., Zhang, Y. Y., Lin, J., and Liu, S. M. (2011). Hypoxia off the Changjiang (Yangtze river) estuary: oxygen depletion and organic matter decomposition. *Mar. Chem.* 125, 108–116. doi: 10.1016/j.marchem.2011.03.005

Zuo, J. L., Song, J. M., Yuan, H. M., Li, X. G., Li, N., and Duan, L. Q. (2019). Impact of kuroshio on the dissolved oxygen in the East China sea region. *J. Oceanol. Limnol.* 37, 513–524. doi: 10.1007/s00343-019-7389-5

Conflict of Interest: The authors declare that the research was conducted in the absence of any commercial or financial relationships that could be construed as a potential conflict of interest.

Copyright © 2021 Liu, Gan, Wu, Hu, Cai and Deng. This is an open-access article distributed under the terms of the Creative Commons Attribution License (CC BY). The use, distribution or reproduction in other forums is permitted, provided the original author(s) and the copyright owner(s) are credited and that the original publication in this journal is cited, in accordance with accepted academic practice. No use, distribution or reproduction is permitted which does not comply with these terms.

frontiers in Marine Science

ORIGINAL RESEARCH
published: 13 August 2020
doi: 10.3389/fmars.2020.00679

Temporal and Spatial Variability of the CO_2 System in a Riverine Influenced Area of the Mediterranean Sea, the Northern Adriatic

Lidia Urbini[1], Gianmarco Ingrosso[2], Tamara Djakovac[3], Salvatore Piacentino[4] and Michele Giani[1]**

[1] National Institute of Oceanography and Applied Geophysics (OGS), Trieste, Italy, [2] Institute of Polar Sciences, National Research Council, Lecce, Italy, [3] Center for Marine Research, Rudjer Boskovic Institute, Rovinj, Croatia, [4] ENEA-CLIMOSS, Palermo, Italy

Coastal ecosystems are subject to multiple processes that drive pH change over time. Therefore, efforts to understand the variability in the coastal carbonate system are crucial to assess the marine system vulnerability to acidification. The variations of the carbon dioxide (CO_2) system were studied, from December 2014 to January 2017, on 6 stations along a transect latitudinally crossing the northern Adriatic, from the Po River delta to the Istrian Peninsula. The study aims to evaluate the influence of riverine inputs and other environmental drivers, such as temperature, air-sea CO_2 exchanges and biological processes, on the carbonate system. Riverine discharges significantly affected the carbonate system, as they are an input of total alkalinity and nutrients. High alkalinity concentrations were measured in low salinity waters and a significant negative correlation between salinity and alkalinity was found. The influence of biological processes was underscored by the significant inverse correlation between pH_T at a constant temperature ($pH_{T25°C}$) and apparent oxygen utilization, and by the positive correlation between chlorophyll *a* and $pH_{T25°C}$ in samplings close to flood events. Moreover, thermic and non-thermic partial pressure (*p*) of CO_2 in surface waters was evaluated. pCO_2 was more strongly influenced by the thermal effect during summer, while the biological effect prevailed in the other seasons. The analysis of air-sea CO_2 fluxes highlighted that the area acts as a sink of CO_2 during winter, spring and autumn and as a source during summer. A biogeochemical simulation was used for bottom and surface waters to estimate future changes in northern Adriatic carbonate chemistry with the increase of anthropogenic CO_2 and temperature, and to understand how biological processes could affect the expected trends. By 2100, under the IPCC scenario of business as usual and without the effect of biological processes, pH_T is expected to decrease by ∼0.3 and the aragonite saturation is expected to decline by ∼1.3, yet not reach undersaturation values. Even though the northern Adriatic is characterized by high alkalinity buffering, pH seasonal variability will likely be more pronounced, due to the strong decoupling of production and respiration processes driven by stratification of the water column.

Keywords: CO_2 system, pH, Adriatic, river, fluxes, nutrients

OPEN ACCESS

Edited by:
Nina Bednarsek, Southern California Coastal Water Research Project, United States

Reviewed by:
Mariana Ribas Ribas, University of Oldenburg, Germany
Matthew Paul Humphreys, Royal Netherlands Institute for Sea Research (NIOZ), Netherlands
Leif Anderson, University of Gothenburg, Sweden

****Correspondence:***
Lidia Urbini
lurbini@inogs.it
Michele Giani
mgiani@inogs.it

Specialty section:
This article was submitted to Coastal Ocean Processes, a section of the journal Frontiers in Marine Science

Received: *11 May 2020*
Accepted: *27 July 2020*
Published: *13 August 2020*

Citation:
Urbini L, Ingrosso G, Djakovac T, Piacentino S and Giani M (2020) Temporal and Spatial Variability of the CO_2 System in a Riverine Influenced Area of the Mediterranean Sea, the Northern Adriatic. Front. Mar. Sci. 7:679. doi: 10.3389/fmars.2020.00679

INTRODUCTION

Atmospheric carbon dioxide (CO_2) levels increased over 40% passing from 280 ppm (parts per million volume), before the Industrial Revolution, to 415 ppm in 2019, as is shown by the Keeling Curve[1]. This is mainly due to fossil fuel combustion, deforestation, cement production and land use change. The increasing concentration surpassed the highest level in the last 800.000 years (Lüthi et al., 2008) and the rate of increase is an order of magnitude faster than has occurred for millions of years (Doney and Schimel, 2007). The oceanic uptake of CO_2 has resulted in the acidification of the ocean (OA), since the beginning of the industrial era; the pH of ocean surface water has decreased by 0.1 units corresponding to a 26% increase in acidity, measured as hydrogen ion concentration (IPCC, 2014) and a further decrease of 0.4 is expected for the end of the century (Orr, 2011). Together with the change in pH, the whole carbonate system is changing rapidly (IPCC, 2013). As a consequence of CO_2 addition to the ocean: the concentration of bicarbonate ions (HCO_3^-) and the concentration of dissolved inorganic carbon (TCO_2) increases, whereas pH, the concentration of carbonate ions (CO_3^{2-}) and the saturation state of the carbonate minerals present in the seawater decreases. These changes can have negative effects on the marine biota, especially on calcifying organisms (Kleypas et al., 1999). Long-term pH reduction due to the anthropogenic CO_2 in the open ocean has been demonstrated in the long-term records acquired in the last decades. However, the effects of acidification processes in coastal areas are still difficult to assess and predict. Coastal ecosystems are more complex and dynamic than that of the open ocean (Borges and Gypens, 2010; Cai et al., 2011; Ingrosso et al., 2016a), thus pH changes and long-term trends in coastal seas are usually considerably more complex (Duarte et al., 2013; Carstensen et al., 2018). These characteristics do not allow a direct transport of OA patterns from open oceans to coastal areas, leaving a remarkable lack in projections about acidification effects. How ocean acidification will affect marine organisms depends on changes in both the long-term, mean and short-term temporal variability of carbonate chemistry (Kwiatkowski and Orr, 2018). The duration of very low pH periods can be relevant for marine organisms both at seasonal or interannual level. The duration of seasonal events with very low pH could increase in the next future and can have long-term consequences. Moreover, the cumulation with other stressors as oxygen depletion and temperature increase (Wallace et al., 2014; Bednaršek et al., 2016), that are becoming more common in the last years, could worsen the impacts on marine organisms in the future.

The analysis of long-term changes in pH across 83 coastal ecosystems showed that these ecosystems present a much broader range (∼20 times larger) of rates of change in pH than the open ocean does (Carstensen and Duarte, 2019). Metabolic effects, represented by net community production and respiration rates, tend to be greater in coastal and estuarine ecosystems (Duarte and Cerbrian, 1996; Gattuso et al., 1998; Anthony et al., 2011). Observations of pH in a variety of coastal habitats indicate site-specific variability at scale ranging from diel to seasonal oscillations (Hofmann et al., 2011). Regional scale processes such as phytoplankton blooms (Kapsenberg and Hofmann, 2016), upwelling (Chan et al., 2017), and freshwater inputs (Fassbender et al., 2016) further modify CO_2 exposures, thus the negative impact of acidification could be enhanced in some coastal ecosystems subject to changes in the eutrophication pressure (Provoost et al., 2010; Wallace et al., 2014). Coastal phytoplankton blooms can increase pH up to 8.6–9.0 (Brussaard et al., 1996). Metabolic-intense ecosystems, such as seagrass meadows, mangroves, salt marshes, coral reefs and macroalgal beds, can support diel changes in pH as high as 1.0 unit. Consequently, long-term trends are difficult to separate from interannual and decadal oscillations.

In the Mediterranean Sea the acidification process seems more rapid than in the Atlantic Ocean, where the decrease range is from -0.0013 to -0.0026 yr^{-1} (Bates et al., 2014). A pH_T decrease of 0.0028 yr^{-1} has been observed in the NW Mediterranean Sea (Kapsenberg et al., 2017) while one of 0.0025 pH_T units yr^{-1} was estimated in the Adriatic Sea (Luchetta et al., 2010) and of 0.009 units yr^{-1} in the Levantine sea (Hassoun et al., 2019). The northern Adriatic (NAd) is a shallow semi-enclosed system strongly influenced by the Po River freshwater discharge, the second largest river in the Mediterranean Sea (Cozzi et al., 2019). Moreover, NAd is one of the few sites in the Mediterranean Sea where dense waters are formed (Font et al., 2009). Winter cooling determines heat loss and evaporation which induce the formation of dense waters (Supič and Vilibic, 2006) which flow southwards partially filling the meso- and south Adriatic pits and partially flowing along the western coast toward the Ionian Sea, contributing to the Mediterranean deep waters (Russo and Artegiani, 1996). Depending on the formation rate, dense water formation in NAd could potentially sequester high levels of anthropogenic carbon dioxide and contribute to acidification of deep waters (Ingrosso et al., 2017). The aim of this work is to investigate the spatial and temporal variability of the carbonate system in a Mediterranean system strongly influenced by riverine discharges, as the NAd, and to determine the main physical and biogeochemical drivers influencing it.

Description of the Area

The study area is the shallow northern Adriatic, with an average bottom depth of about 35 m. The area is a part of the Adriatic Sea (**Figure 1**) and represents the largest shelf area of the entire Mediterranean region (Gačič et al., 2001).

River runoff is particularly strong in the northern basin and it affects circulation by altering the buoyancy of water masses, and the ecosystem by introducing large amounts of nutrients (Zavatarelli et al., 1998), making the northern Adriatic a highly productive area (Pugnetti et al., 2006). Po River flow rates amount to around 45 km^3 yr^{-1} (70% of the total freshwater discharge in the region) with spring and autumn floods up to 10000 m^3 s^{-1} (Cozzi and Giani, 2011).

The Adriatic mean surface circulation is generally cyclonic, with the Eastern Adriatic Current (EAC) flowing northward along the eastern side from the Strait of Otranto to as far north as the Istrian Peninsula, and the return flow, referred to as the

[1]https://scripps.ucsd.edu/programs/keelingcurve/

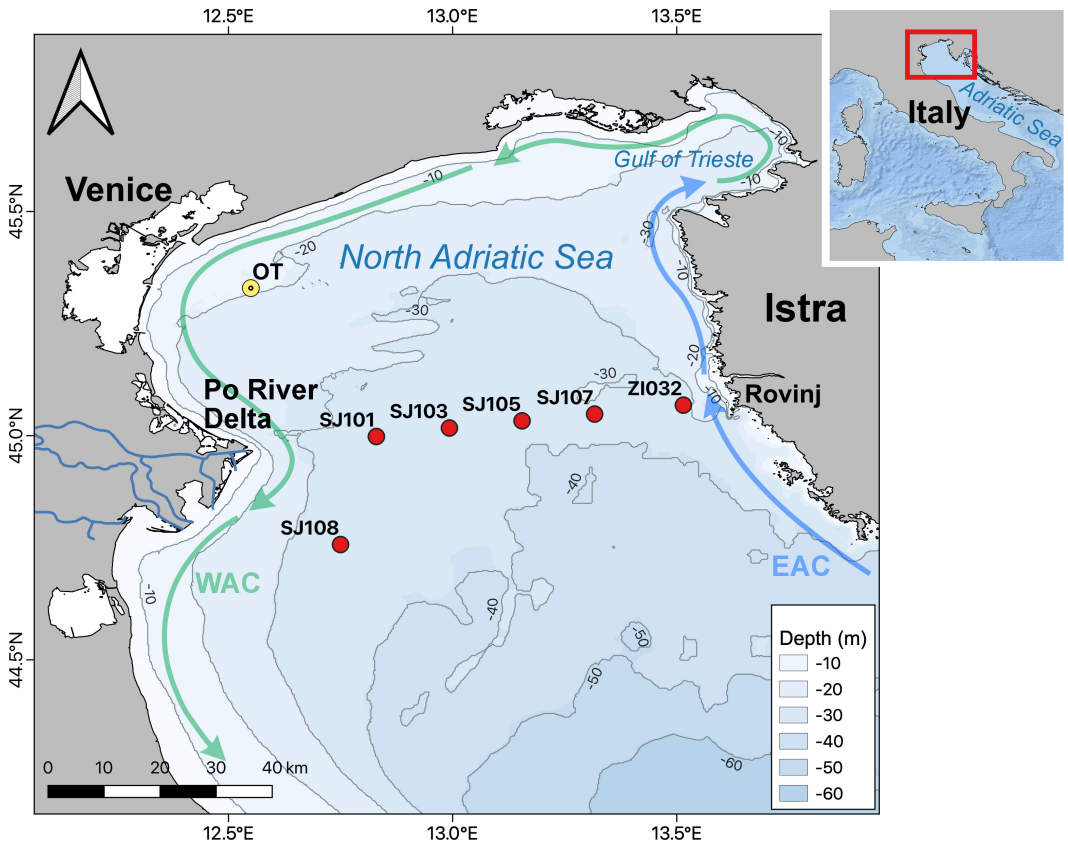


FIGURE 1 | Map of the sampling stations along a transect from Po River delta to Istra, and of the oceanographic tower (OT) Acqua Alta.

Western Adriatic Current (WAC), that runs along the Italian coast (Poulain, 2001). The WAC between the Po River delta and the Gargano Promontory is more concentrated near the Italian coast in winter and spring, while during the other seasons its core is found farther offshore (about 20–30 km from the coast in fall). The WAC and EAC are generally stronger in summer/fall than in winter/spring (Poulain, 2001).

During winter in the NAd the northern Adriatic dense water (NAdDW), the densest water of the entire Mediterranean, is generated (Bensi et al., 2013; Raicich et al., 2013). This water is characterized by low temperature, high salinity and density, usually: T 11.35 ± 1.4°C, S 38.3 ± 0.28 and σ_t > 29.2 kg m^{-3} (Artegiani et al., 1997). In general, NAdDW is formed on the central eastern side of the NAd, whereas the western part of the northern shelf, which is affected by the WAC, is characterized by lower-density water masses (Querin et al., 2013). Additionally, this area is characterized by the occurrence of the northern Adriatic surface water (NAdSW), which corresponds to low salinities and relatively high temperature in summer (Artegiani et al., 1997). Flow of this water is cyclonic due to its mixed positive–negative estuarine circulation (Hopkins et al., 1999) forced by buoyant freshwater from the rivers (mainly the Po River) and by strong air–sea fluxes resulting in loss of buoyancy and dense water formation. Along the eastern side of the basin, an occasional inflow of the modified Levantine intermediate water (MLIW) may occur (Zavatarelli et al., 1998; Manca and Giorgetti, 1999).

MATERIALS AND METHODS

Sampling Scheme

Data were sampled along a transect from the mouth of the Po River to the area of Rovinj in the northern Adriatic basin (**Figure 1**) from December 2014 to January 2017 in 16 oceanographic cruises. During cruises 6 stations (SJ108; SJ101; SJ103; SJ105; SJ107; and ZI032) were sampled. These stations were selected based on circulation patterns to obtain a river-sea gradient and were made to potentially match a seasonal trophic gradient. Water samples for temperature, salinity, pH on total scale (pH_T) A_T, dissolved oxygen (DO), dissolved inorganic nutrients and chlorophyll *a* (Chl-*a*) were collected and analyzed.

All parameters were sampled at 4 depths (0.5, 10, 20, and 2 m above the bottom). DO, pH_T and A_T samples were the first to be drawn from Niskin bottles. pH_T samples were drawn into 120 mL borosilicate glass bottles, with a 1% headspace, poisoned with 50 μL of saturated mercuric chloride ($HgCl_2$), and stored at 4°C in the dark, until analysis. Samples for A_T were filtered on pre-combusted (450°C for 4 h) Whatman GF/F filters to remove phytoplankton cells and particles of $CaCO_3$ derived

from calcifying organisms (Gattuso et al., 2010; Bockmon and Dickson, 2014), collected into borosilicate flasks (250 mL) with 1% headspace, poisoned with 100 μL of saturated $HgCl_2$, and stored in the dark at a 4°C temperature until analysis. For both parameters, analyses were performed by the National Institute of Oceanography and Applied Geophysics (OGS) in Trieste, Italy. DO, nutrients and Chl-a instead, have been analyzed by the Center of Marine Research (CMR) of Rudjer Boskovic Institute (RBI) in Rovinj, Croatia, Istrian Peninsula.

Analytical Measurements of Temperature, Salinity, Dissolved Oxygen, Inorganic Nutrients and Chlorophyll *a*

Temperature was measured by protected reversing thermometers (digital thermometers SIS RTM 4002, precision ± 0.003°C, accuracy ± 0.005°C) attached to the Niskin bottles. Salinity from Niskin bottles samples was determined by high precision salinometer (RBR Precision Instruments MS-310) as the ratio of the value of conductivity of sample and standard (IAPSO standard seawater) using algorithms recommended by UNESCO (1983) with accuracy of ±0.002.

DO and inorganic nutrients were analyzed directly on-board by the CMR/RBI research group, according to methods widely used in oceanography (Parsons et al., 1984). DO was determined by the Winkler titration method, while the saturation percentage was calculated following the Benson and Krause equation (UNESCO, 1986). The method accuracy was ±0.5% with a detection limit of 0.9 μmol kg^{-1} (Parsons et al., 1984). The apparent oxygen utilization (AOU) was determined as the difference between the equilibrium saturation of oxygen's concentration in seawater with the same physical and chemical properties and the measured oxygen concentration. AOU represents an estimate of the oxygen utilized due to biochemical processes, providing an approximation of the balance between biological processes of primary production and respiration.

Dissolved inorganic nutrients concentrations [nitrite N-NO_2, nitrate N-NO_3, phosphate P-PO_4, and silicate Si-Si $(OH)_4$] were analyzed spectrophotometrically (Parsons et al., 1984), moreover, ammonia (N-NH_4) concentrations were determined by a modified technique of the indophenol blue method (Ivančič and Degobbis, 1984). Dissolved inorganic nitrogen (DIN) was obtained as a sum of ammonia, nitrite and nitrate. The absorbance readings for all nutrients were made on Shimadzu UV-Mini 1240 double-beam spectrophotometer using 10 and 5 cm quartz cuvettes. Method accuracies for NO_2, NO_3, NH_4, PO_4 and $Si(OH)_4$ were ±3%, ±3%, ±5%, ±3%, and ±6%, respectively, and detection limits were 0.05, 0.01, 0.1, 0.02, and 0.05 μmol L^{-1}, respectively.

The samples for Chl-a measurement were prefiltered through 290 μm Nybolt net, and then filtered through Whatman GF/C filters (1 μm pore size) on-board, immediately after collection. The filters were stored at −20°C until analyses, which were performed fluorometrically after a 3 h extraction in 90% acetone (in the dark, with grinding after addition of acetone) by using Turner Designs, TD-700 fluorometer at the inland CMR/RBI laboratories. Method accuracy of 78%, and detection limit of 0.02 μg L^{-1} were calculated according to equations of Parsons et al. (1984).

Analytical Determination of Seawater pH_T and Total Alkalinity

pH_T determination was performed at OGS using a double wavelength spectrophotometer (Cary 100 Scan UV-visible) and employing purified dye m-cresol purple 4 mM as indicator, as described in SOP 6b of Dickson et al. (2007). The results were expressed on the 'pH total hydrogen ion scale' (pH_T) at 25°C, with a reproducibility of ±0.001, determined by replicates from the same Niskin bottles. The day of the analysis samples were brought to 25°C and subsampled by siphoning with a tygon tube, avoiding gas exchange, in a 10 cm path-length cylindrical quartz cell; no head-space was left. pH_T was measured within a few hours from the sub-sampling. During the whole analysis, the temperature of the samples was controlled through thermostatic cell holders inside the spectrophotometer, connected to a circulation criothermostat (LAUDA RE415) and monitored with a digital thermometer (VWR Traceable).

The accuracy of pH_T (±0.004) spectrophotometric measurements was assessed through the analysis of Tris buffers supplied by Prof. A.G. Dickson, Scripps Institute of Oceanography, United States. Tris buffer reference value was calculated, at the temperature of the measurements, following DelValls and Dickson (1998).

A_T was analyzed in the laboratory by an open cell potentiometric titration, using a Mettler Toledo G20, at 25°C; ∼100 g of sample were weighed and titrated with HCl 0.1 mol kg^{-1} in NaCl 35‰ as defined by the SOP 3b (Dickson et al., 2007), using a non-linear least squares approach. The HCl was calibrated against seawater certified reference materials (CRMs) for TCO_2 and A_T supplied by Prof. A.G. Dickson, Scripps Institute of Oceanography, USA (Batch numbers #107, #133, #153). A_T calculations were run by Alka Open Cell 2.0, a computer program developed by OGS according to programs listed in SOP 3 of Dickson and Goyet (1994); the program was adapted to work in association with the Mettler Toledo LabX software. A_T reproducibility was <2 μmol kg^{-1} and the accuracy ±4 μmol kg^{-1}, they were assessed by analyzing both CRMs and local reference materials (LRM) of natural seawater; moreover, the OGS laboratory participated in the Inter-laboratory Comparison of Seawater CO_2 Measurements organized by the Scripps Institution of Oceanography in 2013 and 2017. The differences for A_T and pH_T measurements were < 4 μmol kg^{-1} and <0.0004 respectively.

All other carbonate system parameters, including pH_T at *in situ* temperature, seawater partial pressure of CO_2 (pCO_2), TCO_2, and aragonite saturation state (Ω_{ar}), were calculated using the CO2Sys program (Pierrot et al., 2006) through A_T concentration, pH_T (25°C), temperature, salinity, phosphate, and silicate concentration data. Carbonic acid dissociation constants (i.e., pK1 and pK2) proposed by Lueker et al. (2000) as well as the Dickson constant for the ion HSO_4 (Dickson, 1990) and borate dissociation constant of Uppström (1974) were used. Uncertainties for the derived carbonate system parameters have

been calculated using CO2Sys, following Orr et al. (2018). The estimated uncertainties were: ±0.006 for pH_T at *in situ* temperature, ±8 μatm for pCO_2, ±9 μmol kg^{-1} for TCO_2 and ±0.2 for aragonite saturation state.

Thermic (T) and non-thermic (B) pCO_2 in surface waters has been calculated following the procedure described by Takahashi et al. (2002) to distinguish the effect of temperature change from the effect of other processes (i.e., biological processes, advection of water masses..). For each station seasonal T was calculated as the difference between the maximum and the minimum thermic pCO_2 and B as the difference between the maximum and the minimum non-thermic pCO_2. Thermic pCO_2 was calculated as described in equation 1:

$$Thermic\ pCO_2 = pCO_{2mean} \exp[0.0423(T_{obs} - T_{mean})] \quad (1)$$

Where pCO_{2mean} is the mean surface pCO_2 of the investigated period, T_{obs} is the measured temperature and T_{mean} is the mean surface temperature of the investigated period.

While non-thermic pCO_2 was computed as described in equation 2:

$$non - Thermic\ pCO_2 = pCO_{2obs} \exp[0.0423(T_{mean} - T_{obs})] \quad (2)$$

where pCO_{2obs} is the measured surface pCO_2.

In order to remove the variations due to freshwater input, mixing and evaporation/precipitation influence, A_T and TCO_2 were normalized (nA_T and $nTCO_2$) to a different salinity for every year using a traditional normalization style. We are aware that the tradition approach (Millero et al., 1998) could create artificial variance in distributions (Friis et al., 2003), but we chose the classical normalization since we do not have a stable endmember.

For the contour plots the advanced DIVA gridding of the software Ocean Data View (Schlitzer, 2018) was used. Since we are aware of the limitations of this gridding method, we checked the representativeness of the interpolations with the discrete data points.

Air-Sea CO_2 Flux Calculations

The daily air-sea CO_2 flux (FCO_2, mmol m^{-2} day^{-1}) has been calculated following the equation:

$$FCO_2 = K_0 k(pCO_2 - pCO_{2atm}) \quad (3)$$

where:

K_0 is the solubility coefficient of CO_2 at *in situ* temperature and salinity of seawater (Weiss, 1974; Zeebe and Wolf-Gladrow, 2001);

k is the gas transfer velocity (m day^{-1}) and pCO_2 – pCO_{2atm} is the difference between pCO_2 at sea surface and daily mean pCO_2 in atmosphere.

Since several algorithms for k calculation exists, two different parameterizations were used to compute k: the one described by Wanninkhof (2014) in equation 4, hereafter referred to as W14, and the parameterization described by Nightingale et al. (2000) in equation 5, hereafter referred to as N00:

$$k = 0.251u^2 \left(\frac{Sc}{660}\right)^{-\frac{1}{2}} \quad (4)$$

$$k = (0.333u + 0.222u^2) \left(\frac{Sc}{660}\right)^{-\frac{1}{2}} \quad (5)$$

where u is the daily mean wind speed recorded at the oceanographic tower (OT) Acqua Alta (**Figure 1**) and Sc the Schmidt number for CO_2.

If the FCO_2 is < 0 the flux is from air to seawater, on the contrary if FCO_2 is > 0 the flux is from the seawater to the atmosphere.

CO_2 monitoring in air was run with continuous measurements at ENEA Station for Climate Observations on the island of Lampedusa (Italy). CO_2 measurements were made with a Picarro G2401 gas analyzer. Ambient air was taken from a tower at a height of 8 m above the surface, about 50 m above sea level. Water vapor was removed from the sampled air by means of a cryogenic trap at about −60°C. The gas analyzer was calibrated biweekly, using 4 cylinders which concentration is traceable to the WMO CO2-X2007 reference scale (provided by the Max Planck Institute in Jena, Germany, as part of the InGOS European Union Project). Gas from an additional cylinder was injected in the instrument every 6 h as an additional quality control check. Data were subsequently verified by means of standard quality control procedures, the accuracy on 5-min average CO_2 measurements was better than 0.02 ppm.

pCO_{2atm} data of Lampedusa were used because there were no pCO_{2atm} daily measurements available in the offshore NAd for the investigated period.

Buffer Factors and Carbonate Saturation State

The fractional change in concentration of CO_2 over the fractional change in TCO_2 has been referred to as the Revelle factor, or R (Revelle and Suess, 1957; Broecker et al., 1979):

$$R = \frac{\partial \ln[CO_2]}{\partial \ln TCO_2} \quad (6)$$

This quantifies the ocean's sensitivity to an increase in atmospheric CO_2. Moreover, we considered two other buffer factors, β_{TCO2} and β_{AT}, as defined by Egleston et al. (2010):

The parameter β_{AT}, defined as:

$$\beta_{AT} = \left(\frac{\partial \ln[H^+]}{\partial A_T}\right)^{-1} = \frac{A_C^2}{TCO_2} - S \quad (7)$$

measures the resistance to change of the hydrogen ion concentration (or activity) when alkalinity changes at constant

TCO_2, i.e., upon addition of a strong base, directly related to the traditional buffer capacity of the system.

The parameter β_{TCO2}, defined as:

$$\beta_{TCO2} = \left(\frac{\partial \ln[H^+]}{\partial TCO_2}\right)^{-1} = \frac{TCO_2 \; x \; \text{S-A}_C^2}{A_C} \quad (8)$$

measures the resistance to change of the hydrogen ion concentration (or activity) when TCO_2 changes at constant A_T.

Where

$$\begin{aligned} S = {} & [HCO_3^-] + 4[CO_3^{2-}] + \frac{[H^+][B(OH)_4^-]}{K_{hb} + [H^+]} + [H^+] \\ & + [OH^-] + ([H_3PO_4]([H_2PO_4^-] + 2[HPO_4^{2-}] + 3[PO_4^{3-}]) \\ & + [HPO_4^{2-}](2[H_3PO_4] + [H_2PO_4^-] - [PO_4^{3-}]) \\ & + 2[PO_4^{3-}](3[H_3PO_4] + 2[H_2PO_4^-] + [HPO_4^{2-}]))/P_T \\ & + \frac{[H^+][SiO(OH)_3^-]}{K_{Si} + [H^+]} \end{aligned} \quad (9)$$

as revised in the Appendix B of Orr et al. (2018), and

$$A_C = [HCO_3^-] + 2[CO_3^{2-}] \quad (10)$$

We performed the calculations with the routine *buffesm* of the Seacarb (Gattuso et al., 2015) package in R (R Core Team, 2016) employing the same constants used in CO2Sys to calculate the other carbonate system parameters (see section "Analytical Determination of Seawater pH_T and Total Alkalinity").

Seawater CO_2 Chemistry Simulations

In order to estimate future changes in the northern Adriatic Sea carbonate chemistry with the increase of anthropogenic CO_2, and to estimate how biological processes could affect the expected trends, we set up a biogeochemical simulation following Sunda and Cai (2012). In our simulation, we considered how a high level of atmospheric CO_2 could affect the carbonate system of NAd in two water types that usually have pronounced metabolic activity: the bottom waters and NAdSW. The initial carbonate chemistry conditions for these two water types were calculated using their A_T and CO_2 at air-sea equilibrium as a function of their specific temperature and salinity. Atmospheric pCO_2 was set at two levels (400 and 910 ppm) corresponding to present-day and year 2100 Representative Concentration Pathway for high emission scenario (RCP 8.5, van Vuuren et al., 2011; IPCC, 2013). A seawater temperature increase of +2.58°C for the 2100 was also considered in our simulation, as projected by IPCC (2019) for global sea surface under RCP 8.5 scenario. The adopted trend implies a +0.03°C yr^{-1}, which is intermediate between the NAd warming rate reported by Raicich and Colucci (2019) of 0.013 ± 0.005°C yr^{-1} and that of 0.01–0.06°C yr^{-1} reported by Vilibič et al. (2019). The biogeochemical model for respiratory increases or photosynthetic decrease in CO_2 concentration is based on AOU calculations as described by Redfield et al. (1963). Once the initial surface conditions were calculated, aerobic respiration or photosynthetic activity were assumed to increase or decrease TCO_2 respectively, due to respiration or primary production at the Redfield ratio of 106 CO_2 to 138 O_2. Then the resulting TCO_2 was used to calculate the other carbonate chemistry parameters for 2100, assuming reference A_T, salinity and temperature (sea surface temperature in 2100 = present day temperature +2.58°C) specific for each water mass and using the same equilibrium constants as previously described for the carbonate system. A_T was considered constant because in the organic matter, the aerobic oxidation of amine nitrogen to nitric acid has only a small decrease in alkalinity, but this effect is essentially canceled by denitrification under hypoxic conditions, which converts HNO_3 to N_2. All calculations were performed with the Seacarb (Gattuso et al., 2015) and Marelac (Soetaert et al., 2015) packages in R (R Core Team, 2016).

Statistical Analysis

The Shapiro–Wilk test (Shapiro and Wilk, 1965) was used to check the normality of the data. Due to their non-normal distribution a non-parametric approach was adopted. Spearman's coefficient was used for correlations. The Kruskal–Wallis rank sum test (Kruskal and Wallis, 1952) was used to test statistically significant differences between seasons for each parameter whereas the multiple comparison test (Siegel and Castellan, 1988) was used to determine which pair of seasons were different. Analyses were performed with R program and the package *pgirmess*. Seasons were considered as follows: winter (January–March), spring (April–June), summer (July–September), and autumn (October–December). Seasons were defined based on the climatological work of Zavatarelli et al. (1998).

RESULTS

Riverine Influence

Po River discharges strongly influence the NAd, particularly after the freshets; daily variations of Po river flow rate (Q) measured at Pontelagoscuro station (Ferrara, Italy) and discrete sampling days are presented in **Figure 2**.

The mean Po flow rate decreased between 2015 and 2017; in 2015 (from December 2014 to December 2015) was of 1421 m^3 s^{-1}, while in 2016 (from January 2016 to January 2017) was of 1148 m^3 s^{-1}.

The strong effect of the freshwater discharge was observed on the majority of the parameters along the section, highlighted by (i) their seasonal variability, strongly connected to Po River discharges and (ii) the formation of a gradient from the western toward the eastern sector of the basin.

The formation of a horizontal gradient along the transect, is evident from the spatial distribution of salinity, A_T, pH_T and TCO_2 in February 2015 (**Figure 3**), sampled close to a flood event, with values of A_T and TCO_2 higher in the WAC, decreasing eastwards, and values of salinity and pH_T increasing eastwards.

The effect of riverine inputs on the concentration of A_T is also highlighted by its negative correlation with salinity. The most significant correlations were found in surface

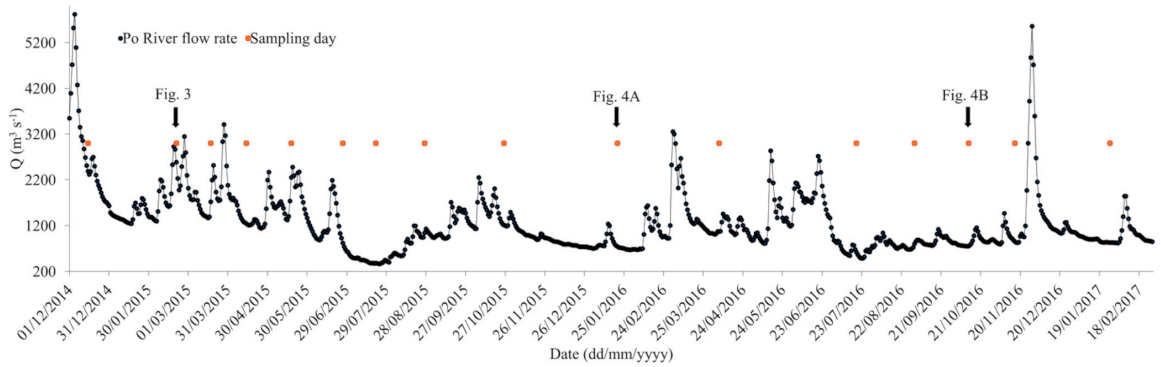


FIGURE 2 | Daily variations of Po river flow rate (Q) measured at Pontelagoscuro station (Ferrara, Italy) and sampling days from December 2014 to January 2017 (red square symbols).

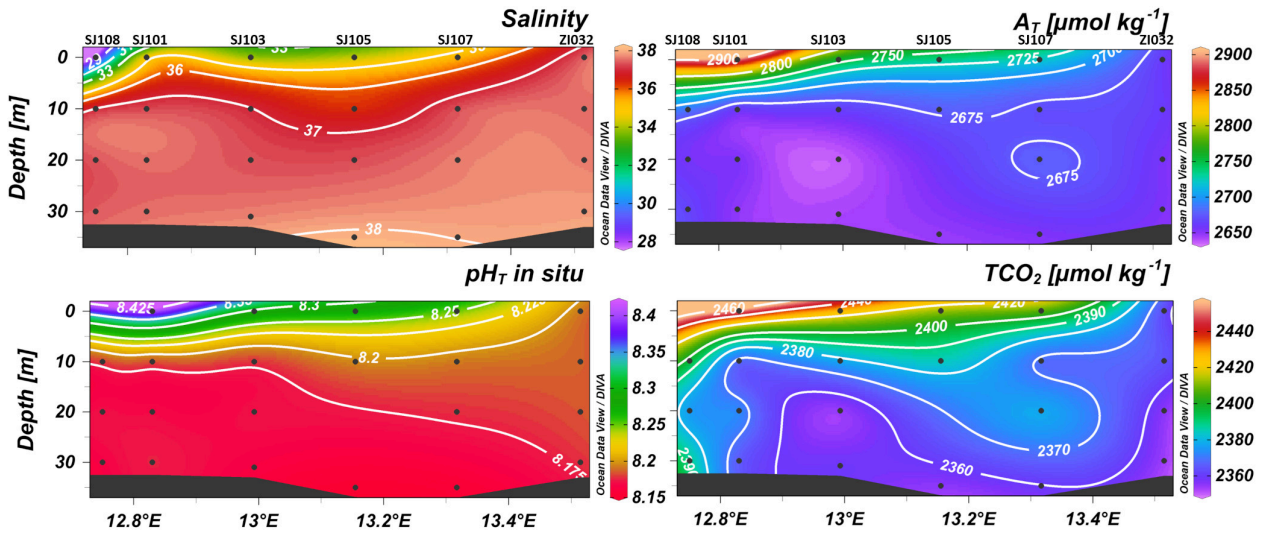


FIGURE 3 | Contour plots of salinity, total alkalinity (A_T), pH_T and dissolved inorganic carbon (TCO_2) versus depth in February 2015 along the transect from Po River (left) to Rovinj (right).

waters during the period of high freshwater discharges: high concentrations of A_T (2668 ± 51 µmol kg^{-1}) were measured in February, March and April 2015 (late winter-spring) when also the strongest correlation with salinity was found ($r = -0.66$; $p < 0.0001$; $n = 69$). However, even considering all the data, the correlation was still significant ($r = -0.50$; $p < 0.0001$; $n = 377$) (**Supplementary Figures 1, 2**).

Beside the effects of temperature, riverine inputs influenced pH_T values mainly due to the fertilization effect. In fact, higher pH_T values were measured at surface during winter/spring period, characterized by higher freshwater discharges that brings inorganic nutrients to support primary production.

The TCO_2 concentration resulted influenced by freshwater discharges, as it is underlined by its negative correlation ($r = -0.79$; $p < 0.001$; $n = 17$) in surface waters with salinity in February, March and April 2015 (**Supplementary Figure 3**).

The effect of riverine inputs on inorganic nutrient concentrations was highlighted by the highly significant negative correlation between salinity in surface waters and nitrate ($r = -0.96$; $p < 0.0001$; $n = 18$), nitrite ($r = -0.90$; $p < 0.0001$; $n = 18$), phosphate ($r = -0.79$; $p < 0.001$; $n = 18$) and silicate ($r = -0.66$; $p < 0.01$; $n = 18$) in samplings close to flood events. The highest concentrations of nitrate (74.42 µmol L^{-1}), silicate (65.35 µmol L^{-1}), phosphate (1.31 µmol L^{-1}), and ammonium (7.38 µmol L^{-1}) have been measured in February 2015 in surface waters close to the Po River delta (**Supplementary Figure 4**).

Influence of Biological Processes

The biological processes in the water column which affect the CO_2 system in the NAd are strongly related to the seasonality, as evidenced by the difference between the winter homogeneity (**Figure 4A**) and the autumn thermohaline stratification (**Figure 4B**).

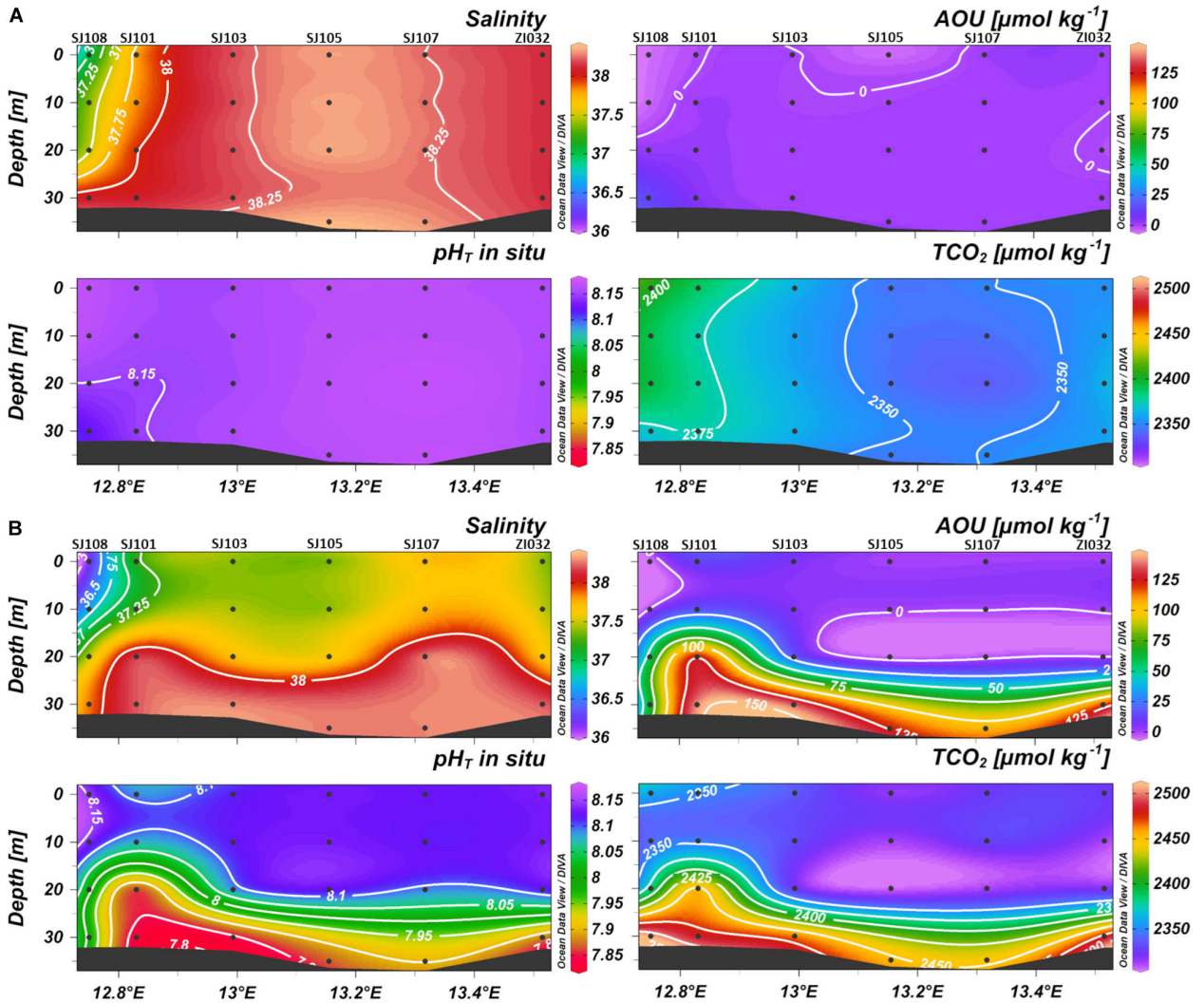


FIGURE 4 | Contour plots of salinity, apparent oxygen utilization (AOU), pH_T and dissolved inorganic carbon (TCO_2) versus depth along the transect in **(A)** January 2016 and **(B)** October 2016, from Po River (left) to Rovinj (right).

During winter (**Figure 4A**) the water column was homogenous for all the parameters, with a weak horizontal gradient of salinity that increased eastwards from the Po River delta. AOU was uniform along the section, with an average value of 1 ± 4 µmol kg^{-1}, indicating that DO was near to saturation. pH_T was high and homogeneous in the whole water column (8.160 ± 0.010 on average), TCO_2 instead followed the weak horizontal gradient of salinity decreasing toward the offshore waters.

During the seasonal stratification (**Figure 4B**), a marked oxygen depletion occurred under the pycnocline, where, due to respiration and organic matter remineralization, carbon dioxide was produced, lowering pH_T and increasing the concentration of TCO_2.

The influence of biological processes on pH_T variations, removing the effect of temperature, is evidenced by the correlation between AOU and $pH_{T25°C}$, which was significant for all the data ($r = -0.59$; $p < 0.0001$; $n = 383$). Considering just the layer below 20 m depth, where respiration processes prevail, the correlation resulted more significant ($r = -0.76$; $p < 0.0001$; $n = 95$) (**Supplementary Figures 5, 6**). Moreover, in bottom waters, the influence of biological processes is underlined by the slope of the regression line between AOU and $nTCO_2$, that had a value of 0.799 (**Supplementary Figure 7**), close to the Redfield ratio of 0.768 (C: AOU = 106: 138).

The relative importance of biology and temperature effects on pCO_2 is expressed by the thermic/non thermic ratio (T/B; **Figure 5**). If the biological effect exceeds the temperature changes, ratio varies from 0 to 1, if the temperature effect is stronger than the biological processes the ratio is greater than 1, the two effects have the same influence if the ratio is 1. During winter, the biological effect on pCO_2 prevailed on the temperature effect in all stations of the transect, but mostly in the two stations closer to the Po River delta (**Figure 5**).

During spring the biological processes still exceeded temperature changes, but less intensively than in winter (**Figure 5**). In summer the thermic effect was stronger in all the stations except the most eastern one, where the ratio was 1. The two stations near the Po River delta were the ones where the temperature effects were stronger. In autumn, the biological effect prevailed in all the stations (**Figure 5**).

A horizontal gradient of Chl-a concentration, decreasing from the western to the eastern waters, was found, more marked in winter-spring 2015 and autumn 2016 (**Supplementary Figure 8**). The biological effect of the trophic gradient is supported by the positive correlation ($r = 0.36$; $p < 0.05$; $n = 71$) between $pH_{T25°C}$, and Chl-a in samplings close to flood events. Moreover, the significant inverse relationship ($r = -0.35$; $p < 0.001$; $n = 95$) in the waters above the pycnocline of pCO_2 and Chl-*a* points out the possible effects of the CO_2 drawdown by phytoplankton.

Seasonal and Interannual Variations

The wide variation of both the physical and chemical properties observed during the two years, strongly influenced the marine carbonate system. Seasonal average values of temperature, salinity, density anomaly (σ_t), AOU, TCO_2 and pH_T are summarized in **Table 1**. Three stations (SJ101, SJ105, and ZI032) were selected to represent the time evolution in the western, central, and eastern NAd (**Figures 6**, **7**). For the western side of the basin, station SJ101 was selected, as it is strongly influenced by riverine discharges and it is representative for the coastal area; similar thermohaline conditions between station SJ108 and SJ101 were found, but a stronger variability characterized SJ101. Station SJ105 was selected to represent the central area of the transect, while station ZI032 was chosen to represent the eastern side of the basin, where southern waters enter into the NAd. The differences between seasons for each parameter were tested with the non-parametric Kruskal–Wallis rank sum test and the results are presented in **Table 2**. Seawater temperature in the water column varied between 8.10 and 29.58°C during the investigated period (**Table 1**), with the surface layer minimum measured in winter (January 2017), and the surface layer maximum reached in summer (July 2015). Seawater temperature resulted significantly different ($p < 0.001$) among each season (**Table 2**). Salinity ranged between 26.36 and 38.53, while σ_t varied between 18.85 and 29.85 kg m^{-3} (**Table 1**). For both parameters the minimum was measured in spring and the maximum in winter. The highest variability along the transect was detected in spring (36.96 ± 1.86 and 27.60 ± 2.10, respectively). Salinity was significantly different ($p < 0.001$) only among spring and winter and among summer and winter (**Table 2**). The variation of observed AOU was consistent with the typical seasonal cycle; during all the investigated period it ranged between −180 and 144 μmol kg^{-1}, with the maximum reached in autumn 2016 at surface and the minimum measured in winter 2015 at bottom. During winter, when the biological activity is usually low, the mean AOU along the whole water column was close to zero (**Table 1**). In spring, primary production was the predominant process, as shown by the negative mean AOU (−10 ± 31 μmol kg^{-1}). In summer the effect of primary production was still evident in the upper layer (−17 ± 11 μmol kg^{-1}), while below 10 m depth, due to stratification, oxygen consumption prevailed (13 ± 38 μmol kg^{-1}). In autumn the water column was oxygen undersaturated, the mean AOU was 25 ± 40 μmol kg^{-1}, due to the prevalence of respiration processes. The concentration of TCO_2 ranged between 2234 and 2582 μmol kg^{-1}, both recorded during spring. In winter and spring high and comparable TCO_2 concentrations were detected. In winter low temperatures enhance the solubility of CO_2 in seawater and TCO_2 increases (physical pump), even if this is a slow process it lasts for a long period. In spring these concentrations are due to freshwater inputs increase. The average TCO_2 value decreased in summer and increased again in autumn, with the seawater cooling. As for AOU, there was a clear difference due the proximity to the Po River delta: higher values of TCO_2 at the bottom, under the pycnocline in the most western stations, and a decrease at the bottom toward the eastern waters.

pH_T seasonal variation strongly depended on thermal seasonal variation of seawater. During all the study period, the variation was of 0.585, with the maximum (8.415) reached in winter and the minimum (7.830) measured in autumn. pH_T values were high in winter (8.182 ± 0.036), when the average temperature was 10.33 ± 1.02°C and gradually decreased with seawater warming in spring (8.129 ± 0.066) and summer (8.062 ± 0.086), The seawater cooling in autumn caused an increase in pH_T (8.084 ± 0.086). pH_T was significantly different ($p < 0.001$) among each season (**Table 2**), with the only exception of spring and autumn. The buffer capacity showed marked seasonal variations (**Table 3**): it was lower in winter and higher in summer. The highest values were observed in summer surface waters, due to the riverine inputs of total alkalinity and high seawater temperature that causes shifts in acid-base dissociation constants. All the buffer factors were significantly correlated ($p < 0.0001$) with temperature, β_{TCO2} directly and β_{AT} and R inversely. In the surface waters, freshwater inputs increased the buffer factors ($p < 0.005$). Interestingly in bottom waters the buffer capacity was higher in winter and lower in summer (the opposite with respect to the upper water column). The saturation state also showed a marked seasonality, with the lowest values during winter and highest during summer, similarly to the buffer factors, in the bottom waters it was the opposite.

The CO_2 System in the Different Water Types

Density, salinity and temperature were used to identify the main water types that characterize the northern Adriatic (**Figure 8**):

(1) the NAdDW: dense and cold water mass formed in winter;
(2) dense and relatively warm bottom waters present from late spring to autumn: they derive from NAdDW which, with warming and partial mixing, becomes progressively less dense;
(3) the NAdSW: surface waters diluted by the Po River, occurring throughout the entire year.

The NAdDW, characterized by σ_t values higher than 29.2 kg m^{-3} (**Figure 8** and **Table 4**), was identified along the transect in January 2016 and 2017. In both periods the seawater

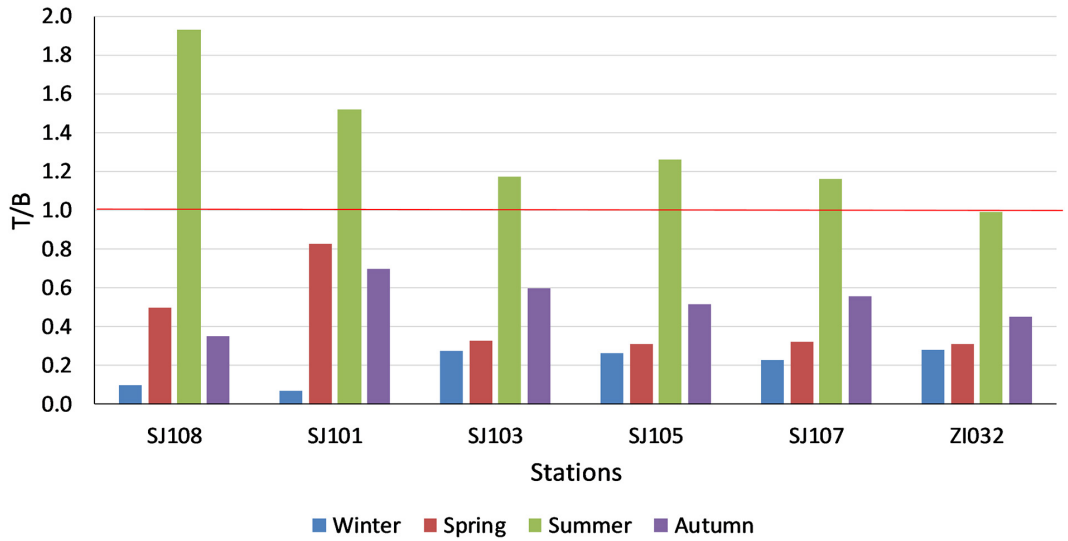


FIGURE 5 | Thermic/not thermic pCO_2 ratio (T/B) in surface waters in the stations of the transect in the different seasons.

TABLE 1 | Summary statistics for temperature, salinity, density anomaly (σ_t), apparent oxygen utilization (AOU), dissolved inorganic carbon (TCO_2), and pH_T at *in situ* temperature along the transect during the four seasons.

Season	*n*	Temperature (°C)	Salinity	σ_t (kg m^{-3})	AOU (μmol kg^{-1})	TCO_2 (μmol kg^{-1})	pH_T
Winter	93	10.33 ± 1.02 (8.10;12.28)	37.53 ± 1.36 (27.84;38.53)	28.86 ± 1.02 (21.61;29.85)	−5 ± 22 (−180;22)	2372 ± 21 (2326;2456)	8.182 ± 0.036 (8.124;8.415)
Spring	94	14.25 ± 3.72 (11.08;24.05)	36.96 ± 1.86 (26.36;38.40)	27.60 ± 2.10 (18.85;29.23)	−10. ± 31 (−144;78)	2373 ± 43 (2234;2582)	8.129 ± 0.066 (8.006;8.393)
Summer	95	21.10 ± 4.77 (12.41;29.58)	37.29 ± 0.94 (34.52;38.30)	26.13 ± 1.92 (21.59;28.82)	5 ± 37 (−54;124)	2346 ± 49 (2286;2498)	8.062 ± 0.047 (7.868;8.173)
Autumn	94	17.57 ± 1.66 (15.42;21.08)	37.51 ± 0.81 (31.43;38.46)	27.29 ± 0.71 (23.10;28.18)	25 ± 40 (−40;144)	2363 ± 49 (2289;2510)	8.084 ± 0.086 (7.830;8.176)

Data are presented as average ± standard deviation and (minimum; maximum).

temperatures were lower than 13°C and the salinity ranged from 37.80 to 38.53. In January 2016 the newly formed dense water filled the intermediate and bottom layers only in the central area of the transect. A remain of NAdDW was still present in April 2016, at the bottom of the central station (σ_t = 29.23 kg m^{-3}). In winter 2017 lower temperature characterized the water column, reaching the minimum of 8.68°C. The dense waters formed as a result of the intense cooling combined with high salinity (37.80 – 38.53) and reached the maximum σ_t of 29.85 kg m^{-3}. The relatively high salinity bottom waters with temperatures above 13°C, were typically present from spring through autumn during the investigated period (**Table 4**). In 2015 the mean salinity was 37.81 ± 0.27, with a mean temperature of 15.56 ± 1.77°C, while in 2016 the mean salinity was 38.17 ± 0.20, with a mean temperature of 16.46 ± 1.28°C. NAdSW, occupied the surface layer reaching the 10 m depth. The dilution was more marked in the western waters, especially during spring. The influence of fresh waters affected the water column differently throughout the seasons. This affect, was evident even in the eastern stations of the transect. Spring months showed the minimum salinity values throughout the year, ranging from 26.36 to 37.46. Salinity increased in summer and was more homogeneous (36.60 ± 0.87), and in autumn increased slightly (37.18 ± 0.97). Salinity values were lower in 2015 for all the seasons. In 2015 Po River discharges were higher (mean discharges: 1421 ± 765 m^3 s^{-1} in 2015 and 1148 ± 615 m^3 s^{-1} in 2016). The carbonate system showed different features in the identified water types: the concentration of A_T was higher in NAdSW, where the absolute maximum and minimum were measured (**Table 4**). Average pH_T values were lower in warm bottom waters, due to respiration process that occur under the pycnocline, as confirmed by AOU values above 0. In contrast, NAdDW were characterized by higher pH_T and mean AOU concentrations close to 0 (**Table 4**). Warm bottom waters were characterized also by the highest average TCO_2

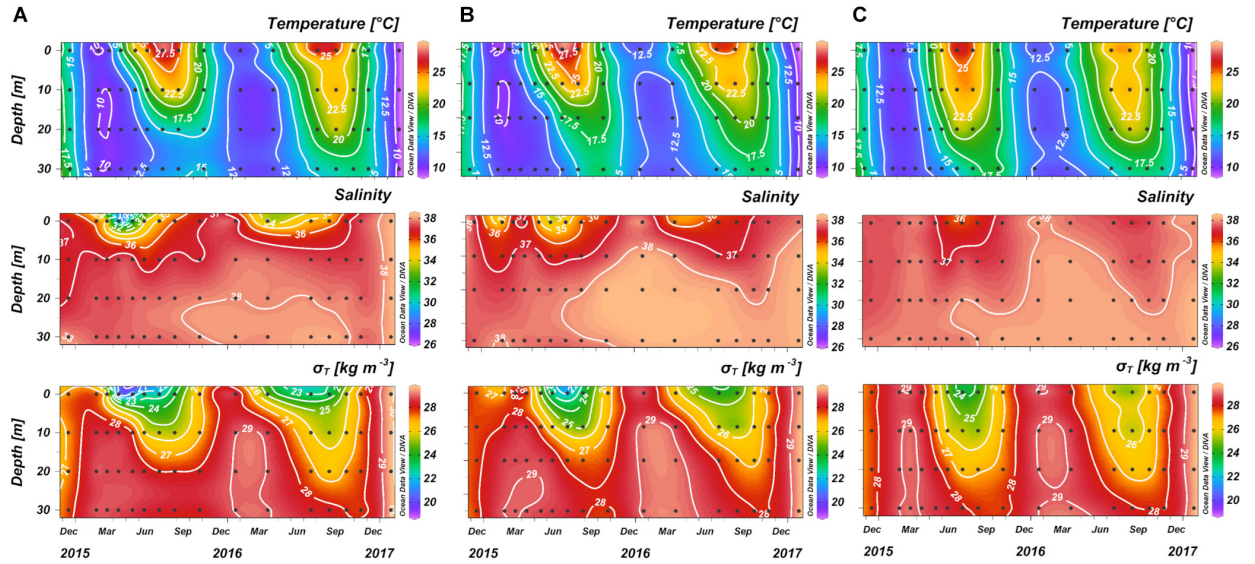


FIGURE 6 | Temporal variations of temperature, salinity, and density anomaly (σ_t) in the stations: **(A)** SJ101, **(B)** SJ105, and **(C)** ZI032.

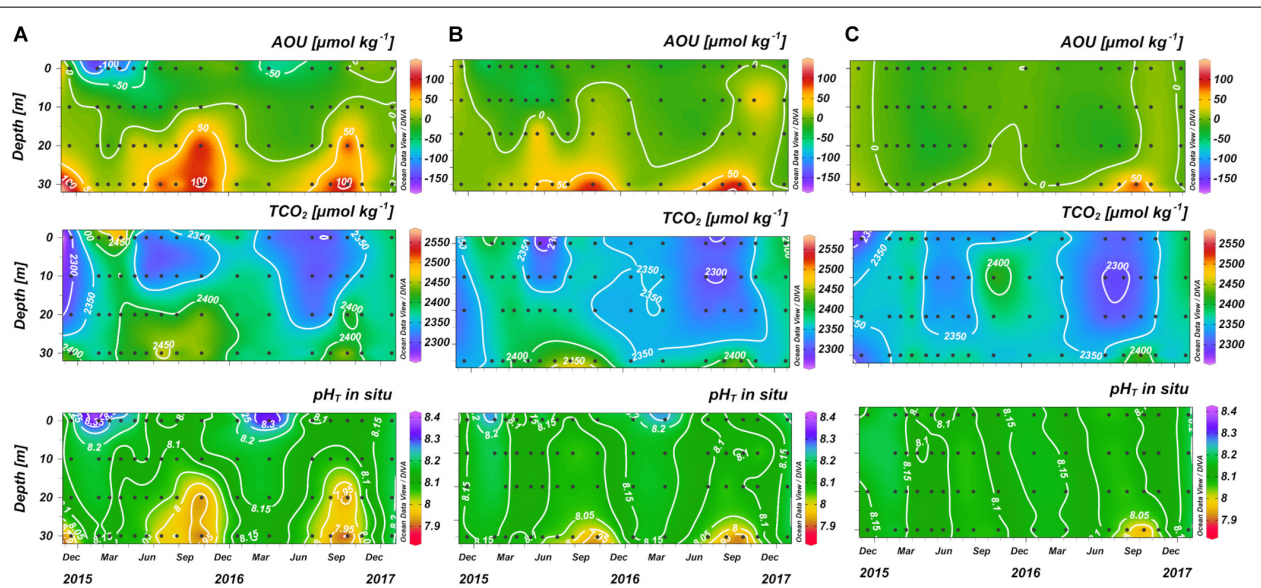


FIGURE 7 | Temporal variations of apparent oxygen utilization (AOU), dissolved inorganic carbon (TCO_2) and pH_T in the stations: **(A)** SJ101, **(B)** SJ105, and **(C)** ZI032.

concentration, while the lowest average TCO_2 concentration was recorded in NAdSW (**Table 4**).

Fluxes of CO_2 at Seawater-Atmosphere Interface

The air-sea CO_2 fluxes in the different seasons computed using W14 and N00 gas transfer velocity are presented in **Table 5**.

The absolute difference between the two parameterizations ranged between 0.5 and 2.3 mmol m^{-2} day^{-1}. During the investigated period FCO_2 ranged from −14.9 mmol m^{-2} day^{-1} to 2.5 mmol m^{-2} day^{-1} adopting W14 parameterization, or from −15.2 mmol m^{-2} day^{-1} to 3.0 mmol m^{-2} day^{-1} according to N00 parameterization. FCO_2 were strongly influenced by riverine inputs, temperature and wind speed. The study area acted as a sink of carbon dioxide during winter, spring and autumn; and as a source of CO_2 during summer (**Table 5**). A clear influx of CO_2 toward the sea was detected in January 2017 in all the stations of the transect (average FCO_2 = −14.2 ± 0.5 mmol m^{-2} day^{-1} −W14 or −14.8 ± 0.5 mmol m^{-2} day^{-1} -N00). This condition was driven by the low seawater temperature, which led to pCO_2 undersaturation in surface waters with respect to the atmosphere, in synergy with a wind speed 8.2 m s^{-1}, more than

TABLE 2 | Results of Kruskal–Wallis rank sum test and multiple comparison test among seasons on different physico-chemical parameters.

	Temperature (°C)		Salinity		A_T (μmol kg^{-1})		pH_T *in situ*		TCO_2 (μmol kg^{-1})	
Kruskal–Wallis rank sum test	χ^2	***p*-value**	χ^2	***p*-value**	χ^2	***p*-value**	χ^2	***p*-value**	χ^2	***p*-value**
	262.17	<0.001	13.99	0.002	3.98	0.26	206.71	<0.001	41.15	<0.001
Multiple comparison test (*p* = 0.05)	**Obs.dif**	**Critical.dif**	**Obs.dif**	**Critical.dif**	**Obs.dif**	**Critical.dif**	**Obs.dif**	**Critical.dif**	**Obs.dif**	**Critical.dif**
Autumn–spring	**83.80**	42.27	14.64	42.27	12.88	41.94	36.09	41.83	**46.67**	41.83
Autumn–summer	**44.92**	42.27	10.75	42.27	9.98	41.83	**65.56**	41.72	37.98	41.72
Autumn–winter	**195.93**	42.27	38.87	42.27	18.77	41.94	**156.43**	41.94	**48.49**	41.94
Spring–summer	**128.71**	42.27	3.89	42.27	22.86	41.83	**101.65**	41.72	**84.65**	41.72
Spring–winter	**112.14**	42.27	**53.51**	42.27	5.89	41.94	**120.35**	41.94	1.82	41.94
Summer–winter	**240.85**	42.27	**49.62**	42.27	28.75	41.83	**222.00**	41.83	**86.47**	41.83

	AOU (μmol kg^{-1})		Ω_{ar}		β_{TCO2}		β_{AT}	
Kruskal–Wallis rank sum test	χ^2	***p*-value**	χ^2	***p*-value**	χ^2	***p*-value**	χ^2	***p*-value**
	68.03	<0.001	44.61	<0.001	41.14	<0.001	41.01	<0.001
Multiple comparison test (*p* = 0.05)	**Obs.dif**	**Critical.dif**	**Obs.dif**	**Critical.dif**	**Obs.dif**	**Critical.dif**	**Obs.dif**	**Critical.dif**
Autumn–spring	**125.92**	42.27	**52.67**	41.83	**53.73**	41.83	**53.41**	27.45
Autumn–summer	**94.82**	42.27	20.97	41.72	19.09	41.72	19.31	27.38
Autumn–winter	**86.55**	42.27	**70.85**	41.94	**67.12**	41.94	**66.90**	27.53
Spring–summer	31.09	42.27	**73.64**	41.72	**72.82**	41.72	**72.73**	27.38
Spring–winter	39.36	42.27	18.18	41.94	13.39	41.94	13.48	27.53
Summer–winter	8.27	42.27	**91.82**	41.83	**86.21**	41.83	**86.21**	27.45

In bold the pair of seasons significantly different.

the double of the mean wind speed of all the other months. The months with the most relevant flux of CO_2 from the sea to the atmosphere were April 2015, just in the offshore stations (mean FCO_2 = 2.3 ± 0.2 mmol m^{-2} day^{-1}-W14; or 2.8 ± 0.2 mmol m^{-2} day^{-1}-N00), and July 2016, except station SJ108 (mean FCO_2 = 0.8 ± 0.4 mmol m^{-2} day^{-1}-W14; or 1.2 ± 0.5 mmol m^{-2} day^{-1}-N00). A different seasonal pattern between stations located close to the Po River mouth and offshore stations was

TABLE 3 | Buffer factors (R, β_{TCO2}, β_{AT}) and aragonite saturation state (Ω_{ar}).

Parameters	Season	*n*	Mean	Minimum	Maximum	Std. Dev.
R	Winter	93	10.72	9.12	11.22	0.26
	Spring	94	10.75	8.67	12.46	0.92
	Summer	95	10.19	8.72	13.27	1.12
	Autumn	94	10.53	9.42	13.80	1.07
β_{TCO2}	Winter	93	0.26	0.25	0.34	0.01
	Spring	94	0.27	0.22	0.34	0.03
	Summer	95	0.28	0.21	0.34	0.03
	Autumn	94	0.27	0.20	0.31	0.03
β_{AT}	Winter	93	−0.29	−0.39	−0.27	0.01
	Spring	94	−0.29	−0.39	−0.24	0.04
	Summer	95	−0.31	−0.38	−0.22	0.04
	Autumn	94	−0.30	−0.34	−0.21	0.03
Ω_{ar}	Winter	93	3.20	2.93	4.99	0.23
	Spring	94	3.34	2.43	5.33	0.69
	Summer	95	3.73	2.17	5.21	0.76
	Autumn	94	3.43	2.03	4.15	0.53

Statistical summary in the different seasons. Number of data, mean, minimum, maximum and standard deviation (Std. Dev.) are reported.

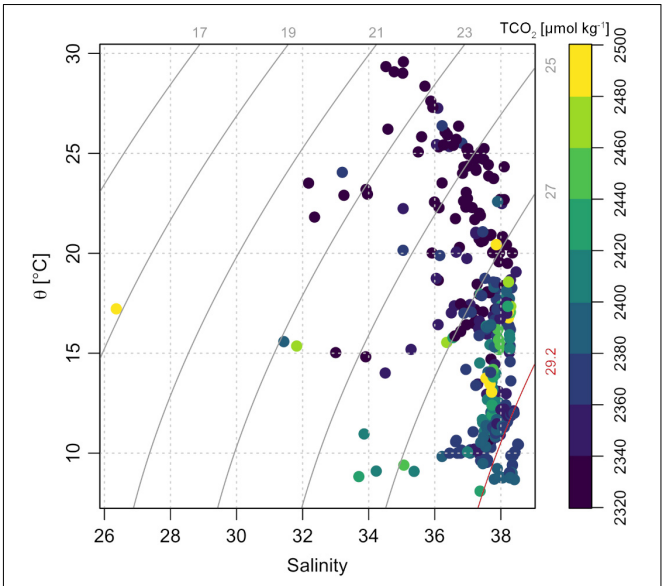


FIGURE 8 | Potential temperature – salinity plot with isopycnes. The color scale represents dissolved inorganic carbon (TCO_2) concentration. The plot was made using the R package oce (Kelley, 2018).

evident. In March 2015 all the stations acted as a sink, whereas in April 2015 the two stations closer to the river acted as a CO_2 sink, with an average FCO_2 of -2.3 ± 1.2 mmol m^{-2} day^{-1}-W14; or -2.8 ± 1.5 mmol m^{-2} day^{-1}-N00, and the other stations of the transect acted as a CO_2 source. This was probably due to an increase of Chl-a and nutrients in the stations inside the river plume, and to an increase of 4°C and a decrease of Chl-a 0.9 μg L^{-1} in the offshore stations, with respect to the previous month. In October 2016 on the contrary, all the stations of the transect acted as a CO_2 sink (mean $FCO_2 = -2.7 \pm 0.9$ mmol m^{-2} day^{-1}-W14; or -2.9 ± 1.0 mmol m^{-2} day^{-1}-N00) except SJ101 that acted as a source of carbon dioxide (1.92.0 mmol m^{-2} day^{-1}-W14; or mmol m^{-2} day^{-1}-N00) due to higher temperature with respect to the adjacent stations.

Future Coastal Acidification

Considering the IPCC RCP 8.5 scenario, business as usual for the year 2100, the atmospheric pCO_2 is projected to reach the value of 910 μatm and global mean sea surface temperature is expected to increase by 2.58°C. Under this scenario and without the effect of biological processes (**Figure 9**, air-equilibrated CO_2 condition) the pH_T is expected to decrease by approximately 0.3 in the northern Adriatic (warm bottom water pH_T = 7.798, NAdSW pH_T = 7.806). In the same way, the Ω_{ar} is expected to decline by about 1.3 units, reaching the value of 2.02 in the warm bottom waters and 2.15 in NAdSW. Respiration of organic matter leads to carbon dioxide production, which results in a greater reduction of pH_T and Ω_{ar}. By considering the warm bottom waters with a mean AOU equal to that measured in our study (AOU = 68 μmol kg^{-1}), pH_T and Ω_{ar} are expected to reach the mean value of 7.679 and 1.58 respectively for the year 2100. The pH_T and Ω_{ar} levels could be further reduced by stronger respiration events, as detected in warm bottom waters during autumn (AOU = 144 μmol kg^{-1}), which could determine strong acidification conditions (pH_T = 7.529) and Ω_{ar} very close to saturation level (Ω_{ar} = 1.15). In the NAdSW the future decline of pH and Ω_{ar} is less extreme, thanks to the predominance of photosynthetic activity that reduces the anthropogenic CO_2 levels at the surface. Therefore, with average AOU levels detected for the NAdSW (−14 μmol kg^{-1}) the acidification in the 2100 could be less marked: pH_T = 7.829 and Ω_{ar} = 2.25. This trend could be further enhanced during events of high primary production (AOU = −181 μmol kg^{-1}) which would rise the pH and carbonate saturation level far away from critical acidification conditions (pH_T = 8.060 and Ω_{ar} = 3.51).

Biogeochemical Processes Driving Carbonate System Seasonal Variation

Analysis of the relationship between $nTCO_2$ and nA_T can provide useful insights into the dominant biogeochemical processes that drive the carbonate system seasonal variation (Borges et al., 2003; Krumins et al., 2013; Sippo et al., 2016; Saderne et al., 2019). The slope of the regression between nA_T and $nTCO_2$ follows a stoichiometric relationship that is informative of a specific metabolic pathway (**Figure 10**). Assuming that organic matter has the Redfield Ratio C: N: P, the slopes for the main biogeochemical processes that occur in the water column or at the sediment-water interface are: aerobic respiration = −0.2, primary production = +0.2, denitrification = 0.8, nitrification = −1, calcium carbonate dissolution = 2.0, calcium carbonate precipitation = −2.0 (Krumins et al., 2013).

In the northern Adriatic, the nA_T-$nTCO_2$ regression was statistically significant for all the seasons (F-statistic > 81.93, $p < 0.001$, $R^2 > 0.47$) and the slopes ranged from 0.80 to 1.23, indicating a combination of biogeochemical processes that affect the carbonate system of the study area. The influence of biological activity on the carbonate system was very clear during summer (**Figure 10B**). By assuming winter as a reference period (slope = 1.15), due to its very low biological activity, and considering water column as a two layer system (i.e., surface and bottom waters), in summer the nA_T-$nTCO_2$ slope of the surface (1.38) was greater than the winter one by about 0.23, which indicate a relevant influence of the primary production (+0.2). On the other hand, the nA_T-$nTCO_2$ slope of the bottom waters (0.42) was 0.73 lower with respect to the winter reference. This could be interpreted as a combined effect of aerobic respiration (−0.2) and nitrification (−1.0), due to high concentration of AOU (46 μmol kg^{-1}) and nitrate close to the bottom (**Supplementary Figure 9**). Therefore, nitrification could be considered a relevant metabolic pathway in this system. The correlation between pH_T and Chl-a, was positive in autumn ($p < 0.01$) and negative in summer ($p < 0.0001$). The negative correlation in summer was probably due to remineralization processes under the pycnocline. Indeed, considering just the upper layer (down to 10 m depth) the correlation was positive ($p < 0.01$) while below 20 m it is still significantly negative ($p < 0.001$). The predominance of remineralization is also confirmed by the negative correlations ($p < 0.01$) between pH_T and inorganic nutrients. This underscores the strong decoupling of production and respiration processes driven by seasonal stratification of water column in the area.

DISCUSSION

Po River Role on Carbonate System Variability

Po River discharges are the major source of freshwater (47.17 km^3 yr^{-1}) and nutrients in the northern Adriatic basin (Cozzi and Giani, 2011), and, in concurrence with meteorological forcing, they drive a seasonal stratification regime and circulation pattern (Spillman et al., 2007). The distribution of land nutrients discharged by the river, follows the structure of the haline fronts, spreading, in particular conditions, along the entire basin (Russo and Artegiani, 1996) and showing a complex patchiness characterized by horizontal and vertical gradients (Cozzi et al., 2002). This patchiness strongly influences the distribution of the carbonate system parameters in all seasons and was also subject to the strength of the WAC and the EAC, which influences the spreading of riverine discharges.

The salinity seasonal average along the transect was low during spring–summer and high during autumn–winter (**Table 1**),

TABLE 4 | Summary of temperature, salinity, density anomaly (σ_t), chlorophyll *a* (Chl-a), total alkalinity (A_T), pH_T at *in situ* temperature, dissolved inorganic carbon (TCO_2) and apparent oxygen utilization (AOU) in the different water types.

Water type	*n*	Temperature (°C)	Salinity	σ_t (kg m^{-3})	Chl-a (μg L^{-1})	A_T (μmol kg^{-1})	pH_T	TCO_2 (μmol kg^{-1})	AOU (μmol kg^{-1})
NAdDW	26	9.64 ± 1.04	38.29 ± 0.18	29.58 ± 0.17	0.72 ± 0.18	2672 ± 8	8.180 ± 0.011	2378 ± 13	−0 ± 5
		(8.68; 12.12)	(37.80; 38.53)	(29.20; 29.85)	(0.48; 1.06)	(2652; 2690)	(8.139; 8.196)	(2344; 2398)	(−11; 15)
Warm bottom waters	49	16.00 ± 1.60	37.99 ± 0.30	28.04 ± 0.40	0.62 ± 0.41	2657 ± 29	8.014 ± 0.087	2402 ± 52	68 ± 43
		(13.06; 20.44)	(37.10; 38.30)	(26.83; 28.82)	(0.13; 1.81)	(2625; 2801)	(7.830; 8.145)	(2313; 2510)	(−10; 144)
NAdSW	192	17.35 ± 5.90	36.74 ± 1.65	26.62 ± 2.14	0.97 ± 1.14	2685 ± 40	8.138 ± 0.063	2350 ± 42	−14 ± 24
		(8.10; 29.58)	(26.36; 38.36)	(18.85; 29.72)	(0.09; 6.58)	(2621; 2920)	(8.023; 8.415)	(2234; 2582)	(−180; 48)

Data are presented as average ± standard deviation and (minimum; maximum).

following the same seasonal pattern of other riverine influenced areas of the NAd (e.g., Gulf of Trieste, Ingrosso et al., 2016a). The general negative relationship between A_T and salinity is consistent with the findings of Cantoni et al. (2012) and Ingrosso et al. (2016a; 2016b), highlighting that the NAd acts as a source of alkalinity for the Mediterranean Sea. The A_T-salinity correlation in the surface layer differed between seasons. A_T values extrapolated at S = 0 varied from 2892 μmol kg^{-1} in autumn to 3616 μmol kg^{-1} in winter, while the TCO_2 values at S = 0 varied from 2242.79 μmol kg^{-1} in summer to 2889.11 μmol kg^{-1} in winter, indicating a potential high temporal variability of riverine A_T and TCO_2 end-member. The supply of nutrients sustains the large productivity of the coastal zone especially during winter and spring, triggering intense phytoplankton blooms. This biological effect is underscored by the correlation between Chl-*a* and pCO_2.

Buffer Capacity and Saturation State

Despite the marked seasonal "acidification," the carbonate system never reached the undersaturation state: even with the lowest pH_T value (7.830) the saturation state of aragonite (Ω_{ar}) was 2.04. This was probably due to the freshwater discharges, which increases the ratio alkalinity dissolved inorganic carbon and thus the buffering capacity of the system, as demonstrated by the lower Revelle factors at lower salinities. As the ratio A_T/TCO_2 in the oceans decreases in response to the uptake of atmospheric CO_2, the buffer factors will decrease consequently. The net result will be a less efficient absorption of CO_2 from the atmosphere and a greater sensitivity of $[CO_2]$, $[H^+]$, and Ω to environmental changes (Egleston et al., 2010). NAd was supersaturated with respect to both calcite and aragonite along the whole water column. Interestingly an opposite trend was found in bottom waters with respect to the upper water column. The buffer capacity and the saturation state were higher in winter and lower in summer in bottom waters, yet in surface they were lower in winter and higher in summer. This difference is due to the influence of riverine inputs and temperature at surface, which causes shifts in acid-base dissociation constants and a consequent increase of the buffering capacity. At the bottom, however, the segregation of seawater under the pycnocline causes an increase of respiration and organic matter remineralization processes, that lowers pH_T and increases the concentration of TCO_2, decreasing the saturation state of aragonite and the buffering capacity of the system. The 2-year average of the Revelle factor that we found (10.5 ± 0.9) is in agreement with previous studies for the Adriatic Sea (Luchetta et al., 2010; Álvarez et al., 2014; Ingrosso et al., 2016a). This underscores the high uptake capacity for the anthropogenic CO_2 of the NAd (Ingrosso et al., 2017).

TABLE 5 | Seasonal air-sea CO_2 fluxes (FCO_2) calculated using different gas transfer velocities: Wanninkhof (2014)-W14 and Nightingale et al. (2000)-N00.

FCO_2 (mmol m^{-2} d^{-1}) calculated using different gas transfer velocities				
	Winter	Spring	Summer	Autumn
W14	−5.5 ± 5.9	−0.6 ± 1.0	0.4 ± 0.3	−0.8 ± 0.8
N00	−6.3 ± 5.9	−0.8 ± 1.2	0.5 ± 0.4	−1.0 ± 0.7

Data are presented as average ± standard deviation.

Air-Sea CO_2 Fluxes Spatial and Temporal Variations

According to the "continental shelf pump" hypothesis (Tsunogai et al., 1999), winter cooling depresses seawater pCO_2 below saturation, whereas nutrients inputs and biological CO_2 drawdown in summer and the vertical export of organic matter and horizontal export of CO_2, maintain the CO_2 sink of the continental shelf throughout the year (Bates, 2006). On the basis of data available from 87 continental shelves, Chen et al. (2013) stated that most of the temperate regions are CO_2-undersaturated and absorb CO_2 from the atmosphere during most of the year. Summer is an exception as seawater warming increases pCO_2 and surface water becomes a weak CO_2 source (Chen et al., 2012). Our data show that the NAd acts prevalently as CO_2 sink with higher influxes during the winter cooling, as found in specific areas of NAd (i.e., the Gulf of Trieste, Cantoni et al., 2012; Turk et al., 2013; Ingrosso et al., 2016a) and in the modeling study which considered the whole sub-basin (Cossarini et al., 2015b). In agreement with the findings of Chen et al. (2013), the CO_2 effluxes are limited to the stratified period, mainly in spring or summer, as also found in the Gulf of Trieste by Ingrosso et al. (2016b). CO_2 fluxes were directly correlated with the sea surface temperature (W14: $r = 0.62$; $p < 0.0001$; $n = 96$ – N00: $r = 0.64$; $p < 0.0001$; $n = 96$), this highlights the importance of the thermodynamic driver, that leads to effluxes at high temperatures, and influxes when temperatures are lower.

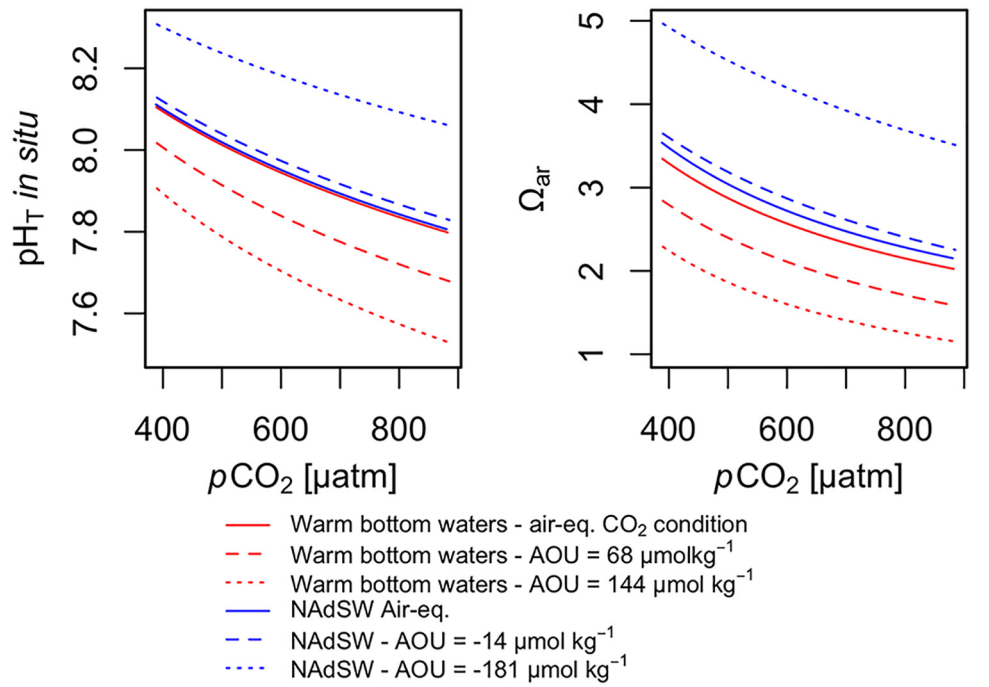


FIGURE 9 | Simulated effect of atmospheric pCO_2 increase on pH_T and Ω_{ar} considering: (1) warm bottom waters and NAdSW at air-equilibrated CO_2 conditions (without biological effect), (2) warm bottom waters with medium AOU (68 µmol kg^{-1}) and high AOU (144 µmol kg^{-1}) (3) NAdSW with medium AOU (–14 µmol kg^{-1}) and high AOU (–181 µmol kg^{-1}). All the modeled future changes in carbonate chemistry were calculated assuming a mean sea surface warming of 2.58°C for the year 2100 under the RCP 8.5 scenario.

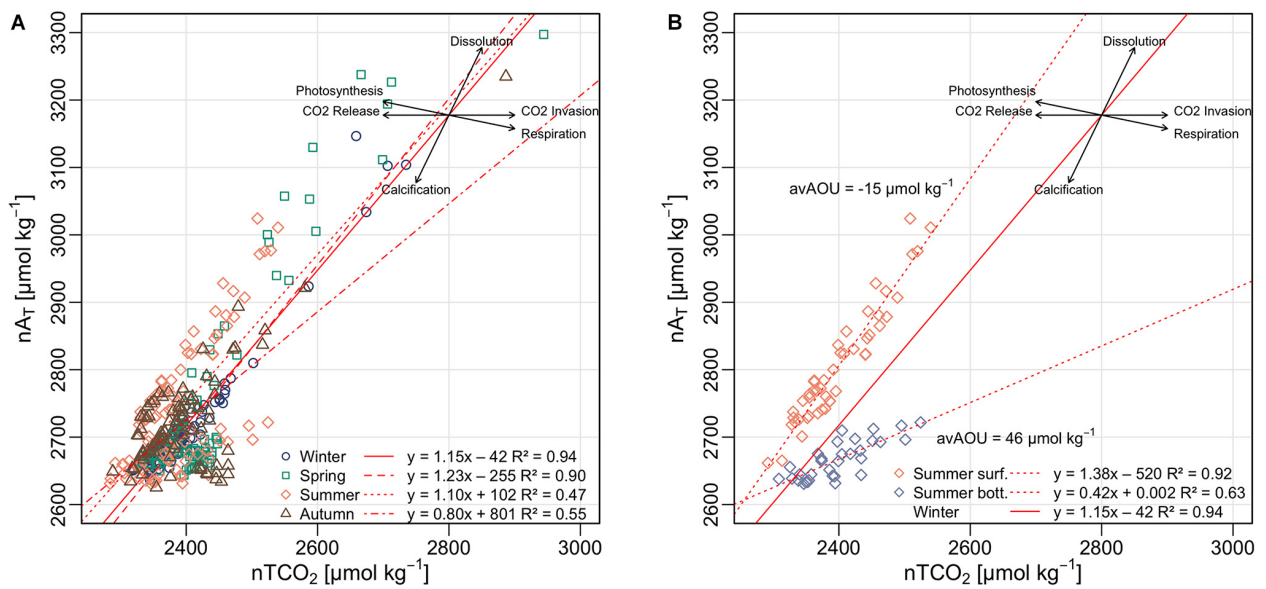


FIGURE 10 | (A) nA_T – $nTCO_2$ relationship in the NAd and linear regressions of the different seasons. **(B)** Summer nA_T – $nTCO_2$ relationship of the surface and bottom waters. The vectors are represented following the stoichiometric ratios of the main biogeochemical processes in order to visualize the dominant processes driving the CO_2 system.

If we consider an increase in temperature of 21.5°C (measured between winter and summer) and we keep all other factors constant, the mean pCO_2 of the shelf changes from 318 to 762 µatm. This demonstrates that temperature causes an increase of 21 µatm °C^{-1}, pCO_2 increases by 6.6% for an increase of 1°C, slightly higher than the 4.3% for an increase of 1°C

reported by Takahashi et al. (1993), for a salinity range of 34–36 and a temperature range of 2–20°C. This emphasizes that the thermodynamic effect is relevant to determine the supersaturation in summer, and thus causing the system to be a source of carbon dioxide, if the heterotrophic processes prevail. The strongest influxes were observed near the Po River delta, at station SJ108 (mean of all the investigated period in station SJ108: $FCO_2 = -2.4 \pm 3.9$ mmol m^{-2} day^{-1}-W14; or -2.8 ± 4.3 mmol m^{-2} day^{-1}-N00), in agreement with the "continental shelf pump" hypothesis, whereas the effluxes occurred mostly in the central eastern waters. The observed spatial variations are attributable to a higher drawdown due to higher phytoplankton biomass in the western waters, influenced by riverine inputs. Measurements performed in the northernmost part of the NAd, the Gulf of Trieste, showed that Bora wind, a typical cold ENE wind, can determine higher daily inflows of the CO_2 from the atmosphere ($-22.6/-24.2$ mmol m^{-2} day^{-1}, Turk et al., 2013). Moreover, during winter a significant correlation between TCO_2 and temperature was found ($r = -0.69$; $p < 0.0001$; $n = 93$) in surface waters, evidencing the role of the dense water formation in the CO_2 absorption and transport southwards. Our average efflux in summer was 0.4 ± 0.34 mmol m^{-2} day^{-1}-W14; or 0.5 ± 0.4 mmol m^{-2} day^{-1}-N00, with a peak of 1.4 mmol m^{-2} day^{-1}-W14; or 2.0 mmol m^{-2} day^{-1}-N00 observed in July 2016 in station SJ101, but higher values, up to 11.4 ± 7.6 mmol m^{-2} day^{-1} where reported for the Gulf of Trieste (Turk et al., 2013). The strongest efflux was measured in April 2015, in the offshore waters, while the waters in the river plume acted as a sink. This difference was probably due to a prevalence of the biological processes in stations SJ108 and SJ101, inside the plume, where the input of Chl-a and nutrients supported primary production, and a predominance of the thermodynamic effect in the offshore waters, where temperature increased by 4°C with respect to the previous month. This hypothesis is supported by the T/B ratio analysis, that resulted higher than 1 (temperature effect stronger than the biological processes) in the central-eastern waters and below 1 in the coastal waters near the Po delta.

Future Trends

Estimating the long-term trend and variability of pH and saturation state in coastal areas is challenging and different modeling approaches have been used. Sunda and Cai (2012) showed that in waters like the Gulf of Mexico hypoxic zone, the combined effects of increasing anthropogenic pCO_2 and respiratory increases in TCO_2 on pH will be more than additive and will exert a synergistic interaction. While in areas like the Baltic Sea hypoxic zone there will be no synergism, but the effect of both processes together in lowering pH will still be worse than from either process alone (Sunda and Cai, 2012). With a similar methodological approach, Feely et al. (2018) demonstrated that pH and Ω_{ar} decrease related to the future anthropogenic CO_2 emissions will be more severe in coastal waters affected by respiration-induced hypoxia. Shen et al. (2020), by using a retrospective coupled hydrodynamic-biogeochemical model simulations, demonstrated that pH variability in the mid Chesapeake Bay was primarily influenced by acidification and biological process, while river basification along with acidification played a key role in regulating the long-term Ω_{ar} variability. Our parameterization is in good agreement with these previous works, since we found a strong influence of biological processes on the future acidification in the northern Adriatic. Following the RCP 8.5 scenario, in warm bottom waters respiration could reach the mean value of 7.679 and 1.58 for pH_T and Ω_{ar}, respectively. This acidification could be magnified by stronger respiration events, as detected during autumn, leading to lower pH_T values and to a Ω_{ar} very close to the saturation level. This could be enhanced by the increase in hypoxic events and may cause significant negative impacts on ecosystems that are already stressed. On the other hand, in the NAdSW the future decline of pH and Ω_{ar} is less extreme, due to the predominance of photosynthetic activity, which reduces the anthropogenic CO_2 levels at the surface. In this case, acidification in 2100 could be less marked and such condition could be further enhanced during events of high primary production that serve to raise the pH and carbonate saturation level far away from acidification conditions. However, it is important to consider our simulation as a simple estimation of the future CO_2 system in the NAd based on physical-chemical constraints and considering different biological thresholds. Ocean acidification, warming and increased stratification will drive changes in marine microbial community (Dutkiewicz et al., 2015) and in their metabolic processes. We did not consider this aspect into our simulation since it is not yet known how these changes will alter global ecosystem functions, such as net primary production/respiration and export or air-sea gas exchange (Doney et al., 2020).

Comparison With Other Areas

CO_2 Exchanges With the Atmosphere

Our CO_2 influxes measured during winter 2017 (-14.2 ± 0.4 mmol m^{-2} day^{-1} -W14 or -14.8 ± 0.5 mmol m^{-2} day^{-1} -N00), when north-easterly Bora wind was blowing in the Gulf of Trieste, are comparable with the estimates of other temperate regions under freshwater influence. The Aegean Sea as a whole absorbs CO_2 during winter at a rate ranging from -6.2 to -11.8 mmol m^{-2} day^{-1} (Krasakopoulou et al., 2009), while in the East China Sea in winter a -13.7 ± 5.7 mmol m^{-2} day^{-1} was measured (Chou et al., 2011). Estimating a mean annual flux based on the mean values for each season, we would get -0.4 mol m^{-2} y^{-1}-W14 or -0.5 mol m^{-2} y^{-1}-N00 for the year 2014/2015 and -0.8 mol m^{-2} y^{-1}-W14 or -0.9 mol m^{-2} y^{-1}-N00 for the year 2016/2017 which ranges from 35 to 85% (W14) or from 44 to 94% (N00)of the previous estimates of -1.0 and -1.06 mol m^{-2} y^{-1} made by Catalano et al. (2014) and by Cossarini et al. (2015b), respectively. This CO_2 absorption from the atmosphere is of the same order of magnitude as the -1.8 mol m^{-2} y^{-1} estimated for the north-west European shelf by Kitidis et al. (2019) and as the -0.8 mol m^{-2} y^{-1} estimated for the Biscay Bay (Borges et al., 2006). Similar annual fluxes were reported also in the Otaru Bay (Sakamoto et al., 2008), in the New Jersey coast (Boehme et al., 1998) and in the East China Sea (Wang et al., 2000). Our results also underline that in NAd, as in other temperate areas as East China Sea, west European continental shelves (Tsunogai et al., 1999; Thomas et al., 2004;

Borges, 2005; Bozec et al., 2005; Prowe et al., 2009), lower estuary of Guadalquivir Estuary and the Bay of Cádiz (Ribas-Ribas et al., 2011a), seawater pCO_2 remains below atmospheric CO_2 values for most of the year and these shelves are net CO_2 sinks.

Our fluxes are, however, about five folds lower than the annual estimate of the Chukchi Sea shelf (Bates, 2006). This is due to the lower temperature and higher productivity of the Arctic region.

Carbonate System

Coastal ecosystems display a complex set of interacting processes that drive high pH variability over time.

An analysis of long-term pH measured in coastal waters around the world showed that seasonal variability could be as high as 1.4 pH units (Carstensen and Duarte, 2019). High-latitudes sites with low alkalinity buffering display largest seasonal ranges in pH, typically up to 1 unit as found in Baltic Sea and Danish straits (Carstensen et al., 2018; Carstensen and Duarte, 2019). Whereas pH in low- mid-latitude sites and with high alkalinity buffering typically vary less than 0.4 over the year. In our study despite high total alkalinity, the seasonal variability in pH was 0.59, which is a variation comparable with the one found in the gulf of Trieste by Cantoni et al. (2012). High seasonal change in temperature (ranging from 8.10 to 29.58°C) and strong decoupling of production and respiration processes likely explain this result. Effect of mixing on observed pH variability is, however, expected to be low, because coastal ecosystems receiving freshwater with $A_T > 1200\ \mu mol\ kg^{-1}$ have modest variation in pH across a salinity gradient (Carstensen and Duarte, 2019). The effect of mixing on pH is typically more pronounced in sites with low and medium buffering, such as Northern Baltic Sea (Beldowski et al., 2010) and Chesapeake Bay (Brodeur et al., 2019) respectively, where changing salinity overall controls the mean pH levels.

Metabolic imbalance between production and respiration processes, which remove or add dissolved inorganic carbon respectively, is a key driver of pH change in this coastal ecosystem. Under present day conditions, biological metabolism results in a pH change of 0.59 in NAd (from 8.415 at the surface to 7.830 at the bottom waters). The metabolic-driven chemistry change of the carbonate system expected for 2100 (under RCP 8.5 scenario) is similar to present day condition, with pH variability range of 0.53 (8.060 to 7.529). This pH range is more pronounced than the one observed in the Gulf of Mexico, where oxidation-driven increases in CO_2 result in pH_T decreases of 0.46 under present day condition, and 0.51 under for 2100 under RCP 8.5 scenario (Feely et al., 2018).

In our study area a negative correlation between A_T and salinity was found, especially in samplings close to flood events, showing that riverine inputs increase seawater total alkalinity. Negative A_T-salinity correlations were also found in coastal areas of the Mediterranean Sea (Schneider et al., 2007; Cossarini et al., 2015a), in the North Aegean Sea (Krasakopoulou et al., 2017) and in the study of Ribas-Ribas et al. (2011b) near the mouth of the Guadalquivir River, Bay of Càdiz.

Thanks to the high A_T and TCO_2 riverine inputs the NAd was supersaturated, during all the seasons, with respect to both calcite and aragonite throughout the whole water column, in contrast to other coastal area where strong undersaturation (<0.6) is reached, as found in the Baltic Sea (Tyrrell et al., 2008), Long Island Sound (Wallace et al., 2014), and the lower St. Lawrence estuary (Mucci et al., 2011). In Chesapeake Bay for example Ω_{ca} is <1 in the bottom waters of the upper bay, but it is >1 in the lower bay (Brodeur et al., 2019). In the northern Gulf of Mexico indeed, notwithstanding a high acidification with pH in bottom waters of 7.85 or less, the Ω_{ar} is 2.63 ± 0.25 (Laurent et al., 2017) due to high alkalinity brought by Mississippi River (Wang et al., 2013).

CONCLUSION

This work presents temporal and seasonal variability of the CO_2 system in the waters of the NAd based 16 cruises.

Po River influence contributes to maintain a gradient from coast to offshore. The freshwater discharges in NAd increase total alkalinity and total inorganic carbon, changing the buffer capacity of the system. In surface waters the riverine contribution enhances the buffer capacity, which is also positively correlated to temperature and reaches the higher values in summer.

Phytoplankton blooms triggered by river-borne nutrients fertilization, contribute to increase the pH in the upper part of the water column. The riverine discharges contribute also to enhance the saturation state in surface waters. With the progression of the sea warming and the formation of a marked pycnocline, in bottom waters the respiration and degradation of organic matter decrease pH, that reaches the minimum values in autumn.

The strong seasonal variability of the saturation state between winter and summer is mainly driven by the effect of temperature on the carbonate solubility, however, due to the CO_2 increase under the pycnocline, the lowest values are reached during summer and autumn.

It is remarkable that in NAd, notwithstanding the high buffer capacity of the system, there is a high seasonal variability of pH (0.59) and also within the same season the pH variation between surface and bottom waters is of a similar amplitude. This finding highlight that the system could be very sensitive to changes in the balance between primary productivity and respiration processes.

The analysis of CO_2 fluxes emphasized that the NAd acts overall as a sink of CO_2, but with marked seasonal and spatial variations driven by wind strength, riverine inputs, temperature and biological processes. The CO_2 absorbed from the atmosphere in the NAd contributes to the transport of anthropogenic CO_2 in the deeper layers of the Mediterranean Sea through the dense waters formed in the area. The estimated annual influxes of CO_2 are comparable to the fluxes measured in other temperate continental shelves.

The estimation of the future seawater CO_2 chemistry for the end of the century highlights that, under business-as-usual scenario and without the effect of biological processes, pH_T could decline by 0.3 and aragonite saturation by 1.3. Moreover, in the warm bottom waters during high respiration events Ω_{ar} could reach the value of 1.15. This value is very close to the saturation level and could negatively affect the marine biota, especially calcifying organisms, and subsequently lead to repercussions on the marine ecosystem.

Our results are important to advance the knowledge and the understanding of the global carbon cycle and will likely be of use for future studies to address potential changes in the NAd coastal acidification.

DATA AVAILABILITY STATEMENT

Data are available at PANGAEA®. Doi: https://doi.pangaea.de/10.1594/PANGAEA.916129.

AUTHOR CONTRIBUTIONS

LU, MG, and GI wrote the draft. MG and TD conceived the study and the experimental design. LU performed the CO_2 system analyses. TD collected the data from the field survey. SP performed the analyses of the pCO_2 in air. All the authors interpreted all data, revised and approved the final version of the manuscript.

FUNDING

This research was carried out in the framework of Acid.It project financially supported by the Italian Ministry of Education, University and Research, and to other projects supported by Croatian Ministry of Science, Education and Sports.

ACKNOWLEDGMENTS

The authors would like to thank the crew of R/V Vila Velebita, and all the other CMR-RBI colleagues who contributed to sampling and analysis. Mauro Bastianini of CNR-ISMAR for the meteorological data measured at the oceanographic tower "Acqua Alta", Damiano Sferlazzo, Alcide di Sarra, Tatiana Di Iorio, and Francesco Monteleone of ENEA for their contributions, Giulia Cataluffi who contributed to the CO_2 system analyses, Erin Cox for the assistance and support during the writing. Measurements at Lampedusa contribute to the Integrated Carbon Observation System (ICOS), European Multidisciplinary Seafloor and water-column Observatory (EMSO), and Aerosols, Clouds and Trace Gases (ACTRIS) Research Infrastructures. We are in debt to Gianpiero Cossarini and Giorgio Bolzon of OGS for the Alka Open Cell 2.0 software development. We kindly acknowledge the three reviewers for the constructive comments that improved the quality of the manuscript.

SUPPLEMENTARY MATERIAL

The Supplementary Material for this article can be found online at: https://www.frontiersin.org/articles/10.3389/fmars.2020.00679/full#supplementary-material

REFERENCES

Álvarez, M., Sanleón-Bartolomé, H., Tanhua, T., Mintrop, L., Luchetta, A., and Cantoni, C. (2014). The CO2 system in the Mediterranean Sea: a basin wide perspective. *Ocean Sci.* 10, 69–92. doi: 10.5194/os-10-69-2014

Anthony, K. R. N., Kleypas, J. A., and Gattuso, J. P. (2011). Coral reefs modify their seawater carbon chemistry–implications for impacts of ocean acidification. *Glob, Chan. Biol.* 17, 3655–3666. doi: 10.1111/j.1365-2486.2011.02510.x

Artegiani, A., Bregant, D., Paschini, E., Pinardi, N., Raicich, F., and Russo, A. (1997). The adriatic sea general circulation: part I. Air-sea interaction and water mass structure; Part II. Baroclinic circulation structure. *J. Phys. Oceanogr.* 27, 1492–1532.

Bates, N. R. (2006). Air-sea CO2 fluxes and the continental shelf pump of carbon in the Chukchi Sea adjacent to the Arctic Ocean. *J. Geophys. Res.* 111, 1–21. doi: 10.1029/2005JC003083

Bates, N. R., Astor, Y. M., Church, M. J., Currie, K., Dore, J. E., and González-Dávila, M. (2014). A time-series view of changing ocean chemistry due to ocean uptake of anthropogenic CO2 and ocean acidification. *Oceanogr.* 27, 126–141. doi: 10.5670/oceanog.2014.16

Bednaršek, N., Harvey, C. J., Kaplan, I. C., Feely, R. A., and Mozina, J. (2016). Pteropods on the edge: cumulative effects of ocean acidification, warming, and deoxygenation progress. *Oceanography* 145, 1–24. doi: 10.1016/j.pocean.2016.04.002

Beldowski, J., Löffler, A., Schneider, B., and Joensuu, L. (2010). Distribution and biogeochemical control of total CO2 and total alkalinity in the Baltic Sea. *J. Mar, Syst.* 81, 252–259. doi: 10.1016/j.jmarsys.2009.12.020

Bensi, M., Cardin, V., Rubino, A., Notarstefano, G., and Poulain, P. M. (2013). Effects of winter convection on the deep layer of the Southern Adriatic Sea in 2012. *J. Geophys. Res.* 118, 6064–6075. doi: 10.1002/2013JC009432

Bockmon, E. E., and Dickson, A. G. (2014). A seawater filtration method suitable for total dissolved inorganic carbon and pH analyses. *Limnol. Oceanogr. Methods* 12, 191–195. doi: 10.4319/lom.2014.12.191

Boehme, S. E., Sabine, C. L., and Reimers, C. E. (1998). CO2 fluxes from a coastal transect: a time-series approach. *Mar. Chem.* 63, 49–67. doi: 10.1016/s0304-4203(98)00050-4

Borges, A. V. (2005). Do we have enough pieces of the jigsaw to integrate CO2 fluxes in the coastal ocean? *Estuaries* 28, 3–27. doi: 10.1007/bf02732750

Borges, A. V., Djenidi, S., Lacroix, G., Théate, J., Delille, B., and Frankignoulle, M. (2003). Atmospheric CO2 flux from mangrove surrounding waters. *Geophys. Res. Lett.* 30:1558. doi: 10.1029/2003GL017143

Borges, A. V., and Gypens, N. (2010). Carbonate chemistry in the coastal zone responds more strongly to eutrophication than ocean acidification. *Limnol. Oceanogr.* 55, 346–353. doi: 10.4319/lo.2010.55.1.0346

Borges, A. V., Schiettecatte, L. S., Abril, G., Delille, B., and Gazeau, F. (2006). Carbon dioxide in European coastal waters. *Estuar. Coast. Shelf Sci.* 70, 375–387. doi: 10.1016/j.ecss.2006.05.046

Bozec, Y., Thomas, H., Elkalay, K., and de Baar, H. J. W. (2005). The continental shelf pump for CO2 in the North Sea—evidence from summer observation. *Mar. Chem.* 93, 131–147. doi: 10.1016/j.marchem.2004.07.006

Brodeur, J. R., Chen, B., Su, J., Xu, Y.-Y., Hussain, N., and Scaboo, K. M. (2019). Chesapeake bay inorganic carbon: spatial distribution and seasonal variability. *Front. Mar. Sci.* 6:99. doi: 10.3389/fmars.2019.00099

Broecker, W. S., Takahashi, T., Simpson, H. J., and Peng, T. H. (1979). Fate of fossil fuel carbon dioxide and the global carbon budget. *Science* 206, 409–418. doi: 10.1126/science.206.4417.409

Brussaard, C. P. D., Gast, G. J., van Duyl, F. C., and Riegman, R. (1996). Impact of phytoplankton bloom magnitude on a pelagic microbial food web. *Mar, Ecol. Prog. Ser.* 144, 211–221. doi: 10.3354/meps144211

Cai, W.-J., Hu, X., Huang, W.-J., Murrell, M. C., Lehrter, J. C., and Lohrenz, S. E. (2011). Acidification of subsurface coastal waters enhanced by eutrophication. *Nat. Geosci.* 4, 766–770. doi: 10.1038/ngeo1297

Cantoni, C., Luchetta, A., Celio, M., Cozzi, S., Raicich, F., and Catalano, G. (2012). Carbonate system variability in the Gulf of Trieste (North Adriatic Sea). *Estuar. Coast. Shelf Sci.* 115, 51–62. doi: 10.1016/j.ecss.2012.07.006

Carstensen, J., Chierici, M., Gustafsson, B. G., and Gustafsson, E. (2018). Long-term and seasonal trends in estuarine and coastal carbonate systems. *Glob. Biogeochem. Cycles* 32, 497–513. doi: 10.1002/2017gb005781

Carstensen, J., and Duarte, C. M. (2019). Drivers of pH Variability in Coastal Ecosystems. *Environ. Sci. Technol.* 53, 4020–4029. doi: 10.1021/acs.est.8b03655

Catalano, G., Azzaro, M., Bastianini, M., Bellucci, L. G., Bernardi Aubry, F., and Bianchi, F. (2014). The Carbon budget in the northern Adriatic Sea, a winter case study. *J. Geophys. Res* 119, 1399–1417. doi: 10.1002/2013JG002559

Chan, F., Barth, J. A., Blanchette, C. A., Byrne, R. H., Chavez, F., and Cheriton, O. (2017). Persistent spatial structuring of coastal ocean acidification in the California Current System. *Sci. Rep.* 7:2526. doi: 10.1038/s41598-017-02777

Chen, C.-T. A., Huang, T.-H., Chen, Y.-C., Bai, Y., He, X., and Kang, Y. (2013). Air–sea exchanges of CO2 in the world's coastal seas. *Biogeosciences* 10, 6509–6544. doi: 10.5194/bg-10-6509-2013

Chen, C. T. A., Huang, T. H., Fu, Y. H., Bai, Y., and He, X. (2012). Strong sources of CO2 in upper estuaries become sinks of CO2 in large river plumes. *Curr. Opin. Env. Sust.* 4, 179–185. doi: 10.1016/j.cosust.2012.02.003

Chou, W.-C., Gong, G.-C., Tseng, C.-M., Sheu, D. D., Hung, C.-C., and Chang, L.-P. (2011). The carbonate system in the East China Sea in winter. *Mar. Chem.* 123, 44–55. doi: 10.1016/j.marchem.2010.09.004

Cossarini, G., Lazzari, P., and Solidoro, C. (2015a). Spatiotemporal variability of alkalinity in the Mediterranean Sea. *Biogeosciences* 12, 1647–1658. doi: 10.5194/bg-12-1647-2015

Cossarini, G., Querin, S., and Solidoro, C. (2015b). The continental shelf carbon pump in the northern Adriatic Sea (Mediterranean Sea): influence of wintertime variability. *Ecol. Modelling* 314, 118–134. doi: 10.1016/j.ecolmodel.2015.07.024

Cozzi, S., and Giani, M. (2011). River water and nutrient discharges in the Northern Adriatic Sea: current importance and long term changes. *Cont. Shelf Res.* 31, 1881–1893. doi: 10.1016/j.csr.2011.08.010

Cozzi, S., Ibáñez, C., Lazar, L., Raimbault, P., and Giani, M. (2019). Flow regime and nutrient-loading trends from the largest south european watersheds: implications for the productivity of mediterranean and Black Sea's Coastal Areas. *Water* 11:1. doi: 10.3390/w11010001

Cozzi, S., Lipizer, M., Cantoni, C., and Catalano, G. (2002). Nutrient balance in the ecosystem of the north western Adriatic Sea. *Chem. Ecol.* 18, 1–12. doi: 10.1080/02757540212685

DelValls, T. A., and Dickson, A. G. (1998). The pH of buffers based on 2-amino-2-hydroxymethyl-1,3-propanediol ('tris') in synthetic sea water. *Deep Sea Res Part I* 45, 1541–1554. doi: 10.1016/s0967-0637(98)00019-3

Dickson, A. G. (1990). Standard potential of the reaction – AgCl(S) +1/2h-2(g)=Ag(S) + HCl(Aq) and the standard acidity constant of the ion HSO4- in synthetic sea water from 273.*15* to 318.15 K. *J. Chem. Thermodyn.* 22, 113–127. doi: 10.1016/0021-9614(90)90074-z

Dickson, A. G., and Goyet, C. (1994). *Handbook of Methods for the Analysis of the Various Parameters of the Carbon dioxide System of Sea Water. Version 2*. DOE (No. ORNL/CDIAC-74. Oak Ridge, TN: Oak Ridge National Lab.

Dickson, A. G., Sabine, C. L., and Christian, J. R. (eds) (2007). *Guide to Best Practices for Ocean CO2 Measurements*, Vol. 3. Sidney: North Pacific Marine Science Organization.

Doney, S. C., Busch, D. S., Cooley, S. R., and Kroeker, K. J. (2020). The impacts of ocean acidification on marine ecosystems and reliant human communities. *Annu. Rev. Environ. Resour.* 45, 11.1–11.30.

Doney, S. C., and Schimel, D. (2007). Carbon and climate system coupling on timescales from the precambrian to the anthropocene. *Annu. Rev. Environ. Resour.* 32, 31–66. doi: 10.1146/annurev.energy.32.041706.124700

Duarte, C. M., and Cerbrian, J. (1996). The fate of marine autotrophic production. *Limnol. Oceanogr.* 41, 1758–1766. doi: 10.4319/lo.1996.41.8.1758

Duarte, C. M., Hendriks, I. E., Moore, T. S., Olsen, Y. S., Steckbauer, A., and Ramajo, L. (2013). Is ocean acidification an open ocean syndrome? understanding anthropogenic impacts on seawater pH. *Estuar. Coast.* 36, 221–236. doi: 10.1007/s12237-013-9594-3

Dutkiewicz, S., Morris, J. J., Follows, M. J., Scott, J., Levitan, O., Dyhrman, S. T., et al. (2015). Impact of ocean acidification on the structure of future phytoplankton communities. *Nature Climate Change* 5, 1002–1006. doi: 10.1038/nclimate2722

Egleston, E. S., Sabine, C. L., and Morel, F. M. M. (2010). Revelle revisited: buffer factors that quantify the response of ocean chemistry to changes in DIC and alkalinity. *Glob. Biogeochem. Cycles* 24:GB1002. doi: 10.1029/2008GB003407

Fassbender, A. J., Sabine, C. L., and Feifel, K. M. (2016). Consideration of coastal, carbonate chemistry in understanding biological calcification. *Geophys. Res. Lett.* 43, 4467–4476. doi: 10.1002/2016GL068860

Feely, R. A., Okazaki, R. R., Cai, W. J., Bednaršek, N., Alin, S. R., and Byrne, R. H. (2018). The combined effects of acidification and hypoxia on pH and aragonite saturation in the coastal waters of the California current ecosystem and the northern Gulf of Mexico. *Cont. Shelf Res.* 152, 50–60. doi: 10.1016/j.csr.2017.11.002

Font, J., Béranger, K., Bryden, H., Budillon, G., Fuda, J. L., and Gačič, M. (2009). *Executive Summary of CIESM Workshop 38 "Dynamics of Mediterranean Deep Waters*. Monaco: CIESM Workshop Monographs.

Friis, K., Körtzinger, A., and Wallace, D. W. R. (2003). The salinity normalization of marine inorganic carbon chemistry data. *Geophys. Res. Lett.* 30:1085. doi: 10.1029/2002GL015898

Gačič, M., Lascaratos, A., Manca, B. B., and Mantziafou, A. (2001). "Adriatic deep water and interaction with the eastern mediterranean Sea," in *Physical Oceanography of the Adriatic Sea*, eds B. Cushman-Roisin, M. Gačič, P. M. Poulain, and A. Artegiani, (Dordrecht: Springer), doi: 10.1007/978-94-015-9819-4_4

Gattuso, J.-P., Epitalon, J.-M., and Lavigne, H. (2015). *Seacarb: Seawater Carbonate Chemistry. R Package Version 3.0.14*. Available online at: https://cran.r-project.org/web/packages/seacarb/index.html

Gattuso, J.-P., Frankignoulle, M., and Wollast, R. (1998). Carbon and carbonate metabolism in coastal aquatic ecosystems. *Annu. Rev, Ecol. Syst.* 29, 405–434. doi: 10.1146/annurev.ecolsys.29.1.405

Gattuso, J.-P., Lee, K., Rost, B., and Schulz, K. (2010). "Approaches and tools to manipulate the carbonate chemistry," in *Guide for Best Practices in Ocean Acidification Research and Data Reporting*, eds U. Riebesell, V. J. Fabry, L. Hansson, and J.-P. Gattuso, (Luxembourg: Office for Official Publications of the European Union).

Hassoun, A. E. R., Raad, N., Fakhri, M., Abboud-Abi Saab, M., Gemayel, E., and De Carlo, E. (2019). The carbonate system of the eastern-most mediterranean sea, levantine sub-basin: variations and drivers. *Deep Sea Res. II* 164, 54–73. doi: 10.1016/j.dsr2.2019.03.008

Hofmann, A. F., Peltzer, E. T., Walz, P. M., and Brewer, P. G. (2011). Hypoxia by degrees: establishing definitions for a changing ocean. *Deep Sea Res. I* 58, 1212–1226. doi: 10.1016/j.dsr.2011.09.004

Hopkins, T. S., Artegiani, A., Kinder, C., and Pariante, R. (1999). "A discussion of the northern Adriatic circulation and flushing as determined from the ELNA hydrography," in *The Adriatic Sea*, Vol. 32, eds T. S. Hopkins, A. Artegiani, G. Cauwet, D. Degobbis, and A. Malej, (Brussel: European Commission), 85–106.

Ingrosso, G., Bensi, M., Cardin, V., and Giani, M. (2017). Anthropogenic CO2 in a dense water formation area of the Mediterranean Sea. *Deep Sea Res. I* 123, 118–128. doi: 10.1016/j.dsr.2017.04.004

Ingrosso, G., Giani, M., Comici, C., Kralj, M., Piacentino, S., and De Vittor, C. (2016a). Drivers of the carbonate system seasonal variations in a Mediterranean gulf. *Estuar. Coast. Shelf Sci.* 168, 58–70. doi: 10.1016/j.ecss.2015.11.001

Ingrosso, G., Giani, M., Cibic, T., Karuza, A., Kralj, M., and Del Negro, P. (2016b). Carbonate chemistry dynamics and biological processes along a river–sea gradient (Gulf of Trieste, northern Adriatic Sea). *J. Mar. Syst.* 155, 35–49. doi: 10.1016/j.jmarsys.2015.10.013

IPCC, (2013). "The physical science basis," in *Contribution of Working Group I the Fifth Assessment Report of the Intergovernmental Panel on Climate Change*, eds T. F. Stocker, D. Qin, G.-K. Plattner, M. Tignor, S. K. Allen, J. Boschung, et al. (Cambridge: Cambridge University Press), 1535.

IPCC, (2014). "Climate change 2014: synthesis report," in *Contribution of Working Groups I, II and III to the Fifth Assessment Report of the Intergovernmental Panel on Climate Change*, eds R. K. Pachauri, and L. A. Meyer, (Geneva: IPCC), 151.

IPCC, (2019). "Technical Summary," in *IPCC Special Report on the Ocean and Cryosphere in a Changing Climate*, eds H.-O. Pörtner, D. C. Roberts, V. Masson-Delmotte, P. Zhai, M. Tignor, E. Poloczanska, et al. (Geneva: IPCC).

Ivančič, I., and Degobbis, D. (1984). An optimal manual procedure for ammonia analysis in natural waters by the indophenol blue method. *Water Res.* 18, 1143–1147. doi: 10.1016/0043-1354(84)90230-6

Kapsenberg, L., Alliouane, S., Gazeau, F., Mousseau, L., and Gattuso, J.-P. (2017). Coastal ocean acidification and increasing total alkalinity in the northwestern Mediterranean Sea. *Ocean Science* 13, 411–426. doi: 10.5194/os-13-411-2017

Kapsenberg, L., and Hofmann, G. E. (2016). Ocean pH time-series and drivers of variability along the northern Channel Islands. California, USA. *Limnol. Oceanogr.* 61, 953–968. doi: 10.1002/lno.10264

Kelley, D. E. (2018). *The OCE Package. In Oceanographic Analysis With R*. New York, NY: Springer, 91–101.

Kitidis, V., Shutler, J. D., Ashton, I., Warren, M., Brown, I., and Findlay, H. (2019). Winter weather controls net influx of atmospheric CO2 on the northwest European shelf. *Sci. Rep.* 9:20153. doi: 10.1038/s41598-019-56363-5

Kleypas, J. A., Buddemeier, R. W., Archer, D., Gattuso, J.-P., Langdon, C., and Opdyke, B. N. (1999). Geochemical consequences of increased atmospheric carbon dioxide on coral reefs. *Science* 284, 118–120. doi: 10.1126/science.284.5411.118

Krasakopoulou, E., Rapsomanikis, S., Papadopoulos, A., and Papathanassiou, E. (2009). Partial pressureand air–sea CO2 flux in the aegean sea during February 2006. *Cont. Shelf Res.* 29, 1477–1488. doi: 10.1016/j.csr.2009.03.015

Krasakopoulou, E., Souvermezoglou, E., Giannoudi, L., and Goyet, C. (2017). Carbonate system parameters and anthropogenic CO2 in the North Aegean Sea during October 2013. *Cont. Shelf Res.* 147, 69–81. doi: 10.1016/j.csr.2017.04.002

Krumins, V., Gehlen, M., Arndt, S., Van Cappellen, P., and Regnier, P. (2013). Dissolved inorganic carbon and alkalinity fluxes from coastal marine sediments: model estimates for different shelf environments and sensitivity to global change. *Biogeosciences* 10, 371–398. doi: 10.5194/bg-10-371-2013

Kruskal, W. H., and Wallis, W. A. (1952). Use of ranks in one-criterion variance analysis. *J. Am. Stat. Assoc.* 47, 583–621. doi: 10.1080/01621459.1952.10483441

Kwiatkowski, L., and Orr, J. C. (2018). Diverging seasonal extremes for ocean acidification during the twenty-first century. *Nat. Clim. Change* 8, 141–145. doi: 10.1038/s41558-017-0054-0

Laurent, A., Fennel, K., Cai, W. -J., Huang, W. -J., Barbero, L., and Wanninkhof, R. (2017). Eutrophication-induced acidification of coastal waters in the northern Gulf of Mexico: insights into origin and processes from a coupled physical-biogeochemical model. *Geophys. Res. Lett.* 44, 946–956. doi: 10.1002/2016GL071881

Luchetta, A., Cantoni, C., and Catalano, G. (2010). New observations of CO2 induced acidification in the Northern Adriatic Sea, over the last quarter century. *Chem. Ecol.* 26, 1–17. doi: 10.1080/02757541003627688

Lueker, T., Dickson, A. G., and Keeling, C. D. (2000). Ocean pCO2 calculated from dissolved inorganic carbon, alkalinity, and equations for K1 and K2: validation based on laboratory measurements of CO2 in gas and seawater at equilibrium. *Mar. Chem.* 70, 105–119. doi: 10.1016/s0304-4203(00)00022-0

Lüthi, D., Le Floch, M., Bereiter, B., Blunier, T., Barnola, J.-M., and Siegenthaler, U. (2008). High-resolution carbon dioxide concentration record 650,000–800,000?years before present. *Nature* 453, 379–382. doi: 10.1038/nature06949

Manca, B., and Giorgetti, A. (1999). "Flow patterns of the main water masses across transversal areas in the Southern Adriatic Sea: seasonal variability," in *The Eastern Mediterranean as a Laboratory Basin for the Assessment of Contrasting Ecosystems*, eds P. Malanotte-Rizzoli, and V. N. Eremeev, (Netherlands: Kluwer Acad), 495–506. doi: 10.1007/978-94-011-4796-5_37

Millero, F. J., Lee, K., and Roche, M. (1998). Distribution of alkalinity in the surface waters of the major oceans. *Mar. Chem.* 60, 111–130. doi: 10.1016/s0304-4203(97)00084-4

Mucci, A., Starr, M., Gilbert, D., and Sundby, B. (2011). Acidification of Lower Sy. Lawrence Estuary Bottom Waters. *Atmos. Ocean* 49, 206–218. doi: 10.1080/07055900.2011.599265

Nightingale, P. D., Malin, G., Law, C. S., Watson, A. J., Liss, P. S., Liddicoat, M. I, et al. (2000). In situ evaluation of air-sea exchange parametrizations using novel conservative and volatile tracers. *Global Biogeochem. Cycles* 14, 373–387. doi: 10.1029/1999gb900091

Orr, J. C. (2011). "Recent and future changes in ocean carbonate chemistry," in *Ocean Acidification*, eds J. P. Gattuso, and L. Hansson, (Oxford: Oxford Univ. Press), 41–66.

Orr, J. C., Epitalon, J.-M., Dickson, A. G., and Gattuso, J.-P. (2018). Routine uncertainty propagation for the marine carbon dioxide system. *Mar. Chem.* 207, 84–107. doi: 10.1016/j.marchem.2018.10.006

Parsons, T. R., Maita, Y., and Lalli, C. M. (1984). *A Manual of Chemical and Biological Methods for Seawater Analysis*. Oxford: Pergamon Press.

Pierrot, D., Lewis, E., and Wallace, D. W. R. (2006). *MS Excel Program Developed for CO2 System Calculations. Technical Report*. Oak Ridge, TN: U.S. Department of Energy.

Poulain, P. M. (2001). Adriatic Sea surface circulation as derived from drifter data between 1990 and 1999. *J. Mar. Syst.* 29, 3–32. doi: 10.1016/s0924-7963(01)00007-0

Provoost, P., van Heuven, S., Soetaert, K., Laane, R. W. P. M., and Middleburg, J. J. (2010). Seasonal and long term changes in pH in the Dutch coastal zone. *Biogeosciences* 7, 3869–3878. doi: 10.5194/bg-7-3869-2010

Prowe, A. E. F., Thomas, H., Pätsch, J., Kühn, W., Bozec, Y., Schiettecatte, L.-S., et al. (2009). Mechanisms controlling the air–sea CO2 flux in the North Sea. *Cont. Shelf Res.* 29, 1801–1808. doi: 10.1016/j.csr.2009.06.003

Pugnetti, A., Camatti, E., Mangini, O., Morabito, G., Oggioni, A., and Saggiomo, V. (2006). Phytoplankton production in Italian freshwater and marine ecosystems: state of the art and perspectives. *Chem. Ecol.* 22(Suppl. 1), S49–S69.

Querin, S., Cossarini, G., and Solidoro, C. (2013). Simulating the formation and fate of dense water in a midlatitude marginal sea during normal and warm winter conditions. *J. Geophys. Res.: Oceans* 118, 1–16. doi: 10.1002/jgrc.20092

R Core Team, (2016). *R: A Language and Environment for Statistical Computing*. Vienna: R Foundation for Statistical Computing.

Raicich, F., and Colucci, R. R. (2019). A near-surface sea temperature time series from Trieste, northern Adriatic Sea (1899–2015). *Earth Syst. Sci. Data* 11, 761–768. doi: 10.5194/essd-11-761-2019

Raicich, F., Malacic, V., Celio, M., Giaiotti, D., Cantoni, C., and Colucci, R. R. (2013). Extreme air-sea interactions in the Gulf of Trieste (North Adriatic) during the strong Bora event in winter 2012. *J. Geophys. Res.* 118, 5238–5250. doi: 10.1002/jgrc.20398

Redfield, A. C., Ketchum, B. H., and Richards, F. A. (1963). "The influence of organisms on the chemical composition of seawater," in *The Sea*, ed. M. N. Hill, (New York, NY: Interscience), 26–77.

Revelle, R., and Suess, H. E. (1957). Carbon dioxide exchange between atmosphere and ocean and the question of an increase of atmospheric CO2 during the past decades. *Tellus* 9, 18–27. doi: 10.3402/tellusa.v9i1.9075

Ribas-Ribas, M., Gómez-Parra, A., and Forja, J. M. (2011a). Air–sea CO2 fluxes in the north-eastern shelf of the Gulf of Cádiz (southwest Iberian Peninsula). *Mar. Chem.* 123, 56–66. doi: 10.1016/j.marchem.2010.09.005

Ribas-Ribas, M., Gómez-Parra, A., and Forja, J. M. (2011b). Seasonal distribution of the inorganic carbon system and net ecosystem production in the north eastern shelf of the Gulf of Cadiz (Southwest Iberian Peninsula). *Cont. Shelf Res.* 31, 1931–1942. doi: 10.1016/j.csr.2011.09.003

Russo, A., and Artegiani, A. (1996). Adriatic Sea hydrography. *Sci. Mar.* 60, 33–43.

Saderne, V., Baldry, K., Anton, A., Agustí, S., and Duarte, C. M. (2019). Characterization of the CO2 system in a coral reef, a seagrass meadow, and a mangrove forest in the central Red Sea. *J. Geophys. Res.* 124, 7513–7528. doi: 10.1029/2019JC015266

Sakamoto, A., Watanabe, Y. W., Osawa, M., Kido, K., and Noriki, S. (2008). Time series of carbonate system variables off Otaru coast in Hokkaido, Japan. *Estuar. Coast. Shelf Sci.* 79, 377–386. doi: 10.1016/j.ecss.2008.04.013

Schlitzer, R. (2018). *Ocean Data View, Version 5.1.5*. Available at http://odv.awi.de (accessed June 03, 2020).

Schneider, A., Wallace, D. W. R., and Kortzinger, A. (2007). Alkalinity of the Mediterranean Sea. *Geophys. Res. Lett.* 34:L15608. doi: 10.1029/2006GL028842

Shapiro, S. S., and Wilk, M. B. (1965). An analysis of variance test for normality (complete samples). *Biometrika* 52, 591–611. doi: 10.1093/biomet/52.3-4.591

Shen, C., Testa, J. M., Li, M., and Cai, W. J. (2020). Understanding anthropogenic impacts on pH and aragonite saturation in Chesapeake Bay: insights from a 30-year model study. *J. Geophys. Res.: Biogeosciences* 125:e2019JG005620. doi: 10.1029/2019JG005620

Siegel, S., and Castellan, N. J. Jr. (1988). *Nonparametric Statistics for the Behavioral Sciences*. New York, NY: McGraw-Hill Int, 213–214.

Sippo, J. Z., Maher, D. T., Tait, D. R., Holloway, C., and Santos, I. R. (2016). Are mangroves drivers or buffers of coastal acidification? Insights from alkalinity and dissolved inorganic carbon export estimates across a latitudinal transect. *Global Biogeochem. Cycles* 30, 753–766. doi: 10.1002/2015GB005324

Soetaert, K., Petzoldt, T., and Meysman, F. (2015). *Marelac: Tools for Aquatic Sciences. R Package Version 2.1.5*.

Spillman, C. M., Imberger, J., Hamilton, D. P., Hipsey, M. R., and Romero, J. R. (2007). Modelling the effects of Po River discharge, internal nutrient cycling

and hydrodynamics on biogeochemistry of the Northern Adriatic Sea. *J. Mar. Syst.* 68, 167–200. doi: 10.1016/j.jmarsys.2006.11.006

Sunda, W. G., and Cai, W.-J. (2012). Eutrophication induced CO2-acidification of subsurface coastal waters: interactive effects of temperature, salinity, and atmospheric pCO2. *Environ. Sci. Technol.* 46, 10651–10659. doi: 10.1021/es300626f

Supič, N., and Vilibic, I. (2006). Dense water characteristics in the northern Adriatic in the 1967-2000 interval with respect to surface fluxes and Po river discharge rates. *Estuar. Coast. Shelf Sci.* 66, 580–593. doi: 10.1016/j.ecss.2005.11.003

Takahashi, T., Olafsson, J., Goddard, J. G., Chipman, D. W., and Sutherland, S. C. (1993). Seasonal variation of CO2 and nutrients in the high-latitude surface oceans: a comparative study. *Global Biogeochem.Cycles* 7, 843–847.

Takahashi, T., Sutherlan, S. C., Sweeney, C., Poisson, A., Metzl, N., and Tilbrook, B. (2002). Global sea–air CO2 flux based on climatological surface ocean pCO2, and seasonal biological and temperature effects. *Deep-Sea Res. II* 49, 1601–1622. doi: 10.1016/s0967-0645(02)00003-6

Thomas, H., Bozec, Y., Elkalay, K., and De Baar, H. J. W. (2004). Enhanced open ocean storage of CO2 from shelf sea pumping. *Science* 304, 1005–1008. doi: 10.1126/science.1095491

Tsunogai, S., Watanabe, S., and Sato, T. (1999). Is there a "continental shelf pump" for the absorption of atmospheric CO2? *Tellus* 51B, 701–712. doi: 10.3402/tellusb.v51i3.16468

Turk, D., Book, J. W., and McGills, W. R. (2013). pCO2 and CO2 exchange during high bora winds in the Northern Adriatic. *J. Mar. Syst.* 11, 65–71. doi: 10.1016/j.jmarsys.2013.02.010

Tyrrell, T., Schneider, B., Charalampopoulou, A., and Riebesel, U. (2008). Coccolithophores and calcite saturation state in the Baltic and Black Seas. *Biogeosciences* 5, 485–494. doi: 10.5194/bg-5-485-2008

UNESCO, (1983). "Algorithms for computation of fundamental properties of seawater," in *UNESCO Technical Papers in Marine Science*, (Paris: UNESCO).

UNESCO, (1986). "Progress on oceanographic tables and standards 1983 e 1986, Work and recommendations of the Unesco/SCOR/ICES/IAPSO Joint Panel," in *UNESCO Technical Papers in Marine Science*, (Paris: UNESCO).

Uppström, L. R. (1974). The boron/chlorinity ratio of deep-sea water from the Pacific Ocean. *Deep Sea Res.* 21, 161–162. doi: 10.1016/0011-7471(74)90074-6

van Vuuren, D., Edmonds, J., Kainuma, M., Riahi, K., Thomson, A., and Hibbard, K. (2011). The representative concentration pathways: an overview. *Clim. Change* 109, 5–31. doi: 10.1007/s10584-011-0148-z

Vilibič, I., Zemunik, P., Šepič, J., Dunič, N., Marzouk, O., Mihanovič, H., et al. (2019). Present climate trends and variability in thermohaline properties of the northern Adriatic shelf. *Ocean Sci.* 15, 1351–1362. doi: 10.5194/os-15-1351-2019

Wallace, R. B., Baumann, H., Grear, J. S., Aller, R. C., and Gobler, C. J. (2014). Coastal ocean acidification: the other eutrophication problem. *Estuar. Coast. Shelf Sci.* 148, 1–13. doi: 10.1016/j.ecss.2014.05.027

Wang, S. L., Chen, C. T. A., Hong, G. H., and Chung, C. S. (2000). Carbon dioxide and related parameters in the East China Sea. *Cont. Shelf Res.* 20, 525–544. doi: 10.1016/s0278-4343(99)00084-9

Wang, Z. A., Wanninkhof, R., Cai, W.-J., Byrne, R. H., Hu, X., and Peng, T.-H. (2013). The marine inorganic carbon system along the Gulf of Mexico and Atlantic coasts of the United States: insights from a transregional coastal carbon study. *Limnol. Oceanogr.* 58, 325–342. doi: 10.4319/lo.2013.58.1.0325

Wanninkhof, R. (2014). Relationship between wind speed and gas exchange over the ocean revisited. *Limnol. Oceanogr. Methods* 12, 351–362. doi: 10.4319/lom.2014.12.351

Weiss, R. F. (1974). Carbon dioxide in water and seawater: the solubility of a non-ideal gas. *Mar. Chem.* 2, 203–215. doi: 10.1016/0304-4203(74)90015-2

Zavatarelli, M., Raicich, F., Artegiani, A., Bregant, D., and Russo, A. (1998). Climatological Biogeochemical characteristics of the Adriatic Sea. *J. Mar. Syst.* 18, 227–263. doi: 10.1016/s0924-7963(98)00014-1

Zeebe, R. E., and Wolf-Gladrow, D. (2001). *CO2 in Seawater: Equilibrium, Kinetics, Isotopes*. Amsterdam: Elsevier Oceanography Series.

Conflict of Interest: The authors declare that the research was conducted in the absence of any commercial or financial relationships that could be construed as a potential conflict of interest.

Copyright © 2020 Urbini, Ingrosso, Djakovac, Piacentino and Giani. This is an open-access article distributed under the terms of the Creative Commons Attribution License (CC BY). The use, distribution or reproduction in other forums is permitted, provided the original author(s) and the copyright owner(s) are credited and that the original publication in this journal is cited, in accordance with accepted academic practice. No use, distribution or reproduction is permitted which does not comply with these terms.

frontiers in Marine Science

ORIGINAL RESEARCH
published: 12 November 2020
doi: 10.3389/fmars.2020.588465

Effects of Wind-Driven Lateral Upwelling on Estuarine Carbonate Chemistry

Ming Li[1], Renjian Li[1], Wei-Jun Cai[2], Jeremy M. Testa[3] and Chunqi Shen[3]*

[1] Horn Point Laboratory, University of Maryland Center for Environmental Science, Cambridge, MD, United States, [2] School of Marine Science and Policy, University of Delaware, Newark, DE, United States, [3] Chesapeake Biological Laboratory, University of Maryland Center for Environmental Science, Solomons, MD, United States

Estuaries are productive ecosystems that support extensive vertebrate and invertebrate communities, but some have suffered from an accelerated pace of acidification in their bottom waters. A major challenge in the study of estuarine acidification is strong temporal and spatial variability of carbonate chemistry resulting from a wide array of physical forces such as winds, tides and river flows. Most past studies of carbonate system dynamics were limited to the along channel direction, while lateral dynamics received less attention. Recent observations in Chesapeake Bay showed strong lateral asymmetry in the partial pressure of carbon dioxide (pCO_2) and air-sea CO_2 flux during a single wind event, but comparable responses to different wind events has yet to be investigated. In this work, a coupled hydrodynamic-carbonate chemistry model is used to understand wind-driven variability in the estuarine carbonate system. It is found that wind-driven lateral upwelling ventilates high DIC (Dissolved Inorganic Carbon) and CO_2 deep water and raises surface pCO_2, thereby modifying the air-sea CO_2 flux. The upwelling also advects low pH water onto the adjacent shoals and reduces the aragonite saturation state Ω_{arag} in these shallow water environments, producing large temporal pH fluctuations and low pH events. Regime diagrams are constructed to summarize the effects of wind events on temporal pH and Ω_{arag} fluctuations and the lateral gradients in DIC, pH, and pCO_2 in the estuary. This modeling study provides a mechanistic explanation for the observed wind-driven lateral variability in DIC and pCO_2 and reproduces large pH and Ω_{arag} fluctuations that could be driven by physical forcing. Given that current and historic mainstem Bay oyster beds are located in shallow shoals affected by this upwelling, a large fraction of the oyster beds (100–300 km^2) could be exposed to carbonate mineral under-saturated ($\Omega_{arag} < 1$) conditions during wind events. This effect should be considered in the management of acidification-sensitive species in estuaries.

Keywords: carbonate chemistry, air-sea CO_2 flux, pH, estuary, winds, upwelling, oyster

OPEN ACCESS

Edited by:
Xianghui Guo,
Xiamen University, China

Reviewed by:
Zhongming Lu,
Hong Kong University of Science and Technology, Hong Kong
Lei Ren,
Sun Yat-sen University, China

****Correspondence:***
Ming Li
mingli@umces.edu

Specialty section:
This article was submitted to Coastal Ocean Processes, a section of the journal Frontiers in Marine Science

Received: *28 July 2020*
Accepted: *14 October 2020*
Published: *12 November 2020*

Citation:
Li M, Li R, Cai W-J, Testa JM and Shen C (2020) Effects of Wind-Driven Lateral Upwelling on Estuarine Carbonate Chemistry. Front. Mar. Sci. 7:588465. doi: 10.3389/fmars.2020.588465

INTRODUCTION

Riverine water typically has lower dissolved inorganic carbon (DIC) and total alkalinity (TA) values and a higher DIC/TA ratio than seawater (Salisbury et al., 2008; Huang et al., 2015; Cai et al., 2021). Because of this difference between the river and ocean end members, distributions of TA, DIC, pCO_2 (partial pressure of carbon dioxide), and pH in estuaries feature strong gradients

in the along-channel direction (Cai and Wang, 1998; Borges and Gypens, 2010; Cai et al., 2011). In stratified estuaries, strong vertical gradients in DIC and pH also develop where phytoplankton photosynthesis in the surface euphotic layer consumes DIC and respiration of organic material in the bottom layer produces DIC (Feely et al., 2010; Cai et al., 2011, 2017). These strong horizontal and vertical gradients make estuarine carbonate chemistry susceptible to disruptions from physical forcing. Turbulent mixing generated by tides and winds may mix acidic bottom water upward, leading to large changes in the air-sea CO_2 flux (Cai et al., 2017; Paerl et al., 2018). Advection by tidal and wind driven currents across the horizontal gradient may cause large short-term pH fluctuations at fixed locations, which may add further stress to organisms for coping with extreme low pH events (Ribas-Ribas et al., 2013; Saderne et al., 2013; Pacellaa et al., 2018). There is an increasing recognition for the large temporal pH variability and extreme pH values in estuarine and coastal environments (Hofmann et al., 2011; Baumann et al., 2015; Baumann and Smith, 2018; Carstensen and Duarte, 2019), but most research has focused on metabolically driven pH fluctuations such as the diel photosynthesis/respiration cycle (Saderne et al., 2013; Baumann and Smith, 2018; Pacellaa et al., 2018). Relatively few studies have addressed how physical processes affect high-frequency carbonate chemistry in estuaries.

Wind-driven lateral upwelling is a well-known physical phenomenon in estuaries. Along-channel winds drive cross-channel transports via lateral Ekman transport in the surface layer of estuaries, leading to upwelling or downwelling flows at side boundaries and clockwise or counter-clockwise circulations in cross-channel sections. These lateral flows can transport momentum (Lerczak and Geyer, 2004; Scully et al., 2009), alter stratification (Lacy et al., 2003; Li and Li, 2011), and transport sediment (Geyer et al., 2001; Chen and Sanford, 2009). Using a numerical model of Chesapeake Bay, Li and Li (2012) found that the clockwise circulation generated under up-estuary winds is much stronger than the counterclockwise circulation generated under down-estuary winds. Xie et al. (2017) analyzed long-term mooring data at a cross-channel section in Chesapeake Bay and found that the lateral circulation strength increased linearly with wind speeds under up-estuary winds but was a parabolic and weaker function of wind speeds under down-estuary winds.

Wind-driven lateral circulation and upwelling can transport biologically important materials such as nutrients and oxygen between the deep channel and shallow shoals (Malone et al., 1986; Sanford et al., 1990; Reynolds-Fleming and Luettich, 2004; Wilson et al., 2008). In Chesapeake Bay, Malone et al. (1986) observed higher phytoplankton production over the flanks of the main channel relative to production over the channel and attributed it to nutrient exchanges by the lateral circulation. Episodic upwelling of hypoxic water from the deep channel to shallow shoals has been observed in several estuaries, including Mobile Bay (Loesch, 1960), the Neuse River (Eggleston et al., 2005), Long Island Sound (Wilson et al., 2008), and Chesapeake Bay (Sanford et al., 1990; Breitburg, 1992). These upwelling events have the potential to generate short-lived, but severely negative conditions for organisms residing in these otherwise favorable shallow habitats, where in extreme cases, flurries of organisms congregate near shorelines as the escape to the upwelled waters (e.g., a crab "jubilee"). In a modeling study of Chesapeake Bay, Scully (2010) showed that wind-driven lateral exchange of oxygen between well-oxygenated shallow shoals and hypoxic deep channel may be more important than direct turbulent mixing in supplying oxygen to the hypoxic deep channel.

CO_2 dynamics often mirror O_2 dynamics, since all chemical species are advected or diffused by the same physical processes (currents and mixing) while the production and consumption of DIC and O_2 are affected by common biological processes such as phytoplankton production and organic matter respiration. However, while surface-water O_2 equilibrates with the atmospheric concentration relatively quickly, surface-water pCO_2 is slow to adjust and rarely reaches equilibrium with respect to the atmospheric pCO_2 due to the buffering effect of a much greater DIC pool on aqueous CO_2 (Cai et al., 2020, 2021). Thus the effects of short-term wind effects may be different between O_2 and CO_2. Huang et al. (2019) made repeated measurements of temperature, salinity, and pCO_2 in surface waters at a cross-channel transect in the middle reach of Chesapeake Bay. They observed large temporal and spatial variations of pCO_2 during a northerly wind event. The air-sea CO_2 flux over the eastern one-third of this transect was 20–40% higher than the flux over the middle section whereas the CO_2 flux over the western one-third of this transect was 30% lower. Huang et al. (2019) hypothesized that northerly (down-estuary) winds generated upwelling on the eastern shore, enhancing the release of respired CO_2 from acidic subsurface water. This raises a question whether southerly (up-estuary) winds will generate higher pCO_2 on the western shoal and under what wind conditions this lateral upwelling mechanism is effective in generating the lateral asymmetry in the CO_2 flux. A related question is how this wind-driven lateral upwelling affects the overall carbonate chemistry in an estuary.

Our study site, Chesapeake Bay, is an ideal system to address these questions, given that it is a large eutrophic estuary with relatively low buffer capacity (Cai et al., 2017) and wind forcing is comparable to tidal forcing (Zhong and Li, 2006; **Figure 1A**). It stretches for about 320 km from the mouth of the Susquehanna River at Havre de Grace, Maryland to its seaward end at Cape Charles and Cape Henry, Virginia. It is shallow, with a mean water depth of 6.5 m. However, a deep paleochannel running in the north-south direction dominates the bathymetry in the middle reaches of the main Bay. Chesapeake Bay is a partially mixed estuary: vertical salinity differences of 2–8 stratify the water column (Carter and Pritchard, 1988). It features a two-layer circulation with speeds on the order of 0.1 m s^{-1} (e.g., Goodrich and Blumberg, 1991). Compared with other estuaries, tidal forcing in the Bay is relatively modest with tidal range rarely exceeding 1 m (Browne and Fisher, 1988). Winds are episodic with dominant periods of 2–7 days.

Recent observations have mapped out the distributions of DIC, TA, pCO_2, and pH in the main stem of Chesapeake Bay (Brodeur et al., 2019; Friedman et al., 2020). DIC and TA increased from surface to bottom and from north to south over

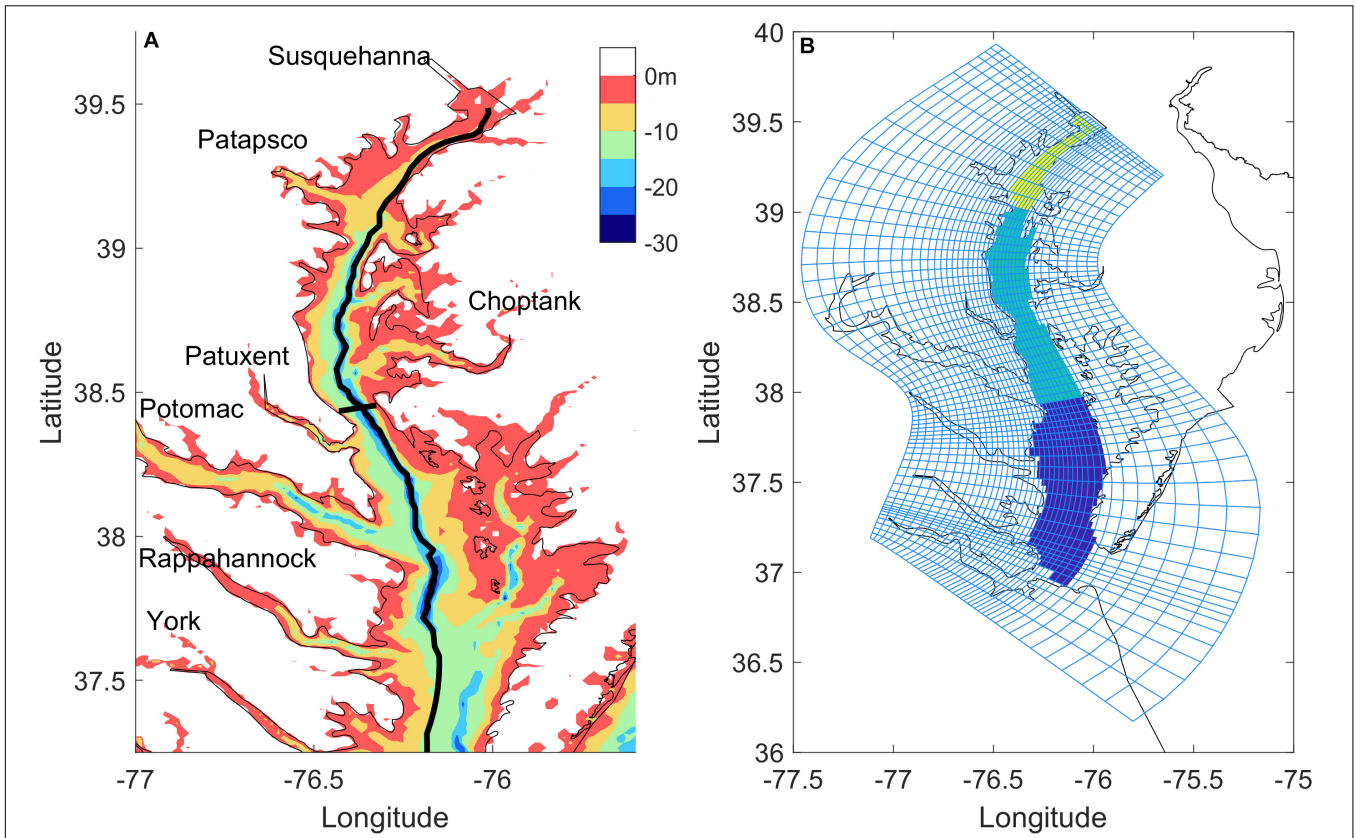


FIGURE 1 | Map showing bathymetry **(A)** and model grids **(B)** for Chesapeake Bay. The black lines in **(A)** marks the along-channel section and a cross-channel section in the mid-Bay used in later analysis. The shaded areas in **(B)** represent the upper, middle, and lower-Bay regions.

the course of 2016. Upper, mid-, and lower bay DIC and TA ranged from 1000 to 1300, 1300 to 1800, and 1700 to 1900 μmol kg^{-1}, respectively. The pH range was large, with the maximum value of 8.5 at the surface and the minimum as low as 7.1 in bottom water in the upper and mid-bay (Brodeur et al., 2019). Significant spatial variability of pCO_2 was observed throughout the mainstem, with net uptake of atmospheric CO_2 during each season in the middle Bay and weak seasonal outgassing of CO_2 near the outflow to the Atlantic Ocean (Chen et al., 2020; Friedman et al., 2020). High-frequency pH data from a moored sensor showed high frequency fluctuations of DIC, pH, and pCO_2 influenced by circulation and biological processes (Shadwick et al., 2019). Coupled hydrodynamic-biogeochemical-carbonate chemistry models (ROMS-RCA-CC) have been developed for Chesapeake Bay (Shen et al., 2019a). Shen et al. (2019a) focused their modeling analysis on the large-scale carbonate chemistry dynamics and validation against field observations. Furthermore, Shen et al. (2019b) and Shen et al. (2020) conducted 30-year hindcast simulations to examine ecosystem metabolism and carbon balance and investigated the anthropogenic impacts on pH and aragonite saturation state. This modeling study takes the next step to investigate how physical processes affect carbonate chemistry in this estuary, seeking to test the lateral upwelling mechanism over a range of wind conditions, in particular during the up-estuary wind condition not observed in Huang et al. (2019). It also builds upon previous studies of O_2 dynamics to further our understanding of CO_2 dynamics.

MATERIALS AND METHODS

To investigate how winds affected carbonate chemistry in Chesapeake Bay, we used coupled hydrodynamic-biogeochemical-carbonate chemistry models to conduct hindcast simulations. The coupled models have three sub-models. The hydrodynamic model, based on the Regional Ocean Modeling System (ROMS, Shchepetkin and McWilliams, 2005; Haidvogel et al., 2008), has 80 × 120 grid points (∼1 km resolution) in the horizontal direction and 20 vertical sigma layers, as shown in **Figure 1B** (Li et al., 2005). ROMS simulates water level, currents, temperature and salinity. The biogeochemical model is based on the Row-Column Aesop (RCA) model, and includes a water-column component (Isleib et al., 2007) and a sediment diagenesis component (Di Toro, 2001). RCA simulates pools of organic and inorganic nutrients, two phytoplankton groups, and dissolved oxygen concentrations (Testa et al., 2014). The carbonate chemistry (CC) model simulates DIC, TA, and mineral calcium carbonate (aragonite $CaCO_3$) (Shen et al., 2019a,b, 2020). DIC is consumed by phytoplankton growth/photosynthesis and calcium carbonate precipitation. The sources of DIC include air-sea CO_2

flux, phytoplankton respiration, oxidation of organic matter, calcium carbonate dissolution, sulfate reduction, and sediment-water fluxes. Calcium carbonate dissolution and precipitation is the primary source/sink for TA, but the contributions of several other biogeochemical processes (e.g., nitrification and sulfate reduction) to TA are also modeled (Shen et al., 2019a). Other carbonate chemistry parameters such as pH and pCO_2 are calculated from the CC model outputs using CO2SYS program (Lewis and Wallace, 1998).

The ROMS hydrodynamic model is forced by river flows at eight major tributaries, by wind stress and heat fluxes across the sea surface, and by sea level and climatology of temperature and salinity at the open boundary (Li et al., 2005, 2015; Cheng et al., 2013; Xie and Li, 2018). At the upstream boundary of the eight major tributaries, freshwater inflows measured at USGS gauging stations were prescribed. Tidal forcing at the open ocean boundary was decomposed into tidal constituents from TPXO7 (TOPEX/Poseidon) data-assimilative global tidal model (Egbert and Erofeeva, 2002). For non-tidal forcing at the offshore boundary, de-tided daily sea-level observations acquired at NOAA Duck station were used. Air-sea momentum and heat fluxes were computed by applying standard bulk formulae (Fairall et al., 2003) to NARR (North America Regional Reanalysis from National Center for Environmental Prediction) products.

The RCA biogeochemical model is forced by loads of dissolved and particulate materials from the eight major rivers. Riverine constituent concentrations for phytoplankton, silica, particulate and dissolved organic carbon, phosphorus, and nitrogen, and inorganic nutrients (ammonium, nitrate, phosphate) were obtained or derived from Chesapeake Bay Program biweekly monitoring data[1] as described in Testa et al. (2014). The ocean boundary concentrations were acquired from the World Ocean Atlas 2013 and Filippino et al. (2011). Atmospheric deposition was not considered.

The CC carbonate chemistry model is forced by the atmospheric CO_2, the riverine loads and offshore concentration of TA and DIC. Time series of TA measurements in riverine inputs were obtained from the USGS station in the Susquehanna and Potomac Rivers (Raymond et al., 2000). The riverine DIC concentrations were calculated through CO2SYS with the available TA and pH (Shen et al., 2020). The computed DIC is in very good agreement with the observed DIC when direct DIC measurements were made during the field cruises of 2016 (**Supplementary Figure S1**). Carbonate chemistry data for the other smaller tributaries were estimated using empirical relationships as functions of freshwater discharge (Shen et al., 2019a). TA at the ocean boundary was directly estimated with the empirical equation based upon salinity and temperature at the ocean boundary (Cai et al., 2010). DIC at the offshore boundary was calculated with the available TA, fCO_2 from SOCAT (Bakker et al., 2016), salinity and temperature using CO2SYS. The atmosphere pCO_2 was set to be 400 ppm.

Regional ocean modeling system was initialized with outputs from a hindcast simulation from 1 January to 31 December 2012. The initial conditions of RCA were based on Chesapeake Bay Program monitoring data in December 2012. Initial conditions for DIC and TA were calculated from the two-end member mixing model. Model hindcast simulation for this study lasted from 1 January to 31 December 2013.

The ROMS-RCA-CC models have been validated against a wide variety of observational data (e.g., Li et al., 2005, 2006, 2016; Zhong and Li, 2006; Testa et al., 2014; Xie and Li, 2018; Shen et al., 2019a,b, 2020; Ni et al., 2020). The ROMS hydrodynamic model has been validated against water level measurements at tidal gauge stations (Zhong and Li, 2006; Zhong et al., 2008), salinity and temperature time series at monitoring stations (Li et al., 2005; Ni et al., 2020), salinity distributions collected during hydrographic surveys, and current measurements (Li et al., 2005). In particular, Xie and Li (2018) showed that ROMS reproduced the wind-driven lateral circulation patterns, including the current field and salinity distribution at a cross-channel section in the mid-Bay. The RCA biogeochemical model has been validated against biogeochemical data at a number of stations in Chesapeake Bay (including NO_3, PO_4, NH_4, chlorophyll-a, dissolved oxygen, and organic carbon, nitrogen, and phosphorus), integrated metrics of hypoxic volume, rates of water-column primary production and respiration, and nutrient fluxes across the sediment-water surface (Brady et al., 2013; Testa et al., 2013, 2014, 2017; Li et al., 2016; Ni et al., 2020). The CC model has been validated against extensive surveys of DIC, TA, and pH collected during ten cruises in 2016 (Shen et al., 2019a) and long term (1985–2015) measurements of pH at a number of monitoring stations (Shen et al., 2019b, 2020). The model-predicted along-channel distribution of air-sea CO_2 flux is also in good agreement with that calculated from the observational data (Shen et al., 2019a). This paper uses the well-validated coupled hydrodynamic-biogeochemical-carbonate chemistry models to investigate how winds affect carbonate chemistry in this estuary.

RESULTS

We examined the effects of up-estuary and down-estuary winds on lateral upwelling and carbonate system variability. Detailed modeling analysis revealed that interactions between wind direction and bathymetry determined the strength of upwelling and the associated bottom-surface exchange of low-pH and high-pCO_2 water. Regime diagrams were constructed to summarize the wind effects on carbonate system in the estuary and support a discussion of the associated impacts on Maryland's oyster beds.

An example sequence of a southerly wind event followed by a northerly wind event illustrated the contrasting responses of pH to winds. Southerly (up-estuary) winds blew over Chesapeake Bay between 22.00 LST (Local Standard Time) 18 September and 6.00 LST 22 September 2013, with a maximum wind speed of ∼7.5 m s^{-1} (**Figure 2A**). This was followed by northerly (down-estuary) winds between LST 6.00 on 22 September and LST 0.00 on 25 September 2013, with a maximum wind speed of ∼7.3 m s^{-1}. **Figures 2B–D** show how the surface and bottom water pH responded to winds at three locations (the western shoal, central

[1]https://www.chesapeakebay.net/what/data

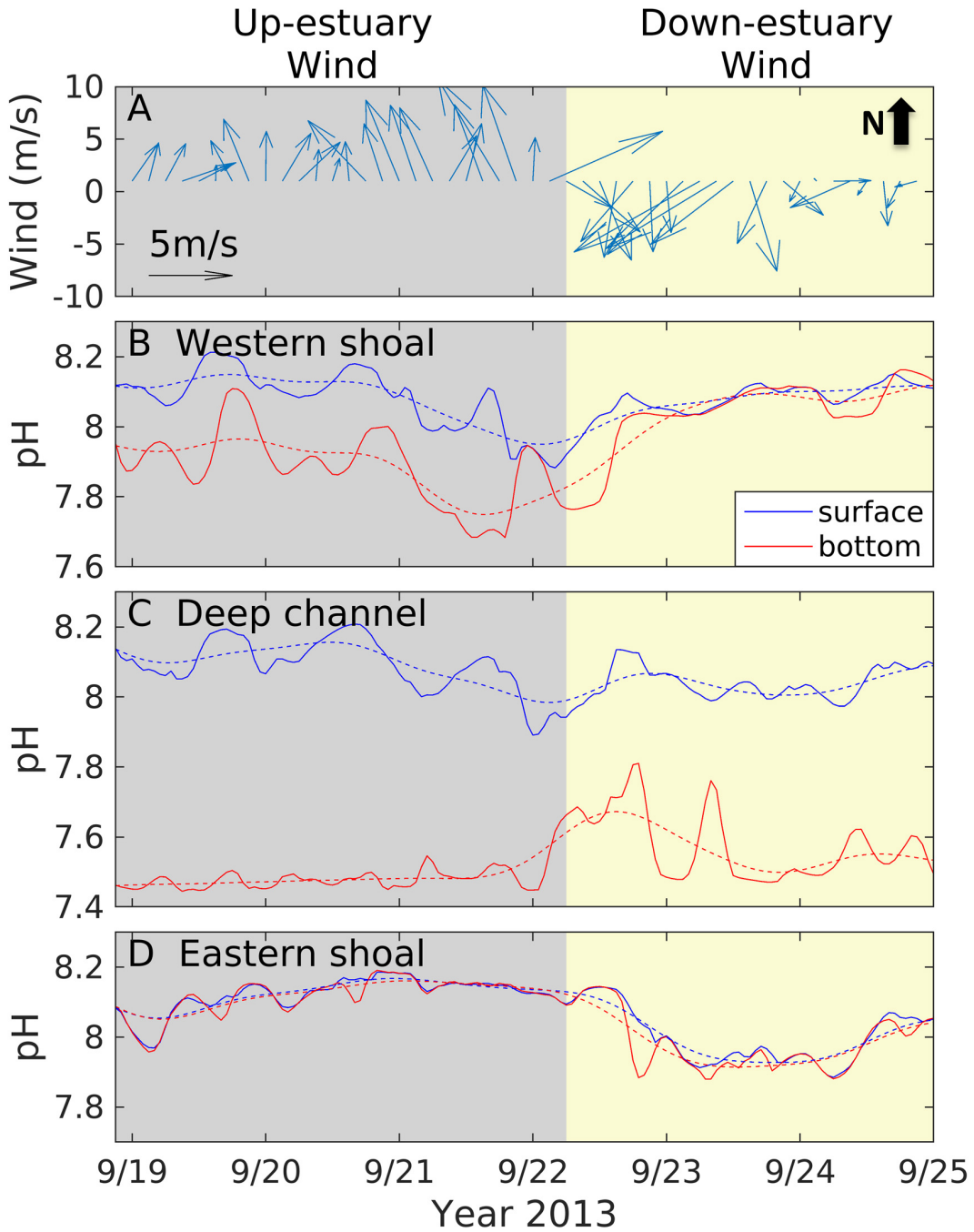


FIGURE 2 | Time series of wind speed vector **(A)**, surface (blue) and bottom (red) pH at a location on the western shoal **(B)**, in the center channel **(C)**, and on the eastern shoal **(D)** in a mid-Bay section (marked as black line in **Figure 1A**). The three locations are further marked as red dashed lines in **Figure 4D**. The solid lines are original time series including tidal fluctuations and the dashed lines are low-passed with a 34-h Butterworth filter.

deep channel, and the eastern shoal) in a mid-Bay cross section. During the up-estuary wind event, the surface/bottom pH on the western shoal decreased from 8.1/7.9 to 7.9/7.7 while pH on the eastern shoal increased from 8 to 8.2 (**Figures 2B,D**). During the following down-estuary wind event, the opposite trend appeared: the surface/bottom pH on the western shoal increased from 7.9/7.8 to 8.2/8.1 while pH on the eastern shoal decreased from 8.1 to 7.9. In the deep channel, the bottom pH was much lower than the surface pH and the vertical pH difference decreased from ∼0.6 to ∼0.4 during the strong winds (21–23 September) (**Figure 2C**). The differences in the pH time series at the three locations highlight the short-term variations in pH and

carbonate chemistry in the estuary in response to wind forcing. Thus, we conducted a series of model simulations to quantify the carbonate system response to (a) weak winds, (b) up-estuary winds, and (c) down-estuary winds.

Weak Wind

As a baseline for comparison, we plot the distributions of physical and carbonate chemistry fields during a period when wind speeds were below 2 m s^{-1}, e.g., 22.00 LST 3 October – 10.00 LST 5 October (**Figures 3**, **4**). The tidally averaged current displayed a typical two-layer gravitational circulation, with seaward flow in the surface layer down to ∼10 m and landward flow in the underlying bottom layer (**Figure 3A**). The along-channel salinity distribution showed sloping isohalines typical of a partially mixed estuary, with the top-bottom salinity difference reaching ∼6 in the deep mid-Bay (**Figure 3B**). DIC and TA showed a similar along-channel distribution (**Figures 3C,D**). However, DIC had a larger vertical gradient than TA since phytoplankton production consumed DIC in the surface euphotic layer and respiration of organic material produced DIC in the bottom layer. The relative impacts of primary production and respiration on TA are small as is expected. pH also showed a strong longitudinal gradient, with lower pH values in the upper Bay due to the influence of poorly buffered, high-CO_2 riverine water and higher pH values in the lower Bay due to well-buffered oceanic water (**Figure 3E**). In addition, pH had a strong vertical gradient, with the top-to-bottom pH difference reaching 0.8 in the upper part of the mid-Bay. The aragonite saturation state Ω_{arag} showed a similar along-channel distribution as pH, falling below 1 in the upper Bay and bottom waters of the mid-Bay but reaching 2–3 in the surface waters of the mid-Bay and everywhere in the lower Bay (**Figure 3F**). The surface pCO_2 exceeded atmospheric equilibrium value in the upper Bay (north of 39.2°N), was undersaturated in the mid-Bay (37.5–39.2°N), and reached a near-equilibrium status in the lower Bay (south of 37.5°N) (**Figure 3G**). Consequently, the air-sea CO_2 flux showed outgassing of ∼5 mmol C m^{-2} d^{-1} in the upper Bay, and ingassing of (3–4) mmol C m^{-2} d^{-1} in the mid-Bay and near-zero exchange in the lower Bay (**Figure 3H**). When integrated over the main stem of the Bay, there was a net influx of $-10.5\times10^6 g\ C\ d^{-1}$ into the estuary.

Since deep water in the mid-Bay is most susceptible to low pH and low O_2 in the estuary (Brodeur et al., 2019; Shen et al., 2019a), we examined a representative cross-channel section in this region. Salinity was vertically stratified and tilted slightly downward on the western shore as the Coriolis force confined the outflowing brackish water to the west (**Figure 4A**). DIC and TA also showed strong vertical gradients and a slight west-east tilt (**Figure 4B**), with lower DIC and TA within the western surface waters. pH isolines were also slightly tilted, but the lateral gradient in pH (∼0.2) was much smaller than the vertical gradient (∼0.7; **Figure 4D**).

Up-Estuary Wind

Winds led to large changes in the carbonate system. The up-estuary winds forced water in the shallow lower Bay to move

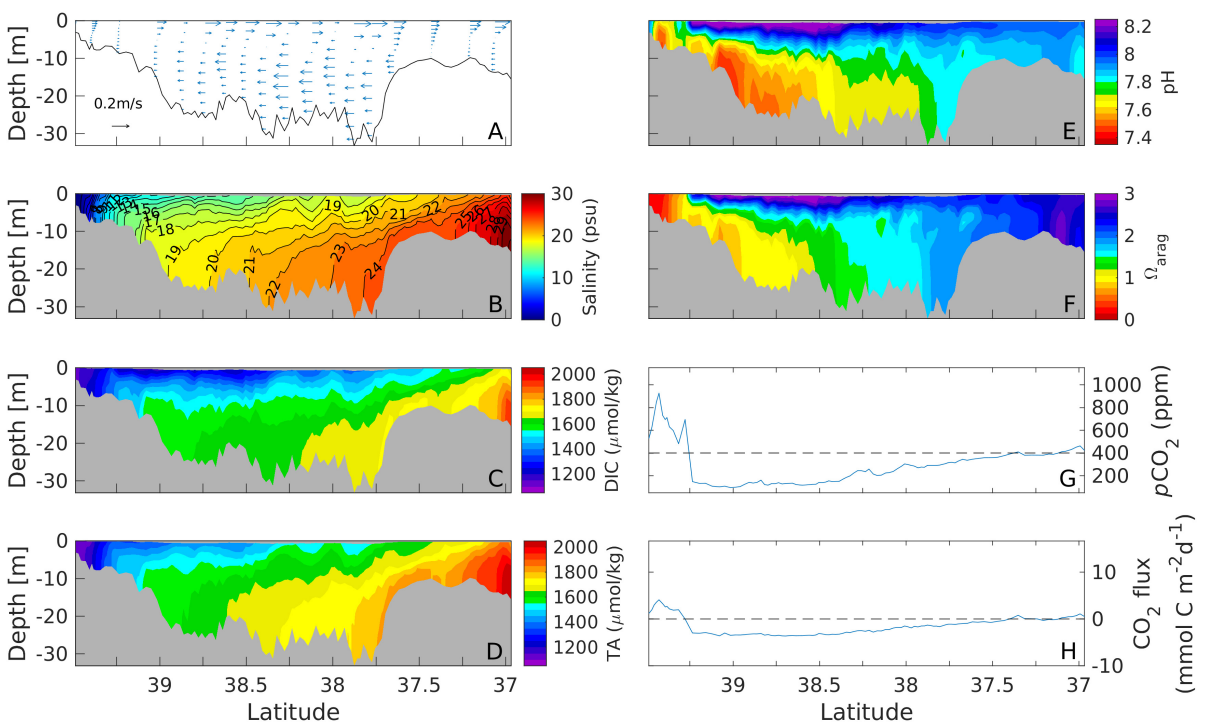


FIGURE 3 | Along channel distributions of subtidal current **(A)**, salinity **(B)**, DIC **(C)**, TA **(D)**, pH **(E)**, Ω_{arag} **(F)**, surface pCO_2 **(G)**, and air-sea CO_2 flux **(H)** during a weak wind period on 2–5 October, 2013. The along-channel section is marked by the black line in **Figure 1A**.

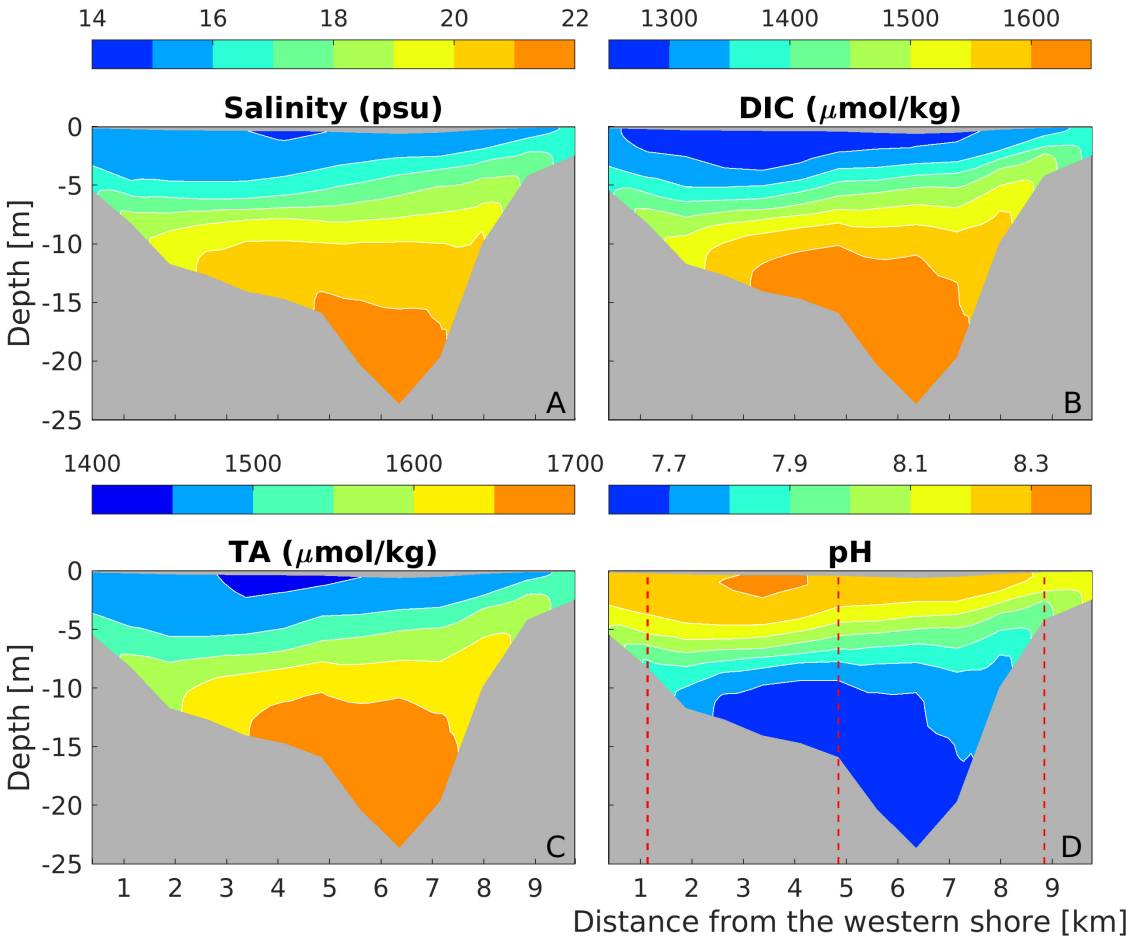


FIGURE 4 | Distributions of salinity **(A)**, DIC **(B)**, TA **(C)**, and pH **(D)** at a mid-bay cross section (marked as the thick black line in **Figure 1A**) during the weak wind period. The red dashed lines in **(D)** mark the three stations used for plotting pH time series in **Figures 2B–D**.

landward at all depths (**Figure 5A**). In the deep mid-Bay, the currents moved landward in the surface layer whereas the pressure gradient due to sea level pileup at the head of the estuary drove the bottom water seaward, thereby reversing the gravitational circulation. This reversed circulation strained the salinity field toward the vertical direction, promoting the ventilation of deep water. Furthermore, wind-driven turbulence generated a surface mixed layer, with its depth reaching ∼10 m between 38.5 and 39°N (**Figure 5B**). The vertical mixing and along-channel straining also strongly modified DIC and TA fields (**Figures 5C,D**). Their vertical gradients were greatly reduced, with nearly a uniform distribution down to a depth of 10–15 m. In the mid and lower Bay, pH was separated into two regions in the vertical direction (8–8.2 in the surface layer and 7.4–7.6 in the bottom layer) and was uniform (7.4) at all depths in the upper Bay (**Figure 5E**). The aragonite saturation state also showed a sharp contrast between the surface and bottom layers, with highly under-saturated conditions in the bottom layer of the mid-Bay. The seaward flows in the bottom layer (**Figure 5A**) – which under these wind conditions were opposite of the direction of mean flows (landward) – advected the under-saturated bottom water further seaward in the mid-Bay (**Figure 5F**).

The southerly winds also impacted pCO_2 and air-sea fluxes. The surface water pCO_2 increased significantly in the mid-Bay as mixing and straining during the wind event raised the surface DIC (**Figure 5G**). Around 39°N, where bathymetry deepens rapidly, ventilation of the bottom water occurred, mixing high DIC-water upward and raising the surface water pCO_2 above atmospheric equilibrium. As a result, the peak in CO_2 efflux at 39°N rivaled the peak in the uppermost part of the Bay (>39.5°N) (compare **Figures 3H**, **5H**). The wind event thus drove outgassing of CO_2 over an extended region in the upper and mid-Bay (down to 38.8°N), with a magnitude of 40 mmol C m^{-2} d^{-1}. Further south in the wide mid-Bay (between 38.8 and 37.5°N), however, the estuary absorbed CO_2 at −20 mmol C m^{-2} d^{-1}. When integrated over the entire estuary, there was a net influx of $-12.1\times10^6 g\ C\ d^{-1}$.

The up-estuary winds also drove a strong clockwise lateral circulation in the cross-channel section, with the eastward velocity in the near-surface layer reaching 0.1 m s^{-1} (**Figure 6A**). This resulted in upwelling on the western shore, with an

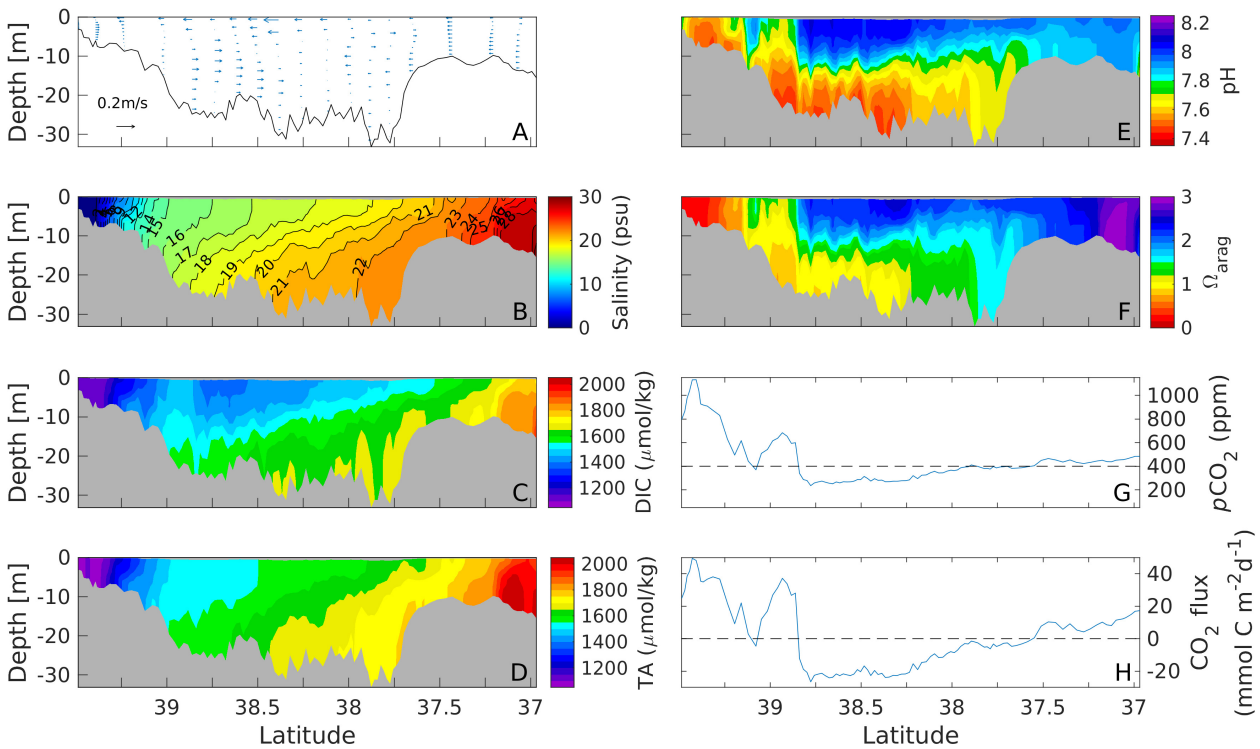


FIGURE 5 | Along channel distributions of subtidal current **(A)**, salinity **(B)**, DIC **(C)**, TA **(D)**, pH **(E)**, Ω_{arag} **(F)**, surface pCO_2 **(G)**, and air-sea CO_2 flux **(H)** during an up-estuary wind event on 18–22 September, 2013.

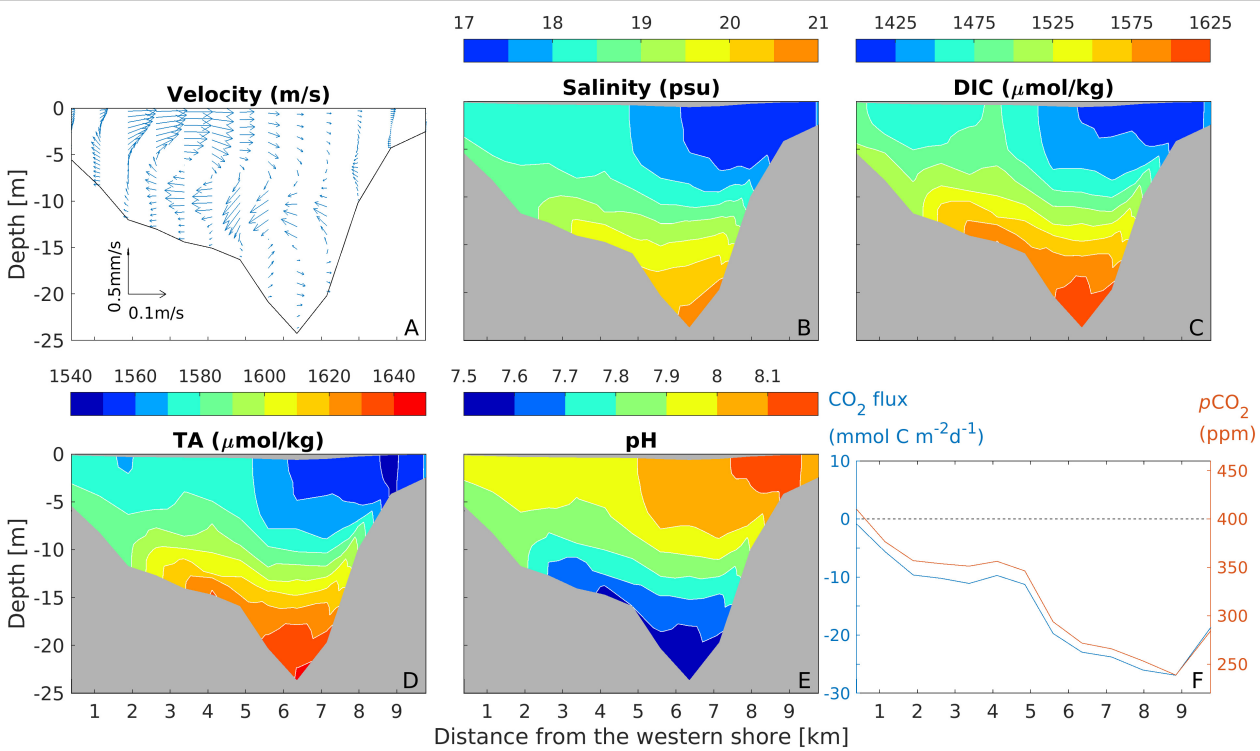


FIGURE 6 | Distributions of lateral-vertical velocity vector **(A)**, salinity **(B)**, DIC **(C)**, TA **(D)**, pH **(E)**, and surface pCO_2 (red) and air-sea CO_2 flux (blue) **(F)** and at the mid-bay section during the up-estuary wind event.

upwelling velocity up to 0.5 mm s^{-1}. Consequently, isohalines were tilted upward on the western part of the cross-section (**Figure 6B**). Wind-driven turbulent mixing also homogenized salinity in the top 5 m. DIC and TA showed a similar upward tilt on the western shore, with the upwelling of high DIC and TA bottom water onto the broad western shore (**Figures 6C,D**). The upwelling changed acidity on the shallow shoals, where pH on the western shore was lowered (**Figure 6E**), reaching minima of 7.5–7.7 during the up-estuary wind (on the sea bed).

The upwelling resulted in much higher pCO_2 value on the western shore (~350–400 ppm) than on the eastern shore (~250 ppm). This lateral difference in the surface-water partial pressure led to a strong lateral gradient in the CO_2 flux (**Figure 6F**). The mid-Bay region has been identified as a carbon sink on an annual scale. During this up-estuary wind event, the surface pCO_2 on the western shore increased, resulting in weak CO_2 flux there. On the other hand, the CO_2 flux on the eastern part of the cross section increased to −30 mmol C m^{-2} d^{-1}, producing a strong carbon sink. No significant change (<2 mg/L in chlorophyll a) in phytoplankton biomass was seen during the wind event (**Supplementary Figure S2**).

Down-Estuary Wind

Following the up-estuary wind event, northerly winds blew down the estuary (**Figure 2A**), with the maximum wind speed of 7 m s^{-1}. The down-estuary winds amplified the two-layer gravitational estuarine circulation, with the landward bottom current reaching 0.2 m s^{-1} (**Figure 7A**). This strong two-layer current strained the salinity field to flatten the isohalines, while the direct wind-induced mixing homogenized salinity in the surface layer down to 10 m (**Figure 7B**). The landward flow in the bottom layer brought in higher salinity oceanic water into the estuary. This intrusion also caused bottom DIC and TA to increase (**Figures 7C,D**). pH showed an almost two-layer structure except in the shallow upper Bay where waters were vertically well mixed. In the mid-Bay, pH was 8.0–8.2 in the surface layer down to a depth of 15 m and 7.4–7.6 in the deep water below (**Figure 7E**). Ω_{arag} showed a similar distribution as pH (**Figure 7F**). Due to strong wind mixing, the surface pCO_2 exceeded the atmospheric value nearly everywhere along the center axis of the Bay (**Figure 7G**) with net estuarine release of CO_2 except in a couple of regions of the mid-Bay (**Figure 7H**). When integrated over the entire estuary and over the wind event, there was a small net influx of $-4.0\times10^6 g\ C\ d^{-1}$. Because the mid-Bay is much wider than the upper Bay, the total CO_2 flux was slightly negative during this down-estuary wind event even though the upper bay was a strong source, as the broad shallow shoals of the mid-Bay were a carbon sink.

In the cross-channel section, the down-estuary winds drove a counter-clockwise lateral circulation, with upwelling on the eastern shore and downwelling on the western shore (**Figure 8A**). Isohalines were tilted upward, with water in the intermediate depths (~15 m) uplifted toward the steep eastern shoal, with the isohalines outcropping at a distance from the coastline

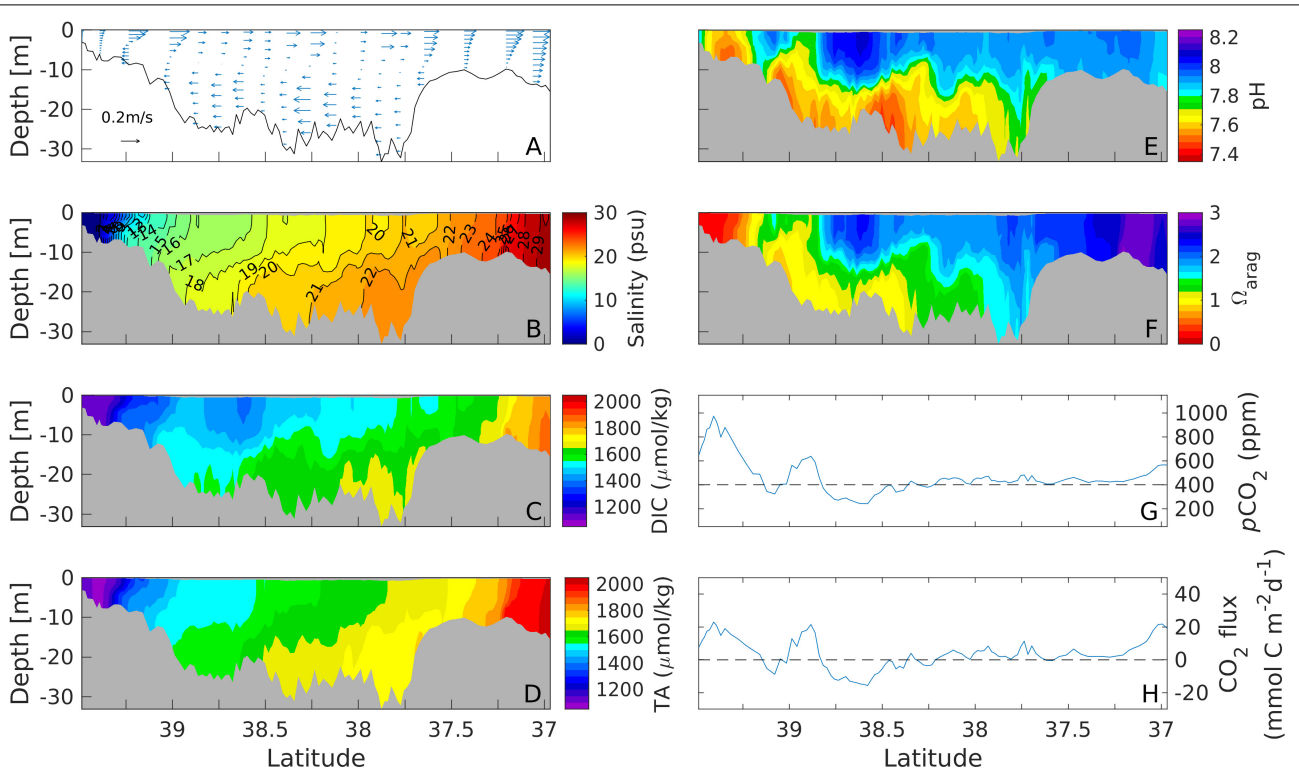


FIGURE 7 | Along channel distributions of subtidal current **(A)**, salinity **(B)**, DIC **(C)**, TA **(D)**, pH **(E)**, Ω_{arag} **(F)**, surface pCO_2 **(G)** and air-sea CO_2 flux **(H)** during a down-estuary wind event on 22–25 September, 2013.

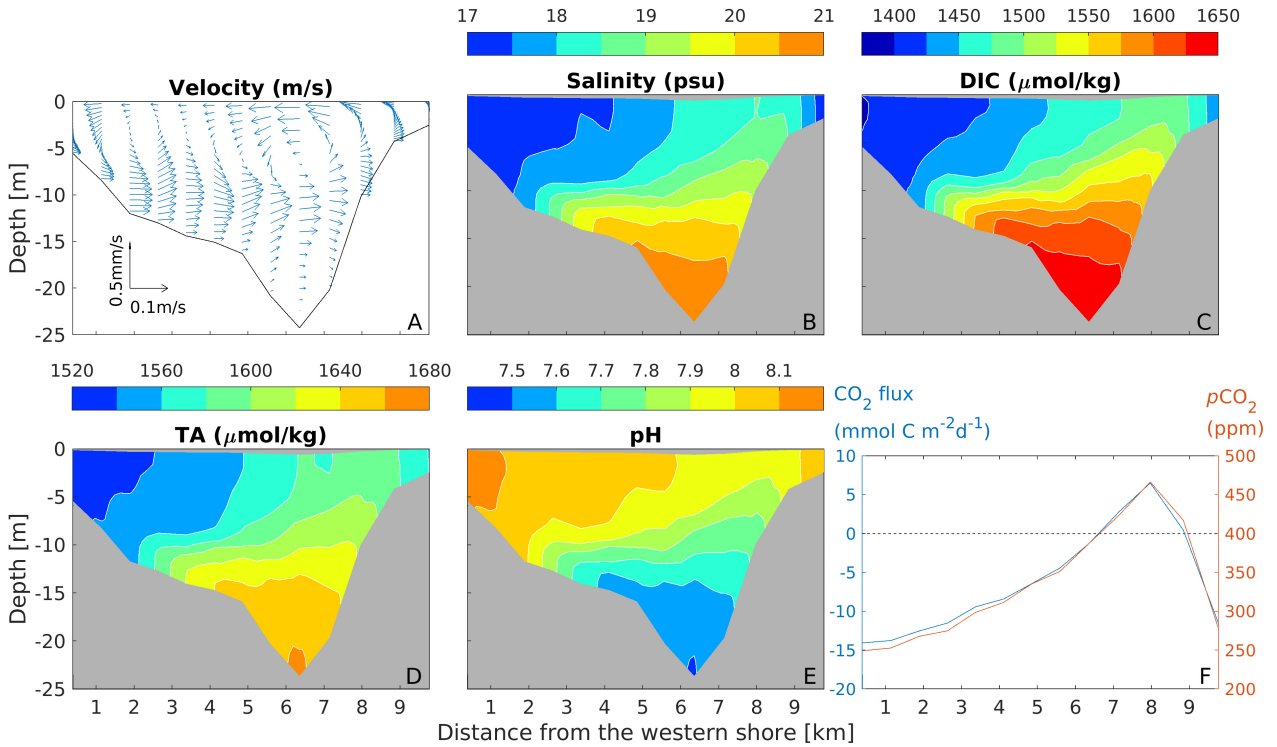


FIGURE 8 | Distributions of lateral-vertical velocity vector **(A)**, salinity **(B)**, DIC **(C)**, TA **(D)**, pH **(E)**, and surface pCO_2 (red) and air-sea CO_2 (blue) **(F)** at the mid-bay section during the down-estuary wind event.

(**Figure 8B**). Due to the steep bathymetry on the eastern flank of the deep channel, the upwelling was the most intense slightly away from the shore rather than at the coastline. Both DIC and TA were uplifted upward over the eastern shoal, with the highest values at about 1 km from the shoreline, as shown in the doming of DIC and TA isohalines (**Figures 8C,D**). In the surface layer down to 15 m depth, pH developed a strong lateral gradient, where pH reached a low value of 7.6–7.7 on the flank of the eastern shoal (5–10 m depth) and a high value of 8.0–8.1 on the western shoal (**Figure 8E**). The ventilation of high DIC water at 1 km off the eastern shoreline caused the surface water pCO_2 there to exceed the atmospheric value. The lateral distribution of air-sea CO_2 flux showed ingassing up to 15 mmol C m^{-2} d^{-1} on the western shoal and outgassing of up to 7 mmol C m^{-2} d^{-1} on the eastern shoal (**Figure 8F**).

Summary of Wind Effects

We have so far focused on the detailed analyses of two wind events. To summarize the overall effects of wind on the carbonate system, we investigated a number of weather events that moved across Chesapeake Bay during 2013. This analysis captured how the carbonate system evolved in different seasons due to changing seasonal prevailing wind directions and seasonal evolution of CO_2 uptake and respiration. Two regime diagrams were constructed to identify general relationships between winds and variations in pH, DIC and other carbonate parameters.

First we investigated wind-driven temporal changes in pH. At the three stations in the mid-Bay cross-section (the cross-section marked in **Figure 1A** and the three stations in this section marked in **Figure 4D**), the time series of surface and bottom water pH were filtered to remove tidal fluctuations and the pH change from the beginning (pH_{begin}) to the end (pH_{end}) of a wind event was calculated:

$$\delta pH = pH_{end} - pH_{begin}. \quad (1)$$

We also calculated similar quantity for the aragonite saturation state:

$$\delta\Omega_{arag} = \Omega_{arag_{end}} - \Omega_{arag_{begin}} \quad (2)$$

where $\Omega_{arag_{begin}}$ and $\Omega_{arag_{end}}$ are the values of Ω_{arag} the beginning and end of each wind event. The wind impulse, defined as

$$I_{wind} = \int_{begin}^{end} \tau_x dt \quad (3)$$

is an integrated measure of wind effects over a wind event and provides a good descriptor of the lateral upwelling effect. Here τ_x is the along-channel wind stress at a mid-Bay location and the integration is over the entire duration of a wind event. **Figures 9A,C,D,F** show that δpH and $\delta\Omega_{arag}$ at the two shallow shoals were approximately linearly proportional to I_{wind}, and that there was additional variability beyond that explained by I_{wind}. With δpH reaching up to $\pm$0.3, pH fluctuated over a wide range during a wind event. Changes in Ω_{arag} were also large,

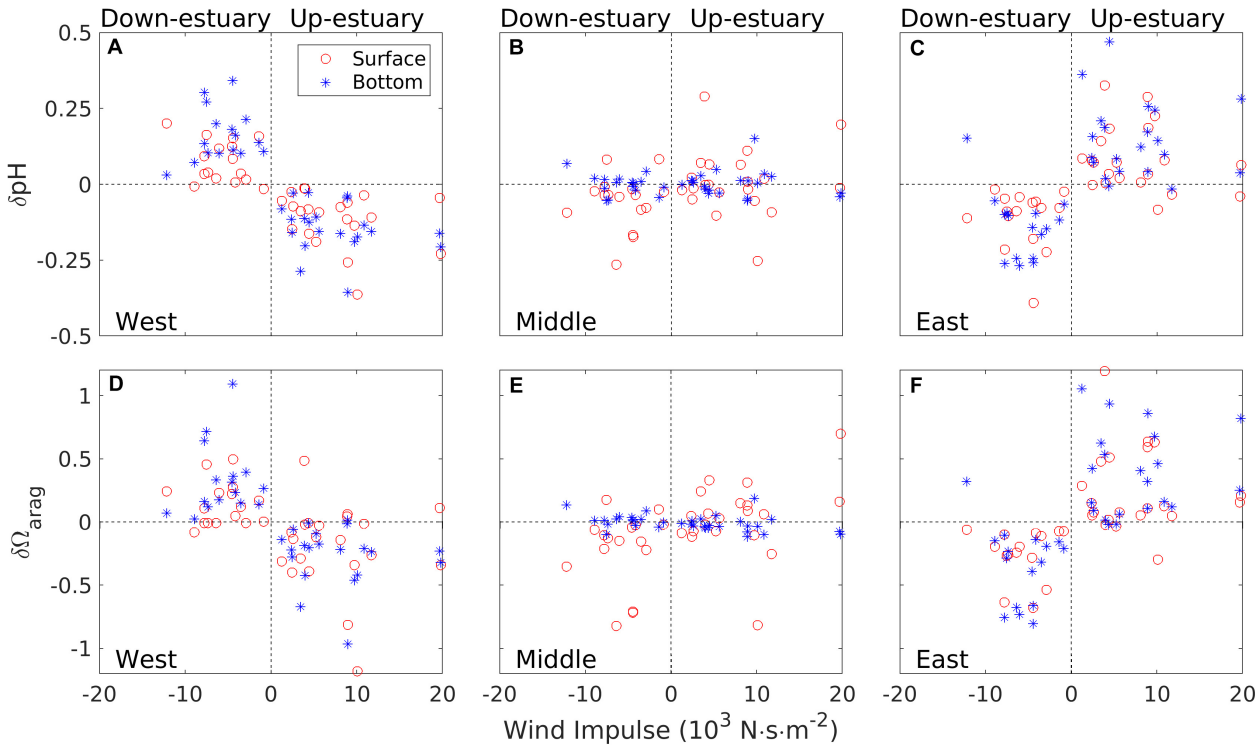


FIGURE 9 | Summary of wind effects on the temporal variations in pH/aragonite saturation state Ω_{arag} at the western shoal location **(A,D)**, the center channel **(B,E)**, and the eastern shoal location **(C,F)**: red open circles for surface pH/ Ω_{arag} and blue stars for bottom pH/ Ω_{arag}.

reaching ±1.0. Under the down-estuary winds, δpH and $\delta\Omega_{arag}$ were positive (increased over time) on the western shoal but negative (decreased) on the eastern shoal. Under the up-estuary winds, δpH and $\delta\Omega_{arag}$ were negative (decreased over time) on the western shoal but positive (increased) on the eastern shoal. They varied out of phase because the lateral upwelling affected the two shoals in opposite ways. In contrast, δpH and $\delta\Omega_{arag}$ in the bottom water of the deep channel showed small changes, indicating that neither the direct wind mixing nor the lateral upwelling had much effect there (**Figures 9B,E**). δpH in the surface water of the deep channel showed much larger changes over each wind event and was mostly negative, indicating wind mixing injected lower pH subsurface water upward and reduced surface pH. In some cases, it became positive, suggesting that horizontal advection and straining may have brought high pH water to the mid-Bay section. $\delta\Omega_{arag}$ in the surface water of the deep channel showed changes compatible to δpH there (**Figure 9E**). With the exception of a few wind events, δpH and $\delta\Omega_{arag}$ in the deep channel showed much smaller fluctuations than those on the shallow shoals.

The lateral differences Δ_yDIC, Δ_ypH , and $\Delta_y pCO_2$ were calculated as the DIC, pH and pCO_2 differences between the eastern and western flanks of the estuarine channel (each covering ∼1/3 of the cross-sectional area), averaged over each wind event. Instead of looking at one cross-channel section, we averaged Δ_yDIC and Δ_ypH over the mid-Bay (marked as the light blue area in **Figure 1B**) and over the entire main stem of the Bay (all shaded areas in **Figure 1B**). **Figure 10A** shows how Δ_yDIC averaged over the mid-Bay varied with I_w. Δ_yDICwas generally negative under the up-estuary winds (positive I_w) and positive under the down-estuary winds (negative I_w). This simply said that DIC was higher on the western shoal than on the eastern shoal under the up-estuary winds. The reverse was true under the down-estuary winds: DIC was higher on the eastern shoal than on the western shoal. Despite the scatter in the plot, Δ_yDIC generally increased with I_w. The stronger the wind speed or the longer the wind duration or both, the stronger the lateral gradient in DIC. There was a bias toward the upper right corner because of the downward tilt of isohalines and DIC-isolines due to the geostrophic balance (see **Figure 4**). Δ_yDIC can reach ±100 μmol/kg. Because the lateral asymmetry was weaker in the narrow upper Bay and shallow lower Bay, ΔDIC over the entire Bay was smaller. Due to the geostrophic control in the lower Bay, Δ_yDIC was biased toward the positive value even under many up-estuary wind events (**Figure 10D**). The overall wind effects on the lateral asymmetry in the entire Bay were not as strong as in the mid-Bay.

pH averaged over the top 5 m in the water column also displayed the lateral asymmetry that extended to all seasons and all wind events (**Figures 10B,E**). In the mid-Bay, Δ_ypH > 0 for $I_w > 0$ and Δ_ypH < 0 for $I_w < 0$ (**Figure 10B**). Notwithstanding the scatters, ΔpH appears to be a linear function of I_w for $I_w > 0$. Therefore, pH was lower on the western shoal than on the eastern shoal under the up-estuary

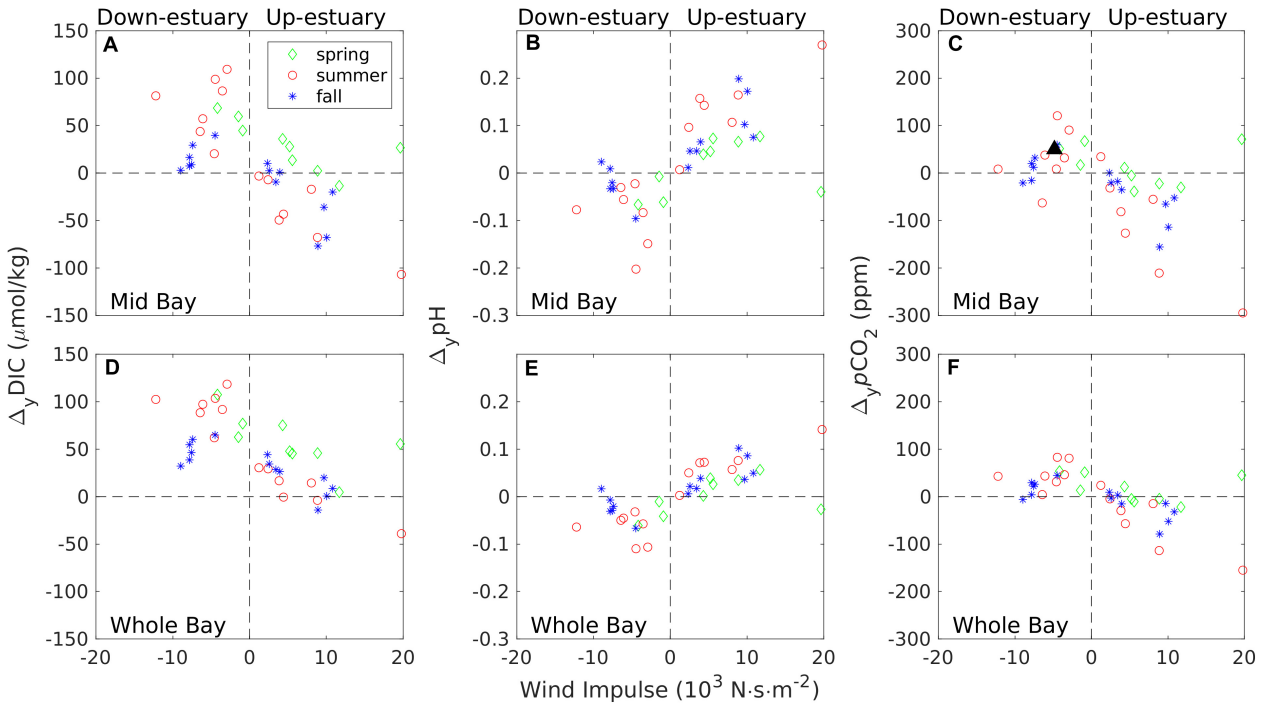


FIGURE 10 | Summary of wind effects on the lateral asymmetry in estuarine carbonate system. Time averaged lateral difference (eastern one third-minus western one third) in DIC **(A,D)**, pH **(B,E)**, and pCO_2 **(C,F)** in the mid-Bay region **(top panel)** or over the entire Bay **(bottom panel)**: spring (March–May, green diamonds), summer (June–August, red circles), fall (September–November, blue stars). The black triangle in **(C)** denoted the observational data from Huang et al. (2019).

winds and this lateral difference Δ_ypH increased with the wind impulse. Under the down-estuary winds, the reverse asymmetry was true: pH was lower on the eastern shoal than on the western shoal. At $I_w < 0$ the magnitude of Δ_ypH was generally less than 0.1 (except two events) whereas Δ_ypH could reach 0.2 at $I_w > 0$. This asymmetry in Δ_ypH is related to the asymmetric response to wind direction: the lateral circulation strength and lateral upwelling are weaker under the down-estuary winds than under the-up-estuary winds (Li and Li, 2012; Xie et al., 2017). When averaged over the entire Bay, Δ_ypH versus I_w showed surprisingly tight relationship as seen in the mid-Bay (**Figure 10E**). The magnitude was smaller, down to ± 0.1, as opposed to ± 0.2 in the mid-Bay.

The lateral upwelling also generated pCO_2 variations in the lateral direction (**Figures 10C,F**). Under the up-estuary winds, pCO_2 on the western shoal was larger than that on the eastern shoal, i.e., $\Delta_y pCO_2 < 0$ and its magnitude increased with the wind impulse. Under the down-estuary winds, the reverse was generally true, with $\Delta_y pCO_2 > 0$. Huang et al. (2019) observed $\Delta_y pCO_2 = 50\ ppm$ during a down-estuary wind event with the maximum wind speed of 7 m/s and wind impulse of $4.84 \times 10^3\ Nsm^{-2}$. The observed data fit well with the scatter plot in **Figure 10C**, indicating a general agreement between the model-predicted and observed pCO_2 lateral differences. The numerical model allowed us to explore a wide range of wind forcing conditions, and **Figures 10C,F** showed that winds can generate lateral pCO_2 differences in the range of $\pm\ 200\ ppm$ in the mid-Bay and in the range of $\pm\ 100\ ppm$ when averaged over the entire estuary.

Effects of Upwelling on Nearshore Habitats

Most of the current and historic mainstem eastern oyster (*Crassostrea virginica*) beds in Maryland are located on the shallow shoals in the mid-Bay between 37.9 and 39.1°N, as shown in **Figure 11A** (Smith, 1997). Wind-driven lateral upwelling could expose these oysters to episodic acidic conditions, particularly during the summer months when pH and Ω_{arag} reach seasonal minima in bottom waters, and exposure of the eastern oyster to low pH and under-saturated waters could have potentially negative consequences for growth and calcification (Waldbusser and Salisbury, 2014; Waldbusser et al., 2015). Under the weak winds, the aragonite saturation state Ω_{arag} on a narrow strip along the western shoal and a broader region on the eastern shoal exceeded 1, suggesting limited influence of deep-channel bottom water on most of the historic oyster beds (**Figure 11B**). In contrast to the shallow shoals, bottom water was highly undersaturated, with Ω_{arag} around 0.5. Under the up-estuary winds, Ω_{arag} fell below 1 almost everywhere on the western shoal, with the minimum value dropping down to 0.6 (**Figure 11C**). On the other hand, Ω_{arag} increased on the eastern shoal, suggesting that dissolution-favorable conditions would not occur. Under the down-estuary winds, the most intense upwelling occurred channel-ward of the eastern coastline (**Figure 8C**) such that Ω_{arag}

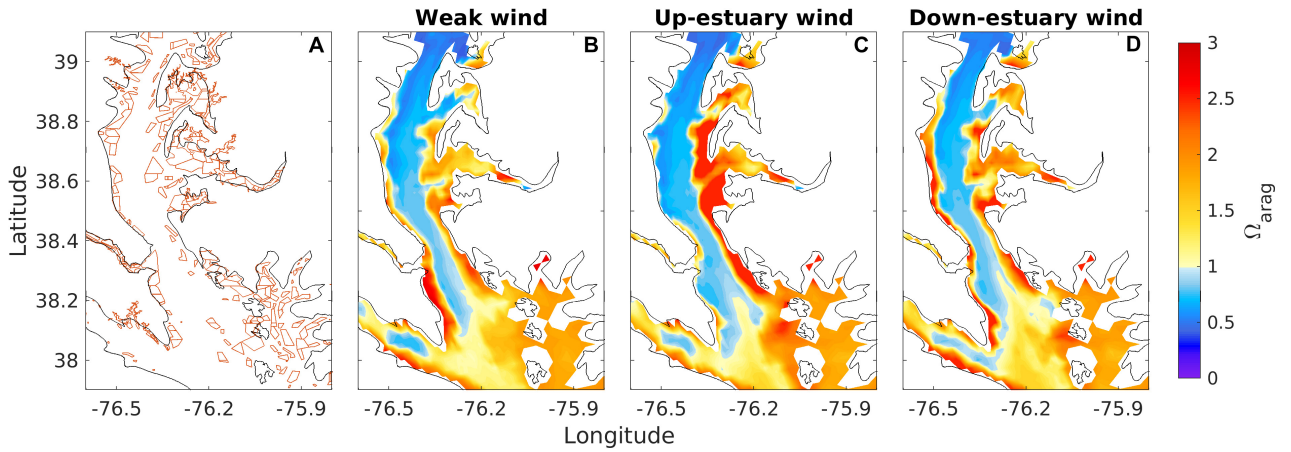


FIGURE 11 | Distribution of Maryland's oyster bed in Chesapeake Bay **(A)** and bottom water aragonite saturation state Ω_{arag} in the oyster habitat under weak **(B)**, up-estuary **(C)**, and down-estuary **(D)** winds during August, 2003.

remained above 1 over the shallowest regions on the eastern shoal (**Figure 11D**). During the same down-estuary winds, Ω_{arag} increased to 2–3 on the fringe along the western coastline.

The duration of exposure to undersaturated conditions is an important factor for potentially negative growth and calcification effects on bivalves. We calculated the time which the bottom water $\Omega_{arag} < 1$ persisted during each wind event, using the two shallow-shoal locations in the mid-Bay (**Figure 4B**) as examples. During the spring and summer, the bottom water on the western shoal was exposed to undersaturated conditions for a period ranging from 5 to 60 h (**Figure 12A**). The bottom water was rarely exposed to $\Omega_{arag} < 1$ during the fall. Since the location on the eastern shoal is further inshore than the most-intense upwelling region, the bottom water there was exposed to fewer wind events with an extended period of undersaturated conditions (**Figure 12B**).

To examine the regional spatial impacts of wind-driven lateral upwelling, we calculated the size A_{oyster} of the sea bed areas in the mid-Bay during each wind event. We computed the area between 37.9 and 39.1°N where depth <8 m and $\Omega_{arag} < 1$ for three different seasons (spring, summer, and fall). A_{oyster} in spring and summer was a U-shaped function of the wind impulse, implying that more areas of the oyster beds were exposed to undersaturated conditions at higher wind speed or longer wind duration on both the eastern and western shoals (**Figure 12C**). About 100–300 km^2 of this area could be exposed to $\Omega_{arag} < 1$ during the spring and summer seasons, which is about 25–75% of the total oyster bed area. During the fall, pH and Ω_{arag} were higher such that only a small area (generally less than 50 km^2) was affected.

DISCUSSION

This study showed that winds can drive pH fluctuations of up to 0.3 in Chesapeake Bay over a period of a few days. These pH fluctuations are comparable to or larger than the long-term pH (0.1–0.2) decline that has been observed in Chesapeake Bay over the past three decades (Waldbusser et al., 2011; Shen et al., 2020). This adds to a growing body of evidence for large pH variability in coastal and estuarine systems (Carstensen and Duarte, 2019). Hofmann et al. (2011) analyzed high resolution time series of upper ocean pH obtained using autonomous sensors, over a variety of systems from polar to tropical regions. In the four coastal and estuarine sites on the United States West Coast, the standard deviations from the monthly mean pH ranged from 0.07 to 0.13, of a similar magnitude as found here. In a seagrass habitat of Hat Island in Puget Sound, Pacellaa et al. (2018) observed the mean diel range of pH of 0.39, with a maximum observed diel range of 0.74. The diel photosynthesis/respiration cycle was a major driver of this large pH variability, but tidal advection of metabolically altered parcels and wind-driven mixing events also played important roles. Similarly, measurements in a macrophyte meadow of the Baltic Sea showed that pH can vary from 8.22 ± 0.1 in August to 7.83 ± 0.4 in September (Saderne et al., 2013). Daily variations of pCO_2 due to photosynthesis and respiration were a major cause for this pH variability, but local upwelling of elevated pCO_2 water masses with offshore winds drove the variations at a time scale of days to weeks. Thus, winds and local productivity interact to drive high frequency variations in estuaries.

Winds may affect the carbonate system in an estuary or a coastal ocean in a number of ways. Depending on the air-sea difference in pCO_2, winds can drive a large efflux or influx of CO_2 and change surface water DIC and pH (Huang et al., 2015). Wind-driven mixing can mix high DIC, high CO_2 and low pH bottom waters to the surface layer and reduce surface pH (Cai et al., 2017; Moore-Maley et al., 2018). Wind-driven upwelling can deliver acidic and carbonate undersaturated waters onto continental shelves (Feely et al., 2008; Hauri et al., 2009). Our analysis showed that wind-driven lateral upwelling could cause larger pH fluctuations on shallow shoals than those caused by direct wind mixing in Chesapeake Bay (**Figures 2**, **9**). This

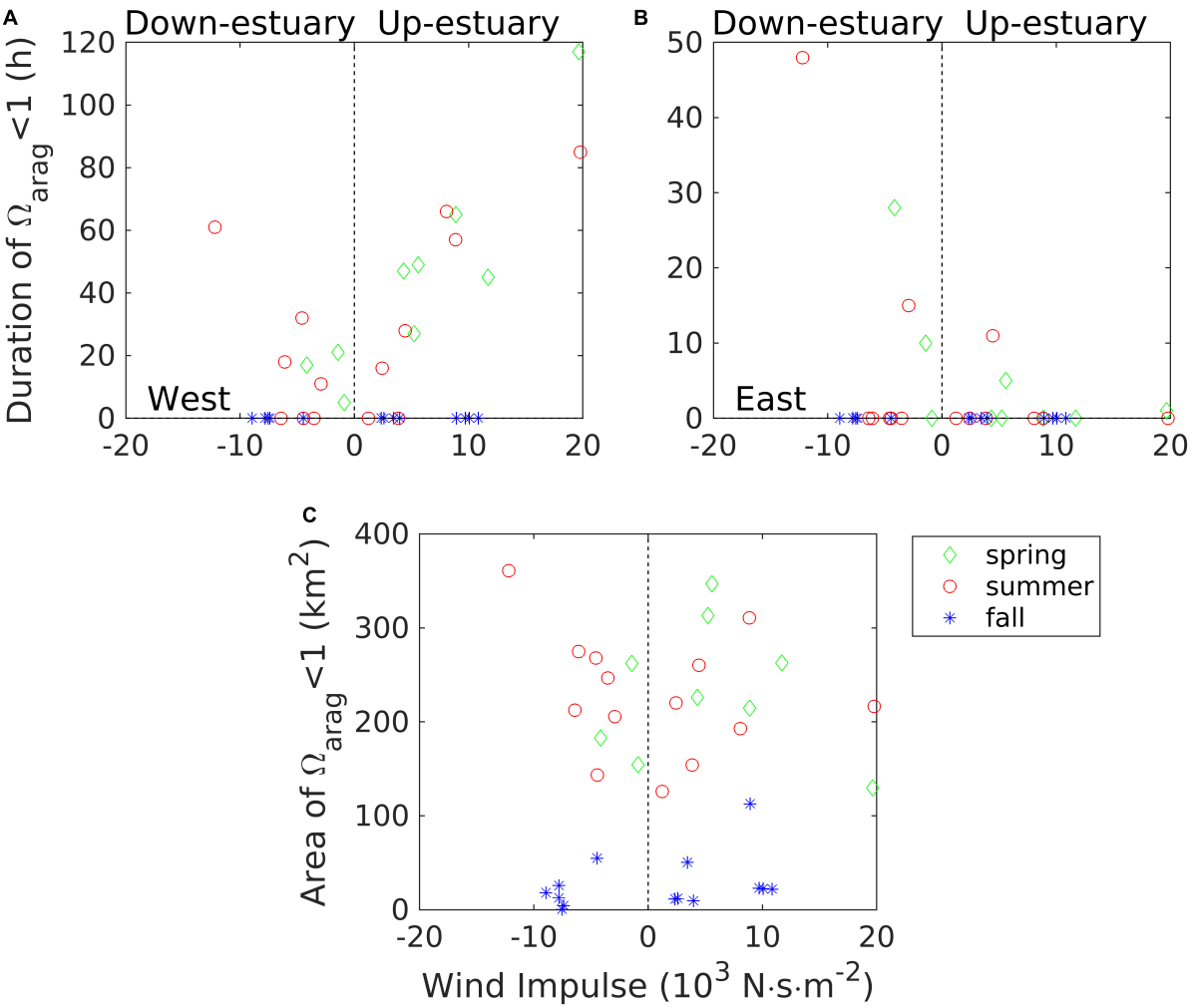


FIGURE 12 | Duration of aragonite saturation state $\Omega_{arag} < 1$ in bottom waters at the western shoal **(A)** and the eastern shoal **(B)** locations in the mid-Bay cross-section. **(C)** The size of mainstem oyster beds in Maryland affected by under-saturated water ($\Omega_{arag} < 1$) during wind events. Green diamonds for spring, red circles for summer, and blue stars for fall.

upwelling mechanism is similar to that in large-scale coastal upwelling systems (e.g., Pacific coast of North America), even though winds are weaker and more variable. The upwelling velocity in Chesapeake Bay is <0.5 mm s^{-1} (**Figures 6A**, **8A**), only a fraction of the typical upwelling velocity (2 mm s^{-1}) found in large coastal upwelling systems (Johnson, 1977). However, it can still deliver deep acidic water to the shallow shoals because water depths in the estuary are only a few to tens of meters. For a synoptic weather event with a mean wind speed of 5 m s^{-1} and a duration of 2 days, the wind impulse is 8.6×10^3 Nsm^{-2}, well within the range reported in **Figures 9**, **12** and typically observed in estuarine and coastal regions. Our result for the dominance of upwelling over mixing in driving pH fluctuations is consistent with a related hypoxia modeling study in which Scully (2010) showed that wind-driven lateral upwelling and ventilation of deep hypoxic water onto shallow shoals are more important than wind mixing in supplying dissolved oxygen to the bottom water. This is probably more so for CO_2 than for O_2 as the air-sea gas exchange flux is generally much smaller for CO_2 than for O_2 (Jiang et al., 2019).

The wind-driven lateral upwelling generated large lateral differences in DIC. The relationship between Δ_yDIC and I_w holds better in the mid-Bay than in the entire estuary (**Figure 10**), as the wind-driven lateral circulation is strongest in the wide mid-Bay that features a deep channel and broad shoals. Moreover, the vertical gradient in DIC and pH there is strongest due to DIC consumption in the surface layer and DIC production in the bottom layer, such that upwelling of acidic deep water has the largest effects on the shallow shoals. In comparison, the lateral circulation is much weaker in the shallow and narrow upper Bay. Strong lateral circulation can develop in the lower Bay (Xie and Li, 2018), but the vertical DIC gradient is much smaller there than that in the mid-Bay such that the upwelling does not induce large changes in surface water DIC. When integrated over the entire Bay, the relationship between $\Delta_y DIC$ and I_w (and the lateral DIC asymmetry) is less robust than in the mid-Bay. Δ_yDIC

is approximately a linear function of I_w under the up-estuary winds but displays more scatters under the down-estuary winds. In a numerical modeling study, Li and Li (2012) showed that at the same wind speed the lateral circulation strength is 2–3 times stronger under the up-estuary winds than under the down-estuary winds. Using velocity measurements collected at a cross-channel array of AD, Xie et al. (2017) observed that the lateral circulation on the western part of the estuarine channel was weakened considerably due to the effect of baroclinic forcing under the down-estuary winds. Therefore, the larger scatter in Δ_yDIC versus I_w under the down-estuary winds is likely caused by the weaker lateral circulation. We note that the scatter seen in **Figure 10** are comparable to that in the plot for the lateral circulation strength reported in Xie et al. (2017) because the wind-driven lateral circulation is not only determined by the wind speed but also affected by river flows, offshore salinity and lateral baroclinic forcing.

Unlike DIC and pH, the air-sea CO_2 flux does not demonstrate a simple dependence on the wind speed/direction or wind impulse (**Supplementary Figures S3–S5**). As Shen et al. (2019a) and Chen et al. (2020) showed recently, Chesapeake Bay is releasing CO_2 into the atmosphere in the upper Bay, absorbing it in the mid-Bay and near the equilibrium condition in the lower Bay. While wind-driven mixing and straining/ventilation can result in locally enhanced CO_2 flux (**Figures 5H**, **7H**) and lateral upwelling can generate cross-channel gradients in CO_2 flux (**Figures 6F**, **8F**), the overall wind effects on the air-sea CO_2 exchange over the entire estuary cannot be easily quantified. As discussed earlier, wind effects are most pronounced in the deep hypoxic mid-Bay where respiration of organic matter creates strong vertical gradients in DIC. Typically, the mid-Bay is a net sink of CO_2 due to strong phytoplankton production in the surface euphotic layer and the surface water pCO_2 is in the range of 200–300 ppm which is less than the atmospheric pCO_2 of 400 ppm. Wind-induced mixing and ventilation in the deep channel raises surface water pCO_2, but the net wind effect on the CO_2 flux depended on whether the surface water pCO_2 remains below or rises above the atmospheric value. If the surface water $pCO_2 < 400$ ppm, the winds would pump more CO_2 into the estuary and this influx/sink increases with the wind speed. For example, the up-estuary wind event U17 caused a peak CO_2 influx of -65.3×10^6 mol C d^{-1} over the mid-Bay and -61.4×10^6 mol C d^{-1} over the entire estuary (**Supplementary Figure S5**). If the surface water $pCO_2 > 400$ ppm, however, the winds will release CO_2 into the atmosphere, turning Chesapeake Bay from a weak CO_2 sink to a source. For example, during the down-estuary wind event D8, the surface water pCO_2 increased to 672.9 ppm, such that there was a peak CO_2 efflux of 133.7×10^6 mol C d^{-1} over the mid-Bay and 340.6×10^6 mol C d^{-1} over the entire estuary (**Supplementary Figure S4**). Similarly, the wind-driven upwelling changes the lateral distribution of pCO_2, but its net effect on the CO_2 flux depends on the balance between the excess and deficits in the CO_2 flux at the two shallow shoals flanking the deep channel. Overall, the complicated non-linear dependence of CO_2 flux on the wind speed and strong spatial variability make it difficult to identify a simple relationship between the CO_2 flux and wind forcing in this estuary. Although numerical model estimates of air-sea@ CO_2 flux can help overcome challenges in making similar estimates from limited and error-prone observations (Herrmann et al., 2020), assigning causation to these changes under dynamic physical forcing is difficult even with model simulations.

Lateral upwelling of oxygen poor, acidic water onto otherwise oxic and high-pH shallow shoals in Chesapeake Bay has been documented in previous studies (e.g., Malone et al., 1986; Sanford et al., 1990; Scully, 2010; Huang et al., 2019), but its potential impact on oyster beds has not been specifically investigated in this estuary. In contrast, upwelling of acidic waters and it impacts on bivalves have been clearly documented along the Pacific coast of North America (e.g., Feely et al., 2008). We found that southerly or southeasterly (up-estuary winds) during the summer led to upwelling of corrosive water onto the western shoal where oyster beds have previously been identified, and that the duration of these events in 2013 led to 1–3 day periods with water with $\Omega_{arag} < 1$. Although Waldbusser et al. (2011) documented reduced biocalcification in juvenile eastern oysters as $W_{calcite}$ declined, they also found that net calcification could occur under moderately corrosive conditions ($W_{calcite}$ ~0.7–1). However, net dissolution in the eastern oyster occurred below $\Omega_{arag} = 0.6$, and studies focused on other juvenile bivalves found reduced growth and mortality under comparable conditions (e.g., Green et al., 2009). The relatively brief duration of upwelling events in Chesapeake Bay may not be sufficiently chronic to induce reduced growth, calcification, or other physiological consequences (Talmage and Gobler, 2010; Keppel et al., 2016), but repeated exposures to these conditions may eventually be detrimental.

To account for accumulated acidification stress on larval bivalves, Gimenez et al. (2018) recently defined a new metric: ocean acidification stress index for shellfish (OASIS):

$$OASIS = \int_{fertilization}^{settlement} \left[(\Omega_{thrsh} - \Omega_{arag}) \frac{1}{1+D_{pft}} \right] dt, \quad if\ (\Omega_{thrsh} - \Omega_{arag}) > 0$$

where Ω_{thrsh} is the selected acidification stress threshold and D_{pft} is the day(s) post-fertilization (spawning day = 0). OASIS has the unit of Ω min day^{-1} and provides a measure of accumulated stress by integrating only the area of the Ω_{arag} time series that falls below the designated threshold over the entire larval period, from fertilization to metamorphosis. Although the experimental study by Gimenez et al. (2018) focused on the Pacific oyster, it is instructive to calculate OASIS using the model results presented in **Figure 12**. We adopted the same conservative threshold of $\Omega_{thrsh} = 1.5$. **Figure 13** shows how the OASIS index at the two shallow shoal locations in the mid-Bay cross section varies with the wind impulse, and the OASIS response largely mirrors that of low Ω_{arag} duration and area (**Figure 12**). OASIS was small during the fall, indicating limited acidification stress on the oyster larvae, but fall conditions may not be as important because oysters typically spawn between June and August (Kennedy, 1996). However, OASIS increased rapidly with I_w during the spring and summer, a time when eastern oyster gametes are beginning to ripen and spawning occurs, respectively (Kennedy, 1996). At the

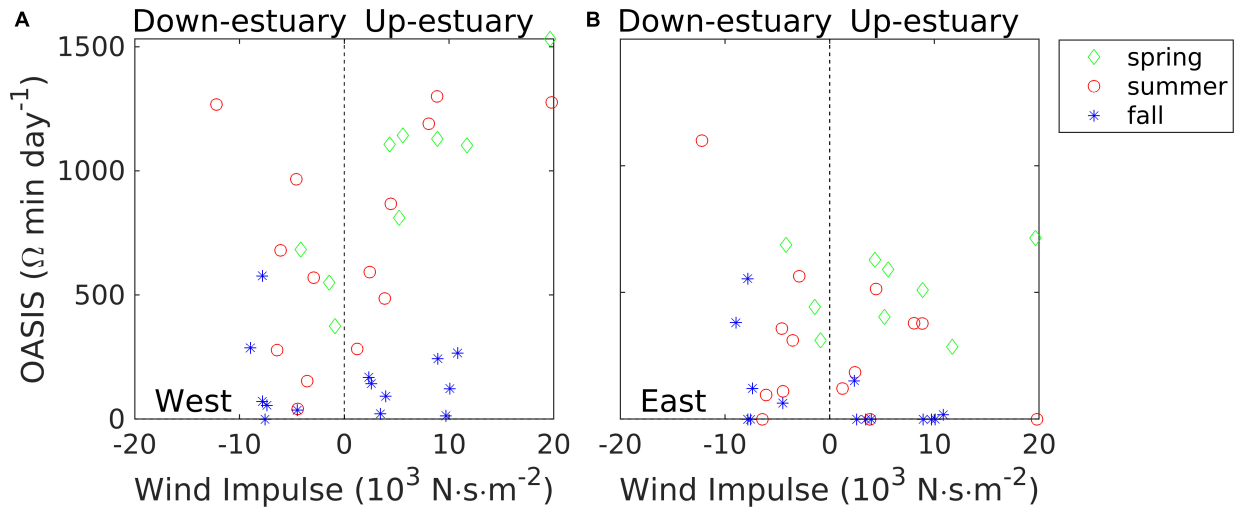


FIGURE 13 | OASIS (Ocean Acidification Stress Index for Shellfish) in bottom waters at the western shoal **(A)** and the eastern shoal **(B)** locations in the mid-Bay cross-section. Green diamonds for spring, red circles for summer, and blue stars for fall.

western shoal location, OASIS reached 500–1500 Ω min day^{-1} in the summer, which could cause a significant reduction in oyster larval survival rate (Gimenez et al., 2018) at a time when spawning is actively occurring. Furthermore, the interaction of exposures to both corrosive and hypoxic waters during these upwelling events may also have synergistic consequences for organisms (e.g., Miller et al., 2016). Clearly, there remains much to be learned concerning the potential impacts of upwelling events on biological communities, and the model simulations presented here provide a quantitative tool for prediction of the severity, duration, and frequency of such events in response to seasonally varying winds.

In summary, we used a numerical model to quantify the impacts of along-axis wind stress on the lateral dynamics of the carbonate system in Chesapeake Bay, a large estuary with moderate tides. Although the upwelling of corrosive and acidified water in response to wind is widely recognized in coastal oceans, this study provides the first mechanistic explanation that wind-driven lateral upwelling can deliver acidified deep water to shallow shoals in estuaries, producing large temporal pH and Ω_{arag} fluctuations. Fluctuations in pH could reach ±0.3, depending on the combined effect of wind speed and wind duration as represented by the wind impulse. Changes in Ω_{arag} were also large, reaching ±1.0. Regime diagrams are constructed to summarize the effects of wind events on temporal pH and Ω_{arag} fluctuations and the lateral gradients in DIC, pH, and pCO_2 in the estuary. Given the potential for expanded low-pH bottom waters under warming-enhanced respiration, elevated riverine inputs, and increasing atmospheric CO_2, Chesapeake Bay may be more vulnerable to more frequent or intense future upwelling events. Future studies of estuarine acidification need to consider the intensity and control of these events, as well as the effects of these physically driven pH fluctuations on organisms' physiological response.

DATA AVAILABILITY STATEMENT

Publicly available datasets were analyzed in this study. This data can be found here: https://zenodo.org/record/3964478#.XyBNRxIh2Uk.

AUTHOR CONTRIBUTIONS

ML, W-JC, and JT conceived and designed the numerical experiments. RL conducted the numerical model simulations. CS assisted in the model configurations. RL and ML analyzed the model results. ML wrote the manuscript with editorial contributions from W-JC and JT. All authors contributed to the article and approved the submitted version.

FUNDING

We are grateful to the NOAA Ocean Acidification Program (NOAA-OAP; Awards NA15NOS4780184 and NA18NOS4780179) for the financial support.

ACKNOWLEDGMENTS

We thank the two reviewers for helpful comments and George Waldbusser for brining our attention to the OASIS calculations. This is UMCES contribution number 5923.

SUPPLEMENTARY MATERIAL

The Supplementary Material for this article can be found online at: https://www.frontiersin.org/articles/10.3389/fmars.2020.588465/full#supplementary-material

REFERENCES

Bakker, D. C. E., Pfeil, B., Landa, C. S., Metzl, N., O'Brien, K. M., Olsen, A., et al. (2016). A multi-decade record of high-quality fCO_2 data in version 3 of the Surface Ocean CO_2 Atlas (SOCAT). *Earth Syst. Sci. Data* 8, 383–413. doi: 10.5194/essd-8-383-2016

Baumann, H., and Smith, E. M. (2018). Quantifying metabolically driven pH and oxygen fluctuations in US nearshore habitats at diel to interannual time scales. *Estuar. Coast.* 41, 1102–1117. doi: 10.1007/s12237-017-0321-3

Baumann, H., Wallace, R. B., Tagliaferri, T., and Gobler, C. J. (2015). Large natural pH, CO2 and O2 fluctuations in a temperate tidal salt marsh on diel, seasonal, and interannual time scales. *Estuar. Coast.* 38, 220–231. doi: 10.1007/s12237-014-9800-y

Borges, A. V., and Gypens, N. (2010). Carbonate chemistry in the coastal zone responds more strongly to eutrophication than to ocean acidification. *Limnol. Oceanogr.* 55, 346–353. doi: 10.4319/lo.2010.55.1.0346

Brady, D. C., Testa, J. M., Di Toro, D. M., Boynton, W. R., and Kemp, W. M. (2013). Sediment flux modeling: calibration and application for coastal systems. *Estua. Coast. Shelf Sci.* 117, 107–124. doi: 10.1016/j.ecss.2012.11.003

Breitburg, D. L. (1992). Episodic hypoxia in Chesapeake Bay: interacting effects of recruitment, behavior, and physical disturbance. *Ecol. Monogr.* 62, 525–546. doi: 10.2307/2937315

Brodeur, J. R., Chen, B., Zhong, J., Xu, Y., Hussain, N., Scaboo, K. M., et al. (2019). Chesapeake Bay inorganic carbon, spatial distribution and seasonal variability. *Front. Mar. Sci.* 6:99. doi: 10.3389/fmars.2019.00099

Browne, D. R., and Fisher, C. W. (1988). *Tide and Tidal Currents in the Chesapeake Bay*. NOAA Technical Report NOS OMA 3 84. Washington, DC: NOAA.

Cai, W., Hu, X., Huang, W., Murrell, M. C., Lehrter, J. C., Lohrenz, S. E., et al. (2011). Acidification of subsurface coastal waters enhanced by eutrophication. *Nat. Geosci.* 4, 766–770. doi: 10.1038/ngeo1297

Cai, W., Huang, W., Luther, G. W., Pierrot, D., Li, M., Testa, J. M., et al. (2017). Redox reactions and weak buffering capacity lead to acidification in the Chesapeake Bay. *Nat. Commun.* 8:369.

Cai, W.-J., Feely, R., Testa, J. M., Li, M., Evans, W., Alin, S., et al. (2021). Natural and anthropogenic drivers of acidification in large estuaries. *Ann. Rev. Mar. Sci.* [Epub ahead of print].

Cai, W.-J., Hu, X., Huang, W.-J., Jiang, L.-Q., Wang, Y., Peng, T. H., et al. (2010). Alkalinity distribution in the western North Atlantic Ocean margins. *J. Geophys. Res. Ocean* 115:C08014. doi: 10.1029/2009JC005482

Cai, W.-J., and Wang, Y. (1998). The chemistry, fluxes and sources of carbon dioxide in the estuarine waters of the Satilla and Altamaha Rivers, Georgia. *Limnol. Oceanogr.* 43, 657–668. doi: 10.4319/lo.1998.43.4.0657

Cai, W.-J., Xu, Y.-Y., Feely, R. A., Wanninkhof, R., Jönsson, B., Alin, S., et al. (2020). Controls on surface water carbonate chemistry along North American ocean margins. *Nat. Commun.* 11:2691. doi: 10.1038/s41467-020-16530-z

Carstensen, J., and Duarte, C. M. (2019). Drivers of pH variability in coastal ecosystems. *Environ. Sci. Technol.* 53, 4020–4029. doi: 10.1021/acs.est.8b03655

Carter, H. H., and Pritchard, D. W. (1988). "Oceanography of Chesapeake Bay," in *Hydrodynamics of Estuaries: Dynamics of Partially-Mixed Estuaries*, Vol. 1, ed. B. Kjerfe (Boca Raton, FL: CRC Press), 1–16.

Chen, B., Cai, W.-J., Brodeur, J. R., Hussain, N., Testa, J. M., Ni, W., et al. (2020). Seasonal and spatial variability in surface pCO_2 and air-water CO_2 flux in the Chesapeake Bay. *Limnol. Oceanogr.* [Epub ahead of print]. doi: 10.1002/lno.11573

Chen, S.-N., and Sanford, L. P. (2009). Axial wind effects on stratification and longitudinal salt transport in an idealized, partially mixed estuary. *J. Phys. Oceanogr.* 39, 1905–1920. doi: 10.1175/2009JPO4016.1

Cheng, P., Li, M., and Li, Y. (2013). Generation of an estuarine sediment plume by a tropical storm. *J. Geophys. Res. Oceans* 118, 1–13. doi: 10.1029/2012JC008225

Di Toro, D. M. (2001). *Sediment Flux Modeling*. New York, NY: Wiley-Interscience.

Egbert, G. D., and Erofeeva, S. Y. (2002). Efficient inverse modeling of barotropic ocean tides. *J. Atmos. Ocean Tech.* 19, 183–204. doi: 10.1175/1520-0426(2002)019<0183:eimobo>2.0.co;2

Eggleston, D. B., Bell, G. W., and Amavisca, A. D. (2005). Interactive effects of episodic hypoxia and cannibalism on juvenile blue crab mortality. *J. Exp. Mar. Biol. Ecol.* 325, 18–26. doi: 10.1016/j.jembe.2005.04.023

Fairall, C. W., Bradley, E. F., Hare, J. E., Grachev, A. A., and Edson, J. B. (2003). Bulk parameterization of air–sea fluxes: updates and verification for the COARE algorithm. *J. Clim.* 16, 571–591. doi: 10.1175/1520-0442(2003)016<0571:bpoasf>2.0.co;2

Feely, R. A., Alin, S. R., Newton, J., Sabine, C. L., Warner, M., Devol, A. H., et al. (2010). The combined effects of ocean acidification, mixing, and respiration on pH and carbonate saturation in an urbanized estuary. *Estuar. Coast. Shelf Sci.* 88, 442–449. doi: 10.1016/j.ecss.2010.05.004

Feely, R. A., Sabine, C. L., Hernandez-Ayon, J. M., Ianson, D., and Hales, B. (2008). Evidence for upwelling of corrosive "acidified" water onto the continental shelf. *Science* 320, 1490–1492. doi: 10.1126/science.1155676

Filippino, K. C., Mulholland, M. R., and Bernhardt, P. W. (2011). Nitrogen uptake and primary productivity rates in themid-Atlantic bight (MAB). *Estuar. Coast. Shelf Sci.* 91, 13–23. doi: 10.1016/j.ecss.2010.10.001

Friedman, J. R., Shadwick, E. H., Friedrichs, M. A. M., Najjar, R. G., De Meo, O. A., Da, F., et al. (2020). Seasonal variability of the CO_2 system in a large coastal plain estuary. *J. Geophys. Res. Oceans* 125:e2019JC015609. doi: 10.1029/2019JC015609

Geyer, W. R., Woodruff, J. D., and Traykovski, P. (2001). Sediment transport and trapping in the Hudson River estuary. *Estuar. Coasts* 24, 670–679. doi: 10.2307/1352875

Gimenez, I., Waldbusser, G. G., and Hales, B. (2018). Ocean acidification stress index for shellfish (OASIS): linking *Pacific oyster* larval survival and exposure to variable carbonate chemistry regimes. *Elem. Sci. Anth.* 6:51. doi: 10.1525/elementa.306

Goodrich, D. M., and Blumberg, A. F. (1991). The fortnightly mean circulation of Chesapeake Bay. *Estuar. Coast. Shelf Sci.* 32, 451–462. doi: 10.1016/0272-7714(91)90034-9

Green, M. A., Waldbusser, G. G., Reilly, S. L., Emerson, K., and O'Donnell, S. (2009). Death by dissolution: sediment saturation state as a mortality factor for juvenile bivalves. *Limnol. Oceanogr.* 54, 1037–1047. doi: 10.4319/lo.2009.54.4.1037

Haidvogel, D. B., Arango, H., Budgell, W. P., Cornuelle, B. D., Curchitser, E., Di Lorenzo, E., et al. (2008). Ocean forecasting in terrain-following coordinates: formulation and skill assessment of the regional ocean modeling system. *J. Comput. Phys.* 227, 3595–3624. doi: 10.1016/j.jcp.2007.06.016

Hauri, C., Gruber, N., Plattner, G.-K., Alin, S., Feely, R. A., Hales, B., et al. (2009). Ocean acidification in the California current system. *Oceanography* 22, 60–71. doi: 10.5670/oceanog.2009.97

Herrmann, M., Najjar, R. G., Da, F., Friedman, J. R., Friedrichs, M. A. M., Goldberger, S., et al. (2020). Challenges in quantifying air-water carbon dioxide flux using estuarine water quality data: case study for Chesapeake Bay. *J. Geophys. Res. Oceans* 125:e2019JC015610. doi: 10.1029/2019JC015610

Hofmann, G. E., Smith, J. E., Johnson, K. S., Send, U., Levin, L. A., Micheli, F., et al. (2011). High-frequency dynamics of ocean pH: a multi-ecosystem comparison. *PLoS One* 6:e28983. doi: 10.1371/journal.pone.0028983

Huang, W.-J., Cai, W.-J., Wang, Y., Lohrenz, S. E., and Murrell, M. C. (2015). The carbon dioxide system on the Mississippi River-dominated continental shelf in the northern Gulf of Mexico: 1. Distribution and air-sea CO_2 flux. *J. Geophys. Res. Oceans* 120, 1429–1445. doi: 10.1002/2014jc010498

Huang, W.-J., Cai, W.-J., Xie, X., and Li, M. (2019). Wind-driven lateral variations of partial pressure of carbon dioxide in a large estuary. *J. Mar. Syst.* 195, 67–73. doi: 10.1016/j.jmarsys.2019.03.002

Isleib, R. P. E., Fitzpatrick, J. J., and Mueller, J. (2007). The development of a nitrogen control plan for a highly urbanized tidal embayment. *Proc. Water Environ. Feder.* 5, 296–320. doi: 10.2175/193864707786619152

Jiang, Z.-P., Cai, W.-J., Chen, B., Wang, K., Han, C., Roberts, B. J., et al. (2019). Physical and biogeochemical controls on pH dynamics in the northern Gulf of Mexico during summer hypoxia. *J. Geophys. Res. Oceans* 124, 5979–5998. doi: 10.1029/2019JC015140

Johnson, D. R. (1977). Determining vertical velocities during upwelling off the Oregon coast. *Deep Sea Res.* 24, 171–180. doi: 10.1016/0146-6291(77)90551-3

Kennedy, V. S. (1996). "Biology of larvae and spat," in *The Eastern Oyster: Crassostrea Virginica*, eds V. S. Kennedy, R. I. E. Newell, and A. F. Eble (Maryland: Maryland Sea Grant College,College Park), 371–421.

Keppel, A. G., Breitburg, D. L., and Burrell, R. B. (2016). Effects of Co-varying diel-cycling hypoxia and pH on growth in the juvenile eastern oyster,

Crassostrea virginica. *PLoS One* 11:e0161088. doi: 10.1371/journal.pone.0161088

Lacy, J. R., Stacey, M. T., Burau, J. R., and Monismith, S. G. (2003). Interaction of lateral baroclinic forcing and turbulence in an estuary. *J. Geophys. Res. Oceans* 108:3089. doi: 10.1029/2002JC001392

Lerczak, J. A., and Geyer, W. R. (2004). Modeling the lateral circulation in straight stratified estuaries. *J. Phys. Oceanogr.* 34, 1410–1428. doi: 10.1175/1520-0485(2004)034<1410:mtlcis>2.0.co;2

Lewis, E. R., and Wallace, D. W. R. (1998). *CO2SYS-Program Developed for CO2 System Calculations*. Tennessee: Carbon Dioxide Inf. Anal. Centre.

Li, M., Lee, Y. J., Testa, J. M., Li, Y., Ni, W., Kemp, W. M., et al. (2016). What drives interannual variability of hypoxia in Chesapeake Bay: climate forcing versus nutrient loading? *Geophys. Res. Lett.* 43, 2127–2134. doi: 10.1002/2015GL067334

Li, M., Zhong, L., and Boicourt, W. C. (2005). Simulations of Chesapeake Bay estuary: sensitivity to turbulence mixing parameterizations and comparison with observations. *J. Geophys. Res. Oceans* 110:C12004. doi: 10.1029/2004JC002585

Li, M., Zhong, L., Boicourt, W. C., Zhang, S., and Zhang, D. (2006). Hurricane-induced storm surges, currents and destratification in a semi-enclosed bay. *Geophys. Res. Lett.* 33:L02604. doi: 10.1029/2005GL024992

Li, Y., and Li, M. (2011). Effects of winds on stratification and circulation in a partially mixed estuary. *J. Geophys. Res. Oceams* 116:C12012. doi: 10.1029/2010JC006893

Li, Y., and Li, M. (2012). Wind-driven lateral circulation in a stratified estuary and its effects on the along-channel flow. *J. Geophys. Res. Oceams* 117:C09005. doi: 10.1029/2011JC007829

Li, Y., Li, M., and Kemp, W. M. (2015). A budget analysis of bottom-water dissolved oxygen in Chesapeake Bay. *Estuar. Coast.* 38, 2132–2148. doi: 10.1007/s12237-014-9928-9

Loesch, H. (1960). Sporadic mass shoreward mgrations of demersal fish and crustaceans in Mobile Bay, Alabama. *Ecology* 41, 292–298. doi: 10.2307/1930218

Malone, T. C., Kemp, W. M., Ducklow, H. W., Boynton, W. R., Tuttle, J. H., and Jonas, B. (1986). Lateral variation in the production and fate of phytoplankton in a partially stratified estuary. *Mar. Ecol. Prog. Ser.* 32, 149–160. doi: 10.3354/meps032149

Miller, S. H., Breitburg, D. L., Burrell, R. B., and Keppel, A. G. (2016). Acidification increases sensitivity to hypoxia in important forage fishes. *Mar. Ecol. Prog. Ser.* 549, 1–8. doi: 10.3354/meps11695

Moore-Maley, B. L., Ianson, D., and Allen, S. E. (2018). The sensitivity of estuarine aragonite saturation state and pH to the carbonate chemistry of a freshet-dominated river. *Biogeosciences* 15, 3743–3760. doi: 10.5194/bg-15-3743-2018

Ni, W., Li, M., and Testa, J. M. (2020). Discerning effects of warming, sea level rise and nutrient management on long-term hypoxia trend in Chesapeake Bay. *Sci. Total Environ.* 737:139717. doi: 10.1016/j.scitotenv.2020.139717

Pacellaa, S. R., Browna, C. A., Waldbusserb, G. G., Labiosac, R. G., and Halesb, B. (2018). Seagrass habitat metabolism increases short-term extremes and long-term offset of CO2 under future ocean acidification. *PNAS* 115, 2870–2875.

Paerl, H. W., Crosswell, J. R., Van Dam, B., Hall, N. S., Rossignol, K. L., Osburn, C. L., et al. (2018). Two decades of tropical cyclone impacts on North Carolina's estuarine carbon, nutrient and phytoplankton dynamics: implications for biogeochemical cycling and water quality in a stormier world. *Biogeochemistry* 141, 307–332. doi: 10.1007/s10533-018-0438-xvolV)

Raymond, P. A., Bauer, J. E., and Cole, J. J. (2000). Atmospheric CO_2 evasion, dissolved inorganic carbon production, and net heterotrophy in the York River estuary. *Limnol. Oceanogr.* 45, 1707–1717. doi: 10.4319/lo.2000.45.8.1707

Reynolds-Fleming, J. V., and Luettich, R. A. (2004). Wind-driven lateral variability in a partially mixed estuary. *Estua. Coast. Shelf Sci.* 60, 395–407. doi: 10.1016/j.ecss.2004.02.003

Ribas-Ribas, M., Anfuso, E., Gomez-Parra, A., and Forja, J. M. (2013). Tidal and seasonal carbon and nutrient dynamics of the Guadalquivir estuary and the Bay of Cadiz (SW Iberian Peninsula). *Biogeosciences* 10, 4481–4491. doi: 10.5194/bg-10-4471-2013

Saderne, V., Fietzek, P., and Herman, P. M. J. (2013). Extreme Variations of pCO2 and pH in a macrophyte meadow of the Baltic Sea in summer: evidence of the effect of photosynthesis and local upwelling. *PLoS One* 8:e62689. doi: 10.1371/journal.pone.0062689

Salisbury, J., Green, M., Hunt, C., and Campbell, J. (2008). Coastal acidification by rivers: a threat to shellfish? *EOS Trans. AGU* 89, 513–514. doi: 10.1029/2008eo500001

Sanford, L. P., Sellner, K. G., and Breitburg, D. L. (1990). Covariability of dissolved-oxygen with physical processes in the summertime Chesapeake Bay. *J. Mar. Res.* 48, 567–590. doi: 10.1357/002224090784984713

Scully, M. E. (2010). Wind modulation of dissolved oxygen in Chesapeake Bay. *Estuar.Coast.* 33, 1164–1175. doi: 10.1007/s12237-010-9319-9

Scully, M. E., Geyer, W. R., and Lerczak, J. A. (2009). The Influence of lateral advection on the residual estuarine circulation: a numerical modeling study of the Hudson River estuary. *J. Phys. Oceanogr.* 39, 107–124. doi: 10.1175/2008jpo3952.1

Shadwick, E. H., Friedrichs, M. A. M., Najjar, R. G., De Meo, O. A., Friedman, J. R., Da, F., et al. (2019). High frequency CO2 system variability over the winter-to-spring transition in a coastal plain estuary. *J. Geophys. Res. Oceans* 124, 7626–7642. doi: 10.1029/2019JC015246

Shchepetkin, A. F., and McWilliams, J. C. (2005). The regional oceanic modeling system (ROMS): a split-explicit, free-surface, topography-following-coordinate oceanic model. *Ocean Model.* 9, 347–404. doi: 10.1016/j.ocemod.2004.08.002

Shen, C., Testa, J. M., Li, M., and Cai, W.-J. (2020). Understanding anthropogenic impacts on pH and aragonite saturation state in Chesapeake Bay: insights from a 30-year model study. *J. Geophys. Res. Biogeosci.* 125:e2019JG005620. doi: 10.1029/2019JG005620

Shen, C., Testa, J. M., Li, M., Cai, W.-J., Waldbusser, G. G., Ni, W., et al. (2019a). Controls on carbonate system dynamics in a coastal plain estuary: a modeling study. *J. Geophys. Res. Biogeosci.* 124, 61–78. doi: 10.1029/2018JG004802

Shen, C., Testa, J. M., Ni, W., Cai, W.-J., Li, M., and Kemp, W. M. (2019b). Ecosystem metabolism and carbon balance in Chesapeake Bay: a 30-year analysis using a coupled hydrodynamic-biogeochemical model. *J. Geophys. Res. Oceans* 124, 6141–6153. doi: 10.1029/2019jc015296

Smith, G. F. (1997). *Maryland's Historical Oyster Bottom: A Geographic Representation of the Traditional Named Oyster Bars*. Oxford: Report of Fisheries Service, Maryland Department of Natural Resources and Cooperative Oxford Laboratory.

Talmage, S. C., and Gobler, C. J. (2010). Effects of past, present, and future ocean carbon dioxide concentrations on the growth and survival of larval shellfish. *PNAS* 107, 17246–17251. doi: 10.1073/pnas.0913804107

Testa, J. M., Brady, D. C., Di Toro, D. M., Boynton, W. R., Cornwell, J. C., and Kemp, W. M. (2013). Sediment flux modeling: nitrogen, phosphorus and silica cycles. *Estuar. Coast. Shelf Sci.* 131, 245–263. doi: 10.1016/j.ecss.2013.06.014

Testa, J. M., Li, Y., Lee, Y. J., Li, M., Brady, D. C., Di, D. M., et al. (2014). Quantifying the effects of nutrient loading on dissolved O2 cycling and hypoxia in Chesapeake Bay using a coupled hydrodynamic – biogeochemical model. *J. Mar. Syst.* 139, 139–158. doi: 10.1016/j.jmarsys.2014.05.018

Testa, J. M., Li, Y., Lee, Y. J., Li, M., Brady, D. C., DiToro, D. M., et al. (2017). "Modeling physical and biogeochemical controls on dissolved oxygen in Chesapeake Bay: lessons learned from simple and complex approaches," in *Modeling Coastal Hypoxia - Numerical Simulations of Patterns, Controls and Effects of Dissolved Oxygen Dynamics*, eds D. Justic, K. Rose, R. Hetland, and K. Fennel (Switzerland: Springer), 95–118. doi: 10.1007/978-3-319-54571-4_5

Waldbusser, G. G., Hales, B., Langdon, C. J., Haley, B. A., Schrader, P., Brunner, E. L., et al. (2015). Saturation-state sensitivity of marine bivalve larvae to ocean acidification. *Nat. Clim. Change* 5, 273–280. doi: 10.1038/nclimate2479

Waldbusser, G. G., and Salisbury, J. E. (2014). Ocean acidification in the coastal zone from an organism's perspective: multiple system parameters, frequency domains, and habitats. *Annu. Rev. Mar. Sci.* 6, 221–247. doi: 10.1146/annurev-marine-121211-172238

Waldbusser, G. G., Voigt, E., Bergschneider, H., Green, M., and Newell, R. E. (2011). Biocalcification in the Eastern Oyster (*Crassostrea virginica*) in relation to long-term trends in Chesapeake Bay pH. *Estua. Coast.* 34, 221–231. doi: 10.1007/s12237-010-9307-0

Wilson, R. E., Swanson, R. L., and Crowley, H. A. (2008). Perspectives on long-term variations in hypoxic conditions in western Long Island Sound. *J. Geophys. Res. Oceans* 113:C12011. doi: 10.1029/2007JC004693

Xie, X., and Li, M. (2018). Effects of wind straining on estuarine stratification: a combined observational and modeling study. *J. Geophys. Res. Oceans* 123, 2363–2380. doi: 10.1002/2017JC013470

Xie, X., Li, M., and Boicourt, W. C. (2017). Baroclinic effects on wind-driven lateral circulation in Chesapeake Bay. *J. Phys. Oceanogr.* 47, 433–445. doi: 10.1175/JPO-D-15-0233.1

Zhong, L., and Li, M. (2006). Tidal energy fluxes and dissipation in the Chesapeake Bay. *Cont. Shelf Res.* 26, 752–770. doi: 10.1016/j.csr.2006.02.006

Zhong, L., Li, M., and Foreman, M. G. (2008). Resonance and sea level variability in Chesapeake Bay. *Cont. Shelf Res.* 28, 2565–2573. doi: 10.1016/j.csr.2008.07.007

Conflict of Interest: The authors declare that the research was conducted in the absence of any commercial or financial relationships that could be construed as a potential conflict of interest.

Copyright © 2020 Li, Li, Cai, Testa and Shen. This is an open-access article distributed under the terms of the Creative Commons Attribution License (CC BY). The use, distribution or reproduction in other forums is permitted, provided the original author(s) and the copyright owner(s) are credited and that the original publication in this journal is cited, in accordance with accepted academic practice. No use, distribution or reproduction is permitted which does not comply with these terms.

frontiers in Marine Science

ORIGINAL RESEARCH
published: 05 November 2020
doi: 10.3389/fmars.2020.594725

Inter-annual Variability of the Carbonate System in the Hypoxic Upper Pearl River Estuary in Winter

Xianghui Guo[1,2,3], Xue Song[1,2], Ying Gao[1,2], Yaohua Luo[1,2], Yi Xu[1], Tao Huang[1] and Lifang Wang[1,2]*

[1] State Key Laboratory of Marine Environmental Science, Xiamen University, Xiamen, China, [2] College of Ocean and Earth Sciences, Xiamen University, Xiamen, China, [3] Fujian Provincial Key Laboratory for Coastal Ecology and Environmental Studies, Xiamen University, Xiamen, China

Hypoxia has become a universal environmental and ecological problem in recent decades. The Pearl River estuary (PRE), the largest estuary in Southern China, is hypoxic year-round in the upper estuary. This study reports the inter-annual variation between 2005 and 2019 in the carbonate system of the hypoxic upper PRE in winter. In January 2005, both dissolved inorganic carbon (DIC) and total alkalinity (TA) concentrations were >3000 μmol kg^{-1} at the upstream-most station and decreased sharply downstream. However, DIC and TA were lower, with concentrations of 2300 and 1950 μmol kg^{-1}, respectively, at the upstream-most in January 2019. At salinities >15, both DIC and TA were conservative and reached steady values at the downstream seawater end-member. The upstream-most station was taken as an example to quantify the influences of biogeochemical processes on DIC and TA, including CO_2 degassing, organic carbon oxidation, pelagic nitrification, $CaCO_3$ dissolution and benthic release. Among the biogeochemical process, a decrease in $CaCO_3$ dissolution (from 734.4 μmol kg^{-1} in 2005 to 168.9 μmol kg^{-1} in 2019) was the major factor driving the decreases of DIC and TA in 2019. In the context of global change, inter-annual variability in biogeochemical process should receive more attention.

Keywords: Pearl River estuary, carbonate system, inter-annual variability, biogeochemical processes, hypoxic

OPEN ACCESS

Edited by:
Zhan Hu,
School of Marine Sciences (CAS), China

Reviewed by:
Meilin WU,
South China Sea Institute of Oceanology (CAS), China
Sun Cuici,
South China Sea Institute of Oceanology (CAS), China

****Correspondence:***
Xianghui Guo
xhguo@xmu.edu.cn

Specialty section:
This article was submitted to Coastal Ocean Processes, a section of the journal Frontiers in Marine Science

Received: *14 August 2020*
Accepted: *12 October 2020*
Published: *05 November 2020*

Citation:
Guo X, Song X, Gao Y, Luo Y, Xu Y, Huang T and Wang L (2020) Inter-annual Variability of the Carbonate System in the Hypoxic Upper Pearl River Estuary in Winter. Front. Mar. Sci. 7:594725. doi: 10.3389/fmars.2020.594725

HIGHLIGHTS

- A significant inter-annual variation in DIC and TA in the hypoxic upper Pearl River estuary was observed between 2005 and 2019.
- Processes influencing DIC and TA were quantified in the hypoxic upper Pearl River estuary.

INTRODUCTION

Hypoxia in estuaries and coasts is a global environmental and ecological problem (Caballero-Alfonso et al., 2015; Fennel and Testa, 2019). Well-known hypoxic zones include the northern Gulf of Mexico (Rabalais and Turner, 2006), the Baltic Sea (Conley et al., 2011; Bendtsen and Hansen, 2013; Carstensen et al., 2014), Chesapeake Bay (Testa and Kemp, 2012; Li et al., 2016), and the East

China Sea off the Changjiang estuary (Li et al., 2002), as well as others. The Pearl River estuary (PRE) is the largest estuary in southern China, and is surrounded by several rapidly developing cities such as Guangzhou, Dongguan, Shenzhen, and others. Hypoxia in the PRE occurs mainly in two zones; one is the year-round hypoxic zone in the upper estuary from Guangzhou to Humen (Zhai et al., 2014), and the other is the seasonal hypoxic zone in summer at the estuary mouth and in waters near Hong Kong (Qian et al., 2018; Wang et al., 2018; Cui et al., 2019). In the hypoxic upper estuary, highly over-saturated CO_2 was observed all year round, with CO_2 partial pressures (pCO_2) up to >7000 μatm and dissolved inorganic carbon (DIC) concentration up to >3000 μmol kg^{-1} in winter (Xu et al., 2005; Dai et al., 2006, 2008; Guo et al., 2008; Zhai et al., 2014).

Viewing the entire PRE, Guo et al. (2008) reported the seasonal variability of carbonate parameters in the main channel of the estuary based on field observations from 2000 to 2005; Liang et al. (2020) simulated the spatial distributions of carbonate parameters in the summer and winter of 2006. In the hypoxic upper PRE, Guo et al. (2008) found that both DIC and total alkalinity (TA) showed large seasonal variations, with much higher values in winter (>3000 μmol kg^{-1}) than in summer (<1700 μmol kg^{-1}). They suggest that seasonal changes in the location of freshwater end-member, biogeochemical processes and hydrologic conditions are the major causes of the variability (Guo et al., 2008). More recently, field observations since 2010 have shown lower DIC and TA values (<2500 μmol kg^{-1}) in winter in the upper PRE (Dai et al., unpublished data). However, DIC and TA of the river waters were much lower than 2000 μmol kg^{-1} (Guo et al., unpublished data). This indicates that the very high DIC and TA concentrations previously found in the upper PRE in winters from 2000 to 2005 might be due to strong local additions from biogeochemical processes.

This study aims to: (1) confirm that DIC and TA in the upper PRE decreased after 2005, and (2) determine the key processes dominating the inter-annual variability in these parameters. In order to solve these two questions, we closely compare data collected from January 2005 and January 2019 in the estuary. The 2005 data were previously published (Guo et al., 2008), and the 2019 data were collected during a cruise at nearly the same locations in the upper PRE as the 2005 data. During the cruise, in addition to measuring carbonate system parameters, dissolved oxygen (DO) and nutrient measurements, and oxygen consumption and nitrification incubations were conducted using the same methods as in January 2005.

MATERIALS AND METHODS

Study Area

The Pearl River is the 2nd largest river in China and the 13th largest river in the world in terms of freshwater discharge, with an annual freshwater discharge of 3.3×10^{11} m^3 $year^{-1}$ (Zhao, 1990; Dai et al., 2014). The Pearl River has three major tributaries: the West River, the North River and the East River, and many local rivers and reticulated channels in the delta (**Figure 1**). The West River originates from the Yunnan–Guizhou Plateau and flows though Yunnan Province, Guizhou Province, the Guangxi Zhuang Autonomous Region and Guangdong Province. The North River and the East River originate from Jiangxi Province and flow through Guangdong Province. The three major tributaries contribute ∼95% of the freshwater discharge of the Pearl River system (Zhao, 1990). The drainage basins of the West River and North River have an abundance of carbonate minerals, while the drainage basin of the East River is rich in silicate minerals. Therefore, the bicarbonate and calcium concentrations in the West and North Rivers are higher than in the East River (Chen and He, 1999). The drainage basin of the Pearl River system is located in the south Asia tropical and subtropical areas, and ∼80% of the freshwater discharge occurs during the wet season from April to October, driven by the Asian monsoon (Zhao, 1990; Dai et al., 2014). The highest discharges of the three main tributaries occur from June to July, and lowest discharges are in winter (December–February, **Figure 2**).

All runoff from the Pearl River system discharges into the northern South China Sea (NSCS) via eight major outlets (from east to west: the Humen, Jiaomen, Hongqimen, Hengmen, Modaomen, Jitimen, Hutiaomen, and Yamen outlets) and through three sub-estuaries: the Lingdingyang, Modaomen, and Huangmaohai (**Figure 1**). Lingdingyang is traditionally called the PRE, which collects the freshwater from the eastern four outlets, including the East River and branches of the North and West Rivers.

The lower Pearl River drainage basin has several rapidly developing cities, such as Guangzhou, Dongguan, and others. Rapid economic and population growth have caused serious environmental problems, such as water pollution and hypoxia. In the early 2000s, whole water column hypoxia and very high ammonia concentrations (>800 μmol kg^{-1} in winter and >300 μmol kg^{-1} in summer) were observed in the upper estuary from Guangzhou to Humen (Dai et al., 2008). Strong aerobic respiration and nitrification induced very high pCO_2 and CO_2 degassing rates (Dai et al., 2006, 2008; Guo et al., 2008). Due to dilution by seawater and relatively weaker biogeochemical processes downstream, nutrient concentrations and pCO_2 decreased sharply downstream of the Humen Outlet, i.e., in the Lingdingyang (Dai et al., 2006; Guo et al., 2009).

Over the past few decades, sewage discharge and treatment rates have both significantly increased. For example, in the city Guangzhou, urban domestic sewage discharge increased from 7.4 billion tons $year^{-1}$ in 1995 to 14.3 billion tons $year^{-1}$ in 2015 (**Figure 3A**). At the same time, the sewage treatment rate also increased, from <10% in 1995 to 48% in 2005, and then to >85% after 2010 (**Figure 3B**). Subsequently, direct sewage discharge without treatment decreased sharply after 2005 (**Figure 3C**) (Bulletin of Statistics of Guangzhou's Environmental Status).[1] As a result, the water quality of the channels flowing through Guangzhou and Dongguan has improved considerably. During the January 2005 cruise, the water was black, had a noticeably bad smell, and wildlife such as fish and birds were not observed. However, in 2019, we observed greener water, flock of egrets, and the absence of previous odors. Therefore, 2005 is a

[1] http://sthjj.gz.gov.cn/gkmlpt/index

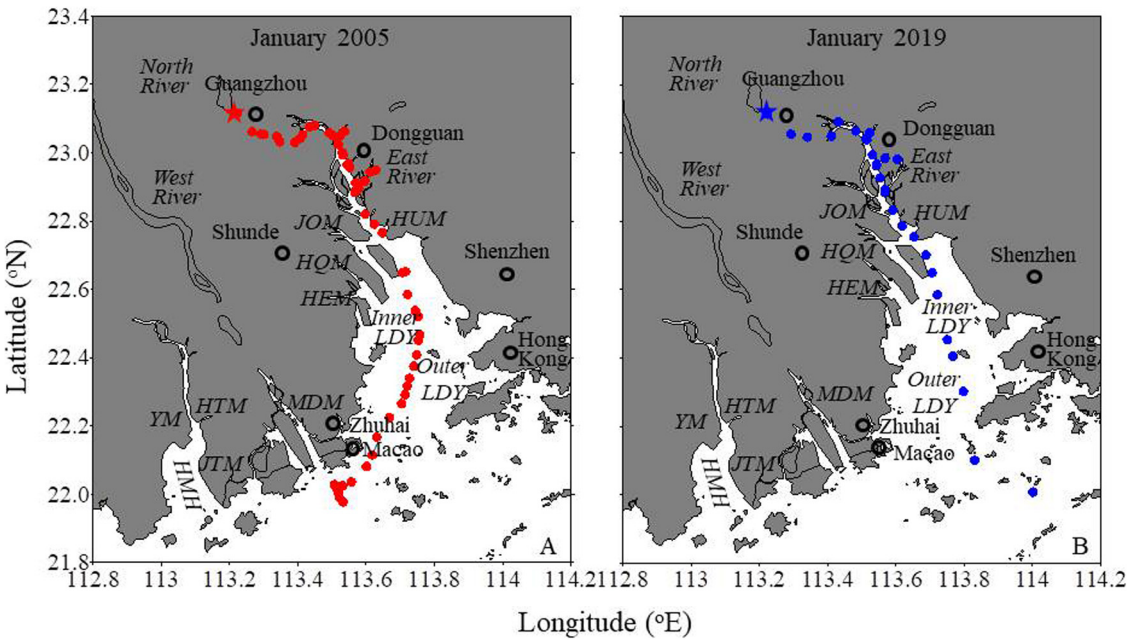


FIGURE 1 | The map of the Pearl River estuary with sampling stations (dots). HUM, JOM, HQM, HEM, MDM, JTM, HTM, and YM are the outlets of Humen, Jiaomen, Hongqimen, Hengmen, Modaomen, Jitimen, Hutiaomen, and Yamen. The black open circles mark the cities. LDY is the Lingdingyang; HMH is the Huangmaohai. The star is the incubation station. Data for the January 2005 cruise are from Guo et al. (2008).

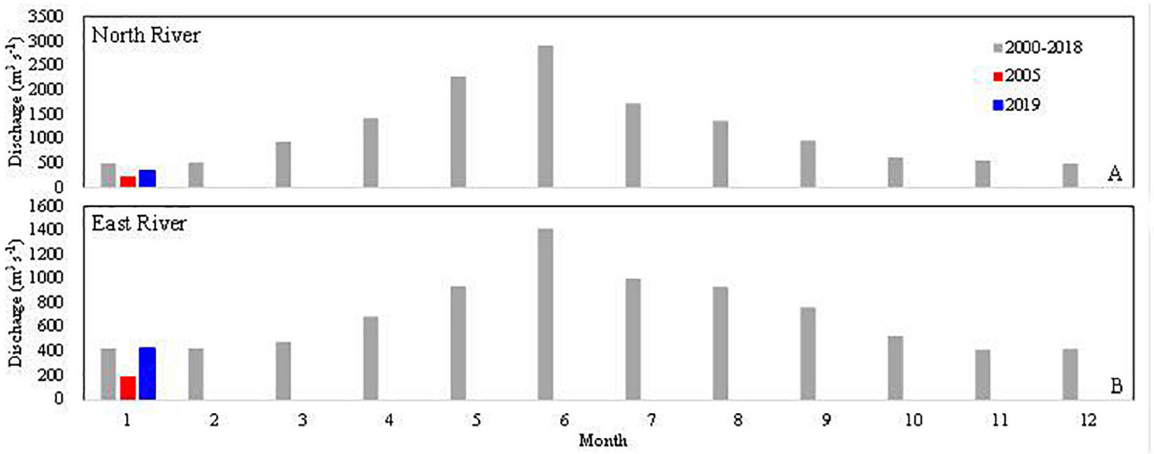


FIGURE 2 | Freshwater discharge downstream of the North River (Shijiao gauge station) and East River (Boluo gauge station). Label of panel **B** is the same with panel **A**. Data are from the Annual Hydrological Report (2000–2018), Hydrology Bureau, Ministry of Water Resources of the China (http://www.pearlwater.gov.cn/).

representative year of the huge impacts of direct sewage discharge and severe pollution, while 2019 is a representative year of water quality restoration.

Sampling and Analysis

Water Sample Collection

Cruises were conducted in the PRE from January 19–23, 2005, and from January 12–18, 2019, onboard the Yue-Dongguan-Yu 00589 and Yue-Zhu-Yu 31008. At each station, depth profiles of salinity and temperature were recorded with a YSI 6600 multi-parameter monitoring system (2005) or an AML BASE.X (sensor exchangeable Instrument) Conductivity-Temperature-Depth/pressure (CTD) sensor package (2019). Water samples were collected with 2 L or 5 L Niskin bottles.

Sub-samples for DO, pH, DIC/TA were taken with Tygon® tubing free of air bubbles, with ample sample overflow in order to minimize any contamination from atmospheric O_2 or CO_2. Samples for DO were sampled with 60 mL BOD (biological oxygen demand) bottles and fixed with Winkler reagents (Carpenter, 1965). Samples for pH were taken into

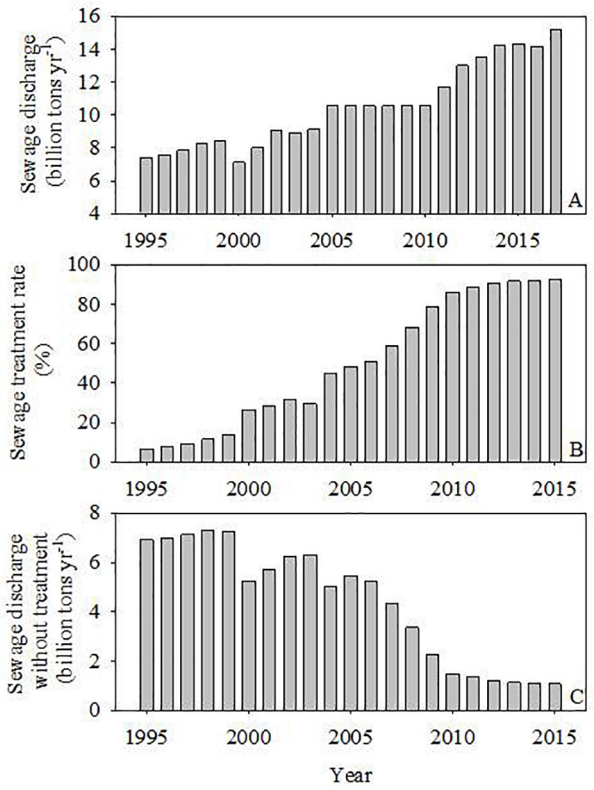


FIGURE 3 | Urban sewage discharges, sewage treatment rate, and sewage discharges without treatment from the city Guangzhou. Each column represents one year. Data were from the Bulletin of Statistics of Guangzhou's Environmental Status (1995–2015), http://sthjj.gz.gov.cn/gkmlpt/content.

120 mL amber glass bottles and poisoned with 100 μL of a saturated $HgCl_2$ solution. During the January 2005 cruise, DIC samples were sampled into 40 mL amber glass vials with 50 μL saturated $HgCl_2$ added; TA samples were sampled into 120 mL high-density Polyethylene (HDPE) bottles with 100 μL saturated $HgCl_2$ added. During the 2019 cruise, samples for DIC and TA measurements were taken into 250 mL borosilicate bottles with grounded stoppers and poisoned with 200 μL of the saturated $HgCl_2$ solution. All DIC and TA samples were stored in the dark at room temperature until analysis. Samples for nutrient and calcium (Ca^{2+}) measurements were filtered with 0.45 μm polyacetate filters. Samples for nitrite (NO_2^-), nitrate and nitrite (N + N), and soluble reactive phosphorus (SRP) were frozen and stored at −20°C until analysis. Samples for ammonium (NH_4^+) and silicate (Si) measurements were stored at −4°C until analysis. Samples for Ca^{2+} measurements were stored in the dark at room temperature.

CO_2 partial pressures of surface water and the atmosphere was measured with an underway system integrating an air-water equilibrator and a Li-Cor 7000 or Picarro G2101-i CO_2 analyzer. Six air-based CO_2 standard gases ranging 200 to 10000 parts per million provided by the National Reference Material Research Center of China were used to calibrate the measurements. Data processing was the same as previously described in Guo et al. (2009). Wind speed was measured with an R.M. Young model 05106 marine wind monitor at ∼10 m above the sea surface. The accuracy of wind speed measurements was ±0.3 m s^{-1}.

In February 18–19 of 2019, surface water samples were collected at gauge stations in the lower North and East Rivers (Shijiao in the North River and Boluo in the East River) to measured DIC, TA, nutrients, and calcium. The samples were taken with a 2 L plexiglass sampler. The sub-sampling, treatment and storage methods are the same as those during the January 2019 cruise.

Rate Incubation Experiments

Bulk oxygen consumption incubations were conducted at the upstream-most station (**Figure 1**) following the method of Dai et al. (2006). Briefly, surface water was pumped into a clean 400 L plastic box. After oxygenation, the water was transferred into two 20 L HDPE cubitainers (Thermo Fisher Scientific) immediately. 10 mL of a saturated $HgCl_2$ solution was added to one of the cubitainers as a control. The incubation was conducted in the dark and the temperature was controlled to match that of the surface water by using running water circulated outside of the cubitainers. Samples were taken every 3–6 h to measure DO. Bulk oxygen consumption rates were estimated from the change in the DO concentration over time.

Incubation experiments for estimating nitrification rates were conducted at the same stations as the bulk oxygen consumption incubations following the method of Dai et al. (2008). Briefly, surface water was sampled with 5 L Niskin bottles. Triplicate samples were filled into 4 L narrow-neck amber glass bottles. Allylthiourea (ATU, final concentration of 100 mg L^{-1}) and $NaClO_3$ (final concentration of 10 mg L^{-1}) were added to the bottles to inhibit the oxidation of NH_4^+ and NO_2^-, respectively. The third bottle was used as a control without reagent addition. Water samples were taken every 4–8 h to measure NO_2^-. NH_4^+ and NO_2^- oxidation rates were estimated from the change in the concentration of NO_2^- over time.

Sample Analysis

Dissolved oxygen samples were measured onboard with the classic Winkler method, and calibrated using a potassium iodate standard solution provided by the Reference Material Center of the Marine Ecology and Environmental Laboratory of the 2nd Institute of Oceanography (Ministry of Natural Resources of the People's Republic of China). The precision of the measurements was better than ±2 μmol kg^{-1}. pH samples were measured onboard within 2 h of sampling with a Corning 350 or Orion 3 Star pH meter and an Orion 8102BN Ross combination electrode calibrated against three NBS buffers (4.01, 7.00, and 10.01 at 25°C, provided by Thermo Fisher Scientific). Samples for pH measurements and buffers were placed in a constant temperature bath at 25 ± 0.01°C for about 1 h before their pH values were measured. Therefore, the measured pH values were at 25°C (pH_{25}) and given on the NBS scale. DIC and TA samples were measured onboard within 1 day of sampling during the 2005 cruise and within 1 week after the 2019 cruise. Analyses of DIC and TA followed the methods previously described by Cai et al. (2004). DIC was measured by collecting and quantifying

the CO_2 released from the sample upon acidification with a non-dispersive infrared detector (Li-Cor 7000) using an Apollo SciTech model AS-C3 DIC Analyzer with a precision of ±2 μmol kg^{-1}. TA was determined by Gran titration with hydrochloric acid using an automated alkalinity titrator (Apollo SciTech model AS-ALK1+) with a precision of better than ±2 μmol kg^{-1}. Both DIC and TA measurements were calibrated with certified reference material (CRM) provided by Dr. A. G. Dickson at the Scripps Institution of Oceanography, to obtain an accuracy of better than ±2 μmol kg^{-1}.

For the January 2019 cruise, Ca^{2+} was measured using the ethylene glycol tetraacetic acid (EGTA) titration method developed by Lebel and Poisson (1976) and modified by Cao and Dai (2011), with a precision of ±0.06%. The measurements were calibrated with artificial seawater based $CaCl_2$ solution. Salinity standard seawater of the International Association for the Physical Sciences of the Oceans (IAPSO) (Batch P158) was adopted as a reference. The measured Ca/salinity ratio of the IAPSO standard seawater was 291.6, which was slightly higher than the reported value of Batch P79 and P86 (290.5 and 290.9) (Olson and Chen, 1982), but slightly lower than the reported values of 292.0 for Batch P78 (Olson and Chen, 1982), 293.0 for Batch P67 (Kanamori and Ikegami, 1980), and 292.3 for Batch P147 (Cao and Dai, 2011). The deviations of the Ca/salinity ratios might be attributed to differences in the ratios of the different batches of the IAPSO standard seawater, and/or the system error among the different laboratories or operators. Nevertheless, our Ca/salinity ratio was very close to the average of the above literature values (291.7). The precision of our measurements (±0.06%) were ±5.8 μmol kg^{-1} for seawater with salinity of 33. For the January 2005 cruise, Ca^{2+} was measured with the ethylenediaminetetraacetic acid (EDTA) titrimetric method (China-EPA, 1987), with a precision of ±0.41%, (±39.5 μmol kg^{-1} for seawater with salinity 33).

Ammonium samples were measured onboard within 3 h of sampling using the indophenol blue method, with a detection limit of 0.1 μmol L^{-1} (Pai et al., 2001). NO_2^- was determined using the pink azo dye method; N + N was determined by copper-cadmium column reduction and the pink azo dye photometric method; SRP was determined with the phosphomolybdenum blue photometric method; silicate samples were determined using the silicomolybdic blue photometric method (Hansen and Koroleff, 1999). NO_2^-, N + N, SRP and silicate samples were all measured with an AA3 Auto-Analyzer (Bran-Lube, GmbH). The detection limits for NO_2^-, N + N, SRP and silicate were 0.04, 0.10, 0.08, and 0.16 μmol L^{-1}, respectively, and the analytical precision was better than 1% for N + N and silicate and 2% for SRP (Han et al., 2012).

Data Processing

The saturation state index (Ω) was defined as the product of the concentrations of Ca^{2+} ($[Ca^{2+}]$) and carbonate ($[CO_3^{2-}]$) divided by the apparent solubility product of $CaCO_3$ (K_{sp}^*) (Eq. 1).

$$\Omega = \frac{[Ca^{2+}] \times [CO_3^{2-}]}{K_{sp}^*} \quad (1)$$

$[Ca^{2+}]$ was the measured Ca^{2+} concentration. $[CO_3^{2-}]$ was calculated from DIC and TA with the program CO2SYS (Version 14) (Pierrot et al., 2006). The dissolution constants of carbonic acid are from Millero (2010). The CO_2 solubility coefficient is from Weiss (1974) and the sulfate dissociation constant from Dickson (1990). The PO_4^{3-} and SiO_2 data are the measured cruise data. K_{sp}^* at 1 standard atmosphere pressure was calculated from temperature and salinity according to the formula of Mucci (1983). The pressure correction of the K_{sp}^* of calcite was from Ingle (1975); the pressure correction of the K_{sp}^* of aragonite was from Millero (1979). The calculated Ω was 0.02–0.37 higher than the values calculated with CO2SYS, which might suggest the contribution of excess Ca^{2+} produced by the dissolution of $CaCO_3$ in the upper estuary.

DO saturation degree (DO%) was defined as the ratio of the measured DO to the DO at saturation (DO_{sat}) (Eq. 2). DO_{sat} was calculated according to the empirical formula of Benson and Krause (1984).

$$DO\ (\%) = (DO/DO_{sat}) \times 100\% \quad (2)$$

The net CO_2 flux (F_{CO2}) between surface water and the atmosphere (or air-sea CO_2 flux) was calculated using the following formula:

$$F_{CO2} = k \times s \times \Delta pCO_2 \quad (3)$$

$$k = 0.27 \times U_{10}{}^2 \times (Sc/660)^{-0.5} \quad (4)$$

where s is the solubility of CO_2 (Weiss, 1974), ΔpCO_2 is the pCO_2 difference between the surface water and the atmosphere, and k is the CO_2 transfer velocity. k was parameterized using the empirical function of Sweeney et al. (2007). U_{10} is the wind speed at 10 m above sea level (in m s^{-1}). Here, the daily average wind speeds were adopted in the FCO_2 calculations.

RESULTS

Salinity, Temperature and DO Saturation Degree

The freshwater sources of the upper PRE are mainly the North River and the East River. The long-term (2000–2018) monthly average freshwater discharge rates of the North and East Rivers are ∼500 and ∼420 m^3 s^{-1} in winter, equivalent to 25–40% of the freshwater discharge in summer (**Figure 2**). The low freshwater discharge in winter may have resulted in the higher salinities observed in the upper PRE in winter than in summer (salinity was 0 from Guangzhou to Humen in summer, Guo et al., 2008).

During both the January 2005 and 2019 cruises, the salinity of the upstream-most station at Guangzhou was <0.5, and increased downstream (**Figures 4A,B**). Salinity at the Humen Outlet ranged from 10 to 20, and increased to >25 in Outer Lingdingyang and 30–33 at the estuary mouth.

Surface water temperatures ranged from 14.6 to 18.8°C in January 2005, with the higher temperatures found in the low latitude zone (<22°N). In January 2019, temperatures

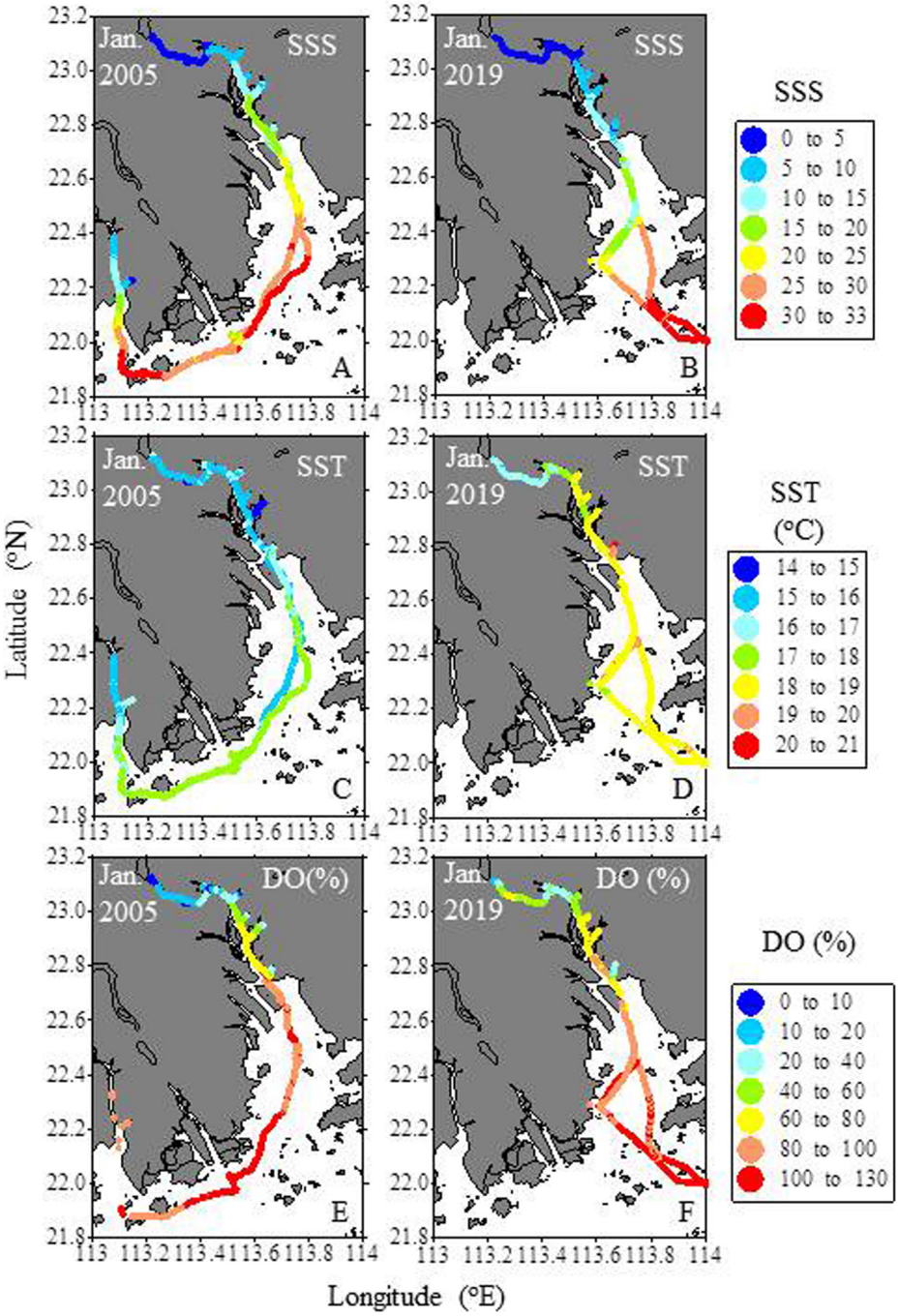


FIGURE 4 | Spatial distributions of salinity (SSS). temperature (SST) and DO saturation degree (DO%) of surface water in the Pearl River estuary in January of 2005 and 2019. The January 2005 data are from Guo et al. (2009).

ranged from 15.9 to 20.5°C, with higher temperatures in the Lingdingyang and outside of the estuary mouth than in the upper estuary (**Figures 4C,D**).

The DO saturation degree in the Guangzhou region ranged from ∼4–31% (12–93 μmol kg^{-1}) in January 2005, and most of this region was hypoxic. Downstream from Guangzhou, the DO saturation degree increased to 60–80% at the Humen Outlet and 80–100% in the Lingdingyang. Outside of the Lingdingyang, DO was slightly oversaturated (**Figure 4E**). In January 2019, DO saturation in the Guangzhou region ranged from 15 to 65% (45–200 μmol kg^{-1}), and hypoxic zones were observed at the two east-west ends of this region. Downstream of Guangzhou, the degree and pattern of DO saturation was similar to that observed in January 2005 (**Figure 4F**). Comparing the data of the two

January cruises reveals that DO was slightly higher in 2019 than in 2005 in the upper estuary (**Figures 4E,F**).

Spatial Distribution of Carbonate System Parameters, DO and Nitrogen-Containing Nutrients

In January 2005, DIC and TA values were as high as ∼3300 and 3100 μmol kg^{-1}, respectively, at the upstream-most station, and decreased sharply downstream. At salinities >15, both DIC and TA showed either a linear decrease or increase with salinity. However, the distributions of DIC and TA in January 2019 were different. At the upstream-most station, DIC and TA concentrations were 2300 and 1950 μmol kg^{-1}, respectively, ∼1000 μmol kg^{-1} lower than those measured at this station in 2005. They both decreased with salinity and reached their minima at salinity of ∼5. At salinities >5, both DIC and TA increased with salinity. Similar to the 2005 survey, at salinities >15, both DIC and TA were conservative (**Figures 5A-1,B-1**). As DIC and TA concentrations in the low salinity zone were much lower in 2019 than in 2005, their concentrations in almost the entire estuarine mixing zone were lower in 2019 than in

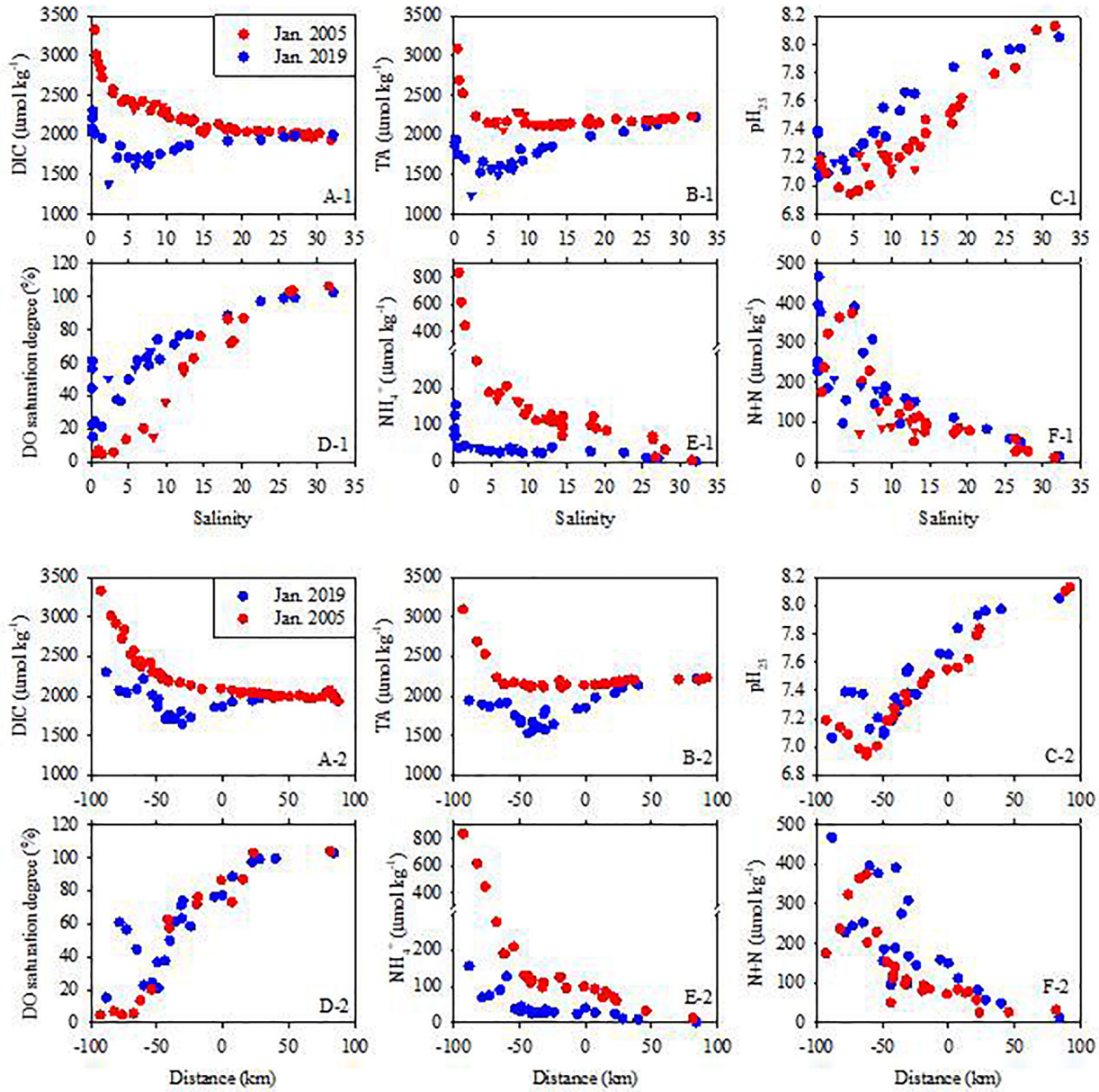


FIGURE 5 | DIC, TA, pH_{25}, DO, ammonium and N + N concentrations in surface water in January of 2005 and 2019. The distance is from Humen Outlet with negative values indicating upstream and positive values downstream locations. The triangles represent the data collected in the lower branches of the East River. For the January 2005 cruise, DIC, TA and pH_{25} data are from Guo et al. (2008), and nutrient data are from Dai et al. (2008). Legends are the same for all panels.

2005 (**Figures 5A-2,B-2**). At salinities >30, TA values in January of 2005 and 2019 were consistent, which indicated the stable characteristics of the seawater compared to the estuarine water (**Figure 5B-1**).

In January 2005, the pH at the upstream-most station was ∼7.2. pH decreased downstream and reached a minimum (6.9) at a salinity of ∼5 (**Figure 5C-1**), which was due mainly to the high rates of nitrification and aerobic respiration (Guo et al., 2008). At salinities >5, pH increased downstream and reached ∼8.11 at a salinity of ∼33 (**Figure 5C-1**). In January 2019, the distribution of pH in the upper estuary was slightly different from that in 2005. Although the pH at the upstream-most station was as low as 7.06, the pH in the middle of the Guangzhou region was as high as ∼7.4 (**Figure 5C-2**). pH decreased again to 7.1 further downstream (60 km upstream Humen Outlet), and then increased with salinity to 8.05 at a salinity of 32.5. Compared with 2005, DO in the Guangzhou region in 2019 was generally higher. However, at the same site downstream of Guangzhou (from the distance of −50 km downstream), the DO saturation degree in 2019 resembled January 2005 (**Figure 5D-2**). The relatively higher pH at stations in the Guangzhou region in January 2019 was accompanied by higher DO concentrations (**Figures 5C-2,D-2**).

In January 2005, NH_4^+ concentrations in the most upper estuary were as high as 800 μmol kg^{-1} and decreased sharply downstream to 3 μmol kg^{-1} at salinities >30 (**Figures 5E-1,E-2**). N + N concentrations increased from 177 μmol kg^{-1} at the upstream-most station to a maximum of 372 μmol kg^{-1} at a salinity of ∼5, and then decreased to 10 μmol kg^{-1} at salinities >30 (**Figures 5F-1,F-2**). The sharp decrease in NH_4^+ concentrations and maximum N + N concentrations in the low salinity zone were due to the presence of strong nitrification (Dai et al., 2008; Guo et al., 2008). In January 2019, the NH_4^+ concentration at the upstream-most station was 150 μmol kg^{-1}, much lower than in 2005. Consequently, NH_4^+ concentrations across the entire estuarine mixing zone were much lower in 2019 than in 2005. However, the N + N concentration at upstream-most stations (up to 463 μmol kg^{-1}) was higher than in 2005 (**Figures 5E-1,E-2,F-1,F-2**). This might be due mainly to the nitrification process during sewage treatment (EPA, 1993). The total concentration of NH_4^+ and N + N at the upstream-most station was also much lower in 2019 than in 2005 (1009.6 vs. 622.7 μmol kg^{-1}), which might be due to the denitrification process during sewage treatment (EPA, 1993).

Distribution of Calcium, and the Saturation State Index of Calcium Carbonate

Calcium concentrations ranged from 1798 to 9410 μmol kg^{-1} in January 2005 and from 989 to 9529 μmol kg^{-1} in January 2019. Although generally the Ca^{2+} concentration increased with salinity, the overall distribution of Ca^{2+} was slightly different between the two winter cruises. In 2005, Ca^{2+} concentrations in the low salinity zone were higher than in 2019. If the conservative mixing line between the North River and seawater was taken as a reference, Ca^{2+} concentrations showed additions in the low salinity zone in January of both 2005 and 2019, and the addition in 2005 was higher than in 2019.

The saturation state indices of both aragonite and calcite were <1 in the upper PRE (upstream of Humen Outlet, salinity <15), suggesting under-saturation for both aragonite and calcite minerals. In the area downstream of the Humen Outlet, Ω_{Ca} increased to ∼5.2 in 2005 and 4.0 in 2019, and Ω_{Ar} increased to 3.2 in 2005 and 2.4 in 2019, at the seawater end-member (**Figure 6**). The higher saturation state indices of calcite and aragonite in the high salinity zone in 2005 were due mainly to a local phytoplankton bloom, which was consistent with the relatively higher pH and DO, but lower DIC, in 2005.

Bulk Oxygen Consumption and Nitrification Rates

Bulk Oxygen Consumption Rate

In January of 2005 and 2019, DO decreased almost linearly during incubations without $HgCl_2$ addition, while DO concentrations remained almost constant for the samples with $HgCl_2$ added (control samples, **Figure 7**). The bulk oxygen consumption rates were 55.88 and 49.44 μmol L^{-1} d^{-1} in 2005 and 2019, respectively (**Table 1**).

In addition, we may use *in situ* DO concentrations to estimate the bulk oxygen consumption rate. In January 2005, DO saturation at the upstream-most station was 311.6 μmol kg^{-1}, while the *in situ* DO concentration was 14.9 μmol kg^{-1}. Therefore, the DO consumption was 296.7 μmol kg^{-1}. Assuming a residence time of 5 days (Guo et al., 2008), the DO consumption rate would be 59.3 μmol L^{-1} d^{-1}. This value is consistent with the value of 55.9 μmol L^{-1} d^{-1} estimated based on the incubations (**Table 1**). In January 2019, the *in situ* DO concentration at Guangzhou was 45.6 μmol kg^{-1} and the DO saturation was 302.7 μmol kg^{-1}. Therefore, the *in situ* DO consumption was 257.1 μmol kg^{-1}. If a residence time of 5 days is adopted (Guo et al., 2008), the bulk oxygen consumption rate is estimated as 51.4 μmol L^{-1} d^{-1}, which is reasonably consistent with values based on the incubations (49.4 μmol L^{-1} d^{-1}, **Table 1**).

Compared to other estuaries, the bulk oxygen consumption rate measured in the upper PRE is similar to that estimated in the polluted Seine River estuary in the spring and fall of 1996 [20–68 μmol L^{-1} d^{-1} assuming an average depth of 5 m, Garnier et al. (2001)]. However, it is higher than that found in the inner Scheldt estuary in the winter of 2003 [18–21 μmol L^{-1} d^{-1}, Gazeau et al. (2005)], or the polluted Huangpu River flowing through the city Shanghai (a branch of the lower Changjiang) in the winter and fall of 2005, which was 4–11 μmol L^{-1} d^{-1} (Zhai et al., 2007). However, it is lower than in salt marsh waters of the southeastern United States measured during the fall of 1995 and summer of 1996 [80 μmol L^{-1} d^{-1}, Cai et al. (1999)].

Nitrification Rate

In January 2005 and 2019, NO_2^- concentrations decreased in the samples with ATU added (inhibiting the oxidation of NH_4^+ to NO_2^-) during the incubations, suggesting the conversion of NO_2^- to NO_3^-. However, the NO_2^- concentration increased in the incubations with $NaNO_3$ added (inhibiting the oxidation

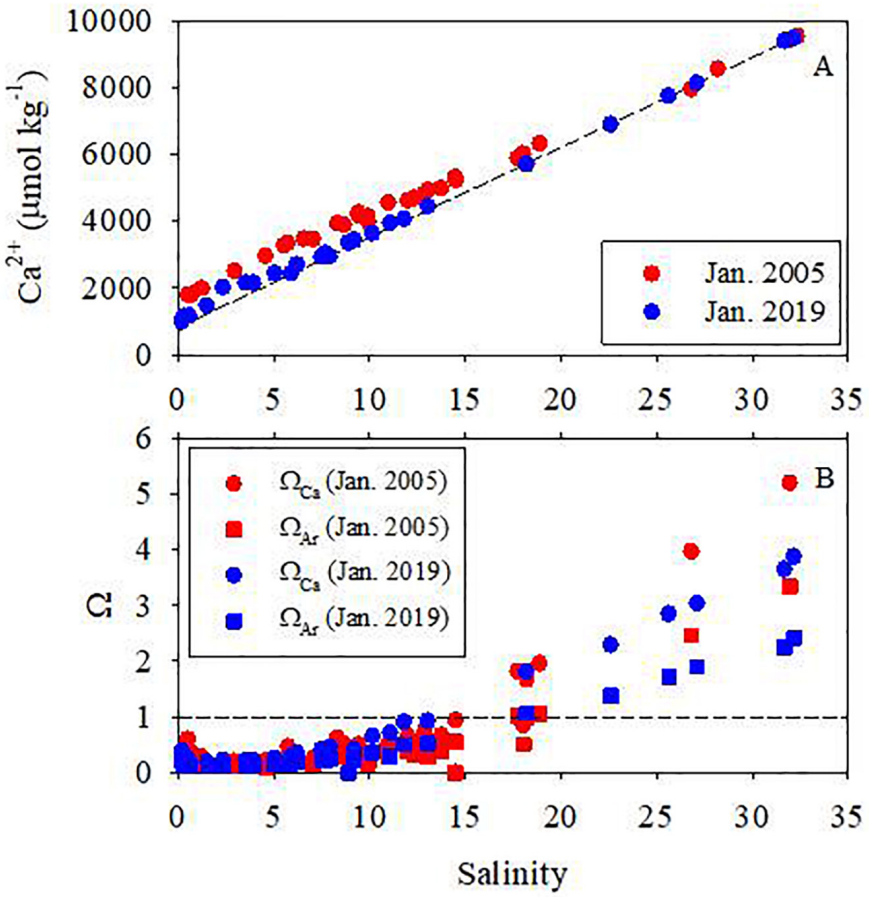


FIGURE 6 | Distributions of Ca^{2+} concentration and saturation state indices of calcite (Ω_{Ca}) and aragonite (Ω_{Ar}) in the surface water of the Pearl River estuary. The dashed line in panel **(A)** is the conservative mixing line. The dashed line in panel **(B)** represents $\Omega = 1$. Legends are the same for both panels.

of NO_2^- to NO_3^-), suggesting the accumulation of NO_2^- by converting NH_4^+ to NO_2^- (**Figure 8**). The estimated NH_4^+ oxidation rate was 3.86 μmol L^{-1} d^{-1} in 2005 and 6.53 μmol L^{-1} d^{-1} in 2019. The NO_2^- oxidation rate was 4.62 μmol L^{-1} d^{-1} in 2005 and 7.75 μmol L^{-1} d^{-1} in 2019 (**Table 1**). Nitrification rates in January of 2019 were higher than in January of 2005, but lower than in spring and summer [up to 31.5 μmol L^{-1} d^{-1}, Dai et al. (2008)]. Although NH_4^+ concentrations were lower in 2019 compared to 2005, the nitrification rate increased, which suggests that NH_4^+ concentrations are controlled by multiple factors. As the influencing factors of nitrification are beyond the scope of this study, we will not discuss it further here.

DISCUSSION

Processes Dominating DIC and TA Addition/Removal in the Upper PRE

Compared to January 2005, DIC and TA concentrations at the upstream-most station in January 2019 were both ∼1000 μmol kg^{-1} lower, but relatively consistent in the seawater end-member between both years. Influenced by the water characterized by very high DIC and TA at the upstream-most station, DIC and TA in the estuarine mixing zone at salinities <20 in January 2019 were much lower than those in January 2005 (**Figure 5**). It should be noted that DIC was slightly lower and pH and DO were slightly higher at the seawater end-member in 2005 (**Figures 5A-1,C-1,D-1**), which might be due to a weak local phytoplankton bloom.

The DIC and TA minima at salinity of ∼5 in 2019 were observed where the East River converges into the main channel of the estuary. Therefore, they might be due to the influence of East River water which was characterized by lower DIC and TA (the blue triangles in **Figures 5A-1,B-1**). DIC and TA in the East River were 605.3 and 566.6 μmol kg^{-1} in February 2019. The characteristically low DIC and TA concentrations of East River water were also reported in Guo et al. (2008). However, DIC and TA did not show this minima in January 2005, which might be due to large DIC and TA additions from local biogeochemical processes, similar to the case in the Guangzhou region.

Although both DIC and TA decreased downstream from the Guangzhou region, the very high DIC and TA values at the upstream-most station (3329.2 and 3093.5 μmol kg^{-1} in January 2005 and 2301.3 and 1947.2 μmol kg^{-1} in January

TABLE 1 | Environmental factors, air-water CO_2 flux (FCO_2), bulk oxygen consumption and nitrification rates of the water of the incubation station in the upper Pearl River estuary.

Time	Temp. (°C)	Salinity	NH_4^+ (μmol kg^{-1})	NO_2^- (μmol kg^{-1})	NO_3^- (μmol kg^{-1})	DO (μmol kg^{-1})	FCO_2 (mmol m^{-2} d^{-1})	O_2 consumption rate (μmol O_2 L^{-1} d^{-1})	NH_4^+ oxidation rate (μmol N L^{-1} d^{-1})	NO_2^- oxidation rate (μmol N L^{-1} d^{-1})
January 2005	16.0	0.69	838.2	68.3	107.9	15.4	175.5 ± 14.5	55.88	3.86	4.62
January 2019	16.4	0.31	155.2	43.2	424.3	45.7	174.5 ± 1.5	49.44	6.53	7.75

Nutrient data and nitrification rates for January 2005 are from Dai et al. (2008).

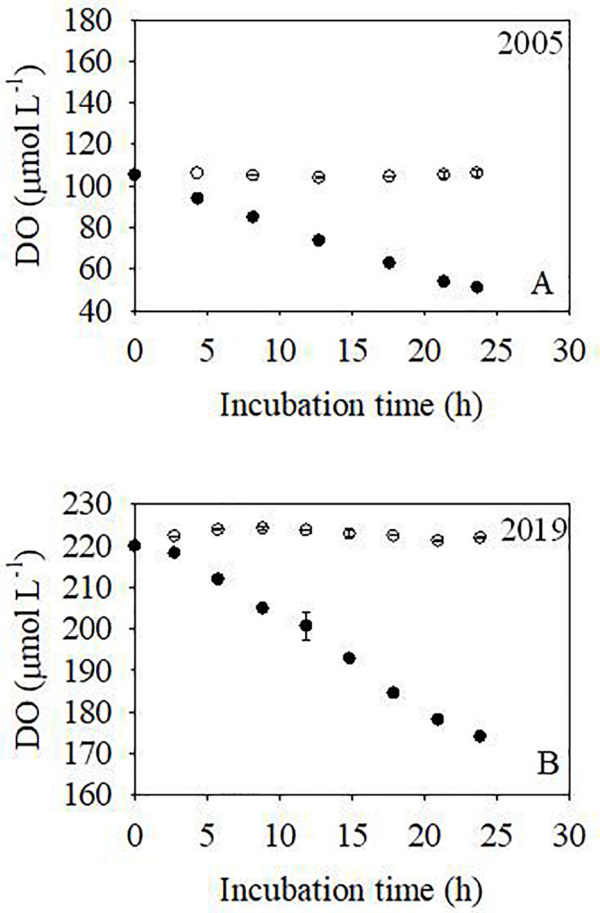


FIGURE 7 | Evolution of DO concentration during the incubations at the upstream-most station (Guangzhou). The solid circles are the samples without $HgCl_2$ addition; the open circles are the controls (samples with $HgCl_2$ added). Legends are the same for both panels.

2019, respectively) were not the river end-member values. The freshwater in the Guangzhou region was mostly from a branch of the North River. DIC and TA in the North River were 1587.5 and 1533.5 μmol kg^{-1} in January 2005 and 1575.4 and 1516.6 μmol kg^{-1} in January 2019 (Guo et al., unpublished data). DIC and TA in the East River were much lower. Therefore, there were local DIC and TA additions (1735.6 and 1549.2 μmol kg^{-1} additions in January 2005 and 707.4 and 539.5 μmol kg^{-1} additions in January 2019) in the Guangzhou region of the upper PRE.

Biogeochemical processes in the Guangzhou region of the upper PRE were very strong (Dai et al., 2006, 2008). Processes influencing DIC and TA concentrations include aerobic respiration, nitrification, air-water exchange of CO_2, and others (Guo et al., 2008). Benthic release is also an important DIC and TA source for the water column (Cai et al., 2015). Additionally, calcium carbonate dissolution or precipitation might also impact the carbonate system in estuarine environments (Abril et al., 2004; Macreadie et al., 2017; Su et al., 2020).

This complicated mixing scheme in the upper PRE makes it difficult to quantify the DIC and TA budget at all stations; thus, we take the upstream-most station as an example to quantify the influences of biogeochemical processes. At this station, the freshwater source was mainly the North River.

Air-Water CO_2 Exchange

The upper PRE was a strong CO_2 source. CO_2 evasion decreases DIC in the water, but has no influence on TA. The average air-water CO_2 exchange rate in the Guangzhou region was 175.5 ± 14.5 and 174.5 ± 1.5 mmol m^{-2} d^{-1} in January of 2005 and 2019, respectively (**Table 1**). If a residence time of 5 days and average water depth of 5 m are adopted (Zhao, 1990; Guo et al., 2008), the influence of CO_2 evasion would have decreased DIC by 175.5 and 174.5 μmol kg^{-1} in January 2005 and 2019, respectively. This shows the influence of CO_2 evasion on DIC was nearly identical in 2019 and 2005.

Pelagic Nitrification

The stoichiometric relationships of NH_4^+ and NO_2^- to DO and H^+ are expressed in Eqs. 5 and 6 (Dai et al., 2006). Only the oxidation of NH_4^+ to NO_2^- influences TA, and the ratio of change in TA to NH_4^+ concentrations is 2. Nitrification decreases TA in the water, but has no influence on DIC. At the upstream-most station, NH_4^+ oxidation rates were 3.86 μmol L^{-1} d^{-1} in January 2005 and 6.53 μmol L^{-1} d^{-1} in January 2019 (**Table 1**). Therefore, the rates of change in TA were 7.7 and 13.1 μmol L^{-1} d^{-1} in 2005 and 2019, respectively. Similarly, taking a residence time of 5 days (Guo et al., 2008), the TA change would be −38.6 and −65.3 μmol L^{-1} in 2005 and 2019.

$$NH_4^+ + 3/2O_2 \rightarrow NO_2^- + 2H^+ + H_2O \quad (5)$$

$$NO_2^- + 1/2\,O_2 \rightarrow NO_3^- \quad (6)$$

Organic Carbon Oxidation

The total oxygen consumption rate includes the oxygen consumption due to nitrification and organic carbon oxidation. During nitrification, the stoichiometric ratio of O_2 to NH_4^+ is 1.5 during the NH_4^+ oxidation process, and the ratio of O_2 to NO_2^- is 0.5 during the NO_2^- oxidation process (Eqs. 5 and 6). The NH_4^+ oxidation rate was 3.86 μmol L^{-1} d^{-1} in 2005 and 6.53 μmol L^{-1} d^{-1} in 2019, and the NO_2^- oxidation rate was 4.62 μmol L^{-1} d^{-1} in 2005 and 7.75 μmol L^{-1} d^{-1} in 2019 (**Table 1**). Therefore, the oxygen consumption rate induced by nitrification was 8.10 μmol O_2 L^{-1} d^{-1} in January 2005 and 13.69 μmol O_2 L^{-1} d^{-1} in January 2019, respectively.

As the total oxygen consumption rate at this station was 55.88 μmol L^{-1} O_2 d^{-1} in January 2005 and 49.44 μmol L^{-1} O_2 d^{-1} in January 2019, the DO consumption rate induced by the oxidation of organic carbon (excluding oxidation of nitrogen) was 47.78 μmol L^{-1} O_2 d^{-1} in January 2005 and 35.75 μmol L^{-1} O_2 d^{-1} in January 2019. According to the stoichiometric ratio of organic carbon oxidation (excluding nitrification of NH_4^+, Eq. 7), the DIC production rate due to organic carbon oxidation would be 47.78 μmol C L^{-1} d^{-1} in January 2005 and 35.75 μmol C L^{-1} d^{-1} in January 2019. If a residence time of 5 days is assumed (Guo et al., 2008), the DIC addition due to organic carbon oxidation would have been 238.9 μmol kg^{-1} in January 2005 and 178.8 μmol kg^{-1} in January 2019.

$$(CH_2O)_{106} + 106\,O_2 \rightarrow 106\,CO_2 + 106\,H_2O \quad (7)$$

$CaCO_3$ Dissolution

As the saturation state of $CaCO_3$ in the upper PRE ($\Omega < 0.5$) was well below the saturation level ($\Omega = 1$), $CaCO_3$ should dissolve. $CaCO_3$ dissolution influences both DIC and TA. We estimated the Ca^{2+} addition resulting from $CaCO_3$ dissolution according to the difference between the observed and estimated conservative mixing Ca^{2+} concentrations. To estimate the conservative Ca^{2+} concentration, we assume two end-member mixing between North River water and seawater. The relationship of the conservative mixing line of Ca^{2+} with salinity is expressed by Eq. 8.

$$[Ca^{2+}]\ (\mu mol\ kg^{-1}) = 278.75 \times \text{salinity} + 822.4 \quad (8)$$

In January 2005, the conservative Ca^{2+} concentration at the upstream-most station was 957.3 μmol kg^{-1}. As the measured Ca^{2+} concentration was 1691.8 μmol kg^{-1}, the Ca^{2+} addition was 734.4 μmol kg^{-1}. Since $CaCO_3$ dissolution adds DIC and TA by 1 and 2 times the amount of $CaCO_3$ dissolved (Eq. 9), the DIC and TA additions resulting from $CaCO_3$ dissolution were 734.4 and 1468.8 μmol kg^{-1}, respectively. Similarly, the conservative and observed Ca^{2+} concentrations were 882.9 and 1051.8 μmol kg^{-1} in January 2019, and the Ca^{2+} addition was 168.9 μmol kg^{-1}. The DIC and TA additions resulting from $CaCO_3$ dissolution were 168.9 and 337.8 μmol kg^{-1}, respectively. These estimates show that $CaCO_3$ dissolution in 2019 was much weaker than in 2005.

$$CaCO_3 + H^+ \leftrightarrow Ca^{2+} + HCO_3^- \quad (9)$$

The relatively lower $CaCO_3$ dissolution in January 2019 might be due to the relatively higher pH (**Figures 5C-1,C-2**). Low pH is favorable for $CaCO_3$ dissolution. Therefore, the relatively lower pH in 2005 might enhance $CaCO_3$ dissolution. However, $CaCO_3$ dissolution increases pH (Eq. 9), which adds the complexity of the relationship between pH and $CaCO_3$ dissolution.

Benthic Release

Denitrification can also influence DIC and TA (Chen, 2002), but as the water column was generally oxygenated (although DO < 60 μmol kg^{-1}) we assumed denitrification was negligible. However, both nitrification and denitrification might occur in the sediments of the PRE, which also influences the carbonate system in the water (Xu et al., 2005). Other anaerobic reactions (reduction of Fe/Mn and/or sulfate) in the sediment might also affect the carbonate system in the water. Anaerobic reactions in sediment consume protons and increase TA in the sediment porewater. Combined with the organic carbon degradation, DIC in porewater in the PRE was much higher than in the water column (Cai et al., 2015). The interactions between sediment and water at the water-sediment interface cause the sediment to release DIC and TA to the water column. A similar phenomenon of sedimentary reactions altering the

carbonate system in the water column was also observed in the northern Gulf of Mexico (Hu et al., 2017; Berelson et al., 2019).

As we didn't measure benthic fluxes during the cruises, we used the benthic DIC flux measured in November 2013 and the benthic TA/DIC ratio reported in the literature to estimate the influence of benthic release on the water column DIC and TA. In November 2013, the benthic DIC release rate at the upstream station was 1200 ± 300 mmol m^2 d^{-1} (Cai et al., 2015).

To account for the large influence of temperature on the rates of biogeochemical processes (Rabus et al., 2002; Govorushko, 2012), we calibrated the biogeochemical process rates in the sediment according to Eq. 10.

$$Q_{10} = e^{10k} \quad (10)$$

Q_{10} refers to the multiple of the increase in the rate of biochemical reactions per temperature increase of 10°C; k refers to the slope of the linear regression between temperature and the logarithm of rates.

The reported Q_{10} of anaerobic reactions in sediment ranges from 2 to 3 (Pomeroy and Wiebe, 2001; Kirchman et al., 2009), so a Q_{10} of 2.5 was taken in the estimation. The temperature in November 2013 when the sampling of Cai et al. (2015) was conducted was 22°C, while temperatures during our January 2005 and 2019 samplings were 16.0 and 16.4°C. Lowering the temperature by 6 and 5.6°C decreases the reaction rates by 1.73 and 1.67, respectively. Assuming that other conditions during our cruises were the same as November 2013, the benthic DIC release rate was 692.5 μmol m^2 d^{-1} in January 2005 and 718.3 μmol m^2 d^{-1} in January 2019.

The ratio of the benthic TA/DIC flux is 0.57–0.95 in the hypoxic northern Gulf of Mexico (Berelson et al., 2019). If this ratio range is similar in the PRE, the benthic TA flux would be 394.7–657.9 mmol m^{-2} d^{-1} in January 2005 and 409.5–682.4 mmol m^{-2} d^{-1} in January 2019.

The Guangzhou region of the upper PRE was well-mixed vertically, so the released benthic DIC and TA were likely homogenized throughout the whole water column. Taking an average water depth of 5 m and a residence time of 5 days (Zhao, 1990; Guo et al., 2008), the DIC and TA additions from the benthic flux would be 695.2 and 394.7–657.9 μmol kg^{-1} in January 2005, and 718.3 and 409.5–682.4 μmol kg^{-1} in January 2019. Therefore, considering the uncertainties in the benthic DIC and TA flux estimates, no conspicuous changes were observed between January 2005 and January 2019.

Inter-annual Variations in DIC and TA in the Upper PRE

The quantification of the above biogeochemical processes at the upstream-most station is shown in **Table 2**. The net influence of these biogeochemical processes was 1490.3 and 1824.9–2088.1 μmol kg^{-1} for DIC and TA in January 2005, and 895.1 and 682.0–954.9 μmol kg^{-1} for DIC and TA in January 2019. The estimates were generally consistent with the observed DIC and TA additions (1735.6 and 1549.2 μmol kg^{-1} in January 2005, and 707.4 and 539.5 μmol kg^{-1} in January 2019) at this station.

TABLE 2 | Quantified influences of biogeochemical processes on DIC and TA (ΔDIC and ΔTA) at Guangzhou in January of 2005 and 2019.

Biogeochemical processes	ΔDIC (μmol kg^{-1})		ΔTA (μmol kg^{-1})	
	2005	2019	2005	2019
CO_2 evasion	−175.5	−174.5	0.0	0.0
Pelagic nitrification	0.0	0.0	−38.6	−65.3
Organic carbon oxidation	238.9	178.8	0.0	0.0
$CaCO_3$ dissolution	734.4	168.9	1468.8	337.8
Benthic release	692.5	718.3	394.7–657.9	409.5–682.4
Net impact	1490.3	891.5	1824.9–2088.1	682.0–954.9
Observed addition	1735.6	707.4	1549.2	539.5

The only DIC sink for upper PRE water in January of both 2005 and 2019 was CO_2 evasion to the atmosphere, while the DIC sources were organic carbon oxidation, $CaCO_3$ dissolution and benthic release. The DIC removal due to CO_2 evasion to the atmosphere was almost the same during the two winter cruises (175.5 and 174.5 μmol kg^{-1} in 2005 and 2019, respectively). Although the DIC addition from organic carbon oxidation in January 2019 was slightly lower than in January 2005 (238.9 μmol kg^{-1} in 2005 vs. 178.8 μmol kg^{-1} in 2019), DIC removal due to CO_2 evasion was almost offset by the DIC addition resulting from organic carbon oxidation during both cruises relative to the size of the overall DIC budget. The most important sources of DIC were $CaCO_3$ dissolution and benthic release. As the benthic release rates were estimated based on previously reported benthic DIC fluxes and only the temperature effect was considered, estimates of benthic DIC release were similar during the two winter cruises as the temperatures were similar. A comparison between the two winter cruises indicates the largest differences were in the DIC addition due to $CaCO_3$ dissolution; DIC addition due to this process was 565.5 μmol kg^{-1} lower in January 2019 than in January 2005, controlling the much lower overall DIC addition observed in January 2019.

The only major sink for TA of the water was pelagic nitrification. As the nitrification rate in January 2019 was slightly higher than in January 2005, the TA removal in 2019 (65.3 μmol kg^{-1}) was slightly greater than in 2005 (38.6 μmol kg^{-1}). As was the case with DIC, the benthic TA release during both the 2005 and 2019 cruises was similar. However, the TA addition due to $CaCO_3$ dissolution in January 2019 was 1131.0 μmol kg^{-1} lower than in 2005, and dominated the decrease in the local TA addition in 2019 in the upper PRE.

Although the above estimates generally explain the inter-annual variations in DIC and TA in the upper PRE between 2005 and 2019, there are differences between the sum of the estimated and the observed addition values. These differences might be due to the different dynamic conditions during the different cruises as well as the uncertainties in estimating benthic DIC and/or TA fluxes. The uncertainties in water residence time, average depth, and other parameters might also add to the uncertainties of the estimates. In addition, the influence of complicated mixing on the biogeochemical processes across the entire estuarine mixing

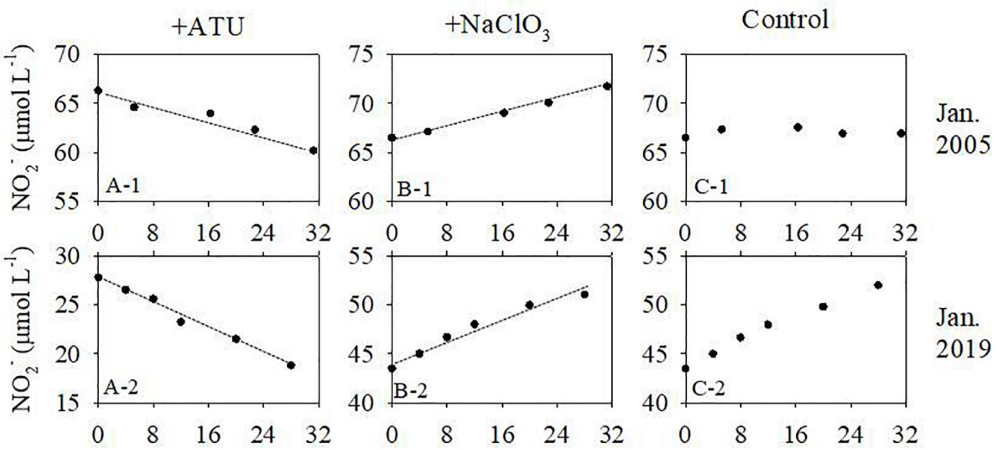


FIGURE 8 | Evolution of NO_2^- concentration during the nitrification incubations. The dashed lines are linear regressions. Data for January 2005 are from Dai et al. (2008). Labels are the same for all panels.

zone is yet to be quantified. The relationship between decreasing $CaCO_3$ dissolution and the improvement of water quality also needs further examination.

Ecological environmental improvement is a universal goal in China and across the world, and this may in turn influence the cycles of biogenic elements. Similar inter-annual variability in biogeochemical parameters or mass fluxes may manifest in other estuaries and coastal zones, which could also influence ocean element cycling and even local climate change. This phenomenon deserves more attention.

CONCLUSION

Dissolved inorganic carbon and TA distributions in the PRE were determined in January of 2005 and 2019. Although they show little difference in the high-salinity lower estuary, both DIC and TA in the heavily perturbed upper estuary showed a ∼1000 μmol kg^{-1} decrease in 2019 compared to 2005. The upstream-most station was used as an example to quantify the influences of biogeochemical processes on DIC and TA. For DIC, the CO_2 degassing was almost compensated by organic carbon oxidation, while benthic release and $CaCO_3$ dissolution contributed to the major additions. For TA, benthic release and $CaCO_3$ dissolution were the major additions, and pelagic nitrification contributed to slight removal. Although the above biogeochemical processes differed between the 2 years, the decrease in $CaCO_3$ dissolution dominated the DIC and TA decreases in the upper PRE in 2019 compared to 2005. In the context of global change, inter-annual variability in the biogeochemical parameters of estuaries and coasts might be universal and deserves more attention.

DATA AVAILABILITY STATEMENT

The raw data supporting the conclusions of this article will be made available by the authors, without undue reservation.

AUTHOR CONTRIBUTIONS

XG collected the oxygen consumption rate data from the January 2005 cruise. All authors collected the data from the January 2019 cruise except LW. XG designed the cruise, took the DIC, TA and pH samples. XS and YG conducted the nitrification and oxygen consumption incubation experiments. YL collected the nutrient and calcium samples. YX measured DO and pCO_2. TH measured the ammonium samples. YG and YL measured the N + N, phosphate and silicate samples. XS and YL measured the DIC, TA and calcium samples. YG and YL collected the North and East Rivers data in February 2019. XG drafted the manuscript and all authors participated the discussion on data interpretation.

FUNDING

This study was supported by the National Natural Science Foundation of China (grant numbers 41876080 and 41706079). The preparation of this manuscript was supported by the Strategic Priority Research Program of Chinese Academy of Sciences (grant number XDB42000000) and Hong Kong Research Grants Council (grant number T21-602/16-R).

ACKNOWLEDGMENTS

We are grateful to the crews of the ships Yue-Dong-Guan-Yu 00589 and Yue-Zhu-Yu 31008 for their help during the cruises. Baoshan Chen is appreciated for collecting the calcium data during the January 2005 cruise. Weifang Chen, Wen Lin, Yan Li, and Zhe Wang at Xiamen University, Dr. Huabin Mao at the South China Sea Institute of Oceanography (Chinese Academy of Sciences) and Ms. Haijuan Chen at Xinzhou Hotel (Guangzhou) are appreciated for their help in preparation and implementation of the cruises. The discussion with Dr. Wei-Jun Cai at University of Delaware was helpful in data interpretation.

REFERENCES

Abril, G., Commarieu, M. V., Maro, D., Fontugne, M., Guerin, F., and Etcheber, H. (2004). A massive dissolved inorganic carbon release at spring tide in a highly turbid estuary. *Geophys. Res. Lett.* 31:L09316.

Bendtsen, J., and Hansen, J. L. S. (2013). Effects of global warming on hypoxia in the Baltic Sea-North Sea transition zone. *Ecol. Model.* 264, 17–26. doi: 10.1016/j.ecolmodel.2012.06.018

Benson, B. B., and Krause, D. (1984). The concentration and isotopic fractionation of oxygen dissolved in freshwater and seawater in equilibrium with the atmosphere. *Limnol. Oceanogr.* 29, 620–632. doi: 10.4319/lo.1984.29.3.0620

Berelson, W. M., McManus, J., Severmann, S., and Rollins, N. (2019). Benthic fluxes from hypoxia-influenced Gulf of Mexico sediments: impact on bottom water acidification. *Mar. Chem.* 209, 94–106. doi: 10.1016/j.marchem.2019.01.004

Caballero-Alfonso, A. M., Carstensen, J., and Conley, D. J. (2015). Biogeochemical and environmental drivers of coastal hypoxia. *J. Mar. Syst.* 141, 190–199. doi: 10.1016/j.jmarsys.2014.04.008

Cai, P., Shi, X., Hong, Q., Li, Q., Liu, L., Guo, X., et al. (2015). Using 224Ra/228Th disequilibrium to quantify benthic fluxes of dissolved inorganic carbon and nutrients into the Pearl River Estuary. *Geochim. Cosmochim. Acta* 170, 188–203. doi: 10.1016/j.gca.2015.08.015

Cai, W.-J., Dai, M. H., Wang, Y. C., Zhai, W. D., Huang, T., Chen, S. T., et al. (2004). The biogeochemistry of inorganic carbon and nutrients in the Pearl River estuary and the adjacent Northern South China Sea. *Continent. Shelf Res.* 24, 1301–1319. doi: 10.1016/j.csr.2004.04.005

Cai, W.-J., Pomeroy, L. R., Moran, M. A., and Wang, Y. C. (1999). Oxygen and carbon dioxide mass balance for the estuarine-intertidal marsh complex of five rivers in the southeastern U S. *Limnol. Oceanogr.* 44, 639–649. doi: 10.4319/lo.1999.44.3.0639

Cao, Z., and Dai, M. (2011). Shallow-water CaCO3 dissolution: evidence from excess calcium in the South China Sea and its export to the Pacific Ocean. *Glob. Biogeochem. Cycles* 25:GB2019.

Carpenter, J. H. (1965). The chesapeake Bay Institute technique for the Winkler dissolved oxygen method. *Limnol. Oceanogr.* 10, 141–143. doi: 10.4319/lo.1965.10.1.0141

Carstensen, J., Andersen, J. H., Gustafsson, B. G., and Conley, D. J. (2014). Deoxygenation of the Baltic Sea during the last century. *Proc. Natl. Acad. Sci. U.S.A.* 111, 5628–5633. doi: 10.1073/pnas.1323156111

Chen, C.-T. A. (2002). Shelf vs. dissolution-generated alkalinity above the chemical lysocline. *Deep Sea Res. II* 49, 5365–5375. doi: 10.1016/s0967-0645(02)00196-0

Chen, J., and He, D. (1999). Chemical characteristics and genesis of major ions in the Pearl River basin. *Acta Sci. Nat. Univ. Pekinesis* 35, 786–793.

China-EPA (1987). Water quality-determination of calcium-EDTA titrametric method. National standards of people's republic of China. *Natl. Environ. Protect. Agency Peoples Republic China* 87, 56–59.

Conley, D. J., Carstensen, J., Aigars, J., Axe, P., Bonsdorff, E., Eremina, T., et al. (2011). Hypoxia is increasing in the Coastal Zone of the Baltic Sea. *Environ. Sci. Technol.* 45, 6777–6783.

Cui, Y., Wu, J., Ren, J., and Xu, J. (2019). Physical dynamics structures and oxygen budget of summer hypoxia in the Pearl River Estuary. *Limnol. Oceanogr.* 64, 131–148. doi: 10.1002/lno.11025

Dai, M., Gan, J., Han, A., Kung, H. S., and Yin, Z. (2014). *Physical Dynamics and Biogeochemistry of the Pearl River Plume, Biogeochemical Dynamics at Major River-Coastal Interface-Linkage with Global Change*. New York: Cambridge University Press, 321–352.

Dai, M., Wang, L., Guo, X., Zhai, W., Li, Q., He, B., et al. (2008). Nitrification and inorganic nitrogen distribution in a large perturbed river/estuarine system: the Pearl River Estuary, China. *Biogeosciences* 5, 1227–1244. doi: 10.5194/bg-5-1227-2008

Dai, M. H., Guo, X. H., Zhai, W. D., Yuan, L. Y., Wang, B. W., Wang, L. F., et al. (2006). Oxygen depletion in the upper reach of the Pearl River estuary during a winter drought. *Mar. Chem.* 102, 159–169. doi: 10.1016/j.marchem.2005.09.020

Dickson, A. G. (1990). Thermodynamics of the dissociation of boric acid in synthetic sea water from 273.15 to 318.15 K Deep. *Sea Res. A Oceanogr. Res. Pap.* 37, 755–766. doi: 10.1016/0198-0149(90)90004-f

EPA (1993). *Manual Nitrogen Control*. Washington DC: Office of Research and Development, Office of Water, United States Environmental Protection Agency.

Fennel, K., and Testa, J. M. (2019). Biogeochemical controls on coastal hypoxia. *Annu. Rev. Mar. Sci.* 11, 105–130. doi: 10.1146/annurev-marine-010318-095138

Garnier, J., Servais, P., Billen, G., Akopian, M., and Brion, N. (2001). Lower Seine River and estuary (France) carbon and oxygen budgets during low flow. *Estuaries* 24, 964–976. doi: 10.2307/1353010

Gazeau, F., Gattuso, J. P., Middelburg, J. J., Brion, N., Schiettecatte, L. S., Frankignoulle, M., et al. (2005). Planktonic and whole system metabolism in a nutrient-rich estuary (the Scheldt estuary). *Estuaries* 28, 868–883. doi: 10.1007/bf02696016

Govorushko, S. M. (2012). Influence of weather-climatic conditions on biospheric processes. *Atmos. Ocean. Phys.* 48, 771–784. doi: 10.1134/s0001433812080051

Guo, X. H., Cai, W.-J., Zhai, W. D., Dai, M. H., Wang, Y. C., and Chen, B. S. (2008). Seasonal variations in the inorganic carbon system in the Pearl River (Zhujiang) estuary. *Continent. Shelf Res.* 28, 1424–1434. doi: 10.1016/j.csr.2007.07.011

Guo, X. H., Dai, M. H., Zhai, W. D., Cai, W. J., and Chen, B. S. (2009). CO2 flux and seasonal variability in a large subtropical estuarine system, the Pearl River Estuary, China. *J. Geophys. Res. Biogeosci.* 114:G03013.

Han, A., Dai, M., Kao, S.-J., Gan, J., Li, Q., Wang, L., et al. (2012). Nutrient dynamics and biological consumption in a large continental shelf system under the influence of both a river plume and costal upwelling. *Limnol. Oceanogr.* 57, 486–502. doi: 10.4319/lo.2012.57.2.0486

Hansen, H. P., and Koroleff, F. (1999). *Determination of Nutrients, Methods of Seawater Analysis*. Toronto: Wiley-VCH, 159–228.

Hu, X., Li, Q., Huang, W.-J., Chen, B., Cai, W.-J., Rabalais, N. N., et al. (2017). Effects of eutrophication and benthic respiration on water column carbonate chemistry in a traditional hypoxic zone in the Northern Gulf of Mexico. *Mar. Chem.* 194, 33–42. doi: 10.1016/j.marchem.2017.04.004

Ingle, S. E. (1975). Solubility of calcite in the ocean. *Mar. Chem.* 3, 301–319. doi: 10.1016/0304-4203(75)90010-9

Kanamori, S., and Ikegami, H. (1980). Computer-processes potentiometric titration for the determination of calcium and magnesium in seawater. *J. Oceanogr. Soc. Jpn.* 36, 177–184.

Kirchman, D. L., Morán, X. A., and Ducklow, H. (2009). Microbial growth in the polar oceans—role of temperature and potential impact of climate change. *Nat. Rev. Microbiol.* 7, 451–459. doi: 10.1038/nrmicro2115

Lebel, J., and Poisson, A. (1976). Potentiometric determination of calcium and magnesium in seawater. *Mar. Chem.* 4, 321–332. doi: 10.1016/0304-4203(76)90018-9

Li, D. J., Zhang, J., Huang, D. J., Wu, Y., and Liang, J. (2002). Oxygen depletion off the Changjiang (Yangtze River) estuary. *Sci. China Ser. D Earth Sci.* 45, 1137–1146. doi: 10.1360/02yd9110

Li, M., Lee, Y. J., Testa, J. M., Li, Y., Ni, W., Kemp, W. M., et al. (2016). What drives interannual variability of hypoxia in Chesapeake Bay: climate forcing versus nutrient loading? *Geophys. Res. Lett.* 43, 2127–2134. doi: 10.1002/2015gl067334

Liang, B., Hu, J. T., Li, S. Y., Ye, Y. X., Liu, D. H., and Huang, J. (2020). Carbon system simulation in the Pearl River Estuary, China: mass fluxes and transformations. *J. Geophys. Res. Biogeosci.* 125:e2019JG005012.

Macreadie, P. I, Serrano, O., Maher, D. T., and Duarte, C. M. B. J. (2017). Addressing calcium crbonate cycling in blue carbon accounting. *Limnol. Oceanogr. Lett.* 2, 195–201. doi: 10.1002/lol2.10052

Millero, F. J. (1979). The thermodynamics of the carbonate system in seawater. *Geochim. Cosmochim. Acta* 43, 1651–1661. doi: 10.1016/0016-7037(79)90184-4

Millero, F. J. (2010). Carbonate constants for estuarine waters. *Mar. Freshw. Res.* 61, 139–142. doi: 10.1071/mf09254

Mucci, A. (1983). The solubility of calcite and aragonite in seawater at various salinities, temperatures, and one atmosphere total pressure. *Am. J. Sci.* 283, 780–799. doi: 10.2475/ajs.283.7.780

Olson, E. J., and Chen, C.-T. A. (1982). Interference in the determination of calcium in seawater. *Limnol. Oceanogr.* 27, 375–380. doi: 10.4319/lo.1982.27.2.0375

Pai, S. C., Tsau, Y.-J., and Yang, T.-I. (2001). pH and buffering capacity problems involved in the determination of ammonia in saline water using the indophenol blue spectrophotometric method. *Anal. Chim. Acta* 434, 209–216. doi: 10.1016/s0003-2670(01)00851-0

Pierrot, D., Lewis, E., and Wallace, W. R. (2006). *MS Excel Program Developed for CO2 System Calculations*. ORNL/CDIAC-105a. Oak Ridge: Carbon Dioxide Information Analysis Center.

Pomeroy, L. R., and Wiebe, W. J. (2001). Temperature and substrates as interactive limiting factors for marine heterotrophic bacteria. *Aquat. Microb. Ecol.* 23, 187–204. doi: 10.3354/ame023187

Qian, W., Gan, J., Liu, J., He, B., Lu, Z., Guo, X., et al. (2018). Current status of emerging hypoxia in a eutrophic estuary: the lower reach of the Pearl River Estuary, China. *Estua. Coast. Shelf Sci.* 205, 58–67. doi: 10.1016/j.ecss.2018.03.004

Rabalais, N. N., and Turner, R. E. (2006). *Oxygen Depletion in the Gulf of Mexico adjacent to the Mississippi River, Past and Present Water Column Anoxia*. Netherlands: Springer, 225–245.

Rabus, R., Bruchert, V., Amann, J., and Konneke, M. (2002). Physiological response to temperature changes of the marine,sulfate-reducing bacterium *Desulfobacterium autotrophicum*. *FEMS Microbiol. Ecol.* 42, 409–417. doi: 10.1111/j.1574-6941.2002.tb01030.x

Su, J., Cai, W.-J., Jean, B., Chen, B., Hussain, N., Yao, Y., et al. (2020). Chesapeake Bay acidification buffered by spatially decoupled carbonate mineral cyclin. *Nat. Geosci.* 13, 441–447. doi: 10.1038/s41561-020-0584-3

Sweeney, C., Gloor, E., Jacobson, A. R., Key, R. M., McKinley, G., Sarmiento, J. L., et al. (2007). Constraining global air-sea gas exchange for CO2 with recent bomb C-14 measurements. *Glob. Biogeochem. Cycles* 21: GB2015.

Testa, J. M., and Kemp, W. M. (2012). Hypoxia-induced shifts in nitrogen and phosphorus cycling in Chesapeake Bay. *Limnol. Oceanogr.* 57, 835–850. doi: 10.4319/lo.2012.57.3.0835

Wang, B., Hu, J., Li, S., Yu, L., and Huang, J. (2018). Impacts of anthropogenic inputs on hypoxia and oxygen dynamics in the Pearl River estuary. *Biogeosciences* 15, 6105–6125. doi: 10.5194/bg-15-6105-2018

Weiss, R. F. (1974). Carbon dioxide in water and seawater: the solubility of a non-ideal gas. *Mar. Chem.* 2, 203–215. doi: 10.1016/0304-4203(74)90015-2

Xu, J. R., Wang, Y. S., Wang, Q. J., and Yin, J. P. (2005). Nitrous oxide concentration and nitrification and denitrification in Zhujiang River estuary, China. *Acta Oceanol. Sin.* 24, 122–130.

Zhai, W. D., Dai, M. H., and Guo, X. H. (2007). Carbonate system and CO2 degassing fluxes in the inner estuary of Changjiang (Yangtze) River, China. *Mar. Chem.* 107, 342–356. doi: 10.1016/j.marchem.2007.02.011

Zhai, W. D., Zheng, N., Huo, C., Xu, Y., Zhao, H. D., Li, Y. W., et al. (2014). Subsurface pH and carbonate saturation state of aragonite on the Chinese side of the North Yellow Sea: seasonal variations and controls. *Biogeosciences* 11, 1103–1123. doi: 10.5194/bg-11-1103-2014

Zhao, H. (1990). *Evolution of the Pearl River Estuary*. Melbourne: Ocean Press.

Conflict of Interest: The authors declare that the research was conducted in the absence of any commercial or financial relationships that could be construed as a potential conflict of interest.

Copyright © 2020 Guo, Song, Gao, Luo, Xu, Huang and Wang. This is an open-access article distributed under the terms of the Creative Commons Attribution License (CC BY). The use, distribution or reproduction in other forums is permitted, provided the original author(s) and the copyright owner(s) are credited and that the original publication in this journal is cited, in accordance with accepted academic practice. No use, distribution or reproduction is permitted which does not comply with these terms.

frontiers in Marine Science

ORIGINAL RESEARCH
published: 26 March 2021
doi: 10.3389/fmars.2021.621243

Seasonal Mixing and Biological Controls of the Carbonate System in a River-Dominated Continental Shelf Subject to Eutrophication and Hypoxia in the Northern Gulf of Mexico

Wei-Jen Huang[1], Wei-Jun Cai[2] and Xinping Hu[3]*

[1] Department of Oceanography, National Sun Yat-sen University, Kaohsiung, Taiwan, [2] School of Marine Science and Policy, University of Delaware, Newark, DE, United States, [3] Harte Research Institute for Gulf of Mexico Studies, Texas A&M University-Corpus Christi, Corpus Christi, TX, United States

OPEN ACCESS

Edited by:
Arnaud Laurent, Dalhousie University, Canada

Reviewed by:
Wei-Dong Zhai, Shandong University, China
Bryce Robert Van Dam, Helmholtz Centre for Materials and Coastal Research (HZG), Germany

****Correspondence:***
Wei-Jen Huang
wjhuang29@mail.nsysu.edu.tw

Specialty section:
This article was submitted to Marine Biogeochemistry, a section of the journal Frontiers in Marine Science

Received: *25 October 2020*
Accepted: *16 February 2021*
Published: *26 March 2021*

Citation:
Huang W-J, Cai W-J and Hu X (2021) Seasonal Mixing and Biological Controls of the Carbonate System in a River-Dominated Continental Shelf Subject to Eutrophication and Hypoxia in the Northern Gulf of Mexico. Front. Mar. Sci. 8:621243. doi: 10.3389/fmars.2021.621243

Large rivers export a large amount of dissolved inorganic carbon (DIC) and nutrients to continental shelves; and subsequent river-to-sea mixing, eutrophication, and seasonal hypoxia (dissolved oxygen < 2 mg·L^{-1}) can further modify DIC and nutrient distributions and fluxes. However, quantitative studies of seasonal carbonate variations on shelves are still insufficient. We collected total alkalinity (TA), DIC, and NO_3^- data from nine cruises conducted between 2006 and 2010 on the northern Gulf of Mexico continental shelf, an area strongly influenced by the Mississippi and Atchafalaya Rivers. We applied a three-end-member model (based on salinity and potential alkalinity) to our data to remove the contribution of physical mixing to DIC and nitrate distribution patterns and to derive the net *in situ* removal of DIC and nitrate (ΔDIC and ΔNO_3^-, respectively). Systematic analyses demonstrated that the seasonal net DIC removal in the near-surface water was strong during summer and weak in winter. The peak in net DIC production in the near-bottom, subsurface waters of the inner and middle sections of the shelf occurred between July and September; it was coupled, but with a time lag, to the peak in the net DIC removal that occurred in the near-surface waters in June. A similar 2-month delay (i.e., January vs. November) could also be observed between their minima. A detailed examination of the relationship between ΔDIC and ΔNO_3^- demonstrates that net biological activity was the dominant factor of DIC removal and addition. Other effects, such as air–sea CO_2 gas exchange, wetland exports, $CaCO_3$ precipitation, and a regional variation of the Redfield ratio, were relatively minor. We suggest that the delayed coupling between eutrophic surface and hypoxic bottom waters reported here may also be seen in the carbon and nutrient cycles of other nutrient-rich, river-dominated ocean margins worldwide.

Keywords: carbon cycle, dissolved inorganic carbon, carbonate saturation state, river plume, Mississippi River

HIGHLIGHTS

- Net CO_2 removal was strong in summer and weak in winter in the near-surface waters.
- Net CO_2 accumulation was strong from July to September and weak in January in the near-bottom, subsurface waters.
- Wetland exports and air–sea gas exchanges are minor factors in dissolved inorganic carbon (DIC) changes.
- A 100 $\mu mol \cdot kg^{-1}$ increase of net DIC removal led to a 1Ω increase in a shelf-wide scale.
- Annually, the peak of net CO_2 removal was about 2 months before the peak of net accumulation.

INTRODUCTION

Continental shelves receive large and highly variable amounts of freshwater, dissolved inorganic carbon (DIC), and nutrients. As such, they may experience seasonal coastal enhanced primary productivity and bottom-water hypoxic [dissolved oxygen (DO) less than 2 $mg \cdot L^{-1}$] events (Borges and Gypens, 2010; Rabalais et al., 2010; Bauer et al., 2013; Breitburg et al., 2018; Oschlies et al., 2018). Seasonal variations in the riverine carbonate system can alter the composition of the river end-member, while subsequent mixing with seawater and the effect this has on the carbonate system equilibrium constants can lead to the formation of a minimum pH and low partial pressure of carbon dioxide (pCO_2) zone (Hu and Cai, 2013; Huang et al., 2018; Laurent et al., 2018). Excessive amounts of riverine nutrients can induce eutrophication, which fuels primary production, removing DIC from the water, increasing the flux of organic matter, and subsequently leading to hypoxic events whereby DIC is released back to the water. Notwithstanding the recent improvements in our conceptual understanding of biogeochemical processes in river-dominated continental shelf systems (Bianchi et al., 2010; Cai et al., 2011; Hu et al., 2017; Legge et al., 2020), quantitative information about the seasonal net DIC removal in the near-surface waters and net DIC release/accumulation in the near-bottom, subsurface waters, respectively, is still insufficient.

Carbon fluxes between wetlands, estuaries, and shelves have been quantified in a global North American carbon budget in Najjar et al. (2018). One component of this budget that has since gained more attention is the contribution of wetlands toward organic carbon storage, especially due to the very high productivity of saltmarsh vegetation along the periphery of the Gulf of Mexico (Thorhaug et al., 2017, 2019). The cross-shelf transport from wetlands to shelves has generated considerable recent research interest (Fry et al., 2015; Anderson et al., 2020). Field studies conducted along the shelf of the northern Gulf of Mexico (nGOM) have reported DIC release rates and associated pH and DO variations in near-bottom, subsurface waters during the summer (Xue et al., 2015; Jiang et al., 2019). The development of hypoxia is also time-dependent, yet few investigations have addressed this issue over monthly to sub-monthly timescale (Turner et al., 2017; Matli et al., 2018). Laurent et al. (2018) used a three-dimensional model to simulate these processes in the nGOM. They found that significant shifts could occur as a result of changes in freshwater discharge and wind direction, particularly where the latter was persistent and favored upwelling.

The Mississippi and Atchafalaya River system is the largest in North America in terms of freshwater discharge (Milliman and Meade, 1983). It exports ~17 Tg $C \cdot year^{-1}$ of DIC to the nGOM (Goolsby et al., 2000; Raymond et al., 2008; Lehrter et al., 2013) but also acts as a sink of atmospheric CO_2 by stimulating primary productivity in the receiving coastal and shelf waters (Huang et al., 2015b). The riverine nitrogen export is about 1–1.5 Tg $N \cdot year^{-1}$ ($T = 10^{12}$), with nitrate (NO_3^-) accounting for two-thirds of the total and nitrite plus ammonium for the remaining third. The marine end-member contributes 30% of the nitrogen inputs to the nGOM shelf (Lehrter et al., 2013), but it is the seasonal fluctuations in the river inputs that modulate the amount of primary production on the shelf (Turner and Rabalais, 2013; Chakraborty and Lohrenz, 2015). On an annual basis, biological productivity on the Louisiana shelf is controlled by the availability of N (Turner and Rabalais, 2013), although P and Si can also be co-limiting over small temporal and spatial scales (Ren et al., 2009; Turner and Rabalais, 2013). Seasonal variations in river inputs and changes in coastal physical and biological conditions should conceptually lead to seasonal variations in air–sea CO_2 gas exchange. Previous studies conducted off the Louisiana Bight in the late 2000s and over a wider portion of the shelf in the 2010s have revealed that these study areas act as a strong CO_2 sink in spring to early summer but switch to a weak source or near-neutral system in fall to winter (Green et al., 2006; Guo et al., 2012; Huang et al., 2015b; Xue et al., 2016). The approach used in these studies was to quantify air–sea CO_2 flux and net DIC removal according to salinity intervals or depth intervals (topography). Comparable studies identifying specific regions of net DIC removal/uptake or release/accumulation down the water column on an annual scale are still rare. In particular, the chemical measurements needed to reveal the interconnections and relationships that drive the seasonal net DIC removal in a river-dominated continental shelf are still lacking.

In this study, we measured total alkalinity (TA) and DIC and calculated pH and calcium carbonate saturation state (Ω_{Arag}) from the river to the marine end-members based on an extensive dataset of nine cruises conducted over 5 years (2006–2010). We systematically removed the effect of river-to-sea mixing on DIC and NO_3^- concentrations using an end-member model and interpreted the residuals as net DIC removal/accumulation; the residuals showed systematic seasonal variations in specified ranges of depths and salinity in both near-surface and near-bottom waters. Based on these results, we discuss the combined effects of mixing and biological activity on the non-linear variations observed in pH and Ω_{Arag}. We then investigate the processes affecting the carbonate system by analyzing the covariation of net DIC removal/accumulation and NO_3^- across the studied area. Finally, we synthesize our improved understanding of these processes via a conceptual model for the whole region.

METHODS

Sampling and Analytical Methods

Seawater salinity, temperature, DIC, TA, and nutrient data were collected on nine cruises in the nGOM (**Figure 1** and **Table 1**). Five cruises (2009 to 2010) were cross-shelf surveys (**Figure 1**). Four previous cruises (2006–2007) were focused on an area that has been covered for more than three decades for hypoxia mapping and investigation[1].

Water samples for TA and DIC were taken from Niskin bottles that were attached to a conductivity, temperature, and pressure package (CTD) following standard procedures. Water samples for TA and DIC were filtered through a purged cartridge filter (Whatman® 6724-6004) directly into borosilicate glass bottles and were poisoned with 100 μl of saturated $HgCl_2$ solution immediately after sampling to arrest biological activity. Then the samples were kept at low temperatures (∼4°C) until analysis at the University of Georgia. DIC samples (0.75 ml) were acidified by adding 1 ml of 10% H_3PO_4, and the CO_2 released was quantified by using a CO_2 detector (LI-COR® 6262 or 7000) (AS-C3 Apollo SciTech). TA was analyzed on a temperature-controlled, semi-automated titrator (AS-ALK2 Apollo SciTech) following the open-cell Gran titration method. Both TA and DIC measurements were referenced against certified reference materials from A. G. Dickson at Scripps Institution of Oceanography. The precision of TA and DIC measurements was 0.1% (Cai and Wang, 1998; Huang et al., 2012a). The concentration of NO_3^- was measured according to wet chemistry methods (APHA, 1989) with a continuous flow analyzer (Astoria-Pacific International) during 2006–2007 cruises done by Lehrter et al. (2013) and during the 2008–2010 cruises done by Chakraborty and Lohrenz (2015). On each cruise, DO, chlorophyll *a* (Chl-*a*), and NO_3^- concentrations were measured by the same group. DO concentrations were measured with the CTD system with excellent stability (Murrell et al., 2013). Apparent oxygen utility (AOU) was calculated by the saturated DO concentration minus the measured DO concentration.

Calculation of pH and Ω_{Arag}

We used TA, DIC, and dissolution constants from Millero et al. (2006) to calculate pH and saturation state for aragonite (Ω_{Arag}) using the R software package seacarb (Gattuso et al., 2016). Since aragonite is more soluble (lower Ω values) than calcite, we selected Ω_{Arag} over Ω_{Cal} as the carbonate saturation state parameter for this study. Ω_{Arag} is defined as follows:

$$\Omega_{\mathrm{Arag}} = [Ca^{2+}][CO_3^{2-}]K'^{-1}_{sp}, \quad (1)$$

where $[Ca^{2+}]$ is the calcium ion concentration, $[CO_3^{2-}]$ is the carbonate ion concentration, and K'_{sp} is the apparent solubility product of aragonite in seawater at a given salinity, temperature, and pressure (Mucci, 1983). Note that in seacarb, or indeed in other carbonate chemistry equilibrium calculation packages, riverine $[Ca^{2+}]$ is set to 0, and its concentration in seawater is inferred from salinity. Thus, we need to override these settings in order to calculate $[Ca^{2+}]$ in the river plume or estuarine waters. In this study, the riverine calcium concentrations were relatively high, with average concentrations of 1.0 ± 0.1 mmol·kg^{-1} in the Mississippi River end-member (Balle Chase, Louisiana station) and 0.9 ± 0.2 mmol·kg^{-1} in the Atchafalaya River end-member (Morgan City, USGS #07381600). As these two $[Ca^{2+}]$ end-members showed no significant difference, the Mississippi end-member value was used in our calculations. $[Ca^{2+}]$ of 10.28 mmol·kg^{-1} at a salinity of 35 was used as the ocean end-member, and the concentrations along the salinity gradient were then calculated using the following linear equation:

$$[Ca^{2+}] = 0.266 \times \mathrm{Salinity} + 1.0(\mathrm{mmol \cdot kg^{-1}}) \quad (2)$$

In situ salinity and temperature values were used to calculate K_{sp} in surface samples and were adjusted to ambient pressure where necessary with the equations provided by Millero (1995) and the corrected constants provided by Zeebe and Wolf-Gladrow (2001).

The effect of $[Ca^{2+}]$ variation can be canceled mainly by the change of K_{sp}' when they are both a function of salinity without riverine $[Ca^{2+}]$ (Xue et al., 2017). The change of $[Ca^{2+}]$ with this new slope in Eq. (2) may still be proportional to the change of K_{sp}' in high salinities but may not sufficiently covary in low salinities. As the low-salinity region (<18) covers a relatively small part of this shelf (<3%) (Huang et al., 2015b), we focus our discussion on Ω_{Arag} variations at higher salinities (>18).

We estimated the uncertainty for Ω_{Arag} and pH due to the measurement uncertainties in TA (±0.1%) and DIC (±0.1%) by the bootstrap method (Efron, 1992). We assumed each uncertainty occurred randomly in TA and DIC, and we used TA of 2,400 μmol·kg^{-1} and DIC of 2,050 μmol·kg^{-1} as an example to calculate their corresponding Ω_{Arag} with seacarb. The average value and its standard deviation of 500 iterations were 3.87 and 0.02 in Ω_{Arag} unit (±0.5%), respectively. Similarly, the impact of uncertainties of the same TA and DIC values on the calculated pH value was ± 0.0026 pH unit (±0.03%).

Net Dissolved Inorganic Carbon Removal (ΔDIC) and Nitrate Removal (ΔNO_3^-) Over the Water Column

To assess the spatial pattern of net DIC removal or accumulation (ΔDIC) in both near-surface and near-bottom, subsurface waters, we need to remove the mixing effect on DIC and to quantify ΔDIC and net NO_3^- removal (ΔNO_3^-) over the shelf area. To this end, we applied a three-end-member mixing model, as the two rivers are often fairly different in their chemical properties. We used "f" as the fractional contribution of (1) freshwater from the Mississippi River (subscripted "M"), (2) freshwater from the Atchafalaya River (subscripted "A"), and (3) seawater (subscripted "S"). "Sal" is the observed salinity, and "S" is used to represent the salinity of each end-member. The results of this three-end-member method comprise the bulk of

[1]http://www.gulfhypoxia.net/

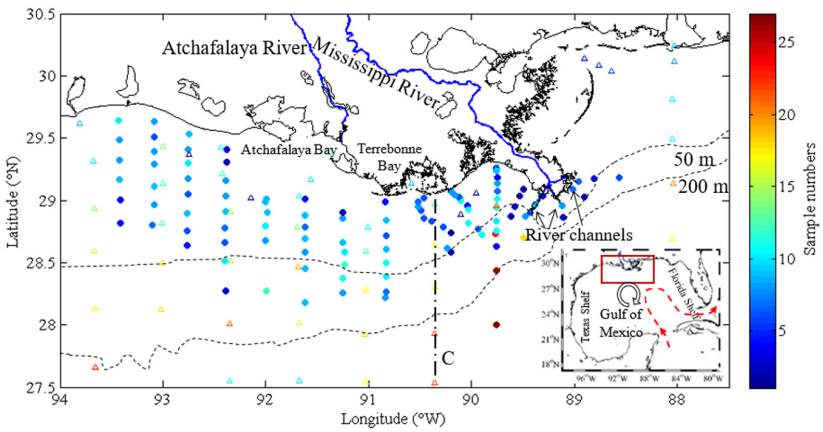


FIGURE 1 | The study area and sampling frequency map. Nine cruises surveyed the nGOM (the red rectangle in the inset) near the Mississippi and Atchafalaya Rivers (blue lines) and several wetlands, lakes, and bays. The sampling stations covered the shelf and also parts of the open Gulf. Generally, most of the stations were visited four times, and the stations on Louisiana Bight were visited with a higher frequency. Transect C (dashed line) was labeled to show the cross-shelf variation in later sections. The red dashed line indicates Loop Current, and the circle with an arrow represents a loop current eddy and its direction, respectively, in the inset. nGOM, northern Gulf of Mexico.

this report. Following Guo et al. (2012); Huang et al. (2012a), the model equations are as follows:

$$1 = f_M + f_A + f_S, \quad (3)$$

$$Sal = S_M \times f_M + S_A \times f_A + S_S \times f_S, \quad (4)$$

In a three-end-member model, we need another conservative tracer in addition to salinity. Here, we used a slightly modified alkalinity term. In the river plume, TA is affected by conservative mixing as well as biological NO_3^- drawdown (ΔNO_3^-). Thus, we have

$$TA = TA_M \times f_M + TA_A \times f_A + TA_S \times f_S + \Delta NO_3^-, \quad (5)$$

This TA modification is linked to NO_3^- use or regeneration,

$$NO_3^- = NO_3^-{}_M \times f_M + NO_3^-{}_A \times f_A + NO_3^-{}_S \times f_S - \Delta NO_3^-. \quad (6)$$

By combining Eq. (6) with Eq. (5), a conservative property called "potential alkalinity," TA+NO_3^- (Brewer and Goldman, 1976; Peng et al., 1987; Bates et al., 1998) can be derived:

$$(TA + NO_3^-) = (TA + NO_3^-)_M \times f_M + (TA + NO_3^-)_A \times f_A + (TA + NO_3^-)_S \times f_S \quad (7)$$

As both TA and NO_3^- are known, the fractional contribution of each end-member (f_M, f_A, and f_S) can be solved by substituting in end-member values (**Supplementary Tables 1**, **2**) and using Eqs. (3), (4), and (7) with a non-negative solver (NNLS in MATLAB).

Thereafter, any biological modification during the mixing can be expressed as the difference between the observation and a conservative value predicted by the mixing model. For example, ΔDIC can be calculated by subtracting measured DIC from the DIC value based on conservative mixing:

$$\Delta DIC = DIC_M \times f_M + DIC_A \times f_A + DIC_S \times f_S - DIC \quad (8)$$

Positive ΔDIC values in the near-surface waters are defined as net DIC removal, and negative values in the near-bottom, subsurface waters are defined as net DIC accumulation. Similarly, the biological modification can be calculated via Eq. (6).

We allowed for the fact that the marine end-member may change depending on the season and plume trajectory (**Table 1** and **Supplementary Table 1**). The shelf water has a residence time of about 1 month during winter and over 3 months during summer (Zhang and Hetland, 2012; Xue et al., 2013). We selected one marine end-member from high-salinity offshore waters in

TABLE 1 | Summary of survey cruises.

Year	Date	Vessel	River discharge[#]	NO_x flux[#]
			10^3 $m^3 \cdot s^{-1}$	10^9 g N
2006	6/6–6/11	*Bold*	12.2	60.2
2006	9/6–9/11	*Bold*	7.5	19.7
2007	5/2–5/7	*Bold*	25.4	148.0
2007	8/18–8/24	*Bold*	12.1	31.2
2009	1/9–1/20	*Cape Hatteras*	23.9	92.6
2009	4/20–5/1	*Cape Hatteras*	30.9	151.0
2009	7/19–7/29	*Cape Hatteras*	18.9	73.5
2009	10/28–11/7	*Hugh R. Sharp*	35.5	86.3
2010	3/9–3/21	*Cape Hatteras*	27.8	121.0

Corresponding river discharge and NO_x flux are monthly data.
[#]USGS, Hypoxia in the Gulf of Mexico Studies, http://toxics.usgs.gov/hypoxia/index.html.

each cruise as the standard deviation of each monthly TA average in the offshore water (0 to 100 m, salinity > 36) was mostly less than 14 $\mu mol \cdot kg^{-1}$ (<0.5%) (**Supplementary Table 3**).

Finally, we gained insight into the controlling processes responsible for the ΔDIC and ΔNO_3^- variations by analyzing the observed ΔDIC vs. ΔNO_3^- relationship, as $CaCO_3$ precipitation/dissolution affects the slope and air–sea gas exchange affects the intercept of the theoretical relationship.

Supportive Lines of Mixing and Biological Activities for pH and Ω_{Arag}

In special cases, such as in areas near one river or when the chemical differences of the two river end-members are much smaller than biological modifications during mixing, the above three-end-member model may be simplified into a two-end-member model. An advantage of a two-end-member model is that only one conservative tracer (i.e., salinity) is enough for calculations. Another benefit is that one can readily show the biological modification as the deviations from a linear plot of property against the conservative tracer (i.e., a NO_3^- or DIC vs. salinity plot). Thus, we chose to apply a two-end-member model to examine non-linear biological modifications on our data in the near-surface water in this study area. Note that the majority of our results are still based on the three-end-member model in the section "Net Dissolved Inorganic Carbon Removal (ΔDIC) and Nitrate Removal (ΔNO_3) Over the Water Column."

We simplified the mixing case by using the combination of river end-members and the marine end-members to demonstrate the seasonal effects of mixing and biological activities on pH and Ω_{Arag}. During the combination of river end-members, the freshwater discharge was considered and used two thirds from the Mississippi River end-member and one third from the Atchafalaya River end-member (**Supplementary Table 1**). We considered that TA and DIC are conservative (TA_{mix2} and DIC_{mix2}, respectively) for mixing to calculate the conservative pH (pH_{mix2}) and Ω_{Arag} (Ω_{Arag_mix2}) for each season with seacarb. The abbreviation of "mix2" represented "two-end-member mixing" to distinguish the difference from the three-end-member mixing model in the following section.

$$TA_{mix2} = TA_{M1} \times f_{M1} + TA_{S1} \times f_{S1} \quad (9)$$

$$DIC_{mix2} = DIC_{M1} \times f_{M1} + DIC_{S1} \times f_{S1} \quad (10)$$

where subscribed "M1" and "S1" are end-member values for the mixed river and the marine end-members, respectively; f_{M1} and f_{S1} are fractions from the mixed river and the marine end-members. Using TA_{mix2} and DIC_{mix2}, we can calculate pH_{mix2} and $\Omega_{Arag-mix2}$.

We considered the influence of net biological production to evaluate the effect of net DIC uptake on pH and Ω_{Arag}. We used the deficit of NO_3^- between measurements and the conservative mixing ($\Delta NO_3^-_{bio2}$) as biological uptake to simulate biological effects on TA (TA_{bio2}) and DIC (DIC_{bio2}). The NO_3^- to salinity relationship was non-linear in each season and was discontinuous in a few salinity ranges. To fulfill these missing nitrate values in these salinity ranges, we extrapolated data to the few missing nitrate data points by using a non-linear nitrate-to-salinity relationship for each season (**Supplementary Figure 1**). We then used the deficit between the non-linear relationship and the linear conservative mixing line in each salinity bin to calculate $\Delta NO_3^-_{bio2}$. For each unit of biological uptake, $\Delta NO_3^-_{bio2}$ can increase one TA by one unit (Brewer and Goldman, 1976; Wolf-Gladrow et al., 2007) in addition to the conservative mixing (Eq. 11) and can induce a DIC change of 106/16 of $\Delta NO_3^-_{bio2}$ through the Redfield ratio (C/N = 106/16) (Eq. 12).

$$TA_{mix2+bio2} = TA_{M1} \times f_{M1} + TA_{S1} \times f_{S1} + \Delta NO_3^-_{bio2} \quad (11)$$

$$DIC_{mix2+bio2} = DIC_{M1} \times f_{M1} + DIC_{S1} \times f_{S1} - \Delta NO_3^-_{bio2} \times 106/16 \quad (12)$$

$TA_{mix2+bio2}$ and $DIC_{mix2+bio2}$ were used to calculate the combined effect of mixing and biological-induced pH ($pH_{_mix2+bio2}$) and Ω_{Arag} ($\Omega_{Arag_mix2+bio2}$) values for each season (seacarb with the same K_1 and K_2 used again). Additional information about the DIC buffer factor is provided with **Supplementary Information**.

To sum up, this two-end-member model can quickly give us the effect of mixing and biological uptake on changes of pH and Ω_{Arag} in the mid-salinity surface water.

RESULTS

Seasonal Properties to Salinity Relationships

Freshwater discharge, TA (**Table 2**), and NO_x (including nitrate and nitrite) fluxes varied seasonally and were generally high during the spring and low during the late summer and fall (**Figure 2**) (United States Geological Survey, Hypoxia in the Gulf of Mexico Studies)[2].

The effects of the freshwater discharge further characterized the seasonal variations in the TA and salinity relationships (**Figures 3A–D**). When considering the TA–salinity relationship, TA values were high in low-salinity waters during the summer due to the reduction of river discharge (for example, riverine TA was over 2,500 $\mu mol \cdot kg^{-1}$ in June) (**Table 2**). In contrast, TA values were low during the late fall, winter, and early spring when discharge was high (for example, riverine TA was ∼1,800 $\mu mol \cdot kg^{-1}$ in November 2009) (**Figures 2**, **3**A–D). Overall, the TA data were generally in the range or close to the boundary composed of two rivers and one marine end-members, indicating possible three-end-member mixings (**Figures 3A–D**).

Relative to the near-linear TA and salinity relationship, DIC concentrations in middle salinities were much lower than those in high salinities on the DIC-to-salinity relationship (**Figures 3E–H**). Net DIC removal in middle salinities was clear during

[2]http://toxics.usgs.gov/hypoxia/index.html

TABLE 2 | Salinity, temperature, pH, DIC, TA, Ca^{2+}, and Ω_{Arag} values at the Mississippi and Atchafalaya Rivers and Terrebonne Bay.

Sta.	Date	Lat. (°N)	Lon. (°W)	Sal.	Temp. (°C)	pH	DIC, μmol·kg^{-1}	TA, μmol·kg^{-1}	TA/DIC	Ca^{2+}, mmol·kg^{-1}	Ω_{Arag}
	Mississippi River										
MR1	01/11/09	29.0340	89.3264	1.50	7.95	7.76	2,109	2,072	0.98	1.37	0.90
MR1	03/20/10	29.0461	89.3174	0.53	10.55	8.16	2,425	2,399	0.99	1.11	1.96
MR1	04/22/09	29.0398	89.3220	0.36	15.23	7.78	2,192	2,142	0.98	1.07	1.64
M02	05/07/07	28.9677	89.3845	0.90	18.72	8.51	2,305	2,308	1.00	1.21	1.06
M01	06/06/06	29.0378	89.3093	1.06	25.59	7.91	2,641	2,651	1.00	1.25	3.08
M02	06/06/06	28.9675	89.3854	2.53	25.73	7.92	2,599	2,627	1.01	1.64	2.43
MR1	07/20/09	29.0326	89.3289	1.36	29.55	7.83	2,636	2,594	0.98	1.33	1.88
M02	08/19/07	28.9625	89.3871	5.38	31.53	8.04	2,333	2,403	1.03	2.40	1.31
M01	09/06/06	29.0353	89.3266	6.60	30.79	8.08	2,466	2,563	1.04	2.72	2.34
M02	09/06/06	28.9691	89.3831	7.71	30.88	8.12	2,385	2,570	1.08	3.02	4.32
MR1	10/31/09	29.0303	89.3310	0.15	16.69	7.68	1,823	1,794	0.98	1.01	2.14
	Atchafalaya Bay/River										
E0	01/14/09	29.3842	91.3724	0.15	8.14	7.63	1,663	1,592	0.96	1.01	0.91
E0	03/15/10	29.3835	91.3733	0.30	12.49	8.20	1,438	1,371	0.95	1.05	0.66
E0	04/24/09	29.3846	91.3726	0.18	18.54	7.64	1,898	1,813	0.96	1.02	1.21
E0	07/24/09	29.3845	91.3722	0.35	28.85	7.86	2,438	2,404	0.99	1.06	3.12
E0	11/03/09	29.3822	91.3750	0.08	17.21	7.27	1,073	985	0.92	0.99	0.45
	Terrebonne Bay										
C0	01/12/09	29.1340	90.5879	29.67	16.14	8.24	2,155	2,487	1.15	8.86	3.95
C0	03/13/10	29.1351	90.5902	22.17	16.62	7.98	1,911	2,126	1.11	6.87	2.79
C0	04/22/09	29.1334	90.5884	25.95	23.26	8.36	1,891	2,198	1.16	7.87	3.83
C0	07/22/09	29.1361	90.5900	28.27	28.96	8.19	2,049	2,289	1.12	8.49	3.14
C0	11/01/09	29.1383	90.5905	25.79	19.88	8.20	2,091	2,359	1.13	7.83	3.39

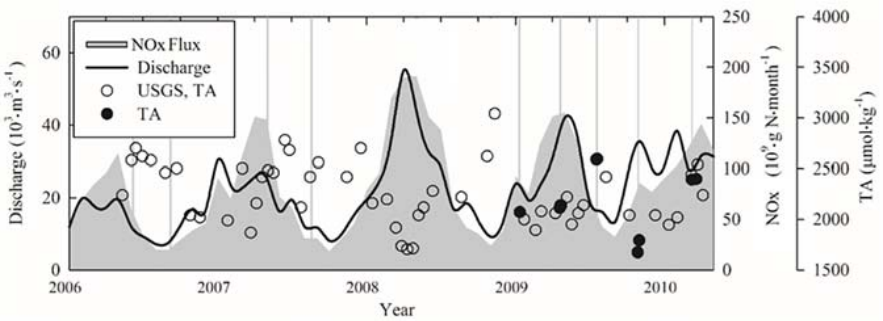


FIGURE 2 | The temporal variations of river discharge, TA values, and nitrogen flux. Throughout the course of our sampling, freshwater discharge (black line) and the NO_x flux (gray area) from the Mississippi and Atchafalaya Rivers [U.S. Geological Survey (USGS) data] varied seasonally. USGS TA values (open circles) were close to our measured TA (solid circles). Vertical gray lines indicate the beginning date of the sampling cruise in **Table 1**. TA, total alkalinity.

the summer. Chl-*a*-to-salinity relationships corresponds to the net DIC removal. High Chl-*a* concentrations (over 30 μg·L^{-1}) were observed in salinities of 20 to 30 in the near-surface water during the spring and summer cruises, medium Chl-*a* concentrations (<20 μg·L^{-1}) during the fall, and low Chl-*a* concentrations (∼<5 μg·L^{-1}) in the winter (**Supplementary Figure 6**). Moreover, changing river DIC end-members (**Table 2**) and levels of deficits displayed the seasonal variations on the DIC-to-salinity relationships (**Figures 3E–H**). High DIC river end-members and large DIC deficits were present from May to September (**Figures 3E,F**), and low DIC river end-members and reduced DIC deficits were present from November to March (**Figures 3G,H,E**). When freshwater discharge quickly decreased from spring to summer, DIC river end-member can promptly increase and create non-linear mixing curves on the DIC-to-salinity relationship. We considered this issue, and we adopted a river end-member a few weeks earlier than the sampling cruise to perform the calculation in the section "Net Dissolved Inorganic Carbon Removal (dDIC) and Nitrate Removal (dNO_3_) Over the Water Column."

Values of measured pH and Ω_{Arag} displayed maximum values in middle salinities during each season (**Figure 4**), particularly during the summer (**Figures 4B,F**). Similarly, the highest Ω_{Arag} in middle salinities was over 6.0 during the spring, increased to

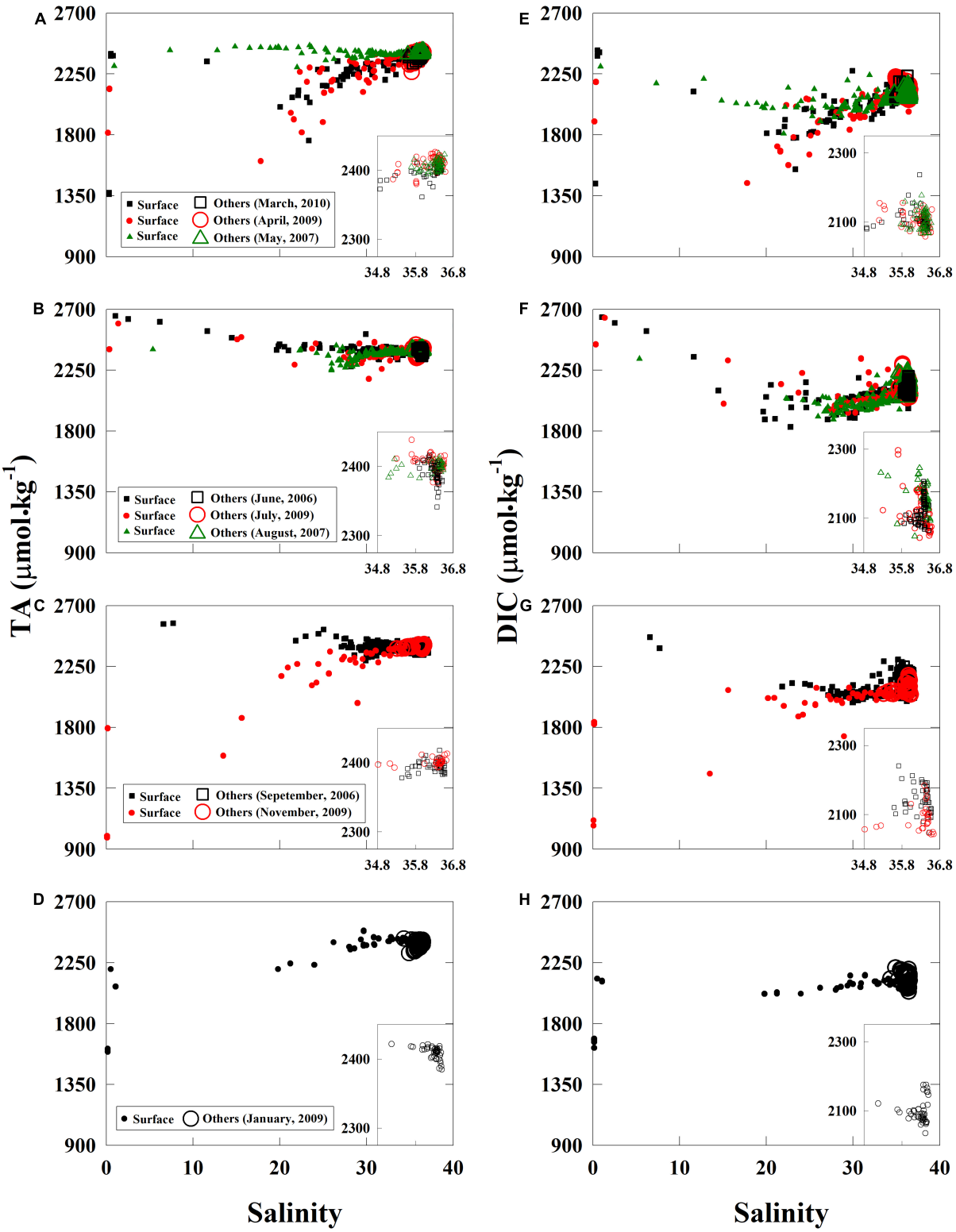


FIGURE 3 | Total alkalinity and DIC-to-salinity relationships. Fluctuating TA and DIC river end-members dominated the seasonal variations in the near-surface water **(A–H)**. In the near-surface water (solid marker) during the summer, DIC measurements were lower in middle salinities than those in high salinities and displayed clear DIC removals **(F)**. In the near-bottom, subsurface, and deep waters (open marker), DIC extended a high concentration arm at high salinities at the marine end-members. We clarify the relationships between 20- and 100-m depth in the inset of each panel **(A–H)**. TA, total alkalinity; DIC, dissolved inorganic carbon.

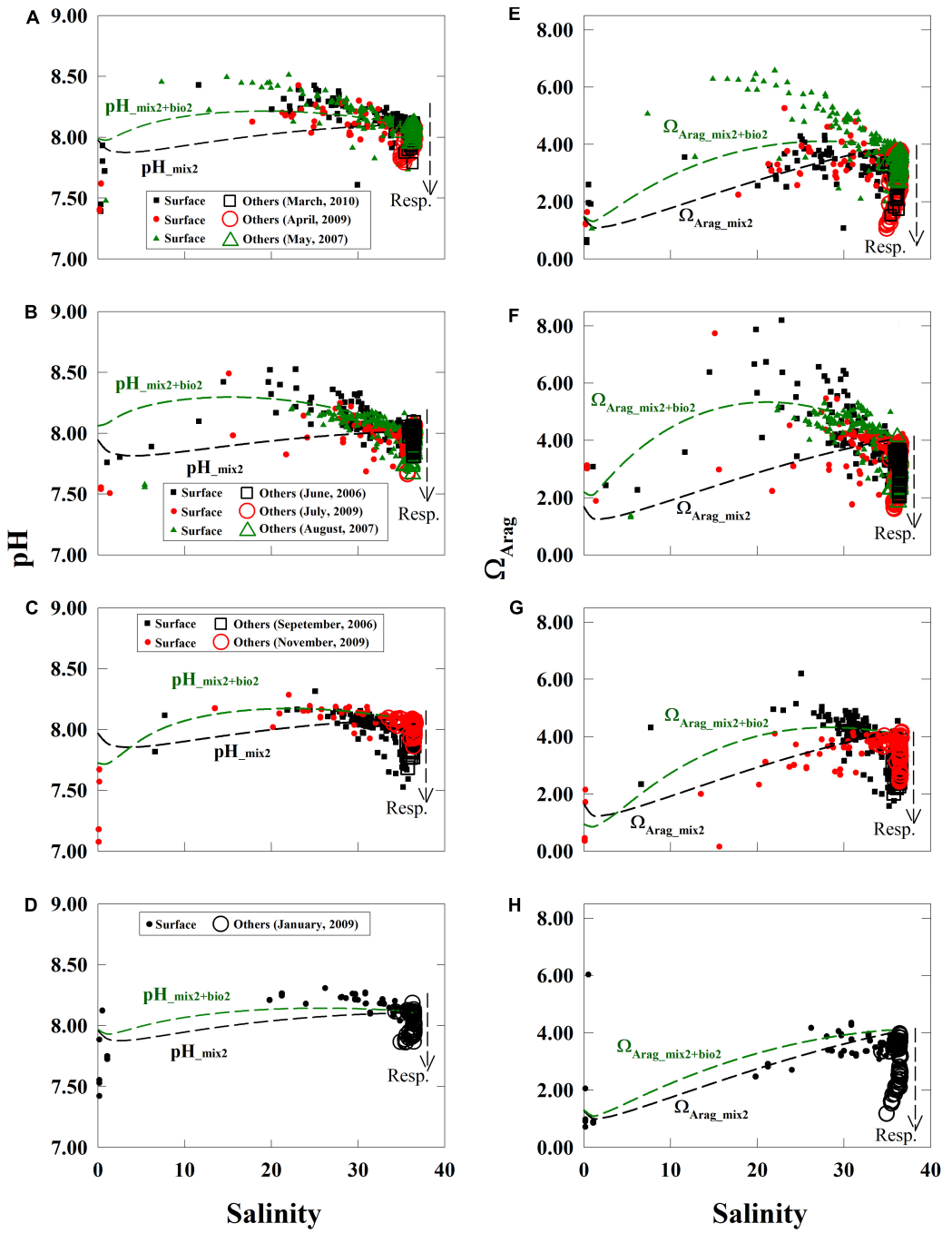


FIGURE 4 | Relationships between pH and Ω_{Arag} to salinity. Values of pH and Ω_{Arag} displayed non-linear relationships with salinity in the near-surface waters (filled symbols, depth < 5 m) and displayed low values in near-bottom, subsurface, and deep waters (open symbols, depth > 5 m) **(A–H)**. Values of pH and Ω_{Arag} values from November to January were close to their supporting conservative curves and **(C,D,G,H)** were close to the supporting curves with biological activity from May to August **(A,B,E,F)** in the near-surface waters. Respiration induced extensions arms of pH and Ω_{Arag} from the sea end-member can be observed in each panel (open markers). The supporting lines in this figure are based on the section "Supportive Lines of Mixing and Biological Activities for pH and Ω_{Arag}". TA, total alkalinity; DIC, dissolved inorganic carbon.

over 7.0 in the summer, was below 7.0 in the fall, and reduced to below 5.0 in the winter (**Figures 4E–H**).

We had drawn supporting lines by simplified simulations (section "Supportive Lines of Mixing and Biological Activities for pH and Ω_{Arag}") to help us to display non-linear distribution patterns of mixing or biological activities in **Figure 4**. Conservative simulations for $pH_{_mix2}$ and Ω_{Arag_mix2} were curves due to the carbonate system (**Figure 4**) and varied seasonally

in the near-surface water (**Figure 4**). Our NO_3^- fitting curves based on measured data were concaved upward in all seasons, showing a strong contrast to their respective ideal linear mixing lines (**Figure 5** and **Supplementary Figure 1**). The NO_3^- deficit from the conservative mixing line to the fitting curve of measured data was large in spring, kept increasing in summer, and reduced from fall to winter (**Figure 5**). This deficit of NO_3^- was converted to net biological DIC uptake to simulate $pH_{_mix+bio2}$ and $\Omega_{Arag_mix+bio2}$ (**Figure 4**, methods in the section "Supportive Lines of Mixing and Biological Activities for pH and Ω_{Arag}"). The differences between $pH_{_mix2}$ and $pH_{_mix2+bio2}$, and between Ω_{Arag_mix2} and $\Omega_{Arag_mix2+bio2}$, are effects on these properties by the net biological uptake (**Figure 4**). These effects of net biological uptake on each carbonate parameters varied seasonally in middle-to-high salinities, increasing from spring to summer and decreasing from fall to winter. Finally, those measured pH and Ω_{Arag} values were close to the conservative mixing curves during November and January (**Figures 4C,D,G,H**) and were close to the biological activity scenario, particularly during May and June (**Figures 4A,B,E,F**). Note that the result of supporting lines in the section "Supportive Lines of Mixing and Biological Activities for pH and Ω_{Arag}" was only presented in **Figures 4**, **5**.

In high-salinity waters, an arm of high DIC (**Figures 3E–H**), pH (**Figures 4A–D**), and Ω_{Arag} (**Figures 4E–H**) extended from the marine end-member. Sources of these waters were near-bottom shelf waters or subsurface and deep (>200 m) waters, and these values deviated from simulations in the near-surface water, showing net DIC release. Additionally, extension arms of low values of DIC buffer factor in high salinities were in DIC buffer factor to salinity relationships (**Supplementary Figures 7A-D**).

To sum up, four distribution patterns characterized the carbonate parameters along the river-to-sea salinity gradient: (1)

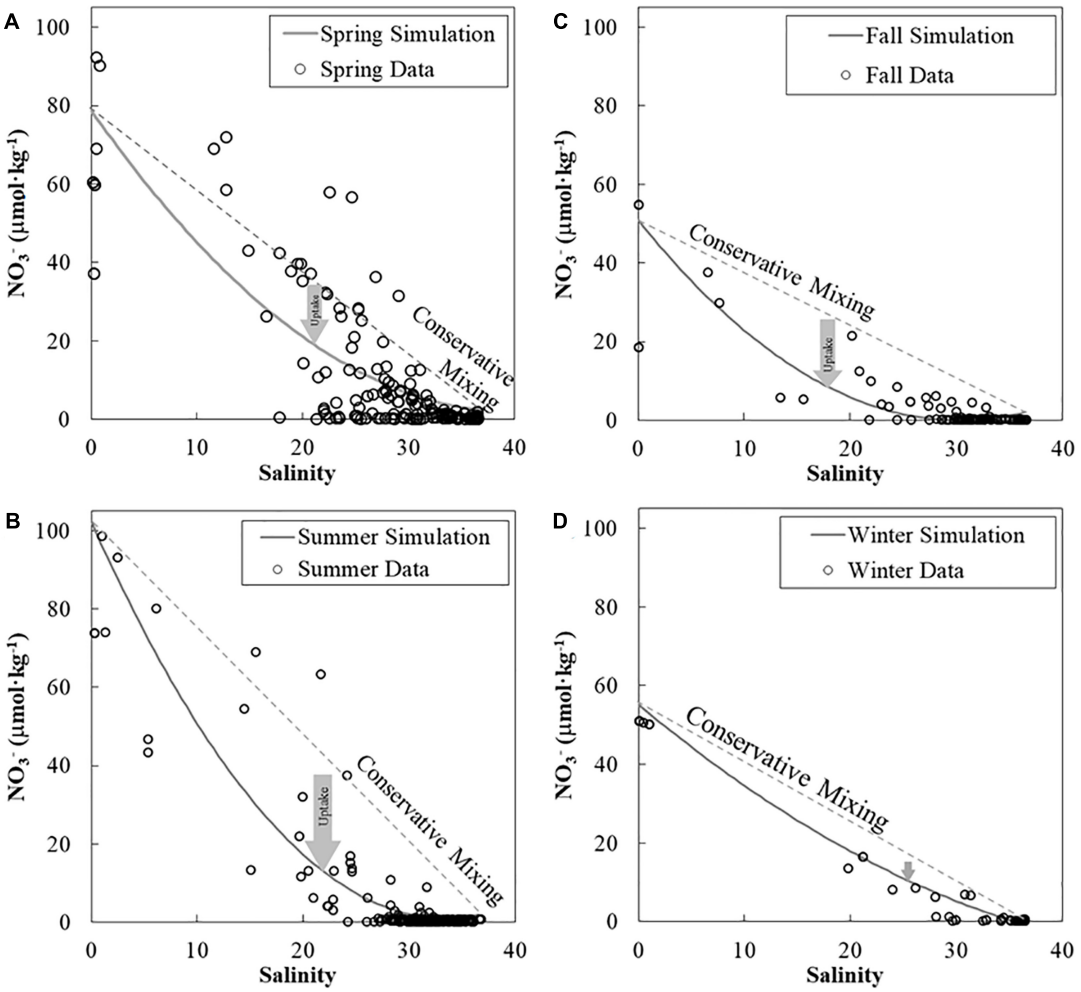


FIGURE 5 | Nitrate-to-salinity relationships in the near-surface water in four seasons. The nitrate river end-member increased from the spring **(A)** to the summer **(B)** and decreased to the fall **(C)** and winter **(D)**. We used nitrate measurements (symbols) in each season to fit a concave upward curve to fulfill the lack of data in a few salinity bins. The deficit of nitrate between the nitrate measurement (concave-upward curve) and the conservative mixing line (that is, net nitrate removal) was also high in the summer and low in the winter. The deficit of NO_3^- in this figure was only used in the section "Supportive Lines of Mixing and Biological Activities for pH and Ω_{Arag}" to convert to biological DIC uptake and to calculate the supporting lines of effects of mixing plus biological uptake in **Figure 4**. Note that results from the section "Supportive Lines of Mixing and Biological Activities for pH and Ω_{Arag}" are only used for **Figure 4**. DIC, dissolved inorganic carbon.

river TA and DIC end-members varied seasonally (**Figure 3**), (2) pH- and Ω_{Arag}-to-salinity relationships showed concave-downward curves in the near-surface waters (**Figure 4**), (3) the deficits between the observed pH and Ω_{Arag} data to the conservative mixing curves changed seasonally (**Figure 4**), and (4) an arm was extended from the marine end-members of pH and Ω_{Arag} (**Figure 4**).

Distributions of Multi-year Average Salinity and ΔDIC in the Near-Surface Water

The distribution of ΔDIC (calculated by the three-end-member model) generally demonstrated non-conservative effects during the dispersal process in the near-surface water compared with salinity (**Figure 6**). The salinity contour lines of 18 and 33 were parallel to the coastline and demonstrated the principle dispersal range between them (**Figure 6A,B**). High and positive ΔDIC values (strong net DIC removal) were at the Louisiana Bight, and ΔDIC was nearly zero at non-plume regions on a shelf-wide scale in most cases (**Figure 6C,D**), implying strong net DIC uptake just next to the river mouth and descending toward the far-field of this river plume. Note that the ΔDIC values hereafter were quantified by using the three-end-member model in the section "Net Dissolved Inorganic Carbon Removal (ΔDIC) and Nitrate Removal (ΔNO_3) Over the Water Column."

Vertical Cross-Shelf Distributions and Their Seasonal Variations

Distinct carbonate variations were between the near-surface water; and the near-bottom, subsurface waters, and their values and distributions varied seasonally. ΔDIC values were more positive while Ω_{Arag} values were high in the near-surface water close to the coast, and ΔDIC became negative while Ω_{Arag} values were low in the near-bottom, subsurface, and deep waters (**Figure 7**) on the cross-shelf transect C in the middle of this shelf (**Figure 1**). Note that ΔDIC in **Figure 7** was from the result of three-end-member mixing in the section "Net Dissolved Inorganic Carbon Removal (ΔDIC) and Nitrate Removal (ΔNO_3) Over the Water Column." These cross-shelf changes in ΔDIC and Ω_{Arag} further displayed seasonal variations (**Figure 7**). In January, high DIC removal (ΔDIC ~ 100 $\mu mol \cdot kg^{-1}$) and high Ω_{Arag} (>4) values were observed in the inner shelf (**Figures 7a,f**). From March to July, high ΔDIC and Ω_{Arag} were in the near-surface layer, while low values were in the near-bottom, subsurface waters (**Figures 7a–e** for ΔDIC, **Figures 7f–j** for Ω_{Arag}). During the late fall (November), low ΔDIC values were observed on the inner shelf, while high Ω_{Arag} values were recorded on the outer shelf (**Figures 7e,j**). Moreover,

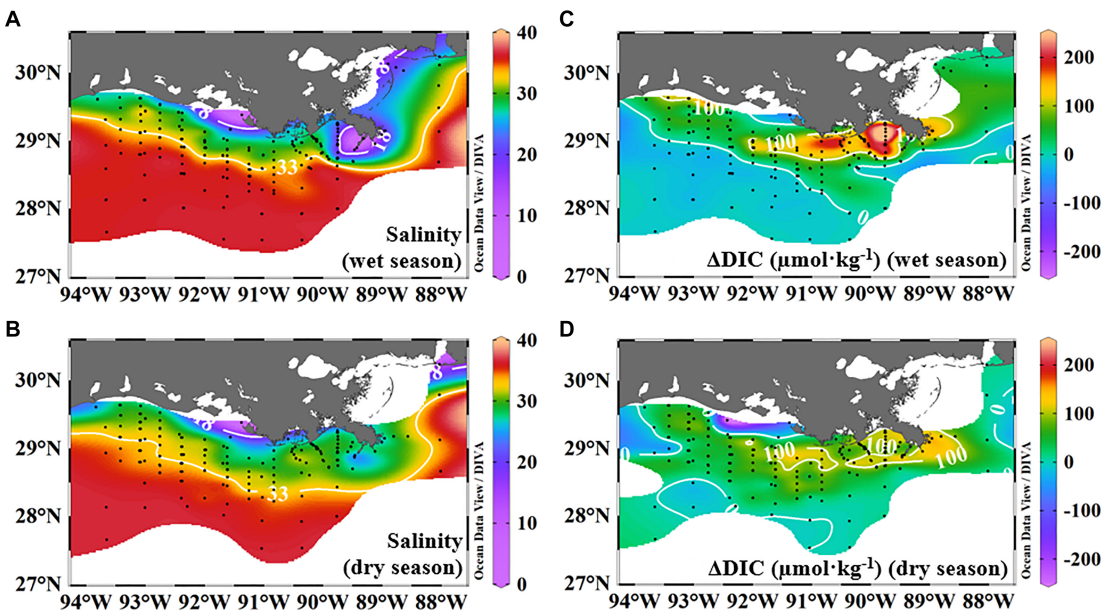


FIGURE 6 | Distributions of multi-year average salinity and ΔDIC in the near-surface water during wet and dry seasons. Average salinity was from salinities of nine cruises to show the general trend of river plume trajectory. Salinities lower than 18 were along the inner shelf, and salinities between 18 and 33 were observed along the inner to middle shelves **(A,B)**. The salinity contour line of 33 was to the north of 28.5°N in the wet season and to the south in the dry season **(A,B)**. Net DIC removal/accumulation (ΔDIC) values calculated in section "Net Dissolved Inorganic Carbon Removal (ΔDIC) and Nitrate Removal (ΔNO_3) Over the Water Column" by the three-end-member model were averaged to display the general trend of ΔDIC over the plume trajectory. High, positive ΔDIC values were observed next to the river channel in the middle field of this plume, displaying ~200 $\mu mol \cdot kg^{-1}$ in the wet season and <150 $\mu mol \cdot kg^{-1}$ in the dry season **(C,D)**. Negative or ΔDIC values close to zero were on the southwestern and outer shelves in both seasons **(C,D)**. Note the positive ΔDIC value in the near-surface waters is defined as net DIC removal. DIC, dissolved inorganic carbon.

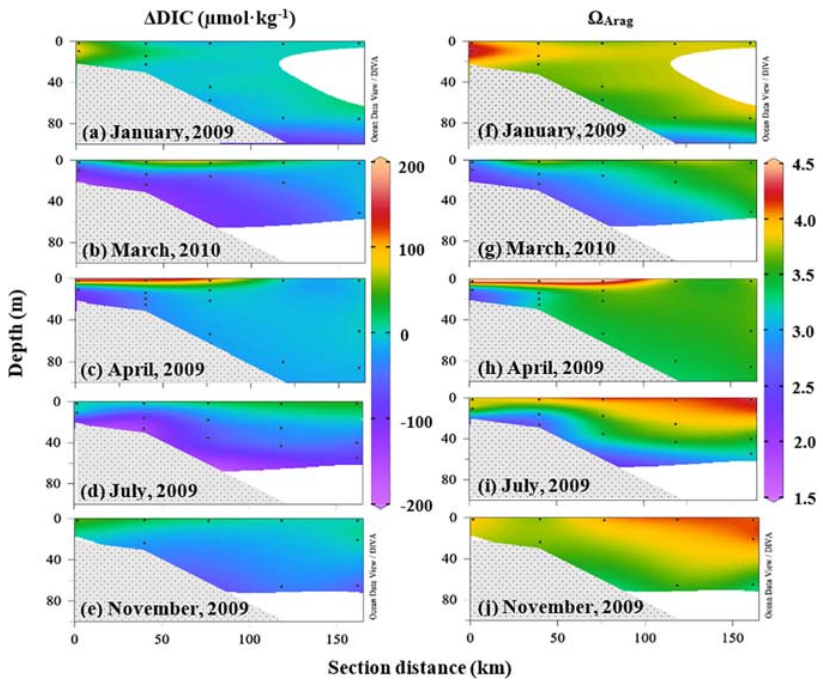


FIGURE 7 | Cross-shelf distributions of ΔDIC and Ω_{Arag}. ΔDIC and Ω_{Arag} displayed cross-shelf variations and varied seasonally **(a–j)**. In January, high ΔDIC (~100 μmol·kg^{-1}) and high Ω_{Arag} (>4.0) values were in the inner shelf. From March to July, high ΔDIC and Ω_{Arag} were on the near-surface layer, while low values were in the near-bottom, subsurface waters. During late fall (November), weak ΔDIC values were observed in the inner shelf, and high Ω_{Arag} values were on the outer shelf. DIC, dissolved inorganic carbon.

high ΔDIC and Ω_{Arag} values extended from the inner shelf to 100- to 150-km offshore in March 2010 (**Figures 7b,g**).

The Ω_{Arag}-to-depth profile demonstrated the difference in variations of Ω_{Arag} among the near-surface water, near-bottom, subsurface, and deep waters (**Figure 8**). Ω_{Arag} values varied greatly ($1.0 < \Omega_{Arag} < 6.0$) in the surface layer (<5 m) and narrowed to a range between ~2.0 and 5.0 in the subsurface and bottom waters on the middle shelf (20–100 m). Ω_{Arag} values were generally less than 2.0 and decreased toward 1.0 or lower in deeper waters (>200 m) (**Figure 8**).

Strong seasonal variations in ΔDIC and Ω_{Arag} were observed across the shelf, particularly on the inner-to-middle shelf (**Figure 7**). Therefore, we focus on this area to display their monthly variations in two specified regions.

Monthly Variations in ΔDIC, Apparent Oxygen Utility, and Chlorophyll *a* on Specified Regions on the Inner-to-Middle Shelf

We considered the horizontal dispersal (**Figures 6**, **7**) and vertical stratification (**Figure 7**) and organized the monthly ΔDIC on specified conditions on the inner-to-middle shelf to quantify the spatial–temporal ΔDIC variations. (Note that ΔDIC was from the calculation in the section "Net Dissolved Inorganic Carbon Removal (ΔDIC) and Nitrate Removal (ΔNO_3) Over the Water Column" by the three-end-member mixing.) In the near-surface water (specified at sample depth < 5 m, salinity < 35, to the north of 28.2°N), the average of ΔDIC values increased from 14.3 μmol·kg^{-1} in January to 126.6 μmol·kg^{-1} in June and subsequently decreased to nearly zero (–2.9 μmol·kg^{-1}) in November (**Figure 9A**). Interestingly, the seasonal trend of ΔDIC in the specified the near-bottom, subsurface water (20–100 m, to the north of 28.2°N) displayed an opposite pattern; that is, it changed from –13.5 μmol·kg^{-1} in January to –102 μmol·kg^{-1} in July and –13 μmol·kg^{-1} in September and returned to –42.5 μmol·kg^{-1} in November (**Figure 9A**). Though data in March 2010 and July 2009 were affected by special weather events (will be discussed later), monthly average ΔDIC in the specified near-surface and near-bottom, subsurface waters still demonstrated clear seasonal trends (**Figure 9A**). In particular, we noticed that the ΔDIC peak time in the near-surface water (June) was 1-3 months (approximately 2 months hereafter) ahead of the one in the near-bottom, subsurface waters (July to September).

Interestingly, monthly AOU and Chl-*a* both demonstrated similar seasonal trends (**Figures 9B,C**). The AOU seasonal variation in the near-surface water, correspondingly, decreased from 75 to –25 to –19 μmol·kg^{-1} from April to June and gradually increased to 20 μmol·kg^{-1} in November. In contrast, AOU in the near-bottom, subsurface waters displayed a maximum (112 μmol·kg^{-1}) in August and a minimum (4 μmol·kg^{-1}) in April. The AOU peak time in the near-surface water (April to June) was 2-3 months ahead of the one in the near-bottom, subsurface waters (August). Furthermore, monthly Chl-*a* in the near-surface water increased from the

lowest of ∼2 μg·L^{-1} in January to the maximum value of 7.6 μg·L^{-1} in April and again decreased to 2.6 μg·L^{-1} in August (**Figure 9C**). Monthly Chl-*a* concentrations in the near-bottom, subsurface waters were lower than those in the near-surface waters, increasing from a minimum of 0.27 μg·L^{-1} in January to 1.7 μg·L^{-1} in August (**Figure 9C**). The peak time in the near-surface waters (April) was almost 4 months ahead of the one in the near-bottom, subsurface waters (August and September).

DISCUSSION

Mixing and Non-mixing Factors of ΔDIC

Seasonal changes in the carbonate system vary along the plume trajectory and dissipate offshore or away from the river mouths due to mixing and biological activities. For regions near the Mississippi River Delta, Green et al. (2006) have estimated the water residence time (less than 14.5 days) by examining satellite images. For the entire shelf, fluctuating river discharge can change water transit time in the nGOM, resulting in that freshwater volume on the shelf lags the discharge by 21-33 days (Zhang et al., 2012). We generally follow the above two estimations to choose the river end-members in advance of our sampling cruise (**Supplementary Table 1**). Anderson et al. (2020) have estimated the residence time to be short during July (4–68 days) and to be long (11–233 days) during September by using radium radioisotopes. This physical water residence time on the shelf is long enough to support the biogeochemical temporal scales of Chl-*a* and ΔDIC in the section "Monthly Variations in ΔDIC, Apparent Oxygen Utility, and Chlorophyll a on Specified Regions on the Inner-to-Middle Shelf." Moreover, previous studies have demonstrated that mixing dominated regions with salinities lower than 18 in this study area (Green et al., 2006; Lohrenz et al., 2010; Huang et al., 2015b). Mixing can further affect the carbonate system, as pH and Ω_{Arag} are non-conservative, particularly at low-salinity estuaries where minimum buffering and pH zones often occur (Mook and Koene, 1975; Hu and Cai, 2013; Hu et al., 2017).

The net biological activity includes photosynthesis and respiration. Primary production can be affected by the availability of nutrients and environmental factors [such as water temperature, stratification, insolation duration, and light attenuation (k_d)]. Previous studies have demonstrated variations in ΔDIC mostly in the near-surface water at particular seasons (as high as 400–500 μmol·kg^{-1} during spring and as low as < 200 μmol·kg^{-1} during fall) (Guo et al., 2012; Huang et al., 2012a; Fry et al., 2015). Murrell et al. (2013) have reported that gross primary production varied at different salinity ranges (0–18, 18–27, 27–32, and >32), and it can be over 250 mmol·m^{-2}·day^{-1} in the second salinity range (18–27). Furthermore, they also have suggested that GPP and respiration both occurred throughout the water column, and the net ecosystem metabolism switched to net respiration when the water column was >20 m. In line with results of previous studies, ΔDIC was overall positive in the near-surface water and negative in the near-bottom, subsurface waters. Moreover, this study fulfills the seasonal variation in ΔDIC in both near-surface and near-bottom, subsurface waters.

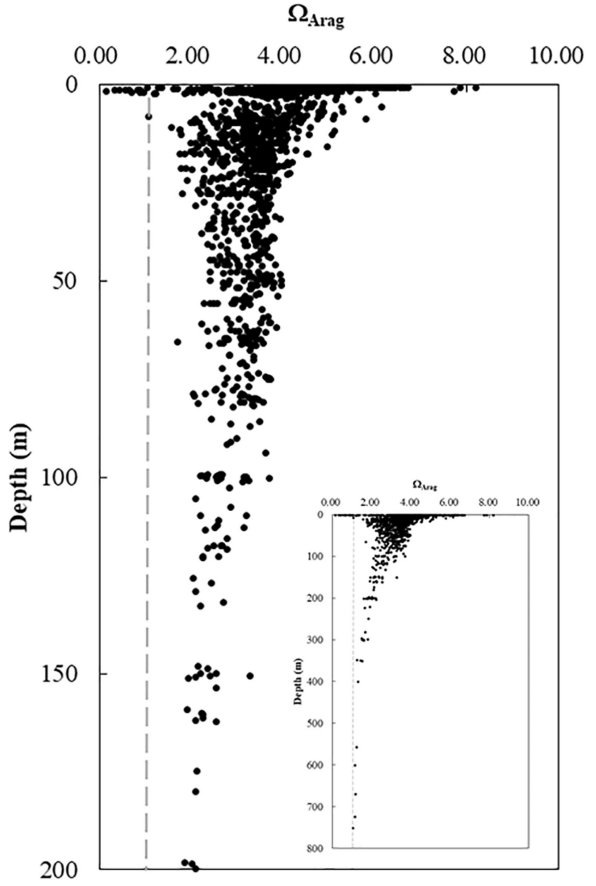


FIGURE 8 | Vertical variations in Ω_{Arag}. Ω_{Arag} varied from 1.0 to 8.0 with large ΔDIC variations in the near-surface water and changed from 2.0 to 4.0 in the subsurface and bottom waters on the shelf. The Ω_{Arag} value gradually decreased from 2.0 at 200 m to close to 1.0 at 800 m (the inset). DIC, dissolved inorganic carbon.

Special weather events may alter the carbonate system by changing the plume dispersal direction or range. In the first case, the near-surface water acted as a weak sink of CO_2 with an eastward river plume and an upwelling-favorable wind in July 2009 (Zhang et al., 2012; Fichot et al., 2014; Huang et al., 2015a), leading to the early development of hypoxia (Feng et al., 2014). At the northern South China Sea, seasonal upwelling in this large-river-dominated continental shelf can reduce acidification in the near-bottom waters (Huang et al., 2020). In the second case, Huang et al. (2013) have reported an extended surface plume over the middle and outer shelves in March 2010 due to an exceptionally widespread plume when winter storms dominated North America.

Effects of Minor Factors on the ΔDIC Variation

We interpret the major and minor effects of carbonate dynamics by examining the regression's slope and intercept ΔDIC and

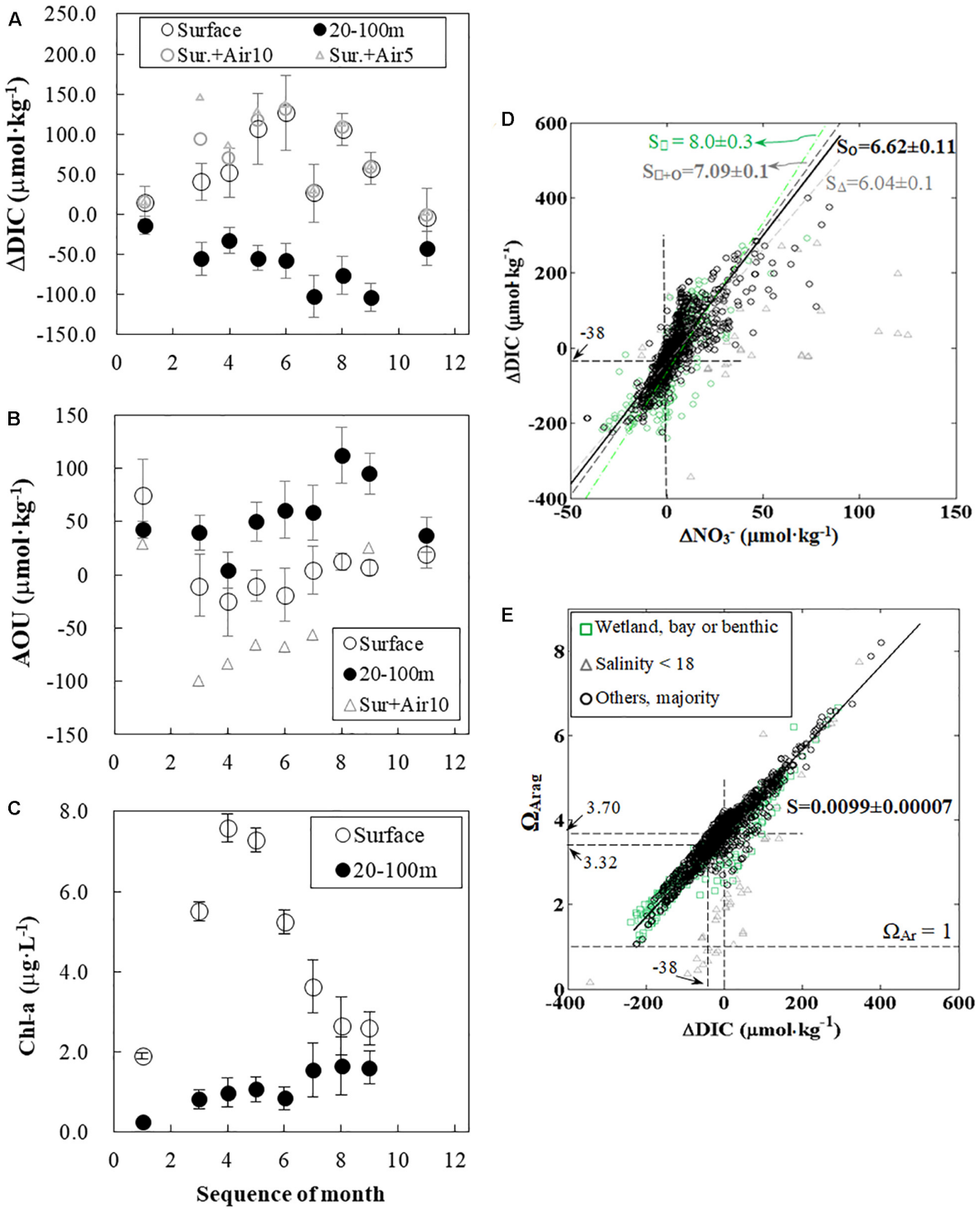


FIGURE 9 | Seasonal variations in ΔDIC, AOU, Chl-*a*, and relationships between ΔDIC, ΔNO_3^-, and Ω_{Arag}. In the near-surface water, the average of ΔDIC values increased from January to June and subsequently decreased to nearly zero (–2.9 μmol·kg^{-1}) in November. Interestingly, the seasonal trend of ΔDIC in the near-bottom, subsurface waters displayed an opposite pattern, decreasing from January to July and September and increasing until November. ΔDIC values in panel **(A)** were averaged from the specific water in each cruise by the result of three-end-member model (section "Net Dissolved Inorganic Carbon Removal (ΔDIC) and Nitrate Removal (ΔNO_3) Over the Water Column"). The effect of air–sea CO_2 gas exchanges from Huang et al. (2015b) on ΔDIC was usually less than 10% (assuming 5- and 10-m mixing layer depth for triangle markers and open gray circles, respectively) **(A)**. AOU in the near-surface waters and near-bottom, subsurface waters displayed a time delay in their peak; that is, April to June vs. August **(B)**. The effect of air–sea O_2 gas exchange on AOU in the near-surface water was large, and peak time was still similar (assuming 10-m mixing layer depth, triangle markers). Air–sea CO_2 and O_2 fluxes were exceptionally large in March **(A,B)**.Chl-*a*

(Continued)

FIGURE 9 | Continued
concentrations were low (<2 μg·L^{-1}) in January, increased to >7 μg·L^{-1} in April, and decreased back to <3 μg·L^{-1} in August and September in the near-surface water **(C)**. In the near-bottom, subsurface waters, Chl-*a* was < 3 μg·L^{-1} and increased from January to September **(C)**. Bars in panels **(A–C)** represent ± 1 standard deviation of the average. Furthermore, ΔDIC values from each sample in all cruises were positively correlated to the corresponding ΔNO_3^- values (d). The slope of the regression line of majority data (circles) was close to the Redfield ratio, and the intercept was –38 μmol·kg^{-1} **(D)**. Besides, this slope could likely be affected by low salty water (triangle markers), wetland exports (square markers), $CaCO_3$ precipitation, and the regional change of the Redfield ratio **(D)**. Finally, Ω_{Arag} values from all samples were also positively correlated to the corresponding ΔDIC **(E)**. The multi-year effect of being a CO_2 sink (0 to –38 μmol·kg^{-1}) can lead to a decrease of Ω_{Arag} from 3.70 to 3.32 **(E)**. **(B,C)** share the same legend. Note that the positive ΔDIC value in surface waters is defined as net DIC removal. DIC, dissolved inorganic carbon; AOU, apparent oxygen utility; Chl-*a*, chlorophyll *a*.

ΔNO_3^-. We assume that ΔDIC is composed of net biological removals (ΔOC), $\Delta CaCO_3$, and the proportion of DIC affected by air–sea CO_2 gas exchanges ($\Delta DIC_{air-sea}$).

$$\Delta DIC = \Delta OC + \Delta CaCO_3 + \Delta DIC_{air-sea}, \quad (13)$$

where positive $\Delta DIC_{air-sea}$ represents a CO_2 source to the atmosphere and a negative value represents CO_2 sink. We further assume that the $CaCO_3$ precipitation/dissolution is proportional to ΔOC ($\Delta CaCO_3 = \beta \times \Delta OC$) (Chen et al., 1995, 2017).

$$\Delta DIC = (1 + \beta) \times \Delta OC - \Delta DIC_{air-sea} \quad (14)$$

Furthermore, ΔOC can be converted to ΔDIC through the Redfield ratio (α = C/N = 106/16). Eq. (14) can thus be converted to an equation including α and β, as follows:

$$\Delta DIC = \alpha(1 + \beta) \times \Delta NO_3^- + \Delta DIC_{air-sea} \quad (15)$$

We organize the relationship between ΔDIC and ΔNO_3^- in Eq. (15) (**Figure 9D**), which showed a slope and an intercept reflecting α(1 + β) and the air–sea CO_2 flux, respectively. In the major response region, the slope reflecting C:N ratio in the relationship between ΔDIC and ΔNO_3^- is 6.62 ± 0.11 (n = 1,213) (**Figure 9D**) (by type II regression as both ΔDIC and ΔNO_3^- have uncertainties). This slope value over a shelf-wide area is consistent with previous studies with less temporal and spatial coverage (Huang et al., 2012a; Xue et al., 2015).

We quantitatively discuss the regional variation of the Redfield ratio (α in Eq. 15) and the $CaCO_3$ formation ($\Delta CaCO_3$, β in Eq. 15). The effect of net community calcification (NCC) is usually lower than net community production (NCP) (that is, NCC:NCP<<1). For instance, the decrease of DIC can be mostly due to NCP instead of NCC during a coccolithophore bloom in the northwest European continental margin (Suykens et al., 2010). Martiny et al. (2013), which suggested that stoichiometry varies among phytoplankton species in addition to the traditional Redfield ratio (Redfield, 1958). On the same cruises from 2009 to 2010, Chakraborty and Lohrenz (2015) have observed that diatoms and cyanobacteria dominated the phytoplankton community in this study area. The C/N ratio of diatoms can be higher than the Redfield ratio (Geider and LaRoche, 2002), and the ratio of cyanobacteria can be lower than the Redfield ratio (Martiny et al., 2013). We focus on the data in the major response area (excluding two exceptional regions in **Figure 9D**) and adopt the proportion of NCC to NCP of 5% at the Atlantic Ocean (Tyrrell and Young, 2009) and 1–3% in the global scale (Balch, 2018) with traditional Redfield C/N ratios ($\alpha \cong 6.625$, $6.125 < \alpha < 6.64$), resulting in a range of α(1 + β) between 6.186 and 6.972. This theoretical range of α(1 + β) was consistent with our observation of 6.62 ± 0.11. Thus, we suggest that the net removal of DIC and nitrate ratio can also be affected by the proportion between NCC and NCP in the aerobic water column. The benthic CO_2 flux during hypoxia may provide an additional DIC source (Hu et al., 2017) and, together with N_2 degassing through denitrification reported by Xue et al. (2015), and may lead to a potential higher C/N ratio in the water column respiration. Besides, though organic matters can affect alkalinity values during the titration process (Hernández-Ayon et al., 2007), this contribution has been suggested to be minor compared with our analytical precision (0.1%) (Yang et al., 215).

Two areas, one affected by salinities lower than 18 and the other affected by export from wetlands/bays, may also lead to changes in the slope between ΔDIC and ΔNO_3^- (**Figure 9D**). The area affected by low salinities is likely dominated by mixing, as mentioned in the sections "Seasonal Properties to Salinity Relationships and Mixing and Non-mixing Factors of ΔDIC." For example, the changing DIC river end-member in the section "Seasonal Properties to Salinity Relationships" may also affect the ΔDIC result in low salinities. We focused on the result on the shelves where middle to high salinities were dominant. The other data that are affected by the wetlands/bays display a slope of 8.0 ± 0.3 (n = 245) (see **Supplementary Information** for details about these effects) on the ΔDIC and ΔNO_3^- diagram (**Figure 9D**). The slope of data from the above two areas (7.09 ± 0.1) is very close to the C/N ratio of 7.16 ± 0.15 from particulate organic matter (POM) in this study area in late July from 2006 to 2010 (n = 429) as reported by Fry et al. (2015). This is likely to be because particulate organic carbon (POC) and dissolved organic carbon (DOC) from Barataria Bay might be more labile (likely increase DIC) than the incubated plume water ("the bay water contributes higher potential lability of 35% than the plume water, which is 15%") (Fry et al., 2015). Thus, organic matter from Barataria Bay may slightly affect α in this study. Moreover, a higher Si/N ratio in the northern Louisiana Bight may be related to the export from the wetland (Huang et al., 2012a). The water's Si/N ratio may affect both the composition of phytoplankton and respiration (Turner et al., 1998). Berelson et al. (2019) have observed that fluxes of dissolved Si and DIC are significantly correlated on the hypoxia-influenced sediment on this study area, and they

have suggested the importance of diagenesis of biogenic Si and organic carbon.

Recent observations demonstrated that DIC export through wetlands to the nGOM could be important (Anderson et al., 2020). Subsurface groundwater (SGD) can be a pathway and has been noticed in the past two decades (Bugna et al., 1996; McCoy et al., 2007; McCoy and Corbett, 2009; Befus et al., 2017; Coleman et al., 2017). DIC export through SGD can be low in snowmelt and wet seasons and high during the dry season in the Mississippi River basin (Cai et al., 2020). However, the role of SGD in the carbon budget of North America is still unclear (Najjar et al., 2018).

The intercept of this regression line (with a slope of 6.62 for the majority of this study area, **Figure 9D**) for ΔDIC and ΔNO_3^- can reflect the net effect of air–sea CO_2 gas exchange on DIC when $\Delta NO_3^- = 0$ and $\Delta DIC = \Delta DIC_{air-sea} = -38$ $\mu mol \cdot kg^{-1}$ as expressed in Eq. (15). The assumption of ΔNO_3^- equals to 0 in this regression line does not imply zero biological activity, but the net biological activity (net ecosystem photosynthesis minus respiration) is zero. The intercept is below zero, implying that this study area generally acts as a CO_2 sink according to the net results of high biological DIC uptake and release on this highly dynamic shelf. Our interpretation is consistent with the direct measurements of pCO_2 in this study region (Huang et al., 2015b). We count these direct measurements of air–sea CO_2 gas exchange in each month and suggest that the effect of air–sea gas exchanges for each month was usually less than 10% to 20% of ΔDIC (**Figure 9A** and **Supplementary Table 4**). The effect of air–sea CO_2 gas exchange on surface ΔDIC in March was exceptionally strong, as the plume coverage was exceptionally large due to the winter storm (Huang et al., 2013). Moreover, air–sea O_2 gas exchange can also supply additional DO for AOU in the near-surface water (details in **Supplementary Table 5**). The AOU peak in the near-surface water was still in April when we exclude the exceptional case in March.

To sum up, the slope of the ΔDIC and ΔNO_3^- diagram shows that Redfield-type biological activities were dominant in this study area with several minor factors. Exports from the wetland into the inner shelf region are complex and can be studied in the future.

Assessments of the Relationship Between ΔDIC and Ω_{Arag}

Dissolved inorganic carbon uptake can increase Ω_{Arag} values (**Figure 9E**), resulting in a near-linear relationship. The observed Ω_{Arag} to ΔDIC relationship has a slope of 0.0099 ± 0.00007 (nearly 0.01) and an intercept of 3.70 for those waters with an average salinity of 33.5 (±1.85). Note that the influence of two areas (wetland/bay or benthic process, and low salty region) has been excluded in this regression. Slope and intercept of this regression can reveal the effects of photosynthesis, respiration, and air–sea gas exchange on the Ω_{Arag} variation. Xiong et al. (2019) have suggested that high Ω_{Arag} values were insensitive to salinity changes than low ones. They also have considered the combined effect of salinity and ΔDIC changes on Ω_{Arag} variations. They suggest that the effect of a unit of salinity decrease on Ω_{Arag} decline can be counteracted by a DIC uptake of 9.43 $\mu mol \cdot kg^{-1}$, displaying that model simulations can reveal details in carbonate variations in a single event. In a global scale, Ω_{Arag} is expected to increase 1.06 or 0.91 unit for every 100 increase of [TA–DIC] at the *in situ* condition or a condition in 25°C and 3 dbar, respectively (Xue and Cai, 2020). The change of [TA–DIC] was highly related to changes of $[CO_3^{2-}]$ and $[CO_2^*]$, which proportion subjects to the pH level. Wang et al. (2017) have reported that Ω_{Arag} is expected to decrease by 1 for every 100 $\mu mol \cdot kg^{-1}$ increase of DIC in the western Gulf of Maine. A consistent value (that is, 100 ΔDIC $\mu mol \cdot kg^{-1}$ to 1 Ω_{Arag}) from the Gulf of Maine and this study area provides a shelf-wide result from various seasons on a regional scale. As the carbonate system and biological activities can vary regionally, we suggest that this slope between ΔDIC and Ω_{Arag} value may also change correspondingly. This slope of ∼0.01 in this study may represent the one at high productivity and high TA coastal regions and can help mimic marine *in situ* Ω_{Arag} variations.

The net effect of being a CO_2 sink through DIC on Ω_{Arag} can be calculated by applying $\Delta DIC = \Delta DIC_{air-sea} = -38$ $\mu mol \cdot kg^{-1}$ to the Ω_{Arag} function of ΔDIC ($\Omega_{Arag} = 0.0099 \times \Delta DIC + 3.70$), displaying a result of 3.32 (**Figure 9E**). As the atmospheric partial pressure of carbon dioxide (pCO_2) has increased over our 5-year study period (Huang et al., 2015b), the effect of varying atmospheric pCO_2 on the air–sea gas exchange would only lead to 2% of Ω_{Arag} change in the near-surface waters (Wanninkhof et al., 2015). This difference of 0.38 in the Ω_{Arag} changes (3.70–3.32 = 0.38) should mostly represent the effect of air–sea CO_2 gas exchange through the water column DIC on Ω_{Arag}. Though the riverine nitrogen-induced biological activity can trigger a larger variation than the influence of air–sea CO_2 gas exchange on Ω_{Arag} variations, we suggest that the former factor only controls the seasonal Ω_{Arag} variation and that the latter one controls the Ω_{Arag} value on a longer time scale (decadal). Low Ω_{Arag} values in low salinities ($S < 18$) in **Figure 9E** are consistent with results provided by Xiong et al. (2019), who have simulated the effect of salinity changes on ΔDIC and indicate that Ω_{Arag} decreases with a reduction in salinity at a given ΔDIC. Besides, a few Ω_{Arag} values lower than the regression line (**Figure 9E**) may signal the benthic processes affecting the inorganic carbon system (Murrell et al., 2013; Fry et al., 2015; Hu et al., 2017). A few outliers are from depths of 350 to 720 m, except one from 8 m at the river mouth, and all had temperature < 10°C. Here, deep waters (200 to 700 m) are from regions other than the Gulf of Mexico, such as the Caribbean (Rivas et al., 2005).

Finally, we suggest that the relative proportion of each carbonate-related biogeochemical process on a river-dominated continental shelf is as follows: mixing (roughly ∼<200 $\mu mol \cdot kg^{-1}$ in salinities > 18 waters, **Figures 3E–H**) and NCP (0 to 120 $\mu mol \cdot kg^{-1}$ in monthly average, **Figure 9A**) (>70%)≫ effect of air–sea CO_2 gas exchange on DIC (38 $\mu mol \cdot kg^{-1}$ in average, **Figure 9D**) (∼<10–20%, depending on the pCO_2 level induced by other factors) > $CaCO_3$ precipitation and the variation of stoichiometry (<7% by

evaluating α and β in the section "Effects of Minor Factors on the ΔDIC Variation").

Seasonal Conceptual Model

We use a seasonal conceptual model to integrate the spatial–temporal ΔDIC variations in this river-dominated continental shelf (**Figure 10**). Seasonal variations in river end-members, shelf circulation, shelf-water residence time, wind direction, cross-shelf transportation, bays and wetlands export (including SGD), and also biogeochemical processes (such as autotrophic or heterotrophic activities, benthic processes, carbonate precipitation or dissolution, and air–sea gas exchanges) all contribute to the carbonate system in this shelf. At the connecting regions, these biogeochemical parameters (such as DIC, pH, and Ω_{Arag}) are diluted by mixing with the pelagic ocean or varied by exports from bays or wetlands.

When we focused on the majority of this shelf, we successfully quantified two regions of this shelf with seasonal variations (**Figure 10A**). The near-surface waters (0–5 m, 18 ≤ salinity < 35, to the north of 28.2°N) displayed a peak of Chl-*a* and AOU in April and a peak of net DIC removal in June (**Figure 10B**). The 2-month delay between these two peaks implied a peak of heterotrophic activity, which should not be earlier than June. Furthermore, a Chl-*a* maximum was in August in the near-bottom, subsurface waters (20 m < depth < 100 m, S = 35, to the north of 28.2°N), but net DIC accumulation and the AOU peak were still observed around August in this region too (specified as section "Monthly Variations in ΔDIC, Apparent Oxygen Utility, and Chlorophyll a on Specified Regions on the Inner-to-Middle Shelf") (**Figure 10C**). Finally, it is worth noting that the seasonal variation of AOU in the near-bottom, subsurface waters is about a 2- to 3-month delay to the near-surface one. Furthermore, the seasonal variation of ΔDIC in the near-bottom, subsurface waters is about a 2- to 2.5-month delay to the near-surface one. This difference in the delay time between AOU and ΔDIC is probably because the buffer capacity was lacking in DO and was strong in the carbonate system.

SUMMARY

The fluctuating river end-members dominated the seasonal changes in river TA and DIC in the property-to-salinity relationship. The application of the three-end-member model on our dataset produced ΔDIC over nine cruises from 2006 to 2010. Non-linear variations in pH and Ω_{Arag} values were close to the conservative mixing curves during November and January (**Figures 4C,D,G,H**) and were close to the biological activity curves, particularly during May and June (**Figures 4A,B,E,F**).

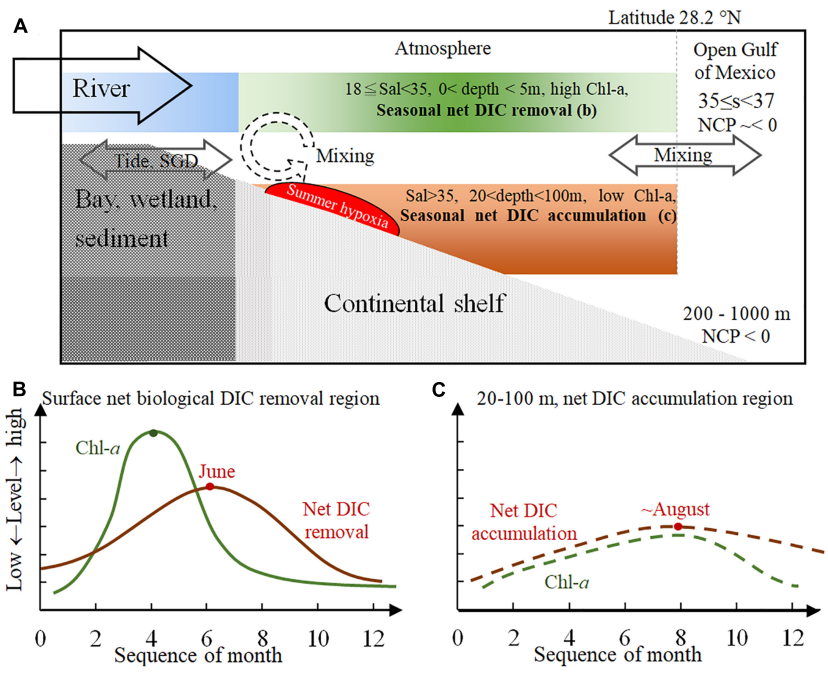


FIGURE 10 | The seasonal conceptual model for the carbonate system on a large river-dominated continental shelf. Mixing dominated waters with low salinities (<18) in the river channel and tidal exchange can facilitate the water exchange (including subsurface groundwater) in the bay and wetland. The continental shelf is a high dynamics system where strong biological uptake and release occur simultaneously. This study is the first to propose quantified regions to distinguish the areas of net DIC removal and net DIC accumulation. The shallow water (<5 m) with salinity between 18 and 35 **(A)** displayed high Chl-*a* and seasonal net DIC removal **(B)**, and the salty near-bottom, subsurface waters (salinity > 35, 20 < depth < 100 m) **(A)** showed low Chl-*a* and seasonal net DIC accumulation/release **(C)**. The peak of net DIC accumulation was about 2 months after the peak of net DIC removal, displaying the seasonal relationship between these two biogeochemical hotspots along the water column on the continental shelf. DIC, dissolved inorganic carbon; Chl-*a*, chlorophyll *a*.

We suggest that the relative proportion of each controlling factor on ΔDIC on a river-dominated continental shelf is mixing and NCP (>70%) ≫ effect of air–sea CO_2 gas exchange on DIC (∼<10–20%) > $CaCO_3$ precipitation and the variation of stoichiometry (<7%). As a result of these natural factors, we suggest a realistic, ecosystem-based relationship; that is, a nearly 100 $\mu mol \cdot kg^{-1}$ increase of net DIC removal can lead to a 1-unit increase of Ω_{Arag} for future studies. Furthermore, there is a 2-month delay in biogeochemical processes between net DIC removal in the near-surface water and net DIC accumulation in the near-bottom, subsurface waters. We argue that, for regions including eutrophic surface and hypoxic bottom waters, a similar seasonal delay in the carbonate system between these two waters may last on an annual basis and occur worldwide.

DATA AVAILABILITY STATEMENT

The original contributions presented in the study are included in the article/**Supplementary Material**, further inquiries can be directed to the corresponding author/s.

AUTHOR CONTRIBUTIONS

W-JH designed the study, conducted most field trips, analyzed most TA samples, wrote the manuscript, and organized all the data. W-JC supervised the fieldwork and experiments and edited the manuscript. XH participated in several cruises, analyzed some TA samples, and edited the manuscript. All authors contributed to the article and approved the submitted version.

FUNDING

Data presented in the manuscript were collected over several project periods when all authors were members of the Cai coastal ocean CO_2 research group at the University of Georgia. Funded primarily by NSF grants OCE-1559279 and OCE-0752110 and NASA grant NNH13ZDA001N and NNX14AM37G for W-JC, MOST#104-2611-M-110-023-MY2 at Taiwan to W-JH, and GOMRI RFP II-020 for additional support to W-JC and XH.

ACKNOWLEDGMENTS

This work was dedicated to Yongchen Wang, who provided critical efforts in experiments. We thank the captains and crews on R/V *Cape Hatteras*, RV *Pelican*, OSV *Bold*, and RV *Hugh R. Sharp*. We also thank Michael Murrel for inviting us to participate in the cruises in 2006 and 2007, Allan Shiller for the cruise in 2008, and Steven E. Lohrenz for leading the cruises in 2009 and 2010. Feizhou Chen, Chenhua Han, Liang Xue, and Baoshan Chen all helped with our fieldwork and sample analysis. We appreciate the help from Fei-Ling Yuan at the Department of Oceanography, National Sun Yat-sen University. Comments from two reviewers have improved this study.

SUPPLEMENTARY MATERIAL

The Supplementary Material for this article can be found online at: https://www.frontiersin.org/articles/10.3389/fmars.2021.621243/full#supplementary-material

REFERENCES

Anderson, M. M., Maiti, K., Xue, Z. G., and Ou, Y. (2020). Dissolved inorganic carbon transport in the surface-mixed layer of the Louisiana Shelf in Northern Gulf of Mexico. *J. Geophys. Res. Oceans* 125:e2020JC016605. doi: 10.1029/2020JC016605

APHA (1989). *Standard Methods for the Examination of Water and Wastewater*, 17th Edn. Washington, DC: American Public Health Association.

Balch, W. M. (2018). The ecology, biogeochemistry, and optical properties of Coccolithophores. *Ann. Rev. Mar. Sci.* 10, 71–98. doi: 10.1146/annurev-marine-121916-063319

Bates, N. R., Hansell, D. A., Carlson, C. A., and Gordon, L. I. (1998). Distribution of CO_2 species, estimates of net community production, and air-sea CO_2 exchange in the Ross Sea polynya. *J. Geophys. Res.* 103, 2883–2896. doi: 10.1029/97jc02473

Bauer, J. E., Cai, W.-J., Raymond, P. A., Bianchi, T. S., Hopkinson, C. S., and Regnier, P. A. G. (2013). The changing carbon cycle of the coastal ocean. *Nature* 504, 61–70. doi: 10.1038/nature12857

Befus, K. M., Kroeger, K. D., Smith, C. G., and Swarzenski, P. W. (2017). The magnitude and origin of groundwater discharge to Eastern U.S. and Gulf of Mexico coastal waters. *Geophys. Res. Lett.* 44, 10396–10406. doi: 10.1002/2017GL075238

Berelson, W. M., McManus, J., Severmann, S., and Rollins, N. (2019). Benthic fluxes from hypoxia-influenced Gulf of Mexico sediments: impact on bottom water acidification. *Mar. Chem.* 209, 94–106. doi: 10.1016/j.marchem.2019.01.004

Bianchi, T. S., DiMarco, S. F., Cowan, J. H. Jr., Hetland, R. D., Chapman, P., Day, J. W., et al. (2010). The science of hypoxia in the Northern Gulf of Mexico: a review. *Sci. Total Environ.* 408, 1471–1484.

Borges, A. V., and Gypens, N. (2010). Carbonate chemistry in the coastal zone responds more strongly to eutrophication than to ocean acidification. *Limnol. Oceanogr.* 55, 346–353.

Breitburg, D., Levin, L. A., Oschlies, A., Grégoire, M., Chavez, F. P., Conley, D. J., et al. (2018). Declining oxygen in the global ocean and coastal waters. *Science* 359:6371. doi: 10.1126/science.aam7240

Brewer, P. G., and Goldman, J. C. (1976). Alkalinity changes generated by phytoplankton growth. *Limnol. Oceanogr.* 21, 108–117.

Bugna, G. C., Chanton, J. P., Cable, J. E., Burnett, W. C., and Cable, P. H. (1996). The importance of groundwater discharge to the methane budgets of nearshore and continental shelf waters of the northeastern Gulf of Mexico. *Geochim. Cosmochim. Acta* 60, 4735–4746. doi: 10.1016/S0016-7037(96)00290-6

Cai, W.-J., Hu, X., Huang, W.-J., Murrell, M. C., Lehrter, J. C., Lohrenz, S. E., et al. (2011). Acidification of subsurface coastal waters enhanced by eutrophication. *Nat. Geosci.* 4, 766–770. doi: 10.1038/ngeo1297

Cai, W.-J., and Wang, Y. (1998). The chemistry, fluxes, and sources of carbon dioxide in the estuarine waters of the Satilla and Altamaha Rivers. *Georgia. Limnol. Oceanogr.* 43, 657–668.

Cai, Y., You, C. F., Wu, S. F., Cai, W. J., and Guo, L. (2020). Seasonal variations in strontium and carbon isotope systematics in the Lower Mississippi River: implications for chemical weathering. *Chem. Geol.* 553:119810. doi: 10.1016/j.chemgeo.2020.119810

Chakraborty, S., and Lohrenz, S. E. (2015). Phytoplankton community structure in the river-influenced continental margin of the northern Gulf of Mexico. *Mar. Ecol. Prog. Ser.* 521, 31–47.

Chen, C.-T. A., Lui, H.-K., Hsieh, C.-H., Yanagi, T., Kosugi, N., Ishii, M., et al. (2017). Deep oceans may acidify faster than anticipated due to global warming. *Nat. Clim. Chang.* 7, 890–894. doi: 10.1038/s41558-017-0003-y

Chen, C.-T. A., Wang, S.-L., and Bychkov, A. S. (1995). Carbonate chemistry of the Sea of Japan. *J. Geophys. Res.* 100, 13737–13745. doi: 10.1029/95JC00939

Coleman, D. J., Kolker, A. S., and Johannesson, K. H. (2017). Submarine groundwater discharge and alkaline earth element dynamics in a deltaic coastal setting. *Hydrol. Res.* 48, 1169–1176. doi: 10.2166/nh.2016.285

Efron, B. (1992). "Bootstrap methods: another look at the jackknife," in *Breakthroughs in Statistics: Methodology and Distribution*, eds S. Kotz and N. L. Johnson (New York, NY: Springer), 569–593. doi: 10.1007/978-1-4612-4380-9_41

Feng, Y., Fennel, K., Jackson, G. A., DiMarco, S. F., and Hetland, R. D. (2014). A model study of the response of hypoxia to upwelling-favorable wind on the northern Gulf of Mexico shelf. *J. Mar. Syst.* 131, 63–73. doi: 10.1016/j.jmarsys.2013.11.009

Fichot, C. G., Lohrenz, S. E., and Benner, R. (2014). Pulsed, cross-shelf export of terrigenous dissolved organic carbon to the Gulf of Mexico. *J. Geophys. Res. Oceans* 119, 1176–1194. doi: 10.1002/2013JC009424

Fry, B., Justić, D., Riekenberg, P., Swenson, E. M., Turner, R. E., Wang, L., et al. (2015). Carbon dynamics on the Louisiana Continental Shelf and cross-shelf feeding of hypoxia. *Estuar. Coast.* 38, 703–721. doi: 10.1007/s12237-014-9863-9

Gattuso, J.-P., Epitalon, J.-M., Lavigne, H., Orr, J., Gentili, B., Hofmann, A., et al. (2016). *seacarb: Seawater Carbonate Chemistry R Package Version 3.0*.

Geider, R. J., and LaRoche, J. (2002). Redfield revisited: variability of C:N:P in marine microalgae and its biochemical basis. *Eur. J. Phycol.* 37, 1–17. doi: 10.1017/s0967026201003456

Goolsby, D. A., Battaglin, W. A., Aulenbach, B. T., and Hooper, R. P. (2000). Nitrogen flux and sources in the Mississippi River Basin. *Sci. Total Environ.* 248, 75–86.

Green, R. E., Bianchi, T. S., Dagg, M. J., Walker, N. D., and Breed, G. A. (2006). An organic carbon budget for the Mississippi River turbidity plume and plume contributions to air-sea CO_2 fluxes and bottom water hypoxia. *Estuar. Coast.* 29, 579–597. doi: 10.1007/BF02784284

Guo, X., Cai, W.-J., Huang, W.-J., Wang, Y., Chen, F., Murrell, M. C., et al. (2012). Carbon dynamics and community production in the Mississippi River plume. *Limnol. Oceanogr.* 57, 1–17. doi: 10.4319/lo.2012.57.1.0001

Hernández-Ayon, J. M., Zirino, A., Dickson, A. G., Camiro-Vargas, T., and Valenzuela, E. (2007). Estimating the contribution of organic bases from microalgae to the titration alkalinity in coastal seawaters. *Limnol. Oceanogr. Meth.* 5, 225–232. doi: 10.4319/lom.2007.5.225

Hu, X., and Cai, W. J. (2013). Estuarine acidification and minimum buffer zone - a conceptual study. *Geophys. Res. Lett.* 40, 5176–5181. doi: 10.1002/grl.51000

Hu, X., Li, Q., Huang, W. J., Chen, B., Cai, W. J., Rabalais, N. N., et al. (2017). Effects of eutrophication and benthic respiration on water column carbonate chemistry in a traditional hypoxic zone in the Northern Gulf of Mexico. *Mar. Chem.* 194, 33–42. doi: 10.1016/j.marchem.2017.04.004

Huang, W.-J., Cai, W.-J., Castelao, R. M., Wang, Y., and Lohrenz, S. E. (2013). Effects of a wind-driven cross-shelf large river plume on biological production and CO_2 uptake on the Gulf of Mexico during spring. *Limnol. Oceanogr.* 58, 1727–1735. doi: 10.4319/lo.2013.58.5.1727

Huang, W.-J., Cai, W.-J., Powell, R. T., Lohrenz, S. E., Wang, Y., Jiang, L.-Q., et al. (2012a). The stoichiometry of inorganic carbon and nutrient removal in the Mississippi River plume and adjacent continental shelf. *Biogeosciences* 9, 2781–2792. doi: 10.5194/bg-9-2781-2012

Huang, W.-J., Kao, K.-J., Lin, Y.-S., Chen, C.-T., and Liu, J. T. (2020). Daily to weekly impacts of mixing and biological activity on carbonate dynamics in a large river-dominated shelf. *Estuar. Coast. Shelf Sci.* 245:106914. doi: 10.1016/j.ecss.2020.106914

Huang, W.-J., Wang, Y., and Cai, W.-J. (2012b). Assessment of sample storage techniques for total alkalinity and dissolved inorganic carbon in seawater. *Limnol. Oceanogr. Meth.* 10, 711–717. doi: 10.4319/lom.2012.10.711

Huang, W.-J., Cai, W.-J., Wang, Y., Hu, X., Chen, B., Lohrenz, S. E., et al. (2015a). The response of inorganic carbon distributions and dynamics to upwelling-favorable winds on the northern Gulf of Mexico during summer. *Cont. Shelf Res.* 111, 211–222. doi: 10.1016/j.csr.2015.08.020

Huang, W.-J., Cai, W.-J., Wang, Y., Lohrenz, S. E., and Murrell, M. C. (2015b). The carbon dioxide system on the Mississippi River-dominated continental shelf in the northern Gulf of Mexico: 1. Distribution and air-sea CO_2 flux. *J. Geophys. Res. Oceans* 120, 1429–1445. doi: 10.1002/2014JC010498

Huang, W.-J., Kao, K.-J., Liu, L.-L., Liao, C.-W., and Han, Y.-L. (2018). An assessment of direct dissolved inorganic carbon injection to the coastal region: a model result. *Sustainability* 10:1174. doi: 10.3390/su10041174

Jiang, Z., Cai, W., Chen, B., Wang, K., Han, C., Roberts, B. J., et al. (2019). Physical and biogeochemical controls on pH dynamics in the northern Gulf of Mexico during summer hypoxia. *J. Geophys. Res. Oceans* 124, 5979–5998. doi: 10.1029/2019jc015140

Laurent, A., Fennel, K., Ko, D. S., and Lehrter, J. (2018). Climate change projected to exacerbate impacts of coastal eutrophication in the Northern Gulf of Mexico. *J. Geophys. Res. Oceans* 123, 3408–3426. doi: 10.1002/2017JC013583

Legge, O., Johnson, M., Hicks, N., Jickells, T., Diesing, M., Aldridge, J., et al. (2020). Carbon on the Northwest European shelf: contemporary budget and future influences. *Front. Mar. Sci.* 7:143. doi: 10.3389/fmars.2020.00143

Lehrter, J. C., Ko, D. S., Murrell, M. C., Hagy, J. D., Schaeffer, B. A., Greene, R. M., et al. (2013). Nutrient distributions, transports, and budgets on the inner margin of a river-dominated continental shelf. *J. Geophys. Res. Oceans* 118, 4822–4838. doi: 10.1002/jgrc.20362

Lohrenz, S. E., Cai, W.-J., Chen, F., Chen, X., and Tuel, M. (2010). Seasonal variability in air-sea fluxes of CO_2 in a river-influenced coastal margin. *J. Geophys. Res. Oceans* 115:C10034. doi: 10.1029/2009jc005608

Martiny, A. C., Pham, C. T. A., Primeau, F. W., Vrugt, J. A., Moore, J. K., Levin, S. A., et al. (2013). Strong latitudinal patterns in the elemental ratios of marine plankton and organic matter. *Nat. Geosci.* 6, 279–283. doi: 10.1038/ngeo1757

Matli, V. R. R., Fang, S., Guinness, J., Rabalais, N. N., Craig, J. K., and Obenour, D. R. (2018). Space-time geostatistical assessment of hypoxia in the Northern Gulf of Mexico. *Environ. Sci. Technol.* 52, 12484–12493. doi: 10.1021/acs.est.8b03474

McCoy, C. A., and Corbett, D. R. (2009). Review of submarine groundwater discharge (SGD) in coastal zones of the Southeast and Gulf Coast regions of the United States with management implications. *J. Environ. Manage.* 90, 644–651. doi: 10.1016/j.jenvman.2008.03.002

McCoy, C. A., Corbett, D. R., McKee, B. A., and Top, Z. (2007). An evaluation of submarine groundwater discharge along the continental shelf of Louisiana using a multiple tracer approach. *J. Geophys. Res. Oceans* 112, 1–13. doi: 10.1029/2006JC003505

Millero, F. J. (1995). Thermodynamics of the carbon dioxide system in the oceans. *Geochim. Cosmochim. Acta* 59, 661–677. doi: 10.1016/0016-7037(94)00354-O

Millero, F. J., Graham, T. B., Huang, F., Bustos-Serrano, H., and Pierrot, D. (2006). Dissociation constants of carbonic acid in seawater as a function of salinity and temperature. *Mar. Chem.* 100, 80–94. doi: 10.1016/j.marchem.2005.12.001

Milliman, J. D., and Meade, R. H. (1983). World-wide delivery of river sediment to the Oceans. *J. Geol.* 91, 1–21.

Mook, W. G., and Koene, B. K. S. (1975). Chemistry of dissolved inorganic carbon in estuarine and coastal brackish waters. *Estuar. Coast. Mar. Sci.* 3, 325–336. doi: 10.1016/0302-3524(75)90032-8

Mucci, A. (1983). The solubility of calcite and aragonite in seawater at various salinities, temperatures, and one atmosphere total pressure. *Am. J. Sci.* 283, 780–799. doi: 10.2475/ajs.283.7.780

Murrell, M. C., Stanley, R. S., Lehrter, J. C., and Hagy, J. D. III (2013). Plankton community respiration, net ecosystem metabolism, and oxygen dynamics on the Louisiana continental shelf: implications for hypoxia. *Cont. Shelf Res.* 52, 27–38. doi: 10.1016/j.csr.2012.10.010

Najjar, R. G., Herrmann, M., Alexander, R., Boyer, E. W., Burdige, D. J., Butman, D., et al. (2018). Carbon budget of tidal wetlands, estuaries, and shelf waters of Eastern North America. *Global Biogeochem. Cy.* 32, 389–416. doi: 10.1002/2017GB005790

Oschlies, A., Brandt, P., Stramma, L., and Schmidtko, S. (2018). Drivers and mechanisms of ocean deoxygenation. *Nat. Geosci.* 11, 467–473. doi: 10.1038/s41561-018-0152-2

Peng, T.-H., Takahashi, T., Broecker, W. S., and Olafsson, J. (1987). Seasonal variability of carbon dioxide, nutrient and oxygen in the northern North Atlantic surface water: observation and a modeliability of carbon dioxide, nutrient and oxygen in the northern North Atlantic surface water: observation and a model. *Tellus* 39B, 439–458.

Rabalais, N. N., Diaz, R. J., Levin, L. A., Turner, R. E., Gilbert, D., and Zhang, J. (2010). Dynamics and distribution of natural and human-caused hypoxia. *Biogeosciences* 7, 585–619. doi: 10.5194/bg-7-585-2010

Raymond, P. A., Oh, N.-H., Turner, R. E., and Broussard, W. (2008). Anthropogenically enhanced fluxes of water and carbon from the Mississippi River. *Nature* 451, 449–452.

Redfield, A. C. (1958). The biological control of chemical factors in the environment. *Am. Sci.* 46, 205–221.

Ren, L., Rabalais, N., Turner, R., Morrison, W., and Mendenhall, W. (2009). Nutrient limitation on phytoplankton growth in the upper Barataria Basin, Louisiana: microcosm bioassays. *Estuar. Coast.* 32, 958–974. doi: 10.1007/s12237-009-9174-8

Rivas, D., Badan, A., and Ochoa, J. (2005). The ventilation of the deep Gulf of Mexico. *J. Phys. Oceanogr.* 35, 1763–1781. doi: 10.1175/JPO2786.1

Suykens, K., Delille, B., Chou, L., DeBodt, C., Harlay, J., and Borges, A. V. (2010). Dissolved inorganic carbon dynamics and air-sea carbon dioxide fluxes during coccolithophore blooms in the northwest European continental margin (northern Bay of Biscay). *Global Biogeochem. Cy.* 24, 1–14. doi: 10.1029/2009GB003730

Thorhaug, A., Poulos, H. M., López-Portillo, J., Ku, T. C. W., and Berlyn, G. P. (2017). Seagrass blue carbon dynamics in the Gulf of Mexico: stocks, losses from anthropogenic disturbance, and gains through seagrass restoration. *Sci. Total Environ.* 605–606, 626–636. doi: 10.1016/j.scitotenv.2017.06.189

Thorhaug, A., Poulos, H. M., López-Portillo, J., Barr, J., Lara-Domínguez, A. L., Ku, T. C., et al. (2019). Gulf of Mexico estuarine blue carbon stock, extent and flux: mangroves, marshes, and seagrasses: a North American hotspot. *Sci. Total Environ.* 653, 1253–1261. doi: 10.1016/j.scitotenv.2018.10.011

Turner, R., and Rabalais, N. (2013). Nitrogen and phosphorus phytoplankton growth limitation in the northern Gulf of Mexico. *Aquat. Microb. Ecol.* 68, 159–169. doi: 10.3354/ame01607

Turner, R. E., Qureshi, N., Rabalais, N. N., Dortch, Q., Justic, D., Shaw, R. F., et al. (1998). Fluctuating silicate:nitrate ratios and coastal plankton food webs. *Proc. Natl. Acad. Sci. U.S.A.* 95, 13048–13051.

Turner, R. E., Rabalais, N. N., and Justi, D. (2017). Trends in summer bottom-water temperatures on the northern Gulf of Mexico continental shelf from 1985 to 2015. *PLoS One* 12:e0184350. doi: 10.1371/journal.pone.0184350

Tyrrell, T., and Young, J. R. (2009). "Coccolithophores," in *Encyclopedia of Ocean Sciences*, ed. J. H. Steele (Amsterdam: Elsevier), 606–614. doi: 10.1016/B978-012374473-9.00662-7

Wang, Z. A., Lawson, G. L., Pilskaln, C. H., and Maas, A. E. (2017). Seasonal controls of aragonite saturation states in the Gulf ofMaine. *J. Geophys. Res. Oceans* 122, 372–389. doi: 10.1002/2016JC011778

Wanninkhof, R., Barbero, L., Byrne, R., Cai, W.-J., Huang, W.-J., Zhang, J.-Z., et al. (2015). Ocean acidification along the Gulf Coast and East Coast of the USA. *Cont. Shelf Res.* 98, 54–71.

Wolf-Gladrow, D. A., Zeebe, R. E., Klaas, C., Körtzinger, A., and Dickson, A. G. (2007). Total alkalinity: the explicit conservative expression and its application to biogeochemical processes. *Mar. Chem.* 106, 287–300.

Xiong, T., Liu, P., Zhai, W., Bai, Y., Liu, D., Qi, D., et al. (2019). Export flux, biogeochemical effects, and the fate of a terrestrial carbonate system: from Changjiang (Yangtze River) estuary to the East China Sea. *Earth Space Sci.* 6, 2115–2141. doi: 10.1029/2019EA000679

Xue, J., Cai, W. J., Hu, X., Huang, W. J., Lohrenz, S. E., and Gundersen, K. (2015). Temporal variation and stoichiometric ratios of organic matter remineralization in bottom waters of the northern Gulf of Mexico during late spring and summer. *J. Geophys. Res. Oceans* 120, 8304–8326. doi: 10.1002/2015JC011453

Xue, L., and Cai, W. J. (2020). Total alkalinity minus dissolved inorganic carbon as a proxy for deciphering ocean acidification mechanisms. *Mar. Chem.* 222:103791. doi: 10.1016/j.marchem.2020.103791

Xue, L., Cai, W.-J., Sutton, A. J., and Sabine, C. (2017). Sea surface aragonite saturation state variations and control mechanisms at the Gray's Reef time-series site off Georgia, USA (2006-2007). *Mar. Chem.* 195, 27–40. doi: 10.1016/j.marchem.2017.05.009

Xue, Z., He, R., Fennel, K., Cai, W. J., Lohrenz, S., and Hopkinson, C. (2013). Modeling ocean circulation and biogeochemical variability in the Gulf of Mexico. *Biogeosciences* 10, 7219–7234. doi: 10.5194/bg-10-7219-2013

Xue, Z., He, R., Fennel, K., Cai, W.-J., Lohrenz, S., Huang, W.-J., et al. (2016). Modeling pCO_2 variability in the Gulf of Mexico. *Biogeosciences* 13, 4359–4377. doi: 10.5194/bg-13-4359-2016

Yang, B., Byrne, R. H., and Lindemuth, M. (2015). Contributions of organic alkalinity to total alkalinity in coastal waters: a spectrophotometric approach. *Mar. Chem.* 176, 199–207. doi: 10.1016/j.marchem.2015.09.008

Zeebe, R. E., and Wolf-Gladrow, D. A. (2001). *CO_2 in Seawater: Equilibrium, Kinetics, Isotopes*. Elsevier Oceanography Book Series 65, Amsterdam: Elsevier, 346.

Zhang, X., Hetland, R. D., Marta-Almeida, M., and DiMarco, S. F. (2012). A numerical investigation of the Mississippi and Atchafalaya freshwater transport, filling and flushing times on the Texas-Louisiana Shelf. *J. Geophys. Res. Oceans* 117:C11009. doi: 10.1029/2012jc008108

Zhang, Z., and Hetland, R. (2012). A numerical study on convergence of alongshore flows over the Texas-Louisiana shelf. *J. Geophys. Res. Oceans* 117:C11010. doi: 10.1029/2012jc008145

Conflict of Interest: The authors declare that the research was conducted in the absence of any commercial or financial relationships that could be construed as a potential conflict of interest.

The handling editor declared a past collaboration with one of the authors W-JC

Copyright © 2021 Huang, Cai and Hu. This is an open-access article distributed under the terms of the Creative Commons Attribution License (CC BY). The use, distribution or reproduction in other forums is permitted, provided the original author(s) and the copyright owner(s) are credited and that the original publication in this journal is cited, in accordance with accepted academic practice. No use, distribution or reproduction is permitted which does not comply with these terms.

frontiers in Marine Science

ORIGINAL RESEARCH
published: 24 April 2020
doi: 10.3389/fmars.2020.00252

Summertime Oxygen Depletion and Acidification in Bohai Sea, China

Guisheng Song[1,2], Liang Zhao[3], Fei Chai[2], Fangfang Liu[1], Mengting Li[1] and Huixiang Xie[4]**

[1] School of Marine Science and Technology, Tianjin University, Tianjin, China, [2] State Key Laboratory of Satellite Ocean Environment Dynamics, Second Institute of Oceanography, Ministry of Natural Resources, Hangzhou, China, [3] College of Marine and Environmental Sciences, Tianjin University of Science and Technology, Tianjin, China, [4] Institut des Sciences de la mer de Rimouski, Université du Québec à Rimouski, Rimouski, QC, Canada

Increasing attention has recently been drawn to oxygen depletion and ocean acidification in coastal seas and their impacts on the marine ecosystem. Intensive organic matter degradation combined with weak water exchange is considered to be mainly responsible for bottom water oxygen depletion and acidification. Hypoxia and acidification in the bottom water of Bohai Sea have been frequently observed in summer seasons over the past decade. In this study, monthly surveys were conducted along an inshore-offshore transect in the north Bohai Sea from May to August in 2017 and 2018. The physical structure of the water column in the study area was characterized by a well-mixed surface layer and an essentially homogeneous deep layer that were separated by a strong pycnocline over the period from mid-Jun to late August in both years. Dissolved oxygen (DO), pH, and dissolved inorganic carbon (DIC) in the water column were also split into two layers by the pycnocline and varied little in each layer. No significant interannual variations were observed for the temporal progressions of DO, pH and DIC in the bottom water. Average DO concentration and pH in the bottom water linearly decreased with time from May to August while DIC presented an opposite trend. DO became increasingly unsaturated from mid-June to late August when DO decreased to 96 μmol L^{-1} and pH to 7.74. The molar ratio of net oxygen consumption to DIC production was 1.42, similar to the Redfield ratio (1.30). Pelagic respiration (>60%) linked to degradation of fresh organic matter prevailed over sediment respiration (<40%) in contributing to the oxygen depletion and acidification observed in this shallow water body. The duration and intensity of oxygen depletion and acidification in the study area were strongly affected by stormy weather events such as typhoons.

Keywords: oxygen depletion, acidification, dissolved inorganic carbon, organic matter degradation, typhoon, Bohai Sea

OPEN ACCESS

Edited by:
Xianghui Guo,
Xiamen University, China

Reviewed by:
Yuanyuan Xu,
University of Miami, United States
Guoxiang Wu,
Ocean University of China, China

****Correspondence:***
Guisheng Song
guisheng.song@tju.edu.cn
Huixiang Xie
huixiang_xie@uqar.ca

Specialty section:
This article was submitted to Coastal Ocean Processes, a section of the journal Frontiers in Marine Science

Received: *26 February 2020*
Accepted: *30 March 2020*
Published: *24 April 2020*

Citation:
Song G, Zhao L, Chai F, Liu F, Li M and Xie H (2020) Summertime Oxygen Depletion and Acidification in Bohai Sea, China. Front. Mar. Sci. 7:252. doi: 10.3389/fmars.2020.00252

INTRODUCTION

Water masses undergoing oxygen depletion and acidification are expanding globally in both open oceans and coastal seas (Matear and Hirst, 2003; Carstensen et al., 2014). Oxygen depletion and ocean acidification can reduce the ocean's biodiversity (Rabalais et al., 2002; Fabricius et al., 2011) and influence the abundance and activity of bacteria (Galán et al., 2009; Galgani et al., 2014). Prolonged exposure to low oxygen conditions may change the population and community structure

of zooplankton (Keister et al., 2000) and benthic organisms (Vaquer-Sunyer and Duarte, 2008). Ocean acidification can also inhibit the activity of calcifying organisms (Orr et al., 2005; Hoegh-Guldberg et al., 2007) and hence decrease the downward flux of $CaCO_3$ to the deep ocean (Feng et al., 2008). Consequently, oxygen depletion and ocean acidification have potentially important impacts on the structure and function of the marine ecosystem (Diaz and Rosenberg, 2008), the ocean's fisheries industry (Rabalais et al., 2002; Rheuban et al., 2018), and the dynamics of organic and inorganic matter (Galgani et al., 2014).

Oxygen depletion and concomitant acidification in the bottom water of coastal seas stem from a combination of strengthened bacterial respiration and restricted water exchange (Diaz, 2001; Wallace et al., 2014). The increase in bacterial respiration is often linked to eutrophication which enhances primary production (Smodlaka, 1986) and therefore downward particulate organic matter transport to the bottom water and sediments. The relative contributions of pelagic and sedimentary respiration of organic matter to the water column oxygen consumption vary substantially among different hypoxic waters, depending to a large extent on the depth of the water column and the topography of the seabed (Hetland and DiMarco, 2008; Murrell and Lehrter, 2011; Bourgault et al., 2012). Similarly, the relative contributions of fresh, autochthonous organic matter and old, allochthonous organic matter to the water column oxygen consumption differ considerably as well from one hypoxic system to another, depending in part on the quantity and lability of the allochthonous organic matter (Rabalais et al., 2002; Wang et al., 2017; Su et al., 2017, 2020). In addition to organic matter input, stormy weather conditions, such as typhoons and hurricanes, can also strongly impact the duration and intensity of oxygen depletion and acidification in coastal bottom waters, given that these events can dramatically alter the physical stability of the water column and redistribute nutrients therein (McCarthy et al., 2013; Ni et al., 2016; Su et al., 2017).

Located in the northeast China, the Bohai Sea is a semi-closed coastal sea that is connected to the Yellow Sea to the east via the Bohai Channel (**Figure 1**). Eutrophication in the Bohai Sea has been deteriorating in the past 30 years due to industrialization and urbanization along its coast (Zhang et al., 2012; Yu et al., 2013) combined with its limited water exchange with the outside. Increasing eutrophication and strong water column stratification in summer have led to decreasing summertime dissolved oxygen (DO) concentration in the bottom water of the Bohai Sea in the past decades (Zu et al., 2005; Ning et al., 2010). Zhai et al. (2012) first reported the occurrence of significant oxygen depletion and acidification in the nearshore bottom water of the northeastern and northern Bohai Sea, with pH and DO decreasing by 0.29 and 170 $\mu mol\ kg^{-1}$, respectively, from June to August. Later studies demonstrated that summertime oxygen depletion in the Bohai Sea shows a two-core feature corresponding to the two cold cores located in the bottom water of the western and northern Bohai Sea (Zhao et al., 2017; Wei et al., 2019). Currently, little is known about the duration, intensity, and interannual variability of the summertime oxygen depletion and acidification in the Bohai Sea. Moreover, the source (pelagic vs. sedimentary) and nature (fresh vs. old) of the organic matter dominating oxygen consumption in the bottom water of the Bohai Sea remain unclear, though organic matter degradation has been considered to be responsible for the observed oxygen depletion and acidification there (Zhai et al., 2012; Zhao et al., 2017; Wei et al., 2019). In this study, we investigated the temporal evolution of DO, pH, and dissolved inorganic carbon (DIC) in the bottom water on the west coast of the Bohai Sea over two summer seasons to assess the rates of oxygen consumption and acidification and the pelagic vs. sedimentary contribution to the observed oxygen depletion and acidification. We also assessed the impact of Typhoon Rumbia, which passed over the Bohai Sea during late summer of 2018, on bottom water oxygen depletion and acidification in the study area.

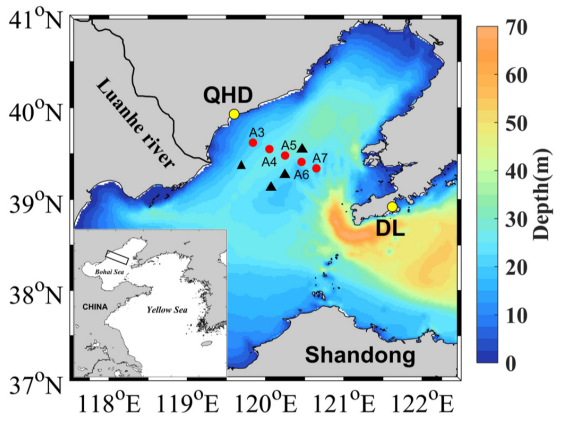


FIGURE 1 | Map of sampling stations. See **Table 1** for the coordinates of the sampling stations and other sampling information. Red points denote stations sampled in 2017 and 2018 and the black triangles represent stations visited in June and August 2011 by Zhai et al. (2012) (see section Oxygen Depletion and Acidification in the Bottom Layer). QHD and DL denote Qinhuangdao City and Dalian City, respectively.

SAMPLE COLLECTION AND ANALYSIS

DO, pH, and DIC were investigated during the summers of 2017 and 2018 along an inshore-offshore transect across the known oxygen depletion area with four cruises being conducted each year (**Figure 1** and **Table 1**). The transect, located off

TABLE 1 | Coordinates, water depth, and sampling dates.

Station	Lat. (°N)	Long. (°E)	Water depth (m)	Sampling dates (YD)	
				2017	2018
A3	39.618	119.840	21	178, 203, 234	162, 200, 220, 237
A4	39.548	120.046	25	144, 178, 203, 234	162, 200, 220, 237
A5	39.478	120.252	27	144, 178, 203, 234	162, 200, 220, 237
A6	39.408	120.458	23	144, 178, 203, 234	162, 200, 220, 237
A7	39.377	120.551	23	NA	162, 200, 220, 237

YD, day of the year; NA, samples were not collected.

Qinhuangdao City, crossed the southwest of the bowl-shaped depression extending from northeast to southwest (**Figure 1**; Zhou et al., 2017). In summer, cyclonic circulation is dominant in this area, and horizontal transport in bottom water is weak, with the current velocity <30 cm s^{-1} (Zhou et al., 2017). Water samples were collected from 4 to 6 depths using a 5 L Niskin bottle and vertical profiles of temperature and salinity were simultaneously acquired using a RBR maestro multi-parameter. Upon on the deck, water in the Niskin bottle was immediately transferred into 100-mL brown glass bottles, 60-mL transparent glass bottles, and 250-mL polypropylene bottles for DO, DIC, and pH measurements, respectively. Sample transfer, storage, and analysis for DO followed the Winkler method (Grasshoff et al., 1999). An auto-titrator (Brand: Mettler Toledo, model: G10S) was used for DO analysis, and the relative standard deviation for all triplicate samples was <2%. pH and DIC samples were also transferred without air contamination by sufficient overflowing. pH samples were stored in the dark at room temperature (∼22°C) and DIC in dark at 4°C. Saturated $HgCl_2$ solution (250 μL) was added into the DIC samples to prevent biological activities during storage. pH was measured on board right after the sample was warmed to lab temperature (22 ± 0.5°C), using a bench pH meter (Brand: Mettler Toledo; Model: S210) equipped with an Inlab® Expert Pro pH probe. Before use, the pH meter was calibrated with three NIST (NBS) buffers at pH 4.00, 7.01, and 9.24 (22°C) purchased from Mettler Toledo. The pH values of the buffers at 22°C were linearly interpolated from their corresponding certified pH values at 20 and 25°C. Then a Tris buffer, provided by A. G. Dickson's lab at Scripps Institution of Oceanography, was used to convert the NBS scale (pH_{NBS}) to the total hydrogen ion concentration scale (i.e., pH_T). The measured pH_{NBS} of the Tris buffer was 0.12 ± 0.01 (n = 24) higher than its pH_T value at 22°C which was converted from the certified pH_T value at 25°C using the excel conversion file provided by A. G. Dickson's lab. The difference between pH_{NBS} and pH_T obtained here was comparable with those reported previously (Zhai et al., 2012; Cai et al., 2017). For each sample, at least three pH_{NBS} values, along with temperature, were recorded. If the differences among the three values were less than 0.01, their average was taken as the measured pH_{NBS} of this sample. The pH_T values of the samples at the measured temperatures were retrieved by subtracting 0.12 from the pH_{NBS} values and then corrected to the *in situ* temperatures and pressures using the CO2Sys software (Pierrot et al., 2006). The uncertainty of pH measurement was estimated to be 0.005 ± 0.008 pH units based on 360 sets of triplicate measurements. DIC concentrations for all duplicate subsamples were measured in triplicate injections using a Shimadzu TOC-Lcph analyzer in a land-based lab, with the coefficient of variation <2%. The analyzer was daily calibrated with a certified DIC reference standard (batch# 174, provided by A. G. Dickson's lab) with a mean concentration of 2050.84 ± 0.66 μmol kg^{-1} or 2099.14 ± 0.68 μmol L^{-1} at the temperature of calibration and sample analysis (20°C). The relative standard deviation was 0.75% based on five triplicate analyses of the DIC reference standard. The unit of DIC concentrations were expressed in μmol L^{-1}.

After the collection of the water samples, current velocity at station A5 was continuously recorded for 47 h with a Nortek Acoustic Doppler Velocimetry (ADV) from 22:00 of day of year 220 (YD 220) in 2018. The downward-looking ADV sampling volume was set up at ∼0.3 m above the bottom, with a sampling rate of 32 Hz. Continuous temperature, salinity and DO concentration in this layer were determined by the RBR maestro multi-parameter. The mean downward oxygen flux through the bottom boundary layer (i.e., oxygen consumption by sedimentary organic matter, F_{BBL}) at the interval of 0.5 h was calculated using Equation (1) (Wang et al., 2016):

$$F_{BBL} = \frac{0.1DC_{BBL}2^{T/T_m}}{3.7L_{Br}^{\#}} \quad (1)$$

where D is the oxygen diffusion coefficient (m^2 s^{-1}), C_{BBL} is the DO concentration in the bottom boundary layer (μmol L^{-1}), T denotes the temperature in the bottom boundary layer and T_m the mean temperature of the dataset during the continuous measurement. $L_{Br}^{\#}$ could be calculated based on the measured current velocity according to Wang et al. (2013). The oxygen diffusion coefficient (D) was obtained based on the bottom water temperature and salinity (Ramsing and Gundersen, 1994). Both C_{BBL} and T were measured by the RBR maestro multi-parameter (see above).

Meanwhile, the turbulent kinetic energy (TKE) dissipation rate (ε) was hourly scanned using a vertical microstructure profiler (VMP-200) manufactured by Rockland Scientific International (RSI). The VMP was equipped with two high-frequency shear probes with a sampling frequency of 512 Hz. The TKE dissipation rate ε was estimated by fitting the empirical Nasmyth spectrum to the measured shear spectra with the calculation methods have been clearly depicted before (Gregg, 1999; Wolk et al., 2002; Xu et al., 2020). Hourly DO vertical profiles at this station were synchronously determined by another RBR maestro multi-parameter. The oxygen sensors used above were corrected with the corresponding titrated DO concentrations during sampling on YD 220(2018). The eddy diffusivity K_ρ (m^2 s^{-1}) was estimated using the formula (Osborn, 1980):

$$K_\rho = \Gamma \frac{\varepsilon}{N^2} \quad (2)$$

where Γ (unitless) is the mixing efficiency and is assigned to be a constant of 0.2 (Osborn, 1980), ε the TKE dissipation rate (W kg^{-1}), and N^2 the squared buoyancy frequency (s^{-2}). N^2 was calculated based on the density profile according to Jackett and McDougall (1995). Then the vertical turbulent oxygen diffusion flux through the pycnocline (F_p, mmol m^{-2} s^{-1}) was estimated using Equation (3) (Rippeth et al., 2009):

$$F_p = K_\rho \left(\frac{\triangle DO}{\triangle z} \right) \quad (3)$$

where Δz stands for the thickness of the pycnocline and ΔDO for the difference in DO concentration between the upper and lower boundary of the pycnocline. ΔDO/Δz thus denotes the vertical gradient of DO across the pycnocline.

RESULTS AND DISCUSSION

Physical and Biological Settings

The water depth along the transect ranged from 21 to 27 m, with the maximum occurring at station A5 (**Table 1**). The depth ranges of the pycnoclines, where N^2 exceeded 0.001 s^{-2}, at the sampling stations are shown in **Table 2**. Note that the pycnocline was undetectable, per the criterium of $N^2 > 0.001$ s^{-2}, across the entire transect on YD 144 (24 May) in 2017 and at station A3 on YD 237 (25 August) in 2018, though weak stratification was visually noticeable on both occasions based on the vertical profiles of water temperature, salinity, and density (**Figure 2**). The absence of a fully developed pycnocline on YD 144(2017) was due to the relatively low surface water temperature (14.5–16.2°C) preventing the formation of a strong stratification. The passage of Typhoon Rumbia over the Bohai Sea on YD 231-232(2018), which created intensive turbulence, was mainly responsible for the weak stratification on YD 237(2018). Owning to the abrupt heavy wind just within 15 h before sampling on YD 203(2017), the depths of the pycnocline were much deeper than that during other cruises (**Figure 2** and **Table 2**). During the other cruises, the water column was separated into a well-mixed surface layer ("surface layer" hereafter) and a nearly homogenous deep layer ("bottom layer" hereafter) by a strong thermocline or pycnocline (**Figure 2** and **Supplementary Figures S1, S2**). In each layer, the water temperature and salinity (and thus density) varied little. Despite the lack of a quantifiable pycnocline, a bottom layer with depth > 16 m was assigned to YD 144(2017) based on the visually observable decrease in temperature and increase in density at the middle of the water column (14–16 m) (**Figure 2**). The vertical profile of temperature almost mirrored that of density, indicating that temperature was the dominant factor controlling the distribution of density. In contrast, the halocline was much weaker and the bottom-surface difference in salinity

TABLE 2 | Depth range of the pycnocline based on the buoyance frequency (N^2).

Sampling date	Range of pycnocline (m)				
	A3	A4	A5	A6	A7
			2017		
YD 144[b]	NA[a]	–	–	–	NA
YD 178	6–9	7–9	7–10	5–8	NA
YD 203	13–17	11–17	12–18	13–15	NA
YD 234	12–14	11–13	12–14	9–10	NA
			2018		
YD 162	7–10	12–14	12–15	12–13	7–11
YD 200	8–9	8–10	8–9	7–9	8–9
YD 220	11–13	12–16	10–14	9–11	8–13
YD 237[b]	–	20–21	15–18	9–11	7–9

[a]*Station A3 on YD 144(2017) and station A7 in 2017 were not visited (see **Table 1**).*
[b]*No significant pycnoclines detected at stations A4–A6 on YD 144(2017), and at station A3 on YD 237(2018), based on the N^2 values.*

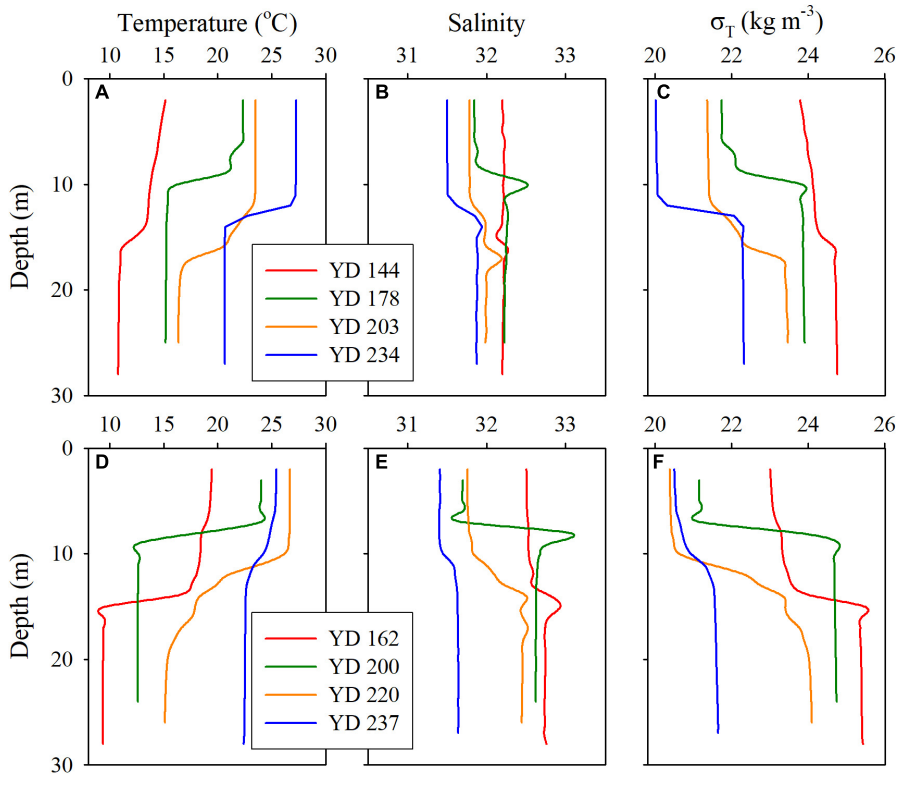


FIGURE 2 | Vertical profiles of temperature **(A,D)**, salinity **(B,E)**, and density **(C,F)** for each cruise at station A5 in 2017 (upper panels) and 2018 (lower panels).

was mostly <0.87 across the entire transect. The lower-than-expected surface salinity on YD 200(2018) was due to the heavy precipitation in July. Water temperature generally increased with time in the whole water column. Yet surface water temperature along the entire transect on YD 237(2018) was 1.60 ± 0.94°C lower than that on YD 220(2018) due to the strong water column mixing by Typhoon Rumbia. Salinity slightly decreased from May to August in both years but the decrease was larger in 2018 because of a relatively heavier precipitation in 2018. As expected from the temporal trends of temperature and salinity, density gradually decreased from May to August in both years.

Vertical Profiles of DO, pH_T, and DIC

The vertical profiles of DO, pH_T, and DIC displayed a double-layer feature similar to that of density, i.e., homogeneous or weak gradients in the surface and bottom layers and rapid changes within the pycnoclines (**Figures 3**). DO and pH_T in the surface layer were higher than in the bottom layer while DIC exhibited an inverse pattern. The temporal variations in pH_T, DO, and DIC in the surface layer were generally less regular and smaller than those in the bottom layer. These phenomena can be attributed to more complex processes in controlling the dynamics of pH_T, DO, and DIC in the surface layer (e.g., air-sea exchange, photosynthesis, respiration) than those in the bottom layer (mainly respiration only). In 2017, pH_T and DO decreased while DIC increased progressively in the bottom layer from late May (YD 144) to late August (YD 234) (**Figures 3A–C**). In 2018, a similar temporal trend was seen in the bottom layer from mid-June (YD 162) to early August (YD 220) but this trend was sharply reversed in late August (YD 237) (**Figures 3D–F**) as a result of the disruption of the stable vertical structure of the water column by Typhoon Rumbia (**Figure 2F**).

Oxygen Depletion and Acidification in the Bottom Layer

Since the water mass was essentially homogenous beneath the pycnocline (**Supplementary Figures S1, S2**), the average values of DO, pH_T, and DIC in bottom water (see section Physical and Biological Settings) along the entire transect were calculated for discussion. For each sampling year, DO, pH_T, and DIC changed linearly with YD (**Table 3**). Student's *t*-test did not show significant interannual variations for the progressions of DO, pH_T and DIC over the sampling periods ($p > 0.45$). The daily decreasing rates of DO and pH_T obtained from the present study, i.e., the regressed slopes in **Table 3**, were also comparable with those in summer 2011 (DO: 2.13 ± 0.14 μmol L^{-1} d^{-1}; pH_T: 0.0038 ± 0.0006 d^{-1}) observed near our sampling transect (Zhai et al., 2012; **Figure 1**). These results demonstrate little interannual

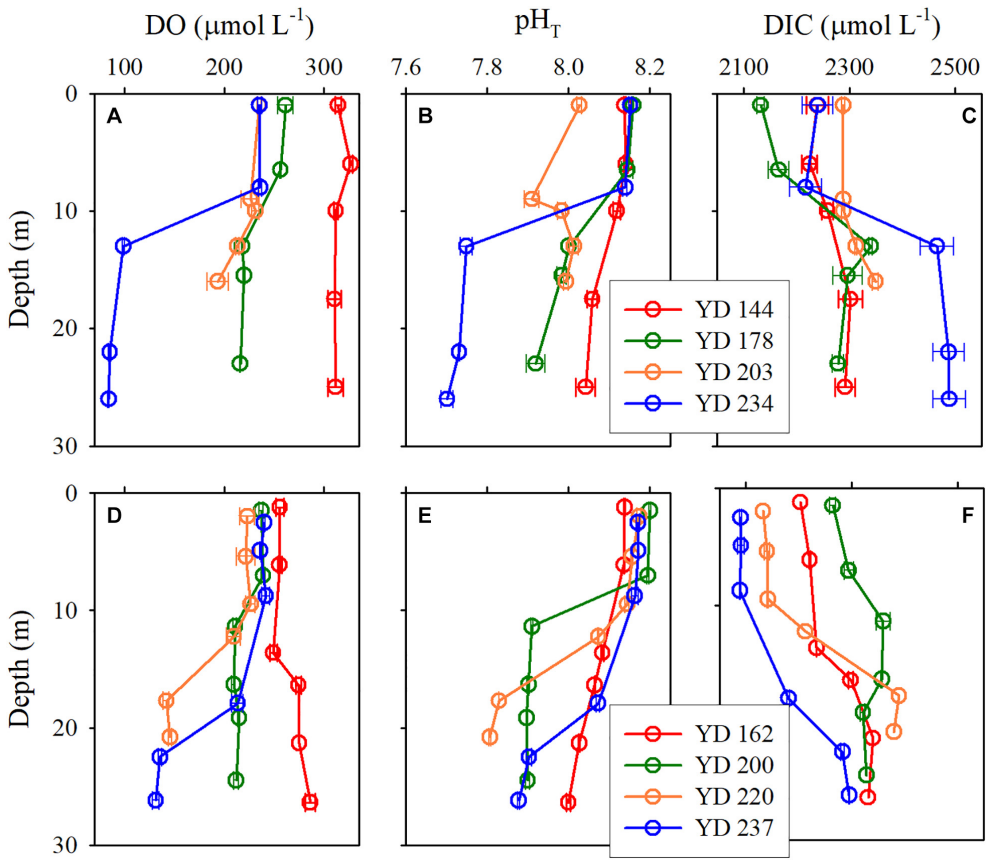


FIGURE 3 | Vertical profiles of DO **(A,D)**, pHT **(B,E)**, and DIC **(C,F)** for each cruise at station A5 in 2017 (upper panels) and 2018 (lower panels).

variations in the rates of oxygen consumption and the associated acidification in the bottom water of the study area from 2011 to 2018. For the above comparison, the pH_T at 25°C (pH_{25}) reported by Zhai et al. (2012) was converted to *in situ* temperature pH_T using the method presented in section Sample Collection and Analysis. In addition, DO concentration was also converted from the units of μmol kg^{-1} to μmol L^{-1} using the samples' potential densities. Owing to lack of interannual variability, we combined our 2-year data to simplify discussion. The composite data lead to a net oxygen consumption rate of 2.18 μmol L^{-1} d^{-1}, a net DIC production rate of 1.54 μmol L^{-1} d^{-1}, and an acidification rate of 0.0037 pH d^{-1} (**Figure 4** and **Table 4**). The oxygen consumption rate was similar to that in the North Sea–Baltic Sea transition zone (0.28–2.8 μmol L^{-1} d^{-1}) (Hansen and Bendtsen, 2014), but lower than that in the northern Gulf of Mexico (3.8–106 μmol L^{-1} d^{-1}) (Murrell and Lehrter, 2011; McCarthy et al., 2013). The ratio of the oxygen depletion rate to the acidification rate is 589 μmol L^{-1} pH^{-1}, comparable to the modeled ratio (588 μmol kg^{-1} pH^{-1}) for the northern Gulf of Mexico and the East China Sea with present atmospheric CO_2 level (Cai et al., 2011).

Based on the regression of DO saturation degree against YD (**Figure 5** and **Table 4**), DO in the bottom water switched from oversaturation to undersaturation on YD 164 (June 13), decreasing gradually from 264.7 ± 38.4 μmol L^{-1} to 90.3 ± 8.1 μmol L^{-1}, or by 66% ± 17% over a period of ∼80 days from YD 164. Simultaneously, pH_T progressively decreased from 8.03 ± 0.06 to 7.74 ± 0.07, or by 0.29 ± 0.09. The extent of oxygen depletion in our study area is comparable to those in the Gulf of St. Lawrence (Bourgault et al., 2012) and the Pearl River estuary (Qian et al., 2018) but substantially lower than those in the Chesapeake Bay (Cai et al., 2017), the northern Gulf of Mexico (Cai et al., 2011), and the Yangtze River estuary (Ni et al., 2016; Wang et al., 2017) which all experience severe summertime hypoxia (DO < 32 μmol L^{-1}). The pH in bottom water in the Bohai Sea in August is lower than that in the bottom water of the neighboring north Yellow Sea (7.88 ± 0.06) (Zhai et al., 2014), but higher than those in the northern Gulf of Mexico and the Chesapeake Bay, where pH in bottom water is <7.6 (Cai et al., 2011, 2017). Furthermore, the acidification degree (i.e., ΔpH) in the bottom water of the Bohai Sea is moderate relative to those in the north Yellow Sea (0.14 ± 0.07) (Zhai et al., 2014), the northern Gulf of Mexico (0.3–0.4) (Cai et al., 2011), and the Chesapeake Bay (∼0.4) (Cai et al., 2017).

TABLE 3 | Results of linear regression of the mean DO, pH_T, and DIC in bottom water against day of the year (YD) performed separately for 2017 and 2018.

Parameter	Function	R^2	*p*
	2017		
DO	Y = (-2.25 ± 0.20)X + (631.5 ± 38.7)	0.984	<0.01
pH_T	Y = (-0.0037 ± 0.0006)X + (8.63 ± 0.12)	0.944	0.03
DIC	Y = (1.60 ± 0.37)X + (2051.9 ± 64.8)	0.919	0.04
	2018		
DO	Y = (-2.03 ± 0.14)X + (601.7 ± 27.0)	0.995	0.02
pH_T	Y = (-0.0039 ± 0.0001)X + (8.67 ± 0.01)	0.999	<0.01
DIC	Y = (1.41 ± 0.40)X + (2079.5 ± 78.5)	0.925	0.18

YD 237(2018) was excluded due to the influence of Typhoon Rumbia.

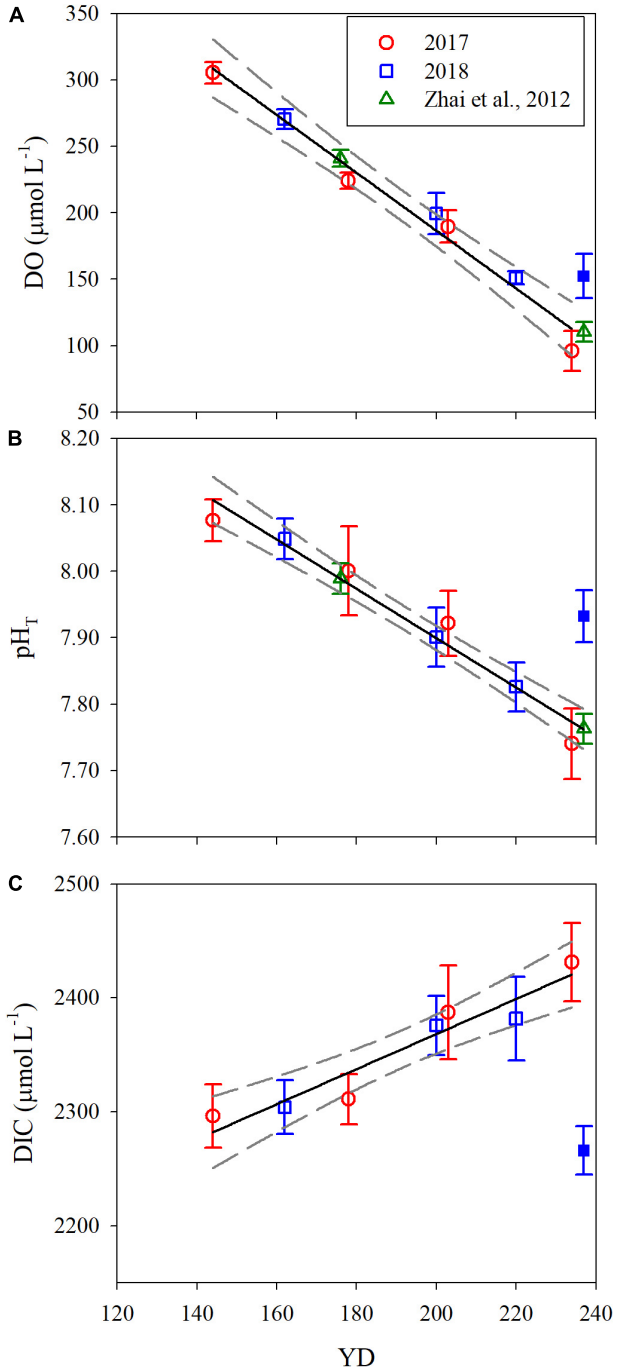


FIGURE 4 | Temporal evolution of the mean DO **(A)**, pH_T **(B)**, and DIC **(C)** in bottom water along the sampling transect. YD stands for day of the year. Error bars are 1 standard deviation. The solid and dashed lines are the linear fit to the data and 95% confidence interval, respectively. The solid blue points on YD 237 were excluded for data fitting.

TABLE 4 | Results of linear regression of the mean values of DO, pH_T, and DIC in bottom water against day of the year (YD) based on the composite data of 2017 and 2018.

Parameter	Function	R^2	*p*
DO	Y = (-2.18 ± 0.15)X + (622.2 ± 29.5)	0.976	<0.0001
pH_T	Y = (-0.0037 ± 0.0002)X + (8.64 ± 0.05)	0.965	<0.0001
DIC	Y = (1.54 ± 0.22)X + (2060.4 ± 42.3)	0.909	<0.001

YD 237(2018) was excluded due to the influence of Typhoon Rumbia.

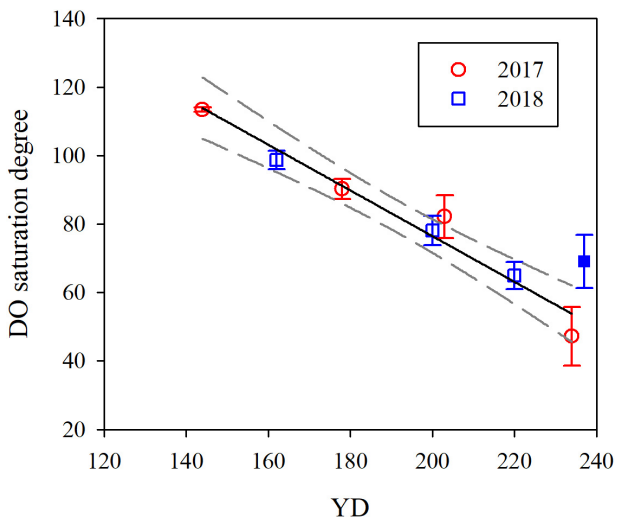


FIGURE 5 | Temporal evolution of the mean DO saturation degree in bottom water. YD stands for day of the year. Error bars are 1 standard deviation. The solid and dashed lines are the linear fit to the data and 95% confidence interval, respectively. The solid blue point was excluded for data fitting. The regressed equation is: Y = (-0.67 ± 0.06) X + (210.0 ± 12.0), R^2 = 0.96, p = 0.001.

Note that the data for YD 237(2018) was not included for the regression analysis shown in **Figure 4** and **Table 4** due to the influence of Typhoon Rumbia. The passage of the typhoon over the sampling area on YD 231-232(2018) greatly weakened the pycnocline, leading to enhanced vertical mixing of DO and DIC. Horizontal exchange with adjacent waters richer in DO but poorer in DIC might also be increased due to the elevated turbulence. Consequently, DO and pH_T in bottom water on YD 237(2018) were 46.7 μmol L^{-1} and 0.17 higher and DIC was 159.5 μmol L^{-1} lower than expected from the fit to the data excluding YD 237(2018) (**Figure 4** and **Table 4**). This result also indicates that the typhoon effect persisted at least to the end of our sampling campaign, ∼5 days after the typhoon event. Previous studies have demonstrated that typhoons could terminate bottom water oxygen depletion in the estuaries of the Yangtze River and Pearl River (Ni et al., 2016; Su et al., 2017). However, phytoplankton blooms often ensue following stormy weather events due to large supplies of nutrients to surface water via enhanced vertical mixing and freshwater discharge, leading to a renewed and even exacerbated bottom water oxygen depletion and acidification (McCarthy et al., 2013; Su et al., 2017; Wang et al., 2017). In the Bohai Sea, bottom water oxygen depletion and acidification could disappear in early- or mid-September due to weakened water column stratification by stronger wind mixing (Huang et al., 1999; Xu et al., 2020). Hence, stormy weather events in late summer are not expected to allow the water column to fully re-establish stratification before seasonal surface water cooling sets in, thereby reducing both the intensity and duration of the bottom water oxygen depletion and acidification.

Pelagic vs. Sediment Oxygen Consumption

The oxygen diffusion flux through the pycnocline (i.e., the diapycnal diffusion flux) derived from Equation (3) for station A5 on YD 220–222(2018) ranged from 0 to 0.93 mmol m^{-2} d^{-1} and averaged 0.19 ± 0.21 mmol m^{-2} d^{-1} (**Figure 6A**). The concurrently determined oxygen flux at the water-sediment boundary layer, i.e., the sediment oxygen consumption rate, ranged from 0.27 to 10.26 mmol m^{-2} d^{-1} and averaged 6.32 ± 2.44 mmol m^{-2} d^{-1} (**Figure 6B**), which is comparable to that in the Oregen continental shelf (3.2–9.8 mmol m^{-2} d^{-1}) (Reimers et al., 2012), and lower than those in the northern Gulf of Mexico (1.3–26.0 mmol m^{-2} d^{-1}) (Murrell and Lehrter, 2011; McCarthy et al., 2013) and the Yangtze River estuary (9.1–62.5 mmol m^{-2} d^{-1}) (Zhang et al., 2017). At station A5, the net oxygen consumption rate in the bottom layer derived from regressing DO against time was 2.34 ± 0.34 μmol L^{-1} d^{-1}, translating into a depth-integrated net oxygen consumption rate of 30.42 ± 4.42 mmol m^{-2} d^{-1} on YD 220(2018) when the bottom layer was 13 m thick (**Tables 1**, **2**). The diapycnal diffusion flux was thus negligible (<1%) compared to the net oxygen consumption rate in the bottom layer and can be ignored for the discussion below. The sediment oxygen consumption contributed 21% to the net oxygen consumption in the overlying bottom water. If assuming negligible monthly variations in the current velocity in the bottom water, the sediment oxygen consumption rate at station A5 during each cruise was estimated using the bottom-most DO concentration, temperature and salinity (**Table 5**). The results suggest the sediment oxygen consumption rate generally decreases with time, with its contribution to the net oxygen consumption in bottom water ranged from 13.4 to 42.1%. Before sampling, very heavy wind occurred over night on YD 202-203(2017), which induced the pycnocline deeper (**Figure 2** and **Table 2**). So the depth-integrated net oxygen consumption rate on YD 203(2017) was much smaller, and consequently the sedimentary contribution was highest. The sedimentary contribution on YD 237(2018) was about three times of that on YD 234(2017), due to the influence of Typhoon Rumbia. The results demonstrated the dominant role of pelagic respiration in generating the observed oxygen depletion in the bottom layer. This argument is also supported by most DO vertical profiles showing little change in DO concentration toward the seafloor (**Figure 3**).

The molar ratio of oxygen consumption to DIC production in the bottom water (O_2/DIC hereafter) was calculated to be 1.42 ± 0.22 based on the slopes of the fitted DO vs. YD and DIC vs. YD equations (**Table 4**). This ratio is statistically indifferent from the Redfield ratio (1.30), suggesting that microbial oxidation

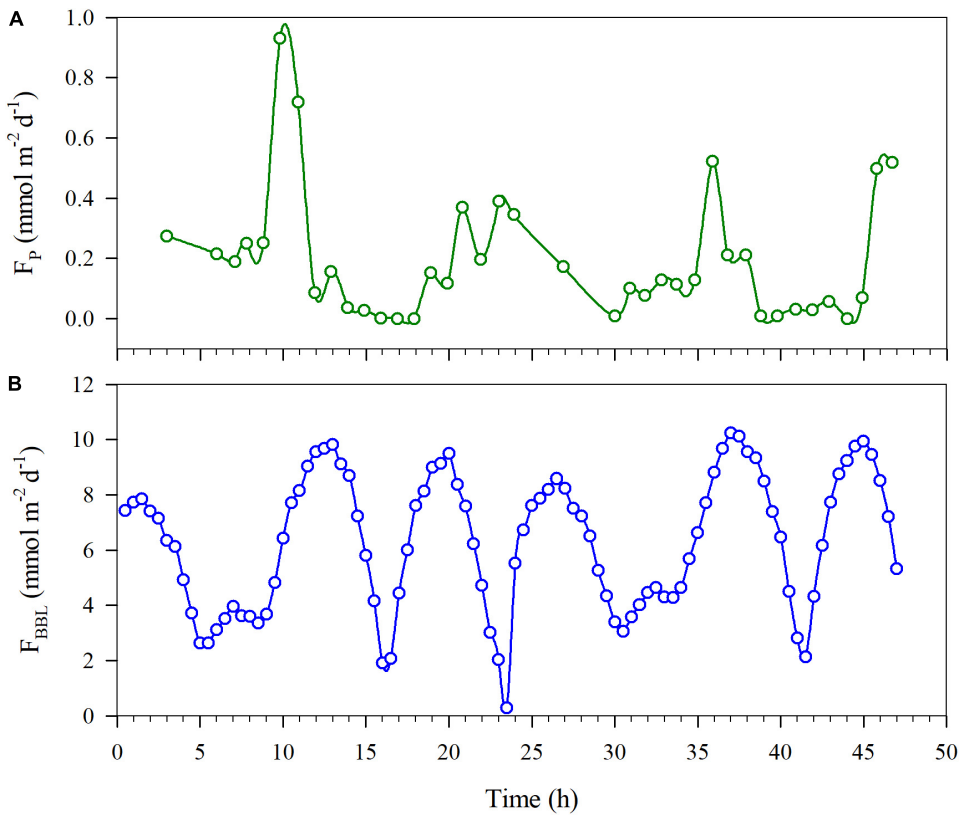


FIGURE 6 | Estimated DO fluxes at station A5 through the pycnocline (F_p) **(A)** and through the bottom boundary layer (F_{BBL}) **(B)** as a function of time.

of particulate organic matter freshly produced by marine plankton (e.g., phytodetritus) dominated oxygen consumption, as has been observed in the Gulf of Mexico (Rabalais et al., 2002; Green et al., 2006), the Yangtze River estuary (Wang et al., 2017), the Pearl River estuary (Qian et al., 2018), and the Chesapeake Bay (Su et al., 2020). Since pelagic respiration was the main contributor (>60%) to the oxygen depletion (see above), the oxidation of fresh, autochthonous particulate organic matter should have primarily transpired in the water column rather than in the sediment, even though the water column was very shallow (<30 m). This result was consistent with that in the shallow (<30 m) hypoxic zone in the Chesapeake Bay where the pelagic respiration contributes ∼70% to the bottom oxygen depletion (Li et al., 2015). However, in shallow waters,

TABLE 5 | Estimated DO fluxes through the bottom boundary layer (F_{BBL}) and their contributions to the net oxygen consumption rate in bottom water at station A5, along with other parameters in the bottom water.

Cruise	Temperature (°C)	Salinity	DO (μ mol L^{-1})	D (×10^{-9} m^2 s^{-1})	F_{BBL} (mmol m^{-2} d^{-1})	Contribution (%)
			2017			
YD 144	10.8	32.21	311.6	1.505	11.25	NA
YD 178	15.2	32.23	216.0	1.713	8.87	22.3
YD 203	20.3	32.02	193.5	1.909	8.86	42.1
YD 234	20.7	31.87	84.3	2.011	4.07	13.4
			2018			
YD 162	9.4	32.73	286.1	1.417	9.72	34.6
YD 200	12.7	32.32	212.0	1.588	8.07	19.2
YD 220	16.9	31.98	145.7	1.809	6.32	20.8
YD 237	22.7	31.29	158.0	2.103	7.97	37.8

D, the oxygen diffusion coefficient; NA, not available.

sediment oxygen consumption often plays a dominant role, e.g., in the western side of the Gulf of Mexico near the Atchafalaya River plume (<30 m) (Hetland and DiMarco, 2008) and the Yangtze River estuary (30–50 m) (Zhang et al., 2017). Pelagic-dominated oxygen consumption occurs in relatively deeper water bodies, such as the lower St. Lawrence estuary (>300 m deep) (Bourgault et al., 2012) where the residence time of particulate organic matter in the water column is relatively long. Pelagic-dominated oxygen consumption can also take place in shallow waters with limited sediment deposition, such as in the Louisiana Bight near the Mississippi River plume where suspended particles in the river plume can barely reach the seafloor before entering the deeper (>40 m) shelf water (Corbett et al., 2006; Green et al., 2006; Hetland and DiMarco, 2008). The factors leading to the pelagic-dominated oxygen consumption in the shallow water off Qinhuangdao, Bohai Sea, is unclear but could be linked to abundant loads of slow-sinking, fine organic particles in the water column that originated from phytoplankton blooms.

SUMMARY AND CONCLUSION

Oxygen depletion of ∼90 μmol L^{-1} and acidification of ∼0.3 pH unit occurred in the bottom water of the Bohai Sea off Qinhuangdao City during the summers of 2017 and 2018. Combined with literature data, no significant interannual variations were observed in the rates of oxygen depletion and acidification from 2011 to 2018. The bottom water had therefore remained in a stable condition in terms of net community respiration over that period. The ratio of oxygen consumption to DIC production in the bottom water (1.42 ± 0.22) was close to the Redfield ratio (1.30), demonstrating that degradation of freshly produced organic matter dominated oxygen consumption. Sedimentary organic matter degradation contributed <40% of the oxygen depletion and acidification in the overlying bottom water. The passage of Typhoon Rumbia over the Bohai Sea in the late summer of 2018 strongly weakened the bottom water oxygen depletion and acidification. This study demonstrates that pelagic respiration can thus prevail over sediment respiration in generating oxygen depletion and acidification in shallow coastal systems and stormy weather events can substantially alter the duration and intensity of oxygen depletion and acidification in coastal areas.

DATA AVAILABILITY STATEMENT

The raw data supporting the conclusions of this article will be made available by the authors, without undue reservation, to any qualified researcher.

AUTHOR CONTRIBUTIONS

GS, LZ, FC, and HX designed the project. GS, LZ, and FL collected and analyzed the water samples. GS, LZ, and ML processed the data. GS and HX prepared the manuscript with input from all other authors.

FUNDING

This study was financially supported by the Natural Key Research and Development Program of China (2016YFC1401602), National Natural Science Foundation of China (41606098, 41876018, and 41806018), and Tianjin Natural Science Foundation (19JCZDJC40600 and 16JCQNJC08000). GS held a visiting scholarship (QNHX1811) at Second Institute of Oceanography, Ministry of Natural Resources during this study.

ACKNOWLEDGMENTS

We thank W. Zhai for providing the 2011 DO and pH data, our colleagues for their help with the sample collection, and the crews for their cooperation during the cruises.

SUPPLEMENTARY MATERIAL

The Supplementary Material for this article can be found online at: https://www.frontiersin.org/articles/10.3389/fmars.2020.00252/full#supplementary-material

REFERENCES

Bourgault, D., Cyr, F., Galbraith, P. S., and Pelletier, E. (2012). Relative importance of pelagic and sediment respiration in causing hypoxia in a deep estuary. *J. Geophys. Res.* 117:C08033. doi: 10.1029/2012JC007902

Cai, W.-J., Hu, X., Huang, W., Murrell, M. C., Lehrter, J. C., Lohrenz, S. E., et al. (2011). Acidification of subsurface coastal waters enhanced by eutrophication. *Nat. Geosci.* 4, 766–770. doi: 10.1038/ngeo1297

Cai, W.-J., Huang, W., Luther, G. W. III, Pierrot, D., Li, M., Testa, J., et al. (2017). Redox reactions and weak buffering capacity lead to acidification in the Chesapeake Bay. *Nat. Commun.* 8:369. doi: 10.1038/s41467-017-00417-7

Carstensen, J., Andersen, J. H., Gustafsson, B. G., and Conley, D. J. (2014). Deoxygenation of the Baltic Sea during the last century. *Proc. Natl. Acad. Sci. U.S.A.* 111, 5628–5633. doi: 10.1073/pnas.1323156111

Corbett, D. R., McKee, B. A., and Duncan, D. (2006). An evaluation of mobile mud dynamics in the Mississippi River deltaic region. *Cont. Shelf Res.* 26, 2125–2140.

Diaz, R. J. (2001). Overview of hypoxia around the world. *J. Environ. Quality* 30, 275–281. doi: 10.2134/jeq2001.302275x

Diaz, R. J., and Rosenberg, R. (2008). Spreading dead zones and consequences for marine ecosystems. *Science* 321, 926–929. doi: 10.1126/science.1156401

Fabricius, K. E., Langdon, C., Uthicke, S., Humphrey, C., Noonan, S., De'ath, G., et al. (2011). Losers and winners in coral reefs acclimatized to elevated carbon dioxide concentrations. *Nat. Climat. Change* 1, 165–169. doi: 10.1038/nclimate1122

Feng, Y., Warner, M. E., Zhang, Y., Sun, J., Fu, F.-X., Feng, Y., et al. (2008). Interactive effects of increased pCO2, temperature and irradiance on the marine coccolithophore *Emiliania huxleyi* (Pyrmnesiophyceae). *Eur. J. Phycol.* 43, 87–98. doi: 10.1080/09670260701664674

Galán, A., Molina, V., Thamdrup, B., Woebken, D., Lavik, G., Kuypers, M. M. M., et al. (2009). Anammox bacteria and the anaerobic oxidation of ammonium in

the oxygen minimum zone off northern Chile. *Deep Sea Res. II* 56, 1021–1031. doi: 10.1016/j.dsr2.2008.09.016

Galgani, L., Stolle, C., Endres, S., Schulz, K. G., and Engel, A. (2014). Effects of ocean acidification on the biogenic composition of the sea-surface microlayer: results from a mesocosm study. *J. Gepphys. Res. Oceans* 119, 7911–7924. doi: 10.1002/2014jc010188

Grasshoff, K., Kremling, K., and Ehrhardt, M. (1999). *Methods of Seawater Analysis. Third, Completely Revised and Extended Edition*. Weinheim: Wiley-VCH Verlag GmbH.

Green, R. E., Bianchi, T. S., Dagg, M. J., Walker, N. D., and Breed, G. A. (2006). An organic carbon budget for the Mississippi River turbidity plume and plume contributions to air-sea CO2 fluxes and bottom water hypoxia. *Estuar. Coast.* 29, 579–597. doi: 10.1007/bf02784284

Gregg, M. C. (1999). Uncertainties and limitations in Measuring *varepsilon* and χW. *J. Atmos. Oceanic Technol.* 16, 1483–1490.

Hansen, J. L. S., and Bendtsen, J. (2014). Seasonal bottom water respiration in the North Sea-Baltic Sea transition zone: rate, temperature sensitivity and sources of organic material. *Mar. Ecol. Prog. Ser.* 499, 19–34. doi: 10.3354/meps10633

Hetland, R. D., and DiMarco, S. F. (2008). How does the character of oxygen demand control the structure of hypoxia on the Texas-Louisiana continental shelf? *J. Mar. Syst.* 70, 49–62. doi: 10.1016/j.jmarsys.2007.03.002

Hoegh-Guldberg, O., Mumby, P. J., Hooten, A. J., Steneck, R. S., Greenfield, P., Gomez, E., et al. (2007). Coral reefs under rapid climate change and ocean acidification. *Science* 318, 1737–1742.

Huang, D., Su, J., and Backhaus, J. O. (1999). Modelling the seasonal thermal stratification and baroclinic circulation in the Bohai Sea. *Cont. Shelf Res.* 19, 1485–1505. doi: 10.1016/s0278-4343(99)00026-6

Jackett, D. R., and McDougall, T. J. (1995). Minimal adjustment of hydrographic profiles to achieve static stability. *J. Atmos. Ocean. Technol.* 12, 381–389. doi: 10.1175/1520-0426(1995)012<0381:maohpt>2.0.co;2

Keister, J. E., Houde, E. D., and Breitburg, D. L. (2000). Effects of bottom-layer hypoxia on abundances and depth distributions of organisms in Patuxent River. *Chesapeake Bay. Mar. Ecol. Prog. Ser.* 205, 43–59. doi: 10.3354/meps205043

Li, Y., Li, M., and Kemp, W. M. (2015). A budget analysis of bottom-water dissolved oxygen in Chesapeake Bay. *Estuar. Coast.* 38, 2132–2148. doi: 10.1007/s12237-014-9928-9

Matear, R. J., and Hirst, A. C. (2003). Long-term changes in dissolved oxygen concentrations in the ocean caused by protracted global warming. *Global Biogeochem. Cycles* 17:1125. doi: 10.1029/2002GB001997

McCarthy, M. J., Carine, S. A., Liu, Z., Ostrom, N., and Gardner, W. S. (2013). Oxygen consumption in the water column and sediments of the northern Gulf of Mexico hypoxic zone. *Estuar. Coast. Shelf Sci.* 123, 46–53. doi: 10.1016/j.ecss.2013.02.019

Murrell, M. C., and Lehrter, J. C. (2011). Sediment and lower water column oxygen consumption in the seasonally hypoxic region of the Louisiana Continental Shelf. *Estuar. Coast.* 34, 912–924. doi: 10.1007/s12237-010-9351-9

Ni, X., Huang, D., Zeng, D., Zhang, T., Li, H., and Chen, J. (2016). The impact of wind mixing on the variation of bottom dissolved oxygen off the Changjiang Estuary during summer. *J. Mar. Syst.* 154, 122–130. doi: 10.1016/j.jmarsys.2014.11.010

Ning, X., Lin, C., Su, J., Liu, C., Hao, Q., Le, F., et al. (2010). Long-term environmental changes and the responses of the ecosystems in the Bohai Sea during 1960-1996. *Deep Sea Res. II* 57, 1079–1091. doi: 10.1016/j.dsr2.2010.02.010

Orr, J. C., Fabry, V. J., Aumont, O., Bopp, L., Doney, S. C., Feely, R. A., et al. (2005). Anthropogenic ocean acidification over the twenty-first century and its impact on calcifying organisms. *Nature* 437, 681–686. doi: 10.1038/nature04095

Osborn, T. R. (1980). Estimates of the local rate of diffusion from dissipation measurements. *J. Phys. Oceanogr.* 10, 83–89. doi: 10.1175/1520-0485(1980)010<0083:eotlro>2.0.co;2

Pierrot, D., Lewis, E., and Wallace, D. W. R. (2006). *MS Excel Program Developed for CO2 System Calculations*. Oak Ridge, TN: U.S. Department of energy, doi: 10.3334/CDIAC/otg.CO2SYS_XLS_CDIAC105a

Qian, W., Gan, J., Liu, J., He, B. Y., Lu, Z., Guo, X., et al. (2018). Current status of emerging hypoxia in a eutrophic estuary: the lower reach of the Pearl River estuary, China. *Estuar. Coast. Shelf Sci.* 205, 58–67. doi: 10.1016/j.ecss.2018.03.004

Rabalais, N. N., Turner, R. E., and Wiseman, W. J. Jr. (2002). Gulf of Mexico hypoxia, A. K. A. "the dead zone". *Annu. Rev. Ecol. Syst.* 33, 235–263. doi: 10.1146/annurev.ecolsys.33.010802.150513

Ramsing, N., and Gundersen, J. (1994). Seawater and Gases-Tabulated Physical Parameters of Interest to People Working with Microsensors in Marine Systems, Version 2.0, Unisense Internal Report. doi: 10.1146/annurev.ecolsys.33.010802.150513

Reimers, C. E., Özkan-Haller, H. T., Berg, P., Devol, A., McCann-Grosvenor, K., and Sanders, R. D. (2012). Benthic oxygen consumption rates during hypoxic conditions on the Oregon continental shelf: evaluation of the eddy correlation method. *J. Geophys. Res.* 117:C020021. doi: 10.1029/2011JC007564

Rheuban, J. E., Doney, S. C., Cooley, S. R., and Hart, D. R. (2018). Projected impacts of future climate change, ocean acidification, and management on the US Atlantic sea scallop (*Placopecten magellanicus*) fishery. *PLoS One* 13:E0203536. doi: 10.1371/journal.pone.0203536

Rippeth, T. P., Wiles, P., Palmer, M. R., Sharples, J., and Tweddle, J. (2009). The diapycnal nutrient flux and shear-induced diapycnal mixing in the seasonally stratified western Irish Sea. *Cont. Shelf Res.* 29, 1580–1587. doi: 10.1016/j.csr.2009.04.009

Smodlaka, N. (1986). Primary production of the organic matter as an indicator of the eutrophication in the northern Adriatic sea. *Sci. Total Environ.* 56, 211–220. doi: 10.1016/0048-9697(86)90325-6

Su, J., Cai, W.-J., Brodeur, J., Hussain, N., Chen, B., Testa, J. M., et al. (2020). Source partitioning of oxygen-consuming organic matter in the hypoxic zone of the Chesapeake Bay. *Limnol. Oceanogr.* 9999, 1–17. doi: 10.1002/lno.11419

Su, J., Dai, M., He, B., Wang, L., Gan, J., Guo, X., et al. (2017). Tracing the origin of the oxygen-consuming organic matter in the hypoxic zone in a large eutrophic estuary: the lower reach of the Pearl River estuary. *Chin. Biogeosci.* 14, 4085–4099. doi: 10.5194/bg-14-4085-2017

Vaquer-Sunyer, R., and Duarte, C. M. (2008). Thresholds of hypoxia for marine biodiversity. *Proc. Natl. Acad. Sci. U.S.A.* 105, 15452–15457. doi: 10.1073/pnas.0803833105

Wallace, R. B., Baumann, H., Grear, J. S., Aller, R. C., and Gobler, C. J. (2014). Coastal ocean acidification: the other eutrophication problem. *Estuar. Coast. Shelf Sci.* 148, 1–13. doi: 10.1016/j.ecss.2014.05.027

Wang, B., Chen, J., Jin, H., Li, H., Huang, D., and Cai, W.-J. (2017). Diatom bloom-derived bottom water hypoxia off the Changjiang estuary, with and without typhoon influence. *Limnol. Oceanogr.* 62, 1552–1560.

Wang, J., Wei, H., Lu, Y., and Zhao, L. (2013). Diffusive boundary layer influence by bottom boundary hydrodynamics in tidal flows. *J. Geophys. Res. Oceans* 118, 5994–6005. doi: 10.1002/2013jc008900

Wang, J., Zhao, L., Fan, R., and Wei, H. (2016). Scaling relationships for diffusive boundary layer thickness and diffusive flux based on in situ measurements in coastal seas. *Prog. Oceanogr.* 144, 1–14. doi: 10.1016/j.pocean.2016.03.001

Wei, Q., Wang, B., Yao, Q., Xue, L., Sun, J., Xin, M., et al. (2019). Spatiotemporal variations in the summer hypoxia in the Bohai Sea (China) and controlling mechanisms. *Mar. Pollut. Bull.* 138, 125–134. doi: 10.1016/j.marpolbul.2018.11.041

Wolk, F., Yamazaki, H., Seuront, L., and Lueck, R. G. (2002). A 431 new free-fall profiler for measuring biophysical microstructure. *J. Atmos. Oceanic Technol.* 19, 780–793. doi: 10.1175/1520-0426(2002)019<0780:anffpf>2.0.co;2

Xu, P., Yang, W., Zhao, L., Wei, H., and Nie, H. (2020). Observations of turbulent mixing in the Bohai Sea during weakly stratified period. *Acta Oceanol. Sin.* 42, 1–9. doi: 10.3969/j.issn.0253-4193.2020.03.001

Yu, C., Liang, B., Bao, C., Li, M., Hu, Y., Lan, D., et al. (2013). Study on eutrophication status and trend in Bohai Sea. *Mar. Environ. Sci.* 32, 175–177.

Zhai, W.-D., Zhao, H., Zheng, N., and Xu, L. (2012). Coastal acidification in summer bottom oxygen-depleted waters in northwestern-northern Bohai Sea from June to August in 2011. *Chin. Sci. Bull.* 57, 1062–1068. doi: 10.1007/s11434-011-4949-2

Zhai, W.-D., Zheng, N., Huo, C., Xu, Y., Zhao, H., Li, Y., et al. (2014). Subsurface pH and carbonate saturation state of aragonite on the Chinese side of the North Yellwo Sea: seasonal variations and controls. *Biogeosciences* 11, 1103–1123. doi: 10.5194/bg-11-1103-2014

Zhang, H., Zhao, L., Sun, Y., Wang, J., and Wei, H. (2017). Contribution of sediment oxygen demand to hypoxia development off the Changjiang Estuary. *Estuar. Coast. Shelf Sci.* 192, 149–157. doi: 10.1016/j.ecss.2017.05.006

Zhang, Z., He, X., Zhang, Z., Han, G., Wang, Y., and Wang, L. (2012). Eutrophication status, mechanism and its coupling effect with algae blooming in Bohai. *Mar. Environ. Sci.* 31, 465–483.

Zhao, H.-D., Kao, S.-J., Zhai, W.-D., Zang, K., Zheng, N., Xu, X., et al. (2017). Effects of stratification organic matter remineralization and bathymetry on summertime oxygen distribution in the Bohai Sea. *China. Cont. Shelf Res.* 134, 15–25. doi: 10.1016/j.csr.2016.12.004

Zhou, F., Huang, D., Xue, H., Xuan, J., Yan, T., Ni, X., et al. (2017). Circulations associated with cold pools in the Bohai Sea on the Chinese continental shelf. *Cont. Shelf Res.* 137, 25–38. doi: 10.1016/j.csr.2017.02.005

Zu, T., Bao, X., Xie, J., and Wu, D. (2005). Distribution and variation trends of the environmental factors in the central section of the Bohai Sea. *J. Ocean Univ. Chin.* 35, 889–894.

Conflict of Interest: The authors declare that the research was conducted in the absence of any commercial or financial relationships that could be construed as a potential conflict of interest.

Copyright © 2020 Song, Zhao, Chai, Liu, Li and Xie. This is an open-access article distributed under the terms of the Creative Commons Attribution License (CC BY). The use, distribution or reproduction in other forums is permitted, provided the original author(s) and the copyright owner(s) are credited and that the original publication in this journal is cited, in accordance with accepted academic practice. No use, distribution or reproduction is permitted which does not comply with these terms.

frontiers in Marine Science

ORIGINAL RESEARCH
published: 25 March 2021
doi: 10.3389/fmars.2021.642041

Ocean Acidification State in the Highly Eutrophic Tokyo Bay, Japan: Controls on Seasonal and Interannual Variability

Michiyo Yamamoto-Kawai[1], Soichiro Ito[1], Haruko Kurihara[2] and Jota Kanda[1]*

[1] Department of Ocean Sciences, Tokyo University of Marine Science and Technology, Tokyo, Japan, [2] Department of Science, University of the Ryukyus, Nishihara, Japan

Seasonal and interannual variabilities in the partial pressure of CO_2 (pCO_2), pH, and calcium carbonate saturation state (Ω) were investigated in the highly eutrophicated Tokyo Bay, Japan, based on monthly observations that were conducted from 2011 to 2017. There were large variabilities in these parameters for surface and bottom waters due to photosynthesis and respiration, respectively. Warming/cooling and freshwater input also altered the surface Ω. During the observation period, calcium carbonate undersaturation was observed twice in the anoxic bottom waters in summer. The data indicate that anaerobic remineralization under anoxic conditions lowers the Ω, causing undersaturation. These findings suggest that de-eutrophication can decelerate ocean acidification in the bottom waters of Tokyo Bay. However, if atmospheric CO_2 exceeds 650 ppm, aragonite undersaturation will be a common feature in the summer bottom water, even if hypoxia/anoxia are alleviated by de-eutrophication.

Keywords: ocean acidification, hypoxia, eutrophication, coastal region, anoxic remineralization

OPEN ACCESS

Edited by:
Xianghui Guo,
Xiamen University, China

Reviewed by:
Naohiro Kosugi,
Meteorological Research Institute, Japan
Liang Xue,
First Institute of Oceanography, Ministry of Natural Resources, China

****Correspondence:***
Michiyo Yamamoto-Kawai
michiyo@kaiyodai.ac.jp

Specialty section:
This article was submitted to Coastal Ocean Processes, a section of the journal Frontiers in Marine Science

Received: *15 December 2020*
Accepted: *05 March 2021*
Published: *25 March 2021*

Citation:
Yamamoto-Kawai M, Ito S, Kurihara H and Kanda J (2021) Ocean Acidification State in the Highly Eutrophic Tokyo Bay, Japan: Controls on Seasonal and Interannual Variability. Front. Mar. Sci. 8:642041. doi: 10.3389/fmars.2021.642041

INTRODUCTION

Ocean acidification (OA) is defined as the progressive reduction in the pH of ocean over an extended period of time, typically decades or longer (Field et al., 2011). Changes of seawater carbonate chemistry associated to OA, such as an increase in partial pressure of seawater CO_2 (pCO_2) concentration and a decrease in calcium carbonate ($CaCO_3$) saturation state (Ω) are also included in the discussion of the effects of OA (Royal Society, 2005; IPCC, 2014). The increased CO_2 concentration promotes the photosynthesis by primary producers such as phytoplankton and seagrass (Hinga, 2002; Palacios and Zimmerman, 2007; Hendriks et al., 2010), while the decreased Ω adversely affects the calcification, as well as the growth and survival of calcifying organisms (e.g., Kroeker et al., 2010). The increased CO_2 concentration also affects the growth of otoliths ($CaCO_3$ structures in ears), metabolic rate and behavior of some fishes (Heuer and Grosell, 2014 for review). The co-occurrence of OA with other environmental changes, such as warming and deoxygenation lead to further biological complications (Kroeker et al., 2013; Gao et al., 2019; Doney et al., 2020). It has been found that an elevated CO_2 concentration reduces the tolerance of fish and bivalves to low oxygen conditions (Hancock and Place, 2016; Miller et al., 2016; Gobler and Baumann, 2016). In addition, the synergistic effects of OA and the warming

of seawater negatively impact the calcification, reproduction, and survival of marine organisms (Harvey et al., 2013).

The current OA, caused primarily by the uptake of anthropogenic CO_2 from the atmosphere, is occurring at a rate higher than that observed at any other time in the last 300 million years (Hönisch et al., 2012). The high OA rate, together with other anthropogenic perturbations, pose a threat to marine organisms, and thus to human society (Bednaršek et al., 2016; Hall-Spencer and Harvey, 2019; Stewart-Sinclair et al., 2020). Coastal regions are of particular importance to human society, providing ∼40% of the global ecosystem goods and services (Costanza et al., 1997). However, due to the complex natural processes and anthropogenic effects, it is difficult to understand and predict the progress of OA in coastal regions. For instance, freshwater discharge from land lowers the salinity and alkalinity and thus lowers the buffer capacity of coastal seawater, making it sensitive to anthropogenic CO_2 addition (Salisbury et al., 2008; Hu and Cai, 2013). An excessive loading of man-made nutrients from land, a phenomenon known as eutrophication, causes massive algal production (blooms) and the subsequent decomposition of large amounts of sinking organic matter causes hypoxia (oxygen concentrations $\leq$ 2 mg L^{-1} or $\leq$ 61 μmol kg^{-1}) in coastal waters worldwide (Breitburg et al., 2018). Eutrophication can thwart OA in the surface waters by increasing the biological CO_2 uptake; however, it amplifies OA in bottom waters by increasing the amount of CO_2 released from the decomposed organic matter (respiration) and also by reducing the buffer capacity (CO_2-rich water has lower buffer capacity; Cai et al., 2011; Duarte et al., 2013; Wallace et al., 2014; Zhao et al., 2020). Large seasonal variations in the physical and biogeochemical conditions of shallow coastal regions can also result in large pH and Ω fluctuations, suggesting that the progress of OA causes coastal waters to seasonally exceed the biologically harmful pH and Ω thresholds faster than offshore waters (Pacella et al., 2018; c.f., McNeil and Matear, 2008). Depending on the balance between the OA (caused by anthropogenic CO_2) and other processes, the coastal regions can undergo a variety of changes from rapid acidification to basification (Duarte et al., 2013; Ishizu et al., 2019). Furthermore, all of these natural and anthropogenic processes can differ across regions. Therefore, to predict the future environmental conditions, it is essential to quantitatively understand the processes affecting OA in each coastal region (e.g., Cai et al., 2011; Laurent et al., 2017; Feely et al., 2018; Rheuban et al., 2019).

In this study, we investigate the state of OA in Tokyo Bay, a highly eutrophicated bay in Japan. Our previous study was the first report on the Ω of water in Tokyo Bay based on monthly observations at two stations, which were conducted from April 2011 to January 2012 (Yamamoto-Kawai et al., 2015). Of these two stations, larger seasonal variabilities in the physical and biogeochemical parameters were observed at F3, the inner bay station, than at F6, the middle bay station. Herein, the seasonal and interannual variations in the various carbonate chemistry parameters, viz., CO_2, pH, and Ω are quantitatively examined to understand the processes affecting the of OA in Tokyo Bay, based on the monthly observations made at F3 from April 2011 to December 2017.

STUDY AREA

Tokyo Bay is a semi-enclosed bay with a mean depth of 19 m (**Figure 1**). The freshwater discharge from rivers (∼400 m^3 s^{-1}) and the inflow of offshore waters drives the estuarine circulation in the bay. The residence time of water in the bay is 1–3 months (Okada et al., 2011). The environment of Tokyo Bay has significantly changed over the last century (see Furukawa and Okada, 2006 for review). The nutrient loading from the surrounding metropolitan areas to the bay rapidly increased in the 1950s and the 1960s. The massive algal bloom (commonly referred to as the "red tide"), mainly caused by the dinoflagellates and diatoms, and the resulting bottom water hypoxia/anoxia have been repeatedly observed since the 1960s (Ishii et al., 2008; Kodama and Horiguchi, 2011). Since most river discharge enters from the north-west side, severe eutrophication and prolonged hypoxia/anoxia are observed in the inner part of the bay (e.g., Kodama and Horiguchi, 2011). Hypoxia/anoxia promotes the anaerobic oxidation of organic matter such as denitrification and sulfate reduction (e.g., Krumins et al., 2013). The bottom water with toxic hydrogen sulfide produced by the sulfate-reducing bacteria can rise by wind mixing, killing the fish and shellfish at the northern coast of the bay. This phenomenon is known as "blue tide" because the hydrogen sulfide in upwelled water is oxidized to elemental sulfur, causing the water to appear whitish blue (Takii et al., 2002). In addition, the area of the tidal flats decreased by ∼90% over the past century, thereby decreasing the shellfish habitat and destroying the network for benthic larvae transport. Due to these environmental changes, the total fish caught annually in Tokyo Bay decreased from $> 1 \times 10^5$ tons in the 1950s (∼90% of shellfish) to 4×10^4 tons in the 1990s (Furukawa and Okada, 2006). Although the implementation of sewage treatment decreased the nutrient concentration in the bay after the 1980s (Kanda et al., 2008; Kubo et al., 2019), red tide and summer bottom hypoxia are still observed every year. The progress of OA can impose additional stress to the ecosystem of Tokyo Bay, which has been suffering from eutrophication and hypoxia.

MATERIALS AND METHODS

Monthly observations (a total of 77 times) were carried out at F3, a time-series station (35.51°N, 139.83°E, bottom depth = 23 m; **Figure 1**) from April 2011 to December 2017. Station F3 is located in the inner bay region. Seawater samples were collected using Niskin bottles mounted on a conductivity-temperature-depth (CTD)/rosette on the *R/V Seiyo-maru* of Tokyo University of Marine Science and Technology at target depths of 0 m, 5 m, 10 m, 15 m, and bottom. Actual depths of sampling were 1–3 m for the target depth of 0 m, 2–8 m for 5 m, 10–14 m for 10 m, 14–18 m for 15 m, and 19–24 m for the bottom.

Samples for dissolved inorganic carbon (DIC) and total alkalinity (TA) were preserved using a saturated mercuric chloride solution (0.1% by volume). The DIC was determined

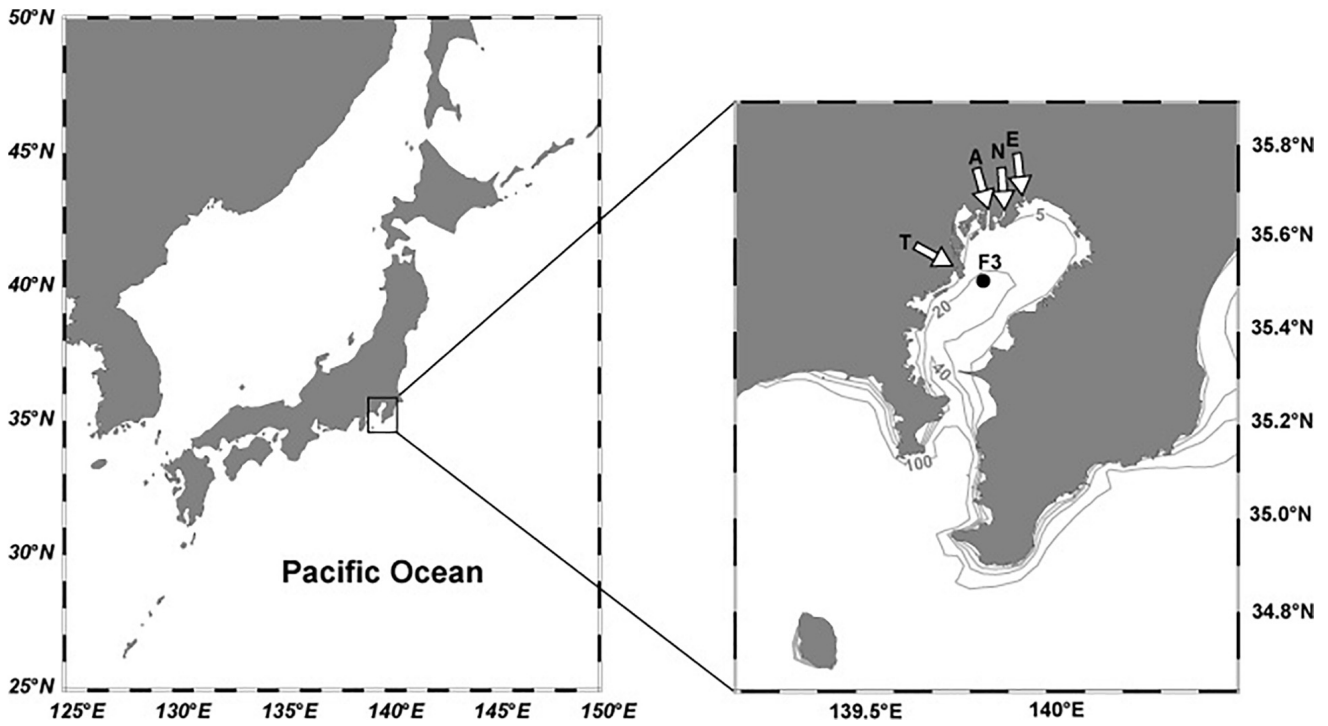


FIGURE 1 | Map of Tokyo Bay and the sampling location. White arrows indicate the major rivers (E, Edogawa; N, Nakagawa; A, Arakawa; T, Tamagawa rivers). Gray lines with numbers indicate the bathymetry in meters.

using the CO_2 extraction-coulometry method (Dickson et al., 2007). The TA was measured using a spectrophotometric method (Yao and Byrne, 1998) for samples from April 2011 to January 2012, and by an open titration method (Dickson et al., 2007) for all other samples. The DIC and TA were calibrated against certified reference materials provided by Dr. Dickson at Scripps Institution of Oceanography and/or KANSO Technos, Japan. The pooled standard deviations obtained from replicate analysis were 2.5 and 2.8 μmol kg^{-1} for TA and DIC, respectively. The dissolved oxygen (DO) and chlorophyll *a* (Chl *a*) concentrations were measured using a RINKO DO sensor (JEFF Advantec Co., Ltd.) and a Seapoint chlorophyll fluorometer (Seapoint sensors, Inc.), respectively. The percentage of oxygen saturation (DO%) was calculated at standard air pressure with solubility of Weiss (1970). We also used nutrient data till October 2015, reported in Kubo et al. (2019).

The DIC, TA, temperature (T), salinity (S), and phosphate and silicate concentrations were used to calculate the *in situ* partial pressure of CO_2 (pCO_2), pH (total scale), and **Ω** of the collected samples using the CO2SYS program (Lewis and Wallace, 1998), along with the K_1 and K_2 constants reported by Mehrbach et al. (1973), refit by Dickson and Millero (1987), and K_{SO4} constant of Dickson (1990). The phosphate and silicate concentrations of Kubo et al. (2019), who reported data till October 2015, were used. After October 2015, we used the mean of the monthly phosphate and silicate concentrations calculated from 2011 to 2015 at each depth. For **Ω**, only the saturation state of aragonite (**Ω**ar) is reported. The calcite saturation state is approximately 1.5 times higher than that of **Ω**ar.

RESULTS AND DISCUSSION

Seasonal Variability

Figure 2 shows mean values of physical and biogeochemical parameters for each month and each target depth (0, 5, 10, 15 m, and bottom). In December and January, all observed parameters show relatively uniform values from the surface to the bottom, because of vertical mixing induced by cooling and winds. From January to August, the T increases from 10.7 to 26.8°C in the surface layer and from 12.5 to 21.2°C in bottom layer (**Figure 2A**). The S below 10 m remains largely unchanged throughout the year, ranging between 33 and 34 at the bottom (**Figure 2B**). In contrast, there is a large seasonal variability in S at 0 and 5 m, decreases to 26.1 and 29.7, respectively, in September. This indicate that river discharge significantly lowers S in the top 5 m layer at F3. The average T and S for all observations were 17.5°C and 32.0, respectively.

Chl *a* concentrations in the top 5 m layer also show large seasonal variability (**Figure 2C**). The highest Chl *a* concentration of 28 μg L^{-1} was observed in the surface water in May. Interestingly, the Chl *a* concentration increased from December to January at all depths (**Figure 2C**), suggesting the enhancement of primary production during January. In addition, the concurrent decrease in the phosphate and silicate

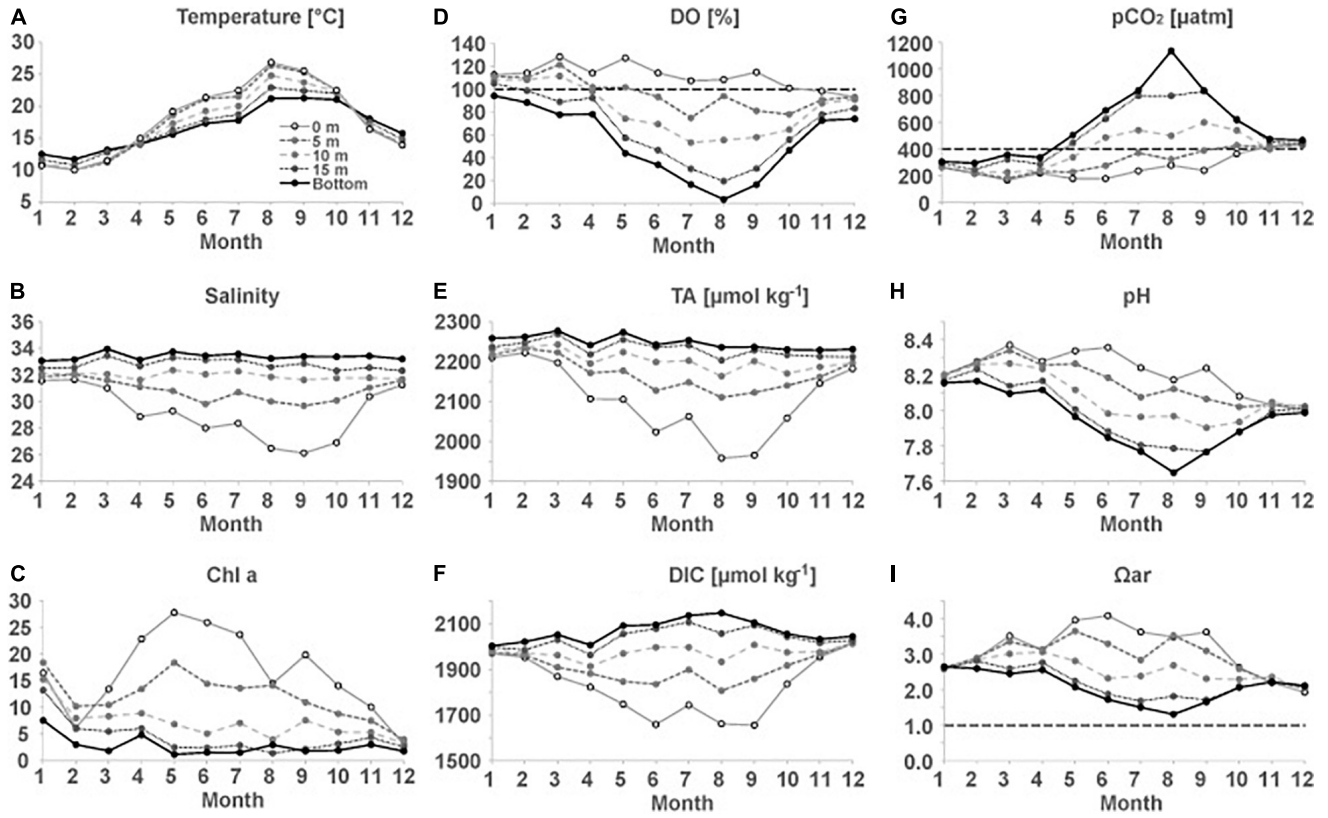


FIGURE 2 | Seasonal variations in **(A)** T, **(B)** S, **(C)** Chl *a*, **(D)** DO%, **(E)** TA, **(F)** DIC, **(G)** pCO_2, **(H)** pH, and **(I)** Ωar at station F3. Black horizontal dashed lines in **(D,G,I)** indicate the O_2 saturation, CO_2 saturation (relative to mean atmospheric CO_2 for the observation period), and aragonite saturation (Ωar = 1), respectively.

concentrations from December to January (not shown) indicates the occurrence of photosynthesis by diatoms. This finding is consistent with previous studies, which have reported winter photosynthesis by diatoms in Tokyo Bay, stimulated by episodic stratification with favorable light conditions and abundant nutrients (Shibata and Aruga, 1982; Nomura and Yoshida, 1997).

The surface DO was slightly undersaturated in December (94.5 ± 3.9%), but increased to 115.0 ± 15.5% in January due to the production of DO by photosynthesis. Despite continued photosynthesis and warming (lowers gas solubility in seawater), DO% does not largely increase from spring to summer, possibly due to the release of O_2 to the atmosphere by an air-sea gas exchange. From spring to summer, the DO in the bottom water at F3 largely decreases because of decomposition of organic matter, reaching as low as 3.3% (7.4 µmol kg^{-1}) in August. Bottom water is in hypoxic condition (≤61 µmol kg^{-1}) from July to September. In August, water at 15 m also reaches hypoxic condition. After September, vertical mixing supplies oxygen from the atmosphere to the bottom waters, increasing the DO levels (**Figure 2D**).

Carbonate chemistry should be affected by above mentioned seasonal variation in cooling/warming, freshwater mixing, biological activity such as photosynthesis and respiration. Seasonal variations in TA and DIC were similar to those in S, showing low values during summer in the top 5 m layer due to mixing with river water (**Figures 2B,E,F**). The DIC below 10 m increases from spring to summer due to the accumulation of CO_2 from decomposition of organic matter. The seasonal and interannual variations in the carbonate parameters (calculated from TA and DIC) differ from those in TA or DIC (**Figures 2G–I**). The seasonal variation in pCO_2 is much larger in the bottom layer than in the surface layer. Surface water tends to be undersaturated with respect to atmospheric CO_2 (∼400 µatm) from January to October, while it is oversaturated with CO_2 from November to December (**Figure 2G**). The bottom water also tends to be undersaturated from January to April and the pCO_2 in the bottom water increased as the DO% decreased, reaching 1,134 µatm in August. From September to November, the bottom pCO_2 rapidly decreases, indicating the transfer of CO_2 to the upper waters and the atmosphere by an enhanced vertical mixing in fall; however, CO_2 oversaturation was still observed in December, following which, winter photosynthesis decreases the pCO_2 till the water is undersaturated with respect to the atmosphere in January (**Figure 2G**). The seasonal variations in the pH mirrors that of pCO_2 (**Figure 2H**). Bottom pH is as low as 7.6 in August. Ωar is high in the surface waters during summer (**Figure 2I**), in spite of freshwater mixing that lowers Ωar (Salisbury et al., 2008; Yamamoto-Kawai et al., 2011). This means that effect of biological activity (i.e., uptake of CO_2 by photosynthesis) exceeds

the effect of freshening. The bottom Ωar reaches a minimum value of 1.3 in August.

Interannual Variability

Although 7 years of observations are not sufficient to determine the acidification trends in the highly variable Tokyo Bay, the interannual variabilities in the physical and biogeochemical parameters can be investigated. Interannual variability in T is not so large, compared to seasonal variability (**Figure 3A**). For example, surface T in August ranged only between 25.31°C (in 2015) and 28.86°C (in 2013). In contrast, surface S shows large interannual variability (**Figure 3B**). Extreme surface freshening was observed in September 2011 (S = 15.87), April 2014 (S = 20.75), June 2014 (S = 22.95), August 2016 (S = 19.49), and October 2016 (S = 16.30), while surface S was greater than 28 throughout 2013 (**Figure 2A**). In the layer below 10 m depth, S is relatively constant throughout the study period. Accordingly, extreme surface freshening leads to strong stratification at around 5 m.

Though a seasonal maximum Chl *a* concentration of 28 μg L^{-1} was found in May in **Figure 2C**, greater concentrations were observed during other months too (**Figure 3C**). According to Nomura (1998), a Chl *a* concentration > 30 μg L^{-1} indicates the occurrence of red tide in Tokyo Bay, and such high concentrations were observed every year from 2011 to 2014, with the highest Chl *a* concentration (92 μg L^{-1}) in June 2014. The observed Chl *a* concentrations were lower than 30 μg L^{-1} after 2015. The extent of DO oversaturation was extremely high (>150%) in the surface layers in 2012, 2013, and 2014. These observations along with the high Chl *a* concentrations suggest that the primary productivity was higher in the earlier years of the observation period (**Figures 3C,D**). On the contrary, a significant undersaturation of DO in surface water (<80%, down to 47%) was observed in July and August 2015, October 2016, and July 2017, indicating the mixing with waters affected by respiration at the bottom of F3 or somewhere in upstream regions. In October 2016, the low DO% in extremely low S water (S = 16.3) suggests that the respiratory processes took place near the river mouth and then advected to F3.

Bottom hypoxia (DO ≤ 61 μmol kg^{-1}, DO% < 25%) was observed every summer. Anoxic conditions (DO = 0 μmol kg^{-1}) were observed in the bottom layer in August 2013, July 2015, and August 2015, and at a depth of 16 m in July 2014 (**Figure 3D**). Not anoxia, but very low concentration of DO (<5.0 μmol kg^{-1}, DO% < 2%) were observed in the bottom water in all other years. Although hypoxia and anoxia are induced by the stratification and decomposition of organic matter produced by primary production, the occurrence of anoxia at

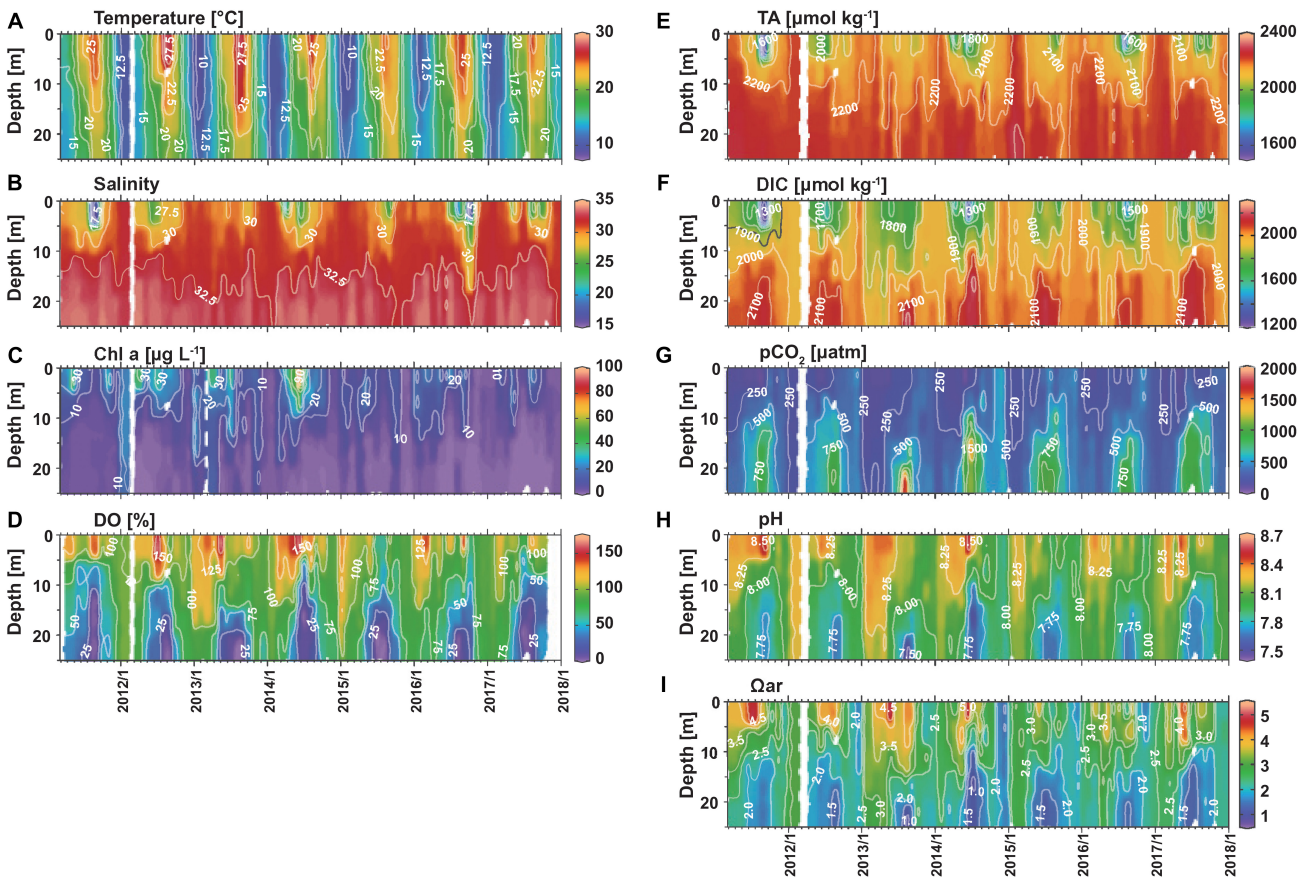


FIGURE 3 | Time series of **(A)** T, **(B)** S, **(C)** Chl *a*, **(D)** DO%, **(E)** TA, **(F)** DIC, **(G)** pCO_2, **(H)** pH, and **(I)** Ωar at station F3.

the bottom does not seem to be directly related to the strength of stratification (stronger in 2011 and 2016 by freshening; **Figure 3B**) or surface productivity (higher in 2011–2014 than 2015–2017; **Figure 3C**). This is likely because bottom anoxia was not a special event for 2013, 2014, and 2015, but almost occurs every year, and our observations happened to be made during a short anoxic period in 2013, 2014, and 2015. This is supported by the data of public water quality measurement near our study site (at 9 stations in the area of 35.46–35.53°N, 139.74–139.85°E; data can be downloaded from websites of Tokyo Metropolitan Government Bureau of Environment and Kanagawa prefecture Environment and Agriculture Bureau). The minimum DO values at or below detection limit [<0.5 mg L^{-1} (Tokyo) or 0.1 mg L^{-1} (Kanagawa)] were reported every summer at 1–4 of 9 stations, suggesting possible occurrence of localized anoxia. However, such low DO condition was not observed for two consecutive months at each station. These results suggest that anoxia in this region is not uncommon, but is a localized, short-term event. This is consistent with previous studies reporting that bottom DO in Tokyo Bay varies in a short period of time due to the wind-driven intrusion of offshore water (Fujiwara and Yamada, 2002; Sato et al., 2012). The intrusion of offshore water supplies oxygen and also moves hypoxic/anoxic water toward the coast and to the subsurface layer (Fujiwara and Yamada, 2002). This explains the observation of anoxic water at a depth of 16 m, not at the bottom in July 2014.

Interannual variations in TA and DIC are similar to that of S in the upper layer (**Figures 3E**, **4F**). Especially low TA and DIC were observed in September 2011, April 2014, June 2014, and August 2016 when extreme freshening was observed. Although extreme freshening was also observed in October 2016, TA and DIC were relatively high. In the deeper layer, T shows relatively small interannual variability. The bottom DIC in summer is high in 2013, 2014, 2015, and 2017.

Lower pCO_2, higher pH and Ωar were observed in the summer surface waters during the first half of the observation period (**Figures 3G–I**). Extremely high pCO_2 (>1,500 μatm), low pH (<7.5) and low Ωar (<1) were observed in the bottom layer in August 2013 and at a depth of 16 m in July 2014, when anoxic condition was also observed. This is the first record of aragonite undersaturation in Tokyo Bay. Although bottom anoxia was observed in July and August 2015, the carbonate parameters did not show extreme values and Ωar was higher than 1 (1.2 and 1.4, respectively). In November and December of 2014, high pCO_2, low pH, and low Ωar were observed in the whole water column compared to other years. This should reflect the accumulation of large amounts of CO_2 during the preceding summer in the layer below 10 m (**Figure 3G**), indicating that the properties of summer bottom water later affect the properties in winter. Another process causing interannual variation in the winter carbonate properties is winter photosynthesis (Shibata and Aruga, 1982; Nomura and Yoshida, 1997): relatively low pCO_2, high pH and high Ωar were observed in the whole water column in January 2012 and February 2013 when Chl *a* was relatively high.

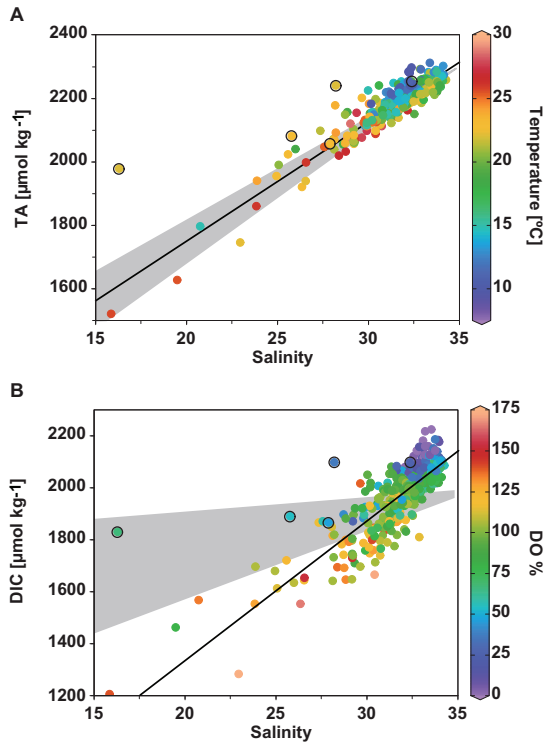


FIGURE 4 | Relationships between **(A)** TA and S, colored by T, **(B)** DIC and S, colored by DO%. Black lines represent the least square linear fits of each plot. Gray area shows the mixing of offshore water (*S* = 34.82, TA = 2,293 μmol kg^{-1}, DIC = 1,960∼1,990 μmol kg^{-1}) with river water (*S* = 0, TA = 1,013 ± 156 μmol kg^{-1}, DIC = 1,047∼1,800 μmol kg^{-1}). Circled data points represent the observations of the water samples collected in October 2016.

Processes Affecting Carbonate Chemistry in Tokyo Bay

Physical Processes Occurring With Air-Sea CO_2 Equilibrium

In this section, the processes responsible for the seasonal and interannual variations in the carbonate parameters in Tokyo Bay are quantitatively discussed. As shown in **Figure 4**, both DIC and TA are linearly correlated with S, indicating the significant influence of mixing of offshore water (high in S, DIC, and TA) with freshwater (low in S, DIC, and TA). The TA and DIC values were higher than expected from S in October 2016 (circled data in **Figure 4**) when freshening was observed from the surface (*S* = 16.3) to a depth of 16 m (S = 28.2 at 16 m) in the water column. Although the reason is not completely understood, the low DO% (68% at the surface) suggests that this anomaly arises from the input of local freshwater input with especially high TA and DIC and local respiratory processes in the regions near the coast or the river mouth. Except for the data recorded in October 2016, TA correlated well with S and the regression line of TA is 37.61 (± 0.73) × S + 998.4 (± 23.1) (black line in **Figure 4A**, $r = 0.94$, $n = 368$), which is in good agreement with that obtained by Taguchi et al. (2009) for surface waters in 2008

(TA = 36.77 × S + 1,006, r = 0.99, n = 59), following a mixing line between offshore water [North Pacific Sub-Tropical Mode Water (NPSTW), S = 34.82, TA = 2293 μmol kg^{-1}] and river water (S = 0, TA ∼1,000 μmol kg^{-1}). This indicates that the waters in Tokyo Bay can be expressed as a mixture of these two components. Deviations from the regression line in the low-salinity waters may reflect the variations in TA in the river water and the contribution of precipitation (TA = 0). The correlation between DIC and S, except for data from October 2016, is expressed by DIC = 53.7 (± 1.7) × S + 261.5 (± 54.8) (black line in **Figure 4B**, r = 0.85, n = 367). Compared to the TA-S plot, there were more data scattering and deviations from the mixing line between the DIC values of offshore waters (DIC = 1,960–1,900 μmol kg^{-1} at S = 34.82 from Ishii et al., 2011) and river waters (1,047 ± 164 μmol kg^{-1} in the Tamagawa River and 1,499 ± 222 μmol kg^{-1} in the Arakawa River from May 2011 to April 2012, Kubo, 2015; ∼1,800 μmol kg^{-1} in the Tamagawa River in April 1993, Ogawa and Ogura, 1997) in the DIC-S plot. Water samples with high S and low DO% showed an elevated DIC, while surface waters with low S and high DO% showed a lower DIC than that expected from the mixing line, indicating the significant influence of photosynthesis and respiration on the DIC concentrations. The DIC should also have been affected by warming/cooling and air-sea gas exchanges.

To separately and quantitatively assess the effects of the physical processes on the carbonate parameters, we have assumed that the TA and DIC values were affected only by the physical processes, i.e., mixing with freshwater and warming/cooling. Under this assumption, the TA (TA^{phys}) can be predicted from the S values assuming two end-member mixing of offshore water with river water (TA^{phys} = 36.76 × S + 1,013). For the offshore waters, the S and TA values of Taguchi et al. (2009) were used (34.82 and 2293 μmol kg^{-1}, respectively). This TA value was in agreement with that of Ishii et al. (2011), who reported a mean salinity-normalized TA of 2,305 μmol kg^{-1} at S = 35, corresponding to 2,293 μmol kg^{-1} at S = 34.82 in the Kuroshio region, southwest of Tokyo Bay. For the river water, a TA of 1,013 μmol kg^{-1}, the mean of monthly observations of four major rivers (the Edogawa, Arakawa, Nakagawa, and Tamagawa rivers, ± 156 μmol kg^{-1}, n = 42), was used (reported in the appendix of the 2018 annual report on water quality by the Bureau of Waterworks Tokyo Metropolitan Government)[1]. The DIC can be also predicted from the S and end-member DIC values. However, the mixing of river water with offshore water causes an oversaturation of pCO_2 in the waters compared with the atmospheric pCO_2. Accordingly, the DIC should decrease from the river mouth to the observation site by the outgassing of CO_2, as observed in Tokyo Bay (Kubo et al., 2017) and other coastal regions (e.g., Zhao et al., 2020). Therefore, we used pCO_2 instead of DIC, by assuming that pCO_2 in the physics only case (pCO_2^{phys}) is at equilibrium with atmospheric pCO_2 at TA^{phys} and observed T and S conditions. For this calculation, the monthly mean dry air CO_2 concentration (xCO_2) observed at Mauna Loa (NOAA/PMEL) was converted to pCO_2 at 100% humidity, standard air pressure, and the observed water T. Then, the DIC, pH and Ω of the waters, under the assumption that only physical processes are taking place, are calculated as:

$$\mathrm{DIC}^{phys}, \mathrm{pH}^{phys} \text{or} \Omega^{phys} = f(\mathrm{T}_{obs}, \mathrm{S}_{obs}, \mathrm{TA}^{phys}, \mathrm{pCO}_2^{phys})$$

where the function f refers to the CO2SYS thermodynamic equations, T_{obs} and S_{obs} are observed T and S. DIC_{phys} shows relatively large variability (ranging from 1,481 to 2,071 μmol kg^{-1}) under the equilibration with atmospheric pCO_2, reflecting significant effects of T, S, and TA on DIC (**Figure 5A**). Of these, the effect of T can be estimated by comparing DIC_{phys} with that calculated by replacing T_{obs} by mean T of 17.5°C. It is estimated that summer warming to 27°C decreases DIC by ∼70 μmol kg^{-1} and winter cooling to 11°C increases DIC by ∼50 μmol kg^{-1}. This indicates that the large variability in DIC_{phys} is mostly caused by freshening (**Figure 5A**). Nevertheless, when compared to the observed seasonal and interannual variabilities in the carbonate parameters, those calculated for the physical processes with an air sea CO_2 equilibrium were significantly lower (**Figures 2F–I**, **3F–I**, **5A–D**, note that the scales of the y-axis in **Figures 5B,C** are much smaller than those in **Figures 2G,H**, **3G,H**). **Figure 5C** shows that the pH^{phys} reflects seasonal variations and long-term trend of pCO_2^{phys}. In addition, it is apparent that the pH^{phys} is affected by S. However, even under extreme freshening, the pH^{phys} is lowered by only ∼0.03, suggesting that the effects of mixing of seawater with river water and warming/cooling on the pH are small after sufficient air–sea gas exchange has occurred, even in Tokyo Bay with large seasonal variability in T and S. Seasonal variation in the Ω^{phys} values is relatively large (**Figure 5D**). In general, Ω^{phys} values are high in the summer (∼2.8) and low in winter (∼1.8), and the data are positively correlated with T (r = 0.86), reflecting the effect of T on solubility of aragonite (Mucci, 1983). In addition, surface freshening lowers the Ω^{phys} by ∼1 (for example, the difference between the Ω^{phys} value at 0 m (S = 15.87) and that at 5 m (S = 29.82) in September 2011 is 1.3). Due to the combined effects of T and freshening, the lowest and second lowest Ω^{phys} values (Ω^{phys} = 1.3 and 1.4) were observed in the surface waters in April 2014 (S = 20.75, T = 15°C) and October 2016 (S = 16.3 and T = 22°C), respectively, not in the freshest but warm water in September 2011 (S = 15.9, T = 26°C, Ω^{phys} = 1.6). In terms of interannual variability, freshwater mixing is the major factor affecting the Ω^{phys} values since T has a small interannual variation (**Figure 2A**). These findings suggest that warming/cooling induces the seasonal variation in Ω^{phys}, whereas fluctuations in freshwater mixing cause the interannual variations in the surface Ω^{phys} in Tokyo Bay.

Other Processes

The net effect of processes other than physical processes on the carbonate parameters can be estimated by the differences between the observed values and those calculated under the physical processes only condition;

$$\Delta DIC, \Delta \mathrm{pCO}_2, \Delta \mathrm{pH}, \text{or} \Delta \Omega \mathrm{ar} = f(\mathrm{T}_{obs}, \mathrm{S}_{obs}, \mathrm{DIC}_{obs}, \mathrm{TA}_{obs}) - f(\mathrm{T}_{obs}, \mathrm{S}_{obs}, \mathrm{TA}^{phys}, \mathrm{pCO}_2^{phys}).$$

[1]http://www.waterworks.metro.tokyo.jp/suigen/nempo/

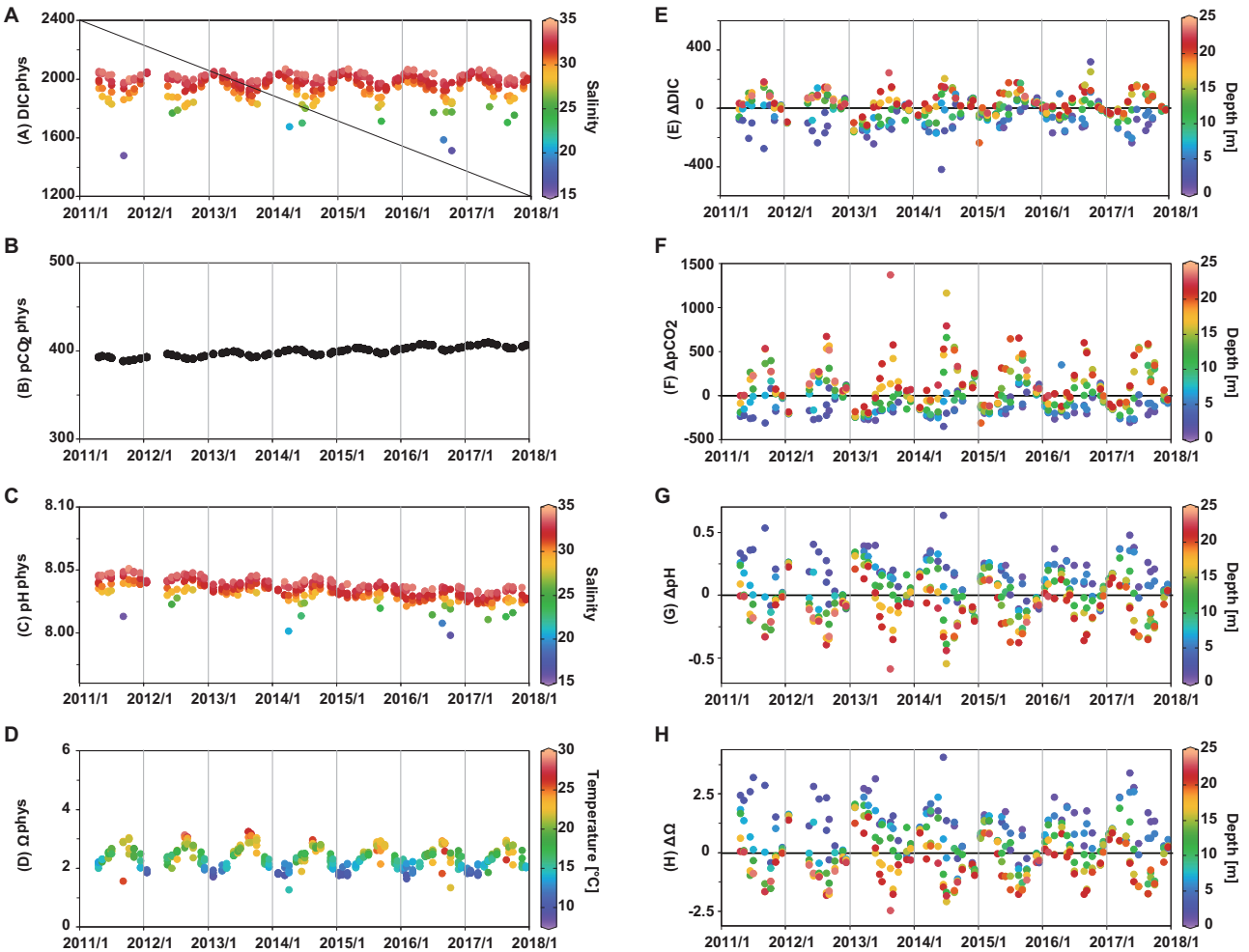


FIGURE 5 | Seasonal and interannual variations in **(A)** DIC^{phys} **(B)** $pCO_2{}^{phys}$, **(C)** pH^{phys}, **(D)** Ω^{phys}, **(E)** ΔDIC, **(F)** ΔpCO_2, **(G)** ΔpH, and **(H)** ΔΩ at all observation depths. **(A,C)** are colored by S, **(D)** is colored by T, and **(E–H)** are colored by depth.

The other processes that affect the carbonate parameters include photosynthesis, remineralization, formation and dissolution of $CaCO_3$, and air-sea CO_2 disequilibrium. Uncertainties and fluctuations in the end-member TA values used to estimate the carbonate parameters for the physical processes-only case can affect the ΔDIC, ΔpCO_2, ΔpH, and ΔΩar values (Δ values). The seasonal and interannual variations in the Δ values are similar to those in the observed carbonate parameters (**Figures 2F–I**, **3F–I**, **5E–H**), indicating the importance of non-physical processes in Tokyo Bay. The average net effects of these processes in the surface (bottom) waters are as follows: DIC = −76 ± 102 μmol kg^{-2} (+ 50 ± 73 μmol kg^{-2}), pCO_2 = −130 ± 127 μatm (+ 192 ± 283 μatm), pH = + 0.17 ± 0.17 (−0.12 ± 0.17), and Ωar = + 1.0 ± 0.9 (−0.4 ± 0.7). The relationships between carbonate parameters (ΔpCO_2, ΔpH, and ΔΩar) and the DO% (**Figure 6**) indicate that photosynthesis and aerobic respiration are the major processes controlling the Δ values. In waters with high DO oversaturation, the effect of non-physical processes is high: maximum values (ΔpCO_2: −345 μatm; ΔpH: + 0.6; ΔΩar: + 3.3) were observed in the water with the highest DO% (174%). Relatively low ΔpCO_2 along with high ΔpH and ΔΩar values were observed in the surface waters during the first half of the observation period (**Figure 5**). These findings are consistent with the higher photosynthesis rate in the earlier years, as indicated by the higher Chl *a* concentration and DO% (**Figures 3C,D**).

During summer, high ΔpCO_2 values (>1,000 μatm) were estimated for the anoxic and aragonite undersaturated bottom waters collected on 19 August, 2013 and 04 July, 2014 (**Figure 5F**). An increase in the pCO_2 without a corresponding change in the DO level under anoxic conditions (**Figure 6A**) suggests the influence of anaerobic processes, such as denitrification and sulfate reduction in the sediment, which are followed by a DIC efflux to the overlying bottom water. Both denitrification and sulfate reduction are known to occur in the sediments of Tokyo Bay (Koike and Hattori, 1978;

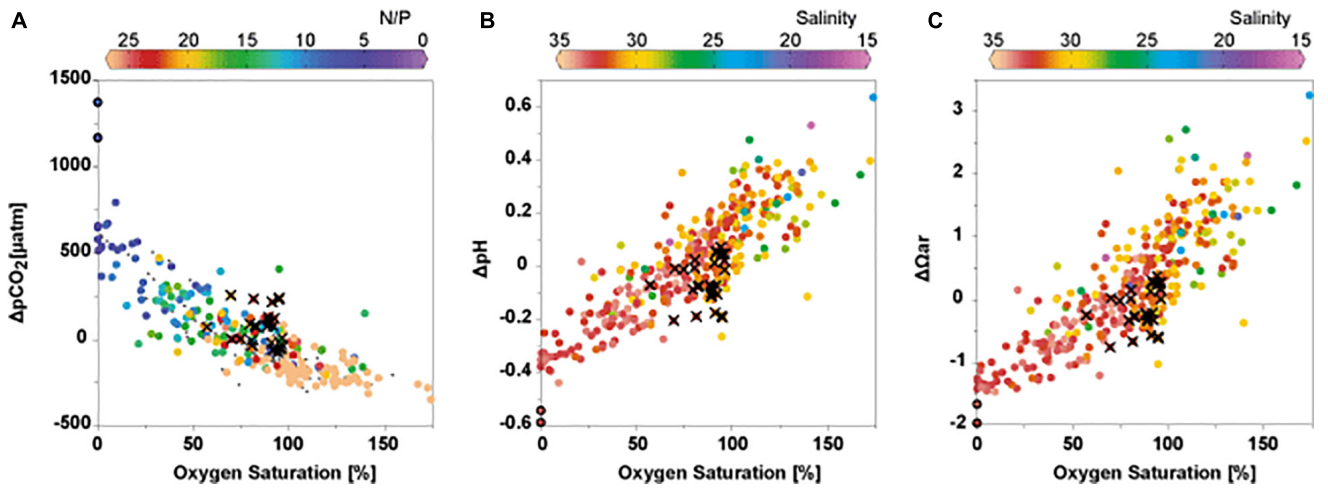


FIGURE 6 | (A) ΔpCO_2, **(B)** ΔpH, and **(C)** $\Delta\Omega$ plotted against oxygen saturation %. Color indicates ratio of DIN (nitrate + nitrite + ammonia) over phosphate in **(A)**, and S in **(B,C)**. Gray dots are data after November 2015, when nutrient data are not available. Crosses represent data for samples collected in December. Black circles demonstrate the aragonite undersaturations and anoxic waters observed in August 2013 and July 2014.

Nishio et al., 1982; Takii et al., 2002). Significant denitrification in the bottom waters is also expected to occur in summer (Koike, 1993). In our observations, relationship between dissolved inorganic nitrogen (DIN: nitrate + nitrite + ammonia) and dissolved inorganic phosphorous (phosphate) indicates effects of anaerobic processes. As shown in **Figure 6**, N/P ratio in low oxygen water is much lower than the Redfield ratio of 16 (Redfield et al., 1963), although surface water in the bay has much larger N/P ratio (Kubo et al., 2019). The low N/P ratio can be caused by denitrification (removal of DIN) and/or efflux of phosphate from anoxic sediments (Golterman, 2001). Low N/P values are found in low DO% waters overall, not only in anoxic waters (**Figure 6**). This indicates that anaerobic remineralization, not only in anoxic bottom waters but also in anoxic bottom sediments, influences bottom water properties in the region. The DIN deficit (DIN – P × 16) in summer hypoxic/anoxic bottom water (DO < 61 μmol kg^{-1} at 20 m in July, August, and September) was −24.0 μmol kg^{-1} (−38.4 ∼ −9.0 μmol kg^{-1}). If this deficit represent the removal of DIN by denitrification, DIC produced by denitrification is estimated to be 21.2 μmol kg^{-1} (8.0∼33.9 μmol kg^{-1}; DIN deficit/(104 + 16) × 106; cf. Gruber and Sarmiento, 1997). Without this DIC, carbonate parameters in summer bottom water would change significantly: pCO_2 decreases by 136 μatm while pH and Ωar increases by 0.06 and 0.18, respectively. However, given that DIN deficit can be caused by efflux of phosphate from sediments (Golterman, 2001) and that N/P ratios in Tokyo Bay without denitrification should be greater than 16 (Kubo et al., 2019), these estimates could be either underestimates or overestimates. Nevertheless, these results demonstrate the importance of anaerobic remineralization processes on carbonate parameters in Tokyo Bay.

Figures 3 and **5** show that anaerobic remineralization in the water and sediments increases pCO_2 to as high as > 1,500 μatm and ΔpCO_2 as high as > 1,000 μatm, leading to sporadic aragonite undersaturation in the bottom waters. Notably, aragonite undersaturation and anoxia were observed at a depth of 16 m, and not in the bottom waters (22 m) in July 2014. The higher Ωar and DO values in the waters above and below 16 m imply that the aragonite undersaturation and anoxia were not developed *in situ* at station F3, but they initially occurred in the surrounding areas and then advected to station F3. Such advection of low DO water has been reported as a subsurface hypoxic water mass in a previous study focused on Tokyo Bay (Fujiwara and Yamada, 2002). In July and August 2015, when bottom anoxia was also observed, the Ωar values were greater than 1. It seems that ΔDIC in these waters were relatively high (∼175 μmol kg^{-2}) but were not enough to cause aragonite undersaturation. As ΔDIC should reflect total amount of organic matter remineralized through both aerobic and anaerobic oxidation, anoxic water does not necessarily always accompany aragonite undersaturation.

The scatter in **Figure 6** reflect the effects of non-physical processes other than photosynthesis and respiration on the carbonate parameters. For example, the waters collected in December tended to have higher ΔpCO_2 and lower ΔpH and ΔΩar values than those that were expected from the DO% (**Figure 6**), possibly due to the occurrence of an air–sea CO_2 disequilibrium after vertical mixing. Vertical mixing during fall/winter brings CO_2-enriched and DO-depleted bottom water to the surface. An air–sea gas exchange changes the properties to attain a DO% = 100% and Δ = 0. However, as compared to the DO exchange rate, the CO_2 exchange rate is considerably lower (e.g., Zeebe and Wolf-Gladrow, 2001), which causes deviations from the expected carbonate parameters, as observed in the data for waters collected in December (**Figure 6**). The large extent of scattering for the low-salinity waters in the ΔpH-DO% and ΔΩar-DO% plots may also reflect differences in gas exchange rate between the oxygen and CO_2. Variability in the TA of freshwater end-members is another possible reason for the scattering.

Furthermore, the dissolution of $CaCO_3$ has been suggested by the high TA relative to the S values in low-**Ω** bottom waters of some coastal regions (e.g., Cross et al., 2013; Wang et al., 2017). In Tokyo Bay, elevated TA values were observed (**Figure 4A**) in cold waters during winter, and not in the low-**Ω**ar bottom waters during the summer. This elevation from the regression line in **Figure 4A** was observed every year, by an average of 24 μmol kg^{-1} (n = 65) and up to 81 μmol kg^{-1} for waters at T < 13°C. Since the **Ω**ar values of these waters are high (2.8 ± 0.5) and that sedimentary dissolution of $CaCO_3$ is a slow process (time required for complete dissolution of available aragonite solid is 20,000 days at **Ω** = 0.5, Cross et al., 2013), the elevated TA values are probably not caused by $CaCO_3$ dissolution. An increase in the TA during winter is not evident in offshore subtropical source water (Ishii et al., 2011) and in river water (Bureau of Waterworks Tokyo Metropolitan Government). Since surface water at higher latitudes tends to have higher TA at the same salinity level (Takatani et al., 2014), the observed increase in TA could be explained if water of northern-origin flows into Tokyo Bay every winter. However, to the best of the authors' knowledge, this has not been reported. Particulate and dissolved organic matter (POM and DOM) are known to affect the TA of coastal water samples (Cai et al., 1998; Kim et al., 2006; Hernández-Ayon et al., 2007; Kim and Lee, 2009). However, the POM and DOM concentrations observed at our study sites are high in summer and low in winter (Kubo et al., 2015; Kubo and Kanda, 2017). Therefore, the elevated TA during winter cannot be explained by the organic contributions. Anaerobic remineralization processes such as denitrification and sulfate reduction can also increase the TA (Hu and Cai, 2011; Krumins et al., 2013). Although increase in TA was not evident in the hypoxic/anoxic summer bottom water, sediment denitrification can be stimulated in winter by supplying O_2 to promote nitrification or NO_3 itself into nitrate-limited sediment (Bonaglia et al., 2014). Quantitative analysis of the TA efflux from the sediment may clarify the reason for the TA elevation in winter waters and its importance in the carbonate system of Tokyo Bay.

Future Progress of Ocean Acidification

In this section, the future changes in the pH and **Ω**ar values of surface and bottom waters at station F3 are estimated. As per the report by Yamamoto-Kawai et al. (2015), the future DIC values are calculated as DIC = DIC_{EQ} + ΔDIC, where DIC_{EQ} is the DIC of the water that is in equilibrium with atmospheric CO_2, and ΔDIC represents an air–sea disequilibrium caused by an insufficient air–sea gas exchange, biological activities, etc. Using the CO2SYS program, the mean DIC_{EQ} of the study period with atmospheric xCO_2 of 400 ppm is estimated from the monthly mean T_{obs}, S_{obs}, and TA^{phys}. Then, ΔDIC is calculated by subtracting DIC_{EQ} from the monthly mean of the observed DIC. This is similar to the calculations for the carbonate parameters in the physical processes-only case and the Δ values, with the only difference being that monthly mean values were used instead of each individual observation. Under the assumption that the ΔDIC remains unchanged over time, ΔDIC is added to DIC_{EQ} estimated for the water under future xCO_2 conditions. Future changes in the pH and **Ω**ar were then estimated using the derived DIC along with T_{obs}, S_{obs}, and TA^{phys} values.

Figure 7 shows changes in pH and **Ω**ar with increasing atmospheric xCO_2. It is predicted that in future, the decrease in the pH of surface waters will be larger in winter than that in summer (**Figure 7C**). In contrast, the decrease in the pH of bottom waters will be larger in summer than that in winter, due to the lower buffer capacity of waters with higher pCO_2. Aragonite undersaturation in bottom waters will be a common event in August when the atmospheric xCO_2 values reach 500 ppm (in the year 2043 and 2057 in RCP 8.5 and RCP6.0 scenario, respectively). When the atmospheric xCO_2 is 700 ppm (in the year 2073 in RCP8.5, after the end of this century in RCP6.0), aragonite undersaturation in the bottom waters lasts for ∼3 months from July to September (**Figure 7B**).

Yamamoto-Kawai et al. (2015) have estimated that since 1950/1960s, eutrophication has increased the summer bottom water DIC by 46 μmol kg^{-1} and decreased summer surface water DIC by 46 μmol kg^{-1}. When we remove these changes in DIC in the calculation of future pH and **Ω**ar for summer months (from June to September), results change significantly (**Figure 7**). Under the atmospheric xCO_2 of 700 ppm, removal of eutrophication effect decreases pH by ∼0.10 and **Ω**ar by ∼0.48 in the surface water (red filled circles and red open circles). In the bottom water, the pH and **Ω**ar values increase by ∼0.14 and 0. 30, respectively (red filled squares and red open squares) And aragonite undersaturation occurs only in August. In addition, in the absence of eutrophication, the rate of decrease in pH (for every 100 ppm increase in xCO_2) is reduced from 0.076 to 0.067 in December and from 0.102 to 0.096 in August (mean rate for xCO_2 range from 400 to 700 ppm; **Figure 7**). The mean **Ω**ar in August becomes < 1 when the xCO_2 value reaches 650 ppm (in the year 2067 and 2095 in the RCP 8.5 and 6.0 scenarios, respectively), indicating that de-eutrophication can postpone the timing of bottom aragonite undersaturation by 24 and 38 years, RCP 8.5 and RCP6.0 scenarios, respectively. Nevertheless, de-eutrophication should be accompanied with an effort to maintain low atmospheric xCO_2 values (below 650 ppm) to ensure that the water in Tokyo Bay is oversaturated with respect to aragonite throughout the year.

SUMMARY AND CONCLUSION

Seven years of observations have revealed the seasonal and interannual variations in the carbonate parameters and the processes affecting the carbonate system in Tokyo Bay. In the surface layer, the **Ω**ar increases by ∼1.0 from winter to summer because of warming. The sporadic extreme freshening caused by river water input lowers the **Ω**ar by ∼1.0. These physical processes do not cause large variations in pCO_2 and pH when a CO_2 equilibrium is achieved by an air-sea gas exchange. In contrast, the active photosynthetic processes in this highly eutrophic bay significantly impact the carbonate parameters. Surface water was undersaturated with respect to atmospheric CO_2 for most months, making the bay a strong

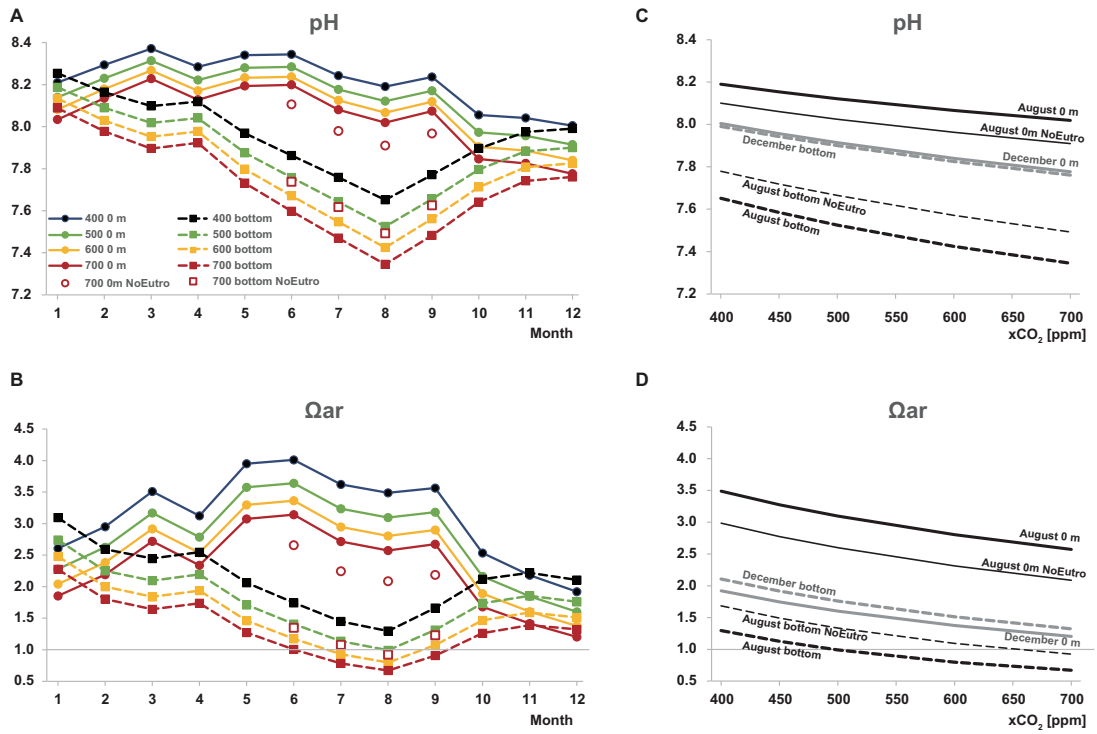


FIGURE 7 | Predicted changes in **(A,C)** pH and **(B,D)** Ωar in the surface (solid lines) and the bottom (dashed lines) waters with increasing atmospheric xCO_2. **(A,B)** Show seasonal variations. **(C,D)** Indicate future progress of ocean acidification in August (black lines) and December (gray lines). Estimated pH and Ωar values in the absence of eutrophication are indicated as open symbols **(A,B)** or thin lines **(C,D)**.

CO_2 sink (Kubo et al., 2017). Quantitative evaluation shows that photosynthesis, together with other non-physical processes, decreases the pCO_2 in surface waters by up to 345 μatm, causing both the pH and Ωar of surface waters to increase by up to 0.6 and 3.3, respectively. In the bottom layer, remineralization is the major process controlling the carbonate parameters. Aragonite undersaturation was observed twice during the study period in anoxic waters. The relationship between pCO_2 and DO% suggests that anaerobic remineralization under anoxic conditions lowered the Ωar value, causing undersaturation. This suggests that anoxic conditions can enhance ocean acidification at bottom water which can be critical to the benthic marine organisms. In addition, advection of the anoxic and aragonite undersaturated seawater to the upper water column can be detrimental to the planktonic organisms in Tokyo Bay.

If the concentration of atmospheric CO_2 continues to increase, aragonite undersaturation of the summer bottom water will be a common event in the Tokyo Bay in the near future. De-eutrophication, resulting from pollution control, can decelerate ocean acidification and postpone the occurrence of prolonged aragonite undersaturation in the bottom waters. De-eutrophication will also improve the oxygen conditions in summer bottom waters, thereby suppressing anoxic remineralization and sporadic aragonite undersaturation. However, if atmospheric CO_2 exceeds 650 ppm, aragonite undersaturation will be a common feature in the summer bottom waters, even if hypoxia/anoxia are alleviated by de-eutrophication.

DATA AVAILABILITY STATEMENT

The raw data supporting the conclusions of this article will be made available by the authors, without undue reservation.

AUTHOR CONTRIBUTIONS

MY-K and HK contributed the concept and design of the study. JK, MY-K, and SI collected the samples during field samplings and analyzed the samples. MY-K drafted the manuscript. All authors contributed to the manuscript revision, read, and approved the submitted version.

ACKNOWLEDGMENTS

We thank the crews of the R/V Seiyo-maru as well as the many participants in the sampling cruises. We also thank Dr. Atsushi Kubo for providing us with the nutrient data. We are grateful to the Fleet Management Office at the Tokyo University of Marine Science and Technology for their assistance in coordinating the observations.

REFERENCES

Bednaršek, N., Harvey, C. J., Kaplan, I. C., Feely, R. A., and Možina, J. (2016). Pteropods on the edge: cumulative effects of ocean acidification, warming, and deoxygenation. *Prog. Oceanogr.* 145, 1–24. doi: 10.1016/j.pocean.2016.04.002

Bonaglia, S., Deutsch, B., Bartoli, M., Marchant, H. K., and Brüchert, V. (2014). Seasonal oxygen, nitrogen and phosphorus benthic cycling along an impacted Baltic Sea estuary: regulation and spatial patterns. *Biogeochemistry* 119, 139–160. doi: 10.1007/s10533-014-9953-6

Breitburg, D., Levin, L. A., Oschlies, A., Grégoire, M., Chavez, F. P., Conley, D. J., et al. (2018). Declining oxygen in the global ocean and coastal waters. *Science* 359:eaam7240.

Cai, W. J., Hu, X., Huang, W. J., Murrell, M. C., Lehrter, J. C., Lohrenz, S. E., et al. (2011). Acidification of subsurface coastal waters enhanced by eutrophication. *Nat. Geosci.* 4, 766–770. doi: 10.1038/ngeo1297

Cai, W.-J., Wang, Y., and Hodson, R. E. (1998). Acid-base properties of dissolved organic matter in the estuarine waters of Georgia, USA. *Geochimica et Cosmochimica Acta* 62, 473–483. doi: 10.1016/s0016-7037(97)00363-3

Costanza, R., d'Arge, R., De Groot, R., Farber, S., Grasso, M., Hannon, B., et al. (1997). The value of the world's ecosystem services and natural capital. *Nature* 387, 253–260.

Cross, J. N., Mathis, J. T., Bates, N. R., and Byrne, R. H. (2013). Conservative and non-conservative variations of total alkalinity on the southeastern Bering Sea shelf. *Mar. Chem.* 154, 100–112. doi: 10.1016/j.marchem.2013.05.012

Dickson, A. G. (1990). Thermodynamics of the dissociation of boric acid in synthetic seawater from 273.15 to 318.15 K. *Deep Sea Res. A. Oceanogr. Res. Papers* 37, 755–766. doi: 10.1016/0198-0149(90)90004-f

Dickson, A. G., Sabine, C. L., and Christian, J. R. (2007). *Guide to Best Practices for Ocean CO2 Measurements*. British Columbia: North Pacific Marine Science Organization.

Dickson, A. G., and Millero, F. J. (1987). A comparison of the equilibrium constants for the dissociation of carbonic acid in seawater media. *Deep Sea Res. A. Oceanogr. Res. Papers* 34, 1733–1743. doi: 10.1016/0198-0149(87)90021-5

Doney, S. C., Busch, D. S., Cooley, S. R., and Kroeker, K. J. (2020). The impacts of ocean acidification on marine ecosystems and reliant human communities. *Annu. Rev. Environ. Resour.* 45, 83–112. doi: 10.1146/annurev-environ-012320-083019

Duarte, C. M., Hendriks, I. E., Moore, T. S., Olsen, Y. S., Steckbauer, A., Ramajo, L., et al. (2013). Is ocean acidification an open-ocean syndrome? understanding anthropogenic impacts on seawater pH. *Estuaries Coasts* 36, 221–236. doi: 10.1007/s12237-013-9594-3

Feely, R. A., Okazaki, R. R., Cai, W. J., Bednaršek, N., Alin, S. R., Byrne, R. H., et al. (2018). The combined effects of acidification and hypoxia on pH and aragonite saturation in the coastal waters of the California current ecosystem and the northern Gulf of Mexico. *Continental Shelf Res.* 152, 50–60. doi: 10.1016/j.csr.2017.11.002

Field, C. B., Barros, V., Stocker, T. F., Dahe, Q., Mach, K. J., Plattner, G.-K., et al. (2011). *IPCC Workshop on Impacts of Ocean Acidification on Marine Biology and Ecosystems*. US: Carnegie Institution, Stanford.

Fujiwara, T., and Yamada, Y. (2002). Inflow of oceanic water into Tokyo Bay and generation of a subsurface hypoxic water mass. *J. Geophys. Res. Oceans* 107, 13–11.

Furukawa, K., and Okada, T. (2006). "Tokyo Bay: its environmental status—past, present, and future," in *The Environment in Asia Pacific Harbours*, ed. E. Wolanski (Dordrecht: Springer), 15–34. doi: 10.1007/1-4020-3655-8_2

Gao, K., Beardall, J., Häder, D. P., Hall-Spencer, J. M., Gao, G., and Hutchins, D. A. (2019). Effects of ocean acidification on marine photosynthetic organisms under the concurrent influences of warming, UV radiation and deoxygenation. *Front. Mar. Sci.* 6:322.

Gobler, C. J., and Baumann, H. (2016). Hypoxia and acidification in ocean ecosystems: coupled dynamics and effects on marine life. *Biol. Lett.* 12:20150976. doi: 10.1098/rsbl.2015.0976

Golterman, H. L. (2001). Phosphate release from anoxic sediments or 'What did Mortimer really write?' *Hydrobiologia*, 450, 99–106. doi: 10.1023/A:1017559903404

Gruber, N., and Sarmiento, J. L. (1997). Global patterns of marine nitrogen fixation and denitrification. *Global Biogeochem. Cycles* 11, 235–266. doi: 10.1029/97gb00077

Hall-Spencer, J. M., and Harvey, B. P. (2019). Ocean acidification impacts on coastal ecosystem services due to habitat degradation. *Emerg. Top. Life Sci.* 3, 197–206. doi: 10.1042/etls20180117

Hancock, J. R., and Place, S. P. (2016). Impact of ocean acidification on the hypoxia tolerance of the woolly sculpin, *Clinocottus analis*. *Conserv. Physiol.* 4:cow040. doi: 10.1093/conphys/cow040

Harvey, B. P., Gwynn-Jones, D., and Moore, P. J. (2013). Meta-analysis reveals complex marine biological responses to the interactive effects of ocean acidification and warming. *Ecol. Evol.* 3, 1016–1030. doi: 10.1002/ece3.516

Hendriks, I. E., Duarte, C. M., and Álvarez, M. (2010). Vulnerability of marine biodiversity to ocean acidification: a meta-analysis. *Estuar. Coast. Shelf Sci.* 86, 157–164. doi: 10.1016/j.ecss.2009.11.022

Heuer, R. M., and Grosell, M. (2014). Physiological impacts of elevated carbon dioxide and ocean acidification on fish. *Am. J. Physiol. Regul. Integr. Comp. Physiol.* 307, R1061–R1084.

Hinga, K. R. (2002). Effects of pH on coastal marine phytoplankton. *Mar. Ecol. Prog. Ser.* 238, 282–300. doi: 10.3354/meps238281

Hu, X., and Cai, W. J. (2011). An assessment of ocean margin anaerobic processes on oceanic alkalinity budget. *Global Biogeochem. Cycles* 25. doi: 10.1007/978-3-662-05127-6_10

Hu, X., and Cai, W. J. (2013). Estuarine acidification and minimum buffer zone—a conceptual study. *Geophys. Res. Lett.* 40, 5176–5181. doi: 10.1002/grl.51000

Hönisch, B., Ridgwell, A., Schmidt, D. N., Thomas, E., Gibbs, S. J., Sluijs, A., et al. (2012). The geological record of ocean acidification. *Science* 335, 1058–1063.

IPCC (2014). "Climate change 2014: synthesis report," in *Contribution of Working Groups I, II and III to the Fifth Assessment Report of the Intergovernmental Panel on Climate Change, Core Writing Team*, eds R. K. Pachauri and L. A. Meyer (Geneva: IPCC).

Ishii, M., Hasegawa, K., and Kakino, J. (2008). Long-term fluctuations of the water quality in Tokyo Bay judged from a data set of Chiba prefecture. *Bull. Jpn. Soc. Fish. Oceanogr.* 72, 189–199. doi: 10.1007/bf02489226

Ishii, M., Kosugi, N., Sasano, D., Saito, S., Midorikawa, T., and Inoue, H. Y. (2011). Ocean acidification off the south coast of Japan: a result from time series observations of CO2 parameters from 1994 to 2008. *J. Geophys. Res. Oceans* 116. doi: 10.1029/2010JC006831

Ishizu, M., Miyazawa, Y., Tsunoda, T., and Ono, T. (2019). Long-term trends in pH in Japanese coastal seawater. *Biogeosciences* 16, 4747–4763. doi: 10.5194/bg-16-4747-2019

Kanda, J., Chomthaison, P., Horimoto, N., Yamaguchi, Y., and Ishimaru, T. (2008). Time-series variations in nutrient concentrations at two monitoring stations in Tokyo Bay. *J. Jpn. Soc. Water Environ.* 31, 559–564. doi: 10.2965/jswe.31.559

Kim, H. C., Lee, K., and Choi, W. (2006). Contribution of phytoplankton and bacterial cells to the measured alkalinity of seawater. *Limnol. Oceanogr.* 51, 331–338. doi: 10.4319/lo.2006.51.1.0331

Kim, H. C., and Lee, K. (2009). Significant contribution of dissolved organic matter to seawater alkalinity. *Geophys. Res. Lett.* 36:L20603.

Kodama, K., and Horiguchi, T. (2011). Effects of hypoxia on benthic organisms in Tokyo Bay, Japan: a review. *Mar. Pollut. Bull.* 63, 215–220. doi: 10.1016/j.marpolbul.2011.04.022

Koike, I. (1993). "Micorbiota," in *Tokyo Bay*, ed. N. Ogura (Tokyo: Koseisha Koseikaku).

Koike, I., and Hattori, A. (1978). Denitrification and ammonia formation in anaerobic coastal sediments. *Appl. Environ. Microbiol.* 35, 278–282. doi: 10.1128/aem.35.2.278-282.1978

Kroeker, K. J., Kordas, R. L., Crim, R. N., and Singh, G. G. (2010). Meta-analysis reveals negative yet variable effects of ocean acidification on marine organisms. *Ecol. Lett.* 13, 1419–1434. doi: 10.1111/j.1461-0248.2010.01518.x

Kroeker, K. J., Kordas, R. L., Crim, R., Hendriks, I. E., Ramajo, L., Singh, G. S., et al. (2013). Impacts of ocean acidification on marine organisms: quantifying sensitivities and interaction with warming. *Global Change Biol.* 19, 1884–1896. doi: 10.1111/gcb.12179

Krumins, V., Gehlen, M., Arndt, S., Van Cappellen, P., and Regnier, P. (2013). Dissolved inorganic carbon and alkalinity fluxes from coastal marine sediments: model estimates for different shelf environments and sensitivity to global change. *Biogeosciences* 10, 371–398. doi: 10.5194/bg-10-371-2013

Kubo, A. (2015). *Carbon Cycling in Tokyo Bay*. [dissertation], Tokyo University of Marine Science and Technology, Japan.

Kubo, A., Hashihama, F., Kanda, J., Horimoto-Miyazaki, N., and Ishimaru, T. (2019). Long-term variability of nutrient and dissolved organic matter concentrations in Tokyo Bay between 1989 and 2015. *Limnol. Oceanogr.* 64, S209–S222.

Kubo, A., Maeda, Y., and Kanda, J. (2017). A significant net sink for CO2 in Tokyo Bay. *Sci. Rep.* 7:44355.

Kubo, A., Yamamoto-Kawai, M., and Kanda, J. (2015). Seasonal variations in concentration and lability of dissolved organic carbon in Tokyo Bay. *Biogeosciences* 12:269. doi: 10.5194/bg-12-269-2015

Kubo, A., and Kanda, J. (2017). Seasonal variations and sources of sedimentary organic carbon in Tokyo Bay. *Mar. Pollut. Bull.* 114, 637–643. doi: 10.1016/j.marpolbul.2016.10.030

Laurent, A., Fennel, K., Cai, W. J., Huang, W. J., Barbero, L., and Wanninkhof, R. (2017). Eutrophication-induced acidification of coastal waters in the northern Gulf of Mexico: insights into origin and processes from a coupled physical-biogeochemical model. *Geophys. Res. Lett.* 44, 946–956. doi: 10.1002/2016gl071881

Lewis, E. R., and Wallace, D. W. R. (1998). *Program Developed for CO2 System Calculations (No. cdiac: CDIAC-105)*. U.S: Department of Energy Office of Scientific and Technical Information.

Hernández-Ayon, M. J., Zirino, A., Dickson, A. G., Camiro-Vargas, T., and Valenzuela-Espinoza, E. (2007). Estimating the contribution of organic bases from microalgae to the titration alkalinity in coastal seawaters. *Limnol. Oceanogr. Methods* 5, 225–232. doi: 10.4319/lom.2007.5.225

McNeil, B. I., and Matear, R. J. (2008). Southern Ocean acidification: a tipping point at 450-ppm atmospheric CO2. *Proc. Natl. Acad. Sci. U.S.A.* 105, 18860–18864. doi: 10.1073/pnas.0806318105

Mehrbach, C., Culberson, C. H., Hawley, J. E., and Pytkowicx, R. M. (1973). Measurement of the apparent dissociation constants of carbonic acid in seawater at atmospheric pressure 1. *Limnol. Oceanogr.* 18, 897–907. doi: 10.4319/lo.1973.18.6.0897

Miller, S. H., Breitburg, D. L., Burrell, R. B., and Keppel, A. G. (2016). Acidification increases sensitivity to hypoxia in important forage fishes. *Mar. Ecol. Prog. Ser.* 549, 1–8. doi: 10.3354/meps11695

Mucci (1983). The solubility of calcite and aragonite in seawater at various salinities, temperatures, and one atmosphere total pressure. *Am. J. Sci.* 283, 780–799. doi: 10.2475/ajs.283.7.780

Nishio, T., Koike, I., and Hattori, A. (1982). Denitrification, nitrate reduction, and oxygen consumption in coastal and estuarine sediments. *Appl. Environ. Microbiol.* 43, 648–653. doi: 10.1128/aem.43.3.648-653.1982

Nomura, H. (1998). Changes in red tide events and phytoplankton community composition in Tokyo Bay from the histrorical plankton records in a period between 1907 and 1997. *Umi no Kenkyu* 7, 159–178. doi: 10.5928/kaiyou.7.159

Nomura, H., and Yoshida, M. (1997). Recent occurrence of phytoplankton in the hyper-eutrophicated inlet, Tokyo Bay, central Japan. *La Mer* 35, 107–121.

Ogawa, N., and Ogura, N. (1997). Dynamics of particulate organic matter in the Tamagawa Estuary and inner Tokyo Bay. *Estuar. Coast. Shelf Sci.* 44, 263–273. doi: 10.1006/ecss.1996.0118

Okada, T., Nakayama, K., Takao, T., and Furukawa, K. (2011). Influence of freshwater input and bay reclamation on long-term changes in seawater residence times in Tokyo Bay, Japan. *Hydrol. Process.* 25, 2694–2702. doi: 10.1002/hyp.8010

Pacella, S. R., Brown, C. A., Waldbusser, G. G., Labiosa, R. G., and Hales, B. (2018). Seagrass habitat metabolism increases short-term extremes and long-term offset of CO2 under future ocean acidification. *Proc. Natl. Acad. Sci. U.S.A.* 115, 3870–3875. doi: 10.1073/pnas.1703445115

Palacios, S. L., and Zimmerman, R. C. (2007). Response of eelgrass Zostera marina to CO2 enrichment: possible impacts of climate change and potential for remediation of coastal habitats. *Mar. Ecol. Prog. Ser.* 344, 1–13. doi: 10.3354/meps07084

Redfield, A. C., Ketchum, B. H., and Richards, F. A. (1963). "The influence of organisms on the composition of seawater," in *The Sea*, ed. M. N. Hill (Geneva: Interscience Publishers), 26–77.

Rheuban, J. E., Doney, S. C., McCorkle, D. C., and Jakuba, R. W. (2019). Quantifying the effects of nutrient enrichment and freshwater mixing on coastal ocean acidification. *J. Geophys. Res. Oceans* 124, 9085–9100. doi: 10.1029/2019jc015556

Royal Society (2005). *Ocean Acidification Due to Increasing Atmospheric Carbon Dioxide*. London: The Royal Society.

Salisbury, J., Green, M., Hunt, C., and Campbell, J. (2008). Coastal acidification by rivers: a threat to shellfish? *Eos Trans. Am. Geophys. Union* 89, 513–513. doi: 10.1029/2008eo500001

Sato, C., Nakayama, K., and Furukawa, K. (2012). Contributions of wind and river effects on DO concentration in Tokyo Bay. *Estuar. Coast. Shelf Sci.* 209, 91–97. doi: 10.1016/j.ecss.2012.05.023

Shibata, Y., and Aruga, Y. (1982). Variation of chlorophyll a concentration and photosynthetic activity of phytoplankton in Tokyo Bay. *La Mer* 20, 75–92.

Stewart-Sinclair, P. J., Last, K. S., Payne, B. L., and Wilding, T. A. (2020). A global assessment of the vulnerability of shellfish aquaculture to climate change and ocean acidification. *Ecol. Evol.* 10, 3518–3534. doi: 10.1002/ece3.6149

Taguchi, F., Fujiwara, T., Yamada, Y., Fujita, K., and Sugiyama, M. (2009). Alkalinity in costal seas around Japan. *Bull. Coast. Oceanogr.* 47, 71–75.

Takatani, Y., Enyo, K., Iida, Y., Kojima, A., Nakano, T., Sasano, D., et al. (2014). Relationships between total alkalinity in surface water and sea surface dynamic height in the Pacific Ocean. *J. Geophys. Res. Oceans* 119, 2806–2814.

Takii, S., Tanaka, H., Kohata, K., Nakamura, Y., Ogura, H., and Takeshita, S. (2002). Seasonal changes in sulfate reduction in sediments in the inner part of Tokyo Bay. *Microbes Environ.* 17, 10–17. doi: 10.1264/jsme2.2002.10

Wallace, R. B., Baumann, H., Grear, J. S., Aller, R. C., and Gobler, C. J. (2014). Coastal ocean acidification: the other eutrophication problem. *Estuar. Coast. Shelf Sci.* 148, 1–13. doi: 10.1016/j.ecss.2014.05.027

Wang, Z. A., Lawson, G. L., Pilskaln, C. H., and Maas, A. E. (2017). Seasonal controls of aragonite saturation states in the G ulf of M aine. *J. Geophys. Res. Oceans* 122, 372–389. doi: 10.1002/2016jc012373

Weiss, R. F. (1970). *The Solubility of Nitrogen, Oxygen and Argon in Water and Seawater. in Deep Sea Research and Oceanographic Abstracts*. Amsterdam: Elsevier, 721–735.

Yamamoto-Kawai, M., Kawamura, N., Ono, T., Kosugi, N., Kubo, A., Ishii, M., et al. (2015). Calcium carbonate saturation and ocean acidification in Tokyo Bay, Japan. *J. Oceanogr.* 71, 427–439. doi: 10.1007/s10872-015-0302-8

Yamamoto-Kawai, M., McLaughlin, F. A., and Carmack, E. C. (2011). Effects of ocean acidification, warming and melting of sea ice on aragonite saturation of the Canada Basin surface water. *Geophys. Res. Lett.* 38. doi: 10.1029/2010GL045501

Yao, W., and Byrne, R. H. (1998). Simplified seawater alkalinity analysis: use of linear array spectrometers. *Deep Sea Res. I Oceanogr. Res. Papers* 45, 1383–1392. doi: 10.1016/s0967-0637(98)00018-1

Zeebe, R. E., and Wolf-Gladrow, D. (2001). *CO2 in Seawater: Equilibrium, Kinetics, Isotopes (No. 65)*. Texas: Gulf Professional Publishing.

Zhao, Y., Liu, J., Uthaipan, K., Song, X., Xu, Y., He, B., et al. (2020). Dynamics of inorganic carbon and pH in a large subtropical continental shelf system: interaction between eutrophication, hypoxia, and ocean acidification. *Limnol. Oceanogr.* 65, 1359–1379. doi: 10.1002/lno.11393

Conflict of Interest: The authors declare that the research was conducted in the absence of any commercial or financial relationships that could be construed as a potential conflict of interest.

Copyright © 2021 Yamamoto-Kawai, Ito, Kurihara and Kanda. This is an open-access article distributed under the terms of the Creative Commons Attribution License (CC BY). The use, distribution or reproduction in other forums is permitted, provided the original author(s) and the copyright owner(s) are credited and that the original publication in this journal is cited, in accordance with accepted academic practice. No use, distribution or reproduction is permitted which does not comply with these terms.

frontiers in Marine Science

ORIGINAL RESEARCH
published: 11 June 2021
doi: 10.3389/fmars.2021.590020

Continuous Monitoring and Future Projection of Ocean Warming, Acidification, and Deoxygenation on the Subarctic Coast of Hokkaido, Japan

Masahiko Fujii[1,2], Shintaro Takao[3], Takuto Yamaka[2], Tomoo Akamatsu[2], Yamato Fujita[2], Masahide Wakita[4], Akitomo Yamamoto[5] and Tsuneo Ono[6]*

[1] Faculty of Environmental Earth Science, Hokkaido University, Sapporo, Japan, [2] Graduate School of Environmental Science, Hokkaido University, Sapporo, Japan, [3] Center for Global Environmental Research, National Institute for Environmental Studies, Tsukuba, Japan, [4] Mutsu Institute for Oceanography, Japan Agency for Marine-Earth Science and Technology, Aomori, Japan, [5] Japan Agency for Marine-Earth Science and Technology, Yokohama, Japan, [6] National Research Institute of Far Seas Fisheries, Fisheries Research Agency, Yokohama, Japan

OPEN ACCESS

Edited by:
Richard Alan Feely, National Oceanic and Atmospheric Administration (NOAA), United States

Reviewed by:
Dwight Kuehl Gledhill, National Oceanic and Atmospheric Administration (NOAA), United States
Kim Irene Currie, National Institute of Water and Atmospheric Research (NIWA), New Zealand

***Correspondence:**
Masahiko Fujii
mfujii@ees.hokudai.ac.jp

Specialty section:
This article was submitted to Coastal Ocean Processes, a section of the journal Frontiers in Marine Science

Received: *31 July 2020*
Accepted: *10 May 2021*
Published: *11 June 2021*

Citation:
Fujii M, Takao S, Yamaka T, Akamatsu T, Fujita Y, Wakita M, Yamamoto A and Ono T (2021) Continuous Monitoring and Future Projection of Ocean Warming, Acidification, and Deoxygenation on the Subarctic Coast of Hokkaido, Japan. Front. Mar. Sci. 8:590020. doi: 10.3389/fmars.2021.590020

As the ocean absorbs excessive anthropogenic CO_2 and ocean acidification proceeds, it is thought to be harder for marine calcifying organisms, such as shellfish, to form their skeletons and shells made of calcium carbonate. Recent studies have suggested that various marine organisms, both calcifiers and non-calcifiers, will be affected adversely by ocean warming and deoxygenation. However, regardless of their effects on calcifiers, the spatiotemporal variability of parameters affecting ocean acidification and deoxygenation has not been elucidated in the subarctic coasts of Japan. This study conducted the first continuous monitoring and future projection of physical and biogeochemical parameters of the subarctic coast of Hokkaido, Japan. Our results show that the seasonal change in biogeochemical parameters, with higher pH and dissolved oxygen (DO) concentration in winter than in summer, was primarily regulated by water temperature. The daily fluctuations, which were higher in the daytime than at night, were mainly affected by daytime photosynthesis by primary producers and respiration by marine organisms at night. Our projected results suggest that, without ambitious commitment to reducing CO_2 and other greenhouse gas emissions, such as by following the Paris Agreement, the impact of ocean warming and acidification on calcifiers along subarctic coasts will become serious, exceeding the critical level of high temperature for 3 months in summer and being close to the critical level of low saturation state of calcium carbonate for 2 months in mid-winter, respectively, by the end of this century. The impact of deoxygenation might often be prominent assuming that the daily fluctuation in DO concentration in the future is similar to that at present. The results also suggest the importance of adaptation strategies by local coastal industries, especially fisheries, such as modifying aquaculture styles.

Keywords: ocean acidification, deoxygenation, subarctic, coast, monitoring, future projection, mitigation, adaptation

INTRODUCTION

Global change-driven global ocean warming, acidification, and deoxygenation are all thought to be caused primarily by excessive anthropogenic CO_2 emissions. Various studies have suggested that the rise in water temperature caused by global change will alter habitats and marine ecosystem functions [e.g., Intergovernmental Panel on Climate Change (IPCC), 2014]. However, the impacts of ocean acidification and deoxygenation are difficult to detect directly, and relatively little evidence has been reported.

Ocean acidification leads to lower pH in the surface ocean and the pH has already been lowered by 0.1 globally over the past century (Orr et al., 2005). The global average oceanic pH is currently around 8.1 and is anticipated to decrease to 7.8 by the end of this century (e.g., Feely et al., 2008; Intergovernmental Panel on Climate Change (IPCC), 2014). Recent studies have suggested that ocean acidification will affect marine organisms that form shells or bodies made of calcium carbonate (calcifiers) because these chemicals are more easily dissolved or harder to generate in high-CO_2, low-pH environments. The impact of ocean acidification on calcifiers has already been reported, such as the significant mortality of oyster (*Crassostrea gigas*) larvae (Feely et al., 2008; Barton et al., 2012) and damage to the carapaces of larval Dungeness crabs (*Metacarcinus magister*; Bednaršek et al., 2020) in the high-CO_2 environment of the Pacific northwest coast of the United States of America. Several studies have shown that ocean acidification also affects the life stages of calcifiers differently, and the larvae are more vulnerable to high CO_2 (e.g., Kurihara, 2008; Kimura et al., 2011; Waldbusser et al., 2015; Zhan et al., 2016; Onitsuka et al., 2018; Foo et al., 2020). Ocean acidification also affects non-calcifiers, such as by impairing the fertilization of eggs (e.g., Morita et al., 2009) and olfactory discrimination and homing ability (e.g., Munday et al., 2009, 2014; Dixson et al., 2015). Therefore, similar to ocean warming, ocean acidification also affects marine ecosystems widely.

Deoxygenation has long been recognized as a local phenomenon, such as that caused by blooms of red tides and subsequent extremely low dissolved oxygen (DO) concentration environments in the bottom layers. Recently, world-wide deoxygenation has been observed as a result of ocean warming followed by lower oxygen saturation in warmer waters, reduced air-sea oxygen exchange with stratification of the surface layer and increased consumption of DO by enhanced respiration and dissolution of organic matter at higher temperatures (e.g., Turner et al., 2005; Vaquer-Sunyer and Duarte, 2008; Rabalais et al., 2010; Frieder et al., 2012; Marumo and Yokota, 2012; Schmidtko et al., 2017; Christian and Ono, 2019). Deoxygenation affects various marine organisms more directly and acutely than ocean acidification. Moreover, recent studies have suggested combined multi-stressor synergistic effects of ocean acidification and deoxygenation on calcifiers that may magnify the adverse impacts (e.g., Melzner et al., 2013; DePasquale et al., 2015; Gobler and Baumann, 2016; IPCC, 2018).

Recent observational studies have shown that both physical and biogeochemical parameters regulating ocean acidification and deoxygenation vary markedly in space and time. For example, the spatiotemporal variability is generally much larger in coastal oceans than in open oceans (e.g., Wootton et al., 2008; Dai et al., 2009; Rabalais et al., 2010; Hofmann et al., 2011; Frieder et al., 2012; Baumann et al., 2014). The greater temporal variability is characterized by the larger seasonal and daily variation in coastal ocean parameters. Daily minimum saturation state value of aragonite (a polymorph of calcium carbonate; Ω_{arag}) of around 1, which is close to the undersaturated and is unsuitable for calcifiers, have already been recorded at night in some coastal oceans (e.g., Frieder et al., 2012). The daily minimum DO is similarly low in the coastal oceans, where deoxygenation is caused by coexisting drivers of global change and local human impacts, such as additive oxygen utilization stimulated by nutrient inputs from the land and aquaculture (e.g., Melzner et al., 2013; Wallace et al., 2014).

However, fewer studies have examined the effects of ocean acidification and deoxygenation on subarctic coasts compared to tropical and subtropical coasts (e.g., Hofmann et al., 2011), although several have examined the subarctic open ocean (e.g., Wakita et al., 2017). This is mainly because of the difficulty in deploying multi-year monitoring, especially in winter when bad weather often prevents observations. It is important to elucidate the impact of global change, especially ocean acidification, on subarctic coasts for two reasons. First, ocean acidification is considered to affect calcifiers in subarctic oceans more significantly than in tropical, subtropical, and temperate oceans, because high-latitude systems are generally less buffered than low latitude systems and likely experience a higher frequency occurrence of under-saturated conditions. The other is because there is a high local fishery dependence on marine calcifiers. Most of the subarctic coasts in Japan are in Hokkaido Prefecture, which also accounts for one-fourth of the total fish catch, half of the calcifier catch, and 60% of the shellfish catch in Japan (Ministry of Agriculture, Forestry and Fisheries website: https://www.maff.go.jp/e/index.html). Therefore, it is very important to elucidate the current status of ocean acidification and deoxygenation and predict the possible future status from the perspective of local societies and the marine ecosystem of the subarctic coasts.

To assess the impacts of ocean acidification and deoxygenation on coastal organisms properly, we need to make long-term, high-frequency measurements of environmental parameters in subarctic regions. To investigate the diurnal variation in physical and biogeochemical properties related to ocean warming and acidification and deoxygenation in the subarctic region, this study measured physical and biogeochemical parameters to elucidate the temporal variation and its causes in the subarctic coastal region. The results were used for future projection toward the end of this century. Based on the combined results, we hope to develop scientific guidelines to combat the impact of global change on marine ecosystems and relevant local industries along subarctic coasts.

MATERIALS AND METHODS

Monitoring Site

We established a site for monitoring and modeling physical and biogeochemical properties in Oshoro Bay, Hokkaido, Japan, as a representative subarctic coast site in Japan (**Figure 1**;

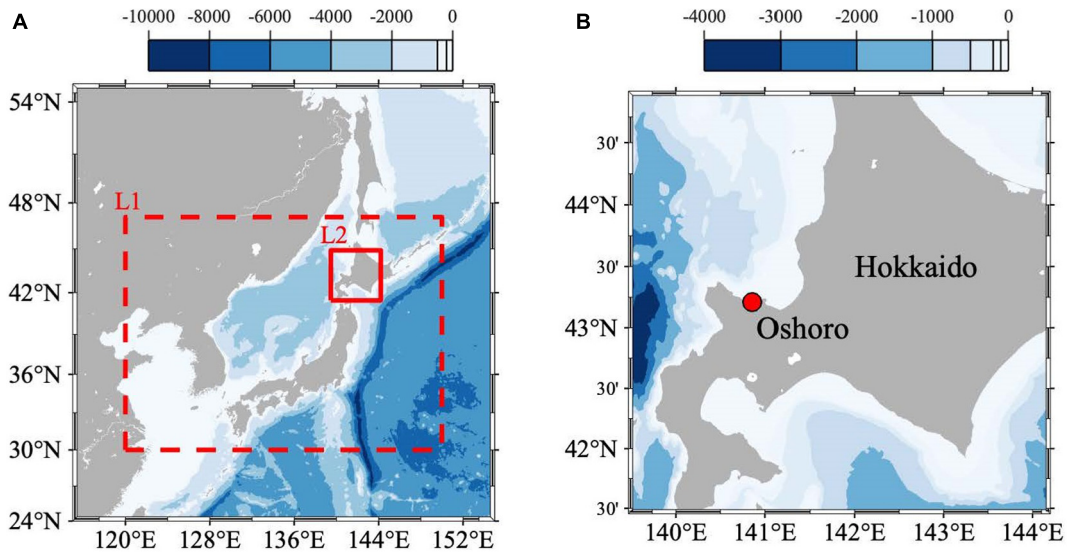


FIGURE 1 | (A) Model domains and bathymetry (color: m) of the double-nested Regional Ocean Modeling System (ROMS). The domains of the 1/3- (L1) and 1/15- (L2) degree models are surrounded by the dashed and solid red squares, respectively. **(B)** The location of the study site (140°51'30"E and 43°12'34"N) is indicated by the dotted red circle in the zoomed-in region of the ROMS-L2 domain.

Christian and Ono, 2019; Yamaka, 2019). The site is in the subarctic region of the Japan Sea and the longitude and latitude is 140.86°E and 43.21°N, respectively. Fisheries are a main local industry, and the target species include sea urchin (*Strongylocentrotus intermedius*), kelps (*Laminaria* spp.), Ezo abalone (*Haliotis discus hannai*), and scallops (*Mizuhopecten yessoensis*); all are representative subarctic fisheries species (Yamaka, 2019).

Monitoring

Since March 30, 2017, we have measured continuously temperature and salinity as physical parameters, and DO and pH (total scale) as biogeochemical parameters. A conductivity and temperature sensor (INFINITY-CTW ACTW-USB; JFE Advantech) was used to measure temperature and salinity hourly, while DO was measured hourly with a RINKO W AROW-USB (JFE Advantech). The accuracy of temperature, conductivity and DO is ±0.01°C, ±0.01 mS cm^{-1}, and non-linearity ± 2% FS (at 1 atm, 25°C), respectively. The range of the DO sensor was 0–20 mg l^{-1} DO concentration (or 0–200% DO saturation) and data beyond this range were eliminated. Calibration of the DO sensor was carried out by two-point (zero and span) calibration using 0 and 100% (saturated) oxygen waters. The two sensors have mechanical wipers that periodically sweep the sensing surface to keep the initial accuracy, avoiding bio-fouling without chemical materials and frequent maintenances.

To measure pH hourly, glass electrode pH sensors (SP-11 and SPS-14; Kimoto Electric) were used. The reproducibility of pH sensors is ±0.001. The sensors were calibrated against two seawater scale pH standard buffer solutions, 2-amino-2-hydroxymethyl-1, 3-propanediol (TRIS) and 2-aminopyridine (AMP). The sensors were withdrawn for maintenance and calibration at 1- to 3-month intervals to minimize measurement biases caused by bio-fouling and measurement drift. At each calibration, it was confirmed that the sensor kept its Nernst response (ca. 0.05916V/pH at 25°C and 35.0 salinity) within the range of ±0.5%.

Seawater samples were collected when the sensors were calibrated and analyzed using a total alkalinity (TA) titration analyzer (ATT-05; Kimoto Electric) to obtain the TA and a coulometer (MODEL 3000A; Nippon ANS) to determine the dissolved inorganic carbon (DIC) concentration (Wakita et al., 2017, 2021; Yamaka, 2019). The values were calibrated against certified reference material (CRM) provided by Prof. A. G. Dickson (Scripps Institution of Oceanography, University of California San Diego) and KANSO. The precision of the analyses of both the DIC and TA was smaller than ±2 μmol kg^{-1} based on replicate samples. Then, the pH (total scale) at the *in situ* temperature were calculated from the carbonate dissociation constants in Lueker et al. (2000) and temperature, salinity, TA, and DIC using CO2SYS (Pierrot et al., 2006). pH at time t [pH(t)] obtained by the sensor was then corrected its drift by the following equation:

$$\mathrm{pH}\,(t) \;= \mathrm{pH}_m\,(t) + \left(\mathrm{pH}_{\mathrm{sample}}(t_e) - \mathrm{pH}_m(t_e)\right) \;\times \frac{t - t_i}{t_e - t_i}, \tag{1}$$

where $\mathrm{pH}_m(t)$ represents measured value of pH by the sensor at the time t, $\mathrm{pH}_{\mathrm{sample}}(t_e)$ and $\mathrm{pH}_m(t_e)$ is the pH at the end time of each deployment (t_e) obtained by the seawater sample and sensor, respectively, and t_i is the start time of each deployment.

Equation (1) assumes that drift of the pH sensor increases linearly with time over the whole period of single deployment. However, actual time course of sensor drift is not linear, so this may cause significant error in the pH(t) value after the drift correction. In 2020, we made a 55-days deployment of the same

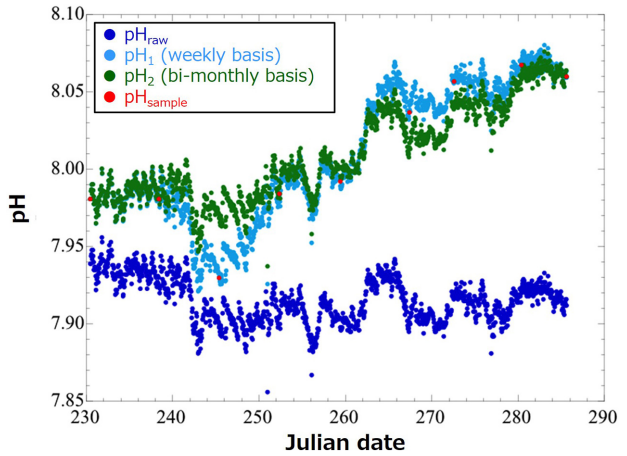


FIGURE 2 | Time-series of pH values in the Miyako Bay in August through October 2020. Dots in blue denote raw pH values obtained by a pH sensor (SP-11; pH_{raw}). Those in red demote pH values calculated by referring to pH values of water samples (pH_{sample}). Those in light blue and green show pH values after calibration and bias correction by pH values obtained by water samples weekly (pH_1; in light blue) and bi-monthly (at the initial and end time of the deployment; pH_2; in green).

pH sensor (SP-11) that we deployed in this study into the Miyako Bay, a bay in northern Japan having similar feature with that of the Oshoro Bay. At this time, we calculated pH(t) using the same Eq. (1) but with pH_{sample} data obtained by weekly basis [$pH_1(t)$] and those obtained by bi-monthly basis [at the initial and end time of the deployment; $pH_2(t)$], and compared the drift-corrected values (**Figure 2**). We found that the root mean square of difference between $pH_1(t)$ and $pH_2(t)$ over the whole deployment period was 0.015. We interpreted this value as the measure of the uncertainty of pH(t) originated from different frequency of the drift correction (10 days and 2 months in this case). Therefore, we evaluate that the uncertainty of pH(t) calculated in this study is in the same order and is small enough for monitoring in the coastal regions with relatively larger daily and seasonal variations.

Ω_{arag} of the seawater samples were calculated from the carbonate dissociation constants in Lueker et al. (2000) and temperature, salinity, TA, and DIC using CO2SYS (Pierrot et al., 2006). Ω_{arag} was also estimated using CO2SYS, with TA, the monitored temperature, and salinity. As no continuous monitoring TA data exist, we used the TA value obtained with a regression equation for north of 30°N in the North Pacific (Lee et al., 2006):

$$\begin{aligned} \mathrm{TA}(\mu\mathrm{mol\ kg^{-1}}) &= 2305 + 53.23\ (\mathrm{salinity} - 35) + 1.85 \\ &(\mathrm{salinity} - 35)^2 - 14.72\ (\mathrm{temperature}\ (^\circ\mathrm{C}) - 20) \\ &-0.158\ (\mathrm{temperature}\ (^\circ\mathrm{C}) - 20)^2 + 0.062 \\ &(\mathrm{temperature}\ (^\circ\mathrm{C}) - 20) \times \mathrm{longitude}\ (^\circ), \end{aligned} \quad (2)$$

where the longitude of the study site is 140.86°E (**Figure 1B**).

Modeling

The current and future states of physical and biogeochemical parameters were simulated using the Regional Ocean Modeling System (ROMS). Of the versions of ROMS, we chose ROMS-Agrif (Penven et al., 2006), which embeds an ecosystem model (Pelagic Interactions Scheme for Carbon and Ecosystem Studies (PISCES); Aumont et al., 2003) in the ROMS. The bathymetry was expressed using the Earth 1 Arc Minute Topography Model (ETOPO1; Amante and Eakins, 2009).

The ROMS was downscaled (nested) twice (**Figure 1A**; Yamaka, 2019; Akamatsu, 2020). The first ROMS (L1) had a horizontal resolution of 1/3 degree and a temporal resolution of 1 h. To simulate physical and biogeochemical parameters using L1, boundary and initial conditions were needed. For this simulation, the Comprehensive Ocean-Atmosphere Data Set (COADS) 2005 (Da Silva et al., 1994) was used for the atmospheric forcing. For the oceanic physical and biogeochemical forcing, the World Ocean Atlas (WOA) 2009 (Goyet et al., 2000; Aumont and Bopp, 2006; Antonov et al., 2010; Garcia et al., 2010; Locarnini et al., 2010) was used. For future projection, the climate model outputs of the MIROC-EMS (model description and basic results of CMIP5-20c3m; Watanabe et al., 2011). Representative Concentration Pathways (RCP) 2.6 and 8.5 scenarios were used. The outputs of L1 were used as boundary and initial conditions to drive a second ROMS (L2) with a horizontal resolution of 1/15 degree and a temporal resolution of 1 h. The model was spun up for 5 years by driving with the 10-year mean current (1996–2005) and future (2086–2095) boundary conditions and the model outputs for the last 5 years were averaged and analyzed in this study.

When the monthly-averaged model results were compared with the corresponding observed results, the model results still differed from the observed results and the extent of model-observation misfits differs largely among parameters and months (**Figure 3**). One of the possible reasons for the model-observation misfits is because the spatial resolution of L2 is still a bit too coarse to simulate the Oshoro bay. The other possible reason is because the model does not embed local processes such as inputs of freshwater and terrestrial nutrients to the coast, and primary production by seagrass/seaweeds. For example, as explained in 3.1, substantially low salinity was observed from late winter to early spring (in March and April), which was caused by the inflow of snow-melt water discharged directly to the bay from the surrounding land (Nakata et al., 2001). Such observed processes were not able to be reproduced by the model. Also, as well as phytoplankton bloom, abrupt primary production by seagrass/seaweeds is dominant in spring (in April through June) in the study site, which is not reproduced explicitly by the ecosystem model used in this study in which phytoplankton are assumed to be primary producers. This might lead to relative underestimation of modeled DO in spring even though the modeled temperature is underestimated, too. In this study, the biases between the observed and modeled results were corrected using a procedure adapted by Yara et al. (2011). Hence,

$$\Phi_f = \Phi_{\mathrm{obs}} + \Delta\Phi, \quad (3)$$

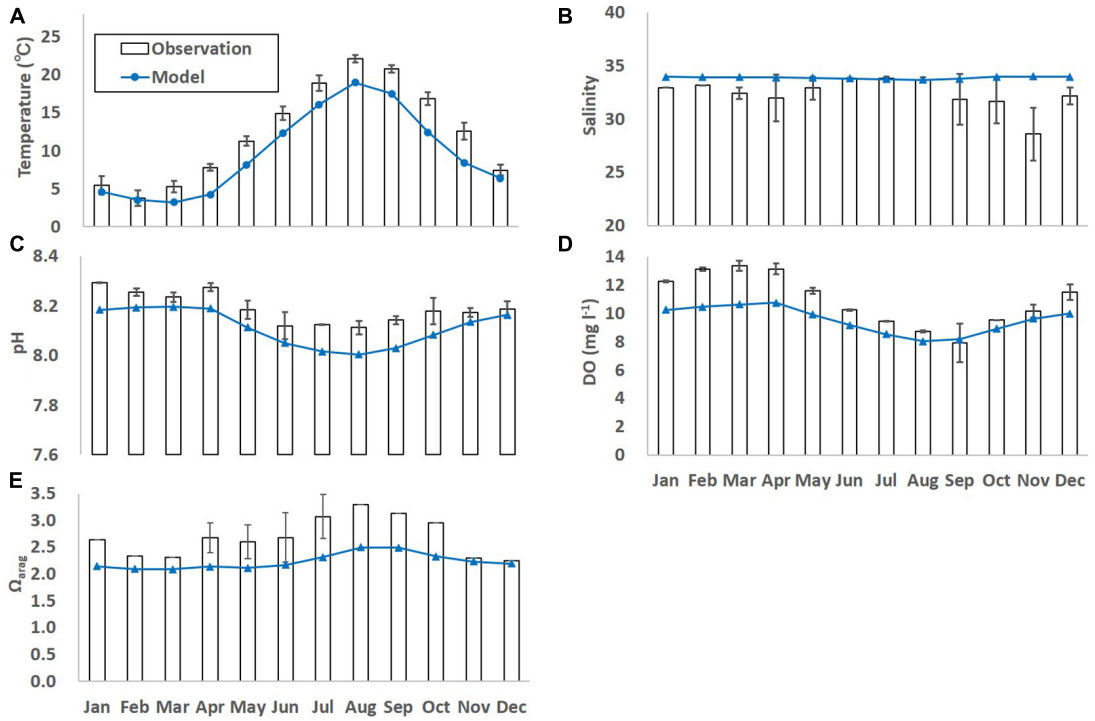


FIGURE 3 | Monthly-mean observed and modeled **(A)** temperature (°C), **(B)** salinity, **(C)** dissolved oxygen (DO; mg l^{-1}), **(D)** pH, and **(E)** Ω_{arag}. The error bars denote one standard deviation of the observed results. Black bars and blue lines denote observed and model results for the current states, respectively.

$$\Delta\Phi = \Phi_f - \Phi_p, \quad (4)$$

where Φ_f is the future modeled value of a parameter, and Φ_{obs} and Φ_p are the present observed and modeled values of the parameter, respectively.

RESULTS

Physical Parameters

Large seasonal fluctuation in the water temperature was found (**Figure 4A**). The maximum and minimum temperatures during the monitoring period were 24.3°C in August 2018 and 0.9°C in February 2019, respectively. These were similar to observations at three sites at depths of 0 and 5 m in the same bay in the 1990s (Nakata et al., 2001).

The salinity also fluctuated seasonally, but in a more complicated manner (**Figure 4B**). The maximum and minimum salinity during the monitoring period was 35.9 in July 2017 and 10.8 in November 2017, respectively. The salinity was relatively low from late winter to early spring as a result of the inflow of snow-melt water discharged directly to the bay from the surrounding land, as also mentioned in Nakata et al. (2001). The low salinity that appeared sporadically in November 2017 was first found by the continuous monitoring. This sudden low salinity was thought to be associated with an extreme storm on November 11, 2017.

Biogeochemical Parameters

The DO also showed strong seasonal fluctuation, and was generally high in boreal winter (January – March) and low in boreal summer (July – September; **Figure 4C**). The maximum and minimum DO during the monitoring period was 19.8 mg l^{-1} in April 2018 and 7.2 mg l^{-1} in August 2017, respectively. The seasonal fluctuation was characterized by the difference in oxygen saturation with temperature, and was high in cold water and low in warm water. The DO concentration is negatively correlated with temperature year-round, with a strong annual mean negative correlation of $R = -0.86$ (**Table 1** and **Figure 5A**).

The DO also showed clear daily fluctuation, unlike the physical parameters. A maximum amplitude of 9.5 mg l^{-1} was recorded in May 2018 during the spring bloom (**Figure 4C**; Yamaka, 2019). The maximum amplitude was comparable to or larger than reported in other coastal regions (e.g., 220 μmol kg^{-1} or around 6.9 mg l^{-1}; Frieder et al., 2012). DO is generally higher in the daytime and lower at night (**Figure 6A**). The daily fluctuation in DO concentration is consistent with DO produced by photosynthesis by primary producers, such as phytoplankton, seaweeds, and seagrasses in the daytime and DO consumption by the respiration of all marine organisms at night. Therefore, the daily amplitude of DO concentration was relatively large in boreal spring (April - June) when photosynthesis was active, and the monthly-mean value was the largest in April (1.6 mg l^{-1}; **Figure 7A**).

Accordingly, pH showed similar seasonal and daily fluctuations (**Figures 4D,E**, **6B,C**). The maximum and minimum

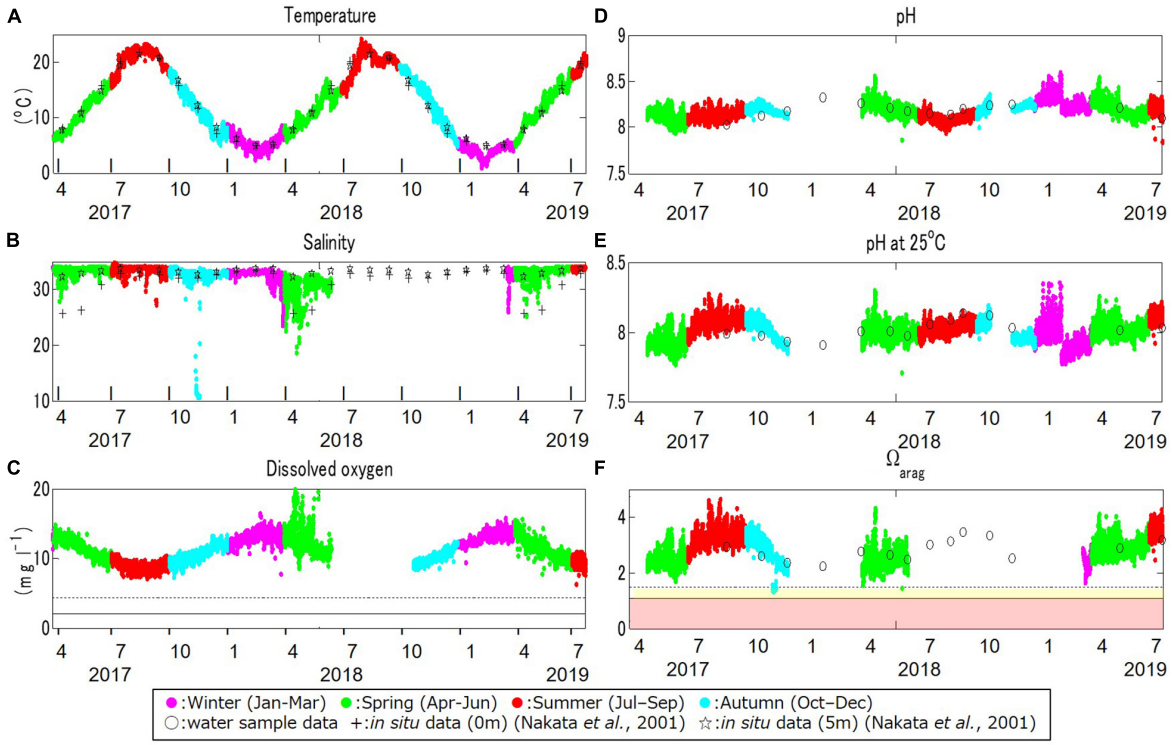


FIGURE 4 | Time series monitoring data for **(A)** temperature (°C), **(B)** salinity, **(C)** dissolved oxygen (DO; mg l^{-1}), **(D)** pH, **(E)** pH standardized at 25°C (pH_25°C), and **(F)** the aragonite saturation state (Ω_{arag}) at the study site, in boreal winter (January through March; in magenta), spring (April through June; in green), summer (July through September; in red), and autumn (October through December; in light blue), from March 30, 2017, to July 22, 2019. Crosses and stars in **(A,B)** denote the observational data at 0 and 5 m depths at the study site obtained in a previous study (Nakata et al., 2001). Open dots in **(D–F)** denote *in-situ* values obtained by water samples. The dotted and solid lines in **(C)** denote the critical level for deoxygenation in Turner et al. (2005) and Vaquer-Sunyer and Duarte (2008; 2.0 mg l^{-1}), and Marumo and Yokota (2012; 4.29 mg l^{-1}), respectively. Yellow and red domains in (f) denote the marginal and critical level of ocean acidification for calcifiers compiled in previous studies (between 1.1 and 1.5 and below 1.1 for Ω_{arag}, respectively; e.g., Waldbusser et al., 2015; Onitsuka et al., 2018).

TABLE 1 | Monthly- and annual-mean observed correlation coefficients between (a) temperature (T) and dissolved oxygen (DO),and (b) temperature and pH standardized at 25°C (pH_25°C) at the study site.

	(a) T vs. DO	(b) T vs. pH_25°C
Jan	−0.44	−0.05
Feb	−0.11	−0.21
Mar	−0.24	0.57
Apr	−0.26	0.24
May	−0.49	0.25
Jun	−0.27	0.55
Jul	−0.64	0.42
Aug	−0.31	0.31
Sep	−0.45	0.16
Oct	−0.45	0.14
Nov	**−0.84**	**0.95**
Dec	**−0.78**	0.14
Annual mean	**−0.86**	0.60

Bold values are less than −0.7 or larger than 0.7 (i.e., strong correlations). N/A: no data.

pH during the monitoring period was 8.72 (pH_25°C = 8.35) in February 2019 and 7.86 (pH_25°C = 7.71) in June 2018, respectively. Similar to DO, the seasonal and daily fluctuations were primarily characterized by physical and biogeochemical processes, respectively. The pH is dependent on temperature and is high in cold water and low in warm water, which contributes to the seasonal fluctuation in pH. The monitored pH_25°C had a positive correlation with the temperature (an annual-mean correlation coefficient of R = 0.60; **Table 1** and **Figure 5B**), although the correlation varied seasonally.

Similar to the DO concentration, there was a daily fluctuation in pH, which was high in the daytime and low at night, due to photosynthesis by primary producers in the daytime and respiration by marine organisms at night (**Figures 6B,C**). The daily amplitude was relatively large in April, when photosynthesis is predominant, and the monthly-mean was the largest in April (0.11; **Figure 7B**), similar to that of the DO concentration. The pH also fluctuated sporadically. The maximum diurnal fluctuation in the study period was 0.64 (0.42 for pH_25°C), which occurred in January 2019 (**Figures 6C**, **7C**), and was comparable to fluctuations in estuarine (0.99), near-shore (0.49), and kelp forest (0.36-0.54) sites in other coastal regions (Hofmann et al., 2011; Frieder et al., 2012). These results indicate that coastal marine species in Oshoro Bay temporarily

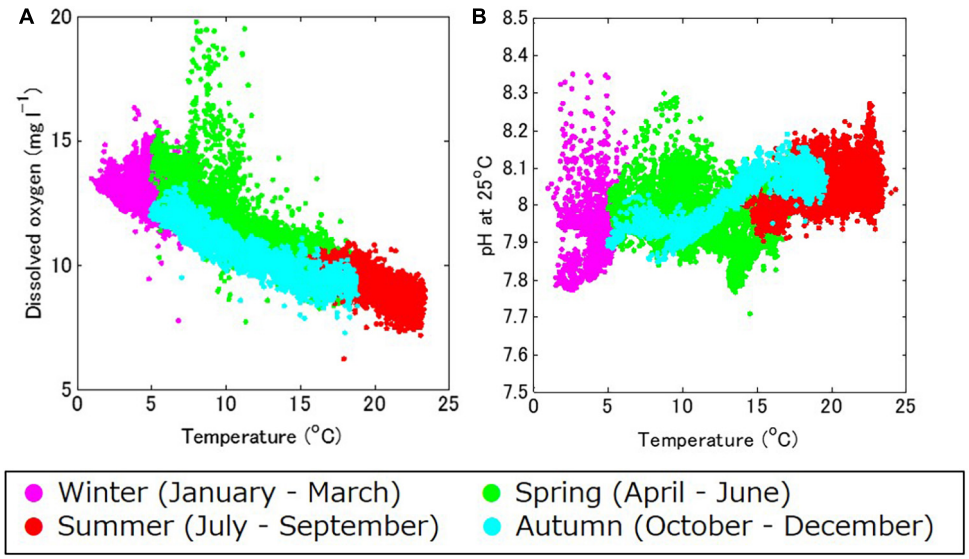


FIGURE 5 | (A) Temperature–dissolved oxygen (DO), and **(B)** temperature–pH standardized at 25°C (pH_25°C) diagrams for the study site, in winter (January through March; in magenta), spring (April through June; in green), summer (July through September; in red), and autumn (October through December; in light blue).

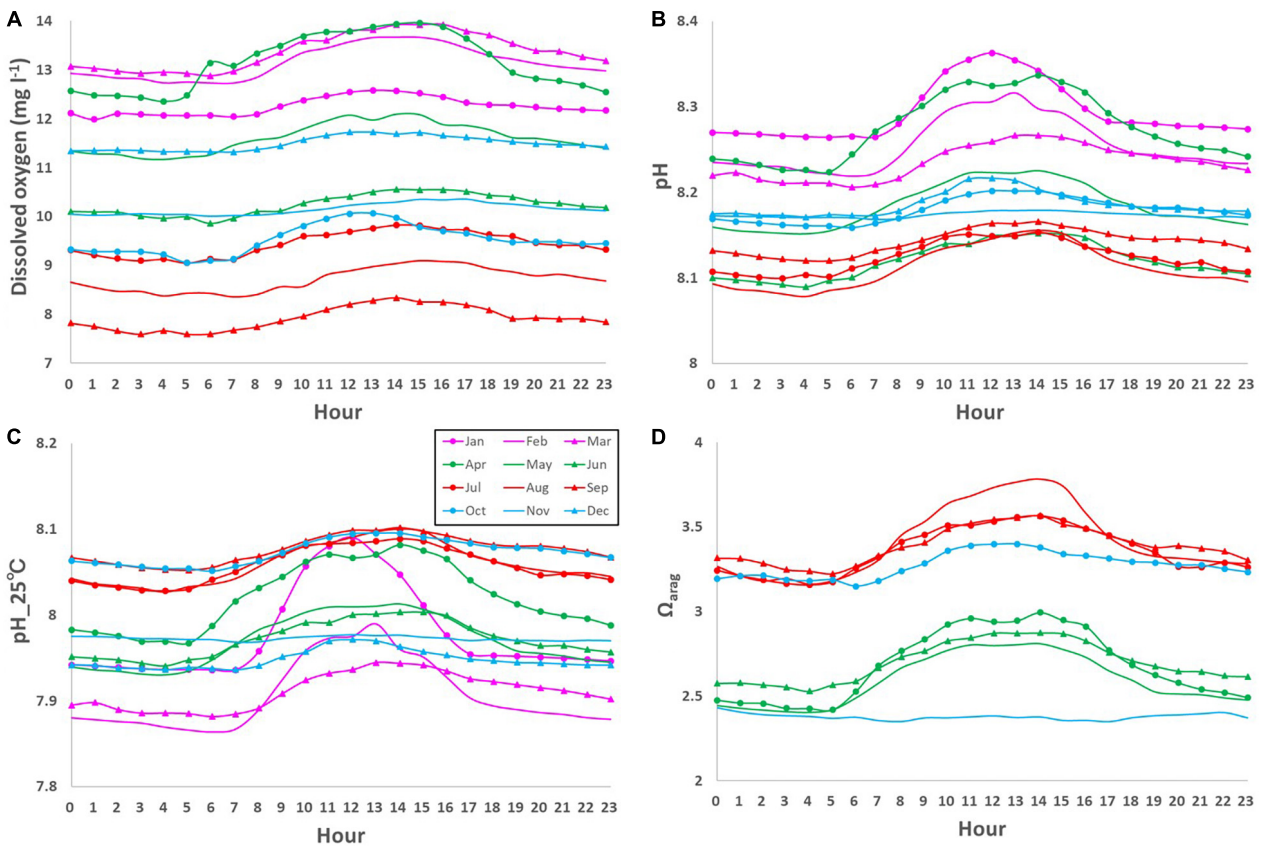


FIGURE 6 | Monthly-mean daily fluctuations in **(A)** dissolved oxygen (DO; mg l^{-1}), **(B)** pH, **(C)** pH_25°C, and **(D)** Ω_{arag} from 0 am to 11 pm.

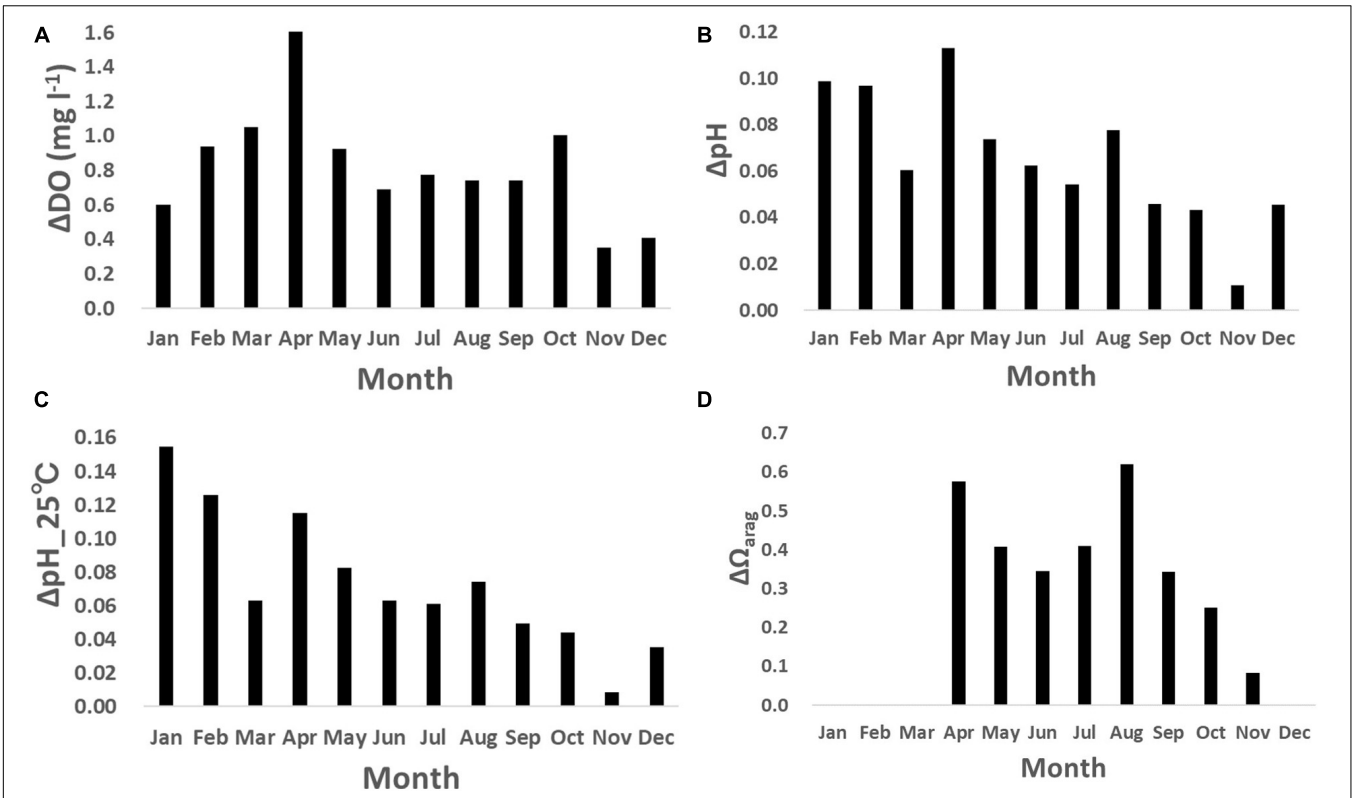


FIGURE 7 | Monthly-mean daily amplitude of **(A)** dissolved oxygen (DO; mg l^{-1}), **(B)** pH, **(C)** pH_25°C, and **(D)** Ω_{arag}.

experienced low pH resulting from the wide diurnal variation in pH, similar to other coastal regions.

The Ω_{arag}, another ocean acidification metric, also showed significant seasonal and daily fluctuations, but in a more complicated way (**Figure 4F**). The maximum and minimum Ω_{arag} was 4.7 in August 2017 and 1.3 in November 2017, respectively. The extremely low Ω_{arag} in November 2017 is thought to be associated with an extreme storm on November 11, 2017, which caused low temperature and salinity. The sporadic lowering of Ω_{arag}, which is close to the critical level of ocean acidification (Ω_{arag} = 1.1; Onitsuka et al., 2018) was first found by multi-year monitoring. No Ω_{arag} values were available when either the salinity or pH data were not obtained. Therefore, it is likely that we failed to capture the annual minimum value of Ω_{arag} in this study. However, referring to observed seasonal fluctuations in Ω_{arag} (e.g., Ishii et al., 2011; Wakita et al., 2017, 2021), the annual minimum should appear in winter when the water temperature is low and the value may have already reached close to the critical level of acidification.

Similar to the DO concentration and pH, the daily fluctuation in Ω_{arag} was also prominent and it was high in the daytime and low at night, driven by daily fluctuation of carbon and oxygen dynamics through photosynthesis by primary producers in the daytime and respiration by marine organisms at night (**Figure 6D**). Although we did not cover the overall temporal fluctuation of Ω_{arag} because of missing data necessary for calculating the value (**Figure 4F**), the observed maximum daily fluctuation during the study period was 2.3 in April 2018, when the spring bloom was dominant. The monthly-mean daily amplitude was as large as 0.6 in spring and summer (**Figure 7D**).

Future Projections

The annual-mean projected rise in water temperature from the present to the end of this century was 2.2°C for the RCP 2.6 scenario and 5.5°C for the RCP 8.5 scenario (**Figure 8A**). The rise in temperature was followed by significant lowering of the DO concentration, pH, and Ω_{arag} in the future (**Figures 8B–D**). However, the extent differed between the RCP scenarios: compared to their present states both physical and biogeochemical parameters are anticipated to change significantly for RCP 8.5, but much more moderately for RCP 2.6. The estimated extent of the projected results for RCP 2.6 is closer to the present values than those for RCP 8.5, which concurred with other future projections (e.g., Takao et al., 2015).

The projected annual-mean DO concentration decreased by 0.43 mg l^{-1} for RCP 2.6 and 1.02 mg l^{-1} for RCP 8.5, from the present (**Figure 8B**). Similarly, the projected annual-mean pH decreased by 0.06 for RCP 2.6 and 0.38 for RCP 8.5, from the present (**Figure 8C**). The projected pH reduction for RCP 2.6 and RCP 8.5 is comparable to that projected globally in previous studies (0.06–0.07 and 0.30–0.33, respectively; e.g.,

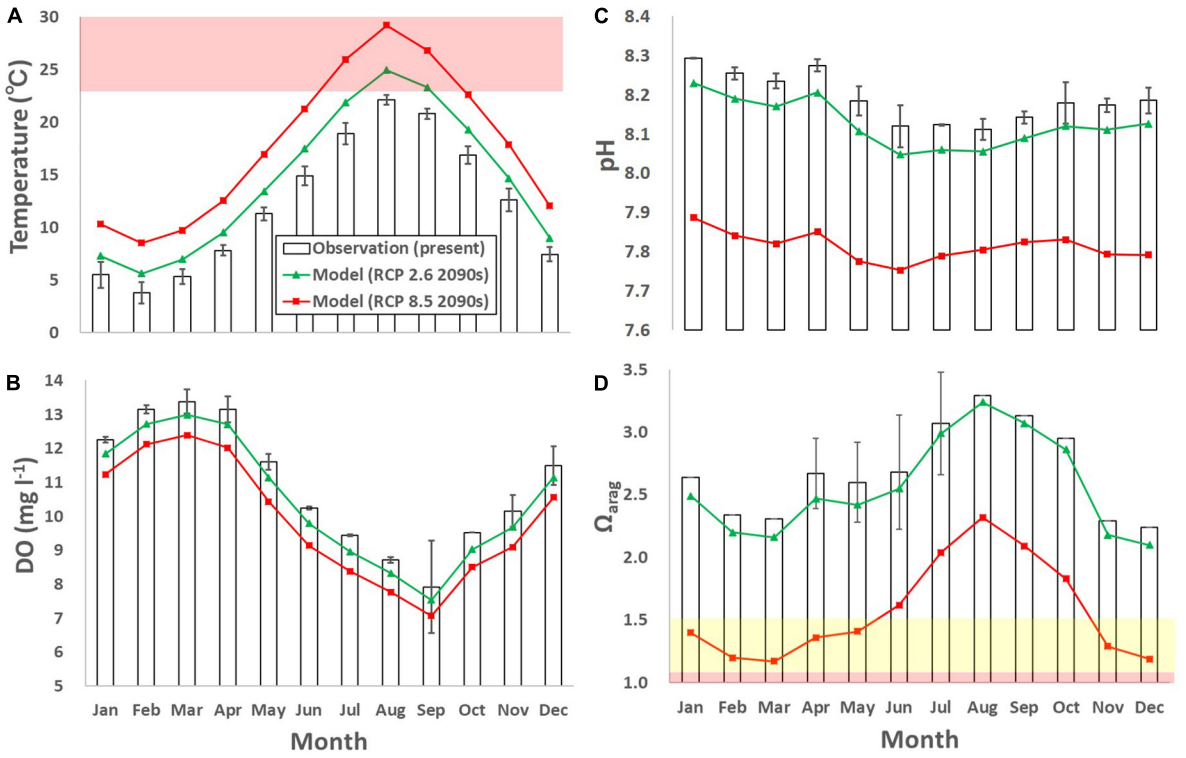


FIGURE 8 | Monthly-mean observed and modeled **(A)** temperature (°C), **(B)** dissolved oxygen (DO; mg l^{-1}), **(C)** pH, and **(D)** Ω_{arag}. The error bars denote one standard deviation of the observed results. Green and red lines denote model results for the 2090s with the RCP 2.6 and 8.5 scenarios, respectively. The red domain in **(A)** denotes the critical level of ocean warming for sea urchins and scallops (over 23°C; Hoshikawa, 2006; Shibano et al., 2014), both of which are main fisheries targets of the subarctic coast. Yellow and red domains in **(D)** denote the marginal and critical level of ocean acidification for calcifiers compiled in previous studies (between 1.1 and 1.5 and below 1.1 for Ω_{arag}, respectively; e.g., Waldbusser et al., 2015; Onitsuka et al., 2018).

IPCC AR5, Jiang et al., 2019). The projected annual-mean Ω_{arag} decreased by 0.1 for RCP, 2.6 and 1.1 for RCP 8.5, from the present (**Figure 8D**).

DISCUSSION

Criteria for Ocean Warming, Acidification, and Deoxygenation

Several studies have reported marginal levels for calcifiers for ocean acidification of Ω_{arag} = ca. 1.1–1.5 [e.g., Waldbusser et al., 2015 for bivalve larvae, Zhan et al., 2016 for sea urchin (*S. intermedius*), and Onitsuka et al., 2018 for Ezo abalone larvae]. The marine environment is suitable for calcifiers above the marginal levels and unsuitable (critical) below them, while the levels differ with species abundance, life stages and locations.

The monitoring showed that the Ω_{arag} did not reach the critical level in the study period, but was sometimes marginal (**Figure 4F**). For the RCP 8.5 scenario, the monthly-mean Ω_{arag} is very often marginal in the 2090s. Considering that the future daily fluctuations of the biogeochemical parameters presumably magnify as the buffer capacity weakens, the daily minimum values will more often reach critical levels for calcifiers (<1.1 for Ω_{arag}). Previous experimental results showed that the growth and malformation rates of larval Ezo abalone decreased and increased greatly, respectively, when the larvae were exposed in experimental seawater in which the Ω_{arag} was about 1.1, even for only 2–3 days (Onitsuka et al., 2018). This implies that more frequent future critical levels may severely damage calcifiers, especially during their early stages when they are relatively vulnerable to high CO_2. This will also affect local industries, especially shellfisheries. Because around 60% of the shellfish and half of the calcifiers in Japan are caught in subarctic seas in which the Ω_{arag} is relatively low, ocean acidification is of great concern and the social demand for adaptive fisheries, such as changing the aquaculture style as mentioned in section "Suggestion for future adaptation," in response to global change is high.

Similarly, several studies have reported various critical levels for deoxygenation in which the DO concentration is <2.0 mg l^{-1} (Turner et al., 2005; Vaquer-Sunyer and Duarte, 2008) or 4.29 mg l^{-1} (Marumo and Yokota, 2012). Our monitoring results show that the minimum DO concentration during the study period (7.2 mg l^{-1} in August 2017) was still above the critical level (**Figure 4C**). However, similar to pH and Ω_{arag}, if we assume that the daily fluctuation in DO concentration in the future is similar to that at present, i.e., the maximum daily fluctuation is as large as 9.5 mg l^{-1}, the daily minimum DO concentration might often reach critical levels of less than 2.0 mg l^{-1} in the future.

Along with ocean acidification and deoxygenation, concurrent ocean warming may also affect marine organisms, including calcifiers. For example, the main fisheries targets in the study site are vulnerable to warm temperatures. A representative critical temperature level was reported to be 23°C for sea urchins and scallops (Hoshikawa, 2006; Shibano et al., 2014). Temperatures over 23°C are not common at the study site now, but are projected to appear for 2 months for the RCP 2.6 scenario and 3 months for the RCP 8.5 scenario in summer (**Figure 8A**). This means that calcifiers along the subarctic coast will suffer from ocean acidification in winter and ocean warming in summer in the future.

Suggestion for Future Adaptation

The large difference in the future projections between the RCP 2.6 and 8.5 scenarios clearly shows the need to reduce anthropogenic CO_2 and other greenhouse gas emissions as per the Paris Agreement, which has a target similar to the RCP 2.6 pathway, to alleviate fatal impacts of global change on marine organisms along subarctic coasts. It is also important to adapt to the upcoming impacts of global change. Adaptation strategies include modifying local industries in subarctic coastal regions, such as fisheries, and tourism such as eating around seafoods and recreational scuba diving. Because of overused fisheries resources, aquaculture plays a greater role in maintaining a steady supply of fisheries resources. Shellfish such as scallops, oysters, and abalone, and sea urchins are all calcifiers, and therefore, are concerned to be more or less affected by ocean acidification. However, the vulnerability to low pH and Ω_{arag} differs with various aspects such as the species abundance, life stage and habitats. For example, possible adaptation strategies to upcoming ocean acidification include changing the aquaculture style, such as raising larval calcifiers in low CO_2 conditions manipulated artificially, such as on-land aquaculture (e.g., Fujii, 2020), following the scientific insights that early larvae are relatively vulnerable to high CO_2 (e.g., Kurihara, 2008; Kimura et al., 2011; Waldbusser et al., 2015; Onitsuka et al., 2018; Foo et al., 2020). Combined impacts of global warming and ocean acidification are generally concerned to magnify the adverse effects on calcifiers, while global warming may partly and temporally alleviate the impacts of ocean acidification by rise in alkalinity from the land, as already evidenced in some other subarctic regions (e.g., Watanabe et al., 2009; Salisbury and Jönsson, 2018).

Regarding deoxygenation, low oxygen conditions are due to local human impacts, as well as global change and subsequent ocean warming. As local human impacts such as nutrification from the land are easier to alleviate than global change, further regulation of nutrient discharge to the coasts should delay the serious impacts of deoxygenation on marine organisms (e.g., Rabalais et al., 2010). However, the extent of regulation of nutrient discharge has not yet been quantified and further analytical studies are required.

CONCLUSION

This study was the first multi-year *in-situ* monitoring study of a subarctic coast and produced future projections of physical and biogeochemical parameters related to global change-driven ocean warming, acidification, and deoxygenation. The monitoring identified new characteristics of physical and biogeochemical parameters at the study site, such as sporadic changes in salinity and DO, which revealed that marine creatures sometimes experience marginal levels of ocean acidification. Our future projection results suggest that in the future high CO_2 world, calcifiers that are accustomed to current subarctic environments may be seriously damaged by ocean warming in summer and ocean acidification in mid-winter, and possibly by deoxygenation assuming that the daily fluctuation in DO concentration in the future is similar to that at present. Therefore, the mitigation of global change by following the Paris Agreement is of great importance for saving marine ecosystems and local industries, although local adaptation strategies are also required, such as adjusting aquaculture styles.

DATA AVAILABILITY STATEMENT

The raw data supporting the conclusions of this article will be made available by the authors, without undue reservation.

AUTHOR CONTRIBUTIONS

MF, ST, TY, TA, YF, MW, AY, and TO contributed to the study conception and design. All authors contributed to the manuscript revision and have read and approved the submitted version.

FUNDING

This study was supported by the Integrated Research Program for Advancing Climate Models (TOUGOU) Grant Numbers JPMXD0717935498 and JPMXD0717935715 from the Ministry of Education, Culture, Sports, Science, and Technology (MEXT), Japan, the Japan Society for the Promotion of Science (JSPS) KAKENHI Grant Number JP 15H04536, 16H01792, and 20H04349, Study of Biological Effects of Acidification and Hypoxia (BEACH) of the Environment Research and Technology Development Fund Grant Number JPMEERF20202007 of the Environmental Restoration and Conservation Agency of Japan, and Hokkaido University Functional Enhancement Project.

ACKNOWLEDGMENTS

We thank Hisashi Endo, Haruko Kurihara, Koji Suzuki, Michiyo Yamamoto-Kawai, and Takeshi Yoshimura for their fruitful discussion and helps on monitoring and water sample analyses. We also thank Norishige Yotsukura, Koji Shibazaki, and Norifumi Sugimoto of the Oshoro Marine Station, Hokkaido University, and Wakako Takeya and Serina Maehara for their support with the monitoring, and Hiroyoshi Sumita of Kaiyoutansa for his suggestion regarding monitoring and installation. Thanks are also extended to Richard Feely and two reviewers for their practical and useful comments.

REFERENCES

Akamatsu, T. (2020). *Projecting the Impacts of Climate Change On Coral Distribution In The Temperate Area Of Japan*. Master's thesis. Graduate School of Environmental Science, Hokkaido University, 66.

Amante, C., and Eakins, B. W. (2009). "ETOPO1 1 Arc-minute global relief model: procedures, data sources and analysis," in *NOAA Technical Memorandum NESDIS, NGDC 24*, (Washington, DC: NOAA), 19.

Antonov, J. I., Seidov, D., Boyer, T. P., Locarnini, R. A., Mishonov, A. V., Garcia, H. E., et al. (2010). *WORLD OCEAN ATLAS 2009, Volume 2: Salinity. NOAA Atlas NESDIS 69*. Washington, DC: NOAA, 184.

Aumont, O., and Bopp, L. (2006). Globalizing results from ocean in situ iron fertilization studies. *Global Biogeochem. Cycles* 20:GB2017.

Aumont, O., Maier-Reimer, E., Blain, S., and Monfray, P. (2003). An ecosystem model of the global ocean including Fe, Si, P colimitations. *Global Biogeochem. Cycles* 17:GB1060.

Barton, A., Hales, B., Waldbusser, G. G., Langdon, C., and Feely, R. A. (2012). The Pacific oyster, *Crassostrea gigas*, shows negative correlation to naturally elevated carbon dioxide levels: Implications for near-term ocean acidification effects. *Limnol. Oceanogr.* 57, 698–710. doi: 10.4319/lo.2012.57.3.0698

Baumann, H., Wallace, R. B., Tagliaferri, T., and Gobler, C. J. (2014). Large natural pH, CO_2 and O_2 fluctuations in a temperate tidal salt marsh on diel, seasonal, and interannual time series. *Estuaries Coast.* 38, 220–231. doi: 10.1007/s12237-014-9800-y

Bednaršek, N., Feely, R. A., Beck, M. W., Alin, S. R., Siedlecki, S. A., Calosi, P., et al. (2020). Exoskeleton dissolution with mechanoreceptor damage in larval Dungeness crab related to severity of present-day ocean acidification vertical gradients. *Sci. Total Environ.* 716:136610. doi: 10.1016/j.scitotenv.2020.136610

Christian, J., and Ono, T. (Eds) (2019). Ocean acidification and deoxygenation in the North Pacific Ocean. *PICES Spec. Publ.* 6:101.

Da Silva, A. M., Young, C. C., and Levitus, S. (1994). *Atlas of Surface Marine Data 1994, Vol. 1, Algorithms and Procedures, NOAA Atlas NESDIS 6*. Washington, DC: NOAA, 74.

Dai, M., Lu, Z., Zhai, W., Chen, B., Cao, Z., Zhou, K., et al. (2009). Diurnal variations of surface seawater pCO_2 in contrasting coastal environments. *Limnol. Oceanogr.* 54, 735–745. doi: 10.4319/lo.2009.54.3.0735

DePasquale, E., Baumann, H., and Gobler, C. J. (2015). Vulnerability of early life stage Northwest Atlantic forage fish to ocean acidification and low oxygen. *Mar. Ecol. Prog. Ser.* 523, 145–156. doi: 10.3354/meps11142

Dixson, D. L., Jennings, A. R., Atema, J., and Munday, P. L. (2015). Odor tracking in sharks is reduced under future ocean acidification conditions. *Glob. Chang. Biol.* 21, 1454–1462. doi: 10.1111/gcb.12678

Feely, R. A., Sabine, C. L., Hernandez-Ayon, J. M., Ianson, D., and Hales, B. (2008). Evidence for upwelling of corrosive "acidified" water onto the continental shelf. *Science* 320, 1490–1492. doi: 10.1126/science.1155676

Foo, S. A., Koweek, D. A., Munari, M., Gambi, M. C., Byrne, M., and Caldeira, K. (2020). Responses of sea urchin larvae to field and laboratory acidification. *Sci. Total Environ.* 723:138003. doi: 10.1016/j.scitotenv.2020.138003

Frieder, C. A., Nam, S. H., Martz, T. R., and Levin, L. A. (2012). High temporal and spatial variability of dissolved oxygen and pH in a nearshore California kelp forest. *Biogeosciences* 9, 3917–3930. doi: 10.5194/bg-9-3917-2012

Fujii, M. (2020). Effects of ocean warming and acidification on marine ecosystem and societies in Japanese coasts. *Fish. Eng.* 56, 191–195.

Garcia, H. E., Locarnini, R. A., Boyer, T. P., and Antonov, J. I. (2010). "World Ocean Atlas 2009, Volume 3: dissolved oxygen, apparent oxygen utilization, and oxygen saturation," in *NOAA Atlas NESDIS 70*, ed. S. Levitus (Washington, DC: NOAA), 344.

Gobler, C. J., and Baumann, H. (2016). Hypoxia and acidification in ocean ecosystems: coupled dymanics and effects on marine life. *Biol. Lett.* 12:20150976. doi: 10.1098/rsbl.2015.0976

Goyet, C., Healy, R. J., and Ryan, J. P. (2000). *Global Distribution of Total Inorganic Carbon and Total Alkalinity Below the Deepest Winter Mixed Layer Depths. ORNL/CDIAC-127 NDP-076, 40*. Oak Ridge, TN: Oak Ridge National Laboratory, U.S. Department of Energy,

Hofmann, G. E., Smith, J. E., Johnson, K. S., Send, U., Levin, L. A., Micheli, F., et al. (2011). High-frequency dynamics of ocean pH: a multi ecosystem comparison. *PLoS One* 6:e28983. doi: 10.1371/journal.pone.0028983

Hoshikawa, H. (2006). Change of sea water temperature and recruitment of sea urchin along the coast of the Sea of Japan in Hokkaido. *Kaiyo Monthly* 38, 205–209.

Intergovernmental Panel on Climate Change (IPCC) (2014). *Climate Change 2014: Impacts, Adaptation, and Vulnerability. Part A: Global and Sectoral Aspects*. Contribution of Working Group II to the Fifth Assessment Report of the Intergovernmental Panel on Climate Change. Cambridge: Cambridge University Press, 1132.

IPCC (2018). *Global Warming of 1.5°C. An IPCC Special Report on the Impacts of Global Warming of 1.5°C Above Pre-Industrial Levels and Related Global Greenhouse Gas Emission Pathways, in the Context of Strengthening the Global Response to the Threat of Climate Change, Sustainable Development, and Efforts to Eradicate Poverty*. Geneva: IPCC.

Ishii, M., Kosugi, N., Sasano, D., Saito, S., Midorikawa, T., and Inoue, H. Y. (2011). Ocean acidification off the south coast of Japan: a result from time series observations of CO_2 parameters from 1994 to 2008. *J. Geophys. Res.* 116:C06022. doi: 10.1029/2010JC006831

Jiang, L.-Q., Carter, B. R., Feely, R. A., Lauvset, S. K., and Olsen, A. (2019). Surface ocean pH and buffer capacity: past, present and future. *Sci. Rep.* 9:18624. doi: 10.1038/s41598-019-55039-4

Kimura, R., Takami, H., Ono, T., Onitsuka, T., and Nojiri, Y. (2011). Effects of elevated pCO_2 on the early development of the commercially important gastropod, Ezo abalone Haliotis discus hannai. *Fish. Oceanogr.* 20, 357–366. doi: 10.1111/j.1365-2419.2011.00589.x

Kurihara, H. (2008). Effects of CO_2-driven ocean acidification on the early developmental stages of invertebrates. *Mar. Ecol. Prog. Ser.* 373, 275–284. doi: 10.3354/meps07802

Lee, K., Lan, T., Tong, L. T., Millero, F. J., Sabine, C. L., Dickson, A. G., et al. (2006). Global relationships of total alkalinity with salinity and temperature in surface waters of the world's oceans. *Geophys. Res. Lett.* 33:L19605. doi: 10.1029/2006GL027207

Locarnini, R. A., Mishonov, A. V., Antonov, J. I., Boyer, T. P., Garcia, H. E., Baranova, O. K., et al. (2010). "World Ocean Atlas 2009, Volume 1: temperature," in *NOAA Atlas NESDIS 68*, ed. S. Levitus (Washington, DC: NOAA), 184.

Lueker, T. J., Dickson, A. G., and Keeling, C. D. (2000). Ocean pCO_2 calculated from dissolved inorganic carbon, alkalinity, and equations for K1 and K2: validation based on laboratory measurements of CO_2 in gas and seawater at equilibrium. *Mar. Chem.* 70, 105–119. doi: 10.1016/s0304-4203(00)00022-0

Marumo, K., and Yokota, M. (2012). Review on the hypoxia formation and its effects on aquatic organisms. *Rep. Mar. Ecol. Res. Inst.* 15, 1–21.

Melzner, F., Thomsen, J., Koeve, W., Oschilies, A., Gutowska, M. A., Bange, H. W., et al. (2013). Future ocean acidification will be amplified by hypoxia in coastal habitats. *Mar. Biol.* 160, 1875–1888. doi: 10.1007/s00227-012-1954-1

Morita, M., Suwa, R., Iguchi, A., Nakamura, M., Shimada, K., Sakai, K., et al. (2009). Ocean acidification reduces sperm flagellar motility in broadcast spawning reef invertebrate. *Zygote* 18, 103–107. doi: 10.1017/s0967199409990177

Munday, P. L., Cheal, A. J., Dixson, D. L., Rummer, J. L., and Fabricius, K. E. (2014). Behavioral impairments in reef fishes caused by ocean acidification at CO_2 seeps. *Nat. Clim. Chang.* 4, 487–492. doi: 10.1038/nclimate2195

Munday, P. L., Dixson, D. L., Donelson, J. M., Jones, G. P., Pratchett, M. S., Devitsina, G. V., et al. (2009). Ocean acidification impairs olfactory discrimination and homing ability of a marine fish. *Proc. Natl. Acad. Sci. U.S.A.* 106, 1848–1852. doi: 10.1073/pnas.0809996106

Nakata, A., Yagi, H., Miyazono, A., Yasunaga, T., Kawai, T., and Iizumi, H. (2001). Relationships between sea surface temperature and nutrient concentrations in Oshoro Bay, Hokkaido, Japan. *Sci. Rep. Hokkaido Fish. Exp. Stn.* 59, 31–41.

Onitsuka, T., Takami, H., Muraoka, D., Matsumoto, Y., Nakatsubo, A., Kimura, R., et al. (2018). Effects of ocean acidification with pCO_2 diurnal fluctuations on survival and larval shell formation of Ezo abalone, *Haliotis discus* hannai. *Mar. Environ. Res.* 134, 28–36. doi: 10.1016/j.marenvres.2017.12.015

Orr, J. C., Fabry, V. J., Aumout, O., Bopp, L., Doney, S. C., Feely, R. A., et al. (2005). Anthropogenic ocean acidification over the twenty-first century and its impact on calcifying organisms. *Nature* 437, 681–686. doi: 10.1038/nature04095

Penven, P., Debreu, L., Marchesiello, P., and McWilliams, J. C. (2006). Application of the ROMS embedding procedure for the Central California Upwelling System. *Ocean Model.* 12, 157–187. doi: 10.1016/j.ocemod.2005.05.002

Pierrot, D., Lewis, E., and Wallace, D. W. R. (2006). *MS Excel program developed for CO_2 system calculations. ORNL/CDIAC-105a*. Oak Ridge, TN: Carbon Dioxide Information Analysis Center, Oak Ridge National Laboratory, doi: 10.3334/CDIAC/otg.CO2SYS_XLS_CDIAC105a

Rabalais, N. N., Díaz, R. J., Levin, L. A., Turner, R. E., Gilbert, D., and Zhang, J. (2010). Dynamics and distribution of natural and human-caused hypoxia. *Biogeosciences* 7, 585–619. doi: 10.5194/bg-7-585-2010

Salisbury, J. E., and Jönsson, B. F. (2018). Rapid warming and salinity changes in the Gulf of Maine alter surface ocean carbonate parameters and hide ocean acidification. *Biogeochemistry* 141, 401–418. doi: 10.1007/s10533-018-0505-3

Schmidtko, S., Stramma, L., and Visbeck, M. (2017). Decline in global oceanic oxygen content during the past five decades. *Nature* 542, 335–339. doi: 10.1038/nature21399

Shibano, R., Fujii, M., Yamanaka, Y., Yamano, H., and Takao, S. (2014). Spatial and temporal dynamics of coastal sea surface temperature and catches of Japanese scallop *Mizuhopecten yessoensis* in Hokkaido. *Bull. Jpn. Soc. Fish. Oceanogr.* 78, 259–267.

Takao, S., Kumagai, N. H., Yamano, H., Fujii, M., and Yamanaka, Y. (2015). Projecting the impacts of rising water temperatures on the distribution of seaweeds around Japan under multiple climate change scenarios. *Ecol. Evol.* 5, 213–223. doi: 10.1002/ece3.1358

Turner, R. E., Rabalais, N. N., Swenson, E. M., Kasprzak, M., and Romaire, T. (2005). Summer hypoxia in the northern Gulf of Mexico and its prediction from 1978 to 1995. *Mar. Environ. Res.* 59, 65–77. doi: 10.1016/j.marenvres.2003.09.002

Vaquer-Sunyer, R., and Duarte, C. M. (2008). Thresholds of hypoxia for marine biodiversity. *Proc. Natl. Acad. Sci. U.S.A.* 105, 15452–15457. doi: 10.1073/pnas.0803833105

Wakita, M., Nagano, A., Fujiki, T., and Watanabe, S. (2017). Slow acidification of the winter mixed layer in the subarctic western North Pacific. *J. Geophys. Res. Oceans* 122, 6923–6935. doi: 10.1002/2017jc013002

Wakita, M., Sasaki, K., Nagano, A., Abe, H., Tanaka, T., Nagano, K., et al. (2021). Rapid reduction of pH and $CaCO_3$ saturation state in the Tsugaru Strait by the intensified Tsugaru Warm Current during 2012–2019. *Geophys. Res. Lett.* doi: 10.1029/2020GL091332

Waldbusser, G. G., Hales, B., Langdon, C. J., Haley, B. A., Shrader, P., Brunner, E. L., et al. (2015). Ocean acidification has multiple modes of action on bivalve larvae. *PLoS One* 10:e0128376. doi: 10.1371/journal.pone.0128376

Wallace, R. B., Baumann, H., Grear, J. S., Aller, R. C., and Gobler, C. J. (2014). Coastal ocean acidification: the other eutrophication problem. *Estuar. Coast. Shelf Sci.* 148, 1–13. doi: 10.1016/j.ecss.2014.05.027

Watanabe, S., Hajima, T., Sudo, K., Nagashima, T., Takemura, T., Okajima, H., et al. (2011). MIROC-ESM 2010: model description and basic results of CMIP5-20c3m experiments. *Geosci. Model Dev.* 4, 845–872. doi: 10.5194/gmd-4-845-2011

Watanabe, Y. W., Nishioka, J., Shigemitsu, M., Mimura, A., and Nakatsuka, T. (2009). Influence of riverine alakalinity on carbonate species in the Okhotsk Sea. *Geophys. Res. Lett.* 36:L15606. doi: 10.1029/2009GL038520

Wootton, J. T., Pfister, C. A., and Forester, J. D. (2008). Dynamic patterns and ecological impacts of declining ocean pH in a high-resolution multi-year dataset. *Proc. Natl. Acad. Sci. U.S.A.* 105, 18848–18853. doi: 10.1073/pnas.0810079105

Yamaka, T. (2019). *Assessment and future projection of variational characteristics of global warming and ocean acidification proxies in Oshoro Bay, Hokkaido*. Master's thesis. Graduate School of Environmental Science, Hokkaido University, 74.

Yara, Y., Oshima, K., Fujii, M., Yamano, H., Yamanaka, Y., and Okada, N. (2011). Projection and uncertainty of the poleward range expansion of coral habitats in response to sea surface temperature warming: a multiple climate model study. *Galaxea* 13, 11–20. doi: 10.3755/galaxea.13.11

Zhan, Y., Hu, W., Liu, M., Duan, M., Huang, X., Chang, Y., et al. (2016). The impact of CO_2-driven ocean acidification on early development and calcification in the sea urchin Strongylocentrotus intermedius. *Mar. Pollut. Bull.* 112, 291–302. doi: 10.1016/j.marpolbul.2016.08.003

Conflict of Interest: The authors declare that the research was conducted in the absence of any commercial or financial relationships that could be construed as a potential conflict of interest.

Copyright © 2021 Fujii, Takao, Yamaka, Akamatsu, Fujita, Wakita, Yamamoto and Ono. This is an open-access article distributed under the terms of the Creative Commons Attribution License (CC BY). The use, distribution or reproduction in other forums is permitted, provided the original author(s) and the copyright owner(s) are credited and that the original publication in this journal is cited, in accordance with accepted academic practice. No use, distribution or reproduction is permitted which does not comply with these terms.

frontiers in Marine Science

ORIGINAL RESEARCH
published: 14 January 2021
doi: 10.3389/fmars.2020.590236

High-Resolution Carbonate System Dynamics of Netarts Bay, OR From 2014 to 2019

*William Fairchild and Burke Hales**

College of Earth, Ocean, and Atmospheric Sciences, Oregon State University, Corvallis, OR, United States

Netarts Bay is a shallow, temperate, tidal lagoon located on the northern coast of Oregon and the site of the Whiskey Creek Shellfish Hatchery (WCSH). Data collected with an autonomous continuous flow-through system installed at WCSH capable of high-resolution (1 Hz) partial pressure of aqueous CO_2 (pCO_2) and hourly total dissolved inorganic carbon (TCO_2) measurements, with combined measurement uncertainties of $< 2.0\%$ and 0.5%, respectively, is analyzed over the 2014–2019 interval. Summer upwelling, wintertime downwelling, and *in situ* bay biogeochemistry represent significant modes of the observed variability in carbonate system dynamics. Summer upwelling is associated with large amplitude diel pCO_2 variability, elevated TCO_2 and alkalinity, but weak variability in salinity. Wintertime downwelling is associated with bay freshening by both local and remote sources, a strong tidal signature in salinity, TCO_2, and alkalinity, with diel pCO_2 variability much less amplified when compared to summer. Further, analysis of alkalinity-salinity relationships suggests multiple water masses inhabiting the bay during 1 year: mixing of end-members associated with direct precipitation, coastal rivers, southward displacement of the Columbia River plume, California Current surface and deep upwelled waters. The importance of in-bay processes such as net community metabolism during intervals of high productivity are apparent. These direct measurements of pCO_2 and TCO_2 have been useful to local hatchery owners who have monitored intake waters following historic seed-production failures related to high-CO_2 conditions exacerbated by ocean acidification.

Keywords: ocean acidification, estuarine biogeochemistry, time-series, coastal oceanography, carbonate chemistry, Netarts Bay, Oregon

OPEN ACCESS

Edited by:
Hongjie Wang,
Pacific Marine Environmental Laboratory (NOAA), United States

Reviewed by:
Andrea J. Fassbender,
Monterey Bay Aquarium Research Institute (MBARI), United States
Sophie Chu,
University of Washington, United States

***Correspondence:**
Burke Hales
burke.hales@oregonstate.edu

Specialty section:
This article was submitted to Coastal Ocean Processes, a section of the journal Frontiers in Marine Science

Received: *31 July 2020*
Accepted: *11 December 2020*
Published: *14 January 2021*

Citation:
Fairchild W and Hales B (2021) High-Resolution Carbonate System Dynamics of Netarts Bay, OR From 2014 to 2019. Front. Mar. Sci. 7:590236. doi: 10.3389/fmars.2020.590236

INTRODUCTION

Shallow coastal ecosystems, coral reefs, and temperate estuaries are among the most vulnerable oceanographic regimes currently threatened by exposure to elevated atmospheric CO_2 and related anthropogenic forcings (Peirson et al., 2015). Enhanced nutrient loading from anthropogenically modified runoff, habitat loss, introduction of invasive species, altered freshwater flow, dredging, expanding 'dead zones' characterized by prolonged hypoxic episodes, and trace metal contamination represent some of the many stressors facing modern estuarine systems (Kennish, 2002; Diaz and Rosenberg, 2008). Additionally, rising sea levels, ocean acidification, and loss of global marine biomass further complicate these vital ecosystems' health and stability and the goods and services they provide (Rabalais et al., 2009).

Near-shore monitoring studies of oceanic CO_2 in the Pacific Northwest have primarily been limited to shipboard measurements in tandem with buoy observations during upwelling intervals (van Geen et al., 2000; Ianson et al., 2003; Hales et al., 2005; Feely et al., 2008; Nemcek et al., 2008; Evans et al., 2011) while more recent work in the Columbia River, Puget Sound, and Salish Sea have introduced CO_2 data at higher spatiotemporal resolution (Evans et al., 2013, 2019; Fassbender et al., 2018). The lack of extensive spatiotemporal sampling represents a hurdle in understanding how the dynamic coastal ocean and estuarine environments are interacting with and responding to the cascading and complex problems associated with ongoing climate change. Biophysical processes within shallow coastal shelves and estuarine bodies occur across variable time and space scales (Waldbusser and Salisbury, 2014), from hours to interannual, and forecasting how these environments will respond to climate change continues to be challenging, requiring more expansive and higher resolution coastal monitoring networks.

Despite poor data coverage, our understanding of ocean acidification's impact on organismal life cycles, specifically for larval and juvenile bivalves, shows these organisms experiencing physiological stress across varying levels of pCO_2, pH, and/or saturation state at levels currently observed during various periods of the year (Waldbusser et al., 2011, 2015a; Barton et al., 2012; White et al., 2013). Ocean acidification-related symptoms include, but are not limited to, compromised shell integrity, increased mortality, and reduced recruitment success. *Crassostrea gigas*, for example, shows enhanced sensitivity to water conditions during the first 48 h of calcification (Barton et al., 2012). An under sampling of the coastal ocean in both time and space in assessment of coastal water chemistry may result in these bivalve-poor water conditions to be overlooked entirely.

However, high-resolution carbonate sampling is not mission-critical to understand in real-time how ocean acidification is threatening habitat stability, organismal life cycles, and even fisheries economies. During the summer of 2009, Whiskey Creek Shellfish Hatchery in Netarts Bay, OR, sustained significant and prolonged larval oyster mortality in response to intake water which was corrosive and fatal to their broodstock (Barton et al., 2012). A liquid flow-through pCO_2/TCO_2 instrument was installed in 2011 to monitor in-take water conditions in real time (Vance, 2012). Coincident with water chemistry monitoring, hatchery operators moved the growing season to earlier in the year and began conditioning incoming seawater with sodium carbonate to elevate saturation states to optimal shellfish growing levels. In an industry worth $270 million regionally and one which employs 3000 + people (Barton et al., 2015), implementation of this strategy to mitigate the severe effects of ocean acidification on bivalve mortality continues to be beneficia for hatchery operators at Whiskey Creek. Recreational shellfishing, on the other hand, will be more directly impacted by changing ocean carbonate chemistry since the intertidal zone and shallow estuarine shellfish habitats are directly exposed to dynamic carbonate conditions.

Netarts Bay is a temperate, well-mixed, tidal lagoon located 90 km south of the Columbia River mouth on the Oregon Pacific coast (**Figure 1**). Draining only a 4100 Ha watershed, the bay is marine-dominated, receiving freshwater input only from about a dozen very small streams, primarily during the winter storm seasons (McCallum, 1977). A 6 km-long sandspit stretching north-to-south forms the seaward boundary of the estuary and the primary exchange of water occurs at the ∼100 m wide tidal channel located at the northern end of the spit. The net effect of bay hydrology and tidal dynamics results in rapid flushing and water residence times < 12 h (Glanzman, 1971); a single ebb-flood cycle can replace approximately 2/3 of the bay's water during intervals of spring tides.

For this study, we analyzed 6-year time series of high-resolution carbonate chemistry measurements taken from Netarts Bay, OR, with the goal to analyze hydrographic and carbonate trends, establish modern baselines, and examine scales of variability that are not often resolved from discrete sampling methods.

MATERIALS AND METHODS

Whiskey Creek Shellfish Hatchery (WCSH; 45.403°N, 123.944°W) is located on the eastern bank of Netarts Bay, approximately 2 km south of the bay's mouth. During the 2007–2008 growing season, hatcheries up and down the Pacific Northwest coast, including WCSH, experienced intermittent but significant mass larval mortality, which was later directly linked to high-CO_2 content in intake waters (Barton et al., 2012, 2015). Beginning in 2011, Vance (2012) installed an automated system that combined pCO_2 and TCO_2 measurements, following the TCO_2 system as described by Bandstra et al. (2006) combined with the pCO_2 system described by Hales et al. (2004) modified to use a showerhead-style equilibrator. This precursor system was redesigned prior to 2014 and has been in operation more or less continuously in its current configuration since then.

Briefly, hatchery seawater is branched into an adjacent side-laboratory, passing through a SeaBird Electronics 45 MicroTSG (SBE45) which continuously measures *in situ* temperature and conductivity, allowing determination of salinity. The intake pipe remains submerged 0.5 m above the seafloor at an average depth 2 m. Downstream of the TSG is an enclosed-headspace shower-head equilibrator in which the seawater flows over a porous bubbler tube where the recirculated headspace gas is introduced to the equilibration chamber. High water flow rates and vigorous bubbling ensures complete equilibration of the headspace gas CO_2 with the dissolved CO_2 in the sample stream. The headspace gas is recirculated in a closed loop, passing through a detector unit (LI-840A[1]), where the CO_2 content of the gas is measured via infrared spectrometry.

Once an hour, the instrument performs a TCO_2 sequence closely following the method of Bandstra et al. (2006). Water is drawn from the main seawater flow through a custom 40-micron tangential-flow filter at a pump-controlled 20 mL/min

[1]licor.com

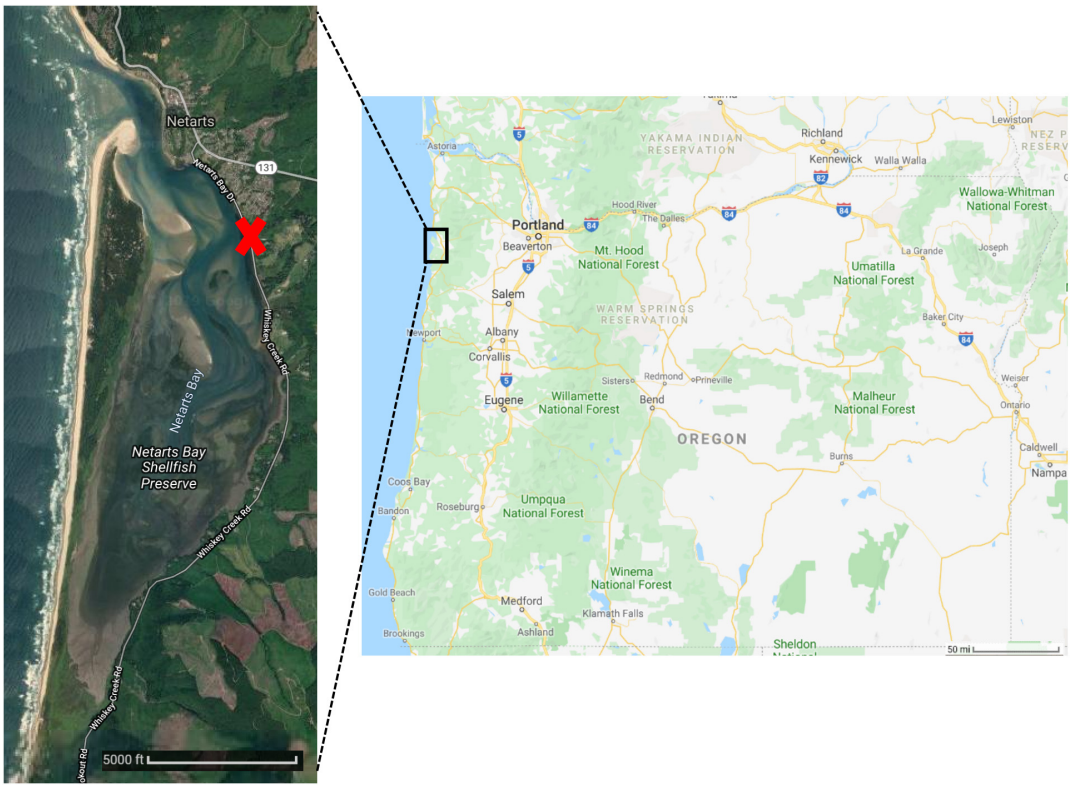


FIGURE 1 | Oregon state map **(Right)** and satellite imagery of Netarts Bay **(Left)**. Red X marks site of Whiskey Creek Shellfish Hatchery (WCSH). Images courtesy of Google Earth.

and acidified with a 0.1 mL/min flow of a solution of 30% concentrated HCl in distilled water. The acidified liquid sample stream flows through the lumen-side of a hydrophobic microporous membrane contactor (Liquicell G543), while a CO_2-free gas stream controlled at 900 ml/min by a molecular mass-flow controller (Alicat Scientific) flows counter to the liquid stream on the shell-side of the contactor. A steady-state mass balance governs the CO_2 composition of the outlet gas stream. With precisely controlled gas and liquid flows, the xCO_2 of the effluent gas stream, measured by the LI-840A, is proportional to the TCO_2 of the sample water.

The instrument is controlled by a computer and a custom acquisition and control program developed in LabView. Data (LI-840A, mass flow, and SBE45 output, and several operational analog sensors) are sampled and stored at 1-Hz frequency. At user-specified intervals (30 s here), the program calculates medians of the continuous data (pCO_2, salinity, and temperature), applies calibrations and corrections, and performs carbonate-system calculations to give real-time estimates of water alkalinity, pH_t (presented here on the total hydrogen ion scale), and $CaCO_3$ mineral saturation states.

Calibrations and Standards

Both gas and liquid-phase standards are run automatically at user-specified intervals (6 h for this work) to verify detector accuracy and the relationship between TCO_2 outlet strip gas and inlet-water TCO_2 concentration. Gas standards are a set of three cylinders of gravimetrically prepared mixtures of CO_2 in ultrapure air, typically spanning the range of 200–2000 ppm, but there were variations over the course of this study. The LI-840A is factory-linearized over a range of 0–20000 ppm, and we have verified this linearity up to 7000 ppm in the laboratory. In the instances where the natural dynamic range exceeds the calibration range, we are confident that our linear regression (R^2 typically > 0.999, $n \geq 3$) can be extended to any CO_2 level observed here. Liquid standards are three solutions of $NaHCO_3$ and Na_2CO_3 in deionized water, in proportions selected to maintain near-ambient solution pCO_2 at TCO_2 concentrations of 1200, 1800, and 2400 μmol/kg. The liquid calibration is likewise highly linear (R^2 typically > 0.999, $n \geq 3$). Calibration sequences are processed, and regressions performed in real time. At each calibration interval, measurements of outside air xCO_2 and barometric pressure are made.

Raw LI-840A xCO_2 measurements are corrected using linear regressions performed from bracketing gas standard sequences using gases of known CO_2 mixing ratio. A drift correction is applied to the converted data using a linear interpolation in time between adjacent standard sequences. Calibrated xCO_2 during pCO_2 operations are converted to pCO_2 using the total headspace pressure, which is undetectably different from ambient atmospheric pressure. Calibrated xCO_2 data during TCO_2 operations are converted to TCO_2 in μM using the

set of liquid standard sequences which bookend any given TCO_2 measurement, and subsequently converted to μmol/kg using sample density calculated from the SBE45 temperature and salinity. A density and CRM correction are applied post-conversion to arrive at units of μmol/kg. Synchronizing hourly TCO_2 measurements with temperature, salinity, and time-weighted interpolated pCO_2 value allows for calculation of hourly alkalinity (Eq. 1), pH_t, and mineral saturation with use of a program such as CO2Sys or CO2Calc, though we use our own calculation program here (CarbCalc; developed by B. Hales). For the custom CarbCalc function, we use the dissociation constants of water provided by Millero (2010), calcite and aragonite solubility constants from Mucci (1983), and constants for equilibrium of carbonic acid from Millero (2010) and boric acid by Dickson (1990).

$$Alkalinity = \left[HCO_3^-\right] + 2\left[CO_3^{2-}\right] + \left[B\,(OH)_4^-\right] + \left[OH^-\right] - [H^+] \quad (1)$$

To cross-check the accuracy of the instrument's TCO_2 response, certified reference materials (CRM) provided by Scripps Institute of Oceanography (Dickson laboratory) were run roughly every other month throughout the study. These CRMs contain highly accurate and precisely known concentrations of TCO_2 and alkalinity. On-site TCO_2 measurements of these CRM's consistently produce correction factors 0.985 ± 0.005 (n = 14), so we applied a single correction of 0.985 to our TCO_2 data over the duration of the study. This implies an uncertainty of ± 0.5% (∼10 μmol/kg) in TCO_2, which exceeds that achievable in a more controlled operation (Bandstra et al., 2006), but is quite small in the context of this dynamic setting where TCO_2 ranges from 1200 to 2300 μmol/kg during the year.

On a weekly basis, discrete check samples were collected in 350 ml amber glass bottles downstream of the equilibration chamber, poisoned with mercuric chloride, and capped with metal bottle caps. These samples were analyzed in the Hales' laboratory at Oregon State University using combined pCO_2/TCO_2 measurements as described above but modified for discrete samples. Check samples (n = 237) reveal that pCO_2 measurements at WCSH are within ± 5% of the discrete-sampler system, while TCO_2 measurements are within ± 1%. Discrepancies between the two measurements can arise from human error such as inconsistent sampling procedure, failure to adequately poison the discrete sample bottle, and occasional transcription errors. We believe these disagreements represent extreme bounds on the uncertainty of the system, particularly for pCO_2 which is more robust in the continuous equilibration than in discrete bottle samples. For example, the equilibration of a discrete liquid sample containing headspace gas, albeit relatively small in volume, inherently and unpreventably alters the exact chemistry of the sample. The asymptote of an infinitesimal headspace and an infinite water sample is more closely approached by a fixed, recirculated gaseous headspace equilibrated with a continuous flow of seawater than by the discrete liquid sample in a bottle.

Full data processing, including a suite of statistical analyses, was performed using compiled language and programs written in RStudio (version 1.2.5033). Complete annual data coverage proved challenging due to several internal and external circumstances. Such instances included times of seawater flow stoppage, either in the main hatchery supply—specifically during late September when hatchery operations slow down and pipes are cleaned or replaced—or in the branch to the laboratory, clogs in the headspace recirculation airflow, LI-840A detector failures, HCl depletion, etc. These failures were recognizable from anomalous system variables, such as flow or pressure readings, atypical temperature and salinity readings (i.e., negative salinities), among others. QA/QC was applied manually to remove instances of system malfunction. Despite various setbacks, we were able to process and analyze ∼75% of measurements taken from 2014 to 2019.

RESULTS

The time series data presented below represent a highly dynamic system, with multiple timescales of variability. Our examination of the data revealed four key timescales of variability: diel, which persists throughout the year; seasonal, reflecting the transition between predominantly upwelling summer and predominantly downwelling winter conditions; summer-event variability associated with upwelling/relaxation cycles; and winter-event variability associated with storms and precipitation events. There are other scales of variability present, such as sub-hourly, but our discussion will focus on elucidating those listed above, using the data from 2017 as exemplary in terms of data coverage before presenting the 2014–2019 composite.

Summer and Winter 7-Day Direct Observations

Plots of the measurements of temperature, salinity, and pCO_2 at 30-s resolution, and TCO_2 at hourly resolution for two 7-day periods in February and June of 2017 are shown in **Figure 2**. Modeled tide height, relative to Crescent City, CA (NOAA reference station ID: 9419750) is shown as a spline-fit of daily high-and-low tides (data courtesy of https://tidesandcurrents.noaa.gov/), and shading represents local day- and night-time, yellow and blue, respectively.

Plots of a 7-day interval in February of 2017 (day-of-year 48–55) are shown in **Figure 2** (left). Temperature varies weakly between 9.4 and 11.2°C without obvious diel or tidal character. Salinity varies strongly between 26 and 31, with a clear tidal covariance. pCO_2 ranges between 325 and 420 μatm with evident diel amplitude, but with a dramatically smaller dynamic range than seen in the summer. The overall trend of decreasing pCO_2 throughout the afternoon and build-up throughout nighttime persists in winter. TCO_2 ranges from 1620 to 2000 μmol/kg, which is large compared to the summer observations. That variability is largely positively correlated to salinity for this period (r^2 = 0.91, n = 153), with diel variability and pCO_2 co-variance less evident than seen in summer.

A weekly snapshot of summertime in June of 2017 is detailed in **Figure 2** (right). In-bay temperature ranges between 14 and 17.5°C with little systematic variability from day-of-year

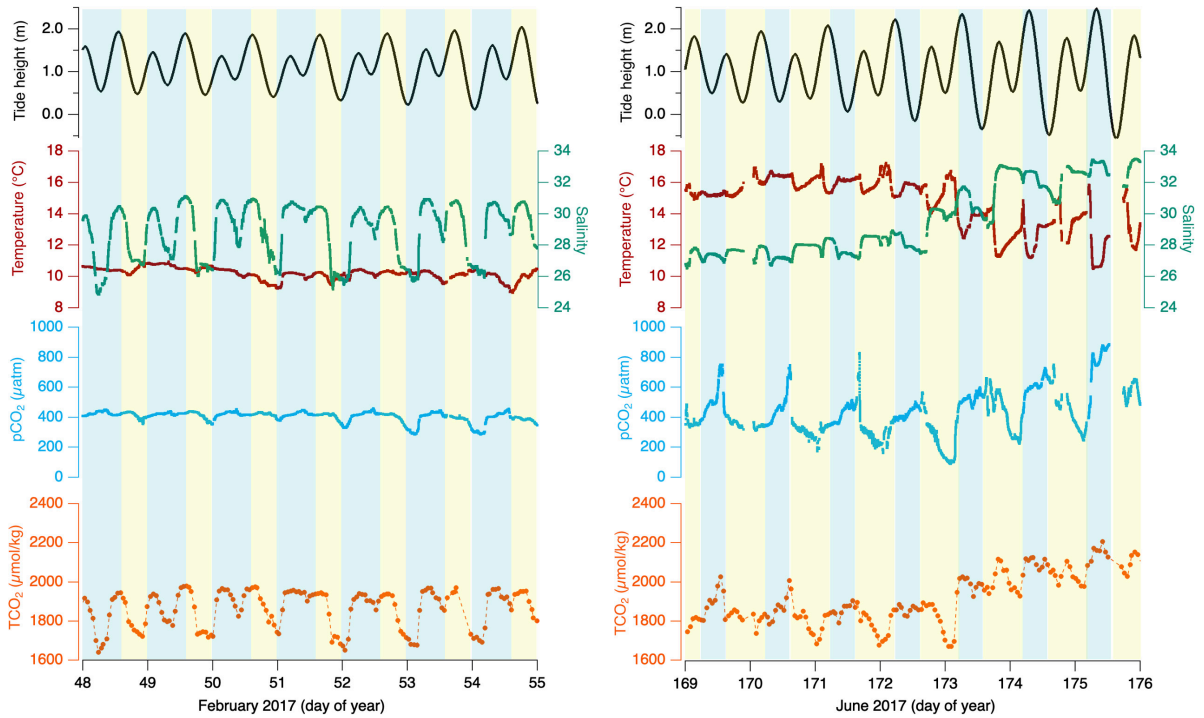


FIGURE 2 | 7-day period winter **(Left)** and summer **(Right)** 2017 for Netarts Bay, OR, time in day of year UTC. Temperature (red line), salinity (teal line), pCO_2 (cyan line), TCO_2 (orange dots connected by dashed line), and estimated tide height (black line). Blue shading indicates local nighttime and yellow shading indicates local daytime.

169–173 until decreasing in temperature but growing in tidal variability from day 173 to 176. Salinity experiences variability more closely synchronized with the local tide stage, initially varying between 26.2 and 28 until day 173, when salinity increases to 33.5 and remains high through day 176. pCO_2 shows strong diel variability from $<$ 200 to $>$ 800 µatm in this interval. pCO_2 tends to increase during the night hours, peaking either immediately before or shortly after sunrise, and then rapidly falls throughout the day, reaching daily minima in late afternoon or early evening. Early in the observation period, TCO_2 shows clear pCO_2-synchronous diel variability with dawn maxima around 1900 µmol/kg and late afternoon minima around 1700 µmol/kg, until late in day 173, when TCO_2 shows a large increase (∼150 µmol/kg) coinciding with the step up in salinity. Following day 173, TCO_2 continues to show pCO_2-synchronous diel variability with morning maxima slightly over 2100 µmol/kg and evening minima slightly under 2000 µmol/kg.

Summer and Winter 7-Day Derived Observations

As discussed in the methods section, hourly TCO_2 measurements are combined with a synchronized, time-interpolated pCO_2 value to calculate hourly alkalinity, pH_t, saturation state, and a series of other carbonate variables including individual inorganic carbon species as determined through thermodynamic relationships. **Figure 3** plots alkalinity, pH_t, and the saturation state of aragonite (Ω_a) for the same two 7-day intervals of **Figure 2**. **Figure 3** (left) shows the corresponding wintertime-interval alkalinity, pH_t, and Ω_a. Alkalinity varies by a large range compared to the summer interval, from 1700 to 2100 µeq/kg; however, the variability is more strongly coupled to salinity variability than to any diel pattern. Ω_a varies between ∼1 and 1.5, with an apparent mixture of covariance between salinity and pCO_2. pH_t varies between ∼7.9 and 8.1, and, while late-day maxima correspond to late-day pCO_2 minima, there are additional variations that hint at a relation to salinity.

For the summer interval (right), alkalinity is largely covariant with the TCO_2 data in the first 4 days of the interval, varying from 1900 to 2100 µmol/kg. In the final 3 days, alkalinity increases with the step up in salinity, and then experiences minimal variability between 2100 and 2150 µmol/kg for the remainder of the record. The saturation state ranges from 1.0 to over 4.6 in similar diel cycling as the pH_t values, and thus anti-correlated with *in situ* pCO_2, with lowest saturation states in late-evening or early morning, and highest values in late afternoon. pH_t behavior is primarily anti-correlated with the pCO_2 observations ($r^2 = -0.93$, $n = 31$), showing the diel pattern of lowest values ∼7.8 in the early morning, and highest values, ∼8.1 or higher, in late afternoon or early evening.

Single Year Direct Observations

Annual patterns for the direct measurements taken during the representative year 2017 are shown in **Figures 4A–F**. The leading inferred drivers at the seasonal timescale are the

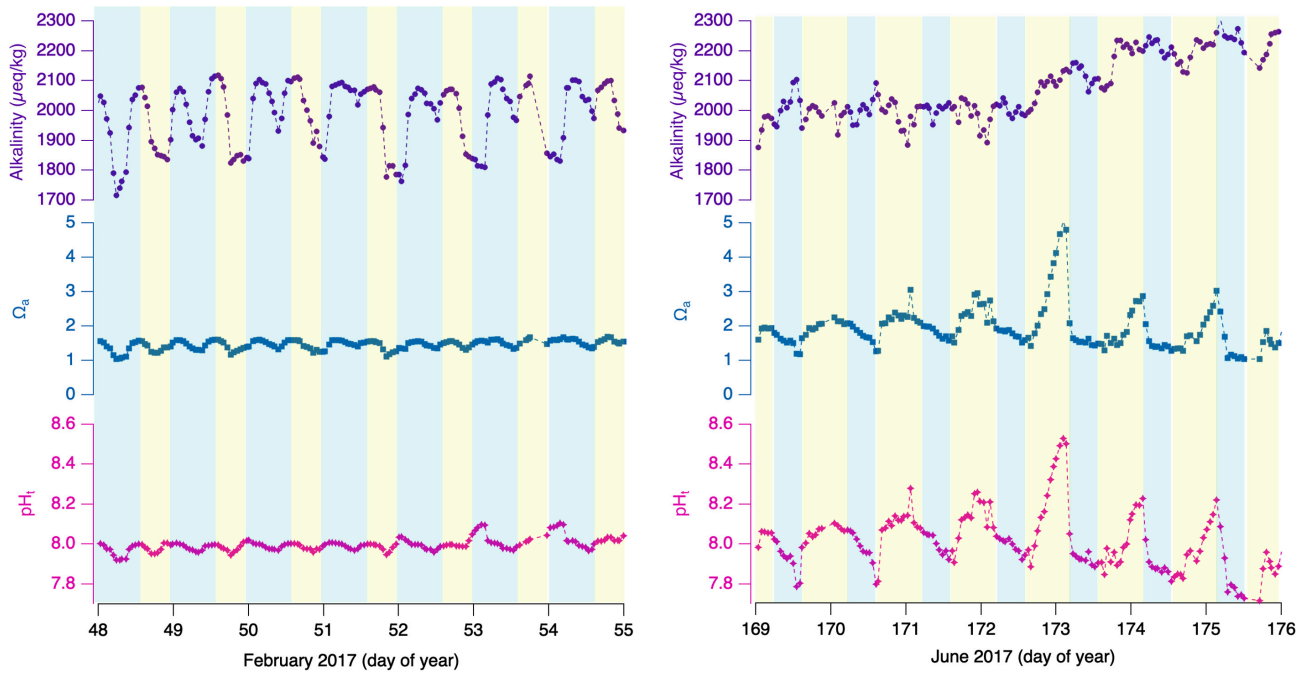


FIGURE 3 | 7-day period winter **(Left)** and summer **(Right)** 2017 for Netarts Bay, OR. Calculated alkalinity (purple dots connected by dashed line), saturation state of aragonite (Ω_a, blue squares connected by dashed line), and pH (pink stars diamonds connected by dashed line). Blue shading indicates local nighttime and yellow shading indicates daytime.

upwelling/downwelling forcing and the related precipitation. In winter, winds are predominantly poleward and lead to onshore convergence and downwelling. Frequently accompanying poleward wind forcing are storm events that bring instances of high precipitation to the bay. In summer, the winds reverse to become primarily equatorward, causing coastal divergence and upwelling. Little precipitation occurs throughout these summer months. Not shown for the location is the annual photoperiod variation from ∼8.5 to 15.5 h between winter and summer solstices. Separating the winter and summer seasons are spring and fall transition periods, where the character of the dominant season fades and that of the forthcoming season grows.

The influence of these seasonal forcings are evident in the temperature and salinity time series. While the coldest temperatures are seen in winter, summertime minimum temperatures are nearly as low (∼8°C), corresponding to the highest bay salinities and reflecting the influence of deep upwelling-source water. However, winter-time temperatures show relatively little variability (8–12°C), with maxima rarely > 12°C, while summer maximum temperatures are routinely > 15°C. Salinity shows nearly opposite character. The highest values approach 34 in summer, when there is relatively little variability. In contrast, winter salinity is rarely above 32, and minimum values corresponding to high-precipitation events fall as low as 16. The seasonality is perhaps most evident in the dramatic change in the pCO_2 variability. In winter, pCO_2 values rarely exceed 500 μatm, and rarely fall below 300 μatm. In contrast, summer pCO_2 ranges between minima ∼190 μatm and maxima ∼1600 μatm.

TCO_2 variability show distinctly different behavior from pCO_2 when examined in the composite year as compared to the weekly snapshots. In winter, when pCO_2 variability is minimal, TCO_2 dynamic range is greatest. Winter TCO_2 maxima are only ∼2050 μmol/kg, and the lowest annual values, ∼1400 μmol/kg are seen then. These low TCO_2 events correspond with freshening events that dilute ocean-source water TCO_2, while having little effect on pCO_2. During summer, the TCO_2 values are overall higher (∼2000 – 2250 μmol/kg). and show less dynamic range than winter.

Single Year Derived Observations

The full 2017-year observations the derived terms alkalinity, Ω_a, and pH_t, are shown in **Figures 4G–I**. Alkalinity shows similar wintertime variability to TCO_2, with lower maximum concentrations (compared to summer) and strong salinity- and TCO_2-covariance leading to a dynamic range of ∼1400 – 2200 μmol/kg. During summer, alkalinity reaches its highest values near 2300 μmol/kg, while variability is low with minimum values rarely falling below 2200 μmol/kg. Wintertime Ω_a generally falls in the range of 1–2, except for some values ∼0.5 corresponding to the lowest observed salinities. Summertime dynamics show extreme ranges from ∼0.7 to 5, coinciding with the similarly maximal dynamic range in pCO_2 and pH_t. Winter pH_t shows little variability, mostly captured with the range 7.9–8.1. Springtime pH_t values are amplified relative to winter, ranging from 7.6 to 8.5, meanwhile summer pH_t shows strong variability between 7.5 and 8.4. The spring transition out of the dominant wintertime regime

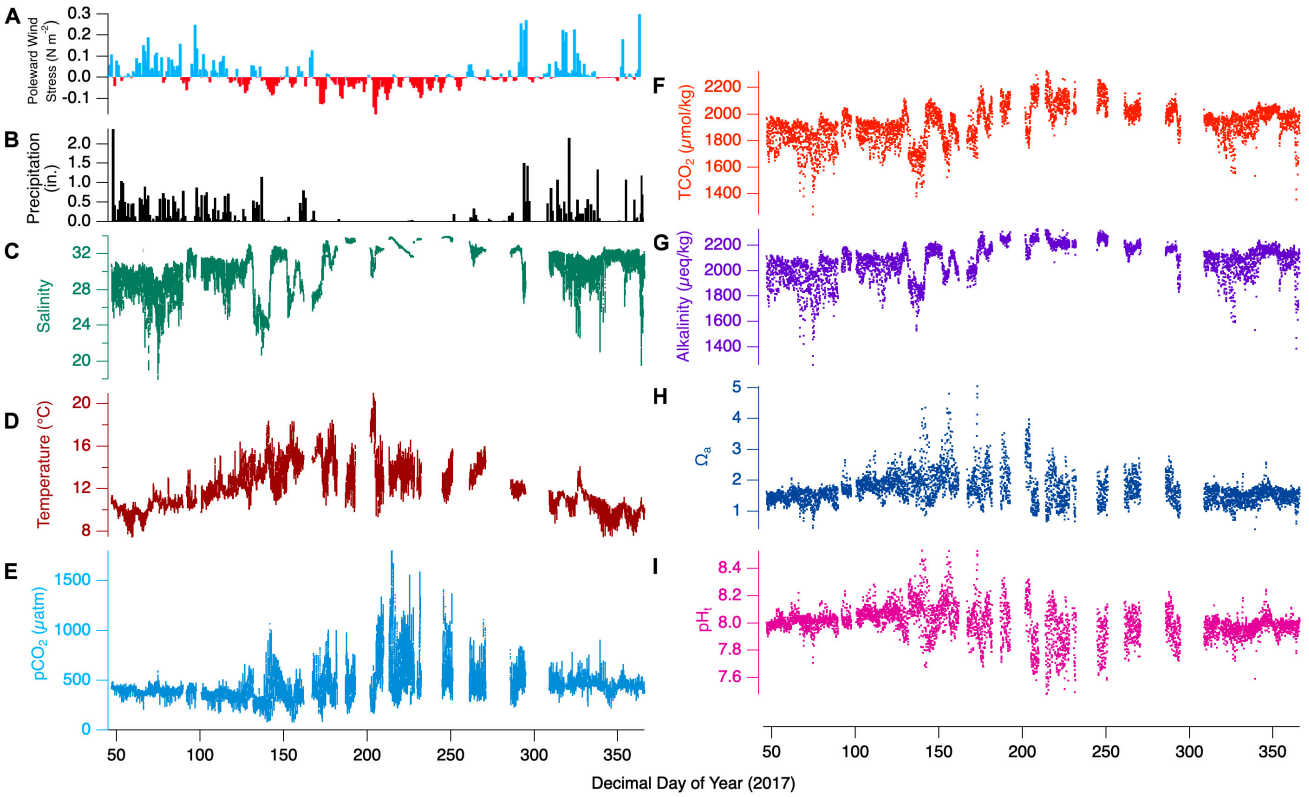


FIGURE 4 | Full 2017-year observations for Netarts Bay, OR. **(A)** Poleward wind stress, **(B)** daily precipitation in inches, **(C)** salinity (teal line), **(D)** temperature (red line), **(E)** pCO_2 (cyan line), **(F)** TCO_2 (orange dots), **(G)** calculated alkalinity (purple dots), **(H)** aragonite saturation state (Ω_a, blue dots), and **(I)** pH (pink dots), for the full 2017 timeseries. Wind stress data courtesy of http://damp.coas.oregonstate.edu/windstress/; Precipitation data courtesy of https://www.ncdc.noaa.gov/cdo-web/.

shows elevated values of pH_t and Ω_a, with maxima of 8.5 and 5.0, respectively. Similarly, alkalinity and TCO_2 values become elevated in tandem with intermittent equatorward wind and spring-transition upwelling related events. The reverse occurs during the fall transition as poleward winds become dominant and downwelling prevails.

Composite Year Direct Observations

Compositing all years' wind stress, precipitation, salinity, temperature, TCO_2, and pCO_2 data provides the full range of variability in the basic carbonate measurements taken at Netarts Bay from 2014 to 2019 (**Figures 5A–F**). Over all 6 years, temperature ranges from ∼5–20°C, salinity from ∼15 to 34, pCO_2 from ∼100 to 2500 µatm, and TCO_2 from ∼1400 to 2250 µmol/kg. The 2017-year discussed previously falls within the 6-year composite, and the general patterns hold: winter is dominated by poleward winds and high precipitation, while summer is dominated by equatorward winds and nearly absent precipitation. Wintertime pCO_2 and temperature exhibit lower variability while summer values show dynamic ranges that nearly encompass the full data-set dynamic range. Wintertime salinity and TCO_2 show lower maxima than seen in summer, and the lowest minima seen all year, while values are higher and less variant in summer.

Composite-Year Derived Observations

Figures 5G–I adds all years' calculated alkalinity, pH_t, and Ω_a observations to the previously discussed pCO_2 and TCO_2. Alkalinity ranges from ∼1150 to 2400 µeq/kg, Ω_a from ∼0.3 to 5.0, and pH_t from ∼7.5 to 8.6. As above, the general patterns seen for the 2017-year persist: alkalinity is overall lower in winter but experiences the largest variability with extreme minima that correspond to the lowest salinity events, while summer alkalinity experiences its highest values and lower variability. Ω_a shows low variability mostly captured in the range 1–2 in winter, with instances of very low Ω_a associated with the lowest-salinity events, while summer conditions show large variability, ranging from 0.7 to 5.0. pH_t variability is low in winter months and exceeds 1 pH unit in summer, coincident with the large observed range in pCO_2.

DISCUSSION

Timescales and Drivers of Variability

Netarts Bay experiences dynamic variability across multiple hydrographic and carbonate parameters at timescales from diel to tidal to several days to seasonal. This variability occurs in response to a variety of factors, namely in-bay metabolic

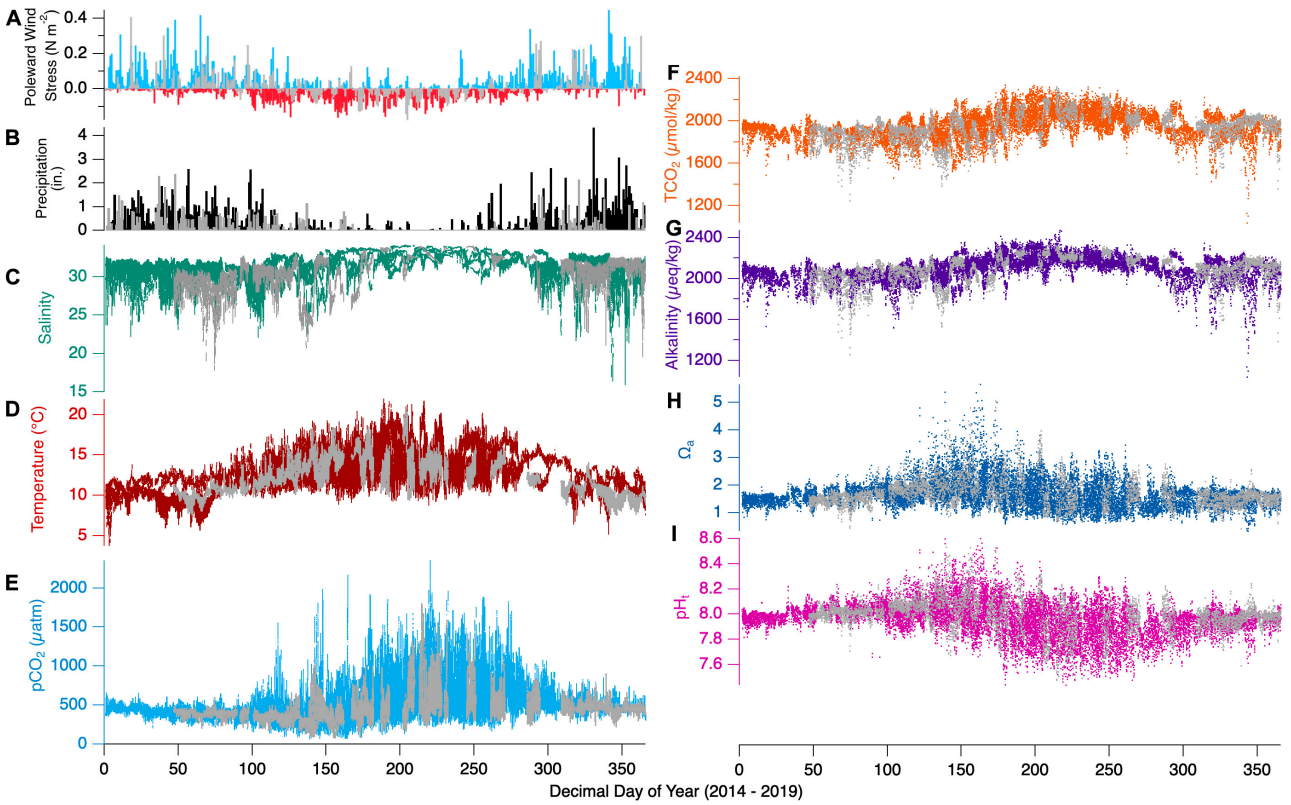


FIGURE 5 | Composite observations for Netarts Bay 2014–2019. **(A)** Poleward wind stress, **(B)** daily precipitation in inches, **(C)** salinity (teal line), **(D)** temperature (red line), **(E)** pCO_2 (cyan line), **(F)** TCO_2 (orange dots), **(G)** calculated alkalinity (purple dots), **(H)** aragonite saturation state (Ω_a,blue dots), and **(I)** pH (pink dots). Dark gray shading of each parameter represents the 2017 data set. Wind stress data available at: http://damp.coas.oregonstate.edu/windstress/Precipitation data courtesy of https://www.ncdc.noaa.gov/cdo-web/.

processes, advection of various water masses into the bay, adjacent coastal wind forcing, and daytime insolation. In this section we examine and hypothesize certain factors driving the observed variability at multiple timescales.

Diel Synchrony and Tide Phasing

The previously described diel variability of in-bay pCO_2 is characterized by a gradual decline throughout the afternoon until a diel minimum is reached in late afternoon or early evening, followed by a gradual build up overnight until an early morning maximum is reached. This pattern is evident in both summer and winter, though with lower amplitude in winter (**Figure 2**). Coincident with the diel variability, however, is a strong tidal forcing that cannot be clearly separated from the diel forcing in the 1-week snapshots presented earlier. With relatively short water residence times (∼12 h), tidal forcing is evident in salinity, and to some degree TCO_2 and alkalinity variability, particularly in winter. The semi-diurnal tides are not perfectly in phase with the diel variability, however, but shift forward nearly 40 min each day. Therefore, if tidal forcing were the dominant control, we would see the pCO_2 variability reverse phase with respect to the day on ∼fortnightly intervals. **Figures 6A,B** shows pCO_2 and TCO_2 variability across two 5-day periods in summer 2017 with tide phasing shifted roughly 90 degrees between the top and bottom graph. In each representation, pCO_2 trends down during daylight hours to reach a late-day minimum and increases overnight to an early morning maximum. Similarly, wintertime conditions show diel pCO_2 behavior which trend down in response to daytime insolation and rise slightly overnight (**Figures 6C,D**) even when comparing periods of orthogonal tide heights.

The apparent driver of this diel variability is the net metabolism driven by a composite of processes in the bay. The balance between primary production, which consumes CO_2 in the presence of sunlight and nutrients to create organic matter, and respiration, which releases CO_2 during the degradation of organic matter, drives diel pCO_2 variability. During summer, when the photoperiod is extended due to higher incident solar angle and prolonged daylight, insolation is at its maxima; coincidentally, upwelling supplies the bay and coastal ocean with elevated nutrients (Oregon coast upwelled-water NO_3^- > 35 μM; Hales et al., 2005). The abundant epibenthic primary producers and the high surface-area:volume ratio of the bay-floor relative to the water column leads to extensive modification of the overlying water, despite rapid tidal flushing. Broadly, the reverse occurs once the lights turn off and heterotrophic metabolism tips the scales, producing an abundance of TCO_2. This addition of dissolved carbon dioxide

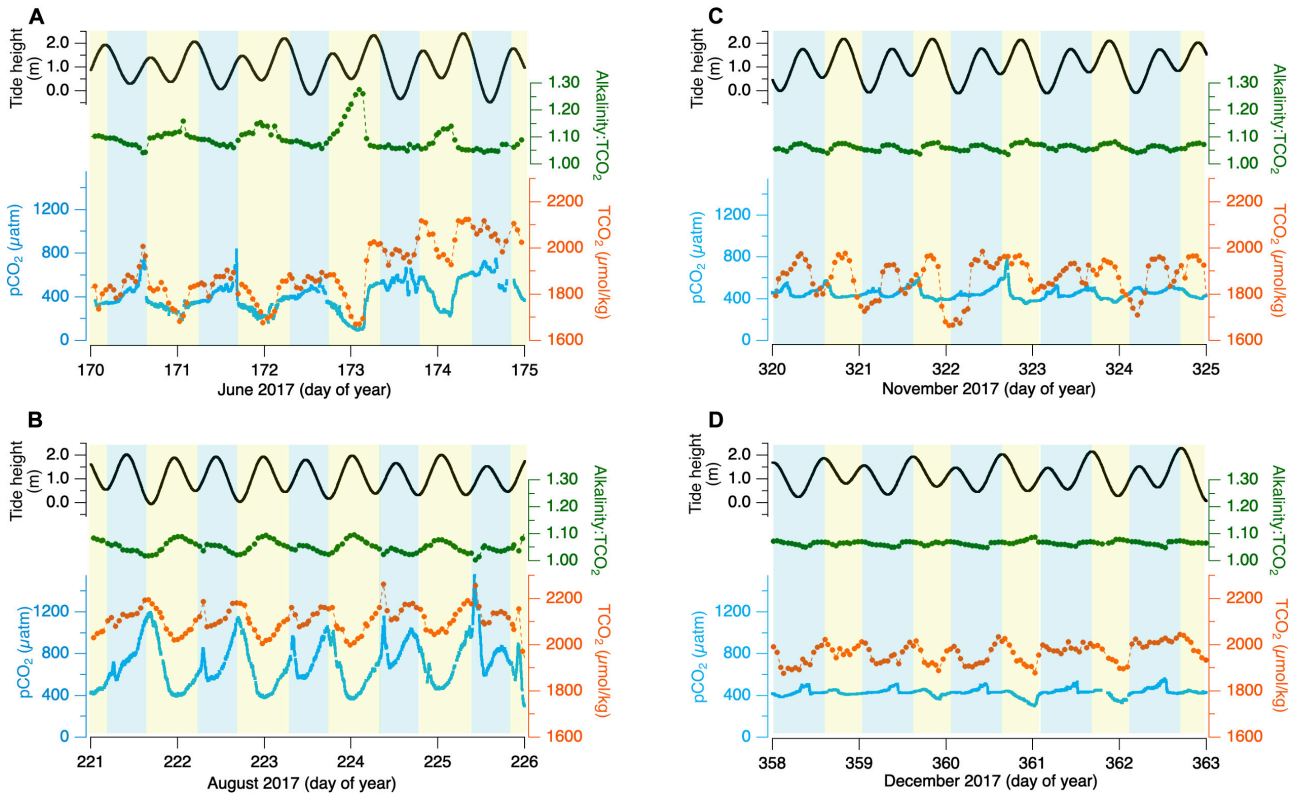


FIGURE 6 | pCO_2 (blue line), TCO_2 (orange dots connected by a line), Alk:TCO_2 ratio (red starts connected by a line), and estimated tide height (black line) for two 7-day periods during summer **(A,B)** and winter **(C,D)** of 2017 with tide-phasing ~90° between top and bottom. Blue shading indicates local nighttime and yellow shading indicates daytime.

shifts the carbonate chemistry such that pCO_2 at times passes 2000 µatm as seen in the early morning spring months of 2019 (data not shown) in response to strong and sustained equatorward winds and subsequent offshore upwelling.

This mechanism is supported further by the close coherence of pCO_2 and TCO_2 during the productive summer season, while alkalinity variability remains small. Aerobic net community metabolism impacts primarily TCO_2, with much smaller impact on alkalinity, and thus carries an implied pCO_2 and TCO_2 covariance. For T ~ 12°C, S ~ 33, the relative change in pCO_2 is 12 times the relative change of TCO_2 [Revelle Factor of 12 (Revelle and Suess, 1957; Broecker et al., 1979; Sundquist et al., 1979)], for all other variables constant. Relative variability in pCO_2 daily minimum and maximum for the intervals depicted ranges 10–20 times that for TCO_2, adding support to the idea that net metabolism, modulated by diel insolation cycles, is the primary driver of summertime bay carbonate-system variability.

Nested within the day-night variability is an apparent tidal signature, most evident in the "dual-peaks" signature in the pCO_2 behavior in **Figure 6B**. This tidal signal is complicated, however, by the variable synchronicity between ocean upwelling and relaxation, the tide state, and insolation. For example, during strong upwelling, high-pCO_2 freshly upwelled water will be present adjacent to the bay-mouth. If this water flows into the bay in the evening following a sunny day when in-bay productivity has reduced the pCO_2 of bay waters, the rising tide will coincide with rising bay pCO_2. Conversely, if relaxation has allowed productive ocean waters with depleted pCO_2 to be pushed against the shore and these waters enter the bay early in the morning after in-bay respiration has increased bay-water pCO_2, the rising tide will correspond with falling bay pCO_2. The persistent diel insolation-coupled periodicity in summertime, despite the range of ocean conditions and tide/insolation phasing emphasizes the dominance of in-bay metabolism.

The wintertime conditions are somewhat more challenging to explain, as the diel variability in pCO_2 is muted but persists in the face of clearly tidally modulated alkalinity and TCO_2. Even within broad ranges of TCO_2 and alkalinity, pCO_2 is largely driven by changes in the ratio of TCO_2:alkalinity (**Figures 6C,D**). Although there are important variations in the salinity-alkalinity relationships, discussed below, the leading factor is freshwater dilution of ocean water, which largely preserves the oceanic TCO_2:alkalinity ratio. The large tidally driven salinity-covariant TCO_2 variability is thus compensated by covarying alkalinity. The responding factors like pCO_2 and pH_t show distinct patterns of variability, with the diel character persisting. The metabolic signature is expected to be suppressed relative to summer. Lower insolation angle, shorter photoperiod, and increased cloudiness limit the potential maximum photosynthetic rate, and wintertime coastal waters carry significantly lower nutrient concentrations

than upwelled source waters (Wetz et al., 2006). This reduced metabolic signature is consistent with observed reductions in in-bay biomass during winter, when the extensive seagrass beds seen in summer have vanished.

Event-Scale Variability

Imposed onto the observed carbonate dynamics are event-scale processes which act on timescales of days to weeks. The predominantly summertime equatorward winds which drive offshore Ekman transport and upwelling occur in cycles of strong wind-forcing/relaxation periods. The duration, timing of onset, and intensity of these cycles are governed by synoptic-scale high-pressure systems and occur on variable time and space scales along the West Coast (Pringle and Dever, 2009; Aristizábal et al., 2017). One such transition from wind relaxation to upwelling is captured in the 2017 summer interval (**Figures 2**, **3**), which show a clear hydrographic and carbonate-variable influence of high-salinity, -TCO_2 and -alkalinity deep-upwelled-source water entering the bay coincident with a strengthening of equatorward wind. The wind-relaxation event which occurred prior, days 169–173, was concurrent with salinity, TCO_2 and alkalinity below 32, 2000 μmol/kg, and 2100 μeq/kg, respectively. The wind-stress time-series for the full year 2017 (**Figure 4**) shows days to weeks of prevailing equatorward winds followed by instances of brief relaxation periods and/or light poleward winds. These relaxation cycles coincide with warmer water temperatures, lower and more tidally synchronized salinity and alkalinity, and a slight dampening of diel pCO_2 dynamics in response to reduced input of dissolved nutrients as the bay's primary water source shifts from deep upwelled water to open Pacific Ocean surface water.

Event-scale variability occurs throughout the downwelling-wintertime regime as well as when the influence of predominantly California current water ($S \sim 32.5$) is interrupted by brief but intense storm-dominated conditions. During the winter of 2017, multiple low-pressure fronts moved over the Oregon coast (**Figure 4**), depositing several inches of rain over brief (∼48-h, days 361–363) windows. The combination of direct dilution and mixing of local coastal freshwater endmembers represented by discharge from small mountainous rivers resulted in large negative salinity, alkalinity, and TCO_2 departures from the overall background downwelling conditions. Rapid tidal flushing and a return to precipitation-free downwelling in the days following storm conditions quickly returned the bay to normal wintertime variability.

Seasonal Upwelling and Downwelling

At seasonal timescales, we observe large differences in character and variability of nearly all hydrographic and carbonate parameters between the summer and winter. The clear driver of these stark summer-winter differences is the regional transition from upwelling-dominated high-insolation summer conditions with equatorward winds and low precipitation, to downwelling-dominated low-insolation winter conditions with frequent intense precipitation events. These background seasonal differences set the stage for the distinct behavior and variability timescales seen in the different seasons.

Interceding these two states are transition seasons where the character of the dominant season fades and the impending season emerges. In the fall transition, upwelling favorable winds wane in the September-October timeframe, while the winter storms build in October-November. In the spring transition, intervals between winter storm events have building upwelling character. The bay's seasons are thus driven largely by the initiation and termination of coastal upwelling and downwelling. There have been detailed studies regarding the variability of the onset of upwelling in this region (Pierce et al., 2006); similarly wintertime precipitation events are highly variable interannually.

Behavior of Alkalinity

For much of the open surface ocean, alkalinity is affected primarily by local removal (by evaporation and/or ice formation) and addition (by precipitation and/or ice-melt) of near zero-alkalinity fresh water (Brewer et al., 1986; Lee et al., 2006). Mixing of water masses results in single, conservative (linear) alkalinity-salinity relationships that can be applied within large oceanic sub-regions (Takahashi et al., 2014). We have compared regionally published alkalinity-salinity relationships for North Pacific subregion (Takahashi et al., 2014, Eq. 2; Cullison Gray et al., 2011, Eq. 3, adapted from the published form for consistency) to that acquired from the comprehensive 2014 –2019 WCSH measurements (**Figure 7**; Eq. 4):

$$Alkalinity = 44.88 * \left(Salinity\right) + 724.6 \tag{2}$$

$$Alkalinity = 50.8 * \left(Salinity - 31.25\right) + 2131$$

$$Alkalinity = 50.8 * \left(Salinity\right) + 543 \tag{3}$$

$$Alkalinity = 53.1 * \left(Salinity\right) + 440 \tag{4}$$

While the WCSH results are broadly consistent with the other regional regressions, particularly at salinities approaching open Pacific Ocean surface waters ($S > 32$, average salinity-based alkalinity predictions deviated ± 15 *upmu*eq/kg when compared to observed), there are multiple and discrete trends which depart from both the regional relationships and the comprehensive WCSH alkalinity/salinity relationship. These differences appear to be real and mechanistic. Although the Takahashi et al. (2014) relationship is based on a nitrate-corrected 'potential alkalinity' and the Cullison Gray et al. (2011) results are not, the difference between their mostly open-ocean products is likely to be only a few μeq/kg. Our results are also uncorrected for nitrate, and while the corrections for our data are likely to be higher, they are still expected to be less than ∼35 μeq/kg (given the NO_3^- levels in upwelled source water; Hales et al., 2005) and without clear salinity dependence. While all three relationships are broadly consistent with each other at the highest salinities, there is a clear tendency toward higher salinity dependence (slope) and lower apparent freshwater endmember (intercept) in the WCSH data, as well as deviation of the direct alkalinity determinations

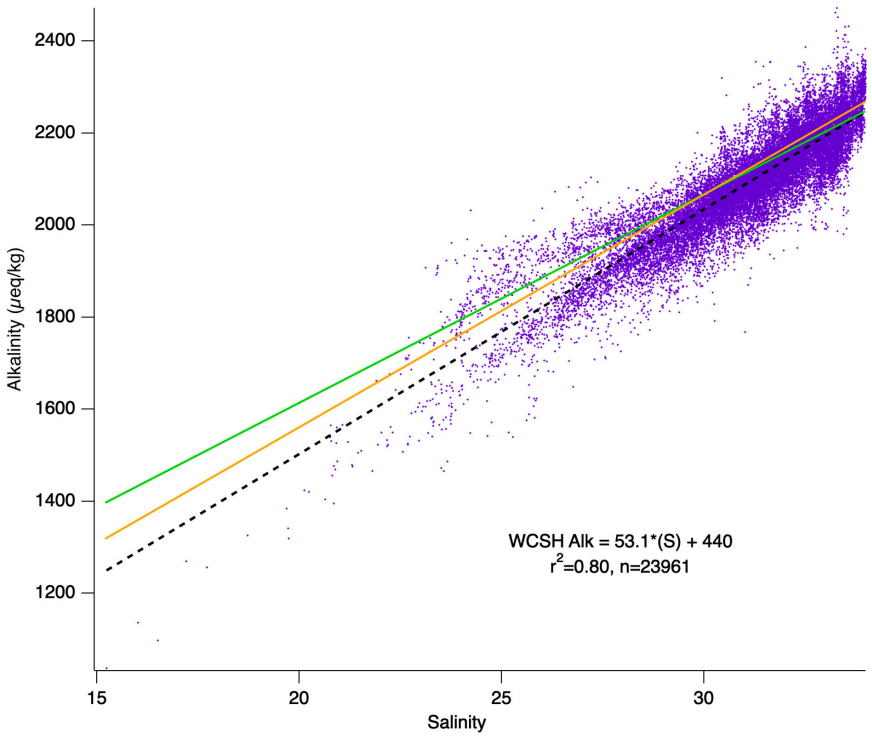


FIGURE 7 | Composite alkalinity-salinity regression for all years 2014–2019 and associated correlation statistics. Purple dots represent hourly calculated alkalinity data and black dashed line represents a simple linear-fit. Published regional alkalinity-salinity relationships from from Cullison Gray et al. (2011; orange), and Takahashi et al. (2014; green) are overlain.

from the regression of the full WCSH dataset that exceed the analytical uncertainty.

The existence of regional predictive relationships for alkalinity from the relatively more-easily measured salinity, as well as the large-scale coherence between salinity and alkalinity seen in our data, offers potential for assessing ocean acidification-relevant parameters using measurement of a single parameter, such as pCO_2, and a salinity-based estimate of alkalinity. Our direct determinations of alkalinity, however, show several systematic departures from all three 'regional' predictions that exceed our analytical uncertainty. These cause significant error in calculation of un-measured parameters, and can be broadly divided into two categories: conservative mixing with multiple end-members; and non-conservative behavior driven by in-bay metabolic-processes.

Identifying Multiple End-Members

From late fall to early spring, metabolic activity in the bay is suppressed and salinity variability is comparatively high relative to summer conditions. During these intervals, there is strong linear covariance between alkalinity and salinity over a variety of timescales with R^2 values frequently exceeding 0.9. During these months, WCSH alkalinity is well-predicted by the full-dataset, Cullison Gray et al. (2011), and Takahashi et al. (2014) relationships when the salinity is relatively high and the variability is moderate (**Figure 8A**, days 72–74; **Figure 8B**, days 128–131). This likely reflects mixing of California Current surface waters with mixed winter-time Oregon shelf waters (Wetz et al., 2006; Whitney and Garvine, 2006; Banas et al., 2009; Pfeiffer-Herbert et al., 2016). More extreme freshening, however, causes systematic deviation from the regional predictions, in both the positive and negative sense. **Figure 8A**, day 74 shows a strong alkalinity decrease coinciding with freshening driven by a 24-h period of intense local rainfall and watershed runoff. In this case, the directly determined alkalinity is 200–280 μeq/kg lower than the regional predictions, reflecting the very-low alkalinity of precipitation and event-driven runoff from Netarts Bay's small watershed. Regression of alkalinity vs. salinity in these events (inset) suggests a freshwater endmember of 115 μeq/kg, low even in comparison to coast range river water (~300 μeq/kg; Pfeiffer-Herbert et al., 2016; Hales, unpublished) and indicative of the importance of direct precipitation on the bay. For this precipitation event, the WCSH-regression alkalinity (Eq. 4) combined with the directly measured pCO_2 resulted in overestimates of the actual TCO_2 by 164 ± 28 μmol/kg, pH_t by 0.06 ± 0.01, and Ω_a by 0.10 ± 0.02. In comparison, the Cullison Gray et al. (2011) alkalinity model would overestimate TCO_2 by 192 ± 33 μmol/kg, pH_t by 0.07 ± 0.01 and Ω_a by 0.10 ± 0.02. Likewise, the Takahashi et al. (2014) alkalinity model would overestimate TCO_2, pH_t, and Ω_a as much as 257 ± 48 μmol/kg, 0.09 ± 0.02, and 0.14 ± 0.03, respectively.

Other low-salinity deviations show the opposite effect. **Figure 8B**, days 132–135 shows low-alkalinity conditions, also driven by strong freshening of bay-water. Rather than falling below the regionally predicted alkalinity, observations exceed

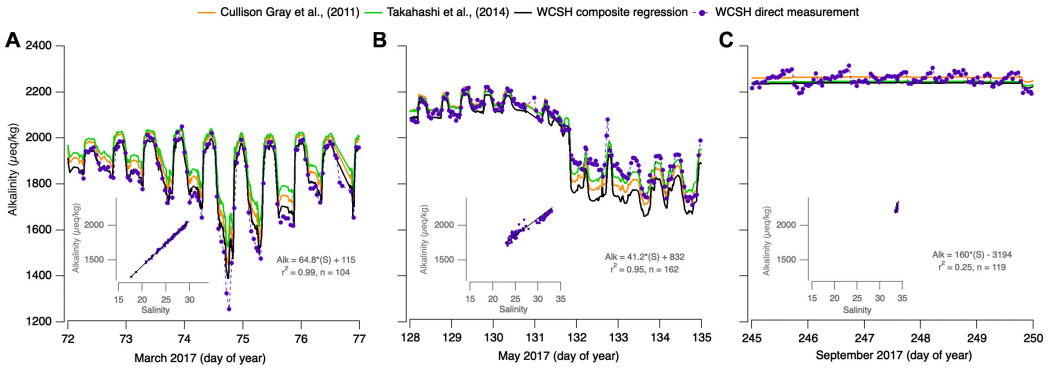


FIGURE 8 | Reconstruction and comparison of directly determined WCSH alkalinity (purple dots connected by a dashed line) and WCSH-composite regression determined alkalinity (black line) against two published regional alkalinity-salinity relationships from Cullison Gray et al. (2011) (orange), and Takahashi et al. (2014) (green). Three intervals are depicted: downwelling interceded by a precipitation event on day 74 **(A)**, apparent Columbia River plume intrusion days 132–135 **(B)**, and persistently high salinity during an upwelling interval **(C)**. Associated alkalinity-salinity regression insets for **(A–C)** are displayed in gray.

the regional salinity-based predictions, by 64–134 μeq/kg. In this case, oscillating upwelling/downwelling forcing as the spring transition is approached is thought to introduce Columbia River plume waters into the bay. Under downwelling forcing, coastal flow is poleward and onshore, typically trapping the plume along the Washington coastline. Under the opposite flow of upwelling forcing, the plume is pushed equatorward, 100 km or more south of the river mouth, but typically sits offshore near the shelf break (Banas et al., 2009). Periods of upwelling, followed by reversals to downwelling are thought to push the southward-displaced plume onshore (Mazzini et al., 2015), thus bringing Columbia-induced freshening to the bay mouth. In this case, regressions (**Figure 8B**, inset) indicate a freshwater endmember of 832 μeq/kg, higher than any of the regional relationships and consistent with the composition of Columbia River water (USGS National Stream Quality Accounting Network[2]; Evans et al., 2013). These deviations are significant not just in alkalinity, but in the parameters that might be calculated from a predicted alkalinity and WCSH-measured pCO_2. For Cullison Gray et al. (2011) TCO_2 estimates would be underpredicted by as much as 188 ±37 μmol/kg; pH by 0.04 ± 0.01 and Ω_a by 0.52 ± 0.08. Similarly, Takahashi et al. (2014) at times would underpredict TCO_2 by 182 ± 34 μmol/kg; pH by 0.05 ± 0.01 and Ω_a by 0.44 ± 0.08. WCSH-regression alkalinity resulted in the largest observed underestimations in TCO_2, pH_t, and Ω_a of 224 ± 41 μmol/kg, 0.06 ± 0.01, and 0.56 ± 0.12, respectively.

Metabolic-Process Dominance

The strong alkalinity-salinity coupling observed during downwelling-favorable conditions tends to break down during persistent upwelling intervals. During these summertime conditions, precipitation and local-river discharge is effectively absent, the Columbia River plume is far offshore, and the in-bay salinity variability is minimal. In spite of this, alkalinity variability is high and significantly in excess of our analytical uncertainty. Even when regressions were statistically significant with high linearity, the coefficients were geochemically unrealistic: slopes with magnitudes many times any reported values and with both positive and negative sign. Similarly, observed alkalinity was as much as 58 μeq/kg different from the regional relationships (**Figure 8C**), in both positive and negative senses. These results suggested that any alkalinity-salinity covariance was fortuitous, and that the alkalinity variability was driven by processes other than mixing or dilution/concentration. Regression of these data (**Figure 8C**, inset) generates low predictive power (R^2 = 0.25) and geochemically unrealistic slope and intercept values. Parameters calculated from WCSH-regression alkalinity and those provided by Cullison Gray et al. (2011) and Takahashi et al. (2014) were all similarly in error: TCO_2 overestimated at times by 108 ± 21μmol/kg, pH_t by 0.02 ± 0.01, Ω_a by 0.14 ± 0.02.

Non-physical processes that can change bay alkalinity include the consumption/release of protons in proportion to nitrate uptake/regeneration during oxic photosynthesis/respiration; $CaCO_3$ formation and dissolution; and suboxic respiration such as sulfate reduction and pyrite formation (Brewer and Goldman, 1976; Hu and Cai, 2011; Cai et al., 2017). While any of these processes are probably occurring, net calcification seems most likely to have the greatest effect. Aerobic nitrate cycling should result in anti-correlated alkalinity:TCO_2 with a ∼1:7 ratio (Dickson, 1981; Wolf-Gladrow et al., 2007), and this is not evident. Further, net autotrophy within the bay, as suggested by the seasonal buildup of seagrass beds, would seemingly result in a growing alkalinity over the course of the summer season, which is also not observed. In contrast, summer alkalinity frequently departs negatively from expected salinity dependences. The only process that can drive these negative departures in the face of strong biological pCO_2 depletion is net precipitation of $CaCO_3$. It is hard to quantify the net $CaCO_3$ precipitation independently, but the bay is a location of abundant and resilient shellfish communities.

Implications for Ocean Acidification

Whiskey Creek Shellfish Hatchery experienced the immediate impacts of ocean acidification during the 2008 growing season

[2]https://nrtwq.usgs.gov/nwqn/#/

when intake water containing naturally elevated CO_2 –further enhanced by anthropogenic CO_2—killed off millions of larval shellfish, placing the hatchery in danger of permanent shutdown (Barton et al., 2012, 2015). Along the adjacent coastal shelf, water influenced by anthropogenic carbon has been documented upwelling onto the shelf (Feely et al., 2008), creating potentially corrosive conditions for marine calcifiers and threatening to fundamentally alter the marine food-web. Instances of ocean acidification-related shellfish mortality and various other implications of changing carbonate chemistry are expected to continue worsening through the end of century (IPCC, 2014), and the work of coastal monitoring and public communication and engagement will be essential toward developing potential mitigation strategies.

In the coastal environment with dramatically variable carbonate chemistry within relatively small spatial scales, monitoring ocean acidification requires a broad network of buoys, field scientists, and volunteers (Hofmann et al., 2011; Takeshita et al., 2015). These operations are often times many millions of dollars (Strong et al., 2014) and the commercial fisheries and shellfish industries rely on accurate, reliable assessment of coastal water quality as it relates to specific organisms. Frequently, pH probes are used to measure pH because they are relatively easy tools to use. However, pH measurements come with inherent measurement uncertainties and often are unreliable predictors of more relevant ocean acidification parameters for marine calcifiers such as Ω_a (Gimenez et al., 2019), specifically in salinity-variable settings such as estuaries. Similarly, coastal mooring sites reveal that low pH and low Ω_a do not necessarily overlap (Sutton et al., 2016). A 3-year study of Willapa Bay carbonate chemistry revealed that for a nominal pH_t value of 7.7, Ω_a ranged from < 0.5 to 1.5 (Hales et al., 2017) suggesting that reliance on pH probes alone, without consideration of other carbonate variables, may over- or underestimate optimal seawater growing conditions for hatchery owners. For a nominal pH of 7.7 across all years at WCSH, Ω_a ranged from 0.9 to 1.8.

Understanding and predicting organismal response to ocean acidification represents a primary challenge in determining the fate of marine calcifiers in the face of an increasingly corrosive marine environment. For example, laboratory studies suggest that *Crassostrea gigas* (Pacific oyster) larvae begin to experience acute physiological stress in seawater with $\Omega_a < 1.7$; below 1.4 significant developmental stunting and potential larval shellfish mortality can occur (Barton et al., 2012; Waldbusser et al., 2015b); while $\Omega_a < 1.0$ and the system thermodynamically favors dissolution of mineral calcium carbonate back into solution. In the context of WCSH, which primarily raise *C. gigas* larvae, monitoring and adjusting intake water Ω_a (Waldbusser et al., 2015a) have led to increased hatchery success (Barton et al., 2015), and far fewer instances of mass larval mortality.

Utilizing hourly calculated Ω_a at WCSH for all years of this study, Ω_a measured less than 1.7 during 58% of instances, < 1.4 for 31% of instances, and < 1.0 6% of the time, with the most frequent events < 1.4 occur during the late-summer months (**Figure 5H**). While the ecological thresholds for optimal and suboptimal shellfish spawning are well known for *C. gigas*, the exact timing of natural larval shellfish spawning remains an ongoing research question. For WCSH, few native oyster populations are found within the bay owing in part to lack of suitable substrate, while mussels are found inhabiting the rocky tidal shores near the mouth of the bay. Clams represent the dominant native shellfish population of Netarts Bay. The success of any native shellfish population which may inhabit the bay is critically dependent on overlapping spawning times with optimal carbonate conditions—particularly within the first 48-h when shellfish are at the highest risk of mortality in corrosive conditions (Waldbusser et al., 2015a).

The Impact of Anthropogenic CO_2

The Pacific ocean inventory of CO_2 is increasing at a rate of approximately 0.41 ± 0.13 mol C/m^2/yr (0.82 ± 0.26 Pg C/yr) (Quay et al., 2017) primarily by means of ocean surface gas exchange with the atmosphere. Estimates place the total increase in concentration of TCO_2 in upper surface ocean layers along the west coast of North America on the order of 37–63 μmol/kg, although these values vary spatially (Khatiwala et al., 2013; Feely et al., 2016). Using a conservative nominal value of 37 μmol/kg ($\Delta TCO_{2,anth}$) added to this region of the ocean since 1850, we estimated what conditions would have been like for WCSH without any added anthropogenic carbon by subtracting 37 μmol/kg from the TCO_2 observations and recalculating pH_t and Ω_a.

On average, the addition of 37 μmol/kg TCO_2 to the oceans has resulted in average WCSH pH_t and Ω_a values approximately 0.1 and 0.30 units lower, respectively, when compared to pre-industrial estimates. This is in line with global evaluations that surface ocean pH_t has declined 0.1 units since the start of the Industrial Revolution (Feely et al., 2004) and that surface ocean saturation state is in a current state of global decline (Friedrich et al., 2012; Jiang et al., 2015). Applying a conservative fixed anthropogenic TCO_2 addition of 37 μmol/kg for all years 2014–2019 (**Figure 9**), we find the relative impact of anthropogenic carbon on pH_t and Ω_a is variable throughout upwelling and downwelling events, with no statistically significant interannual variation from 2014 to 2019. Astoundingly, when Ω_a conditions are elevated during the late-spring/early-summer months (**Figure 5H**), the apparent contribution of anthropogenic carbon to reduced Ω_a is at its greatest (**Figure 9**, top). Moreover, the contribution of $\Delta TCO_{2,anth}$ to pH_t appears to be at its annual minimum during this period, suggesting a decoupling mechanism between pH_t and Ω_a. While our evaluation likely underestimates the true value of $\Delta TCO_{2,anth}$ for Oregon coast source water and assumes $\Delta TCO_{2,anth}$ remains fixed between 2014 and 2019, we find the results useful in demonstrating the way in which Netarts Bay is effected by ocean acidification. Implementing a fixed $\Delta TCO_{2,anth}$ reveals both a decline in the mean pH_t and saturation state, as well as more frequent low- pH_t, low-saturation state events (**Figure 10**). Using this estimate, the frequency of low saturation state events ($\Omega_a < 1.5$) has increased nearly 240% while that of undersaturation ($\Omega_a < 1.0$) events has increased sevenfold. Continued oceanic uptake of carbon will continue to push pH_t and Ω_a below their modern values, with high-latitude surface

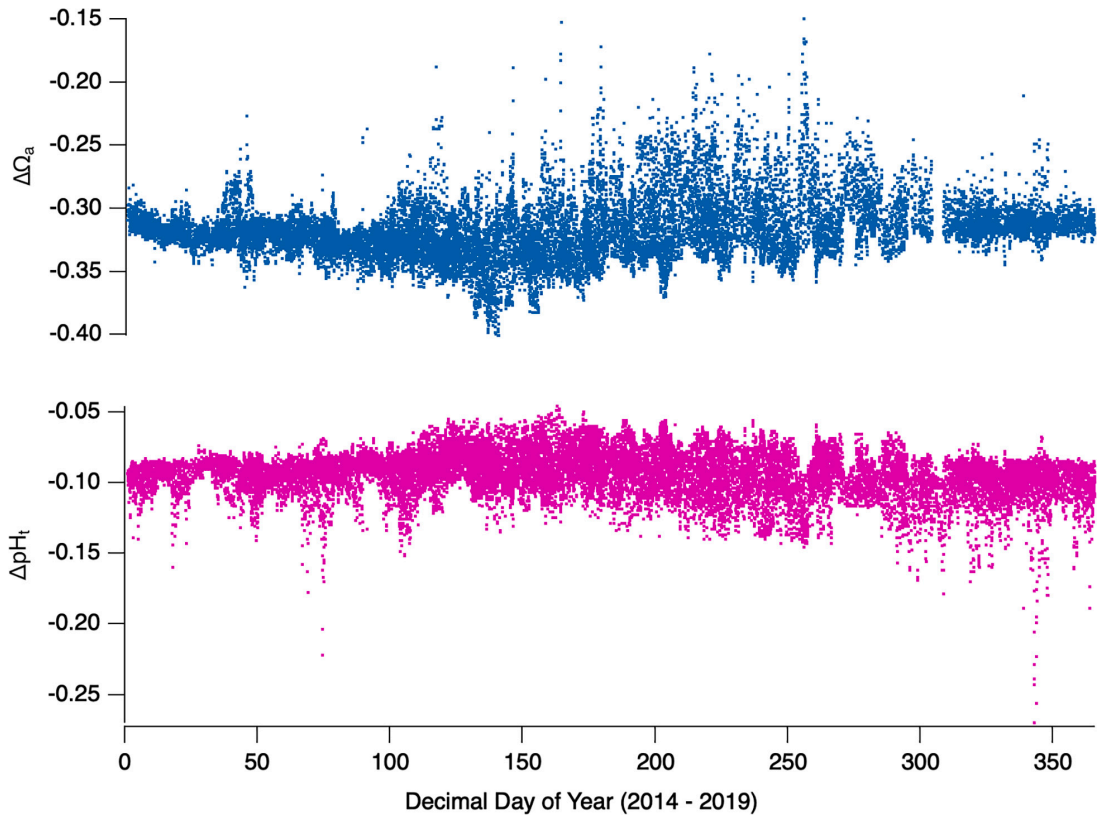


FIGURE 9 | $\Delta\Omega_a$ (top) and ΔpH_t (bottom) calculated for all years 2014–2019 at WCSH using a conservative nominal value of 37 μmol/kg TCO_2 added to west coast of United States surface water since 1850. Values represent approximate negative departures due to anthropogenic CO_2.

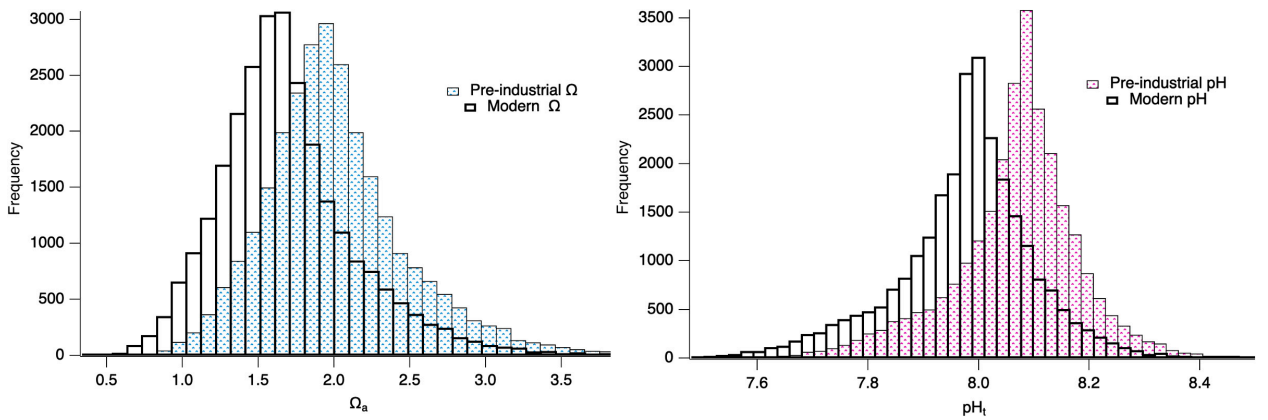


FIGURE 10 | Histogram plot of all hourly calculated Ω_a **(Left)** and pH_t **(Right)** for the 2014–2019 WCSH timeseries.

waters expected to be fully undersaturated by the end of century (Feely et al., 2009).

CONCLUSION

Netarts Bay is a metabolically dynamic, ocean-dominated estuarine environment with hydrographic and carbonate-system variability occurring on multiple timescales. Summer upwelling, wintertime downwelling, and *in situ* bay biogeochemistry represent significant drivers of the observed variability in carbonate dynamics. Data presented here show the seasonality, intensity, and duration of high-pCO_2 events while illuminating diel, seasonal, and annual patterns of carbonate-system dynamics. Direct estimates of total alkalinity from paired pCO_2 and TCO_2 measurements suggest local biogeochemical

processes not captured by regional, open-ocean alkalinity-salinity relationships. Additionally, in line with global estimates of global surface ocean pH_t and calcium carbonate saturation decline, we find that WCSH has experienced an approximate decline in pH_t and Ω_a of ∼0.1 and ∼0.30 units, respectively, since 1850.

DATA AVAILABILITY STATEMENT

The raw data supporting the conclusions of this article will be made available by the authors, without undue reservation.

AUTHOR CONTRIBUTIONS

BH was responsible for instrument development. BH and WF were responsible for data acquisition, analysis, and interpretation.

FUNDING

Funding from NOAA OAP and IOOS programs through an Ocean Technology Transfer award (NA14NOS0120151) and sustained support to NANOOS (NA16NOS0120019).

ACKNOWLEDGMENTS

The data are available: https://ir.library.oregonstate.edu/concern/datasets/9z903634r?locale=en. We would like to thank the continued participation of the WCSH team, including the sterling leadership of Sue Cudd and Alan Barton, faculty participation and assistance in routine maintenance of the laboratory including Marnie Jo Zirbel, Dale Hubbard, and Joe Jennings, as well as undergraduate and graduate student assistance from Carrie Weekes, Selina Lambert, and Michael Moses.

REFERENCES

Aristizábal, M. F., Fewings, M. R., and Washburn, L. (2017). Effects of the relaxation of upwelling-favorable winds on the diurnal and semidiurnal water temperature fluctuations in the Santa Barbara channel, California. *J. Geophys. Res. Oceans* 122, 7958–7977. doi: 10.1002/2017JC013199

Banas, N. S., MacCready, P., and Hickey, B. M. (2009). The Columbia River plume as cross-shelf exporter and along-coast barrier. *Cont. Shelf Res.* 29, 292–301. doi: 10.1016/j.csr.2008.03.011

Bandstra, L., Hales, B., and Takahashi, T. (2006). High-frequency measurements of total CO2: method development and first oceanographic observations. *Mar. Chem.* 100, 24–38. doi: 10.1016/j.marchem.2005.10.009

Barton, A., Hales, B., Waldbusser, G. G., Langdon, C., and Feely, R. A. (2012). The *Pacific oyster*, *Crassostrea gigas*, shows negative correlation to naturally elevated carbon dioxide levels: implications for near-term ocean acidification effects. *Limnol. Oceanography* 57, 698–710. doi: 10.4319/lo.2012.57.3.0698

Barton, A., Waldbusser, G., Feely, R., Weisberg, S., Newton, J., Hales, B., et al. (2015). Impacts of coastal acidification on the Pacific Northwest shellfish industry and adaptation strategies implemented in response. *Oceanography* 25, 146–159. doi: 10.5670/oceanog.2015.38

Brewer, P. G., Bradshaw, A. L., and Williams, R. T. (1986). "Measurements of total carbon dioxide and alkalinity in the North Atlantic Ocean in 1981," in *The Changing Carbon Cycle: A Global Analysis*, eds J. R. Trabalka and D. E. Reichle (New York, NY: Springer), 348–370. doi: 10.1007/978-1-4757-1915-4_18

Brewer, P. G., and Goldman, J. C. (1976). Alkalinity changes generated by phytoplankton growth1: alkalinity changes. *Limnol. Oceanography* 21, 108–117. doi: 10.4319/lo.1976.21.1.0108

Broecker, W. S., Takahashi, T., Simpson, H. J., and Peng, T.-H. (1979). Fate of fossil fuel carbon dioxide and the global carbon budget. *Science* 206, 409–418. doi: 10.1126/science.206.4417.409

Cai, W.-J., Huang, W.-J., Luther, G. W., Pierrot, D., Li, M., Testa, J., et al. (2017). Redox reactions and weak buffering capacity lead to acidification in the Chesapeake Bay. *Nat. Commun.* 8:369. doi: 10.1038/s41467-017-00417-7

Cullison Gray, S. E., DeGrandpre, M. D., Moore, T. S., Martz, T. R., Friederich, G. E., and Johnson, K. S. (2011). Applications of in situ pH measurements for inorganic carbon calculations. *Mar. Chem.* 125, 82–90. doi: 10.1016/j.marchem.2011.02.005

Diaz, R. J., and Rosenberg, R. (2008). Spreading dead zones and consequences for marine ecosystems. *Science* 321, 926–929. doi: 10.1126/science.1156401

Dickson, A. G. (1981). An exact definition of total alkalinity and a procedure for the estimation of alkalinity and total inorganic carbon from titration data. *Deep Sea Res. Part A. Oceanographic Res. Papers* 28, 609–623. doi: 10.1016/0198-0149(81)90121-7

Dickson, A. G. (1990). Thermodynamics of the dissociation of boric acid in synthetic seawater from 273.15 to 318.15 K. *Deep Sea Res. Part A. Oceanographic Res. Papers* 37, 755–766. doi: 10.1016/0198-0149(90)90004-F

Evans, W., Hales, B., and Strutton, P. G. (2013). pCO2 distributions and air–water CO2 fluxes in the Columbia River estuary. *Estuarine, Coastal Shelf Sci.* 117, 260–272. doi: 10.1016/j.ecss.2012.12.003

Evans, W., Pocock, K., Hare, A., Weekes, C., Hales, B., Jackson, J., et al. (2019). Marine CO2 patterns in the Northern Salish Sea. *Front. Mar. Sci.* 5:536. doi: 10.3389/fmars.2018.00536

Evans, W., Hales, B., and Strutton, P. G. (2011). Seasonal cycle of surface ocean pCO2 on the oregon shelf. *J. Geophys. Res. Atmospheres* 116, C05012. doi: 10.1029/2010JC006625

Fassbender, A. J., Alin, S. R., Feely, R. A., Sutton, A. J., Newton, J. A., Krembs, C., et al. (2018). Seasonal carbonate chemistry variability in marine surface waters of the US Pacific Northwest. *Earth System Sci. Data* 10, 1367–1401. doi: 10.5194/essd-10-1367-2018

Feely, R. A., Alin, S. R., Carter, B., Bednaršek, N., Hales, B., Chan, F., et al. (2016). Chemical and biological impacts of ocean acidification along the west coast of North America. *Estuarine, Coastal Shelf Sci.* 183, 260–270. doi: 10.1016/j.ecss.2016.08.043

Feely, R. A., Doney, S. C., and Cooley, S. R. (2009). Ocean acidification : present conditions and future changes in a high-CO2 world. *Oceanography* 22, 36–47. doi: 10.5670/oceanog.2009.95

Feely, R. A., Sabine, C. L., Hernandez-Ayon, J. M., Ianson, D., and Hales, B. (2008). Evidence for upwelling of corrosive "Acidified" water onto the continental shelf. *Science* 320, 1490–1492. doi: 10.1126/science.1155676

Feely, R. A., Sabine, C. L., Lee, K., Berelson, W., Kleypas, J., Fabry, V. J., et al. (2004). Impact of anthropogenic CO2 on the CaCO3 system in the oceans. *Science* 305, 362–366. doi: 10.1126/science.1097329

Friedrich, T., Timmermann, A., Abe-Ouchi, A., Bates, N. R., Chikamoto, M. O., Church, M. J., et al. (2012). Detecting regional anthropogenic trends in ocean acidification against natural variability. *Nat. Climate Change* 2, 167–171. doi: 10.1038/nclimate1372

Gimenez, I., Waldbusser, G. G., Langdon, C. J., and Hales, B. R. (2019). The dynamic ocean acidification manipulation experimental system: separating carbonate variables and simulating natural variability in laboratory flow-through experiments. *Limnol. Oceanography: Methods* 17, 343–361. doi: 10.1002/lom3.10318

Glanzman (1971). *Tidal Hydraulics, Flushing Characteristics and Water Quality of Netarts Bay*. Corvallis: Oregon State University.

Hales, B., Chipman, D., and Takahashi, T. (2004). High-frequency measurement of partial pressure and total concentration of carbon dioxide in seawater using microporous hydrophobic membrane contactors. *Limnol. Oceanography: Methods* 2, 356–364. doi: 10.4319/lom.2004.2.356

Hales, B., Moum, J. N., Covert, P., and Perlin, A. (2005). Irreversible nitrate fluxes due to turbulent mixing in a coastal upwelling system. *J. Geophys. Res.: Oceans* 110, doi: 10.1029/2004JC002685

Hales, B., Suhrbier, A., Waldbusser, G. G., Feely, R. A., and Newton, J. A. (2017). The carbonate chemistry of the "Fattening line," Willapa Bay, 2011-2014. *Estuar. Coasts; Port Republic* 40, 173–186. doi: 10.1007/s12237-016-0136-7

Hofmann, G. E., Smith, J. E., Johnson, K. S., Send, U., Levin, L. A., Micheli, F., et al. (2011). High-Frequency dynamics of ocean pH: a Multi-Ecosystem comparison. *PLoS One* 6:e28983. doi: 10.1371/journal.pone.0028983

Hu, X., and Cai, W.-J. (2011). An assessment of ocean margin anaerobic processes on oceanic alkalinity budget: anaerobic alkalinity production. *Global Biogeochem. Cycles* 25:GB3003. doi: 10.1029/2010GB003859

Ianson, D., Allen, S. E., Harris, S. L., Orians, K. J., Varela, D. E., and Wong, C. S. (2003). The inorganic carbon system in the coastal upwelling region west of Vancouver Island, Canada. *Deep Sea Res. Part I: Oceanographic Res. Papers* 50, 1023–1042. doi: 10.1016/S0967-0637(03)00114-6

Jiang, L.-Q., Feely, R. A., Carter, B. R., Greeley, D. J., Gledhill, D. K., and Arzayus, K. M. (2015). Climatological distribution of aragonite saturation state in the global oceans. *Global Biogeochem. Cycles* 29, 1656–1673. doi: 10.1002/2015GB005198

Kennish, M. J. (2002). Environmental threats and environmental future of estuaries. *Environmental Conserv.* 29, 78–107. doi: 10.1017/S0376892902000061

Khatiwala, S., Tanhua, T., Mikaloff Fletcher, S., Gerber, M., Doney, S. C., Graven, H. D., et al. (2013). Global ocean storage of anthropogenic carbon. *Biogeosciences* 10, 2169–2191. doi: 10.5194/bg-10-2169-2013

Lee, K., Tong, L. T., Millero, F. J., Sabine, C. L., Dickson, A. G., Goyet, C., et al. (2006). Global relationships of total alkalinity with salinity and temperature in surface waters of the world's oceans. *Geophys. Res. Lett.* 33:L19605. doi: 10.1029/2006GL027207

Mazzini, P. L. F., Risien, C. M., Barth, J. A., Pierce, S. D., Erofeev, A., Dever, E. P., et al. (2015). Anomalous near-surface low-salinity pulses off the central Oregon Coast. *Sci. Rep.* 5:17145. doi: 10.1038/srep17145

McCallum, L. (1977). *Netarts Bay, Oregon: An Assessment of Human Impact on an Estuarine System*. Ph.D. thesis, Department of Geography, Portland State University, Portland. doi: 10.15760/etd.2548

Millero, F. J. (2010). Carbonate constants for estuarine waters. *Mar. Freshwater Res.* 61, 139–142. doi: 10.1071/MF09254

Mucci, A. (1983). The solubility of calcite and aragonite in seawater at various salinities, temperatures, and one atmosphere total pressure. *Am. J. Sci.* 283, 780–799. doi: 10.2475/ajs.283.7.780

Nemcek, N., Ianson, D., and Tortell, P. D. (2008). A high-resolution survey of DMS, CO2, and O2/Ar distributions in productive coastal waters. *Global Biogeochem. Cycles* 22:GB2009. doi: 10.1029/2006GB002879

Peirson, W., Davey, E., Jones, A., Hadwen, W., Bishop, K., Beger, M., et al. (2015). Opportunistic management of estuaries under climate change: a new adaptive decision-making framework and its practical application. *J. Environ. Manag.* 163, 214–223. doi: 10.1016/j.jenvman.2015.08.021

Pfeiffer-Herbert, A. S., Prahl, F. G., Hales, B., Lerczak, J. A., Pierce, S. D., and Levine, M. D. (2016). High resolution sampling of methane transport in the Columbia River near-field plume: implications for sources and sinks in a river-dominated estuary. *Limnol. Ocean.* 61, S204–S220. doi: 10.1002/lno.10221

Pierce, S. D., Barth, J. A., Thomas, R. E., and Fleischer, G. W. (2006). Anomalously warm July 2005 in the northern California current: historical context and the significance of cumulative wind stress. *Geophys. Res. Lett.* 33. doi: 10.1029/2006GL027149

Pringle, J. M., and Dever, E. P. (2009). Dynamics of wind-driven upwelling and relaxation between Monterey Bay and point arena: local-, regional-, and gyre-scale controls. *J. Geophys. Res.: Oceans* 114. doi: 10.1029/2008JC005016

Quay, P., Sonnerup, R., Munro, D., and Sweeney, C. (2017). Anthropogenic CO2 accumulation and uptake rates in the Pacific Ocean based on changes in the 13C/12C of dissolved inorganic carbon. *Global Biogeochem. Cycles* 31, 59–80. doi: 10.1002/2016GB005460

Rabalais, N. N., Turner, R. E., Diaz, R. J., and Justic, D. (2009). Global change and eutrophication of coastal waters. *ICES J. Mar. Sci.* 66, 1528–1537. doi: 10.1093/icesjms/fsp047

Revelle, R., and Suess, H. E. (1957). Carbon dioxide exchange between atmosphere and ocean and the question of an increase of atmospheric CO 2 during the past decades. *Tellus* 9, 18–27. doi: 10.1111/j.2153-3490.1957.tb01849.x

Strong, A. L., Kroeker, K. J., Teneva, L. T., Mease, L. A., and Kelly, R. P. (2014). Ocean acidification 2.0: managing our changing coastal ocean chemistry. *BioScience* 64, 581–592. doi: 10.1093/biosci/biu072

Sundquist, E. T., Plummer, L. N., and Wigley, T. M. L. (1979). Carbon dioxide in the ocean surface: the homogeneous buffer factor. *Science* 204, 1203–1205. doi: 10.1126/science.204.4398.1203

Sutton, A. J., Sabine, C. L., Feely, R. A., Cai, W.-J., Cronin, M. F., McPhaden, M. J., et al. (2016). Using present-day observations to detect when anthropogenic change forces surface ocean carbonate chemistry outside preindustrial bounds. *Biogeosciences* 13, 5065–5083. doi: 10.5194/bg-13-5065-2016

Takahashi, T., Sutherland, S. C., Chipman, D. W., Goddard, J. G., Ho, C., Newberger, T., et al. (2014). Climatological distributions of pH, pCO2, total CO2, alkalinity, and CaCO3 saturation in the global surface ocean, and temporal changes at selected locations. *Mar. Chem.* 164, 95–125. doi: 10.1016/j.marchem.2014.06.004

Takeshita, Y., Frieder, C. A., Martz, T. R., Ballard, J. R., Feely, R. A., Kram, S., et al. (2015). Including high-frequency variability in coastal ocean acidification projections. *Biogeosciences* 12, 5853–5870. doi: 10.5194/bg-12-5853-2015

van Geen, A., Takesue, R. K., Goddard, J., Takahashi, T., Barth, J. A., and Smith, R. L. (2000). Carbon and nutrient dynamics during coastal upwelling off Cape Blanco, Oregon. *Deep Sea Res. Part II: Top. Stud. Oceanography* 47, 975–1002. doi: 10.1016/S0967-0645(99)00133-2

Vance, J. M. (2012). *Proof-of-Concept: Automated High-Frequency Measurements of pCO2 and TCO2 and Real-time Monitoring of the Saturation State of Calcium Carbonate*. Thesis, Oregon State University: Corvallis, OR.

Waldbusser, G. G., Hales, B., Langdon, C. J., Haley, B. A., Schrader, P., Brunner, E. L., et al. (2015a). Ocean acidification has multiple modes of action on bivalve larvae. *PLoS One* 10:e0128376. doi: 10.1371/journal.pone.0128376

Waldbusser, G. G., Hales, B., Langdon, C. J., Haley, B. A., Schrader, P., Brunner, E. L., et al. (2015b). Saturation-state sensitivity of marine bivalve larvae to ocean acidification. *Nat. Climate Change* 5, 273–280. doi: 10.1038/nclimate2479

Waldbusser, G. G., and Salisbury, J. E. (2014). Ocean acidification in the coastal zone from an organism's perspective: multiple system parameters, frequency domains, and habitats. *Ann. Rev. Mar. Science* 6, 221–247. doi: 10.1146/annurev-marine-121211-172238

Waldbusser, G. G., Voigt, E. P., Bergschneider, H., Green, M. A., and Newell, R. I. E. (2011). Biocalcification in the Eastern oyster (*Crassostrea virginica*) in relation to long-term trends in chesapeake bay pH. *Estuaries Coasts* 34, 221–231. doi: 10.1007/s12237-010-9307-0

Wetz, M. S., Hales, B., Chase, Z., Wheeler, P. A., and Whitney, M. M. (2006). Riverine input of macronutrients, iron, and organic matter to the Coastal Ocean off Oregon, U.S.A., during the Winter. *Limnol. Oceanography* 51, 2221–2231. doi: 10.4319/lo.2006.51.5.2221

White, M. M., McCorkle, D. C., Mullineaux, L. S., and Cohen, A. L. (2013). Early exposure of bay scallops (Argopecten irradians) to high CO_2 causes a decrease in larval shell growth. *PLoS One* 8:e61065. doi: 10.1371/journal.pone.0061065

Whitney, M. M., and Garvine, R. W. (2006). Simulating the delaware bay buoyant outflow: comparison with observations. *J. Phys. Oceanography* 36, 3–21. doi: 10.1175/JPO2805.1

Wolf-Gladrow, D. A., Zeebe, R. E., Klaas, C., Körtzinger, A., and Dickson, A. G. (2007). Total alkalinity: the explicit conservative expression and its application to biogeochemical processes. *Mar. Chem.* 106, 287–300. doi: 10.1016/j.marchem.2007.01.006

Conflict of Interest: The authors declare that the research was conducted in the absence of any commercial or financial relationships that could be construed as a potential conflict of interest.

Copyright © 2021 Fairchild and Hales. This is an open-access article distributed under the terms of the Creative Commons Attribution License (CC BY). The use, distribution or reproduction in other forums is permitted, provided the original author(s) and the copyright owner(s) are credited and that the original publication in this journal is cited, in accordance with accepted academic practice. No use, distribution or reproduction is permitted which does not comply with these terms.

frontiers in Marine Science

ORIGINAL RESEARCH
published: 29 June 2021
doi: 10.3389/fmars.2021.629412

The Mid-Atlantic Bight Dissolved Inorganic Carbon System Observed in the March 1996 DOE Ocean Margins Program (OMP)—A Baseline Study

Ting-Hsuan Huang[1,2], Wei-Jun Cai[3], Penny Vlahos[4], Douglas W. R. Wallace[5], Ernie R. Lewis[6] and Chen-Tung Arthur Chen[1]*

[1] Department of Oceanography, National Sun Yat-sen University, Kaohsiung, Taiwan, [2] National Applied Research Laboratories, Taiwan Ocean Research Institute, Kaohsiung, Taiwan, [3] School of Marine Science and Policy, University of Delaware, Newark, NJ, United States, [4] Department of Marine Sciences, University of Connecticut, Groton, CT, United States, [5] Department of Oceanography, Dalhousie University, Halifax, NS, Canada, [6] Environmental and Climate Sciences Department, Brookhaven National Laboratory, Upton, NY, United States

OPEN ACCESS

Edited by:
Xianghui Guo, Xiamen University, China

Reviewed by:
Antón Velo, Instituto de Investigaciones Marinas (CSIC), Spain
Chris Langdon, University of Miami, United States

***Correspondence:**
Wei-Jun Cai
wcai@udel.edu

Specialty section:
This article was submitted to Coastal Ocean Processes, a section of the journal Frontiers in Marine Science

Received: *14 November 2020*
Accepted: *24 May 2021*
Published: *29 June 2021*

Citation:
Huang T-H, Cai W-J, Vlahos P, Wallace DWR, Lewis ER and Chen C-TA (2021) The Mid-Atlantic Bight Dissolved Inorganic Carbon System Observed in the March 1996 DOE Ocean Margins Program (OMP)—A Baseline Study. Front. Mar. Sci. 8:629412. doi: 10.3389/fmars.2021.629412

The United States Department of Energy (DOE)'s Ocean Margins Program (OMP) cruise EN279 in March 1996 provides an important baseline for assessing long-term changes in the carbon cycle and biogeochemistry in the Mid-Atlantic Bight (MAB) as climate and anthropogenic changes have been substantial in this region over the past two decades. The distributions of O_2, nutrients, and marine inorganic carbon system parameters are influenced by coastal currents, temperature gradients, and biological production and respiration. On the cross-shelf direction, pH decreases seaward, but carbonate saturation state (Ω_{Arag}) does not exhibit a clear trend. In contrast, Ω_{Arag} increases from north to south, while pH has no clear spatial patterns in the along-shelf direction. In order to distinguish between the effects of physical mixing of various water masses and those of biological activities on the marine inorganic carbon system, we use the potential temperature-salinity diagram to identify water masses, and differences between observations and theoretical mixing concentrations to measure the non-conservative (primarily biological) effects. Our analysis clearly shows the degree to which ocean margin pH and Ω_{Arag} are regulated by biological activities in addition to water mass mixing, gas exchange, and temperature. The correlations among anomalies in dissolved inorganic carbon, phosphate, nitrate, and apparent oxygen utilization agree with known biological stoichiometry. Biological uptake is substantial in nearshore waters and in shelf-slope mixing areas. This work provides valuable baseline information to assess the more recent changes in the marine inorganic carbon system and the status of coastal ocean acidification.

Keywords: Mid-Atlantic Bight, inorganic carbon system, water mass mixing, carbonate saturation, nutrient supply

INTRODUCTION

Coastal waters link the three main carbon reservoirs: land, ocean, and atmosphere, and are recognized as a major component of the global carbon cycle and budget. Although the surface area of continental margins amounts to only 7–8% of that of the ocean as a whole, the margins contribute 10–30% of global oceanic primary production (Liu et al., 2000, 2010; Vlahos et al., 2002; Jahnke, 2010; Chavez et al., 2011; Chen et al., 2013). Terrestrial materials flow into the continental shelf through river plumes and groundwater discharge. Coastal ocean processes such as tides, upwelling, onwelling, and net advective transport are the main physical pathways for terrestrial material exchange with oceanic water. In addition, gas exchange and deposition provide the main interactions between the atmosphere and coastal water. Besides mediating the exchange of carbon among the three main carbon reservoirs, biogeochemical processes, and anthropogenic impacts further compound the complexity of the marine inorganic carbon system in continental margins (Mackenzie et al., 2005; Muller-Karger et al., 2005; Jahnke, 2010; Cai, 2011; Bauer et al., 2013).

The Mid-Atlantic Bight (MAB) is a hydrographically and geochemically complex continental margin ecosystem that has been investigated intensively over the past 30 years (Csanady and Hamilton, 1988; Walsh, 1988; Biscaye et al., 1994; Wang et al., 2013; Wanninkhof et al., 2015; Cai et al., 2020; Xu et al., 2020). The slope water, coastal river plume water, southward-flowing Labrador Current, and northeastward-flowing Gulf Stream constitute the multiple and varied components of the shelf water in the MAB. Air temperature differences, buoyancy effects, tidal mixing, wind force, eddies, and shelf break jets all contribute to the physical exchange processes of water masses. Furthermore, biological processes such as photosynthesis, remineralization, bacterial motility, and denitrification also affect the marine inorganic carbon cycle in the MAB (Beardsley et al., 1976; Chapman and Beardsley, 1989; Linder and Gawarkiewicz, 1998; Gawarkiewicz et al., 2001; Aluwihare et al., 2002; Fennel et al., 2006; Lentz, 2008).

To improve the knowledge of biogeochemical processes in the continental shelf to the slope region, the United States Department of Energy (DOE) supported several research projects including the Ocean Margins Program (OMP), whose goal was to estimate the carbon and biogenic elemental storage, biogeochemical transformations, and fluxes across different interfaces (Jahnke and Verity, 1994). Hydrographic data were collected in the course of eight cruises between 1993 and 1996, and physical and biological parameters have been studied extensively according to these results. The reported results indicate that the MAB ecosystem is net autotrophic, and phytoplankton absorbs the inorganic carbon and generates organic matter that would otherwise be chemically altered and exported to the open ocean (Bauer et al., 2002; DeGrandpre et al., 2002; Hopkinson et al., 2002; Vlahos et al., 2002). However, the dissolved inorganic carbon (DIC) and total alkalinity (TA) data collected during this program have not been previously reported. A thorough analysis of the OMP inorganic carbon dataset will not only improve our understanding of how inorganic carbon system parameters are regulated by complex coastal ocean physical and biological processes but also will provide a valuable baseline to examine how climate and anthropogenic changes have modified inorganic carbon system parameters since the 1990s. This exercise is particularly relevant to current community efforts to determine and understand coastal ocean acidification with ongoing regional field observations every 3 to 5 years (Wang et al., 2013; Wanninkhof et al., 2015; Xu et al., 2017; Cai et al., 2020).

This study focuses on spatial distributions of the inorganic carbon system parameters, water mass mixing, and biological activities in the MAB in March 1996. More specifically, it focuses on the exchange between nearshore and shelf water, and between shelf and slope water (or Gulf Stream), and the mixing of these water masses that takes place largely along isopycnals or *via* mixing in the benthic boundary layer over the shelf and shelf-break. In subsequent papers, we will compare this wintertime and baseline analysis with summer data from OMP to assess seasonal variations and with more recent observations to assess the carbon cycle, anthropogenic carbon accumulation, and biogeochemical changes in this region.

STUDY AREA, ANALYTICAL METHODS, AND MIXING MODE

Cruise Description and Regional Hydrographic Background

The MAB is commonly defined by boundaries at the coast, the shelf/slope front, and two imaginary lines across the shelf: one south of Nantucket Shoals and one east of Cape Hatteras (Mountain, 1991; **Figure 1**). The cruise data were collected throughout the entire MAB from March 1–10, 1996. The timing of the cruise was chosen to capture late winter conditions when shelf water temperatures are at their annual minimum (e.g., Mountain, 2003). The six transects (**Figures 1A,B**) sampled from north to south are the Nantucket Shoals (NS), Long Island (LI), New Jersey (NJ), Delaware (DE), Chesapeake Bay (CB), and Cape Hatteras (CH), and each transect traversed from the shelf to the upper slope, with the bottom depth reaching 1,000 m at the most offshore stations, except in the NS transect. However, water samples for inorganic carbon measurements were generally collected only in the upper 200 m to allow for high vertical sample resolution within the depth and density ranges of slope waters that could exchange directly with shelf waters. In addition, there is no significant exchange between the shelf water and the slope water below 200 m (Csanady and Hamilton, 1988; **Supplementary Figure 1**).

In the vicinity of the MAB, the main alongshore currents are an equatorward-flowing, cold, and fresh coastal current (Chapman and Beardsley, 1989) supplied by the Labrador Current, and the northward-flowing, warm, and salty Gulf Stream (**Figure 1A**). The Slope Sea separates the shelf waters from the Gulf Stream as far south as Cape Hatteras, with the western Slope Sea (within the MAB) being a closed cyclonic gyre, and the eastern Slope Sea having a more open cyclonic circulation. The Labrador Current flows out of the Canadian

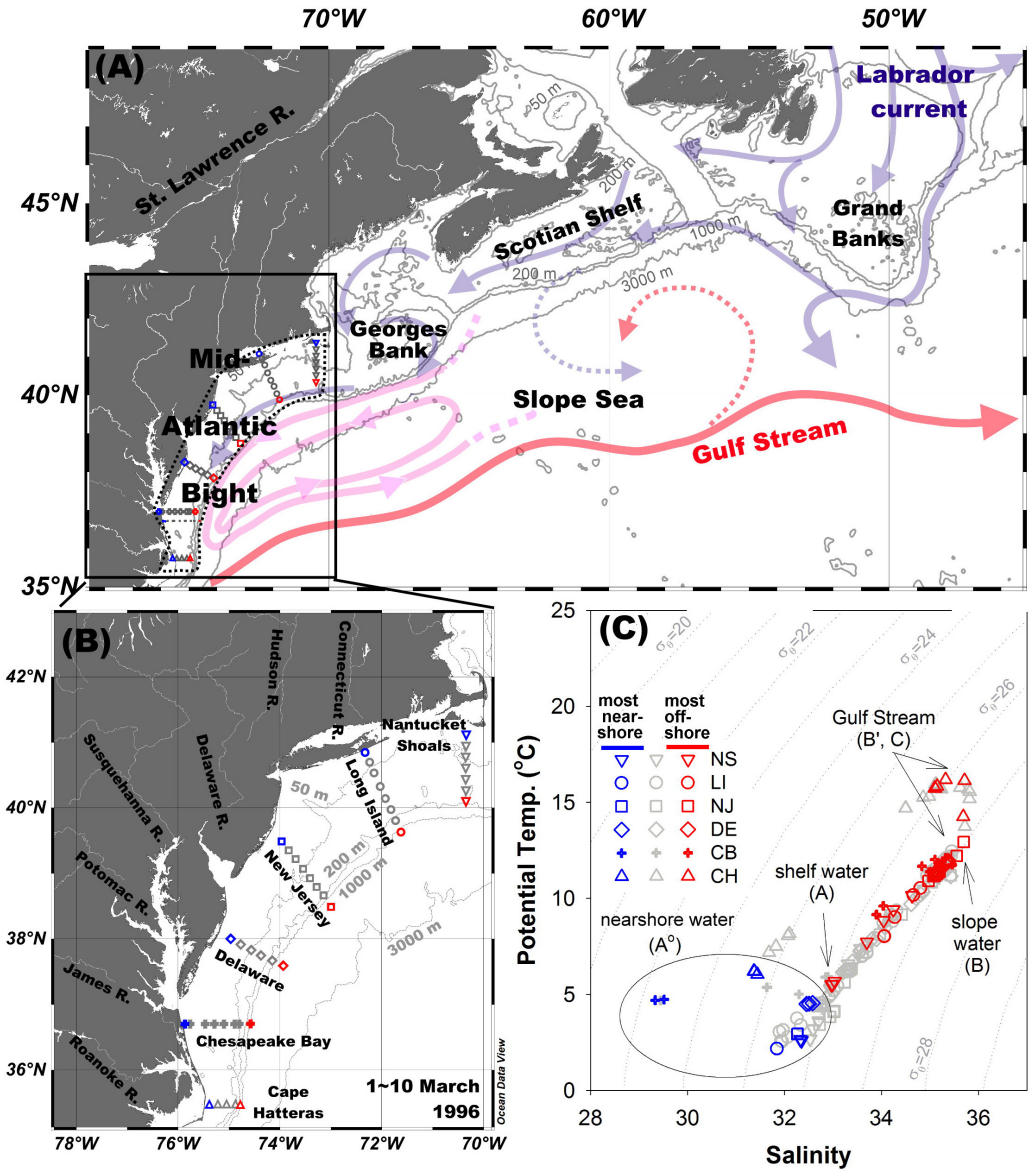


FIGURE 1 | (A) Schematic representation of the Gulf Stream, Labrador Current, and Slope Sea modified from Saba et al. (2015) and Townsend et al. (2006). **(B)** The location of sampled sites. **(C)** Potential temperature and salinity diagram. The different symbols correspond to different transects. Although symbols are not differentiated for depths, red, and blue colors are used to represent the most nearshore stations and offshore stations, respectively, while the light shaded symbols are the stations in-between. The six transects from north to south are: Nantucket Shoals (NS), Long Island (LI), New Jersey (NJ), Delaware (DE), Chesapeake Bay (CB), and Cape Hatteras (CH).

Arctic and mixes with the Gulf Stream and its extension, the North Atlantic Current, at the Grand Banks. Further south, the Labrador Current water exchanges with fresher water from the Gulf of St. Lawrence, and flows along the Scotian Shelf, and through the Gulf of Maine where mixing with a cross-isobath, onshore flow of warmer and saltier slope waters creates the characteristic shelf water mass of the MAB (Csanady and Hamilton, 1988; Chapman and Beardsley, 1989; Dong and Kelly, 2003; Townsend et al., 2006; **Figure 1A**). Within the MAB, there is additional local freshwater supply from rivers *via* several large bays, but the major freshwater sources for the MAB are the Chesapeake Bay, Labrador Current, and St. Lawrence River. A shelf-slope front that separates shelf waters from the Slope Sea has a variable location but lies typically over the 80-m isobath and is characterized by a salinity around ca. 34 and a sigma theta around 26.5 (**Supplementary Figure 1**).

Analytical Methods and Study Area

The shipboard salinity and temperature data were collected with a Neil Brown Mark III (NBIS) conductivity temperature depth (CTD) device (Flagg et al., 2002). Nitrate (NO_3^-) and phosphate (PO_4^-) concentrations were determined by using a

Technicon Autoanalyzer (Technicon AA-II, SEAL Analytical, Inc.) with spectrophotometric methods similar to those described in Wilson et al. (1989). The precision of these methods was around ± 2% (Atlas et al., 1971; Hager et al., 1972; Knap et al., 1996). The DIC concentrations were measured using a single operator multi-parameter metabolic analyzer (SOMMA) with a precision of ± 0.06% and an accuracy of ca. ± 2 μmol kg^{-1}, with values checked against Certified Reference Materials (CRM) (Dickson, 2010), and TA concentrations were determined with a Metrohm 665 Dosimat titrator and an Orion 720A pH meter with a ROSS glass pH electrode and an Orion double junction Ag, AgCl reference electrode through a nonlinear least squares approach with ±2 μmol kg^{-1} precision and were corrected with the difference between the CRM stated and analyzed values (Johnson, 1992; Johnson et al., 1993; DOE, 1994; Jahnke and Verity, 1994; Knap et al., 1996). The apparent oxygen utilization (AOU) values were calculated from the difference between the theoretical oxygen (O_2) saturation values and O_2 concentrations determined by Winkler titrations (Chen, 1981; Garcia and Gordon, 1992); positive values of AOU represent O_2 undersaturation, and negative values reflect O_2 oversaturation. Most samples were analyzed on board during the cruise.

Carbonate chemistry calculations require any two of the four commonly measured parameters—TA, DIC, pH, and fCO_2 (fugacity of CO_2) or pCO_2 (partial pressure of carbon dioxide)—to determine the other two. The CO2SYS program (Lewis and Wallace, 1998; Pierrot et al., 2006) used measured DIC and TA concentrations to calculate values of pH on the total scale, using carbonic acid dissociation constants (K_1, K_2) of Lueker et al. (2000). Also calculated using the CO2SYS was the aragonite saturation, Ω_{Arag}, defined as $[Ca^{2+}][CO_3^{2-}]/K_{Arag}$, where K_{Arag} is the solubility constant (Mucci, 1983), and the calcium concentration was determined from salinity (Millero, 1995). Finally, $pH_{in\ situ}$ and Ω_{Arag} were calculated at *in situ* temperature and pressure.

Water Mass Mixing Model

Potential temperature–salinity (θ-S) diagrams (**Figure 1C**) are widely utilized to represent and quantify mixing of different water masses (Helland-Hansen, 1916; Mamayev, 1975). The geometry of the θ-S diagram, together with the assumption of no heat or gas exchange with the atmosphere, yields a set of closed system equations that allow quantitative water mass analysis (Tomczak, 1981). The source water types (known as endmembers) were identified for each transect in the MAB based on the bounding extremes and inflection points in the potential θ-S diagrams (**Table 1** and **Supplementary Figures 1, 2**). The nearshore water endmembers were the points with the lowest salinity at each transect. The shelf water endmembers were the inflection points within the salinity range around 33–34, where the water column generally showed stratification. If there was another inflection point between the nearshore water and the shelf water, it would be identified as the nearshore water endmember 2, which reflects the mixing situation in shallow waters. The slope water was determined as the highest salinity point on the θ-S plot and was generally located around the isopycnal of 27 (**Supplementary Figure 1**). In the southern MAB, the Gulf Stream rather than the slope water served as the highest salinity endmembers for the CB and CH transects.

In this work, each transect was divided into two mixing regimes: a mixing between nearshore and shelf water, and a mixing between shelf and slope water (or the Gulf Stream for the two southern transects). The fraction of each water mass was estimated by a two-endmember mixing or a three-endmember mixing (when there were two nearshore water endmembers). The mass balance equations of a water sample (j) that is a mixture of various source water types (i) are:

$$1 = \sum_i X_{ij} \quad (1)$$

$$T_j = \sum_i X_{ij} \times T_i \quad (2)$$

$$S_j = \sum_i X_{ij} \times S_i \quad (3)$$

where the subscript i refers to an individual seawater endmember or water type, and X_{ij} is the fractional contribution of the endmember (i) to a water sample (j). T_j and S_j are the temperatures and salinities of the samples, and T_i and S_i are the temperatures and salinities of the individual endmembers. Equation 1 is the mass balance of water and Equation 3 that of salt, both of which must be conserved. Salinity can vary due not only to mixing of different water types but also to precipitation and evaporation, but it is assumed that the latter processes have little influences on the water and salt masses during the sampling period. Strictly speaking, temperature (Equation 2) is not a conserved quantity, but it is nearly directly proportional to heat content, which is conserved. Water temperatures can also be affected by heat exchange with the atmosphere, but this is not considered in the mixing model. In the calculation of mixing model, the estimated salinities are consistent with corresponding data points, but temperature differences between estimated and measured values range from –1.3 to 0.9°C.

Theoretical mixing concentrations of biogeochemical parameters can be viewed as conservative and predicted based on the proportions and concentrations of different source water types as follows:

$$A^\circ_j = \sum_j X_{ij} \times A_i \quad (4)$$

where A°_j refers to the theoretical, or conservative, mixing concentration in sample j, of a biogeochemical parameter such as AOU, phosphate, nitrate, or DIC, and A_i represents the concentrations of that biogeochemical parameter in the endmembers. The differences

$$dA = A_j - A^\circ_j \quad (5)$$

between the observed sample concentrations A_j and theoretical concentrations predicted on the basis of conservative mixing

TABLE 1 | Comparisons among nearshore water, shelf water, and slope water in temperature, salinity, phosphate, nitrate, DIC, and AOU in the NS, LI, NJ, DE, CB, and CH transects.

	Temperature (°C)						Salinity					
Transect	**Nearshore water 1**	**Nearshore water 2**	**Shelf water**	**Slope water**	**Gulf Stream 1 (40 m)**	**Gulf Stream 2 (203 m)**	**Nearshore water 1**	**Nearshore water 2**	**Shelf water**	**Slope water**	**Gulf Stream 1 (40 m)**	**Gulf Stream 2 (203 m)**
NS	2.635 (2.5–2.76)	2.671 (2.65–2.69)	4.504 (4.5–4.508)	12.202 (11–14)	-	-	32.329 (32.326–32.329)	32.532 (32.529–32.535)	32.837 (32.837–32.839)	35.554 (35.432–35.683)	-	-
LI	2.172 (2.13–2.21)	3.05 (2.92–3.22)	4.409 (4.22–4.55)	12.202 (11–14)	-	-	31.844 (31.843–31.844)	31.902 (31.885–31.908)	32.728 (32.732–32.728)	35.554 (35.432–35.683)	-	-
NJ	2.932 (2.902–4.43)	4.085 (3.97–5)	5.631 (5.63–5.632)	12.202 (11–14)	-	-	32.267 (32.246–32.267)	33.015 (33.015–33.025)	33.24 (33.239–33.341)	35.554 (35.432–35.683)	-	-
DE	4.505 (3.005–5.937)	-	6.701 (5.201–8.146)	12.202 (11–14)	-	-	32.457 (32.398–32.457)	-	33.399 (33.399–33.451)	35.554 (35.432–35.683)	-	-
CB	4.692 (3.192–5.51)	-	6.929 (5.43–7.265)	12.202 (11–14)	21.336 (20.3–24.9)	-	29.334 (29.332–29.334)	-	33.539 (33.539–33.541)	35.554 (35.432–35.683)	36.434 (36.26–36.74)	-
CH	6.207 (4.707–7.374)	-	14.694 (8.14–20.96)	-	21.336 (20.3–24.9)	11.127 (11–11.8)	31.366 (31.34–31.366)	-	34.50 (34.38–34.52)	-	36.434 (36.26–36.74)	35.413 (35.33–35.5)
	Phosphate (μmol kg^{-1})						**Nitrate (μmol kg^{-1})**					
Transect	**Nearshore water 1**	**Nearshore water 2**	**Shelf water**	**Slope water**	**Gulf Stream 1 (40 m)**	**Gulf Stream 2 (203 m)**	**Nearshore water 1**	**Nearshore water 2**	**Shelf water**	**Slope water**	**Gulf Stream 1 (40 m)**	**Gulf Stream 2 (203 m)**
NS	0.27 (0.269–0.271)	0.30 (0.28–0.31)	0.64 (0.638–0.641)	1.07 (1.02–1.13)	-	-	0 (0–0.18)	0 (0–0.25)	5.17 (5.01–5.33)	17.49 (16.7–18.28)	-	-
LI	0.48 (0.47–0.49)	0.44 (0.43–0.45)	0.70 (0.698–0.702)	1.07 (1.02–1.13)	-	-	1.93 (1.91–1.95)	2.03 (2–2.07)	5.89 (5.82–5.97)	17.49 (16.7–18.28)	-	-
NJ	-	-	0.55 (0.49–0.6)	1.07 (1.02–1.13)	-	-	-	-	1.2 (0.2–2.19)	17.49 (16.7–18.28)	-	-
DE	0.25 (0.24–0.26)	-	0.44 (0.43–0.45)	1.07 (1.02–1.13)	-	-	0.41 (0.32–0.52)	-	0.61 (0.49–0.65)	17.49 (16.7–18.28)	-	-
CB	0.00	-	0.34 (0.28–0.39)	1.07 (1.02–1.13)	0.00 (0–0.26)	-	0.48 (0.47–0.48)	-	0.13 (0.12–0.14)	17.49 (16.7–18.28)	0.25 (0–3.7)	-
CH	0.20 (0.16–0.24)	-	0.19 (0.15–0.22)	-	0.00 (0–0.26)	1.27 (1.19–1.33)	0.55 (0.53–0.58)	-	2.15 (2.11–2.17)	-	0.25 (0–3.7)	20.38 (18.8–21.9)
	DIC (μmol kg^{-1})						**AOU (μmol kg^{-1})**					
Transect	**Nearshore water 1**	**Nearshore water 2**	**Shelf water**	**Slope water**	**Gulf Stream 1 (40 m)**	**Gulf Stream 2 (203 m)**	**Nearshore water 1**	**Nearshore water 2**	**Shelf water**	**Slope water**	**Gulf Stream 1 (40 m)**	**Gulf Stream 2 (203 m)**
NS	1,972 (1,970–1,977)	1,999.9 (1,998–2,015)	2,056.9 (2,055–2,058)	2,148.7 (2,146–2,152)	-	-				97.3 (89–105)		
LI	2,001.6 (2,001–2,002)	1,990.7 (1,990.2–1,991.4)	2,045.9 (2,045.4–2,046.4)	2,148.7 (2,146–2,152)	-	-				97.3 (89–105)		
NJ	1,971.4 (1,971.2–1,971.6)	2,013.6 (2,013.4–2,013.8)	2,027.6 (2,027.2–2,028.1)	2,148.7 (2,146–2,152)	-	-	-27.299 (-27.4—27.2)	-10.773 (-11.1—10.2)	-16.08 (-16.2—15.9)	97.3 (89–105)		
DE	1,986.2 (1,984.5–1,987.8)	-	2,026.2 (2,024.6–2,027.8)	2,148.7 (2,146–2,152)	-	-	-22.584 (-23.5—21.8)		-15.52 (-16.3—14.6)	97.3 (89–105)		
CB	1,883.9 (1,883.8–1,884)	-	2,010.4 (2,007–2,013.8)	2,148.7 (2,146–2,152)	2,037.1 (2,021–2,051)	-	-12.139 (-12.4—11.9)		-12.97 (-13.2—12.7)	97.3 (89–105)		
CH	1,965.3 (1,964.3–1,965.8)	-	2,019.6 (2,019.1–2,020.2)		2,037.1 (2,021–2,051)	2,169.5 (2,164–2,175)	-4.162 (-6.5—1.7)		-1.054 (-3.6—1.3)		-0.1 (-21–20.2)	117.99 (108.7–127.2)

The nearshore and shelf water masses vary with each transect, but slope water is assumed as having constant values excluding at the CH where the slope water data change to Gulf Stream values. The number in brackets indicates the range of ± 10% for the slope values and the coefficients of determination in the ***Figure 7****. DIC, dissolved inorganic carbon; AOU, apparent oxygen utilization; NS, Nantucket Shoals; LI, Long Island; NJ, New Jersey; DE, Delaware; CB, Chesapeake Bay; CH, Cape Hatteras.*

reflect anomalies mainly resulting from biological processes such as production and remineralization.

RESULTS AND DISCUSSION

Surface Distributions of Current, Physical, Chemical, and Biological Parameters

Consistent with regional circulation (see the *Cruise description and regional hydrographic background* section), surface temperature, salinity, nitrate, DIC, and TA in the MAB increase across the shelf from the shore to the Slope Sea (**Figure 2**). The lower temperatures occur in the most nearshore stations of NS, LI, and NJ because of the more important role of heat loss in shallow water to the atmosphere during winter, Labrador Current input, and coastal river inputs. The temperature of nearshore water also slightly increases with decreasing latitude due to the increased solar radiation and decreased influence of the Labrador Current. The highest temperature is at the most offshore station of CH due to the influence of the Gulf Stream (**Figure 2A**). The distribution of salinity is slightly different from that of temperature, with river discharge diminishing the salinity in the nearshore region, and more Labrador Current dominance leading to low salinity in the northern part of the shelf. The greatest onshore–offshore salinity contrast occurs in the CB and CH transects due to the large amount of freshwater input from the Chesapeake Bay and the greater influences of the Gulf Stream and slope water at the most offshore stations (**Figure 2B**).

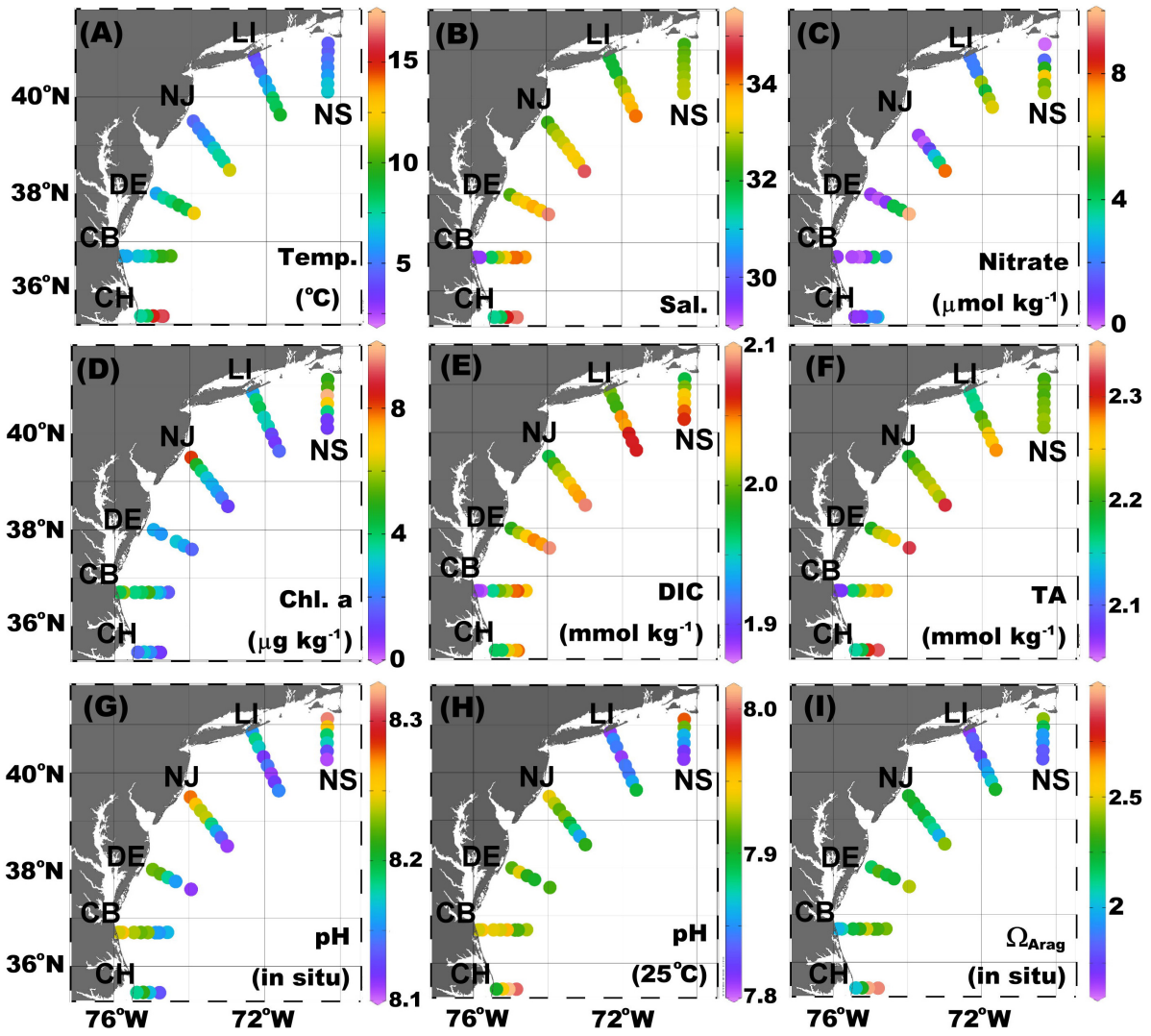


FIGURE 2 | Surface distribution of **(A)** temperature, **(B)** salinity, **(C)** nitrate, **(D)** chlorophyll a (Chl-a), **(E)** dissolved inorganic carbon (DIC), **(F)** total alkalinity (TA), **(G)** $pH_{in\ situ}$, **(H)** pH_{25C}, and **(I)** aragonite saturation state (Ω_{Arag}) in the Mid-Atlantic Bight (MAB). The color dots from red to purple depicts the value from high to low. $pH_{in\ situ}$ was calculated on the total scale at *in situ* temperature and pressure, and pH_{25C} was calculated in 25°C and zero pressure. Ω_{Arag} was calculated at the *in situ* temperature and pressure.

In general, river discharges bring nitrate to the nearshore regions, as does mixing with slope water. However, in the MAB region, major river inputs are processed within large estuaries such as the Chesapeake and Delaware Bays with relatively long water residence times (Boynton et al., 1995; Kemp et al., 1997; Sharp et al., 2009). As a result, riverine nitrate and DIC are consumed, and pCO_2 is reduced in lower estuaries before reaching the shelf (Joesoef et al., 2015; Cai et al., 2017; Chen et al., 2020). Nutrients and DIC are also used for biological production in the MAB inner shelf, even during the late winter, as evidenced by relatively high Chlorophyll a (Chl-a) concentrations (**Figures 2C–E**). As river water is characterized by much lower DIC and TA concentrations than seawater, the surface DIC and TA distributions largely reflect the salinity distribution (**Figures 2B,E,F**). On the contrary, $pH_{in\ situ}$ values decrease seaward with increasing salinity (**Figure 2G**). This pattern is a combined result of water mass mixing with an increasing temperature to the offshore direction and a stronger biological production (which increases pH) in nearshore waters. In the northern transects, it appears that strong biological activities play a more important role as pH normalized to 25°C has a similar pattern to the $pH_{in\ situ}$ and as Chl-a values are clearly higher at nearshore stations (**Figures 2G–I**). In the southernmost transect (CH), however, once the temperature is scaled or normalized to a common temperature of 25°C, pH_{25C} increases toward the Gulf Stream endmember. Biological CO_2 could have a stronger impact in increasing pH in cold waters than in warm waters (Cai et al., 2020). The distribution of Ω_{Arag} is less consistent in the cross-shelf direction, decreasing seaward along the NS transect but increasing seaward in other transects.

Vertical Distributions of Physical, Chemical, and Biological Parameters

Shallow inner shelf waters are vertically well mixed because of strong winds and cooling, as indicated by an overlap of symbols in the θ-S diagram from the same station (blue symbols in **Figure 1C**). The salinity maximum ($S = 35.82$) at offshore regions likely results from the subtropical subsurface water, reflecting the influence of the Gulf Stream (Gawarkiewicz et al., 1992; Marchese and Gordon, 1996), and this impact is particularly noticeable across the entire CH transect from coast to the shelf break (**Figure 1C** and **Supplementary Figure 1**), which is close to where the Gulf Stream leaves the coast. This vertical mixing results in a hook shape in the θ-S diagram for the CH transect at the highest salinity (S ≈ 34.5–35.8) and temperature (T ≈ 13.7–16.2°C), where the subtropical subsurface water mixes with coastal river plume water from the Chesapeake Bay (triangle symbols in **Figure 1C**). The most offshore stations (red symbols in **Figure 1C**) from the NS to the CB sections reflect the influence of the slope water (S ≈ 35.6), and the waters in the layer of $\sigma_T \approx 26.5$–27 cluster in a small salinity and temperature range (**Figure 1C**). Excluding the lowest and highest salinity areas, the main trend shown in **Figure 1C** is nearly a linear relation between θ and S (S ≈ 33.0–35.6, T ≈ 4.7–12.2°C), reflecting the mixing between the low-salinity inner shelf water (S ≈ 32–33.5) and the higher-salinity slope water (S ≈ 35.6).

The cross-shelf sections of temperature, salinity, nitrate, Chl-a, DIC, TA, $pH_{in\ situ}$, and Ω_{Arag} for each transect are presented in **Figures 3**, **4**. Cold and freshwater occupies the shelf, whereas warm and salty water sits over the slope, with the boundary between these two water masses marked by the persistent shelf-break front (green area in **Figures 3A–F**, yellow area in **Figures 3G–L**). The colder and fresher shelf water extends seaward in the upper layer, while the warmer and saltier slope water onwells shoreward in the bottom layer from the NS to the CB transects (**Figures 3A–L**). In the alongshore direction, the northern MAB region (NS-NJ) is colder, fresher, and has a larger extent of vertical mixing on the shelf than in the southern region (DE–CH), reflecting a north-to-south change in the volume of the shelf water (Mountain, 1991). At the nearshore end of CB transect, the water from the Chesapeake Bay greatly reduces both salinity and temperature. The highest temperature and salinity waters occupy the shelf break edge of the CH transect (**Figures 3F,L**), consistent with its proximity to the Gulf Stream, which turns northeastward around Cape Hatteras (Rossby and Benway, 2000).

As noted in the *Surface distributions of current, physical, chemical, and biological parameters* section, inner shelf waters tend to have low nitrate concentrations, which increase seaward due to wintertime mixing with deeper, subsurface waters with high nutrient concentrations that occur in the Slope Sea (**Figures 3M–R**). However, nitrate concentrations are also high inside the shelf-break at about the 50-m depth in the CB transect due to bottom recycling driven by high biological production in the surface water (**Figure 3Q**; Fisher et al., 1988). Generally, concentrations of Chl-a are high along the coastal shelf and decrease with distance from shore, and at some shallow stations, (e.g., those <50 m, **Figure 3S**) concentrations are highest near the bottom due to either wind-enhanced mixing or bottom shoreward nutrient supply (**Figures 3S–X**; Makinen and Moisan, 2012).

Dissolved inorganic carbon and TA values on the shelf are between 1,850 and 2,050 and 2,050 and 2,250 μmol kg^{-1}, respectively, whereas the slope water is characterized by DIC and TA that are higher than 2,100 and 2,300 μmol kg^{-1}, respectively (**Figures 4A–L**). The lowest DIC and TA are found at the most nearshore station in the CB transect (**Figures 4E,K**), consistent with the lowest salinity found there because of river plume water influences (**Figure 3K**). The highest DIC and TA originate from the subsurface water of the Slope Sea that partially onwells to the edge of the shelf (**Figures 4A–L**). Similar to the surface distributions, $pH_{in\ situ}$ values are consistently higher in the nearshore water columns and decrease seaward (**Figures 4M–R**), whereas Ω_{Arag} distributions are variable (**Figures 4S–X**). The lower $pH_{in\ situ}$ values are also present near the bottom or in the subsurface water.

Latitudinal Distribution of Aragonite Saturation State

Ω_{Arag} increases from north to south with the increase in TA/DIC ratio and temperature (**Figure 2**). This trend is largely determined by the temperature dependences of CO_2 solubility,

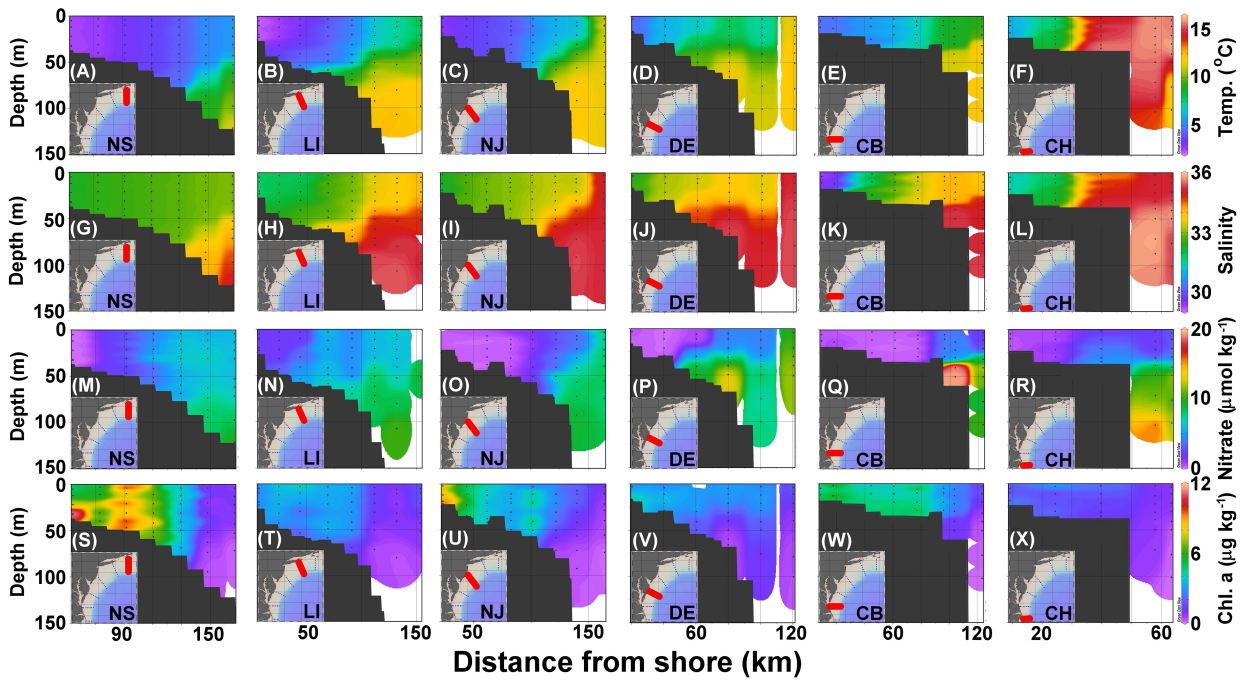


FIGURE 3 | Cross section of temperature **(A–F)**, salinity **(G–L)**, nitrate **(M–R)**, and Chl-a **(S–X)** in the NS, LI, NJ, DE, CB, and CH transects (**Figure 1**) corresponding to panels ordered from left to right. The black dots represent sampled locations and depths.

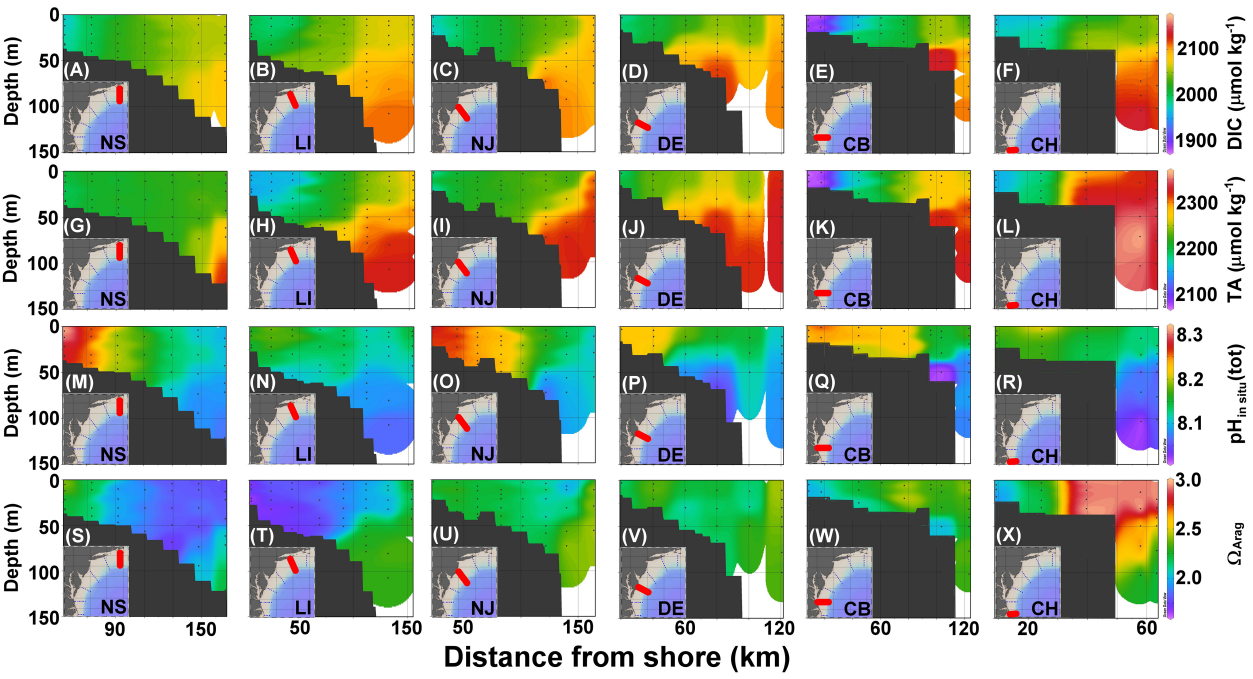


FIGURE 4 | Cross section of DIC **(A–F)**, TA **(G–L)**, $pH_{in\ situ}$ **(M–R)**, and Ω_{Arag} **(S–X)** in the NS, LI, NJ, DE, CB, and CH transects (**Figure 1**) corresponding to panels ordered from left to right. The black dots represent sampled locations and depths.

the solubility of aragonite, and the dissociation constants of carbonic acid (Millero et al., 2006; Cai et al., 2020). Jiang et al. (2015) have derived a regional empirical formula based on the data collected from 1970 to 2010 to predict the surface water Ω_{Arag} in the Atlantic Ocean from sea surface temperature (SST) and concluded that the tight correlation

between Ω_{Arag} and temperature is mainly a result of the different air–sea CO_2 exchange fluxes induced by the north–south temperature gradient rather than a direct thermodynamic effect of temperature. In other words, more CO_2 is taken up by cold water in the north, thus, converting more CO_3^{2-} to HCO_3^- and leading to a higher DIC and a lower TA/DIC ratio than in the warmer water in the south (Takahashi et al., 2014; Xu et al., 2017; Cai et al., 2020). A similar correlation exists for the MAB shelf water (the dotted line in **Figure 5**), likely for the same reason, even though TA and environmental conditions change greatly and are often patchy in these coastal waters. The average Ω_{Arag} in the MAB surface waters is generally lower than the value predicted using Jiang's formula because the TA/DIC ratio in nearshore water is generally lower than the open ocean surface waters (note that the TA/DIC ratio is ≤ 1.0 in most rivers and typically near 1.15 in open ocean waters). Such latitudinal pattern does not exist in the surface $pH_{in\ situ}$ distribution as it is more controlled by the local biological activities. The closely linked, but somewhat different, responses of $pH_{in\ situ}$ and Ω_{Arag} to temperature, mixing, and biological production observed here are consistent with those reported in Cai et al. (2020) at a large, though less fine, spatial scale in the waters off the northern American eastern coast.

Correlations Among Apparent Oxygen Utilization, Dissolved Inorganic Carbon, Nutrients, and Total Alkalinity

Property–property plots such as those presented in **Figure 6** can reveal whether associated variables follow the same physical mixing process or are altered by biological processes. Here, we have categorized data into two groups: (i) mixture of shelf water with slope water or Gulf Stream water (gray circles) and (ii) mixture of nearshore water with shelf water (black cross symbols). For DIC-TA plot, the slope of the black symbols, located near the shore, is consistent with linear mixing (two black solid lines) between seawater and riverine (nearshore) endmembers based on the riverine TA data from the United States Geological Survey (USGS) for the same period and assuming TA ≈ DIC (Cai et al., 2010). As noted earlier, as riverine concentrations of DIC are subject to modification by net biological production in large estuaries and low-salinity inner shelf waters (**Figure 6A**), it may therefore be more appropriate to use nearshore endmembers instead of river endmembers to examine mixing and biological effects. The black crosses with high DIC concentrations (a few symbols above the solid lines) on the northern shelf indicate another low-salinity endmember (**Figure 6A**; **Table 1**).

Graphs of DIC vs phosphate, nitrate vs phosphate, and AOU vs DIC, are shown in **Figures 6B–D**, respectively. Overall, most of the slopes in these plots differ from the stoichiometry given by the Redfield ratios (Redfield, 1958), which are expected from biological processing alone (C:P = 106:1; N:P = 16:1; O:C = 138:106), due to the mentioned physical mixing. For biological activities, the low nitrate makes nitrogen, rather than phosphate, the limiting nutrient (black cross symbols in **Figure 6C**), and similar distributions also exists in Georges Bank and the Gulf of Maine (Townsend and Thomas, 2002). In most of the inner shelf water (black cross in **Figure 6C**), nitrate falls below the expected Redfield ratio and may be the result of a more rapid regeneration for phosphate than nitrate (Paytan and McLaughlin,

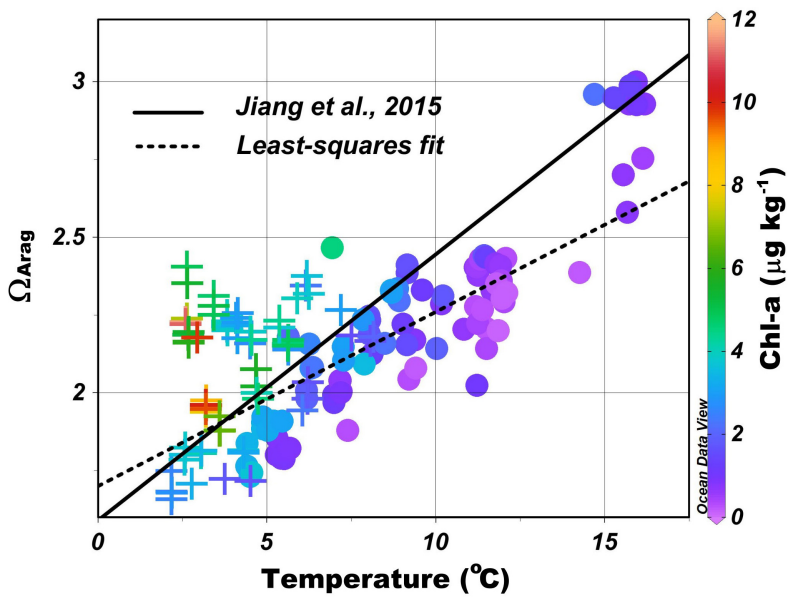


FIGURE 5 | Aragonite saturation state (Ω_{Arag}) as a function of sea surface temperature (SST), with least-squares fit, $\Omega_{Arag} = 0.056 \times SST + 1.70$ (dotted line). Circles represent samples between the shelf water and the slope water/Gulf Stream, and crosses represent samples between the nearshore and the shelf waters. Symbols with different colors represent different levels of Chl-a concentration. The black line represents the empirical formula from Jiang et al. (2015): $\Omega_{Arag} = 0.0855 \times SST + 1.59$.

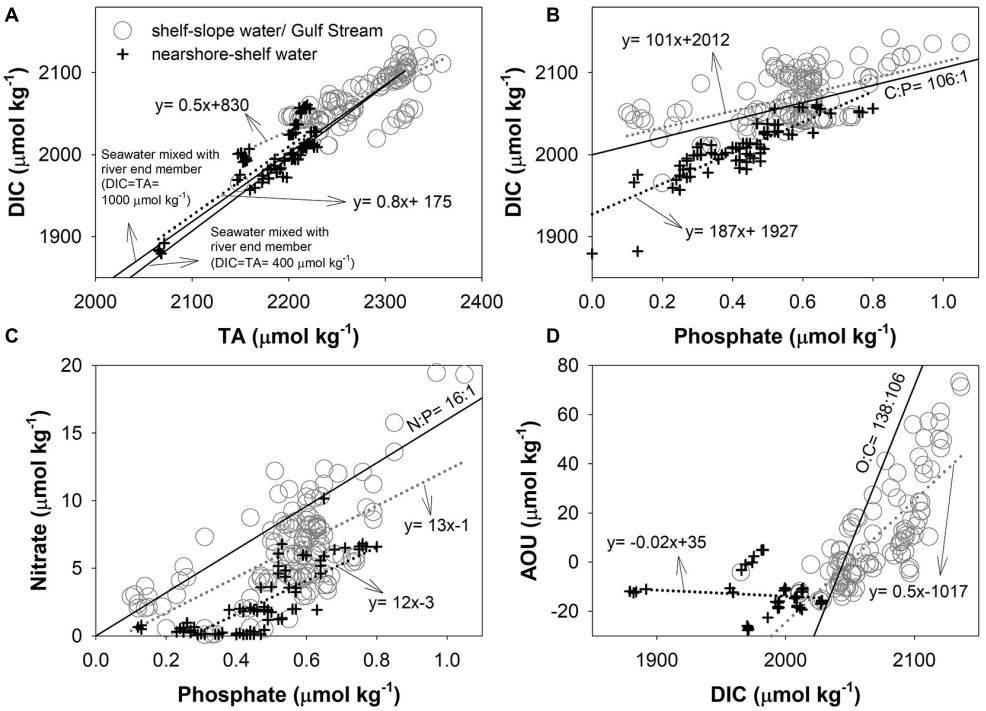


FIGURE 6 | (A) DIC vs. TA, **(B)** DIC vs. phosphate, **(C)** nitrate vs. phosphate, and **(D)** apparent oxygen utilization (AOU) vs. DIC. Gray circles represent samples between the shelf water and the slope water/Gulf Stream, and black crosses represent the seasonal samples between the plume nearshore and the shelf water. The gray and black dot lines are linear regression lines for data represented by gray circles and black crosses. The two black lines in **(A)** denote the theoretical mixing between riverine endmember and shelf water **(A)**, and the lines in other plots are the Redfield ratios. For the theoretical mixing line, two river concentrations (DIC ≈ TA = 400 or 1,000 μmol kg^{-1}) are used to bracket a range of river endmembers in this region.

2007). Denitrification and gas exchange can also affect the relations (see discussion in the *Separation of water mixing and biological effects* section). Because of a combination of complex mixing and biological activities operating in different regions of the MAB, a simple interpretation of water column processes based on observed property–property relations is unlikely, and a more rigorous treatment of mixing is needed to elucidate the influences of biological processes on nutrient and inorganic carbon distributions.

Separation of Water Mixing and Biological Effects

In order to distinguish biological effects from water mass mixing on the property distributions and to examine stoichiometric ratios during biological processes, we use the mixing model to separate the effects of these two processes. We first use the results of linear programming optimization (Goodarzi et al., 2014)—that is, Equations 1–3—to calculate the fractions of various water masses that contribute at each location. Then, the estimated fractions of identified water masses are used to calculate the theoretical concentrations of biochemical parameters. Finally, the difference between the observed property and the mixing predicted value is defined as the anomaly, which is attributed to non-conservative biological processes (atmospheric exchange is neglected here). The source water types are determined from the θ-S diagram as detailed earlier (**Figure 1C**), and nutrient and DIC concentrations are then used to distinguish the water masses with similar θ-S values (**Table 1**). Although the identified endmembers may vary both spatially and temporally, the concept and procedure proposed here, nonetheless, allow us to effectively separate biological processes from physical mixing. However, it must be noted that this approach does not provide a measure on the biological activities in the endmembers, such as that in the highly productive nearshore waters.

The adopted endmember values differ between different transects (**Table 1**). The phosphate concentration of nearshore water at the CB transect is zero, consistent with reports that phosphate is limited in the Chesapeake Bay during winter (Prasad et al., 2010). The low nitrate concentration of nearshore waters at the NS transect may result from the near-zero nitrate of the Gulf of Maine surface water (Townsend et al., 2010). The AOU of nearshore water increases from the NJ to the CH transect, and the DIC concentration either decreases or remains nearly constant. It is worth noting that nearshore or coastal river plume water is most heterogeneous and variable, and can be divided into two sub-types (nearshore water-1 and nearshore water-2) in the northern transects (NS-NJ), where nearshore water-1 is slightly colder and fresher than nearshore water-2. Surface cooling and vertical mixing in nearshore areas may contribute to the lower temperature there, and cause the winter-only mid-shelf front in the northern MAB (Ullman and Cornillon, 2001). The nitrate concentration of shelf water in the NS and LI are similar to the

reported values for the Georges Bank (**Table 1**; Townsend and Thomas, 2001; Bisagni, 2003). For the shelf water endmember, the nutrient and DIC concentrations decrease southward from the NS to the CB, but the salinity increases consistent with the water flow direction, showing a reduced Labrador Current influence (**Table 1**).

Using the water mass endmembers identified above and the mixing model presented in the *Water mass mixing model* section, we are able to separate the effects of biological processes from the water mass mixing using correlations among the biogeochemical anomalies, dDIC, dP, dN, and dAOU presented in **Figure 7**, calculated using Equations 1–5. Each plot is divided into four quadrants based on the sign of the anomalies, with positive and negative values representing addition to or removal from the theoretical mixing values, respectively. In particular, the anomalies in quadrant I denote the addition of DIC and inorganic nutrients and consumption of O_2 due to organic matter decomposition, and those in quadrant III represents removal of DIC and inorganic nutrients and production of O_2 by biological production and other processes (see discussion below).

Most anomalies from the mid and outer shelves (gray circles in **Figure 7**) occur in quadrants I and III, and those on the inner shelf (black crosses in **Figure 7**) cluster near the origin. dDIC, dP, dN, and dAOU anomalies in the mixed shelf and slope (Gulf Stream) waters (gray circles in **Figure 7**) are negative in quadrant III, meaning that these concentrations are removed by biogeochemical activities. Thus, the MAB ecosystem tends to be autotrophic during late winter, a result consistent with a recent numerical model study (Friedrichs et al., 2019). In the mixed nearshore-shelf waters, most of the dissolved oxygen is oversaturated (black crosses in **Figure 7D**, AOU < 0 in **Figure 6D**), and the excess oxygen escapes to the atmosphere (dAOU ~ 0), while the DIC is consumed by phytoplankton (dDIC < 0). While both O_2 supersaturation and CO_2 deficit are compensated by gas exchange in the surface or shallow waters, the impacts on the dAOU and dDIC are different. This is because air–sea exchange is more rapid for O_2 than for CO_2, and more importantly, the impact of the carbonate buffering system, i.e., the gas exchange-induced changes in aquatic CO_2 are buffered by a much larger carbon pool of HCO_3^--CO_3^{2-} (Wallace and Wirick, 1992; DeGrandpre et al., 1998; Carrillo et al., 2004; Zhai et al., 2009).

The extent to which biological processes determine the anomalies of various parameters can be examined by comparing ratios of the anomalies to the Redfield ratios, as noted above. The dDIC/dP ratio of 96.8 ± 4.8 is slightly lower than the Redfield ratio of C:P = 106, likely because of the decrease of processes that compensate dDIC, such as an increase due to absorbing atmospheric CO_2 (**Figure 7A**). The surface seawater in the MAB was a moderately strong atmospheric CO_2 sink during late winter in 1996 (DeGrandpre et al., 2002; Signorini et al., 2013). The air–sea CO_2 flux will tend to compensate biological DIC removal or addition; that is, to reduce dDIC in the third quadrant and to reduce oversaturated CO_2 in the first quadrant (**Figure 7A**).

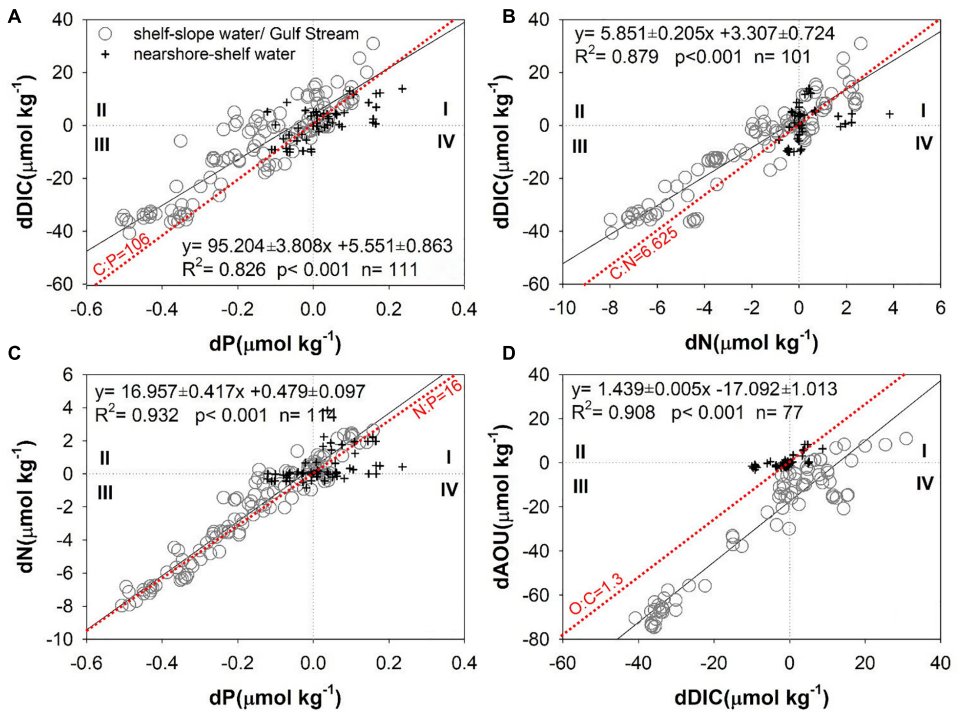


FIGURE 7 | (A) dDIC vs. dP, **(B)** dDIC vs. dN, **(C)** dN vs. dP, and **(D)** dAOU vs. dDIC in the MAB. Gray circles represent samples between the shelf water and the slope water/Gulf Stream, and black crosses represent the samples between the nearshore and the shelf water. Black lines denote least squares fits calculated with a model II regression (Laws and Archie, 1981; Sokal and Rohlf, 2012), and the red dot lines are the Redfield ratios.

Another reason for the dDIC/dP ratio being lower than the Redfield ratio is that it does not adequately account for recycled phosphate. The dDIC/dN ratio of 5.85 ± 0.21 is similar to the Redfield ratio C:N = 6.625 and to that reported by Hedges et al. (2002), C:N = 6.23 (**Figure 7B**), yet lower than that reported by Chen et al. (1996), C:N = 7.69. Denitrification will also diminish nitrate, and substantial denitrification may occur on the seafloor (Seitzinger and Giblin, 1996; Fennel, 2010). However, as the dN/dP ratio of 16.96 ± 0.42 is similar to the Redfield ratio of N:P = 16 (**Figure 7C**), we conclude that the impact of benthic denitrification on water column N is quite limited in winter, probably because of the diminished denitrification under low temperature (Brin et al., 2014) and high oxygen concentration due to a well-mixed condition during wintertime. Finally, the

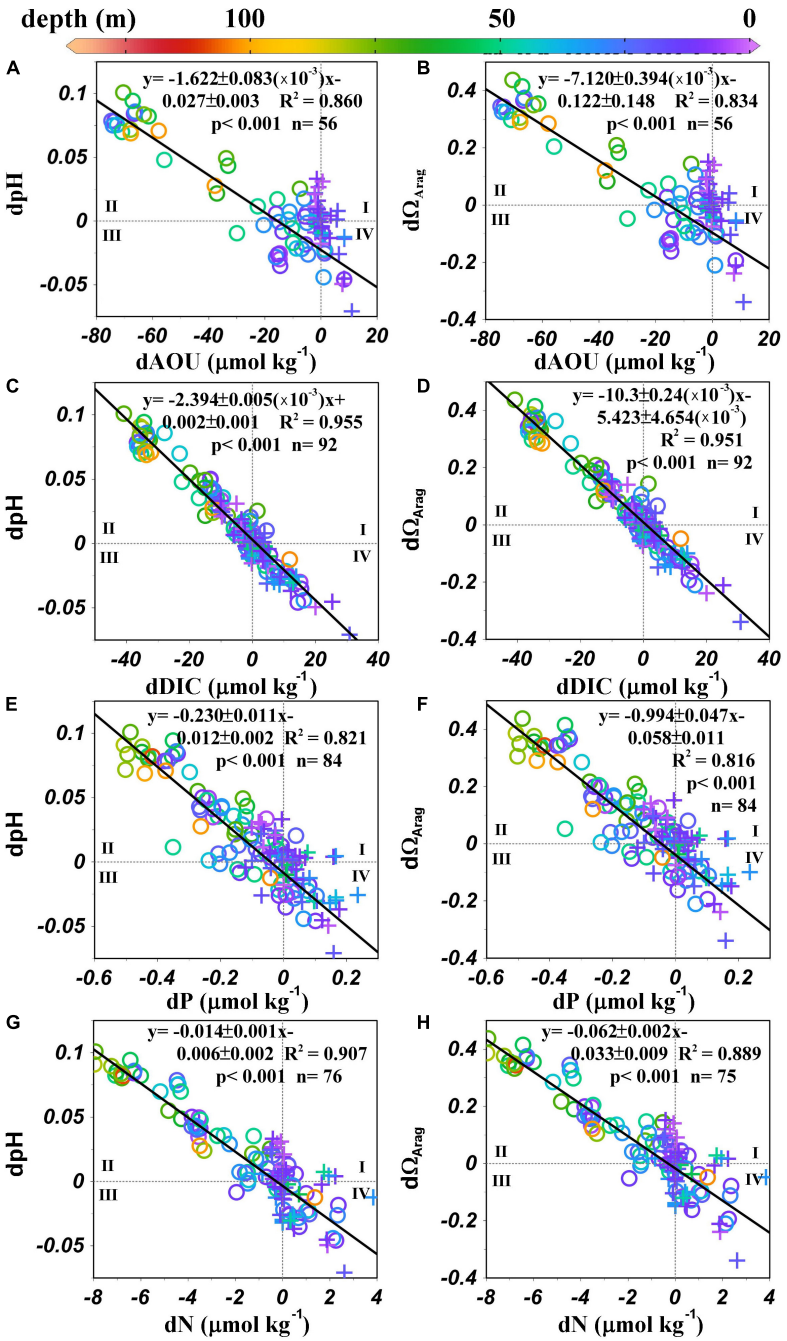


FIGURE 8 | (A) $dpH_{in\ situ}$ vs. dAOU, **(B)** $d\Omega_{Arag}$ vs. dAOU, **(C)** $dpH_{in\ situ}$ vs. dDIC, **(D)** $d\Omega_{Arag}$ vs. dDIC, **(E)** $dpH_{in\ situ}$ vs. dP, **(F)** $d\Omega_{Arag}$ vs. dP, **(G)** $dpH_{in\ situ}$ vs. dN, and **(H)** $d\Omega_{Arag}$ vs. dN in the MAB. Circles represent samples collected between the shelf water and the slope water/Gulf Stream, and crosses represent samples collected between the nearshore water and the shelf water. Black lines denote least-squares fits calculated with a model II regression.

dAOU/dDIC ratio of 1.44 ± 0.01 is also similar to the Redfield ratio for these quantities, O:C = 1.30, as well as with those reported by Chen et al. (1996), O:C = 1.27, and Hedges et al. (2002), O:C = 1.45 (**Figure 7D**). Slight differences in ratios may be actual differences across sampled areas or may result from deviations in endmembers. Overall, the results capture biological effects well and support the validity of a water mass mixing approach.

Biological Control on pH and Aragonite Saturation State

As suggested in the *Surface distributions of current, physical, chemical, and biological parameters* section, $pH_{in\ situ}$ indicates a biological control mechanism. After removing the influence of physical mixing, strong correlations remain between positive $dpH_{in\ situ}$ and negative dAOU, dDIC, dP, and dN (**Figures 8A,C,E,G**), indicating that the increase in $pH_{in\ situ}$ and the decreases in AOU, DIC, and nutrient concentrations are controlled by the same biological process. The same strong correlation occurs between positive $d\Omega_{Arag}$ and negative dAOU, dDIC, dP, and dN (**Figures 8B,D,F,H**). Biological production releases oxygen (negative AOU) and consumes DIC, hydrogen ions (increases pH), and nutrient concentrations, which are represented by anomalies in the second quadrant of **Figure 8** (corresponding to quadrant III in **Figure 7**). In contrast, the anomalies in the fourth quadrant of **Figure 8** result from organic matter decomposition (corresponding to quadrant I in **Figure 7**), which increases the AOU, DIC, hydrogen ions (decreases pH), and nutrient anomalies. Regression lines of dDIC, $dpH_{in\ situ}$, dN, dP, and $d\Omega_{Arag}$ all pass through the origin, indicating that these quantities are influenced by the same biological processes, and supporting the overall validity of the mixing and mass balance model and our choices of the endmember values (circles in **Figures 7**, **8**).

In contrast, consistently in all anomaly plots, at dDIC = 0 or dpH = 0 or $d\Omega_{Arag}$ = 0, dAOU values scatter from –20 to 0 μmol kg^{-1} in the mixed shelf-slope waters (gray circles in **Figures 7D**, **8A,B**). While we have no independent supporting evidence (for example, information from an inert gas such as argon), we suggest this negative shift in dAOU is caused by air bubble-induced O_2 supersaturation (Craig and Hayward, 1987; Wallace and Wirick, 1992; Cassar et al., 2009; Emerson and Bushinsky, 2016). During wintertime, strong winds and deep mixed layer depth could facilitate increased O_2 solubility at high hydrological pressure in the offshore water. A changing O_2 gas solubility due to bubbling effect is a physical process that is not considered in our water mass mixing model and is, thus, a non-conservative term as far as the mixing is concerned, although it is non-biological either. This process would have little effect on the CO_2 system as it is buffered by the HCO_3^- and CO_3^{2-}.

SUMMARY

Using the late wintertime dataset collected under the Ocean Margins Program in March 1996, we have characterized four main biogeochemically distinguishable water masses distributed within the MAB: the nearshore, shelf, slope, and Gulf Stream waters. Generally, the nearshore (or coastal river plume) and shelf waters occupy the inner shelf and have high Chl-a concentration and stronger biological production, whereas the slope and the Gulf Stream waters occupy the outer shelf and the slope area. Among these water masses, the nearshore water is colder and fresher, with lower AOU, DIC, nitrate, and TA concentrations than the slope water. On the cross-shelf direction, $pH_{in\ situ}$ decreases seaward reflecting a strong biological control in addition to water mass mixing, gas exchange, and temperature, but Ω_{Arag} is more variable and does not exhibit a clear trend. However, $pH_{in\ situ}$ has no clear spatial patterns on the along-shelf direction, whereas Ω_{Arag} increases from north to south, reflecting the strong influence of the CO_2 solubility on carbonate saturation state.

The hydrography of the MAB is complex because of the current patterns compounded with other effects, such as tidal and cross-frontal mixing. To distinguish between physical and biological effects, we adopted a water mass mixing model, using endmembers derived from θ-S diagrams. By accounting for physical effects through the mixing model, anomalies due to biological effects could be isolated and were shown to be consistent with the Redfield ratios. Moreover, the intrusion of the slope water onto the outer shelf is found to further support biological production, even during late winter conditions providing further information to support across-front organic carbon flux for the MAB study.

DATA AVAILABILITY STATEMENT

The datasets presented in this study can be found in online repositories. The names of the repository/repositories and accession number(s) can be found in the article/**Supplementary Material**.

AUTHOR CONTRIBUTIONS

T-HH, W-JC, and C-TC prepared the manuscript. DW and EL conceived and conducted the original experiments. PV and EL reviewed and edited the manuscript. All authors contributed to the article and approved the submitted version.

FUNDING

W-JC is supported by the NOAA Ocean Acidification Program and NSF Chemical Oceanography. This publication was also supported by the NSF EPSCoR Grant No. 1757353 and the State of Delaware. This paper was initially prepared in 2015 when T-HH was a visiting scholar at the University of Delaware. T-HH was financed by the National Science Council of Taiwan (103-2917-I-110-004-) during her visit.

ACKNOWLEDGMENTS

We thank the Captains and crews of the vessels, and others for their contribution to the Ocean Margins Program data collection and archive.

SUPPLEMENTARY MATERIAL

The Supplementary Material for this article can be found online at: https://www.frontiersin.org/articles/10.3389/fmars.2021.629412/full#supplementary-material

REFERENCES

Aluwihare, L. I., Repeta, D. J., and Chen, R. F. (2002). Chemical composition and cycling of dissolved organic matter in the Mid-Atlantic Bight. *Deep Sea Res. II Top. Stud. Oceanogr.* 49, 4421–4437. doi: 10.1016/S0967-0645(02)00124-8

Atlas, E. L., Gordon, L., Hager, S., and Park, P. K. (1971). *A Practical Manual for Use of the Technicon Autoanalyzer in Seawater Nutrient Analyses in: Technical Report*. Corvallis, OR: Oregon State University.

Bauer, J. E., Cai, W.-J., Raymond, P. A., Bianchi, T. S., Hopkinson, C. S., and Regnier, P. A. (2013). The changing carbon cycle of the coastal ocean. *Nature* 504, 61–70. doi: 10.1038/nature12857

Bauer, J. E., Druffel, E. R., Wolgast, D. M., and Griffin, S. (2002). Temporal and regional variability in sources and cycling of DOC and POC in the northwest Atlantic continental shelf and slope. *Deep Sea Res. II Top. Stud. Oceanogr.* 49, 4387–4419. doi: 10.1016/S0967-0645(02)00123-6

Beardsley, R., Boicourt, W., and Hansen, D. (1976). "Physical oceanography of the Middle Atlantic Bight," in *Middle Atlantic Continental Shelf and the New York Bight*, ed. M. G. Gross (Lawrence, KS: American Society of Limnology and Oceanography), 20–34.

Bisagni, J. (2003). Seasonal variability of nitrate supply and potential new production in the Gulf of Maine and Georges Bank regions. *J. Geophys. Res. Oceans* 108:8015. doi: 10.1029/2001JC001136

Biscaye, P. E., Flagg, C. N., and Falkowski, P. G. (1994). The shelf edge exchange processes experiment, SEEP-II: an introduction to hypotheses, results and conclusions. *Deep Sea Res. II Top. Stud. Oceanogr.* 41, 231–252. doi: 10.1016/0967-0645(94)90022-1

Boynton, W., Garber, J., Summers, R., and Kemp, W. (1995). Inputs, transformations, and transport of nitrogen and phosphorus in Chesapeake Bay and selected tributaries. *Estuaries Coasts* 18, 285–314. doi: 10.2307/1352640

Brin, L. D., Giblin, A. E., and Rich, J. J. (2014). Environmental controls of anammox and denitrification in southern New England estuarine and shelf sediments. *Limnol. Oceanogr.* 59, 851–860.

Cai, W.-J. (2011). Estuarine and coastal ocean carbon paradox: CO_2 sinks or sites of terrestrial carbon incineration? *Annu. Rev. Mar. Sci.* 3, 123–145. doi: 10.1146/annurev-marine-120709-142723

Cai, W. J., Hu, X., Huang, W. J., Jiang, L. Q., Wang, Y., Peng, T. H., et al. (2010). Alkalinity distribution in the western North Atlantic Ocean margins. *J. Geophys. Res. Oceans* 115:C08014. doi: 10.1029/2009JC005482

Cai, W.-J., Huang, W.-J., Luther, G. W., Pierrot, D., Li, M., Testa, J., et al. (2017). Redox reactions and weak buffering capacity lead to acidification in the Chesapeake Bay. *Nat. Commun.* 8:369. doi: 10.1038/s41467-017-00417-7

Cai, W.-J., Xu, Y.-Y., Feely, R. A., Wanninkhof, R., Jönsson, B., Alin, S. R., et al. (2020). Controls on surface water carbonate chemistry along North American ocean margins. *Nat. Commun.* 11:2691.

Carrillo, C. J., Smith, R. C., and Karl, D. M. (2004). Processes regulating oxygen and carbon dioxide in surface waters west of the Antarctic Peninsula. *Mar. Chem.* 84, 161–179. doi: 10.1016/j.marchem.2003.07.004

Cassar, N., Barnett, B., Bender, M., Kaiser, J., Hamme, R., and Tilbrook, B. (2009). Continuous high-frequency dissolved O2/Ar measurements by equilibrator inlet mass spectrometry. *Anal. Chem.* 81, 1855–1864. doi: 10.1021/ac802300u

Chapman, D. C., and Beardsley, R. C. (1989). On the origin of shelf water in the Middle Atlantic Bight. *J. Phys. Oceanogr.* 19, 384–391. doi: 10.1175/1520-04851989019<0384:OTOOSW<2.0.CO;2

Chavez, F. P., Messié, M., and Pennington, J. T. (2011). Marine primary production in relation to climate variability and change. *Annu. Rev. Mar. Sci.* 3, 227–260. doi: 10.1146/annurev.marine.010908.163917

Chen, B., Cai, W. J., Brodeur, J. R., Hussain, N., Testa, J. M., Ni, W., et al. (2020). Seasonal and spatial variability in surface pCO2 and air–water CO2 flux in the Chesapeake Bay. *Limnol. Oceanogr.* 65, 3046–3065. doi: 10.1002/lno.11573

Chen, C.-T. A. (1981). Oxygen solubility in seawater. *Solubility Data Ser.* 7, 41–55.

Chen, C.-T. A., Huang, T.-H., Chen, Y.-C., Bai, Y., He, X., and Kang, Y. (2013). Air–sea exchanges of CO_2 in the world's coastal seas. *Biogeosciences* 10, 6509–6544. doi: 10.5194/bg-10-6509-2013

Chen, C.-T. A., Lin, C.-M., Huang, B.-T., and Chang, L.-F. (1996). Stoichiometry of carbon, hydrogen, nitrogen, sulfur and oxygen in the particulate matter of the western North Pacific marginal seas. *Mar. Chem.* 54, 179–190. doi: 10.1016/0304-4203(96)00021-7

Craig, H., and Hayward, T. (1987). Oxygen supersaturation in the ocean: Biological versus physical contributions. *Science* 235, 199–202. doi: 10.1126/science.235.4785.199

Csanady, G., and Hamilton, P. (1988). Circulation of slopewater. *Cont. Shelf Res.* 8, 565–624. doi: 10.1016/0278-4343(88)90068-4

DeGrandpre, M., Hammar, T., and Wirick, C. (1998). Short-term pCO_2 and O_2 dynamics in California coastal waters. *Deep Sea Res. II Top. Stud. Oceanogr.* 45, 1557–1575. doi: 10.1016/S0967-0645(98)80006-4

DeGrandpre, M., Olbu, G., Beatty, C., and Hammar, T. (2002). Air–sea CO_2 fluxes on the US Middle Atlantic Bight. *Deep Sea Res. II Top. Stud. Oceanogr.* 49, 4355–4367. doi: 10.1016/S0967-0645(02)00122-4

Dickson, A. G. (2010). Standards for ocean measurements. *Oceanography* 23, 34–47.

DOE (1994). *Handbook of Methods for the Analysis of the Various Parameters of the Carbon Dioxide System in Sea Water*. San Diego, CA: ORNL/CDIAC-74.

Dong, S., and Kelly, K. A. (2003). Seasonal and interannual variations in geostrophic velocity in the Middle Atlantic Bight. *J. Geophys. Res. Oceans* 108:3172. doi: 10.1029/2002JC001357

Emerson, S., and Bushinsky, S. (2016). The role of bubbles during air-sea gas exchange. *J. Geophys. Res. Oceans* 121, 4360–4376. doi: 10.1002/2016JC011744

Fennel, K. (2010). The role of continental shelves in nitrogen and carbon cycling: Northwestern North Atlantic case study. *Ocean Sci.* 6:539. doi: 10.5194/os-6-539-2010

Fennel, K., Wilkin, J., Levin, J., Moisan, J., O'Reilly, J., and Haidvogel, D. (2006). Nitrogen cycling in the Middle Atlantic Bight: results from a three-dimensional model and implications for the North Atlantic nitrogen budget. *Glob. Biogeochem. Cycles* 20:GB3007. doi: 10.1029/2005GB002456

Fisher, T. R., Harding, L. W., Stanley, D. W., and Ward, L. G. (1988). Phytoplankton, nutrients, and turbidity in the Chesapeake, Delaware, and Hudson estuaries. *Estuarine Coast. Shelf Sci.* 27, 61–93. doi: 10.1016/0272-7714(88)90032-7

Flagg, C. N., Pietrafesa, L. J., and Weatherly, G. L. (2002). Springtime hydrography of the southern Middle Atlantic Bight and the onset of seasonal stratification. *Deep Sea Res. II Top. Stud. Oceanogr.* 49, 4297–4329. doi: 10.1016/S0967-0645(02)00121-2

Friedrichs, M. A., St-Laurent, P., Xiao, Y., Hofmann, E., Hyde, K., Mannino, A., et al. (2019). Ocean circulation causes strong variability in the Mid-Atlantic Bight nitrogen budget. *J. Geophys. Res. Oceans* 124, 113–134. doi: 10.1029/2018JC014424

Garcia, H. E., and Gordon, L. I. (1992). Oxygen solubility in seawater: better fitting equations. *Limnol. Oceanogr.* 37, 1307–1312. doi: 10.4319/lo.1992.37.6.1307

Gawarkiewicz, G., Bahr, F., Beardsley, R. C., and Brink, K. H. (2001). Interaction of a slope eddy with the shelfbreak front in the Middle Atlantic Bight. *J. Phys. Oceanogr.* 31, 2783–2796. doi: 10.1175/1520-04852001031<2783:IOASEW<2.0.CO;2

Gawarkiewicz, G., Church, T. M., Luther, G. W., Ferdelman, T. G., and Caruso, M. (1992). Large-scale penetration of Gulf Stream water onto the Continental Shelf north of Cape Hatteras. *Geophys. Res. Lett.* 19, 373–376. doi: 10.1029/92GL00225

Goodarzi, E., Ziaei, M., and Hosseinipour, E. Z. (2014). "Linear optimization," in *Introduction to Optimization Analysis in Hydrosystem Engineering,* eds E. Goodarzi, M. Ziaei, and E. Z. Hosseinipour (Cham: Springer International Publishing), 17–53.

Hager, S. W., Atlas, E. L., Gordon, L. I., Mantyla, A. W., and Park, P. K. (1972). A comparison at sea of manual and autoanalyzer analyses of phosphate, nitrate, and silicate. *Limnol. Oceanogr.* 17, 931–937. doi: 10.4319/lo.1972.17.6.0931

Hedges, J., Baldock, J., Gélinas, Y., Lee, C., Peterson, M., and Wakeham, S. (2002). The biochemical and elemental compositions of marine plankton: a NMR perspective. *Mar. Chem.* 78, 47–63. doi: 10.1016/S0304-4203(02)00009-9

Helland-Hansen, B. (1916). Nogen hydrografiske metoder, Forhandlinger ved de Skandinaviske Naturforskeres Möde. 16, 357–359.

Hopkinson, C. S., Vallino, J. J., and Nolin, A. (2002). Decomposition of dissolved organic matter from the continental margin. *Deep Sea Res. II Top. Stud. Oceanogr.* 49, 4461–4478. doi: 10.1016/S0967-0645(02)00125-X

Jahnke, R., and Verity, P. (1994). in *Ocean Margins Program*, ed. U. S. D. O. Energy (Oak Ridge, TN: DOE Office of Scientific and Technical Information).

Jahnke, R. A. (2010). "Global synthesis," in *Carbon and Nutrient Fluxes in Continental Margins*, eds K.-K. Liu, L. Atkinson, R. Quinones, and L. Talaue-McManus (Berlin: Springer-Verlag), 597–615.

Jiang, L. Q., Feely, R. A., Carter, B. R., Greeley, D. J., Gledhill, D. K., and Arzayus, K. M. (2015). Climatological distribution of aragonite saturation state in the global oceans. *Glob. Biogeochem. Cycles* 29, 1656–1673. doi: 10.1002/2015GB005198

Joesoef, A., Huang, W.-J., Gao, Y., and Cai, W.-J. (2015). Air–water fluxes and sources of carbon dioxide in the Delaware Estuary: spatial and seasonal variability. *Biogeosciences* 12, 6085–6101. doi: 10.5194/bg-12-6085-2015

Johnson, K. (1992). *Single-Operator Multiparameter Metabolic Analyzer (SOMMA) For Total Carbon Dioxide (C_T) with Coulometric Detection. Operator's Manual*. Upton, NY: Brookhaven National Lab.

Johnson, K., Wills, K. D., Butler, D. B., Johnson, W. K., and Wong, C. S. (1993). Coulometric total carbon dioxide analysis for marine studies: maximizing the performance of an automated gas extraction system and coulometric detector. *Mar. Chem.* 44, 167–187.

Kemp, W., Smith, E., Marvin-DiPasquale, M., and Boynton, W. (1997). Organic carbon balance and net ecosystem metabolism in Chesapeake Bay. *Mar. Ecol. Progr. Ser.* 150, 229–248. doi: 10.3354/meps150229

Knap, A., Michaels, A., Close, A., Ducklow, H., and Dickson, A. (1996). *Protocols for the Joint Global Ocean Flux Study (JGOFS) Core Measurements, JGOFS, Reprint of the IOC Manuals and Guides No. 29*. Paris: Intergovernmental Oceanographic Commission.

Laws, E., and Archie, J. (1981). Appropriate use of regression analysis in marine biology. *Mar. Biol.* 65, 13–16.

Lentz, S. J. (2008). Observations and a model of the mean circulation over the Middle Atlantic Bight continental shelf. *J. Phys. Oceanogr.* 38, 1203–1221. doi: 10.1175/2007JPO3768.1

Lewis, E., and Wallace, D. W. R. (1998). *Program Developed for CO_2 System Calculations*. Oak Ridge, TN: Oak Ridge National Laboratory.

Linder, C. A., and Gawarkiewicz, G. (1998). A climatology of the shelfbreak front in the Middle Atlantic Bight. *J. Geophys. Res. Oceans* 103, 18405–18423. doi: 10.1029/98JC01438

Liu, K., Iseki, K., and Chao, S. (2000). "Continental margin carbon fluxes," in *The Changing Ocean Carbon Cycle: a Midterm Synthesis of the Joint Global Ocean Flux Study*, eds R. B. Hanson, H. W. Ducklow, and J. G. Field (Cambridge, MA: Cambridge University Press), 187–239.

Liu, K.-K., Atkinson, L., Quiñones, R. A., and Talaue-McManus, L. (2010). "Biogeochemistry of continental margins in a global context," in *Carbon and Nutrient Fluxes in Continental Margins*, eds K.-K. Liu, L. Atkinson, R. Quinþones, and L. Talaue-McManus (Berlin: Springer), 3–24.

Lueker, T. J., Dickson, A. G., and Keeling, C. D. (2000). Ocean pCO_2 calculated from dissolved inorganic carbon, alkalinity, and equations for K1 and K2: validation based on laboratory measurements of CO_2 in gas and seawater at equilibrium. *Mar. Chem.* 70, 105–119. doi: 10.1016/S0304-4203(00)00022-0

Mackenzie, F., Andersson, A., Lerman, A., and Ver, L. M. (2005). "Boundary exchanges in the global coastal margin: implications for the organic and inorganic carbon cycles," in *The Global Coastal Ocean: Multiscale Interdisciplinary Processes*, eds A. R. Robinson and K. Brink (Cambridge, MA: Harvard University press), 193–225.

Makinen, C. P., and Moisan, T. A. (2012). Phytoplankton assemblage patterns in the southern Mid-Atlantic Bight. *Bot. Mar.* 55, 445–457. doi: 10.1515/bot-2012-0110

Mamayev, O. I. (1975). *Temperature-Salinity Analysis of World Ocean Waters*. New York, NY: Elsevier.

Marchese, P. J., and Gordon, A. L. (1996). The eastern boundary of the Gulf Stream recirculation. *J. Mar. Res.* 54, 521–540. doi: 10.1357/0022240963213510

Millero, F. J. (1995). Thermodynamics of the carbon dioxide system in the oceans. *Geochim. Cosmochim. Acta* 59, 661–677. doi: 10.1016/0016-7037(94)00354-O

Millero, F. J., Graham, T. B., Huang, F., Bustos-Serrano, H., and Pierrot, D. (2006). Dissociation constants of carbonic acid in seawater as a function of salinity and temperature. *Mar. Chem.* 100, 80–94. doi: 10.1016/j.marchem.2005.12.001

Mountain, D. G. (1991). The volume of shelf water in the Middle Atlantic Bight: seasonal and interannual variability, 1977–1987. *Cont. Shelf Res.* 11, 251–267.

Mountain, D. G. (2003). Variability in the properties of Shelf Water in the Middle Atlantic Bight, 1977–1999. *J. Geophys. Res. Oceans* 108:3014.

Mucci, A. (1983). The solubility of calcite and aragonite in seawater at various salinities, temperatures, and one atmosphere total pressure. *Am. J. Sci.* 283, 780–799. doi: 10.2475/ajs.283.7.780

Muller-Karger, F. E., Varela, R., Thunell, R., Luerssen, R., Hu, C., and Walsh, J. J. (2005). The importance of continental margins in the global carbon cycle. *Geophys. Res. Lett.* 32:L01602. doi: 10.1029/2004GL021346

Paytan, A., and McLaughlin, K. (2007). The oceanic phosphorus cycle. *Chem. Rev.* 107, 563–576. doi: 10.1021/cr0503613

Pierrot, D., Lewis, E., and Wallace, D. (2006). *MS Excel Program Developed for CO_2 System Calculations*. Oak Ridge, TN: Carbon Dioxide Information Analysis Center.

Prasad, M. B. K., Sapiano, M. R., Anderson, C. R., Long, W., and Murtugudde, R. (2010). Long-term variability of nutrients and chlorophyll in the Chesapeake Bay: a retrospective analysis, 1985–2008. *Estuaries Coasts* 33, 1128–1143. doi: 10.1007/s12237-010-9325-y

Redfield, A. C. (1958). The biological control of chemical factors in the environment. *Am. Sci.* 46, 205–221.

Rossby, T., and Benway, R. (2000). Slow variations in mean path of the Gulf Stream east of Cape Hatteras. *Geophys. Res. Lett.* 27, 117–120. doi: 10.1029/1999GL002356

Saba, V. S., Hyde, K. J., Rebuck, N. D., Friedland, K. D., Hare, J. A., Kahru, M., et al. (2015). Physical associations to spring phytoplankton biomass interannual variability in the US Northeast Continental Shelf. *J. Geophys. Res. Biogeosci.* 120, 205–220.

Seitzinger, S. P., and Giblin, A. E. (1996). Estimating denitrification in North Atlantic continental shelf sediments. *Biogeochemistry* 35, 235–260. doi: 10.1007/BF02179829

Sharp, J. H., Yoshiyama, K., Parker, A. E., Schwartz, M. C., Curless, S. E., Beauregard, A. Y., et al. (2009). A biogeochemical view of estuarine eutrophication: seasonal and spatial trends and correlations in the Delaware Estuary. *Estuaries Coasts* 32, 1023–1043. doi: 10.1007/s12237-009-9210-8

Signorini, S. R., Mannino, A., Najjar, R. G., Friedrichs, M. A. M., Cai, W.-J., Salisbury, J., et al. (2013). Surface ocean pCO_2 seasonality and sea-air CO_2 flux estimates for the North American east coast. *J. Geophys. Res. Oceans* 118, 5439–5460. doi: 10.1002/jgrc.20369

Sokal, R. R., and Rohlf, F. J. (2012). *Biometry: the Principles and Practice of Statistics in Biological Research*. New York, NY: W.H. Freeman and Company.

Takahashi, T., Sutherland, S. C., Chipman, D. W., Goddard, J. G., Ho, C., Newberger, T., et al. (2014). Climatological distributions of pH, pCO_2, total CO_2, alkalinity, and $CaCO_3$ saturation in the global surface Ocean, and temporal changes at selected locations. *Marine Chemistry* 164, 95–125. doi: 10.1016/j.marchem.2014.06.004

Tomczak, M. (1981). A multi-parameter extension of temperature/salinity diagram techniques for the analysis of non-isopycnal mixing. *Progr. Oceanogr.* 10, 147–171. doi: 10.1016/0079-6611(81)90010-0

Townsend, D. W., Rebuck, N. D., Thomas, M. A., Karp-Boss, L., and Gettings, R. M. (2010). A changing nutrient regime in the Gulf of Maine. *Cont. Shelf Res.* 30, 820–832. doi: 10.1016/j.csr.2010.01.019

Townsend, D. W., and Thomas, A. C. (2001). Winter–spring transition of phytoplankton chlorophyll and inorganic nutrients on Georges Bank. *Deep Sea Res. II Top. Stud. Oceanogr.* 48, 199–214. doi: 10.1016/S0967-0645(00)00119-3

Townsend, D. W., Thomas, A. C., Mayer, L. M., Thomas, M. A., and Quinlan, J. A. (2006). "Oceanography of the northwest Atlantic continental shelf," in *The Global Coastal Ocean: Interdisciplinary Regional Studies and Syntheses*, eds

A. R. Robinson and K. Brink (Cambridge, MA: Harvard University Press), 119–168.

Townsend, D. W., and Thomas, M. (2002). Springtime nutrient and phytoplankton dynamics on Georges Bank. *Mar. Ecol. Progr. Ser.* 228, 57–74. doi: 10.3354/meps228057

Ullman, D. S., and Cornillon, P. C. (2001). Continental shelf surface thermal fronts in winter off the northeast US coast. *Cont. Shelf Res.* 21, 1139–1156.

Vlahos, P., Chen, R. F., and Repeta, D. J. (2002). Dissolved organic carbon in the Mid-Atlantic Bight. *Deep Sea Res. II Top. Stud. Oceanogr.* 49, 4369–4385. doi: 10.1016/S0967-0645(02)00167-4

Wallace, D., and Wirick, C. (1992). Large air–sea gas fluxes associated with breaking waves. *Nature* 356:694. doi: 10.1038/356694a0

Walsh, J. J. (1988). *On the Nature of Continental Shelves*. San Diego, CA: Academic Press.

Wang, Z. A., Wanninkhof, R., Cai, W.-J., Byrne, R. H., Hu, X., Peng, T.-H., et al. (2013). The marine inorganic carbon system along the Gulf of Mexico and Atlantic coasts of the United States: insights from a transregional coastal carbon study. *Limnol. Oceanogr.* 58, 325–342. doi: 10.4319/lo.2013.58.1.0325

Wanninkhof, R., Barbero, L., Byrne, R., Cai, W.-J., Huang, W.-J., Zhang, J.-Z., et al. (2015). Ocean acidification along the Gulf Coast and East Coast of the USA. *Cont. Shelf Res.* 98, 54–71. doi: 10.1016/j.csr.2015.02.008

Wilson, C., Behrens, W. J., Flagg, C. N., Wallace, D. W. R., Wilke, R. J., and Wyman, K. D. (1989). *Shelf Edge Exchange Processes, II: SEEP2-08, R/V ENDEAVOR Cruise 188. Hydrographic Data Report*. Upton, NY: Brookhaven National Laboratory.

Xu, Y. Y., Cai, W. J., Gao, Y., Wanninkhof, R., Salisbury, J., Chen, B., et al. (2017). Short-term variability of aragonite saturation state in the central Mid-Atlantic Bight. *J. Geophys. Res. Oceans* 122, 4274–4290. doi: 10.1002/2017JC012901

Xu, Y. Y., Cai, W. J., Wanninkhof, R., Salisbury, J., Reimer, J., and Chen, B. (2020). Long-term changes of carbonate chemistry variables along the North American East Coast. *J. Geophys. Res. Oceans* 125:e2019JC015982.

Zhai, W., Dai, M., and Cai, W.-J. (2009). Coupling of surface pCO_2 and dissolved oxygen in the northern South China Sea: impacts of contrasting coastal processes. *Biogeosciences* 6, 2589–2598. doi: 10.5194/bg-6-2589-2009

Conflict of Interest: The authors declare that the research was conducted in the absence of any commercial or financial relationships that could be construed as a potential conflict of interest.

Copyright © 2021 Huang, Cai, Vlahos, Wallace, Lewis and Chen. This is an open-access article distributed under the terms of the Creative Commons Attribution License (CC BY). The use, distribution or reproduction in other forums is permitted, provided the original author(s) and the copyright owner(s) are credited and that the original publication in this journal is cited, in accordance with accepted academic practice. No use, distribution or reproduction is permitted which does not comply with these terms.

frontiers in Marine Science

ORIGINAL RESEARCH
published: 13 December 2021
doi: 10.3389/fmars.2021.611781

Ecosystem Metabolism Modulates the Dynamics of Hypoxia and Acidification Across Temperate Coastal Habitat Types

Ryan B. Wallace[1], Bradley J. Peterson[2] and Christopher J. Gobler[2]**

[1] Environmental Studies and Sciences, Adelphi University, Garden City, NY, United States, [2] School of Marine and Atmospheric Sciences, Stony Brook University, Stony Brook, NY, United States

OPEN ACCESS

Edited by:
Hongjie Wang, Pacific Marine Environmental Laboratory, National Oceanic and Atmospheric Administration (NOAA), United States

Reviewed by:
Xianghui Guo, Xiamen University, China
Jacob Carstensen, Aarhus University, Denmark
Stephen Roger Pacella, United States Environmental Protection Agency (EPA), United States

***Correspondence:**
Ryan B. Wallace
rwallace@adelphi.edu
Christopher J. Gobler
Christopher.gobler@stonybrook.edu

Specialty section:
This article was submitted to Coastal Ocean Processes, a section of the journal Frontiers in Marine Science

Received: *29 September 2020*
Accepted: *16 November 2021*
Published: *13 December 2021*

Citation:
Wallace RB, Peterson BJ and Gobler CJ (2021) Ecosystem Metabolism Modulates the Dynamics of Hypoxia and Acidification Across Temperate Coastal Habitat Types. Front. Mar. Sci. 8:611781. doi: 10.3389/fmars.2021.611781

Changes in photosynthetic and respiration rates in coastal marine habitats cause considerable variability in ecosystem metabolism on timescales ranging from diel to tidal to seasonal. Here, temporal and spatial dynamics of dissolved oxygen (DO), carbonate chemistry, and net ecosystem metabolism (NEM) were quantified from spring through fall in multiple, distinct, temperate estuarine habitats: seagrass meadows, salt marshes, an open water estuary, and a shallow water habitat dominated by benthic macroalgae. DO and pH_T (total scale) measurements were made *via* high frequency sensor arrays coupled with discrete measurements of dissolved inorganic carbon (DIC) and high-resolution spatial mapping was used to document intra-habitat spatial variability. All habitats displayed clear diurnal patterns of pH_T and DO that were stronger than tidal signals, with minimums and maximums observed during early morning and afternoon, respectively. Diel ranges in pH_T and DO varied by site. In seagrass meadows and the open estuarine site, pH_T ranged 7.8–8.4 and 7.5–8.2, respectively, while DO exceeded hypoxic thresholds and aragonite was typically saturated ($\Omega_{Ar} > 1$). Conversely, pH_T in a shallow macroalgal and salt marsh dominated habitats exhibited strong diel oscillations in pH_T (6.9–8.4) with diel acidic ($pH_T < 7$) and hypoxic (DO < 3 mg L^{-1}) conditions often observed during summer along with extended periods of aragonite undersaturation ($\Omega_{Ar} < 1$). The partial pressure of carbon dioxide (pCO_2) exceeded 3000 and 2000 μatm in the salt marsh and macroalgal bed, respectively, while pCO_2 never exceeded 1000 μatm in the seagrass and open estuarine site. Mesoscale (50–100 m) spatial variability was observed across sites with the lowest pH_T and DO found within regions of more restricted flow. NEM across habitats ranged from net autotrophic (macroalgae and seagrass) to metabolically balanced (open water) and net heterotrophic (salt marsh). Each habitat exhibited distinct buffering capacities, varying seasonally, and modulated by adjacent biological activity and variations in total alkalinity (TA) and DIC. As future predicted declines in pH and DO are likely to shrink the spatial extent of estuarine refuges from acidification and hypoxia, efforts are required to expand seagrass meadows and the aquaculture of macroalgae to maximize their ecosystem benefits and maintain these estuarine refuges.

Keywords: acidification, hypoxia, estuary, respiration, carbon dioxide, pH, dissolved oxygen, ecosystem metabolism

INTRODUCTION

Estuaries are among the most biologically productive ecosystems on the planet and serve as critical habitats for early life stage finfish and shellfish (Baird et al., 1991; Sogard and Able, 1991; Able, 2005; Barbier et al., 2010). Estuaries play a vital role by providing important ecosystem services including acting as filtration barriers between terrestrial and marine environments as well as buffer zones, protecting coastal regions and stabilizing shorelines (Valiela, 2006). The habitats within estuaries are biologically and metabolically diverse, ranging from highly productive salt marsh ecosystems to mesotrophic-to-oligotrophic open water estuaries (Caffrey, 2004). Primary production is essential to the functioning of these aquatic ecosystems and, depending on estuarine habitat, can be generated from a variety of sources including macroalgae, seagrasses, salt marsh grasses, benthic microalgae, and phytoplankton. Although primary production (and thus O_2 production) within estuarine environments can be elevated on short timescales (hours to days), respiration within these systems catalyzes energy production sourced from allochthonous and autochthonous carbon, making estuaries predominantly net heterotrophic ecosystems (Smith and Mackenzie, 1987; Caffrey, 2004; Cloern et al., 2014). However, there are many examples of net autotrophy where shallow, macrophyte dominated estuaries with minimal organic matter loading can be considered a net CO_2 sink (Maher and Eyre, 2012). Microbial metabolic rates driving ecosystem metabolism can vary on hourly time scales in estuarine environments causing rapid changes in dissolved gases (O_2, CO_2), and changes in estuarine pH over short temporal and spatial scales (Baumann and Smith, 2018).

Salt marshes are highly productive ecosystems well-known for high rates of metabolic activity that increase dramatically from winter to summer months (Nixon and Oviatt, 1973). Tidal fluctuations can also have strong influences on shallow salt marshes with high tides often transporting more oxygenated waters into marshes (O'Boyle et al., 2013; Baumann et al., 2015). Salt marsh-dominated estuaries generally have a detritus-based food web (Odum, 1971) and respiration rates that are highly accelerated, facilitating the net consumption of DO (Nixon and Oviatt, 1973). In contrast to DO, substantially less is known regarding the dynamics of carbonate chemistry in salt marshes (Wang et al., 2016; Wang et al., 2018).

Seagrass meadows are found in the shallow waters of every continent except Antarctica (Duarte et al., 2010) and provide food, habitat, and nursery areas for a variety of invertebrate and vertebrate species (Beck et al., 2001; Heck et al., 2003; Orth et al., 2006). Seagrass beds can be important sources of organic production, sequestering carbon within the surrounding sediment and exporting detritus (Suchanek et al., 1985; Duarte et al., 2005; Orth et al., 2006). Previous studies have shown that low pH can also occur in seagrass beds at night, where periods of undersaturation can cause carbonate-sediment dissolution (Camp et al., 2016; Cyronak et al., 2018). In addition, organic material within seagrass beds can degrade, increasing DIC and enhancing carbonate dissolution in these shallow water habitats (Unsworth et al., 2012). Photosynthetic rates in seagrass beds can also be limited by carbon availability, specifically in the form of CO_2 (Beer and Koch, 1996) and this may be especially evident in many northeast United States estuaries as much of the remaining seagrass beds are now restricted to low turbidity areas (Dennison et al., 1993) with minimal shoreline development (Roman et al., 2000; Short et al., 2006; Blake et al., 2014), but also higher salinity and lower CO_2 (Wallace et al., 2014). The species of seagrass indigenous to the Northeast United States (*Zostera marina*) has been well-studied and much of the oxygen produced by this species is released into the surrounding water column (Sand-Jensen and Borum, 1983; Caffrey and Kemp, 1991). Conversely, as a significant carbon sink (Orth et al., 2006) these highly productive seagrass meadows rapidly assimilate CO_2 and may provide zones of elevated aragonite saturation (Ω_{Ar}), even within eutrophic estuaries (Hendriks et al., 2014; Pacella et al., 2018).

Macroalgae-dominated estuarine regions are common in both tropical and temperate regions around the world and are often dominated by chlorophytes such as *Ulva* spp. that can form dense blooms referred to as "green tides" (Smetacek and Zingone, 2013). Regions commonly impacted by the accumulation of green macroalgal biomass include the east coast of North America (Ye et al., 2011), the Bohai Sea in China (Liu et al., 2009; Liu et al., 2010), and Brittany, France (Ménesguen and Piriou, 1995) where blooms are often dominated by morphologically indistinguishable species of the genus *Ulva* (Blomster et al., 2002). *Ulva*-dominated ecosystems can drive large fluctuations in DO on both diurnal and seasonal timescales *via* photosynthesis and respiration. Middelboe and Hansen (2007a) found that in a macroalgae-dominated, wave exposed area, DO was supersaturated during the day (125% saturation) and near saturated conditions at night (91% saturation). In more poorly flushed, temperate regions, dense stands of macroalgae and *Ulva* spp. blooms can promote diurnal and seasonal hypoxia and anoxia (Valiela et al., 1992; Wallace and Gobler, 2015). Despite the well-documented occurrence of hypoxia within macroalgal-dominated communities (Valiela et al., 1992; Valiela, 2006), no study to date has co-currently assessed DO dynamics and carbonate chemistry within such temperate ecosystems, despite previous studies that have shown that *Ulva* spp. can have negative impacts on multiple calcifying animals (Magre, 1974; Johnson and Welsh, 1985).

Tidal and metabolic variability can drive intense temperature, pH, and DO fluctuations in coastal environments occurring over short time scales (Wootton et al., 2008; Cai et al., 2011; Riche et al., 2014). With recent advances in high frequency *in situ* sensors (Bergveld, 2003; Hofmann et al., 2011; Fietzek et al., 2014), biogeochemical cycles can be monitored with high temporal resolution. Net metabolism in coastal ecosystems has been studied for decades (Smith and Mackenzie, 1987; Gattuso et al., 1998; Caffrey, 2004; Borges et al., 2008), although most of these efforts lacked the high frequency, high resolution data needed to resolve the temporal and spatial dynamics of rate processes within these systems (Borges et al., 2008). In addition, most studies of ecosystem metabolism in estuaries have focused either on high frequency O_2 measurements or less frequent, lower resolution pH or carbon measurements. There has been little focus on high frequency and high-resolution

measurements of both O_2 and pH (Rosenau et al., 2021) coupled with measurements of carbonate chemistry. Studies that have focused on the monitoring of high frequency carbonate chemistry in coastal environments (Baumann et al., 2015; Saderne et al., 2015; Wang et al., 2015), have lacked simultaneous comparisons of distinct habitats. Such approaches would permit an evaluation of the relative strength and direction (net autotrophic vs. net heterotrophic) of ecosystem metabolism as well as their comparative suitability as habitats for calcifying and other marine organisms.

Therefore, this study was undertaken to compare four common northeast United States coastal habitats within the same general estuarine system, with respect to the dynamics of net ecosystem metabolism (NEM), carbonate chemistry, DO, and pH_T. Questions addressed in this study included: How do rates of NEM compare across estuarine habitat types? What are the fine temporal and spatial scales of carbonate chemistry across estuarine habitats? How do specific estuarine habitats compare as refugia from coastal acidification? Continuous measurements were specifically made within multiple salt marshes and seagrass beds, as well as in macroalgae beds and open-water estuarine regions over a 5-year period. Continuous measurements of DO and pH_T were complemented with discrete measurements of carbonate chemistry, allowing for a comprehensive assessment of the suitability of the various habitats for calcifying and other marine organisms.

MATERIALS AND METHODS

Site Description

Four distinct coastal habitat types within a ∼200 km^2 region on eastern Long Island were examined for this study; two seagrass meadows in eastern Shinnecock Bay (SG-1; 40.85849, −72.45107 and SG-2; 40.86001, −72.49834; **Figure 1**), one salt marsh in western Shinnecock Bay (SM-1; 40.81992, −72.56497; **Figure 1**), two salt marshes in the Peconic Estuary (SM-2; 40.90555, −72.59280 and SM-3; 40.92970, −72.42583; **Figure 1**), an open water location in the Peconic Estuary (OW-1; 40.97672, −72.46638; **Figure 1**), and a shallow water ecosystem dominated by benthic macroalgae (*Ulva* spp.) in the Peconic Estuary (MA-1; 41.01861, −72.47134; **Figure 1**). In addition, cruises were performed across the Peconic Estuary and Shinnecock Bay to place habitat-specific observations in a larger, estuary-wide perspective.

The seagrass sites were located at the southeastern extent of Long Island's South Shore Estuary Reserve, which hosts some of the most expansive seagrass (*Z. marina*) stands remaining on Long Island (∼81 km^2; Carlson et al., 2009). *Z. marina* shoot density at site SG-1 was 827 shoots m^{-2} (SD ± 148.3, $n = 30$) and was 224 shoots m^{-2} (SD ± 27.9, $n = 18$) at site SG-2, a density range considered typical of healthy stands (Olesen and Sand-Jensen, 1994). Site SG-1 is a ∼2 km^2 seagrass bed located ∼2.6 km ENE of Shinnecock Inlet where water is exchanging with the Atlantic Ocean and SG-2 is a ∼1 km^2 bed that runs along the western shoreline located ∼2.5 km NNW of Shinnecock Inlet and has extensive macroalgae interspersed within the seagrass bed. The mean depth at SG-1 was 1.26 m with a mean daily range of 1.02 m and the mean depth at SG-2 was 1.09 m with a mean daily range of 1.06 m. Salt marsh site SM-1 was located along the southwest shore of Shinnecock Bay, where there are dense stands of salt marsh islands and tidal creeks stretching for ∼ 6 km and extending up to 0.8 km wide. The mean depth at SM-1 was 0.59 m with a mean daily range of 0.75 m. The two additional salt marsh sites lie at opposite ends of the Peconic Estuary. Site SM-2 lies along the south shore of Flanders Bay and represents the northern boundary of a 3.23 km^2 protected salt marsh known as Hubbard County Park. The mean depth at SM-2 was 0.94 m with a mean daily range of 0.84 m. Site SM-3 is located in the Scallop Pond Preserve, one of Long Island's least developed coastal wetlands encompassing an area of ∼2 km^2. Site SM-3 was slightly deeper than the other two marsh sites with a mean depth of 1.68 and a 1.01 m mean daily range. The open water location is in the north shore of Robin's Island in a mesotrophic to oligotrophic section of the Peconic Estuary, strongly flushed by tides (Hardy, 1976) and known to host robust bay scallop (*Argopecten irradians*) populations (Tettelbach et al., 2013). The mean depth at this location was 2 m with a mean daily range of 0.92 m. The macroalgae-dominated site was located in the Haywater Cove, Cutchogue, NY, which receives extensive nutrient loads from adjacent residential and agricultural areas. The study area exhibited 100% benthic coverage with *Ulva* spp. at 101 ± 13 g^{-1} DW m^{-2} during this study and the mean depth was 1.08 m with a mean daily range of 0.84 m.

Time Series

At all locations a Satlantic SeaFET Ocean pH sensor and a YSI EXO2 multiparameter sonde were affixed horizontally atop a 0.3 m polycarbonate cage that permitted complete flow of water and prevented interaction with sediments. The sensor array at the open water location (site OW-1; **Figure 1**) was suspended from a fixed bulkhead ∼1 m (low tide) above the sediment surface. The EXO2 multiparameter platform had sensors for temperature (°C), conductivity (μS cm^{-1}), DO (optical; mg L^{-1} and % saturation), pH_{NBS} (National Bureau of Standards), and chlorophyll *a* fluorescence (RFU) that made measurements at 10 min intervals from ∼May through ∼October, over multiple years, 2014–2018. Copper mesh was fitted over all sensors and a central wiping mechanism was attached to the multiparameter sondes (180 min. wipe interval) to minimize biofouling. The SeaFET pH sensor measured pH_T (total H^+ scale), is designed specifically for long term field deployments (e.g., Martz et al., 2010; Hofmann et al., 2011) and, like the multiparameter sensors, logged pH_T levels every 10 min from ∼May through ∼October. The NBS scale measures H^+ activity and the total H^+ scale measures H^+ concentration where converting between scales can introduce significant error. The differences between scales can range from hundredths to tenths of a pH unit where the total H^+ scale is generally considered to be the most appropriate for estuarine and coastal systems (Pimenta and Grear, 2018). Maintenance and data transfer on each sensor array were performed on a weekly to bi-weekly basis during which sensors and brackets were removed, cleaned, and tested. Additionally, discrete sampling

and field calibrations were performed on a weekly to bi-weekly basis. Discrete measurements were made using a YSI 600QS fitted with a temperature/conductivity sensor, a rapid pulse polarographic DO sensor, and a pH electrode/Ag/Ag-Cl reference probe that provided pH measurements on the NBS scale. The handheld DO sensor was calibrated on a weekly to bi-weekly basis using a 2-point calibration technique in which the sensor was inserted into a 100% air saturated chamber until the sensor reached temperature equilibrium. Following the air-saturated calibration, the sensor was submersed in a saturated sodium sulfite solution (O_2 scavenger) to achieve a zero-point calibration. This two-point calibration technique improves accuracy of DO measurements in estuarine systems that are prone to intense diurnal fluctuations (Baumann et al., 2015). Conductivity sensors were calibrated at the beginning of the field season using a 50,000 $\mu S\ cm^{-1}$ conductivity solution and only calibrated again if significant drift was observed in the data (>0.2 psu). The pH sensor affixed to the EXO2 was calibrated at 25°C on a weekly to bi-weekly basis using a 3-point calibration procedure in which sensors were submerged in three NIST certified pH buffer solutions (4, 7, and 10: ±0.02). In addition, discrete measurements of pH_T were made using a Honeywell DuraFET III pH electrode (Ion Selective Field Effect Transistor; ISFET) integrated to a Honeywell Analytical Process Analyzer (APT) 4000PH series. The DuraFET was calibrated seasonally and when significant drift was observed (±0.02) by submersion in a 25°C equimolal Tris buffer in synthetic seawater of salinity 35 prepared by Dr. Andrew Dickson's lab (University of California San Diego, Scripps Institution of Oceanography; Batch 26). The pH_T of field samples were corrected for temperature and salinity as per Martz et al. (2010). Post-processing of data was conducted to account for fouling errors and/or sensor calibration drift. In order to adjust for potential data inconsistencies, data corrections were applied when combined absolute values due to errors exceeded water quality data correction criteria as described by USGS (see **Supplementary Table 2**; Wagner et al., 2006). Data errors resulting from biofouling were assessed by determining differences between pre- and post-cleaning measurements and a sensor fouling error would then be applied to the data as necessary (Wagner et al., 2006). Similarly, calibration drift was assessed pre- and post-calibration by determining a drift error based on the sensor measurements in standard/buffer solutions and the temperature-compensated value of the standard/buffer solution (Wagner et al., 2006). Data corrections were applied between maintenance intervals where drift corrections are assumed to occur at a constant rate and therefore linearly interpolated between maintenance intervals (Bartholoma, 2003). Generally, a single variable data correction was applied unless the data range was significant relative to the maintenance interval, in which case a second data correction based on percent error was applied (see **Supplementary Table 2** descriptions for formulas applied; Wagner et al., 2006). There were a few occasions during this study in which sensors failed due to fouling and other issues in which case data was removed. Spatial and temporal trends in chemical sensor data was assessed using a Spearman rank order correlation.

Discrete Samples

Discrete water samples were collected using a 2-L handheld WildCo® Van Dorn horizontal water sampler and/or peristaltic pump during daylight hours. Dissolved inorganic carbon (DIC) samples were obtained by inserting Tygon® tubing from the Van Dorn bottle into 330 mL borosilicate glass BOD bottles and allowing sample water to overflow with two full volumes of water. All samples were preserved on site by adding 100 µL of saturated $HgCl_2$ solution and were sealed with a glass stopper using Apiezon L ultra-high vacuum grease. Poisoned DIC samples were analyzed by coulometric titration using a UIC Inc. CM5017O coulometer interfaced to a VINDTA 3D delivery system. As a quality assurance measure, certified reference material generated by Dr. Andrew Dickson's lab (University of California San Diego, Scripps Institution of Oceanography) was analyzed immediately before and after sample titration and yielded full recovery during this entire study (99.99% ± 0.05). Carbonate chemistry parameters were calculated from measured levels of DIC, pH_T, temperature, salinity, phosphate, silicate, concentrations of boron (Lee et al., 2010), sulfate (Morris and Riley, 1966), fluorine (Riley, 1965), the dissociation constant of potassium fluoride (Dickson and Riley, 1979), the dissociation constant of potassium sulfate (Dickson, 1990), the solubility coefficient of CO_2 (Weiss, 1974), the vapour pressure of H_2O above seawater (Weiss and Price, 1980), and the first and second dissociation constants of carbonic acid in seawater (Millero, 2010) using the program CO2SYS.[1] Additional water samples were collected for analysis of chlorophyll *a*, nitrate/nitrite, ammonium, orthophosphate, particulate organic carbon (POC), and particulate organic nitrogen (PON). Chlorophyll *a* samples were filtered in triplicate through 0.2 µm polycarbonate filters and were extracted *via* organic solvent (acetone) and quantified using a Turner Designs© Trilogy Laboratory Fluorometer with an excitation wavelength of 485 nm and an emission wavelength of 685/10 nm. Water collected for dissolved inorganic nutrient analyses was filtered on site through pre-combusted (2 h at 450°C) glass fiber filters (GF/F) and filtrate was colorimetrically analyzed *via* a Hach QuikChem 8500 Flow Injection Analysis system. Water collected for POC/N were processed by collecting particles onto pre-combusted, GF/F and were analyzed using a CE instruments Flash 1112 elemental analyzer (Sharp, 1974). Differences in the chemical characteristics of sites were compared by means of one-way ANOVAs with Bonferroni tests used to assess difference among groups. Non-normal data was transformed prior to statistical tests.

Spatial Mapping

Surface water DO, pH_{NBS}, and pCO_2 levels were horizontally profiled across several systems and estuaries during the day to characterize spatial patterns within each distinct habitat. *In situ* pCO_2 levels were measured using a Contros HydroC CO_2 sensor. The HydroC measures pCO_2 levels *via* non-dispersive infrared spectrometry (NDIR) after dissolved gasses within seawater permeate a hydrophobic membrane and equilibrate with the inner pumped gas circuit (Fiedler et al., 2012; Fietzek et al., 2014).

[1] https://cdiac.ess-dive.lbl.gov/ftp/co2sys/

Surface water mapping cruises encompassed the Peconic Estuary in its entirety, with additional secondary cruises conducted in the Haywater Cove region (site MA-1), and the Scallop Pond region (site SM-3) using a 1″ diameter rigid ram intake (Madden and Day, 1992) affixed to the rear transom of a small vessel, extending 0.5 m below the air-sea interface with 3–4 flow chambers customized to specific sensor arrays. A debubbler was installed in-line where the system was first primed to generate laminar flow. If significant bubbling was detected *via* pressure sensor, data was removed. In order to examine fine scale variations within the seagrass meadow, a rigid intake was developed for the seagrass sampling location (SG-1) in which water was sampled continuously from 10 cm above the sediment water interface using a laminar flow pump. All sampling locations were geo-referenced using a GPS receiver (GlobalSat BU-353S4; SiRFstar IV) transmitting at 1 Hz. Horizontal survey data was interpolated using the simple kriging method and the semivariogram function was used to relate semivariance to sampling lag (Curran, 1988). Additional point data was interpolated using a diffusion kernel technique with an additive raster barrier. This diffusion interpolation was useful as high resolution data warranted an interpolation that uses a distance metric (optimally varying kernel) that calculates the cost of travel from one cell of a raster to the next (Krivoruchko and Gribov, 2004). This technique yielded predictions based on a grid matrix and accounted for any region with insufficient data or areas that have non-transparent barriers (i.e., coastlines) for chemical propagation (Gribov and Krivoruchko, 2011).

Habitat Metabolism

Ecosystem metabolism was calculated at five sampling locations (SG-1, SG-2, SM-3, MA-1, and OW-1), enabling comparison of distinct metabolic rates throughout the entire field season. Diffusion of oxygen (O_{2d}) across the air-sea interface (kg s^{-1}) was calculated at 10 min intervals using a bulk liquid-phase mass transfer coefficient (Eq. 1) as described in Ro et al. (2007), where DO_A is the DO concentration at equilibrium with the atmosphere (kg m^{-3}), DO_w is the DO concentration in the water (kg m^{-3}), A is the mass transfer area (m^2), and k_L is the bulk liquid-phase oxygen mass transfer coefficient (m/s). k_L was derived using Eq. 2 as described by Ro et al. (2007) where Sc is the Schmidt number, defined as the kinematic viscosity of water divided by the diffusion coefficient of O_2 gas (Wanninkhof, 1992). U_{10} is the wind speed at a reference height of 10 m (m/s), which was derived from continuous data collected at the Stony Brook Southampton Marine Sciences Center, Southampton, NY, United States which is <15 km from all study sites,[2] ρ_A indicates the density of air, and ρ_W indicates the density of water.

$$O_{2d} = k_L * A(DO_A - DO_W) \quad (1)$$

$$k_L = \left[170.6 * Sc^{-1/2} U_{10}^{1.81} \left(\frac{\rho_A}{\rho_W}\right)^{1/2}\right] 2.78 * 10^{-6} \quad (2)$$

[2]https://lishore.org/l17/latest.php

For each 10 min interval, O_2 diffusion (O_{2d}) was subtracted from the change in DO concentrations (g m^{-3}) multiplied by depth (z) of measurement (m), resulting in time-integrated oxygen flux (O_{2f} g m^{-2}) as described in Caffrey (2004) (Eq. 3).

$$O_{2f} = \sum_{i=1}^{t} (DO_t - DO_{(t-1)}) * z - (O_{2d}) \quad (3)$$

Estimates of daily metabolic rates were calculated by subtracting total respiration from gross production. Oxygen fluxes during daylight hours (net production) were calculated and summed oxygen fluxes at night were multiplied by −1 to determine evening respiration rates (Caffrey, 2004). Gross production and total respiration rates were estimated using net production and evening respiration values (Caffrey, 2004). Day and evening hours for all calculations were determined using daily civil twilight times (Sun is 6° below azimuth; EDT) at each sampling location.

Calculated metabolic rates based on fixed sensor deployments may be susceptible to error due to tidal advection where water masses with distinct DO histories may influence observed DO sensor measurements (Beck et al., 2015). In order to address this issue, we calculated an NEM error range for each site based on the distance between sites sampled and adjacent monitoring arrays (Van Dam et al., 2019). Mean spatial concentration gradients were estimated for each site by dividing the mean DO concentration by the distance between sites in km (x), multiplied by water velocity (v; Van Dam et al., 2019). We used a mean water velocity of 2.5 cm/s for all stations, which was the mean velocity over a tidal cycle at station SG-2. This error range, $\left[\left(\frac{\triangle DO}{\triangle x}\right) * v\right]$, was then calculated for each 10 min interval and the summation per day was incorporated into our NEM calculations (Van Dam et al., 2019). Due to the shallow depth at most sites, the impact of gas transfer on water column DO concentrations may also be significant and therefore NEM is subject to additional error related to O_2 re-aeration. To account for this re-aeration adjustment, the calculated gas transfer velocity (Eq. 2) was added to the error range and the summation per day was further incorporated into the NEM calculations. Therefore, the resulting uncertainty bounds presented in **Figure 5** represent the combined effects of lateral mixing and variability in gas transfer velocities.

RESULTS

Continuous, Multi-Day Deployments in Salt Marshes and Seagrass Beds

During the summer and fall of 2014, high frequency measurements of DO and pH_T were made over short temporal scales at seagrass station 1 and salt marsh stations 1 and 2 (SG-1, SM-1, and SM-2; **Figures 1**, **2**). During the mid-summer seagrass deployment, salinity ranged from 27 to 30, DO ranged from 6 to 10 mg L^{-1}, and pH_T ranged from 7.7 to 8.1, with minimum DO and pH_T values occurring in the early morning (**Figure 2A**) while maximum values were recorded during the early evening

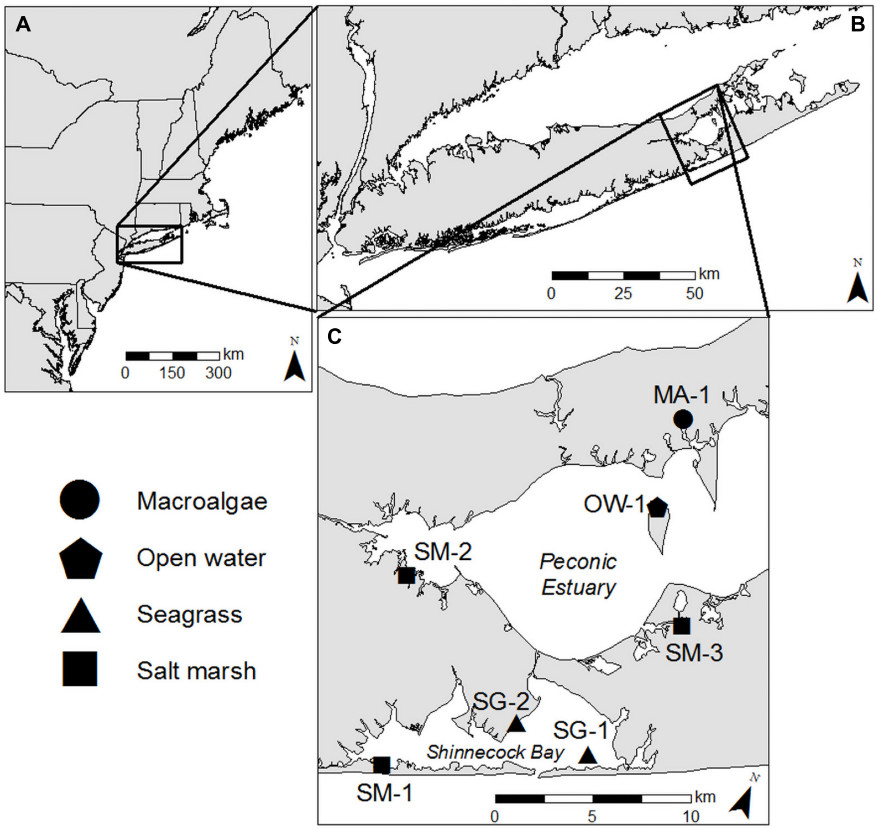


FIGURE 1 | (A) Map of Northeastern United States with **(B)** Long Island, **(C)** Shinnecock Bay, and Great Peconic Bay inset. Black shapes indicate sampling locations and shapes correspond to distinct habitats sampled.

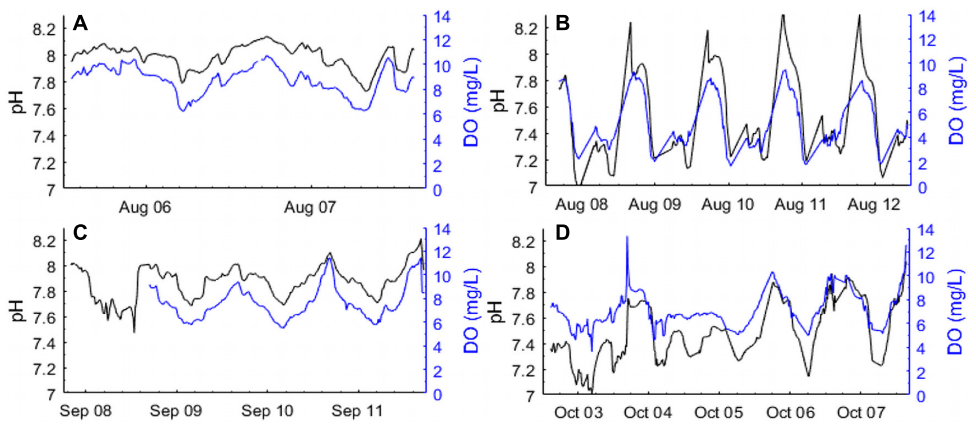


FIGURE 2 | High frequency diurnal measurements of pH_T (Black lines; total H^+ scale) and dissolved oxygen (Blue lines; DO mg L^{-1}) in **(A)** a seagrass bed (SG-1) in August, **(B)** a salt marsh (SM-1) in August, **(C)** a seagrass bed (SG-1) in September, and **(D)** a salt marsh (SM-2) in October of 2014.

and coincided with a high tide on August 6 (**Figure 2A**). During the same time period, sensors at the salt marsh detected values that were lower and more dynamic, with DO ranging from 2 to 10 mg L^{-1}, pH_T ranging from 7.0 to 8.2 (**Figure 2B**), with both parameters being tightly coupled with each other ($\rho = 0.67$; $p < 0.0001$) and tidal height ($\rho = 0.36$ and 0.24 for DO and pH_T, respectively, $p < 0.0001$ for both; **Figure 2B**). During fall, the seagrass meadow displayed a slightly larger pH_T and DO range, 7.6–8.1 and 6–11 mg L^{-1} relative to summer, with similar diurnal patterns (**Figure 2C**). The fall salt marsh deployment revealed weaker diurnal patterns, higher minimum DO concentrations (min. DO 4–5 mg L^{-1}), but continued low

pH_T conditions, within a minima of 7.0 and maximum pH_T values never exceeding 8.0 (**Figure 2D**).

Continuous, Seasonal Deployments Across Four Habitat Types

In 2015, a multi-habitat study was established from May to early October for three locations: salt marsh station 3 (SM-3), seagrass station 1 (SG-1), and a macroalgae station (MA-1), with an open water station studied from late June to mid-November (OW-1; **Figure 1**). Analysis of high-frequency DO and pH_T data revealed substantial differences in means and variances between sites (**Table 1** and **Figure 3**). Within the salt marsh habitat, DO steadily decreased from ∼7 to ∼5 mg L^{-1} throughout the summer, before increasing slightly in fall (**Figure 3A**) while mean pH_T values were dynamic but low, ranging from 7.0 to 7.7 from May through October (**Figure 3B**). Mean DO over the entire sampling season in the salt marsh was 5.3 mg L^{-1} and mean pH_T was 7.4 (**Table 1** and **Figures 3A,B**). Within the macroalgae-dominated system, pH_T and DO were highly dynamic over diurnal time scales (**Figures 3C,D**) with DO supersaturated (DO > 8 mg L^{-1}) and pH_T ranging from 7.5 to 8.4 during much of May and June (**Figure 3C**). During late June and July, this site began to experience nocturnal hypoxia (<3 mg DO L^{-1}; **Figure 3C**) and acidified conditions (pH_T < 7.5; **Figure 3D**). In September, DO and pH_T levels within the macroalgae-dominated site were slightly higher than late summer conditions as mean DO ranged from 4 to 10 mg L^{-1} and mean pH_T ranged from 7.6 to 8.2 (**Figure 3D**). For the sampling season, the macroalgae station had a mean DO of 8.53 mg L^{-1} and a pH_T of 7.81 (**Table 1** and **Figures 3C,D**). Within the seagrass bed, DO and pH_T levels were consistently higher than the salt marsh site and displayed little seasonal variance compared to the macroalgae site. Mean DO throughout the entire season was 7.85 mg L^{-1} and the mean daily range was 4.5 mg L^{-1} while the mean pH_T was 8.01 with a mean daily range of 0.34 (**Table 1** and **Figures 3E,F**). The open water location exhibited the lowest seasonal variance among the sites with mean values of DO and pH_T of 7.34 ± 0.56 mg L^{-1} and 7.87 ± 0.06, respectively, and mean ranges of 2.19 mg L^{-1} and 0.25, respectively (**Table 1** and **Figures 3G,H**).

All four habitats exhibited similar diurnal patterns in pH_T and DO, being lowest during the morning hours (**Figure 4**; 4:00–8:00 EDT), and highest in the afternoon (**Figure 4**; 12:00–21:00 EDT). In the salt marsh, acidic (pH_T < 7) and hypoxic conditions (DO < 3 mg L^{-1}) were common in the morning hours, with a maximum pH_T of up to 7.8 in the evening when DO often exceeded 7 mg L^{-1} (**Figure 4A**). The macroalgal dominated ecosystem had the largest pH_T and DO range with the pH_T ranging from 6.9 to 8.8 and DO ranging from 0 to 20 mg L^{-1} (**Figure 4B**). Hypoxic / anoxic events were most commonly observed from 04:00 to 09:00 EDT when pH_T values were usually 7.0–7.5 (**Figure 4B**). In contrast, pH_T and DO within the macroalgae site rarely decreased below 7.6 and 7 mg L^{-1}, respectively, from 15:00 to 20:00 EDT, and was often supersaturated with respect to DO at this time (**Figure 4B**). The seagrass site was less dynamic than the salt marsh and macroalgae-dominated sites with pH_T values exceeding 8 and supersaturated DO values commonly observed between 13:00 and 20:00 EDT (**Figure 4C**). In contrast to the salt marsh and macroalgae site, neither hypoxic nor acidic conditions were observed within the seagrass meadow throughout this study (**Figure 4C**). The open water location exhibited the lowest diurnal variability as pH_T ranged from 7.5 to 8.2 and DO ranged from 5 to 10 mg L^{-1} with mild afternoon increases in pH_T and DO (**Figure 4D**).

TABLE 1 | Daily mean ± SD, maximum, minimum, variance, and range in four distinct coastal habitats.

DO (mg L^{-1})	SM-3	MA-1	SG-1	OW-1
Mean	5.26	8.53	7.85	7.34
Mean daily SD	1.81	3.26	1.18	0.56
Mean daily max	8.17	14.68	10.44	8.42
Mean daily min	1.90	4.33	5.93	6.23
Mean daily var	3.51	15.15	1.67	0.37
Mean daily range	6.28	10.36	4.51	2.19
pH_T	**SM-3**	**MA-1**	**SG-1**	**OW-1**
Mean	7.38	7.81	8.01	7.87
Mean daily SD	0.18	0.24	0.09	0.06
Mean daily max	7.66	8.14	8.19	7.99
Mean daily min	7.04	7.36	7.85	7.74
Mean daily var	0.04	0.07	0.01	0.00
Mean daily range	0.62	0.78	0.34	0.25

A salt marsh (SM-3), a macroalgal bed (MA-1), a seagrass bed (SG-1), and an open water estuary (OW-1).

Daily ecosystem metabolism rates further highlighted differences between habitats. The salt marsh was predominantly net heterotrophic (NEM < 0) with production exceeding respiration on only a handful of days over the deployment (**Figure 5A**). NEM averaged −2.22 ± 3.54 g O_2 m^{-2} d^{-1} within the salt marsh over the entire sampling season (**Figure 5A**). In contrast, the macroalgae station was primarily autotrophic (NEM > 0), but highly variable, ranging from >20 to −7 g O_2 m^{-2} d^{-1} (**Figure 5B**). The highest rates of net productivity were observed in June and July before decreasing and becoming slightly net heterotrophic by September (**Figure 5B**). The seagrass sites exhibited lesser variability than the macroalgae and salt marsh sites and was a more metabolically balanced ecosystem averaging 0.65 ± 1.73 g O_2 m^{-2} d^{-1} through the sampling season (**Figure 5C**). NEM increased and became slightly more variable during late summer, as the mean NEM before July 15 was 0.40 ± 1.11 and nearly doubled to 0.76 ± 1.93 g O_2 m^{-2} d^{-1} from mid-July through August (**Figure 5C**). By October, NEM within the seagrass meadow was consistently positive and less variable (**Figure 5C**). NEM was the least dynamic within the open water site, being slightly net heterotrophic, −0.13 ± 0.85 g O_2 m^{-2} d^{-1} (**Figure 5D**).

Inter-annual, inter-month, and intra-habitat variability of seagrass metabolism was assessed by comparing month-by-month, diurnal dynamics of DO and pH_T in two seagrass meadows (SG-1 in 2015 and SG-2 in 2016; **Figure 1**). At both sites, DO and pH_T showed consistent diurnal patterns that intensified through summer, with site two displaying a larger degree of diel variation during the sampling period (**Figure 6**).

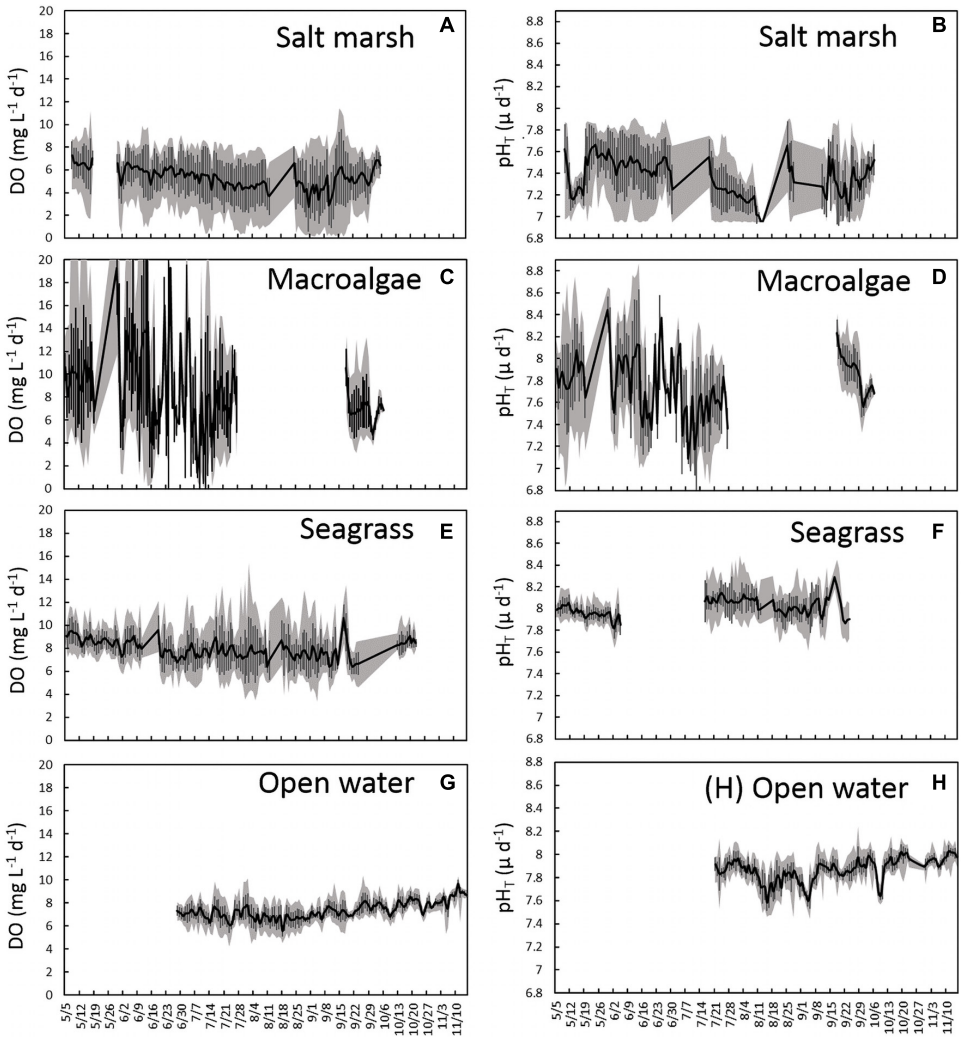


FIGURE 3 | Time series plots representing mean **(A)** DO mg L^{-1} d^{-1} ± SD and **(B)** pH_T d^{-1} ± SD (black lines and error bars) in a salt marsh (SM-3), **(C)** DO mg L^{-1} d^{-1} ± SD and **(D)** pH_T d^{-1} ± SD (black lines and error bars) in a macroalgae-dominated creek (MA-1), **(E)** DO mg L^{-1} d^{-1} ± SD and **(F)** pH_T d^{-1} ± SD (black lines and error bars) in a seagrass bed (SG-1), and **(G)** DO mg L^{-1} d^{-1} ± SD and **(H)** pH_T d^{-1} ± SD (black lines and error bars) in an open water estuary (OW-1). The gray shaded area represents the maximum daily range each day.

Through the summer, the second seagrass site displayed stronger daytime super-saturation of DO (>10 mg L^{-1}) and during August and September, this site frequently displayed pH_T and DO values below 7.7 and 5 mg L^{-1} in the early morning hours (**Figure 6**).

Dynamics of Carbonate Chemistry

Distinct differences in the carbonate system and total alkalinity (TA) were apparent across habitats (**Figure 7**). The salt marsh ($n = 15$) and seagrass ($n = 25$) sites had similar medians with respect to TA (∼2150 μmol kg^{-1} SW) and a large seasonal range (**Figure 7A** and **Supplementary Table 3**; 600 and 550 μmol kg^{-1} SW, respectively) where the seagrass site had a greater salinity range and higher peak salinity (**Supplementary Table 3**). TA at the macroalgae station was significantly lower ($p < 0.001$; **Supplementary Table 3**; **Figure 7A**; median ∼1850 μmol kg^{-1} SW, $n = 9$) and reached a minimum of ∼1600 μmol kg^{-1} SW (**Figure 7A**). The macroalgae station also had the lowest salinity compared to all other sites sampled, decreasing to 24 during periods of intense precipitation (**Supplementary Table 3**). TA at the open water site was more consistent, remaining between ∼1900 and ∼2000 μmol kg^{-1} SW (**Figure 7A**; $n = 19$) and was also significantly lower than the salt marsh and seagrass habitats ($p < 0.001$; **Supplementary Table 3**), but the mean was not statistically distinguishable from the macroalgae site ($p > 0.05$; ANOVA; Bonferroni test; **Supplementary Table 3**). DIC exhibited patterns similar to TA although the salt marsh had a significantly larger range and higher median than the other three sites ($p < 0.0001$; **Supplementary Table 3**; **Figure 7B**; range ∼700 μmol kg^{-1} SW, median ∼ 2100 μmol kg^{-1} SW). The larger DIC range and higher values at the salt marsh site were, at least in part, due to greater metabolic CO_2 fluxes

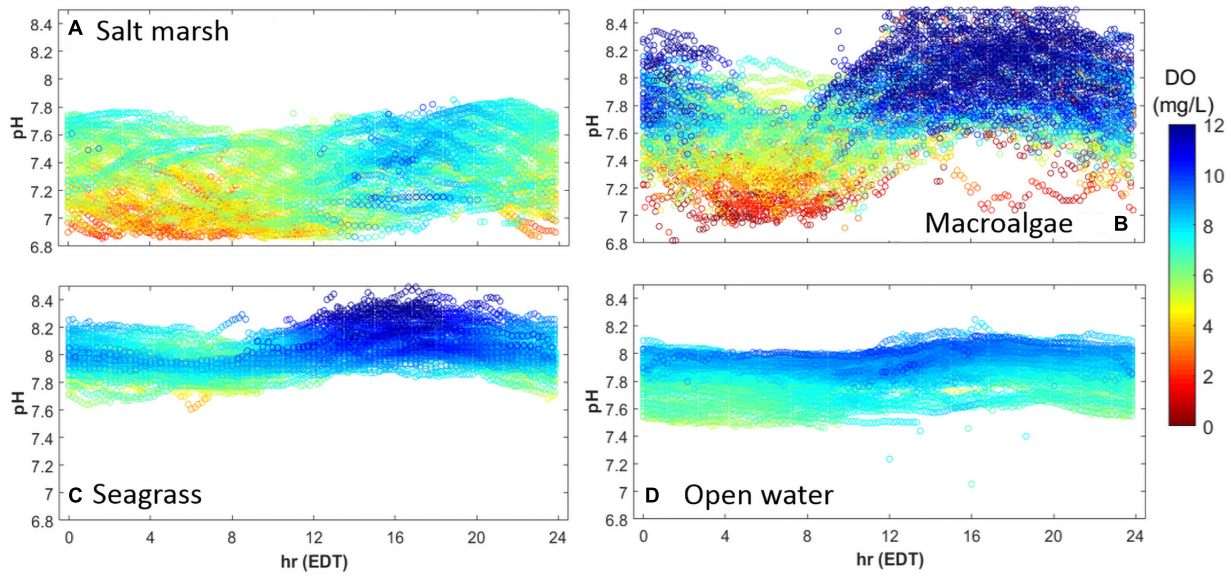


FIGURE 4 | Diurnal patterns of pH_T (y-axis) and DO (mg L^{-1}; color) in an **(A)** salt marsh, **(B)** macroalgal dominated (*Ulva* sp.) region, **(C)** seagrass meadow, and **(D)** open water estuary, May–October, 2015. Sites identical to **Figure 3**.

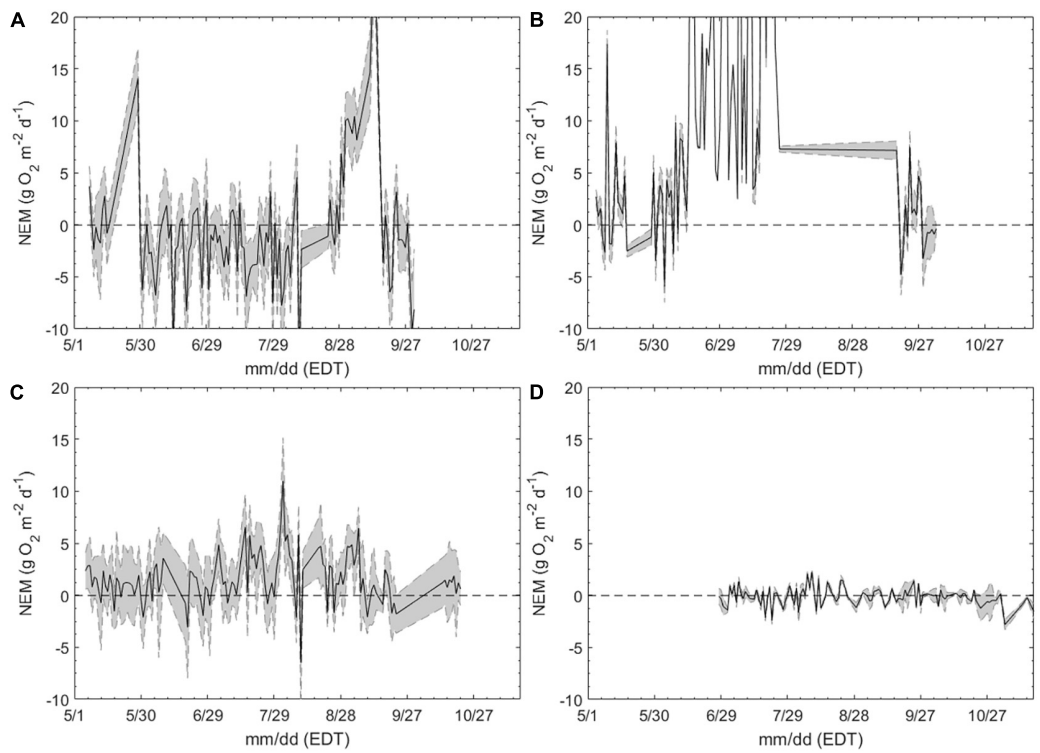


FIGURE 5 | Daily net ecosystem metabolism (NEM; g O_2 m^{-2} d^{-1}) in a **(A)** salt marsh (SM-3), **(B)** a macroalgae bed (MA-1), **(C)** a seagrass bed (SG-1), and **(D)** an open water estuary (OW-1), May – October, 2015. Sites identical to **Figures 3**, **4**. Shaded region bound by dashed lines indicates the calculated uncertainty due to the combined effects of lateral mixing and variability in gas transfer velocity.

emanating from the salt marsh (**Figure 7C**). Mean pCO_2 levels in the salt marsh were 2,315 ± 1,228 μatm, significantly higher than all other sites ($p < 0.0001$; **Supplementary Table 3**; **Figure 7C**). The pCO_2 levels displayed large variation at the macroalgae location, fluctuating from <200 to 2,000 μatm (mean = 1,060 ± 637 μatm) and were lowest at the open water

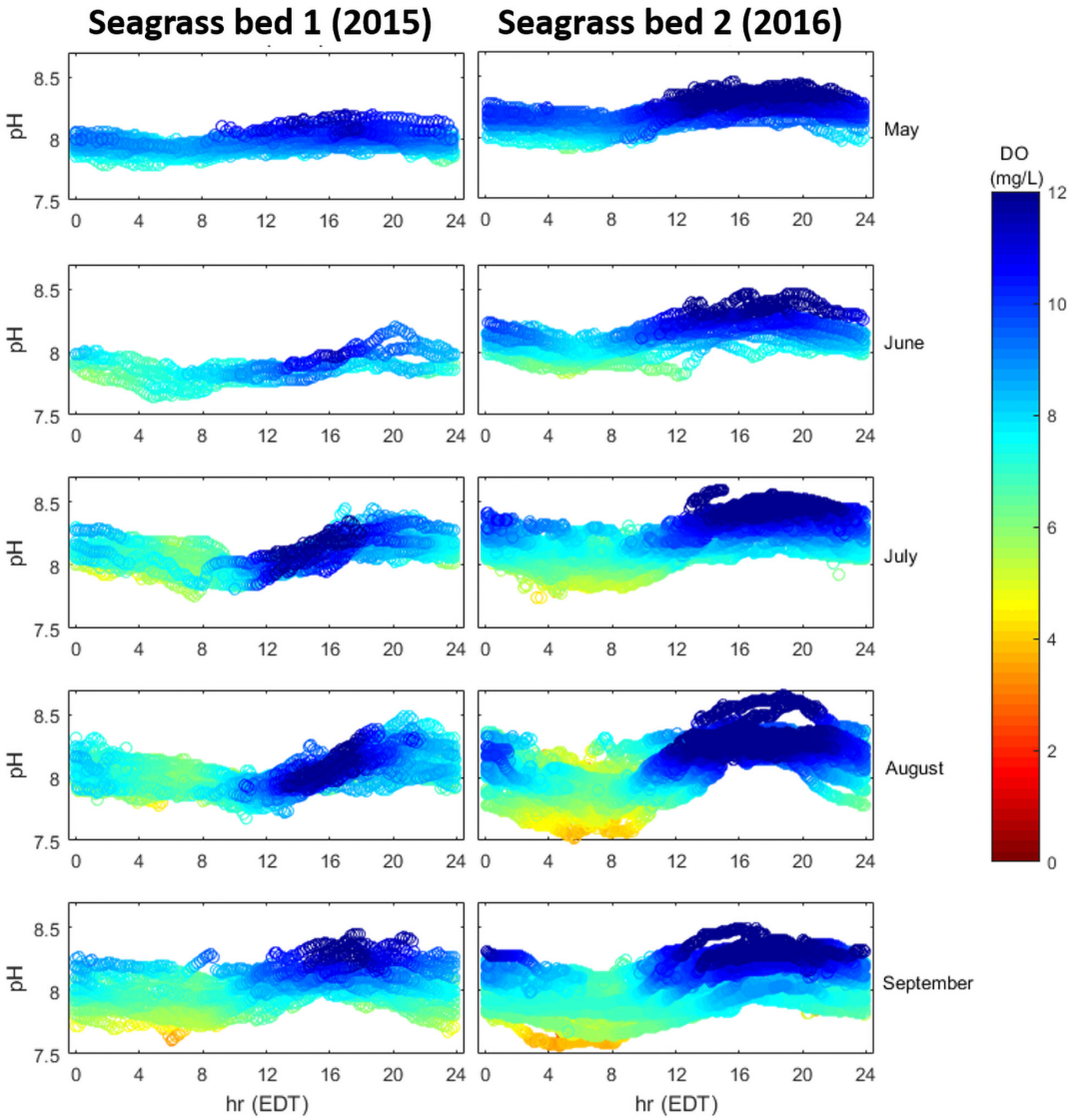


FIGURE 6 | Diurnal patterns of pH_T (y-axis) and DO (mg L^{-1}; colormap) in two seagrass meadows (SG-1 and SG-2), May–September, 2015 and 2016, respectively.

and seagrass sites (mean = 500 ± 140 μatm and 498 ± 184 μatm, respectively; **Figure 7C**). Although the macroalgae site was often undersaturated with respect to aragonite ($\Omega_{Ar} < 1$), it also exhibited the largest range (<0.5–>4.5), whereas the seagrass bed was always saturated (Ω_{Ar} 1–3.5) and had the highest Ω_{Ar} while the site was almost always undersaturated ($\Omega_{Ar} < 1$; **Figure 7D**). Mean Ω_{Ar} levels within the seagrass beds and open water sites were significantly higher than the salt marsh site ($p < 0.001$; **Supplementary Table 3**) and Ω_{Ar} within the seagrass beds was also significantly higher than the macroalgae site ($p < 0.01$; **Supplementary Table 3**). The Revelle factor (Rf) can be useful for assessing an environment's ability to buffer against increasing CO_2 with a higher Rf yielding a lower buffering capacity. Increases in Rf indicate a decreased buffer capacity allowing for the fractional change in pCO_2 in relation to the fractional change in DIC to increase (Revelle and Suess, 1957; Egleston et al., 2010). The Rf exhibited by the salt marsh and macroalgae-dominated sites were significantly higher than those of seagrass and open water sites ($p < 0.05$; **Supplementary Table 4**; **Figure 7E**). The macroalgae station had a much larger range in which the Rf decreased to <8 and exceeded 18 (**Figure 7E**). In contrast, the seagrass and open water location were between 10 and 16 (**Figure 7E**).

High-Resolution Mapping of Coastal Habitats

The spatial variability within each habitat was examined *via* high-resolution, horizontal mapping. Across the open waters of the Peconic Estuary (Great Peconic Bay) in August, DO ranged from 6.5 to 8.7 mg L^{-1}, while pH_{NBS} ranged from 7.82 to 7.98 (**Figure 8**) with values generally increasing from

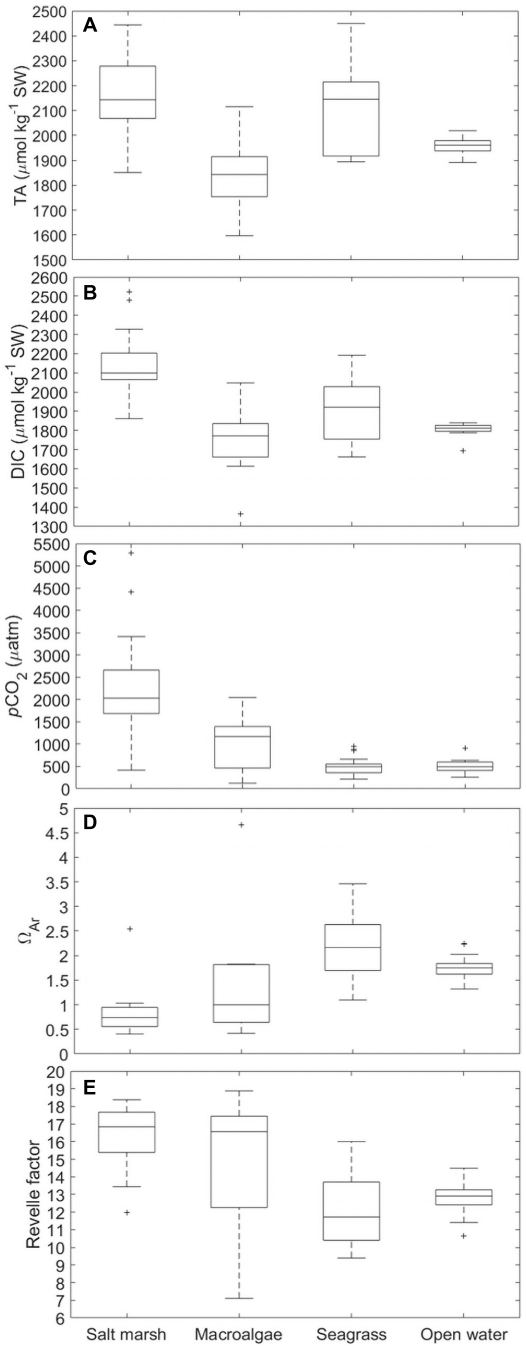


FIGURE 7 | Box and whisker plots of **(A)** TA (μmol kg^{-1} SW), **(B)** DIC (μmol kg^{-1} SW), **(C)** pCO_2 (μatm), **(D)** Ω_{Ar}, and **(E)** Revelle factor for four habitat types (SM-3, MA-1, SG-1, OW-1). On each box, the central mark indicates the median, and the bottom and top edges of the box indicate the 25th and 75th percentiles, respectively. The whiskers extend to the most extreme data points not considered outliers, and the outliers are plotted individually using the "+" symbol.

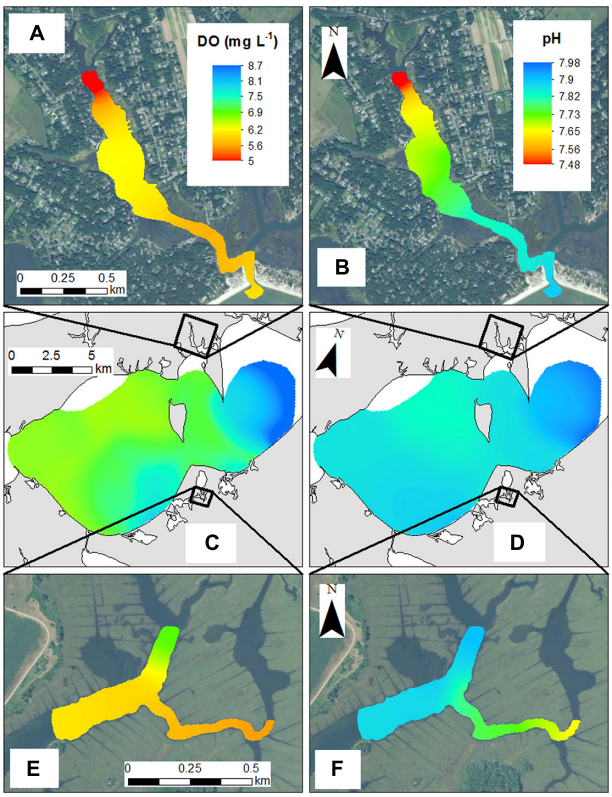


FIGURE 8 | High resolution surveys of **(A)** DO (mg L^{-1}) within the macroalgae (MA-1) sampling region, **(B)** pH within the macroalgae (MA-1) sampling region, **(C)** DO (mg L^{-1}) in the Peconic Estuary (OW-1), **(D)** pH in the Peconic Estuary (OW-1), **(E)** DO (mg L^{-1}) within a salt marsh habitat (SM-3), and **(F)** pH within a salt marsh habitat (SM-3). All cruises were conducted in August.

west to east toward the mouth of the estuary. Levels of pCO_2 ranged from 580 to 700 μatm (Wallace, unpublished data). In contrast, the macroalgae and salt marsh along the northern and southern shores in the same estuary, respectively, were more spatially heterogeneous. Daytime DO within the macroalgae region ranged from >6.5 mg L^{-1} at the mouth of the cove to <5 mg L^{-1} toward the head while daytime pH_{NBS} ranged from 7.48 within the cove to 7.82 at the mouth (**Figure 8**). Within the salt marsh region, similar spatial differences were detected as daytime DO ranged between 5.6 and 6.2 mg L^{-1} within the marsh to >7 mg L^{-1} in the tributary exchanging with the Peconic Estuary, a total distance of only ∼400 m (**Figure 8**). The pH_{NBS} trends were similar with daytime pH_{NBS} ranging from 7.6 to 7.7 within the marsh and exceeding 7.8 within the deeper navigational channel toward the estuary (**Figure 8**). The salt marsh pH_{NBS} and DO values during the cruise were slightly elevated compared to the continuous measurements in this system as the salt marsh cruise was conducted during the late afternoon when DO and pH_{NBS} values are generally at their peak (**Figure 4A**; O'Boyle et al., 2013; Baumann et al., 2015; Wang et al., 2016). In addition, sampling was conducted during a flood tide, two conditions that increase both DO and pH_{NBS}.

The seagrass bed (SG-1) in Shinnecock Bay displayed sharp spatial differences in pCO_2 (**Figure 9**). Surface waters of Shinnecock Bay in August had pCO_2 levels that ranged from 550

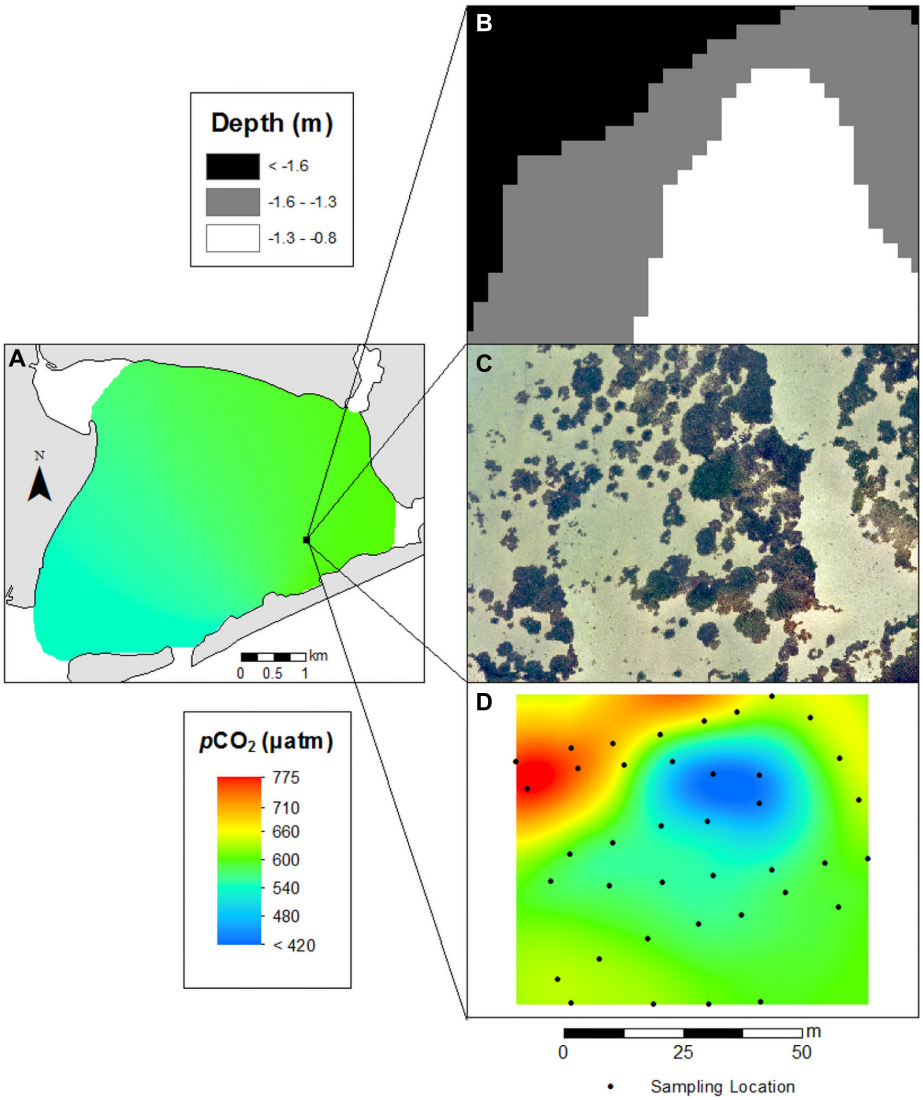


FIGURE 9 | (A) High resolution survey of pCO_2 in eastern Shinnecock Bay. **(B)** High resolution depth measurements (3 m horizontal resolution), **(C)** high resolution drone imagery, and **(D)** pCO_2 measurements sampled at 10 cm above the sediment-water interface encompassing a 6300 m^2 region surrounding seagrass site SG-1.

to 600 µatm (**Figure 9**). Within the seagrass bed, regions with a depth <1 m and dense patches of seagrass had pCO_2 levels as low as 400 µatm whereas deeper regions with no seagrass had pCO_2 exceeding 700 µatm (**Figure 9**).

DISCUSSION

High frequency pH_T and DO measurements coupled with discrete sampling across four distinct coastal habitats revealed stark differences in carbonate chemistry and ecosystem metabolism during this study. High-resolution sampling conducted across each habitat highlighted acute spatial variability present within each environment. While each habitat displayed similar relative diurnal patterns of pH_T and DO, the intensity of variance of these conditions differed significantly among habitats. Spring through fall is a period of maximal metabolic rates in estuaries (D'Avanzo et al., 1996; Caffrey, 2004; Middelboe and Hansen, 2007b; Baumann et al., 2015). Such rates will interact with other factors such as volume of estuarine waters, residence time, and tidal forcing to shape differing local extrema of DO and pH_T. The coastal habitats examined here are representative of many temperate estuaries that harbor juvenile finfish and shellfish (Nixon and Oviatt, 1973; Sogard and Able, 1991; Roman et al., 2000; Beck et al., 2001; Duffy, 2006), making an understanding of the DO and carbonate chemistry dynamics within these systems important for fisheries management and aquaculture practices (Wallace et al., 2014; Tomasetti and Gobler, 2020).

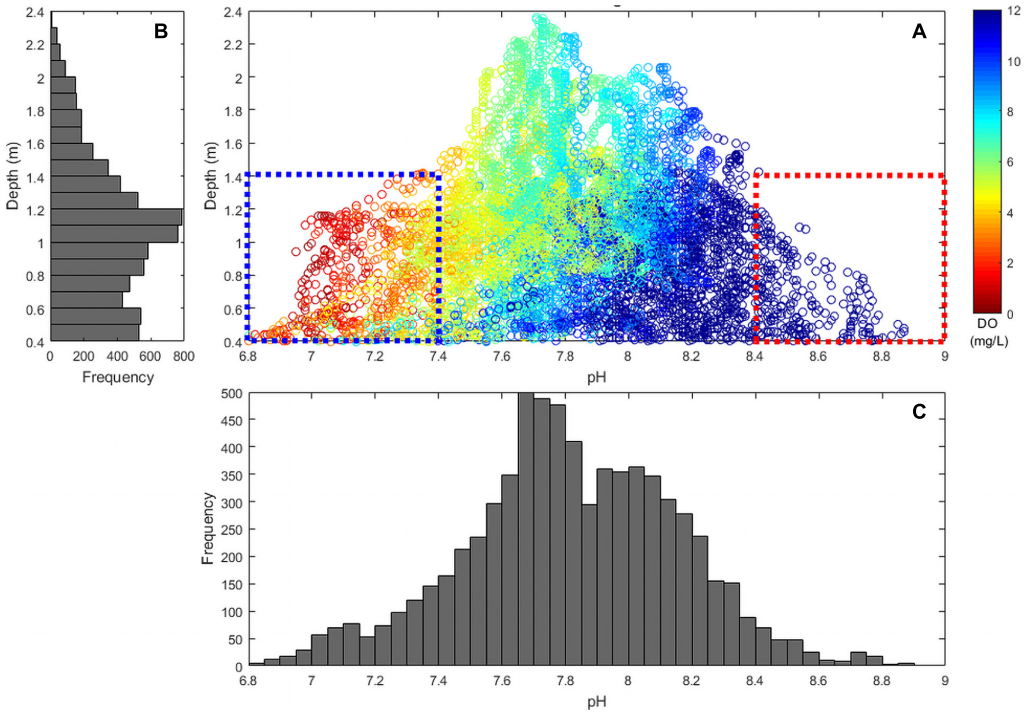


FIGURE 10 | Comparison of **(A)** depth (y-axis), pH_T (x-axis), and DO (mg L^{-1}; color) in a macroalgal dominated (*Ulva* sp.) region (MA-1), May–October, 2015. Blue dashed box indicates low pH_T and DO during low tides and red dashed box indicates high pH_T and DO during low tides. Frequency distribution of **(B)** depth and **(C)** pH_T samples are indicated by adjacent histograms.

Seasonal Inter-Habitat Variability in Net Ecosystem Metabolism and Carbonate Chemistry

The open water habitat of this study was the most metabolically balanced region (**Figure 5D**) and displayed temporal stability (**Figures 3G,H**, **4D**) and spatial homogeneity (**Figure 8**) representative of tidally dominated estuaries where vertical mixing prevents stratification of the water column (Hardy, 1976; Fischer et al., 2013). This system was slightly net heterotrophic over the course of this study (mean NEM $= -0.14 \pm 0.9$) as sampling was conducted primarily during summer months when respiration rates are maximal in temperate coastal systems (D'Avanzo et al., 1996; Iriarte et al., 1997; Tait and Schiel, 2013) and the spring phytoplankton bloom has since subsided in Long Island coastal waters (Riley and Conover, 1967; George et al., 2015). Both pH_T and DO ranges were consistent with other estuarine or near-shore environments that have been examined on both the east and west coast of the United States (Caffrey, 2004; Hofmann et al., 2011; Baumann and Smith, 2018), but certainly was greater than open ocean environments (Hofmann et al., 2011; Sutton et al., 2019). Correspondingly, the Rf is in the range expected for this class of environments (Feely et al., 2018).

The seagrass meadows examined here exhibited slightly larger diurnal ranges of both pH_T (0.34 vs. 0.25) and DO (4.51 vs. 2.19 mg L^{-1}) compared to the open water site (**Table 1** and **Figures 4C,D**) and were generally net autotrophic over diel timescales from the late spring through the early fall (**Table 1** and **Figures 5C**, **6**). The seagrass systems were also distinctive in hosting the lowest levels of pCO_2 (<400 μatm) and the highest Ω_{Ar} ($\Omega_{Ar} > 3$), conditions that would make them localized refuges against coastal ocean acidification (Hendriks et al., 2014; Wallace et al., 2014; Camp et al., 2016; Pacella et al., 2018). During warm and calm conditions, seagrass meadow photosynthesis will locally increase DO and decrease pCO_2 levels above and below the solubility in the water column, respectively (Dennison, 2009). This would account for the higher increase in DO and pH_T at seagrass bed 2, as this region is more sheltered from prevailing southwesterly winds that are common on Long Island during the summer months (Blumberg and Galperin, 1990). In addition, while both seagrass meadows were the same species (*Z. marina*), a greater macroalgal biomass at seagrass bed 2 resulted in more elevated community photosynthetic rates thus resulting in higher DO and pH_T levels (Jackson, 1987; Beer and Koch, 1996; Chung et al., 2011). Furthermore, the calmer conditions coupled with the seasonal decomposition of this mixed macrophyte community contributed toward the lower DO and pH_T levels during the late summer months.

Diel Inter-Habitat Variability in Net Ecosystem Metabolism and Carbonate Chemistry

In contrast to the open water and seagrass sites, the salt marshes and the macroalgae sites exhibited significantly larger diel ranges

in both pH_T and DO throughout the season (**Table 1** and **Figures 5A,B**) with these parameters being tightly coupled at both sites ($\rho = 0.674$ and 0.837, $p < 0.0001$). Although both locations tidally exchange with the adjacent Peconic Estuary, strong metabolic processes within these habitats drove significant variation on diel timescales (Wootton et al., 2008). In addition to rapid rates of photosynthesis and respiration, restricted exchange with the larger Peconic Estuary maximizes the influence of these metabolic processes on water column chemistry (Wallace et al., 2014).

During peak daylight hours, both pH_T and DO were consistently depressed within the salt marsh ($pH_T < 7.8$, DO < 8 mg L^{-1}), resulting from the cumulative effects of both biological respiration (Turner, 1978; Burnett, 1997) and tidal exchange (Gardner and Gorman, 1984; Baumann et al., 2015). While the signature of diurnal metabolism was clear, tidal exchange played a lesser, but significant role as pH_T and DO tended to increase during increasing tidal height ($\rho = 0.242$ and $\rho = 0.357$, $p < 0.0001$ for both). Similarly, Baumann et al. (2015) reported that during the summer months in a Long Island salt marsh, pH_T and DO declined during the ebbing tide whereas the flooding tide increased pH_T and DO due to lower biological activity within an adjacent open water estuarine system (Long Island Sound). In addition, hypoxic and acidified conditions are maximized when low tides occur during peak hours of net heterotrophy (**Figure 4C**; ∼4:00–8:00 EDT). Although photosynthetic rates of *Spartina* in salt marshes are high, most oxygen within blades is lost to the atmosphere and oxygen produced from the root system is rapidly reduced within the sediment (Gleason et al., 1982). Hence, the net transport of oxygen from the marsh to the water column is small and confined to higher tidal cycles which is distinct from other estuarine submerged aquatic vegetation studied here.

In contrast to salt marshes, the shallow macroalgae-dominated system was net autotrophic throughout most of the season, although periods of net heterotrophy became more common late in the season and under extreme tides. The tidal range at the macroalgae site was ∼2 m (0.4–2.4 m) and as water depth decreased below 1.4 m, both pH_T and DO reached extreme values. For example, DO only exceeded 200% saturation and only decreased below 50% saturation when tidal height was <1.4 m (**Figure 10**). In addition, these lower tidal periods were the only periods in which pH_T exceeded 8.4 and when both hypoxic and acidified conditions were observed (DO < 3 mg L^{-1} and $pH_T < 7.4$; **Figure 10**). Super saturated O_2 conditions and elevated pH_{NBS} ($pH_{NBS} > 9$) have been synchronously observed in other shallow macroalgal dominated marine ecosystems (Howland et al., 2000; Menéndez et al., 2001; Middelboe and Hansen, 2007b), but such shallow, highly productive habitats are not ordinarily associated with acidification and hypoxia. Coastal macroalgal habitats have long been considered nutrient buffer zones that can alter shallow water biogeochemistry and exchange solutes at the sediment-water interface (Duarte et al., 2013; Sundbäck and McGlathery, 2013). In shallow tidal systems, such as described here, large macroalgal aggregations can intensify water column DO and pH_T extremes during lower tide cycles on diel and seasonal timescales. During summer months when macroalgal biomass accumulates in calm, shallow water habitats, DO fluctuations can be large and DO concentrations are high (Middelboe and Hansen, 2007b). At the end of the summer and/or during extreme heat waves, macroalgal communities decay, creating the potential for hypoxia, anoxia, and acidification *via* respiration (Apinis et al., 1956; Han and Liu, 2014; Lenzi, 2014).

Buffer Capacity in Distinct Coastal Habitats

As CO_2 concentrations increase seasonally in coastal zones (Wallace et al., 2014), buffering capacity has become an important ecosystem service in estuaries. Each habitat examined here differed in their buffering capacities that changed seasonally and were modified through biological activity, salinity, and variations in TA and DIC. TA was highest within the salt marsh and seagrass locations (TA $>$ 2400 μmol kg^{-1} SW; **Figures 7A,B**) with seagrass having significantly lower DIC (DIC $<$ 1700 μmol kg^{-1} SW) and pCO_2 (<400 μatm) due to increased carbon uptake and its closer proximity to ocean water with higher salinity (and thus TA) and lower CO_2 concentrations. All sites examined during this study, with the exception of the open water site, had large ranges in Rf likely associated with biologically mediated CO_2 uptake and drawdown. The Rf in ocean surface waters generally ranges from 8 to 18 (Feely et al., 2018) and these values can provide valuable insight into the discrete responsiveness of pH_T, TA, DIC, and Ω_{Ar} when considering future changes in pCO_2 (Egleston et al., 2010). Although the mean Rf at the open water site (mean $Rf = 13$) was lower than both the salt marsh (mean $Rf = 17$) and macroalgae site (mean $Rf = 16.5$; $p < 0.0001$ and $p < 0.05$, respectively), the open water site never decreased below 11 and exhibited a narrow range (11–14; **Figure 7**). Considering the lower buffer capacity of the Peconic Estuary and the limited influence of biological activity, increases in CO_2 uptake will both accelerate and intensify acidification within this larger, open water system. In addition to the potential for increased CO_2 uptake *via* the atmosphere, further increases in CO_2 could emanate *via* transport of carbon from wetlands and/or areas with dense stands of macrophytes (Cai, 2011; Najjar et al., 2018) and with a lower buffer capacity, as pCO_2 increases, Rf would also increase, increasing the likelihood of this estuary being inhospitable for bivalve populations (Grear et al., 2020).

While TA and DIC are key indicators of buffering capacity and are often intimately linked in estuaries (Hagens et al., 2015), intense metabolic activity can decouple these pools, altering habitat buffering and suitability for calcifying organisms. For example, TA and DIC within the salt marshes became decoupled in the late summer (**Supplementary Tables 2, 3**), likely associated with increased anaerobic activity. Higher TA was observed when samples were collected at lower tidal levels suggesting TA production *via* anaerobic processes (Wang and Cai, 2004) such as the net production of bicarbonate (HCO_3^-) by sulfate reducing microorganisms (Berner et al., 1970; Hu and Cai, 2011) and TA generation *via* denitrification (Hu and Cai, 2011). Although ebbing tides from salt marshes yielded low pH_T water, this water will also have a higher buffering capacity

compared to higher pH_T waters observed during flood tides (Wang et al., 2016). This increased buffering capacity during lower tidal states coupled with increased oxygen production during higher tides when marsh grasses were submerged, resulted in occasional late summer net autotrophy (**Figure 5A**) and may further buffer against increased acidified conditions commonly observed in Northeast United States estuaries during the late summer (Wallace et al., 2014). A decoupling of DIC and TA was also observed in the late summer/early fall at the macroalgal dominated site during periods of pCO_2 undersaturation and decreasing HCO_3^- concentrations, as CO_3^{2-} concentrations increased, resulting in a transformed DIC speciation (**Supplementary Table 3**). When pCO_2 levels reached a minimum (<200 μatm), a drawdown in HCO_3^- was also evident, indicating the potential utilization of HCO_3^- when pCO_2 levels were low to support increased photosynthetic rates (Axelsson et al., 1995; Rautenberger et al., 2015). This seemed to be further enhanced during periods of increased solar radiation when DIC concentrations decreased as light intensity increased, indicating increased photosynthetic rates (Nejrup et al., 2013). TA was consistently lower at the macroalgal location and this was primarily due to the close proximity to the head of the creek where freshwater input decreased both salinity and TA (**Supplementary Table 2**), especially after heavy precipitation events where TA variations associated with freshwater addition can account for up to 80% of TA variability (Lee et al., 2006). Additionally, increased HCO_3^- uptake by macroalgae may have contributed to decreased TA *via* release of H^+ by macroalgae *via* active extrusion pump as pH_T in the surrounding water column reaches extreme levels (Uusitalo, 1996; Axelsson et al., 2000).

Intra-Habitat Variation in DO, pH, and pCO_2

Beyond inter-habitat differences revealed during this study, high resolution sampling showed significant intra-habitat variation. More restricted regions sampled within the salt marsh and macroalgae-dominated sites exhibited the lowest surface DO (<5.5 and <5 mg L^{-1}, respectively) and pH_{NBS} (<7.65 and <7.5, respectively), indicating that tidal mixing of adjacent waters with higher DO/pH_{NBS} would alleviate these conditions. Conversely, these fringing habits may significantly influence carbonate chemistry within larger adjacent systems *via* export of low DO - pH, DIC enriched waters (Chu et al., 2018). This inorganic carbon pump is especially evident in salt marsh-dominated systems (Wang and Cai, 2004) and may be a significant contributor of CO_2 to the surrounding estuary (Wang et al., 2018). The flux from other habitats such as macroalgal beds can also seasonally contribute DIC to surrounding estuarine systems while sequestering carbon during periods of intense growth (Krause-Jensen et al., 2018). During the summer and fall, temperature marine habitats such as salt marshes and dense macroalgal assemblages, and especially the most restricted regions within these habitats with the lowest DO and pH, are high risk environments for early life stage finfish and shellfish that are known to be highly sensitive to these conditions (Talmage and Gobler, 2010; Baumann et al., 2012; Gobler and Baumann, 2016).

High resolution surface mapping across Shinnecock Bay revealed spatial homogeneity with respect to pCO_2 for much of the estuary but a high degree of spatial heterogeneity within the seagrass bed (**Figure 9**). Specifically, pCO_2 levels were reduced by ∼200 μatm below ambient levels within shallow, dense stands of seagrass (**Figure 9**). These trends were driven by increased production within the dense seagrass beds, drawing down pCO_2 levels and increased pCO_2 in deeper regions associated with increased bacterial degradation of leaf litter and associated organic matter (Churchill and Riner, 1978; Mateo and Romero, 1996; Liu et al., 2017). It has been hypothesized that as coastal marine systems continue to acidify, seagrass habitats will become increasingly vital for buffering the surrounding water column (Pacella et al., 2018), creating refuges for many marine organisms, acting as potential CO_2 sinks in coastal habitats (Smith, 1981; Duarte et al., 2010; Camp et al., 2016). Determination of localized carbon budgets and carbonate chemistry will be of increasing importance as CO_2 concentrations in coastal waters continue to rise. The mesoscale variation observed here highlights the complex spatial and temporal patterns in the capacity of coastal habitats to buffer against metabolically driven acidification.

Ecological Implications

Habitats examined during this study harbor wild and aquacultured populations of multiple species of calcifying bivalves (*A. irradians*, *Crassostrea virginica*, *Mercenaria mercenaria*, *Mytilus edulis*) that are sensitive to low Ω_{Ar} values, even when Ω_{Ar} is above the thermodynamic calcification/dissolution threshold ($\Omega_{Ar} > 1$; Barton et al., 2012; Stevens and Gobler, 2018). Given the expected 0.3–0.4 unit decrease in pH in the world's oceans by the end of this century (Orr et al., 2005) and the potential for such changes to extinguish local bivalve populations (Grear et al., 2020) management agencies must identify habitats favorable for sustaining wild and aquacultured bivalves. Within the ∼200 km^2 coastal region examined during this study, we observed that differing habitats displayed distinct ranges in Ω_{Ar}. Seagrass meadows exhibited significantly higher Ω_{Ar} (mean $\Omega_{Ar} > 2$) compared to the salt marshes (mean $\Omega_{Ar} < 1$) and macroalgae dominated habitats (mean $\Omega_{Ar} = 1$; $p < 0.0001$ and $p < 0.05$, respectively). While the larger Peconic Estuary was never undersaturated during this study, during the late summer and early fall Ω_{Ar} values did regularly decrease below 1.7 (**Supplementary Table 3**), a level known to reduce the growth and survival of larval aragonitic bivalves (**Figure 7**; Talmage and Gobler, 2010; Barton et al., 2012) whereas these species will transition to precipitation of calcite in juvenile and adult stages (Haley et al., 2018). Chronic exposure to acidified conditions can cause increased mortality and depressed growth in larval bivalve species (Talmage and Gobler, 2010; Gobler and Talmage, 2013) whereas diel exposure to acidified conditions may alleviate some of these negative effects (Gobler et al., 2017). Regardless, if hypercapnia intensifies as anticipated in the future (Pachauri et al., 2014), restricted open water coastal systems such as the Peconic Estuary will be more vulnerable to the assimilation of atmospheric CO_2 than waters adjacent to wetlands and macrophyte-dominated regions where acute biological activity modulates carbon fluxes,

increasing atmospheric CO_2 sinks *via* increases in productivity (Langley et al., 2009). Given this system hosts a large aquaculture leasing program as well as a large bay scallop (*A. irradians*) fishery, future acidification could potentially result in significant economic loss (Mangi et al., 2018; Grear et al., 2020).

Recently, multi-trophic ocean farming has been considered as a remedial aquaculture practice whereby macroalgae are, for example, co-cultivated with bivalves (Neori, 2009; Clements and Chopin, 2017). Recent laboratory experiments have shown that bivalves grown under elevated pCO_2 conditions experience increased shell and tissue growth when co-cultivated with green algae of the genus *Ulva* when compared to bivalves grown without exposure to this alga (Young and Gobler, 2018). While *Ulva* spp. could also acidify the water column on diel timescales if in a period of decay (**Figure 4B**), multi-trophic systems whereby macroalgae such as kelp or other seaweeds (Chopin et al., 2001; Kim et al., 2015) are grown and harvested prior to decay periods could protect calcifying bivalves and thus may become an increasingly important aquaculture approach in coastal systems as oceans continue to acidify.

In the Northeast United States during summer months, intense diel fluctuations in DO and pH have been documented within salt marshes (Baumann et al., 2015; Wang et al., 2016, this study). The combined effects of hypoxia and acidification on the growth and survival of early life stage shellfish has been documented in recent years (Gobler et al., 2014; Stevens and Gobler, 2018) and the levels and intensity of diel changes in pH_T and DO observed in both the salt marshes and the macroalgae site during this study (**Figure 4**), have been shown to depress growth rates and decrease survival of bivalve larvae (*A. irradians.*, *M. mercenaria*, *C. virginica*) in laboratory experiments (Clark and Gobler, 2016; Gobler et al., 2017). Presently, wild populations of *A. irradians*, *C. virginica*, and *M. mercenaria* are primarily restricted to open water habitats or within seagrass beds in the Peconic Estuary and Shinnecock Bay (NYSDEC, 2015). Conversely, salt marshes examined during this study were dominated exclusively by the ribbed mussel (*Geukensia demissa*), an intertidal species that is able to tolerate extended exposure to the atmosphere, extreme temperatures, and hypoxic conditions (Jost and Helmuth, 2007; Fields et al., 2014). *G. demissa* specifically relies on anaerobic respiration during periods of atmospheric exposure (Fields et al., 2014), and when submerged, this physiological mechanism would enable this species to be more tolerant of hypoxia and perhaps increased CO_2 concentrations when compared to other bivalves. Hence, future bivalve restoration efforts within nearshore habitats that may be vulnerable to current or future acidification may be more successful building populations of *G. demissa* which is clearly tolerant of a wide range of pH and DO conditions found in salt marshes.

CONCLUSION

This study highlights the temporal and spatial variation of DO and carbonate chemistry parameters observed during months associated with peak productivity as well as the onset and demise of hypoxia in temperate coastal habitats. Importantly, these are also periods where larval and juvenile stage fish and shellfish are vulnerable to acidification and hypoxia (Clark and Gobler, 2016; Stevens and Gobler, 2018) and are present in these habitats (Chambers and Trippel, 1997; Ishimatsu et al., 2008; Salisbury et al., 2008). While the co-occurrence of hypoxia and acidification within coastal systems has been documented, these conditions are frequently associated with deeper coastal regions that experience intense eutrophication and/or upwelling (Borges and Gypens, 2010; Feely et al., 2010; Cai et al., 2011; Wallace et al., 2014). Concurrent hypoxia and acidification in shallow water habitats that experience moderate nutrient loading is poorly understood and generally related to seasonal and diel ecosystem metabolism (Baumann and Smith, 2018; Lowe et al., 2019). This study highlights the suitability of various habitats as refuges from present and future hypoxia and acidification, as well as regions that are already inhospitable for many resource bivalves. Future efforts that seek to expand seagrass meadows and the aquaculture of macroalgae are likely to expand local refuges from hypoxia and acidification and thus maximize their ecosystem benefits.

DATA AVAILABILITY STATEMENT

The original contributions presented in the study are included in the article/**Supplementary Material**, further inquiries can be directed to the corresponding authors.

AUTHOR CONTRIBUTIONS

RW and CG designed the research methodology and wrote the manuscript. RW collected field data, performed the laboratory analysis, and processed and analyzed the data. All authors contributed to the article and approved the submitted version.

FUNDING

Funding for these experiments was obtained from the New York Sea Grant (award # R-FMB-38), the Laurie Landeau Foundation, and the Simons Foundation.

ACKNOWLEDGMENTS

We thank Ryan Anderson, Robert McCabe, Andrew Lundstrom, and Craig Schenone for research assistance during this project. We also thank the staff of the Stony Brook Southampton Marine Sciences Center for their logistical support.

SUPPLEMENTARY MATERIAL

The Supplementary Material for this article can be found online at: https://www.frontiersin.org/articles/10.3389/fmars.2021.611781/full#supplementary-material

REFERENCES

Able, K. W. (2005). A re-examination of fish estuarine dependence: evidence for connectivity between estuarine and ocean habitats. *Estuar. Coast. Shelf Sci.* 64, 5–17. doi: 10.1016/j.ecss.2005.02.002

Apinis, A., Chesters, C. G. C., and Turner, M. (1956). Studies of the decomposition of seaweeds and seaweed products by micro-organisms. *Proc. Linn. Soc. Lond.* 166, 87–97. doi: 10.1111/j.1095-8312.1956.tb00753.x

Axelsson, L., Mercado, J. M., and Figueroa, F. L. (2000). Utilization of HCO_3^- at high pH by the brown macroalga *Laminaria saccharina*. *Eur. J. Phycol.* 35, 53–59. doi: 10.1080/09670260010001735621

Axelsson, L., Ryberg, H., and Beer, S. (1995). Two modes of bicarbonate utilization in the marine green macroalga Ulva lactuca. *Plant Cell Environ.* 18, 439–445. doi: 10.1111/j.1365-3040.1995.tb00378.x

Baird, D., McGlade, J. M., and Ulanowicz, R. E. (1991). The comparative ecology of six marine ecosystems. *Philos. Trans. R. Soc. B Biol. Sci.* 333, 15–29. doi: 10.1098/rstb.1991.0058

Barbier, E. B., Hacker, S. D., Kennedy, C., Koch, E. W., Stier, A. C., and Silliman, B. R. (2010). The value of estuarine and coastal ecosystem services. *Ecol. Monogr.* 81, 169–193. doi: 10.1890/10-1510.1

Bartholoma, S. D. (2003). *User's manual for the National Water Information System of the U.S. Geological Survey: automated Data Processing System (ADAPS), Open-File Report, Version 4.3; Supercedes OFR 97-635 ed*. Virginia, United States: U.S. Geological Survey

Barton, A., Hales, B., Waldbusser, G. G., Langdon, C., and Feely, R. A. (2012). The Pacific oyster, *Crassostrea gigas*, shows negative correlation to naturally elevated carbon dioxide levels: implications for near-term ocean acidification effects. *Limnol. Oceanogr.* 57, 698–710. doi: 10.4319/lo.2012.57.3.0698

Baumann, H., and Smith, E. M. (2018). Quantifying metabolically driven pH and oxygen fluctuations in US nearshore habitats at diel to interannual time scales. *Estuaries Coasts* 41, 1102–1117. doi: 10.1007/s1223

Baumann, H., Talmage, S. C., and Gobler, C. J. (2012). Reduced early life growth and survival in a fish in direct response to increased carbon dioxide. *Nat. Clim. Chang.* 2, 38–41. doi: 10.1038/nclimate1291

Baumann, H., Wallace, R. B., Tagliaferri, T., and Gobler, C. J. (2015). Large natural pH, CO_2 and O_2 fluctuations in a temperate tidal salt marsh on diel, seasonal, and interannual time scales. *Estuaries Coasts* 38, 220–231. doi: 10.1007/s12237-014-9800-y

Beck, M. W., Hagy, J. D. III, and Murrell, M. C. (2015). Improving estimates of ecosystem metabolism by reducing effects of tidal advection on dissolved oxygen time series. *Limnol. Oceanogr. Methods* 13, 731–745.

Beck, M. W., Heck, K. L., Able, K. W., Childers, D. L., Eggleston, D. B., Gillanders, B. M., et al. (2001). The identification, conservation, and management of estuarine and marine nurseries for fish and invertebrates: a better understanding of the habitats that serve as nurseries for marine species and the factors that create site-specific variability in nursery quality will improve conservation and management of these areas. *BioScience* 51, 633–641. doi: 10.1641/0006-3568(2001)051[0633:ticamo]2.0.co;2

Beer, S., and Koch, E. (1996). Photosynthesis of marine macroalgae and seagrasses in globally changing CO_2 environments. *Mar. Ecol. Prog. Ser.* 141, 199–204. doi: 10.3354/meps141199

Bergveld, P. (2003). Thirty years of ISFETOLOGY: what happened in the past 30 years and what may happen in the next 30 years. *Sens. Actuators B Chem.* 88, 1–20. doi: 10.1016/S0925-4005(02)00301-5

Berner, R. A., Scott, M. R., and Thomlinson, C. (1970). Carbonate alkalinity in the pore waters of anoxic marine sediments. *Limnol. Oceanogr.* 15, 544–549. doi: 10.4319/lo.1970.15.4.0544

Blake, R. E., Duffy, J. E., and Richardson, J. P. (2014). Patterns of seagrass community response to local shoreline development. *Estuaries Coasts* 37, 1549–1561. doi: 10.1007/s12237-014-9784-7

Blomster, J., Back, S., Fewer, D. P., Kiirikki, M., Lehvo, A., Maggs, C. A., et al. (2002). Novel morphology in Enteromorpha (Ulvophyceae) forming green tides. *Am. J. Bot.* 89, 1756–1763. doi: 10.3732/ajb.89.11.1756

Blumberg, A. F., and Galperin, B. (1990). "On the Summer Circulation in New York Bight and Contiguous Estuarine Waters," in *Residual Currents and Long-term Transport*, ed. R. T. Cheng (New York, NY: Springer), 451–468. doi: 10.1029/ce038p0451

Borges, A. V., and Gypens, N. (2010). Carbonate chemistry in the coastal zone responds more strongly to eutrophication than ocean acidification. *Limnol. Oceanogr.* 55, 346–353. doi: 10.4319/lo.2010.55.1.0346

Borges, A. V., Ruddick, K., Schiettecatte, L.-S., and Delille, B. (2008). Net ecosystem production and carbon dioxide fluxes in the Scheldt estuarine plume. *BMC Ecol.* 8:15. doi: 10.1186/1472-6785-8-15

Burnett, L. E. (1997). The challenges of living in hypoxic and hypercapnic aquatic environments. *Am. Zool.* 37, 633–640. doi: 10.1093/icb/37.6.633

Caffrey, J. M. (2004). Factors controlling net ecosystem metabolism in U.S. estuaries. *Estuaries* 27, 90–101. doi: 10.1007/BF02803563

Caffrey, J. M., and Kemp, W. M. (1991). Seasonal and spatial patterns of oxygen production, respiration and root-rhizome release in *Potamogeton perfoliatus* L. and *Zostera marina* L. *Aquat. Bot.* 40, 109–128. doi: 10.1016/0304-3770(91)90090-R

Cai, W.-J. (2011). Estuarine and Coastal Ocean Carbon Paradox: CO_2 Sinks or Sites of Terrestrial Carbon Incineration? *Ann. Rev. Mar. Sci.* 3, 123–145. doi: 10.1146/annurev-marine-120709-142723

Cai, W.-J., Hu, X., Huang, W.-J., Murrell, M. C., Lehrter, J. C., Lohrenz, S. E., et al. (2011). Acidification of subsurface coastal waters enhanced by eutrophication. *Nat. Geosci.* 4, 766–770. doi: 10.1038/ngeo1297

Camp, E. F., Suggett, D. J., Gendron, G., Jompa, J., Manfrino, C., and Smith, D. J. (2016). Mangrove and seagrass beds provide different biogeochemical services for corals threatened by climate change. *Front. Mar. Sci.* 3:52. doi: 10.3389/fmars.2016.00052

Carlson, P., Peterson, B., Dennison, W., Heck, K. L., Fonseca, M., Pickerell, C., et al. (2009). *Final Report of the New York State Seagrass Task Force: recommendations to the New York State Governor and Legislature*. New York, NY: New York Department of State.

Chambers, R. C., and Trippel, E. (1997). *Early Life History and Recruitment in Fish Populations*. Netherlands: Springer.

Chopin, T., Buschmann, A. H., Halling, C., Troell, M., Kautsky, N., Neori, A., et al. (2001). Integrating seaweeds into marine aquaculture systems: a key toward sustainability. *J. Phycol.* 37, 975–986. doi: 10.1046/j.1529-8817.2001.01137.x

Chu, S. N., Wang, Z. A., Gonneea, M. E., Kroeger, K. D., and Ganju, N. K. (2018). Deciphering the dynamics of inorganic carbon export from intertidal salt marshes using high-frequency measurements. *Mar. Chem.* 206, 7–18. doi: 10.1016/j.marchem.2018.08.005

Chung, I. K., Beardall, J., Mehta, S., Sahoo, D., and Stojkovic, S. (2011). Using marine macroalgae for carbon sequestration: a critical appraisal. *J. Appl. Phycol.* 23, 877–886. doi: 10.1007/s10811-010-9604-9

Churchill, A. C., and Riner, M. I. (1978). Anthesis and seed production in *Zostera marina* L. from Great South Bay, New York, U.S.A. *Aquat. Bot.* 4, 83–93. doi: 10.1016/0304-3770(78)90009-8

Clark, H. R., and Gobler, C. J. (2016). Diurnal fluctuations in CO_{-2} and dissolved oxygen concentrations do not provide a refuge from hypoxia and acidification for early-life-stage bivalves. *Mar. Ecol. Prog. Ser.* 558, 1–14. doi: 10.3354/meps11852

Clements, J. C., and Chopin, T. (2017). Ocean acidification and marine aquaculture in North America: potential impacts and mitigation strategies. *Rev. Aquac.* 9, 326–341. doi: 10.1111/raq.12140

Cloern, J. E., Foster, S. Q., and Kleckner, A. E. (2014). Phytoplankton primary production in the world's estuarine-coastal ecosystems. *Biogeosciences* 11, 2477–2501. doi: 10.5194/bg-11-2477-2014

Curran, P. J. (1988). The semivariogram in remote sensing: an introduction. *Remote Sens. Environ.* 24, 493–507. doi: 10.1016/0034-4257(88)90021-1

Cyronak, T., Andersson, A. J., D'Angelo, S., Bresnahan, P., Davidson, C., Griffin, A., et al. (2018). Short-Term Spatial and Temporal Carbonate Chemistry Variability in Two Contrasting Seagrass Meadows: implications for pH Buffering Capacities. *Estuaries Coasts* 41, 1282–1296. doi: 10.1007/s12237-017-0356-5

D'Avanzo, C., Kremer, J. N., and Wainright, S. C. (1996). Ecosystem production and respiration in response to eutrophication in shallow temperate estuaries. *Mar. Ecol. Prog. Ser.* 141, 263–274. doi: 10.3354/meps141263

Dennison, W. C. (2009). Seagrasses: biology, ecology and conservation. *Botanica Marina* 52, 365–366. doi: 10.1515/BOT.2009.009

Dennison, W. C., Orth, R. J., Moore, K. A., Stevenson, J. C., Carter, V., Kollar, S., et al. (1993). Assessing Water Quality with Submersed Aquatic Vegetation:

habitat requirements as barometers of Chesapeake Bay health. *BioScience* 43, 86–94. doi: 10.2307/1311969

Dickson, A. G. (1990). Standard potential of the reaction: AgCl(s) + 12H2(g) = Ag(s) + HCl(aq), and and the standard acidity constant of the ion HSO4- in synthetic sea water from 273.15 to 318.15 K. *J. Chem. Thermodyn.* 22, 113–127. doi: 10.1016/0021-9614(90)90074-z

Dickson, A. G., and Riley, J. P. (1979). The estimation of acid dissociation constants in sea-water media from potentiometric titrations with strong base. II. The dissociation of phosphoric acid. *Mar. Chem.* 7, 101–109. doi: 10.1016/0304-4203(79)90002-1

Duarte, C. M., Hendriks, I. E., Moore, T. S., Olsen, Y. S., Steckbauer, A., Ramajo, L., et al. (2013). Is ocean acidification an open-ocean syndrome? Understanding anthropogenic impacts on seawater pH. *Estuaries Coasts* 36, 221–236. doi: 10.1007/s12237-013-9594-3

Duarte, C. M., Marbà, N., Gacia, E., Fourqurean, J. W., Beggins, J., Barrón, C., et al. (2010). Seagrass community metabolism: assessing the carbon sink capacity of seagrass meadows. *Global Biogeochem. Cycles* 24:8. doi: 10.1029/2010GB003793

Duarte, C. M., Middelburg, J. J., and Caraco, N. (2005). Major role of marine vegetation on the oceanic carbon cycle. *Biogeosciences* 2, 1–8. doi: 10.5194/bg-2-1-2005

Duffy, J. E. (2006). Biodiversity and the functioning of seagrass ecosystems. *Mar. Ecol. Prog. Ser.* 311, 233–250. doi: 10.3354/meps311233

Egleston, E. S., Sabine, C. L., and Morel, F. M. M. (2010). Revelle revisited: buffer factors that quantify the response of ocean chemistry to changes in DIC and alkalinity. *Global Biogeochem. Cycles* 24:GB1002. doi: 10.1029/2008GB003407

Feely, R. A., Alin, S. R., Newton, J., Sabine, C. L., Warner, M., Devol, A., et al. (2010). The combined effects of ocean acidification, mixing, and respiration on pH and carbonate saturation in an urbanized estuary. *Estuar. Coast. Shelf Sci.* 88, 442–449. doi: 10.1016/j.ecss.2010.05.004

Feely, R. A., Okazaki, R. R., Cai, W.-J., Bednaršek, N., Alin, S. R., Byrne, R. H., et al. (2018). The combined effects of acidification and hypoxia on pH and aragonite saturation in the coastal waters of the California current ecosystem and the northern Gulf of Mexico. *Cont. Shelf Res.* 152, 50–60. doi: 10.1016/j.csr.2017.11.002

Fiedler, B., Fietzek, P., Vieira, N., Silva, P., Bittig, H. C., and Körtzinger, A. (2012). *In situ* CO_2 and O_2 measurements on a profiling float. *J. Atmos. Ocean. Technol.* 30, 112–126. doi: 10.1175/JTECH-D-12-00043.1

Fields, P. A., Eurich, C., Gao, W. L., and Cela, B. (2014). Changes in protein expression in the salt marsh mussel *Geukensia demissa*: evidence for a shift from anaerobic to aerobic metabolism during prolonged aerial exposure. *J. Exp. Biol.* 217, 1601–1612. doi: 10.1242/jeb.101758

Fietzek, P., Fielder, B., Steinhoff, T., and Körtzinger, A. (2014). In situ quality assessment of a novel underwater pCO_2 sensor based on membrane equilibration and NDIR spectrometry. *J. Atmos. Ocean. Technol.* 31, 181–196. doi: 10.1175/JTECH-D-13-00083.1

Fischer, H. B., List, J. E., Koh, C. R., Imberger, J., and Brooks, N. H. (2013). *Mixing in inland and coastal waters*. Cambridge, Massachusetts: Academic Press.

Gardner, L. R., and Gorman, C. (1984). The summertime net transport of dissolved oxygen, salt and heat in a salt marsh basin, North Inlet, S.C. *Estuar. Coast. Shelf Sci.* 19, 331–339. doi: 10.1016/0272-7714(84)90029-5

Gattuso, J.-P., Frankignoulle, M., and Wollast, R. (1998). Carbon and carbonate metabolism in coastal aquatic ecosystems. *Annu. Rev. Ecol. Syst.* 29, 405–434. doi: 10.1146/annurev.ecolsys.29.1.405

George, J. A., Lonsdale, D., Merlo, L. R., and Gobler, C. J. (2015). The interactive roles of temperature, nutrients, and zooplankton grazing in controlling the winter–spring phytoplankton bloom in a temperate, coastal ecosystem, Long Island Sound. *Limnol. Oceanogr.* 60, 110–126. doi: 10.1002/lno.10020

Gleason, D. F., Zimmerman, R. J., and Minello, T. J. (1982). Carbon-sources for Penaeid shrimp in a salt-marsh. *Am. Zool.* 22:964.

Gobler, C. J., and Baumann, H. (2016). Hypoxia and acidification in ocean ecosystems: coupled dynamics and effects on marine life. *Biol. Lett.* 12:20150976. doi: 10.1098/rsbl.2015.0976

Gobler, C. J., Clark, H. R., Griffith, A. W., and Lusty, M. W. (2017). Diurnal fluctuations in acidification and hypoxia reduce growth and survival of larval and juvenile bay scallops (*Argopecten irradians*) and hard clams (*Mercenaria mercenaria*). *Front. Mar. Sci.* 3:282. doi: 10.3389/fmars.2016.00282

Gobler, C. J., DePasquale, E. L., Griffith, A. W., and Baumann, H. (2014). Hypoxia and acidification have additive and synergistic negative effects on the growth, survival, and metamorphosis of early life stage bivalves. *PLoS One* 9:e83648. doi: 10.1371/journal.pone.0083648

Gobler, C. J., and Talmage, S. C. (2013). Short- and long-term consequences of larval stage exposure to constantly and ephemerally elevated carbon dioxide for marine bivalve populations. *Biogeosciences* 10, 2241–2253. doi: 10.5194/bg-10-2241-2013

Grear, J. S., O'Leary, C. A., Nye, J. A., Tettelbach, S. T., and Gobler, C. J. (2020). Effects of coastal acidification on North Atlantic bivalves: interpreting laboratory responses in the context of in situ populations. *Mar. Ecol. Prog. Ser.* 633, 89–104. doi: 10.3354/meps13140

Gribov, A., and Krivoruchko, K. (2011). Local polynomials for data detrending and interpolation in the presence of barriers. *Stoch. Environ. Res. Risk Assess.* 25, 1057–1063. doi: 10.1007/s00477-011-0488-2

Hagens, M., Slomp, C., Meysman, F., Seitaj, D., Jerome, H., Borges, A., et al. (2015). Biogeochemical processes and buffering capacity concurrently affect acidification in a seasonally hypoxic coastal marine basin. *Biogeosciences* 12, 1561–1583. doi: 10.5194/bg-12-1561-2015

Haley, B. A., Hales, B., Brunner, E. L., Kovalchik, K., and Waldbusser, G. G. (2018). Mechanisms to Explain the Elemental Composition of the Initial Aragonite Shell of Larval Oysters. *Geochem. Geophys. Geosyst.* 19, 1064–1079. doi: 10.1002/2017gc007133

Han, Q., and Liu, D. (2014). Macroalgae blooms and their effects on seagrass ecosystems. *J. Ocean Univ. China* 13, 791–798. doi: 10.1007/s11802-014-2471-2

Hardy, C. D. (1976). *A preliminary description of the Peconic Bay estuary*. University, NY: Stony Brook, Marine Sciences Research Center.

Heck, K. L., Hays, G., and Orth, R. J. (2003). Critical evaluation of the nursery role hypothesis for seagrass meadows. *Mar. Ecol. Prog. Ser.* 253, 123–136. doi: 10.3354/meps253123

Hendriks, I. E., Olsen, Y. S., Ramajo, L., Basso, L., Steckbauer, A., Moore, T. S., et al. (2014). Photosynthetic activity buffers ocean acidification in seagrass meadows. *Biogeosciences* 11, 333–346. doi: 10.5194/bgd-10-12313-2013

Hofmann, G. E., Smith, J. E., Johnson, K. S., Send, U., Levin, L. A., Micheli, F., et al. (2011). High-frequency dynamics of ocean pH: a multi-ecosystem comparison. *PLoS One* 6:e28983. doi: 10.1371/journal.pone.0028983

Howland, R. J. M., Tappin, A. D., Uncles, R. J., Plummer, D. H., and Bloomer, N. J. (2000). Distributions and seasonal variability of pH and alkalinity in the Tweed Estuary, UK. *Sci. Total Environ.* 251-252, 125–138. doi: 10.1016/S0048-9697(00)00406-X

Hu, X., and Cai, W.-J. (2011). An assessment of ocean margin anaerobic processes on oceanic alkalinity budget. *Global Biogeochem. Cycles* 25:GB3003. doi: 10.1029/2010GB003859

Iriarte, A., Madariaga, I., Diez-Garagarza, F., Revilla, M., and Orive, E. (1997). Primary plankton production, respiration and nitrification in a shallow temperate estuary during summer. *J. Exp. Mar. Biol. Ecol.* 208, 127–151. doi: 10.1016/S0022-0981(96)02672-X

Ishimatsu, A., Hayashi, M., and Kikkawa, T. (2008). Fishes in high-CO_2, acidified oceans. *Mar. Ecol. Prog. Ser.* 373, 295–302. doi: 10.3354/meps07823

Jackson, G. A. (1987). Modelling the growth and harvest yield of the giant kelp *Macrocystis pyrifera*. *Mar. Biol.* 95, 611–624. doi: 10.1007/BF00393105

Johnson, D. A., and Welsh, B. L. (1985). Detrimental effects of *Ulva lactuca* (L.) exudates and low oxygen on estuarine crab larvae. *J. Exp. Mar. Biol. Ecol.* 86, 73–83. doi: 10.1016/0022-0981(85)90043-7

Jost, J., and Helmuth, B. (2007). Morphological and ecological determinants of body temperature of *Geukensia demissa*, the Atlantic ribbed mussel, and their effects on mussel mortality. *Biol. Bull.* 213, 141–151. doi: 10.2307/25066630

Kim, J. K., Kraemer, G. P., and Yarish, C. (2015). Use of sugar kelp aquaculture in Long Island Sound and the Bronx River Estuary for nutrient extraction. *Mar. Ecol. Prog. Ser.* 531, 155–166. doi: 10.3354/meps11331

Krause-Jensen, D., Lavery, P., Serrano, O., Marbà, N., Masque, P., and Duarte, C. M. (2018). Sequestration of macroalgal carbon: the elephant in the Blue Carbon room. *Biol. Lett.* 14:20180236. doi: 10.1098/rsbl.2018.0236

Krivoruchko, K., and Gribov, A. (2004). "Geostatistical Interpolation and Simulation in the Presence of Barriers," in *geoENV IV — Geostatistics for Environmental Applications. Quantitative Geology and Geostatistics*, eds X. Sanchez-Vila, J. Carrera, and J. J. Gómez-Hernández (Dordrecht: Springer).

Langley, J. A., McKee, K. L., Cahoon, D. R., Cherry, J. A., and Megonigal, J. P. (2009). Elevated CO_2 stimulates marsh elevation gain, counterbalancing

sea-level rise. *Proc. Natl. Acad. Sci. U. S. A.* 106, 6182–6186. doi: 10.1073/pnas.0807695106

Lee, K., Kim, T.-W., Byrne, R. H., Millero, F. J., Feely, R. A., and Liu, Y.-M. (2010). The universal ratio of boron to chlorinity for the North Pacific and North Atlantic oceans. *Geochim. Cosmochim. Acta* 74, 1801–1811. doi: 10.1016/j.gca.2009.12.027

Lee, K., Tong, L. T., Millero, F. J., Sabine, C. L., Dickson, A. G., Goyet, C., et al. (2006). Global relationships of total alkalinity with salinity and temperature in surface waters of the world's oceans. *Geophys. Res. Lett.* 33:LI9605. doi: 10.1029/2006GL027207

Lenzi, M. (2014). What can be Done about Massive Macroalgal Blooms? *J. Aquac. Res. Dev.* 5:292. doi: 10.4172/2155-9546.1000292

Liu, D., Keesing, J. K., Xing, Q., and Shi, P. (2009). World's largest macroalgal bloom caused by expansion of seaweed aquaculture in China. *Mar. Pollut. Bull.* 58, 888–895. doi: 10.1016/j.marpolbul.2009.01.013

Liu, F., Pang, S. J., Xu, N., Shan, T. F., Sun, S., Hu, X., et al. (2010). *Ulva* diversity in the Yellow Sea during the large-scale green algal blooms in 2008–2009. *Physiol. Res.* 58, 270–279. doi: 10.1111/j.1440-1835.2010.00586.x

Liu, S., Jiang, Z., Deng, Y., Wu, Y., Zhao, C., Zhang, J., et al. (2017). Effects of seagrass leaf litter decomposition on sediment organic carbon composition and the key transformation processes. *Sci. China Earth Sci.* 60, 2108–2117. doi: 10.1007/s11430-017-9147-4

Lowe, A. T., Bos, J., and Ruesink, J. (2019). Ecosystem metabolism drives pH variability and modulates long-term ocean acidification in the Northeast Pacific coastal ocean. *Sci. Rep.* 9:963. doi: 10.1038/s41598-018-37764-4

Madden, C. J., and Day, J. W. (1992). An instrument system for high-speed mapping of chlorophyll a and physico-chemical variables in surface waters. *Estuaries* 15, 421–427. doi: 10.2307/1352789

Magre, E. J. (1974). *Ulva lactuca* L. negatively affects *Balanus balanoides* (L.) (*Cirripedia Thoracica*) in tidepools. *Crustaceana* 27, 231–234. doi: 10.1163/156854074X00758

Maher, D. T., and Eyre, B. D. (2012). Carbon budgets for three autotrophic Australian estuaries: implications for global estimates of the coastal air-water CO2 flux. *Global Biogeochem. Cycle* 26:GB1032.

Mangi, S. C., Lee, J., Pinnegar, J. K., Law, R. J., Tyllianakis, E., and Birchenough, S. N. R. (2018). The economic impacts of ocean acidification on shellfish fisheries and aquaculture in the United Kingdom. *Environ. Sci. Policy* 86, 95–105. doi: 10.1016/j.envsci.2018.05.008

Martz, T. R., Connery, J. G., and Johnson, K. S. (2010). Testing the Honeywell Durafet® for seawater pH applications. *Limnol. Oceanogr. Methods* 8, 172–184. doi: 10.4319/lom.2010.8.172

Mateo, M. A., and Romero, J. (1996). Evaluating seagrass leaf litter decomposition: an experimental comparison between litter-bag and oxygen-uptake methods. *J. Exp. Mar. Biol. Ecol.* 202, 97–106. doi: 10.1016/0022-0981(96)00019-6

Menéndez, M., Martínez, M., and Comín, F. A. (2001). A comparative study of the effect of pH and inorganic carbon resources on the photosynthesis of three floating macroalgae species of a Mediterranean coastal lagoon. *J. Exp. Mar. Biol. Ecol.* 256, 123–136. doi: 10.1016/S0022-0981(00)00313-0

Ménesguen, A., and Piriou, J.-Y. (1995). Nitrogen loadings and macroalgal (*Ulva* sp.) Mass Accumulation in Brittany (France). *Ophelia* 42, 227–237. doi: 10.1080/00785326.1995.10431506

Middelboe, A. L., and Hansen, P. J. (2007a). Direct effects of pH and inorganic carbon on macroalgal photosynthesis and growth. *Mar. Biol. Res.* 3, 134–144. doi: 10.1080/17451000701320556

Middelboe, A. L., and Hansen, P. J. (2007b). High pH in shallow-water macroalgal habitats. *Mar. Ecol. Prog. Ser.* 338, 107–117. doi: 10.3354/meps338107

Millero, F. J. (2010). Carbonate constants for estuarine waters. *Mar. Freshw. Res.* 61, 139–142. doi: 10.1071/mf09254

Morris, A. W., and Riley, J. P. (1966). The bromide/chlorinity and sulphate/chlorinity ratio in sea water. *Deep Sea Res. Oceanogr. Abstr.* 13, 699–705. doi: 10.1016/0011-7471(66)90601-2

Najjar, R. G., Herrmann, M., Alexander, R., Boyer, E. W., Burdige, D. J., Butman, D., et al. (2018). Carbon budget of tidal wetlands, estuaries, and shelf waters of eastern North America. *Global Biogeochem. Cycles* 32, 389–416. doi: 10.1002/2017GB005790

Nejrup, L. B., Staehr, P. A., and Thomsen, M. S. (2013). Temperature- and light-dependent growth and metabolism of the invasive red algae *Gracilaria vermiculophylla* – a comparison with two native macroalgae. *Eur. J. Phycol.* 48, 295–308. doi: 10.1080/09670262.2013.830778

Neori, A. (2009). Essential role of seaweed cultivation in integrated multi-trophic aquaculture farms for global expansion of mariculture: an analysis. *J. Appl. Phycol.* 20, 567–570. doi: 10.1007/s10811-007-9206-3

Nixon, S. W., and Oviatt, C. A. (1973). Ecology of a New England salt marsh. *Ecol. Monogr.* 43, 463–498. doi: 10.2307/1942303

NYSDEC (2015). *State Wildlife Action Plan (SWAP) An Approach to Conserve At-Risk Fish and Wildlife Species*. Albany, NY: New York Department of State.

O'Boyle, S., McDermott, G., Noklegaard, T., and Wilkes, R. (2013). A Simple Index of Trophic Status in Estuaries and Coastal Bays Based on Measurements of pH and Dissolved Oxygen. *Estuaries Coasts* 36, 158–173. doi: 10.1007/s12237-012-9553-4

Odum, W. E. (1971). *Pathways of energy flow in a south Florida estuary*. Bloomington: Indiana University, University of Miami Sea Grant Program.

Olesen, B., and Sand-Jensen, K. (1994). Biomass-density patterns in the temperate seagrass *Zostera marina*. *Mar. Ecol. Prog. Ser.* 109, 283–291. doi: 10.3354/meps109283

Orr, J. C., Fabry, V. J., Aumont, O., Bopp, L., Doney, S. C., Feely, R. A., et al. (2005). Anthropogenic ocean acidification over the twenty-first century and its impact on calcifying organisms. *Nature* 437, 681–686. doi: 10.1038/nature04095

Orth, R. J., Carruthers, T. J. B., Dennison, W. C., Duarte, C. M., Fourqurean, J. W., Heck, K. L., et al. (2006).). A global crisis for seagrass ecosystems. *BioScience* 56, 987–996.

Pacella, S. R., Brown, C. A., Waldbusser, G. G., Labiosa, R. G., and Hales, B. (2018). Seagrass habitat metabolism increases short-term extremes and long-term offset of CO_2 under future ocean acidification. *Proc. Natl. Acad. Sci. U. S. A.* 115, 3870–3875. doi: 10.1073/pnas.1703445115

Pachauri, R. K., Allen, M., Barros, V., Broome, J., Cramer, W., Christ, R., et al. (2014). "Climate Change 2014," in *Synthesis Report. Contribution of Working Groups I, II and III to the Fifth Assessment Report of the Intergovernmental Panel on Climate Change*. eds R. Pachauri and L. Meyer (Geneva, Switzerland: IPCC).

Pimenta, A. R., and Grear, J. (2018). *Guidelines for Measuring Changes in Seawater pH and Associated Carbonate Chemistry in Coastal Environments of the Eastern United States*. Washington, D.C: U.S. EPA Office of Research and Development

Rautenberger, R., Fernández, P. A., Strittmatter, M., Heesch, S., Cornwall, C. E., Hurd, C. L., et al. (2015). Saturating light and not increased carbon dioxide under ocean acidification drives photosynthesis and growth in *Ulva rigida*. *Planta* 5, 874–888. doi: 10.1002/ece3.1382

Revelle, R., and Suess, H. E. (1957). Carbon Dioxide Exchange Between Atmosphere and Ocean and the Question of an Increase of Atmospheric CO2 during the Past Decades. *Tellus* 9, 18–27. doi: 10.3402/tellusa.v9i1.9075

Riche, O., Johannessen, S. C., and Macdonald, R. W. (2014). Why timing matters in a coastal sea: trends, variability and tipping points in the Strait of Georgia, Canada. *J. Mar. Syst.* 131, 36–53. doi: 10.1016/j.jmarsys.2013.11.003

Riley, G. A., and Conover, S. M. (1967). Phytoplankton of Long Island Sound 1954-1955. *Bull. Bingham Oceanogr. Collection* 19, 5–34.

Riley, J. P. (1965). The occurrence of anomalously high fluoride concentrations in the North Atlantic. *Deep Sea Res. Oceanogr. Abstr.* 12, 219–220. doi: 10.1016/0011-7471(65)90027-6

Ro, K. S., Hunt, P. G., and Poach, M. E. (2007). Wind-Driven Surficial Oxygen Transfer. *Crit. Rev. Environ. Sci. Technol.* 37, 539–563. doi: 10.1080/10934520600754714

Roman, C. T., Jaworski, N., Short, F. T., Findlay, S., and Warren, R. S. (2000). Estuaries of the northeastern United States: habitat and land use signatures. *Estuaries* 23, 743–764. doi: 10.2307/1352997

Rosenau, N. A., Galavotti, H., Yates, K. K., Bohlen, C. C., Hunt, C. W., Liebman, M., et al. (2021). Integrating High-Resolution Coastal Acidification Monitoring Data Across Seven United States Estuaries. *Front. Mar. Sci.* 8:679913. doi: 10.3389/fmars.2021.679913

Saderne, V., Fietzek, P., Aßmann, S., Körtzinger, A., and Hiebenthal, C. (2015). Seagrass beds as ocean acidification refuges for mussels? High resolution measurements of pCO_2 and O_2 in a *Zostera marina* and *Mytilus edulis* mosaic habitat. *Biogeosci. Discuss.* 12, 11423–11461. doi: 10.5194/bgd-12-11423-2015

Salisbury, J., Green, M., Hunt, C., and Campbell, J. (2008). Coastal acidification by rivers: a new threat to shellfish? *Eos* 89:513. doi: 10.1029/2008EO500001

Sand-Jensen, K., and Borum, J. (1983). Regulation of growth of eelgrass (*Zostera marina* L.) in Danish coastal waters. *Mar. Technol. Soc. J.* 17, 15–21.

Sharp, J. H. (1974). Improved analysis for particulate organic carbon and nitrogen from seawater. *Limnol. Oceanogr.* 19, 984–989. doi: 10.4319/lo.1974.19.6.0984

Short, F. T., Koch, E. W., Creed, J. C., Magalhães, K. M., Fernandez, E., and Gaeckle, J. L. (2006). SeagrassNet monitoring across the Americas: case studies of seagrass decline. *Mar. Ecol.* 27, 277–289. doi: 10.1111/j.1439-0485.2006.00095.x

Smetacek, V., and Zingone, A. (2013). Green and golden seaweed tides on the rise. *Nature* 504, 84–88. doi: 10.1038/nature12860

Smith, S. V. (1981). Marine Macrophytes as a Global Carbon Sink. *Science* 211, 838–840. doi: 10.1126/science.211.4484.838

Smith, S. V., and Mackenzie, F. T. (1987). The ocean as a net heterotrophic system: implications From the carbon biogeochemical cycle. *Global Biogeochem. Cycles* 1, 187–198. doi: 10.1029/GB001i003p00187

Sogard, S. M., and Able, K. W. (1991). A comparison of eelgrass, sea lettuce macroalgae, and marsh creeks as habitats for epibentic fishes and decapods. *Estuar. Coast. Shelf Sci.* 33, 501–519. doi: 10.1016/0272-7714(91)90087-R

Stevens, A. M., and Gobler, C. J. (2018). Interactive effects of acidification, hypoxia, and thermal stress on growth, respiration, and survival of four North Atlantic bivalves. *Mar. Ecol. Prog. Ser.* 604, 143–161. doi: 10.3354/meps12725

Suchanek, T. H., Williams, S. L., Ogden, J. C., Hubbard, D. K., and Gill, I. P. (1985). Utilization of shallow-water seagrass detritus by Carribbean deep-sea macrofauna: $\delta^{13}C$ evidence. *Deep Sea Res. A Oceanogr. Res. Pap.* 32, 201–214. doi: 10.1016/0198-0149(85)90028-7

Sundbäck, K., and McGlathery, K. (2013). "Interactions Between Benthic Macroalgal and Microalgal Mats," in *Interactions Between Macro- and Microorganisms in Marine Sediments, Coastal and Estuarine Studies*, eds E. Kristensen, R. R. Haese, and J. E. Kostka (Washington, DC: American Geophysical Union), 7–29. doi: 10.1029/ce060p0007

Sutton, A. J., Feely, R. A., Maenner-Jones, S., Musielwicz, S., Osborne, J., Dietrich, C., et al. (2019). Autonomous Seawater pCO_2 and pH Time Series From 40 Surface Buoys and the Emergence of Anthropogenic Trends. *Earth Syst. Sci. Data* 11, 421–439. doi: 10.5194/essd-11-421-2019

Tait, L. W., and Schiel, D. R. (2013). Impacts of Temperature on Primary Productivity and Respiration in Naturally Structured Macroalgal Assemblages. *PLoS One* 8:e74413. doi: 10.1371/journal.pone.0074413

Talmage, S. C., and Gobler, C. J. (2010). Effects of past, present, and future ocean carbon dioxide concentrations on the growth and survival of larval shellfish. *Proc. Nat. Acad. Sci. U. S. A.* 107, 17246–17251. doi: 10.1073/pnas.0913804107

Tettelbach, S. T., Peterson, B. J., Carroll, J. C., Hughes, S. W. T., Bonal, D. M., Weinstock, A., et al. (2013). Priming the larval pump: resurgence of bay scallop recruitment following initiation of intensive restoration efforts. *Mar. Ecol. Prog. Ser.* 478, 153–172. doi: 10.3354/meps10111

Tomasetti, S. J., and Gobler, C. J. (2020). Dissolved oxygen and pH criteria leave fisheries at risk. *Science* 368, 372–373. doi: 10.1126/science.aba4896

Turner, R. E. (1978). Community plankton respiration in a salt marsh estuary and the importance of macrophytic leachates. *Limnol. Oceanogr.* 23, 442–451. doi: 10.4319/lo.1978.23.3.0442

Unsworth, R. K. F., Collier, C. J., Henderson, G. M., and McKenzie, L. J. (2012). Tropical seagrass meadows modify seawater carbon chemistry: implications for coral reefs impacted by ocean acidification. *Environ. Res. Lett.* 7:024026. doi: 10.1088/1748-9326/7/2/024026

Uusitalo, J. (1996). Uusitalo, Jarmo. "Algal carbon uptake and the difference between alkalinity and high pH ("alkalinization"), exemplified with a pH-drift experiment. *Sci. Mar.* 60, 129–134.

Valiela, I. (2006). *Global Coastal Change*. Malden, MA: Wiley-Blackwell.

Valiela, I., Foreman, K., LaMontagne, M., Hersh, D., Costa, J., Peckol, P., et al. (1992). Couplings of watersheds and coastal waters: sources and consequences of nutrient enrichment in Waquoit Bay. Massachusetts. *Estuaries* 15, 443–457. doi: 10.2307/1352389

Van Dam, B. R., Lopes, C., Osburn, C. L., and Fourqurean, J. W. (2019). Net heterotrophy and carbonate dissolution in two subtropical seagrass meadows. *Biogeosciences* 16, 4411–4428.

Wagner, R. J., Boulger, R. W. Jr., Oblinger, C. J., and Smith, B. A. (2006). *Guidelines and Standard Procedures for Continuous Water-Quality Monitors: station Operation, Record Computation, and Data Reporting*. Reston, VA: U.S. Geological Survey, 51.

Wallace, R. B., Baumann, H., Grear, J. S., Aller, R. C., and Gobler, C. J. (2014). Coastal ocean acidification: the other eutrophication problem. *Estuar. Coast. Shelf Sci.* 148, 1–13. doi: 10.1016/j.ecss.2014.05.027

Wallace, R. B., and Gobler, C. J. (2015). Factors controlling blooms of microalgae and macroalgae (*Ulva rigida*) in a eutrophic, urban estuary: jamaica Bay, NY, USA. *Estuaries Coasts* 38, 519–533. doi: 10.1007/s12237-014-9818-1

Wang, S. R., Iorio, D. D., Cai, W.-J., and Hopkinson, C. S. (2018). Inorganic carbon and oxygen dynamics in a marsh-dominated estuary. *Limnol. Oceanogr.* 63, 47–71. doi: 10.1002/lno.10614

Wang, Z. A., and Cai, W.-J. (2004). Carbon dioxide degassing and inorganic carbon export from a marsh-dominated estuary (the Duplin River): a marsh CO_2 pump. *Limnol. Oceanogr.* 49, 341–354. doi: 10.4319/lo.2004.49.2.0341

Wang, Z. A., Kroeger, K. D., Ganju, N. K., Gonneea, M. E., and Chu, S. N. (2016). Intertidal salt marshes as an important source of inorganic carbon to the coastal ocean. *Limnol. Oceanogr.* 61, 1916–1931. doi: 10.1002/lno.10347

Wang, Z. A., Sonnichsen, F. N., Bradley, A. M., Hoering, K. A., Lanagan, T. M., Chu, S. N., et al. (2015). An In-situ Sensor Technology for Simultaneous Spectrophotometric Measurements of Seawater Total Dissolved Inorganic Carbon and pH. *Environ. Sci. Technol.* 49, 4441–4449. doi: 10.1021/es504893n

Wanninkhof, R. (1992). Relationship between wind speed and gas exchange over the ocean. *J. Geophys. Res. Oceans* 97, 7373–7382. doi: 10.1029/92jc00188

Weiss, R. F. (1974). Carbon dioxide in water and seawater: the solubility of a non-ideal gas. *Mar. Chem.* 2, 203–215. doi: 10.1016/0304-4203(74)90015-2

Weiss, R. F., and Price, B. A. (1980). Nitrous oxide solubility in water and seawater. *Mar. Chem.* 8, 347–359.

Wootton, J. T., Pfister, C. A., and Forester, J. D. (2008). Dynamic patterns and ecological impacts of declining ocean pH in a high-resolution multi-year dataset. *Proc. Natl. Acad. Sci. U. S. A.* 105, 18848–18853. doi: 10.1073/pnas.0810079105

Ye, N. H., Zhang, X. W., Mao, Y. Z., Liang, C. W., Xu, D., Zou, J., et al. (2011). 'Green tides' are overwhelming the coastline of our blue planet: taking the world's largest example. *Ecol. Res.* 26, 477–485. doi: 10.1007/s11284-011-0821-8

Young, C. S., and Gobler, C. J. (2018). The ability of macroalgae to mitigate the negative effects of ocean acidification on four species of North Atlantic bivalve. *Biogeosciences* 15, 6167–6183. doi: 10.5194/bg-15-6167-2018

Conflict of Interest: The authors declare that the research was conducted in the absence of any commercial or financial relationships that could be construed as a potential conflict of interest.

Publisher's Note: All claims expressed in this article are solely those of the authors and do not necessarily represent those of their affiliated organizations, or those of the publisher, the editors and the reviewers. Any product that may be evaluated in this article, or claim that may be made by its manufacturer, is not guaranteed or endorsed by the publisher.

Copyright © 2021 Wallace, Peterson and Gobler. This is an open-access article distributed under the terms of the Creative Commons Attribution License (CC BY). The use, distribution or reproduction in other forums is permitted, provided the original author(s) and the copyright owner(s) are credited and that the original publication in this journal is cited, in accordance with accepted academic practice. No use, distribution or reproduction is permitted which does not comply with these terms.

frontiers in Marine Science

ORIGINAL RESEARCH
published: 18 March 2021
doi: 10.3389/fmars.2021.604330

Early Diagenesis in the Hypoxic and Acidified Zone of the Northern Gulf of Mexico: Is Organic Matter Recycling in Sediments Disconnected From the Water Column?

Christophe Rabouille[1]†, Bruno Lansard[1], Shannon M. Owings[2], Nancy N. Rabalais[3], Bruno Bombled[1], Edouard Metzger[4], Julien Richirt[4], Eryn M. Eitel[2], Anthony D. Boever[2], Jordon S. Beckler[5] and Martial Taillefert[2]*

[1] Laboratoire des Sciences du Climat et de l'Environnement, UMR 8212 CEA-CNRS-UVSQ, CEA-Orme des Merisiers, IPSL and Université Paris-Saclay, Gif-sur-Yvette, France, [2] School of Earth and Atmospheric Sciences, Georgia Institute of Technology, Atlanta, GA, United States, [3] Department of Oceanography and Coastal Sciences, Louisiana State University, Baton Rouge, LA, United States, [4] LPG-BIAF, UMR 6112 CNRS, Université d'Angers, Angers, France, [5] Harbor Branch Oceanographic Institute, Florida Atlantic University, Boca Raton, FL, United States

OPEN ACCESS

Edited by:
Arnaud Laurent,
Dalhousie University, Canada

Reviewed by:
Mathilde Hagens,
Wageningen University and Research, Netherlands
Gerdhard L. Jessen,
Universidad Austral de Chile, Chile

***Correspondence:**
Christophe Rabouille
rabouill@lsce.ipsl.fr
orcid.org/0000-0003-1211-717X

Specialty section:
This article was submitted to Coastal Ocean Processes, a section of the journal Frontiers in Marine Science

Received: 09 September 2020
Accepted: 16 February 2021
Published: 18 March 2021

Citation:
Rabouille C, Lansard B, Owings SM, Rabalais NN, Bombled B, Metzger E, Richirt J, Eitel EM, Boever AD, Beckler JS and Taillefert M (2021) Early Diagenesis in the Hypoxic and Acidified Zone of the Northern Gulf of Mexico: Is Organic Matter Recycling in Sediments Disconnected From the Water Column? Front. Mar. Sci. 8:604330. doi: 10.3389/fmars.2021.604330

Hypoxia and associated acidification are growing concerns for ecosystems and biogeochemical cycles in the coastal zone. The northern Gulf of Mexico (nGoM) has experienced large seasonal hypoxia for decades linked to the eutrophication of the continental shelf fueled by the Mississippi River nutrient discharge. Sediments play a key role in maintaining hypoxic and acidified bottom waters, but this role is still not completely understood. In the summer 2017, when the surface area of the hypoxic zone in the nGoM was the largest ever recorded, we investigated four stations on the continental shelf differentially influenced by river inputs of the Mississippi-Atchafalaya River System and seasonal hypoxia. We investigated diagenetic processes under normoxic, hypoxic, and nearly anoxic bottom waters by coupling amperometric, potentiometric, and voltammetric microprofiling with high-resolution diffusive equilibrium in thin-films (DET) profiles and porewater analyses. In addition, we used a time-series of bottom-water dissolved oxygen from May to November 2017, which indicated intense O_2 consumption in bottom waters related to organic carbon recycling. At the sediment-water interface (SWI), we found that oxygen consumption linked to organic matter recycling was large with diffusive oxygen uptake (DOU) of 8 and 14 mmol m^{-2} d^{-1}, except when the oxygen concentration was near anoxia (5 mmol m^{-2} d^{-1}). Except at the station located near the Mississippi river outlet, the downcore pore water sulfate concentration decrease was limited, with little increase in alkalinity, dissolved inorganic carbon (DIC), ammonium, and phosphate suggesting that low oxygen conditions did not promote anoxic diagenesis as anticipated. We attributed the low anoxic diagenesis intensity to a limitation in organic substrate supply, possibly linked to the reduction of bioturbation during the hypoxic spring and summer.

Keywords: diagenesis, hypoxia, acidification, organic matter, continental shelf, oxygen, sediments, RiOMar

INTRODUCTION

Ocean de-oxygenation is a major concern due to warming and eutrophication, especially in the coastal zone (Pörtner et al., 2007; Diaz and Rosenberg, 2008; Gilbert et al., 2010; Zhang et al., 2010; Breitburg et al., 2018; Capet et al., 2020). The occurrence, frequency and extent of hypoxic events (dissolved oxygen concentration $< 63\ \mu mol\ L^{-1}$) are increasing in many coastal zones due to global warming and local eutrophication. The oxygenation of sea water is fundamental to biological and biogeochemical processes. Its decline can cause major changes in ocean productivity, biodiversity, and biogeochemical cycles. Despite the recognized impact of hypoxia on many coastal ecosystems, the numerous benthic processes which promote or limit its negative effects are largely under-investigated. Oxygen availability affects remineralization processes and associated sources and sinks of important nutrient elements, such as nitrogen, phosphorus, and iron (Breitburg et al., 2018). In the general context of ocean acidification caused by anthropogenic CO_2 invasion (Orr et al., 2005), coastal acidification shows some specific features. In addition to surface invasion of CO_2, coastal acidification is amplified by the microbial respiration of terrigenous and marine organic matter in bottom waters, and the accumulation of DIC in stratified waters (Cai et al., 2011). In coastal regions, seasonal hypoxia is generally associated with significant bottom water acidification because of concomitant DIC production and oxygen consumption during aerobic mineralization of organic matter thus imposing a double stressor to coastal ecosystems (Cai et al., 2011). Sediments play a key role in maintaining hypoxic and acidified bottom waters, but this role is still not completely understood (Middelburg and Levin, 2009).

The northern Gulf of Mexico (nGoM) and the Louisiana shelf near the Mississippi River delta includes one of the largest seasonal hypoxic zones of the coastal ocean (Rabalais et al., 2002). Coastal eutrophication associated with nutrient input from the Mississippi River watershed is responsible for the onset of hypoxia through increased primary production, organic matter sedimentation, and mineralization in the bottom waters of the stratified water column (Rabalais et al., 2002; Turner et al., 2006, 2008; Bianchi et al., 2010; Fennel and Testa, 2019). The aerobic microbial degradation of organic matter also generates *in situ* ocean acidification by the formation of metabolic CO_2 without significant total alkalinity (TA) production (Cai et al., 2011). The consumption of bottom water oxygen in the nGoM is intense and correlated to the vertical flux of organic matter originating from primary production in the Mississippi River plume and adjacent continental shelf waters (Redalje et al., 1994; Rabalais et al., 2014; Wang et al., 2018). This organic matter flux promotes a rise in bacterial oxygen consumption with depletion time of several days to a few weeks (Chin-Leo and Benner, 1992; Amon and Benner, 1998; Rabalais et al., 2007; Rabouille et al., 2008). Mobile muds contribute to sediment redistribution and export across the continental shelf (Corbett et al., 2004, 2007; McKee et al., 2004) and to oxygen consumption in the bottom water during resuspension events (Moriarty et al., 2018). In addition to water column respiration, sediment oxygen demand was identified as an important contributor to hypoxia (Turner et al., 2008) with benthic oxygen consumption rates obtained by *in situ* benthic chambers ranging from 5 to 50 mmol $O_2\ m^{-2}\ d^{-1}$ (Morse and Rowe, 1999; Rowe et al., 2002; Berelson et al., 2019) and by *ex situ* sediment core incubations ranging from 10 to 20 mmol $O_2\ m^{-2}\ d^{-1}$ (Murrell and Lehrter, 2011). It was also proposed that dissolved inorganic carbon (DIC) benthic fluxes contribute to the acidification of bottom waters (Hu et al., 2017). As anoxic mineralization in sediments produces alkalinity (Krumins et al., 2013; Rassmann et al., 2020), benthic alkalinity fluxes may also mitigate bottom water acidification if the TA/DIC flux ratio is above one (Hu and Cai, 2011). Several 3D models dealing with hypoxia in the nGoM utilized sediment oxygen consumption (SOC) representations and DIC fluxes to explain the onset and maintenance of hypoxia and the related acidification throughout the summer season (Hetland and DiMarco, 2008; Fennel et al., 2013; Laurent et al., 2017). Specific sediment models were also developed with the aim of understanding oxygen fluxes and their relationship with organic matter deposition and oxygen concentration in the water column (Morse and Eldridge, 2007; Laurent et al., 2016). Benthic-pelagic exchange processes were recognized as key features of mathematical models for accurate representation of hypoxia occurrence and persistence in the nGoM (Fennel et al., 2013; Feist et al., 2016).

Yet, benthic processes involved in bottom water oxygen consumption and acidification remain poorly characterized. After the pioneering work of Lin and Morse (1991) on pyrite formation in the Gulf of Mexico, which included pore water depth profiles of sulfur species (SO_4^{2-}, ΣH_2S), few pore water data have been published in the following 20 years. Morse and Rowe (1999) investigated the benthic biogeochemistry at three stations beneath the Mississippi river plume and some other data have been published in a later paper (Morse and Eldridge, 2007). Pore water data obtained at five stations across the Louisiana shelf for 5 years (2002–2007) were published in a report (Murrell et al., 2013) without a thorough discussion of the underlying biogeochemical processes. Later, these processes were partially discussed for two of the five stations (Devereux et al., 2015; Laurent et al., 2016), although a larger collection of pore water profiles was published more recently (Devereux et al., 2019) together with sulfate reduction rate measurements. In contrast to the large sediment oxygen demands reported in the above studies, all data sets indicated poorly active subsurface sediments with limited increase of metabolite concentrations (NH_4^+, DIC) in shelf sediments under the river plume and adjacent continental shelf waters.

In most of these studies, the contribution of benthic processes, in particular the role of dissolved iron, manganese and sulfide oxidation at the oxic-anoxic interface in sediments, to the onset and persistence of hypoxic bottom waters throughout the summer was not investigated thoroughly. Furthermore, the role of benthic processes on DIC and TA fluxes to bottom waters and its link to acidification during both normoxic and hypoxic periods was not considered, despite the potential release of alkalinity produced by increased anoxic diagenesis (Krumins et al., 2013; Rassmann et al., 2020).

In this paper, the role of early diagenesis in Louisiana shelf sediments on bottom water hypoxia was investigated in the

summer of 2017, when the surface area of the hypoxic zone was the largest ever recorded (Rabalais and Turner, 2019). Surface sediments and pore waters within and beyond the hypoxic zone were examined using multiple techniques, including *in situ* and *ex situ* micro-electrodes, diffusive equilibrium in thin films (DET) probes and classical pore water extractions. Time series data (7 months) of bottom water dissolved oxygen from a fixed station in 20-m water depth collected simultaneously were also included to examine the oxygen conditions before, during, and after hypoxia and assess the dynamics of oxygen consumption in the water column. The main objectives of this paper are to: (i) examine the contribution of water column, interface and subsurface sediments to the overall oxygen demand of bottom waters; (ii) investigate whether anoxic early diagenesis in subsurface sediments (metal oxides and sulfate reduction) is enhanced by hypoxic conditions; and (iii) examine the contribution of early diagenesis to bottom water acidification through benthic DIC and TA production and their potential release to the overlying waters.

MATERIALS AND METHODS

Site Characteristics and Sampling

The Louisiana shelf near the Mississippi River delta in the nGoM is one of the largest seasonal hypoxic zones of the coastal ocean (Rabalais et al., 2002; Rabouille et al., 2008). These sediments contain high concentrations of particulate organic carbon (POC) which decrease slightly from the River mouth (1.4% OC dry weight) to the shelf (1.1% OC dw) (Goni et al., 1997; Gordon and Goni, 2004; Bianchi et al., 2014). Although terrestrial organic carbon from C3 and C4 plants is present, a decreasing proportion of terrestrial organic carbon and a progressive replacement by marine organic matter is observed westward (Waterson and Canuel, 2008) with a proportion of 60–80% of marine OC in shelf sediments. Most of the recycled carbon is derived from marine organic carbon as attested by the $\delta^{13}C$ signature of bottom water DIC (Wang et al., 2018). The export of POC to the Mississippi canyon is also significant (Bianchi et al., 2006) and probably related to mobile mud resuspension and transport (Corbett et al., 2004, 2007). Sedimentation rates indicate large sedimentation near the river outlet (>2.5 cm y^{-1}) with values ranging between 0.1 and 0.7 cm y^{-1} on the Louisiana shelf (Gordon and Goni, 2004; Corbett et al., 2006).

The MissRhoDia 1 cruise was conducted in the nGoM in the plume of the Mississippi River on the R/V *Savannah*, operated by the Skidaway Institute of Oceanography at the University of Georgia (United States), from July 19th to August 13th 2017. Four stations were investigated on the Louisiana continental shelf along a 170 km east-west transect from the river mouth to the open shelf (**Figure 1**). Station 2b was located near the Mississippi River delta at 65 m depth, whereas the three other stations (4, MK, and 5B) were located on the Louisiana shelf around the 20 m isobath in and around the reported hypoxic zone. Indeed, the reported hypoxia frequency for these three stations are 50–100% during the hypoxic season (Rabalais and Turner, 2019). Four other stations were investigated during the same cruise on the slope and are presented in a companion paper (Owings et al., 2021). At each station, CTD profiles were measured, bottom water was sampled with Niskin bottles, one microprofiler deployment was conducted and three sediment cores were collected using a MC-800 multicorer (Ocean Instruments) and immediately treated on board: one for porosity, one for voltammetry followed by porewater extraction, and one for DET measurements. In addition, dissolved oxygen time series in bottom waters obtained in 2017 at station C6C are included, as a subset of the time series obtained over the last 20 years by LUMCON (Rabalais and Turner, 2019).

CTD and Bottom Water Measurements

Seawater samples were collected using a rosette system (10 × 6-L Niskin bottles) equipped with a conductivity-temperature-depth sensor (CTD, Seabird® SBE 19), a dissolved O_2 sensor (Seabird® SBE 43), a turbidity sensor (ECO-BB, Wet Lab®) and a fluorometer (Seapoint®). The temperature, conductivity, turbidity and fluorometer probes were calibrated by the manufacturer. Bottom water samples were collected using the CTD/Rosette as close as possible to the seafloor approximately 1.5–2 m above the seabed. Temperature and salinity were immediately measured using a manual thermometer (precision 0.1°C) and a thermo-salinometer (WTW 331, precision 0.1). DIC and TA samples were collected in 500 mL borosilicate glass bottles, poisoned with 100 μL of saturated $HgCl_2$ and measured by the SNAPO-CO2 at the LOCEAN French laboratory (Paris, France). These analyses were performed by a potentiometric closed-cell titration (DOE, 1994), on 120 mL sample volumes, at 25°C and with a precision of 0.15%. Bottom water pH was measured on board in triplicates by the unpurified m-cresol spectrophotometric method of Clayton and Byrne (1993) at 25°C with uncertainties < 0.01 pH units. The pH at *in situ* conditions was then calculated using the CO2sys program (Pierrot et al., 2006) with *ex situ* pH, TA, salinity, temperature, and pressure as inputs parameters. Following the recommendations of Orr et al. (2015), all calculations with CO2sys were performed using the acid dissociation constants of carbonate Ka1 and Ka2 reported by Lueker et al. (2000) and total dissolved boron (B_T) reported by Uppström (1974). The *in situ* pH is reported on the total proton scale (pH_T). In order to validate our pH values, we compared the obtained *in situ* pH_T to that calculated using measured DIC and TA (SNAPO-CO2) at *in situ* pressure, salinity and temperature by the CO2sys program. These two independent values were in good agreement within 0.015 pH units or better.

Continuous O_2 Records in Bottom Waters

Data from the C6C station (O2 on **Figure 1**) were obtained every 15 min for bottom water dissolved oxygen from May 2017 to Nov 2017. The data were collected at 1 m above the seabed using dissolved oxygen meters YSI6600 calibrated before and after deployment with Winkler titrations. Water quality probes were replaced optimally at 4- to 6-week intervals to ensure adequate battery life and to avoid fouling, which was minimal because of low oxygen concentrations and high turbidity at these depths.

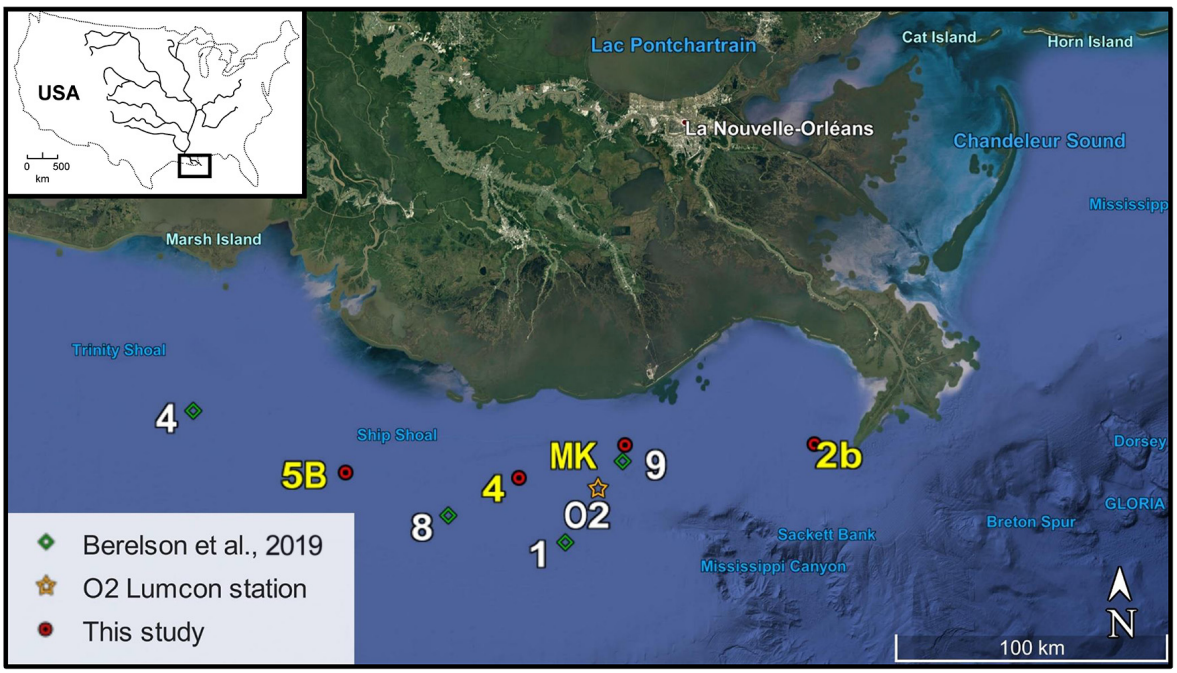


FIGURE 1 | Map of the Louisiana shelf showing the location of the four stations (2b, MK, 4, and 5B) sampled by the R/V *Savannah* in July-August 2017. Station O2 (orange star) refers to the seasonal monitoring station C6C maintained by LUMCON with bottom water oxygen measurements, whereas stations 1, 8, and 9 (green diamonds) refer to Berelson et al. (2019) benthic chamber measurements.

Independent measurements of oxygen were also obtained with a profiling YSI6820 on dive trips when changing the water quality probes to provide an independent quality control on the dissolved oxygen concentration of the deployed YSI6600. The YSI6820 was also pre- and post-calibrated and compared to Winkler titrations in the laboratory.

In situ Micro-Electrode Measurements in Sediment

The *in situ* distributions of O_2 and pH at the sediment-water interface (SWI) were obtained using a benthic micro-profiler (Rassmann et al., 2016, 2020) equipped with five Clark Au/Ag oxygen microelectrodes, two pH glass microelectrodes, two pH references (Ag/AgCl) and one resistivity electrode. After landing on the sediment, the sensing head of the lander carrying the microelectrodes moved vertically over 4 cm across the SWI with a resolution of 200 μm. The O_2 microelectrodes were calibrated with a two-point calibration technique using the bottom water O_2 concentration determined by Winkler titration and the anoxic pore waters. The pH microelectrodes were calibrated using NBS buffers (pH 4.00, 7.00, and 9.00 at 20°C), and electrode slopes were used to calculate pH variations (ΔpH) in the pore waters at *in situ* temperature. The ΔpH values were then added to the spectrophotometrically determined pH_T of the bottom waters to obtain pore water pH_T. Signal drift of O_2 and pH microelectrodes during profiling was checked to be less than 5%. Diffusive Oxygen Uptake rates (DOU) were calculated for each micro-profile using the observed O_2 concentration gradient calculated over 400 μm in the sediment, the porosity value and the O_2 diffusion coefficient at *in situ* temperature (Broecker and Peng, 1974) corrected for tortuosity. The oxygen penetration depth (OPD) was operationally defined as the depth where O_2 concentrations dropped below 1 μmol L^{-1} (Rabouille and Gaillard, 1991).

Sediment Porosity Measurements

For each station, a sediment core was dedicated to porosity measurements. The core was sub-cored using a 50-ml plastic syringe with end cut off and then cut into 2 mm slices on the first centimeter, every 5 mm on the next 9 cm and finally on 2 cm slices for the rest of the core (Cathalot et al., 2010). The sediments from each section were stored in petri dishes and frozen. Porosity was measured in the laboratory based on the salt-corrected mass difference between wet and dry samples (1 week at 60°C) and a sediment density of 2.65 g cm^{-3}.

Voltammetric *ex situ* Profiling

A replicate core collected from the same MC800 deployment was profiled in millimeter increments for dissolved oxygen [$O_{2(aq)}$], thiosulfate ($S_2O_3^{2-}$), total dissolved sulfide ($\Sigma H_2S = H_2S + HS^- + S^0 + S_x^{2-}$), dissolved iron(II) ($Fe^{2+}$), and dissolved manganese(II) (Mn^{2+}) with 100 μm gold/mercury (Au/Hg) voltammetric microelectrodes (Owings et al., 2021). The electrodes were prepared daily and deployed on a computer-controlled micromanipulator with a DLK 70 electrochemical analyzer (Analytical Instrument Systems, Inc.) in a three-electrode system (Ag/AgCl reference, Pt counter, and Au/Hg working electrodes) as reported previously

(Brendel and Luther, 1995; Luther et al., 2008). All measurements were performed according to Owings et al. (2021). Except for $O_{2(aq)}$ which was calibrated using the Winkler-determined overlying water measurements, five-point external calibrations in 0.54 M NaCl were performed with Mn^{2+} as pilot ion, and $S_2O_3^{2-}$, Fe^{2+}, and ΣH_2S were quantified from the pilot ion method (Brendel and Luther, 1995) with the following minimum detection limits (MDLs): ∼15 μM for Mn^{2+}, ∼25 μM for Fe^{2+}, and ∼0.2 μM for ΣH_2S. The electrochemical system also allows detection of organic complexes of Fe(III) [org-Fe(III)] (Taillefert et al., 2000) and aqueous iron sulfide clusters [$FeS_{(aq)}$] as intermediates in the precipitation of $FeS_{(s)}$ (Theberge and Luther, 1997). As the chemical composition of these species is variable and not well defined, they cannot be quantified and are thus reported in normalized current intensities (Meiggs and Taillefert, 2011).

Pore Water Extraction and Analyses

After voltammetric profiles were completed, typically 3 h after core recovery, the same core was transferred to a glove bag (Sigma Aldrich) with a N_2 atmosphere for sectioning in 7–10 mm increments down to 12.5 cm and then in 20 mm increments down to the bottom of the core (Owings et al., 2021). For station 2b, the increment was increased to 50 mm after 20 cm depth. Sediment sections were partitioned into 50 mL Falcon tubes, centrifuged for 10 min at 3,000 rpm under N_2 atmosphere to extract pore waters, which were then immediately filtered through 0.2-micron Whatman® nitrocellulose Puradisc syringe filters into 15 mL Falcon tubes under N_2 atmosphere. The pore waters were then split for onboard analyses of dissolved iron [Fe(II) and Fe(III)] speciation, dissolved manganese (Mn_d), dissolved inorganic phosphate (DIP), DIC, and TA. The remaining aliquots were acidified (HCl 0.1 N) and preserved at 4°C or at −20°C until analysis at Georgia Tech (NH_4^+, SO_4^{2-}, NO_3^-).

Pore water TA measurements were conducted according to Dickson et al. (2007), with a 3 mL open-cell potentiometric titration (Rassmann et al., 2016) using 0.01 M HCl, which was calibrated every day using Seawater Reference Material (standard batch #150) provided by the Scripps Institution of Oceanography (A. G. Dickson laboratory). Error in this analysis represents the standard deviation from the mean of duplicate samples and averages 0.5%. DIC was determined by flow injection analysis, if necessary after 5 mM $ZnCl_2$ amendment to avoid dissolved sulfide interference (Hall and Aller, 1992) with an uncertainty of 2–3%. Total dissolved Mn (Mn_d) was determined in duplicate using the porphyrin kinetic spectrophotometric method (Madison et al., 2011) modified to account for dissolved Fe^{2+} interferences (Owings et al., 2021). Mn_d was quantified by converting the final absorbance to concentration using the molar absorptivity ($\varepsilon = 91.2 \pm 0.4 \times 10^{-3}$ μM cm^{-1}) determined from external calibration curves with Mn^{2+} (MDL: 0.11 μM, 3σ of blanks, $n = 24$). Dissolved orthophosphates (ΣPO_4^{3-}) were quantified with the methylene blue method after correction for silica interference (Murphy and Riley, 1962). Finally, dissolved Fe^{2+} was quantified using the ferrozine method without hydroxylamine whereas total dissolved Fe (Fe_d) was determined by reacting a separate aliquot with hydroxylamine hydrochloride (0.2 M) in the dark for 24 h. Dissolved Fe^{3+} was obtained by subtracting the dissolved Fe^{2+} concentration from total dissolved Fe (Stookey, 1970; Viollier et al., 2000). Dissolved ammonium (NH_4^+) was quantified by the indophenol blue method (Strickland and Parsons, 1972) and anions (SO_4^{2-}, NO_2^-, and NO_3^-) *via* HPLC with UV detection using a 3.2 mM $NaCO_3$/1.0 mM $NaHCO_3$ buffer (SO_4^{2-}; Minimum detection limit = 114 μM respectively) and 54 mM NaCl (NO_2^- NO_3^-, MDL = 0.12, and 0.11 μM) eluents (Beckler et al., 2014). All standard deviations reported for pore water measurements represent analytical error propagated from calibration curves.

"Diffusive Equilibrium in Thin Films" Profiling

Two-dimensional (2D) distributions of total dissolved iron (Fe_d) were obtained by insertion of a 2D-DET probe into a separate sediment core collected simultaneously at each station. The 2D-DET probe was composed of a polycarbonate plate as support, a 100 × 40 × 0.5 mm hydrated polyacrylamide gel (details in Jézéquel et al., 2007) and a 0.1 mm-thick PVDF membrane (Durapore®). Before deployment, the probe was deoxygenated by N_2 bubbling for at least 3 h. Probes were inserted in the sediment cores for 3 h for chemical equilibrium with the pore waters. During this time, oxygen concentration in the core overlying water was maintained by bubbling an N_2/air mix. Temperature of the core was also maintained at *in situ* value using a Thermo-Fisher cryostat. At the same time, a 0.5 mm-thick gel was also equilibrated with a solution of ascorbic acid (30 mM) and ferrozine (12.2 mM) to form a reagent gel. After retrieval, the probe gel was laid onto the reagent gel. After 15 min, a magenta color whose intensity is proportional to total iron content was read using an office flatbed scanner. Standardization was realized according to Cesbron et al. (2014) with $(NH_4)_2Fe(SO_4)_2{\cdot}6H_2O$ and ascorbic acid solutions. Scanned images were processed using ImageJ software and the green band was used for calibration and quantification (Jézéquel et al., 2007). For comparison to extracted porewaters, average profiles were calculated using the mean and standard deviations of all pixels within the same depth interval as core slices.

Calculation of the Carbonate Saturation State

Calcium carbonate ($CaCO_3$) saturation states with respect to calcite (Ω_{Ca}) and aragonite (Ω_{Ar}), reported classically as the ion activity product divided by the apparent solubility equilibrium constant of calcite or aragonite, were calculated using the CO2SYS program (Pierrot et al., 2006) following the recommendations of Orr et al. (2015), using measured values of pH, TA, temperature, salinity, DIP, and silicate from Berelson et al. (2019). Calcium carbonate saturation states at a millimeter scale near the SWI were calculated from *in situ* pH profiles and linear interpolation of the centimeter-scale TA profiles. The uncertainties of Ω_{Ca} and Ω_{Ar} were estimated using the standard deviation of the mean *in situ* pH profiles and the pore water TA ($\pm$ 15 μmol kg^{-1}).

Integrated Reaction Rate Calculations Using PROFILE

To quantify the mineralization of organic carbon in shelf sediments, integrated reaction rates of DIC production were calculated using the PROFILE software (Berg et al., 1998) using different bioirrigation rate constants (α in y^{-1}). Alpha coefficients were constant with depth until 5–6 cm depth below which they rapidly decreased to 0. Four to five values were used for each profile fit in order to bracket the best fit for each station. Measured porosity profiles were used with diffusion coefficients adjusted to the observed water temperature and salinities. Fits to the measured DIC concentration profiles were optimized by the software and computed integrated reaction rates were then converted to mmol m^{-2} d^{-1}.

RESULTS

Water Column Measurements

Vertical distributions of temperature, salinity, fluorescence, turbidity, and dissolved O_2 concentration in the water column are shown in **Figure 2**. Surface water temperatures ranged from 28 to 30°C, with the lowest temperature observed near the Mississippi River delta (St. 2b), and water temperatures remained consistently high to 20 m in depth (≥28°C). The water column showed a haline stratification at all stations, with the lowest surface salinity measured at St. 4 (S = 12), which was probably most directly in the path of the freshwater discharge, and the highest surface salinity observed at St. 5B (S = 24). In contrast, bottom water salinities were close to marine waters (**Table 1**). This haline stratification (Wiseman et al., 1997) was correlated to a strong gradient in dissolved O_2 concentration from the surface to the bottom. Dissolved O_2 concentrations were slightly supersaturated around 240 μmol L^{-1} in surface waters at St. MK and 4, reached close to 190 μmol L^{-1} at St. 2b, and were slightly lower at Station 5B (180 μmol L^{-1}). Dissolved O_2 concentrations decreased with depth at all stations (**Figure 2**). Bottom water O_2 concentration reached 109 and 106 μmol L^{-1} at St. 2b and 4, respectively (**Table 1**). Near-hypoxic values were observed at St. MK (64 μmol L^{-1}) while hypoxic values were observed at St. 5B (18 μmol L^{-1}). Bottom water pH_T followed the decrease in oxygen concentrations, with larger values at stations 2b and 4, slightly lower pH_T at St. MK, and a minimum was measured at St. 5B (**Table 1**). The Chl-*a* concentration was relatively low (2–5 mg m^{-3}) within the uppermost 10 m of the water column at all stations and decreased below the pycnocline (**Figure 2**) to reach a constant value of 2 mg m^{-3} except at St. 2b. The turbidity signal was relatively high above the pycnocline at stations 2b, MK and 4, which are located in the coastal waters around the Mississippi river mouth, and decreased deeper. A nepheloid layer was mostly detected close to the seafloor at St. MK, and to a lesser extent at St. 2b and 5B.

Bottom Water Oxygen Time Series

Dissolved oxygen time series in bottom waters are reported for 7 months at site C6C in the center of the seasonal hypoxic zone. The bottom water oxygen concentrations were consistent with independent measurements conducted during maintenance visits (red diamonds). The time series indicated extended periods of hypoxia in May-June, July, and August-September with re-oxygenation of the bottom waters in June after the tropical storm Cindy on June 21st and in September-October (**Figure 3**). Periods of rapid consumption of oxygen occurred during the summer: at the beginning of July (1st July), the oxygen concentration in the bottom waters dropped from 150 μmol L^{-1} to hypoxia (63 μmol L^{-1}) in 30 h. Similarly, on July 16th, the oxygen concentration switched from hypoxia to near anoxia in only 2 days.

Oxygen and pH Micro-Profiles

The *in situ* distribution of oxygen at the SWI revealed a large decrease of oxygen concentration in the first millimeters of the sediment (**Figure 4**). Stations MK and 5B, which showed the lowest oxygen concentration in the bottom water, nearly hypoxic and hypoxic respectively, showed highly reproducible profiles and were characterized by average OPD of 0.4–0.6 mm (**Table 2**). In contrast, St. 4 and 2b, in oxic conditions, displayed more heterogeneous sediment profiles with average OPD of 1.6–2.0 mm. DOU rates ranged between 5 and 15 mmol m^{-2} d^{-1} and decreased with decreasing bottom water O_2 from St. 2b to St. 5B (**Table 2**).

The *in situ* pH_T microprofiles acquired using the benthic micro-profiler were characterized by large pH decreases below the SWI (**Figure 5A**). Two types of profiles were observed. At the shelf stations (4, MK, and 5B), pH showed a large decrease in the oxic zone (a few millimeters) and stabilized around 6.8–7.0 at depth. On the contrary, pH profiles at the river mouth station (St. 2b) showed a less intense decrease across the oxic-anoxic interface, a rebound below the OPD, followed by a secondary decrease to reach a minimum value around 7.4 ± 0.1 at depth (**Figure 5**). The pH stabilized within 2 cm below the SWI in all profiles.

In bottom waters, Ω_{Ca} and Ω_{Ar} showed oversaturation with respect to calcite and aragonite. They ranged between 2.5 and 4 for calcite and between 1.7 and 2.6 for aragonite, with maximal values at St. 4 and minimal values at St. 5B (**Figure 5B**). At St. 2b, the pore water saturation state decreased with depth across the oxycline. Although pore waters remained oversaturated with respect to calcite ($\Omega_{Ca} > 1$), pore waters reached aragonite saturation ($\Omega_{Ar} = 1$) at the OPD at this station. As the pH rebounded deeper in the sediment, the pore waters returned to oversaturation with respect to both calcite and aragonite and decreased again during anoxic diagenesis. Similarly, at St. 4, MK, and 5B, Ω_{Ca} and Ω_{Ar} both decreased across the SWI from above saturation in the overlying waters to near saturation or undersaturation at the OPD. However, whereas Ω_{Ca} remained close to one at all stations by 3 cm depth, Ω_{Ar} showed clear undersaturation below the SWI reaching values as low as 0.50, 0.64, and 0.45 at depth at St. 4, MK, and 5B. Thus, dissolution of aragonite likely occurs in these sediments bathed with hypoxic and acidified waters, whereas calcite dissolution appears to be limited in surface sediments.

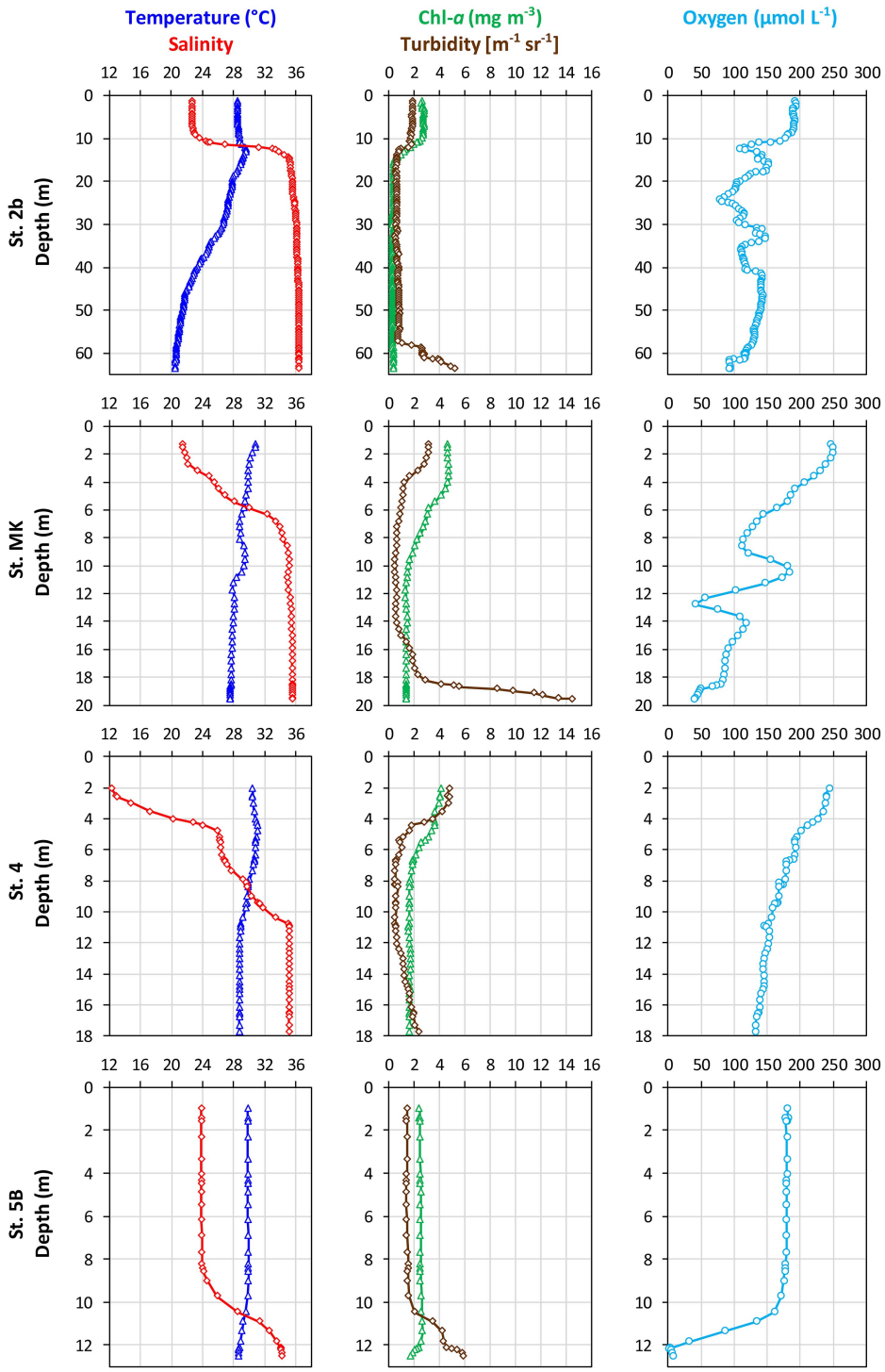


FIGURE 2 | Water column distribution of temperature (°C), salinity, Chl-a concentration (mg m^{-3}), turbidity (m^{-1} sr^{-1}), and dissolved O_2 concentration (µmol L^{-1}) measured *in situ* with the CTD/Rosette at the four stations on the Louisiana shelf (in July-August 2017).

Pore Water Profiles and DET Distributions

Pore water profiles showed diagenetic footprints with generally increasing DIC, TA, NH_4^+, and DIP concentrations downcore (**Figure 6**). However, pore water profiles were characterized by contrasting signatures depending on their location: St. 2b displayed large DIC and TA production in pore waters with deeper concentrations greater than 10 mmol kg^{-1}, accompanied

TABLE 1 | Position, depth, and sampling date of the four stations on the Louisiana shelf (nGoM) along with parameters recorded in the bottom waters (T, S, O_2, pH, TA, and DIC).

Station	Date	Lat (°N)	Long (°W)	Depth (m)	T_{BW} (°C)	S_{BW}	O_{2-BW} (μmol L^{-1})	pH_{T-BW}	TA_{BW} (μmol kg^{-1})	DIC_{BW} (μmol kg^{-1})
2b	Aug-6-2017	28°54.0	89°35.4	64.5	20.9	36.5	108.8 ± 0.2	7.88 ± 0.01	2,420 ± 4	2,218 ± 3
MK	Jul-26-2017	28°54.1	90°17.8	20.3	27.8	35.9	64.0 ± 0.5	7.78 ± 0.01	2,383 ± 4	2,184 ± 3
4	Jul-29-2017	28°47.7	90°41.5	19.2	28.8	35.8	106.2 ± 0.4	7.82 ± 0.01	2,389 ± 4	2,164 ± 3
5B	Aug-1-2017	28°48.6	91°20.3	15.4	28.8	34.2	17.6 ± 0.5	7.62 ± 0.01	2,366 ± 4	2,244 ± 3

pH is reported at in situ condition. The error represents the standard deviation between replicate measurements (n = 3).

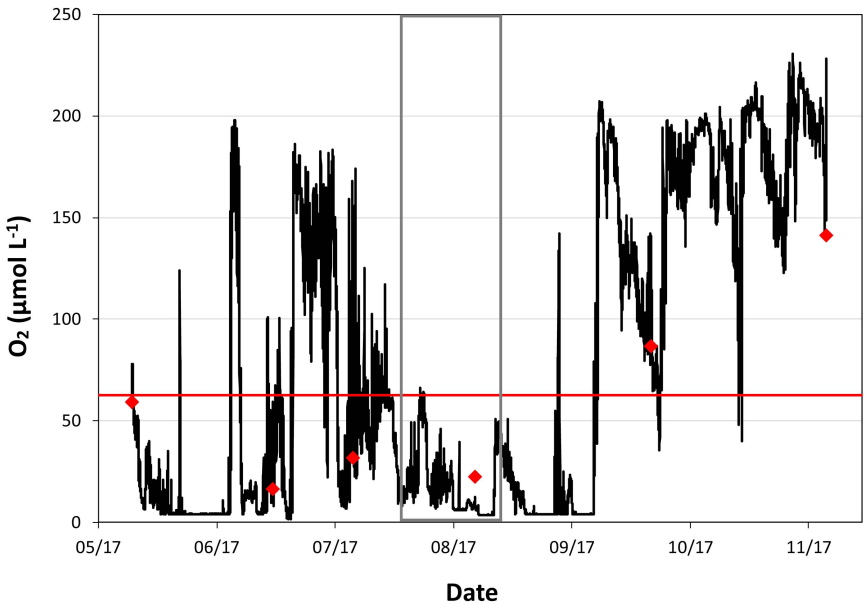


FIGURE 3 | Time series of dissolved oxygen concentration in bottom water (μmol L^{-1}) at Station C6C (O2 on **Figure 1**) showing substantial variability linked to tropical storms (Cindy on June 21st 2017) and subsequent water column mixing followed by rapid de-oxygenation at the beginning of July 2017 and later. The red line indicates the level of hypoxia (O_2 = 63 μmol L^{-1}). Red diamonds represent dates of sensor replacements and independent measurements of oxygen (see section "Materials and Methods"). Gray rectangle represents the sampling period during MissRhoDia 1 cruise.

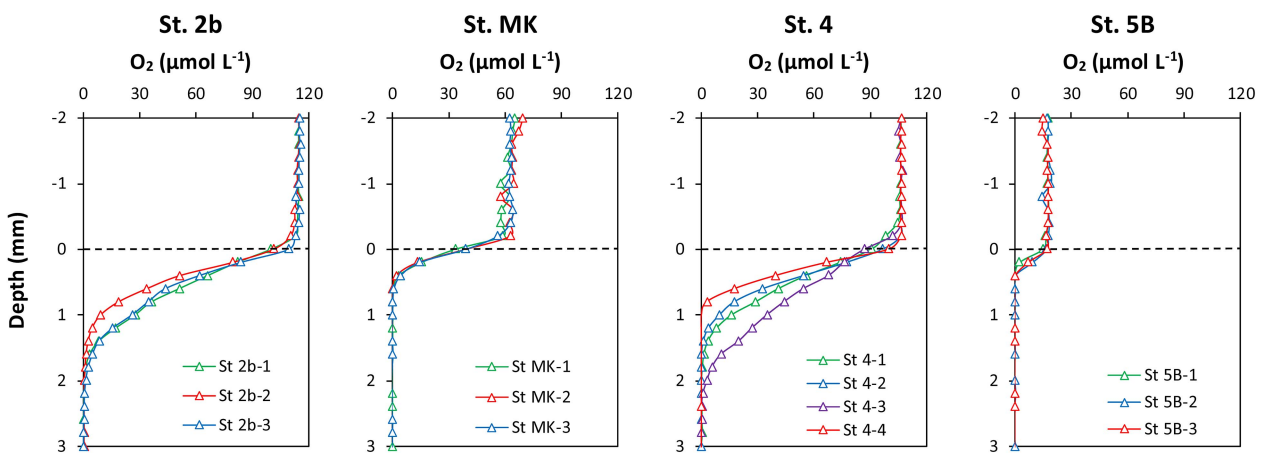


FIGURE 4 | *In situ* dissolved oxygen micro-profiles obtained in sediments from the four stations on the Louisiana shelf in July 2017. The horizontal dashed line represents the sediment-water interface.

TABLE 2 | Oxygen concentration in bottom water (O_2^{BW}), diffusive oxygen uptake (DOU), and oxygen penetration depth (OPD) at the Louisiana shelf in July-August 2017.

Stations	O_{2-BW} (μmol L^{-1})	DOU (mmol m^{-2} d^{-1})	OPD (mm)
2b	108.8	15.1 ± 3.0	2.0 ± 0.2
MK	64	8.0 ± 0.8	0.6 ± 0.0
4	106.2	14.1 ± 6.2	1.6 ± 0.5
5B	17.6	4.8 ± 0.3	0.4 ± 0.0

The DOU and OPD errors represent the standard deviation from the mean values obtained from individual profiles (n = 3–4).

by a large SO_4^{2-} concentration decrease of around 10 mM. The production of DIC was correlated with an increase of up to 1 mM NH_4^+ and 300 μM DIP. Nitrate concentration showed a rapid decrease from the bottom water and stabilization at depth to low values (2–3 μM). Dissolved Mn and Fe showed large and similar increases in the first centimeters below the SWI (up to 300 μM) and a slow decrease with depth. It is noteworthy that Fe^{3+} dominated dissolved iron speciation (**Figure 6**). On the contrary, the diagenetic signatures at all other stations (St. 4, MK, and 5B) were different: they were characterized by slight increases in DIC and TA (2–3 mmol kg^{-1}), with occasional decrease at depth such as observed at St. MK or 5B (**Figure 6**). Limited decreases in SO_4^{2-} (<2 mM) were visible on profiles, and small increases of NH_4^+ and DIP concentration (<250 μM and <100 μM respectively) were also observed. Dissolved Fe and Mn showed subsurface peaks of smaller amplitude than St. 2b (around 50 μM Mn and 100 μM Fe) except at St. 5B where the dissolved Mn subsurface peak reached 300 μM.

The 2D distribution of dissolved iron obtained with the DET probe revealed little lateral variability except at the onset of dissolved iron production (**Figure 7**). In particular, no sign of large disturbance by burrows or other biogenic structures were observed on 2D images except at St. 2b. This is confirmed by the small standard deviation of the pixel lines on the gel image as calculated in the 1-D profiles (black lines). Dissolved iron concentrations from extracted pore waters (red dots) and gel bands averaged over the same depth interval (black dots) were in a good agreement except for St. 2b where the dissolved iron peak in extracted pore waters were about 300 μM and located at 1 cm depth. Such variability between cores suggests heterogeneity at this station, which is the closest to the river delta. Dissolved iron was not detected above 0.5 cm depth at all stations except for St. 4, which showed a single enriched zone at the SWI. At St. 2b, dissolved iron appeared at 2 cm depth, reached 150 μM at 3 cm, and remained stable further down in contrast to the extracted pore water profile. At St. 4 and MK, dissolved iron was present just below the SWI and reached a

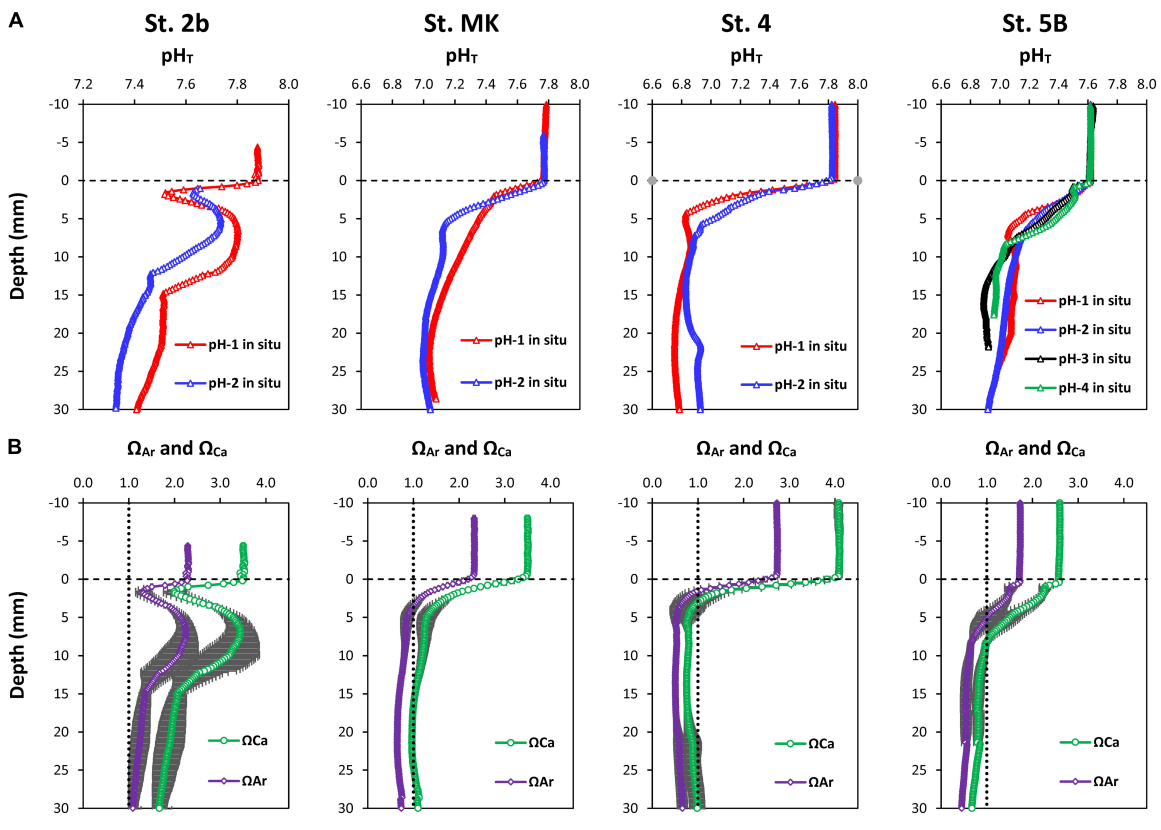


FIGURE 5 | (A) Replicate pH micro-profiles obtained *in situ* at the sediment-water interface of the Louisiana shelf in July-August 2017. **(B)** Calcium carbonate saturation state with respect to calcite and aragonite with their uncertainties calculated for each station from the average pH micro-profile and interpolated TA profile using the CO2SYS program (see text for details). The vertical dashed line represents saturation with calcite or aragonite.

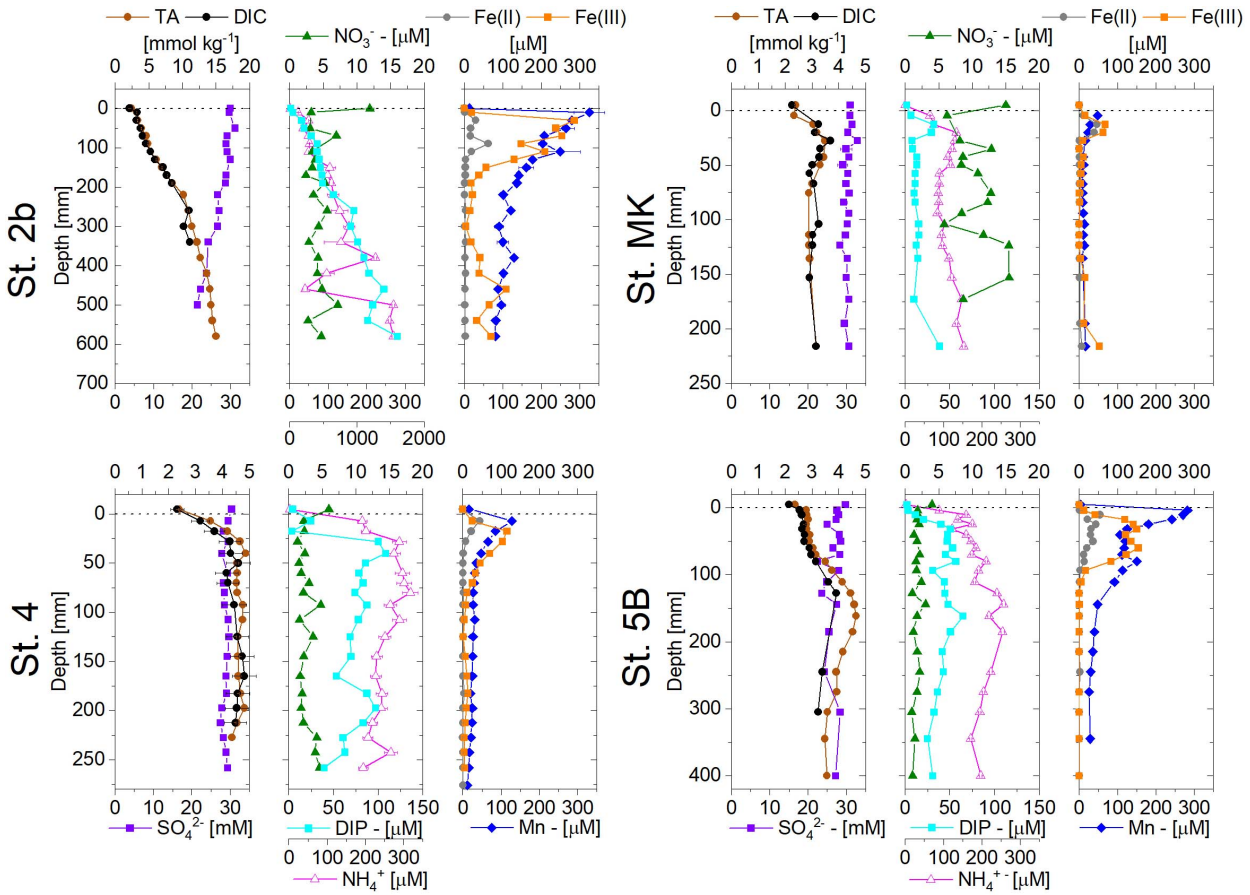


FIGURE 6 | Pore water profiles of TA, DIC, SO_4^{2-}, NO_3^-, NH_4^+, DIP, and dissolved Mn, dissolved Fe(II), and Fe(III) obtained at the four stations on the Louisiana shelf in July-August 2017. The dashed line shows the location of the sediment-water interface. Note that Station 2b has a different depth axis (down to 700 mm).

maximum concentration of about 100 and 70 µM, respectively, near 2 cm depth. Below, dissolved iron concentration slowly decreased to 50 and 30 µM at 8 cm depth, respectively. Station 5B showed the highest Fe_d concentration in the DET, with 200 µM at 2.5 cm depth.

Voltammetric Profiles

Voltammetric microprofiles measured immediately after sediment core collection revealed that metal reduction occurred at all stations albeit with different intensities (**Figure 8**). At St. 2b, dissolved Mn^{2+} showed a pronounced peak up to 1,000 µM at 5 cm with lower values in deeper layers, while dissolved iron showed a coinciding peak in org-Fe(III) rather than Fe^{2+} concentrations at 5 cm depth. At the other stations the dissolved metal signals were much lower except at St. 5B, which showed Mn^{2+} and Fe^{2+} peaks of 250 and 750 µM and pervasive occurrence of org-Fe(III) complexes in much larger current intensities. The large concentrations of dissolved Fe at St. 2b and 5B were also visible in the pore water extraction (**Figure 6**) and 2-D DET profiles (**Figure 7**).

The most striking difference between St. 2b and the other shelf stations was revealed by the total dissolved sulfide (ΣH_2S) and $FeS_{(aq)}$ depth profiles. A ΣH_2S peak reaching 200 µM was detected between 5 and 15 cm with simultaneous production of $FeS_{(aq)}$ clusters over the same depth range, suggesting particulate FeS formation at St. 2b which was corroborated by solid phase data (Owings et al., 2021). In contrast, the other stations did not display any detectable dissolved sulfide (except < 10 µM at depth at St. 5B), nor $FeS_{(aq)}$ clusters throughout these cores.

DISCUSSION

The Louisiana shelf undergoes seasonal hypoxia and acidification, as a result of the biogeochemical mineralization of organic matter and subsequent oxygen consumption and DIC production in the stratified water column. The shelf waters and biogeochemical condition are influenced by the discharge of the Mississippi Atchafalaya River system, increased primary production and thermal warming in spring and summer (Rabalais et al., 2002; Cai et al., 2011; Laurent et al., 2017; Fennel and Testa, 2019). In this discussion, the oxygen depletion in the water column and its dynamics are explored, the effect of diagenetic processes

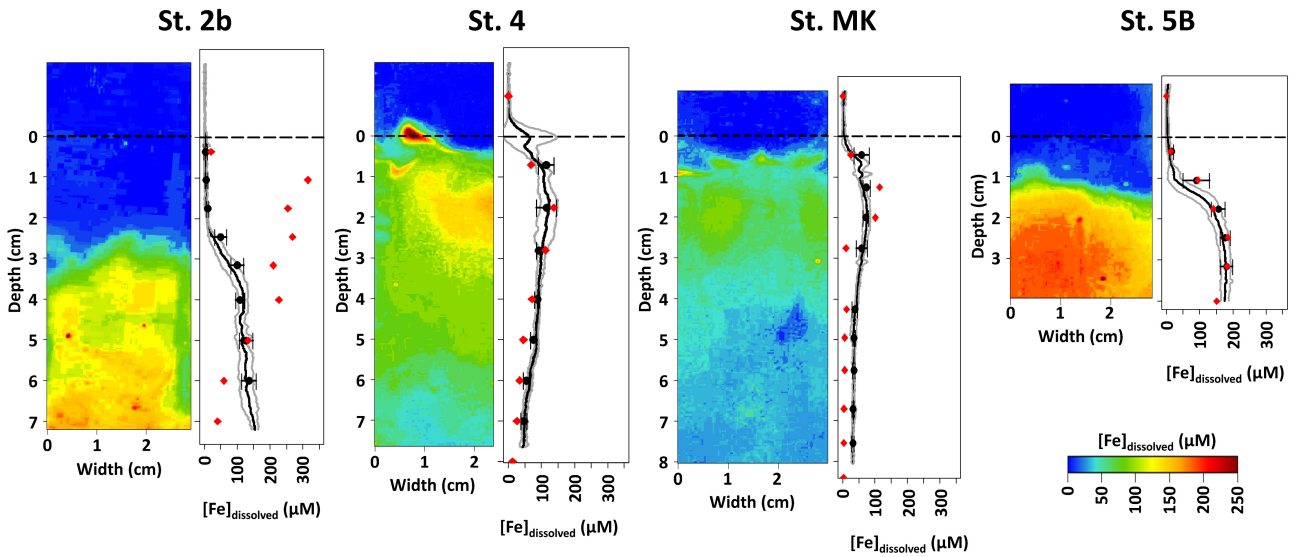


FIGURE 7 | Dissolved iron ($Fe_{dissolved}$) spatial distribution obtained by diffusive equilibrium in thin films (2D-DET) (colored panel) and dissolved Fe averaged profiles obtained from DET (black dots and line) compared to extracted pore water profiles (red dots) at the four stations on the Louisiana shelf in July-August 2017. Gray contours represent 1σ of the distribution of dissolved Fe for each line of pixel.

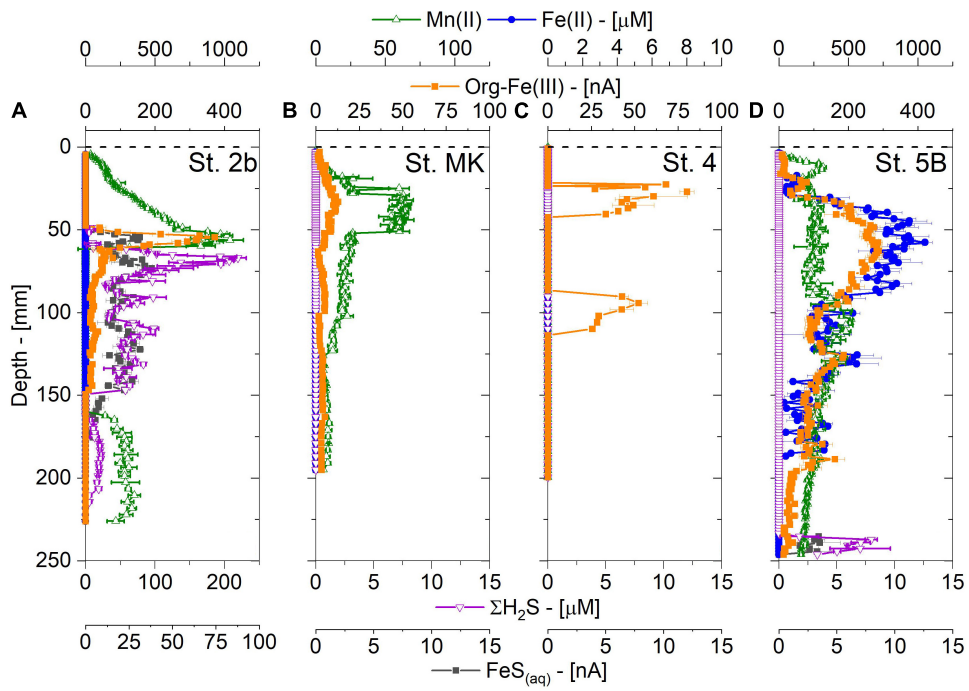


FIGURE 8 | Depth profiles of dissolved Mn^{2+}, Fe^{2+}, organic-Fe (III), ΣH_2S, and $FeS_{(aq)}$ obtained by Au/Hg voltammetric microelectrodes at the four stations (**A–D** for stations 2b, MK, 4 and 5B respectively) on the Louisiana shelf (nGoM) in July-August 2017.

in generating or maintaining hypoxia and contributing to acidification on the shelf is discussed, including the diagenetic processes underlying this oxygen consumption, and a conceptual framework is presented that may explain both the present results and biogeochemical data obtained from previous studies.

High O_2 Consumption in the Water Column and at the Sediment-Water Interface

Oxygen depletion was particularly developed in the summer 2017 (Rabalais and Turner, 2019). Hypoxia was present all over the

Louisiana shelf, in a continuous band from the Mississippi River delta to the Texas shelf at depths between 10 and 20 m. In fact, the hypoxic zone reached its maximum area in 2017, based on a record dating back to 1985 (Rabalais and Turner, 2019).

The shelf water column measurements from the present study showed a gradient of oxygen depletion from oxic at St. 4, to nearly hypoxic at St. MK and hypoxic at St. 5B (**Figure 3**). The water column of all stations revealed both thermal and haline stratification, although the vertical salinity gradient due to seawater dilution in the Mississippi River plume (6–10 m thick at our stations) contributed mainly to this stratification. As the plume was turbid, primary production was limited and Chl-*a* never exceeded 5 mg m^{-3} at the surface in contrast to previous studies that demonstrated larger chlorophyll content in the distal plume in spring and summer (Dagg et al., 2008; Lohrenz et al., 2008). The presence of a significant concentration of Chla in bottom waters can probably be related to freshly settled detritus as previously suggested (Dortch et al., 1994). The bottom boundary layer was characterized by an increase in turbidity (St. 2b, MK, and 5B), which can be related to the nepheloid layer (Corbett et al., 2004, 2007). Oxygen concentrations were at or below the hypoxic level at stations MK and 5B, showing a clear sign of oxygen consumption in the shelf waters (Turner et al., 2008). It has been proposed that the "time to reach hypoxia" from oxic conditions could be around 1 month on the Louisiana shelf (ranging from a few weeks to 2 months; Chin-Leo and Benner, 1992; Dortch et al., 1994; Amon and Benner, 1998) as a result of the aerobic microbial degradation of organic matter and water temperature. Time series in bottom waters at St. C6C indicated that oxygen consumption leading to the hypoxic threshold can be even more rapid in summer, reaching a few days (**Figure 2**). As the oxygen consumption in the nGoM bottom waters is attributed to the excess organic matter linked to high primary production during spring algal bloom (Rabalais et al., 2002; Turner et al., 2008) and microbial activity is high in the water column (Dortch et al., 1994; Amon and Benner, 1998), it can be inferred that the observed rapid drop in bottom water oxygen concentration is related to the mineralization of a large quantity of labile organic matter.

In addition to the rapid consumption of oxygen by aerobic microbial respiration in the stratified bottom waters, the surface sediment also plays a prominent role in consuming dissolved oxygen. Large SOC, which represents the sum of DOU and the fauna-mediated O_2 flux, have been already documented in the area (Rowe et al.; 2002; Murrell and Lehrter, 2011; Lehrter et al., 2012), indicating that SOC could significantly contribute to the oxygen drawdown in bottom waters (20–30%; Dortch et al., 1994; Murrell and Lehrter, 2011; Feist et al., 2016). The data presented in **Figure 4**, displaying low OPD in sediments, suggest large oxygen consumption possibly linked to the degradation by aerobic respiration of organic matter deposited at the SWI. Indeed, the DOU rates (**Table 2**) were high at St. 2b, 4, and MK (respectively, 15, 14, and 8 mmol m^{-2} d^{-1}) where O_2 concentrations were above hypoxic level. The DOU rate was lower at St. 5B (4.8 mmol m^{-2} d^{-1}) limited by O_2 concentration below the hypoxic threshold. DOU is most often lower than SOC because bioirrigation is not considered in DOU (Glud et al., 1998; Glud, 2008). Despite this difference, the DOU rates obtained in this study were comparable to the SOC values obtained by Lehrter et al. (2012); 5.2 ± 2.5 mmol m^{-2} d^{-1} for mid shelf stations), Murrell and Lehrter (2011); shelf average 11.6 ± 2.2 mmol m^{-2} d^{-1}), Rowe et al. (2002); 13 ± 3 mmol m^{-2} d^{-1} at St. C6 close to C6C and St. MK), and Berelson et al. (2019); 4 and 12 mmol m^{-2} d^{-1} at St. 1 and 9; **Figure 1**). These high oxygen consumptions indicate that the sediment plays a significant role in controlling bottom water oxygen concentrations. As dissolved O_2 was confined to a narrow layer at the top of the sediment column, where labile OM from the water column accumulates (OPD = 0.5–2 mm, **Figure 4**), the consumption of oxygen could largely be due to the mineralization of labile organic matter recently deposited at the SWI. Dissolved metal re-oxidation may also play a role in DOU rates, as diffusive flux calculations indicate that a maximum of 20% of oxygen uptake could be used for Mn re-oxidation at St. 5B. SOC would therefore participate in the overall oxic mineralization and O_2 consumption in the bottom waters. It is noteworthy that this large oxic mineralization at the SWI would also contribute to the acidification of bottom waters, as aerobic respiration produces metabolic CO_2 with negligible TA, therefore decreasing the bottom water pH. This is apparent on the gradient from St. 4 to St. 5B where bottom water pH drops by 0.2 units and O_2 from 106 to 18 μmol L^{-1} (**Table 1**). The pH and O_2 values measured in the bottom water are in good agreement with previous data reported for the Louisiana Shelf (see Annex 1; Cai et al., 2011).

Low Intensity of Early Diagenesis in Shelf Sediments

A close examination of the pore water profiles obtained from the Mississippi River delta (St. 2b) to the shelf reveals a contrasted situation. A large increase in metabolite concentrations was observed at St. 2b near the Mississippi River delta where previous papers have indicated high accumulation of terrestrial organic matter (Bianchi et al., 2002). DIC, NH_4^+, and DIP concentrations reach values of 10 mmol kg^{-1}, 1.5 mM, and 200 μM, respectively (**Figure 6**), which together indicate a high mineralization activity in these sediments. At the same time dissolved iron and manganese peaked in surface pore waters with concentrations above 300 μM in the first few centimeters (**Figures 6–8**) indicating significant Fe and Mn reductions. Accompanied by the large decrease in SO_4^{2-} (**Figure 6**) and the presence of dissolved sulfide and $FeS_{(aq)}$ (**Figure 8**), pore water data indicates active sulfate reduction at this station (St. 2b).

In contrast, metabolite concentration increases observed at the other shelf stations (4, MK, and 5B) were limited with maximum DIC concentrations of 5 mmol kg^{-1} ($\Delta DIC < 3$ mmol kg^{-1}), and low NH_4^+ production (<100 μM). At the same time, low SO_4^{2-} decrease in pore waters ($\Delta SO_4 < 2$ mM) was observed at these three stations. The shelf pore water data are similar to other profiles obtained in the same area [St. C06 – Devereux et al. (2019); St. Z02 – Devereux et al. (2015) and Laurent et al. (2016)]. In shelf sediments other than St. 2b, sulfate reduction seemed to be minimal as shown by the absence of sulfide or $FeS_{(aq)}$ clusters in pore waters (**Figure 8**). Only metal diagenesis

(Mn and Fe reduction) appeared to be active in shelf sediments. Both pore water extractions (**Figure 6**) and 2-D DET profiles (**Figure 7**) displayed remarkably similar dissolved Fe(II) profiles, which showed distinct and coherent peaks (80–300 μM) in subsurface sediments indicative of substantial iron reduction in these sediments. Dissolved Mn and Fe peaks were weaker at St. 4 and MK than at St. 5B. This latter station is located westward under the direct influence of the Atchafalaya River, which delivers Mn- and Fe-rich detrital particles to fuel the sedimentary Mn and Fe cycles. It is noteworthy that St. 2b shows similar enhanced Fe and Mn diagenesis probably due to similar inputs of detrital material by the Mississippi River (Owings et al., 2021). Sulfate reduction generally constitutes a major diagenetic pathway in coastal marine sediments which receive significant organic matter inputs (Canfield et al., 1993). The low decrease of SO_4^{2-} in pore water profiles at St. 4, MK, and 5B is clearly indicative that early diagenesis in Louisiana shelf sediments is not intense compared to Station 2b.

In order to quantify the organic carbon mineralization in these shelf sediments, the PROFILE software (Berg et al., 1998) was used and fitted to the DIC profiles of the four investigated stations. As bioirrigation is a major control on benthic fluxes in coastal areas (Glud et al., 1998) and some profiles show a double-bend pattern typical of irrigated profiles (e.g., the DIC profile at St. 2b), different bioirrigation rate constants (α in y^{-1}) were used to calculate integrated DIC production rates in these sediments. In each case, the best fit of the PROFILE model to the data is displayed in **Table 3**.

Integrated DIC production calculated using the PROFILE model at the River delta station 2b matched the carbon remineralization (16.5 mmol m^{-2} d^{-1}) rate calculated for the same station from a complete diagenetic model run at steady-state (Owings et al., 2021). Integrated DIC production rates revealed that the mineralization rate at this station (St. 2b) is greater than the average mineralization rate at the other stations on the Louisiana shelf (St. 4, MK, and 5B), even though mineralization rates are highly variable with a strong positive link to bottom water oxygen levels (**Table 3**). The large DIC production rate at St. 2b is accompanied by a large SO_4^{2-} decrease which indicates prevalent sulfate reduction in sediments near the Mississippi River delta. In contrast, lower DIC productions at St. 4, MK, and 5B (average 6.8 ± 5 mmol m^{-2} d^{-1}) were related to limited SO_4^{2-} decreases indicating low sulfate reduction rates. These findings indicate that anoxic diagenesis was not favored in the nearly-hypoxic (MK) and hypoxic (5B) zones of the Louisiana shelf. These results rather suggest that manganese and iron reduction were the most active pathways and produced the majority of DIC at these two stations, while sulfate reduction was negligible.

Integrated DIC production rates from the present study on the Louisiana shelf (0.7–12 mmol m^{-2} d^{-1}) can be compared to benthic DIC fluxes at steady-state. They fall in the lower range of core incubations measurements (averages 15.2 ± 2.1 mmol m^{-2} d^{-1} for shelf stations; Lehrter et al., 2012) and are lower than *in situ* benthic DIC fluxes measured in August 2011 (18–59 mmol m^{-2} d^{-1}; Berelson et al., 2019). In the case of the Lehrter et al. (2012) study, interannual and seasonal variability may explain the observed difference as half of the measurements were conducted during spring, before deposition of the spring bloom to the sediment. Nevertheless, the benthic DIC fluxes measured at station Z02-Z03 (equivalent to station MK and 5B) were approximately double (or triple) the integrated DIC production rates calculated in the present study. The largest benthic DIC flux (59 mmol m^{-2} d^{-1}; Station 9) in Berelson's study could be attributed to a diagenetic hot spot, as the other fluxes (stations 1 and 8) hovered around 18–19 mmol m^{-2} d^{-1}, in the upper range of Lehrter's values. Thus, benthic DIC fluxes, either obtained by *in situ* measurements or *ex situ* sediment incubations, showed values that were approximately two to three times larger than the internal production of DIC calculated in the present study using DIC depth profiles and bioirrigation. One possible bias of this comparison is the fact that fluxes and integrated DIC production rates were obtained from different years and seasons. Indeed, although previously published DIC fluxes cover a large range, their average shows a clear difference by a factor of two to three with the integrated DIC production rate calculated in this study.

We can thus hypothesize that such differences could be related to the efficient mineralization of organic matter at the SWI, which is not captured by standard centimeter-scale pore water profiles used for PROFILE calculations. In this hypothesis, oxic mineralization and metabolic CO_2 production at the SWI could be a major component of DIC fluxes measured by whole core incubations despite not being detected in pore water profiles due to the low vertical resolution. Calcium carbonate dissolution near the SWI is another potential process that may increase DIC fluxes (Rao et al., 2014). The surface sediment (**Figure 5B**) showed near-saturation with respect to calcite (Ω_{Ca} = 0.8–1) and undersaturation with respect to aragonite (Ω_{Ar} = 0.5). Although carbonate minerals in these sediments probably consist of detritic calcite and foraminifera shells (calcite), to the best of our knowledge, the type of calcium carbonate present in the Louisiana shelf sediments is not known. More importantly, the $CaCO_3$ content of these sediments is apparently low, with an average 0.5% inorganic carbon by weight (Gordon and Goni, 2004). As the calcium carbonate content is low, with an even lower proportion of aragonite, and porewaters were saturated with calcite in surface sediments, it is reasonable to assume that carbonate dissolution is limited and does not contribute significantly to the DIC flux.

TABLE 3 | Integrated DIC production (in mmol m^{-2} d^{-1}) for the station studied in 2017.

	Integrated DIC production (mmol m^{-2} d^{-1})	O_2 (μmol L^{-1})	α (y^{-1})
St. 2b	16.5	108.8	40
St. MK	7.7	64	40
St. 4	12	106.2	20
St. 5B	0.7	17.6	0

Oxygen concentration in the bottom water is provided together with the irrigation rate constant (α expressed in y^{-1}) found for the best fit of the model to the data.

Accordingly, if benthic DIC fluxes based on core incubations or benthic chamber measurements (18–19 mmol m^{-2} d^{-1}; Berelson et al., 2019; 15.2 mmol m^{-2} d^{-1}; Lehrter et al., 2012) were two to three times larger than internal sediment production of DIC based on depth profiles (6.8 ± 5 mmol m^{-2} d^{-1} for station 4, MK, and 5B), the present hypothesis implies that a significant proportion of the benthic DIC production could take place at the SWI by deposition and rapid remineralization of organic matter. The proportion of "surface mineralization" could be even greater for station 5B where less mineralization was calculated from the depth profiles (**Table 3**). This hypothesis clearly requires field-based measurements of concomitant DIC fluxes and concentration profiles for testing (e.g., Rassmann et al., 2020).

Overall, the findings of the present study based on oxygen time series in the water column, DOU calculations, and DIC flux discrepancy between benthic exchange fluxes and integrated rates suggest that consumption of organic matter at stations 4, MK, and 5B on the Louisiana shelf was intense in the water column and at the SWI (first few millimeters), but that recycling of organic matter was limited in deeper sediments (2–20 cm).

Proposed Mechanism: Dysfunction of Bioturbation During Hypoxic Stages

Numerous publications have described the life conditions of demersal and benthic fauna in the context of hypoxia (Rabalais et al., 2001a,b, 2002; Levin et al., 2009; Middelburg and Levin, 2009; Briggs et al., 2015; Devereux et al., 2019; Rabalais and Baustian, 2020). Hypoxic areas are known as "Dead Zones" due to the scarcity of fishable species that leave the area when oxygen is below the hypoxic threshold of 63 μmol L^{-1} (Rabalais et al., 2001b). Below this threshold, burrowing invertebrates are stressed and ultimately die as oxygen levels decrease and persist over time (Rabalais et al., 2002; Levin et al., 2009; Middelburg and Levin, 2009; Metzger et al., 2014; Riedel et al., 2014). It can thus be hypothesized that the bioturbation function of the ecosystem, which relies on macrofaunal invertebrates' activity, is largely affected by hypoxia. Yet, bioturbation, when active, is the major transport of organic substrate to deeper sediment layers and thus fuels microbial activity at depth (Burdige, 2006). Information on bioturbation or bioirrigation during the summer hypoxic phases in the Louisiana shelf is scarce. Briggs et al. (2015) used sediment profiling imagery (SPI), X-rays, and radionuclides to investigate biogenic structures and bioturbation activity on the Louisiana shelf in spring and late summer (September) and concluded that sites with a high exposure to seasonal hypoxia (75%) displayed smaller biogenic structures at a lower density than less impacted sites. At these stations located on the fringes of hypoxia (Rabalais and Baustian, 2020), they showed that bioturbation recovered rapidly in September, after an oxygen intrusion event in the bottom waters. A similar observation was made by Devereux et al. (2019) in late September, with oxic waters and active bioturbation in the sediment of seasonally hypoxic zones. Baustian and Rabalais (2009) and Rabalais and Baustian (2020) indicated that sediments in area of the northern GoM severely impacted by seasonal hypoxia contain smaller, less diverse infauna with lower biomass that are primarily opportunists and either surface deposit feeders or subsurface deposit feeders in the upper centimeter of the sediments, where the organic matter is deposited. They also indicated that macrofaunal density drops during hypoxic phases (Baustian and Rabalais, 2009) from low to even lower abundances. Most benthic infauna in the nGoM hypoxic zone during spring 1990 through fall 1991 were located within the upper 2 cm of the sediments (Rabalais et al., 2001b).

Visual inspection of sediment cores indicated minimal burrowing infauna. The lack of benthic biogenic structures at stations 4, MK, and 5B is corroborated by the 2D-DET images of dissolved iron (**Figure 7**) which showed little horizontal heterogeneity, contrarily to typical observation in coastal bioturbated sediments. Several studies showed that iron is sensitive to bioturbation with complete depletion within burrows when bio-irrigation is active. Abandoned burrows also affect pore water chemistry by generating iron-enriched environments within their walls (e.g., Robertson et al., 2009; Thibault de Chanvalon et al., 2017; Aller et al., 2019). The lack of structures on 2D-DET observations indicate that bioactivity was sparse and probably absent at the time of sampling at these shelf stations.

Interestingly, a generally low bioturbation intensity throughout the year, that is further depressed during hypoxic and anoxic conditions, could explain the suggested disconnect between the intense carbon mineralization in the bottom waters

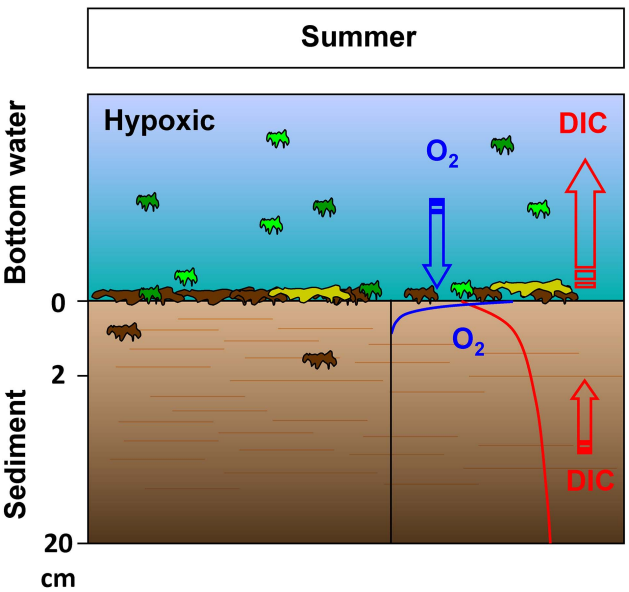


FIGURE 9 | Proposed conceptual model for the summer period: The generally low bioturbation throughout the year and its decrease in summer, concomitantly with the increase in organic matter deposition from the water column, limits organic matter penetration into the sediment by reducing the mixing of new particles with the deeper sediments (horizontal red bars indicate horizontally-layered structure with limited transport). The transport of reactive organic matter is thus limited throughout the year and especially in summer during hypoxic periods, therefore generating a biogeochemically inactive sediment interior (small red arrow in the sediment indicating low DIC internal production) and an active sediment-water interface with important mineralization (large red arrow for total DIC flux).

and sediment interior (**Figure 9**). Bottom waters and surface sediments probably show large mineralization activity, as evidenced by the rapid (**Figures 3**, **4**) O_2 consumption related to the large quantities of labile organic matter raining from surface waters during the spring/summer. Conversely, labile substrate availability is probably restricted in the deeper sediments as a result of the low bioturbation year-round because of the dominance of surface deposit feeders (**Figure 9**). In this scenario, oxygen consumption and DIC production at the SWI would be strengthened during the summer period, as long as oxygen remains near the hypoxic threshold, due to the deposition of labile organic matter at the sediment surface (**Figure 9**). In this case, oxygen consumption at the SWI may increase acidification of bottom waters as a result of the DIC produced during oxic degradation (**Supplementary Figure 1**). A powerful counteracting mechanism would rely on alkalinity production during anoxic mineralization. Indeed, in these sediments, metal reduction (Mn and Fe) is active, which may produce significant alkalinity concentration. However, reoxidation of these dissolved reduced metals with oxygen at the SWI generally consumes most of the alkalinity produced by these reduction reactions (Hu and Cai, 2011). This produces limited net TA fluxes and limits acidification mitigation by benthic alkalinity production. Compounded by the lack of sulfate reduction as a result of the decrease in labile organic inputs in the sediment interior, net alkalinity-generating processes such as FeS production and burial following sulfate reduction (Hu and Cai, 2011; Rassmann et al., 2020), which mitigate acidification in the coastal ocean, are most probably limited at the investigated stations.

CONCLUSION

This study investigated early diagenesis in Louisiana shelf sediments using high resolution techniques near the SWI (amperometric, voltammetric, and potentiometric microelectrodes; DET) and state-of-the-art pore water extractions. A spring to fall time series of bottom water oxygen concentration was also used to investigate hypoxia generation and the biogeochemical dynamics of oxygen consumption in the water column.

From these data, it was possible to conclude that organic matter recycling in the water column near the SWI is disconnected from diagenesis in the sediment interior. Indeed, oxygen consumption was particularly active in the water column during summer as a result of the warm temperature and availability of labile organic matter. Dissolved oxygen was rapidly depleted in the water column, and prolonged periods of hypoxia existed during the summer stratification, therefore attesting the intensity of organic matter mineralization and the lability of the organic substrates. The onset of hypoxia was accompanied by large recycling of organic matter at the SWI as evidenced by dissolved oxygen microprofiles and DOU rates. In contrast, early diagenesis in the shelf sediment interior (St. 4, MK, and 5B) was not intense as revealed by the limited increase in pore water metabolites (DIC, NH_4^+, and DIP), little decrease in SO_4^{2-} concentration and small DIC production rates in the sediment interior. This leads to the conclusion that hypoxia does not favor anoxic diagenesis on the Louisiana shelf, at least at the investigated stations.

The lack of connectivity between surface and subsurface sediments was attributed to the lack of bioturbation year-round and especially in summer, when fresh labile organic matter is deposited at the sediment surface. Hypoxic conditions, starting at the end of the spring prevent benthic macrofauna from burying fresh organic matter within the sediment, therefore limiting substrate availability in the deeper sediment layers (2–20 cm). This lack of organic matter entrainment to the sediment interior may have a profound effect on the onset and maintenance of hypoxia and acidification in bottom waters. Indeed, aerobic processes at the SWI consume oxygen and produce DIC without alkalinity, which favor hypoxia and acidifies the bottom waters without any "temporary storage" typically associated with mixing by bioturbation in the deeper sediment layers and slow diffusion in the pore waters. In addition, alkalinity-producing processes linked to anoxic diagenesis (production and burial of FeS) are absent in these hypoxic sediments, thus preventing mitigation of overlying water acidification.

DATA AVAILABILITY STATEMENT

The datasets presented in this study can be found in the SEANOE online repository: https://www.seanoe.org/data/00630/74215/.

AUTHOR CONTRIBUTIONS

CR and BL wrote the first draft of the manuscript. SO, BB, EM, JR, EE, AB, JB, MT, and CR participated to the cruise, collected the samples, and, with the addition of BL, performed the analysis. NR provided oxygen time series data. All authors contributed to the manuscript by text writing, editions and comments.

FUNDING

Funding was provided by INSU-EC2CO/LEFE MissRhoDia project to the French groups (LSCE and BIAF), NSF to the Georgia Tech group (OCE-1438648), National Academies of Science, Engineering, and Medicine Gulf Research Program (Early Career Grant 2000007281) to JB, and the Chateaubriand Fellowship of the Office for Science and Technology of the Embassy of France in the United States (MOPGA program) awarded to SO, support from the United States National Oceanic and Atmospheric Administration (NA16OAR4320199) and the National Science Foundation (OCE-1559312) to NR.

ACKNOWLEDGMENTS

We would like to thank the captain and crew of the RV *Savannah* for their help with the operations at sea. We acknowledge the help

of L. Brethous, B. P. Fields, E. Buckley, and A. Stancil for the work at sea and further analysis in the laboratory. DIC and TA measurements in the water column were performed at SNAPO-CO2 in Paris (France). **Figure 7** was created using R software (R Core Team, 2017). This is LSCE contribution number 7501.

SUPPLEMENTARY MATERIAL

The Supplementary Material for this article can be found online at: https://www.frontiersin.org/articles/10.3389/fmars.2021.604330/full#supplementary-material

REFERENCES

Aller, R. C., Aller, J. Y., Zhu, Q., Heilbrun, C., Klingensmith, I., and Kaushik, A. (2019). Worm tubes as conduits for the electrogenic microbial grid in marine sediments. *Sci. Adv.* 5:eaaw3651. doi: 10.1126/sciadv.aaw3651

Amon, R. M. W., and Benner, R. (1998). Seasonal patterns of bacterial abundance and production in the Mississippi River plume and their importance for the fate of enhanced primary production. *Microb. Ecol.* 35, 289–300. doi: 10.1007/s002489900084

Baustian, M. M., and Rabalais, N. N. (2009). Seasonal composition of benthic macroinfauna exposed to hypoxia in the northern Gulf of Mexico. *Est. Coast* 32, 975–983. doi: 10.1007/s12237-009-9187-3

Beckler, J. S., Nuzzio, D. B., and Taillefert, M. (2014). Development of single-step liquid chromatography methods with ultraviolet detection for the measurement of inorganic anions in marine waters. *Limnol. Oceanogr. Meth.* 12, 563–576. doi: 10.4319/lom.2014.12.563

Berelson, W., McManus, J., Severmann, S., and Rollin, N. (2019). Benthic fluxes from hypoxia-influenced Gulf of Mexico sediments: Impact on bottom water acidification. *Mar. Chem.* 209, 94–106. doi: 10.1016/j.marchem.2019.01.004

Berg, P., Risgaard-Petersen, N., and Rysgaard, S. (1998). Interpretation of measured concentration profiles in sediment pore water. *Lirnnol. Oceanogr.* 437, 1500–1510. doi: 10.4319/lo.1998.43.7.1500

Bianchi, S. T., DiMarco, S., Cowan, J. H. Jr., Hetland, R. D., Chapman, P., Day, J. W., et al. (2010). The science of hypoxia in the Northern Gulf of Mexico: A review. *Sci. Tot. Environ.* 408, 1471–1484. doi: 10.1016/j.scitotenv.2009.11.047

Bianchi, S. T., Goni, M. A., Allison, M. A., Chen, M. A., and McKee, B. A. (2014). "Sedimentary carbon dynamics of the Atchafalaya and Mississippi River delta system and associated margin," in *Biogeochemical dynamics at major river-coastal interfaces: linkages with global change*, eds S. T. Bianchi, M. A. Allison, and W. J. Cai (New York: Cambridge University Press), 473–502. doi: 10.1017/CBO9781139136853.024

Bianchi, T. S., Allison, M. A., Canuel, E. A., Corbett, D. R., McKee, B. A., Sampere, T. P., et al. (2006). Rapid Export of Organic Matter to the Mississippi Canyon. *Eos* 87, 565–573. doi: 10.1029/2006EO500002

Bianchi, T. S., Mitra, S., and McKee, B. A. (2002). Sources of terrestrially-derived organic carbon in lower Mississippi River and Louisiana shelf sediments: implications for differential sedimentation and transport at the coastal margin. *Mar. Chem.* 77, 211–223. doi: 10.1016/S0304-4203(01)00088-3

Breitburg, D., Levin, L. A., Oschlies, A., Grégoire, M., Chavez, F. P., Conley, D. J., et al. (2018). Declining oxygen in the global ocean and coastal waters. *Science* 359:aam7240. doi: 10.1126/science.aam7240

Brendel, P. J., and Luther, G. W. III (1995). Development of a gold amalgam voltammetric microelectrode for the determination of dissolved Fe, Mn, O2, and S(-II) in porewaters of marine and freshwater sediments. *Environ. Sci. Tech.* 29, 751–761. doi: 10.1021/es00003a024

Briggs, K. B., Hartmann, V. A., Yeager, K. M., Shivarudrappa, S., Diaz, R. J., Osterman, L. E., et al. (2015). Influence of hypoxia on biogenic structure in sediments on the Louisiana continental shelf. *Estuar. Coast. Shelf Sci.* 164:147e160. doi: 10.1016/j.ecss.2015.07.019

Broecker, W. S., and Peng, T. H. (1974). Gas exchange rates between air and sea. *Tellus* 26, 21–35. doi: 10.3402/tellusa.v26i1-2.9733

Cai, W.-J., Hu, X., Huang, W.-J., Murrell, M. C., Lehrter, J. C., Lohrenz, S. E., et al. (2011). Acidification of subsurface coastal waters enhanced by eutrophication. *Nat. Geosci.* 4, 766–770. doi: 10.1038/ngeo1297

Canfield, D. E., Jorgensen, B. B., Fossing, H., Glud, R., Gundersen, J., Ramsing, N. B., et al. (1993). Pathways of organic carbon oxidation in three continental margin sediments. *Mar. Geol.* 113, 27–40. doi: 10.1016/0025-3227(93)90147-N

Capet, A., Cook, P., Garcia-Robledo, E., Hoogakker, B., Paulmier, A., Rabouille, C., et al. (2020). Facing Marine Deoxygenation. *Front. Mar. Sci.* 7:46. doi: 10.3389/fmars.2020.00046

Cathalot, C., Rabouille, C., Pastor, L., Deflandre, B., Viollier, E., Buscail, R., et al. (2010). Temporal variability of carbon recycling in coastal sediments influenced by rivers: assessing the impact of flood inputs in the Rhone River prodelta. *Biogeosciences* 7, 1187–1205. doi: 10.5194/bg-7-1187-2010

Cesbron, F., Metzger, E., Launeau, P., Deflandre, B., Delgard, M.-L., Thibault, et al. (2014). Simultaneous 2D Imaging of Dissolved Iron and Reactive Phosphorus in Sediment Porewaters by Thin-Film and Hyperspectral Methods. *Environ. Sci. Technol.* 48, 2816–2826. doi: 10.1021/es404724r

Chin-Leo, G., and Benner, R. (1992). Enhanced bacterioplankton production and respiration at intermediate salinities in the Mississippi River plume. *Mar. Ecol. Prog. Ser.* 82, 87–103. doi: 10.3354/meps087087

Clayton, T. D., and Byrne, R. H. (1993). Spectrophotometric seawater pH measurements: total hydrogen ion concentration scale calibration of m-cresol purple and at-sea results. *Deep Sea Res.* 40, 2115–2129. doi: 10.1016/0967-0637(93)90048-8

Corbett, D. R., Dail, M., and McKee, B. A. (2007). High-frequency time-series of the dynamic sedimentation processes on the western shelf of the Mississippi River Delta. *Contin. Shelf Res.* 27, 1600–1615. doi: 10.1016/j.csr.2007.01.025

Corbett, D. R., McKee, B. A., and Allison, M. (2006). Nature of decadal-scale sediment accumulation on the western shelf of the Mississippi River delta. *Continent. Shelf Res.* 26, 2125–2140. doi: 10.1016/j.csr.2006.07.012

Corbett, D. R., McKee, B. A., and Duncan, D. (2004). An evaluation of mobile mud dynamics in the Mississippi River deltaic region. *Mar. Geol.* 209, 91–112. doi: 10.1016/j.margeo.2004.05.028

Dagg, M. J., Bianchi, T. S., McKee, B. A., and Powell, R. (2008). Fates of dissolved and particulate materials from the Mississippi river immediately after discharge into the northern Gulf of Mexico, USA, during a period of low wind stress. *Contin. Shelf Res.* 28, 1443–1450. doi: 10.1016/j.csr.2006.12.009

Devereux, R., Lehrter, J. C., Beddick, D. L. J., Yates, D. F., and Jarvis, B. M. (2015). Manganese, iron,and sulfur cycling in Louisiana continental shelf sediments. *Contin. Shelf Res.* 99, 46–56. doi: 10.1016/j.csr.2015.03.008

Devereux, R., Lehrter, J., Cicchetti, G., Beddick, D. L. J., Yates, D. F., Jarvis, B. M., et al. (2019). Spatially variable bioturbation and physical mixing drive the sedimentary biogeochemical seascape in the Louisiana continental shelf hypoxic zone. *Biogeochem* 143, 151–169. doi: 10.1007/s10533-019-00539-8

Diaz, R. J., and Rosenberg, R. (2008). Spreading Dead Zones and Consequences for Marine Ecosystems. *Science* 321, 926–929. doi: 10.1126/science.1156401

Dickson, A. G., Sabine, C. L., and Christian, J. R. (Eds.) (2007). *Guide to Best Practices for Ocean CO_2 Measurements*. Sidney, BC: PICES Special Publication.

DOE (1994). "Handbook of methods for the analysis of the various parameters of the carbon dioxide system in sea water.Version 2," in *ORNL/CDIAC-74*, eds A. G. Dickson and C. Goyet (Washington, D.C: DOE).

Dortch, Q., Rabalais, N. N., Turner, R. E., and Rowe, G. T. (1994). Respiration rates and hypoxia on the Louisiana shelf. *Estuaries* 17, 862–872. doi: 10.2307/1352754

Feist, T. J., Pauer, J. J., Melendez, W., Lehrter, J., DePetro, P. A., Rygwelski, K. R., et al. (2016). Modeling the relative importance of nutrient and carbon loads, boundary fluxes, and sediment fluxes on Gulf of Mexico hypoxia. *Envir. Sci. Technol.* 50, 8713–8721. doi: 10.1021/acs.est.6b01684

Fennel, K., and Testa, J. M. (2019). Biogeochemical controls on coastal hypoxia. *Annu. Rev. Mar. Sci.* 11, 4.1–4.26. doi: 10.1146/annurev-marine-010318-095138

Fennel, K., Hu, J. T., Laurent, A., Marta-Almeida, M., and Hetland, R. D. (2013). Sensitivity of hypoxia predictions for the northern Gulf of Mexico to sediment oxygen consumption and model nesting. *J. Geophys. Res.* 118, 990–1002. doi: 10.1002/jgrc.20077

Gilbert, D., Rabalais, N. N., Díaz, R. J., and Zhang, J. (2010). Evidence for greater oxygen decline rates in the coastal ocean than in the open ocean. *Biogeosciences* 7, 2283–2296. doi: 10.5194/bg-7-2283-2010

Glud, R. N. (2008). Oxygen dynamics of marine sediments. *Mar. Biol. Res.* 4, 243–289. doi: 10.1080/17451000801888726

Glud, R. N., Holby, O., Hoffmann, F., and Canfield, D. E. (1998). Benthic mineralization and exchange in Arctic sediments (Svalbard, Norway). *Mar. Ecol. Prog. Ser.* 173, 237–251. doi: 10.3354/meps173237

Goñi, M. A., Ruttenberg, K. C., and Eglinton T. I. (1997). Sources and contribution of terrigenous organic carbon to surface sediments in the Gulf of Mexico, *Nature* 389, 275–278. doi: 10.1038/38477

Gordon, E. S., and Goni, M. A. (2004). Controls on the distribution and accumulation of terrigenous organic matter in sediments from the Mississippi and Atchafalaya River margin. *Mar. Chem.* 92, 331–352. doi: 10.1016/j.marchem.2004.06.035

Hall, P. J., and Aller, R. C. (1992). Rapid, small-volume, flow injection analysis for SCO2, and NH4+ in marine and freshwaters. *Limnol. Oceanogr.* 37, 1113–1119. doi: 10.4319/lo.1992.37.5.1113

Hetland, R. D., and DiMarco, S. F. (2008). How does the character of oxygen demand control the structure of hypoxia on the Texas-Louisiana continental shelf? *J. Mar. Syst.* 70, 49–62. doi: 10.1016/j.jmarsys.2007.1003.1002

Hu, X. P., and Cai, W. J. (2011). An assessment of ocean margin anaerobic processes on oceanic alkalinity budget. *Glob. Biogeochem. Cycles* 21:GB3003. doi: 10.1029/2010GB003859

Hu, X. P., Li, Q., Huang, W. J., Chen, B. S., Cai, W. J., Rabalais, N. N., et al. (2017). Effects of eutrophication and benthic respiration on water column carbonate chemistry in a traditional hypoxic zone in the northern Gulf of Mexico. *Mar. Chem.* 194, 33–42. doi: 10.1016/j.marchem.2017.04.004

Jézéquel, D., Brayner, R., Metzger, E., Viollier, E., Prévot, F., and Fiévet, F. (2007). Two-dimensional determination of dissolved iron and sulfur species in marine sediment pore-waters by thin-film based imaging. Thau lagoon (France). *Estuar. Coast. Shelf Sci.* 72, 420–431. doi: 10.1016/j.ecss.2006.11.031

Krumins, V., Gehlen, M., Arndt, S., Van Cappellen, P., and Regnier, P. A. G. (2013). Dissolved inorganic carbon and alkalinity fluxes from coastal marine sediments: model estimates for different shelf environments and sensitivity to global change. *Biogeosci* 10, 371–398. doi: 10.5194/bg-10-371-2013

Laurent, A., Fennel, K., Cai, W. J., Huang, W. J., Barbero, L., and Wanninkhof, R. (2017). Eutrophication-induced acidification of coastal waters in the northern Gulf of Mexico: Insights into origin and processes from a coupled physical biogeochemical model. *Geophys. Res. Let.* 44:2016GL071881. doi: 10.1002/2016GL071881

Laurent, A., Fennel, K., Wilson, R., Lehrter, J., and Devereux, R. (2016). Parameterization of biogeochemical sediment–water fluxes using in situ measurements and a diagenetic model. *Depart. Oceanogr.* 13, 77–94. doi: 0.5194/bg-13-77-2016

Lehrter, J. C., Beddick, D. L. J., Devereux, R., Yates, D. F., and Murrell, M. C. (2012). Sediment-water fluxes of dissolved inorganic carbon, O2, nutrients, and N2 from the hypoxic region of the Louisiana continental shelf. *Biogeochem* 109, 233–252. doi: 10.1007/s10533-011-9623-x

Levin, L. A., Ekau, W., Gooday, A. J., Jorissen, F. J., Middelburg, J. J., Naqvi, W. A., et al. (2009). Effects of natural and human-induced hypoxia on coastal benthos. *Biogeosc* 6, 2063–2098. doi: 10.5194/bg-6-2063-2009

Lin, S., and Morse, J. W. (1991). Sulfate reduction and iron sulfide mineral formation in Gulf of Mexico anoxic sediments. *Amer. J. Sci.* 201, 55–89. doi: 10.2475/ajs.291.1.55

Lohrenz, S. E., Redalje, D. G., Cai, W. J., Acker, J., and Dagg, M. J. (2008). A retrospective analysis of nutrients and phytoplankton productivity in the Mississippi River plume. *Contin. Shelf Res.* 28, 1466–1475. doi: 10.1016/j.csr.2007.06.019

Lueker, T. J., Dickson, A. G., and Keeling, C. D. (2000). Ocean pCO2 calculated from dissolved inorganic carbon, alkalinity, and equations for K1 and K2: validation based on laboratory measurements of CO2 in gas and seawater at equilibrium. *Mar. Chem.* 70, 105–119. doi: 10.1016/S0304-4203(00)00022-0

Luther, G. W., Glazer, B., Ma, S., Trouwborst, R., Moore, T., Metzger, E., et al. (2008). Use of voltammetric solid-state (micro)electrodes for studying biogeochemical processes: Laboratory measurements to real time measurements with an in situ electrochemical analyzer (ISEA). *Mar. Chem.* 108, 221–235. doi: 10.1016/j.marchem.2007.03.002

Madison, A. S., Tebo, B. M., and Luther, G. W. III (2011). Simultaneous determination of soluble manganese(III), manganese(II) and total manganese in natural (pore)waters. *Talanta* 84, 374–381. doi: 10.1016/j.talanta.2011.01.025

McKee, B. A., Aller, R. C., Allison, M. A., Bianchi, T. S., and Kineke, G. C. (2004). Transport and transformation of dissolved and particulate materials on continental margins influenced by major rivers: benthic boundary layer and seabed processes. *Contin. Shelf Res.* 24, 899–926. doi: 10.1016/j.csr.2004.02.009

Meiggs, D., and Taillefert, M. (2011). The effect of riverine discharge on biogeochemical processes in estuarine sediments. *Limnol. Oceanogr.* 56, 1797–1810. doi: 10.4319/lo.2011.56.5.1797

Metzger, E., Langlet, D., Viollier, E., Koron, N., Riedel, B., Stachowitsch, M., et al. (2014). Artificially induced migration of redox layers in a coastal sediment from the Northern Adriatic. *Biogeosc* 11, 2211–2224. doi: 10.5194/bg-11-2211-2014

Middelburg, J. J., and Levin, L. A. (2009). Coastal hypoxia and sediment biogeochemistry. *Biogeosci* 6, 1273–1293. doi: 10.5194/bg-6-1273-2009

Moriarty, J. M., Harris, C. K., Friedrichs, M. A. M., Fennel, K., and Xu, K. H. (2018). Impact of seabed resuspension on oxygen and nitrogen dynamics in the northern Gulf of Mexico: A numerical modeling study. *J. Geophys. Res.* 123, 7237–7263. doi: 10.1029/2018JC013950

Morse, J. W., and Eldridge, P. M. (2007). A non-steady state diagenetic model for changes in sediment biogeochemistry in response to seasonally hypoxic/anoxic conditions in the "dead zone" of the Louisiana shelf. *Mar. Chem.* 106, 239–255. doi: 10.1016/j.marchem.2006.02.003

Morse, J. W., and Rowe, G. T. (1999). Benthic biogeochemistry beneath the Mississippi river plume. *Estuaries* 22, 206–214. doi: 10.2307/1352977

Murphy, J., and Riley, J. P. (1962). A modified single solution method for the determination of phosphate in natural waters. *Analyt. Chim. Acta* 27, 31–36. doi: 10.1016/S0003-2670(00)88444-5

Murrell, M. C., Aukamp, J. R., Beddick, D. L. J., Devereux, R., Greene, R. M., Hagy, J. D. I., et al. (2013). *Gulf of Mexico hypoxia research program data report: 2002-2007*. Washington, DC: U. S. Environmental Protection Agency.

Murrell, M., and Lehrter, J. (2011). Sediment and lower water column oxygen consumption in the seasonally hypoxic region of the Louisiana continental shelf. *Estuar. Coasts* 34, 912–924. doi: 10.1007/s12237-010-9351-9

Pörtner, H.-O., Roberts, D. C., Masson-Delmotte, V., Zhai, P., Tignor, M., Poloczanska, E., et al., (eds.) (In press). *IPCC Special Report on the Ocean and Cryosphere in a Changing Climate*.

Orr, J. C., Epitalon, J. M., and Gattuso, J. P. (2015). Comparison of ten packages that compute ocean carbonate chemistry. *Biogeosciences* 12, 1483–1510. doi: 10.5194/bg-12-1483-2015

Orr, J. C., Fabry, V. J., Aumont, O., Bopp, L., Doney, S. C., Feely, R. A. et al. (2005). Anthropogenic ocean acidification over the twenty-first century and its impact on calcifying organisms. *Nature* 437, 681–686. doi: 10.1038/nature04095

Owings, S., Brethous, L., Eitel, E. M., Fields, B. P., Boever, A., Beckler, J., et al. (2021). Differential manganese and iron recycling and transport in continental margin sediments of the Northern Gulf of Mexico. *Mar. Chem.* 229:103908. doi: 10.1016/j.marchem.2020.103908

Pierrot, D., Lewis, E., and Wallace, D. W. R. (2006). *MS Excel Program Developed for CO2 System Calculations. . ORNL/CDIAC-105a*. Tennessee: Carbon Dioxide Information Analysis Center.

R Core Team (2017). *R: A Language and Environment for Statistical Computing*. Vienna: R Foundation for Statistical Computing. Available online at: http://www.R-project.org/

Rabalais, N. N., and Baustian, M. M. (2020). Historical shifts in benthic infaunal diversity in the northern Gulf of Mexico since the appearance of seasonally severe hypoxia. *Divers* 12:49. doi: 10.3390/d12020049

Rabalais, N. N., and Turner, R. E. (2019). Gulf of Mexico Hypoxia: Past, Present, and Future. *Limnol. Oceanogr. Bull.* 28, 117–124. doi: 10.1002/lob.10351

Rabalais, N. N., Cai, W. J., Cartensen, J., Conley, D. J., Fry, B., Hu, X., et al. (2014). Eutrophication-driven deoxygenation in the coastal ocean. *Oceanography* 27, 172–183. doi: 10.5670/oceanog.2014.21

Rabalais, N. N., Harper, D. E. J., and Turner, R. E. (2001a). "Responses of nekton and demersal and benthic fauna to decreasing oxygen concentrations," in *Coastal hypoxia: consequences for living resources and ecosystems. Coastal and estuarine studies*, eds N. N. Rabalais and R. E. Turner (Washington, D.C: American Geophysical Union), 115–128. doi: 10.1029/CE058p0115

Rabalais, N. N., Smith, L. E., Harper, D. E. J., and Justic, D. (2001b). "Effects of seasonal hypoxia on continental shelf benthos," in *Coastal hypoxia:*

consequences for living resources and ecosystems. Coastal and estuarine studies, eds N. N. Rabalais and R. E. Turner (Washington, D.C: American Geophysical Union), 211–240. doi: 10.1029/CE058p0211

Rabalais, N. N., Turner, R. E., and Wiseman, W. J. (2002). Gulf of Mexico hypoxia, a.k.a. "the dead zone". *Ann. Rev. Ecol. Syst.* 33, 235–263. doi: 10.1146/annurev.ecolsys.33.010802.150513

Rabalais, N. N., Turner, R. E., Sen Gupta, B. K., Boesch, D. F., Chapman, P., and Murrell, M. C. (2007). Hypoxia in the northern Gulf of Mexico: does the science support the plan to reduce, mitigate, and control hypoxia? *Estuar. Coast.* 30, 753–772. doi: 10.1007/BF02841332

Rabouille, C., and Gaillard, J. F. (1991). A coupled model representing the deep-sea organic carbon mineralization and oxygen-consumption in surficial sediments. *J. Geophys. Res. Oceans* 96, 2761–2776. doi: 10.1029/90jc02332

Rabouille, C., Conley, D. J., Dai, M. H., Cai, W. J., Chen, C. T. A., Lansard, B., et al. (2008). Comparison of hypoxia among four river-dominated ocean margins: The Changjiang (Yangtze), Mississippi, Pearl, and Rhone rivers. *Contin. Shelf Res.* 28, 1527–1537. doi: 10.1016/j.csr.2008.01.020

Rao, A. M. F., Malkin, S. Y., Montserrat, F., and Meysman, F. J. R. (2014). Alkalinity production in intertidal sands intensified by lugworm bioirrigation. *Estuar. Coast. Shelf Sci.* 148, 36–47. doi: 10.1016/j.ecss.2014.06.006

Rassmann, J., Eitel, E., Cathalot, C., Brandily, C., Lansard, B., Taillefert, M., et al. (2020). Benthic alkalinity and DIC fluxes in the Rhône River prodelta generated by decoupled aerobic and anaerobic processes. *Biogeosciences* 17, 13–33. doi: 10.5194/bg-17-13-2020

Rassmann, J., Lansard, B., Pozzato, L., and Rabouille, C. (2016). Carbonate chemistry in sediment porewaters of the Rhône River delta driven by early diagenesis (northwestern Mediterranean). *Biogeosciences* 13, 5379–5394. doi: 10.5194/bg-13-5379-2016

Redalje, D. G., Lohrenz, S. E., and Fahnenstiel, G. L. (1994). The relationship between primary production and the vertical export of particulate organic matter in a river-impacted coastal ecosystem. *Estuar* 17, 829–838. doi: 10.2307/1352751

Riedel, B., Pados, T., Pretterebner, K., Schiemer, L., Steckbauer, A., Haselmair, A., et al. (2014). Effect of hypoxia and anoxia on invertebrate behaviour: ecological perspectives from species to community level. *Biogeosc* 11, 1491–1518. doi: 10.5194/bg-11-1491-2014

Robertson, D., Welsh, D. T., and Teasdale, P. R. (2009). Investigating biogenic heterogeneity in coastal sediments with two-dimensional measurements of iron(II) and sulfide. *Environ. Chem.* 6, 60–69. doi: 10.1071/EN08059

Rowe, G. T., Kaegi, M. E. C., Morse, J. W., Boland, G. S., and Briones, E. G. E. (2002). Sediment community metabolism associated with continental shelf hypoxia, Northern Gulf of Mexico. *Estuaries* 25, 1097–1106. doi: 10.1007/BF02692207

Stookey, L. L. (1970). Ferrozine- A New Spectrophotometric Reagent for Iron. *Anal. Chem.* 42, 779–781. doi: 10.1021/ac60289a016

Strickland, J. D. H., and Parsons, T. R. (1972). *A practical handbook of sea-water analysis*. Ottawa: Fisheries Research Board of Canada, 167.

Taillefert, M., Bono, A. B., and Luther, G. W. (2000). Reactivity of Freshly Formed Fe(III) in Synthetic Solutions and (Pore)Waters: Voltammetric Evidence of an Aging Process. *Environ. Sci. Technol.* 34, 2169–2177. doi: 10.1021/es990120a

Theberge, S. M., and Luther, G. W. (1997). Determination of the Electrochemical Properties of a Soluble Aqueous FeS Species Present in Sulfidic Solutions. *Aquat. Geochem.* 3, 191–211. doi: 10.1023/A:1009648026806

Thibault de Chanvalon, A., Metzger, E., Mouret, A., Knoery, J., Geslin, E., et al. (2017). Two-dimensional mapping of iron release in marine sediments at submillimetre scale. *Mar. Chem.* 191, 34–49. doi: 10.1016/j.marchem.2016.04.003

Turner, R. E., Rabalais, N. N., and Justic, D. (2006). Predicting summer hypoxia in the northern Gulf of Mexico: Riverine N, P, and Si loading. *Mar. Poll. Bull.* 52, 139–148. doi: 10.1016/j.marpolbul.2005.08.012

Turner, R. E., Rabalais, N. N., and Justic, D. (2008). Gulf of Mexico hypoxia: Alternate states and a legacy. *Envir. Sci. Technol.* 42, 2323–2327. doi: 10.1021/es071617k

Uppström, L. R. (1974). The Boron/Chlorinity Ratio of Deep-Sea Water from the Pacific Ocean. *Deep Sea Res. Oceanogr.* 21, 161–162. doi: 10.1016/0011-7471(74)90074-6

Viollier, E., Inglett, P. W., Hunter, K., Roychoudhury, A. N., and Van Cappellen, P. (2000). The ferrozine method revisited: Fe(II)/Fe(III) determination in natural waters. *Appl. Geochem.* 15, 785–790. doi: 10.1016/S0883-2927(99)00097-9

Wang, H. J., Hu, X. P., Rabalais, N. N., and Brandes, J. (2018). Drivers of oxygen consumption in the northern Gulf of Mexico hypoxic waters—A stable carbon isotope perspective. *Geophys. Res. Let.* 45, 10528–10538. doi: 10.1029/2018GL078571

Waterson, E. J., and Canuel, E. A. (2008). Sources of sedimentary organic matter in the Mississippi River and adjacent Gulf of Mexico as revealed by lipid biomarker and 13CTOC analyses. *Org. Geochem.* 39, 422–439. doi: 10.1016/j.orggeochem.2008.01.011

Wiseman, W. J., Rabalais, N. N., Turner, R. E., Dinnel, S. P., and MacNaughton, A. (1997). Seasonal and interannual variability within the Louisiana coastal current: stratification and hypoxia. *J. Mar. Syst.* 12, 237–248. doi: 10.1016/S0924-7963(96)00100-5

Zhang, J., Gilbert, D., Gooday, A., Levin, L., Naqvi, S. W. A., Middelburg, J. J. et al. (2010). Natural and human-induced hypoxia and consequences for coastal areas: synthesis and future developmen. *Biogeosc* 7, 1443–1467. doi: 10.5194/bg-7-1443-2010

Conflict of Interest: The authors declare that the research was conducted in the absence of any commercial or financial relationships that could be construed as a potential conflict of interest.

Copyright © 2021 Rabouille, Lansard, Owings, Rabalais, Bombled, Metzger, Richirt, Eitel, Boever, Beckler and Taillefert. This is an open-access article distributed under the terms of the Creative Commons Attribution License (CC BY). The use, distribution or reproduction in other forums is permitted, provided the original author(s) and the copyright owner(s) are credited and that the original publication in this journal is cited, in accordance with accepted academic practice. No use, distribution or reproduction is permitted which does not comply with these terms.

frontiers in Marine Science

ORIGINAL RESEARCH
published: 15 May 2020
doi: 10.3389/fmars.2020.00324

Massive Methane Loss During Seasonal Hypoxia/Anoxia in the Nearshore Waters of Southeastern Arabian Sea

V. Sudheesh[1], G. V. M. Gupta[1] and S. W. A. Naqvi[2†]*

[1] Centre for Marine Living Resources and Ecology, Ministry of Earth Sciences, Kochi, India, [2] National Institute of Oceanography, Panaji, India

Repeat observations over the Kochi and Mangalore shelves of the southeastern Arabian Sea (SEAS) during April to December 2012 revealed substantial accumulation of methane (CH_4) in the nearshore waters (48.6 ± 34.4 nM) compared to the outer shelf (2.9 ± 0.7 nM). Sediment methanogenesis and estuarine discharge appear to be the major sources of CH_4 in the nearshore regions during non-upwelling period. But under oxygen deficient conditions that prevail during the upwelling period, extremely low concentrations of CH_4 in the nearshore anoxic region of Mangalore (14 ± 2 nM) compared to similar region of hypoxic Kochi shelf (35.5 ± 15.4 nM) have been observed. We propose that this is mainly due to its greater loss through anaerobic oxidation and in part by the reduced sedimentary inputs by weak bioturbation over Mangalore relative to Kochi. On an annual basis, SEAS is found to be a net source of CH_4 to the atmosphere with its efflux ranging from 0.03 to 170 μmol m^{-2} d^{-1} (21.9 ± 36.7 μmol m^{-2} d^{-1}). Following a zonal extrapolation approach, the estimated CH_4 efflux from the SEAS (7–14°N; 3.2 Gg y^{-1}) accounts for up to ∼16% of the total CH_4 emission from the Arabian Sea.

Keywords: methane, upwelling, coastal anoxia/hypoxia, anaerobic oxidation, bioturbation, methane flux

OPEN ACCESS

Edited by:
Xianghui Guo,
Xiamen University, China

Reviewed by:
Guiling Zhang,
Ocean University of China, China
Kunpeng Zang,
National Marine Environmental Monitoring Center, China

****Correspondence:***
G. V. M. Gupta
gvmgupta@gmail.com;
gvmgupta@cmlre.gov.in

†Present address:
S. W. A. Naqvi,
Council of Scientific and Industrial Research, New Delhi, India

Specialty section:
This article was submitted to Coastal Ocean Processes, a section of the journal Frontiers in Marine Science

Received: *07 January 2020*
Accepted: *21 April 2020*
Published: *15 May 2020*

Citation:
Sudheesh V, Gupta GVM and Naqvi SWA (2020) Massive Methane Loss During Seasonal Hypoxia/Anoxia in the Nearshore Waters of Southeastern Arabian Sea. Front. Mar. Sci. 7:324. doi: 10.3389/fmars.2020.00324

INTRODUCTION

Coastal seas, important sites of methane (CH_4) production, are estimated to contribute up to ∼20% emission of all greenhouse gases (IPCC, 2013). Despite their relatively small geographical coverage (16%), the shelf region accounts for 75% of the oceanic CH_4 emission (Bange et al., 1994). Tropical oceans are found to be a net source of CH_4 although their effective contribution to the global CH_4 budget is relatively small (<4%; Reeburgh, 2007; Kirschke et al., 2013). Marine CH_4 is produced under anaerobic conditions in sediments, interior of suspended particles, and in the guts of zooplankton (de Angelis and Lee, 1994; Karl and Tilbrook, 1994; Boetius et al., 2000). CH_4 production in the coastal zones is linked to high phytoplankton biomass (Tilbrook and Karl, 1995; Oudot et al., 2002; Damm et al., 2008), its seepage from sea bed reserves (Borges et al., 2016) and sediment-water exchange is augmented by upwelling (Kock et al., 2008; Brown et al., 2014). CH_4 is also likely to be produced by aerobic decomposition of methylphosphonate releasing phosphorus in phosphate poor environments (Karl et al., 2008). Inland waters and estuaries also contribute to high

coastal CH_4 concentrations (Jayakumar et al., 2001; Rao and Sarma, 2016, 2017; Upstill-Goddard and Barnes, 2016).

CH_4 emission from coastal zones exhibit large variability due to variations in primary production, decomposition of organic matter, upwelling intensity, etc. (Rehder et al., 2002; Kock et al., 2008). A good example for this is the eastern Arabian Sea (EAS) coastal (alias west coast of India) upwelling system, one of the most intense oxygen deficient shelf systems of world's ocean, where the magnitude of CH_4 emissions has not been well quantified. The previous studies on CH_4 from the EAS reported its high surface supersaturation (89–2521%) and several fold higher effluxes compared to oceanic averages (Owens et al., 1991; Patra et al., 1998; Jayakumar et al., 2001; Shirodkar et al., 2018). A significant part of its supersaturation is apparently contributed by the release from sediments along the Indian continental shelf (Karisiddaiah and Veerayya, 1994, 1996). Bange et al. (1998) reported near saturation of CH_4 in the central Arabian Sea (103–107%) and supersaturation in the coastal upwelling off Oman (up to 156%) and in an upwelling filament (up to 145%). On the other hand, highly productive regions of west coast of India, with one of the largest low-oxygen zone in the world (Naqvi et al., 2006, 2009), favor *in situ* production of CH_4 in the water column (Owens et al., 1991; Jayakumar et al., 2001).

Most of the CH_4 data from the Arabian Sea (AS) correspond to offshore regions and very few datasets are available from the coastal regions. Patra et al. (1998) and Jayakumar et al. (2001) have reported considerable spatial and temporal variation in CH_4 distribution and fluxes along the EAS, with highest concentration of ∼24 nM during the late summer monsoon. Naqvi et al. (2005, 2010) have reviewed the importance and cycling of CH_4 mostly based on the data generated during the Arabian Sea Process Study (1992–1997). They have reported that the coastal wetlands along the west coast of India potentially contribute CH_4 to the nearby coastal regions. Recently, Shirodkar et al. (2018) reported moderate accumulation of CH_4 under oxygen deficient conditions over the EAS shelf during the late summer monsoon. Most of the studies on CH_4 cycling along the EAS shelf were based on the observations from its central region where intense oxygen deficiency (anoxic/suphidic) prevailed seasonally. Although strong upwelling also occurs over the southeastern Arabian Sea (SEAS), the existence of both anoxic/sulphidic and hypoxic conditions (Gupta et al., 2016; Sudheesh et al., 2016) makes this region different. The present study examined the CH_4 distribution and its emissions from the water column to evaluate the influence of upwelling and estuarine contribution over the SEAS shelf. Accordingly, the study focused on (i) factors influencing the distribution and variability of CH_4 concentrations, (ii) role of deoxygenation and macrofauna on CH_4 concentrations, and (ii) its fluxes from the SEAS shelf.

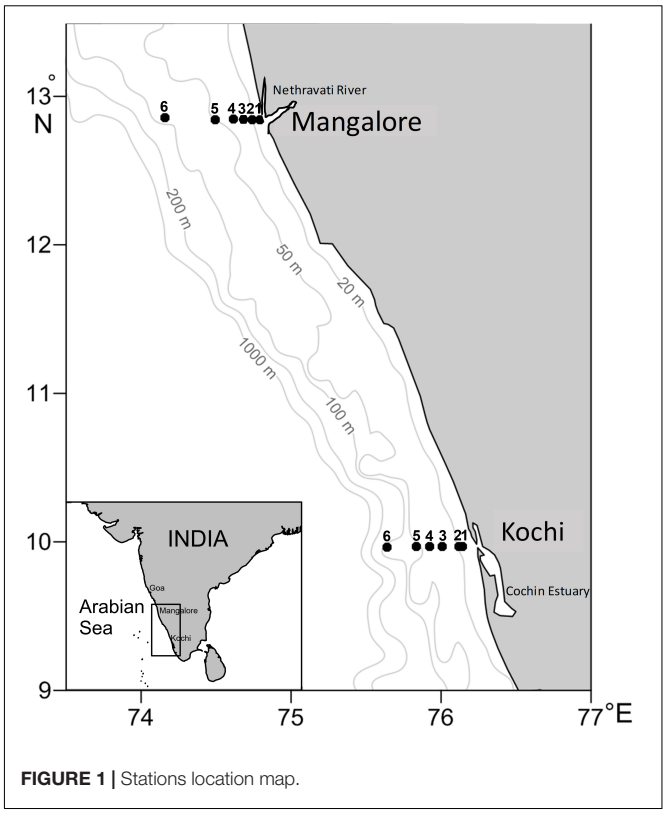


FIGURE 1 | Stations location map.

MATERIALS AND METHODS

Study Area

The present study focuses on the SEAS, between ∼7° and 14°N (**Figure 1**). The biogeochemistry of the SEAS is closely linked to the seasonally changing coastal currents by northward and southward flowing West India Coastal Current (WICC) during winter monsoon (WM) and summer monsoon (SM), respectively (Shankar et al., 2002; Amol et al., 2018). The transition seasons viz. spring inter-monsoon (SIM) and fall inter-monsoon (FIM) exhibit mixed signals between SM and WM (Shankar et al., 2002). The SEAS is largely impacted by monsoonal forcing on the mixed layer variations and nutrient cycling. The seasonal reversal of surface circulation enables the southward transport of high salinity waters from the northern Arabian Sea during SM, and northward transport of low salinity waters during WM. The oxygen minimum zone (OMZ; DO < 20 μM) in the AS is among the largest in the world and its advection onto the continental shelf during SM results in severe coastal hypoxia causing drastic changes in the biogeochemical properties including the emission of greenhouse gases (Naqvi et al., 2000; Naqvi and Jayakumar, 2000; Gupta et al., 2016; Sudheesh et al., 2016, 2017). Many small rivers like Mandovi and Zuari in Goa, Netravati in Mangalore flow across the coastal plain and drain into the northern part of SEAS. Cochin (Kochi) estuary (CE), the largest estuarine system of the southwest coast of India, debouch freshwater into the southern part of SEAS, and its annual mean discharge is much higher (12.33 km^3) compared to other major estuaries like Zuari (3.25 km^3), Mandovi (3.31 km^3) and Netravati (11.06 km^3) of this region (Krishna et al., 2016). The CE, one of the largest estuarine systems along the southwest coast of India, is a highly heterotrophic system impacted with increased anthropogenic activities (Thottathil et al., 2008; Gupta et al., 2009) and opens directly at the present study site. Recent studies

have, however, shown that the CE is acting as heavy sink zone due to high turnover rates of nitrogen, hence its export impact on coastal biogeochemistry is limited mostly to the nearshore region (Bhavya et al., 2016, 2017, 2018; Gupta et al., 2016). During the SM upwelling, shelf waters of southern SEAS experience hypoxia but anoxic conditions prevail both in the water column and sediments of the northern SEAS, triggering varying degree of denitrification over these shelves (Sudheesh et al., 2016).

Sample Collection and Analysis

Repeat observations in the shelf waters off Kochi (~10°N), SEAS were conducted from April to December 2012 (7 times) onboard FORV *Sagar Sampada* covering four seasons viz. spring inter-monsoon (SIM: April), summer monsoon (SM: June-September), fall inter-monsoon (FIM: October), and winter monsoon (WM: November-December). Samples were also collected from a nearby transect off Mangalore (12.8°N) during SIM (April), SM (September) and WM (December) to compare CH_4 dynamics in the two shelf regions. Along both transects, six stations each were occupied at water depths of 13, 20, 30, 40, 50, and 100 m (**Figure 1**). Both transects can be classified into four zones *viz.* nearshore (station 1), inner shelf (stations 2 and 3), mid-shelf (stations 4 and 5), and outer shelf (station 6).

Temperature and salinity profiles were recorded using Sea-Bird CTD profiler (911 plus). Water samples were collected from different depths using Niskin samplers (mounted to CTD rosette for coastal stations). Samples for dissolved oxygen (DO) were collected in 60 ml glass bottles. 0.5 ml each of Winkler reagent was added to the sample to fix DO. After acidification the liberated iodine was titrated against 0.001 N sodium thiosulphate using starch-based visual end point detection (Grasshoff et al., 1999). The small amount of DO carried by the reagents was not subtracted and sodium azide was not used to prevent nitrite interference in the Winkler method. The detection limit is ~2 μM. Samples for nitrate (NO_3^-) and nitrite (NO_2^-) were analyzed spectrophotometrically (Thermo Evolution 201) within few hours of collection following standard procedures (Grasshoff et al., 1999). The analytical precision, expressed as standard deviation based on replicate analyses, was ± 0.01 and ± 0.05 μM for NO_2^- and NO_3^-, respectively. Samples (2 L) for chlorophyll (Chl*a*) estimation were filtered onboard through Whatman 47 mm GF/F filter (0.7 μm) under gentle vacuum (<50 mm Hg) and stored at −20°C until analysis. Chl*a* on the filters were extracted with 90% acetone at 4°C in the dark for 12 h and measured fluorometrically (Joint Global Ocean Flux Study, 1994). Samples for particulate organic carbon (POC) were filtered through pre-combusted (4 h at 450°C) 47 mm Whatman GF/F filters and stored at −20°C until analysis. The samples were dried at 40°C overnight, fumigated with HCl in a desiccator for 6 h to remove the inorganic carbon, again dried overnight and analyzed using CHN analyser (Flash EA 2000, Thermo, United States).

Water samples for CH_4 and nitrous oxide (N_2O) were collected in 60 ml glass bottles immediately following the sampling of DO. Samples were poisoned using saturated mercuric chloride (0.5% v/v) to arrest the microbial activity. The neck of the bottles was sealed using parafilm and samples were kept in dark until analysis. Dissolved CH_4 and N_2O were analyzed by multiple phase equilibration technique (McAuliffe, 1971). The details of N_2O analysis were already described by Sudheesh et al. (2016). Briefly, 25 ml of sample was equilibrated with an equal volume of ultrapure helium in a gas-tight syringe by vigorous shaking at room temperature for 5 min. The headspace gas was then injected through a 5 ml sampling loop into a gas chromatograph (Shimadzu) equipped with a Flame Ionization Detector for CH_4 and ^{63}Ni Electron Capture Detector for N_2O. The separation was achieved over a stainless steel column (1.8 m length and 2 mm ID) packed with molecular sieve 5A (80/100 mesh, Toshvin) maintained at a temperature of 60°C (40°C for N_2O). The instrument was calibrated by several dilutions of CH_4 standard (Scotty II Analyzed Gases) procured from Supelco Inc., United States. All the carrier gases and combustion gases used in the analysis were of ultra-pure grade. Air samples were frequently run to monitor instrument response, which was quite linear within the range of concentrations encountered during the course of this study.

Equilibrium solubility of CH_4 in the surface waters at the observed temperature and salinity was calculated according to Wiesenburg and Guinasso (1979) using an average atmospheric CH_4 mole fraction of 2.03 ppm as reported recently by Rao and Sarma (2017) for the east coast of India.

The percentage saturation of CH_4 was calculated as,

$$\mathrm{CH_4\ saturation} = (\mathrm{C_w}/\mathrm{C_a}) \times 100$$

where, C_w is the measured concentration of dissolved CH_4 and C_a is the equilibrium concentration in seawater.

The sea-air exchange flux density was computed from

$$F = k(C_w - C_a)$$

where, k (cm h^{-1}) is the gas exchange velocity derived as a function of wind speed (U, m s^{-1}) according to Wanninkhof (2014):

$$k = 0.251 * U^2 * (Sc/660)^{-0.5}$$

Sc, the Schmidt number for CH_4, was calculated from temperature (t) according to the polynomial fit given by Wanninkhof (2014). Continuous wind speed recorded along the ship's cruise track using automated weather station installed onboard (10 m above sea surface) was used to obtain daily average wind speed and was used for sea-air flux calculations.

RESULTS AND DISCUSSION

Spatio-Temporal Variation in Shelf Hydrography, Dissolved Oxygen and Nutrients

The spatio-temporal variations in hydrographical properties, DO and nutrients observed during this study were presented earlier in detail by Gupta et al. (2016) and Sudheesh et al. (2016). Briefly, upwelling off Kochi was found to initiate at the shelf break during January-March, progressed steadily to mid shelf by April and to inner shelf by May. It intensified over the entire

shelf from June to August, began to retreat rapidly in September and completely disappeared by October. Under intense solar radiation, sea surface temperature (SST) showed a maximum (>30°C) in April. By May, SST over the inner shelf dropped by 2.8–3.4°C (**Table 1**) due to upwelling and the cooling trend continued till the SM peaked in August. Thereafter, with the withdrawal of upwelling, SST again increased till December (**Figure 2A**). The mixed layer depth (MLD, defined as 0.2 kg m^{-3} density difference from surface) was thin (∼20 m) during SM and thick (∼50 m) over the outer shelf during WM. During SM, the influence of fresh water could be noticed from the sea surface salinity (SSS) which dropped by about 1.5–2.0 during April-June (**Table 1**), and varied between 33.8 (July) and 31.65 (September).

Like Kochi, coastal waters off Mangalore also exhibited clear seasonality in hydrographical properties. Surface waters were warm in April (>30°C) and significantly cooler in September (<27°C, **Figure 3A**) due to strong upwelling. Thereafter, SST again increased by December (>29°C). The depth of 26°C isotherm (D_{26}), which is used to track the progression of upwelling, shoaled from ∼70 m to <10 m between April and September off Mangalore whereas the same shoaled only up to 20 m off Kochi. This indicates a more vigorous upwelling over the Mangalore shelf during September (late SM) when this process was already waning off Kochi. Strong stratification prevailed in September with low salinity waters (29–33) occupying the upper 5 m of the water column up to mid-shelf off Mangalore due to the SM runoff (**Figure 3B**). Such an intense upwelling and runoff during the SM led to much stronger thermohaline stratification off Mangalore relative to off Kochi.

With the advent of upwelling, the Kochi shelf experienced oxygen depletion by June and the intense hypoxic conditions in subsurface waters persisted in July (**Figures 2**, **4**; Sudheesh et al., 2016). Between April and June, the water column below 30 m turned intensely hypoxic (DO < 50 μM) and the euphotic zone was enriched with nutrients (NO_3^-: 8 ± 7 μM; NO_2^-: 0.7 ± 0.9 μM) (see Supplementary Figures S1–S5 of Gupta et al., 2016). The concentration of DO decreased up to 7 μM in bottom waters and NO_2^- concentration reached a maximum of 3.2 μM in June due to possible sedimentary denitrification off Kochi. Relative to Kochi, the more sustained and intense upwelling of suboxic/anoxic waters over the Mangalore shelf resulted in bottom water anoxia during September (**Figures 2**, **3**). The resultant intense reducing conditions in the nearshore bottom waters and sediments were manifested by the occurrence of denitrification and sulfate reduction (Sudheesh et al., 2016). Intense H_2S smell was noticed from the bottom waters and surface sediments up to its inner shelf during this period, though its concentration was not measured. But Naqvi et al. (2009) have reported build-up of H_2S as high as 15.4 μM in these anoxic shallow regions during September. The near-absence of transient reduced forms like NO_2^- and N_2O in the nearshore waters off Mangalore indicated complete denitrification to molecular N_2 (Sudheesh et al., 2016).

CH_4 Distribution

Dissolved CH_4 concentrations over the Kochi (**Figure 2D**) and Mangalore (**Figure 3D**) shelves were generally in excess of saturation values with a gradual decrease from the inner shelf toward the outer shelf. Over the annual cycle, CH_4 concentrations off Kochi ranged from 10.6 to 152 nM (52.5 ± 34.3 nM) in the nearshore, from 2.3 to 23.6 nM (7.6 ± 5.0 nM) over the inner shelf, from 2.1 to 13.4 nM (3.5 ± 1.8 nM) over the mid-shelf and from 2.1 to 5.0 nM (3.0 ± 0.7 nM) over the outer shelf. Similarly, CH_4 concentration off Mangalore varied from 8.9 to 133 nM (39.5 ± 34.2 nM), from 5 to 17 nM (10.0 ± 3.4 nM), from 1.8 to 6.2 nM (3.0 ± 1.1 nM), and from 1.8 to 4.0 nM (2.6 ± 0.6 nM) for the nearshore, inner shelf, mid-shelf and outer shelf regions, respectively. Relatively high CH_4 concentrations were recorded in the mid-shelf and outer shelf regions during the peak SM upwelling (June-July), but the nearshore regions showed high concentrations during non-upwelling periods except in April off Mangalore. High tide conditions during the sampling time in April could have resulted in lower contribution of CH_4 from the adjoining Netravati estuary to the nearshore region off Mangalore.

Between April and September, when upwelling occurred over both the shelves, the cooler bottom waters (24–26°C) of the outer shelf characterized by somewhat elevated CH_4 concentrations (>3 nM) shoaled up from ∼80 to 20 m (**Figures 2D**, **3D**), but returned back following the retrieval of

TABLE 1 | Monthly variation in temperature, salinity, and CH_4 saturation and fluxes in the surface waters of SEAS.

S. No.	Month	Temperature (°C)	Salinity	CH_4 conc. (nM)	Saturation (%)	Air-sea flux (μmol m^{-2} d^{-1})
Kochi						
1	April	30.1–30.7	33.9–34.9	3.3–152.4	116–7456	0.5–170
2	May	26.7–29.6	34.5–35.1	–	–	–
3	June	26.0–27.3	32.9–34.6	4.2–22	195–1003	3.8–35.8
4	July	25.9–27.1	33.8–34.9	3.0–31.5	144–1432	2.2–66.7
5	September	25.9–27.4	31.6–34.0	3.2–50.4	150–2253	1.4–62.3
6	October	27.4–29.3	34.3–34.9	3.2–103	154–4918	1.4–120
7	November	29.5–30.2	33.0–34.7	2.1–87.3	101–4195	0.04–111.7
8	December	29.5–29.9	34.5–35.3	2.1–105	102–5135	0.1–115.1
Mangalore						
9	April	30.1–31.4	34.6–35.2	2.1–40.7	107–2055	0.2–32.2
10	September	26.8–27.5	27.1–33.1	2.1–14.9	101–660	0.1–20.9
11	December	29.3–29.9	34.6–35.2	2.2–133	106–6436	0.03–30.3

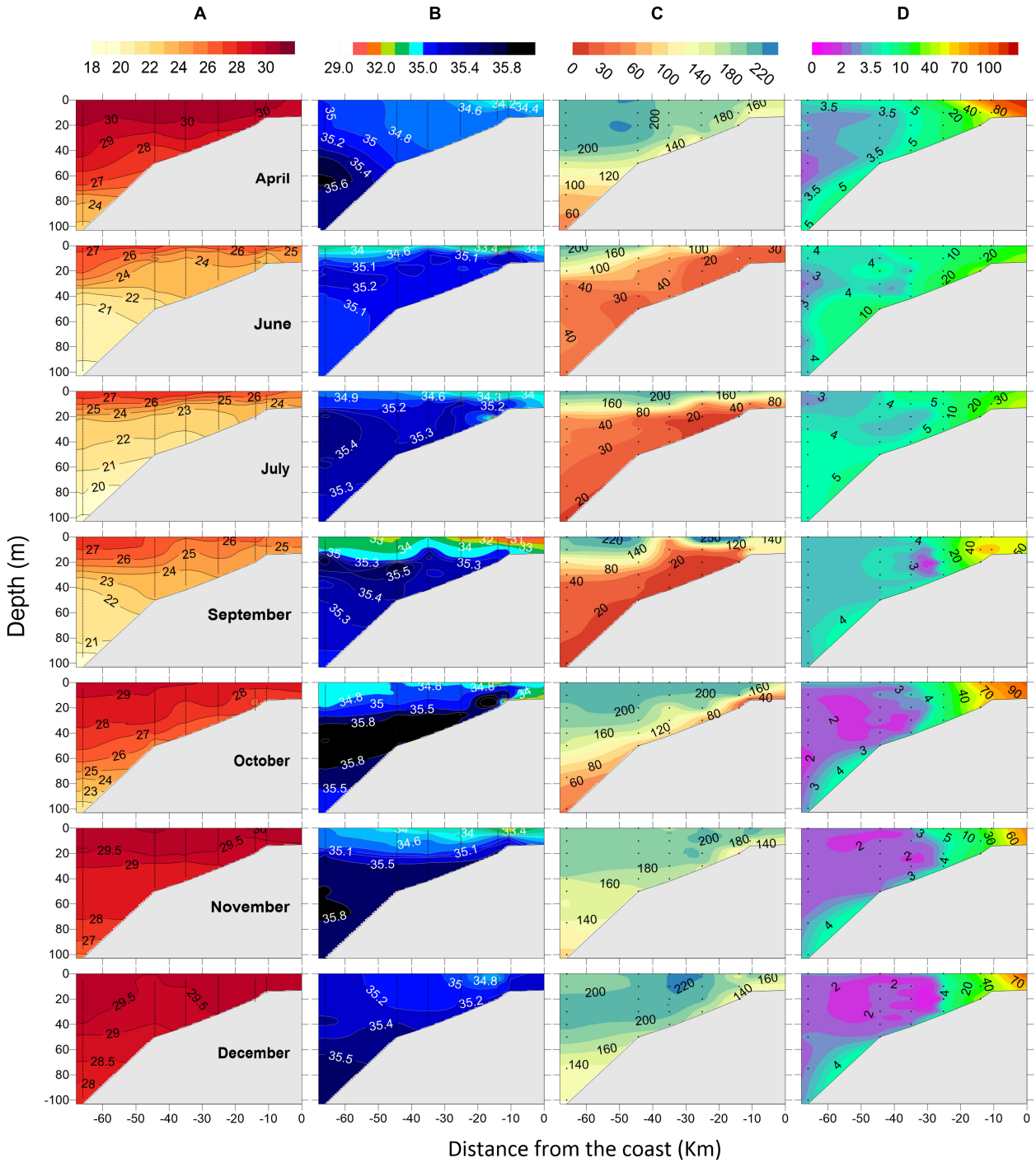


FIGURE 2 | Monthly distribution of **(A)** temperature (°C), **(B)** salinity, **(C)** dissolved oxygen (μM), and **(D)** methane (nM) off Kochi.

upwelling. This upliftment of subsurface waters led to relatively high CH_4 supersaturation in the upper water column of the outer shelf during the summer monsoon (148 ± 25%) than non-monsoon periods (120 ± 22%). This is consistent with the results of earlier studies that reported high CH_4 supersaturation (124–286%) during the summer monsoon due to offshore upliftment of subsurface CH_4 maxima (Owens et al., 1991; Bange et al., 1998; Patra et al., 1998; Upstill-Goddard et al., 1999; Shirodkar et al., 2018).

The CH_4 distribution generally showed a sharp decrease away from the coast (**Figures 2D**, **3D**). Our parallel studies (unpublished) from the Cochin estuary (CE, **Figure 1**), a

wetland eutrophic ecosystem, showed that CH_4 levels in its lower estuary were consistently high in April (SIM): 300 ± 246 nM, September (SM): 334 ± 277 nM and December (WM): 217 ± 93 nM (**Supplementary Figure S1**). Sediments of CE in these regions have been found to contain organic carbon in high concentrations (3–5%) associated with high clay fraction (60–90%) (Martin et al., 2011) and its high decomposition rate (Gupta et al., 2009; Rao and Sarma, 2016) results in substantially high benthic CH_4 fluxes to overlying water column (2.54–210 mg m^{-2} h^{-1}, Verma et al., 2002). CH_4 exported out of the CE through tidal exchange and runoff can influence its adjoining nearshore and inner shelf concentrations. This effect is significantly seen during dry non-upwelling periods, for example, in April and December when Kochi coastal waters are warm and saline (**Figure 2** and **Table 1**), its nearshore waters are observed with higher surface concentrations of CH_4 (152 and 105 nM) compared to bottom (110 and 70 nM) (**Figure 4**). In contrast, such estuarine effect is not significantly pronounced during monsoon as upwelling brings about 100 times lower CH_4 concentrations (3.5 ± 0.5 nM; **Figure 2**) compared to estuarine concentrations (334 ± 277 nM; **Supplementary Figure S1**), thereby the nearshore CH_4 concentrations (35 ± 21 nM; **Figure 4**) are significantly diluted by these two source waters. It must be noted that the significant thermohaline stratification prevailed during monsoon (**Figure 2**) will prevent the surfacing of upwelling waters. But there used to be spells of weak stratification when wind induced vertical mixing brings low CH_4 subsurface waters to surface.

Significant correlations of CH_4 with Chl*a* ($p < 0.001$) and POC ($p < 0.005$) in nearshore waters during non-upwelling periods (**Figure 5**) indicate that apart from the estuarine inputs high phytoplankton production can also lead to water column methanogenesis (Owens et al., 1991; Karl et al., 2008). It can also be argued that tidal export flux of nutrients, apart from CH_4, from the CE promotes phytoplankton production in the nearshore region; and this unrelated phenomenon is being "misrepresented" as a correlation between CH_4 and Chl*a*. The oligotrophic environments, as observed at mid and outer shelves during the non-upwelling period, may also favor CH_4 production as reported elsewhere. For example, Karl et al. (2008) have argued that CH_4 is produced aerobically through decomposition of methylphosphonate that might serve as a source of phosphorus in phosphate poor environments. However, Damm et al. (2010) reported CH_4 production in nitrate-depleted systems that contained sufficient phosphate.

Consistently high concentrations of CH_4 in bottom waters over both the shelves irrespective of season (**Figures 2D**, **3D**)

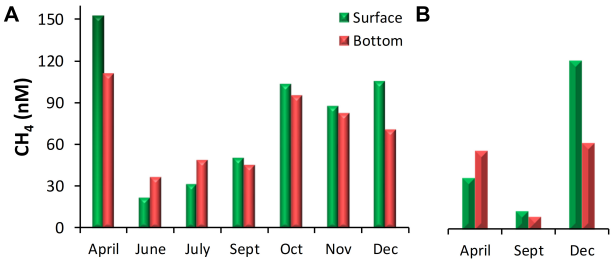


FIGURE 4 | CH_4 concentrations in the nearshore waters of **(A)** Kochi and **(B)** Mangalore.

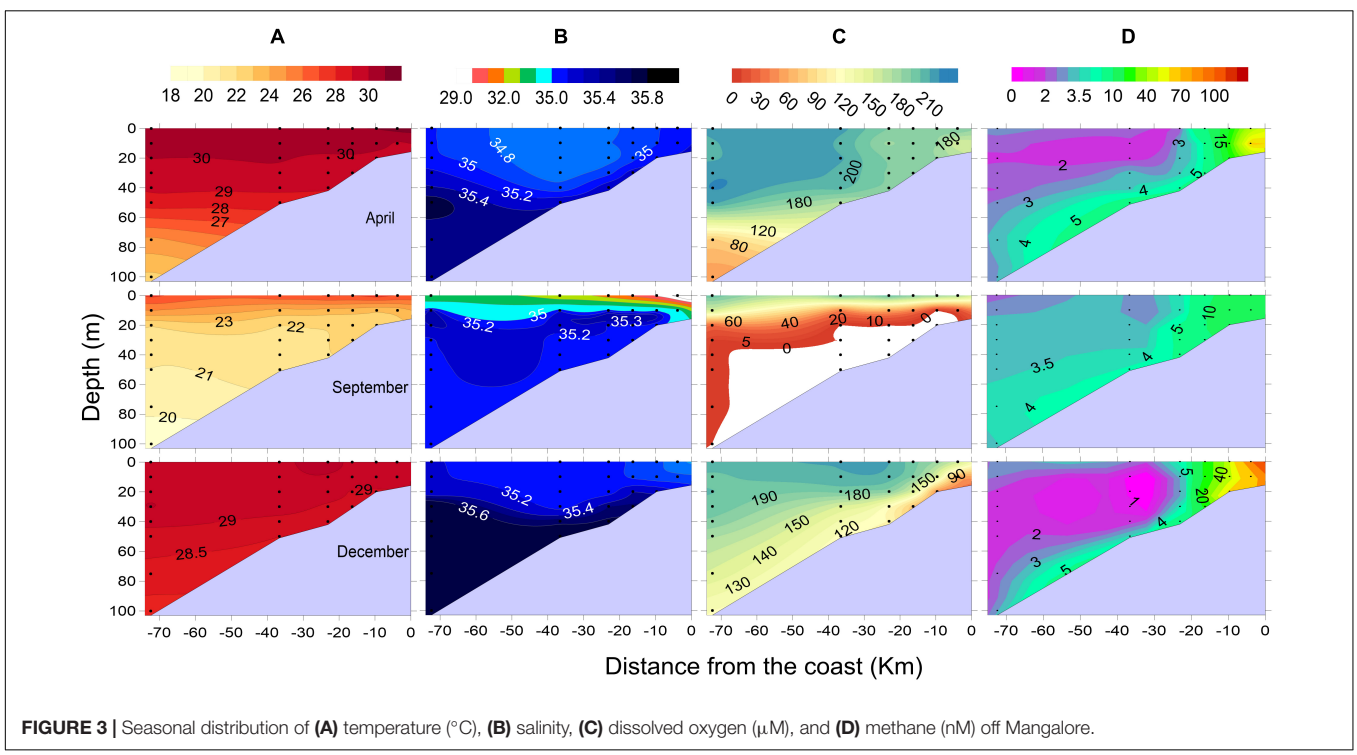


FIGURE 3 | Seasonal distribution of **(A)** temperature (°C), **(B)** salinity, **(C)** dissolved oxygen (μM), and **(D)** methane (nM) off Mangalore.

clearly pointed to its benthic origin. Karisiddaiah and Veerayya (1994, 1996) reported large reservoir of CH_4 few meters beneath the sediments of western continental shelf of India. During dry periods, the seepage of this CH_4 probably maintains high levels in the overlying waters due to stable and less turbulent conditions. Sediment methanogenesis and CH_4 diffusion to the overlying waters, augmented through sedimentary disturbances by benthic organisms, is expected to be the main source of CH_4 in bottom waters (Reeburgh, 2007; Naqvi et al., 2010; Borges et al., 2016). This is in agreement with high CH_4 production rates (0.2–3.1 $\mu g\ CH_4\ g^{-1}\ d^{-1}$) measured in the upper 25 cm of nearshore sediments of the central west coast of India (Gonsalves et al., 2011). Significantly high CH_4 concentrations over the inner shelf observed in the present study are supported by the results of Gireeshkumar et al. (2017) who reported up to 400 nM of CH_4 in the nearshore bottom waters of Alapuzha region (~9.2°N), south of present study area.

Methane Cycling Under Hypoxia/Anoxia

One of the most important factors that control biogeochemical cycling of CH_4 is the redox state of the environment, which is primarily determined by the ambient oxygen concentration. Hypoxic/anoxic shelf waters, in general, serve as significant source for CH_4 to the atmosphere (Naqvi et al., 2010). The shift in the redox state of the waters from oxic to anoxic (reducing) has been found to have a variable effect on CH_4 accumulation (Naqvi et al., 2010, and references therein). This is more important in case of highly productive coastal upwelling systems, including SEAS, where the hypoxic/anoxic conditions prevailed seasonally. High CH_4 accumulation up to 5.2 μM in the nearshore bottom waters has been reported in the upwelling waters off Namibia during intense anoxia (Monteiro et al., 2006; Brüchert et al., 2009; **Table 2**). Though the biological production in these upwelling waters (1.8 g C $m^{-2}\ day^{-1}$) is comparable with that in the SEAS (up to 2.2 g C $m^{-2}\ day^{-1}$; Shirodkar et al., 2018, and reference therein), the massive outbreaks of gases – mostly H_2S and CH_4 – from its anoxic seafloor have long been known to occur (Emeis et al., 2004), making this region different from the SEAS. The other upwelling systems like off Peru and Chile are also well known for acute oxygen deficiency including sulphidic conditions (Dugdale et al., 1977; Schunck et al., 2013) due to extremely high sediment organic carbon, especially off Peru (20–40%: Fossing, 1990) compared to the SEAS (<4%; Shirodkar et al., 2018, and references therein). This can fuel sedimentary CH_4 production and elevate its concentrations in the overlying water column, though to our knowledge CH_4 data is not available from these nearshore waters. But from a deeper Chilean shelf site (~92 m) high CH_4 concentrations of ~80 nM were recorded (Farias et al., 2009). However, contrary to expectation, the present study showed significant reduction in CH_4 concentrations in the nearshore waters of both the shelves, when hypoxic/anoxic conditions associated with upwelling prevailed (**Figure 4**). Upwelling enhances biological production and the reworking/remineralisation of this fresh organic matter may significantly elevate the sedimentary CH_4 production (Gonsalves et al., 2011); this is expected to be more at Mangalore than Kochi shelf due to relatively intense upwelling and elevated phytoplankton production in the former region (Sudheesh et al., 2016). Yet, in September, lowest CH_4 concentrations from entire study were recorded in the sub-pycnocline anoxic waters off Mangalore up to the inner shelf (13.9 ± 2.7 nM) compared to those over the hypoxic shelf off Kochi (39.0 ± 14.8 nM) (**Figures 2**, **3**, **6**). Such extreme low concentrations of CH_4 are in consistent with those reported earlier from the same region/season (Naqvi et al., 2009).

The lower than expected CH_4 levels in bottom waters over both the shelves during SM is possible due to mixing with relatively low CH_4 concentrations in upwelling waters (**Figures 2D**, **3D**). The upwelling intensity and associated dilution effect over the Kochi is at peak during peak SM (June–July), resulting in low concentrations of CH_4 in its nearshore waters (**Figure 2**). But by late SM (September), the upwelling is in its recession thereby the weak dilution effect has facilitated accumulation of CH_4 in the shallow stations near to the coast. However, unlike at Kochi, the upwelling over the Mangalore shelf during September is still sustained thereby the continued dilution effect has reduced the CH_4 concentrations (**Figure 3**). Despite this intra-seasonal variability, the degree of dilution effect over both the shelves is expected to be similar, if so, the mixing alone

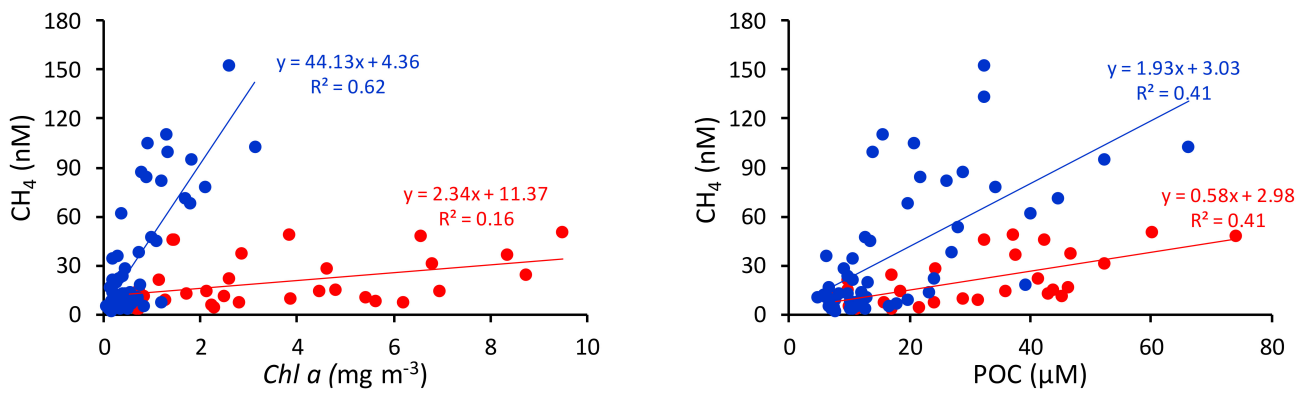


FIGURE 5 | Relationship of CH_4 with POC and Chl*a* in the nearshore waters of SEAS during summer monsoon (red) and rest of the year (blue).

TABLE 2 | Comparison of CH_4 concentration from natural coastal hypoxic systems.

Region	Surface/mixed layer con. in nM	Sea to air flux (μmol m^{-2} d^{-1})	References
Eastern Tropical North Pacific Mexican Margin (open)	3.2–5.7	0.5–2.7	Sansone et al., 2004
Mexican Margin (Gulf of California Basins)	3–4.5	0.5–5.9	Sansone et al., 2004
Eastern Tropical South Pacific (Off central Chile)	3.1–29.2	0.05–59.5	Farías et al., 2009
Eastern Tropical North Atlantic (Off Mauritinia)	2–5. 0	0.5–0.8	Kock et al., 2008
Eastern Tropical South Atlantic (Off Namibia)	2.2–2870	3–752	Monteiro et al., 2006
Bay of Bengal (East coast of India)	3.2–38.3	0.22–24.9	Berner et al., 2003
Bay of Bengal (East coast of India)	1.9–23.6	26.5 ± 31.9	Rao and Sarma, 2017
Eastern Arabian Sea shelf	2.6–47.6	0.58–63.7	Jayakumar, 1999
Eastern Arabian Sea shelf	1.7–19.8	-0.52–26.56	Shirodkar et al., 2018
Southeastern Arabian Sea shelf	2.1–152	0.03–170	Present study

cannot explain the observed lowest concentrations of CH_4 off Mangalore during September.

Earlier studies by Naqvi et al. (2009) and our parallel studies by Sudheesh et al. (2016) reported that during upwelling the Mangalore shelf witnessed shifting from suboxic conditions in peak SM to anoxic conditions by late SM (**Figure 3**), which led to significant N loss through heterotrophic denitrification during peak phase but switched to autotrophic denitrification during late phase (Pratihary et al., 2014) when sediments of nearshore and inner shelf turned to sulphidic (Naqvi et al., 2009). Such autotrophic denitrification under sulphidic conditions has reduced NO_3^- to molecular N_2 leading to complete loss of N with near absence of intermittent reduced forms like NO_2^- and N_2O in the subpycnocline waters up to inner shelf. Similar absence of NO_3^- and NO_2^- were also reported recently off Goa (just north of present study) due to complete denitrification supported by labile sediment organic matter and intense sulfate reduction rates (Naik et al., 2017). Coincidentally, CH_4 concentrations in these sulphidic waters are also distinctly low (**Figures 3**, **6**), inferring either a lower sedimentary efflux or greater loss through oxidation under intense reducing conditions.

It has been shown recently that high rates of CH_4 oxidation are sustained in the intensely oxygen depleted coastal environments (Steinle et al., 2017) and the CH_4 removal through anaerobic oxidation is supported by complete denitrification (Ettwig et al., 2010; Haroon et al., 2013). The sedimentary CH_4 has also been stated to undergo microbially mediated anaerobic oxidation by NO_2^-, Fe^{3+}, Mn^{4+}, and sulfate (Boetius et al., 2000; Beal et al., 2009; Haroon et al., 2013). The marked low concentrations of CH_4 coinciding with extremely low concentrations of NO_2^- and N_2O (**Figures 6**, **7**) under excessive presence of H_2S (Naqvi et al., 2009) over the Mangalore shelf are therefore possibly infer that greater loss of CH_4 is augmented by complete denitrification and/or intense sulfate reduction. Gas charged sediments with pockets of CH_4 were observed in the inner shelf regions of SEAS (Mazumdar et al., 2009) and the accumulation of H_2S has been attributed to the oxidation of CH_4 by sulfate in these shallow sediments (Naik et al., 2017), as well as from coastal sediments off Namibia and elsewhere (Fossing et al., 2000; Brüchert et al., 2003). The recent finding on significant influence of anaerobic oxidation of CH_4 driven sulfate reduction across the sulfate-methane transition zone in the sediment cores of SEAS (Fernandes et al., 2020) has further strengthened above arguments. Indeed, a careful examination of annual climatology developed based on monthly/fortnightly averaged records over the Goa inner shelf (see Plate 2 of Naqvi et al., 2009) clearly depicted intra-seasonal shift during SM: NO_2^- (∼4 μM) and N_2O (∼200 μM) were enriched under no sulphidic conditions during peak SM (August) but by late SM (September–October) they were down by an order of magnitude when the waters turned to sulphidic; many times CH_4 enrichment was not experienced under such intense sulphidic and denitrified conditions (Shirodkar et al., 2018). Similarly, Mangalore shallow waters were also observed with substantial low concentrations of NO_2^- and N_2O (<2 μM and ∼40 nM, respectively) under intense sulphidic conditions (up to ∼15 μM of H_2S) during September 2001 (Naqvi et al., 2009), which is also the case from the present study (**Figures 6**, **7**). There were also occasions at off Goa and Mangalore when maximum CH_4 enrichment occurred under strong reducing conditions without being sulphidic (Shirodkar et al., 2018). Though the role of anoxia in CH_4 accumulation/removal is not straightforward (Shirodkar et al., 2018) as was also seen from our data (figure not shown), the co-occurrence of poor CH_4, and NO_2^- and N_2O (**Figure 7**) along with high H_2S concentrations (Naqvi et al., 2009) can infer that CH_4 removal is succeeded by anaerobic oxidation. Recent studies suggest that nitrite-dependent anaerobic CH_4 oxidation (n-damo) is an important pathway for its loss in aquatic systems (Ettwig et al., 2010; Hu et al., 2014). However, Shirodkar et al. (2018) based on their incubation experiments of anoxic waters with ^{15}N-labeled NO_2^- in the presence/absence of CH_4 have found that n-damo is not significant off Goa. If this is true, we expect very high accumulation of N_2O as n-damo is known to bypass its formation. But the present as well as earlier studies (Naqvi et al., 2009) have clearly showed no substantial build-up of N_2O (**Figures 6**, **7**) during sulphidic periods in September, implying that the role of n-damo in CH_4 sink cannot be ruled out completely.

On the other hand, Kochi shelf being remained at hypoxic conditions has prevailed with anoxic sediments only at ∼20 cm below the surface at nearshore (unpublished data) when such sediments exist even close to sediment-water interface at Mangalore (Pratihary et al., 2014; Naik et al., 2017). This restricts to the occurrence of non-sulphidic and weak sediment

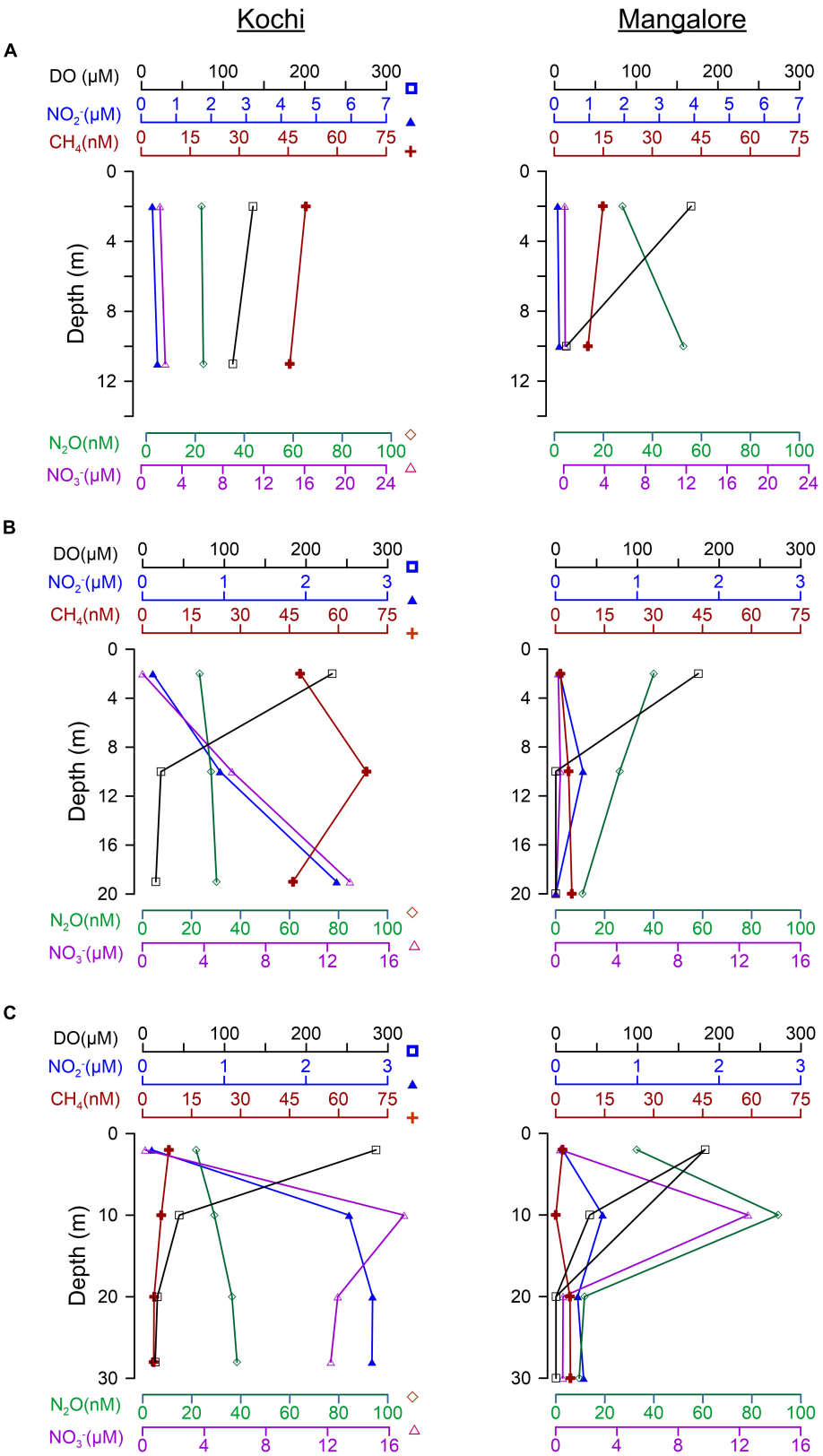


FIGURE 6 | Comparison of vertical profiles for DO, NO_3^-, NO_2^-, N_2O, and CH_4 between Kochi and Mangalore for 13, 20, and 30 m stations (**A–C**, respectively) during September 2012.

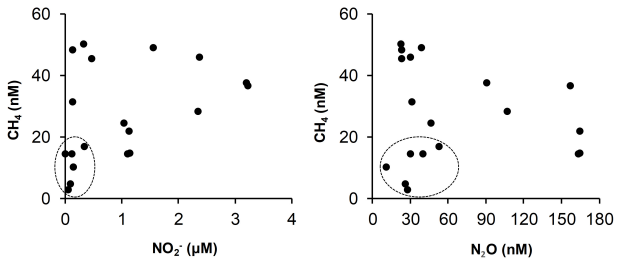


FIGURE 7 | Relationship between CH_4 concentrations and transient denitrified products in the nearshore regions during SM. Circled points depicting lowest concentrations correspond to Mangalore during September.

denitrified/reduced conditions at Kochi (Sudheesh et al., 2016), as evidenced by relatively higher concentrations of NO_2^- and N_2O, which does not support significant loss of CH_4 relative to Mangalore (**Figures 6**, **7**).

Apart from anaerobic oxidative loss of CH_4, its low concentrations during SM are also possible to some extent due to less sedimentary diffusive efflux by the benthic fauna. In the SEAS shelf, macro infaunal communities are overwhelmingly dominated by deposit feeding opportunistic polychaetes (Abdul Jaleel et al., 2015). During the SM, the density and diversity of larger benthic fauna (prawns, crabs, molluscs, etc.) become insignificant and groups which are sensitive to hypoxia, like echinoderms, are either absent or least abundant (Parameswaran et al., 2018). Summer monsoon being the recruitment period for many marine organisms, the benthic fauna from the SEAS shelf is characterized by proliferation of juveniles but their abundance depends on the intensity of hypoxia (Abdul Jaleel et al., 2015). As stated earlier, unlike at Mangalore, Kochi surface sediments are just short of being anoxic in nature. Accordingly, benthic fauna in less stressful (hypoxic) environment off Kochi are able to survive and function, albeit at lower abundance and diversity, thereby contributing to sediment-water exchanges through bioturbation (Sivadas et al., unpublished). In contrast, the more stressful anoxic (sulphidic) conditions off Mangalore are expected to cause exclusion of the macro and megafauna, impacting ecosystem functions such as bioturbation and bio-irrigation (Levin et al., 2009). Our recent studies (unpublished) showed that even meiofaunal density in these anoxic regions have suffered maximum with almost an order of less magnitude compared to those in hypoxic regions. A significant reduction in sediment reworking (∼75%) by the less abundant burrowing organisms in such intense reducing environment (Sturdivant et al., 2012) is expected to cause lower CH_4 diffusion rate (Bonaglia et al., 2017) at Mangalore relative to Kochi.

It has been shown that CH_4 accumulation in the oxygen depleted waters over the eastern Arabian Sea shelf during late SM is gradually decreasing southwards from ∼22 to 104 nM off Goa, 14–70 nM off Karwar (between Goa and Mangalore) and 10–18 nM off Mangalore but increased to 80–84 nM off Kochi (Shirodkar et al., 2018). Though this trend is matching with the present results, it is unclear of what controls such trend. Our study, therefore, offers a plausible explanation that the reduction in CH_4 concentrations in the nearshore anoxic/hypoxic waters of Mangalore/Kochi during SM can largely be defined by the degree of CH_4 loss through its anaerobic oxidation and to some extent by its differential sedimentary diffusion rates controlled by the benthic bioturbation potential. Though the oxygen depleted coastal upwelling regions are the largest source of greenhouse gasses to the atmosphere amongst the world oceans, intense anoxic/sulphidic periods at times are beneficial in naturally reducing the potential impact of this greenhouse effect by converting CH_4 to CO_2 and/or bypassing N_2O production.

Quantification of CH_4 Emissions

The CH_4 saturation levels off Kochi ranged from 101% to 7456% (**Table 1**) with maximum values in the nearshore region (2839 ± 1965%) followed by inner shelf (464 ± 183%), mid-shelf (148 ± 32%), and outer shelf (145 ± 27%). Similar saturation levels (101–6, 435%) were recorded off Mangalore where they also decreased drastically from nearshore (2011 ± 2132%) to inner shelf (546 ± 285%) and then to mid-shelf (156 ± 38%) and outer shelf (115 ± 16%). Relatively high nearshore saturation levels of CH_4 off Kochi compared to those off Mangalore are attributed to greater CH_4 contribution from the adjoining highly eutrophic CE relative to the Netravati estuary. The saturation levels observed over the mid and outer shelves were within the range reported earlier from the continental shelf of India by Jayakumar et al. (2001) and Shirodkar et al. (2018).

The air-sea CH_4 emissions from SEAS (7–14°N) ranged from 3 to 170 μmol m^{-2} d^{-1} in the nearshore, 2.3–23.5 μmol m^{-2} d^{-1} in the inner shelf, 0.04–3.9 μmol m^{-2} d^{-1} in the mid-shelf and 0.03–3.8 μmol m^{-2} d^{-1} in the offshore regions. The computed fluxes from the mid and outer shelves are comparable with earlier studies from the Arabian Sea (Owens et al., 1991; Patra et al., 1998; Jayakumar et al., 2001; Shirodkar et al., 2018) and other coastal upwelling systems (**Table 2**). However, significantly higher fluxes from the nearshore region underscore the importance of these regions in contributing to the global CH_4 flux as reported from elsewhere (Borges et al., 2016). On an annual basis, the air-sea CH_4 emissions from the near-shore region of the SEAS (57.7 ± 45.4 μmol m^{-2} d^{-1}) are 2–3 times higher than the global average for the continental shelves (22–37 μmol m^{-2} d^{-1} by Bange et al., 1994; 30 μmol m^{-2} d^{-1} by Borges et al., 2016) and ∼200 times higher than the global average of open oceanic waters (0.2–0.5 μmol m^{-2} d^{-1} by Rhee et al., 2009).

The annual sea-air flux of CH_4 from the SEAS shelf (7–14°N) was estimated following a zonal and gridded extrapolation method (Sudheesh et al., 2016). Accordingly, the SEAS shelf was divided into two zones viz. 7–11°N and 11–14°N latitudes, which represent the Kochi and Mangalore shelves respectively. In addition, each of these shelf zones were subdivided into six grid boxes according to the water depth (viz. 0–15, 15–25, 25–35, 35–45, 45–75, 75–200 m), which correspond to six monitoring stations respectively from each transect. The fluxes from each grid box were computed by multiplying the surface area of each grid box with the corresponding station CH_4 flux density. The sum of these grid box fluxes yielded CH_4 flux of 2.6 and 0.6 Gg y^{-1} to the zones 7–11°N and 11–14°N, respectively. Combining these

zones, CH_4 efflux from the SEAS shelf (7–14°N) is estimated at 3.2 Gg y^{-1}, which is equivalent to ∼16% of total emission from the Arabian Sea (∼20 Gg y^{-1}; Bange et al., 1998 – flux computed according to Wanninkhof, 1992). The CH_4 emissions from the offshore regions of Arabian Sea have been reported to account for <1% of its global oceanic emissions (Naqvi et al., 2005), however, the inclusion of emissions from the coastal Arabian Sea would elevate the contribution to global oceanic fluxes. It is suggested that the zonal integration approach followed in this study should be undertaken all along the western continental shelf of India to reduce uncertainties in estimation of CH_4 emissions from the Arabian Sea.

CONCLUSION

The present study shows that the SEAS is a significant source of CH_4 to the atmosphere. Higher CH_4 concentrations were recorded in the nearshore region which gradually decreased toward offshore. Significantly high CH_4 concentrations in the nearshore waters during non-upwelling period are presumably due to its combined inputs from sediments, *in-situ* production and estuarine export flux through tidal flushing. Contrary to expectation, increase in CH_4 concentrations during seasonal hypoxic/anoxic periods was not observed. Instead, a decrease in CH_4 concentration occurred in nearshore region of Mangalore during bottom water anoxic events in late summer is largely attributed to its greater sedimentary loss through anaerobic oxidation and in part by its reduced supply from sediment due to weak bioturbation. The estimated CH_4 efflux varied between 0.03 and 170 μmol m^{-2} d^{-1} with an annual emission of 3.2 Gg from the SEAS (7–14°N), which is ∼16% of the previously reported total CH_4 emission from the Arabian Sea. However, further studies are needed to understand the changes in CH_4 emissions from the Indian continental shelves arising from the ongoing regional (e.g., eutrophication) and global (e.g., warming) environmental changes.

DATA AVAILABILITY STATEMENT

All datasets generated for this study are included in the article/**Supplementary Material**.

AUTHOR CONTRIBUTIONS

GG conceived the study. VS and GG conducted field studies and processed the data. All authors prepared the manuscript.

ACKNOWLEDGMENTS

We thank Secretary, Ministry of Earth Sciences (MoES), Government of India and Director, Centre for Marine Living Resources and Ecology (CMLRE) for the support of this study. Drs. Damodar Shenoy and Hema Naik, National Institute of Oceanography, Goa helped in extending the lab facilities for CH_4 analysis. Thanks to Dr. Sanjeev Kumar, Physical Research Laboratory for analyzing POC samples. Thanks also to the FORV Sagar Sampada vessel management group for allotting the cruises and to the fishing hands and crew members for their onboard support during the cruises. VS thanks CMLRE for financial support. The data presented are archived at www.incois.gov.in. This work was undertaken as part of the SIBER-India program of MoES and executed under the Marine Living Resources program of CMLRE. This is CMLRE contribution number 113.

SUPPLEMENTARY MATERIAL

The Supplementary Material for this article can be found online at: https://www.frontiersin.org/articles/10.3389/fmars.2020.00324/full#supplementary-material

FIGURE S1 | Surface CH_4 concentrations in the Cochin estuary during 2012.

REFERENCES

Abdul Jaleel, K. U., Parameswaran, U. V., Gopal, A., Khader, C., Ganesh, T., Sanjeevan, V. N., et al. (2015). Evaluation of changes in macrobenthic standing stock and polychaete community structure along the south eastern Arabian Sea shelf during the monsoon trawl-ban. *Cont. Shelf Res.* 102, 9–18. doi: 10.1016/j.csr.2015.04.011

Amol, P., Vijith, V., Fernando, V., Pednakar, P., and Singh, J. P. (2018). Impact of local and remote winds on the shelf circulation off the central west coast of India. *Ocean Dyn.* 68, 1607–1623.

Bange, H. W., Bartell, U. H., Rapsomanikis, S., and Andreae, M. O. (1994). Methane in the Baltic and North Seas and a reassessment of the marine emissions of methane. *Glob. Biogeochem. Cycles* 8:465. doi: 10.1029/94GB02181

Bange, H. W., Ramesh, R., Rapsomanikis, S., and Andreae, M. O. (1998). Methane in surface waters of the Arabian Sea. *Geophys. Res. Lett.* 25, 3547–3550.

Beal, E. J., House, C. H., and Orphan, V. J. (2009). Manganese- and iron-dependent marine methane oxidation. *Science* 325, 184–187. doi: 10.1126/science.1169984

Berner, U., Poggenburg, J., Faber, E., Quadfasel, D., and Frische, A. (2003). Methane in ocean waters of the Bay of Bengal: its sources and exchange with the atmosphere. *Deep. Res. II Top. Stud. Oceanogr.* 50, 925–950. doi: 10.1016/S0967-0645(02)00613-6

Bhavya, P. S., Kumar, S., Gupta, G. V. M., Sudharma, K. V., and Sudheesh, V. (2018). Spatio-temporal variation in δ^{13}CDIC of a tropical eutrophic estuary (Cochin estuary, India) and adjacent Arabian Sea. *Cont. Shelf Res.* 153, 75–85. doi: 10.1016/j.csr.2017.12.006

Bhavya, P. S., Kumar, S., Gupta, G. V. M., and Sudheesh, V. (2017). Carbon uptake rates in the cochin estuary and adjoining coastal Arabian Sea. *Estuar. Coast.* 40, 447–456. doi: 10.1007/s12237-016-0147-4

Bhavya, P. S., Kumar, S., Gupta, G. V. M., Sudheesh, V., Sudharma, K. V., Varrier, D. S., et al. (2016). Nitrogen uptake dynamics in a tropical eutrophic estuary (Cochin, India) and adjacent coastal waters. *Estuar. Coast.* 39, 54–67. doi: 10.1007/s12237-015-9982-y

Boetius, A., Ravenschlag, K., Schubert, C. J., Rickert, D., Widdel, F., Gieseke, A., et al. (2000). A marine microbial consortium apparently mediating anaerobic oxidation of methane. *Nature* 407, 623–626. doi: 10.1038/nrmicro2944

Bonaglia, S., Brüchert, V., Callac, N., Vicenzi, A., Chi Fru, E., and Nascimento, F. J. A. (2017). Methane fluxes from coastal sediments are enhanced by macrofauna. *Sci. Rep.* 7:13145. doi: 10.1038/s41598-017-13263-w

Borges, A. V., Champenois, W., Gypens, N., Delille, B., and Harlay, J. (2016). Massive marine methane emissions from near-shore shallow coastal areas. *Sci. Rep.* 6:27908. doi: 10.1038/srep27908

Brown, I. J., Torres, R., and Rees, A. P. (2014). The origin of sub-surface source waters define the sea-air flux of methane in the Mauritanian Upwelling, NW Africa. *Dyn. Atmos. Ocean.* 67, 39–46. doi: 10.1016/j.dynatmoce.2014.06.001

Brüchert, V., Jørgensen, B. B., Neumann, K., Riechmann, D., Schlösser, M., and Schulz, H. (2003). Regulation of bacterial Sulphate reduction and hydrogen sulfide fluxes in the central Namibian coastal upwelling zone. *Geochim. Cosmochim. Acta* 67, 4505–4518.

Brüchert, V., Currie, B., and Peard, K. R. (2009). Hydrogen sulphide and methane emissions on the central Namibian shelf. *Prog. Oceanog.* 83, 169–179.

Damm, E., Helmke, E., Thoms, S., Schauer, U., Nöthig, E., Bakker, K., et al. (2010). Methane production in aerobic oligotrophic surface water in the central Arctic Ocean. *Biogeosciences* 7, 1099–1108. doi: 10.5194/bgd-6-10355-2009

Damm, E., Kiene, R. P., Schwarz, J., Falck, E., and Dieckmann, G. (2008). Methane cycling in Arctic shelf water and its relationship with phytoplankton biomass and DMSP. *Mar. Chem.* 109, 45–59. doi: 10.1016/j.marchem.2007.12.003

de Angelis, M. A., and Lee, C. (1994). Methane production during zooplankton grazing on marine phytoplankton. *Limnol. Ocean.* 39, 1298–1308. doi: 10.1126/science.233.4770.1314

Dugdale, R. C., Goering, J. J., Barber, R. T., Smith, R. L., and Packard, T. T. (1977). Denitrification and hydrogen sulfide in the Peru upwelling region during 1976. *Deep Sea Res.* 24, 601–608. doi: 10.1016/0146-6291(77)90530-6

Emeis, K. C., Brüchert, V., Currie, B., Endler, R., Ferdelman, T., Kiessling, A., et al. (2004). Shallow gas in shelf sediments of the Namibian coastal upwelling ecosystem. *Cont. Shelf Res.* 24, 627–642. doi: 10.1016/j.csr.2004.01.007

Ettwig, K. F., Butler, M. K., Le Paslier, D., Pelletier, E., Mangenot, S., Kuypers, M. M. M., et al. (2010). Nitrite-driven anaerobic methane oxidation by oxygenic bacteria. *Nature* 464, 543–548. doi: 10.1038/nature08883

Farías, L., Fernández, C., Faúndez, J., Cornejo, M., and Alcaman, M. E. (2009). Chemolithoautotrophic production mediating the cycling of the greenhouses gases N_2O and CH_4 in an upwelling ecosystem. *Biogeosciences* 6, 3053–3069. doi: 10.5194/bg-6-3053-2009

Fernandes, S., Mazumdar, A., Peketi, A., Anand, S. S., Rengarajan, R., Jose, A., et al. (2020). Sulfidization processes in seasonally hypoxic shelf sediments: a study off the West coast of India. *Mar. Petrol. Geol.* 117:104353. doi: 10.1016/j.marpetgeo.2020.104353

Fossing, H. (1990). Sulfate reduction in shelf sediments in the upwelling region off Central Peru. *Cont. Shelf Res.* 10, 355–367. doi: 10.1016/0278-4343(90)90056-R

Fossing, H., Ferdelman, T. G., and Berg, P. (2000). Sulfate reduction and methane oxidation in continental margin sediments influenced by irrigation (South-East Atlantic off Namibia). *Geochim. Cosmochim. Acta* 64, 897–910.

Gireeshkumar, T. R., Mathew, D., Pratihary, A. K., Naik, H., Narvekar, K. U., Araujo, J., et al. (2017). Influence of upwelling induced near shore hypoxia on the Alappuzha mud banks, South West Coast of India. *Cont. Shelf Res.* 139, 1–8. doi: 10.1016/j.csr.2017.03.009

Gonsalves, M.-J., Fernandes, C. E. G., Fernandes, S. O., Kirchman, D. L., and Bharathi, P. A. L. (2011). Effects of composition of labile organic matter on biogenic production ofmethane in the coastal sediments of the Arabian Sea. *Environ. Monit. Assess.* 182, 385–395. doi: 10.1007/s10661-011-1883-3

Grasshoff, K., Kremling, K., and Ehrhardt, M. (1999). *Methods of Seawater Analysis*. Hoboken, NJ: Wiley.

Gupta, G. V. M., Sudheesh, V., Sudharma, K. V., Saravanane, N., Dhanya, V., Dhanya, K. R., et al. (2016). Evolution to decay of upwelling and associated biogeochemistry over the southeastern Arabian Sea shelf. *J. Geophys. Res. Biogeosci.* 121, 159–175. doi: 10.1002/2015JG003163

Gupta, G. V. M., Thottathil, S. D., Balachandran, K. K., Madhu, N. V., Madeswaran, P., and Nair, S. (2009). CO_2 supersaturation and net heterotrophy in a tropical estuary (Cochin, India): influence of anthropogenic effect: carbon dynamics in tropical estuary. *Ecosystems* 12, 1145–1157. doi: 10.1007/s10021-009-9280-2

Haroon, M. F., Hu, S., Shi, Y., Imelfort, M., Keller, J., Hugenholtz, P., et al. (2013). Anaerobic oxidation of methane coupled to nitrate reduction in a novel archaeal lineage. *Nature* 500, 567–570. doi: 10.1038/nature12375

Hu, B.-L., Shen, L.-D., Lian, X., Zhu, Q., Liu, S., Huang, Q., et al. (2014). Evidence for nitrite-dependent anaerobic methane oxidation as a previously overlooked microbial methane sink in wetlands. *Proc. Natl. Acad. Sci. U.S.A.* 111, 4495–4500. doi: 10.1073/pnas.1318393111

IPCC, (2013). *Climate Change 2013: The Physical Science Basis. Contribution of Working Group I to the Fifth Assessment Report of the Intergovernmental Panel on Climate Change*. Cambridge: Cambridge University Press.

Jayakumar, D. A. (1999). *Biogeochemical Cycling of Methane and Nitrous Oxide in the Northern Indian Ocean*. Ph. D. Thesis, Goa University, Goa.

Jayakumar, D. A., Naqvi, S. W. A., Narvekar, P. V., and George, M. D. (2001). Methane in coastl and offshore waters of the Arabian Sea. *Mar. Chem.* 74, 1–13.

Joint Global Ocean Flux Study, (1994). *Protocols for the Joint Global Ocean Flux Study (JGOFS) Core Measurements, IOC Manual and Guides, 29, 119–122, 155–162*. Paris: UNESCO.

Karisiddaiah, S. M., and Veerayya, M. (1994). Methane-bearing shallow gas-charged sediments in the eastern Arabian Sea: a probable source for greenhouse gas. *Cont. Shelf Res.* 14, 1361–1370. doi: 10.1016/0278-4343(94)90053-1

Karisiddaiah, S. M., and Veerayya, M. (1996). Potential distribution of subsurface methane in the sediments of the eastern Arabian Sea and its possible implications. *J. Geophys. Res.* 101, 25887–25895.

Karl, D. M., Beversdorf, L., Björkman, K. M., Church, M. J., Martinez, A., and Delong, E. F. (2008). Aerobic production of methane in the sea. *Nat. Geosci.* 1, 473–478. doi: 10.1038/ngeo234

Karl, D. M., and Tilbrook, B. D. (1994). Production and transport of methane in oceanic particulate organic matter. *Nature* 368, 732–734.

Kirschke, S., Bousquet, P., Ciais, P., Saunois, M., Canadell, J. G., Dlugokencky, E. J., et al. (2013). Three decades of global methane sources and sinks. *Nat. Geosci.* 6, 813–823. doi: 10.1038/ngeo1955

Kock, A., Gebhardt, S., and Bange, H. W. (2008). Methane emissions from the upwelling area off Mauritania (NW Africa). *Biogeosciences* 5, 1119–1125.

Krishna, M. S., Prasad, M. H. K., Rao, D. B., Viswanadham, R., Sarma, V. V. S. S., and Reddy, N. P. C. (2016). Export of dissolved inorganic nutrients to the northern Indian Ocean from the Indian monsoonal rivers during discharge period. *Geochim. Cosmochim. Acta* 172, 430–443. doi: 10.1016/j.gca.2015.10.013

Levin, L. A., Ekau, W., Gooday, A. J., Jorissen, F., Middelburg, J. J., Naqvi, S. W. A., et al. (2009). Effects of natural and human-induced hypoxia on coastal benthos. *Biogeosciences* 6, 2063–2098. doi: 10.5194/bgd-6-3563-2009

Martin, G. D., Nisha, P. A., Balachandran, K. K., Madhu, N. V., Nair, M., Shaiju, P., et al. (2011). Eutrophication induced changes in benthic community structure of a flow-restricted tropical estuary (Cochin backwaters), India. *Environ. Monit. Assess.* 176, 427–438. doi: 10.1007/s10661-010-1594-1

Mazumdar, A., Peketi, A., Dewangan, P., Badesab, F., Ramprasad, T., Ramana, M. V., et al. (2009). Shallow gas charged sediments off the Indian west coast: genesis and distribution. *Mar. Geol.* 267, 71–85.

McAuliffe, C. (1971). GC determination of solutes by multiple phase equilibrations. *Chem. Tech.* 1, 46–50.

Monteiro, P. M. S., Van Der Plas, A., Mohrholz, V., Mabille, E., Pascall, A., and Joubert, W. (2006). Variability of natural hypoxia and methane in a coastal upwelling system: oceanic physics or shelf biology? *Geophys. Res. Lett.* 33:L16614. doi: 10.1029/2006GL026234

Naik, R., Naqvi, S. W. A., and Araujo, J. (2017). Anaerobic carbon mineralisation through Sulphate reduction in the inner shelf sediments of Eastern Arabian Sea. *Estuar. Coast.* 40, 134–144.

Naqvi, S., Naik, H., Jayakumar, A., Pratihary, A. K., Narvenkar, G., Kurian, S., et al. (2009). Seasonal anoxia over the western Indian continental shelf. *Geophys. Monogr.* 185, 333–345.

Naqvi, S. W. A., and Jayakumar, D. A. (2000). Ocean biogeochemistry and atmospheric composition: significance of the Arabian Sea. *Curr. Sci.* 78, 289–299.

Naqvi, S. W. A., Bange, H. W., Farías, L., Monteiro, P. M. S., Scranton, M. I., and Zhang, J. (2010). Marine hypoxia/anoxia as a source of CH_4 and N_2O. *Biogeosciences* 7, 2159–2190. doi: 10.5194/bg-7-2159-2010

Naqvi, S. W. A., Bange, H. W., Gibb, S. W., Goyet, C., Hatton, A. D., and Upstill-Goddard, R. C. (2005). Biogeochemical ocean-atmosphere transfers in the Arabian Sea. *Prog. Oceanogr.* 65, 116–144. doi: 10.1016/j.pocean.2005.03.005

Naqvi, S. W. A., Jayakumar, D. A., Narvekar, P. V., Naik, H., Sarma, V. V. S. S., D'Souza, W., et al. (2000). Increased marine production of N_2O due to intensifying anoxia on the Indian continental shelf. *Nature* 408, 346–349. doi: 10.1038/35042551

Naqvi, S. W. A., Naik, H., Jayakumar, D. A., Shailaja, M. S., and Narvekar, P. A. (2006). "Seasonal Oxygen Deficiency over the western continental shelf of India," in *Past Present Water Column Anoxia*, ed. L. Neretin (Dordrecht: Springer), 195–224.

Oudot, C., Jean-Baptiste, P., Fourré, E., Mormiche, C., Guevel, M., Ternon, J. F., et al. (2002). Transatlantic equatorial distribution of nitrous oxide and methane. *Deep Res. I Oceanogr. Res. Pap.* 49, 1175–1193. doi: 10.1016/S0967-0637(02)00019-5

Owens, N. P. J., Law, C. S., Mantoura, R. F. C., Burkill, P. H., and Llewellyn, C. A. (1991). Methane flux to the atmosphere from the Arabian Sea. *Nature* 354, 293–295.

Parameswaran, U. V., Abdul Jaleel, K. U., Sanjeevan, V. N., Gopal, A., Vijayan, A. K., Gupta, G. V. M., et al. (2018). Diversity and distribution of echinoderms in the South Eastern Arabian Sea shelf under the influence of seasonal hypoxia. *Prog. Oceanogr.* 165, 189–204. doi: 10.1016/j.pocean.2018.06.005

Patra, P. K., Lal, S., and Venkataramani, S. (1998). Seasonal variability in distribution and fluxes of methane in the Arabian Sea. *J. Geophys. Res.* 103, 1167–1176.

Pratihary, A. K., Naqvi, S. W. A., Narvenkar, G., Kurian, S., Naik, H., Naik, R., et al. (2014). Benthic mineralization and nutrient exchange over the inner continental shelf of western India. *Biogeosciences* 11, 2771–2791.

Rao, G. D., and Sarma, V. V. S. S. (2016). Variability in concentrations and fluxes of methane in the Indian Estuaries. *Estuar. Coast.* 39, 1639–1650. doi: 10.1007/s12237-016-0112-2

Rao, G. D., and Sarma, V. V. S. S. (2017). Influence of river discharge on the distribution and flux of methane in the coastal Bay of Bengal. *Mar. Chem.* 197, 1–10. doi: 10.1016/j.marchem.2017.11.002

Reeburgh, W. (2007). Oceanic methane biogeochemistry. *Chem. Rev.* 107, 486–513. doi: 10.1021/cr050362v

Rehder, G., Collier, R. W., Heeschen, K., Kosro, P. M., Barth, J., and Suess, E. (2002). Enhanced marine CH_4 emissions to the atmosphere off Oregon caused by coastal upwelling. *Glob. Biogeochem. Cycles* 16, 2-1–2-11. doi: 10.1029/2000gb001391

Rhee, T. S., Kettle, A. J., and Andreae, M. O. (2009). Methane and nitrous oxide emissions from the ocean: a reassessment using basin-wide observations in the Atlantic. *J. Geophys. Res. Atmos.* 114:D12304. doi: 10.1029/2008JD011662

Sansone, F. J., Graham, A. W., and Berelson, W. M. (2004). Methane along the western Mexican margin. *Limnol. Oceanogr.* 49, 2242–2255. doi: 10.4319/lo.2004.49.6.2242

Schunck, H., Lavik, G., Desai, D. K., Großkopf, T., Kalvelage, T., Löscher, C. R., et al. (2013). Giant hydrogen sulfide plume in the oxygen minimum zone off Peru supports Chemolithoautotrophy. *PLoS One*. 8:e68661. doi: 10.1371/journal.pone.0068661

Shankar, D., Vinayachandran, P., and Unnikrishnan, A. S. (2002). The monsoon currents in the north Indian Ocean. *Prog. Oceanog.* 52, 63–120. doi: 10.1007/s10661-015-4701-5

Shirodkar, G., Naqvi, S. W. A., Naik, H., Pratihary, A. K., Kurian, S., and Shenoy, D. M. (2018). Methane dynamics in the shelf waters of the West coast of India during seasonal anoxia. *Mar. Chem.* 203, 55–63. doi: 10.1016/j.marchem.2018.05.001

Steinle, L., Maltby, J., Treude, T., Kock, A., Bange, H. W., Engbersen, N., et al. (2017). Effects of low oxygen concentrations on aerobic methane oxidation in seasonally hypoxic coastal waters. *Biogeosciences* 14, 1631–1645. doi: 10.5194/bg-14-1631-2017

Sturdivant, S. K., Díaz, R. J., and Cutter, G. R. (2012). Bioturbation in a declining oxygen environment, in situ observations from wormcam. *PLoS One* 7:e34539. doi: 10.1371/journal.pone.0034539

Sudheesh, V., Gupta, G. V. M., Sudharma, K. V., Naik, H., Shenoy, D. M., Sudhakar, M., et al. (2016). Upwelling intensity modulates N_2O concentrations over the western Indian shelf. *J. Geophys. Res. Ocean.* 121, 8551–8565. doi: 10.1002/2016JC012166

Sudheesh, V., Movitha, M., Hatha, A. A. M., Renjith, K. R., Resmi, P., Rahiman, M., et al. (2017). Effects of seasonal anoxia on the distribution of phosphorus fractions in the surface sediments of southeastern Arabian Sea shelf. *Cont. Shelf Res.* 150, 57–64. doi: 10.1016/j.csr.2017.09.011

Thottathil, S. D., Balachandran, K. K., Gupta, G. V. M., Madhu, N. V., and Nair, S. (2008). Influence of allochthonous input on autotrophic-heterotrophic switch-over in shallow waters of a tropical estuary (Cochin Estuary). *India. Estuar. Coast. Shelf Sci.* 78, 551–562. doi: 10.1016/j.ecss.2008.01.018

Tilbrook, B. D., and Karl, D. M. (1995). Methane sources, distributions and sinks from California coastal waters to the oligotrophic North Pacific gyre. *Mar. Chem.* 49, 51–64. doi: 10.1016/0304-4203(94)00058-L

Upstill-Goddard, R. C., and Barnes, J. (2016). Methane emissions from UK estuaries: re-evaluating the estuarine source of tropospheric methane from Europe. *Mar. Chem.* 180, 14–23. doi: 10.1016/j.marchem.2016.01.010

Upstill-Goddard, R. C., Barnes, J., and Owens, N. J. P. (1999). Nitrous oxide and methane during the 1994 SW monsoon in the Arabian Sea/northwestern Indian Ocean. *J. Geophys. Res. Ocean.* 104, 30067–30084. doi: 10.1029/1999jc900232

Verma, A., Subramanian, V., and Ramesh, R. (2002). Methane emissions from a coastal lagoon: Vembanad Lake. *West Coast, India. Chemosphere* 47, 883–889. doi: 10.1016/s0045-6535(01)00288-0

Wanninkhof, R. (1992). Relationship between wind speed and gas exchange overn the ocean. *J. Geophys. Res.* 97, 7373–7382. doi: 10.1029/92JC00188

Wanninkhof, R. (2014). Relationship between wind speed and gas exchange over the ocean revisited. *Limnol. Oceanogr.* 12, 351–362. doi: 10.4319/lom.2014.12.351

Wiesenburg, D. A., and Guinasso, N. L. Jr. (1979). Equilibrium solubilities of methane, carbon monoxide and hydrogen in water and seawater. *J. Chem. Eng. Data* 24, 356–360.

Conflict of Interest: The authors declare that the research was conducted in the absence of any commercial or financial relationships that could be construed as a potential conflict of interest.

Copyright © 2020 Sudheesh, Gupta and Naqvi. This is an open-access article distributed under the terms of the Creative Commons Attribution License (CC BY). The use, distribution or reproduction in other forums is permitted, provided the original author(s) and the copyright owner(s) are credited and that the original publication in this journal is cited, in accordance with accepted academic practice. No use, distribution or reproduction is permitted which does not comply with these terms.

frontiers in Marine Science

ORIGINAL RESEARCH
published: 13 August 2020
doi: 10.3389/fmars.2020.00678

Massive Nitrogen Loss Over the Western Indian Continental Shelf During Seasonal Anoxia: Evidence From Isotope Pairing Technique

Amit Sarkar[1,2], Syed Wajih Ahmad Naqvi[1,3], Gaute Lavik[4], Anil Pratihary[1,4], Hema Naik[1], Gayatri Shirodkar[1] and Marcel M. M. Kuypers[4]*

[1] CSIR-National Institute of Oceanography, Dona Paula, India, [2] Kuwait Institute for Scientific Research, Salmiya, Kuwait, [3] Council of Scientific & Industrial Research, New Delhi, India, [4] Max Planck Institute for Marine Microbiology, Bremen, Germany

The western Indian continental shelf houses the world's largest naturally formed coastal low-oxygen zone that develops seasonally during the summer monsoon. We investigated multiple reductive nitrogen transformation pathways and quantified their rates in this system through anaerobic incubations with additions of ^{15}N-labeled substrates during the anoxic period for three consecutive years (2008–2010). Addition of ^{15}N labeled ammonium ($^{15}NH_4^+$) resulted in low to moderate anaerobic ammonia oxidation (Anammox) rates in about half of our incubations from the oxygen depleted waters. In contrast, incubations with labeled nitrite ($^{15}NO_2^-$) led to large production of $^{30}N_2$ over $^{29}N_2$ in all incubation experiments, indicating denitrification to be the dominant N-loss pathway. Rates of dissimilatory nitrate/nitrite reduction to ammonium (DNRA) were found to be highly variable and were lower by an order of magnitude than the denitrification rates. Extrapolation of average rates over the sampling periods and volume of anoxic waters showed large nitrogen removal (3.70–11.1 Tg year^{-1}) which is about three times as high as the previously reported estimate (1.3–3.8 Tg year^{-1}). Despite the small area it occupies, this shallow seasonal anoxic zone may account for as much as 20–60% the of the total annual fixed nitrogen loss in the perennial oxygen minimum zone of the Arabian Sea.

Keywords: seasonal hypoxia/anoxia, denitrification, anammox, DNRA, nitrogen loss

OPEN ACCESS

Edited by:
Hongjie Wang,
University of Delaware, United States

Reviewed by:
Antonio Bode,
Instituto Español de Oceanografía (IEO), Spain
Xuefeng Peng,
University of California, Santa Barbara, United States

****Correspondence:***
Amit Sarkar
amitsarkar81@gmail.com

Specialty section:
This article was submitted to Coastal Ocean Processes, a section of the journal Frontiers in Marine Science

Received: *27 April 2020*
Accepted: *27 July 2020*
Published: *13 August 2020*

Citation:
Sarkar A, Naqvi SWA, Lavik G, Pratihary A, Naik H, Shirodkar G and Kuypers MMM (2020) Massive Nitrogen Loss Over the Western Indian Continental Shelf During Seasonal Anoxia: Evidence From Isotope Pairing Technique. Front. Mar. Sci. 7:678. doi: 10.3389/fmars.2020.00678

INTRODUCTION

As in other parts of the North Indian Ocean, hydrography and biogeochemistry over the western Indian continental shelf (WICS) are also dominated by seasonal reversals of surface currents associated with the monsoons (Schott and McCreary, 2001; Naqvi et al., 2006a). During the winter or the Northeast Monsoon (NEM) the West India Coastal Current (WICC) anomalously flows poleward, causing downwelling and oligotrophic, well-oxygenated conditions off the Indian west coast. By contrast, the region behaves as a mini eastern boundary upwelling system during the summer or the Southwest Monsoon (SWM) when the WICC flows toward the equator. The equatorward flow induces upwelling, which is weak except off the southwest coast of India and the west coast of Sri Lanka where winds are more favorable. As a result, there is only modest

enhancement of primary productivity and consequent oxygen demand in near-bottom waters (Naqvi et al., 2010a). However, despite moderate oxygen demand there are several factors that contribute to development of intense anoxia in near bottom waters: (1) The upwelled water, derived from the upper part of the mesopelagic oxygen minimum zone of the Arabian Sea is oxygen-depleted to begin with, although not anoxic; (2) Due to slow upwelling the upwelled water remains over the shelf for a long time; and (3) The cold, saline upwelled water is capped by a thin (<10 m) warm, fresher lens, unusual for any upwelling system, formed due to intense precipitation in the coastal zone during the SWM, resulting in very strong stratification very close to the surface, thereby greatly restricting oxygen diffusion from the surface. The exact time of formation of this coastal OMZ varies strongly. It seems to gradually evolve from the south to the north. Upwelling along the WICS has been reported to start in the south (8°N, off Cochin) probably during spring (in March) (Stramma et al., 1996; Schott and McCreary, 2001), gradually extending northward. In the north (19°N, off Mumbai) the effect of upwelling is felt at least until early December (Naik, 2003; Shankar et al., 2005). This time span far exceeds the duration of the SWM. However, strong water column stratification starts in June due to intense rainfall in coastal areas, which facilitates the formation of the low oxygen zone. The oxygen deficiency intensifies with time resulting in the prevalence of reducing conditions – conversion the oxidized nitrogen to molecular nitrogen (N_2) followed by reduction of sulfate (SO_4^{2-}) to hydrogen sulfide (H_2S) – by July–August. In the north (e.g., off Mumbai) such conditions develop later in the season and last up to October–November. Thus, overall, reducing conditions over the WICS prevail for at least 3 months (90 days) (Naik, 2003; Naqvi et al., 2006b). These processes operate over a large geographical area, making the WICS the single largest low-oxygen system of its kind in the world, occupying an area of ∼200,000 km^2 (O_2 < 20 μM) – an order of magnitude bigger than the area of the famous dead zone of the Gulf of Mexico (area with O_2 < 62.5 μM: 22,000 km^2 – Rabalais et al., 2010). The shallow anoxic zone in the eastern Arabian Sea is believed to provide significant feedback to the global climate change through unusually high emissions of N_2O (nitrous oxide) and DMS (dimethyl sulfide) (Naqvi et al., 2000; Shenoy et al., 2012).

As evident from the chemical data – a decrease in nitrate (NO_3^-) and a concomitant accumulation of nitrite (NO_2^-) – reductive nitrogen removal from this system typically begins to occur during the later phase of the SWM in July/August and continues till October/early November (Naqvi et al., 2009). The reducing zones can be categorized into "suboxic" (functionally identified by the presence of secondary NO_2^-, although it must be pointed out that recent work by Thamdrup et al. (2012) has shown that the secondary NO_2^--bearing waters are also functionally anoxic) and anoxic (sulfidic); these zones are geographically separated, often located over the mid- and inner parts of the shelf (Naqvi et al., 2009). Direct measurements of N-loss rates and the processes involved are very scarce from WICS. Heterotrophic denitrification ($NO_3^- \rightarrow NO_2^- \rightarrow NO \rightarrow N_2O \rightarrow N_2$), in which bacteria use NO_3^- as an electron acceptor for organic matter oxidation (Froelich et al., 1979), was long believed to be the only process removing fixed nitrogen from the ocean, until anammox was recognized to be another major N-loss pathway (Dalsgaard et al., 2003; Kuypers et al., 2003). In previous studies undertaken over the WICS, rates reaching up to 837 nmol L^{-1} d^{-1} were determined based on changes in $NO_3^- + NO_2^-$ concentration over time at fixed sampling locations (Naik, 2003). Similar rate was also calculated assuming that the initial NO_3^- content of 20 μM in the upwelled water was fully utilized over a month (Naqvi et al., 2006b). Overall annual N-loss in the range of 1.2–3.6 Tg was arrived at by scaling up these rates to the entire shelf for the duration of the seasonal anoxia. However, these estimates should be considered as minimum estimates as replenishment of the nitrate pool had not been taken into account. Devol et al. (2006) estimated N-loss at a few coastal stations by incubating samples spiked with $^{15}NO_3^-$ on board ship and measuring the growth of ^{15}N-labeled N_2. The average rate was found to be to 33.2 nmol N L^{-1} d^{-1}. The highest rate measured by these authors was 207 nmol N L^{-1} d^{-1}, only about a quarter of the rate inferred from the overall changes in the nutrient concentrations. However, these measurements suffered from several uncertainties. For example, they did not take into account the possible N-loss through anammox. Moreover, the signal of labeled N_2 produced from $^{15}NO_3^-$ may be significantly diluted due to mixing of $^{15}NO_2^-$, originated during the first step of denitrification pathway, with high ambient substrate pool of $^{14}NO_2^-$. This may lead to underestimation (Holtappels et al., 2011). Also, none of the studies undertaken so far have considered the dissimilatory nitrate/nitrite reduction to ammonium (DNRA) that could have major implications for the estimation of the N-loss by labeling experiments (Jensen et al., 2011; Song et al., 2016) as well as for the estimates based on temporal changes in nitrate concentration (i.e., while DNRA removes NO_3^- or NO_2^-, it is not an N-loss process). Moreover, dissolved inorganic nitrogen (DIN) loading in this region is believed to have significantly increased in recent years due to enhanced synthetic fertilizer consumption in South Asia (∼17 × 10^{12} g N a^{-1}), exhibiting an increase by factor of 50 since 1960s (Naqvi et al., 2009). Seitzinger et al. (2005) estimated that the South Asian rivers could account for as much as 4.2 Tg year^{-1} of the global riverine DIN input of 20.8 tgN year^{-1} to the ocean in 1990. However, the concentrations of NO_3^- reported from some of the rivers draining into the Arabian Sea are quite moderate (e.g., 8–9 μM from the Zuari estuary of Goa – Bardhan et al., 2015). In addition, Naqvi et al. (2010b) estimated annual deposition of ∼0.16 Tg of nitrogen from the atmosphere over the WICS which most probably is also increasing due to fossil fuel burning and industrialization (Duce et al., 2008). Consequently, the N-loss estimated from upwelled NO_3^- may be considerably lower than actual.

The main aim of the present study is to identify and quantify the multiple potential reductive nitrogen processes operating in the water column over the WICS during the period of anoxia by employing various combinations of ^{15}N-labeled substrates. This is the first report evaluating relative contributions of denitrification and anammox to N-loss and also the significance of DNRA from this

region. As the experiments were conducted for three consecutive years the results also provide an idea of the inter-annual variability.

MATERIALS AND METHODS

Sampling Locations and Physicochemical Profiling of Water Column

Samples were collected from several stations located along coast-perpendicular transects during three cruises carried out from 2008 to 2010, on the Coastal Research Vessel *Sagar Sukti* (SaSu#183 and SaSu#205) and using a fishing trawler (CaTS#78). The period of observations was restricted to the time – from late August to late September – when severe oxygen deficiency develops over the WICS. In 2008, only the transect off Goa (15.52^{o}N/73.76^{o}E to 15.423^{o}N/73.283^{o}E) was sampled, whereas in 2009 and 2010 observations along two additional southern transects, off Karwar (14.478^{o}N/74.25^{o}E to 14.325^{o}N/73.768^{o}E) and Mangalore (13.14^{o}N/74.64^{o}E to 12.87^{o}N/74.108^{o}E), were also made (**Figure 1** and **Supplementary Tables S1, S2**). Physicochemical characteristics of the water column (temperature, salinity, dissolved oxygen, inorganic nutrients, chlorophyll *a* and turbidity) were determined at each sampling site. N-loss rates were measured over the inner shelf (depth < 30 m) and mid shelf (depths 30–50 m) where strong reducing conditions prevailed.

A Sea-Bird Electronics CTD system (SBE 911) was used for obtaining continuous profiles of temperature and salinity. Niskin samplers (5 L) fitted with reversing thermometers and mounted on synthetic ropes were used for sampling of seawater from selected depths based on the CTD/O_2 profiles. Dissolved O_2 was measured in each sample following the Winkler titrimetric method (Grasshoff et al., 1983, precision < 1.34 μM). Sub-samples for nutrients (unfiltered) were frozen on *Sagar Sukti* cruises and stored in an ice box on the CaTS field trip for analyses in the shore laboratory using a SKALAR autoanalyzer (precisions ± 0.06, ± 0.01, ± 0.01, ± 0.01 μM for NO_3^-, NO_2^-, NH_4^+ and PO_4^{3-}, respectively). In most cases, NO_2^- concentrations were also measured onboard immediately after sampling following the procedure of Bendschneider and Robinson (1952). The lower detection limit of the NO_2^- measurement was 0.05 μM. Deficiency in DIN was estimated

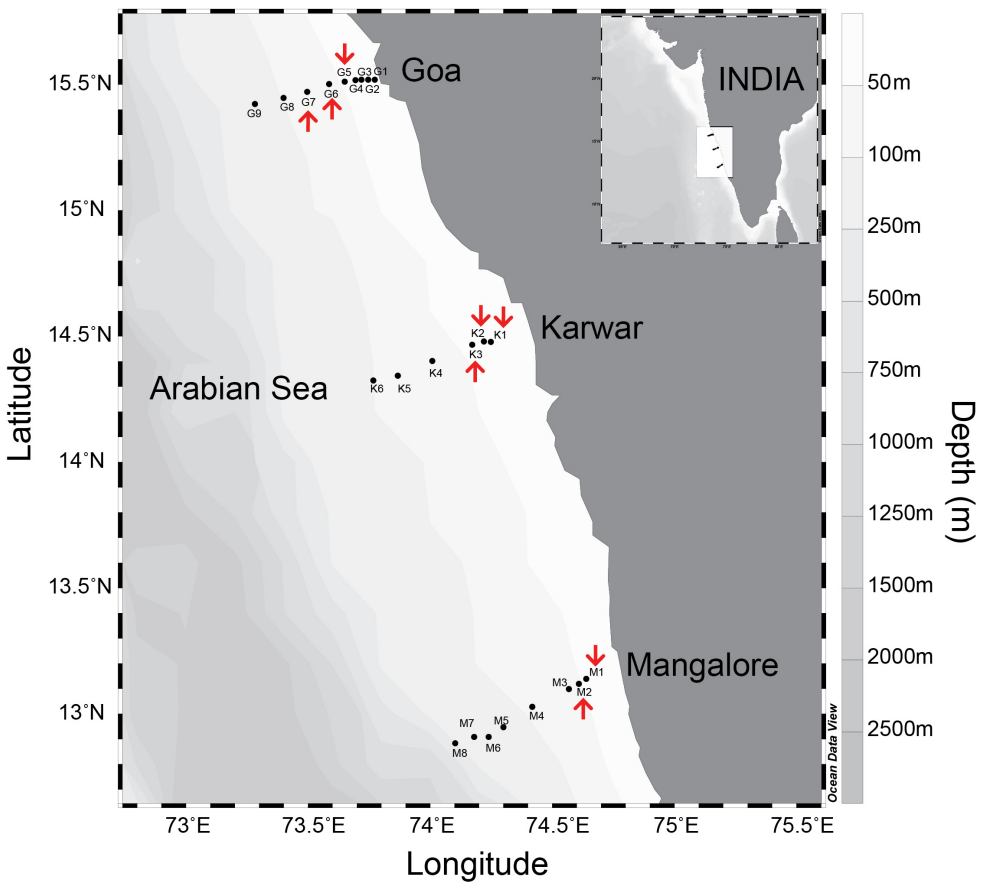


FIGURE 1 | Study area in the eastern Arabian Sea along western continental shelf of India. Biogeochemical monitoring locations on each coast perpendicular transects are indicated by closed circle points. The stations marked with "red arrows" are where ^{15}N-incubations experiments were performed.

from $N^*(\mu M) = [(NO_3^- + NO_2^- + NH_4^+) - 16 \times PO_4^{3-} + 2.9]$ following Gruber and Sarmiento (1997). Chlorophyll *a* samples were collected in 1-liter amber colored HDPE bottles and were filtered immediately through glass-fiber filters (GF/F, 47 mm diameter, 0.7 μm pore size, Whatman) under low vacuum. The filter papers were soaked in 90% acetone and stored at −20°C in the dark to extract the pigments. Quantitative estimation of chlorophyll *a* was done after 24 h spectrofluorometrically at 655 nm wavelength (Strickland and Parsons, 1972). Precision of chlorophyll *a* measurement was ± 0.001 mg m^{-3}.

Isotope Pairing Experiments

Depending on the depth and thickness of the perceived reducing layer, incubation experiments were restricted to 1–3 depths. In 2008, incubations were conducted at two stations at two depths each off Goa (**Figure 2**, O_2 panel marked in diamond symbol). In 2009, three stations each along Goa and Karwar and 1 station off Mangalore were sampled. In 2010, three stations were sampled off Goa, two off Karwar and one off Mangalore (**Figure 2**, **Table 1**, and **Supplementary Figures S2, S3**). Water samples for incubation experiments were taken immediately after the retrieval of samplers in 250-ml glass serum bottles. Water approximating three times of the volume of the bottle was allowed to overflow before the sample was sealed using butyl rubber septum, taking care not to trap any air bubble, and crimped with aluminum cap. Samples were purged with helium for 20 min to reduce the background N_2 concentration as well as to remove oxygen that might have been inadvertently introduced during sampling. After purging with helium for 15 min, various substrates ($^{15}NH_4^+$, $^{15}NO_2^-$ and $^{15}NO_2^- + {}^{14}NH_4^+$, Sigma-Aldrich stable isotope labeled products) were added to serum bottles and purging was continued for another 5 min to ensure removal of oxygen added along with the substrates and also proper mixing. The final concentration of each substrate was 8 μM. Samples were then quickly transferred into 12-ml Labco Exetainers carefully avoiding any atmospheric contamination and incubated in dark at near *in situ* temperature for 36–48 h. Microbial activities were terminated at approximately equal time intervals by adding 100 μl saturated $HgCl_2$ solution after introducing 2 ml of helium headspace (Holtappels et al., 2011). Exetainers were stored upside

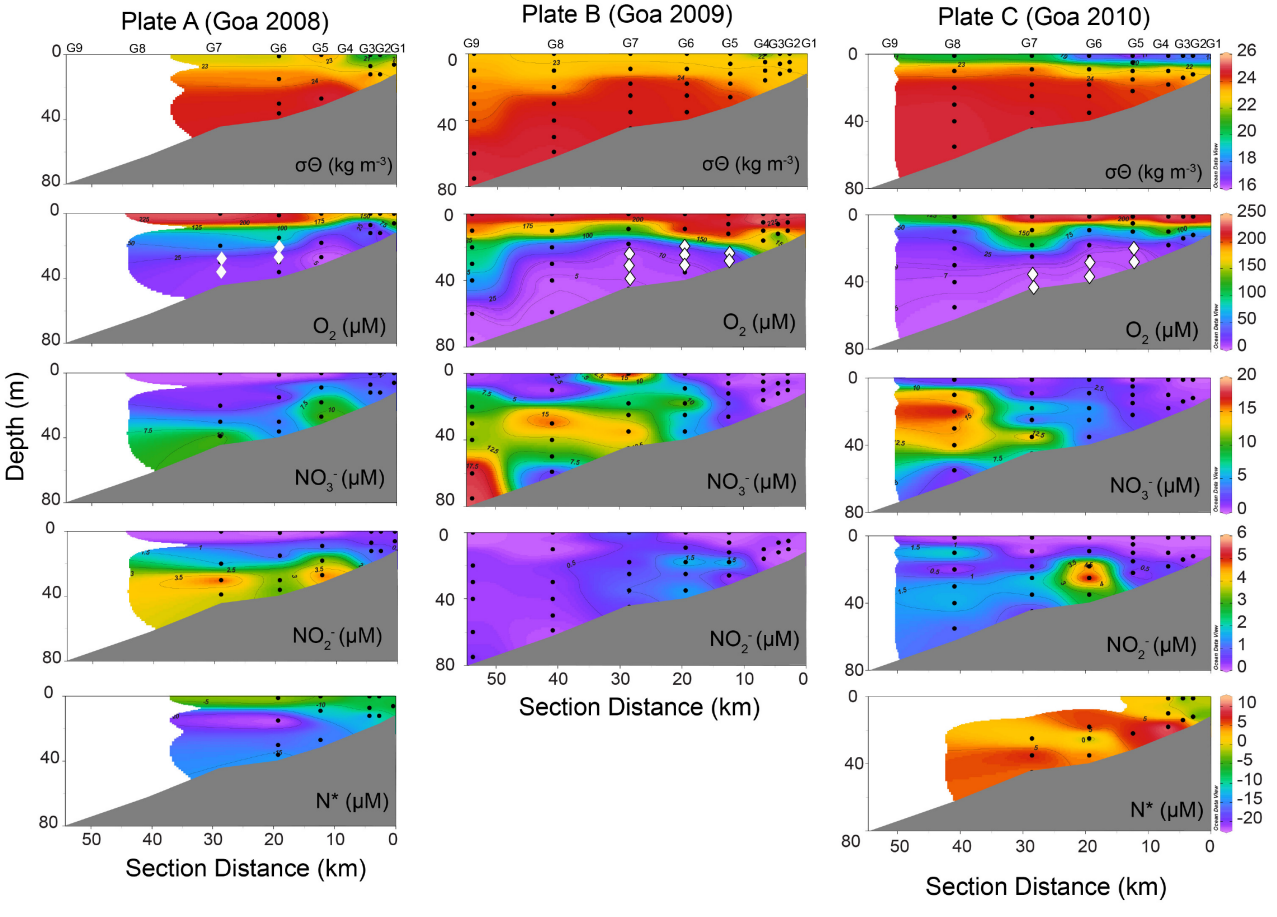


FIGURE 2 | Distribution of physicochemical properties including potential density (σ_θ), dissolved oxygen (O_2), nitrate (NO_3^-), nitrite (NO_2^-), and nitrogen deficit (N^*) in the water column along coast perpendicular transect off Goa based on observations carried out during three consecutive years Plate A. 2008, Plate B. 2009, and Plate C. 2010. Depths marked as "diamond-◊" on O_2 panels in all 3 years represents the depths where ^{15}N-incubation experiments were conducted.

TABLE 1 | Calculated rates (mean and stdev values) of different nitrogen transformation process (anammox rates obtained from both 15NH4+ and 15NO2− incubations) along with ancillary chemical data.

Year	Transects	Site	Depth (m)	O_2 (μM)	NO_3^- (μM)	NO_2^- (μM)	NH_4^+ (μM)	Denitrification (μmol $N_2 L^{-1}$ d^{-1})	Anammox (μmol N_2 L^{-1} d^{-1}) based on $^{15}NH_4^+$ incubation	Anammox (μmol N_2 L^{-1} d^{-1}) based on $^{15}NO_2^-$ incubation	DNRA (μmol$N_2 L^{-1} d^{-1}$)
2008	Goa	G6	30	11.1	3.20	2.7	1.58	1.90 ± 0.16	0.02 ± 0.004	0.52 ± 0.1	n/m
			35	13.9	4.08	2.6	0.06	0.91 ± 0.08	0.01 ± 0.003	0.68 ± 0.001	n/m
		G7	35	10.4	4.05	4.4	0.89	1.93 ± 0.24	0.01 ± 0.001	0.89 ± 0.1	n/m
			40	BDL	11.9	3.03	0.24	1.21 ± 0.95	nd	n/m	n/m
2009	Goa	G5	18	BDL	2.19	2.1	n/m	4.37 ± 0.20	nd	n/m	nd
			25	BDL	0.98	0.07	n/m	8.62 ± 1.10	nd	n/m	nd
		G6	18	32.0	12.6	1.9	n/m	0.45 ± 0.01	nd	n/m	nd
			25	10.5	4.9	0.8	n/m	1.15 ± 0.48	detected	0.91 ± 0.45	nd
			35	2.88	4.67	1.11	n/m	2.25 ± 0.37	nd	n/m	0.32 ± 0.07
		G7	25	4.4	12.6	0.8	n/m	0.53 ± 0.13	detected	0.20 ± 0.10	Nd
			35	BDL	15.9	1.1	n/m	1.31 ± 0.27	detected	0.50 ± 0.21	0.03 ± 0.01
			45	4.5	12.4	0.6	n/m	0.90 ± 0.04	detected	0.01 ± 0.05	nd
	Karwar	K1	15	BDL	1.6	3.08	n/m	9.29 ± 4.52	detected	nd	nd
			20	BDL	2.7	2.83	n/m	7.75 ± 2.25	nd	n/m	nd
		K2	10	24.7	n/m	6.4	n/m	9.34 ± 1.32	nd	n/m	0.14 ± 0.02
			20	7.3	n/m	6.8	n/m	0.66 ± 0.10	nd	n/m	nd
			30	3.9	n/m	6.8	n/m	0.25 ± 0.03	detected	0.07 ± 0.02	0.19 ± 0.009
		K3	18	39.9	18.2	0.5	n/m	0.15 ± 0.03	nd	n/m	nd
			25	5.7	13.6	3.5	n/m	0.33 ± 0.06	nd	n/m	nd
			35	2.9	9.5	2.7	n/m	0.19 ± 0.03	nd	n/m	nd
			44	3.7	11.4	4.9	n/m	0.21 ± 0.01	nd	n/m	0.02 ± 0.006
	Mangalore	M1	24	BDL	n/m	2.5	n/m	10.03 ± 1.7	nd		0.1 ± 0.02
2010	Goa	G5	15	17.9	1.1	0.5	8.3	3.54 ± 2.3	0.02 ± 0.001	0.08 ± 0.29	nd
			25	4.7	1.9	0.1	9.1	0.43 ± 0.08	0.43 ± 0.02	0.79 ± 0.12	0.15 ± 0.006
		G6	30	3.8	4.4	5.5	3.7	0.61 ± 0.02	0.003 ± 0.001	0.35 ± 0.15	nd
			35	3.8	2.6	2.7	4.0	0.24 ± 0.1	0.01 ± 0.003	0.33 ± 0.21	nd
		G7	40	3.9	4.6	0.4	2.1	2.83 ± 0.66	0.24 ± 0.008	1.88 ± 0.43	nd
	Karwar	K2	22	3.8	0.9	1.1	3.3	3.05 ± 1.16	0.014 ± 0.002	1.19 ± 0.68	nd
			26	2.48	5.7	0.1	4.3	0.12 ± 0.03	0.011 ± 0.001	0.12 ± 0.03	nd
		K3	35	6.7	15.7	1.2	3.1	0.03 ± 0.006	0.03 ± 0.01	0.05 ± 0.02	nd
			50	2.0	2.7	0.1	5.2	0.03 ± 0.004	0.01 ± 0.001	0.04 ± 0.02	nd
	Mangalore	M2	20	n/m	11.8	5.9	1.8	3.66 ± 2.11	0.03 ± 0.001	nd	0.04 ± 0.002
			35	17.6	15.8	8.4	2.2	2.77 ± 0.50	0.05 ± 0.001	nd	nd

n/m = not measured, nd = not detected; BDL = below detection limit.

down until analysis to prevent gas loss from the headspace through the septa.

Analysis and Calculation of Denitrification, Anammox, and DNRA Rates

The stable isotopic composition of N_2, measured as $^{28}N_2$, $^{29}N_2$, and $^{30}N_2$ in the headspace, was determined within a few weeks of collection using a continuous flow mass spectrometer coupled with a custom build gas chromatograph (Fisons VG Optima, Manchester, United Kingdom). 100 μl of headspace sample was slowly and carefully drawn from the vial and injected into the GC-IRMS system using gas-tight syringe. Deionized water was used to compensate for the slight under-pressure in the headspace arising from outward He diffusion during storage as well as to make up for the volume of the gas withdrawn. Air was injected as the standard before and after each batch of eight samples. Concentrations of $^{29}N_2$ and $^{30}N_2$ produced during incubation were calculated as described by Holtappels et al. (2011). After analysis of the labeled N_2, $^{15}NO_2^-$ amended samples were used for DNRA rate measurements. The isotopic composition of NH_4^+ in the samples was determined after chemically converting it to N_2 with sodium hypobromite (NaOBr) solution using the same mass spectrometer (Warembourg, 1993; Preisler et al., 2007).

The rates were computed as the slope of linear regression of ^{15}N-production over time. Concentrations of N_2 produced via denitrification and anammox pathways were calculated following Thamdrup and Dalsgaard (2002). N_2 production via denitrification was computed from $^{15}NO_2^-$ incubation as:

Denitrification = $^{30}N_2 \times [F_{NO2}]^{-2}$

Where, F_{NO2} refers to the ^{15}N-mole fraction in the NO_2^- pool.

Anammox was quantified from the $^{15}NH_4^+$ incubation considering the mole fractions of ^{15}N in the substrate pool (F_{NH4}) and excess $^{29}N_2$:

Anammox=$^{29}N_2 \times [F_{NH4}]^{-1}$

In some cases (at stations G6 and G7 off Goa, and station K2 off Karwar in 2009) where NH_4^+ concentrations were not available, anammox rates were calculated from $^{15}NO_2^-$ incubation as:

Anammox=$^{29}N_2 \times [F_{NO2}]^{-2}$–[Denitrification $\times$ 2 $\times$ (1−F_{NO2})]

Dissimilatory nitrate/nitrite reduction to ammonium rates were calculated from the slope of linear regression of ^{15}N-labeled NH_4^+ production with time in the NO_2^- spiked samples (Jensen et al., 2011).

RESULTS

Physicochemical Characteristics

The physicochemical conditions along various transects visited in the 3 years were very similar in that water column was strongly stratified in all cases (as exemplified by transect off Goa in **Figure 2**). In 2008 and 2009, surface water had potential density (σ_θ) of ∼20–22.5 kg m^{-3} that increased to 23.5–24.5 kg m^{-3} in the cooler and more saline subsurface upwelled water below the thermocline (**Figure 2**, Plates A and B). Due to a more intense rainfall in 2010, surface σ_θ values were much lower (**Figure 2**, Plate C). In all cases, surface waters were mostly oxygen saturated or slightly supersaturated (>200 μM) but O_2 concentrations declined sharply (<10 μM, often reaching non-detectable limit) below the thin surface layer. Presence of sulfide was noticed by its strong odor along all transects in 2009. Surface water was mostly nutrient depleted. Over the deeper outer shelf (depth > 50 m) NO_3^- levels were higher (>15 μM) below the surface, but the concentrations decreased steadily toward the coast. Lower NO_3^- levels in oxygen-depleted water over the inner- and mid-shelf regions often coincided with elevated NO_2^- (up to 6 μM) indicating vigorous anaerobic microbial NO_3^- reduction (**Figure 2**). Dissolved NH_4^+, whenever measured, showed some accumulation in NO_3^- reducing water, either being produced through organic matter mineralization and/or DNRA or originating from the underlying sediment. Except for the year 2010, off Goa, strongly negative N* values in subsurface waters over the shelf indicated high fixed N-loss under suboxic/anoxic conditions (**Figure 2**, Plates A and C). The two southern transects (off Karwar and Mangalore) also showed similar physicochemical characteristics (**Supplementary Figures S2, S3**).

Nitrogen Reduction Pathways Over the WICS

Denitrification was detected in all samples, as indicated by significant ($r^2 \geq 0.7$) production of $^{30}N_2$ in $^{15}NO_2^-$-spiked incubations. In fact, most of the N-loss over the shelf appears to be through this process (**Table 1** and **Supplementary Figure S4**, 1 to 33). Production of $^{30}N_2$ exceeded that of $^{29}N_2$ in a majority of experiments, maintaining the theoretical production ratio of 2 (1−F_{NO2})/F_{NO2} through random isotope pairing as proposed by Nielsen (1992). In 2008, denitrification rates along the Goa transect ranged from 0.91 ± 0.08 to 1.93 ± 0.24 μmol N_2 L^{-1} d^{-1}. Higher denitrification rates were observed in 2009 at the inner shelf stations. At station G5, the denitrification rate averaged 6.49 ± 0.65 μmol N_2 L^{-1} d^{-1}; even higher rates were measured along the two southern transects, 9.34 ± 1.32 μmol N_2 L^{-1} d^{-1} off Karwar and 10.03 ± 1.7 μmol N_2 L^{-1} d^{-1} off Mangalore (**Table 1**). In 2010, denitrification rates were considerably lower over the inner shelf as compared to those in 2009. However, at the mid shelf stations inter-annual variations were less pronounced. Using all the 3 year's data, the average denitrification rate was calculated as 2.45 ± 0.63 μmol N_2 L^{-1} d^{-1}.

Anammox activity was confirmed by results of $^{15}NH_4^+$ incubations that led to significant $^{29}N_2$ production in over half (60%) of the all experiments (**Table 1** and **Supplementary Figure S5**, 1 to 20). Anammox rates were calculated using $^{29}N_2$ production rates from both $^{15}NH_4^+$ and $^{15}NO_2^-$ incubations; these are presented in **Table 1**. The rates were significantly different from each other (Independent samples *t*-test, $p < 0.05$) with consistently higher rates from $^{15}NO_2^-$ incubations. This is expected due to the differences in ^{15}N enrichment in the substrate pool (Bulow et al., 2010 and references there in). For consistency, in the present study we considered anammox rates derived only from $^{15}NH_4^+$ incubation which is recommended to be more direct and precise. In 2008, anammox rates ranged between 0 and 0.02 ± 0.004 μmol N_2 L^{-1} d^{-1}. This process was mostly undetectable in 2009. In 2010, overall anammox rates were higher but highly variable from below detection to 0.43 μmol N_2 L^{-1} d^{-1}. The average anammox rate derived from all our $^{15}NH_4^+$ incubations was ∼0.06 ± 0.004 μmol N_2 L^{-1} d^{-1}. These numbers are two orders of magnitude lower than the above-mentioned denitrification rate.

Dissimilatory nitrate/nitrite reduction to ammonium activities were seen only sporadically. In both 2009 and 2010, DNRA activity was found at one depth along the Goa transect, and anammox was not detected in 2008. Off Karwar DNRA was found at 3 depths in 2009, but it was absent in 2010. A completely opposite trend was observed off Mangalore. The average DNRA rate (109.25 ± 22.1 nmol N_2 L^{-1} d^{-1}) was higher than that observed over the Omani shelf (highest ∼40 nmol N_2 L^{-1} d^{-1}).

Spatial and Inter Annual Variability of Nitrogen Reduction Processes

The spatio-temporal trends in denitrification and anammox rates were tested using non-parametric Mann Whitney *t*-test (two-tailed). Due to large intra-annual variability, no inter-annual variability was evident in both processes (**Supplementary Figures S10a,b**). However, denitrification rates along the Goa coast were significantly lower than that at the Karwar

coast at $p \leq 0.1$ (p: 0.10), and Mangalore coast at $p < 0.05$ (P: 0.04). Anammox rates were different only between Karwar and Mangalore at a significance level of $p \leq 0.1$ (p: 0.07). Denitrification was found to be more active at the oxic-suboxic/anoxic interface compared to deeper water (**Figures 3A,B**). In 2009, low rates of denitrification were measured at the base of the oxycline at stations G6 (**Figure 3B**) and K3 where O_2 concentrations were > 30 μM (**Table 1**). These O_2 levels probably inhibited denitrification at these stations. In fact, with just a few exceptions, low levels of denitrification (only 10–25% of the mean of all measured rates) were consistently found in waters containing measurable O_2. Anammox activity

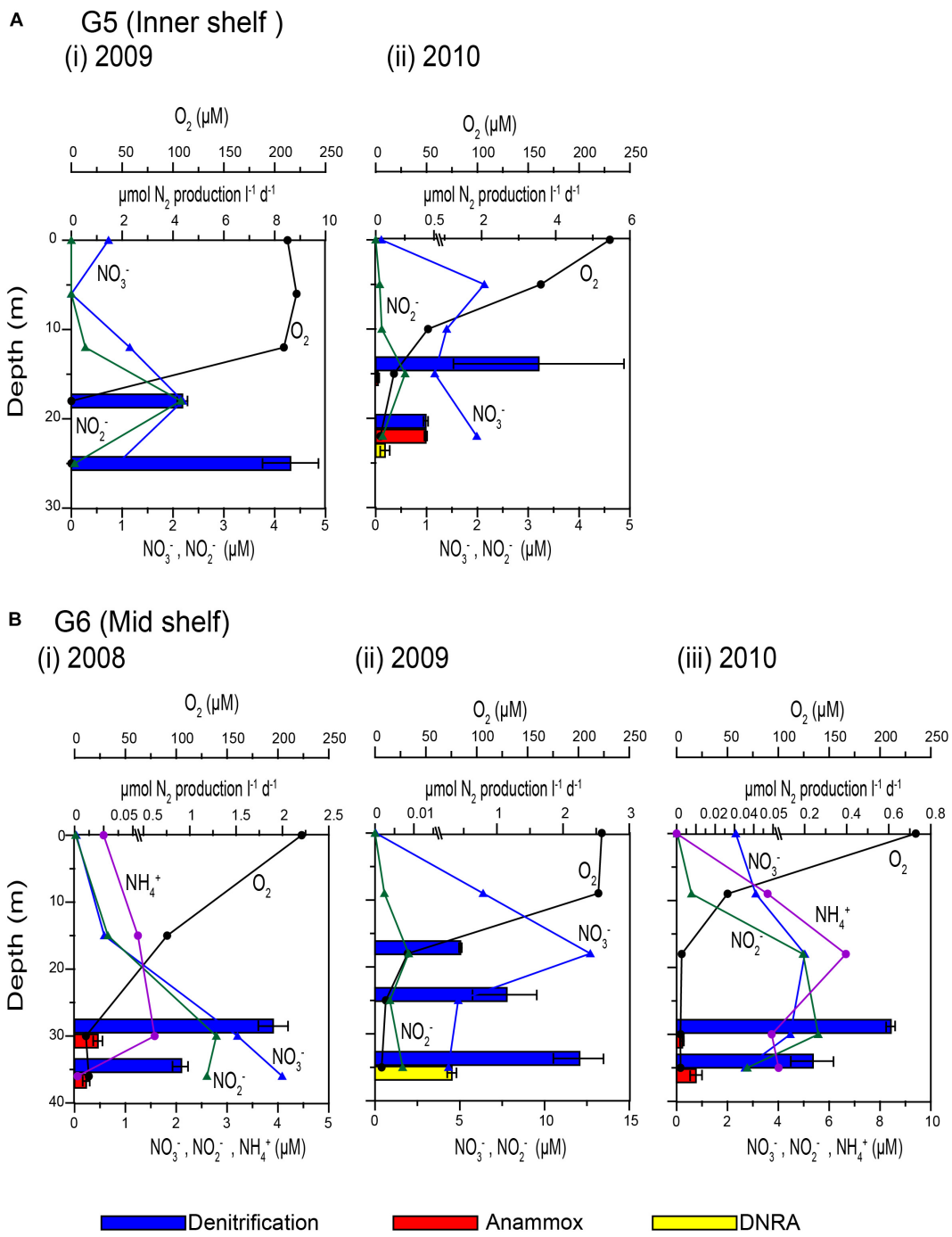


FIGURE 3 | Depth wise variations in concentrations of dissolved oxygen, nitrate, nitrite and ammonium (connected vertical profiles) and N_2 production rates measured by isotope pairing experiments (horizontal bars): **(A)** G5 inner shelf station off Goa (i) 2009 and (ii) 2010 and **(B)** G6 mid shelf station off Goa during (i) 2008, (ii) 2009, and (iii) 2010.

was low and stochastic to infer any trend in its depth distribution (**Table 1** and **Figures 3A,B**). In 2010, anammox rates in bottom waters at stations G5 and G7 off Goa, were not only higher than those at the oxycline but also the highest recorded in this study (**Table 1** and **Figures 3A,B**). However, at most of the depths where the anammox activity was detected O_2 levels were low but often measurable (<5 μM).

Overall denitrification rates did not show large inter annual variations over the 3 years period of the study. Over the inner shelf, average denitrification rate was higher in 2009 (6.49 ± 0.65 μmol N_2 L^{-1} d^{-1}) compared to 2010 (1.98 ± 1.1 μmol N_2 L^{-1} d^{-1}, respectively). In comparison, average anammox average rate was the highest in 2010 (0.07 ± 0.004 μmol N_2 L^{-1} d^{-1}), seven times more than the rates measured in 2008 (0.01 ± 0.002 μmol N_2 L^{-1} d^{-1}). In 2009, near-bottom waters at most inner shelf stations were found to be sulfidic (**Supplementary Figure S1**). At these stations denitrification rates were exceedingly high while anammox activity was not detected (**Figure 3A**).

N-Loss Rates Over the WICS

Despite the intra-annual variability observed at individual stations/sections, our data show quite similar average denitrification rates for 3 years. The mean values of our 3-year N-loss rates through denitrification and anammox were 2.45 ± 0.6 and 0.06 ± 0.004 μmol N_2 L^{-1} d^{-1}, respectively. For up-scaling these values over the entire shelf we followed the assumption previously made by Naqvi et al. (2000) and Naik (2003). Naqvi et al. (2000) estimated the area of the hypoxic zone over the WCSI to be 180,000 km^2. However, O_2 levels over this entire area are not low enough to support reductive N-loss, and as a lower limit about one third of the entire shelf, 60,000 km^2, was assumed to functionally anoxic. The total volume of reducing water was estimated to range between 1.2 and 3.6 × 10^{12} m^3 taking the thickness of the reducing layer to be 20 m. Applying our 3 years average N-loss rates to this volume and assuming the reducing condition to last for 90 days, the overall N-loss would range from 3.70 ± 0.091 to 11.1 ± 2.72 Tg $year^{-1}$ via denitrification, and from 0.09 ± 0.01 to 0.27 ± 0.03 Tg $year^{-1}$ via anammox (**Table 2**).

DISCUSSION

Oxygen Deficiency and Associated Biogeochemical Properties

Consistent with earlier observations (Naqvi et al., 2009, 2010a), suboxic (Winkler O_2 < 10 μM; NO_3^- and NO_2^- > 0 μM) and anoxic (O_2 = 0 μM; H_2S > 0 μM) conditions were found to prevail over the inner-shelf and mid shelf regions in the present study as well. This oxygen deficient environment that evidently supported reductive nitrogen transformations (Hannig et al., 2007; Lavik et al., 2009; Naqvi et al., 2010a) was chosen for ^{15}N labeling experiments (**Figure 2**, depths marked by diamond in O_2 panels). Oxygenated surface water had extremely low NO_3^- concentrations (< 1 μM at most of the stations) with very few exceptions. Average surface chlorophyll *a* concentration was ∼2 mg m^{-3}, with the highest concentration (7.01 mg m^{-3}) occurring at a station M8. Earlier observations made during the SWM also revealed high surface chlorophyll levels (e.g., 2.63 mg m^{-3} at station G5 – Maya et al., 2011). Bhavya et al. (2017) reported average carbon uptake rate of 0.23 mg C l^{-1} d^{-1} water over the coast of Mangalore; this was significantly higher than production during the pre-monsoon but slightly lower than that during the post-monsoon period. In the coastal Arabian Sea primary production has been reported to be the largest contributor to the carbon stock (Barber et al., 2001). Therefore, the low NO_3^- levels in surface waters observed in the present study are probably due to biological uptake which in turn makes organic matter available to support microbial respiration in sub surface layers, increasing the O_2 demand (Devol et al., 2006). Hypoxic water below the surface over the outer shelf was NO_3^- rich (∼15 μM), but NO_3^- was gradually depleted as the water upwelled and moved up the shelf. Accumulation of NO_2^- in the suboxic water over the inner- and mid-shelf points to active denitrification that apparently varied in strength spatially. When the NO_3^- was fully utilized, sulfate reduction commenced leading to buildup of H_2S and NH_4^+. The highest NH_4^+ concentrations (up to 9.1 μM) in low-oxygen waters (**Table 1**) are consistent with earlier measurements by Naqvi et al. (2009). Concentration of H_2S was not measured in the present study; however, its frequent presence over the inner shelf was indicated by strong odor. Soon after our observations off Goa in 2009, station located on Goa transect was visited for time series sampling and a build-up of sulfide in subsurface water was noticed (**Supplementary Figure S1**, reaching concentration as high as ∼12 μM (Shenoy et al., 2012). Overall, our results show the presence of intensely O_2-depleted waters underlying a shallow and sharp pycnocline suitable for suboxic/anoxic microbial processes like denitrification, anammox and DNRA.

Regulation of Nitrogen Reduction Pathways Over the WICS

In the present study, denitrification was found to be the dominant fixed nitrogen removal process. The average denitrification rate (2.45 ± 0.6 μmol N_2 L^{-1} d^{-1}) was more than double of the previously reported value derived from the observed NO_3^- + NO_2^- loss over time (Naik, 2003) and almost two orders of magnitude higher than the estimates derived from incubation of samples spiked with $^{15}NO_3^-$ (Devol et al., 2006). Contrastingly, anammox process, measured and detected for the first time over the WICS, was found to occur to a much lesser extent (∼0.06 ± 0.004 μmol N_2 L^{-1} d^{-1}). In $^{15}NH_4^+$ incubations, production of $^{30}N_2$ was not detected thereby ruling out significant involvement of micro-aerobic ammonium oxidation as reported from the Black Sea (Lam et al., 2007). Nevertheless, our anammox rate over the Indian shelf in the eastern Arabian Sea is comparable with the rate measured off Oman in the western Arabian Sea where this process was found to be the dominant nitrogen loss pathway (Jensen et al., 2011). This indicates that anammox is not limited by the substrate availability as both NO_3^- and NH_4^+ were mostly available in near-bottom waters sampled by us. The growth rate of

TABLE 2 | Total nitrogen loss (mean and standard deviation values) from eastern Arabian Sea from present study and comparison with earlier data extrapolated to the OMZ area and thickness adopted from Naqvi et al. (2000).

Source	Area of Coastal OMZ (Km^2)	Thickness OMZ (m)	Average Denitrification ($\mu mol\ N_2\ L^{-1}\ d^{-1}$)	Average Anammox ($\mu mol\ N_2\ L^{-1}\ d^{-1}$)	Removal of Fixed Nitrogen (Tg N $year^{-1}$)	
					Denitrification	Anammox
Present study	60–180	20	2.45 ± 0.6	0.06 ± 0.004	3.70 ± 0.91–11.11 ± 2.72	0.09 ± 0.01–0.27 ± 0.03
Devol et al., 2006	60–180	20	0.033	n/m	0.05–0.15	n/m
Naik, 2003	60–180	20	0.83 ± 0.6	n/m	1.3–3.8	n/m

n/m = not measured.

anammox bacteria are reported to be very slow, with doubling times of 10–30 days in bio-reactors under controlled conditions (Strous et al., 1998). Lower doubling times of 5.5–7.5 days were obtained in specialized membrane bioreactor (van der Star et al., 2008); however, the growth of anammox organisms is believed to be even slower in the OMZs (Dalsgaard et al., 2012). In the eastern Arabian Sea non-sulphidic (suboxic) anaerobic conditions generally persist only for a few weeks and within this relatively short time anammox bacteria may not be able to build the necessary biomass to utilize the relatively abundant ammonia. In this study DNRA was independently found to occur in some samples in the absence of detectable anammox activity. Along the shelves off Peru and Oman, occurrence of DNRA and its close coupling with anammox has been reported to account for the production of $^{30}N_2$ in experiments conducted with $^{15}NO_2^-$ (Kartal et al., 2007; Jensen et al., 2011). However, our incubations with $^{15}NO_2^- + {}^{14}NH_4^+$ did not show any effect on $^{30}N_2$ production compared to incubations with $^{15}NO_2^-$ alone. If DNRA-anammox were coupled, then addition of $^{14}NH_4^+$ would have diluted the $^{15}NH_4^+$ pool thereby resulting in a lower $^{30}N_2$ yield (Kartal et al., 2007; Song et al., 2016). Furthermore, only ∼24% of the samples yielded positive results in our direct measurement of $^{15}NH_4^+$ production from $^{15}NO_2^-$ in 2009 and 2010, and showed no correlation with the anammox rates. The average DNRA rate (109.6 ± 22.1 nmol $N_2\ L^{-1}\ d^{-1}$) was higher than that observed over the Omani shelf (highest ∼40 nmol $N_2\ L^{-1}\ d^{-1}$). This indicates that while DNRA could make some contribution to the observed NH_4^+ accumulation over the Indian shelf, the sedimentary flux of NH_4^+ is perhaps more important as Pratihary et al. (2014) reported very high benthic NH_4^+ efflux (3.74 mmol $m^{-2}\ d^{-1}$) based on whole core incubations in this region.

The ambient O_2 concentration did not show any clear control over denitrification ($r = 0.22$, $p > 0.05$) and anammox ($r = 0.17$, $p > 0.05$) in present study. However, it must be noted that the Winkler O_2 measurements at near-zero levels may result in systematic overestimation. There are several reports on the sensitivity of denitrification to ambient O_2 concentrations ranging from 0.2 to 5 μM in non-sulphidic O_2-depleted waters (Dalsgaard et al., 2014, 2012; Bristow et al., 2017). For the first step of denitrification – nitrate reduction to nitrite – a somewhat high O_2 tolerance (>25 μM) was noticed from the OMZ waters off Namibia and Peru (Kalvelage et al., 2011) than what is inferred from the field data (Thamdrup et al., 2012). Earlier observations in the Baltic Sea (Rönner and Sörensson, 1985) showed that O_2 concentrations of ∼9–11 μM could inhibit denitrification; this is supported by the results of Jensen et al. (2009) from the Mariager Fjord. Like denitrification, anammox is also sensitive to the ambient O_2 concentration. In the Black Sea, anammox bacteria were found to be active at low levels of O_2 (4–8 μM) but showed complete inhibition at 13–14 μM (Jensen et al., 2008). Elsewhere in the oceans tolerance of anammox to O_2 has been found to vary from nanomolar levels in the OMZs to as high as ∼15 μM in shallow waters (Kalvelage et al., 2011; Dalsgaard et al., 2012). As stated earlier, the Winkler O_2 data used in some of these studies are not very reliable at vanishingly low levels. However, if real, this variability may be explained either by adaptation of anammox organisms to variable O_2 conditions in coastal waters or by the presence of aggregated particles providing anaerobic micro-niches (Kalvelage et al., 2011; Klawonn et al., 2015). Time series observations by Shenoy et al. (2012) carried out for 3 days at station G5 showed highly fluctuating O_2 concentrations on very short time scales (hours), indicating that the anammox and possibly also denitrifying bacteria might be better adapted to these varying O_2 concentrations. Thus, due to multiple uncertainties it is not possible to categorically address the issue of O_2 control on rates measured in the present study.

In many of the incubation experiments carried out by us, an initial lag phase of 10–12 h occurred before linear increase of ^{15}N labeled N_2 production. Around 70% of experiments with $^{15}NO_2^-$ amendments in which denitrification were detected and ∼30% experiments with $^{15}NH_4^+$ which confirmed anammox activity showed such a lag phase. The most likely explanation of this time lag, also observed by us in similar incubations of anoxic reservoir samples (Naqvi et al., 2018), is that the microbes that perform denitrification and anammox were present in the water but were activated only when O_2 level fell below the threshold (functionally anoxic). The possible causes of the presence of O_2 in our samples subjected to incubation are discussed below. The data from the lag phase were not considered for calculation of rates and only the linear portion of the curve was used for this purpose. In some cases, a large (exponential) increase in labeled N_2 production, departing from the linear trend, was also seen toward the end of the experiments. These data points, ostensibly arising from the so-called "bottle effect," were not used for the rate calculation either. For these reasons, the rates computed by us should be considered as conservative. It is worth mentioning that average denitrification rates estimated from all experiments

without lag phases (1.78 ± 0.19 μmol N_2 L^{-1} d^{-1}) were marginally lower than those from experiments with lag phases (2.74 ± 0.8 μmol N_2 L^{-1} d^{-1}). Even our lower mean values are more than twice the earlier estimates from the WICS (0.83 μmol N_2 L^{-1} d^{-1} – Naik, 2003). Contrastingly, in case of anammox, rates calculated from $^{15}NH_4^+$ experiments with lag phase in $^{29}N_2$ production were relatively far lower (0.01 ± 0.003 μmol N_2 L^{-1} d^{-1}) than those from experiments showing linear production from the beginning (0.08 ± 0.004 μmol N_2 L^{-1} d^{-1}). This suggests that anammox rates could not have been overestimated.

In isotope pairing technique (IPT) a time lag of ∼40 h in labeled N_2 production has been observed previously in $^{15}NO_3^-$ incubations (Dalsgaard et al., 2003). This can be attributed to the time taken for the conversion of NO_3^- to NO_2^- pool before N_2 production starts. In modified IPT involving $^{15}NO_2^-$ as the substrate, time lag could arise from the inhibitory effect of traces of O_2 on denitrification/anammox in the incubated samples. The length of time lag has been found to be directly proportional to the O_2 concentration (Baumann et al., 1997). Results of O_2 amendment experiments by Jensen et al. (2008) revealed that the presence of ∼13.5 μM of O_2 could produce 30 h lag before labeled N_2 production commenced. There are several possibilities of O_2 contamination occurring during experiments involving the IPT. Dalsgaard et al. (2014) pointed out that O_2 could leach out from the PVC samplers to anoxic water samples. However, purging with helium for 15 min in 250-ml samples collected in serum bottles should take care of such contamination; this has been practiced as standard operating protocol in many previous studies, both in water from oceanic OMZs (Dalsgaard et al., 2003; Kuypers et al., 2005; Jensen et al., 2008; Holtappels et al., 2011) and anoxic freshwaters (Naqvi et al., 2018). However, there still remains a possibility that some O_2 contamination could occur while transferring samples from serum bottles to Labco exetainers. De Brabandere et al. (2014) also demonstrated that Labco exetainers often used for incubations, as was also done in our study, could suffer from significant O_2 diffusion through their butyl septa. Considering O_2 consumption rates of 0.13 μmol l^{-1} h^{-1} in $^{15}NO_2^-$ incubation (Jensen et al., 2008), ∼1.3 μM O_2 might have produced a time lag of 10–12 h in our experiments. The initial time lag was seen in samples having measurable O_2 levels (often > 10 μM). We strongly believe that He purging for 20 min was sufficient to completely remove O_2 initially and that the production of lag phase is most likely due to subsequent contamination. Interestingly, no time lag was observed in the case of samples that contained traces of sulfide, as in our 2009 experiments. We hypothesize that traces of O_2 introduced through contamination could have been quickly utilized for the oxidation of sulfide, but as discussed below we do not rule out the possibility of the occurrence of chemolithotrophic denitrification in the presence of sulfide (Lavik et al., 2009).

Over the Peruvian and Namibian shelves, re-suspension of sediments and presence of copious marine snow are expected to be most conducive for creating particle associated micro-anaerobic niches within which substantial N-loss could occur (Kuypers et al., 2005; Woebken et al., 2007; Kalvelage et al., 2011, 2013). Co-variation of turbidity and anammox rates was observed in these areas. The water column over the western Indian shelf is more turbid (1–4 NTU, measured in 2009), than off Peru and Namibia (0.05–0.1 NTU; Kuypers et al., 2005). In the present study, water turbidity (**Figure 4A**) showed statistically significant correlation with denitrification ($r = 0.47$, $p < 0.05$). This suggests N removal through denitrification may also occur in particle-associated micro-anaerobic niches over the WICS.

The availability of NO_3^- and organic matter are expected to regulate heterotrophic denitrification (Ward et al., 2008; Dalsgaard et al., 2012) as well as anammox (Kalvelage et al., 2013; Callbeck, 2017) in oceanic oxygen-deficient zones. In our study, in some cases, we noticed high denitrification rates to be associated with higher chlorophyll *a* (a proxy of organic matter availability) as well as lower NO_3^- levels (reflecting denitrification/anammox activities). NO_3^- showed statistically significant inverse relation ($r = -0.43$, $p < 0.05$), whereas chlorophyll *a* yielded non-significant correlations with the measured denitrification rates ($r = 0.20$; $p > 0.05$) (**Figure 4B**).

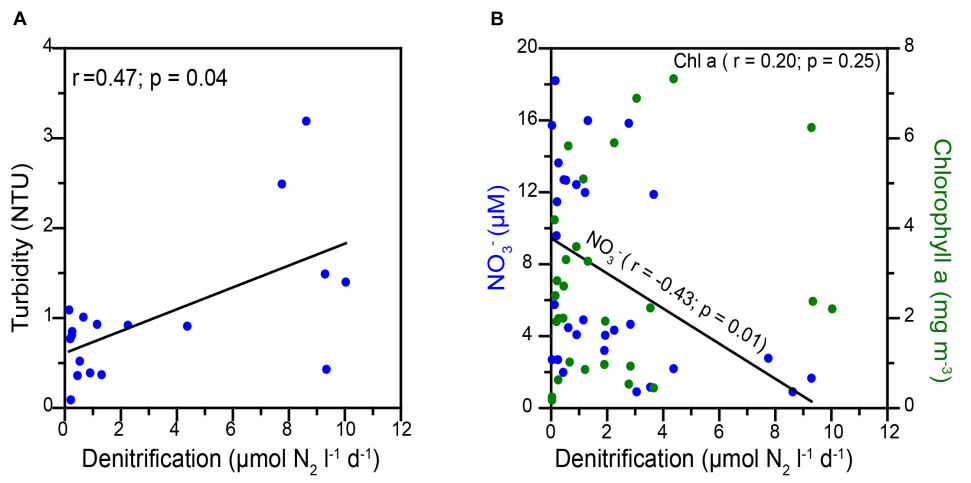


FIGURE 4 | Correlations between **(A)** Denitrification versus turbidity and **(B)** denitrification versus nitrate (blue circles) and chlorophyll *a* (green circle).

This indicates that the N-loss was not limited by organic matter over the Indian shelf.

Sulfide has been reported to inhibit anammox activity (Dalsgaard et al., 2003; Jensen et al., 2008), and this may account for lower anammox rates in our samples in 2009. Recent studies have also shown that sulfide can act as an electron donor for autotrophic denitrification. Various groups of microbes capable of sulfide driven chemolithoautotrophic denitrification have been detected in anoxic waters of the Baltic Sea (Brettar et al., 2006; Hannig et al., 2007), in Saanich Inlet (Zaikova et al., 2010), off Namibia (Lavik et al., 2009) and off Peru (Schunck et al., 2013). These bacteria are known to be fast growing and capable of forming blooms within days to weeks (Lavik et al., 2009). Therefore, it is not unlikely that the high rate of denitrification measured in 2009 arises at least in part from autotrophic denitrification by sulfide-oxidizing microbes. However, it must be pointed out that based on results of incubations alone one cannot distinguish between heterotrophic and autotrophic denitrification processes. Nevertheless, since all our denitrification rates were determined in waters with measurable nitrate/nitrite concentrations and were calculated from the linear increase in N_2 production, it is clear that these processes, whether autotrophic or heterotrophic, is mainly responsible for the apparent N-loss over the Indian shelf. The denitrification rate is of the same order of magnitude but more than double as the NO_3^- loss rate observed in the region (Naik, 2003). On the other hand, the estimated anammox rates are much lower.

N-Removal Versus Uptake Over the Western Indian Continental Shelf During Seasonal Anoxia

The overall nitrogen removal over the WICS is estimated to range between 3.70 ± 0.91 and 11.1 ± 2.72 Tg annually. This corresponds to ∼8–24% of the N-loss estimated for the open ocean OMZ of the Arabian Sea by Bulow et al. (2010) and as high as 24–60% of the model-based value (DeVries et al., 2012). In comparison, anammox contributes only 0.09 ± 0.01–0.27 ± 0.03 Tg to the N-loss per year. Our estimate is also almost three times higher than the previous estimate derived from changes in nitrate concentrations over time (Naik, 2003). The main shortcoming of this estimate that is based on complete removal of an initial NO_3^- concentration of ∼24 μM in the upwelled water over a month at a fixed sampling location (Naik, 2003), is that it ignores additional inputs of NO_3^-. A number of autochthonous and allochthonous sources of fixed nitrogen exist over WICS during the SWM season. As mentioned earlier, atmospheric deposition and land runoff contribute significantly toward the nitrogen inventory (Seitzinger et al., 2005; Naqvi et al., 2010b; Bardhan et al., 2015) which is believed to have increased in recent times. Moreover, high (millimolar) concentrations of NO_3^- are also found in ground water of Goa very close to coast and the submarine groundwater discharge is expected to be a significant but hitherto poorly quantified source of fixed nitrogen to coastal waters.

A considerable amount of fixed nitrogen is removed by the phytoplankton. The chlorophyll *a* (averaging to 2.74 mg m^{-3}) observed in the present study indicates moderately high primary production. Bhavya et al. (2017) reported a carbon uptake rate of 38.8 μmol C l^{-1} d^{-1} from coastal waters of the eastern Arabian Sea during the SWM. Using the Redfield stoichiometry (Redfield et al., 1963) this would correspond to a fixed N demand of 5.8 μmol L^{-1} d^{-1}. However, most of this nitrogen is expected to be regenerated in subsurface waters and thus made available to microbes facilitating the N-loss processes. Once the bottom waters of the WICS turn SO_4^{2-} reducing, after the oxidized N has been fully utilized, the nitrogen regenerated is in the reduced form (NH_4^+). However, it is eventually expected to be oxidized to NO_3^-. Thus, the nitrogen taken up by the autotrophs does not leave the system. The overall N-loss from the system through denitrification and anammox with the former dominating far exceed inputs through upwelling.

CONCLUSION

The present study provides the first results, based on direct measurements using the isotope pairing method of denitrification, anammox and DNRA rates over the world's largest naturally formed coastal low-O_2 zone that develops seasonally over the western Indian continental shelf. The results reveal that denitrification is the predominant process responsible for N-loss at rates that are among the highest reported from any aquatic system. Although anammox was also commonly detected in low O_2 waters its rates were much lower. DNRA was less commonly observed, and at still lower rates. Large spatial and inter annual variations in environmental conditions seem to control the magnitude of different pathways. Denitrification rates were higher over the inner shelf and at the interface of the oxic-suboxic/anoxic layers. Higher rates were observed off Karwar and Mangalore than off Goa. Evolution of sulfate reducing condition and occurrence of dissolved hydrogen sulfide might inhibit anammox activity but stimulate denitrification through chemolithoautotrophy. As in case of the OMZ off Peru, where the measured N-loss rate is the highest over the shelf but the accumulated N* signal is maximal in the offshore OMZ (Kalvelage et al., 2013; Thomsen et al., 2016), strong exchange of water between the coastal and the open ocean OMZ may export N-loss signals (i.e., N* and N_2/Ar ratios, Devol et al., 2006; DeVries et al., 2012) to the open ocean in the Arabian Sea as well.

DATA AVAILABILITY STATEMENT

The original contributions presented in the study are included in the article/**Supplementary Material**, further inquiries can be directed to the corresponding author.

AUTHOR CONTRIBUTIONS

SN and MK designed the experiments. AS, SN, AP, GS, and HN performed all the experiments. AS and SN

analyzed all the samples. AS, SN, and GL processed the data. AS wrote the manuscript with inputs from SN and GL. All authors contributed to the article and approved the submitted version.

FUNDING

Financial support for this research was provided by the European Commission through the award of a Marie Curie International Incoming Fellowship to SN to Max-Planck Society, Germany and the SIBER-INDIA program (Ministry of Earth Sciences, India). The Council of Scientific & Industrial Research (India) supported AS and GS through the award of Senior Research Fellowships.

ACKNOWLEDGMENTS

We thank all the Master and crew of CRV *Sagar Sukti* and H. Dalvi and A. Methar for extending their assistance in sample collections. We thank Dr. Rakhesh Madhusoodhanan, KISR, Kuwait for support with the statistical analysis.

SUPPLEMENTARY MATERIAL

The Supplementary Material for this article can be found online at: https://www.frontiersin.org/articles/10.3389/fmars.2020.00678/full#supplementary-material

REFERENCES

Barber, R. T., Marra, J., Bidigare, R. C., Codispoti, L. A., Halpern, D., Johnson, Z., et al. (2001). Primary productivity and its regulation in the Arabian Sea during 1995. *Deep Sea Res. Part II Top. Stud. Oceanogr.* 48, 1127–1172. doi: 10.1016/s0967-0645(00)00134-x

Bardhan, P., Karapurkar, S. G., Shenoy, D. M., Kurian, S., Sarkar, A., Maya, M. V., et al. (2015). Carbon and nitrogen isotopic composition of suspended particulate organic matter in Zuari Estuary, west coast of India. *J. Mar. Syst.* 141, 90–97. doi: 10.1016/j.jmarsys.2014.07.009

Baumann, B., Snozzi, M., Vandermeer, J. R., and Zehnder, A. J. B. (1997). Development of stable denitrifying cultures during repeated aerobic-anaerobic transient periods. *Wat. Res.* 31, 1947–1954. doi: 10.1016/s0043-1354(97)00053-5

Bendschneider, K., and Robinson, R. J. (1952). A new spectrophotometric method for the determination of nitrite in sea water. *J. Mar. Res.* 11, 87–96.

Bhavya, P. S., Kumar, S., Gupta, G. V. M., and Sudheesh, V. (2017). Carbon uptake rates in the Cochin estuary and adjoining coastal Arabian Sea. *Estuar. Coast.* 40, 447–456. doi: 10.1007/s12237-016-0147-4

Brettar, I., Labrenz, M., Flavier, S., Botel, J., Kuosa, H., Christen, R., et al. (2006). Identification of a Thiomicrospira denitrificans like epsilon proteo bacterium as a catalyst for autotrophic denitrification in the central Baltic Sea. *Appl. Environ. Microbiol.* 72, 1364–1372. doi: 10.1128/aem.72.2.1364-1372.2006

Bristow, L. A., Callbeck, C. M., Larsen, M., Altabet, M. A., Dekaezemacker, J., Forth, M., et al. (2017). N2 production rates limited by nitrite availability in the Bay of Bengal oxygen minimum zone. *Nat. Geosci.* 10:24. doi: 10.1038/ngeo2847

Bulow, S. E., Rich, J. J., Naik, H. S., Pratihary, A. K., and Ward, B. B. (2010). Denitrification exceeds anammox as a nitrogen loss pathway in the Arabian Sea oxygen minimum zone. *Deep Sea Res. Part I Oceanogr. Res. Pap.* 57, 384–393. doi: 10.1016/j.dsr.2009.10.014

Callbeck, C. M. (2017). *Distribution and Activity Of Anammox And Sulphide-Oxidizing Nitrate-Reducing Bacteria In Oxygen Minimum Zones.* Doctoral dissertation, Universität Bremen, Bremen.

Dalsgaard, T., Canfield, D. E., Petersen, J., Thamdrup, B., and Acuña-González, J. (2003). N2 production by the anammox reaction in the anoxic water column of GolfoDulce, Costa Rica. *Nature* 422, 606–608. doi: 10.1038/nature01526

Dalsgaard, T., Stewart, F. J., Thamdrup, B., De Brabandere, L., Revsbech, N. P., Ulloa, O., et al. (2014). Oxygen at nanomolar levels reversibly suppresses process rates and gene expression in anammox and denitrification in the oxygen minimum zone off northern Chile. *mBio* 5:e001966-14.

Dalsgaard, T., Thamdrup, B., Farías, L., and Revsbech, N. P. (2012). Anammox and denitrification in the oxygen minimum zone of the eastern South Pacific. *Limnol. Oceanogr.* 57, 1331–1346. doi: 10.4319/lo.2012.57.5.1331

De Brabandere, L., Canfield, D. E., Dalsgaard, T., Friederich, G. E., Revsbech, N. P., Ulloa, O., et al. (2014). Vertical partitioning of nitrogen-loss processes across the oxic-anoxic interface of an oceanic oxygen minimum zone. *Environ. Microbiol.* 16, 3041–3054. doi: 10.1111/1462-2920.12255

Devol, A. H., Uhlenhopp, A. G., Naqvi, S. W. A., Brandes, J. A., Jayakumar, D. A., Naik, H., et al. (2006). Denitrification rates and excess nitrogen gas concentrations in the Arabian Sea oxygen deficient zone. *Deep Sea Res. Part I Oceanogr. Res. Pap.* 53, 1533–1547. doi: 10.1016/j.dsr.2006.07.005

DeVries, T., Deutsch, C., Primeau, F., Chang, B., and Devol, A. (2012). Global rates of water-column denitrification derived from nitrogen gas measurements. *Nat. Geosci.* 5, 547–550. doi: 10.1038/ngeo1515

Duce, R. A., LaRoche, J., Altieri, K., Arrigo, K. R., Baker, A. R., Capone, D. G., et al. (2008). Impacts of atmospheric anthropogenic nitrogen on the open ocean. *Science* 320, 893–897.

Froelich, P. N., Klinkhammer, G. P., Bender, M. L., Luedtke, N. A., Heath, G. R., Cullen, D., et al. (1979). Early oxidation of organic matter in pelagic sediments of eastern equatorial Atlantic: suboxic diagenesis. *Geochim. Cosmochim. Acta* 43, 1075–1090. doi: 10.1016/0016-7037(79)90095-4

Grasshoff, K., Ehrhardt, M., and Kremling, K. (1983). *Methods Of Seawater Analysis*. Weinheim: Verlag Chemie.

Gruber, N., and Sarmiento, J. L. (1997). Global patterns of marine nitrogen fixation and denitrification. *Glob. Biogeochem. Cycles* 11, 235–266. doi: 10.1029/97gb00077

Hannig, M., Lavik, G., Kuypers, M. M. M., Woebken, D., Martens-Habbena, W., and Jürgens, K. (2007). Shift from denitrification to anammox after inflow events in the central Baltic Sea. *Limnol. Oceanogr.* 52, 1336–1345. doi: 10.4319/lo.2007.52.4.1336

Holtappels, M., Lavik, G., Jensen, M. M., and Kuypers, M. M. M. (2011). 15N-labelling experiments to dissect the contributions of heterotrophic denitrification and anammox to nitrogen removal in the OMZ waters of the ocean. *Methods Enzymol.* 486, 223–251. doi: 10.1016/b978-0-12-381294-0.00010-9

Jensen, M. M., Kuypers, M. M. M., Lavik, G., and Thamdrup, B. (2008). Rates and regulation of anaerobic ammonium oxidation and denitrification in the Black Sea. *Limnol. Oceanogr.* 53, 23–36. doi: 10.4319/lo.2008.53.1.0023

Jensen, M. M., Lam, P., Revsbech, N. P., Nagel, B., Gaye, B., Jetten, M. S. M., et al. (2011). Intensive nitrogen loss over the Omani Shelf due to anammox coupled with dissimilatory nitrite reduction to ammonium. *ISME J.* 5, 1660–1670. doi: 10.1038/ismej.2011.44

Jensen, M. M., Petersen, J., Dalsgaard, T. and Thamdrup, B. (2009). Pathways, rates, and regulation of $N2_2$ production in the chemocline of an anoxic basin, Mariager Fjord, Denmark. *Mar. Chemis.* 113, 102–113.

Kalvelage, T., Jensen, M. M., Contreras, S., Revsbech, N. P., Lam, P., Günter, M., et al. (2011). Oxygen sensitivity of anammox and coupled N-cycle processes in oxygen minimum zones. *PLoS One* 6:e29299. doi: 10.1371/journal.pone.0029299

Kalvelage, T., Lavik, G., Lam, P., Contreras, S., Arteaga, L., Löscher, C. R., et al. (2013). Nitrogen cycling driven by organic matter export in the South Pacific oxygen minimum zone. *Nat. Geosci.* 6, 228–234. doi: 10.1038/ngeo1739

Kartal, B., Kuypers, M. M. M., Lavik, G., Schalk, J., Op den Camp, H. J. M., Jetten, M. S. M., et al. (2007). Anammox bacteria disguised as denitrifiers: nitrate

reduction to dinitrogen gas via nitrite and ammonium. *Environ. Microbiol.* 9, 635–642. doi: 10.1111/j.1462-2920.2006.01183.x

Klawonn, I., Bonaglia, S., Brüchert, V., and Ploug, H. (2015). Aerobic and anaerobic nitrogen transformation processes in N2-fixing cyanobacterial aggregates. *ISME J.* 9:1456. doi: 10.1038/ismej.2014.232

Kuypers, M. M. M., Lavik, G., Woebken, D., Schmid, M., Fuchs, B. M., Amann, R., et al. (2005). Massive nitrogen loss from the Benguela upwelling system through anaerobic ammonium oxidation. *Proc. Natl. Acad. Sci. U.S.A.* 102, 6478–6483. doi: 10.1073/pnas.0502088102

Kuypers, M. M. M., Sliekers, A. O., Lavik, G., Schmid, M., Jørgensen, B. B., Kuenen, J. G., et al. (2003). Anaerobic ammonium oxidation by anammox bacteria in the Black Sea. *Nature* 422, 608–611. doi: 10.1038/nature01472

Lam, P., Jensen, M., Lavik, G., McGinnis, D. F., Müller, B., Schubert, C. J., et al. (2007). Linking crenarchaeal and bacterial nitrification to anammox in the Black Sea. *Proc. Natl. Acad. Sci. U.S.A.* 104, 7104–7109. doi: 10.1073/pnas.0611081104

Lavik, G., Stührmann, T., Brüchert, V., Van der Plas, A., Mohrholz, V., Lam, P., et al. (2009). Detoxification of sulphidic African shelf waters by blooming chemolithotrophs. *Nature* 457, 581–584. doi: 10.1038/nature07588

Maya, M. V., Karapurkar, S. G., Naik, H., Roy, R., Shenoy, D. M., and Naqvi, S. W. A. (2011). Intraannual variability of carbon and nitrogen stable isotopes in suspended organic matter in waters of the western continental shelf of India. *Biogeosciences* 8, 3441–3456. doi: 10.5194/bg-8-3441-2011

Naik, H. (2003). *Benthic Nitrogen Cycling With Special Reference To Nitrous Oxide In The Coastal And Continental Shelf Environments Of The Eastern Arabian Sea*. Dissertation thesis, Marine Science Department, Goa University, Goa.

Naqvi, S. W. A., Bange, H. W., Farías, L., Monteiro, P. M. S., Scranton, M. I., and Zhang, J. (2010a). Marine hypoxia/anoxia as a source of CH4 and N2O. *Biogeosciences* 7, 2159–2190.

Naqvi, S. W. A., Naik, H., D' Souza, W., Narvekar, P. V., Paropkari, A. L., and Bange, H. W. (2010b). "Carbon and nitrogen fluxes in the North Indian Ocean," in *Carbon And Nutrient Fluxes In Continental Margins: A Global Synthesis*, eds K. K. Liu, L. Atkinson, R. Quinones, and M. L. Talaue (Berlin: Springer).

Naqvi, S. W. A., Jayakumar, D. A., Narvekar, P. V., Naik, H., Sarma, V. V. S. S., D'Souza, W., et al. (2000). Increased marine production of N2O due to intensifying anoxia on the Indian continental shelf. *Nature* 408, 346–349. doi: 10.1038/35042551

Naqvi, S. W. A., Lam, P., Narvenkar, G., Sarkar, A., Naik, H., Pratihary, A., et al. (2018). Methane stimulates massive nitrogen loss from freshwater reservoirs in India. *Nat. Commun.* 9, 1–10.

Naqvi, S. W. A., Naik, H., Jayakumar, A., Pratihary, A. K., Narvenkar, G., Kurian, S., et al. (2009). "Seasonal anoxia over the western Indian continental shelf," in *Indian Ocean Biogeochemical Processes And Ecological Variability 1*, eds J. D. Wiggert, R. R. Hood, S. W. A. Naqvi, K. H. Brink, and S. L. Smith (Berlin: Springer), 333–345. doi: 10.1029/2008gm000745

Naqvi, S. W. A., Naik, H., Jayakumar, D. A., Shailaja, M. S., and Narvekar, P. V. (2006a). "Seasonal oxygen deficiency over the western continental shelf of India," in *Past and Present Water Column Anoxia, NATO Science Series, IV. Earth and Environmental Sciences 64*, ed. L. Neretin (Dordrecht: Springer), 195–224. doi: 10.1007/1-4020-4297-3_08

Naqvi, S. W. A., Naik, H., Pratihary, A. K., DeSouza, W., Narvekar, P. V., Jayakumar, D. A., et al. (2006b). Coastal versus open-ocean denitrification in the Arabian Sea. *Biogeosciences* 3, 621–633. doi: 10.5194/bg-3-621-2006

Nielsen, L. P. (1992). Denitrification in sediment determined from nitrogen isotope pairing. *FEMS Microbiol. Lett.* 86, 357–362. doi: 10.1111/j.1574-6968.1992.tb04828.x

Pratihary, A. K., Naqvi, S. W. A., Narvenkar, G., Kurian, S., Naik, H., Naik, R., et al. (2014). Benthic mineralization and nutrient exchange over the inner continental shelf of western India. *Biogeosciences* 11, 2771–2791. doi: 10.5194/bg-11-2771-2014

Preisler, A., De Beer, D., Lichtschlag, A., Lavik, G., Boetius, A., and Jørgensen, B. B. (2007). Biological and chemical sulphide oxidation in a Beggiatoa inhabited marine sediment. *ISME J.* 1, 341–353. doi: 10.1038/ismej.2007.50

Rabalais, N. N., Diaz, R. J., Levin, L. A., Turner, R. E., Gilbert, D., and Zhang, J. (2010). Dynamics and distribution of natural and human-caused hypoxia. *Biogeosciences* 7:585. doi: 10.5194/bg-7-585-2010

Redfield, A. C., Ketchum, B. H., and Richards, F. A. (1963). "The influence of organisms on the composition of sea-water," in *The Composition Of Seawater: Comparative And Descriptive Oceanography. The Sea: Ideas And Observations On Progress In The Study Of The Seas*, ed. M. N. Hill (New York, NY: Interscience Publishers), 26–77.

Rönner, U., and Sörensson, F. (1985). Denitrification rates in the low-oxygen waters of the stratified Baltic proper. *Appl. Environ. Microbiol.* 50, 801–806.

Schlitzer, R. (2018). *Ocean Data View*. Available online at: https://odv.awi.de

Schott, F., and McCreary, J. P. (2001). The monsoon circulation of the Indian Ocean. *Prog. Oceanogr.* 51:123.

Schunck, H., Lavik, G., Desai, D. K., Großkopf, T., Kalvelage, T., Löscher, C. R., et al. (2013). Giant hydrogen sulphide plume in the oxygen minimum zone off Peru supports chemolithoautotrophy. *PLoS One* 8:e68661. doi: 10.1371/journal.pone.0068661

Seitzinger, S. P., Harrison, J. A., Dumont, E., Beusen, A. H. W., and Bouwman, A. F. (2005). Sources and delivery of carbon, nitrogen, and phosphorus to the coastal zone: an overview of global nutrient export from watersheds (NEWS) models and their application. *Glob. Biogeochem. Cycles* 19:2606.

Shankar, D., Shenoi, S. S. C., Nayak, R. K., Vinayachandran, P. N., Nampoothiri, G., Almeida, A. M., et al. (2005). Hydrography of the eastern Arabian Sea during summer monsoon 2002. *J. Earth Syst. Sci.* 114, 459–474. doi: 10.1007/bf02702023

Shenoy, D. M., Sujith, K. B., Gauns, M., Patil, S., Sarkar, A., Naik, H., et al. (2012). Production of dimethylsulphide during the seasonal anoxia off Goa. *Biogeochemistry* 110, 47–55. doi: 10.1007/s10533-012-9720-5

Song, G. D., Liu, S. M., Kuypers, M. M. M., and Lavik, G. (2016). Application of the isotope pairing technique in sediments where anammox, denitrification, and dissimilatory nitrate reduction to ammonium coexist. *Limnol. Oceanogr. Methods* 14, 801–815. doi: 10.1002/lom3.10127

Stramma, L., Fischer, J., and Schott, F. (1996). The flow field off southwest India at 8N during the southwest monsoon of August 1993. *J. Mar. Res.* 54, 55–72. doi: 10.1357/0022240963213448

Strickland, J. D. H., and Parsons, T. R. (1972). A practical handbook of seawater analysis. *Fish. Res. Board Canada* 167:31.

Strous, M., Heijnen, J. J., Kuenen, J. G., and Jetten, M. S. M. (1998). The sequencing batch reactor as a powerful tool for the study of slowly growing anaerobic ammonium-oxidizing microorganisms. *Appl. Microbiol. Biotechnol.* 50, 589–596. doi: 10.1007/s002530051340

Thamdrup, B., and Dalsgaard, T. (2002). Production of N2 through anaerobic ammonium oxidation coupled to nitrate reduction in marine sediments. *Appl. Environ. Microbiol.* 68, 1312–1318. doi: 10.1128/aem.68.3.1312-1318.2002

Thamdrup, B., Dalsgaard, T., and Revsbech, N. P. (2012). Widespread functional anoxia in the oxygen minimum zone of the Eastern South Pacific. *Deep Sea Res. Part I Oceanogr. Res. Pap.* 65, 36–45. doi: 10.1016/j.dsr.2012.03.00133

Thomsen, S., Kanzow, T., Krahmann, G., Greatbatch, R. J., Dengler, M., and Lavik, G. (2016). The formation of a subsurface anticyclonic eddy in the Peru-Chile Undercurrent and its impact on the near-coastal salinity, oxygen, and nutrient distributions. *J. Geophys. Res. Oceans* 121, 476–501. doi: 10.1002/2015jc010878

van der Star, W. R. L., Miclea, A. I., Van dongen, U. G. J. M., Muyzer, G., Picioreanu, C., and Van Loosdrecht, M. C. M. (2008). The membrane bioreactor: a novel tool to grow anammox bacteria as free cells. *Biotechnol. Bioeng.* 101, 286–294. doi: 10.1002/bit.21891

Ward, B. B., Tuit, C. B., Jayakumar, A., Rich, J. J., Moffet, J., and Naqvi, S. W. A. (2008). Organic carbon, and not copper, controls denitrification in oxygen minimum zones of the ocean. *Deep Sea Res. Part I Oceanogr. Res. Pap.* 55, 1672–1683. doi: 10.1016/j.dsr.2008.07.005

Warembourg, F. R. (1993). "Nitrogen fixation in soil and plant system," in *Nitrogen Isotopes Techniques*, eds R. Knowles and T. H. Blackburn (San Diego, CA: Academic Press), 127–156. doi: 10.1016/b978-0-08-092407-6.50010-9

Woebken, D., Fuchs, B. M., Kuypers, M. M. M., and Amann, R. (2007). Potential interactions of particle-associated anammox bacteria with bacterial and archaeal partners in the Namibian upwelling system. *Appl. Environ. Microbiol.* 73, 4648–4657. doi: 10.1128/aem.02774-06

Zaikova, E., Walsh, D. A., Stilwell, C. P., Mohn, W. W., Tortell, P. D., and Hallam, S. J. (2010). Microbial community dynamics in a seasonally anoxic fjord: Saanich Inlet., British Columbia. *Environ. Microbiol.* 12, 172–191. doi: 10.1111/j.1462-2920.2009.02058.x

Conflict of Interest: The authors declare that the research was conducted in the absence of any commercial or financial relationships that could be construed as a potential conflict of interest.

Copyright © 2020 Sarkar, Naqvi, Lavik, Pratihary, Naik, Shirodkar and Kuypers. This is an open-access article distributed under the terms of the Creative Commons Attribution License (CC BY). The use, distribution or reproduction in other forums is permitted, provided the original author(s) and the copyright owner(s) are credited and that the original publication in this journal is cited, in accordance with accepted academic practice. No use, distribution or reproduction is permitted which does not comply with these terms.

frontiers in Marine Science

ORIGINAL RESEARCH
published: 05 January 2021
doi: 10.3389/fmars.2020.575547

Early Diagenesis in Sediments of the Venice Lagoon (Italy) and Its Relationship to Hypoxia

Daniele Brigolin[1,2†], Christophe Rabouille[3†], Clément Demasy[3], Bruno Bombled[3], Gaël Monvoisin[4] and Roberto Pastres[2]*

[1] Department of Architecture and Arts, Università IUAV di Venezia, Venezia, Italy, [2] Department of Environmental Sciences, Informatics and Statistics, Università Ca' Foscari Venezia, Venezia, Italy, [3] Laboratoire des Sciences du Climat et de l'Environnement, UMR CEA-CNRS-UVSQ et IPSL, Université Paris-Saclay, Gif-sur-Yvette, France, [4] CNRS, GEOPS, Université Paris-Saclay, Orsay, France

This work focuses on sediments of a shallow water lagoon, located in a densely populated area undergoing multiple stressors, with the goal of increasing the understanding of the links between diagenetic processes occurring in sediments, the dynamics of dissolved oxygen (DO) in the water column, and potential consequences of hypoxia. Sediment data were collected over three consecutive years, from 2015 to 2017, during spring–summer, at five stations. Measured variables included: sediment porosity, grain size and organic carbon content, porewater microprofiles of O_2, pH and H_2S, porewater profiles of dissolved inorganic carbon (DIC), total alkalinity (TA), NH_4^+, NO_3^-, dissolved Fe, and SO_4^{2-}. In addition, long-term time series of oxygen saturations in the water column (years 2005–2017) were utilized in order to identify the occurrence and duration of hypoxic periods. The results show that the median DO saturation value in summer months was below 50% (around 110 μmol L^{-1}), and that saturation values below 25% (below the hypoxic threshold) can persist for more than 1 week. Sediment stations can be divided in two groups based on their diagenetic intensity: intense and moderate. At these two groups of stations, the average DIC net production rates, estimated trough a steady-state model (Profile) were, respectively, of 2.8 and 1.0 mmol m^{-2} d^{-1}, SO_4^{2-} consumption rates were respectively 1.6 and 0.4 mmol m^{-2} d^{-1}, while diffusive oxygen uptake fluxes, calculated from the sediment microprofile data, were of 28.5 and 17.5 mmol m^{-2} d^{-1}. At the stations characterized by intense diagenesis, total dissolved sulfide accumulated in porewaters close to the sediment-water interface, reaching values of 0.7 mM at 10 cm. Considering the typical physico-chemical summer conditions, the theoretical time required to consume oxygen down to the hypoxic level by sediment oxygen demand ranges between 5 and 18 days, in absence of mixing and re-oxygenation. This estimation highlights that sediment diagenesis may play a crucial role in triggering and maintaining hypoxia of lagoon waters during the summer season in specific high intensity diagenesis zones. This role of the sediment could be enhanced by changes in regional climate conditions, such as the increase in frequency of summer heat waves.

Keywords: early diagenesis, hypoxia, sulfide, shallow water, coastal urban ecosystems, Adriatic sea

OPEN ACCESS

Edited by:
Richard Alan Feely, Pacific Marine Environmental Laboratory (NOAA), United States

Reviewed by:
Peng Yao, Hohai University, China
Raghab Ray, University of Tokyo, Japan

****Correspondence:***
Daniele Brigolin
dbrigolin@iuav.it

† These authors have contributed equally to this work

Specialty section:
This article was submitted to Coastal Ocean Processes, a section of the journal Frontiers in Marine Science

Received: *23 June 2020*
Accepted: *09 November 2020*
Published: *05 January 2021*

Citation:
Brigolin D, Rabouille C, Demasy C, Bombled B, Monvoisin G and Pastres R (2021) Early Diagenesis in Sediments of the Venice Lagoon (Italy) and Its Relationship to Hypoxia. Front. Mar. Sci. 7:575547. doi: 10.3389/fmars.2020.575547

INTRODUCTION

In shallow coastal and marine environments, sediment is expected to have a primary role in controlling the water column biogeochemistry, by influencing the dynamics of oxygen, carbon and macronutrients (N and P) (Schlesinger and Bernhardt, 2013). Hypoxic conditions, in which dissolved oxygen (DO) concentration falls below 2 mg L^{-1} (62 μmol L^{-1}), represent a major threat for coastal ecosystems worldwide (Zhang et al., 2010; Breitburg et al., 2018), because low levels of oxygen affects the metabolism and survival of the less mobile macrofauna (Rabalais et al., 2002; Vaquer-Sunyer and Duarte, 2008), and because the release of toxic compounds from sediments (e.g., H_2S) can harm vertebrate species (Vaquer-Sunyer and Duarte, 2010). The interaction between sediment biogeochemistry and hypoxia has been thoroughly investigated in ecosystems where large areas are hypoxic or become periodically hypoxic (Diaz and Rosenberg, 2008; Middelburg and Levin, 2009), and is also receiving increasing attention in landlocked stratified environments (e.g., Friedrich et al., 2014; Zhu et al., 2017). Less attention has been given, however, to non-stratified shallow water systems where wind is expected to have a major role in water mixing and reoxygenation (Chapelle et al., 2000, 2001). Nonetheless, the coupling between sediment and water column biogeochemical processes is expected to be significant in these highly productive environments, characterized by intense patterns of deposition/resuspension and accumulation of organic debris in specific areas. As a result of organic matter mineralization, the oxygen demand of surface sediment and the potential release of H_2S, accumulated as a by-product of anoxic diagenesis, could be very high (Burdige, 2006). Moreover, an increase in the frequency of summer heat waves due to climate change, which is currently being observed in the Mediterranean region (MerMex Group, 2011; Galli et al., 2017), could lead to increased stratification and therefore duration and severity of hypoxic events, as already reported for European freshwater lakes during the 2003 heat wave (Jankowski et al., 2006).

Lagoons are good examples of vulnerable shallow ecosystems characterized by multiple pressures (Kennish and Paerl, 2010), as they are often located in close proximity of urban areas and megacities (e.g., Gu et al., 2013). In many instances, these systems are protected by international treaties (e.g., Ramsar Convention, 1971) and directives aimed at preserving water quality (e.g., WFD, European Community, 2000). Indeed, they represent valued natural environments and provide goods and services to coastal communities (Millennium Ecosystem Assessment, 2005; Rova et al., 2019). The Venice lagoon (Italy) represents an ecosystem located in a densely populated area with multiple stressors such as massive tourism, aquaculture, industry, maritime circulation (Solidoro et al., 2010), in which the links between sediment and water column dynamics may play an important role in defining ecosystem functioning.

Previous studies on Venice lagoon sediments have emphasized the mapping and evolution of organic carbon (OC) and contaminants in the solid phase of the sediments (Lucchini et al., 2002; Sfriso et al., 2005) in the context of past eutrophication (Pastres et al., 2004) and its relation to oxygen dynamics (Lovato et al., 2013). Other studies (Gieskes et al., 2015) investigated early diagenesis and porewater composition of lagoon sediments, including dissolved sulfide in relation with dredging and disposal of contaminated sediments. The mineralization of organic matter from sewage discharge in the canals network within the historical city, and its contribution to sulfide release was also investigated (Zaggia et al., 2007; Azzoni et al., 2015). Yet, a comprehensive knowledge of organic matter diagenesis in areas of the lagoon which are not directly influenced by the city discharges is missing.

The goal of the current study is to understand the link between diagenetic processes occurring in sediments and the dynamics of DO in lagoon waters. We set three objectives: (i) measure the oxygen demand of surface sediment in different lagoon depositional systems and understand its relationship with hypoxia in the bottom waters; (ii) categorize lagoon areas with respect to the intensity of early diagenesis and associated oxygen demand, and (iii) assess the potential for H_2S release from sediments during hypoxic events. In order to achieve these goals, sediment data were collected, in spring–summer 2015, 2016, and 2017, at five stations, located in open shallow areas of the lagoon (depth, 1 ± 0.5 m) belonging to different Water Framework Directive (WFD) water bodies, and characterized by different depositional environments in terms of exposure to the winds and riverine influence. The results of the field surveys were interpreted using a set of modeling tools and based on the analysis of long-term time series of oxygen saturation data in the water column (2005–2017), collected by the Ministero delle Infrastrutture e dei Trasporti, formerly Venice Water Authority (Magistrato alle Acque).

STUDY SITE DESCRIPTION: THE VENICE LAGOON

The Venice lagoon is a shallow water body, covering an area of approximately 432 km^2 (Sfriso et al., 2019). Its average depth is approximately 1 m, with only 5% deeper than 5 m (some navigable channels are deeper than 15 m). The lagoon is connected to the Northern Adriatic Sea through three inlets: the tidal exchange can reach 20,000 m^3 s^{-1} at peak flow during spring tides (Umgiesser, 2020). On average, water residence time ranges from a few days in the areas close to the inlets to about one month in the inner part, close to the river tributaries (Cucco and Umgiesser, 2006). Notwithstanding the high anthropogenic impact, the Venice lagoon ecosystem still shows a good resilience, providing a broad range of ecosystem services (Rova et al., 2015, 2019). In compliance with the implementation of the Water Framework Directive 2000/60/EC (European Community, 2000), the lagoon was divided into 11 water bodies, based on a combination of hydrological descriptors, existing pressures and chemical, and ecological status (Hydrographic district of Oriental Alps, HDOA; Autorità di bacino dell'Adige e dell'Alto Adriatico, 2010).

Surface sediment was sampled at the five stations shown in **Figure 1**. With respect to the WFD water bodies, stations ALG1,

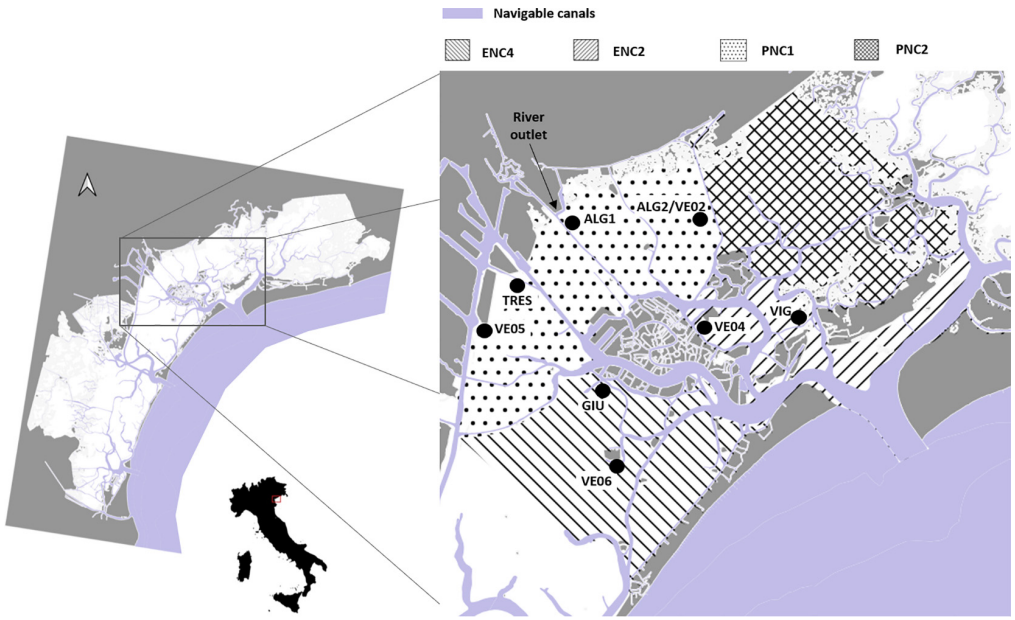


FIGURE 1 | Sediment sampling stations (ALG1, ALG2, TRES, GIU, and VIG), and oxygen monitoring stations (VE 02-04-05-06) reported in the framework of the subdivision adopted by the management plan HDOA (see references in text).

ALG2, and TRES are located in PNC1, VIG in ENC2, and GIU in ENC4. PNC1 stands for Polyhaline Non-Confined 1 water body, with salinity ranging between 20 and 30, while ENC2 and ENC4 are Eurhaline Non-Confined 2 and 4, with salinity between 30 and 40; the three water bodies are NC-non-confined, to differentiate them from those located in the inner parts of the lagoon, characterized by higher water residence time. All stations were located in shallow areas, about 1 m deep. Station ALG2 was located near a Manila clam (*Ruditapes philippinarum*) farming area (Pessa et al., 2018). Stations ALG2, GIU, and TRES were more exposed to wind, with respect to ALG1 and VIG, which are protected, respectively, by an island and a saltmarsh, with the prevalent winds in this area blowing from North-East (Bora) and South-East (Scirocco). The water residence time was higher at stations TRES and ALG1: the latter is also directly affected by freshwater discharges. Four water quality monitoring stations were selected, belonging to the Ministero delle Infrastrutture e dei Trasporti network (**Figure 1**). One of these stations, VE02, was located nearby the ALG2 station.

MATERIALS AND METHODS

Field Campaigns and Data Analysis

The five stations in the central part of the lagoon were sampled in 2015, 2016, and 2017 (**Figure 1** and **Table 1**). At each station, water column was sampled at a depth of 0.5 m with a 5-L Niskin® bottle. At least three 20–40 cm long sediment cores were collected using an Uwitech single tube corer attached to a coring stick. Cores were capped and stored in the shade before returning to the laboratory.

Water Sampling and Analyses

Water temperature was measured with a precision of 0.1°C and salinity with a thermo-salinometer with a precision of 0.1. pH measurements were carried out in 2017 in triplicate within 1 h after sampling by spectrophotometry with unpurified m-cresol purple as indicator dye (Clayton and Byrne, 1993). They are reported on the total proton scale (pH_T) with an uncertainty of ±0.01 pH units. Samples for dissolved inorganic carbon (DIC) and total alkalinity (TA) analysis were stored in 50 ml "grease sealed" glass stoppered bottles, and preserved by adding 100 µl of saturated $HgCl_2$. One bottle was collected at each station, each expedition. TA was measured on 20 ml samples by open cell titration with 0.01 N HCl (Dickson et al., 2007). DIC concentration was analyzed with a DIC analyzer (Apollo/SciTech®) on repeated 1 ml samples (Rassmann et al., 2016). Both measurements showed an uncertainty below 0.5%. Both measurements were calibrated every day using Seawater Reference Material (standard batch #136) provided by the Scripps Institution of Oceanography (A.G. Dickson Laboratory). In 2016, pH was recalculated from DIC, TA, T, and S using the CO2Sys software (Lewis and Wallace, 1998). DO concentrations were determined by Winkler titration (Grasshof et al., 1983) with a precision of ±0.5 µM.

Porosity, Organic Carbon Content, and Grain Size

Sediment porosity profiles were determined by slicing one of the cores with a 2 mm resolution until 10 mm depth, a 5 mm resolution until 60 mm (Cathalot et al., 2010), and a 10 mm resolution down to the bottom of the core. Porosity was calculated as the weight difference between wet

TABLE 1 | Positions of the five sampling stations and field surveys.

	Lat (N)	Long (E)	Depth (m)	Sampling year (s)	Sampled variables	Water body (WFD); closer monitoring station; station characteristics
ALG1	45°27′46 ″	12°17′17″	1.0	2015; 2016; 2017	(WC)T;S;pH;TA;DIC;DO (PW)TA;DIC;SO4;NH4;NO3;pH;TS (S)OC;por;grain size	PNC1; VE02; higher exposure to NE wind; nearby river outlet
ALG2	45°20′02 ″	12°19′56″	1.5	2015; 2016; 2017	(WC)T;S;pH;TA;DIC;DO (PW)TA;DIC;SO4;NH4;NO3;pH (S)OC;por;grain size	PNC1; VE02; exposure to NE and SE winds; close to a shellfish farming lease
GIU	45°25′71 ″	12°18′57″	1.0	2016; 2017	(WC)T;S;pH;TA;DIC;DO (PW)TA;DIC;SO4;NH4;NO3;pH (S)OC;por;grain size	ENC4; VE06; higher exposure to SE winds
TRES	45°26′38 ″	12°16′26″	1.5	2017	(WC)T;S;pH;TA;DIC;DO (PW)TA;DIC;SO4;NH4;NO3;pH;TS (S)OC;por;grain size	PNC1; VE05; higher exposure to SE winds
VIG	45°26′57 ″	12°22′47″	0.8	2016	(WC)T;S;pH;TA;DIC;DO (PW)TA;DIC;SO4;NH4 (S)OC;por;grain size	ENC2; VE04; protected

and dried sediment after 1 week at 60°C, using average sediment density (2.65 g cm^{-3}) and a salt correction based on lagoon water salinity at the site. Organic carbon was measured after removing inorganic carbon using HCl 1.2 N as a wet treatment. Drying was made at 60°C after rinsing and centrifugation. Around 1 g of sediment was decarbonated and the sample size for measurement, in triplicate, was 15–20 mg. Standards for the CHN analyzer calibration were made of pure acetanilide. Measurements were performed on a Fisons Instrument NA 1500 Element Analyzer at LSCE (Cathalot et al., 2013) with a precision of 0.1% dry weight. For grain-size determination, bulk sediment was treated with 0.1 N aqueous solutions of hydrogen peroxide (H_2O_2) and acetic acid (25%) to remove organic materials and carbonate fractions, respectively. The mixture was then rinsed several times (about five rinse cycles) to remove acetic acid residues and gently shaken to achieve deflocculation of sediment. Grain-size distribution of carbonate- and organic-free terrigenous particles in the range of 1.0–2000 μm in the suspension was determined using a Malvern Mastersizer 2000 Particle Size Analyzer at the Laboratoire Géosciences Paris-Sud (GEOPS, Université Paris-Sud/Paris-Saclay). In order to reduce quantity errors, each sample was measured five times and the average of these five measurements was employed to represent the grain-size distribution of each sample.

Porewater Microprofiles of O_2, pH, and H_2S

One of the three cores was used for determining oxygen, pH, and H_2S microprofiles at the three sites, using micro-electrodes (Unisense®) (Rabouille et al., 2003; Cathalot et al., 2012; Rassmann et al., 2016). Cores were maintained at *in situ* temperature using a cooling device and gently bubbled with air, in order to ensure overlying water oxygenation and stirring. Three to four oxygen profiles, two pH profiles, and one H_2S profile were measured within the portion of the core in which no shell debris and macrobenthos were visible at the surface. Vertical profiles were measured with a 200 μm resolution near the sediment-water interface (SWI) and 500–3000 μm resolution below 2 cm to (for pH and H_2S). O_2 microelectrodes were calibrated with a two-point calibration technique using O_2 concentration in the water determined by Winkler titration and the anoxic pore waters. The pH microelectrodes were calibrated using three NBS buffers (pH 4.00, 7.00, and 9.00 at 20°C) for the electrode slope which was recalculated at *in situ* T. The pH variation was then added to the bottom water pH measured at the station for the absolute value (pH_T scale). Signal drift of O_2 and pH microelectrodes during profiling was checked to be less than 5%. Diffusive Oxygen Uptake rates (DOU) were calculated for each micro-profile using the observed O_2 concentration gradient calculated over 400 μm in the sediment, the measured porosity value and the diffusion coefficient at *in situ* temperature (Broecker and Peng, 1974) corrected for tortuosity. Clark-type microsensors (Cathalot et al., 2012), with a platinum guard cathode to ensure a low and stable readings in the absence of sulfide were used for determining sulfides. They were calibrated using H_2S standards prepared daily from a main solution and preserved with $TiCl_3$. The main sulfide solution was re-titrated every day using the classical sulfide titration (Grasshof et al., 1983). The position of the SWI for sulfide electrode was determined visually and the measurement step (initially 200 μm) was adapted to adequately capture the sulfide gradient and measure deeper concentrations (with a 1–3 mm step). Total sulfide (TS) was recalculated using pH and measured H_2S (Jeroschewski et al., 1996).

Porewater Profiles: DIC, Alk, NH_4^+, NO_3^-, Fe^{2+}, SO_4^{2-}

The extraction of sediment pore waters was conducted immediately after returning to the air-conditioned laboratory (1–2 h after core collection) using Rhizon filters with a mean pore size of 0.1 μm (Seeberg-Elverfeldt et al., 2005) in a glove bag flushed with N_2 to create an anoxic atmosphere. The sampling interval was 2 cm in the top 10 and 4 cm underneath. Immediately after collection, pore waters were analyzed for dissolved Fe^{2+} using the ferrozine technique (Stookey, 1970)

and total dissolved iron concentrations the next morning after reduction of total dissolved iron with hydroxylamine. Porewater and water samples were poisoned with $HgCl_2$ for TA and DIC laboratory analysis, acidified for sulfate, and stored in the dark at 4°C until analysis in the laboratory. Subsamples for NH_4^+ were frozen. Another core was sectioned and centrifuged at room temperature for the determination of nitrate (NO_3^-) at higher depth resolution near the SWI (0.5 cm) down to 2 cm, and 1 cm resolution down to 5 cm. After centrifugation, porewaters were filtered using 0.45 μm pore size Minisart and kept frozen until analysis. TA was measured on 3 ml samples by open cell titration with 0.01 N HCl (Dickson et al., 2007). DIC concentrations were analyzed with a DIC analyzer (Apollo/SciTech®) on 1 ml samples as previously described (Rassmann et al., 2016). Certified reference materials were used to calibrate the TA and DIC methods (oceanic CO_2 measurements, Scripps Institution of Oceanography-batch n°136). The relative uncertainty for DIC and TA was ±0.5% of the final value. Sulfate (SO_4^{2-}) concentration was quantified after dilution by a factor of 100 by ion chromatography on an ICS 1000 chromatograph (Dionex) with a relative uncertainty of ±1.6% (Rassmann et al., 2020). To measure ammonium (NH_4^+) concentrations, samples were diluted and analyzed using the indophenol blue method (Grasshof et al., 1983). The uncertainty of the method with small porewater volume was about 5%. NO_3^- was determined using the Vanadium chloride reductant as described in Schnetger and Lehners (2014) followed by the NEDD/sulphanilamide addition and colorimetric measurement. Precision on total NO_x was around 2%.

Time Series of Water Quality Monitoring Data

Bi-hourly time series of DO saturation, water temperature, and salinity, were provided by Ministero delle Infrastrutture e dei Trasporti (provveditorato generale alle OO PP del Veneto, Trentino Alto Adige, Friuli Venezia Giulia, già Magistrato alle Acque di Venezia). Data were collected from March 2005 to December 2018 by the monitoring network SAMANet, set up and managed by the same water authority. Time series pertaining to stations VE02, VE04, VE05, VE06 (**Figure 1**), which were located in the three WFD water bodies, were considered as representative of the water quality at the five stations in which the sediments were collected, VE02 for ALG1 and ALG2, VE04 for VIG, VE06 for GIU, and VE05 for TRES (**Table 1**). Data collected 2 weeks before the field surveys were used for characterizing the hydrological conditions in which sediment samplings were carried out. The time-series of oxygen saturation in summertime (June to September) were reanalyzed for estimating: (i) the weekly average DO saturation (values exceeding ±2.7σ were discarded as outliers), and (ii) the number of consecutive days with minimum O_2 values <25% saturation, which was taken as an indicator of the persistence of an hypoxic event. Indeed, at the average summer temperatures (>20°C) and salinities (>25), this saturation threshold (<55 μmol L^{-1}) is below the hypoxic level (62 μmol L^{-1}).

Porewater Profiles Averaging and Reaction Rate Calculations

The rates of DIC production and SO_4^{2-} consumption were estimated using the Profile software (Berg et al., 1998), using as input the average profiles of DIC and SO_4^{2-} at ALG1 and ALG2 with a resolution of 1 cm. These were obtained by linearly interpolating each profile, and averaging them. The set of input data included also files containing different levels of bio-irrigation. Fits to the measured concentration profiles were optimized and the integrated reaction rates converted in mmol m^{-2} d^{-1}. The uncertainty for the rate calculations is estimated as ±50%.

RESULTS

Water Column, Porewater, and Sediment Profiles

Water physico-chemical parameters measured during the three sampling campaigns, Jun 2015, May 2016, and Sep 2017 (herein 2015; 2016; 2017) are reported in **Table 2**. Temperature ranged from 17.2°C (ALG2-2016) to 26.2°C (ALG1-2015), while salinity varied from 26 psu (ALG2-2015) to 33.1 psu (GIU-2016). Salinity showed limited within-station variability, with the exception of ALG-1 in 2015. DO concentrations were close to saturation except at ALG1 in 2015 (356.3 μM). TA and DIC were markedly larger at stations ALG1 (3067–3417 TA; 2784–2915 DIC) and ALG2 (3036–3281 TA; 2868–2882 DIC), compared with the other stations (min TA 2917, min DIC 2583 at TRES in

TABLE 2 | Water physico-chemical parameters at the five sampled stations, years 2015–2017.

	June 25–26, 2015		May 10–13, 2016				September 22–26, 2017			
Station	**ALG1**	**ALG2**	**ALG1**	**ALG2**	**GIU**	**VIG**	**ALG1**	**ALG2**	**GIU**	**TRES**
T (°C)	26.2	23.9	20.1	17.2	19	17.4	18	18.2	19.3	19.9
S (–)	26.1	26	30.1	27	33.1	32.5	30.6	27.2	31.8	31.9
pH (tot scale)	/	/	/	/	/	/	7.72	7.81	7.85	7.95
TA (μM)	3417	3281	3067	3036	2892	2953	3128	3212	2986	2917
DIC (μM)	2915	2868	2784	2882	2615	2567	2883	2870	2657	2583
Oxygen (μM)	356.3	251.5	173.9	230.1	202.6	283	180	223	220.1	239.3
% sat O_2	162	111	73	90	85	114	73	90	92	102

2017), accompanied by a lower pH at ALG1 (min 7.72 at ALG1, max 7.95 at TRES). Water column physico-chemical parameters recorded at the monitoring station VE 02 during the fortnight preceding each sampling campaign are shown in **Figure 2**. Water temperatures ranged from 14.3°C in late April 2016, to 28.9°C in June 2015 and showed marked differences of environmental conditions during these 3 years. Summer conditions, with water temperatures going above 29°C were present in late June 2015, while transition water temperatures were recorded in May 2016, raising from 12.5 to 22°C, and indicating a spring rapid warming of the water column, approaching a pre-summer condition. The opposite situation was recorded in late September 2017, with water temperatures decreasing from 24 to 15°C, and stabilizing around 18°C during the sampling campaign. Salinity shows large daily variability among the 3 years, being mainly influenced by tidal exchanges and river inputs. Regarding DO, 2015 presents remarkable differences with respect to the two consecutive years, with daily values reaching 250% saturation, and indicating intense primary production.

Figures 3, **4** show the pore water profiles, respectively for the years 2015–2016 and 2017. The core length ranged from 15 to 45 cm, due to the compactness of the sediment and the associated difficulty to sample long cores. DO, DIC, TA, NH_4^+, and SO_4^{2-} were measured on all cores from the initial measurements in 2015 with the addition of pH in 2016 and NO_3^-, Fe^{2+}, and TS profiles in 2017. DIC and TA concentration profiles (**Figures 2**, **3**) showed increasing values downcore at all stations with higher maxima at stations ALG1 and TRES (>10 mM) and lower ones at stations ALG2, GIU, and VIG, where concentrations ranged from 5 to 7 mM. A similar pattern was observed for NH_4^+,with asymptotic concentrations above 500 μM at ALG1 and TRES and lower ones at the other stations (ALG2, GIU, and VIG) except GIU in 2016. In most cases, sulfate depletion was also larger at station ALG1 and TRES (except for ALG1 in 2015), with downcore concentrations lower than 5 mM at station ALG1 in 2016 and 2017 and around 12 mM at TRES. All other stations showed porewater SO_4^{2-} concentrations at depth near or above 20 mM. pH profiles at all stations showed a marked decrease (−0.5 to −0.7 pH unit) just below the SWI, followed by an increase below the oxygen penetration depth and stabilization at depth. NO_3^- concentrations decreased rapidly with depth, and fell below the detection limit below the first centimeter. Dissolved iron (II) profiles were characterized by subsurface maxima, located at a depth ranging from 1 to 3 cm: the highest peak was observed at station ALG1. Total dissolved sulfide, calculated from measured H_2S and pH, showed measurable concentrations in the top layers at two stations (ALG1 and TRES) and exceeded 0.5 mM at the bottom of the core. Vertical distributions of porosity (one profile per station per year), OC content and granulometry (one profile per station in 2017 except VIG in 2016) are shown in **Figure 5**. These parameters were measured in order to provide a background characterization of the stations. Porosity (**Figure 5**) decreased with depth, with the exception of ALG2. The steeper gradient was observed within the upper 20 mm at all sites. OC content ranged from 0.5 to 2%, with largest values in ALG1 and TRES, where algal macro-debris were observed during slicing. These two stations were characterized by the presence of fine silts. Stations GIU and VIG showed very low OC content (0.5%), which correlated negatively with coarser grain size at these stations. ALG2 profile showed a decrease in grain size with depth from coarse to fine silts, which was accompanied by an increase of OC content, from 0.5 to 1%.

Overall, 38 O_2 microprofiles were collected at the five stations. As one can see in **Figure 6**, O_2 concentrations show quasi-monotonic downward decreases, with oxygen penetration

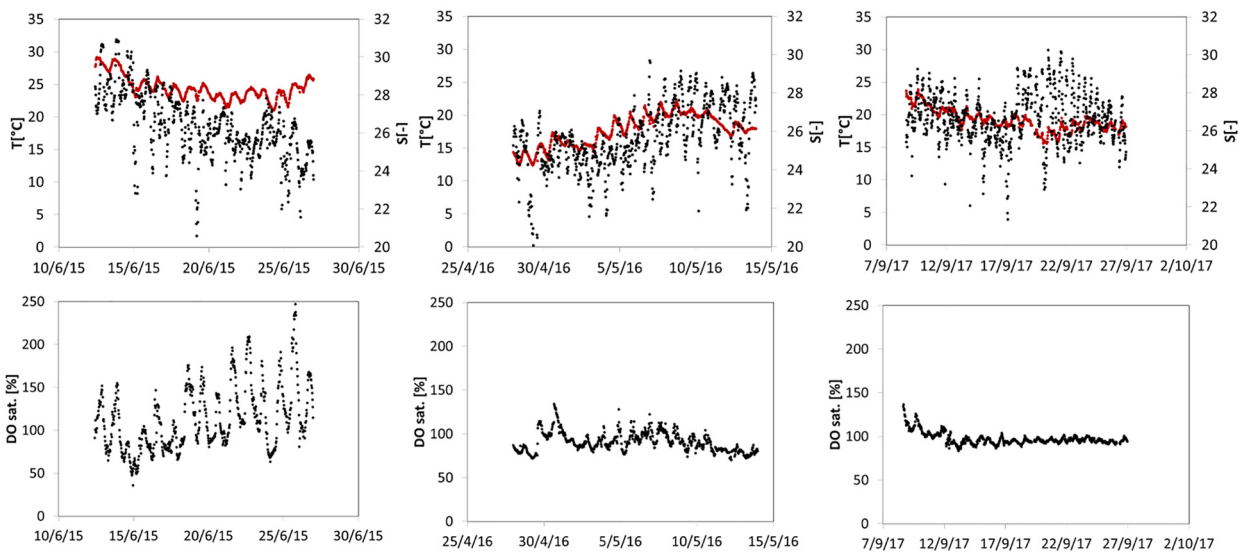


FIGURE 2 | Water column monitoring data at stations VE02 during sampling periods and on the 14 days preceding each campaign. Upper panel: water temperature (red) and salinity (black); lower panel: dissolved oxygen concentration – % with respect to saturation value.

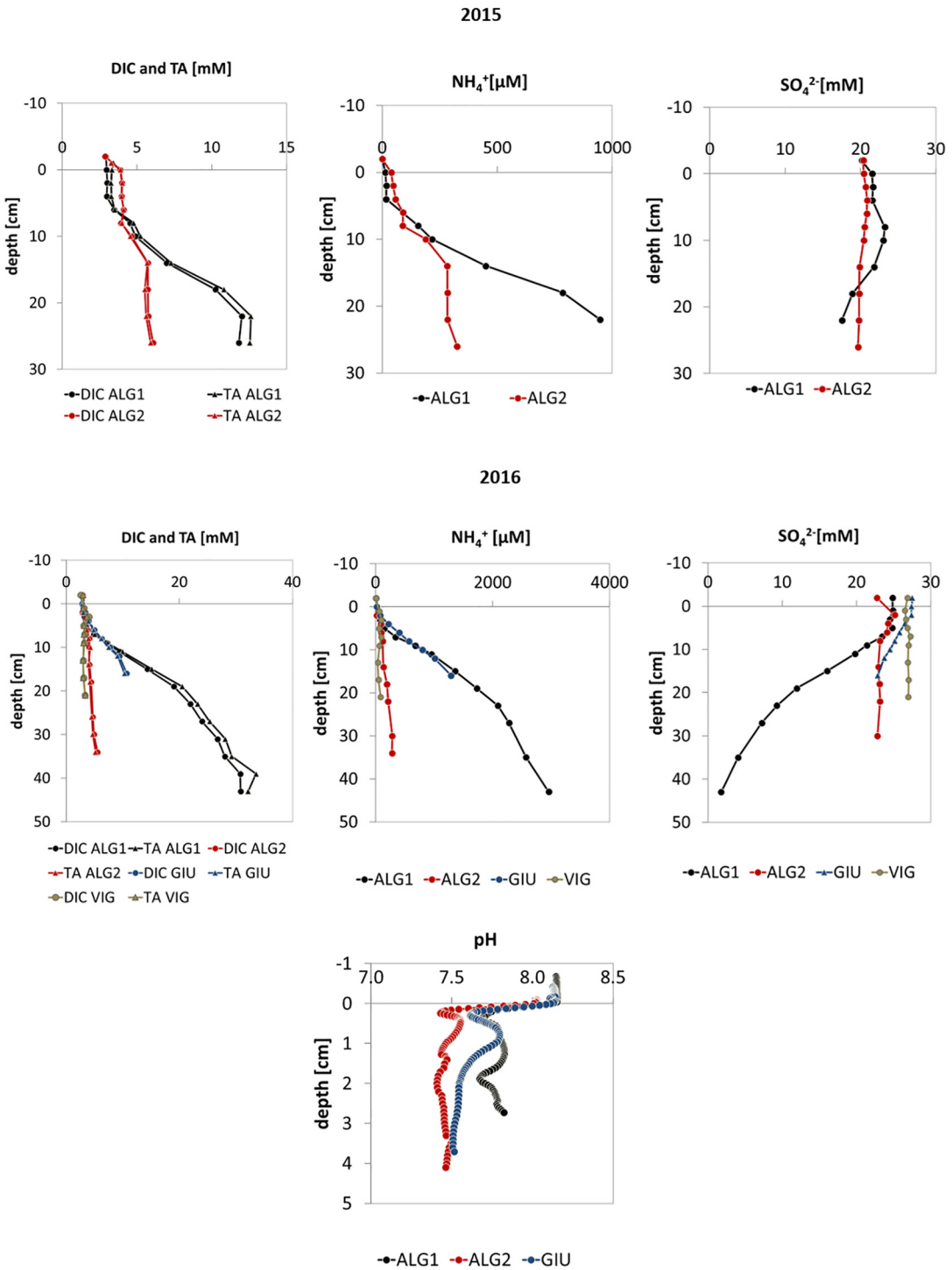


FIGURE 3 | Profiles of DIC, TA, NH_4^+, SO_4^{2-}, and pH in pore waters measured in 2015 and 2016.

depth ranging from 1 to 1.7 mm. Deviations from this general pattern were observed at ALG1 in 2015 with visible burrows and, to a lower extent, at ALG2 in 2017, most likely due to bioirrigation activity. Larger penetration depth and variability were observed at ALG1 in 2015, related to very high concentration of oxygen in the water column (O_2 saturation of 160%), indicating high primary production and intense biological activity during the end of the spring 2015. Diffusive oxygen fluxes (DOU) (**Table 3**) ranged between 8.8 ± 2.7 mmol m^{-2} d^{-1} at GIU and 28.5 ± 12 mmol m^{-2} d^{-1} at ALG1. Stations

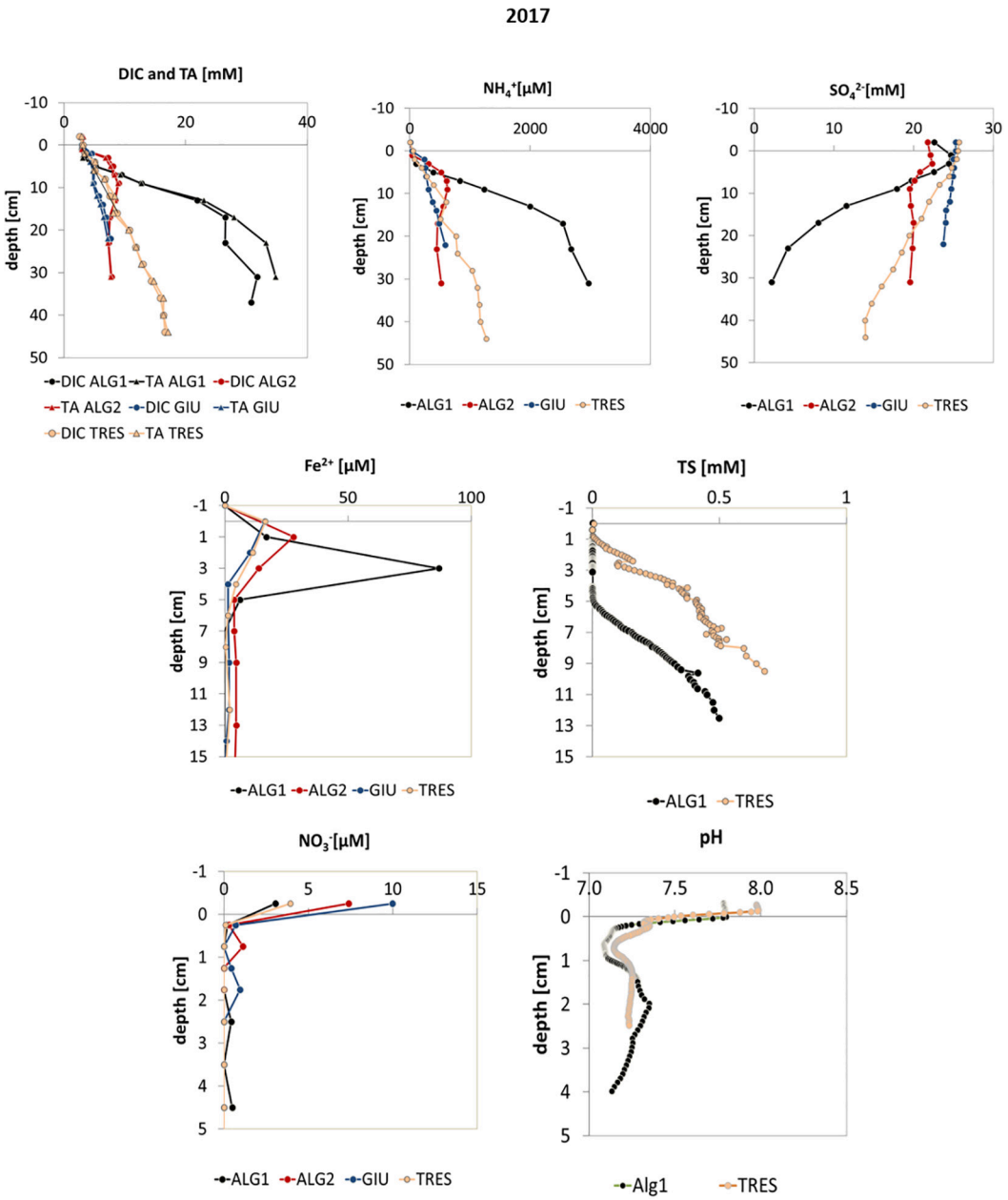


FIGURE 4 | Profiles of DIC, TA, NH_4^+, SO_4^{2-}, Fe^{2+}, and Total Dissolved Sulfide (TS), NO_3^-, and pH in pore waters measured in 2017.

ALG1 and TRES showed the largest average DOU, although the difference with ALG2 was not significant, due to large seasonal variations.

Long-Term DO Monitoring

The box-plot presented in **Figure 7** summarizes the average weekly distribution of DO in summertime at station VE02, based on 12 years of monitoring data. The DO median and minimum values were lower in August, but the last 2 weeks of June also presented critical conditions, with minima below 20% saturation. **Figure 8** presents the index of hypoxia duration for the period comprised between June 1 and September 31, at the four monitoring stations. As can be seen, stations VE02 and VE05, located in the water body PNC1, presented the highest values of the index, up to 23 days at VE02 in 2013.

DISCUSSION

Diagenetic Pathways and Intensity

The oxygen porewater profiles showed limited differences among the five stations, which displayed oxygen penetration depth of

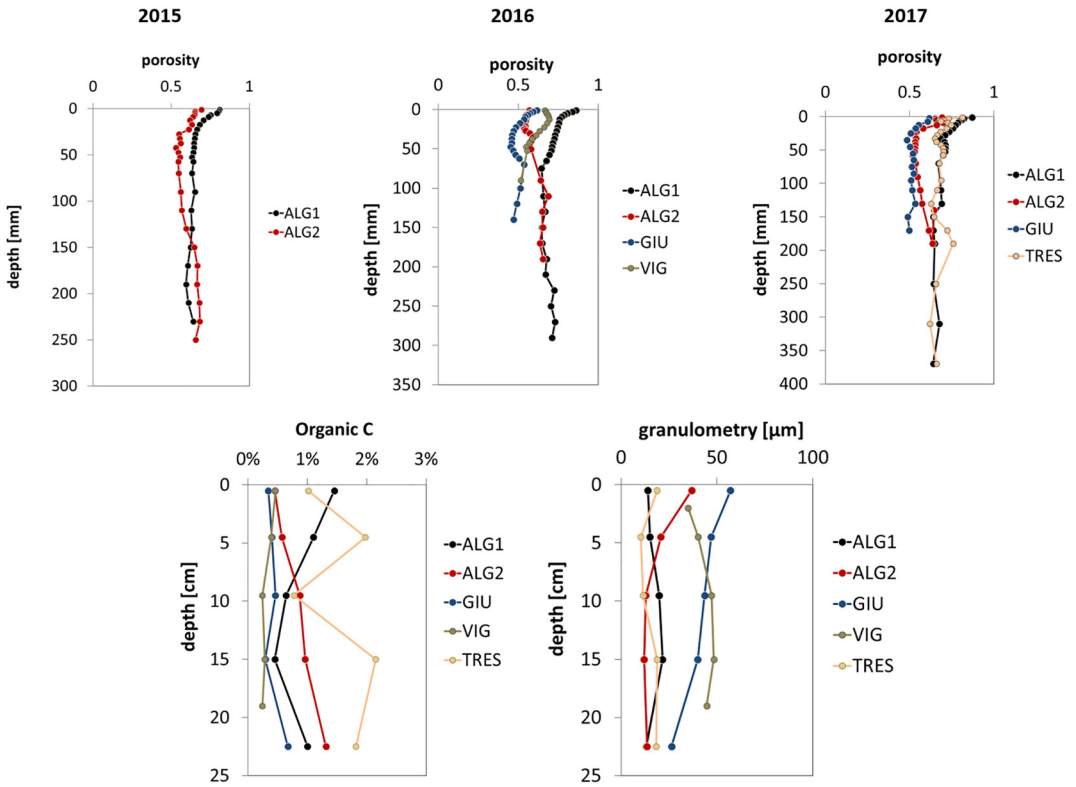


FIGURE 5 | Sediment micro-porosity (2015–2017), OC content (2016–2017), and granulometry (2016–2017) at the five sampling stations.

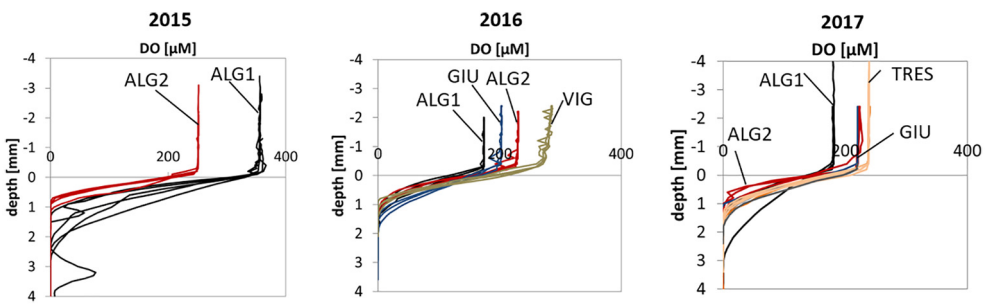


FIGURE 6 | Oxygen microprofiles in porewaters from the years 2015, 2016, 2017: ALG1 black, ALG2 red, GIU blue, VIG gray, TRES orange.

1–1.7 mm. On the contrary, larger DOU values were calculated at stations ALG1, TRES, and ALG2, likely linked to aerobic mineralization and re-oxidation of reduced compounds (Dedieu et al., 2007b; Glud, 2008).

NO_3^- profiles indicated that denitrification was occurring at all sites. However, denitrification did probably not represent a significant diagenetic pathway, given the low concentration of NO_3^- in the water column (<10 µM; Dedieu et al., 2007a). The peaks in Fe^{2+} concentration observed in porewater profiles at all stations indicated that the iron reduction pathway was active at all sites (van Cappellen and Wang, 1996) and, in particular at station ALG1. This is consistent with the increase in pH below the oxic zone at all station (**Figures 2**, **3**), which can be due to iron and probably manganese oxide reduction. The low Fe^{2+} concentration at depth below 5 cm can be explained by the precipitation of FeS or FeS_2 (Rassmann et al., 2020). Sulfate reduction was the most important diagenetic pathway at stations ALG1 and TRES, where the largest SO_4^{2-} gradients and integrated consumptions, as well as the largest increases of dissolved sulfide were observed (**Figure 4**). The difference between the TS increase, about 0.5 mM, and the decrease in porewater sulfate concentration, ranging from 2 to 20 mM, can be explained by the precipitation of iron sulfides (Metzger et al., 2007; Rassmann et al., 2020).

ALG1 and ALG2 were more thoroughly investigated and were visited over 3 consecutive years, in different months over

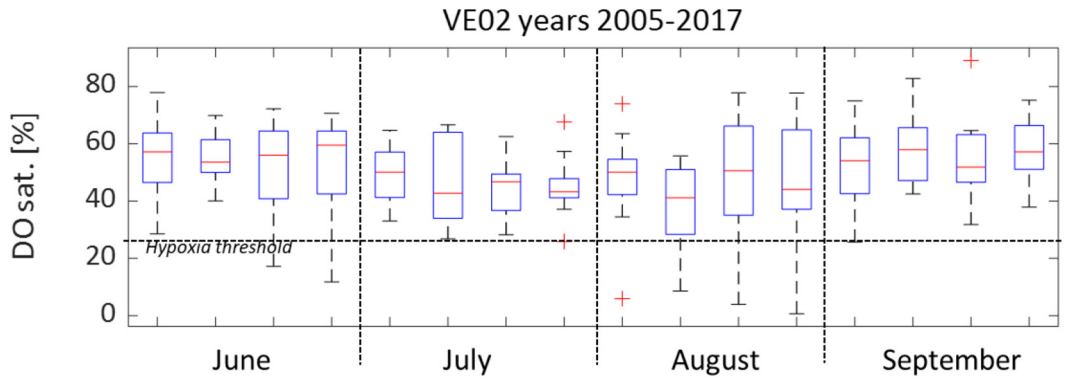


FIGURE 7 | DO saturation at VE02 monitoring station: – box edges indicate the 1st and 3rd quartiles, the central line marks the median, while whiskers indicate extreme (max–min) data points not considered outliers (plotted individually using the "+" symbol).

the spring–summer season. Consequently, they were selected as master stations (MS) of this study, on which we attempted to define differences regarding the intensity in sediment early diagenesis. DIC and SO_4^{2-} were considered as key variables, given the importance of sulfate reduction pathway in organic matter diagenesis in marine sediment. Results from this exercise are presented in **Figure 9**, which shows the average DIC and SO_4^{2-} concentration profiles at the two MS, and marks the two regions in which these parameters were ranging in the different years. It can be seen from the gray envelopes of the DIC and SO_4^{2-} concentration profiles that ALG1 and ALG2 showed clear differences which reflected a variable intensity of diagenesis. By using ΔDIC and ΔSO_4^{2-} defined as the absolute value of the difference between their concentration at the sediment surface and that at the deepest layer of each core, we compared ALG1 and ALG2. The test revealed statistically larger values of ΔDIC and ΔSO_4^{2-} for ALG1 with respect to ALG2 (Mann–Whitney one-tailed; n1 = n2 = 3, $W = 9$, $p = 0.05$).

The DIC integrated productions were significantly larger at ALG1 (2.8 mmol m^{-2} d^{-1}) compared to ALG2 (1.0 mmol m^{-2} d^{-1}), as well as the SO_4^{2-} integrated consumption (1.6 mmol m^{-2} d^{-1} at ALG1 vs 0.4 mmol m^{-2} d^{-1} at ALG1). The ratio among integrated rates of DIC production and SO_4^{2-} consumption was 1.8 at ALG1 and 2.3 at ALG2, which brackets the theoretical ratio of 2 (Rassmann et al., 2016). Along with the DIC and SO_4^{2-} integrated rates, DOU calculated from the microelectrode profiles were used to differentiate the MS (28.5 ± 12 mmol m^{-2} d^{-1} at ALG1 and 17.5 ± 7.4 mmol m^{-2} d^{-1} at ALG2). Based on the differences observed in these three quantities, the two MS presented an "intense diagenesis" behavior (ALG1), and a "moderate diagenesis" behavior (ALG2). The two categories proposed here are consistent with the findings by Gieskes et al. (2015). The authors found TA values around 50 mM and complete consumption of SO_4^{2-} within the upper 40 cm at two of the investigated stations, while the other sites displayed TA values below 10 mM and presented a limited SO_4^{2-} depletion. According to the authors, these differences were primarily related to sediment dredging and subsequent disposal. This constitutes an aspect of primary relevance in the comparison of the two works, since in our case no recent reworking was observed in

TABLE 3 | Diffusive oxygen uptake for the Venice lagoon stations.

Station	Year	DOU (mmol m^{-2} d^{-1})
ALG1	2015	38.2 ± 12.7
	2016	18.8 ± 2.5
	2017	22.1 ± 2.3
ALG1-avg		28.5 ± 12.0
ALG2	2015	23.3 ± 1.1
	2016	8.6 ± 1.3
	2017	19.7 ± 7
ALG2-avg		17.5 ± 7.4
GIU	2017	11.4 ± 1.7
	2016	6.5 ± 0.8
GIU-avg		8.8 ± 2.7
VIG	2016	13.1 ± 1.9
TRES	2017	22.8 ± 3.5

All measurements averages are shown per year and a global average is done per station except for VIG and TRES that were visited only in one occasion.

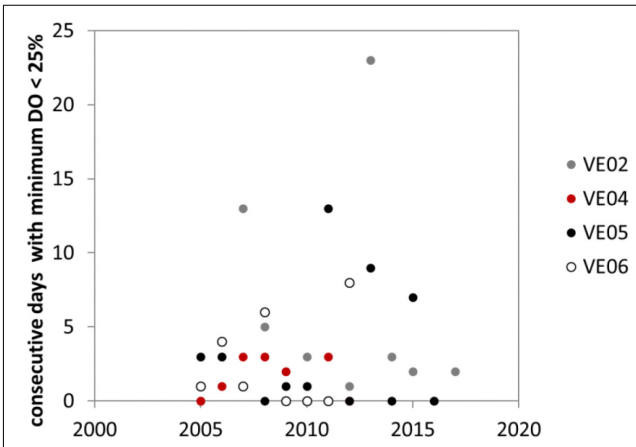


FIGURE 8 | Number of consecutive days with minimum O_2 concentration below 25%.

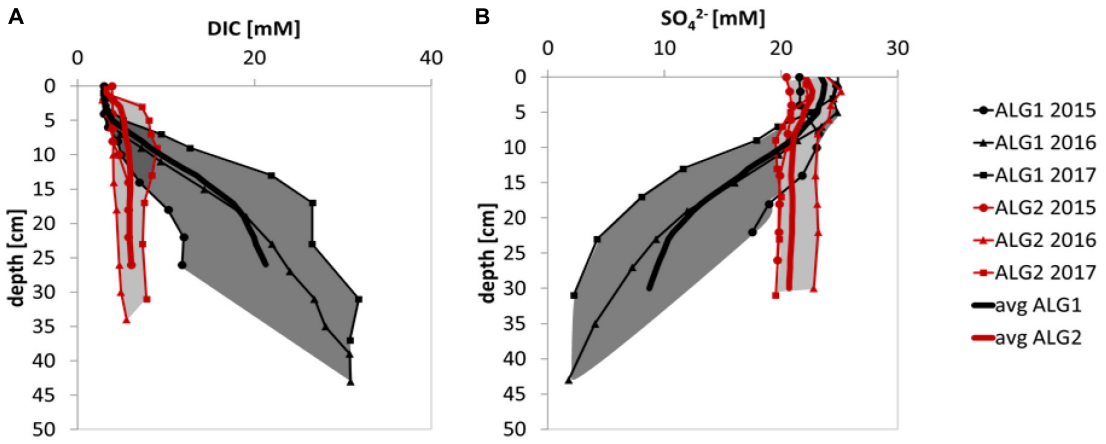


FIGURE 9 | Inter-annual consistency of the sets of data collected at the two CS stations: **(A)** DIC profiles at ALG1 and ALG2; **(B)** SO_4^{2-} profiles at ALG1 and ALG2.

sampled sediments, and all the sampled cores presented intact visual biogenic structures at the core surface. Furthermore, they were collected in shallow water areas which, to the knowledge of the authors, did not experience recent reworking and were placed at a minimum distance of 50 m from the edge of the canals.

Once the difference of the two MS was established, an attempt was made to group the other stations investigated during the three consecutive field campaigns, dividing them between intense diagenesis, at stations resembling ALG1, and moderate diagenesis, at stations closer to ALG2 characteristics. Grouping stations could be relevant for, at least, three reasons: (1) providing information for planning monitoring of crucial sites; (2) guiding data collection for developing a spatial model of lagoon sediments; (3) informing the differential management of sites. Station VIG, sampled in 2016, and station GIU, sampled in 2016 and 2017, show characteristics that are closer to those of MS ALG2 than ALG1, especially in 2017. Indeed, their asymptotic DIC concentration are much lower than the range 12–30 mM, observed at ALG1 (**Figures 2**, **3**). This observation would place the VIG and GIU stations in the "moderate intensity" diagenesis group, which is confirmed by the maximum of NH_4^+ concentration achieved in these two stations. Furthermore, the difference between ALG1 and VIG/GIU is clearly visible in the sulfate profiles: SO_4^{2-} concentration was roughly constant at station VIG and showed a few mM decrease with depth at station GIU. On the contrary, station TRES displays a larger SO_4^{2-} decrease of 10 mM and larger maximal DIC and NH_4^+ concentrations, which reach 16 mM and 1200 μM, respectively. In that respect, even if the highest concentrations of ALG1 are not met at station TRES, this last station is closer to the characteristics of MS ALG1 (intense diagenesis) than ALG2. The difference between the two groups is corroborated by the organic content of surface sediments which is larger at stations ALG1 and TRES than the three other stations.

Indeed, differences in diagenetic intensity among these stations can be related to patterns of organic matter source and accumulation, driven by the spatial heterogeneity in primary producer assemblages. The spatial distribution of macroalgae coverage and standing crop (Sfriso and Facca, 2007), depends on different environmental conditions. One example is the abundance and productivity of Gracilariaceae and *Ulva rigida*, respectively in the areas of TRES and ALG1stations (Sfriso and Sfriso, 2017). These two stations are located close to each other (in absolute terms the two closest stations sampled in this study), but placed on the two sides of the bridge connecting the historical town to the mainland, and characterized by different wind exposures and hence turbidities. Beside differences in biomass density, phenology and degradability, macroalgae coverages can have contrasting impacts on the intensity of diagenesis in terms of reinforcing sediment cohesion and preventing resuspension, in combination with the microphytobenthos community (Yallop et al., 2000; Facca et al., 2002). In terms of physical processes, wind induced resuspension is likely to be more active at station ALG2, as the other stations are partly protected by the bridge (ALG1, and to a lower extent TRES), an island (VIG) or the city of Venice (GIU). This observation is based on a general consideration about the fetch exposure to the two main winds, Bora and Scirocco, and the related bottom shear stress. However, although Scirocco provides the most frequent meteorological forcing, Bora wind blows at speed of 30–40 m/s and is considered to be the geomorphically dominant meteorological condition (Carniello et al., 2009). One relevant mechanism could therefore be related to the resuspension and deposition of organic matter of allochthonous origin during Bora events, in an exchange pattern that could occur between ALG2 and ALG1, which according to the simulations performed by Carniello et al. (2009) belong respectively to areas of erosion and deposition. Anthropogenic drivers also exert an influence in the erosion-sedimentation patterns – e.g., ALG2 is located in proximity of a Manila clam farming area, were dredging could periodically perturb the deposition pattern, while in ALG1, ALG2, and TRES boat traffic and ship wakes can contribute to sediment resuspension and deposition (e.g., Scarpa et al., 2019; Braga et al., 2020).

Overall, it seems reasonable to relate the higher intensity in diagenesis observed in ALG1 and TRES to differences in macroalgal coverage (primary production; sediment

cohesion) and fetch exposure. Nonetheless, it seems difficult to delineate the role and interplay among all the natural and anthropogenic drivers controlling organic matter accumulation without performing dedicated *in situ* measurements, and/or applying models capable of representing lateral transport of suspended particles in different areas of the lagoon (e.g., Ferrarin et al., 2008).

Hypoxia in Venice Lagoon and Potential for Sulfide Release

The analysis of time series indicates that the lagoon waters experience low oxygen concentrations in summer months, with median values of weekly average DO saturation below 50% (**Figure 7**). In conditions of limited mixing, the sediment oxygen demand may contribute to deplete DO in the water column and achieve hypoxia. As an example, considering an oxygen stock at saturation of 220 mmol m^{-2} in 1 m water column (T = 25°C and S = 30 ppt), the theoretical time required for achieving hypoxia would range between 5 and 18 days (DOU respectively of 28.5 mmol m^{-2} day^{-1}, ALG1-avg, and 8.8 mmol m^{-2} day^{-1}, GIU-avg). This basic estimation does not consider oxygen renewal associated to primary production, exchange with the atmosphere and advection, but is a conservative estimate of sediment oxygen consumption by accounting for DOU values only, which represent a fraction only of the total oxygen uptake (Glud, 2008). Interestingly, **Figure 8**, shows that hypoxic events in Venice lagoons last 5–15 days, which is consistent with the time scale of oxygen consumption by sediment diagenesis calculated above. Similar timescales for oxygen depletion have been observed in the Gulf of Mexico (GOM), one of the most documented hypoxic environment in the coastal ocean. Although located in a different coastal setting (open shelf, deeper waters), long term monitoring of DO in bottom water showed that, after mixing events and bottom water oxygen reset, *in situ* oxygen consumption can lead to hypoxia within a few days (Rabalais and Turner, 2019).

The time series analysis showed that in seven events, the number of consecutive hypoxic days exceeded 1 week, twice at VE02 and VE06, and three times at VE05. The fact that stations located in different water bodies experienced prolonged hypoxia supports the hypothesis that the onset of hypoxic conditions is governed by a combined effect of the degradation of planktonic, macroalgae, and microphytobenthos debris (Facca et al., 2002; Sfriso and Facca, 2007), which may occur in surface sediment, and the intensity of water mixing, due to the short term variability of wind conditions (Carniello et al., 2011).

A second aspect of relevance concerns the consequences of hypoxia on water bodies through the release of sulfide. In shallow marine water environments, it represents a major threat for living biota (Vaquer-Sunyer and Duarte, 2010). Release of sulfide is linked to (i) the intensity of diagenesis which increases sulfate-reduction and sulfide production (Cathalot et al., 2012), (ii) the buffer potential of iron as it combines with sulfide to precipitate as FeS and FeS_2 in coastal sediments (Beckler et al., 2016; Rassmann et al., 2020), (iii) the oxygen concentration in the water column (Roden and Tuttle, 1992) as oxygen fuels the re-oxidation loop of H_2S directly or through the iron buffer. In organic rich sediments, such as the Thau lagoon in oyster farms, sulfide production exceeds the buffer iron potential and sulfides are diffuses very close to the SWI (Metzger et al., 2007). H_2S benthic flux also dramatically increases oxygen depletion in the water column during hypoxic phases as H_2S is a strong oxygen sink with 2 moles of O_2 consumed by 1 mole of H_2S, therefore contributing to the spread of oxygen depletion in the stratified water column (Roden and Tuttle, 1992).

$$H_2S + 2\,O_2 \rightarrow SO_4^{2-} + 2\,H^+$$

Our findings show that sulfate reduction is intense at stations ALG1 and TRES, with TS concentrations higher than 0.5 mM at 10–13 cm. Sulfide profiles shows that the concentration rapidly increases with depth (e.g., station TRES in **Figure 4**). Therefore, sulfide could be released to the water column, in case of reduced oxygenation at the SWI. Larger dissolved sulfide concentrations are expected at depth around 20 cm where measurements with micro-electrode could not be carried out. Indeed, as sulfate is nearly completely depleted at station ALG1, sulfide production is likely to be larger below 20 cm depth at this station as already documented at the organic-rich station C5 in the Thau lagoon (Metzger et al., 2007). Stations ALG2, GIU, and VIG, characterized by "moderate diagenesis," showed limited sulfate depletion and little sign of sulfide in porewaters. This is probably the consequence of lower inputs of organic matter and the non-linear interaction with iron which buffers sulfide concentration through Fe-S interactions. In order to improve the management of anoxic crisis in the Venice lagoon and its consequences on the lagoon ecosystem, it would be important to locate and study sulfide occurrence in porewaters and efflux potential. This would help forecasting the consequences of hypoxic crisis on fish and macrobenthos, and potentially remediate in extreme cases.

CONCLUSION

The analysis performed on a >10 years long time-series of monitoring data highlighted the repeated occurrence of low oxygen events during summer, with several consecutive days showing water column saturation values below 25% (in 7 times >1 week). In shallow aquatic systems, the composition of the water column is largely controlled by the exchanges with the sediment. As an illustration, the oxygen uptake values calculated from microelectrode profiles in this study (8.8 and 28.5 mmol m^{-2} day^{-1}), indicate that sediments can have an important role in the onset/maintenance of hypoxic conditions of the water column with a theoretical "consumption time" of water column oxygen ranging from 5 to 18 days. Stations investigated during this study presented different characteristics in terms of intensity of early diagenesis processes, which lead to an attempt of grouping them: (i) intense diagenesis stations, ALG1, TRES, and (ii) moderate diagenesis stations, ALG2, VIG, and GIU. This was performed on the DIC and SO_4^{2-} profiles, considering that the main contrast in diagenetic intensities for the sediment of the Venice lagoon, is reflected in sulfate reduction. The potential for sulfide release in these conditions is higher at stations with

higher diagenetic intensities, having large concentrations of total dissolved sulfide near the SWI. This represents a potential threat to the lagoon ecosystems related to the occurrence of hypoxic events, and should be monitored as such. We also remark that the role of the sediment diagenesis in generating/maintaining hypoxia and contributing to sulfide occurrence in the water column could be enhanced by changes in regional climate conditions, such as the increase in frequency of summer heat waves. Results could constitute a basis for improving existing biogeochemical models of the lagoon (e.g., Lovato et al., 2013), by including a more accurate representation of organic matter degradation processes in sediment (Arndt et al., 2013; Paraska et al., 2014). The future development of existing biogeochemical models in this direction could enhance the capacity of simulating the evolution of the hypoxic conditions, and, therefore, of assessing the risk of hypoxic events.

DATA AVAILABILITY STATEMENT

The datasets presented in this study can be found in online repositories. The names of the repository/repositories and accession number(s) can be found below: Data availability: Data for the sediment part of this article are available on the SEANOE data base as Brigolin Daniele, Rabouille Christophe, Demasy Clément, Bombled Bruno, Pastres Roberto, Brethous Laurie, Monvoisin Gaël (2020). Early diagenesis in sediments of a Mediterranean lagoon (Venice lagoon, Italy) and its relationship to hypoxia. SEANOE. https://doi.org/10.17882/72890. Data for water monitoring are available upon request to Ministero delle Infrastrutture e dei Trasporti – provveditorato generale alle OO PP del Veneto, Trentino Alto Adige, Friuli Venezia Giulia, già Magistrato alle AcquediVenezia.oopp.triveneto-uff1@pec.mit.gov.it.

AUTHOR CONTRIBUTIONS

DB, CR, BB, and RP conceptualized the study. DB, CR, CD, BB, and GM performed the field work and laboratory analysis. DB and CR wrote the manuscript. RP, DB, and CR provided funding to the study. All authors contributed to the article and approved the submitted version.

FUNDING

DB, CR, and BB mobilities were supported by a grant from the Department of Environmental Science, Informatics and Statistics of the University of Venice Ca' Foscari (IRIDE-DHAMACO project).

ACKNOWLEDGMENTS

Water quality data were kindly provided by Ministero delle Infrastrutture e dei Trasporti – provveditorato generale alle OO PP del Veneto, Trentino Alto Adige, Friuli Venezia Giulia, già Magistrato alle Acque di Venezia. We acknowledge the logistic support of Università Ca' Foscari for the sampling activities carried out in the Venice lagoon in 2015, 2016, and 2017, and Prof. F. Pranovi for providing access to his laboratory and to the boat. We also thank L. Brethous for her help during field work and laboratory analysis in 2017, and E.M.D. Porporato for the help with the processing of geospatial data in QGIS.

REFERENCES

Arndt, S., Jørgensen, B. B., Larowe, D. E., Middelburg, J. J., Pancost, R. D., and Regnier, P. (2013). Quantifying the degradation of organic matter in marine sediments: a review and synthesis. *Earth Sci. Rev.* 123, 53–86. doi: 10.1016/j.earscirev.2013.02.008

Autorità di bacino dell'Adige e dell'Alto Adriatico (2010). *Piano di Gestione dei Bacini Idrografici Delle Alpi Orientali. Subunità Idrografica Bacino Scolante, Laguna di Venezia e Mare Antistante*. Available online at: http://www.alpiorientali.it/documenti/list_doc/pub/PdP_doc/04_PG_laguna_di_Venezia_2010_02_24.pdf

Azzoni, R., Nizzoli, D., Bartoli, M., Christian, R. R., and Viaroli, P. (2015). Factors controlling benthic biogeochemistry in urbanized coastal systems: an example from venice (Italy). *Estuar. Coasts* 38, 1016–1031. doi: 10.1007/s12237-014-9882-6

Beckler, J. S., Kiriazis, N., Rabouille, C., Stewart, F. J., and Taillefert, M. (2016). Importance of microbial iron reduction in deep sediments of river-dominated continental-margins. *Mar. Chem.* 178, 22–34. doi: 10.1016/j.marchem.2015.12.003

Berg, P., Risgaard-Petersen, N., and Rysgaard, S. (1998). Interpretation of measured concentration profiles in sediment pore water. *Limnol. Oceanogr.* 43, 1500–1510. doi: 10.4319/lo.1998.43.7.1500

Braga, F., Scarpa, G. M., Brando, V. E., Manfè, G., and Zaggia, L. (2020). COVID-19 lockdown measures reveal human impact on water transparency in the Venice Lagoon. *Sci. Total Environ.* 736:139612. doi: 10.1016/j.scitotenv.2020.139612

Breitburg, D., Levin, L. A., Oschlies, A., Grégoire, M., Chavez, F. P., Conley, D. J., et al. (2018). Declining oxygen in the global ocean and coastal waters. *Science* 359:eaam7240.

Broecker, W. S., and Peng, T.-H. (1974). Gas exchange rates between air and sea. *Tellus* 26, 21–35. doi: 10.1111/j.2153-3490.1974.tb01948.x

Burdige, D. J. (2006). *Geochemistry of Marine Sediments*. Princeton, NJ: Princeton University Press, 609.

Carniello, L., D'Alpaos, A., and Defina, A. (2011). Modeling wind waves and tidal flows in shallow micro-tidal basins Estuarine. *Coast. Shelf Sci.* 92, 263–276. doi: 10.1016/j.ecss.2011.01.001

Carniello, L., Defina, A., and D'Alpaos, L. (2009). Morphological evolution of the Venice lagoon: Evidence from the past and trend for the future. *J. Geophys. Res.* 114:F04002. doi: 10.1029/2008JF001157

Cathalot, C., Lansard, B., Hall, P. O. J., Tengberg, A., Almroth-Rosell, E., Apler, A., et al. (2012). Spatial and temporal variability of benthic respiration in a scottish sea loch impacted by fish farming: a combination of in situ techniques. *Aquat. Geochem.* 18, 515–541. doi: 10.1007/s10498-012-9181-4

Cathalot, C., Rabouille, C., Pastor, L., Deflandre, B., Viollier, E., Buscail, R., et al. (2010). Temporal variability of carbon recycling in coastal sediments influenced by rivers: assessing the impact of flood inputs in the Rhone River prodelta. *Biogeosciences* 7, 1187–1205. doi: 10.5194/bg-7-1187-2010

Cathalot, C., Rabouille, C., Tisnerat-Laborde, N., Toussaint, F., Kerherve, P., Buscail, R., et al. (2013). The fate of river organic carbon in coastal areas: a study in the Rhone River delta using multiple isotopic (delta C-13, Delta C-14) and organic tracers. *Geochim. Cosmochim. Acta* 118, 33–55. doi: 10.1016/j.gca.2013.05.001

Chapelle, A., Lazure, P., and Souchu, P. (2001). Modélisation numérique des crises anoxiques (malaïgues) dans la lagune de Thau (France). *Oceanol. Acta* 24, S87–S97.

Chapelle, A., Menesguen, A., Deslous-Paoli, J. M., Souchu, P., Mazouni, N., Vaquer, A., et al. (2000). Modelling nitrogen, primary production and oxygen in a Mediterranean lagoon: impact of oysters farming and inputs from the watershed. *Ecol. Model.* 127, 161–181. doi: 10.1016/s0304-3800(99)00206-9

Clayton, T. D., and Byrne, R. H. (1993). Spectrophotometric seawater pH measurements: total hydrogen ion concentration scale calibration of m-cresol purple and at-sea results. *Deep Sea Res. Part I* 40, 2115–2129. doi: 10.1016/0967-0637(93)90048-8

Cucco, A., and Umgiesser, G. (2006). Modeling the Venice Lagoon residence time. *Ecol. Model.* 193, 34–51. doi: 10.1016/j.ecolmodel.2005.07.043

Dedieu, K., Rabouille, C., Gilbert, F., Soetaert, K., Metzger, E., Simonucci, C., et al. (2007a). Coupling of carbon, nitrogen and oxygen cycles in sediments from a Mediterranean lagoon: a seasonal perspective. *Mar. Ecol. Prog. Ser.* 346, 45–59. doi: 10.3354/meps07031

Dedieu, K., Rabouille, C., Thouzeau, G., Jean, F., Chauvaud, L., Clavier, J., et al. (2007b). Benthic O-2 distribution and dynamics in a Mediterranean lagoon (Thau, France): an in situ microelectrode study. *Estuar. Coast. Shelf Sci.* 72, 393–405. doi: 10.1016/j.ecss.2006.11.010

Diaz, R. J., and Rosenberg, R. (2008). Spreading dead zones and consequences for marine ecosystems. *Science* 321, 926–929. doi: 10.1126/science.1156401

Dickson, A. G., Sabine, C. L., and Christian, J. R. (eds) (2007). *Guide to Best Practices for Ocean CO_2 Measurements*. London: PICES Special Publication.

European Community (2000). Directive 2000/60/EC of the European Parliament and of the Council of 23 October 2000 Establishing a Framework for Community Action in the Field of Water Policy. Brussels: European Community.

Facca, C., Sfriso, A., and Socal, G. (2002). Changes in abundance and composition of phytoplankton and microphytobenthos due to increased sediment fluxes in the Venice lagoon, Italy. *Estuar. Coast. Shelf Sci.* 54, 773–792. doi: 10.1006/ecss.2001.0848

Ferrarin, C., Umgiesser, G., Cucco, A., Hsu, T.-W., Roland, A., and Amos, C. L. (2008). Development and validation of a finite element morphological model for shallow water basins. *Coast. Eng.* 55, 716–731. doi: 10.1016/j.coastaleng.2008.02.016

Friedrich, J., Janssen, F., Aleynik, D., Wehrli, B., and Wenzhöfer, F. (2014). Investigating hypoxia in aquatic environments: diverse approaches to addressing a complex phenomenon. *Biogeosciences* 11, 1215–1259. doi: 10.5194/bg-11-1215-2014

Galli, G., Solidoro, C., and Lovato, T. (2017). Marine heat waves hazard 3D maps and the risk for low motility organisms in a warming mediterranean sea. *Front. Mar. Sci.* 4:136. doi: 10.3389/fmars.2017.00136

Gieskes, J. M., Han, S., Rathburn, A., Rothwell, G., Pérez, M. E., Porrachia, M., et al. (2015). Anthropogenic contaminants in Venice lagoon sediments and their pore fluids: results from the SIOSED project. *Mar. Chem.* 174, 73–84. doi: 10.1016/j.marchem.2015.05.008

Glud, R. N. (2008). Oxygen dynamics of marine sediments. *Mar. Biol. Res.* 4, 243–289. doi: 10.1080/17451000801888726

Grasshof, K., Ehrhardt, M., and Kremling, K. (1983). *Methods of Seawater Analysis*, 2nd Edn, Weinheim: Verlag Chemie GmbH.

Gu, J., Salem, A., and Chen, Z. (2013). Lagoons of the Nile delta, Egypt, heavy metal sink: with a special reference to the Yangtze estuary of China. *Estuar. Coast. Shelf Sci.* 117, 282–292. doi: 10.1016/j.ecss.2012.06.012

Jankowski, T., Livingstone, D. M., Bührer, H., Forster, R., and Niederhauser, P. (2006). Consequences of the 2003 European heat wave for lake temperature profiles, thermal stability, and hypolimnetic oxygen depletion: implications for a warmer world. *Limnol. Oceanogr.* 51, 815–819. doi: 10.4319/lo.2006.51.2.0815

Jeroschewski, P., Steuckart, C., and Kuhl, M. (1996). An amperometric microsensor for the determination of H2S in aquatic environments. *Anal. Chem.* 68, 4351–4357. doi: 10.1021/ac960091b

Kennish, M. J., and Paerl, H. W. (eds) (2010). *Coastal Lagoons: Critical Habitats of Environmental Change*. Boca Raton, FL: CRC press.

Lewis, E., and Wallace, D. W. R. (1998). *Program Developed for CO_2 System Calculations, ORNL/CDIAC-105*. Oak Ridge, TE: Carbon Dioxide Information Analysis Center, Oak Ridge National Laboratory.

Lovato, T., Ciavatta, S., Brigolin, D., Rubino, A., and Pastres, R. (2013). Modelling dissolved oxygen and benthic algae dynamics in a coastal ecosystem by exploiting real-time monitoring data. *Estuar. Coast. Shelf Sci.* 119, 17–30. doi: 10.1016/j.ecss.2012.12.025

Lucchini, F., Frignani, M., Sammartino, I., Dinelli, E., and Bellucci, L. G. (2002). Composition of Venice lagoon sediments: distributions, sources, settings and recent evolution. *GeoActa* 1, 1–14.

MerMex Group (2011). Marine ecosystems' responses to climatic and anthropogenic forcings in the Mediterranean. *Prog. Oceanogr.* 91, 97–166.

Metzger, E., Simonucci, C., Viollier, E., Sarazin, G., Prevot, F., and Jezequel, D. (2007). Benthic response to shellfish farming in Thau lagoon: porewater signature. *Estuar. Coast. Shelf Sci.* 72, 406–419. doi: 10.1016/j.ecss.2006.11.011

Middelburg, J. J., and Levin, L. A. (2009). Coastal hypoxia and sediment biogeochemistry. *Biogeoscience* 6, 1273–1293. doi: 10.5194/bg-6-1273-2009

Millennium Ecosystem Assessment (2005). *Ecosystems and Human Well-being: Synthesis*. Washington, DC: Island Press.

Paraska, D. W., Hipsey, M. R., and Salmon, S. U. (2014). Sediment diagenesis models: review of approaches, challenges and opportunities. *Environ. Modell. Softw.* 61, 297–325. doi: 10.1016/j.envsoft.2014.05.011

Pastres, R., Solidoro, C., Ciavatta, S., Petrizzo, A., and Cossarini, G. (2004). Long-term changes of inorganic nutrients in the Lagoon of Venice (Italy). *J. Mar. Syst.* 51, 179–189. doi: 10.1016/j.jmarsys.2004.05.011

Pessa, G., Fischetti, D., and Saggese, A. (2018). *Piano d'uso delle aree in Concessione per Venericoltura (Management Plan for Shellfish Farming, in Italian)*. Available online at: http://amministrazionetrasparente.gral.venezia.it (accessed September 10, 2020).

Rabalais, N. N., and Turner, R. E. (2019). Gulf of Mexico Hypoxia: past, present, and future. *Limnol. Oceanogr. Bull.* 28, 117–124. doi: 10.1002/lob.10351

Rabalais, N. N., Turner, R. E., and Wiseman, W. J. (2002). Gulf of Mexico hypoxia, a.k.a. "the dead zone". *Annu. Rev. Ecol. Syst.* 33, 235–263. doi: 10.1146/annurev.ecolsys.33.010802.150513

Rabouille, C., Denis, L., Dedieu, K., Stora, G., Lansard, B., and Grenz, C. (2003). Oxygen demand in coastal marine sediments: comparing in situ microelectrodes and laboratory core incubations. *J. Exper. Mar. Biol. Ecol.* 285, 49–69. doi: 10.1016/s0022-0981(02)00519-1

Ramsar Convention (1971). *Convention on Wetlands of International Importance, Especially as Waterfowl Habitat*. Ramsar: United Nations Educational, Scientific and Cultural Organization (UNESCO).

Rassmann, J., Eitel, E., Cathalot, C., Brandily, C., Lansard, B., Taillefert, M., et al. (2020). Benthic alkalinity and DIC fluxes in the Rhône River prodelta generated by decoupled aerobic and anaerobic processes. *Biogeosciences* 17, 13–33. doi: 10.5194/bg-17-13-2020

Rassmann, J., Lansard, B., Pozzato, L., and Rabouille, C. (2016). Carbonate chemistry in sediment pore waters of the Rhône River delta driven by early diagenesis (NW Mediterranean). *Biogeoscience* 13, 5379–5394. doi: 10.5194/bg-13-5379-2016

Roden, E. E., and Tuttle, J. H. (1992). Sulfide release from estuarine sediments underlying anoxic bottom water. *Limnol. Oceanogr.* 37, 725–738. doi: 10.4319/lo.1992.37.4.0725

Rova, S., Müller, F., Meire, P., and Pranovi, F. (2019). Sustainability perspectives and spatial patterns of multiple ecosystem services in the Venice lagoon: possible roles in the implementation of the EU water framework directive. *Ecol. Indic.* 98, 556–567. doi: 10.1016/j.ecolind.2018.11.045

Rova, S., Pranovi, F., and Müller, F. (2015). Provision of ecosystem services in the lagoon of Venice (Italy): an initial spatial assessment. *Ecohydrol. Hydrobiol.* 15, 13–25. doi: 10.1016/j.ecohyd.2014.12.001

Scarpa, G. M., Zaggia, L., Manfè, G., Lorenzetti, G., Parnell, K., Soomere, T., et al. (2019). The effects of ship wakes in the Venice Lagoon and implications for the sustainability of shipping in coastal waters. *Sci. Rep.* 9:19014.

Schlesinger, W. H., and Bernhardt, E. S. (2013). *Biogeochemistry: An Analysis of Global Change*, 3rd Edn, Amsterdam: Elsevier.

Schnetger, B., and Lehners, C. (2014). Determination of nitrate plus nitrite in small volume marine water samples using vanadium(III)chloride as a reduction agent. *Mar. Chem.* 160, 91–98. doi: 10.1016/j.marchem.2014.01.010

Seeberg-Elverfeldt, J., Schlüter, M., Feseker, T., and Kölling, M. (2005). Rhizon sampling of porewaters near the sediment-water interface of aquatic

systems. *Limnol. Oceanogr. Methods* 3, 361–371. doi: 10.4319/lom.2005.3.361

Sfriso, A., Buosi, A., Mistri, M., Munari, C., Franzoi, P., and Sfriso, A. A. (2019). Long-term changes of the trophic status in transitional ecosystems of the northern Adriatic Sea, key parameters and future expectations: the lagoon of Venice as a study case. *Nat. Conserv.* 34, 193–215. doi: 10.3897/natureconservation.34.30473

Sfriso, A., Favaretto, M., Ceoldo, S., Facca, C., and Marcomini, A. (2005). Organic carbon changes in the surface sediments of the Venice lagoon. *Environ. Int*. 31, 1002–1010. doi: 10.1016/j.envint.2005.05.010

Sfriso, A., and Facca, C. (2007). Distribution and production of macrophytes and phytoplankton in the lagoon of Venice: comparison of actual and past situation. *Hydrobiologia* 577, 71–85. doi: 10.1007/s10750-006-0418-3

Sfriso, A. A., and Sfriso, A. (2017). In situ biomass production of Gracilariaceae and *Ulva rigida*: the Venice Lagoon as a study case. *Bot. Mar.* 60, 271–284.

Solidoro, C., Bandelj, V., Bernardi, F. A., Tagliapietra, D., and Torricelli, P. (2010). "Response of the Venice Lagoon ecosystem to natural and anthropogenic pressures over the last 50 years," in *Coastal Lagoons: Critical Habitats of Environmental Change*, eds J. K. Michael and H. W. Paerl (Boca Raton, FL: CRC Press), 483–511. doi: 10.1201/ebk1420088304-c19

Stookey, L. L. (1970). Ferrozine-A new spectrophotometric reagent for iron. *Anal. Chem.* 42, 779–781. doi: 10.1021/ac60289a016

Umgiesser, G. (2020). The impact of operating the mobile barriers in Venice (MOSE) under climate change. *J. Nat. Conserv.* 54:125783. doi: 10.1016/j.jnc.2019.125783

van Cappellen, P., and Wang, Y. F. (1996). Cycling of iron and manganese in surface sediments: a general theory for the coupled transport and reaction of carbon, oxygen, nitrogen, sulfur, iron, and manganese. *Am. J. Sci.* 296, 197–243. doi: 10.2475/ajs.296.3.197

Vaquer-Sunyer, R., and Duarte, C. M. (2008). Thresholds of hypoxia for marine biodiversity. *Proc. Natl. Acad. Sci. U.S.A.* 105, 15452–15457. doi: 10.1073/pnas.0803833105

Vaquer-Sunyer, R., and Duarte, C. M. (2010). Sulfide exposure accelerates hypoxia-driven mortality. *Limnol. Oceanogr.* 55, 1075–1082. doi: 10.4319/lo.2010.55.3.1075

Yallop, M. L., Paterson, D. M., and Wellsbury, P. (2000). Interrelationships between rates of microbial production, exopolymer production, microbial biomass, and sediment stability in biofilms of intertidal sediments. *Microb. Ecol.* 39, 116–127. doi: 10.1007/s002489900186

Zaggia, L., Rosso, J., and Zonta, R. (2007). Sulphate reduction in the sediment of the Venice canals (Italy). *Mar. Pollut. Bull.* 55, 415–424. doi: 10.1016/j.marpolbul.2007.09.004

Zhang, J., Gilbert, D., Gooday, A. J., Levin, L. A., Naqvi, W. A., Middelburg, J. J., et al. (2010). Natural and human-induced hypoxia and consequences for coastal areas: synthesis and future development. *Biogeoscience* 7, 1443–1467. doi: 10.5194/bg-7-1443-2010

Zhu, Y., McCowan, A., and Perran, L. M. (2017). Effects of changes in nutrient loading and composition on hypoxia dynamics and internal nutrient cycling of a stratified coastal lagoon. *Biogeosciences* 14, 4423–4433. doi: 10.5194/bg-14-4423-2017

Conflict of Interest: The authors declare that the research was conducted in the absence of any commercial or financial relationships that could be construed as a potential conflict of interest.

Copyright © 2021 Brigolin, Rabouille, Demasy, Bombled, Monvoisin and Pastres. This is an open-access article distributed under the terms of the Creative Commons Attribution License (CC BY). The use, distribution or reproduction in other forums is permitted, provided the original author(s) and the copyright owner(s) are credited and that the original publication in this journal is cited, in accordance with accepted academic practice. No use, distribution or reproduction is permitted which does not comply with these terms.

frontiers in Marine Science

ORIGINAL RESEARCH
published: 24 February 2021
doi: 10.3389/fmars.2021.634189

Interactive Effects of Elevated CO_2 Concentration and Light on the Picophytoplankton *Synechococcus*

Nanou Bao[1] *and Kunshan Gao*[1,2]*

[1] State Key Laboratory of Marine Environmental Science, College of Ocean and Earth Sciences, Xiamen University, Xiamen, China, [2] Co-Innovation Center of Jiangsu Marine Bio-industry Technology, Jiangsu Ocean University, Lianyungang, China

Synechococcus is a major contributor to the primary production in tropic and subtropical oceans worldwide. Responses of this picophytoplankton to changing light and CO_2 levels is of general concern to understand its ecophysiology in the context of ocean global changes. We grew *Synechococcus* sp. (WH7803), originally isolated from subtropic North Atlantic Ocean, under different PAR levels for about 15 generations and examined its growth, photochemical performance and the response of these parameters to elevated CO_2 (1,000 μatm). The specific growth rate increased from 6 μmol m^{-2} s^{-1} to reach a maximum (0.547 ± 0.026) at 25 μmol m^{-2} s^{-1}, and then became inhibited at PAR levels over 50 μmol m^{-2} s^{-1}, with light use efficiency (α) and photoinhibition coefficient (β) being 0.093 and 0.002, respectively. When the cells were grown at ambient and elevated CO_2 concentration (400 vs. 1,000 μatm), the high-CO_2 grown cells showed significantly enhanced rates of electron transport and quantum yield as well as significant increase in specific growth rate at the limiting and inhibiting PAR levels. While the electron transport rate significantly increased at the elevated CO_2 concentration under all tested light levels, the specific growth did not exhibit significant changes under the optimal growth light condition. Our results indicate that *Synechococcus* WH7803 grew faster under the ocean acidification (OA) treatment induced by CO_2 enrichment only under limiting and inhibiting light levels, indicating the interactive effects and implying that the picophytoplankton respond differentially at different depths while exposing changing light conditions.

Keywords: CO_2, growth, light, *Synechococcus*, WH7803

OPEN ACCESS

Edited by:
Nina Bednarsek, Southern California Coastal Water Research Project, United States

Reviewed by:
Rajani Kanta Mishra, Ministry of Earth Sciences, India
Michael William Lomas, Bigelow Laboratory for Ocean Sciences, United States
Wanchun Guan, Wenzhou Medical University, China

***Correspondence:**
Kunshan Gao
ksgao@xmu.edu.cn

Specialty section:
This article was submitted to Marine Biology, a section of the journal Frontiers in Marine Science

Received: *27 November 2020*
Accepted: *01 February 2021*
Published: *24 February 2021*

Citation:
Bao N and Gao K (2021) Interactive Effects of Elevated CO_2 Concentration and Light on the Picophytoplankton Synechococcus. Front. Mar. Sci. 8:634189. doi: 10.3389/fmars.2021.634189

INTRODUCTION

Synechococcus is a group of picoplanktonic cyanobacteria, along with *Prochlorococcus* constituting the most widespread and abundant group of marine pico-prokaryotic primary producers (Varkey et al., 2016; Kim et al., 2018). *Synechococcus* strains are distributed widely in both freshwater and oceanic environments, with stain-specific physiological traits under influences of nutrients, temperature and light (Partensky et al., 1999; Callieri et al., 2013; Flombaum et al., 2013; Kim et al., 2018). In marine environments, most species and/or strains of *Synechococcus* are found more abundantly in mesotrophic and moderately oligotrophic marine environments (Scanlan et al., 2009; Domínguez-Martín et al., 2016) in tropical to subtropical oceans from 40°S to 40°N,

contributing by about 16% of the global oceanic annual net primary production (Badger et al., 2006; Flombaum et al., 2013).

Among various strains of *Synechococcus*, WH7803 is featured with the presence of abundant phycoerythrin (PE), awarding it a distinguishable red appearance (Morris and Glover, 1981; Stockner and Antia, 1986). The absorption spectra of PE (450–600 nm) is similar to the spectra at the bottom of euphotic zone where the irradiance intensity is about 1% of the surface, suggesting this strain can be adapted to dim light levels (Fogg, 1986; Glover et al., 1986; Stockner and Antia, 1986; Piazena et al., 2002; Flombaum et al., 2013). However, vertical mixing processes in the oceans can episodically move *Synechococcus* cells to shallower layers where light levels are higher (Flombaum et al., 2013), possibly resulting in photoinhibition (Huner et al., 1998). Based on the light attenuation coefficient (K_d) in the clearest pelagic waters, the theoretical light intensity for WH7803 to survive was estimated to be about 23% of the surface intensity (Smith and Baker, 1981). However, laboratory studies revealed that the optimum light levels for its growth ranged from 25 to 200 μmol m^{-2} s^{-1} of PAR (Glover and Morris, 1981; Alberte et al., 1984; Barlow and Alberte, 1985; Campbell and Carpenter, 1986; Kana and Glibert, 1987). In spite of the reported wide range of PAR for optimal growth, little has been documented on its photophysiological performances under different PAR levels.

With progressive ocean climate changes, on the other hand, it has been predicted that the abundance of *Synechococcus* would increase by about 14%, with its distribution range extended to higher latitudes including the Bering Sea, Gulf of Alaska, and Southern Ocean (Flombaum et al., 2013). While increased levels of CO_2 and higher temperature were both suggested to influence *Synechococcus*, experimental tests on its responses to these drivers have been rarely examined (*Synechococcus* sp. CCMP1334 strain under pCO_2 of 750 ppmv at 24°C, pCO_2 380 ppmv at 24°C, and pCO_2 750 ppmv at 20°C, Fu et al., 2007; Lu et al., 2006). Growth of *Synechococcus* strains can be stimulated (Fu et al., 2007; *Synechococcus* sp. CCMP839 strain under pCO_2 of 800 ppmv, Lu et al., 2006) or unaffected (*Synechococcus elongatus* CCMP1379 strain under pCO_2 of 350, 600, 800 ppmv and *Synechococcus* sp. CCMP839 strain under pCO_2 of 350 and 600 ppmv, Lu et al., 2006) by elevated CO_2 concentrations, showing a strain-specific response when grown under constant light levels (40–45 μmol m^{-2} s^{-1} of PAR). It has been suggested that increased availability of CO_2 and the associated acidic stress can affect phytoplankton growth to different directions, leading to positive, neutral and negative effects under different light levels (Gao et al., 2012) due to carbon concentration mechanisms (CCMs) regulation and involved energetic changes. *Synechococcus* strains possess active CCMs, that can concentrate intracellular CO_2 up to about 1,000 times higher than that in seawater (Badger and Andrews, 1982). Therefore, we hypothesize that *Synechococcus* respond differently under different light levels to elevated CO_2 concentration projected to future ocean acidification (OA), and increasing CO_2 availability and different light levels would result in interactive effects on *Synechococcus* WH7803 strain, which was isolated from subtropical North Atlantic Ocean where anthropogenic CO_2 has been drastically increased with progressive OA (Bates and Johnson, 2020). In this work, we examined physiological performances of the strain WH7803 under various light levels and two CO_2 levels (ambient and elevated levels for the present and end of this century, which were about 400 or 1,000 μatm, respectively), and found that the elevated CO_2 concentration to 1,000 μatm did not affect its growth rate at the optimal growth light level but enhanced it at light-limiting and inhibiting levels.

MATERIALS AND METHODS

Synechococcus WH7803 strain, originally isolated from the North Atlantic Ocean (67.496°W, 33.748°N), was obtained from Professor Rui Zhang's lab at the College of Ocean and Earth, Xiamen University, Xiamen, China. The cells were maintained in A^+ medium in 100 mL Quartz tubes under 6 μmol m^{-2} s^{-1} light intensity with a light-dark period of 12:12 h at 23.5 ± 0.5°C in an illuminating incubator (HP1000G-D, Wuhan Ruihua Instrument and Equipment Co., Ltd., China). Before inoculation, the medium and quartz tubes were sterilized at 110°C for 30 min in an autoclave.

Light (PAR) intensity within the incubator was measured using Datalogging Radiometer Model PMA2100 (Solar Light Company, Inc., United States). Six PAR levels of 6, 13, 25, 38, 50, and 100 μmol m^{-2} s^{-1} were set to grow the *Synechococcus* cells by adjusting distance from the light source and/or covering with neutral filters. The cultures were aerated (30 ml min^{-1}) with filtered air (0.22 μm, PVDF Syringe Filter, AllPure, United States). There were three replicates of culture at each treatment (n = 3). Each culture under different light levels was run for 15 generations before measurements of the physiological and biochemical parameters, including specific growth rate, electron transport rate, effective quantum yield and pigments concentration. The initial cell concentration was set at about 500,000 cells mL^{-1}. The concentration of cells was monitored at 9:00 am every other day.

Then we set up experiments to test how the picophytoplankton respond to future OA under the elevated CO_2 level (1,000 ppmv) based on RCP8.5 senario using the current CO_2 level as control (Gattuso et al., 2010; Gao et al., 2012). CO_2 concentrations in the culture medium were initially set up at 400 (LC) or 1,000 (HC) μatm by using the CO_2 pre-equilibrated medium, which were aerated and prepared through a sterilized filter with outdoor air for LC and the air of 1,000 ppmv CO_2 (achieved by using a plant CO_2 chamber) for HC, respectively. After pre-equilibration, the pH of the medium was measured by a pH meter (Orion Star A211, Thermo Fisher Scientific, United States). In the cultures at LC and HC treatments (pH 8.1 vs. 7.8), the pH_{nbs} was significantly different at the early phase (4 days) with less difference at the end (day 10) of the cultures. The initial cell concentrations in the cultures under both CO_2 levels were 500,000 cells mL^{-1}.

Measurement of Specific Growth Rate

The cell concentration in the cultures was enumerated (each sample for at least 30 s) by a flow cytometer (CytoFLEX S, Beckman Coulter, Inc., United States) with a 488 nm emitter (PE and Chl *a* are both excited by this laser beam, with the

emitted wavelengths of 575 and 675 nm, respectively) (Givan, 2011). The tunnels of the auxiliary software CytExpert 2.0 (Beckman Coulter, Inc., United States) were FSC-A (forward scatter light for diameter), PI-A (690 nm for Chl *a*) and PAO-A (585 nm for PE). When phycoerythrin and chlorophyll *a* in *Synechococcus* cells become excited by 488 light, they emit the characteristic lights as mentioned above. By analyzing those emitted light signals through the software, a *Synechococcus* cell could be distinguished from other particles based on its species-specific emission wavelength characteristics. The specific growth rates were calculated using the following formula based on the enumerated cells (Iturriaga and Mitchell, 1986):

$$\mu = \frac{\ln N - \ln N_0}{\Delta t}$$

where N indicates the cell concentration at T time, N_0 the initial cell concentration at T_0, and Δt the duration (days, $T - T_0$). The non-linear fitting of the specific growth rates to growth light levels was performed using the following formula (Platt et al., 1980):

$$\mu = \mu_{\max}(1 - e^{-\frac{\alpha \times PAR}{\mu \max}}) \times e^{-\frac{\beta \times PAR}{\mu \max}}$$

where *PAR* is the growth light intensity. The μ_{max}, α and β indicate maximal growth rate, light use efficiency and growth photoinhibition coefficient, respectively.

Measurement of Electron Transport Rate and Effective Quantum Yield

Samples for the measurement of relative electron transport rate (*rETR*) were collected directly during the exponential growth phase, which had different concentrations of cells as well as the contents of intracellular chlorophyll. The ETR was measured by using a Multi-color Pulse Amplitude Modulated chlorophyll fluorometer (Multi-color PAM, Walz, Germany), setting measuring wavelength of actinic light at 625 nm (measuring mode Al white, with all samples showing the similar basic fluorescence levels). The range of light curve measurement was from 0 to 798 μmol m^{-2} s^{-1}, which included 13 irradiance steps and each irradiance step was about 10 s. The saturating light pulse (800 ms, 5,000 μmol photons m^{-2} s^{-1}) was applied for determination of ETR. The *rETR* was calculated as follows (Ralph and Gademann, 2005):

$$rETR = \Phi_{\mathrm{PSII}} \times PAR$$

where Φ_{PSII} represents the measured effective quantum yield of photosystem II, and *PAR* the measuring or assay light intensity. Φ_{PSII} was determined by setting actinic light level to the growth light level for each sample that had been grown under different light levels.

Measurement of Pigments Concentrations

A 10 mL of culture from each replicate culture was used for the extraction of Chl *a* and total carotenoids (CARs), and another 10 mL was used for the extraction of APC (allophycocyanin), PC (phycocyanin), and PE (phycoerythrin), respectively. For measurements of Chl *a* and CARs, cells were collected on 0.22 μm GF/F filter and then extracted in 5 mL of pure methanol for 24 h at 4°C in darkness before being centrifuged at 6,000 × *g* for 10 min. The supernatant was scanned for absorbance from 400 to 800 nm by using a spectrophotometer (model DU800 Beckman Coulter, United States). The concentrations of Chl *a* and CARs were determined according to Ritchie (2006) and Strickland and Parsons (1972).

Extractions of APC, PC, and PE were performed according to Lüder et al. (2001) as described by Zhang et al. (2013). Briefly, the collected cells were suspended in 10 mL phosphate buffer. The freezing (liquid nitrogen) and thawing (4°C) processes were repeated for at least four times for each extraction. Optical absorbances of the supernatant after centrifugation were scanned as mentioned above using the spectrophotometer. The concentrations of APC, PC, and PE were calculated according to Lüder et al. (2001).

Data Analysis

One-way ANOVA with post hoc multiple comparisons of Tukey was operated for distinguishing significant ($P < 0.05$) differences using SPSS (PASW 18.0, IBM, United States), since we need to compare more than two groups with the follow-up *post hoc* test for analysis of equality of multiple overall mean values. The significant levels (*p*-values) are given in the Supplementary Material. The fitting and charting were conducted by OriginPro 9.0.0 (64-bit) b45 (OriginLab Corp., United States). All data are presented as the means ± SD of three independent cultures.

RESULTS

The specific growth rate (μ) of *Synechococcus* WH7803 increased from 6 μmol m^{-2} s^{-1} to reach a maximum at 25 μmol m^{-2} s^{-1}, but thereafter declined with increased levels of PAR (**Figure 1**),

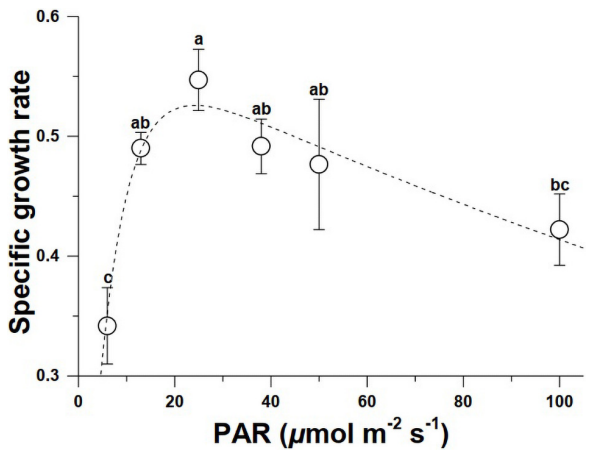


FIGURE 1 | The specific growth rates of *Synechococcus* WH7803 grown under various PAR levels ($n = 3$, triplicate cultures). Different letters above the data indicate significant difference ($p < 0.05$).

resulting in no significance in μ at between 6 and 100 μmol m^{-2} s^{-1} (**Supplementary Table 1**). The results derived from the non-linear fitting of μ revealed that the growth light use efficiency (α) and high light inhibiting coefficient (β) were 0.093 and 0.002, respectively.

The relative electron transport (*rETR*) during photochemical reactions of the cells grown under 6, 12, 25, and 38 μmol m^{-2} s^{-1} of PAR were nearly superimposed, however, the *rETR*s in the cells grown under 50 and 100 μmol m^{-2} s^{-1} significantly increased further with increased levels of PAR (**Figure 2A**). The maximal *rETR* in the cells grown at 100 μmol m^{-2} s^{-1} was nearly twice that grown at 38 μmol m^{-2} s^{-1} or lower PAR levels (**Figure 2A**). The effective quantum yield did not show significant changes (**Figure 2B**) (**Supplementary Table 2**).

When the cells were exposed to elevated CO_2 concentrations for about 10 days under 6 (limiting), 25 (optimal), and 100 (inhibiting) μmol m^{-2} s^{-1} of PAR, its specific growth rate significantly increased at the limiting and inhibiting growth light levels of 6 and 100 μmol m^{-2} s^{-1}, respectively (**Supplementary Table 3**). No significant change was observed between the two CO_2 levels under the optimal light level of 25 μmol m^{-2} s^{-1} (**Figure 3A**). The photosynthetic electron transport rate increased significantly with increased light levels, with higher

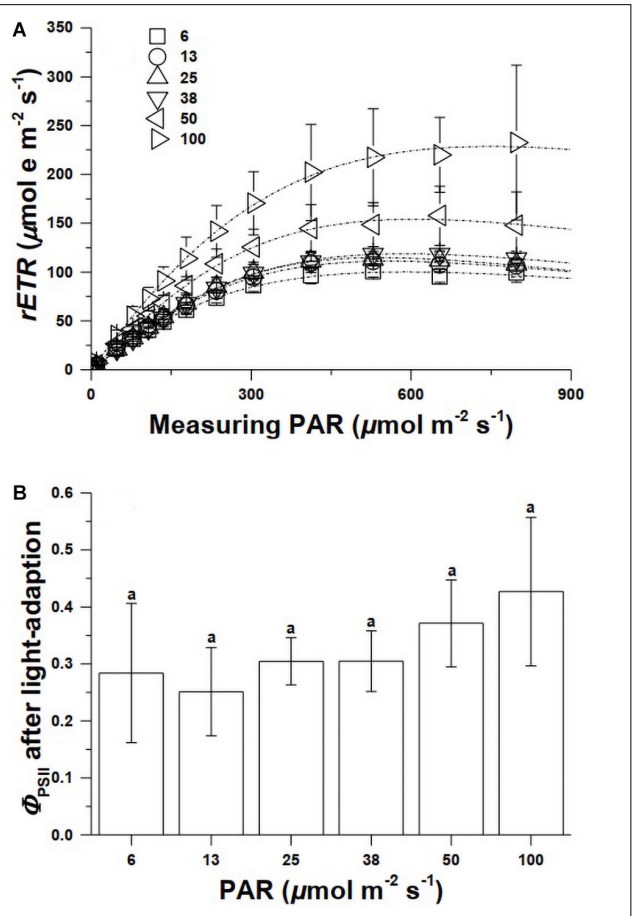


FIGURE 2 | The photosynthetic electron transport vs. light curves of *Synechococcus* WH7803 grown under different PAR levels **(A)**, and the effective quantum yield (Φ_{PSII}) of the cells adapted to growth light levels **(B)** (n = 3, triplicate cultures).

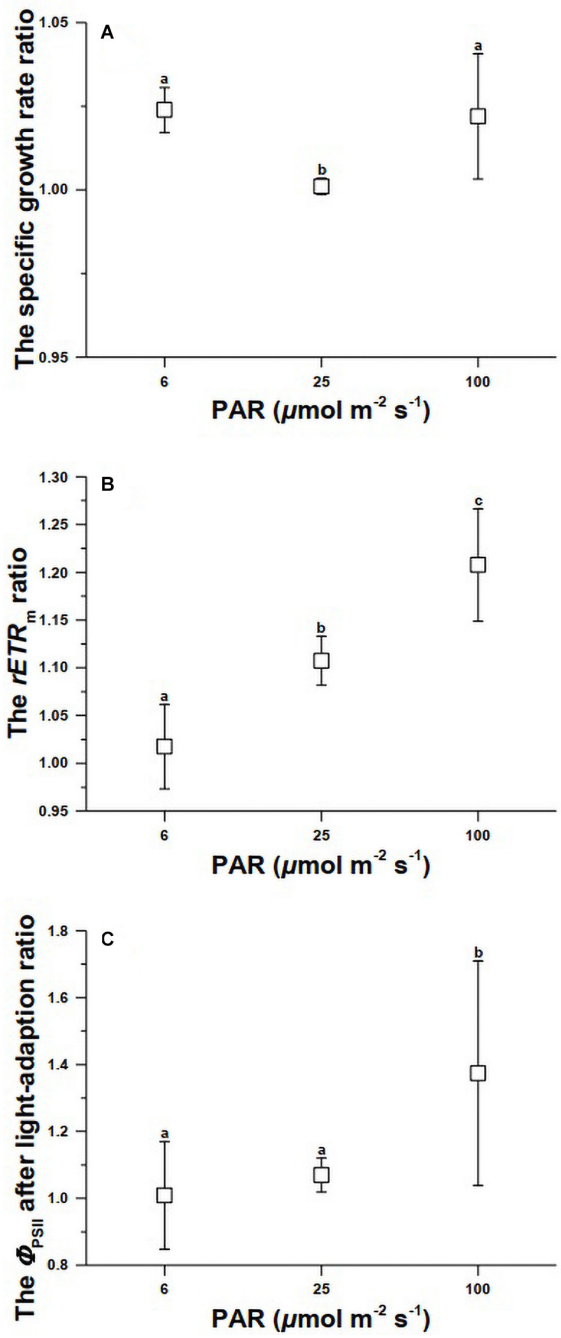


FIGURE 3 | The growth **(A)**, *rETR* **(B)**, and Φ_{PSII} **(C)** ratios of high- to low-CO_2-grown *Synechococcus* cells. Different letters above the data indicate significant difference at $P < 0.05$. The ratios of high CO_2-grown to ambient CO_2 grown cells were based on the data obtained under three levels of light and two levels of CO_2 (18 cultures with each treatment of three replicates). The absolute values for high CO_2-grown cells can be obtained using the ratio and the values in **Figures 1**, **2**.

values in the high CO_2-grown cells (**Figure 3B**) (**Supplementary Table 4**). While elevated CO_2 availability appeared to enhance the quantum yield at all test light levels, significant difference was only found at growth light of 100 μmol m^{-2} s^{-1} (**Figure 3C**), though the specific growth rate was enhanced in the high CO_2-grown cells at both limiting and inhibiting light levels (**Figure 3A**).

While contents of Chl *a* (0.013 ± 0.001 for LC and 0.021 ± 0.001 pg $cell^{-1}$ for HC), carotenoids (0.012 ± 0.002 for LC and 0.019 ± 0.001 pg $cell^{-1}$ for HC) and phycoerythrin (0.208 ± 0.079 for LC and 0.485 ± 0.030 pg $cell^{-1}$ for HC) showed significantly higher values at the optimal growth light of 25 μmol m^{-2} s^{-1}, no significant changes were found among the light levels for allophycocyanin and phycoerythrin (**Table 1**) (**Supplementary Table 5**). However, at any of the growth light levels, all types of photosynthetic pigments increased significantly at the elevated CO_2 level compared to the ambient level, by 58.76, 57.96, 82.10, 177.13, and 132.91%, respectively, for Chl *a*, carotenoids, allophycocyanin, phycocyanin, and phycoerythrin in the cells grown at the optimal light intensity (**Table 1**) (**Supplementary Table 5**).

DISCUSSION

Our results indicate that *Synechococcus* strain WH7803 accelerated its electron transport rate with increased growth light and CO_2 levels, and the elevated CO_2 to 1,000 μatm significantly enhanced its growth under limiting (6 μmol m^{-2} s^{-1}) and inhibiting (100 μmol m^{-2} s^{-1}) light levels, but did not bring about significant effect on it at the optimal light level of 25 μmol m^{-2} s^{-1}. Although the extent of the enhancement due to increased CO_2 availability at the low and high light levels was only by 2–2.5% per day (**Figure 3A**), the accumulative effects over longer periods can hardly be ignored considering the large proportion of *Synechococcus*'s contribution to marine primary productivity. Insignificant effects of elevated CO_2 on *Synechococcus* strains CCM 839 and 1334 were reported when they were grown at optimal light levels of about 40 μmol m^{-2} s^{-1} (Lu et al., 2006; Fu et al., 2007). Our finding first demonstrated the positive effects of elevated CO_2 on *Synechococcus* cells grown under limiting and inhibiting light levels and showed consistency with the previous reports (Lu et al., 2006; Fu et al., 2007) on the CO_2 effects at optimal light intensity.

In the present study, the specific growth rate of *Synechococcus* (WH7803) increased to reach a peak at 25 μmol m^{-2} s^{-1} but then gradually declined at higher light levels, showing a photoinhibition. Barlow and Alberte (1985) showed that *Synechococcus* WH7803 as well as clone WH8018 became light saturated for growth at light levels between 25 and 50 μmol m^{-2} s^{-1}, and was severely inhibited at 250 μmol m^{-2} s^{-1}. This is consistent with our growth vs. light curves (**Figure 1**). While Morris and Glover (1981) reported that growth of *Synechococcus* (WH7803) saturated at 45 μmol m^{-2} s^{-1}, Kana and Glibert (1987) reported that growth of the same strain was saturated at about 200 μmol m^{-2} s^{-1}. Since culture vessels of different materials and culture volumes may lead to different levels of light exposures to the cells within them, such difference in light levels for saturating its growth can be attributed to different transparency of light and to different volumes of culture, since large volume of cultures and the flasks made of polystyrene attenuate or block considerable amount of light. We have used 100 mL Quartz tubes, and the high transparency of the tubes with small volume of water provided higher light exposures to the cells, therefore leading to relatively lower saturating light level for growth (**Figure 1**) compared to other works aforementioned.

Photosynthetic electron transport increased with growth light levels till 100 μmol m^{-2} s^{-1} of PAR, with faster tempo at the elevated CO_2 level across all the growth light levels (**Figure 3B**). The faster electron drainage, which means faster energy supply for physiological processes, can be attributed to enhanced CO_2 assimilation processes and/or photorespiration (Gao et al., 2012). While increased light levels are known to enhance CCMs in phytoplankton species, but elevated CO_2 levels usually down-regulate CCMs (Giordano et al., 2005; Beardall and Raven, 2020), the enhanced electron transport and growth of *Synechococcus* strain WH7803 by elevated CO_2 could be attributed to enhancement of carboxylation under the elevated CO_2, which resulted in faster growth rate under growth limiting and inhibiting light levels (**Figure 3A**). The inhibited growth rate at 100 μmol m^{-2} s^{-1} (**Figure 1**) could be due to light stress, since the cells increased their electron transport with increasing growth light levels to result photoinhibition (**Figure 2**). The reason why growth at optimal growth light level was not enhanced by the elevated CO_2 could be attributed to balanced carbon loss and

TABLE 1 | The per cell concentrations of pigments (pg $cell^{-1}$) of *Synechococcus* WH7803 grown under different light and CO_2 levels (n = 3, triplicate cultures).

Pigments (pg $cell^{-1}$)	LC			HC		
	6 μ mol m^{-2} s^{-1}	25 μ mol m^{-2} s^{-1}	100 μ mol m^{-2} s^{-1}	6 μ mol m^{-2} s^{-1}	25 μ mol m^{-2} s^{-1}	100 μ mol m^{-2} s^{-1}
Chl *a*	0.005 ± 0.000^{aA}	0.013 ± 0.001^{bA}	0.007 ± 0.001^{aA}	0.006 ± 0.000^{aB}	0.021 ± 0.001^{bB}	0.039 ± 0.002^{cB}
CARs	0.004 ± 0.000^{aA}	0.012 ± 0.002^{bA}	0.009 ± 0.001^{cA}	0.006 ± 0.000^{aB}	0.019 ± 0.001^{bB}	0.035 ± 0.003^{cB}
APC	0.187 ± 0.006^{aA}	0.393 ± 0.175^{aA}	0.234 ± 0.033^{aA}	0.302 ± 0.015^{aB}	0.716 ± 0.050^{bB}	1.204 ± 0.193^{cB}
PC	0.079 ± 0.003^{aA}	0.105 ± 0.067^{aA}	0.097 ± 0.012^{aA}	0.127 ± 0.008^{aB}	0.292 ± 0.021^{bB}	0.460 ± 0.067^{cB}
PE	0.130 ± 0.004^{aA}	0.208 ± 0.079^{bA}	0.120 ± 0.017^{cA}	0.209 ± 0.013^{aB}	0.485 ± 0.030^{bB}	0.753 ± 0.120^{cB}

LC and HC indicate CO_2 partial pressures of 400 and 1,000 μatm, respectively. Different types of pigments are shown as Chl a, CARs (carotenoids), APC (allophycocyanin), PC (phycocyanin), and PE (phycoerythrin). Different letters above the data indicate significant difference, with the superscripted lowercases and uppercases representing that for light levels at the same CO_2 and for CO_2 levels at the same light level, respectively.

carboxylation, since the acidic stress associated with elevated CO_2 can stimulate respiratory carbon loss in phytoplankton (see the review by Gao and Campbell (2014) and literatures therein).

Synechococcus strains are known to operate active CCMs, though they lack extracellular carbonic anhydrase (Badger and Andrews, 1982; Price, 2011). Elevated CO_2 concentrations down-regulate the CCMs in microalgae and cyanobacteria, with depressed activity of carbonic anhydrase (Beardall and Raven, 2020). The down-regulated operation of CCMs in *Synechococcus* strain WH7803 could have saved energy (operation of CCMs requires energy expenditure), and the saved energy helps to enhance growth of *Synechococcus* strain WH7803 when light is limiting. That is, it is not the CO_2 fertilization effect that led to enhanced growth of the picophytoplankton under limited light condition. When CCMs become down-regulated, photorespiration or Rubisco-catalyzed oxygenation can speed up at high light levels due to decreased ratio of CO_2 to O_2 (Bailey et al., 2008). In the present work, when *Synechococcus* strain WH7803 was grown under inhibiting light level (100 μmol m^{-2} s^{-1}), its photorespiration might have been enhanced to result in negative effects on growth under the elevated CO_2. However, on the contrary, the increased CO_2 availability enhanced its growth significantly under the high light (**Figure 3A**). It has been shown that *Synechococcus* releases CO_2 by about 30% of the CCMs concentrated DIC while its CCMs operate (Badger et al., 1985), elevated CO_2 concentration in milieu might have counteracted the CO_2 release, therefore aiding the cells with enhancement of electron transport and quantum yield (**Figures 3B,C**) with stimulated growth (**Figure 3A**). More photosynthetic carbon fixation would demand more energy. In the present work, the picophytoplankton increased its photosynthetic pigments with increased levels of light and CO_2, which is consistent with that reported by Fu et al. (2007). Increased availability of CO_2 significantly increased the cells' light capturing capacity, as reflected in the increased photosynthetic pigments (**Table 1**). Under the high levels of light and CO_2, the cells of *Synechococcus* showed the highest increase in Chl. a content to ensure sufficient energy supply to support increased levels of carboxylation and photorespiration, which has been shown to increase under OA conditions (Gao et al., 2012).

In natural marine environments, phytoplankton cells are exposed to different light levels spatio-temporally. *Synechococcus* strains are usually distributed in the lower part of euphotic zone, being exposed relatively low light. However, during noon period or during periods of intensive mixing, the picophytoplankton cells may episodically exposed to high inhibiting light levels. Therefore, elevated CO_2 concentrations can positively and negatively affect its productivity at different depths or times during daytime. Consequently, the effects of OA on *Synechococcus* productivity could be strain-, depth-, and time-dependent, showing spatiotemporal differences in its response to progressive ocean acidification.

DATA AVAILABILITY STATEMENT

The raw data supporting the conclusions of this article will be made available by the authors, without undue reservation.

AUTHOR CONTRIBUTIONS

KG and NB contributed to the designing and planning the experiments and writing the manuscript. NB performed the experiments. Both authors contributed to the article and approved the submitted version.

FUNDING

The study was supported by the National Natural Science Foundation (41890803 and 41720104005).

ACKNOWLEDGMENTS

The authors thank Prof. Rui Zhang for his kind support, and are grateful to Prof. Sven Beer for his helpful comments on the data during his visit to the Xiamen University. The authors also thank Dr. Aziz Ullah for his technical assistance during his visit to the Xiamen University.

SUPPLEMENTARY MATERIAL

The Supplementary Material for this article can be found online at: https://www.frontiersin.org/articles/10.3389/fmars.2021.634189/full#supplementary-material

REFERENCES

Alberte, R. S., Wood, A. M., Kursar, T. A., and Guillard, R. R. L. (1984). Novel phycoerythrins in marine *Synechococcus* spp – characterization and evolutionary and ecological implications. *Plant Physiol.* 75, 732–739. doi: 10.1104/pp.75.3.732

Badger, M. R., and Andrews, T. J. (1982). Photosynthesis and inorganic carbon usage by the marine cyanobacterium, *Synechococcus* sp. *Plant Physiol.* 70, 517–523. doi: 10.1104/pp.70.2.517

Badger, M. R., Bassett, M., and Comins, H. N. (1985). A model for HCO_3^- accumulation and photosynthesis in the cyanobacterium *Synechococcus* sp – theoretical predictions and experimental-observations. *Plant Physiol.* 77, 465–471. doi: 10.1104/pp.77.2.465

Badger, M. R., Price, G. D., Long, B. M., and Woodger, F. J. (2006). The environmental plasticity and ecological genomics of the cyanobacterial CO_2 concentrating mechanism. *J. Exp. Bot.* 57, 249–265. doi: 10.1093/jxb/eri286

Bailey, S., Melis, A., Mackey, K. R. M., Cardol, P., Finazzi, G., van Dijken, G., et al. (2008). Alternative photosynthetic electron flow to oxygen in marine *Synechococcus*. *Biochim. Biophy. Acta* 1777, 269–276. doi: 10.1016/j.bbabio.2008.01.002

Barlow, R. G., and Alberte, R. S. (1985). Photosynthetic characteristics of phycoerythrin-containing marine *Synechococcus* spp .I. Responses to growth photon flux-density. *Mar. Biol.* 86, 63–74. doi: 10.1007/bf00392580

Bates, N. R., and Johnson, R. J. (2020). Acceleration of ocean warming, salinification, deoxygenation and acidification in the surface subtropical North Atlantic Ocean. *Commun. Earth Environ.* 1:33. doi: 10.1038/s43247-020-00030-5

Beardall, J., and Raven, J. A. (2016). "Carbon acquisition by microalgae," in *The Physiology of Microalgae. Developments in Applied Phycology*, Vol. 6, eds M. Borowitzka, J. Beardall, and J. Raven (Switzerland: Springer, Cham). doi: 10.1007/978-3-319-24945-2_4

Beardall, J., and Raven, J. A. (2020). "Acquisition of inorganic carbon by microalgae and cyanobacteria," in *Microbial Photosynthesis*, ed. Q. Wang (Singapore: Springer Singapore), 151–168. doi: 10.1007/978-981-15-3110-1_8

Callieri, C., Coci, M., Corno, G., Macek, M., Modenutti, B. E., Balseiro, E. G., et al. (2013). Phylogenetic diversity of nonmarine picocyanobacteria. *FEMS Microbiol. Ecol.* 85, 293–301. doi: 10.1111/1574-6941.12118

Campbell, L., and Carpenter, E. J. (1986). Diel patterns of cell-division in marine *Synechococcus* spp (Cyanobacteria) – use of the frequency of dividing cells technique to measure growth-rate. *Mar. Ecol. Prog. Ser.* 32, 139–148. doi: 10.3354/meps032139

Domínguez-Martín, M. A., Díez, J., and García-Fernández, J. M. (2016). Physiological studies of glutamine synthetases I and III from *Synechococcus* sp. WH7803 Reveal Differential Regulation. *Front. Microbiol.* 7:969. doi: 10.3389/FMICB.2016.00969

Flombaum, P., Gallegos, J. L., Gordillo, R. A., Rincon, J., Zabala, L. L., Jiao, N., et al. (2013). Present and future global distributions of the marine cyanobacteria *Prochlorococcus* and *Synechococcus*. *Proc. Natl. Acad. Sci. U.S.A.* 110, 9824–9829. doi: 10.1073/pnas.1307701110

Fogg, G. E. (1986). Ocean ecology: light and ultraphytoplankton. *Nature* 319:96. doi: 10.1038/319096a0

Fu, F. X., Warner, M. E., Zhang, Y., Feng, Y., and Hutchins, D. A. (2007). Effects of increased temperature and CO_2 on photosynthesis, growth, and elemental ratios in marine *Synechococcus* and *Prochlorococcus* (Cyanobacteria). *J. Phycol.* 43, 485–496. doi: 10.1111/j.1529-8817.2007.00355.x

Gao, K., and Campbell, D. A. (2014). Photophysiological responses of marine diatoms to elevated CO_2 and decreased pH: a review. *Funct. Plant Biol.* 41, 449–459. doi: 10.1071/FP13247

Gao, K., Xu, J., Gao, G., Li, Y., Hutchins, D. A., Huang, B., et al. (2012). Rising CO_2 and increased light exposure synergistically reduce marine primary productivity. *Nat. Clim. Chang.* 2, 519–523. doi: 10.1038/NCLIMATE1507

Gattuso, J. P., Lee, K., Rost, B., and Schulz, K. G. (2010). "Approaches and tools to manipulate the carbonate chemistry," in *Guide to Best Practices for Ocean Acidification Research and Data Reporting*, eds J.-P. Gattuso, K. Lee, B. Rost, and K. G. Schulz (Luxembourg: Publications Office of the European Union), 41–52.

Giordano, M., Beardall, J., and Raven, J. A. (2005). CO_2 concentrating mechanisms in algae: mechanisms, environmental modulation, and evolution. *Annu. Rev. Plant Biol.* 56, 99–131. doi: 10.1146/ANNUREV.ARPLANT.56.032604.144052

Givan, A. L. (2011). "Flow cytometry: an introduction," in *Flow Cytometry Protocols*, eds T. S. Hawley, and R. G. Hawley (Totowa, NJ: Humana Press), 1–29. doi: 10.1002/9781118487969.ch1

Glover, H. E., Keller, M. D., and Guillard, R. R. L. (1986). Light quality and oceanic ultraphytoplankters. *Nature* 319, 142–143. doi: 10.1038/319142a0

Glover, H. E., and Morris, I. (1981). Photosynthetic characteristics of coccoid marine cyanobacteria. *Arch. Microbiol.* 129, 42–46. doi: 10.1007/bf00417177

Huner, N. P. A., Oquist, G., and Sarhan, F. (1998). Energy balance and acclimation to light and cold. *Trends Plant Sci.* 3, 224–230. doi: 10.1016/s1360-1385(98)01248-5

Iturriaga, R., and Mitchell, B. G. (1986). Chroococcoid cyanobacteria – a significant component in the food web dynamics of the open ocean. *Mar. Ecol. Prog. Ser.* 28, 291–297. doi: 10.3354/meps028291

Kana, T. M., and Glibert, P. M. (1987). Effect of irradiances up to 2000 E m^{-2} s^{-1} on marine *Synechococcus* WH7803-I. Growth, pigmentation, and cell composition. *Deep Sea Res. A* 34, 479–495. doi: 10.1016/0198-0149(87)90001-x

Kim, Y., Jeon, J., Kwak, M. S., Kim, G. H., Koh, I., and Rho, M. (2018). Photosynthetic functions of *Synechococcus* in the ocean microbiomes of diverse salinity and seasons. *PLos One* 13:e0190266. doi: 10.1371/journal.pone.0190266

Lu, Z. Q., Jiao, N. Z., and Zhang, H. Y. (2006). Physiological changes in marine picocyanobacterial *Synechococcus* strains exposed to elevated CO_2 partial pressure. *Mar. Biol. Res.* 2, 424–430. doi: 10.1080/17451000601055419

Lüder, U. H., Knoetzel, J., and Wiencke, C. (2001). Acclimation of photosynthesis and pigments to seasonally changing light conditions in the endemic Antarctic red macroalga *Palmaria decipiens*. *Polar Biol.* 24, 598–603. doi: 10.1007/s003000100260

Morris, I., and Glover, H. (1981). Physiology of photosynthesis by marine coccoid cyanobacteria - some ecological implications. *Limnol. Oceanogr.* 26, 957–961. doi: 10.4319/lo.1981.26.5.0957

Partensky, F., Hess, W. R., and Vaulot, D. (1999). *Prochlorococcus*, a marine photosynthetic prokaryote of global significance. *Microbiol. Mol. Biol. Rev.* 63, 106–127. doi: 10.1128/MMBR.63.1.106-127.1999

Piazena, H., Perez-Rodrigues, E., Hader, D. P., and Lopez-Figueroa, F. (2002). Penetration of solar radiation into the water column of the central subtropical Atlantic Ocean – optical properties and possible biological consequences. *Deep Sea Res. II Top. Stud. Oceanogr.* 49, 3513–3528. doi: 10.1016/s0967-0645(02)00093-0

Platt, T., Gallegos, C. L., and Harrison, W. G. (1980). Photoinhibition of photosynthesis in natural assemblages of marine-phytoplankton. *J. Mar. Res.* 38, 687–701.

Price, G. D. (2011). Inorganic carbon transporters of the cyanobacterial CO_2 concentrating mechanism. *Photosynth. Res.* 109, 47–57. doi: 10.1007/s11120-010-9608-y

Ralph, P. J., and Gademann, R. (2005). Rapid light curves: a powerful tool to assess photosynthetic activity. *Aquat. Bot.* 82, 222–237. doi: 10.1016/j.aquabot.2005.02.006

Ritchie, R. J. (2006). Consistent sets of spectrophotometric chlorophyll equations for acetone, methanol and ethanol solvents. *Photosynth. Res.* 89, 27–41. doi: 10.1007/s11120-006-9065-9

Scanlan, D. J., Ostrowski, M., Mazard, S., Dufresne, A., Garczarek, L., Hess, W. R., et al. (2009). Ecological genomics of marine picocyanobacteria. *Microbiol. Mol. Biol. Rev.* 73, 249–299. doi: 10.1128/MMBR.00035-08

Smith, R. C., and Baker, K. S. (1981). Optical-properties of the clearest natural-waters (200-800 nm). *Appl. Opt.* 20, 177–184. doi: 10.1364/ao.20.000177

Stockner, J. G., and Antia, N. J. (1986). Algal picoplankton from marine and freshwater ecosystems – a multidisciplinary perspective. *Can. J. Fish. Aquat. Sci.* 43, 2472–2503. doi: 10.1139/f86-307

Strickland, J. D. H., and Parsons, T. R. (1972). *A Practical Handbook of Seawater Analysis*. Ottawa, ON: The Alger Press Ltd.

Varkey, D., Mazard, S., Ostrowski, M., Tetu, S. G., Haynes, P., and Paulsen, I. T. (2016). Effects of low temperature on tropical and temperate isolates of marine *Synechococcus*. *ISME J.* 10, 1252–1263. doi: 10.1038/ISMEJ.2015.179

Zhang, Y., Jiang, H.-B., and Qiu, B.-S. (2013). Effects of UVB radiation on competition between the bloom-forming cyanobacterium *Microcystis aeruginosa* and the Chlorophyceae *Chlamydomonas microsphaera*. *J. Phycol.* 49, 318–328. doi: 10.1111/jpy.12038

Conflict of Interest: The authors declare that the research was conducted in the absence of any commercial or financial relationships that could be construed as a potential conflict of interest.

Copyright © 2021 Bao and Gao. This is an open-access article distributed under the terms of the Creative Commons Attribution License (CC BY). The use, distribution or reproduction in other forums is permitted, provided the original author(s) and the copyright owner(s) are credited and that the original publication in this journal is cited, in accordance with accepted academic practice. No use, distribution or reproduction is permitted which does not comply with these terms.

frontiers in Marine Science

ORIGINAL RESEARCH
published: 25 May 2020
doi: 10.3389/fmars.2020.00323

Response of Phytoplankton Assemblages From Naturally Acidic Coastal Ecosystems to Elevated pCO_2

Natalia Osma[1,2], Laura Latorre-Melín[1], Bárbara Jacob[3], Paulina Y. Contreras[4], Peter von Dassow[1,5,6] and Cristian A. Vargas[1,2,4]*

[1] Millennium Institute of Oceanography (IMO), University of Concepción, Concepción, Chile, [2] Department of Aquatic Systems, Faculty of Environmental Science, University of Concepción, Concepción, Chile, [3] Patagonian Ecosystems Research Center (CIEP), Coyhaique, Chile, [4] Center for the Study of Multiple-Drivers on Marine Socio-Ecological Systems (MUSELS), University of Concepción, Concepción, Chile, [5] Department of Ecology, Pontifical Catholic University of Chile, Santiago, Chile, [6] UMI 3614 Evolutionary Biology and Ecology of Algae, CNRS, Sorbonne University, Pontificia Universidad Católica de Chile, Universidad Austral de Chile, Station Biologique, Roscoff, France

The interplay of coastal oceanographic processes usually results in partial pressures of CO_2 (pCO_2) higher than expected from the equilibrium with the atmosphere and even higher than those expected by the end of the century. Although this is a well-known situation, the natural variability of seawater chemistry at the locations from which tested organisms or communities originate is seldom considered in ocean acidification experiments. In this work, we aimed to evaluate the role of the carbonate chemistry dynamics in shaping the response of coastal phytoplankton communities to increased pCO_2 levels. The study was conducted at two coastal ecosystems off Chile, the Valdivia River estuary and the coastal upwelling ecosystem in the Arauco Gulf. We characterized the seasonal variability (winter/summer) of the hydrographic conditions, the carbonate system parameters, and the phytoplankton community structure at both sites. The results showed that carbonate chemistry dynamics in the estuary were mainly related to seasonal changes in freshwater discharges, with acidic and corrosive conditions dominating in winter. In the Arauco Gulf, these conditions were observed in summer, mainly associated with the upwelling of cold and high pCO_2 (>1,000 μatm) waters. Diatoms dominated the phytoplankton communities at both sites, yet the one in Valdivia was more diverse. Only certain phytoplankton groups in this latter ecosystem showed a significant correlations with the carbonate system parameters. When the impact of elevated pCO_2 levels was investigated by pCO_2 manipulation experiments, we did not observe any significant effect on the biomass of either of the two communities. Changes in the phytoplankton species composition and abundance during the incubations were related to other factors, such as competition and growth phases. Our findings highlight the importance of the natural variability of coastal ecosystems and the potential for local adaptation in determining responses of coastal phytoplankton communities to increased pCO_2 levels.

Keywords: climate change, environmental variability, carbonate chemistry, community structure, coastal upwelling, estuary

OPEN ACCESS

Edited by:
Nina Bednarsek, Southern California Coastal Water Research Project, United States

Reviewed by:
José Pinho, University of Minho, Portugal
Jun Sun, Tianjin University of Science and Technology, China

****Correspondence:***
Natalia Osma
natalia.osma@imo-chile.cl

Specialty section:
This article was submitted to Coastal Ocean Processes, a section of the journal Frontiers in Marine Science

Received: *13 November 2019*
Accepted: *21 April 2020*
Published: *25 May 2020*

Citation:
Osma N, Latorre-Melín L, Jacob B, Contreras PY, von Dassow P and Vargas CA (2020) Response of Phytoplankton Assemblages From Naturally Acidic Coastal Ecosystems to Elevated pCO_2. Front. Mar. Sci. 7:323. doi: 10.3389/fmars.2020.00323

1. INTRODUCTION

Human activities over the last two centuries have triggered changes in the global climate system at a pace unprecedented over the past 300 Myr (Caldeira and Wickett, 2003). On a global scale, the air-sea surface gas exchange has promoted an oceanic uptake of about one third of the recent anthropogenic CO_2 emissions (Sabine et al., 2004; Gruber et al., 2019), leading to an alteration of the seawater carbonate chemistry and a reduction in seawater pH of 0.1 units (Hoegh-Guldberg and Bruno, 2010). This process is well-known as ocean acidification (OA, Orr et al., 2005) and is expected to further decrease average oceanic pH between 0.14 and 0.35 units by the end of the century (Caldeira and Wickett, 2003), which will likely have substantial consequences for marine ecosystems (Bopp et al., 2013).

Models predicting future changes in the carbonate chemistry associated to OA can be fairly accurately applied in the open ocean, where the environmental heterogeneity is rather low (Hofmann et al., 2011). Nevertheless, anticipating the synergic effects of OA in coastal ecosystems becomes more complex, owing to the high fluctuations in the physical-chemical properties in short temporal and spatial scales that occurs in these regions (Booth et al., 2012; Waldbusser and Salisbury, 2014). The partial pressure of CO_2 (pCO_2) in the coastal domain exhibits a higher natural variability related both to biological processes, such as respiration and photosynthesis (Shamberger et al., 2011; Buapet et al., 2013; Saderne et al., 2013), as well as to oceanographic processes including the upwelling of deep waters and the discharge of fresh water from rivers (e.g., Cao et al., 2011; Vargas et al., 2016). The dynamic interplay of these coastal processes may result in pCO_2 levels in surface waters higher than expected from the equilibrium with the atmosphere (Hofmann et al., 2011; Wallace et al., 2014). One factor significantly contributing to pCO_2 variability in coastal areas is the discharge of riverine waters (Cao et al., 2011; Vargas et al., 2016). These waters are typically more acidic and corrosive than oceanic waters as they present low pH values and a reduced buffering capacity linked to their low alkalinity (Raymond and Cole, 2003; Vargas et al., 2018). In addition, the remineralization of the organic matter transported by rivers by heterotrophic organisms results in high DIC and pCO_2 levels. In this regard, estuarine environments constitute one naturally acidified coastal ecosystem, where the pCO_2 values can reach several thousands microatmospheres (Borges et al., 2006; Wallace et al., 2014), representing a potential source of CO_2 to the atmosphere. The other example is observed in upwelling-influenced coastal zones, where the upwelling-favorable winds promote the transport to the surface of naturally acidic subsurface waters characterized by low pH (<8) and high pCO_2 (>600 μatm) levels, resulting in a decrease of the seawater pH in the nearshore area (Feely et al., 2008). However, at the same time, these nutrient-rich upwelled waters stimulate primary production, which lower the concentration of dissolved inorganic carbon (DIC), ultimately reducing the levels of pCO_2. Owing to such local acidification processes in the coastal zone, marine organisms inhabiting this areas are constantly exposed to low pH/high pCO_2 conditions and, therefore, may be operating at the limit of their physiological tolerances. Further acidification of the water through OA may lead to a synergistic effect (Gruber, 2011) and bring their physiology beyond these thresholds. Conversely, it may also occur that local adaptation to these highly variable environments confers on these organisms a higher resilience capacity to face sudden changes and increases in the pCO_2 conditions (e.g., Duarte et al., 2013; Vargas et al., 2017). All these potential effects and consequences are still a mater of investigation.

The impact of high pCO_2 levels on the phytoplankton community has been previously characterized in several distinct ecosystems, e.g., the Northern Sea (Burkhardt et al., 2001), equatorial Pacific (Tortell et al., 2002) or Southern ocean (Tortell et al., 2008; Trimborn et al., 2013), among many others. However, these studies have shown contrasting responses of the phytoplankton community structure to increased CO_2 levels. For instance, at high pCO_2 conditions, Tortell et al. (2002) observed a decrease in the abundance of diatoms and an increase of the non-siliceous groups whereas Tortell et al. (2008) reported an increase in primary production and abundance of the chain-forming diatoms *Chaetoceros* spp. Hare et al. (2007), in turn, showed that diatoms were replaced by nanoflagellates under these same conditions. Therefore, there is not a clear consensus about which groups will be benefited in a high pCO_2 environment. In this light, knowing the carbonate system dynamics of the ecosystems where the phytoplankton communities inhabit may be crucial to correctly interpret the outcome of these investigations (Hofmann et al., 2011; Vargas et al., 2017). Unfortunately, this information is usually lacking in the investigation of the impact of OA.

In the present work, we provide insights into the natural seasonal variability of the carbonate system and the phytoplankton community structure and physiology at two contrasting coastal areas off central Chile: an estuarine ecosystem (Valdivia River estuary), and a coastal upwelling ecosystem influenced by freshwater discharges (Arauco Gulf). In addition, the response of these phytoplankton communities to elevated pCO_2 levels is studied using CO_2 manipulation experiments. The objective of this study was 2-fold: (1) to evaluate the relationship between the seasonal variability of the seawater chemistry and the phytoplankton community at two contrasting coastal ecosystems, and (2) to study the response of these communities to elevated pCO_2 levels. Our hypothesis was that phytoplankton communities inhabiting highly variable, naturally acidic coastal ecosystems, such as estuaries, river-influenced areas and/or coastal upwellings, are adapted to high pCO_2 conditions.

2. METHODS

2.1. Description of Study Sites

In this study we investigated two coastal ecosystems off Central Chile which experience naturally high and variable pCO_2 conditions: The river-influenced coastal upwelling area off Concepción, in the northern part of the Arauco Gulf (36° 42–58′ S, 73°12–17′ W), and the Valdivia River estuarine system (39°46′–53′ S, 73°25′ W) (**Figure 1**). The Arauco Gulf is an equatorward facing embayment characterized by intense seasonal upwelling events between September and March (austral Spring-Summer) caused by an increase in the southwesterly wind stress

(Sobarzo et al., 2007; Letelier et al., 2009). During these events, surface waters over the continental shelf edge are typically supersaturated in CO_2, resulting in strong across-shore pCO_2 gradients (Torres et al., 2011). In its northern part, the Arauco Gulf is influenced by freshwater discharges from the Biobío River, whose plume typically moves southward within the bay. Average flow rates of this river range between 200 and 3,000 $m^3\ s^{-1}$ (Valle-Levinson et al., 2003), with maximum values observed during the rainy season in winter (June-August) and minimum values during summer (January-March). Likewise, Biobío River runoff constitutes a significant source of nutrients (silicate, nitrate and phosphate), trace metals and dissolved organic and inorganic carbon (DOC and DIC) for the adjacent coastal ocean (Pérez et al., 2015; Vargas et al., 2016). The Valdivia River estuary, in turn, constitutes one of the most important estuarine systems from central-southern Chile in terms of mean area and freshwater discharges. Hydrographic conditions reveals that it is a partially mixed type estuary, widely affected by tidal cycles (Pino et al., 1994). It presents a seasonal rainfall regime, with an annual average freshwater discharge of 592 $m^3\ s^{-1}$ and maximum and minimum flow rates in austral winter (July) and summer (March), respectively (Garcés-Vargas et al., 2013).

In this study, we conducted four sampling campaigns between 2014 and 2016, both during austral winter and summer; two in the Valdivia River estuary (August 2014 and January 2015) and two in the Arauco Gulf (September 2015 and January 2016). Each sampling was accomplished in 1 day and consisted in an along-shore transect of five stations (**Figure 1**), covering areas influenced by fresh-water discharges and areas without this influence.

2.2. Sampling and Hydrographic Measurements

The hydrological information on daily river flows were obtained from the Dirección General de Aguas (www.dga.cl) of the Chilean Ministry of Public Work. Seasonal variability in the freshwater discharges of the Biobío and Valdivia Rivers during the sampling years is shown in **Figure 1**. During each campaign, the water column was characterized through vertical profiles of temperature, salinity and oxygen recorded using a SeaBird SBE-19 plus conductivity-temperature-depth (CTD) equipped with a Westar fluorometer. Water samples for chlorophyll *a* (Chl *a*; 200-300 mL), nutrients [NO_3^-, NO_2^-, PO_4^{3-}, and $Si(OH)_4$; 25 mL], DIC and the $\delta^{13}C$ isotopic signature of DIC (40 mL), as well as for phytoplankton abundance (250 mL) were collected with 5 L Niskin bottles at 2, 10, 25, and 50 m (only at GA3 and GA5) in the Arauco Gulf, and at 1, 3, and 5 m (plus two additional depths at 8 and 10 m only at VE4 and VE5) in the Valdivia River estuary. In addition, samples for Total Alkalinity (TA) in the Arauco Gulf and for pH in the Valdivia estuary were obtained at the same sampling depths, which were used to estimate both the pCO_2 and the saturation state of aragonite (Ω_{arag}) (see below). Chl *a* samples were directly filtered through GF/F (total Chl *a* concentration), and stored at −20°C until analysis in the laboratory by fluorometry (Turner Design TD-700) according to Parsons et al. (1984). Water samples for nutrients analysis were pre-filtered (GF/F), frozen (−20°C) and subsequently analyzed following (Strickland and Parsons, 1968).

Gross primary productivity (GPP) and community respiration (CR) was estimated at two stations in each study area (**Figure 1**), both during winter and summer campaigns. One station was selected at the inner part of the Valdivia River estuary (VE2) and another one offshore in Corral Bay (VE5), at 20 km from the coast. Similarly, in the Arauco Gulf, one station was located inside the Biobío river plume (GA3) at 4 km from the coast, and the other one northward outside the influence of this river plume (GA1), at ∼40 km from the coast. *In situ* incubations to determine GPP and CR were conducted at two depth levels (1 and 3 m) in the Valdivia River estuary and at three depth levels within the euphotic zone (2, 10, and 15 m) in the Arauco Gulf. Discrete-depth measurements of GPP and CR were integrated to 5 and 20 m depths (in Valdivia estuary and the Arauco Gulf, respectively) using the trapezoidal approximation.

Finally, two additional water samplings were carried out to perform the carbonate system manipulation experiments with phytoplankton assemblages from both coastal upwelling and estuarine ecosystems. In the Valdivia River estuary, about 70 L of surface water was collected using 10 L-Niskin bottles at the inner part of the estuary (VE2) in August 2014. Here, the CO_2 manipulation experiments were conducted at the Coastal Station of Calfuco (Universidad Austral de Chile, 39° 78′ S, 73° 39′ W). In the Arauco Gulf, the sampling took place in November 2016 at the upwelling center off Lavapié Point (37° 08′ S, 73° 34′ W). A similar water volume (∼70 L) was collected using a suction pump in clean plastic containers and was immediately transported to the mesocosm facilities at the Marine Biological Station of Dichato (Universidad de Concepción, 36° 33′ S, 72° 39′ W). Major physical-chemical parameters, such as temperature, salinity, nutrient concentration and CO_2 system parameters (i.e., DIC and pH), as well as Chl *a* concentration and phytoplankton abundance were likewise determined during these field collections in order to have the *in situ* conditions of the experimental water.

2.3. Analysis and Estimation of the Carbonate System Parameters

All the parameters were analyzed according to Riebesell et al. (2010). Seawater pH was measured potentiometrically in a 25 ml-thermostatted cell at 25 ± 0.1°C using a Metrohm 713 pH meter (input resistance >1,013 Ohm, 0.1 mV sensitivity, and nominal resolution 0.001 pH units) with a glass combined double junction Ag/AgCl electrode (Metrohm model 6.0219.100), calibrated with 8.089 Tris buffer (25°C) according to DOE (1994). pH values are given on the total hydrogen scale (pH_T). For DIC and its $\delta^{13}C$ isotopic measurements, a subsample of 40 ml was collected with a sterile syringe, filtered through a GF/F filter (previously pre-combusted at 450°C for 4–5 h) directly into 40 ml glass 200 Series I-CHEM® vials and poisoned with a saturated solution of $HgCl_2$ to stop biological activity. The septa of the vials were substituted by butyl rubber septa to prevent diffusion of CO_2 (DOE, 1994). Samples were run on an OI Analytical total inorganic carbon-total organic carbon (TIC-TOC) Analyzer

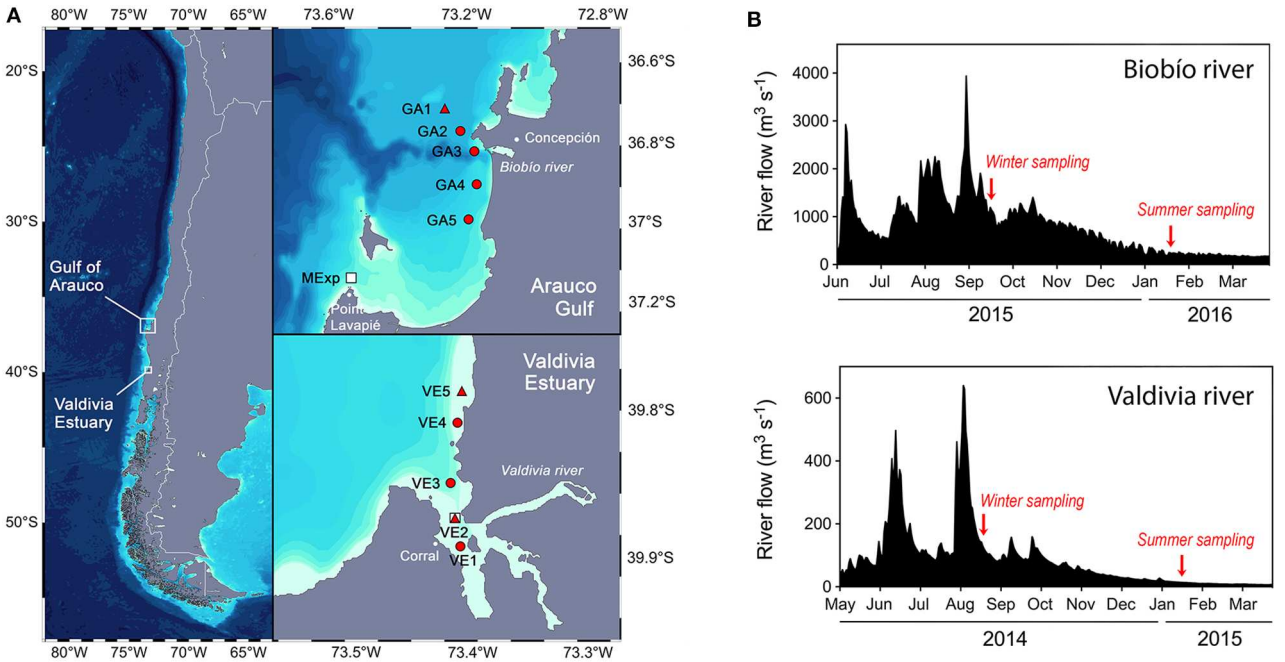


FIGURE 1 | (A) Along-shore transects with the stations position at the two study areas off Central Chile, the Arauco Gulf (GA) and the Valdivia river estuary (VE). Hydrographic and chemical parameters as wells as phytoplankton abundance were measured at all stations. Primary productivity and community respiration were determined at two selected stations in each sampling site (red triangles): one station was located closer to the river mouth, showing a higher influence of fresh water discharges (GA3 and VE2), whereas the other station was located out of this influence (GA1 and VE5). This sampling was repeated in winter and summer at GA (2015–2016) and VE (2014–2015). Squares represent the location where the water was collected for the pCO_2- mesocosms experiments, i.e., Lavapié Point (MExp) and VE2. **(B)** River discharges from the Biobío River (top) and the Valdivia river (bottom) for the year of the corresponding samplings. Red arrows indicates the day of the samplings at each site.

(Aurora Model 1030), first run to determine the parts per million carbon organic/inorganic concentration and then for the $\delta^{13}C$ isotopic signature. The TIC-TOC analyzer was interfaced with a Finnigan Mat DeltaPlus isotope ration mass spectrometer for analysis by continuous flow. Data were normalized using internal standards. The analytical precision was 2% for the quantitative DIC measurements and ±0.2‰ for the isotopes. All the analysis were conducted in the G. G. Hatch Stable Isotope Laboratory at the University of Ottawa, Canada. Samples for total alkalinity (TA) were collected in 250 ml- glass bottles, fixed with a saturated solution of $HgCl_2$, and subsequently measured in the laboratory by potentiometric titration with HCl following the closed-cell method described in DOE (1994).

pH and DIC values (Valdivia estuary), and TA and DIC values (Arauco Gulf) were used in the software CO2SYS (Pierrot et al., 2006) to calculate the rest of the carbonate system parameters (i.e., pCO_2, TA and pH_T in Valdivia estuary and Arauco Gulf, respectively) and the Ω_{arag}. Temperature, salinity, and nutrient [PO_4^{3-} and $Si(OH)_4$] data were likewise included in these calculations. The carbonic acid dissociation constants (K_1 and K_2) were taken from Mehrbach et al. (1973) as refit by Dickson and Millero (1987) for marine waters (salinity >30 psu) and those by Millero (2010) for estuarine waters (salinity between 1 and 30 psu). The $KHSO_4$ equilibrium constant determined by Dickson (1990) was applied for all calculations.

2.4. Phytoplankton Community Structure, Gross Primary Production (GPP), and Community Respiration (CR)

Phytoplankton samples for microscopy were fixed with 2% acidic Lugol solution and analyzed following the Utermöhl technique (Utermöhl et al., 1958), with classification until the lowest possible taxonomical level, using an Olympus IX51 microscope. GPP and CR were estimated from changes in the dissolved oxygen (DO) concentrations after incubating BOD bottles at *in situ* light conditions and in the dark (Strickland, 1960). At all samplings, the incubation time was <12 h and 3–4 replicates of each light condition (i.e., *in situ* and dark) were run. DO was determined before and after the incubation using the OxyMini® optode system (WPInst.). Net community production (NCP) was calculated as the difference in the DO concentration between light (GPP) and dark (CR) BOD bottles after the incubation.

2.5. Carbonate System Manipulation Experiments

Once in the laboratory, the seawater collected at each sampling site for the experiments was pre-filtered through a 200 μm mesh to eliminate large zooplankton. After acclimation to the corresponding pCO_2 treatment for 12 h (Valdivia estuary) or 22 h (Arauco Gulf), seawater was transferred to polycarbonate

20L- bottles to start the experiments. Semi-automatic mesocosm systems for seawater carbonate chemistry manipulation of similar characteristics were employed at the two locations. The different pCO_2 treatments were attained by continuously bubbling the seawater with either ambient (low pCO_2 treatment) or CO_2-enriched air (high pCO_2 treatment). Air/CO_2 mixtures were produced using a bulk technique, based on mixing filtered, dry air with ultra pure CO_2 at a known flow rate using Mass Flow Controllers (MFC; Aalborg Model GFC). In the Valdivia River estuary the low pCO_2 level was set at ∼380 μm (control level, IPCC 2014), whereas in the Arauco Gulf the low pCO_2 level was set at 700 μm corresponding to the *in situ* value during field sampling (i.e., "control" treatment). For the estuarine community, the high pCO_2 treatment was ∼900 μm whereas, for the coastal upwelling area, we considered an experimental treatment of 1600 μm pCO_2. The upwelled water was already CO_2-saturated (700 μm pCO_2), and therefore we assumed a higher ΔCO_2 of around 900 μatm. In both cases, these high pCO_2 levels can naturally occur in these ecosystems (Vargas et al., 2017). Four replicates per treatment were run during the experiments, that lasted for 5 days and were conducted under temperature controlled conditions and 12/12 days/night light regime. The water inside the incubation bottles was gently mixed using rotor-powered blades, in order to prevent sedimentation of the phytoplankton cells. Subsamples for nutrients, carbonate system parameters, chlorophyll *a* and phytoplankton abundance were collected every day (except nutrients in the Arauco Gulf, which were sampled *in situ*, and on days 2 and 4 during the experiments) and analyzed as stated above.

2.6. Statistical Analyses

Pairwise comparisons were conducted applying the Student *t*-test and were considered significant at $p < 0.05$. The phytoplankton community was characterized using the Shannon-Wiener Diversity index (H'), Margalef's species richness (d), and Pielou's evenness index (J_0) at each station and sampling time, using logarithms to the base 2 in the calculation of H′. It should be noted that these indices are not true species-level diversity indexes as some of the organisms could only be identified to the genus level (e.g., *Chaetoceros* spp. and *Thalassiossira* spp.). The correlation between environmental and biological variables was addressed by means of the Spearman correlation coefficient, which were considered significant at $p < 0.05$. Furthermore, a Generalized Linear Model (GLM) was applied to significantly correlated variables to evaluate the dependence between the biological variables and the environmental factors at each study site.

3. RESULTS

3.1. Hydrography

Clear seasonal differences in the hydrographic conditions were observed at the two sampling sites. The Biobío and Valdivia rivers discharges showed a typical annual pattern during the sampling years, with maximum values in winter and minima in summer (**Figure 1B**). Accordingly, fresh water influence was higher in winter at both areas, although in Valdivia, almost the entire water column at the inner estuarine stations was dominated by riverine waters (VE1-VE3, **Figure 2**) whereas in the Arauco Gulf this influence was limited to the surface waters in the southernmost stations (GA3–GA5, **Figure 3**). The water column along the transects was well-mixed and characterized by low temperatures (11–12°C) and oxygenated waters (> 3 ml L^{-1}) during this season. In summer, in contrast, the warming of the surface waters caused the stratification of the water column, with temperatures decreasing 9°C in the upper 5 m in the Valdivia estuary (**Figure 2**) and 4°C in the upper 20 m in the Arauco Gulf (**Figure 3**). In the Valdivia estuary, the reduced river flow during this season limited the influence of freshwater to the first 4 m at the inner part of the estuary (VE1-VE3), whereas the influence of more oceanic waters characterized by higher nutrient levels (both $NO_3^- + NO_2^-$ and PO_4^{-3}) increased. In the Arauco Gulf, the low oxygen values (<1 ml L^{-1}) together with the high PO_4^{-3} concentrations below 20 m showed the influence of an upwelling of oxygen-poor nutrients-rich subsurface waters in summer, especially at stations GA1, GA2, and GA5 (**Figure 3**). However, $NO_3^- + NO_2^-$ concentration did not follow the same pattern as the concentrations in summer were lower than in winter, which may be attributed to an enhanced nitrogen uptake by phytoplankton during the spring-summer blooms. $Si(OH)_4$ concentrations, in turn, were significantly higher in Valdivia than in the Arauco Gulf (*t*-test, $p < 0.05$) but were associated with freshwater inputs at both sites, with maximum values at the Biobío river mouth (GA3) in the Arauco Gulf and at the inner estuarine stations (VE1–VE3) in Valdivia.

3.2. Carbonate System Dynamics at Two Coastal Ecosystems

As with the hydrographic conditions, carbonate system parameters showed marked seasonal differences. The dynamics of the carbonate system in the Valdivia estuary were driven by the interplay between predominant freshwater discharges in winter and the influence of more oceanic waters in summer (**Figure 4**). In winter, the water column at the inner part of the estuary (VE1-VE3) was characterized by low DIC concentrations (<1,250 μmol kg^{-1}), low TA (<1,700 μmol kg^{-1}), low pCO_2 levels (< 300 μatm), and corrosive conditions ($\Omega_{arag} < 1$), due to low alkalinity/salinity conditions associated to high freshwater inputs from the Valdivia river (**Figure 1B**). Depleted $\delta^{13}C_{DIC}$ values indicated the contribution of riverine DIC to the total pool of DIC in this estuarine portion. The pH_T values showed intermediate values during the winter campaign, ranging between 7.60 and 7.99 units. In summer, however, the pH_T ranged from as low as 7.48 at the stations outside of the river plume (i.e., VE4 and VE5) to as high as 8.03 at the surface waters of VE1 and VE3 stations. The influence of oceanic waters extended from the coastal stations to the inner portion of the estuary during this season, being characterized by low pH_T, and high DIC concentrations (>1,700 μmol kg^{-1}), TA values (>2,000 μmol kg^{-1}), and pCO_2 levels (>700 μatm) (**Figure 4**).

In the Arauco Gulf, the highest pH_T values were recorded at the surface waters in winter, ranging between 8.19 and 8.56 units (**Figure 5**), while the lowest DIC concentrations (1535

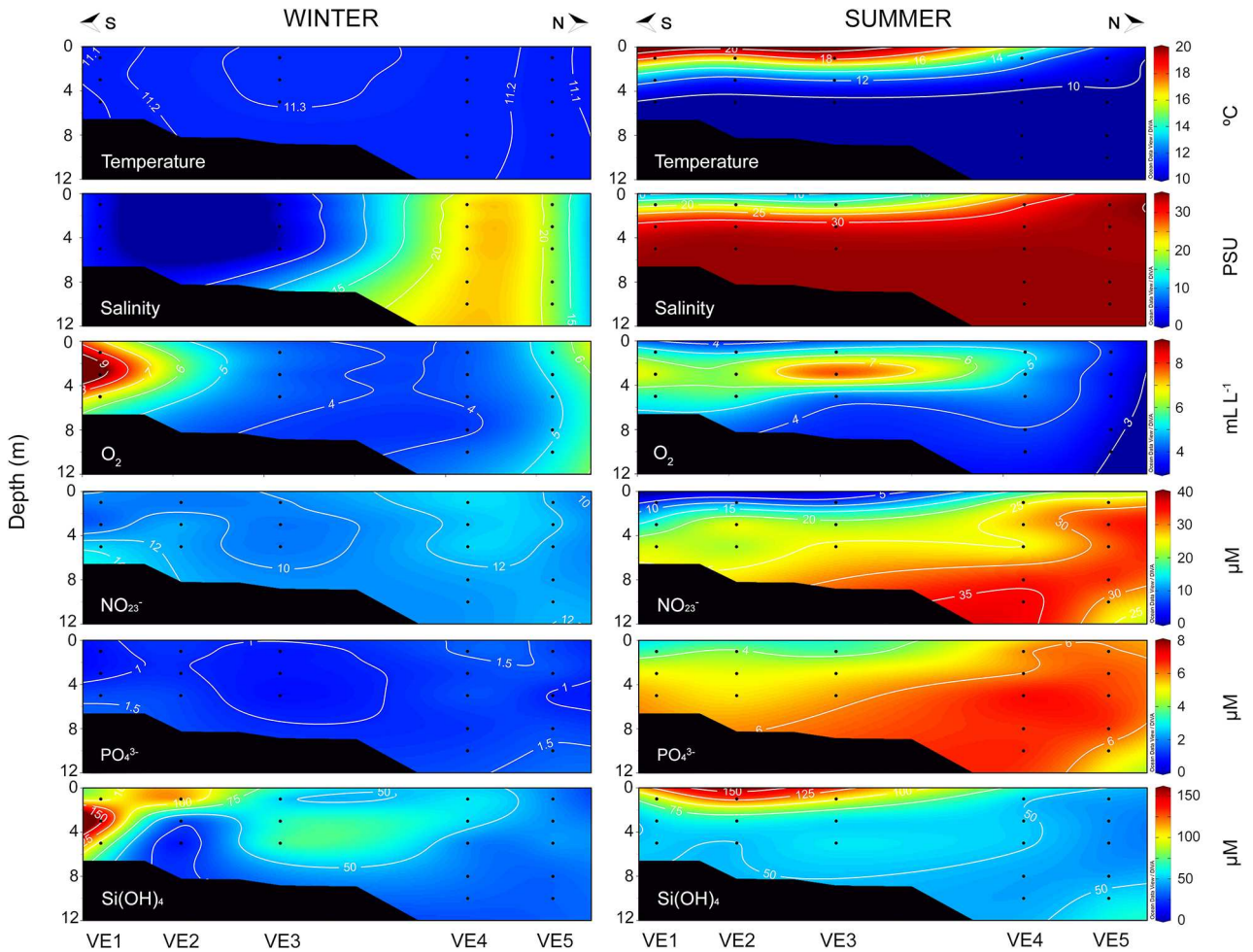


FIGURE 2 | Hydrographic characterization of temperature, salinity, oxygen (O_2), and nutrients [NO_3^- plus NO_2^-, PO_4^{3-}, and $Si(OH)_4$] along the transects sampled at the Valdivia river estuary during winter 2014 **(left)** and summer 2015 **(right)**.

μmol kg^{-1}) and TA levels (1,731 μmol kg^{-1}) for this area were determined at the river mouth station GA3, associated with higher freshwater inputs from the Biobío river during this season (**Figure 1B**). However, the riverine DIC contribution to the DIC pool in the Arauco Gulf was not evident from the $\delta^{13}C_{DIC}$ values. The pCO_2 levels remained relatively low (<300 μatm) throughout most of the transect in winter and Ω_{arag} values revealed supersaturation conditions with respect to aragonite. In summer, in contrast, all the carbonate system parameters (except the TA, which showed a relatively constant value of 2,298 $\pm$ 8 μmol kg^{-1} along the transect) reflected the upwelling of acidic and corrosive subsurface waters mainly at stations GA1, GA2, and GA5 (**Figure 5**). These subsurface waters were also characterized by low pH values (<7.9 units), high DIC concentration (>2,100 μmol kg^{-1}), high pCO_2 levels (>700 μatm), and Ω_{arag} undersaturation conditions (< 1), as compared to other stations (i.e., GA3 and GA4) and season (i.e., winter). $\delta^{13}C_{DIC}$ values also evidenced the influence of fractionated DIC pool (<1‰) associated to low oxygen and corrosive subsurface waters.

In general terms, the more acidic waters (low pH/ high pCO_2) were observed in summer at both the Arauco Gulf and the Valdivia estuary, caused by the influence of subsurface upwelled waters and coastal oceanic waters, respectively. However, in contrast to the Arauco Gulf, the more corrosive conditions Ω_{arag}(< 1) in the water column at the Valdivia estuary were recorded in winter, coinciding with the larger freshwater inputs, which are characterized by a reduced buffering capacity associated to the low TA values (**Figure 5**, **Figure S1**).

3.3. Temporal and Spatial Variations of the Phytoplankton Community

Seasonal differences in the Chl *a* concentration and the abundance of the dominating phytoplankton groups were larger than spatial variations along the transects at both samplings sites. Vertical profiles in the Valdivia estuary showed low Chl *a* concentrations (<2.5 μg L^{-1}) in winter at all stations and depths (**Figure 6**), with integrated values (over the first 5 m) ranging between 5.3 and 8.4 mg m^{-2} (**Table 1**). In summer, this

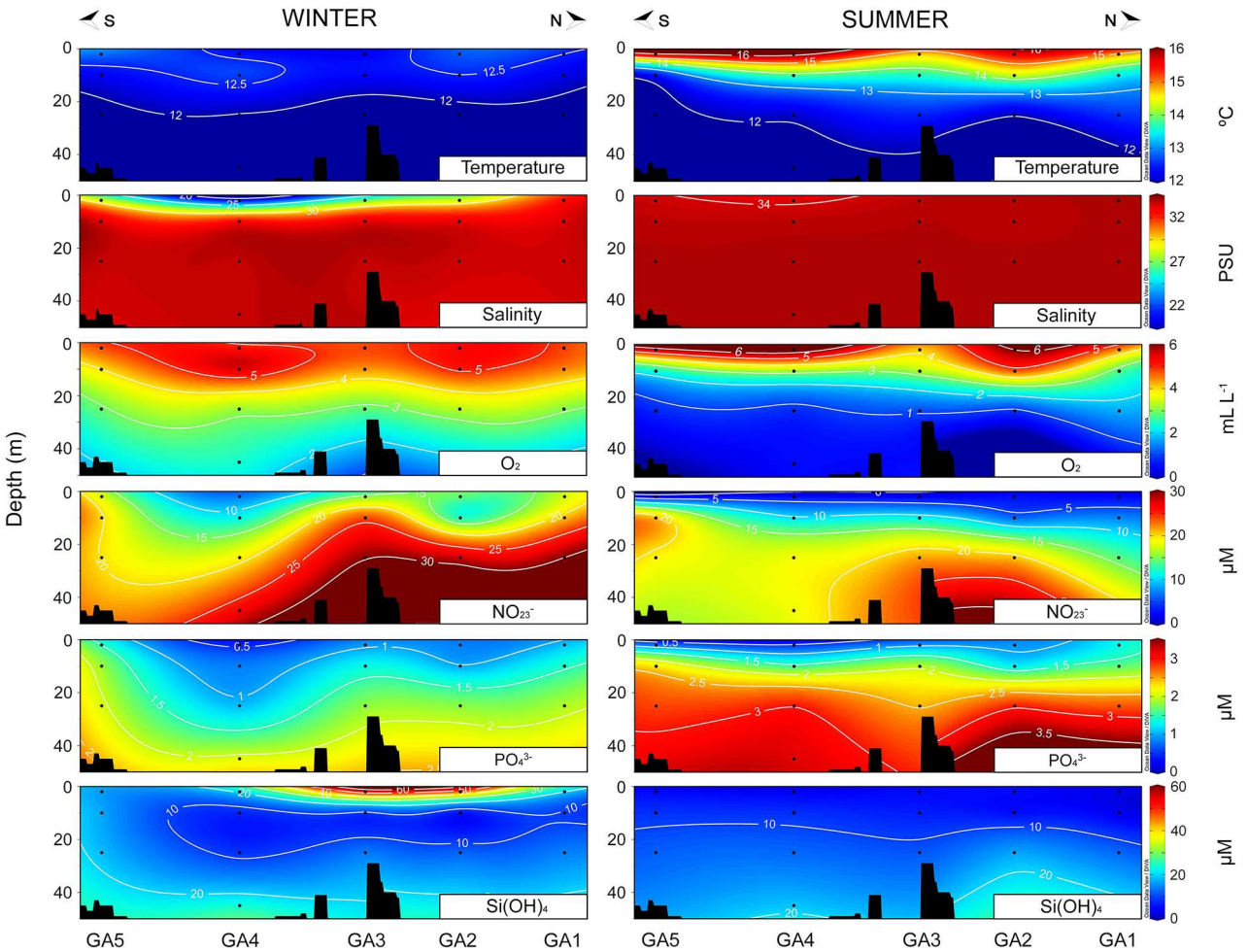


FIGURE 3 | Hydrographic characterization of temperature, salinity, oxygen (O_2), and nutrients [NO_3^- plus NO_2^-, PO_4^{3-}, and $Si(OH)_4$] along the transects sampled at the Arauco Gulf during winter 2015 **(left)** and summer 2016 **(right)**.

concentration increased at all stations but mainly at the inner estuarine section (VE1–VE3), where it achieved maximum values between 7 and 18 μg L^{-1} at subsurface waters and integrated values in the water column of 44.6–65.5 mg m^{-2} (**Table 1**). Similarly, the cell abundance of the different phytoplankton groups was about one order of magnitude larger in summer (**Figure 6**), even though the community was more diverse and the species richness was higher in winter (**Table 1**). Diatoms were the most abundant group throughout the year, contributing between 50 and 94% to the total abundance (**Table S1**), although there was a seasonal change in the dominant species. In winter, *Aulacoseira granulata* and *Thalassionema nitzschioides* accounted for most of the phytoplankton abundance, whereas in summer *Chaetoceros* spp. and *Skeletonema costatum* dominated the water column. A distinct distribution of less abundant groups was also observed along the transect. For instance, chlorophytes were only collected at the inner estuarine stations (**Figure 6**), where they were relatively abundant in winter (14–29%, **Table S1**). Other groups, such as dinoflagellates were present throughout the entire water column, at all stations and samplings, but their relative contribution to the total community changed likely associated to the influence of more oceanic waters as it was higher both at VE4 and VE5 stations and in summer all along the transect (between 10 and 36%, **Table S1**).

In the Arauco Gulf the seasonal patterns of Chl *a* concentration and the cell abundance were similar as in Valdivia, being higher in summer than in winter (**Figure 7**). However, the latter was one order of magnitude higher in the Arauco Gulf during the same season, with maximum values reaching more than 3×10^6 cells L^{-1} at surface waters at GA2 (**Figure 7**) and integrated values (over the first 20 m) of 88.5×10^9 cells m^{-2} (**Table 1**). According to the diversity and species richness indexes (**Table 1**), the plankton community in this coastal ecosystem was less diverse and showed lower species richness in summer, but it was strongly dominated by diatoms throughout the year (relative abundance between 91 and 99%, **Table S2**). As in Valdivia, there was a seasonal change in the species composition at each station. *Chaetoceros* spp. was the most abundant group

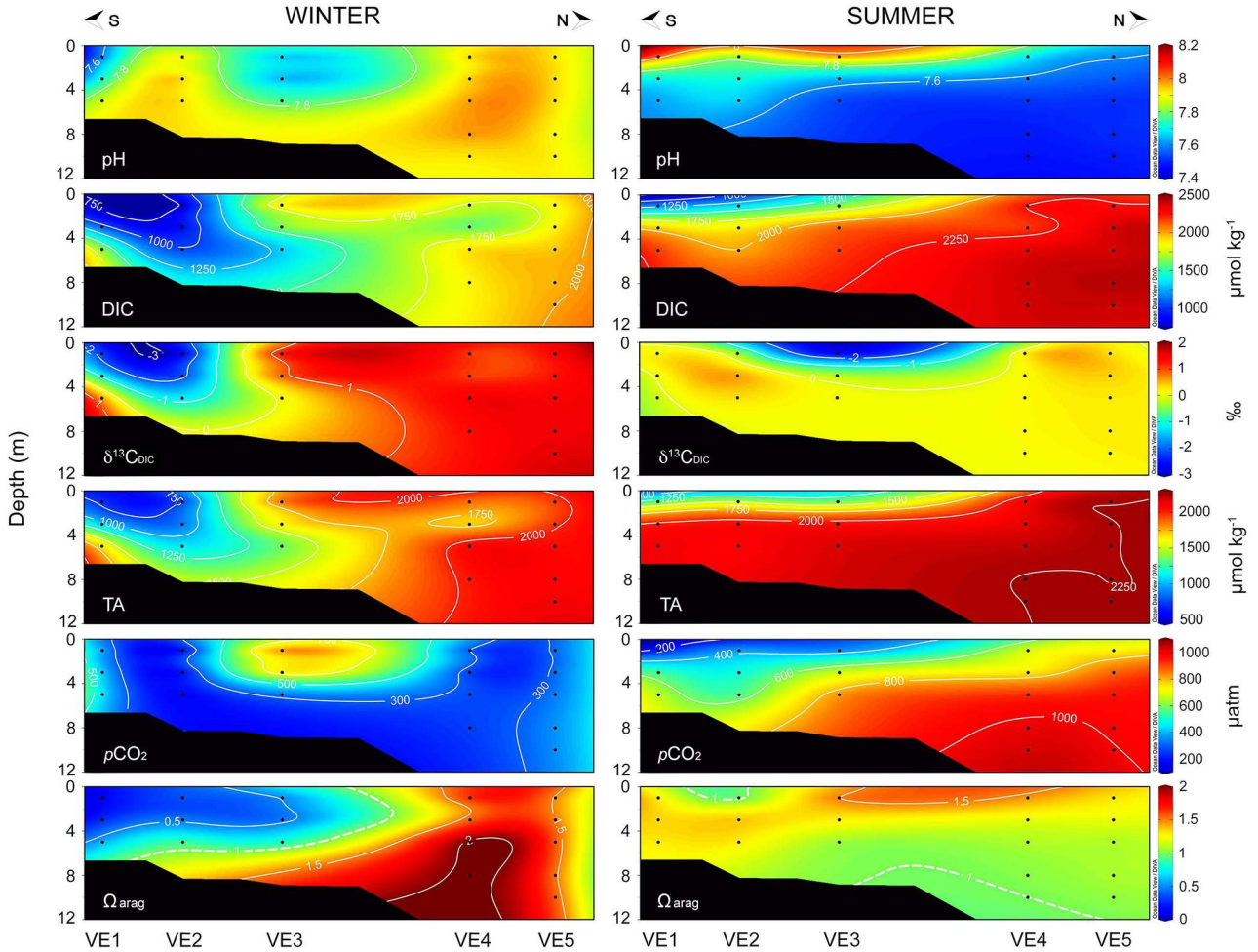


FIGURE 4 | Carbonate system parameters along the transect conducted in the Valdivia river estuary in winter **(left)** and summer **(right)**. From the top to the bottom: pH, dissolved inorganic carbon (DIC), its $\delta^{13}C$ isotope ($\delta^{13}C_{DIC}$), total alkalinity (TA), partial pressure of CO_2 (pCO_2), and the saturation station of aragonite (Ω_{arag}). Dashed line in Ω_{arag} plot represents the isopleth of 1.

at stations GA1 and GA2 in winter (80–86%), whereas the same genus dominated the phytoplankton community at stations GA4 and GA5 in summer (88–82%, **Table S2**). The northernmost stations (GA1–GA3) were dominated by the chain-forming diatom *Leptocylindrus danicus* in summer. It is noteworthy that GA3, the station located at the Biobío river mouth (**Figure 1**), presented the highest diversity and species richness values in winter, not showing a clear dominance of any species or genera (**Table S2**). The contribution of dinoflagellates was low in this area both in winter and summer, ranging from 0.2 to 8.9%, with maximum integrated cell abundances of 35.6×10^7 cells m^{-2} at GA3.

As expected, the largest gross primary production rates (GPP) were recorded during summer campaigns at both study sites (**Table 2**), with values being one order of magnitude higher (>4,000 mg C m^{-2} d^{-1}) in the Arauco Gulf than in the Valdivia River estuary. Seasonal differences in the community respiration (CR) were observed between sites as well. In Valdivia, the highest CR levels were determined at the inner estuarine stations in winter. In the Arauco Gulf, in contrast, the highest values were measured in summer at the more oceanic station (GA1), coinciding with the highest GPP rates supported by the upwelling of nutrient-rich subsurface waters (**Figure 3**). The GPP/CR ratio showed a similar trend at the two coastal ecosystems (**Table 2**), with significantly lower values recorded during winter campaigns (*t*-test, $p < 0.05$).

3.4. Relationship Between Environmental and Biological Variables

Several significant correlations were obtained between the structure and physiological rates of phytoplankton communities and the abiotic factors, such as the hydrographic properties and the carbonate system parameters. **Tables 3**, **4** includes these correlations as well as the results of the GLM model applied to elucidate the role of each environmental factor in predicting the biological variables in Valdivia and the Arauco Gulf, respectively. We observed distinct relationship

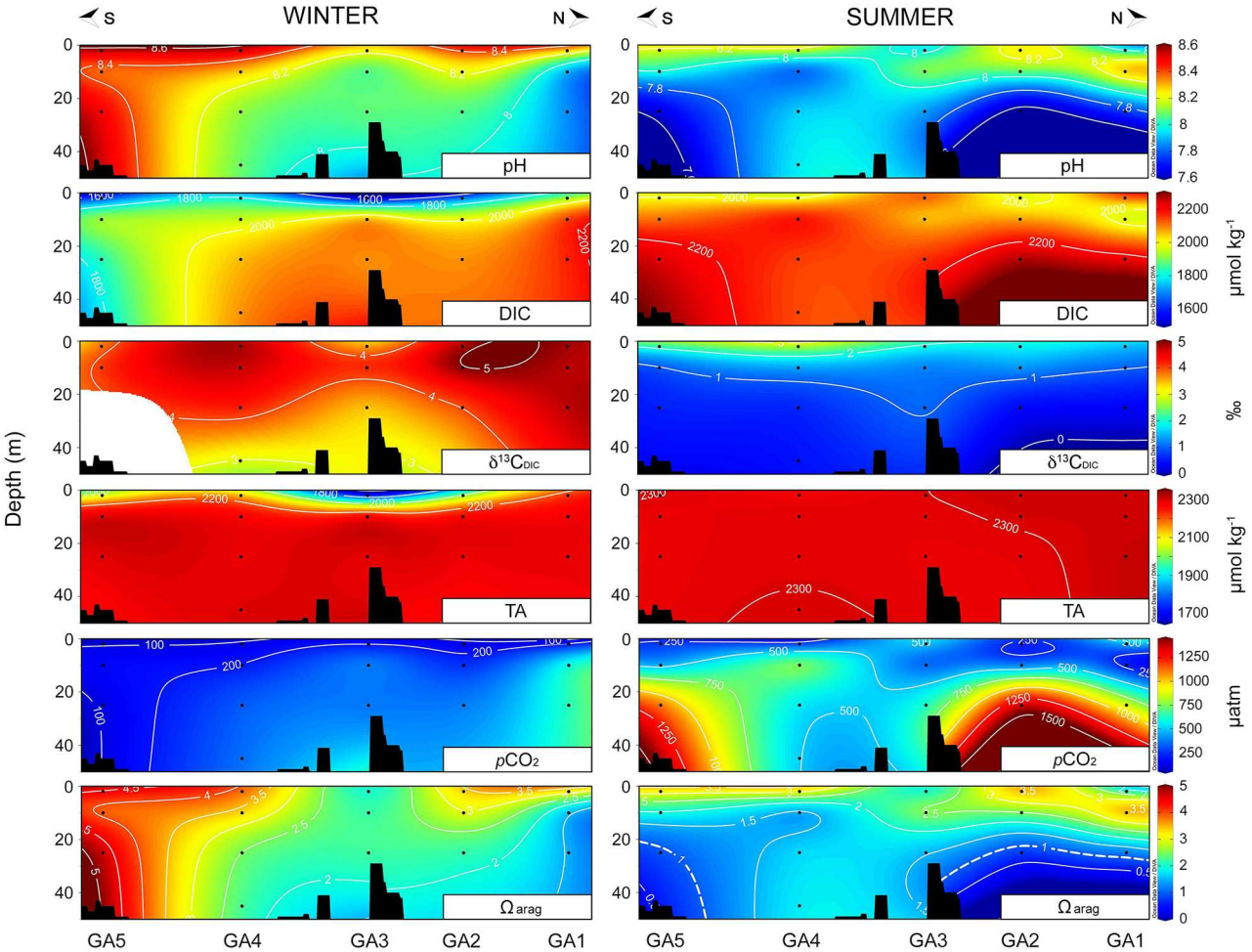


FIGURE 5 | Carbonate system parameters along the transect conducted in the Arauco Gulf in winter **(left)** and summer **(right)**. From the top to the bottom: pH, dissolved inorganic carbon (DIC), its $\delta^{13}C$ isotope ($\delta^{13}C_{DIC}$), total alkalinity (TA), partial pressure of CO_2 (pCO_2), and the saturation station of aragonite (Ω_{arag}). Dashed line in Ω_{arag} plot represents the isopleth of 1.

of the environmental and biological factors between the two sites.

In the Arauco Gulf, the variability of the Chl *a* concentration, the abundance of the different taxonomic groups and the physiological rates were largely explained (44–71%) by variations in temperature and nutrients concentration (**Table 4**). None of the carbonate system parameters was significantly correlated to the considered biological variables in this ecosystem. In contrast, in the Valdivia estuary, the carbonate chemistry in the water column showed a significant role in modulating the abundance of certain taxonomic groups. For instance, change in the Ω_{arag} values explained 14% of the variance in the Chl *a* concentration and 23–40% of the seasonal variability observed in the abundance of euglenophytes, cilliates and silicoflagellates (**Table 3**). The abundance of diatoms and dinoflagellates, in turn, was correlated to the salinity and nutrients concentration, even though the multivariate linear approach considering these factors was only able to explain significantly the variance in dinoflagellates (31%).

3.5. Response of Coastal Phytoplankton Communities to Short-Term Exposure to Elevated pCO_2 Levels

Seawater parameters during field collection (i.e., *in situ*) and for the experimental set up are given in **Figures 8**, **9**. It is noteworthy that the pH/pCO_2 levels established for the two experimental treatments (low/high) were maintained constant over the 5-days experiments, as reflected by the continuous monitoring of pH and pCO_2 values. Natural assemblages of planktonic communities from estuarine and coastal upwelling ecosystems showed distinct responses during the experimental period. In the Valdivia River estuary, the *in situ* values of pH and pCO_2 were of 7.93 and 162 μatm (VE2 in **Figure 5**, winter sampling), respectively. For the experiment, however, we decided to set the low pCO_2/high pH treatment (hereinafter "low treatment") at 380 μatm, a typical and recommended value for control treatments in CO_2 manipulation experiments (IPCC,

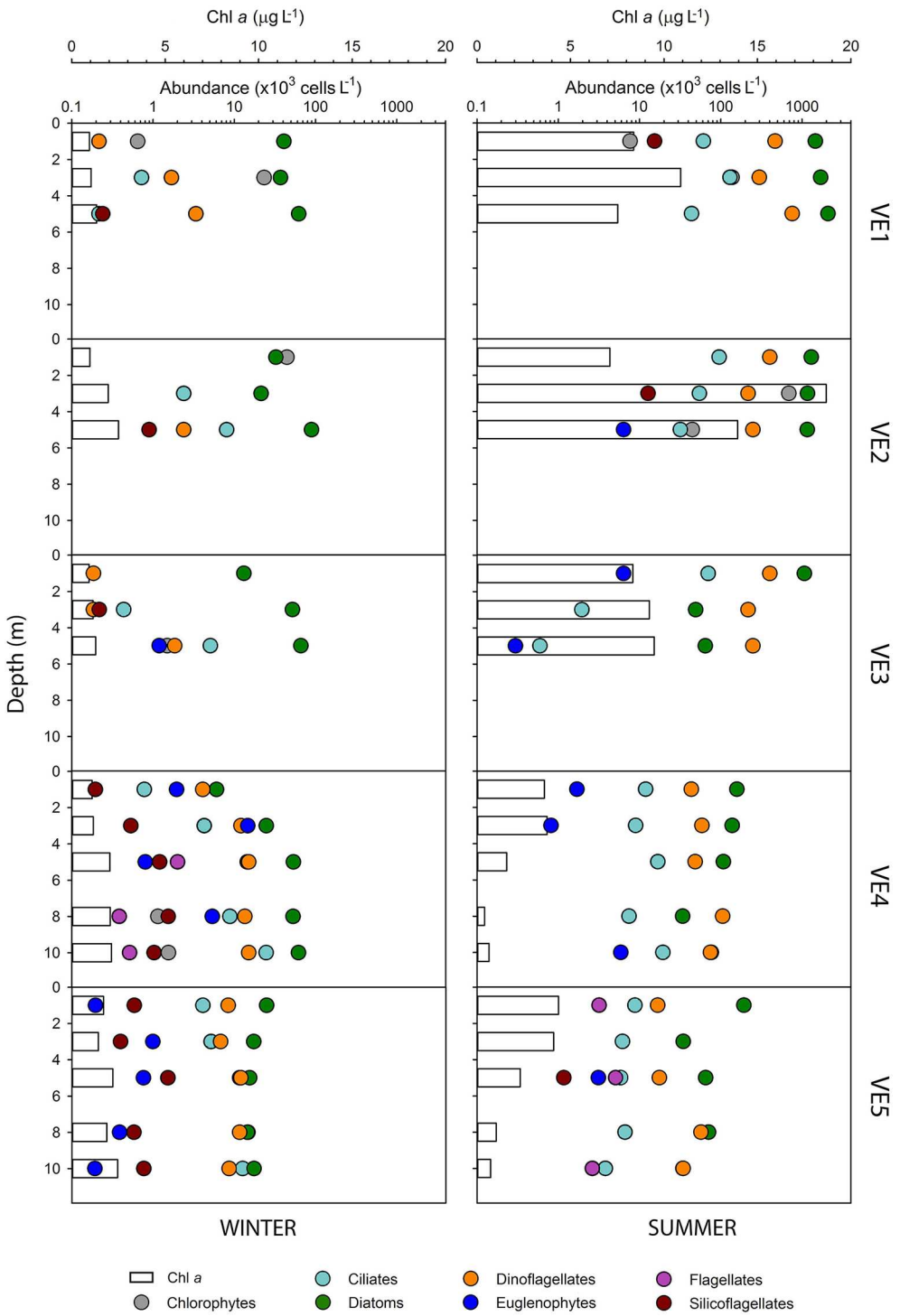


FIGURE 6 | Cell abundance of the phytoplankton groups (*dots*) dominating the community in the Valdivia river estuary during winter **(left)** and summer **(right)**. Note that the abundance is given in log-scale. The bars represents the chlorophyll a concentration at each station and during each seasonal sampling. The legend at the bottom applies to all the panels.

TABLE 1 | Phytoplankton community biodiversity and species richness through the Shannon-Wiener diversity index (H′), Pielou's evenness index (J_0), and Margalef's species richness (d) at both study areas.

Stations	Int. Chl *a* (mg m^{-2})	Int. abundance (× 10^6 cells m^{-2})	H′	J_0	*d*
VALDIVIA ESTUARY					
VE1	5.30–46.08	275.40–11462.68	2.75–2.14	0.74–0.69	3.19–1.29
VE2	8.36–65.51	304.59–9944.58	1.94–2.30	0.60–0.70	1.90–1.61
VE3	5.40–44.61	207.86–4110.04	2.29–2.04	0.68–0.62	2.29–1.70
VE4	6.50–16.29	226.32–1018.41	2.66–1.81	0.81–0.61	2.11–1.30
VE5	8.39–19.25	180.05–623.50	2.28–1.61	0.79–0.57	1.40–1.20
ARAUCO GULF					
GA1	54.10–131.81	552.57–77002.21	0.83–0.24	0.40–0.10	0.53–0.50
GA2	57.81–197.65	2595.14–88513.84	0.57–0.70	0.25–0.30	0.61–0.49
GA3	32.93–151.63	1139.98–22736.50	2.09–0.56	0.79–0.27	0.93–0.41
GA4	74.77–118.82	992.66–2801.09	0.82–0.49	0.46–0.30	0.36–0.27
GA5	35.81–54.04	1295.29–14165.36	1.14–0.37	0.59–0.17	0.43–0.49

The integrated chlorophyll a (Chl a) concentration and phytoplankton abundances are also given, being the integrated depth of 5 m in the Valdivia estuary and of 20 m in the Arauco Gulf. The left and right values in the range corresponds to the winter and summer values, respectively.

2014) and the high pCO_2/low pH treatment (hereinafter "high treatment") at 900 μatm. Both the Chl *a* concentration and the abundance of phytoplankton groups in general showed an exponential increase during this experiment (**Figure 8**). Thus, Chl *a* values in the low treatment, for instance, increased from as low as 1 μg L^{-1} at initial conditions to as high as 15 μg L^{-1} in 5 days. No significant differences were detected between the low and high treatments at the end of the incubation (*t*-test, $p > 0.05$). The fast increase in the phytoplankton growth rates was reflected in the nutrient ratios (**Figure 8**). While the Si/N ratio decreased steadily (from ca. 11 to 9), the N/P ratio increased toward the end of the experiments in both treatments (from ca. 9 to 25). In this regard, there was no significant differences in the N uptake rates between the low and high treatments. The phytoplankton community in these estuarine waters was mainly dominated by diatoms (65% of the total abundance), in agreement to that observed under natural conditions (**Figure 6**). Most of the plankton groups increased their abundance during the incubation at both treatments, except silicoflagellates, which were only present at the beginning of the experiment. Euglenophytes and dinoflagellates showed a moderate increase in both treatments, whereas diatoms and flagellates exhibited the largest increase and were the most abundant groups at the end. When the effect of the elevated pCO_2 level was tested after the 5-days incubation, we only observed significant differences (*t*-test, $p < 0.01$) in the abundance of diatoms and flagellates, being higher in the low treatment. A detailed examination of the species composition of diatoms revealed that the contribution of less abundant species (<1% of the total abundance, grouped as "Other diatoms," **Figure 8**), which corresponded mostly to freshwater diatoms, as well as of *Chaetoceros* spp. decreased toward the end of the experiment. Conversely, taxa, such as *Thalassiosira* spp. and *Skeletonema costatum* increased, mainly at the high pCO_2 treatment.

In the Arauco Gulf, the *in situ* pH and pCO_2 levels were 7.65 and 706 μatm, respectively (**Figure 8**). These values were considered for the low treatment as a measurement of control conditions in upwelling waters, whereas the high treatment was set at 1,600 μatm of pCO_2, considering a Δ pCO_2 of 900 μatm with respect to the control conditions. Nutrient ratios N/P and Si/N remained constant at ca. 11 and 0.73, respectively, indicating no significant uptake of N by phytoplankton and no nutrient limitation during the experiment. Likewise, no significant effect of pCO_2 levels was observed in the concentration of Chl *a*, although it decreased from about 2 μg L^{-1} at *in situ* and initial values to 0.6 μg L^{-1} at the end of the incubation. Similarly, the abundance of diatoms decreased with time at both the high and low treatments, although this decrease was two times higher at high pCO_2 conditions than at low pCO_2 conditions (13.5×10^3 cells L^{-1} d^{-1} vs. 5.9×10^3 cells L^{-1} d^{-1}). This decrease in the cell abundance coincided with an increase in the aggregates formation, as revealed by visual observations of the incubation bottles. The abundance of dinoflagellates, in contrast, did not show any influence of elevated pCO_2 levels nor a decrease with time. In this experiment, the diatom community was dominated by *Thalassiosira* spp. As in the estuarine ecosystem, the less abundant diatom species decreased toward the end of the experiment irrespective of the treatment.

4. DISCUSSION

4.1. The Natural Environmental Variability of Hydrography and Carbonate System for Estuarine and Coastal-Upwelling Phytoplankton Communities

A frequent research gap in OA studies is the lack of information about the natural variability of the seawater chemistry at the locations where the organisms are collected. However, it is increasingly more evident that this knowledge is critical to correctly interpret the outcome of these investigations (e.g., Boyd et al., 2016; Vargas et al., 2017), particularly in studies conducted at highly variable and/or naturally acidic coastal ecosystems. In the present work, we have described the physical-chemical properties of the water column (in terms of temperature, salinity, dissolved oxygen, nutrients concentration and carbonate system parameters) at each study area both during winter and summer, as we expected to record different carbonate chemistry conditions associated to the distinct oceanographic processes dominating the water column during these two seasons.

The seasonal variability in the hydrographic conditions and the phytoplankton community in the Valdivia river estuary and the adjacent coastal area were mostly associated to changes in the extent of the river plume along the transect, which was primarily linked to seasonal changes in the freshwater discharges, as previously described for this area (Vargas et al., 2003; Giesecke et al., 2017). In winter, the low $NO_3^- + NO_2^-$ and PO_4^{-3} concentrations typical for this system (Pérez et al., 2015) together with the limited solar irradiance characteristic at this latitude (Iriarte et al., 2007; González et al., 2010) limited the phytoplankton growth and favored a net heterotrophic system,

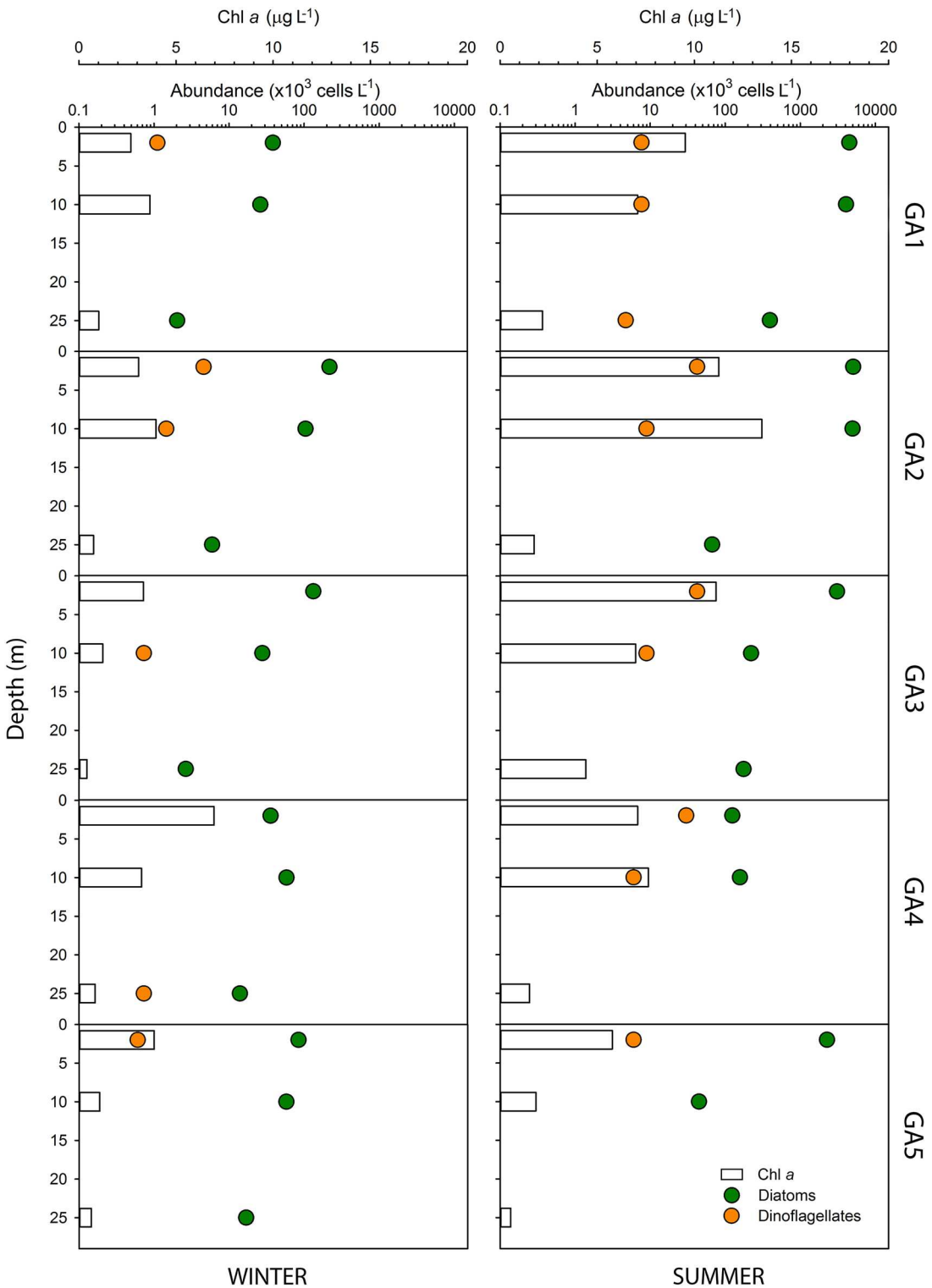


FIGURE 7 | Cell abundance of the phytoplankton groups (*dots*) dominating the community in the Arauco Gulf estuary during winter **(left)** and summer **(right)**. Note that the abundance is given in log-scale. The bars represents the chlorophyll a concentration at each station and during each seasonal sampling. The legend in the lower panel applies to all the panels.

TABLE 2 | Integrated gross primary productivity (GPP), community respiration (CR), net community production (NCP), and the GPP/CR ratio at two station of the Valdivia estuary and the Arauco Gulf during winter and summer.

Stations	Season	GPP	CR	NCP	GPP/CR
VALDIVIA ESTUARY					
VE2	Winter	11.89 ± 2.32	118.15 ± 23.43	−106.26 ± 17.34	0.10 ± 0.06
	Summer	469.37 ± 52.15	62.62 ± 9.98	406.75 ± 43.56	7.50 ± 2.31
VE5	Winte	19.62 ± 3.32	6.66 ± 1.84	12.97 ± 2.43	2.95 ± 0.47
	Summer	295.84 ± 25.22	16.89 ± 1.89	278.95 ± 32.21	17.52 ± 2.99
ARAUCO GULF					
GA1	Winter	231.22 ± 34.68	236.97 ± 30.81	−5.75 ± 0.75	0.98 ± 0.13
	Summer	4699.09 ± 704.86	1222.82 ± 158.97	3476.27 ± 521.44	3.84 ± 0.50
GA3	Winter	140.34 ± 28.07	154.41 ± 23.16	−14.07 ± 1.83	0.91 ± 0.14
	Summer	2311.12 ± 346.67	718.31 ± 143.66	1592.81 ± 318.56	3.22 ± 0.42

*VE2 and GA3 were located close to the Valdivia and the Biobío river mouths (see **Figure 1**), respectively, being influenced by freshwater discharges, mainly in winter. VE5 and GA1 were located out of the river plume influence. The integrated depths are 5 m in the Valdivia estuary and 20 m in the Arauco Gulf. The units for GPP, CR and NCP are mg C m^{-2} d^{-1}, while the GPP/CR is unitless.*

where the CR exceeded GPP (**Table 2**). This high CR was likely associated to the consumption of the organic matter transported by the river. Furthermore, as the relative abundance of the microheterotrophic components of the plankton community was not significantly higher during this time (**Table S1**), the enhanced respiration could be attributed to an increase in the pico- and nanoplankton community associated to freshwater discharges (Iriarte et al., 2018; Cuevas et al., 2019). In summer, the reduction of the river runoff led to a strong stratification in this tidal estuary, with considerable implications for the distribution of Chl *a* in the water column. The surface waters of lower salinity showed low phytoplankton biomass, increasing within the pycnocline and below (**Figure 6**), which is a typical pattern observed in other estuaries and fjord areas (Alldredge et al., 2002; Jouenne et al., 2007). Phytoplankton composition along the transect shifted from a freshwater-water species dominated community during winter toward a marine species dominated community during summer, in agreement to that reported by Giesecke et al. (2017).

The hydrographic features in the Arauco Gulf follow a seasonal pattern, with higher upwelling events during austral spring/summer (Valle-Levinson et al., 2003; Sobarzo et al., 2007) and with a considerable influence of freshwater discharges from the Biobío River in winter (Vargas et al., 2016). Furthermore, water column stratification in this region results from the influence of both temperature and salinity (Sobarzo et al., 2007). Accordingly, our results showed that thermal stratification dominated the water column in summer (associated with an increase in the solar irradiance) whereas salinity stratification was stronger in winter, particularly at those stations influenced by the river plume (GA3–GA5, **Figure 3**). The transport of nutrient-rich subsurface waters to the euphotic zone in summer promoted the phytoplankton growth, reaching Chl *a* values (>10 μg L^{-1}) common for this coastal region (Iriarte and Bernal, 1990; Vargas et al., 2007). Likewise, the nutrient concentrations measured during our samplings are within the range of previously reported values (Vargas et al., 2013; Pérez et al., 2015). The relatively low NO_3^- + NO_2^- values (as compared to the values in winter), together with the high phytoplankton biomass, suggest that our summer sampling took place after an intense upwelling episode. The composition of the phytoplankton taxa found in this study in the Arauco Gulf was in good agreement with that already described for this ecosystem (Anabalón et al., 2007; González et al., 2007) as well as for other upwelling areas (Kudela et al., 2005). On the other hand, the high GPP values found in this (1.4–4.7 g C m^2 d^{-1}) and previous studies (e.g., Daneri et al., 2000; Vargas et al., 2007) highlights the importance of the Humboldt current system off central Chile as one of the most productive systems in the world.

Carbonate chemistry dynamics at both sampling sites were likewise associated to the major local oceanographic forcing's dominating the water column. In Valdivia, the more corrosive conditions were observed at the inner estuarine section in winter, associated with the larger river freshwater discharges (**Figure 4**). This low salinity water was characterized by low DIC concentration and TA (**Figure S1**), which limited the buffering capacity of the system and lead to Ω_{arag} <1. Similar undersaturation conditions have been reported for other estuarine and river plume environments (e.g., Cao et al., 2011; Wallace et al., 2014). In summer, the subsurface intrusion of more oceanic waters, characterized by high pCO_2 and low pH values, was responsible of the undersaturation conditions at the offshore stations (**Figure 4**). The high pH and low pCO_2 levels observed at the surface waters of the inner estuarine portion was most likely caused by the high photosynthetic rates observed during this season (**Table 2**) (Hinga, 2002). In the Arauco Gulf, the more corrosive conditions were registered in summer and were associated to the upwelling episode that apparently happened before our sampling. The subsurface waters were characterized by low pH (<7.6) and high pCO_2 (>1,000 μatm) levels, which led to undersaturation conditions with respect to Ω_{arag}. This is a common feature observed in this (Vargas et al., 2016) and other upwelling ecosystems (e.g., Feely et al., 2008; Hofmann et al., 2011). In winter, the larger influence of freshwater discharges caused the low DIC and TA values determined at the river mouth station (GA3) (Vargas et al., 2016). Overall, the values of the carbonate system parameters determined in this study for both

TABLE 3 | Relationship between biological variables (*Y*) and environmental factors (X_i) at the Valdivia river estuary.

Variables	Factors	Spearman[a]	GLM		
(*Y*)	(X_i)	R^2	σ	*p*-value	R^2
Chl *a*	Ω_{arag}	0.14^{*}	1.87	>0.05	$0.14^{n.s.}$
Diatoms	Salinity	0.12^{*}	-2.28×10^3	>0.05	$0.01^{n.s.}$
	PO_4^{-3}	0.21^{**}	74.17×10^3	>0.05	
Dinoflagellates	Salinity	0.36^{***}	2.03×10^3	>0.05	0.31^{**}
	NO_{23}^{-}	0.17^{*}	-19.75×10^3	<0.01	
	PO_4^{-3}	0.47^{***}	80.04×10^3	>0.01	
Chlorophytes	Temperature	0.12^{*}	5.03×10^3	>0.05	$0.03^{n.s.}$
	pH	0.11^{*}	-282.49×10^3	>0.05	
	pCO_2	0.13^{*}	-0.31×10^3	>0.05	
	NO_{23}^{-}	0.17^{*}	5.63×10^3	>0.05	
	$Si(OH)_4$	0.12^{*}	0.39×10^3	>0.05	
Euglenophytes	Ω_{arag}	0.40^{***}	2.20×10^3	<0.05	0.08^{*}
Cilliates	PO_4^{-3}	0.14^{*}	2.66×10^3	>0.05	$0.04^{n.s.}$
	Ω_{arag}	0.23^{**}	9.86×10^3	>0.05	
Flagellates	$Si(OH)_4$	0.12^{*}	−6.35	>0.05	$0.01^{n.s.}$
Silicoflagellates	pH	0.31^{***}	2.52×10^3	>0.05	$0.02^{n.s.}$
	pCO_2	0.24^{**}	−0.38	>0.05	
	$Si(OH)_4$	0.13^{*}	18.57	>0.05	
	Ω_{arag}	0.25^{**}	−16.78	>0.05	
GPP	$Si(OH)_4$	0.62^{*}	0.67	>0.05	$0.14^{n.s.}$
Diversity	Salinity	0.67^{*}	0.01	>0.05	0.69^{*}
	NO_{23}^{-}	0.45^{*}	−0.02	>0.05	
	PO_4^{-3}	0.45^{*}	−0.13	>0.05	
Sp. richness	Salinity	0.67^{*}	−0.04	>0.05	$0.55^{n.s.}$
	NO_{23}^{-}	0.63^{**}	0.01	>0.05	
	PO_4^{-3}	0.63^{**}	−0.07	>0.05	

*Only variables with significant correlations are presented and were considered to conduct the generalized linear model (GLM). The regression coefficient of predicting factors (σ), their significance in the model (p-value) as well as the adjusted-R^2 for the model are given. [a]The significance of the R^2 values is defined as follows: *p < 0.05, **p < 0.01, ***p < 0.001, $^{n.s.}$ not significant (p > 0.05).*

TABLE 4 | Relationship between biological variables (*Y*) and environmental factors (X_i) at the Arauco Gulf.

Variables	Factors	Spearman[a]	GLM		
(*Y*)	(X_i)	R^2	σ	*p*-value	R^2
Chl *a*	Temperature	0.84^{***}	0.82	>0.05	0.71^{***}
	NO_{23}^{-}	0.68^{***}	−0.23	<0.01	
	PO_4^{-3}	0.33^{***}	−0.32	>0.05	
	$Si(OH)_4$	0.39^{***}	−0.03	>0.05	
Diatoms	Temperature	0.78^{***}	485.50×10^3	>0.05	0.44^{***}
	NO_{23}^{-}	0.60^{***}	-66.91×10^3	>0.05	
	PO_4^{-3}	0.22^{**}	215.53×10^3	>0.05	
	$Si(OH)_4$	0.30^{**}	-15.60×10^3	>0.05	
Dinoflagellates	Temperature	0.63^{***}	5.38×10^3	<0.01	0.53^{***}
	NO_{23}^{-}	0.61^{***}	−105.80	>0.05	
	PO_4^{-3}	0.18^{*}	612.94	>0.05	
	$Si(OH)_4$	0.39^{***}	−5.43	>0.05	
GPP	Temperature	0.58^{**}	271.98	<0.05	0.65^{**}
	NO_{23}^{-}	0.71^{**}	12.48	>0.05	
DCR	Temperature	0.50^{*}	26.26	>0.05	0.66^{*}
	Salinity	0.40^{*}	7.38	>0.05	
	NO_{23}^{-}	0.68^{**}	−0.49	>0.05	
	$Si(OH)_4$	0.35^{*}	1.10	>0.05	
Diversity	Temperature	0.47^{*}	1.01	>0.05	$0.65^{n.s.}$
	Salinity	0.47^{*}	−0.35	>0.05	
	NO_{23}^{-}	0.56^{*}	0.12	>0.05	
	$Si(OH)_4$	0.69^{**}	0.04	>0.05	

*Only variables with significant correlations are presented and were considered to conduct the generalized linear model (GLM). The regression coefficient of predicting factors (σ), their significance in the model (p-value) as well as the adjusted-R^2 for the model are given. [a]The significance of the R^2 values is defined as follows: *p < 0.05, **p < 0.01, ***p < 0.001, $^{n.s.}$ not significant (p > 0.05).*

sites are comparable to those included in recent seasonal analysis of the carbonate chemistry conducted in the same areas by Pérez et al. (2015) and Vargas et al. (2016, 2017). In summary, both sites represent ecosystems which naturally experience very large ranges in carbonate system parameters, despite the important differences in the hydrographical causes of this variability and the particular combinations of carbonate system and other chemical parameters that result.

Previous studies have thus reported the dynamics of the hydrography, carbonate chemistry and phytoplankton community structure separately at the two study sites. However, to our knowledge, this is the first time that the relationship between abiotic factors including the carbonate system parameters and the phytoplankton is investigated along the Chilean coast. We observed significant negative correlations between carbonate system parameters and cell abundances only in certain phytoplankton taxa at the estuarine community (**Table 3**), e.g., silicoflagellates in which changes in the pH and Ω_{arag} values explained about one forth of the changes in their cell abundance. Other phytoplankton groups, such as diatoms and dinoflagellates, were mainly correlated to nutrient concentrations and to other abiotic factors, such as salinity, in the estuarine ecosystem, and temperature in the coastal upwelling ecosystem.

4.2. Influence of Elevated pCO_2 on Contrasting Phytoplankton Assemblages

A principal aim of the present study was to investigate how phytoplankton communities that experience high carbonate system variability and naturally acidified conditions respond to increases in the pCO_2 levels. This study and the previous studies cited show that the annual range of pCO_2 variation is higher in the Arauco Gulf (∼200–1,600 μatm) than in the Valdivia River estuary (∼150–1,000 μatm). These differences were taken into account in the design of the tested experimental conditions, adjusting the tested CO_2 conditions to be more comparable relative to what the communities naturally experience.

Prior to evaluating the effect of increased pCO_2, an overall look at the response of the communities investigated here showed that they exhibited opposite behavior during the incubation, despite that both were dominated by diatoms and presented similar initial values of Chl *a* and total cell abundance. Regardless

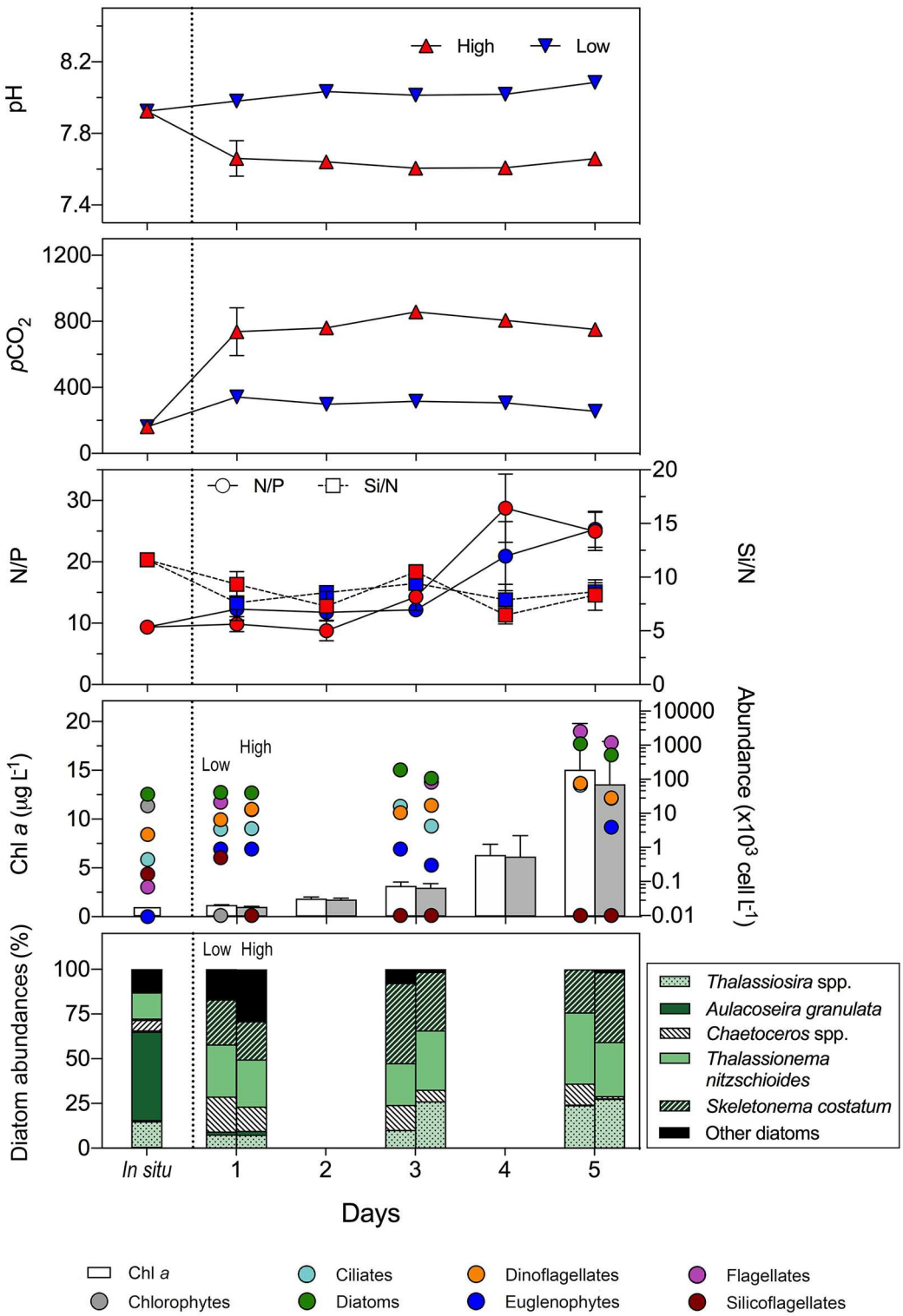


FIGURE 8 | Temporal development of the pH, pCO_2 levels, nutrient ratios (N/P and Si/N), chlorophyll a concentration (Chl *a*), and phytoplankton groups abundance over the course of the mesocosms experiment conducted with the plankton community from the Valdivia estuary (January 2015). The relative contribution of the most abundant (>5%) diatom species is also given. The low and high pCO_2 treatments were of 380 μatm (control level) and 900 μatm, respectively. Average values for four independent replicates are given; error bars stand for the standard deviation. The vertical dashed line separates the *in situ* and the experimental conditions.

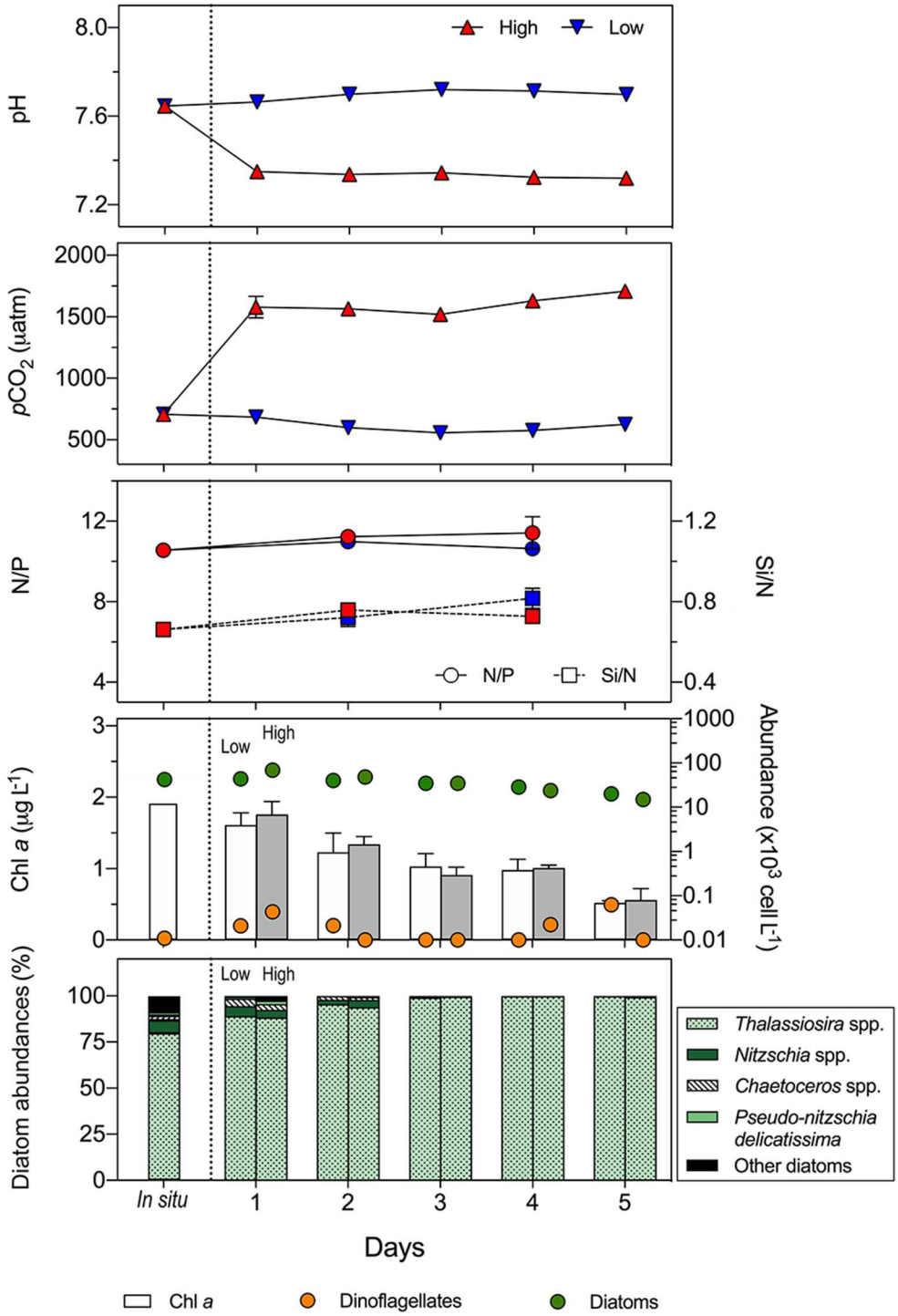


FIGURE 9 | Temporal development of the pH, pCO_2 levels, nutrient ratios (N/P and Si/N), chlorophyll a concentration (Chl *a*), and phytoplankton groups abundance over the course of the mesocosms experiment conducted with the plankton community from the Arauco Gulf (November 2016). The relative contribution of the most abundant (>1%) diatom species is also given. The low and high pCO_2 treatments were of 700 μatm (*in situ* pCO_2 level during the sampling) and 1,600 μatm, respectively. Average values for four independent replicates are given; error bars stand for the standard deviation. The vertical dashed line separates the *in situ* and the experimental conditions.

of the pCO_2 treatment, the community from the Valdivia River estuary showed an exponential increase of both the Chl *a* concentration and the abundance of most of the plankton groups (**Figure 8**), while the phytoplankton community from the Arauco Gulf presented a decreasing trend of the same biological variables toward the end of the incubation (**Figure 9**). Since the two experiments were conducted under nutrient-sufficient conditions, we argue that the reason for this contrasting response is that the two communities were at different growth phases when they were collected from the field, which is a common situation when conducting experiments with naturally-phytoplankton assemblages. In general, the phytoplankton from the Valdivia river estuary was more diverse and was actively growing as reflected by the increase in the N/P ratio (**Figure 9**), which evidenced an enhanced N uptake to support the high growth rates. The phytoplankton from the Arauco Gulf, however, was in a stationary growth phase, according to the constant N/P and Si/N ratios measured during the experiment, and were largely dominated (>75%) by one single diatom genera, *Thalassiosira* spp. These results suggest that this latter community was currently in a post-bloom phase. During this phase, diatoms increase the production of transparent exopolymeric particles (TEP) which enhances cells stickiness and contributes to the subsequent formation of aggregates (Alldredge et al., 1995; Kioerboe et al., 1996; Thornton, 2002) as observed during our experiments. This aggregates formation is likely the cause of the observed cell abundance decrease in both pCO_2 treatments during the experiment with this coastal-upwelling community (**Figure 9**). In any case, considering that the purpose of this work was to evaluate and compare the response of two distinct coastal phytoplankton communities to rising pCO_2, this premise was fulfilled, as the results showed that they differed not only in their taxonomic composition but also in their growth phase.

Owing to the key role of phytoplankton in aquatic food webs as major primary producers, the impact of high pCO_2 conditions on these organisms has been the focus of intense research over the last two decades. These investigations, however, have yielded contrasting results. For instance, some studies with natural phytoplankton assemblages have reported a stimulating effect of elevated pCO_2 on growth rates and primary productivity (Kim et al., 2006; Riebesell et al., 2007; Tortell et al., 2008). Hare et al. (2007), in turn, reported constant primary production under elevated CO_2 in the Bering Sea but a decrease in the diatom contribution to the phytoplankton community. On the other hand, an inhibitory effect has been observed in the formation of the calcareous plankton skeletons, like that of coccolithophorids (Riebesell et al., 2000; Delille et al., 2005), and more recently, other studies have likewise reported negative effects of increased CO_2 in non-calcifying organisms (Feng et al., 2010; Yoshimura et al., 2010; Hama et al., 2011). In the present work, we observed no detectable impact of increased CO_2 on Chl *a* concentration in none of the two phytoplankton communities studied (**Figures 8**, **9**), which aligns well with results from previous micro- and mesocosm OA experiments conducted with diatom-dominated phytoplankton assemblages under the same nutrient sufficient conditions (e.g., Engel et al., 2014; Bach et al., 2017).

Although there was no significant impact on total phytoplankton biomass, there were some possible effects on particular phytoplankton functional groups or even specific taxa within functional groups, particularly in the estuarine community. For example, the total numerical abundances of flagellates, diatoms, and dinoflagellates, was about 25–50% lower under the high pCO_2 treatment. This also suggests that the Chl *a* per cell must have on average been higher under this treatment, to account for the lack of an effect on total Chl *a* concentrations, although we have no direct data at the cellular level for this. Increases in Chl *a* per cell in response to high pCO_2 have been previously reported in multiple dinoflagellates (e.g., Eberlein et al., 2016; Hennon et al., 2017). However, Chl *a* per cell in diatoms has been reported to increase modestly (Crawfurd et al., 2011) to stay the same (e.g., Hennon et al., 2017) or decrease (Jacob et al., 2017) under high pCO_2. Within the diatoms, the genera *Skeletonema* and *Thalassiosira* appeared to benefit more than others. Although *in situ* the community was dominated by freshwater diatoms, such as *A. granulata* (which represented 50% of the numerical abundance), after 5 days these were completely replaced by marine groups. The freshwater diatoms thus probably represent a component that is not growing locally but is advected in, along with other particulate and dissolved organic carbon contributed from the river. *Chaetoceros* spp. also showed modest decrease toward the end.

The mechanisms underlying differences in the response of distinct phytoplankton to elevated pCO_2 can be complex to unravel. On the one hand, a key factor in determining the success of specific functional groups, like diatoms, is their carbon concentrating mechanisms (CCM, Burkhardt et al., 2001; Cassar et al., 2004). Free CO_2 in the ocean is at limiting levels for RuBisCO, the primary carboxilating enzyme used in photosynthesis (Beardall and Raven, 2004). To overcome this constraint, many phytoplankton species have developed an intracellular mechanisms that converts bicarbonate ions ($HCO3^-$) to CO_2 at the active site of this enzyme, thereby supporting higher carbon fixation rates than what would be possible if photosynthesis only relied on diffusive CO_2 uptake (Giordano et al., 2005). The proportion at which both processes operate (i.e., direct CO_2 uptake vs. $HCO3^-$ uptake) varies largely among species (e.g., Reinfelder, 2011; Matsuda and Kroth, 2014), as they differ in the efficiency and regulation of their CCMs (Burkhardt et al., 2001; Rost et al., 2003; Trimborn et al., 2008). Increases in the seawater CO_2 may directly benefit phytoplankton species primarily relying on diffusive CO_2 uptake or those with inefficient CCMs. Species that rely on a resource-intensive CCM, in turn, could also potentially benefit from a downregulation of the CCM in the future, which will allow them to optimize the energy and resources allocation (Rost et al., 2008; Eggers et al., 2014). Nevertheless, this CCM downregulation at increased pCO_2 has been observed to occur primarily under nutrient-limitation conditions (Taucher et al., 2015), and depends on the capacity of each species to switch between carbon acquisition mechanisms. On the other hand, low pH can potentially affect key metabolic rates, such as the ones involved in the maintenance of intracellular homeostasis, which could ultimately counteract the positive effect

of CO_2 fertilization (Wu and Gao, 2010; Bach and Taucher, 2019).

The response of the phytoplankton community from the coastal-upwelling ecosystem in the Arauco Gulf showed no significant effect of short-term exposure to increased pCO_2 in the abundance of either of the two groups that integrated the community, i.e., diatoms and dinoflagellates (**Figure 9**). This finding support our initial hypothesis that exposure to high CO_2 conditions will not challenge phytoplankton communities inhabiting highly variable and acidic habitats. In agreement with our results, a recent review by Bach and Taucher (2019) showed that diatom communities in oceanic environments responded more frequently to rising pCO_2, with negative effects, than in coastal, estuarine, or benthic environments. It is currently beyond doubt that environmental variability can play a key role in promoting local adaptation of organisms so that they tolerate larger range of pH and pCO_2 levels, which are usually characteristics of coastal ecosystems in both temporal and spatial scales (Duarte et al., 2013; Vargas et al., 2017). One study that reflects the importance of local adaptation was the meta-analysis conducted by Vargas et al. (2017) along the Chilean coast. These authors showed that organisms inhabiting areas with high mean pCO_2 and high pCO_2 variability exhibited lower negative effects on physiological traits to elevated pCO_2 conditions, suggesting that local adaptation can play a key role in setting sensitivity of species to changes in pCO_2. In agreement to that reported by these authors for other marine organisms, such as copepods, gastropods or mussels, our results suggest that phytoplankton communities inhabiting the coastal upwelling ecosystem in the Gulf of Arauco are locally adapted to the naturally occurring high pCO_2 levels (**Figure 5**; Vargas et al., 2017), so that short-term exposure to elevated pCO_2 levels does not challenge them.

5. CONCLUSIONS

Our results have shown that changes in the carbonate chemistry in the coastal water may have distinct implications for the phytoplankton communities inhabiting an estuarine and a coastal upwelling systems. Increases of pCO_2 can modify the structure of the estuarine phytoplankton community by decreasing the cell abundance of specific phytoplankton groups, which could have potential bottom-up effects for higher trophic levels. Contrarily, the phytoplankton community from the coastal upwelling ecosystem appears to be locally adapted to changes in the pCO_2 levels. Given the high CO_2 values naturally occurring in this coastal ecosystem, other environmental drivers, such as eutrophication and/or warming may have a larger impact on this phytoplankton assemblage in the future. Overall, these findings highlight the importance of knowing the habitat-specific natural variability of seawater chemistry to better understand the potential impact of elevated pCO_2 conditions at the individual, community and ecosystem levels.

DATA AVAILABILITY STATEMENT

The datasets generated for this study are available on request to the corresponding author.

AUTHOR CONTRIBUTIONS

CV and BJ contributed the concept and design of the study. LL-M, BJ, and PC collected the samples during field samplings, conducted the experiments, and analyzed the samples. NO, PC, and CV organized the database and analyzed the datasets. NO drafted the manuscript with contributions from CV and PD. All authors contributed to the manuscript revision, read, and approved the submitted version.

FUNDING

The present work was fully funded by FONDECYT Project 1170065 to CV and 1181614 to PD. NO was supported by CONICYT Post-doctoral Project 3190365.

ACKNOWLEDGMENTS

The authors also acknowledge support from the Millennium Science Initiative from Chile's Ministry of Economy, Development, and Tourism, through both the Millennium Nucleus MUSELS MINECON NC120086 and the Millennium Institute of Oceanography (IMO), MINECON IC120019.

SUPPLEMENTARY MATERIAL

The Supplementary Material for this article can be found online at: https://www.frontiersin.org/articles/10.3389/fmars.2020.00323/full#supplementary-material

REFERENCES

Alldredge, A. L., Cowles, T. J., MacIntyre, S., Rines, J. E. B., Donaghay, P. L., Greenlaw, C. F., et al. (2002). Occurrence and mechanisms of formation of a dramatic thin layer of marine snow in a shallow Pacific fjord. *Mar. Ecol. Prog. Ser.* 233, 1–12. doi: 10.3354/meps233001

Alldredge, A. L., Gotschalk, C. C., Passow, U., and Riebesell, U. (1995). Mass aggregtion of diatom blooms: insights from a mesocosm study. *Deep Sea Res. II Top. Stud. Oceanogr.* 42, 9–27. doi: 10.1016/0967-0645(95)00002-8

Anabalón, V., Morales, C. E., Escribano, R., and Angélica Varas, M. (2007). The contribution of nano- and micro-planktonic assemblages in the surface layer (0–30 m) under different hydrographic conditions in the upwelling area off Concepción, central Chile. *Prog. Oceanogr.* 75, 396–414. doi: 10.1016/j.pocean.2007.08.023

Bach, L. T., Alvarez-Fernandez, S., Hornick, T., Stuhr, A., and Riebesell, U. (2017). Simulated ocean acidification reveals winners and losers in coastal phytoplankton. *PLoS ONE* 12:e0188198. doi: 10.1371/journal.pone.0188198

Bach, L. T., and Taucher, J. (2019). CO_2 effects on diatoms: a synthesis of more than a decade of ocean acidification experiments with natural communities. *Ocean Sci.* 15, 1159–1175. doi: 10.5194/os-15-1159-2019

Beardall, J., and Raven, J. A. (2004). The potential effects of global climate change on microalgal photosynthesis, growth and ecology. *Phycologia* 43, 26–40. doi: 10.2216/i0031-8884-43-1-26.1

Booth, J. A. T., McPhee-Shaw, E. E., Chua, P., Kingsley, E., Denny, M., Phillips, R., et al. (2012). Natural intrusions of hypoxic, low pH water into nearshore marine environments on the California coast. *Cont. Shelf Res.* 45, 108–115. doi: 10.1016/j.csr.2012.06.009

Bopp, L., Resplandy, L., Orr, J. C., Doney, S. C., Dunne, J. P., Gehlen, M., et al. (2013). Multiple stressors of ocean ecosystems in the 21st century: projections with CMIP5 models. *Biogeosciences* 10, 6225–6245. doi: 10.5194/bg-10-6225-2013

Borges, A. V., Schiettecatte, L.-S., Abril, G., Delille, B., and Gazeau, F. (2006). Carbon dioxide in European coastal waters. *Estuar. Coast. Shelf Sci.* 70, 375–387. doi: 10.1016/j.ecss.2006.05.046

Boyd, P. W., Cornwall, C. E., Davison, A., Doney, S. C., Fourquez, M., Hurd, C. L., et al. (2016). Biological responses to environmental heterogeneity under future ocean conditions. *Glob. Change Biol.* 22, 2633–2650. doi: 10.1111/gcb.13287

Buapet, P., Gullström, M., and Björk, M. (2013). Photosynthetic activity of seagrasses and macroalgae in temperate shallow waters can alter seawater pH and total inorganic carbon content at the scale of a coastal embayment. *Mar. Freshw. Res.* 64, 1040–1049. doi: 10.1071/MF12124

Burkhardt, S., Amoroso, G., Riebesell, U., and Sültemeyer, D. (2001). CO_2 and HCO_3-uptake in marine diatoms acclimated to different CO_2 concentrations. *Limnol. Oceanogr.* 46, 1378–1391. doi: 10.4319/lo.2001.46.6.1378

Caldeira, K., and Wickett, M. E. (2003). Anthropogenic carbon and ocean pH. *Nature* 425:365. doi: 10.1038/425365a

Cao, Z., Dai, M., Zheng, N., Wang, D., Li, Q., Zhai, W., et al. (2011). Dynamics of the carbonate system in a large continental shelf system under the influence of both a river plume and coastal upwelling. *J. Geophys. Res.* 116:G02010. doi: 10.1029/2010JG001596

Cassar, N., Laws, E. A., Bidigare, R. R., and Popp, B. N. (2004). Bicarbonate uptake by Southern Ocean phytoplankton. *Glob. Biogeochem. Cycles* 18, 1–10. doi: 10.1029/2003GB002116

Crawfurd, K. J., Raven, J. A., Wheeler, G. L., Baxter, E. J., and Joint, I. (2011). The response of thalassiosira pseudonana to long-term exposure to increased CO_2 and decreased pH. *PLoS ONE* 6:e0026695. doi: 10.1371/journal.pone.0026695

Cuevas, L. A., Tapia, F. J., IRIARTE, J. L., González, H. E., Silva, N., and Vargas, C. A. (2019). Interplay between freshwater discharge and oceanic waters modulates phytoplankton size-structure in fjords and channel systems of the Chilean Patagonia. *Prog. Oceanogr.* 173, 103–113. doi: 10.1016/j.pocean.2019.02.012

Daneri, G., Dellarossa, V., Quiñones, R., Jacob, B., Montero, P., and Ulloa, O. (2000). Primary production and community respiration in the Humboldt Current System off Chile and associated oceanic areas. *Mar. Ecol. Prog. Ser.* 197, 41–49. doi: 10.3354/meps197041

Delille, B., Harlay, J., Zondervan, I., Stephan, J., Chou, L., Wollast, R., et al. (2005). Response of primary production and calcification to changes of pCO_2 during experimental blooms of the coccolithophorid *Emiliania huxleyi*. *Glob. Biogeochem. Cycles* 19:GB2023. doi: 10.1029/2004GB002318

Dickson, A. G. (1990). Thermodynamics of the dissociation of boric acid in synthetic seawater from 273.15 to 318.15 K. *Deep Sea Res. A Oceanogr. Res. Pap.* 37, 755–766. doi: 10.1016/0198-0149(90)90004-F

Dickson, A. G., and Millero, F. J. (1987). A comparison of the equilibrium constants for the dissociation of carbonic acid in seawater media. *Deep Sea Res. A Oceanogr. Res. Pap.* 34, 1733–1743. doi: 10.1016/0198-0149(87)90021-5

DOE (1994). *Handbook of Methods for the Analysis of the Various Parameters of the Carbon Dioxide System in Seawater*, version 2, 74. Washington, DC: ORNL/CDIAC.

Duarte, C. M., Hendriks, I. E., Moore, T. S., Olsen, Y. S., Steckbauer, A., Ramajo, L., et al. (2013). Is ocean acidification an open-ocean syndrome? Understanding anthropogenic impacts on seawater pH. *Estuar. Coasts* 36, 221–236. doi: 10.1007/s12237-013-9594-3

Eberlein, T., Van de Waal, D. B., Brandenburg, K. M., John, U., Voss, M., Achterberg, E. P., et al. (2016). Interactive effects of ocean acidification and nitrogen limitation on two bloom-forming dinoflagellate species. *Mar. Ecol. Prog. Ser.* 543, 127–140. doi: 10.3354/meps11568

Eggers, S. L., Lewandowska, A. M., Barcelos e Ramos, J., Blanco-Ameijeiras, S., Gallo, F., and Matthiessen, B. (2014). Community composition has greater impact on the functioning of marine phytoplankton communities than ocean acidification. *Glob. Change Biol.* 20, 713–723. doi: 10.1111/gcb.12421

Engel, A., Piontek, J., Grossart, H.-P., Riebesell, U., Schulz, K. G., and Sperling, M. (2014). Impact of CO_2 enrichment on organic matter dynamics during nutrient induced coastal phytoplankton blooms. *J. Plankton Res.* 36, 641–657. doi: 10.1093/plankt/fbt125

Feely, R. A., Sabine, C. L., Hernandez-Ayon, J. M., Ianson, D., and Hales, B. (2008). Evidence for upwelling of corrosive 'acidified' water onto the continental shelf. *Science* 320, 1490–1492. doi: 10.1126/science.1155676

Feng, Y., Hare, C. E., Rose, J. M., Handy, S. M., DiTullio, G. R., Lee, P. A., et al. (2010). Interactive effects of iron, irradiance and CO_2 on Ross Sea phytoplankton. *Deep Sea Res. I* 57, 368–383. doi: 10.1016/j.dsr.2009.10.013

Garcés-Vargas, J., Ruiz, M., Pardo, L. M., Nuñez, S., and Pérez-Santos, I. (2013). Hydrographic features of Valdivia river estuary south-central Chile. *Latin Am. J. Aquat. Res.* 41, 113–125. doi: 10.3856/vol41-issue1-fulltext-9

Giesecke, R., Vallejos, T., Sanchez, M., and Teiguiel, K. (2017). Plankton dynamics and zooplankton carcasses in a mid-latitude estuary and their contributions to the local particulate organic carbon pool. *Cont. Shelf Res.* 132, 58–68. doi: 10.1016/j.csr.2016.07.020

Giordano, M., Beardall, J., and Raven, J. A. (2005). Concentrating mechanisms in algae: mechanisms, environmental modulation, and evolution. *Annu. Rev. Plant Biol.* 56, 99–131. doi: 10.1146/annurev.arplant.56.032604.144052

González, H. E., Calderón, M. J., Castro, L., Clement, A., Cuevas, L. A., Daneri, G., et al. (2010). Primary production and plankton dynamics in the Reloncaví Fjord and the Interior Sea of Chiloé, Northern Patagonia, Chile. *Mar. Ecol. Prog. Ser.* 402, 13–30. doi: 10.3354/meps08360

González, H. E., Menschel, E., Aparicio, C., and Barría, C. (2007). Spatial and temporal variability of microplankton and detritus, and their export to the shelf sediments in the upwelling area off Concepción, Chile (∼36°S), during 2002–2005. *Prog. Oceanogr.* 75, 435–451. doi: 10.1016/j.pocean.2007.08.025

Gruber, N. (2011). Warming up, turning sour, losing breath: ocean biogeochemistry under global change. *Philos. Trans. R. Soc. A* 369, 1980–1996. doi: 10.1098/rsta.2011.0003

Gruber, N., Clement, D., Carter, B. R., Feely, R. A., van Heuven, S., Hoppema, M., et al. (2019). The oceanic sink for anthropogenic CO_2 from 1994 to 2007. *Science* 363, 1193–1199. doi: 10.1126/science.aau5153

Hama, T., Kawashima, S., Shimotori, K., Satoh, Y., Omori, Y., Wada, S., et al. (2011). Effect of ocean acidification on coastal phytoplankton composition and accompanying organic nitrogen production. *J. Oceanogr.* 68, 183–194. doi: 10.1007/s10872-011-0084-6

Hare, C. E., Leblanc, K., DiTullio, G. R., Kudela, R. M., Zhang, Y., Lee, P. A., et al. (2007). Consequences of increased temperature and CO_2 for phytoplankton community structure in the Bering Sea. *Mar. Ecol. Prog. Ser.* 352, 9–16. doi: 10.3354/meps07182

Hennon, G. M. M., Hernndez Limn, M. D., Haley, S. T., Juhl, A. R., and Dyhrman, S. T. (2017). Diverse CO_2-induced responses in physiology and gene expression among eukaryotic phytoplankton. *Front. Microbiol.* 8:2547. doi: 10.3389/fmicb.2017.02547

Hinga, K. R. (2002). Effects of pH on coastal marine phytoplankton. *Mar. Ecol. Prog. Ser.* 238, 281–300. doi: 10.3354/meps238281

Hoegh-Guldberg, O., and Bruno, J. F. (2010). The impact of climate change on the world's marine ecosystems. *Science* 328, 1523–1528. doi: 10.1126/science.1189930

Hofmann, G. E., Smith, J. E., Johnson, K. S., Send, U., Levin, L. A., Micheli, F., et al. (2011). High-frequency dynamics of ocean pH: a multi-ecosystem comparison. *PLoS ONE* 6:e28983. doi: 10.1371/journal.pone.0028983

Iriarte, J. L., and Bernal, P. (1990). Vertical distribution of diatoms and thecate dinoflagellates in the gulf of Arauco: species composition, relative abundance, and the chloropyll maximum layer. *Sci. Mar.* 54, 389–399.

Iriarte, J. L., Cuevas, L. A., Cornejo, F., Silva, N., González, H. E., Castro, L., et al. (2018). Low spring primary production and microplankton carbon biomass in Sub-Antarctic Patagonian channels and fjords (50–53°S). *Arctic Antarctic Alpine Res.* 50, 1–14. doi: 10.1080/15230430.2018.1525186

Iriarte, J. L., González, H. E., Liu, K.-K., Rivas, C., and Valenzuela, C. (2007). Spatial and temporal variability of chlorophyll and primary productivity in surface waters of southern Chile (41.5–43°S). *Estuar. Coast. Shelf Sci.* 74, 471–480. doi: 10.1016/j.ecss.2007.05.015

Jacob, B. G., von Dassow, P., Salisbury, J. E., Navarro, J. M., and Vargas, C. A. (2017). Impact of low pH/high pCO_2 on the physiological response and fatty

acid content in diatom *Skeletonema pseudocostatum*. *J. Mar. Biol. Assoc. U. K.* 97, 225–233. doi: 10.1017/S0025315416001570

Jouenne, F., Lefebvre, S., Véron, B., and Lagadeuc, Y. (2007). Phytoplankton community structure and primary production in small intertidal estuarine-bay ecosystem (eastern English Channel, France). *Mar. Biol.* 151, 805–825. doi: 10.1007/s00227-006-0440-z

Kim, J.-M., Lee, K., Shin, K., Kang, J.-H., Lee, H.-W., Kim, M., et al. (2006). The effect of seawater CO_2 concentration on growth of a natural phytoplankton assemblage in a controlled mesocosm experiment. *Limnol. Oceanogr.* 51, 1629–1636. doi: 10.4319/lo.2006.51.4.1629

Kioerboe, T., Hansen, J., Alldredge, A. L., Jackson, G. A., Passow, U., Dam, H. G., et al. (1996). Sedimentation of phytoplankton during a diatom bloom: rates and mechanisms. *J. Mar. Res.* 54, 1123–1148. doi: 10.1357/0022240963213754

Kudela, R., Pitcher, G., Probyn, T., Figueiras, F., Moita, T., and Trainer, V. (2005). Harmful algal blooms in coastal upwelling systems. *Oceanography* 18, 184–197. doi: 10.5670/oceanog.2005.53

Letelier, J., Pizarro, O., and Nuñez, S. (2009). Seasonal variability of coastal upwelling and the upwelling front off central Chile. *J. Geophys. Res. Oceans* 114, 1–16. doi: 10.1029/2008JC005171

Matsuda, Y., and Kroth, P. G. (2014). "Carbon fixation in diatoms," in *The Structural Basis of Biological Energy Generation*, ed M. F. Hohmann-Marriott (Heidelberg: Springer), 335–362. doi: 10.1007/978-94-017-8742-0_18

Mehrbach, C., Culberson, C. H., Hawley, J. E., and Pytkowicx, R. M. (1973). Measurement of the apparent dissociation constants of carbonic acid in seawater at atmospheric pressure. *Limnol. Oceanogr.* 18, 897–907. doi: 10.4319/lo.1973.18.6.0897

Millero, F. J. (2010). Carbonate constants for estuarine waters. *Mar. Freshw. Res.* 61, 139–142. doi: 10.1071/MF09254

Orr, J. C., Fabry, V. J., Aumont, O., Bopp, L., Doney, S. C., Feely, R. A., et al. (2005). Anthropogenic ocean acidification over the twenty-first century and its impact on calcifying organisms. *Nature* 437, 681–686. doi: 10.1038/nature04095

Parsons, T. R., Maita, Y., and Lalli, C. M. (1984). *A Manual of Chemical and Biological Methods for Seawater Analysis*. New York, NY: Pergamon Press, 173.

Pérez, C. A., DeGrandpre, M. D., Lagos, N. A., Sald i as, G. S., Cascales, E.-K., and Vargas, C. A. (2015). Influence of climate and land use in carbon biogeochemistry in lower reaches of rivers in central southern Chile: implications for the carbonate system in river-influenced rocky shore environments: Riverine contributions to coastal areas. *J. Geophys. Res. Biogeosci.* 120, 673–692. doi: 10.1002/2014JG002699

Pierrot, D., Lewis, E., and Wallace, D. (2006). *CO_2SYS Dos Program Developed for CO_2 System Calculations*. ORNL/CDIAC-105. Oak Ridge, TN: Carbon Dioxide Information Analysis Center; Oak Ridge National Laboratory; US Deparstment of Energy.

Pino, M., Perillo, G. M. E., and Santamarina, P. (1994). Residual fluxes in a cross-section of the Valdivia River estuary, Chile. *Estuar. Coast. Mar. Sci.* 38, 491–505. doi: 10.1006/ecss.1994.1034

Raymond, P. A., and Cole, J. J. (2003). Increase in the export of alkalinity from North America's largest river. *Science* 301, 88–91. doi: 10.1126/science.1083788

Reinfelder, J. R. (2011). Carbon concentrating mechanisms in eukaryotic marine phytoplankton. *Annu. Rev. Mar. Sci.* 3, 291–315. doi: 10.1146/annurev-marine-120709-142720

Riebesell, U., Fabry, V. J., Hansson, L., and Gattuso, J.-P. (2010). *Guide to Best Practices for Ocean Acidification Research and Data Reporting*. Luxembourg: Publications Office of the European Union.

Riebesell, U., Schulz, K. G., Bellerby, R. G. J., Botros, M., Fritsche, P., Meyerhöfer, M., et al. (2007). Enhanced biological carbon consumption in a high CO_2 ocean. *Nature* 450, 545–549. doi: 10.1038/nature06267

Riebesell, U., Zondervan, I., Rost, B., Tortell, P. D., and Morel, F. M. M. (2000). Reduced calcification of marine plankton in response to increased atmospheric CO_2. *Nature* 407, 364–367. doi: 10.1038/35030078

Rost, B., Riebesell, U., Burkhardt, S., and Sültemeyer, D. (2003). Carbon acquisition of bloom-forming marine phytoplankton. *Limnol. Oceanogr.* 48, 55–67. doi: 10.4319/lo.2003.48.1.0055

Rost, B., Zondervan, I., and Wolf-Gladrow, D. (2008). Sensitivity of phytoplankton to future changes in ocean carbonate chemistry: current knowledge, contradictions and research directions. *Mar. Ecol. Prog. Ser.* 373, 227–237. doi: 10.3354/meps07776

Sabine, C. L., Feely, R. A., Gruber, N., Key, R. M., Lee, K., Bullister, J. L., et al. (2004). The oceanic sink for anthropogenic CO_2. *Science* 305, 367–371. doi: 10.1126/science.1097403

Saderne, V., Fietzek, P., and Herman, P. M. J. (2013). Extreme variations of pCO_2 and pH in a macrophyte meadow of the Baltic sea in summer: evidence of the effect of photosynthesis and local upwelling. *PLoS ONE* 8:e62689. doi: 10.1371/journal.pone.0062689

Shamberger, K. E. F., Feely, R. A., Sabine, C. L., Atkinson, M. J., DeCarlo, E. H., Mackenzie, F. T., et al. (2011). Calcification and organic production on a Hawaiian coral reef. *Mar. Chem.* 127, 64–75. doi: 10.1016/j.marchem.2011.08.003

Sobarzo, M., Bravo, L., Donoso, D., Garcés-Vargas, J., and Schneider, W. (2007). Coastal upwelling and seasonal cycles that influence the water column over the continental shelf off central Chile. *Prog. Oceanogr.* 75, 363–382. doi: 10.1016/j.pocean.2007.08.022

Strickland, J., and Parsons, T. R. (1968). *Practical Handbook of Seawater Analysis, 167th Edn*. Fisheries Research Board of Canada Bulletin.

Strickland, J. D. H. (1960). Measuring the production of marine phytoplankton. *Fish. Res. Bd. Canada Bull.* 122:172.

Taucher, J., Jones, J., James, A., Brzezinski, M. A., Carlson, C. A., Riebesell, U., et al. (2015). Combined effects of CO_2 and temperature on carbon uptake and partitioning by the marine diatoms *Thalassiosira weissflogii* and *Dactyliosolen fragilissimus*. *Limnol. Oceanogr.* 60, 901–919. doi: 10.1002/lno.10063

Thornton, D. C. O. (2002). Diatom aggregation in the sea: mechanisms and ecological implications. *Eur. J. Phycol.* 37, 149–161. doi: 10.1017/S0967026202003657

Torres, R., Pantoja, S., Harada, N., González, H. E., Daneri, G., Frangopulos, M., et al. (2011). Air-sea CO_2 fluxes along the coast of Chile: from CO_2 outgassing in central northern upwelling waters to CO_2 uptake in southern Patagonian fjords. *J. Geophys. Res. Oceans* 116, 1–17. doi: 10.1029/2010JC006344

Tortell, P. D., DiTullio, G. R., Sigman, D. M., and Morel, F. M. M. (2002). CO_2 effects on taxonomic composition and nutrient utilization in an Equatorial Pacific phytoplankton assemblage. *Mar. Ecol. Prog. Ser.* 236, 37–43. doi: 10.3354/meps236037

Tortell, P. D., Payne, C. D., Li, Y. Y., Trimborn, S., Rost, B., Smith, W. O., et al. (2008). CO_2 sensitivity of Southern Ocean phytoplankton. *Geophys. Res. Lett.* 35:L04605. doi: 10.1029/2007GL032583

Trimborn, S., Brenneis, T., Sweet, E., and Rost, B. (2013). Sensitivity of Antarctic phytoplankton species to ocean acidification: growth, carbon acquisition, and species interaction. *Limnol. Oceanogr.* 58, 997–1007. doi: 10.4319/lo.2013.58.3.0997

Trimborn, S., Lundholm, N., Thoms, S., Richter, K.-U., Krock, P., Hansen, P. J., et al. (2008). Inorganic carbon acquisition in potentially toxic and non-toxic diatoms: the effect of pH-induced changes in seawater carbonate chemistry. *Physiol. Plant.* 133, 92–105. doi: 10.1111/j.1399-3054.2007.01038.x

Utermöhl, H. (1958). Zur Vervollkomnung der quantita- tiven Phytoplankton-Methodik. Mitteilungen. *Int. Vereiningung Theoret. Angew. Limnol.* 9, 1–38.

Valle-Levinson, A., Atkinson, L. P., Figueroa, D., and Castro, L. (2003). Flow induced by upwelling winds in an equatorward facing bay: Gulf of Arauco, Chile. *J. Geophys. Res. C Oceans* 108:3054. doi: 10.1029/2001JC001272

Vargas, C. A., Araneda, S. E., and Valenzuela, G. (2003). Influence of tidal phase and circulation on larval fish distribution in a partially mixed estuary, Corral Bay, Chile. *J. Mar. Biol. Assoc. U. K.* 83, 217–222. doi: 10.1017/S0025315403006994h

Vargas, C. A., Arriagada, L., Sobarzo, M., Contreras, P. Y., and Saldías, G. (2013). Bacterial production along a river-to-ocean continuum in central Chile: implications for organic matter cycling. *Aquat. Microb. Ecol.* 68, 195–213. doi: 10.3354/ame01608

Vargas, C. A., Contreras, P. Y., Pérez, C. A., Sobarzo, M., Sald i as, G. S., and Salisbury, J. (2016). Influences of riverine and upwelling waters on the coastal carbonate system off Central Chile, and their ocean acidification implications: carbonate system in the coastal ocean. *J. Geophys. Res. Biogeosci.* 121, 1468–1483. doi: 10.1002/2015JG003213

Vargas, C. A., Cuevas, L. A., Silva, N., González, H. E., De Pol-Holz, R., and Narváez, D. A. (2018). Influence of glacier melting and river discharges on the nutrient distribution and DIC recycling in the Southern Chilean Patagonia. *J. Geophys. Res. Biogeosci.* 123, 256–270. doi: 10.1002/2017JG003907

Vargas, C. A., Lagos, N. A., Lardies, M. A., Duarte, C., Manr i quez, P. H., Aguilera, V. M., et al. (2017). Species-specific responses to ocean acidification should account for local adaptation and adaptive plasticity. *Nat. Ecol. Evol.* 1:84. doi: 10.1038/s41559-017-0084

Vargas, C. A., Martínez, R. A., Cuevas, L. A., Pavez, M. A., Cartes, C., González, H. E., et al. (2007). The relative importance of microbial and classical food webs in a highly productive coastal upwelling area. *Limnol. Oceangr.* 52, 1495–1510. doi: 10.4319/lo.2007.52.4.1495

Waldbusser, G. G., and Salisbury, J. E. (2014). Ocean acidification in the coastal zone from an organism's perspective: multiple system parameters, frequency domains, and habitats. *Annu. Rev. Mar. Sci.* 6, 221–247. doi: 10.1146/annurev-marine-121211-172238

Wallace, R. B., Baumann, H., Grear, J. S., Aller, R. C., and Gobler, C. J. (2014). Coastal ocean acidification: the other eutrophication problem. *Estuar. Coast. Shelf Sci.* 148, 1–13. doi: 10.1016/j.ecss.2014.05.027

Wu, Y., and Gao, K. (2010). Combined effects of solar UV radiation and CO_2-induced seawater acidification on photosynthetic carbon fixation of phytoplankton assemblages in the South China Sea. *Chin. Sci. Bull.* 55, 3680–3686. doi: 10.1007/s11434-010-4119-y

Yoshimura, T., Nishioka, J., Suzuki, K., Hattori, H., Kiyosawa, H., and Watanabe, Y. W. (2010). Impacts of elevated CO_2 on organic carbon dynamics in nutrient depleted Okhotsk Sea surface waters. *J. Exp. Mar. Biol. Ecol.* 395, 191–198. doi: 10.1016/j.jembe.2010.09.001

Conflict of Interest: The authors declare that the research was conducted in the absence of any commercial or financial relationships that could be construed as a potential conflict of interest.

Copyright © 2020 Osma, Latorre-Melín, Jacob, Contreras, von Dassow and Vargas. This is an open-access article distributed under the terms of the Creative Commons Attribution License (CC BY). The use, distribution or reproduction in other forums is permitted, provided the original author(s) and the copyright owner(s) are credited and that the original publication in this journal is cited, in accordance with accepted academic practice. No use, distribution or reproduction is permitted which does not comply with these terms.

frontiers in Marine Science

ORIGINAL RESEARCH
published: 20 August 2021
doi: 10.3389/fmars.2021.642208

Elevated pCO_2 Impedes Succession of Phytoplankton Community From Diatoms to Dinoflagellates Along With Increased Abundance of Viruses and Bacteria

*Ruiping Huang[1], Jiazhen Sun[2], Yunlan Yang[1], Xiaowen Jiang[2], Zhen Wang[3], Xue Song[2], Tifeng Wang[2], Di Zhang[2], He Li[2], Xiangqi Yi[1], Shouchang Chen[2], Nanou Bao[2], Liming Qu[2], Rui Zhang[2], Nianzhi Jiao[2], Yahui Gao[3], Bangqin Huang[1], Xin Lin[2], Guang Gao[2] and Kunshan Gao[2]**

[1] State Key Laboratory of Marine Environmental Science, College of the Environment and Ecology, Xiamen University, Xiamen, China, [2] State Key Laboratory of Marine Environmental Science, College of Ocean and Earth Sciences, Xiamen University, Xiamen, China, [3] School of Life Sciences, Xiamen University, Xiamen, China

OPEN ACCESS

Edited by:
Nina Bednarsek,
Southern California Coastal Water Research Project, United States

Reviewed by:
Daniele Ventura,
Sapienza University of Rome, Italy
Dedmer B. Van de Waal,
Netherlands Institute of Ecology (NIOO-KNAW), Netherlands

***Correspondence:**
Kunshan Gao
ksgao@xmu.edu.cn

Specialty section:
This article was submitted to Marine Biology, a section of the journal Frontiers in Marine Science

Received: 15 December 2020
Accepted: 05 August 2021
Published: 20 August 2021

Citation:
Huang R, Sun J, Yang Y, Jiang X, Wang Z, Song X, Wang T, Zhang D, Li H, Yi X, Chen S, Bao N, Qu L, Zhang R, Jiao N, Gao Y, Huang B, Lin X, Gao G and Gao K (2021) Elevated pCO_2 Impedes Succession of Phytoplankton Community From Diatoms to Dinoflagellates Along With Increased Abundance of Viruses and Bacteria. Front. Mar. Sci. 8:642208. doi: 10.3389/fmars.2021.642208

Eutrophic coastal regions are highly productive and greatly influenced by human activities. Primary production supporting the coastal ecosystems is supposed to be affected by progressive ocean acidification driven by increasing CO_2 emissions. In order to investigate the effects of high pCO_2 (HC) on eutrophic plankton community structure and ecological functions, we employed 9 mesocosms and carried out an experiment under ambient (~410 ppmv) and future high (1000 ppmv) atmospheric pCO_2 conditions, using *in situ* plankton community in Wuyuan Bay, East China Sea. Our results showed that HC along with natural seawater temperature rise significantly boosted biomass of diatoms with decreased abundance of dinoflagellates in the late stage of the experiment, demonstrating that HC repressed the succession from diatoms to dinoflagellates, a phenomenon observed during algal blooms in the East China Sea. HC did not significantly influence the primary production or biogenic silica contents of the phytoplankton assemblages. However, the HC treatments increased the abundance of viruses and heterotrophic bacteria, reflecting a refueling of nutrients for phytoplankton growth from virus-mediated cell lysis and bacterial degradation of organic matters. Conclusively, our results suggest that increasing CO_2 concentrations can modulate plankton structure including the succession of phytoplankton community and the abundance of viruses and bacteria in eutrophic coastal waters, which may lead to altered biogeochemical cycles of carbon and nutrients.

Keywords: biogenic silica, community structure, eutrophic coasts, ocean acidification, plankton, viruses

INTRODUCTION

The ocean CO_2 sink has increased from 1.7 ± 0.4 Pg C yr^{-1} in 1980s to 2.5 ± 0.6 Pg C yr^{-1} in 2010s (Friedlingstein et al., 2020), leading to the pH drop of open ocean surface by 0.017–0.027 units per decade (IPCC, 2019), an environmental problem known as ocean acidification (OA). It is predicted that further reduction of around 0.3 pH units will occur by the end of this century under

"business as usual" scenario (IPCC, 2019). Considering the huge changes, it is needed to investigate how marine life will respond directly or indirectly and the consequent changes in biogeochemical cycles. A number of studies have been conducted ranging from single organism to artificial community then to natural community levels, using laboratory, mesocosm and field investigation approaches (see the review by Gao et al., 2019 and literatures therein).

Field mesocosm experiments using natural communities are becoming effective approaches to explore the responses of marine planktonic ecosystems to climate change. Two mesocosm studies deployed in the Raunefjorden, western Norway, showed that *Emiliania huxleyi*, the most abundant coccolithophore species, reduced its growth rates under 710 μatm of pCO_2 during May–June 2001 (Engel et al., 2005), and even lost blooming capacity under 1000–3000 μatm conditions during May–June 2011 (Riebesell et al., 2016). In another mesocosm experiment carried out in the Raunefjorden during May 2006, the dominant group of prasinophyte community changed from *Bathycoccus*-like phylotypes to *Micromonas*-like phylotypes, as pCO_2 increased from current to predicted future levels (Meakin and Wyman, 2011). These results suggest that the OA effects on community structure can vary temporally in the same regions. In addition, highly variable effects of elevated pCO_2 on plankton also attribute to different regions. Under HC conditions, the composition of the community from the temperate Bering Sea shelf and offshore shifted away from diatoms toward nanophytoplankton (Hare et al., 2007). In the temperate Gullmar Fjord at the Swedish west coast, the total diatom biomass were unaffected by pCO_2 during bloom processes, but displayed a positive response to pCO_2 during post-bloom processes (Bach et al., 2016). Off the subtropical eastern coast of Gran Canaria, Spain, the total diatom biomass remained unaffected during oligotrophic conditions, but was significantly positively affected by high CO_2 after nutrient enrichment (Bach et al., 2019). Other plankton also showed varied responses to OA among different regions. The development of zooplankton community was unaffected significantly in the temperate Kongsfjorden Fjord of northwestern Norway (Aberle et al., 2013; Niehoff et al., 2013), but was prevented by increased pCO_2 off the subtropical eastern coast of Gran Canaria, Spain (Riebesell et al., 2018). In the mesocosm experiment conducted in the Kongsfjorden Fjord, bacterioplankton diversity differed significantly between high and low pCO_2 treatments (Zhang et al., 2013). However, pCO_2 did not affect bacterioplankton diversity, in our previous mesocosm experiment conducted in the subtropical eutrophic Wuyuan Bay (Lin et al., 2018). The shifts in plankton community structure will further influence the ecological functions, such as the production, consumption and export of organic matter, with different magnitudes and even directions (de Kluijver et al., 2013; Spilling et al., 2016; Taucher et al., 2020). By integrating and analyzing the results of mesocosm experiments, we noted that planktonic ecosystem level responses to elevated pCO_2 can vary spatiotemporally, which may depend on the initial community structure and other abiotic environmental factors such as nutrient levels.

To date, most mesocosm experiments have been conducted in oligotrophic or non-eutrophicated regions. In the mesocosm experiment employed in the Kongsfjorden during June–July 2010, increase in pCO_2 did not significantly influence chlorophyll *a* (Chl *a*) concentration under oligotrophic conditions, but increased Chl *a* concentration after nutrient fertilization (Schulz et al., 2013). Increased pCO_2 similarly affected Chl *a* concentration after nutrient addition, in the mesocosm experiment employed in Raunefjord during May–June 2011 (Riebesell et al., 2016). In our previous mesocosm experiments which have been carried out in the highly eutrophic Wuyuan Bay, we found that HC treatment did not significantly affect Chl *a* concentration (Liu et al., 2017). The plankton community composition responses to increased pCO_2 also varied in different phases of the mesocosm experiment conducted in the Gullmar Fjord, resulting from plankton communities supported by regenerated nutrients were more sensitive to OA than those having access to higher availability of inorganic nutrients (Bach et al., 2017; Bach et al., 2019). These results suggested that planktonic ecosystem level responses to elevated pCO_2 can be influenced by nutrient levels.

Coastal waters are highly productive that support marine ecosystem and human activities. In these regions, the accumulative effects of natural and anthropogenic climate change are continuing and intensifying the course of eutrophication (Rabalais et al., 2009). With progressive OA, eutrophication is supposed to enhance the CO_2-driven acidification in coastal waters, by an additional drop of 0.13 pH unit relative to open oceans at the end of this century (Cai et al., 2011). Such enhanced OA in pH fluctuating coastal waters can disrupt ecosystem service due to increased energetic demand for ecosystems to sustain. To better understand the consequences of OA in eutrophic coastal regions, further studies should be expanded to look into the ecological responses in different regions and at different seasons under fluctuating and changing environmental conditions. Here, we carried out a mesocosm experiment in the eutrophic coastal region Wuyuan Bay, using *in situ* community during April–May 2018. Apart from monitoring environmental and biogenic changes, we particularly focused on the phytoplankton community succession and the abundance of viruses and bacteria, and the results showed notable correlation between autotrophic assimilation and heterotrophic dissimilation.

MATERIALS AND METHODS

Mesocosms Setup

The mesocosm experiment was conducted in the Facility for the Study of Ocean Acidification Impacts of Xiamen University, located in the subtropical coastal region Wuyuan Bay (24°31′48″ N, 118°10′47″ E), during 9th April–15th May 2018. Nine cylindrical mesocosm bags with 3 m in depth and 1.5 m in diameter, made of transparent thermoplastic polyurethane (TPU), were fixed within steel frames and sheltered by cone lids. The *in situ* seawater were filtered (pore size of 0.01 μm) by water purifier (MU801-4T, Midea, China) and pumped simultaneously into 9 mesocosm bags for 3000 L within 36 h. Bag 2, 4, 6, and

8 were set as control, aerated with ambient air pCO_2 (denoted as AC). To adjust seawater to projected 1000 μatm CO_2 in 2100, bag 1, 3, 5, 7, and 9 were added with approximately 11 L CO_2 saturation seawater (denoted as HC) (Riebesell et al., 2013). Subsequently, AC and HC mesocosm bags were aerated (5 L min^{-1}) with ambient air of ∼410 ppmv CO_2 and pre-mixed air-CO_2 of 1000 ppmv CO_2, respectively, till the end of the experiment. After aerating to homogenize the carbonate system for about 2–3 h, 720 L of *in situ* seawater filtered by 180 μm mash was added simultaneously into 9 mesocosm bags, so that each bag was inoculated with 80 L *in situ* seawater containing a natural microbe community. Subsequently, the mesocosm samples were collected from 0.5 m depths of each bag at 10:00 a.m. every 1–3 days, for physical, chemical and biological analysis.

Physical and Chemical Parameters Measurements

The intensity of solar irradiance was measured with a real-time solar irradiance monitoring device (EKO, Japan). Salinity and temperature were measured using a salinometer and digital thermometer, respectively. The pH was determined instantly using a pH meter (Orion Star A211, Thermo Scientific), which was calibrated against NIST-traceable pH buffers. Samples for dissolved inorganic carbon (DIC) measurements were poisoned with final concentration of 1‰ saturated $HgCl_2$ solution and stored in 40 mL borosilicate glass vials until further analysis. The DIC was determined by acidifying 0.5 mL samples and then measuring CO_2 concentration using a DIC analyzer (AS-C3, Apollo, United States). The other parameters of carbonate system were calculated from DIC and pH_{NBS} using CO2SYS program (Lewis and Wallace, 1998) based on known levels of nutrients, temperature, and salinity.

Samples for nutrient measurements were filtered through 0.45 mm cellulose acetate membrane by suction filter. The filtrate was divided into 2 of 125 mL high density polyethylene bottles: one was stored at −20°C and measured concentrations of NO_3^-, NO_2^-, PO_4^{3-}, and SiO_3^{2-} using an auto-analyzer (AA3, Seal, Germany) at room temperature, and another added with 1‰ chloroform was stored at 4°C and measured concentration of NH_4^+ with indophenol blue spectrophotometry (Tri-223, Spectrum, China) at 25°C.

Chlorophyll *a* Measurement

Water samples of 250–1000 mL were filtered onto GF/F membranes by suction filter with low vacuum pressure (<0.02 MPa), and soaked in pure methanol at 40°C for 1 h. Then the extracts were centrifuged at 6000 × *g* for 10 min, and the absorption spectra of supernatants from 400 to 800 nm were measured using a UV-VIS Spectrophotometer (DU800, Beckman, United States). The Chl *a* concentration was calculated according to the equations from Ritchie (2006).

Viruses and Bacteria Abundance Measurement

Samples filtered by 20 μm mash were collected into 2 mL centrifuge tubes and fixed with glutaraldehyde to a final concentration of 0.5% at room temperature for 15 min, then frozen with liquid nitrogen and stored at −80°C for further measurement. Viruses and bacteria were counted according to forward scatter, side scatter, and fluorescence intensity after samples were stained with SYBR Green I (Molecular Probe, United States), using the Epics Altra II flow cytometer (Beckman Coulter, United States) and Accuri C6 flow cytometer (Becton and Dickinson, United States), respectively (Chen et al., 2019). For the abundance measurement of both viruses and bacteria, fluorescent beads (Molecular Probes) with a diameter of 1 μm were added as an internal standard.

Phytoplankton Community Structure Determination

Water samples of 500–2000 mL were collected into polyethylene bottles and fixed by adding with 1% lugol's iodine. Then the samples were static placed, and concentrated to 25 mL using siphons within 3 days. The concentrated samples were observed using microscopy and plankton chamber to analyze phytoplankton abundance and diversity based on morphological characteristics.

Measurements of Primary Productivity and Respiratory Carbon Loss

Water samples of 120 mL were collected and transferred immediately into 6 glass scintillation vials (3 vials were used for 12 h inoculation and 3 vials were used for 24 h inoculation) before sunrise. The samples were inoculated with 100 μL of 5 μCi (0.185 MBq) $NaH^{14}CO_3$ solution (ICN Radiochemicals, United States) for 12 h and 24 h with similar levels of sunlight and temperature as in the mesocosms. After 12 and 24 h incubation, the cells were filtered onto glass-fiber filters (25 mm, Whatman GF/F, United States), and the filters were stored at −20°C. Later on, the filters were thawed and exposed to HCl fumes overnight and dried at 60°C for 6 h to remove unincorporated labeled carbon, then 3 ml of scintillation cocktail (Hisafe 3, Perkin-Elmer) was added. The incorporated radioactivity was measured by liquid scintillation counting (LS 6500, Beckman Coulter, United States). The respiratory carbon loss during night was calculated as the difference between carbon fixation of 12 h (day-time primary productivity) and 24 h (daily net primary productivity).

Biogenic Silica Measurement

Water samples of 150–500 mL for biogenic silica measurement were collected onto 2 μm polycarbonate membranes, and rinsed with filtered seawater. Each membrane sample was put into 15 mL centrifuge tube, dried and stored in dryers until analysis in the laboratory. The biogenic silica contents were measured by molybdenum-blue-ness spectrophotometry (Brzezinski and Nelson, 1995). Briefly, the samples were placed in a boiling water bath for 40 min, after mixed with 4 mL of 0.2 mol L^{-1} NaOH. Then the samples were cooled on ice, and neutralized with 1 mL of 1 mol L^{-1} HCl. The supernatant, obtained by centrifuging samples at 6000 × *g* for 10 min, were diluted with MilliQ water, and then added with 2 mL of 0.006 mol L^{-1}

ammonium molybdate and stood for 10 min. Finally, the samples were chromogenically reacted with reducing reagent for 3 h. The absorbance of samples was measured at 810 nm using a UV-VIS Spectrophotometer (DU800, Beckman, United States). For the calculation of biogenic silica contents, 0–30 μmol L^{-1} Na_2SiF_6 were used as standards.

Statistical Analyses

The statistical analysis was performed using SPSS Statistics, R and Origin. Independent-samples *t*-test was conducted to check the significant effects of increased pCO_2 at the level of $p < 0.1$, because the variations were larger within ecological replicates than biological replicates. To further detect the pCO_2 effects on Chl *a* concentration, the abundance of viruses and bacteria, BSi concentration, primary productivity and night respiration, the generalized additive mixed-effect modeling (GAMM, R packages "mgcv") was applied to analyze the data with the following procedures (Bach et al., 2017). Three GAMM models (Model I: pCO_2 did not affect the dependent variable, Model II: pCO_2 influenced the constant offset in temporal trends, Model III: pCO_2 changed trend shape) were fitted to each independent variable as a function of time, in which pCO_2 and mesocosm number were set as explanatory and random variables, respectively. To ensure model assumptions were satisfied, we considered heteroscedasticity and temporal autocorrelation of residuals, as well as autoregressive structures. The model with the highest coefficient of correlation (R^2) was defined as the best that described the pCO_2 effects.

RESULTS

Abiotic Environment of Mesocosms

Throughout the mesocosm experiment, most of the days were sunny, with daily mean PAR (photosynthetically active radiation) ranged 690–1075 μmol photons m^{-2} s^{-1} (**Supplementary Figure 1**). The average salinity was 30.4‰, and temperature increased gradually from 21.9 ± 0.1 to 26.1 ± 0.1°C during the period of 9th April–15th May, 2018 (**Figure 1A**).

The differences of pH_{NBS}, pCO_2 and DIC concentration between AC and HC treatments were maintained, respectively, by 0.13–0.31, 230–600 μatm, and 58–130 μmol kg^{-1} throughout the experiment ($p < 0.1$, **Figures 1B–D** and **Supplementary Table 1**). The pH_{NBS} of HC and AC treatments dropped, respectively, from the initial values of 7.79 ± 0.03 and 8.01 ± 0.01, to 7.70 ± 0.05 and 7.87 ± 0.03 on day 4. Correspondingly, the DIC concentration and pCO_2 increased by 26 μmol kg^{-1} and 206 μatm in HC treatment, and by 41 μmol kg^{-1} and 221 μatm in AC treatments, respectively. Then the pH_{NBS} increased to peak values of 7.94 ± 0.13 in HC treatments on day 10 and 8.13 ± 0.03 in AC treatments on day 12, and the corresponding DIC concentration (pCO_2) decreased to 1920 ± 52 μmol kg^{-1} (735 ± 246 μatm) in HC treatments and to 1824 ± 8 μmol kg^{-1} (427 ± 30 μatm) in AC treatments. Subsequently, the pH_{NBS} decreased by 0.21 units in HC treatments and by 0.18 units in AC treatments on day 28, and the corresponding DIC concentration (pCO_2) increased by 36 μmol kg^{-1} (501 μatm) in HC treatments and by 44 μmol kg^{-1} (263 μatm) in AC treatments. Afterward, the carbonate system of both HC and AC treatments sustained relatively stable levels till the end of the experiment.

The nutrient concentrations experienced drastic changes in the early stage of the mesocosm experiment, and maintained stable afterward (**Figure 2**). The initial concentrations of NO_3^-, NO_2^-, NH_4^+, PO_4^{3-}, and $Si(OH)_4$ in all mesocosm bags were 6.73–10.65, 0.49–0.79, 6.07–8.71, 0.18–0.47, and 5.42–9.50 μmol kg^{-1}, respectively. The concentrations of NH_4^+ and PO_4^{3-} decreased rapidly to nearly 0 in both HC and AC treatments on day 2. However, the concentrations of NO_3^-, NO_2^-, and $Si(OH)_4$ increased at first and then decreased. The NO_3^- concentration increased to 20.62 ± 14.87 μmol kg^{-1} in HC treatments and to 12.48 ± 2.77 μmol kg^{-1} in AC treatments on day 2, and then decreased dramatically to 0.10–4.73 μmol kg^{-1} on day 4. The NO_2^- concentration increased up to day 2 and then maintained relatively stable till day 6, with the values of 1.99 ± 1.68 μmol kg^{-1} in HC treatments and 1.20 ± 0.38 μmol kg^{-1} in AC treatments. Subsequently, the NO_2^- concentration decreased to 0.39 ± 0.48 μmol kg^{-1} in HC and to 0.44 ± 0.61 μmol kg^{-1} in AC treatments on day 8. The $Si(OH)_4$ concentration increased to 10.60 ± 2.50 μmol kg^{-1} in HC treatments and to 12.68 ± 3.03 μmol kg^{-1} in AC treatments on day 2, then decreased progressively to 1.08 ± 1.00 μmol kg^{-1} in HC and to 0.64 ± 1.28 μmol kg^{-1} in AC treatments on day 10. After reaching the very low values, the concentrations of all nutrients were stable till the end of the mesocosm experiment. No significant differences in nutrient concentrations were observed between HC and AC treatments during the whole mesocosm experiment ($p > 0.1$), except that the average concentrations of both NO_3^- and NO_2^- were higher (p = 0. 289 and 0.095, respectively) in HC treatments than in AC treatments during the initial stage of the experiment.

Chlorophyll *a* Concentration

As shown in **Figure 3**, the temporal changes in autotrophic biomass were indicated by Chl *a* concentration, during the whole mesocosm experiment. The Chl *a*, with initial concentration of 0.17 μg L^{-1}, increased to 7.91 ± 4.02 μg L^{-1} on day 12 in AC treatments and 6.41 ± 2.80 μg L^{-1} on day 11 in HC treatments. Then it decreased to 0.91 ± 0.31 and to 1.03 ± 0.73 μg L^{-1} on day 22 in AC and HC treatments, respectively. Thereafter, Chl *a* concentration maintained stable till day 25 in AC treatments and to day 28 in HC treatments. Subsequently, it increased slightly to 1.34 ± 1.42 μg L^{-1} in AC treatments and to 1.00 ± 0.75 μg L^{-1} in HC treatments till the end of the experiment. Based on the ln scale of Chl *a* concentration, phytoplankton growth kinetics in both AC and HC treatments was classified into four phases: exponential phase (Phase I) from days 0 to 8, stationary phase (Phase II) from days 8 to 14, decline phase (Phase III) from days 12 to 25 (AC treatment) or day 28 (HC treatment), and exponential phase (Phase IV) of another growth cycle from day 25 (AC treatment) or day 28 (HC treatment) to day 31. The average value of Chl *a* concentration was slightly higher in HC treatments than in AC treatments during

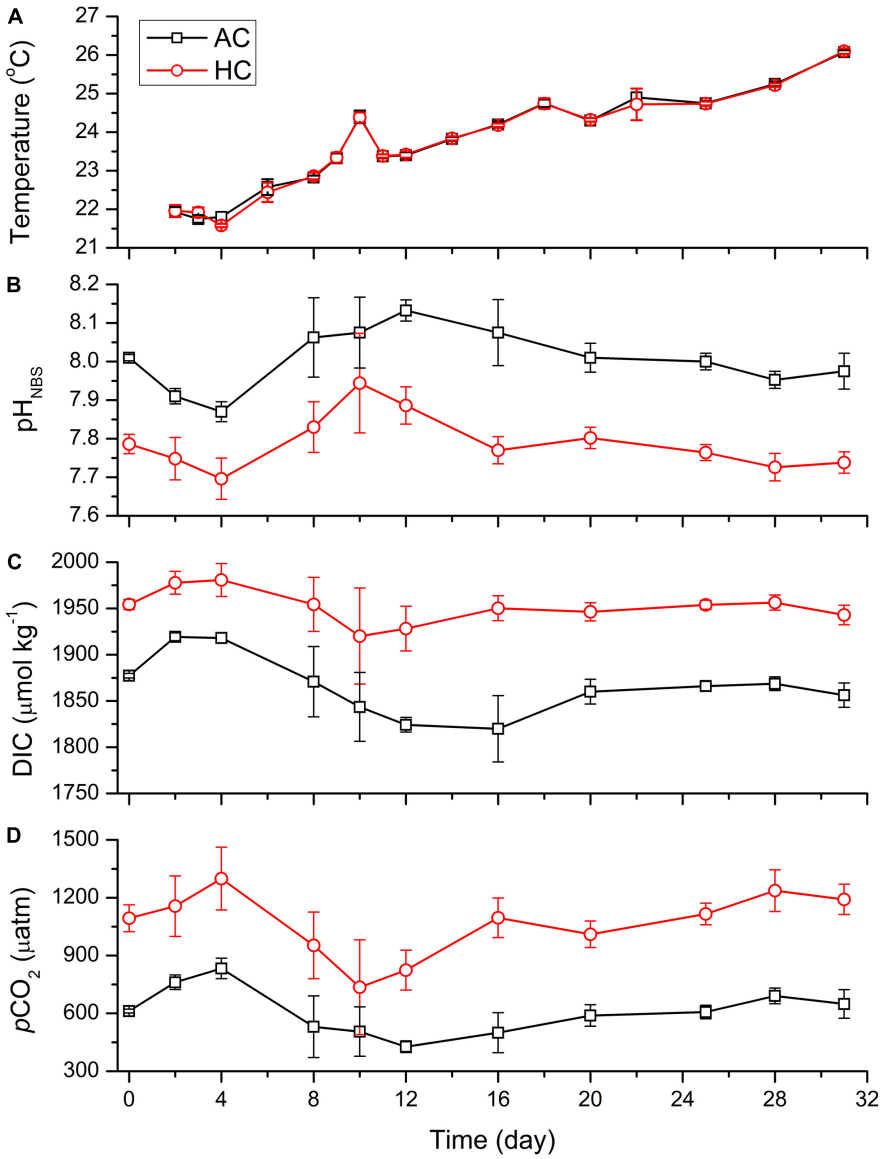


FIGURE 1 | Temporal variations of temperature **(A)**, pH_{NBS} **(B)**, DIC concentration **(C)**, and pCO_2 **(D)** in HC (1000 ppmv) and AC (~410 ppmv) treatments. The pCO_2 was estimated from the measured pH and DIC concentration using CO2SYS program. Data are means ± SD of replicates for HC treatments and for AC treatments.

days 8–16, although the GAMM results showed that HC did not influence the development of Chl *a* concentration (**Table 1**).

Viruses and Bacteria Abundance

The abundance of viruses and bacteria underwent dynamics with different patterns, in both HC and AC treatments (**Figure 4**). The viruses abundance with initial values of 2.01–4.31 × 10^6 particles mL^{-1} increased, with the growth of autotrophic plankton, to 1.65 ± 0.20 × 10^8 particles mL^{-1} in HC treatments on day 10 and to 1.00 × 10^8 ± 0.34 × 10^8 particles mL^{-1} in AC treatments on day 11, respectively. After reaching the peak, the viruses abundance decreased to 3.22 ± 0.94 × 10^7 particles mL^{-1} in HC treatments and to 2.70 ± 0.56 × 10^7 particles mL^{-1} in HC treatments on day 16. Subsequently, the viruses abundance sustained relatively stable values till the end of the experiment in the AC treatments. In the HC treatments, however, it did not change significantly during days 16–22 but increased to 5.46 ± 2.75 × 10^7 particles mL^{-1} during days 25–31. The GAMM analyses revealed that elevated pCO_2 influenced the viruses trend shape (**Table 1** and **Supplementary Figure 2**), with higher abundance in HC during days 6–14 and days 25–31, relative to AC.

The initial abundance of bacteria was 1.78 ± 0.25 × 10^6 cells mL^{-1} in HC treatments or 1.85 ± 0.96 × 10^6 cells mL^{-1} in AC treatments. In the early stage of the experiment, the bacteria abundance increased rapidly to 5.94 ± 0.94 × 10^6 cells mL^{-1} in HC treatments on day 2, which was higher than that in AC treatments of 4.44 ± 0.54 × 10^6 cells mL^{-1} ($p = 0.059$), and then the bacteria abundance decreased till day 4 under both HC and

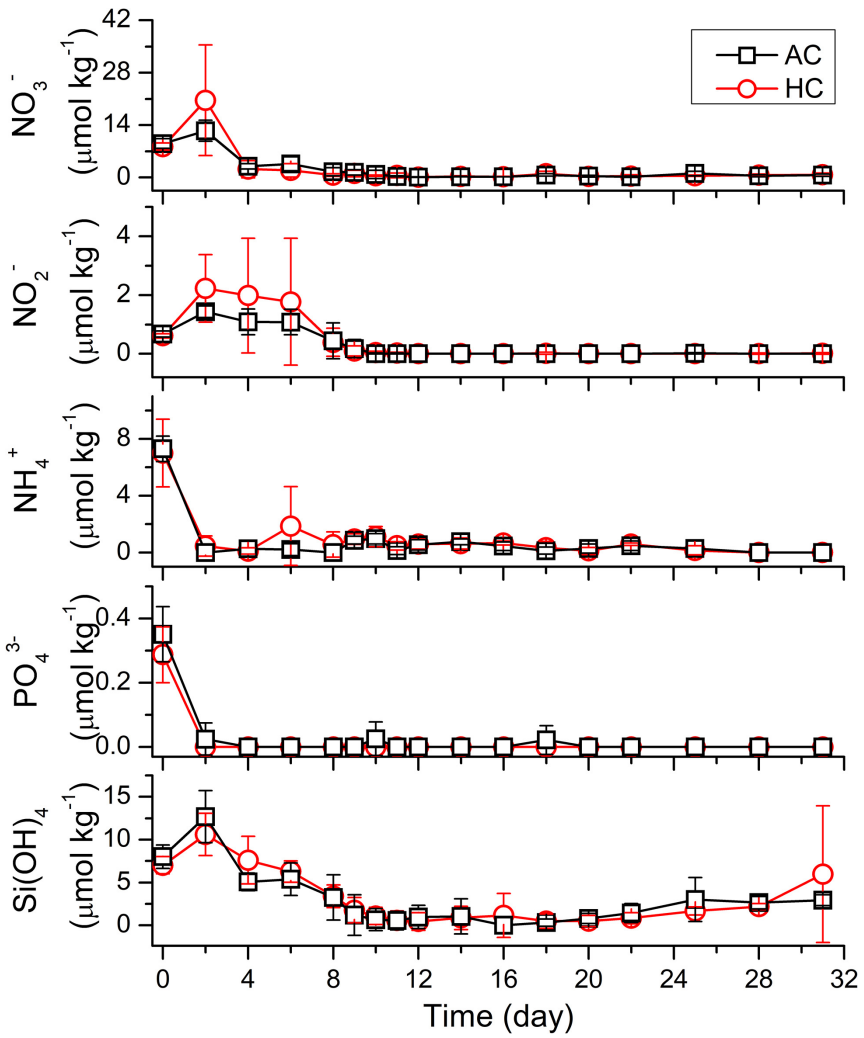


FIGURE 2 | Temporal variations of nutrients (NO_3^-, NO_2^- NH_4^+, PO_4^{3-}, and $Si(OH)_4$) in HC (1000 ppmv) and AC (~410 ppmv) treatments. Data are means ± SD of replicates for HC treatments and for AC treatments.

AC conditions. With the exponential growth of autotrophs (days 4–8), the bacteria abundance increased, however, it decreased in the stationary phase of phytoplankton (days 8–12). A constant offset in bacteria abundance existed between AC and HC, with higher bacteria abundance in HC throughout the experimental period, indicated by GAMM analyses results (**Table 1** and **Supplementary Figure 2**).

Phytoplankton Community Composition and Succession

Using microscopy, a total of 34 genera were identified, in which 26 genera belonged to diatoms and 8 genera to dinoflagellates. From all of the mesocosm bags, the dominant genera were *Chaetoceros*, *Thalassiosira*, *Rhizosolenis*, *Eucampia,* and *Prorocentrum*, and the dominant species were *Chaetoceros curvisetus*, *Rhizosolenis fragilissima*, *Eucampia zoodiacu*, *Cerataulina pelagica,* and *Guinardia delicatula*.

Phytoplankton community structure underwent dynamic succession at phylum levels (**Figure 5**). Diatoms accounted for a proportion of above 90% in both treatments during the period of days 0–16, subsequently decreased to 79.2 ± 13.7% in HC treatments on day 20, being higher than that of 52.2 ± 26.9% in AC treatments, although no significant differences were observed (p = 0.138). The relative abundance of diatoms appeared to decrease to 39.8 ± 28.8% in AC on day 28, but maintained stable by 81.8 ± 14.5% in HC treatments, resulting in more significant differences in relative abundance of diatoms between HC and AC treatments (p = 0.054). Correspondingly, dinoflagellates dominated by *Prorocentrum minimum* and *Peridinium conicoides*, maintained relatively stable abundance with variations less than 10% in HC treatments, but increased to 60.2 ± 28.8% in AC treatments.

The dynamic changes of community structure were more complicated at genus and species levels than at phylum level (**Figure 6** and **Supplementary Figure 3**). The diatom *Guinardia*,

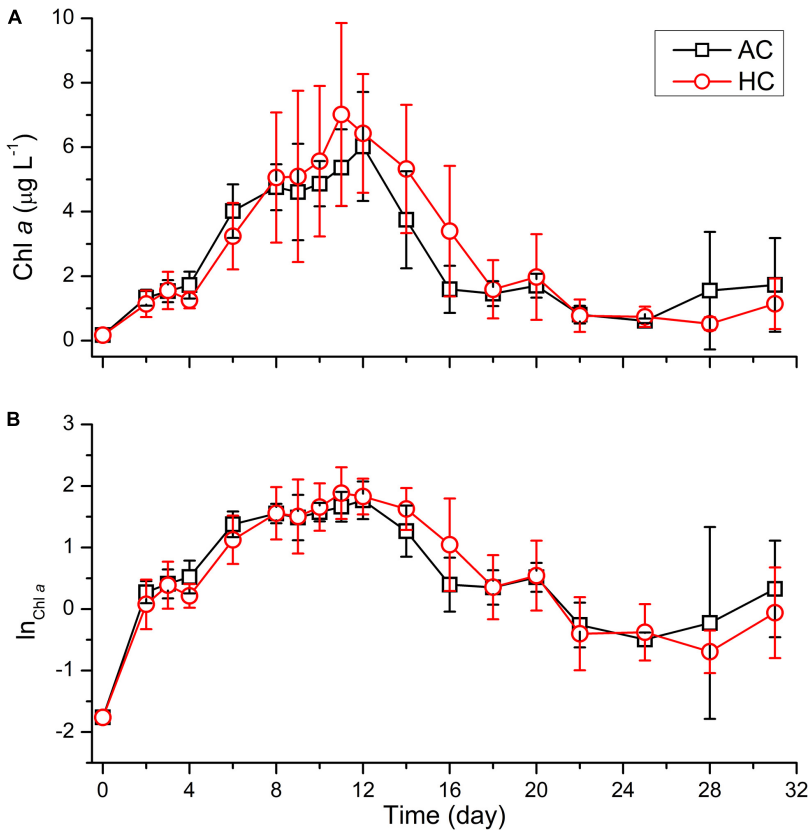


FIGURE 3 | Temporal variations of Chl *a* concentration **(A)** and the ln scale of Chl *a* concentration **(B)** in HC (1000 ppmv) and AC (~410 ppmv) treatments. Data are means ± SD of replicates for HC treatments and for AC treatments.

TABLE 1 | The GAMM analyses results of Chl *a* concentration, the abundance of viruses and bacteria, BSi concentration, primary productivity and night respiration.

Dependent variables	pCO_2 effects	R^2	Temporal autocorrelation	Autoregressive structure	Remark
Chl *a* concentration	type A	0.497	Yes	second order	
Bacteria abundance	type B	0.601	No	0	
Viruses abundance	type C	0.850	No	0	
Day-time primary productivity	type A	0.717	No	0	Chl *a* was added as explanatory variable
Daily net primary productivity	type A	0.642	No	0	Chl *a* was added as explanatory variable
Night-period respiration	type A	0.406	No	0	Chl *a* was added as explanatory variable
BSi concentration	type A	0.739	Yes	0	Temporal autocorrelation could not be resolved

The pCO_2 effects were classified into three types (type A: pCO_2 did not affect the dependent variable, type B: pCO_2 influenced the constant offset in temporal trends, and type C: pCO_2 changed trend shape).

dominated by *G. delicatula*, was the most abundant with relative abundance of 53.4% in terms of total diatom + dinoflagellate species, with cell density of about 9.9×10^4 cells mL^{-1}, after *in situ* community was inoculated into mesocosm bags. However, it decreased rapidly to average relative abundance of 3.2% (density of 2.6×10^3 cells mL^{-1}) and to 1.0% (density of 1.6×10^3 cells mL^{-1}) on day 3 in AC and HC treatments, respectively, and no longer existed from day 6. The diatom *Eucampia* in both HC and AC treatments, mainly composed of *E. zoodiacu*, maintained density of approximately 6×10^4–9×10^4 cells mL^{-1} during days 0–16, then dropped to 0.2×10^4–3.7×10^4 cells mL^{-1} on day 20 and maintained stable afterward. The relative abundance of *Eucampia* increased from initial value of 29% to 61–76% and to 71–75% during days 3–6, and subsequently decreased to 7–16% and to 1–13% on day 10, in HC and AC treatments, respectively. The diatom *Chaetoceros* grew exponentially from 1.4×10^4 cells mL^{-1}, and reached the peak on day 10 with average concentration of 2.9×10^6 cells mL^{-1} in HC and 3.4×10^6 cells mL^{-1} in AC treatments, which accounted for 65.3 and 71.9% of diatom + dinoflagellate assemblages, respectively. Subsequently, the dominant genus in both HC and AC treatments became the diatom *Thalassiosira* and *Rhizosolenis* with the average relative abundance of 53 and 34% on day 16, respectively.

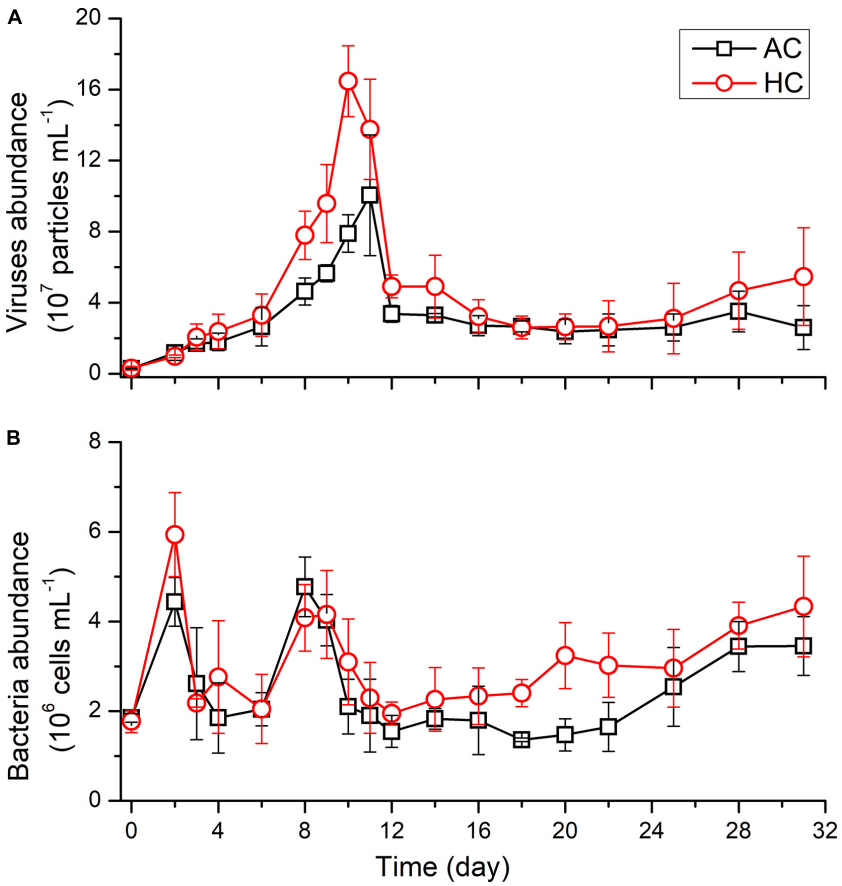


FIGURE 4 | Temporal variations of the abundance of viruses **(A)** and bacteria **(B)** in HC (1000 ppmv) and AC (~410 ppmv) treatments. Data are means ± SD of replicates for HC treatments and for AC treatments.

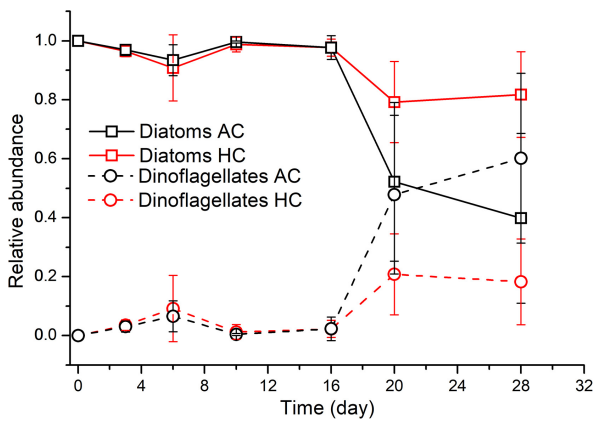


FIGURE 5 | Temporal variations of the relative abundance of diatoms and dinoflagellates in HC (1000 ppmv) and AC (~410 ppmv) treatments. Data are means ± SD of replicates for HC treatments and for AC treatments.

Then the abundance of *Thalassiosira* and *Rhizosolenis* decreased progressively. During the late stage of these experiment, HC stimulated the growth of the diatom *Nitzschia* on day 20, but AC stimulated the growth of the dinoflagellate *Propocentrum* on day 28. As a consequence, the diatom *Nitzschia* had significantly higher relative abundance during days 20–28 ($p = 0.019$), with the dinoflagellate *Propocentrum* accounting for lower proportion on day 28 ($p = 0.078$), in HC relative to AC treatments.

Primary Productivity and Night-Period Respiration

The temporal variations of day-time primary productivity, daily net primary productivity and night respiratory carbon loss normalized to water volume showed similar changing patterns with autotrophic biomass levels indicated by Chl *a* concentration (**Figure 7**). The day-time primary productivity and daily net primary productivity increased with the growth of phytoplankton, from initial values of 24–77 and 21–63 μg C L^{-1}, to the peak values of 573 and 392 μg C L^{-1} on average, respectively, as Chl *a* concentration reached the maximum. Subsequently, the day-time primary productivity and daily net primary productivity decreased progressively, with the decay of algal blooms, with lowered values of 6.5–204 and 6.3–111 μg C L^{-1} after day 22. Respiration carbon loss of phytoplankton during night period increased from 15 μg C L^{-1}

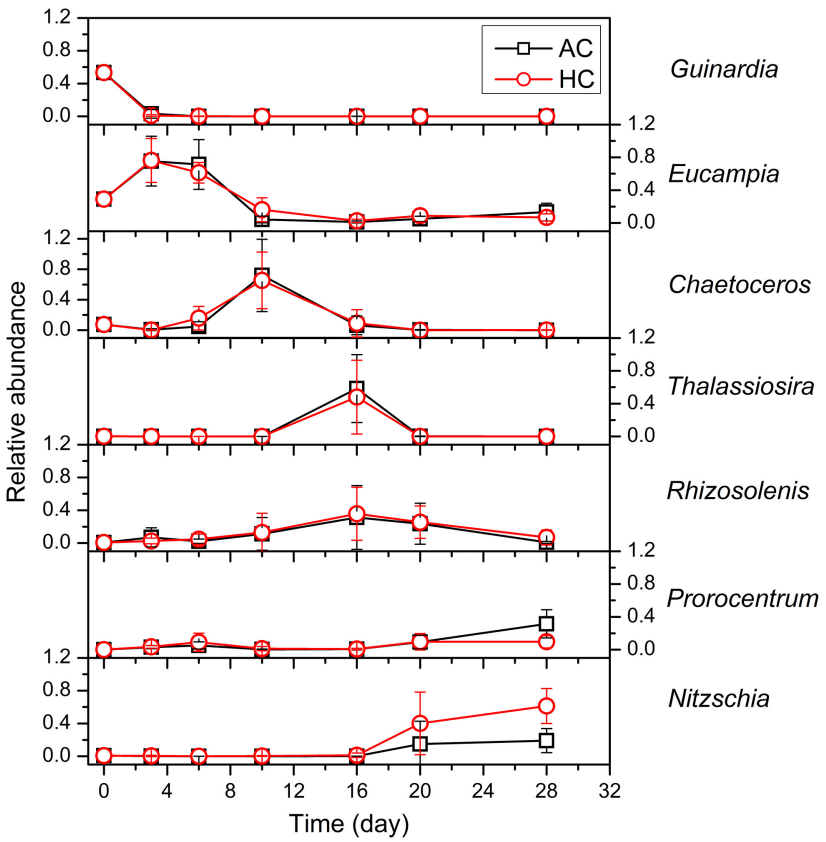


FIGURE 6 | The succession of the dominant phytoplankton at genus level in HC (1000 ppmv) and AC (~410 ppmv) treatments. Data are means ± SD of replicates for HC treatments and for AC treatments.

on average during days 2–8 to 150 μg C L^{-1} on average on day 9. Subsequently, the night period respiration of phytoplankton maintained a rate of 140–180 μg C L^{-1} during the stationary phase of autotrophs, and decreased progressively with the decline of autotrophic blooms. Finally, the respiration stayed 7–9 μg C L^{-1} during days 22–28, and increased slightly at the end of the mesocosm experiment. The daily net primary productivity and day-time primary productivity normalized to Chl *a* increased immediately from the initial values of 17.3 ± 4.0 and 26.8 ± 9.6 μg C (μg Chl *a*)$^{-1}$, to 88.7 ± 23.9 and 100.1 ± 30.3 μg C (μg Chl *a*)$^{-1}$ on day 6, and then sustained relatively stable levels with the average values of 48.2 and 67.9 μg C (μg Chl *a*)$^{-1}$. The night-period respiration normalized to Chl *a*, with lower values of 12.3 μg C (μg Chl *a*)$^{-1}$ during days 0–9, increased drastically and maintained higher values of 12.3 μg C (μg Chl *a*)$^{-1}$. Neither primary productivity nor night respiration of phytoplankton was influenced significantly by HC (**Table 1**), normalized to water volume or to Chl *a*, at any time points examined during the experiment.

Biogenic Silica Contents

Throughout the mesocosm experiment, the differences in temporal development of biogenic silica (BSi) contents were not observed between HC and AC treatments (**Table 1** and **Figure 8**). With development of phytoplankton blooms, the BSi concentration in the water increased and reached peak values of 11.3 ± 0.5 μmol BSi L^{-1} on day 12. Correspondingly, the BSi contents normalized to Chl *a* increased from the initial values of approximately 0.05–2.1 ± 0.8 μmol BSi (μg Chl *a*)$^{-1}$ on day 4, and then maintained relative stable till day 14. Afterward, the BSi concentration in the water decreased, while the BSi contents normalized to Chl *a* increased, with the decay of phytoplankton blooms till the end of the experiment.

DISCUSSION

The results from our mesocosm experiment during the period of late spring and early summer indicate that elevated CO_2 concentration to the level projected for the end of this century, along with natural rise of surface seawater temperature, altered phytoplankton community structure, with impeded succession from diatoms to dinoflagellates and enhanced abundance of free-living viruses and heterotrophic bacteria. Such an ecological response may lead to significant changes in biogeochemical cycles of carbon and nutrients.

The succession from diatoms to dinoflagellates occurred after diatom blooms declined (**Figures 5**, **6**). Under the ambient CO_2 level, the dominant diatom *Nitzschia closterium* was replaced by

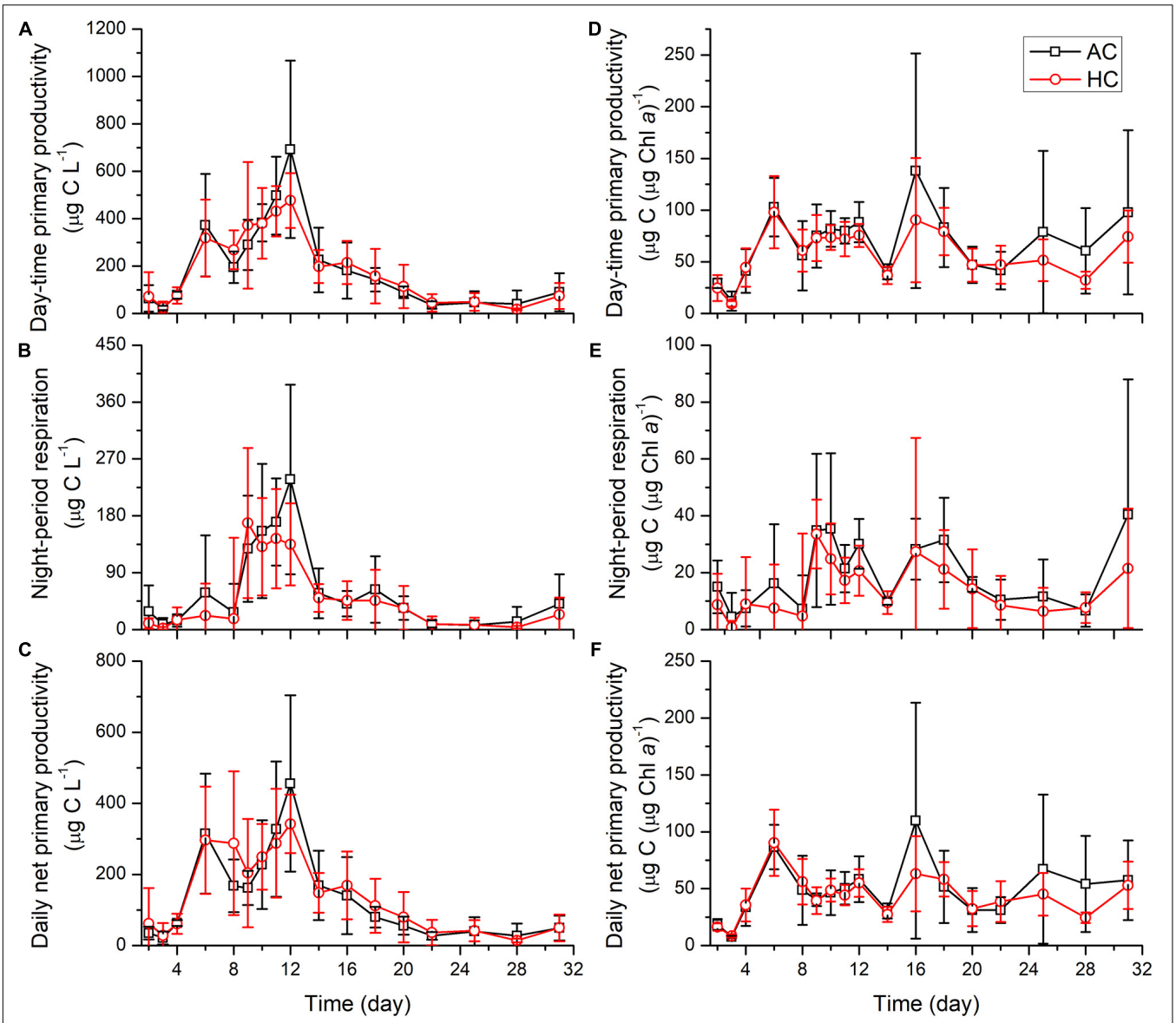


FIGURE 7 | The changes of day-time primary productivity **(A,D)**, night period respiration **(B,E)**, and daily net primary productivity **(C,F)** normalized to water volume (left panels) and to Chl *a* (right panels) levels, in HC (1000 ppmv) and AC (~410 ppmv) treatments. Data are means ± SD of replicates for HC treatments and for AC treatments.

the mixotrophic dinoflagellates *P. minimum* and *P. conicoides*. The phenomenon of succession from diatoms to dinoflagellates have been commonly observed in eutrophic coastal regions (Spilling et al., 2018), which appears to be due to different physiological strategies between the two groups in coping with environmental changes, including CO_2 and temperature changes. It is most likely that mixotrophic dinoflagellates take over the dominance by taking up organic matters after diatoms depleted the inorganic nutrients (Carlsson and Granéli, 1998). Alternatively, dinoflagellates may possess positive interaction with surrounding bacteria consortia to exchange and/or consume matters (Gong et al., 2017). In addition, the heterotrophic metabolism and flagellate motility may boost with increasing temperature. In the present work, water temperature increased by 4.2°C from 21.9 ± 0.1°C at the beginning to 26.1 ± 0.1°C at the end of the experiment (**Figure 1A**). Notably, the competitive capacity of dinoflagellates might become lower in the mesocosms relative to the bay, resulting from low abundance and diversity of dinoflagellates in the bay when the mesocosm experiment was initiated, and from suboptimal growth conditions for dinoflagellates in the mesocosms such as aeration disturbance (Lin et al., 2012; Wohlrab et al., 2020). We also noted that the composition of diatoms changed, with larger cells tending to account for higher proportion (**Figure 6**, Olenina, 2006; Bach et al., 2019). This observation seemed contradict to the strategy of diatoms in coping with nutrients limitation and increasing

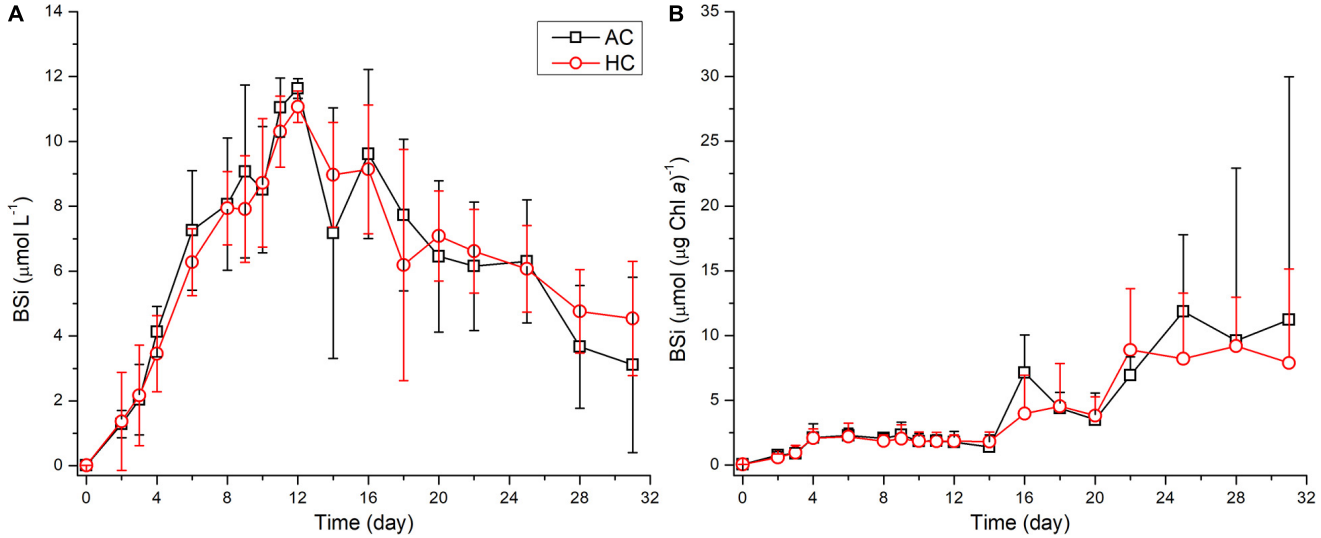


FIGURE 8 | Temporal variations of biogenic silica concentration in the water **(A)** and biogenic silica contents normalized to Chl *a* **(B)**, in HC (1000 ppm) and AC (~410 ppm) treatments. Data are means ± SD **(A)** or means ± SD **(B)** of replicates for HC treatments and for AC treatments.

temperature, which usually results in smaller cells become the dominant (Finkel et al., 2010; Barton et al., 2013). However, larger diatoms have the advantages of storing nutrient for slower growth (Raven, 1987), and heterotrophic refueling of nutrients may also contribute the increased proportion of larger diatoms.

Under the elevated CO_2 concentration, however, the succession of phytoplankton from diatoms to dinoflagellates appeared to occur, but to much less extent, which was not enough for the latter to replace the former for the dominant group (**Figures 5**, **6**). Higher relative abundance of diatoms under HC conditions was also observed in KOSMOS mesocosm experiment conducted in the Gulmar Fjord, Sweden (Bach et al., 2017), as well as at Shikine Island CO_2 seep, Japan (Harvey et al., 2019; Wada et al., 2021). These may attribute to competitive advantages of CCMs in diatoms, under HC conditions. Increased CO_2 availability associated with ocean acidification can fuel phytoplankton biomass when CO_2 becomes limited (Hansen et al., 2007; Berge et al., 2010; Raven et al., 2020). While increased CO_2 levels projected to the end of this century have been shown to down-regulate CCMs in diatoms (see the review by Gao and Campbell, 2014 and literatures therein) and in dinoflagellates (Rost et al., 2006), and the saved energy from operation of CCMs may be beneficial or harmful to phytoplankton growth under limiting and inhibiting light levels, respectively (Gao et al., 2012). Therefore, difference in CCMs efficiency between the two groups might be responsible for the suppressed succession from diatoms to dinoflagellates under the HC. The CO_2 affinity of ribulose 1,5-diphosphate carboxylase/oxidase (Rubisco) for carboxylation is higher in diatoms than dinoflagellates (Reinfelder, 2011). Dinoflagellates possess a high plasticity toward increased pCO_2, while diatoms do not (Van de Waal et al., 2019). Considering the higher CO_2 affinity and lack of CCMs plasticity, diatoms may gain a competitive advantage in DIC uptake under elevated pCO_2 conditions. In addition, OA effects on phytoplankton can be modified by other abiotic factors such as temperature and nutrients, depending on taxa and latitude or weather conditions, and therefore would influence plankton community structure (Sommer et al., 2015; Bach et al., 2016). Diatoms migrated poleward more slowly relative to dinoflagellates, implying that diatoms are more resilient to ocean warming (Chivers et al., 2017), and that diatoms would gain more advantages under OA conditions with increasing temperature. Algal responses to nutrient enrichment may differ at small and intermediate mesocosm volumes but are similar in larger volume mesocosms (>20 L), which are typically used in field (Spivak et al., 2011). Therefore, our experiment with a natural community in >3000 L mesocosm had been performed under different levels of CO_2 could provide basic understanding of the OA impacts on natural plankton communities in eutrophic regions. A previous study showed that plankton communities supported by regenerated nutrients may be more responsive to OA than those having access to higher availability of inorganic nutrients (Bach et al., 2016). Under HC conditions, the dominant diatoms *Nitzschia* spp. have a benefit in nutrient uptake (Qu et al., 2017), and less resources were necessary for diatom inorganic carbon acquisition (Bach et al., 2017). Therefore, elevated pCO_2 along with depletion of nutrients hindered the takeover by dinoflagellates, though a meta-analysis study showed that elevated CO_2 appears to favor dinoflagellates more than diatoms in terms of growth (Seifert et al., 2020). On the other hand, increased bacteria and viruses abundance under HC (**Figure 4**), along with boosted bacterial activity by high temperature (Spilling et al., 2018), could release more nutrients and CO_2 due to enhanced degradation of organic matters, though the inorganic macro-nutrients did not differ obviously (**Figure 2**).

Throughout processes of phytoplankton blooms, higher autotrophic biomass was observed in HC relative to AC, but the

difference was not significant (**Figure 3**). The rapid increase in phytoplankton biomass led to the quick declines in nutrients from days 2 to 4. Phytoplankton biomass continued to increase even when the levels of NO_3^- and PO_4^{3-} were very low. This process may be supported by the degradation of organic matters driven by bacteria, as indicated by increased concentrations of NO_x^- and $Si(OH)_4$, decreased NH_4^+ concentration and increased bacteria abundance on day 2 (**Figure 2**). At the early stage, higher NO_x^- concentration and higher bacteria abundance in HC relative to AC treatments, indicated that OA stimulated more nutrient refueling by bacterial nitrification to support higher phytoplankton biomass. However, the abundances of viruses and bacteria were increased by HC during the growing and declining phase of phytoplankton, respectively, implying that the enhancement of cell lysis by viruses and the negative interaction of bacteria with diatoms (Vincent and Bowler, 2020) may offset the positive effects of OA on autotrophic biomass. In addition, phytoplankton biomass in HC reached the peak one day earlier than AC, which could be attributed to faster exhaustion of nutrients with higher biomass in HC.

While phytoplankton community structure and abundances of viruses and bacteria responded to the elevated pCO_2, no significant changes were observed in primary productivity of phytoplankton assemblages over time, either normalized to water volume or to Chl *a* (**Figure 7**). High pCO_2 also did not significantly influence the production or degradation of BSi (**Figure 8**). Changes in the milieu pH could affect intracellular acid-base homeostasis, which in turn influences silicon metabolism, expansion of vesicle expansion and valve formation (Hervé et al., 2012). In this study, the initial pCO_2 of seawater in AC cultures was 610 μatm, which was higher than that equilibrated with ambient air pCO_2 of about 410 ppmv. This indicated that eutrophication contributed strongly to the CO_2 enrichment and acidification, with a pH drop of 0.15 units. In addition, phytoplankton in this region have adapted to fluctuating pH with 0.11–0.18 units of daily ΔpH, due to high rates of day-time photosynthetic CO_2 removal and night-time respiratory CO_2 release. Non-significant effects of HC on primary productivity and BSi contents may result from high resilience of phytoplankton physiological performance to OA and/or balanced effects of elevated pCO_2 and increased acidic stress (Gao et al., 2019). Although differences in primary productivity or BSi contents were not observed between HC and AC treatments, OA could influence biogeochemical cycles of carbon and nutrients because of varied plankton community structure. BSi contents normalized to Chl *a* maintained stable during the processes of bloom development, but increased with the decline of phytoplankton blooms, reflecting lower rates of BSi remineralizatin by bacteria relative to phytoplankton mortality rates.

In conclusion, our mesocosm experiment demonstrated a community level response to the elevated CO_2 in the eutrophic bay in the coastal waters of the East China Sea, showing repressed species succession of phytoplankton from diatoms to dinoflagellates and enhanced abundance of viruses and heterotrophic bacteria. This finding mirrors observed reduction in biodiversity near shallow CO_2 seeps (Cigliano et al., 2010; Hall-Spencer and Harvey, 2019; Harvey et al., 2021), since acidification would eventually result in "winners" and "losers" (Gattuso et al., 2015). Although we only found that bacteria increased their abundance, it is most likely that their community structure changed, since OA enhanced nitrification at the early stage. The altered bacterial communities by OA were also shown in the waters surrounding a CO_2 seep (Harvey et al., 2020). Increased viruses abundance suggested that OA may enhance viral activity, as shown previously that elevated CO_2 exacerbates viruses attack to its host, a red-tide microalga (Chen et al., 2015). Integratively, OA may alter phytoplankton succession and enhance viral lysis and bacterial degradation, consequently alter biogeochemical processes in eutrophic coastal ecosystems.

DATA AVAILABILITY STATEMENT

The raw data supporting the conclusions of this article will be made available by the authors, without undue reservation.

AUTHOR CONTRIBUTIONS

KG, XL, and GG designed the experiment. TW, XY, DZ, JS, SC, HL, NB, RH, LQ, and XJ preserved normal operation of the mesocosm platform. JS, RH, and SC measured pH, salinity, temperature, primary productivity, and biogenic silica contents. XJ and LQ measured chlorophyll *a* concentration. ZW and YG provided phytoplankton community structure. YY, RZ, and NJ provided viruses and bacteria abundance. XS provided the concentration of nutrient and dissolved inorganic carbon. RH wrote the manuscript. All authors revised the manuscript.

FUNDING

This study was supported by National Natural Science Foundation of China (41720104005, 41721005, 41890803, and 41911530190) and National Key Research and Development Program of China (2016YFA0601400 and 2016YFA0601300).

ACKNOWLEDGMENTS

We sincerely thank Wenyan Zhao, Xianglan Zeng, and Liting Peng for their kind assistance in operation of mesocosm experiment.

SUPPLEMENTARY MATERIAL

The Supplementary Material for this article can be found online at: https://www.frontiersin.org/articles/10.3389/fmars.2021.642208/full#supplementary-material

REFERENCES

Aberle, N., Schulz, K. G., Stuhr, A., Malzahn, A. M., Ludwig, A., and Riebesell, U. (2013). High tolerance of microzooplankton to ocean acidification in an Arctic coastal plankton community. *Biogeosciences* 10, 1471–1481. doi: 10.5194/bg-10-1471-2013

Bach, L. T., Alvarez-Fernandez, S., Hornick, T., Stuhr, A., and Riebesell, U. (2017). Simulated ocean acidification reveals winners and losers in coastal phytoplankton. *PLoS One* 12:e0188198. doi: 10.1371/journal.pone.0188198

Bach, L. T., Hernández-Hernández, N., Taucher, J., Spisla, C., Sforna, C., Riebesell, U., et al. (2019). Effects of elevated CO_2 on a natural diatom community in the subtropical NE Atlantic. *Front. Mar. Sci.* 6:75. doi: 10.3389/fmars.2019.00075

Bach, L. T., Taucher, J., Boxhammer, T., Ludwig, A., Kristineberg KOSMOS Consortium, Achterberg, E. P., et al. (2016). Influence of ocean acidification on a natural winter-to-summer plankton succession: first insights from a long-term mesocosm study draw attention to periods of low nutrient concentrations. *PLoS One* 11:e0159068. doi: 10.1371/journal.pone.0159068

Barton, A. D., Finkel, Z. V., Ward, B. A., Johns, D. G., and Follows, M. J. (2013). On the roles of cell size and trophic strategy in North Atlantic diatom and dinoflagellate communities. *Limnol. Oceanogr.* 58, 254–266. doi: 10.4319/lo.2013.58.1.0254

Berge, T., Daugbjerg, N., Balling Andersen, B., and Hansen, P. J. (2010). Effect of lowered pH on marine phytoplankton growth rates. *Mar. Ecol. Prog. Ser.* 416, 79–91. doi: 10.3354/meps08780

Brzezinski, M. A., and Nelson, D. M. (1995). The annual silica cycle in the Sargasso Sea near Bermuda. *Deep Sea Res. I Oceanogr. Res. Papers* 42, 1215–1237. doi: 10.1016/0967-0637(95)93592-3

Cai, W.-J., Hu, X., Huang, W.-J., Murrell, M. C., Lehrter, J. C., Lohrenz, S. E., et al. (2011). Acidification of subsurface coastal waters enhanced by eutrophication. *Nat. Geosci.* 4, 766–770. doi: 10.1038/ngeo1297

Carlsson, P., and Granéli, E. (1998). "Utilization of dissolved organic matter (DOM) by phytoplankton including harmful species," in *Physiological Ecology of Harmful Algal Blooms*, eds M. A. Donald and D. C. Allan (Heidelberg: Springer), 509–524.

Chen, S., Gao, K., and Beardall, J. (2015). Viral attack exacerbates the susceptibility of a bloom-forming alga to ocean acidification. *Glob. Change Biol.* 21, 629–636. doi: 10.1111/gcb.12753

Chen, X., Wei, W., Wang, J., Li, H., Sun, J., Ma, R., et al. (2019). Tide driven microbial dynamics through virus-host interactions in the estuarine ecosystem. *Water Res.* 160, 118–129. doi: 10.1016/j.watres.2019.05.051

Chivers, W. J., Walne, A. W., and Hays, G. C. (2017). Mismatch between marine plankton range movements and the velocity of climate change. *Nat. Commun.* 8:14434. doi: 10.1038/ncomms14434

Cigliano, M., Gambi, M. C., Rodolfo-Metalpa, R., Patti, F. P., and Hall-Spencer, J. M. (2010). Effects of ocean acidification on invertebrate settlement at volcanic CO_2 vents. *Mar. Biol.* 157, 2489–2502. doi: 10.1007/s00227-010-1513-6

de Kluijver, A., Soetaert, K., Czerny, J., Schulz, K. G., Boxhammer, T., Riebesell, U., et al. (2013). A ^{13}C labelling study on carbon fluxes in Arctic plankton communities under elevated CO_2 levels. *Biogeosciences* 10, 1425–1440. doi: 10.5194/bg-10-1425-2013

Engel, A., Zondervan, I., Aerts, K., Beaufort, L., Benthien, A., Chou, L., et al. (2005). Testing the direct effect of CO_2 concentration on a bloom of the coccolithophorid *Emiliania huxleyi* in mesocosm experiments. *Limnol. Oceanogr.* 50, 493–507. doi: 10.4319/lo.2005.50.2.0493

Finkel, Z. V., Beardall, J., Flynn, K. J., Quigg, A., Rees, T. A. V., and Raven, J. A. (2010). Phytoplankton in a changing world: cell size and elemental stoichiometry. *J. Plankton Res.* 32, 119–137. doi: 10.1093/plankt/fbp098

Friedlingstein, P., O'Sullivan, M., Jones, M. W., Andrew, R. M., Hauck, J., Olsen, A., et al. (2020). Global carbon budget 2020. *Earth Syst. Sci. Data* 12, 3269–3340. doi: 10.5194/essd-12-3269-2020

Gao, K., Beardall, J., Häder, D.-P., Hall-Spencer, J. M., Gao, G., and Hutchins, D. A. (2019). Effects of ocean acidification on marine photosynthetic organisms under the concurrent influences of warming, UV radiation, and deoxygenation. *Front. Mar. Sci.* 6:322. doi: 10.3389/fmars.2019.00322

Gao, K., and Campbell, D. A. (2014). Photophysiological responses of marine diatoms to elevated CO_2 and decreased pH: a review. *Funct. Plant Biol.* 41, 449–459. doi: 10.1071/FP13247

Gao, K., Xu, J., Gao, G., Li, Y., Hutchins, D. A., Huang, B., et al. (2012). Rising CO_2 and increased light exposure synergistically reduce marine primary productivity. *Nat. Clim. Chang.* 2, 519–523. doi: 10.1038/nclimate1507

Gattuso, J.-P., Magnan, A., Billé, R., Cheung, W. W. L., Howes, E. L., Joos, F., et al. (2015). Contrasting futures for ocean and society from different anthropogenic CO_2 emissions scenarios. *Science* 349:aac4722. doi: 10.1126/science.aac4722

Gong, W., Browne, J., Hall, N., Schruth, D., Paerl, H., and Marchetti, A. (2017). Molecular insights into a dinoflagellate bloom. *ISME J.* 11, 439–452. doi: 10.1038/ismej.2016.129

Hall-Spencer, J. M., and Harvey, B. P. (2019). Ocean acidification impacts on coastal ecosystem services due to habitat degradation. *Emerg. Top. Life Sci.* 3, 197–206. doi: 10.1042/ETLS20180117

Hansen, P. J., Lundholm, N., and Rost, B. (2007). Growth limitation in marine red-tide dinoflagellates: effects of pH versus inorganic carbon availability. *Mar. Ecol. Prog. Ser.* 334, 63–71. doi: 10.3354/meps334063

Hare, C. E., Leblanc, K., DiTullio, G. R., Kudela, R. M., Zhang, Y., Lee, P. A., et al. (2007). Consequences of increased temperature and CO_2 for phytoplankton community structure in the Bering Sea. *Mar. Ecol. Prog. Ser.* 352, 9–16. doi: 10.3354/meps07182

Harvey, B., Agostini, S., Kon, K., Wada, S., and Hall-Spencer, J. (2019). Diatoms dominate and alter marine food-webs when CO_2 rises. *Diversity* 11:242. doi: 10.3390/d11120242

Harvey, B. P., Kerfahi, D., Jung, Y., Shin, J.-H., Adams, J. M., and Hall-Spencer, J. M. (2020). Ocean acidification alters bacterial communities on marine plastic debris. *Mar. Pollut. Bull.* 161:111749. doi: 10.1016/j.marpolbul.2020.111749

Harvey, B. P., Kon, K., Agostini, S., Wada, S., and Hall-Spencer, J. M. (2021). Ocean acidification locks algal communities in a species-poor early successional stage. *Glob. Change Biol.* 27, 2174–2187. doi: 10.1111/gcb.15455

Hervé, V., Derr, J., Douady, S., Quinet, M., Moisan, L., and Lopez, P. J. (2012). Multiparametric analyses reveal the pH-dependence of silicon biomineralization in diatoms. *PLoS One* 7:e46722. doi: 10.1371/journal.pone.0046722

IPCC (2019). *Special Report on the Ocean and Cryosphere in a Changing Climate*. Geneva: IPCC.

Lewis, E., and Wallace, D. (1998). *Program Developed for CO_2 System Calculations*. Berkeley, CA: Environmental System Science Data Infrastructure for a Virtual Ecosystem (ESS-DIVE) (United States).

Lin, G., Yang, Q., Lin, W., and Wang, Y. (2012). Distribution characteristic and variation trend of planktonic dinoflagellate in the Taiwan Strait from 2006 to 2007. *Mar. Sci. Bull.* 14, 68–79.

Lin, X., Huang, R., Li, Y., Li, F., Wu, Y., Hutchins, D. A., et al. (2018). Interactive network configuration maintains bacterioplankton community structure under elevated CO_2 in a eutrophic coastal mesocosm experiment. *Biogeosciences* 15, 551–565. doi: 10.5194/bg-15-551-2018

Liu, N., Tong, S., Yi, X., Li, Y., Li, Z., Miao, H., et al. (2017). Carbon assimilation and losses during an ocean acidification mesocosm experiment, with special reference to algal blooms. *Mar. Environ. Res.* 129, 229–235. doi: 10.1016/j.marenvres.2017.05.003

Meakin, N. G., and Wyman, M. (2011). Rapid shifts in picoeukaryote community structure in response to ocean acidification. *ISME J.* 5, 1397–1405. doi: 10.1038/ismej.2011.18

Niehoff, B., Schmithüsen, T., Knüppel, N., Daase, M., Czerny, J., and Boxhammer, T. (2013). Mesozooplankton community development at elevated CO_2 concentrations: results from a mesocosm experiment in an Arctic fjord. *Biogeosciences* 10, 1391–1406. doi: 10.5194/bg-10-1391-2013

Olenina, I. (2006). Biovolumes and size-classes of phytoplankton in the Baltic Sea. *HELCOM Balt. Sea Environ. Proc.* 106:144.

Qu, C.-F., Liu, F.-M., Zheng, Z., Wang, Y.-B., Li, X.-G., Yuan, H.-M., et al. (2017). Effects of ocean acidification on the physiological performance and carbon production of the Antarctic sea ice diatom *Nitzschia* sp. ICE-H. *Mar. Pollut. Bull.* 120, 184–191. doi: 10.1016/j.marpolbul.2017.05.018

Rabalais, N. N., Turner, R. E., Díaz, R. J., and Justić, D. (2009). Global change and eutrophication of coastal waters. *ICES J. Mar. Sci.* 66, 1528–1537. doi: 10.1093/icesjms/fsp047

Raven, J. A. (1987). The role of vacuoles. *New Phytol.* 106, 357–422.

Raven, J. A., Gobler, C. J., and Hansen, P. J. (2020). Dynamic CO_2 and pH levels in coastal, estuarine, and inland waters: theoretical and observed effects on harmful algal blooms. *Harmful Algae* 91:101594. doi: 10.1016/j.hal.2019.03.012

Reinfelder, J. R. (2011). Carbon concentrating mechanisms in eukaryotic marine phytoplankton. *Annu. Rev. Mar. Sci.* 3, 291–315. doi: 10.1146/annurev-marine-120709-142720

Riebesell, U., Aberle-Malzahn, N., Achterberg, E. P., Algueró-Muñiz, M., Alvarez-Fernandez, S., Arístegui, J., et al. (2018). Toxic algal bloom induced by ocean acidification disrupts the pelagic food web. *Nat. Clim. Chang.*8, 1082–1086. doi: 10.1038/s41558-018-0344-1

Riebesell, U., Bach, L. T., Bellerby, R. G. J., Monsalve, J. B., Boxhammer, T., Czerny, J., et al. (2016). Competitive fitness of a predominant pelagic calcifier impaired by ocean acidification. *Nat. Geosci.* 10, 19–23. doi: 10.1038/ngeo2854

Riebesell, U., Czerny, J., von Bröckel, K., Boxhammer, T., Büdenbender, J., Deckelnick, M., et al. (2013). Technical note: a mobile sea-going mesocosm system–new opportunities for ocean change research. *Biogeosciences* 10, 1835–1847. doi: 10.5194/bg-10-1835-2013

Ritchie, R. J. (2006). Consistent sets of spectrophotometric chlorophyll equations for acetone, methanol and ethanol solvents. *Photosynth. Res.* 89, 27–41. doi: 10.1007/s11120-006-9065-9

Rost, B., Richter, K.-U., Riebesell, U. L. F., and Hansen, P. J. (2006). Inorganic carbon acquisition in red tide dinoflagellates. *Plant Cell Environ.* 29, 810–822. doi: 10.1111/j.1365-3040.2005.01450.x

Schulz, K. G., Bellerby, R. G. J., Brussaard, C. P. D., Büdenbender, J., Czerny, J., Engel, A., et al. (2013). Temporal biomass dynamics of an Arctic plankton bloom in response to increasing levels of atmospheric carbon dioxide. *Biogeosciences* 10, 161–180. doi: 10.5194/bg-10-161-2013

Seifert, M., Rost, B., Trimborn, S., and Hauck, J. (2020). Meta-analysis of multiple driver effects on marine phytoplankton highlights modulating role of pCO_2. *Glob. Chang. Biol.* 26, 6787–6804. doi: 10.1111/gcb.15341

Sommer, U., Paul, C., and Moustaka-Gouni, M. (2015). Warming and ocean acidification effects on phytoplankton—from species shifts to size shifts within species in a mesocosm experiment. *PLoS One* 10:e0125239. doi: 10.1371/journal.pone.0125239

Spilling, K., Olli, K., Lehtoranta, J., Kremp, A., Tedesco, L., Tamelander, T., et al. (2018). Shifting diatom—dinoflagellate dominance during spring bloom in the Baltic Sea and its potential effects on biogeochemical cycling. *Front. Mar. Sci.* 5:327. doi: 10.3389/fmars.2018.00327

Spilling, K., Schulz, K. G., Paul, A. J., Boxhammer, T., Achterberg, E. P., Hornick, T., et al. (2016). Effects of ocean acidification on pelagic carbon fluxes in a mesocosm experiment. *Biogeosciences* 13, 6081–6093. doi: 10.5194/bg-13-6081-2016

Spivak, A. C., Vanni, M. J., and Mette, E. M. (2011). Moving on up: can results from simple aquatic mesocosm experiments be applied across broad spatial scales? *Freshw. Biol.* 56, 279–291. doi: 10.1111/j.1365-2427.2010.02495.x

Taucher, J., Boxhammer, T., Bach, L. T., Paul, A. J., Schartau, M., Stange, P., et al. (2020). Changing carbon-to-nitrogen ratios of organic-matter export under ocean acidification. *Nat. Clim. Chang.* 11, 52–57. doi: 10.1038/s41558-020-00915-5

Van de Waal, D. B., Brandenburg, K. M., Keuskamp, J., Trimborn, S., Rokitta, S., Kranz, S. A., et al. (2019). Highest plasticity of carbon-concentrating mechanisms in earliest evolved phytoplankton. *Limnol. Oceanogr. Lett.* 4, 37–43. doi: 10.1002/lol2.10102

Vincent, F., and Bowler, C. (2020). Diatoms are selective segregators in global ocean planktonic communities. *mSystems* 5:e00444-19. doi: 10.1128/mSystems.00444-19

Wada, S., Agostini, S., Harvey, B. P., Omori, Y., and Hall-Spencer, J. M. (2021). Ocean acidification increases phytobenthic carbon fixation and export in a warm-temperate system. *Estuar. Coast. Shelf Sci.* 250:107113. doi: 10.1016/j.ecss.2020.107113

Wohlrab, S., John, U., Klemm, K., Eberlein, T., Forsberg Grivogiannis, A. M., Krock, B., et al. (2020). Ocean acidification increases domoic acid contents during a spring to summer succession of coastal phytoplankton. *Harmful Algae* 92:101697. doi: 10.1016/j.hal.2019.101697

Zhang, R., Xia, X., Lau, S. C. K., Motegi, C., Weinbauer, M. G., and Jiao, N. (2013). Response of bacterioplankton community structure to an artificial gradient of pCO_2 in the Arctic Ocean. *Biogeosciences* 10, 3679–3689. doi: 10.5194/bg-10-3679-2013

Conflict of Interest: The authors declare that the research was conducted in the absence of any commercial or financial relationships that could be construed as a potential conflict of interest.

Publisher's Note: All claims expressed in this article are solely those of the authors and do not necessarily represent those of their affiliated organizations, or those of the publisher, the editors and the reviewers. Any product that may be evaluated in this article, or claim that may be made by its manufacturer, is not guaranteed or endorsed by the publisher.

Copyright © 2021 Huang, Sun, Yang, Jiang, Wang, Song, Wang, Zhang, Li, Yi, Chen, Bao, Qu, Zhang, Jiao, Gao, Huang, Lin, Gao and Gao. This is an open-access article distributed under the terms of the Creative Commons Attribution License (CC BY). The use, distribution or reproduction in other forums is permitted, provided the original author(s) and the copyright owner(s) are credited and that the original publication in this journal is cited, in accordance with accepted academic practice. No use, distribution or reproduction is permitted which does not comply with these terms.

frontiers in Marine Science

ORIGINAL RESEARCH
published: 24 March 2021
doi: 10.3389/fmars.2021.622319

The Combined Effects of Increased pCO_2 and Warming on a Coastal Phytoplankton Assemblage: From Species Composition to Sinking Rate

Yuanyuan Feng[1], Fei Chai[2,3], Mark L. Wells[2,3], Yan Liao[1], Pengfei Li[1], Ting Cai[1], Ting Zhao[1], Feixue Fu[4] and David A. Hutchins[4]*

[1] College of Marine and Environmental Sciences, Tianjin University of Science and Technology, Tianjin, China, [2] State Key Laboratory of Satellite Ocean Environment Dynamics, Second Institute of Oceanography, Ministry of Natural Resources, Hangzhou, China, [3] School of Marine Sciences, University of Maine, Orono, ME, United States, [4] Department of Biological Sciences, University of Southern California, Los Angeles, CA, United States

OPEN ACCESS

Edited by:
Xianghui Guo, Xiamen University, China

Reviewed by:
Allanah J. Paul, GEOMAR Helmholtz Centre for Ocean Research Kiel, Germany
Gang Li, South China Sea Institute of Oceanology (CAS), China
Kalle Olli, Estonian University of Life Sciences, Estonia

***Correspondence:**
Yuanyuan Feng
yfeng@tust.edu.cn;
yyfengcocco@126.com

Specialty section:
This article was submitted to Coastal Ocean Processes, a section of the journal Frontiers in Marine Science

Received: *28 October 2020*
Accepted: *03 March 2021*
Published: *24 March 2021*

Citation:
Feng Y, Chai F, Wells ML, Liao Y, Li P, Cai T, Zhao T, Fu F and Hutchins DA (2021) The Combined Effects of Increased pCO_2 and Warming on a Coastal Phytoplankton Assemblage: From Species Composition to Sinking Rate. Front. Mar. Sci. 8:622319. doi: 10.3389/fmars.2021.622319

In addition to ocean acidification, a significant recent warming trend in Chinese coastal waters has received much attention. However, studies of the combined effects of warming and acidification on natural coastal phytoplankton assemblages here are scarce. We conducted a continuous incubation experiment with a natural spring phytoplankton assemblage collected from the Bohai Sea near Tianjin. Experimental treatments used a full factorial combination of temperature (7 and 11°C) and pCO_2 (400 and 800 ppm) treatments. Results suggest that changes in pCO_2 and temperature had both individual and interactive effects on phytoplankton species composition and elemental stoichiometry. Warming mainly favored the accumulation of picoplankton and dinoflagellate biomass. Increased pCO_2 significantly increased particulate organic carbon to particulate organic phosphorus (C:P) and particulate organic carbon to biogenic silica (C:BSi) ratios, and decreased total diatom abundance; in the meanwhile, higher pCO_2 significantly increased the ratio of centric to pennate diatom abundance. Warming and increased pCO_2 both greatly decreased the proportion of diatoms to dinoflagellates. The highest chlorophyll *a* biomass was observed in the high pCO_2, high temperature phytoplankton assemblage, which also had the slowest sinking rate of all treatments. Overall, there were significant interactive effects of increased pCO_2 and warming on dinoflagellate abundance, pennate diatom abundance, diatom vs. dinoflagellates ratio and the centric vs. pennate ratio. These findings suggest that future ocean acidification and warming trends may individually and cumulatively affect coastal biogeochemistry and carbon fluxes through shifts in phytoplankton species composition and sinking rates.

Keywords: ocean acidification, warming, phytoplankton, diatoms, biogenic silica, sinking rate, coastal environment

INTRODUCTION

Anthropogenic activities have increased atmospheric pCO_2 at a rate of ∼1.8 ppm per year over the last century (IPCC, 2014), with surface seawaters absorbing ∼25% of these CO_2 emissions (Le Quéré et al., 2016). This results in increased CO_2 and HCO_3^- concentrations and decreased pH and CO_3^{2-} concentrations in surface seawaters, collectively referred to as "ocean acidification (OA)" (Caldeira and Wickett, 2003). The average pH of ocean surface waters is predicted to fall from ∼8.1 to ∼7.8 by the end of this century (Feely et al., 2009). In addition, coastal seawater carbonate chemistry can be affected by organic- and acidic sulfate-rich freshwater runoff (Fitzer et al., 2018), or the respiration of organic matter produced as a consequence of eutrophication (Cai et al., 2011), and thus coastal ecosystems are expected to experience more severe acidification (Zhai et al., 2012).

In addition to OA, increasing atmospheric CO_2 also has elevated sea surface temperatures (SST) as a consequence of the greenhouse effect, with predicted 1 to 4°C increases in SST over the next 100 years (Bopp et al., 2013). Observed warming trends are not homogeneous between coastal and oceanic regions (Varela et al., 2018). For example, in Chinese coastal waters, a significant warming trend of ∼0.8–2°C per century has been observed in recent years, almost double that of global SST (Carton and Giese, 2008; Feng and Lin, 2009; Wu et al., 2017).

Both CO_2 and temperature are important environmental drivers controlling marine phytoplankton physiology. The low CO_2 concentrations in seawater can limit the photosynthetic activities of some groups of marine phytoplankton due to the low affinity of the enzyme Ribulose-1,5-bisphosphate carboxylase/oxygenase (RubisCO) for dissolved CO_2 (Riebesell et al., 1993; Falkowski and Raven, 2007). As a consequence, phytoplankton have evolved carbon concentrating mechanisms (CCMs) to enhance carbon availability, but the efficiencies of CCMs differ among groups and taxa. Consequently, the increases in CO_2 concentrations with ocean acidification may have disproportionate effects among different phytoplankton groups/species. For instance, CO_2 enrichment promoted the photosynthetic efficiency of the marine coccolithophore *Emiliania huxleyi* more than the diatom *Skeletonema costatum* or the flagellate *Phaeocystis globosa* (Rost et al., 2003). Rising pCO_2 could thus lead to shifts in phytoplankton taxonomic composition and species succession in the natural environment (Schulz et al., 2017; Bach and Taucher, 2019). It has been shown that CO_2 enrichment can cause a shift in dominance from small pennate to larger centric diatom species in a Southern Ocean phytoplankton community (Tortell et al., 2008; Feng et al., 2010), whereas some other studies found little effect of changing CO_2 concentration on the composition of a coastal phytoplankton assemblage (Kim et al., 2006). In addition, changes in pCO_2 may also play an important role in regulating the biomineralization of calcifying coccolithophores (Raven and Crawfurd, 2012) and siliceous diatoms (Milligan et al., 2004), as well as other physiological processes that alter the overall elemental stoichiometry of phytoplankton (Burkhardt et al., 1999; Hutchins et al., 2009; Finkel et al., 2010). During the past decades, numerous studies have especially focused on the sensitivity of calcification process to ocean acidification, with a general trend of weakened calcification (Riebesell et al., 2000; Beaufort et al., 2011; Krumhardt et al., 2017). While for the silicification process of diatoms, although theoretically the formation of biogenic silica should be facilitated at lower pH (Martin-Jézéquel et al., 2000), controversial results has been reported (Milligan et al., 2004). All of these changes will in turn profoundly influence marine biogeochemical cycles.

Temperature is one of the most fundamental environmental drivers determining the growth, metabolic activities, elemental composition, and distribution of marine phytoplankton (Eppley, 1972). Warming has induced changes in geographic distribution, harmful algal bloom intensity, and biodiversity in marine ecosystems (reviewed by Sommer et al., 2012; Hutchins and Fu, 2017). Previous studies have suggested that CO_2 enrichment and warming may have combined or interactive effects on phytoplankton physiology (Hutchins et al., 2007; Feng et al., 2008) and species succession and biogeochemistry of natural phytoplankton communities (Hare et al., 2007b; Feng et al., 2009; Sommer et al., 2015; Sett et al., 2018).

However, studies examining the influence of multiple environmental driver interactions on marine life are scarce, and more understanding is needed, especially at the community level (Joint et al., 2011; Boyd et al., 2018). Here we present a continuous incubation experiment that investigated the interactive effects of increased pCO_2 and warming on a natural marine phytoplankton assemblage collected from coastal Bohai Sea waters near Tianjin, China, in a region impacted by intense anthropogenic activity. The objective of this study was to investigate the effects of future environmental changes of increased CO_2 concentration and temperature both individually and interactively on phytoplankton assemblage succession, elemental composition, and community sinking rates. The findings help us to understand the consequences of future increases in environmental stressors for biogeochemical processes such as carbon export and elemental cycling by coastal phytoplankton assemblages.

MATERIALS AND METHODS

Experimental Setup and Sampling

Seawater just below the surface (<5 m depth) containing the intact coastal phytoplankton assemblage was collected using a Niskin sampler deployed from a pier near the Tianjin Coastal Recreational Area, Bohai Bay (39.10°N, 117.84°E; temperature: 7°C; salinity: 31; pH: 8.02; nitrate: 8.1 μM; phosphate: 0.4 μM; silicate: 4.2 μM) on March 15, 2017. The whole water was filtered through 100 μm Nitex mesh to eliminate large zooplankton, and then dispensed into 12 4-L clear polycarbonate bottles for incubation. The measured Chl-*a* biomass was low on the 100 μm Nitex mesh, having little effects on the remaining phytoplankton assemblages. Seawater (∼500 L) collected at the same sampling site was filtered through 0.2 μm in-line filters and stored in 25 L clean carboys, to be used for making dilution medium during the continuous culture incubation experiment.

A continuous culture incubation system (Hutchins et al., 2003; Hare et al., 2005, 2007a,b; Feng et al., 2009, 2010) was used to carry out an outdoor experiment under model projected pCO_2 and temperature conditions for the end of this century under some scenarios (IPCC, 2014). Four experimental treatments from full factorial combination of temperature (7 and 11°C) and pCO_2 (400 and 800 ppm) were examined in triplicate bottles: (1) control: 7°C and 400 ppm pCO_2; (2) high pCO_2: 7°C and 800 ppm pCO_2; (3) high temperature: 11°C and 400 ppm pCO_2; and (4) combined: 11°C and 800 ppm pCO_2. Nutrient stock solutions were added to both the initial incubation bottles and the filtered seawater medium to final concentrations of 10 μM nitrate, 1 μM phosphate, and 10 μM silicate. Light levels for the incubations were adjusted using neutral density screens to provide an irradiance of 50% of the incident sea surface level (I_0). The incubation temperatures were maintained by submersing the bottles in a circulating water bath connected to temperature control systems (HC1000BC, Hailea, China) via water pumps. Two different CO_2 levels were adjusted in both the incubation bottles and carboys containing the filtered seawater for dilution, by gentle bubbling (∼4 mL min^{-1}) of ambient air (∼400 ppm) and an air/CO_2 mixture with pCO_2 level of 800 ppm controlled by a gas mixer (CE100, Ruihua, China). The bubbling of the incubation bottles and seawater medium was continuous throughout the whole incubation period in order to maintain the seawater carbonate chemistry.

The phytoplankton community was grown in batch mode during the first 3 days of incubation. The continuous incubation mode with a dilution rate of 0.4 d^{-1} was started on the fourth day (T3) by turning on the peristaltic pumps (Shenchen, China) connected to the bottles through inflow lines going into the bottles from the caps. The dilution rate was chosen based on the average growth rate of the early spring phytoplankton assemblages under nutrient replete conditions in the Bohai Sea (Zou et al., 2001). The outflow outlets were connected at the shoulders of the bottles, in order to maintain a constant volume in the bottles. The bottles were gently shaken and mixed 5–7 times a day to ensure the phytoplankton cells remained suspended.

Samples for pH and total chlorophyll *a* (Chl-*a*) measurements were taken daily directly from the incubation bottles. The daily sampling volume was limited to less than 10% of the incubation volume to avoid significant perturbations of the biomass equilibrium (Feng et al., 2009). Size-fractionated Chl-*a* was sampled only on T0, T3, and T21. The continuous incubation was ended on T21, and samples for measurements of dissolved inorganic carbon (DIC), pH, total alkalinity, Chl-*a*, phytoplankton community structure, biogenic silica (BSi), particulate organic carbon (POC), particulate organic nitrogen (PON), particulate organic phosphorus (POP) and sinking rates were taken on T0 and the final sampling day. T0 samples were taken from the 100 μm Nitex mesh filtered source seawater in triplicates.

Sample Analysis

Seawater Carbonate Chemistry Measurements

Two hundred and fifty mL samples for total alkalinity analysis were preserved with 200 μL of 5% $HgCl_2$ solution in Shott glass bottles (Shott AG, Germany) with screw caps. Alkalinity was then measured using potentiometric titration following the method of Dickson et al. (2007). The accuracy of the method as determined by analysis of Certified Reference Material provided by Andrew Dickson from Scripps Institution of Oceanography was estimated to be ±2 μmol kg^{-1}. Samples for DIC measurements were fixed in 20 mL borosilicate vials with addition of 0.2 mL of 5% $HgCl_2$ solution. The DIC concentration was measured using a total inorganic carbon analyzer (CM140, UIC, United States) by acidification and coulometric detection, and corrected to the Dickson seawater standards (Dickson et al., 2007). The estimated accuracy of the analysis was ± 5 μmol kg^{-1}. pH values were checked daily using a pH meter (S210-B, Mettler Toledo) calibrated with commercial NBS buffers. The seawater carbonate chemistry (data shown in **Supplementary Table 1**, output at the incubation temperatures) was calculated using the program CO2sys (E. Lewis and D. W. R. Wallace) with measured DIC and alkalinity values, using the constants in Mehrbach et al. (1973), re-fitted by Dickson and Millero (1987).

Phytoplankton Chl-*a* Biomass and Assemblage Structure Analyses

20–30 mL samples for Chl-*a* analysis were filtered and extracted in 90% acetone at –20°C in the dark for 24 h, and then measured using a Turner Trilogy fluorometer. Samples for total Chl-*a* biomass analysis were filtered through 0.2 μm polycarbonate filters (Millipore, United States); while size-fractionated Chl-*a* was filtered onto 0.2, 2, and 20 μm polycarbonate filters (Millipore, United States) in series. Samples for phytoplankton taxonomic analysis were preserved with a final concentration of 1% glutaraldehyde and stored at 4°C until analysis. The samples were then concentrated using a 25 mL Utermöhl cell count chamber and counted at 400× magnification under an inverted microscope (AE2000, Motic, China) (Utermöhl, 1958; Thomas, 1997).

Particulate Matter

POC and PON samples (30 mL) were filtered onto pre-combusted (450°C, 2 h) GF/F glass fiber filters (Whatman, United States) and then dried at 55°C. C and N elemental composition was then measured with an elemental analyzer (270, Costech Analytical Technologies, Italy). Thirty mL samples for BSi analysis were filtered onto 0.6 μm polycarbonate filters (Millipore, United States), dried at 60°C, and analyzed using the spectrophotometric method following Brzezinski and Nelson (1995). POP samples (30 mL) were filtered onto pre-combusted GF/F glass fiber filters (Whatman, United States), rinsed with 2 mL of 0.17 mol L^{-1} Na_2SO_4, stored in pre-combusted borosilicate vials with addition of 2 mL of 0.017 mol L^{-1} $MgSO_4$. The samples were then dried and analyzed following the molybdate colorimetric method (Solórzano and Sharp, 1980).

Phytoplankton Sinking Rate

The sinking rate of the phytoplankton assemblage based on Chl-*a* measurements was determined in triplicate samples using the SETCOL method as described in Bienfang (1981). In brief, a plexiglass column (4 cm in diameter, 1 m in length) was filled

up to the top with a homogeneous seawater sample containing the whole phytoplankton assemblage and covered tightly with a glass lid. The column was placed in the dark at the corresponding incubation temperature for a settling time of 3 h, yielding a maximum measurable sinking rate of 8 m d^{-1}. The settling was terminated by carefully draining the upper, middle, and bottom compartments of the column through valved tubing connected through the wall of the column at each depth. The total Chl-*a* concentration of each compartment was then measured, and the sinking rate was calculated using the following equation:

$$S = (C_b \times V_b)/(C_u \times V_u + C_m \times V_m + C_b \times V_b) \times L/t. \quad (1)$$

Here, S is the sinking rate; C_u, C_m, and C_b are the Chl-*a* concentrations in the upper, middle and bottom compartments of the sinking column, respectively; V_u, V_m, and V_b are the volumes in the upper, middle, and bottom compartments, respectively; L is the length of the column; and t is the total sinking time (Bienfang, 1981).

Data Analysis

Statistics

A two-way ANOVA test was used to detect two-way interactions among temperature and CO_2 with the assumptions of homogeneity of variance, independence of observations and independent distribution of variables. Pair-wise tests were conducted using Tukey's multiple comparison *post hoc* analysis. The statistical analysis was performed using GraphPadPrism 7.0 software (GraphPad Software, Inc., San Diego, CA, United States).

Types of Driver Interactions

Two-way interactions among temperature and CO_2 were determined by quantitative comparisons between the observed effects and the model predicted effects of two drivers. The observed effect was calculated as the percentage of change between the combined treatment and control treatment. A model was used for the predictions of two-way effects (Folt et al., 1999; Liao et al., 2019; Feng et al., 2020):

$$\text{Multiplicative effect} = (1 + E_1) \times (1 + E_2) - 1. \quad (2)$$

Here, E1 and E2 denote the individual observed effect of increased pCO_2 and warming on the measured parameter, respectively, calculated as the percentage of changes relative to control treatment.

The interactions among increased pCO_2 and warming were defined as follows:

(1) Synergistic interactive effect: the observed effect > the calculated multiplicative effect (Folt et al., 1999; Boyd and Hutchins, 2012; Boyd et al., 2018);
(2) Antagonistic interactive effect: the observed effect < the calculated multiplicative effect (Folt et al., 1999; Boyd and Hutchins, 2012; Boyd et al., 2018).

Both synergistic and antagonistic interactive effects can be positive (increase) or negative (decrease).

RESULTS

Total and Size-Fractionated Chl-*a* Biomass

The total phytoplankton Chl-*a* biomass kept increasing quickly in the four experimental treatments in the first 5 days of the incubation period (**Figure 1**). The total Chl-*a* concentration on T0 at the sampling site was 14.4 ± 1.4 μg L^{-1}, and it increased throughout the 3-day batch incubation mode. The average value of the total Chl-*a* concentration in the control treatment was lower than those in the other three treatments during the entire course of the incubation (**Figure 1**). By T5, the Chl-*a* concentration in all four treatments were more than double the T0 value, with the highest value observed in the combined

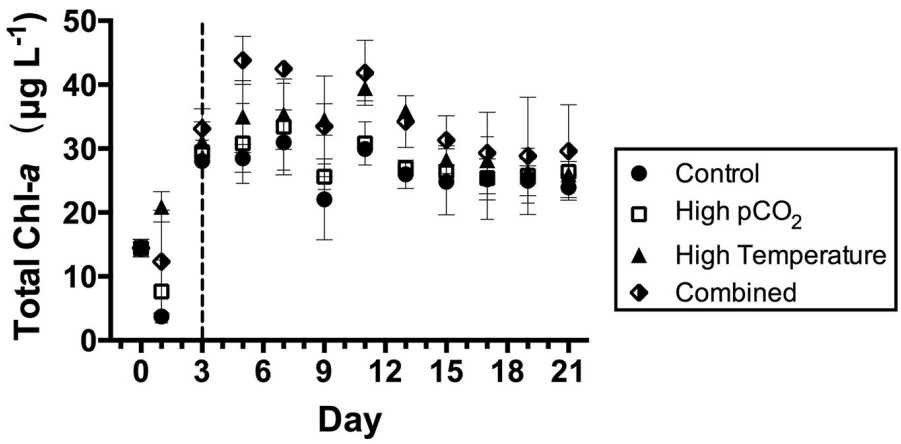


FIGURE 1 | Total Chl-*a* concentrations during the time course of the incubation in the four experimental treatments. Values are the means and error bars are the standard deviations of triplicates. The dashed line separates the two incubation stages: T0–T3 batch growth mode, and T3–T21 continuous growth code with dilution rate of 0.4 d^{-1}.

treatment. During the first 5 days of incubation, the total Chl-*a* concentration was overall higher the two higher temperature treatments (high temperature and combined) compared to that under control and high pCO_2 (**Figure 1**). The total Chl-*a* biomass declined in all the experimental treatments from T11 to T15 and the differences between treatments became less than those in the earlier stage of the incubation. The values also became relatively stable as growth and dilution rates came into balance starting from T15 until the final sampling day (T21, **Figure 1**).

Phytoplankton Chl-*a* biomass size-fractions responded differently to changes in temperature and pCO_2 conditions (**Figure 2**). The initial (T0) phytoplankton assemblage collected for the incubation was dominated by nano-phytoplankton (2–20 μm), contributing 74.5% of the total Chl-*a* biomass. The micro-phytoplankton (>20 μm) and pico-phytoplankton accounted for 18.0 and 7.50% of the total Chl-*a* biomass, respectively (**Figure 2**). The nano-phytoplankton continued to dominate the Chl-*a* biomass (>60%) during the incubation in all the experimental treatments. On the final sampling day, there was a general trend of relatively lower percentages of micro-phytoplankton Chl-*a* biomass but higher percentage of nano-phytoplankton and pico-phytoplankton Chl-*a* biomass under higher temperature. The percentage of Chl-*a* biomass in the micro-phytoplankton group was in general lower in the elevated temperature (high temperature and combined) treatments, with the lowest value (14%) observed in the high temperature treatment. Comparatively, the percentage of total Chl-*a* in micro-phytoplankton was higher ($p < 0.05$, *t*-test) under rising pCO_2 when temperature was the same, with the highest value of 33.2% in the high CO_2 treatment. In contrast, the percentage of nano-phytoplankton increased under elevated temperature but decreased with rising pCO_2, with the highest value (81.4%) in the high temperature treatment and lowest percentage (64.0%) under high CO_2. The percentage of Chl-*a* biomass as pico-phytoplankton was small but showed a similar trend with that of the nano-phytoplankton, with the highest and lowest percentages of pico-phytoplankton being 4.6 and 2.8% under high temperature and high CO_2, respectively ($p < 0.05$, *t*-test, between the two treatments).

Species Composition of the Phytoplankton Assemblage

Microscopic cell counts indicated that the dominant phytoplankton group was diatoms throughout the time course of the incubation, with initial diatom and dinoflagellate abundances of 1090 cells L^{-1} and 300 cells L^{-1}, respectively. On the final sampling day, there were significant differences in the abundances of diatoms (**Figure 3A**) and dinoflagellates (**Figure 3B**) under different temperature and pCO_2 treatments. Diatom abundance was significantly lower (~0.5 fold, $p < 0.05$) in the high pCO_2 and combined treatments compared to the control ($4.518 \pm 0.468 \times 10^4$ cells L^{-1}) and high temperature treatments ($4.221 \pm 0.293 \times 10^4$ cells L^{-1}). However, at the same pCO_2 level, there was no significant difference between different temperature treatments ($p > 0.05$). The dinoflagellate abundance was highest in the high temperature treatment (1016 ± 155 cells L^{-1}, 5.6 fold of the control value). Compared to the control treatment (180 ± 122 cells L^{-1}, the abundance of dinoflagellates was also significantly higher in the high pCO_2 treatment (653 ± 151 cells L^{-1}). However, there was no significant difference between the control and combined treatments. The ratio of diatom to dinoflagellates abundances was highest at control (**Figure 3C**). The ratio significantly decreased by 89, 87, and 74% at high pCO_2, high temperature and combined treatments, respectively.

The species composition of the diatom community was also affected by the CO_2 and temperature treatments. The full list of diatom and dinoflagellate species and their abundances at the beginning and the four experimental treatments on the final sampling day of the incubation are listed in **Table 1**. The two most dominant diatom species at the beginning of the incubation were the centric species *Thalassiosira pacifica* (accounting for 55.91% of the total cell abundance on T0) and the pennate diatom

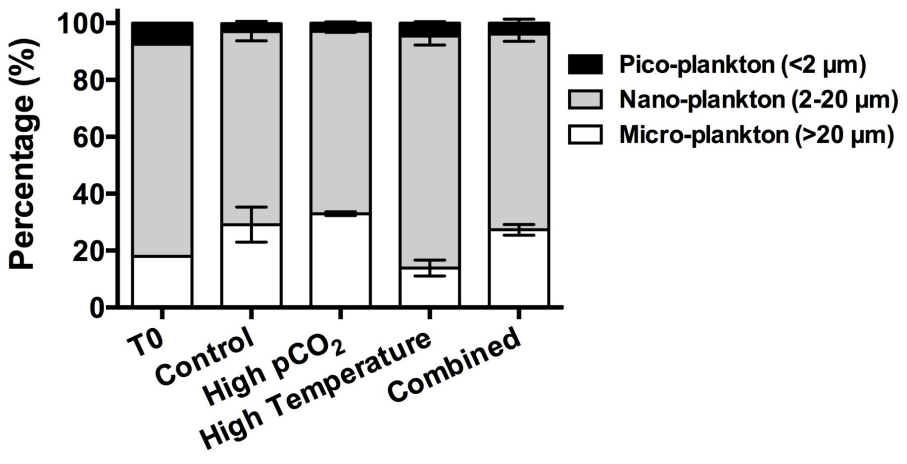


FIGURE 2 | Chl-*a* biomass percentages of micro-phytoplankton (>20 μm), nanoplankton (2–20 μm), and picoplankton (0.2–2 μm) in the beginning of the incubation (T0) and in the four experimental treatments on the final sampling day. Values are the means and error bars are the standard deviations of triplicates.

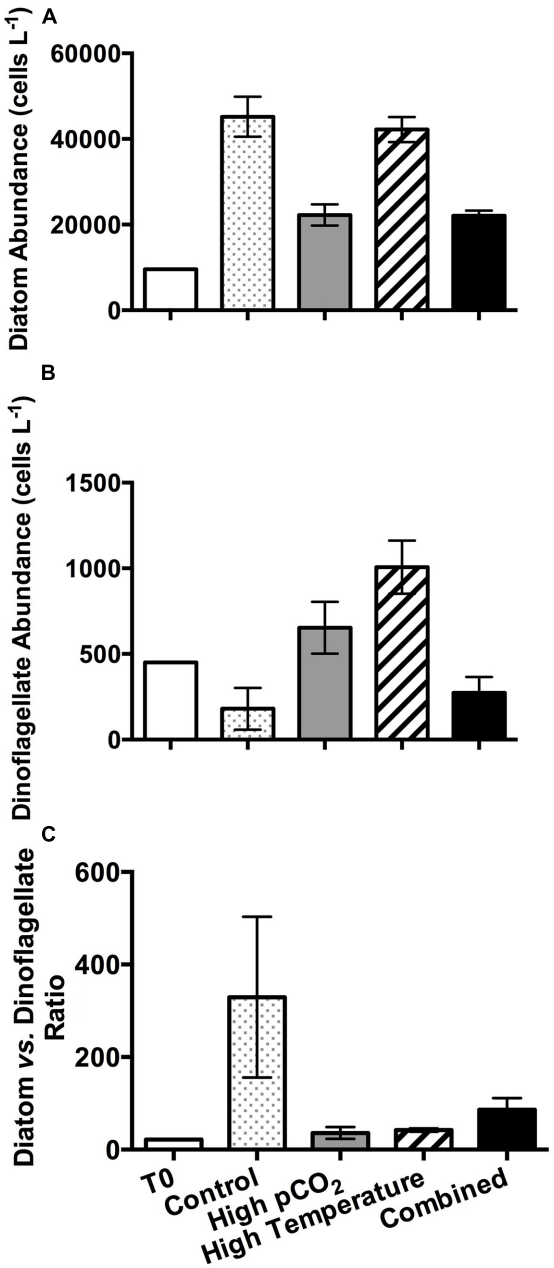


FIGURE 3 | Cell abundances of **(A)** diatoms and **(B)** dinoflagellates and **(C)** ratio of diatom to dinoflagellate abundances in the beginning of the incubation (T0) and in the four experimental treatments on the final sampling day. Values are the means and error bars are the standard deviations of triplicates.

Navicula sp. (18.12%). They continued to be the dominant centric and pennate diatom species respectively in the end of the incubation (**Table 1**). On the final sampling day, both the centric and pennate diatom abundances were significantly lower in the high pCO_2 and combined treatments, compared to the control and high temperature treatments (**Figure 4A**). The lowest abundance of centric diatoms was observed in the high pCO_2 treatment (0.57 fold of the control value), while the abundance of pennate diatoms was lowest in the combined treatment (10% of the control value). In contrast, the ratio of centric to pennate diatom abundance was significantly higher under the higher pCO_2 level, with the highest ratio of 9.8 ± 3.0 (ninefold of the control value) in the combined treatment (**Figure 4B**). Similarly, in the combined treatment, the abundance of the dominant centric diatom species *Thalassiosira pacifica* was highest, while that of the dominant pennate diatom species *Navicula* spp. was lowest among all the four experimental treatments (**Figure 4C**).

Elemental Composition and Community Sinking Rate

The average POC concentration was higher under higher pCO_2, especially with a significantly higher value in the combined treatment relative to the high temperature treatment (**Figure 5A**, $p < 0.05$). Similar to diatom concentration, the BSi concentrations were significantly lower in at higher pCO_2 when temperature was the same (**Figure 5B**, $p < 0.05$). Changing temperature alone had no significant effect on POC; while elevated temperature significantly increased BSi concentration at both pCO_2 levels ($p < 0.05$). The POP concentration was lowest (**Supplementary Data Sheet**) in the high pCO_2 treatment, with no significant difference among the other three treatments. However, there were no significant differences in PON concentrations in the four experimental treatments (**Supplementary Data Sheet**).

Both the POC to PON (C:N) and POC to POP (C:P) ratios were highest in the high pCO_2 treatment (**Figures 6A,B**); whereas there were no significant differences among the other three treatments (**Figures 6A,B**). Similarly, the POC to BSi (C:BSi) ratios were also significantly higher in the high pCO_2 and combined treatments compared to the control and high temperature treatments, with the highest ratio observed under high pCO_2 (25 ± 4, more than twofold of the control value, **Figure 6D**).

The sinking rate of the whole phytoplankton community was lowest in the combined treatment (0.12 ± 0.01 m d^{-1}, half of the control value), which coincided with the markedly higher centric:pennate diatom ratio in this treatment. However, there was no statistically significant difference among the other three treatments (**Figure 7**).

Individual and Interactive Effects of CO_2 and Temperature

The results of two-way ANOVA (**Table 2**) indicate that CO_2 had significant effects on most of the parameters sampled on the final sampling day, including the total diatom, centric diatom and pennate diatom abundances, ratios of diatom vs. dinoflagellate and centric vs. pennate abundances, POC and BSi concentrations, C:N, C:P, C:BSi and sinking rate of the community. Temperature had significant effects on dinoflagellate and pennate diatom abundances, ratios of diatom vs. dinoflagellate and centric vs. pennate abundances, BSi concentration and C:BSi.

For the two-way factorial interaction, CO_2 and temperature had significant interactive effects on the dinoflagellate and pennate diatom abundances, centric vs. pennate ratio and

TABLE 1 | List of all diatom and dinoflagellate species and the cell abundances (cells L^{-1}) identified with microscopy on T0 and the four experimental treatments on the final sampling day and cell volume of the dominant species.

Phytoplankton Species	Sampling Day and Treatments										Cell Volume
	T0		Control		High pCO_2		High Temperature		Combined		
	Cell Abundance	%	Cell Abundance	%	Cell Abundance	%	Cell Abundance	%	Cell Abundance	%	μm^3
Diatoms		95.7		99.7		97.1		97.6		98.7	
Centric Diatoms		70.3		50.6		60.1		53.8		88.6	
Thalassiosira pacifica	1.2×10^4	55.9	$(6.6 \pm 3.0) \times 10^3$	15.3	$(6.5 \pm 0.9) \times 10^3$	28.5	$(4.9 \pm 1.2) \times 10^3$	11.4	$(1.0 \pm 0.1) \times 10^4$	45.9	5655
Thalassiosira rotula	440	2.1	$(2.9 \pm 1.1) \times 10^3$	6.7	$(2.4 \pm 0.3) \times 10^3$	10.5			$(2.3 \pm 0.8) \times 10^3$	10.6	5741
Thalassiosira spp.					$(1.3 \pm 0.2) \times 10^3$	5.7	$(1.5 \pm 0.2) \times 10^3$	3.5	$(1.8 \pm 0.4) \times 10^3$	8.3	5842
Leptocylindrus danicus	690	3.3	$(6.1 \pm 0.4) \times 10^3$	14.1	$(1.4 \pm 0.4) \times 10^3$	6.1	$(4.8 \pm 1.2) \times 10^3$	11.2	$(1.4 \pm 0.5) \times 10^3$	6.4	
Paralia sulcata	520	2.5			293 ± 70	1.2	680 ± 140	1.6			
Climacodium biconcavum	460	2.2	$(2.9 \pm 0.2) \times 10^3$	6.7	307 ± 141	1.3	$(3.2 \pm 0.4) \times 10^3$	7.5	$(1.3 \pm 0.2) \times 10^3$	6.0	
Climacodium frauenfeldianum			273 ± 189	0.6					680 ± 330	3.1	
Ditylum brightwellii	420	2.0	$(1.4 \pm 0.1) \times 10^3$	3.2	253 ± 179	1.1	487 ± 94	1.1	233 ± 90	1.1	
Cyclotella striata	320	1.5	$(1.5 \pm 0.4) \times 10^3$	3.5	387 ± 90	1.7	$(3.7 \pm 0.8) \times 10^3$	8.6	$(1.0 \pm 0.2) \times 10^3$	4.6	
Guinardia delicatula	100	0.5	160 ± 53	0.4	393 ± 61	1.7	440 ± 60	1.0	260 ± 20	1.2	
Guinardia striata					460 ± 40	2.0	640 ± 72	1.5	260 ± 72	1.2	
Chaetoceros sp.	40	0.2							47 ± 30	0.2	
Coscinodiscus sp.	20	0.1	13 ± 23	0.03	34 ± 41	0.1	33 ± 42	0.1			
Detonula pumila							$(2.7 \pm 0.3) \times 10^3$	6.3			
Pennate Diatoms		25.4		49.1		37.0		43.8		10.1	
Navicula sp.	3.8×10^3	18.2	$(8.6 \pm 0.9) \times 10^3$	19.9	$(3.3 \pm 0.6) \times 10^3$	14.5	$(8.4 \pm 2.4) \times 10^3$	19.6	$(1.3 \pm 0.5) \times 10^3$	6.0	1500
Pinnularia spp.	680	3.3	$(5.6 \pm 2.8) \times 10^3$	13.0	$(3.1 \pm 1.2) \times 10^3$	13.6	$(4.4 \pm 0.6) \times 10^3$	10.3	420 ± 381	1.9	
Pseudonitzschia pungens	260	1.2	647 ± 179	1.5	$(1.3 \pm 0.1) \times 10^3$	5.7	640 ± 87	1.5			
Synedra sp.	240	1.2	113 ± 128	0.3	280 ± 87	1.2	360 ± 92	0.8	253 ± 42	1.2	
Nitzschia spp.	160	0.8	532 ± 61	1.2			460 ± 156	1.1			
Nitzschia longissima	80	0.4	$(5.7 \pm 3.8) \times 10^3$	13.2	460 ± 69	2.0	$(4.2 \pm 1.0) \times 10^3$	9.8	220 ± 104	1.0	
Pleurosigma sp.	60	0.3									
Thalassiothrix longissima							340 ± 69	0.8			
Dinoflagellates		4.3		0.3		2.9		2.4		1.3	
Gymnodinium sp.	460	2.2	146 ± 155	0.3	240 ± 20	1.1	326 ± 61	0.8	73 ± 11	0.3	
Oxytoxum parvum	400	1.9			260 ± 72	1.1	680 ± 171	1.6	220 ± 80	1.0	
Podolampas palmipes	40	0.2			153 ± 99	0.7					

The errors are the standard deviations of the triplicate values. The percentage values were calculated based on the average abundance of the triplicate samples.

C:P (**Table 2**). Among these two-way interactive effects, CO_2 and temperature interaction had antagonistic effects on the dinoflagellate abundance, diatom vs. dinoflagellate ratio and C:P, but synergistic effects on the pennate diatom abundance and centric vs. pennate ratio.

DISCUSSION

This study reveals that phytoplankton community size and species composition, elemental ratios, and the sinking rate of the phytoplankton community collected from the Tianjin coastal area all responded to increased pCO_2 and/or warming. Apart from the individual effects, the interaction of CO_2 and temperature had significant interactive effects on some of the examined parameters, thus having implications for marine biogeochemistry in the future environment. It is noteworthy that our continuous incubation experiment is different from the commonly used short-term batch/grow-out culture technique. This continuous incubation method allows the acclimation of the natural phytoplankton assemblage to the experimental conditions for a much longer period of time (21 days in our study). Community changes in a continuous culture system reflect differences in the growth rates of individual phytoplankton species under the experimental conditions, as faster-growing species come to dominate the assemblage

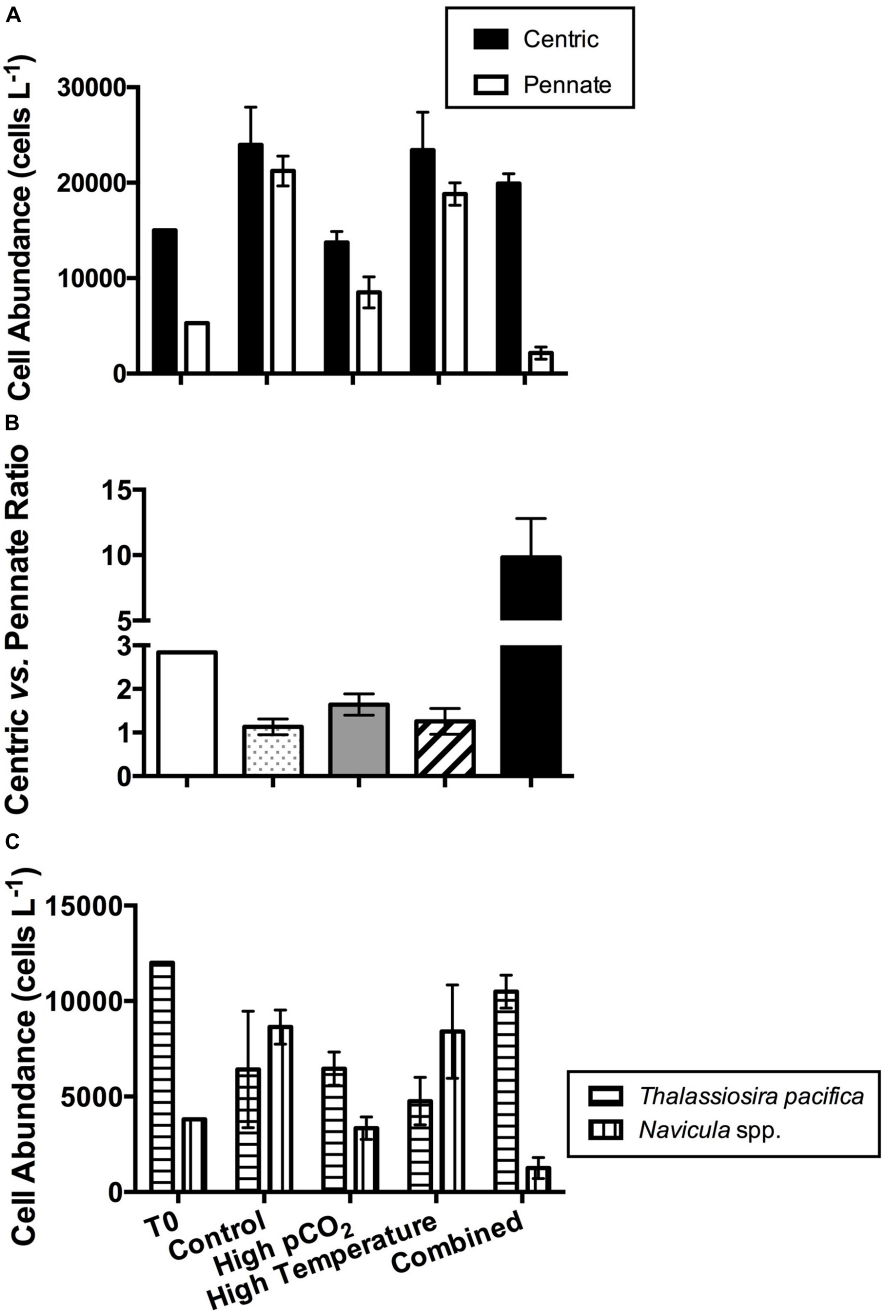


FIGURE 4 | Diatom assemblage composition in the four experimental treatments in the beginning of the incubation (T0) and on the final sampling day: **(A)** cell abundances of centric and pennate diatoms; **(B)** ratio of centric diatom to pennate diatom cell abundances; **(C)** cell abundances of dominant diatom species. Values are the means and error bars are the standard deviations of triplicates.

while slower-growing species are 'washed out' by dilution. In addition, nutrient enrichment, the "bottle effects" and excluding the large grazers may favor certain phytoplankton groups such as diatoms (Buma et al., 1991; Litchman et al., 2007), as suggested by the differences in the sampled parameters between T_0 and T_{final} in our study. Nevertheless, it allows our final sampling to reflect the responses of the natural phytoplankton community to the environmental changes under a relatively steady growth phase (Hutchins et al., 2003; Feng et al., 2009).

Phytoplankton Community Size Structure

The total phytoplankton Chl-*a* biomass was significantly promoted by warming, especially during the batch growth

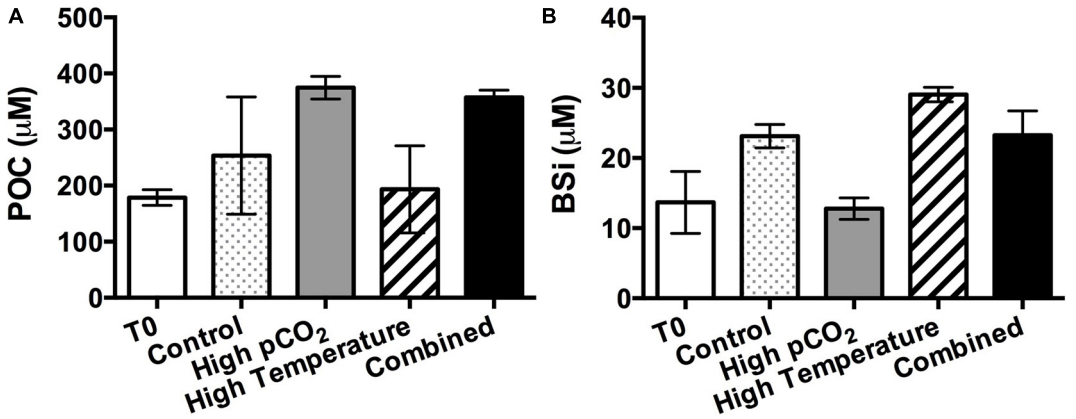


FIGURE 5 | Particulate organic carbon (POC, **A**) and biogenic silica (BSi, **B**) concentrations in the beginning of the incubation (T0) and in the four experimental treatments on the final sampling day. Values are the means and error bars are the standard deviations of triplicates.

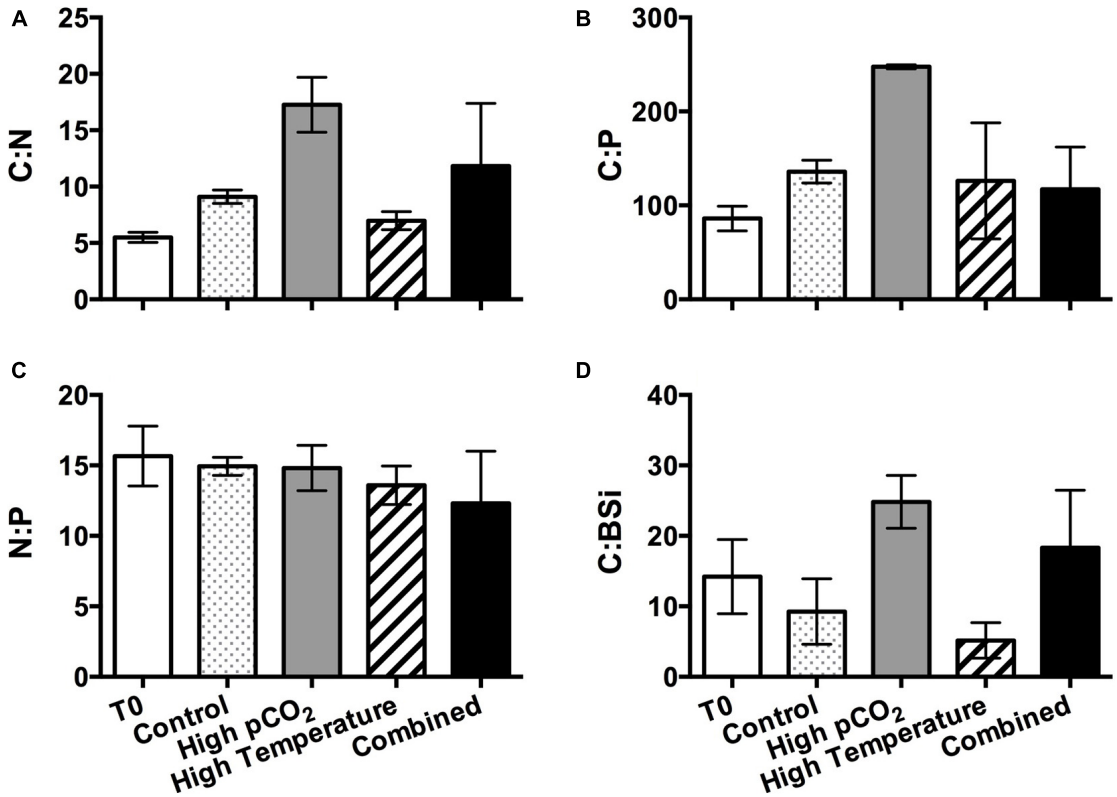


FIGURE 6 | Elemental molar ratios in the beginning of the incubation (T0) and in the four experimental treatments on the final sampling day: **(A)** particulate organic carbon to particulate organic nitrogen ratio (C:N); **(B)** particulate organic carbon to particulate organic phosphorus ratio (C:P); **(C)** particulate organic nitrogen to particulate organic phosphorus ratio (N:P); and **(D)** particulate organic carbon to biogenic silica ratio (C:BSi). Values are the means and error bars are the standard deviations of triplicates.

mode in the first few days with higher values in the high temperature and combined treatments (**Figure 1**). This warming effect is similar to some previous studies on spring phytoplankton assemblages in both coastal regions (Lee et al., 2019) and the open ocean (Feng et al., 2009), mainly due to the thermal stimulation of phytoplankton metabolism within a favorable temperature range (Eppley, 1972). However, a mesocosm study using a phytoplankton assemblage in the coastal Kiel Fjord showed an opposite trend of decreased Chl-*a* biomass under warming, mainly due to the fact that temperature increases of 6°C promoted zooplankton grazing more than phytoplankton growth (Sommer et al., 2015). In our study, however, we deliberately

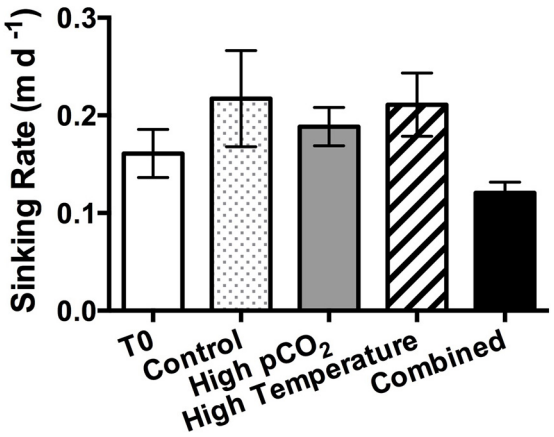


FIGURE 7 | Sinking rates of the phytoplankton community in the beginning of the incubation (T0) and in the four experimental treatments on the final sampling day. Values are the means and error bars are the standard deviations of triplicates.

removed or reduced larger zooplankton numbers at the outset of the study using a coarse mesh screen, yielding much weakened grazing pressure on the phytoplankton biomass, with only few microzooplankton cells detected in the T0 samples. The removal of large grazers, together with the nutrient enrichment, also resulted in the rapid increase in the total Chl-*a* concentration in all the incubation bottles during the batch growth mode.

Size-fractionated Chl-*a* biomass changes suggested that the size of the phytoplankton assemblage may be affected by both temperature and pCO_2. Warming greatly reduced the relative biomass percentage of larger micro-plankton cells, while increasing the nano-plankton and pico-plankton percentages (**Figure 2**). This trend is consistent with some previously published results, showing that elevated temperature may favor smaller species in competition at the community level (Hare et al., 2007a; Daufresne et al., 2009), or simply decrease the cell-size of some species when they grow faster (Atkinson et al., 2003; Sheridan and Bickford, 2011). On the other hand, the larger cell (>20 μm) contribution to total Chl-*a* biomass was increased by CO_2 enrichment under both temperature conditions in our study, and yielded the highest relative abundance of micro-plankton in the high pCO_2 treatment. There is no compelling evidence of CO_2 effects on cell size within individual species (reviewed by Finkel et al., 2010). Therefore, the changes in community size structure were mainly caused by shifts in phytoplankton species, in agreement with a previous study conducted off the coast of Norway (Engel et al., 2008). Compared to small phytoplankton cells, the growth of larger phytoplankton species tends to be more favored by CO_2 enrichment, mainly due to differences in CCM and/or diffusion boundary layer thicknesses (Raven et al., 2008; Finkel et al., 2010).

Phytoplankton Dominance Shifts

Along with the effects of CO_2 and warming on the size structure of the phytoplankton assemblage, changes in CO_2/temperature also caused shifts in the taxonomic composition of the phytoplankton assemblage in our study. Due to the constraints of the microscopic method that small phytoplankton cells (<5 μm) are harder to be distinguished, the species determined here mostly belonged to the micro-plankton and nano-plankton groups. Here we observed that the abundance of dinoflagellates was especially promoted in the high temperature treatment (**Figure 3B**). Although diatoms generally grow much faster than dinoflagellates at the same temperature (Chen and Laws, 2017), the distribution of many dinoflagellate species tends to be more favored in warm waters, compared to diatoms (Finkel et al., 2010; Xiao et al., 2018). Nevertheless,

TABLE 2 | The individual and multiplicative effects of temperature and CO_2 and types of driver interactions on the parameters of the final sampling day of the experiment.

Parameter	CO_2	Temperature	Interaction	Individual effect (%)		Multiplicative effect (%)		Type of interaction
				CO_2	Temperature	Observed	Calculated	
Diatom abundance	*	–	–	–51				
Dinoflagellate abundance	–	*	*	262	459	52	1929	Antagonism
Diatoms vs. dinoflagellates	*	*	*	–89	–87	–74	–99	Antagonism
Centric diatom abundance	*	–	–	–43				
Pennate diatom abundance	*	*	*	–60	–11	–90	–64	Synergism
Centric vs. pennate	*	*	*	45	11	769	61	Synergism
POC concentration	*	–	–	48				
BSi concentration	*	*	–	–45	26			
N:P	–	–	–					
C:N	*	–	–	–45				
C:P	*	–	*	82	–7	–14	69	Antagonism
C:BSi	*	*	–	205	–44			
Sinking rate	*	–	–	–13				

"" represents significance and "–" represents non-significance at the p = 0.05 level using two-way ANOVA test.*
Individual/multiplicative effect was only calculated when there was statistical significance. Types of interaction were only determined for the parameters that CO_2 and temperature had significant interactive effects on. The full two-way ANOVA results can be found in ***Supplementary Table S2****.*

dinoflagellate abundance decreased again in the combined treatment, likely due to the outcome of competition with other nano-phytoplankton and pico-plankton groups. In coastal regions, diatoms and dinoflagellates are the major dominating phytoplankton functional groups (Smayda and Reynolds, 2003). The ratio of diatoms to dinoflagellates is considered to be an environmental indicator, with higher diatoms: dinoflagellates values indicating better seawater quality (Wasmund et al., 2017) and alleviating the eutrophication problem of the water column (Spilling et al., 2018). Changes in phytoplankton species composition may affect the food quality provided to the upper food web (Rose et al., 2009) and reproduction of the zooplankton, with higher copepod reproduction related to relative higher dinoflagellates abundance (Vehmaa et al., 2011). In addition, during costal spring blooms with low grazing pressure, sinking of ungrazed phytoplankton cells contributes to the bottom hypoxia. Diatom cells tend to sink out of the surface layer faster than dinoflagellates and these generally larger cells consume more oxygen during degradation in the subsurface waters; hence, decrease in diatom abundance likely results in reduced oxygen demand of the bottom water in the coastal regions (Spilling and Lindström, 2008). Our results suggest that the proportion of diatoms to dinoflagellates significantly decreased when either pCO_2 or temperature was increased individually or simultaneously, indicating a potential negative feedback of future climate change on the oxygen demand in bottom waters in the Bohai Bay area, as demonstrated for the Baltic Sea (Wasmund et al., 2017).

Both diatom abundance and species composition was significantly affected by changes in pCO_2 (**Figure 3A**). The diatom RubisCO enzyme tends to have a high affinity for CO_2, supplied by efficient CCMs (Gao and Campbell, 2014), and thus diatom photosynthesis may be already saturated under present day CO_2 conditions (Burkhardt et al., 2001; Rost et al., 2003). As a result, although diatoms were still dominant in the phytoplankton assemblage, total diatom abundance as well as centric and pennate diatom abundances were not promoted, but rather all decreased at higher pCO_2 in our study (**Figure 4**). This is most likely due to the outcome of the competition with other phytoplankton groups that were favored more under higher pCO_2. Similarly, a study on the South China Sea phytoplankton community also found diatom abundance declined with elevated CO_2 (Gao et al., 2012). However, the abundance of the dominant centric diatom species *T. pacifica* and the centric vs. pennate diatom ratio showed an opposite trend in our study. The higher centric vs. pennate diatom ratio observed in our study is consistent with previous findings of CO_2 enrichment experiments on the Southern Ocean phytoplankton community, which also reported larger centric diatoms were favored more under rising pCO_2 (Tortell et al., 2008; Feng et al., 2010), further indicating differential responses to CO_2 among different diatom taxonomic groups (Wu et al., 2014). By synthesizing the results of more than a decade research on natural diatom communities responses to OA, Bach and Taucher (2019) also found that more than 65% of the experiments showed changes in diatom species composition with a trend of shifting toward larger species. The taxonomic changes toward larger cells may in turn accelerate the energy transfer efficiency into higher trophic levels in marine food web (Bach and Taucher, 2019). In our study, the centric vs. pennate diatom ratio was further increased in the combined treatment, suggesting potential further influence on the energy transfer in the food web of Bohai Bay area in the future climate change scenario.

Elemental Stoichiometry and Sinking Rate

As a consequence of the shifts in phytoplankton species composition and the direct intra-specific physiological responses to the experimental conditions under different temperature and CO_2 levels, our results also showed significant changes in the elemental composition (POC and BSi concentrations, C:N, C:P, and C:BSi, **Figure 6**) of the phytoplankton community. The significantly higher C:N and C:P ratios in the high pCO_2 treatment were consistent with the results of previous laboratory studies on phytoplankton, including isolates of cyanobacteria (Fu et al., 2007), coccolithophores (Feng et al., 2008), and diatoms (Burkhardt and Riebesell, 1997). This finding likely indicates that CO_2 enrichment promotes carbon fixation more than N and P uptake, and may further have implications on predicting the elemental stoichiometry of the organic matter export by marine phytoplankton into the deeper layers. Nevertheless, Taucher et al. (2020) synthesized the data of *in situ* manipulation experiments on natural plankton community and observed OA-induced 20% increase to 17% decrease in C:N export ratio in the sinking particles. Their results also suggest the C:N export ratio can be regulated greatly by plankton feeding and microbial degradation, as well as other environmental drivers such as temperature and nutrient availability (Taucher et al., 2020 and references therein).

Another significant trend was the increased C:BSi ratios under CO_2 enrichment mainly caused by enhanced POC accumulation and reduced BSi concentration under higher pCO_2. The latter may be attributed not only to reduced total diatom abundance, but also to decreased BSi production by diatoms. Milligan et al. (2004) reported enhanced efflux of silicate from the diatom cells at high pCO_2 while silicate influx was not changed; as a result, the cellular silica quota was reduced with elevated pCO_2 (Milligan et al., 2004). A study on a Southern Ocean diatom assemblage also found decreased community silica production under seawater acidification, but with strain-specific responses (Petrou et al., 2019). In general, mean silica production has a linear relationship with the surface area of diatom cells (McNair et al., 2018), but is not necessarily correlated with the growth rate (Petrou et al., 2019). However, the complete mechanisms of CO_2 regulation of BSi production are still not clearly understood. The silica cell walls of diatoms are considered in the context of functions that include defense from grazing (Hamm et al., 2003) and ballast for sinking and carbon export (Buesseler, 1998). As such, further understanding the regulatory mechanisms for BSi production in the changing marine environment will help to unravel the impacts of environmental changes on carbon export in diatom-dominated waters.

In our study, the sinking rate of the phytoplankton assemblage was lowest in the combined treatment, mainly affected by pCO_2

based on the two-way ANOVA results, despite the lowest BSi concentration being observed in the high pCO_2 treatment. Although the ballasting effect of BSi is an important factor driving the sinking rate of diatoms, the reduced sinking rate in the combined treatment might be attributed to the changes in phytoplankton species composition instead. Compared to the other three experimental treatments, the abundance of the dominant centric diatom species *T. pacifica* was remarkably higher in the combined treatment (**Table 1** and **Figure 4C**). It is noteworthy that *T. pacifica* is a chain-forming species, and the formation of chains can influence buoyancy and slow the sinking rates of the cells (Smayda and Boleyn, 1966). On top of that, the chain length of the chain-forming diatoms tends to increase with rising pCO_2 as in the case of *Asterionellopsis glacialis* (Barcelos e Ramos et al., 2014), while the size of the phytoplankton community may be decreased under elevated temperature, together further reducing the sinking rate in the combined treatment (Denny, 1993). The sinking rate of a phytoplankton community can also be affected the production of transparent exopolymer particles (TEP), which have lower density but facilitate the cells to form large aggregates (Alldredge and Jackson, 1995). As the carbon production in the surface layer is the major contributor of carbon export to depth (Tréguer et al., 2018), if our finding represents a general future trend, OA and warming together may weaken carbon export from the surface layer in diatom-dominated coastal environments. However, we also should consider that, in the real oceanic environment, the actual carbon export to depth will generally be further influenced by grazing and remineralization processes (Armstrong et al., 2002).

Driver Interactions and Implications for the Coastal Biogeochemistry Under Global Change

The findings of our study suggest that both the individual and interactive effects of OA and warming are important to consider for coastal phytoplankton assemblages. There is clear evidence that many environmental drivers are already changing simultaneously in coastal and oceanic regions, including ocean acidification, warming, deoxygenation, changes in nutrient supply, and surface irradiance regimes (IPCC, 2014; Hutchins and Fu, 2017). Therefore, it is urgent to understand the cumulative effects of multiple drivers on the marine biota, and disentangle the interactive patterns of these drivers (Boyd et al., 2018). Our results suggest that CO_2 and temperature synergistically affected pennate diatom abundance and the centric vs. pennate diatom ratio, and had antagonistic effects on dinoflagellate abundance and the ratio of diatom:dinoflagellate abundances. The cumulative effects of OA and warming together may either "amplify" or "shrink" the effects of the individual-driver effects, further emphasizing the importance of considering multiple driver interactions for predicting the biogeochemical responses to future environmental changes. Similarly, a study on the South China Sea phytoplankton community observed that although OA and warming alone promoted the phytoplankton productivity, the combination of the two drivers had an antagonistic effect (Zhang et al., 2018). Sett et al. (2018) also reported strongly shifted diatom species composition by the combined effect of OA and warming. During the past decade, many studies have focused on examining the combined effects of OA and other environmental drivers on natural phytoplankton community (Bach and Taucher, 2019 and references therein). Future work also needs to compile the published results and synthesize the general patterns of the interactive effects of OA and warming on natural phytoplankton assemblages in different oceanic regions.

Overall, our study on a spring bloom phytoplankton assemblage reveals that under future environmental conditions when both OA and warming effects are considered, the centric to pennate diatom ratio will increase, while the diatom:dinoflagellate ratio and phytoplankton-induced sinking rate will significantly decrease in the coastal Bohai Bay area. These changes may further impact carbon export and elemental cycles in the coastal ecosystem, and may impact food and nutritional availability to higher trophic levels, thus affecting coastal fisheries. However, there are limitations to how far we can extrapolate our findings. Our study examined CO_2 and warming effects using a coastal phytoplankton assemblage acclimated to constant experimental conditions. In contrast, CO_2/temperature variability is generally high in the coastal environment (Dai et al., 2009; Li et al., 2016; Kling et al., 2020), especially in regions highly influenced by anthropogenic activities like Bohai Bay. Consequently, coastal phytoplankton assemblages may possess relatively high tolerance limits to thermal and CO_2 shifts. Future studies are needed that examine the effects of ocean acidification and warming in the context of natural fluctuations in pCO_2 and temperature in coastal ecosystems.

DATA AVAILABILITY STATEMENT

The original contributions presented in the study are included in the article/**Supplementary Material**, further inquiries can be directed to the corresponding author/s.

AUTHOR CONTRIBUTIONS

YF designed the study. YL, PL, and TZ conducted the experiments. YL, PL, TZ, TC, and FF analyzed the samples. YF, FC, MW, FF, and DH thoroughly discussed the results and interpreted the data. YF, FC, MW, and DH wrote the manuscript with contributions from all co-authors. All the authors contributed to the article and approved the submitted version.

FUNDING

This work was supported by the National Natural Science Foundation of China grants (nos. 41676160 and 41306118), the Tianjin Natural Science Foundation (19JCYBJC22900), Tianjin Municipal Education Commission Project (2017KJ014), and the open fund of State Key Laboratory of Satellite Ocean

Environment Dynamics, Second Institute of Oceanography (QNHX1803) to YF, and US National Science Foundation grants (OCE 1638804 and OCE 1851222) to DH.

ACKNOWLEDGMENTS

We would like to thank undergraduate students Dandan Hou, Meiqi Li, and Wenzhang Feng at Tianjin University of Science and Technology for helping with seawater collection and experimental setup. We also thank Dr. Guisheng Song's laboratory at Tianjin University for analyzing the dissolved inorganic carbon concentration.

SUPPLEMENTARY MATERIAL

The Supplementary Material for this article can be found online at: https://www.frontiersin.org/articles/10.3389/fmars.2021.622319/full#supplementary-material

REFERENCES

Alldredge, A. L., and Jackson, G. A. (1995). Aggregation in marine systems — preface. *Deep Sea Res. II* 42, 1–7. doi: 10.1016/s0924-7963(02)00049-0

Armstrong, R. A., Lee, C., Hedges, J. I., Honjo, S., and Wakeham, S. G. (2002). A new mechanistic model for organic carbon fluxes in the ocean based on the quantitative association of POC with ballast minerals. *Deep Sea Res. II* 49, 219–236. doi: 10.1016/s0967-0645(01)00101-1

Atkinson, D., Ciotti, B. J., and Montagnes, D. J. S. (2003). Protists decrease in size linearly with temperature: CA. 2.5% degrees C-1. *Proc. R. Soc. B Biol. Sci.* 270, 2605–2611. doi: 10.1098/rspb.2003.2538

Bach, L. T., and Taucher, J. (2019). CO_2 effects on diatoms: a synthesis of more than a decade of ocean acidification experiments with natural communities. *Ocean Sci.* 15, 1159–1175. doi: 10.5194/os-15-1159-2019

Barcelos e Ramos, J., Schulz, K. G., Brownlee, C., Sett, S., and Azevedo, E. B. (2014). Effects of increasing seawater carbon dioxide concentrations on chain formation of the diatom *Asterionellopsis glacialis*. *PLoS One* 9:e90749. doi: 10.1371/journal.pone.0090749

Beaufort, L., Probert, I., de Garidel-Thoron, T., Bendif, E. M., Ruiz-Pino, D., Metzl, N., et al. (2011). Sensitivity of coccolithophores to carbonate chemistry and ocean acidification. *Nature* 476, 80–83. doi: 10.1038/nature10295

Bienfang, P. K. (1981). SETCOL—a technologically simple and reliable method for measuring phytoplankton sinking rates. *Can. J. Fishe. Aquat. Sci.* 38, 1289–1294. doi: 10.1139/f81-173

Bopp, L., Resplandy, L., Orr, J. C., Doney, S. C., Dunne, J. P., Gehlen, M., et al. (2013). Multiple stressors of ocean ecosystems in the 21st century: projections with CMIP5 models. *Biogeosciences* 10, 6225–6245. doi: 10.5194/bg-10-6225-2013

Boyd, P. W., Collins, S., Dupont, S., Fabricius, K., Gattuso, J. P., Havenhand, J., et al. (2018). Experimental strategies to assess the biological ramifications of multiple drivers of global ocean change—a review. *Glob. Chang. Biol.* 24, 2239–2261. doi: 10.1111/gcb.14102

Boyd, P. W., and Hutchins, D. A. (2012). Understanding the responses of ocean biota to a complex matrix of cumulative anthropogenic change. *Mar. Ecol. Prog. Ser.* 470, 125–135. doi: 10.3354/meps10121

Brzezinski, M. A., and Nelson, D. M. (1995). The annual silica cycle in the Sargasso Sea near Bermuda. *Deep Sea Res. Part I Oceanogr. Res. Pap.* 42, 1215–1237. doi: 10.1016/0967-0637(95)93592-3

Buesseler, K. O. (1998). The decoupling of production and particulate export in the surface ocean. *Glob. Biogeochemi. Cycles* 12, 297–310. doi: 10.1029/97gb03366

Buma, A. G., De Baar, H. J., Nolting, R. F., and Van Bennekom, A. J. (1991). Metal enrichment experiments in the Weddell—Scotia Seas: effects of iron and manganese on various plankton communities. *Limnol. Oceanogr.* 36, 1865–1878. doi: 10.4319/lo.1991.36.8.1865

Burkhardt, S., Amoroso, G., Riebesell, U., and Sultemeyer, D. (2001). CO_2 and HCO_3^- uptake in marine diatoms acclimated to different CO_2 concentrations. *Limnol. Oceanogr.* 46, 1378–1391. doi: 10.4319/lo.2001.46.6.1378

Burkhardt, S., and Riebesell, U. (1997). CO_2 availability affects elemental composition (C: N: P) of the marine diatom *Skeletonema costatum*. *Mar. Ecol. Prog. Ser.* 155, 67–76. doi: 10.3354/meps155067

Burkhardt, S., Zondervan, I., and Riebesell, U. (1999). Effect of CO_2 concentration on C: N: P ratio in marine phytoplankton: a species comparison. *Limnol. Oceanogr.* 44, 683–690. doi: 10.4319/lo.1999.44.3.0683

Cai, W.-J., Hu, X., Huang, W.-J., Murrell, M. C., Lehrter, J. C., Lohrenz, S. E., et al. (2011). Acidification of subsurface coastal waters enhanced by eutrophication. *Nat. Geosci.* 4, 766–770. doi: 10.1038/ngeo1297

Caldeira, K., and Wickett, M. E. (2003). Anthropogenic carbon and ocean pH. *Nature* 425, 365–365. doi: 10.1038/425365a

Carton, J. A., and Giese, B. S. (2008). A reanalysis of ocean climate using simple ocean data assimilation (SODA). *Mon. Weather Rev.* 136, 2999–3017. doi: 10.1175/2007mwr1978.1

Chen, B., and Laws, E. A. (2017). Is there a difference of temperature sensitivity between marine phytoplankton and heterotrophs? *Limnol. Oceanogr.* 62, 806–817. doi: 10.1002/lno.10462

Dai, M., Lu, Z., Zhai, W., Chen, B., Cao, Z., Zhou, K., et al. (2009). Diurnal variations of surface seawater pCO_2 in contrasting coastal environments. *Limnol. Oceanogr.* 54, 735–745. doi: 10.4319/lo.2009.54.3.0735

Daufresne, M., Lengfellner, K., and Sommer, U. (2009). Global warming benefits the small in aquatic ecosystems. *Proc. Natl. Acad. Sci. U.S.A.* 106, 12788–12793. doi: 10.1073/pnas.0902080106

Denny, M. (1993). *Air and Water: The Biology and Physics of Life's Media*. Princeton, NJ: Princeton University Press.

Dickson, A. G., and Millero, F. J. (1987). A comparison of the equilibrium-constants for the dissociation of carbonic-acid in seawater media. *Deep Sea Res. Part A Oceanogr. Res. Pap.* 34, 1733–1743. doi: 10.1016/0198-0149(87)90021-5

Dickson, A. G., Sabine, C. L., and Christian, J. R. (2007). *Guide to Best Practices for Ocean CO_2 Measurements*. Sidney, BC: North Pacific Marine Science Organization.

Engel, A., Schulz, K. G., Riebesell, U., Bellerby, R., Delille, B., and Schartau, M. (2008). Effects of CO_2 on particle size distribution and phytoplankton abundance during a mesocosm bloom experiment (PeECE II). *Biogeosciences* 5, 509–521. doi: 10.5194/bg-5-509-2008

Eppley, R. W. (1972). Temperature and phytoplankton growth in the sea. *Fish. Bull.* 70, 1063–1085.

Falkowski, P. G., and Raven, J. A. (2007). *Aquatic Photosynthesis*. Princeton, NJ: Princeton University Press.

Feely, R. A., Doney, S. C., and Cooley, S. R. (2009). Ocean acidification: present conditions and future changes in a high-CO_2 world. *Oceanography* 22, 36–47. doi: 10.5670/oceanog.2009.95

Feng, L., and Lin, X.-P. (2009). Long-term trend of the east china sea surface temperature during 1945¯ 2006. *Period. Ocean Univ. China* 39, 13–18. (In Chinese with English abstract),

Feng, Y., Hare, C. E., Leblanc, K., Rose, J. M., Zhang, Y. H., Ditullio, G. R., et al. (2009). Effects of increased pCO_2 and temperature on the North Atlantic spring bloom. I. The phytoplankton community and biogeochemical response. *Mar. Ecol. Prog. Ser.* 388, 13–25. doi: 10.3354/meps08133

Feng, Y., Hare, C. E., Rose, J. M., Handy, S. M., Ditullio, G. R., Lee, P. A., et al. (2010). Interactive effects of iron, irradiance and CO_2 on Ross Sea phytoplankton. *Deep Sea Res. Part I Oceanogr. Res. Pap.* 57, 368–383. doi: 10.1016/j.dsr.2009.10.013

Feng, Y., Roleda, M. Y., Armstrong, E., Summerfield, T. A., Law, C. S., Hurd, C. L., et al. (2020). Effects of multiple drivers of ocean global change on the physiology and functional gene expression of the coccolithophore *Emiliania huxleyi*. *Glob. Chang. Biol.* 26, 5630–5645. doi: 10.1111/gcb.15259

Feng, Y., Warner, M. E., Zhang, Y., Sun, J., Fu, F. X., Rose, J. M., et al. (2008). Interactive effects of increased pCO_2, temperature and irradiance on the marine

coccolithophore *Emiliania huxleyi* (Prymnesiophyceae). *Eur. J. Phycol.* 43, 87–98. doi: 10.1080/09670260701664674

Finkel, Z. V., Beardall, J., Flynn, K. J., Quigg, A., Rees, T. A. V., and Raven, J. A. (2010). Phytoplankton in a changing world: cell size and elemental stoichiometry. *J. Plankton Res.* 32, 119–137. doi: 10.1093/plankt/fbp098

Fitzer, S. C., Torres Gabarda, S., Daly, L., Hughes, B., Dove, M., O'connor, W., et al. (2018). Coastal acidification impacts on shell mineral structure of bivalve mollusks. *Ecol. Evol.* 8, 8973–8984. doi: 10.1002/ece3.4416

Folt, C. L., Chen, C. Y., Moore, M. V., and Burnaford, J. (1999). Synergism and antagonism among multiple stressors. *Limnol. Oceanogr.* 44, 864–877. doi: 10.4319/lo.1999.44.3_part_2.0864

Fu, F. X., Warner, M. E., Zhang, Y. H., Feng, Y. Y., and Hutchins, D. A. (2007). Effects of increased temperature and CO_2 on photosynthesis, growth, and elemental ratios in marine *Synechococcus* and *Prochlorococcus* (Cyanobacteria). *J. Phycol.* 43, 485–496. doi: 10.1111/j.1529-8817.2007.00355.x

Gao, K., and Campbell, D. A. (2014). Photophysiological responses of marine diatoms to elevated CO_2 and decreased pH: a review. *Funct. Plant Biol.* 41, 449–459. doi: 10.1071/fp13247

Gao, K., Xu, J., Gao, G., Li, Y., Hutchins, D. A., Huang, B., et al. (2012). Rising CO_2 and increased light exposure synergistically reduce marine primary productivity. *Nat. Clim. Chang.* 2, 519–523. doi: 10.1038/nclimate1507

Hamm, C. E., Merkel, R., Springer, O., Jurkojc, P., Maier, C., Prechtel, K., et al. (2003). Architecture and material properties of diatom shells provide effective mechanical protection. *Nature* 421, 841–843. doi: 10.1038/nature01416

Hare, C. E., DiTullio, G. R., Riseman, S. F., Crossley, A. C., Popels, L. C., Sedwick, P. N., et al. (2007a). Effects of changing continuous iron input rates on a Southern Ocean algal assemblage. *Deep Sea Res. I* 54, 732–746. doi: 10.1016/j.dsr.2007.02.001

Hare, C. E., DiTullio, G. R., Trick, C. G., Wilhelm, S. W., Bruland, K. W., Rue, E. L., et al. (2005). Phytoplankton community structure changes following simulated upwelled iron inputs in the Peru Upwelling region. *Aquat. Microb. Ecol.* 38, 269–282. doi: 10.3354/ame038269

Hare, C. E., Leblanc, K., Ditullio, G. R., Kudela, R. M., Zhang, Y., Lee, P. A., et al. (2007b). Consequences of increased temperature and CO_2 for phytoplankton community structure in the Bering Sea. *Mar. Ecol. Prog. Ser.* 352, 9–16. doi: 10.3354/meps07182

Hutchins, D. A., and Fu, F. X. (2017). Microorganisms and ocean global change. *Nat. Microbiol.* 2:17508. doi: 10.1038/nmicrobiol.2017.58

Hutchins, D. A., Fu, F. X., Warner, M. E., Feng, Y., Portune, K., Bernhardt, P. W., et al. (2007). CO_2 control of *Trichodesmium* N_2 fixation, photosynthesis, growth rates, and elemental ratios: implications for past, present, and future ocean biogeochemistry. *Limnol. Oceanogr.* 52, 1293–1340. doi: 10.4319/lo.2007.52.4.1293

Hutchins, D. A., Mulholland, M. R., and Fu, F. X. (2009). Nutrient cycles and marine microbes in a CO_2-enriched ocean. *Oceanography* 22, 128–145. doi: 10.5670/oceanog.2009.103

Hutchins, D. A., Pustizzi, F., Hare, C. E., and Ditullio, G. R. (2003). A shipboard natural community continuous culture system for ecologically relevant low-level nutrient enrichment experiments. *Limnol. Oceanogr. Methods* 1, 82–91. doi: 10.4319/lom.2011.1.82

IPCC (2014). *Climate Change 2014: Synthesis Report. Contribution of Working Groups I, II and II to the FIfth Assessment Report of the Intergovernmental Panel on Climate Change*. Geneva: IPCC.

Joint, I., Doney, S. C., and Karl, D. M. (2011). Will ocean acidification affect marine microbes? *ISME J.* 5, 1–7. doi: 10.1038/ismej.2010.79

Kim, J.-M., Lee, K., Shin, K., Kang, J.-H., Lee, H.-W., Kim, M., et al. (2006). The effect of seawater CO_2 concentration on growth of a natural phytoplankton assemblage in a controlled mesocosm experiment. *Limnol. Oceanogr.* 51, 1629–1636. doi: 10.4319/lo.2006.51.4.1629

Kling, J. D., Lee, M. D., Fu, F.-X., Phan, M. D., Wang, X., Qu, P. P., et al. (2020). Transient exposure to novel high temperatures reshapes coastal phytoplankton communities. *ISME J.* 14, 413–424. doi: 10.1038/s41396-019-0525-6

Krumhardt, K. M. L., Lovenduskib, N. S., Iglesias-Rodriguezc, M. D., and Kleypasd, J. A. (2017). Coccolithophore growth and calcification in a changing ocean. *Prog. Oceanogr.* 159, 276–295. doi: 10.1016/j.pocean.2017.10.007

Le Quéré, C., Andrew, R., Canadell, J. G., Sitch, S., Korsbakken, J. I., Peters, G. P., et al. (2016). Global carbon budget 2016. *Earth Syst. Sci. Data* 8, 605–649.

Lee, K. H., Jeong, H. J., Lee, K., Franks, P. J., Seong, K. A., Lee, S. Y., et al. (2019). Effects of warming and eutrophication on coastal phytoplankton production. *Harm. Algae* 81, 106–118. doi: 10.1016/j.hal.2018.11.017

Li, F., Wu, Y., Hutchins, D. A., Fu, F., and Gao, K. (2016). Physiological responses of coastal and oceanic diatoms to diurnal fluctuations in seawater carbonate chemistry under two CO_2 concentrations. *Biogeosciences* 13, 6247–6259. doi: 10.5194/bg-13-6247-2016

Liao, Y., Feng, Y., Liu, Y., Li, W., Li, J., Ni, H., et al. (2019). The interative effects of nitrogen limitation and ocean acidification on the physiology of the coccolithophore *Emiliania huxleyi* NIWA 1108. *J. Tianjin Univ. Sci. Technol.* 34, 56–62. (In Chinese with English abstract),

Litchman, E., Klausmeier, C. A., Schofield, O. M., and Falkowski, P. G. (2007). The role of functional traits and trade-offs in structuring phytoplankton communities: scaling from cellular to ecosystem level. *Ecol. Lett.* 10, 1170–1181. doi: 10.1111/j.1461-0248.2007.01117.x

Martin-Jézéquel, V., Hildebrand, M., and Brzezinski, M. A. (2000). Review silicon metabolism in diatoms: implications for growth. *J. Phycol.* 36, 821–840. doi: 10.1046/j.1529-8817.2000.00019.x

McNair, H. M., Brzezinski, M. A., Till, C. P., and Krause, J. W. (2018). Taxon−specific contributions to silica production in natural diatom assemblages. *Limnol. Oceanogr.* 63, 1056–1075. doi: 10.1002/lno.10754

Mehrbach, C., Culberson, C. H., Hawley, J. E., and Pytkowic, R. M. (1973). Measurement of apparent dissociation cosntants of carbonic acid in seawater at atmospheric pressure. *Limnol. Oceanogr.* 18, 897–907. doi: 10.4319/lo.1973.18.6.0897

Milligan, A. J., Varela, D. E., Brzezinski, M. A., and Morel, F. M. (2004). Dynamics of silicon metabolism and silicon isotopic discrimination in a marine diatomas a function of pCO_2. *Limnol. Oceanogr.* 49, 322–329. doi: 10.4319/lo.2004.49.2.0322

Petrou, K., Baker, K. G., Nielsen, D. A., Hancock, A. M., Schulz, K. G., and Davidson, A. T. (2019). Acidification diminishes diatom silica production in the Southern Ocean. *Nat. Clim. Chang.* 9, 781–786. doi: 10.1038/s41558-019-0557-y

Raven, J. A., Cockell, C. S., and De La Rocha, C. L. (2008). The evolution of inorganic carbon concentrating mechanisms in photosynthesis. *Philos. Trans. R. Soc. Lond. B Biol. Sci.* 363, 2641–2650. doi: 10.1098/rstb.2008.0020

Raven, J. A., and Crawfurd, K. (2012). Environmental controls on coccolithophore calcification. *Mar. Ecol. Prog. Ser.* 470, 137–166. doi: 10.3354/meps09993

Riebesell, U., Wolfgladrow, D. A., and Smetacek, V. (1993). Carbon dioxide limitation of marine phytoplankton growth rates. *Nature* 361, 249–251. doi: 10.1038/361249a0

Riebesell, U., Zondervan, I., Rost, B., Tortell, P. D., Zeebe, R. E., and Morel, F. M. (2000). Reduced calcification of marine plankton in response to increased atmospheric CO_2. *Nature* 407, 364–367. doi: 10.1038/35030078

Rose, J. M., Feng, Y., Ditullio, G. R., Dunbar, R. B., Hare, C. E., Lee, P. A., et al. (2009). Synergistic effects of iron and temperature on Antarctic phytoplankton assemblages. *Biogeosciences* 6, 3131–3147. doi: 10.5194/bg-6-3131-2009

Rost, B., Riebesell, U., Burkhardt, S., and Sultemeyer, D. (2003). Carbon acquisition of bloom-forming marine phytoplankton. *Limnol. Oceanogr.* 48, 55–67. doi: 10.4319/lo.2003.48.1.0055

Schulz, K. G., Bach, L. T., Bellerby, R. G. J., Bermúdez, R., Büdenbender, J., Boxhammer, T., et al. (2017). Phytoplankton blooms at increasing levels of atmospheric carbon dioxide: experimental evidence for negative effects on prymnesiophytes and positive on small picoeukaryotes. *Front. Mar. Sci.* 4:64. doi: 10.3389/fmars.2017.00064

Sett, S., Schulz, K. G., Bach, L. T., and Riebesell, U. (2018). Shift towards larger diatoms in a natural phytoplankton assemblage under combined high-CO_2 and warming conditions. *J. Plankton Res.* 40, 391–406. doi: 10.1093/plankt/fby018

Sheridan, J. A., and Bickford, D. (2011). Shrinking body size as an ecological response to climate change. *Nat. Clim. Change* 1, 401–406. doi: 10.1038/nclimate1259

Smayda, T. J., and Boleyn, B. J. (1966). Experimental observations on the floatation of marine diatoms. II. *Skeletonema costatum* and *Rhizosolenia setigera*. *Limnol. Oceanogr.* 11, 18–34. doi: 10.4319/lo.1966.11.1.0018

Smayda, T. J., and Reynolds, C. S. (2003). Strategies of marine dinoflagellate survival and some rules of assembly. *J. Sea Res.* 49, 95–106. doi: 10.1016/s1385-1101(02)00219-8

Solórzano, L., and Sharp, J. H. (1980). Determination of total dissolved phosphorus and particulate phosphorus in natural waters. *Limnol. Oceanogr.* 25, 756–760.

Sommer, U., Adrian, R., Bauer, B., and Winder, M. (2012). The response of temperate aquatic ecosystems to global warming: novel insights from a multidisciplinary project. *Mar. Biol.* 159, 2367–2377. doi: 10.1007/s00227-012-2085-4

Sommer, U., Paul, C., and Moustaka-Gouni, M. (2015). Warming and ocean acidification effects on phytoplankton—from species shifts to size shifts within species in a mesocosm experiment. *PLoS One* 10:e0125239. doi: 10.1371/journal.pone.0125239

Spilling, K., and Lindström, M. (2008). Phytoplankton life cycle transformations lead to species-speci?c effects on sediment processes in the Baltic Sea. *Cont. Shelf Res.* 28, 2488–2495. doi: 10.1016/j.csr.2008.07.004

Spilling, K., Olli, K., Lehtoranta, J., Kremp, A., Tedesco, L., Tamelander, T., et al. (2018). Shifting diatom—dinoflagellate dominance during spring bloom in the Baltic Sea and its potential effects on biogeochemical cycling. *Front. Mar. Sci.* 5:327. doi: 10.3389/fmars.2018.00327

Taucher, J., Boxhammer, T., Bach, L. T., Paul, A. J., Schartau, M., Stange, P., et al. (2020). Changing carbon-to-nitrogen ratios of organic-matter export under ocean acidification. *Nat. Clim. Change* 11, 52–57. doi: 10.1038/s41558-020-00915-5

Thomas, C. R. (Ed.) (1997). *Identifying Marine Phytoplankton*. Amsterdam: Elsiever.

Tortell, P. D., Payne, C. D., Li, Y. Y., Trimborn, S., Rost, B., Smith, W. O., et al. (2008). CO_2 sensitivity of Southern ocean phytoplankton. *Geophys. Res. Lett.* 35, 1–5.

Tréguer, P., Bowler, C., Moriceau, B., Dutkiewicz, S., Gehlen, M., Aumont, O., et al. (2018). Influence of diatom diversity on the ocean biological carbon pump. *Nat. Geosci.* 11, 27–37. doi: 10.1038/s41561-017-0028-x

Utermöhl, H. (1958). Zur Vervollkommnung der quantitativen Phytoplankton-Methodik. *Mitt. Int. Ver. Theor. Angew. Limnol.* 9, 1–38. doi: 10.1080/05384680.1958.11904091

Varela, R., Lima, F. P., Seabra, R., Meneghesso, C., and Gómez-Gesteira, M. (2018). Coastal warming and wind-driven upwelling: a global analysis. *Sci. Total Environ.* 639, 1501–1511. doi: 10.1016/j.scitotenv.2018.05.273

Vehmaa, A., Kremp, A., Tamminen, T., Hogfors, H., Spilling, K., and Engström-Öst, J. (2011). Copepod reproductive success in spring-bloom communities with modified diatom and dinoflagellate dominance. *ICES J. Mar. Sci.* 69, 351–357. doi: 10.1093/icesjms/fsr138

Wasmund, N., Kownacka, J., Göbel, J., Jaanus, A., Johansen, M., Jurgensone, I., et al. (2017). The diatom/dinoflagellate index as an indicator of ecosystem changes in the Baltic Sea. 1. Principle and handling instruction. *Front. Mar. Sci.* 4:22. doi: 10.3389/fmars.2017.00022

Wu, R., Li, C., and Lin, J. (2017). Enhanced winter warming in the Eastern China Coastal Waters and its relationship with ENSO. *Atmos. Sci. Lett.* 18, 11–18. doi: 10.1002/asl.718

Wu, Y., Campbell, D. A., Irwin, A. J., Suggett, D. J., and Finkel, Z. V. (2014). Ocean acidification enhances the growth rate of larger diatoms. *Limnol. Oceanogr.* 59, 1027–1034. doi: 10.4319/lo.2014.59.3.1027

Xiao, W., Liu, X., Irwin, A. J., Laws, E. A., Wang, L., Chen, B., et al. (2018). Warming and eutrophication combine to restructure diatoms and dinoflagellates. *Water Res.* 128, 206–216. doi: 10.1016/j.watres.2017.10.051

Zhai, W., Zhao, H., Zheng, N., and Xu, Y. (2012). Coastal acidification in summer bottom oxygen-depleted waters in northwestern-northern Bohai Sea from june to august in 2011. *Chin. Sci. Bull.* 57, 1062–1068. doi: 10.1007/s11434-011-4949-2

Zhang, Y., Wang, T., Li, H., Bao, N., Hall-Spencer, J. M., and Gao, K. (2018). Rising levels of temperature and CO_2 antagonistically affect phytoplankton primary productivity in the South China Sea. *Mar. Environ. Res.* 141, 159–166. doi: 10.1016/j.marenvres.2018.08.011

Zou, L., Zhang, J., Pan, W. X., and Zhan, Y. P. (2001). *In situ* nutrient enrichment experiment in the Bohai and Yellow Sea. *J. Plankton Res.* 23, 1111–1119. doi: 10.1093/plankt/23.10.1111

Conflict of Interest: The authors declare that the research was conducted in the absence of any commercial or financial relationships that could be construed as a potential conflict of interest.

Copyright © 2021 Feng, Chai, Wells, Liao, Li, Cai, Zhao, Fu and Hutchins. This is an open-access article distributed under the terms of the Creative Commons Attribution License (CC BY). The use, distribution or reproduction in other forums is permitted, provided the original author(s) and the copyright owner(s) are credited and that the original publication in this journal is cited, in accordance with accepted academic practice. No use, distribution or reproduction is permitted which does not comply with these terms.

frontiers in Marine Science

ORIGINAL RESEARCH
published: 09 December 2020
doi: 10.3389/fmars.2020.588764

Multi-stressor Extremes Found on a Tropical Coral Reef Impair Performance

Noelle Lucey, Eileen Haskett and Rachel Collin*

Smithsonian Tropical Research Institute, Panama City, Panama

Global change has resulted in oceans that are warmer, more acidic, and lower in oxygen. Individually any one of these stressors can have numerous negative impacts on marine organisms, and in combination they are likely to be particularly detrimental. Understanding the interactions between these factors is important as they often covary, with warming promoting hypoxia, and hypoxia co-occurring with acidification. Few studies have examined how all three factors interact to affect organismal performance, and information is particularly sparse for tropical organisms. Here we documented a strong relationship between high temperatures, low dissolved oxygen (DO), and low pH in and around a tropical bay. We used these field values to inform two multi-stressor experiments. Each experimental factor had two levels, one representing current average conditions and the other representing current extreme conditions experienced in the area. We used sea urchin righting response as a measure of organismal performance for an important reef herbivore. In the first experiment 2-h exposures to a fully factorial combination of temperature, DO, and pH showed that righting success was significantly depressed under low oxygen. To more fully understand the impacts of pH, we acclimated sea urchins to control and low pH for 7 days and subsequently exposed them to the same experimental conditions. Sea urchins acclimated to control pH had significantly reduced righting success compared to animals acclimated to low pH, and righting success was significantly depressed under hypoxia and high temperature, compared to normoxia and ambient temperature. These results show that short, 2 h exposures to the temperature and DO extremes that are already experienced periodically by these animals have measurable detrimental effects on their performance. The positive impact of reduced pH is evident only over longer, 7 days durations, which are not currently experienced in this area.

Keywords: hypoxia, global warming, ocean acidification, *Echinometra*, multiple stressor analysis, coral reef, ocean deoxygenation

OPEN ACCESS

Edited by:
Nina Bednarsek, Southern California Coastal Water Research Project, United States

Reviewed by:
Yanyan Kang, Hohai University, China
Ariel Katharine Pezner, University of California, San Diego, United States
Derek Manzello, National Oceanic and Atmospheric Administration (NOAA), United States
Kirk N. Sato, University of Washington, United States

****Correspondence:***
Noelle Lucey
noelle.lucey@gmail.com

Specialty section:
This article was submitted to Coastal Ocean Processes, a section of the journal Frontiers in Marine Science

Received: *29 July 2020*
Accepted: *17 November 2020*
Published: *09 December 2020*

Citation:
Lucey N, Haskett E and Collin R (2020) Multi-stressor Extremes Found on a Tropical Coral Reef Impair Performance. Front. Mar. Sci. 7:588764. doi: 10.3389/fmars.2020.588764

INTRODUCTION

It is a truth almost universally acknowledged that the world's oceans are warming, becoming more acidic, and losing oxygen (Keeling et al., 2010; Gruber, 2011; Breitburg et al., 2018). Oceans have been rapidly warming since the 1950s (Cheng et al., 2019; IPCC, 2019). This has resulted in reduced global oceanic oxygen concentrations through increased water stratification and decreased oxygen solubility (Keeling et al., 2010; Schmidtko et al., 2017). Oceans also absorb about a quarter

of the carbon dioxide (CO_2) in the atmosphere every year, which is making them more acidic (Doney et al., 2009; Le Quéré et al., 2009). Individually, changes in any one of these factors are likely to impact organismal performance and in severe cases may result in mortality (Diaz, 2001; Kroeker et al., 2010; Yao and Somero, 2014). However, because the three environmental stressors are mechanistically linked (Bopp et al., 2013; Gobler and Baumann, 2016), animals are likely to experience all three stressors in combination in many coastal systems (**Figure 1**) (Breitburg et al., 2015; Reum et al., 2016; Humphreys, 2017).

Most marine organisms need more oxygen when temperatures increase (Fry, 1971; Pörtner, 2010). In coastal habitats, this can result in a reduction in oxygen concentration as a result of increased community metabolism (Gunderson et al., 2016). With increasing organismal oxygen uptake, there is also increasing respiration, which produces carbon dioxide and reacts with the water decreasing the pH. Concentrations of pH and dissolved oxygen (DO) show clear spikes during the day driven by daytime photosynthesis and steep declines at night driven by community respiration (Gobler and Baumann, 2016). The amplitude of these regular daily cycles can increase in response to external inputs, such as storm runoff, weather-driven increases in solar-radiation, and/or decreased wind intensity but are most strongly affected by warming (Tyler et al., 2009).

In addition to diel cycling, warming also clearly exacerbates metabolically-driven extremes in pH and DO on longer episodic or seasonal time scales in coastal systems (Baumann et al., 2014; Baumann and Smith, 2017). Coastal runoff due to intensifying storms, growing populations, and increasing nutrients from untreated wastewaters also fuel coastal community metabolism, and are particularly concerning in the tropics where resources to mitigate these issues are limited (Lonholdt, 2005; Knutson et al., 2010). As climate changes, these fluctuations are likely to become more pronounced (Boyd et al., 2016). These lines of evidence suggest that marine life may already be experiencing multiple stressful conditions at the same time, yet little is known about how these dynamics co-vary in tropical habitats, or what their biological impacts are.

Shallow-water tropical habitats, especially coral reefs which host a significant portion of global marine biodiversity, and estuaries which are important nursery grounds for many commercial species, may be at particular risk from these stressors (Duarte et al., 2013). Recent reviews have argued that modern reefs cannot be fully understood without explicitly considering the impacts of oxygen dynamics (Nelson and Altieri, 2019), and yet hypoxia, more than any other stressor, remains significantly under-studied in tropical locations (Altieri et al., 2017; Hughes et al., 2020). In fact, hypoxia-associated mass mortality events and dead zones associated with warm temperatures have recently been reported for the first time at several tropical sites (Laboy-Nieves et al., 2001; Díaz-Asencio et al., 2015; Altieri et al., 2017; van Tussenbroek et al., 2017). Another review has argued that areas experiencing combined hypoxia and acidification may be significantly under-reported, that natural variability is poorly documented, and that the harmful synergistic interaction between these two stressors are worryingly understudied (Gobler and Baumann, 2016).

One common way to think about the impacts these three co-occurring stressors may have on marine organisms is with aerobic scope, a measure of an organism's ability to take up oxygen from the environment and use it for fundamental activities such as feeding, reproduction, growth, and predator avoidance (Pörtner and Peck, 2010). A decline in aerobic scope can be visualized as a decreased capacity for oxygen uptake and decreased energy for these activities (Fry, 1971; Pörtner, 2010; Claireaux and Chabot, 2016). As temperature increases, aerobic scope is predicted to decrease due to the hindered capacity of the individual to deliver sufficient oxygen to its body tissues and can be visualized as a depressed performance curve (**Figure 1**) (Farrell et al., 2008). As environmental DO and/or pH decreases, aerobic scope is also predicted to decrease, further depressing performance curves (Pörtner and Farrell, 2008). Organism performance at all levels is therefore predicted to be reduced under increasing environmental temperatures, lowered DO and pH, yet ecological validation is still needed (Verberk et al., 2016).

Our aim was to document temperature, DO, and pH conditions throughout a tropical bay and use those conditions to inform multi-factor stressor experiments to understand how current extreme conditions impact the performance of an ecologically important herbivore. Previous work with marine invertebrates has shown that short-term or intermittent exposures to modern-day extreme conditions can result in reduced organismal performance. For example, weekly exposures to 1 mg/L DO for less than 8 h resulted in morphological and metabolic changes in the fireworm, *Hermodice carunculata* (Lucey et al., 2020). The juvenile oyster, *Crassostrea virginica*, raised under diel oxygen cycles where concentrations dipped to 0.5 mg/L exhibited reduced growth rates (Keppel et al., 2016). Herbivory rates of a temperate sea urchin, an amphipod and a snail, all decreased after 48-h reductions of DO from 7.2 to 2.0 mg/L but not after reductions of pH from 7.9 to 7.4, and the combination of the two stressors had the same effect as the hypoxia alone (Ng and Micheli, 2020). Abalone exposed to a 24-h combination of reduced pH (7.5) and DO (5 mg/L) once every 15 days, showed decreased growth and survival compared to controls, as did those exposed only to reduced DO (Kim et al., 2013). Despite these examples, there are few studies that (1) seek to determine if modern-day extremes can have significant impacts on marine organisms and (2) test the effects of multiple stressors in combination (see: Gobler and Baumann, 2016; Gunderson et al., 2016). High temperatures may exacerbate the effects of deoxygenation and acidification making these issues particularly important in the tropics. The objectives of this study were therefore to determine the extreme temperature, pH, and DO values in a tropical reef environment during the last 3 years, and experimentally test the performance of a reef herbivore, the sea urchin *Echinometra lucunter*, using two fully factorial multi-stressor experiments based on measured pH, DO, and temperature values and exposure times. In the first experiment, sea urchins were exposed to stressors for 2 h and then their ability to right themselves was measured. Righting reflects the ability of the feet and spines to function, which is vital to (1) remain attached to the substrate, (2) to find crevices for protection, (3) move around and forage (Barry et al., 2014), and (4) recover

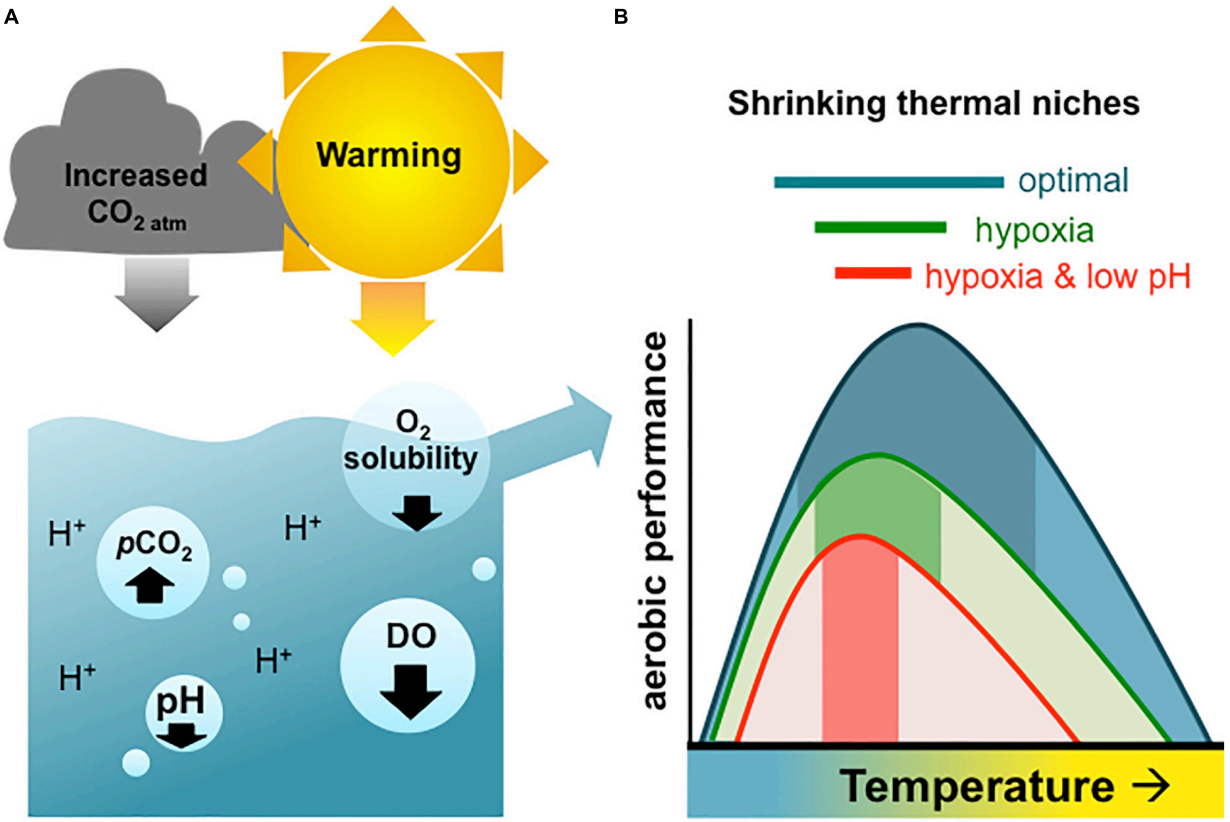


FIGURE 1 | (A) Graphical depiction of atmospheric warming represented as the sun, and increasing atmospheric carbon dioxide (CO_{2atm}) as the cloud, together driving ocean warming, decreasing dissolved oxygen (DO), and lowering pH. The partial pressure of CO_2 (pCO_2) increases from both increasing atmospheric CO_2 that is absorbed into the seawater (i.e., ocean acidification), as well as from biological activity (i.e., respiration) in the marine environment. **(B)** Scheme explaining how these differing stressors are expected to physiologically affect organismal performance, adapted from Pörtner and Farrell (2008). Dark shading within the curves represents the thermal window in which aerobic performance is possible under the different stressor combinations (blue = optimal, green = hypoxia, red = hypoxia and low pH/OA). It is thought that decreasing oxygen availability due to hypoxia and/or low pH can each result in narrowing thermal windows.

if they are somehow dislodged. In the second experiment, we replicated this after first exposing sea urchins to seven days of low pH. We did not expect sea urchin performance, measured as righting success, to be negatively affected by the short 2-h exposures to single-stressor conditions based on measurements in the field; however, we did expect the combination of all three stressors (low pH, high temperature, and low DO) to have some negative effects. We also expected sea urchins that were exposed to low pH conditions for multiple days to be even more negatively affected by multiple stressors. The results of this study provide a current baseline for temperature, oxygen, and pH values on one well-studied tropical coastline, and insight into the relative importance of these specific stressor combinations on an abundant and important herbivore.

MATERIALS AND METHODS

Study Site

Almirante Bay is a large semi-enclosed bay on the Northwest Caribbean coast of Panama (**Figure 2**). Shallow-water ecotypes include mangroves, seagrass beds, fringing, and patch reefs as well as sponge gardens and soft bottoms that are no deeper than 25 m. While this region does not experience large fluctuations in seawater temperature, environmental monitoring has recently detected seasonal changes in a hypoxic water mass in the deep water closest to the mainland. Between August and December, the hypoxic conditions expand and shoal (Lucey et al., 2020), and in recent years, this has caused significantly mortality of corals and associated marine life on reefs as shallow as 3 m (Johnson et al., 2018). However, shallow reefs that remain untouched by episodic hypoxia shoaling from depth can also experience hypoxia at night due to diel DO cycling (Lucey et al., 2020).

Study Organism and Performance

Sea urchins are ecologically important herbivores in shallow-water environments at all latitudes, and are often drivers of benthic community structure (Steneck, 2020). In the Caribbean, *E. lucunter* occurs on shallow exposed reefs and rocky shores (McPherson, 1965; Ebert et al., 2008; Sangil and Guzman, 2016) where their burrows may contribute significantly to erosion and increased habitat complexity (McLean, 1967;

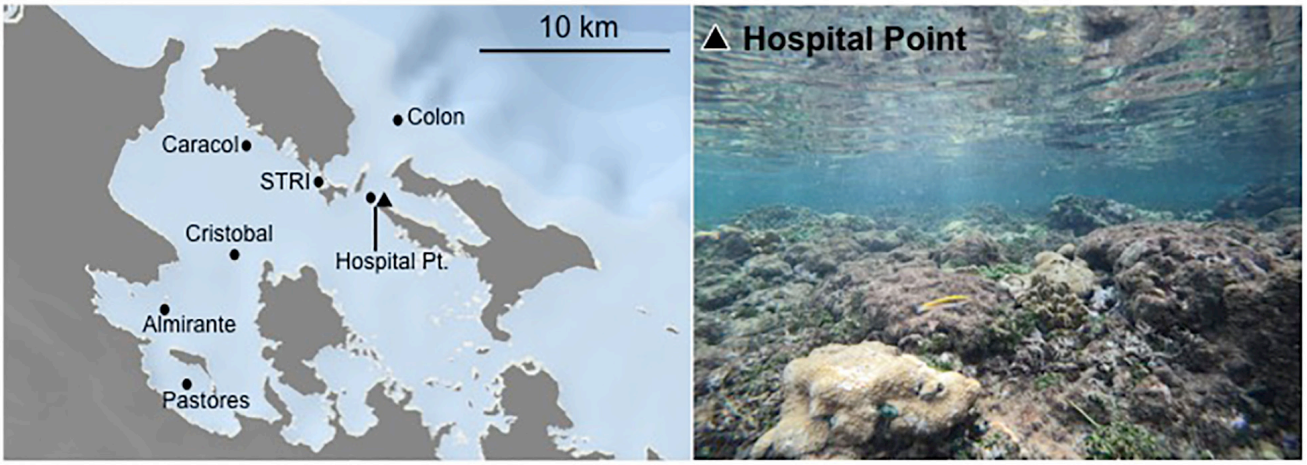


FIGURE 2 | Map of Almirante Bay showing the seven long-term monitoring sites (black dots), with sites "Pastores" and "Almirante" closest to the mainland and "Colon" outside the bay in the open ocean. Continuous monitoring on the Hospital Point reef, where animals were also collected from, is shown on the map as a black triangle and in the photograph on the right.

Schoppe and Werding, 1996). *E. lucunter* are most abundant at 1–5 m but have been found as deep as 45 m (McPherson, 1965). Previous research in Bocas del Toro has demonstrated that *E. lucunter* is one of the most thermally tolerant sea urchin species in the Caribbean (Collin et al., 2018; Perricone and Collin, 2019). To measure adult performance, we used the ability of upturned animals to turn over (righting response; Brothers and McClintock, 2015; Challener and McClintock, 2017; Collin et al., 2018). The righting response has been used to assess the impacts of temperature on echinoderms for 80 years (Kleitman, 1941; Farmanfarmaian and Giese, 1963; Lawrence and Cowell, 1996; Brothers and McClintock, 2015), and presumably requires coordinated sensory and locomotory functions, and therefore reflects whole organism function.

Environmental Conditions

To determine the most extreme values of DO, pH, and temperature throughout the bay over the last 3 years, we analyzed physical monitoring data measured at seven sites between June 2017 and March 2020. Monitoring sites represent the spatial heterogeneity of the area, extending from the mainland, through the bay and in the open ocean (**Figure 2**). Data were collected weekly in the mid-morning by recording depth profiles of parameters throughout the water column with a YSI multiparameter sonde (YSI EXO2 and EXO optical DO—accuracy ± 0.1 mg/L; pH Smart Sensors—accuracy 0.02 units; and Temperature Sensors—accuracy ± 0.01°C, Yellow Springs, United States) as part of the Smithsonian Tropical Research Institute's (STRI's) environmental monitoring program. The sensors were calibrated monthly following the manufacturers instructions (see **Supplementary Material** for details). We used values measured approximately 1 m above the seafloor of each site (∼15–20 m) to comprehensively represent daytime benthic conditions through the 3-year time period.

To determine how the 24-h diel conditions vary on a shallow coral reef, we deployed DO, pH, conductivity, and temperature loggers near one of the long-term monitoring sites, Hospital Point. This is a well-exposed coral reef location, with significant water flow from offshore. Loggers were deployed between July and October 2019 at Hospital Point at 3 m depth and recorded measurements once every hour (HoboOnset loggers: U26-001 HOBO DO Logger–accuracy: 0.2 mg L^{-1}; U24-002 Conductivity Logger accuracy—5%; MX2501 pH and temperature logger—accuracy ± 0.10 pH units and 0.1°C, Onset, MA). Data were downloaded and sensors were cleaned and calibrated monthly according to the manufacture's protocols. Conductivity and temperature measurements were used to adjust DO measurements using HoboPro Software. Measurement precision was based on comparisons to measurements made in the field before and after calibration checks with a YSI Pro2013 multi-parameter handheld (accuracy: DO 0.2 mg/L, Temp. 0.35°C, pH 0.2, Conductivity 0.5%). Further details on calibration and quality control for both the 3-year weekly monitoring dataset and the 3-month hourly dataset are in the **Supplementary Material**.

Experimental Procedures

Echinometra lucunter adults were collected from the reef site near Hospital Point where the loggers were deployed (**Figure 2**). All sea urchins were gently detached from reef and rock substrate between 0 and 3 m depths and placed in coolers of fresh seawater on the boat out of direct sunlight. Within an hour of collection, all sea urchins were transported to the Bocas del Toro Research Station (BRS) and placed in clean holding tanks with unfiltered, continuously flowing seawater and air bubbling to ensure fully oxygenated, ambient temperature seawater conditions. Large rocks with algae were added for shelter and food. In the first experiment, sea urchins were kept in these holding tanks for a maximum of 7 days until the trials and

experiments began, with an average holding time of 3.5 days. In the second experiment, they were kept for a maximum of 18 days, with an average holding time of 11.5 days. Temperature, DO, pH, and salinity were measured with the YSI Pro2013 multiparameter handheld device at the collection site and daily in all holding tanks.

Experiment 1

Sea urchins were collected during the month of May 2019 and exposed to a fully factorial combination of two pH levels: low 7.6 and control 8.1, two temperatures: ambient 29°C and high 32°C, and two DO levels: 1.5 mg/L hypoxic and 5.6 mg/L normoxic (**Table 1**). Experimental exposures were maintained at these levels for 2 h at which point sea urchins were flipped upside-down and righting ability and time measured. Treatment levels were based on the values measured in the field and approximately reflect the more extreme values that occurred infrequently in both time-series datasets (**Table 2**). The "control" values reflect the ambient values, which approximately corresponded with the mid-point of the range of values recorded (**Table 2**).

Trial tanks with 4 L of fresh seawater each held three individuals. Trial tanks were brought to the correct experimental conditions with the animals inside in a 15-min ramping period before trials began. Depending on the treatment, this was accomplished by bubbling regular air for control conditions, and either pure N_2 gas to lower DO, CO_2 gas mixed with air to lower pH, and/or adding small quantities of warmed seawater to reach correct temperature levels. Trial tanks were placed in a water bath with submersible aquarium pumps and heaters to maintain trial temperatures. After the ramping period, water conditions were monitored every 15 min in each tank for the 2-h duration of the trial. To keep seawater parameters stable during trials, either N_2 or regular air was bubbled directly into tanks as needed to maintain DO. Warm seawater and low-pH seawater, made from bubbling CO_2 gas, was prepared before trials and added in small increments if adjustments were necessary throughout the experiment to maintain temperature and pH. Trials were conducted sequentially (see below).

TABLE 1 | Mean and standard deviation of environmental parameters measured in the laboratory during the experimental treatments, and during the 7-day pH acclimation phase of the second experiment.

Factor	Level	*Experiment 1* mean ± SD, *n*	*Experiment 2* mean ± SD, *n*
Temperature°C	Ambient	29.2 ± 0.19, 15	29.1 ± 0.29, 38
	High	31.9 ± 0.27, 15	32.1 ± 0.33, 41
Dissolved oxygen mg/L	Normoxic	5.6 ± 0.35, 15	5.6 ± 0.15, 36
	Hypoxic	1.5 ± 0.09, 16	1.4 ± 0.14, 36
pH	Control	8.1 ± 0.08, 14	7.6 ± 0.05, 42
	Low	7.6 ± 0.04, 15	8.1 ± 0.09, 27
Acclimation pH	Control		8.0 ± 0.05, 9*
	Low		7.6 ± 0.06, 8*

Measurements were taken for each trial tank (n).
**Number of acclimation tanks sea urchins were maintained in during the acclimation phase.*

TABLE 2 | Environmental parameters measured in the field from weekly daytime measurements made from June 2017 to March 2020 near the seafloor, and from hourly measurements made July to October 2019 at the collection site, Hospital Point (in italics).

Site, depth (m)	pH mean (min, max)	DO mg/L mean (min, max)	Temp. °C mean (min, max)
Almirante, 22.6 m	7.91 (7.59, 8.47)	1.74 (0.11, 5.56)	29.00 (26.83, 30.76)
Pastores, 24.1 m	7.92 (7.58, 8.45)	1.89 (0.06, 5.51)	28.96 (26.87, 30.56)
Cristobal, 23.3 m	8.04 (7.59, 8.51)	3.62 (0.37, 6.06)	28.80 (26.80, 30.55)
Caracol, 16.5 m	8.12 (7.58, 8.55)	5.08 (0.53, 6.42)	28.70 (26.52, 30.72)
STRI, 22.1 m	8.06 (7.65, 8.49)	4.05 (0.84, 6.04)	28.78 (26.81, 30.65)
Hospital Pt., 20.5 m	8.11 (7.78, 8.51)	4.75 (2.38, 6.39)	28.73 (26.77, 30.39)
Colon, 20.2 m	8.16 (7.93, 8.53)	5.72 (4.95, 6.29)	28.31 (26.77, 30.23)
Hospital Pt., 3.0 m	8.09 (7.81, 8.64)	5.21 (0.81, 13.89)	29.81 (27.70, 32.70)

Following the 2 h experimental exposure, sea urchins were flipped and time until they were fully righted was measured. Any sea urchin that did not right after 10 min was recorded as a failed righting response. Successful righting usually occurred in <1 min. After righting was measured, urchins were returned to separate holding tanks and 48 h post-trial survival was measured. All animals were released following the 48-h survival analysis at a site 5 km away (i.e., STRI site) from the collection site to ensure individuals were not re-tried. Trials were run daily between May and June 2019. A total of 172 individuals were tested over eight treatment combinations, with three urchins per trial tank, for a total of six to eight trials per treatment.

Experiment 2

The second experiment measured the performance of *E. lucunter* under the three stressors as in Experiment 1, but first urchins were exposed to 7 days of control or chronically low pH. Sea urchins were collected from the same site as above between November and December 2019. After being held in ambient, oxygenated holding tanks with algae-covered rocks/food for an average of 11.5 days, they were placed in 50 L acclimation tanks (18 individuals/acclimation tank). Four control acclimation tanks were maintained at pH > 8.00 with bubbling air, while four low pH acclimation tanks were maintained at pH 7.6 ± 0.06 SE by bubbling air-mixed CO_2 directly into tanks. Temperature and oxygen were kept at ambient levels (29°C and >6.0 mg/L) with submersible aquarium heaters and air pumps maintained. Seawater was refreshed at a rate of 8 L/h in all acclimation tanks. Temperature and DO values were recorded every 10 min (HOBO U30 Station with S-TMB-M0xx temperature probes—accuracy ± 0.2°C; Barreleye Designs DO Controllers with Atlas Scientific galvanic DO probes—accuracy ± 0.05 mg/L). After the 7 days pH exposure, trials were performed following the same protocol as in the first experiment. A total of 299 individuals were

tested over 16 treatment combinations, with three urchins per trial tank for a total of five to six trials per treatment.

In both experiments, the order of trial treatments was systematic to account for the variable of time of collection, and each trial included a small, medium, and large urchin to maintain a balanced size distribution throughout (**Supplementary Summary Tables**). Seawater parameters in the trials were measured using a Thermo Scientific Orion Star A320 optical DO probe (accuracy ± 0.1 mg/L), a Mettler Toledo SevenGo Handheld pH probe calibrated daily with NBS buffers 4, 7, 10 (accuracy ± 0.002), and an Omega high precision thermocouple (±0.05% reading accuracy). Salinity was recorded daily with a handheld multi-parameter YSI Pro2013 (±0.5% reading accuracy).

Temperature, pH, DO, and salinity were measured in the field on collection days, throughout the holding period (pre-experiment), throughout the acclimation period, and during each trial. The conditions experienced by each sea urchin were tracked. Despite necessary variation in the date of collection and time in holding tanks, we maintained similar conditions across all treatments and maintained a strict balance across the unavoidable time constraints of the experiments (**Supplementary Summary Tables**).

Analysis

The effects of pH, DO, temperature, and in the second experiment, pH acclimation, on righting success were analyzed with generalized linear models (GLM) using a binominal distribution and a logit link function. The test diameter of each individual was included as a covariate. The date of collection was included as a covariate in experiment 1, while the days of pre-experiment holding time and acclimation period start date were included as covariates in experiment 2. Fully factorial models were analyzed with step-wise removal of non-significant interactions based on the p-values ($p > 0.1$) (Crawley, 2012). The main effects and covariates were retained in the reduced models. Residual plots were used to assess the quality of model fit (Zuur et al., 2010). In the second experiment, separation was indicated due to the high number of individuals that succeeded, and a Firth penalized likelihood method was employed using the logistf package in R. Analyses with and without the Firth option identified the same significant factors so we retained the model without this correction. Results from experimental assays were analyzed with R v. 3.6.2 (R Core Team, 2020).

RESULTS

Environmental Conditions

Weekly monitoring data show the shallow waters in and around Almirante Bay occasionally experience conditions that are hot, hypoxic, and acidic. Within the last 3 years during the day, temperatures above the seafloor (depth ∼15–20 m) ranged from 26.52 to 30.76°C (mean = 28.8°C ± 0.9 SD), DO ranged from 0.06 to 6.42 mg/L (mean = 3.84 ± 1.9 mg/L) and pH ranged from 7.58 to 8.55 (mean = 8.04 ± 0.2 SD) (**Table 2** and **Figure 3**). There was a clear negative relationship between oxygen and temperature, and a positive correlation between DO and pH (**Figure 3**). The relationship between these parameters was similar among all seven sites, but the sites further from the mainland were less frequently hot, hypoxic, and acidic compared to the sites closer to the mainland (i.e., Colon vs. Almirante; **Figure 3**). The extreme values on the lower limits of the pH and DO ranges occurred between July and December 2019.

The hourly 3-month time-series on the Hospital Point reef, where animals were collected for experiments, experienced large diel fluctuations in pH and DO that scaled with increased temperature. Temperatures ranged from 27.6 to 32.7°C (mean = 29.8°C ± 0.8 SD), pH ranged from 7.81 to 8.64 (mean = 8.09 ± 0.14 SD), and DO ranged from 0.81 to 13.89 mg/L, with a mean value of 5.21 mg/L ± 1.72 SD (**Table 2** and **Figure 4**). Low DO values coincided with low pH values during the night, while warmer temperatures generally occurred during the day when pH and DO were both higher. There were only a few instances when DO values remained under 1.5 mg/L and temperatures above 32°C (e.g., 25 September 2019). These extreme conditions persisted for no more than 4 h at a time (**Figure 4**).

Experiments

For experiment 1, after step-wise removal of non-significant interactions, there was a significant main effect of oxygen on the righting success of *E. lucunter* ($p < 0.001$; **Table 3** and **Figure 5**). No effect of temperature or pH was found. Under normoxic conditions 98.8% ± 1.1 SE of the animals righted successfully in 10 min, while only 67.9% ± 5.1 SE righted successfully in the hypoxic treatments. Animal size did not differ significantly between our treatments, but was a significant covariate, with larger animals less likely to right than small ones regardless of the treatment ($p = 0.020$). This is a normal and expected response found in multiple sea urchin species in laboratory studies (Challener and McClintock, 2017).

For experiment 2, after step-wise removal of non-significant interactions, there were significant main effects of oxygen ($p = 0.005$), temperature ($p = 0.029$) and pH acclimation ($p = 0.007$), with no significant interaction effects on righting success (**Table 3** and **Figure 6**). Righting success under normoxia was 99.3% ± 0.67 SE, while under hypoxia, it was reduced by 9.6% (90% ± 2.4 SE). Righting success was also reduced under warmer temperatures: 98% ± 1.1 SE at ambient and 91.3% ± 2.3 at the high temperature. Unexpectedly, acclimation to low pH for 7 days resulted in an 8.1% increase in righting success compared to "control" pH acclimated animals (98.7% ± 0.93 SE compared to 90.6% ± 2.3 SE, respectively) (**Table 3** and **Figure 6**). Neither the experimental start date, number of days pre-experiment in holding tanks, or size had an effect on righting success.

In the first experiment, seven out of the total 172 urchins tested died within the 48 h recovery period after the trials. All except one of these individuals had been exposed to hypoxia. This one outlier was exposed to low pH and high temperature. In the second experiment, 15 out of a total of 299 died 48 h after trials.

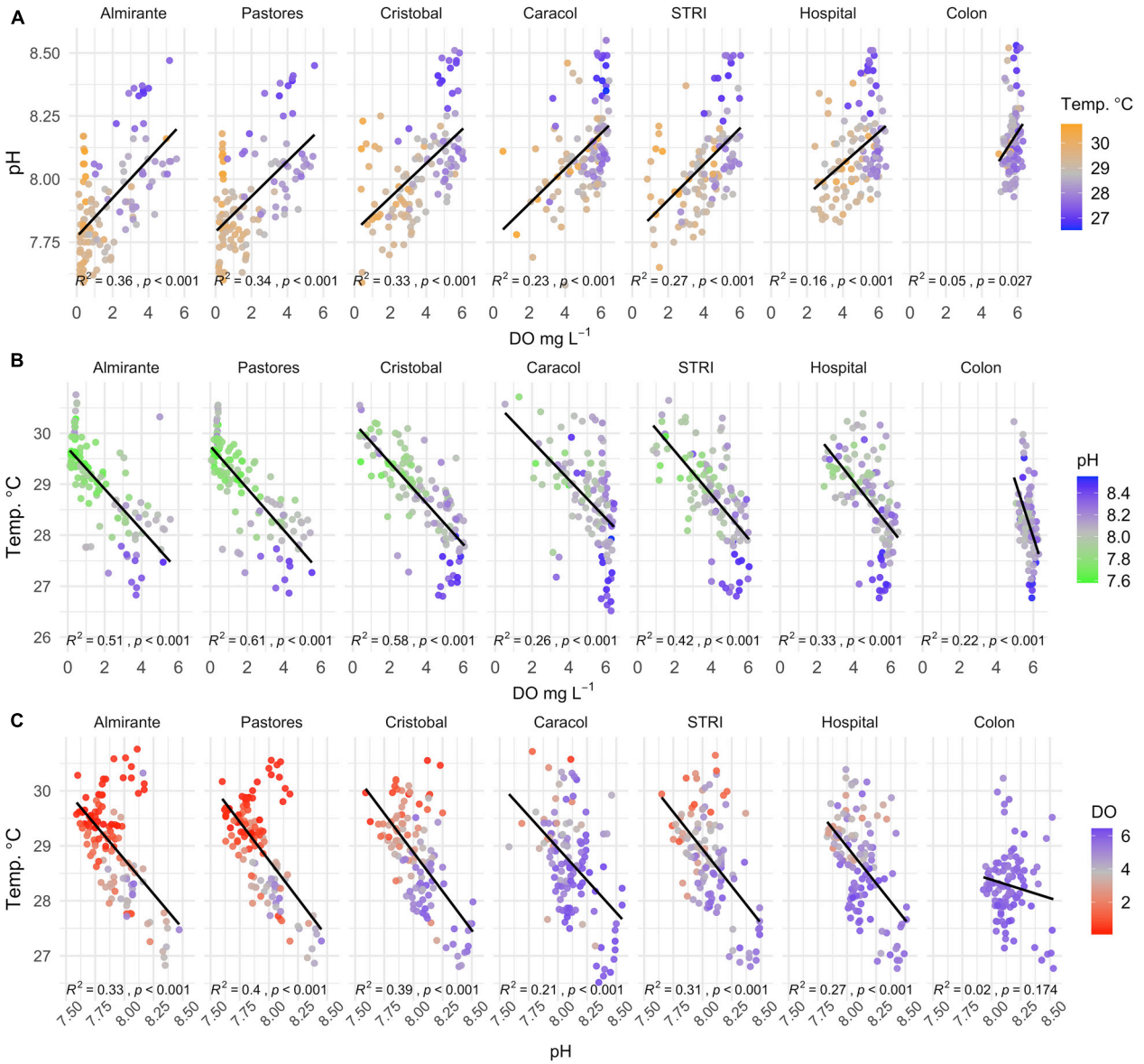


FIGURE 3 | Daytime physical conditions in and around Almirante Bay between June 2017 and March 2020, showing the correlation between pH, dissolved oxygen (DO), and temperature 1 m from the seafloor (~15–20 m). The seven monitoring sites are arranged as a gradient going from the mainland "Almirante" to the open ocean site "Colon." The first row of plots shows DO and pH are positively correlated **(A)**; the second row shows the negative correlation between DO and temperature **(B)**; and the third row shows the negative correlation between pH and temperature **(C)**. The third parameter in each set is colored, with blue colors depicting the most "ambient" end of the range (lowest temperatures, normoxia, highest pH), while grays highlight the calculated mean of each range. R^2 and p-values of Pearson correlation are shown at the bottom of each individual plot.

The prevalent stressor was temperature, with 13 of the 15 urchins exposed to high temperatures.

DISCUSSION

Impacts of Multiple Stressors

Experiments examining the impacts of factorial combinations of multiple stressors provide two important insights into potential real-world responses of organisms to these stressors. They provide information on the relative importance of the stressors and crucially, for factors that co-vary in nature, if the impact of the combined stressors is greater than the individual stressors. However, results can vary based on the levels and durations of the stressors used. Here we aimed to determine which stressors are the most important for the performance of a tropical herbivore, near the center of its range, and under current day extremes. Short-term exposures were used as these stressors show pronounced diel cycles (see below).

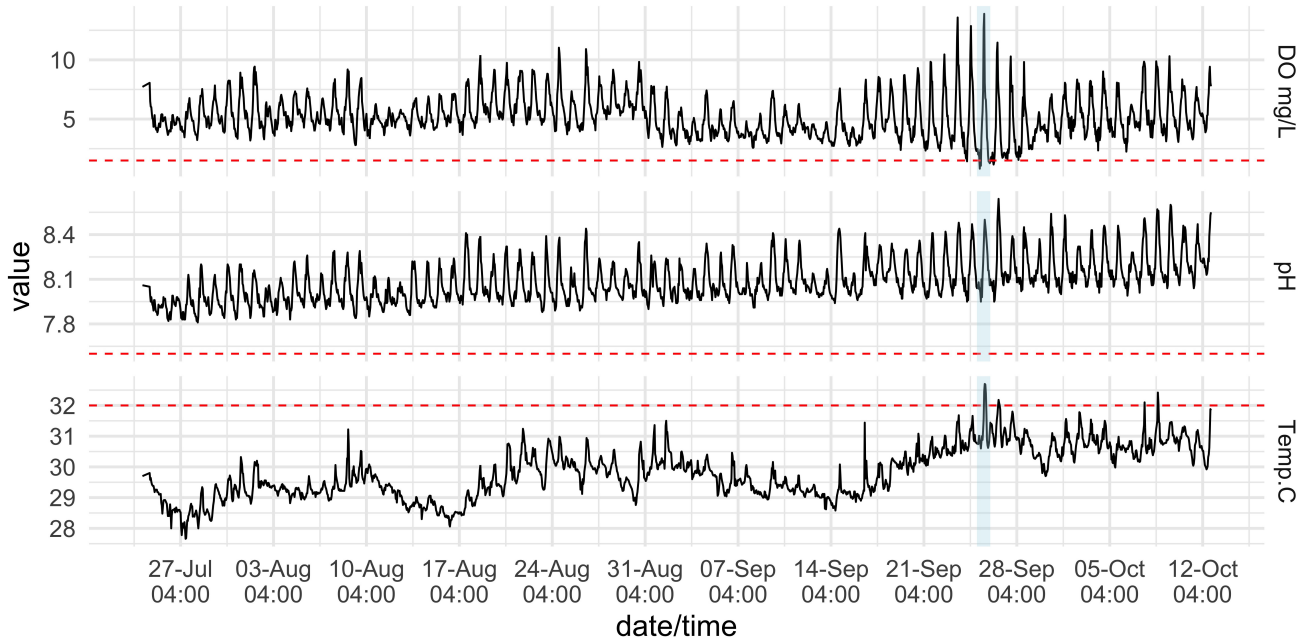


FIGURE 4 | Physical conditions on a coral reef at the inlet to Almirante Bay, Hospital Point. Dissolved Oxygen (DO) (top), pH (middle), and temperature (bottom) measurements recorded hourly from 15 July to 12 October 2019 on the reef where experimental urchins were collected at 3 m depth. Red dotted lines indicate the values that were used in the experiments: 1.5 mg/L DO; 7.6 pH; 32.0°C. Conditions were most severe on Sept. 25th (blue shading).

Of temperature, pH, and DO concentration, we found that DO had the largest negative effect on sea urchin performance in both of our experiments. Warmer temperatures showed a negative effect in the second experiment but not in the first, and short-term exposures to low pH appeared to have no impact. As low pH has been previously demonstrated to have particularly detrimental effects on calcifying sea urchins (Shirayama and Thornton, 2005; Courtney et al., 2013), we included an unrealistically long exposure to low pH in the second experiment, which had a substantial significant positive impact on performance. In neither experiment did we detect significant interactions between stressors, showing that despite the proposed mechanistic link between temperature and oxygen availability, the performance outcomes in this system are independent at these exposures. Taken together these results show that DO concentration and temperature are the most important conditions to consider when predicting environmental impacts on adult *E. lucunter* populations and distribution.

TABLE 3 | Effect of temperature, oxygen, and pH on righting success in both experiments, determined with GLMs.

	Factor	Estimate	Std. error	*Z*-value	*P*-value
Exp. 1	Intercept	9.52	5.48	1.7	0.080
	Oxygen	**3.90**	**1.05**	**3.7**	**<0.001**
	Temperature	−0.14	0.16	−0.8	0.400
	pH	0.07	0.49	0.1	0.880
	Size (test diameter)	**−0.12**	**0.05**	**−2.4**	**0.020**
	Date of collection	−0.31	0.20	−1.6	0.110
Exp. 2	Intercept	2.23	2.42	0.9	0.355
	Oxygen	**3.04**	**1.09**	**2.8**	**0.005**
	Temperature	**−1.63**	**0.75**	**−2.2**	**0.029**
	pH	0.44	0.77	0.6	0.566
	pH acclimation	**2.17**	**0.80**	**2.7**	**0.007**
	Size (test diameter)	−0.38	0.74	−0.5	0.603
	Holding time	0.09	0.07	1.3	0.188
	Experiment Start	0.01	0.08	0.2	0.881

In Experiment 1, stepwise removal of non-significant interactions was made from the fully factorial model with collection data and animal size as covariates. Experiment 2 models included the additional effect of acclimation pH, with experimental start date and holding time as covariates. Nesting trial replicate as a random effect in mixed models produced similar results, but are not reported due to over-parameterization issues.

Although producing consistent results in terms of the factor with the greatest effect (DO), the results of the two experiments differed with respect to the effect of temperature. It is possible that experimental timing contributed to this difference. The sea urchins in experiment 1 were collected at the start of the warm hypoxic season in May and had therefore been naturally acclimated to cooler and better oxygenated conditions in the field. The animals in experiment 2 were collected toward the end of this season in November and had therefore been naturally acclimated to warmer conditions. Chronically warmer temperatures may induce either increased thermal tolerance through acclimation (Angilletta, 2009; Huey et al., 2012; Botero et al., 2015) or may induce increased sensitivity (Stillman, 2003; Boyd et al., 2016), as may have been the case here. As with any study of wild-collected animals, any number of potential confounding effects could have

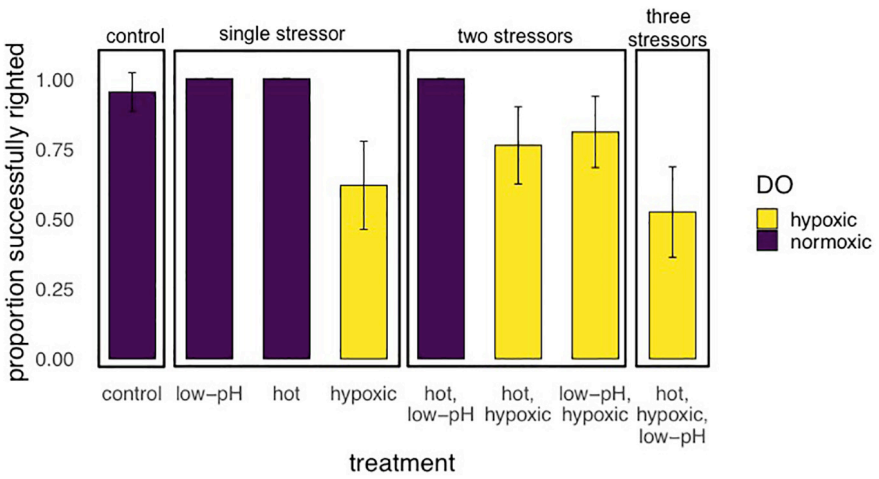


FIGURE 5 | Results of Experiment 1 showing the proportion (mean ± SE) of *E. lucunter* that were able to successful right after 2 h multi-stressor trials with levels of pH at 7.6 or 8.1, DO 1.5 or 6.0 mg/L, and temperatures of either 29 or 32°C. Sea urchins had no experimental acclimation before the trials. Performance was negatively affected by treatments with hypoxia, which are indicated by the yellow bars ($p < 0.001$).

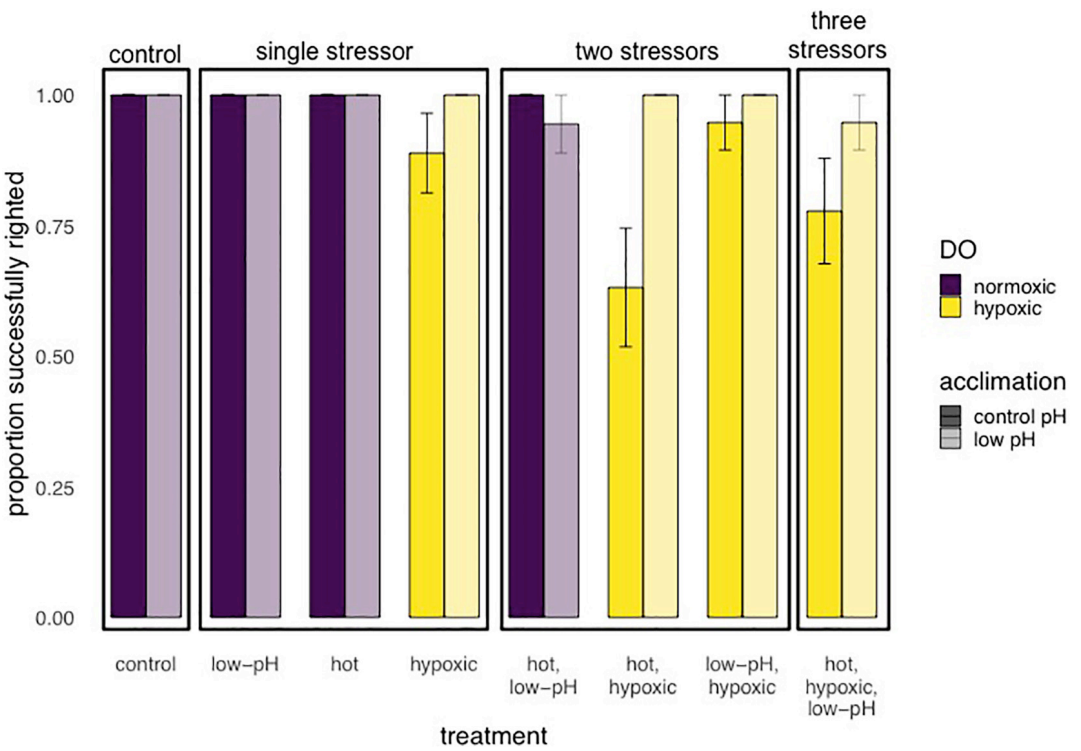


FIGURE 6 | Results of Experiment 2 showing the proportion (mean ± SE) of *E. lucunter* that were able to successful right after 2 h multi-stressor trials, with levels of pH at 7.6 or 8.1, DO 1.5 or 6.0 mg/L, and temperature either 29 or 32°C. Prior to multi-stressor trials, animals were acclimated to either control (ambient) conditions (solid bars: pH 8.0) or low pH (lightly shaded bars pH 7.6). Performance was negatively affected by hypoxia, shown as yellow grouped bars ($p = 0.005$), and higher temperatures ($p = 0.029$). Low pH acclimation significantly improved performance compared to control pH acclimation, shown as lightly shaded bars vs. solid bars, respectively ($p = 0.007$).

been experienced in the field. Unlike the physical conditions, we do not know if other factors like seawater nutrient conditions or diet quality vary seasonally and may have contributed to the inconsistent effect of temperature. Alternatively, the larger overall sample size in experiment 2 may have contributed to our ability to detect a moderately significant effect.

The most surprising experimental result of this study is that 7-day exposures to chronic low pH appeared to improve

performance. Sea urchins acclimated to these conditions may have performed better than those that were kept in ambient control conditions because acclimation to low pH alters and improves the stress response. Some studies have shown that acclimation to one stressor may lead to increased tolerance for another, or a combination of different stressors (Todgham and Stillman, 2013). It has also been shown that a 2-year exposure to low pH and increased temperature positively influenced adult urchins through increased reproduction success (Suckling et al., 2015). Studies of other marine organisms have documented favorable impacts of reduced pH in combination with low oxygen as well. For example, Montgomery et al. (2019) found that lower pH increased hypoxia tolerance in a fish, due to increased affinity of red blood cells for oxygen under the lower pH conditions. Invertebrates that lack hemoglobin have also shown positive impacts of reduced pH. The larvae of the barnacle *Balanus amphitrite* grow more slowly with low oxygen than under normoxia, but this reduction in growth is not evident when larvae are grown with low oxygen and low pH (Campanati et al., 2015). Several studies of adult sea urchins have indicated little impact of reduced pH on performance over the long term (e.g., Hazan et al., 2014; Moulin et al., 2014; Uthicke et al., 2016).

A hint at a possible mechanism behind the improved performance of sea urchins after acclimation to low pH was first given by Spicer (1995) who showed that in *Psammechinus miliaris*, as the partial pressure of oxygen (pO_2) decreased in the environment, it also decreased in the coelomic fluid. This was accompanied by an increase in pH in the coelomic fluid. *Echinometra* and *Stongylocentrous* species have also been shown to use bicarbonate compensation to regulate the acid–base balance of the coelomic fluid, to buffer over the long-term (Stumpp et al., 2012; Moulin et al., 2015), although this ability may vary among species or genera (Calosi et al., 2013). We note that while the acclimation potential and possible mitigating effects of low pH are conceptually interesting, it is not directly ecologically relevant for two reasons. First, the 7-day duration of the low pH acclimation used in our study was longer than any period of such extreme pH measured in the field. Second, while it is not unreasonable to assume that longer durations of pH and hypoxia are possible, or even likely, a low pH acclimation capacity may be irrelevant when such low pH conditions co-occur with extremely low and detrimental DO concentrations.

Diel Variation and Environmental Extremes

Our experiments focus on short-term exposures to multiple potential stressors as organisms are likely exposed to such conditions in the field. During the last 3 years of daytime monitoring, we found a significant correlation between temperature, DO, and pH, confirming that these variables covary. Within the last year, we found the lowest lows of pH and DO, and highest highs of temperature. With continuous monitoring at an exposed, well-mixed shallow reef, we found distinct, even drastic, diel changes in DO and pH. Our experimental results show that, not only could daytime values of DO and temperature be detrimental to *E. lucunter*, but that, as DO and pH are lowest at night, sites that may appear benign from daytime measures may experience stressful conditions during the night.

Although more environmental datasets are becoming available, numerous authors have cited the lack of well-documented environmental conditions as an impediment to designing experiments that reflect realistic levels of stressors, their variability, and durations (Duarte et al., 2013; Gunderson et al., 2016; Hannan et al., 2020). Our continuous data show that average daily fluctuations of 4–5 mg/L in DO, 1–1.5°C in temperature and fluctuations of 0.3 pH units are typical at this well-mixed site. These short-term fluctuations in conditions are not unique to this region. For example, a study of reefs in five locations around the world showed that average diel temperature changes ranged from < 0.5°C in Palmyra to > 3°C in Heron Island and that average diel pH changes ranged from < 0.05 pH units in Bermuda to ∼0.3 units in Heron Island (Cyronak et al., 2019). They also recorded similar variability at a another site in Almirante Bay, comparable to what we measured when conditions at the Hospital Point reef site where relatively cool. However, their 10-day dataset did not capture the variability in DO and pH that we found at the end of September, which occurred when temperature increased. In another study, all three stressors measured on shallow reefs in Hawaii over an 11-month period also showed similar ranges to our data (Guadayol et al., 2014). Previous work has shown that at a protected reef near the mainland (i.e., Almirante; **Figure 2**), daily fluctuations in DO can be as large as 8 mg/L (Lucey et al., 2020) and temperature can reach 33°C (Lucey unpublished). Due to the difficulties of continuous measurements over large spatial scales, none of these ranges may capture infrequent extreme values, but nevertheless show that even well mixed, semi-exposed sites can experience a suite of physiologically stressful conditions daily.

Diel variation is not specific to coral reef habitats, and short-term variations in conditions have also been documented for a variety of other marine habitats. Diel cycles in conditions can be significant for planktonic animals whose vertical migrations may take them between different water masses. For example, in the Baltic Sea copepods experience changes of 5°C and 0.5 pH units during their diel migrations (Almén et al., 2014). Organisms living in mangrove pools in Panama can experience diel changes of as much as 0.5 pH units, and 5°C, ranging from 0 to 100% oxygen saturation (Gedan et al., 2017). Fluctuations in temperature and DO can be even greater in comparable habitats in Belize, while changes in pH were similar (Gedan et al., 2017). Large diel fluctuations are also documented in mangroves in Bermuda (Zablocki et al., 2011) and near mangroves, seagrass, and reefs in the Red Sea (Saderne et al., 2019). Mediterranean seagrass beds can experience diel DO ranges from 1.5 to 6.4 mg/L, and diel pH ranges from 0.06 to 0.24 units (Saderne et al., 2019). Finally, temperate, subtropical, and tropical estuaries also experience extreme fluctuations in DO, temperature, and pH (Baumann et al., 2014; Baumann and Smith, 2017). These studies suggest that large diel fluctuations in environmental conditions are more common than not in coastal ecosystems. Therefore, results from long-term static exposures to potential stressors may not reflect present or future environmental conditions or the organismal responses to them well. Since environmental conditions are often monitored during the day, experiments are likely underestimating the DO and pH stress that organism endure at night. Experiments that apply continuous conditions

may also overestimate the detrimental effects of stressors from which animals may experience daily respite in the field (Shang et al., 2020).

In addition to highlighting the importance of diel fluctuations, we also show a significant correlation between temperature, pH, and DO, which is evident over seven coastal sites during the last 3 years. These sites cover a spatial gradient from the mainland to the open ocean. A correlation between all three variables is evident at all sites along this gradient, albeit with relatively low R^2 values; however, these relationships are most significant in the sites closest to the mainland, such as "Almirante" on the far left, compared to sites closer to the open ocean, such as "Colon" on the far right, which has the lowest R^2 (**Figure 3**). This replicated relationship between DO, pH, and temperature in coastal waters emphasizes the importance of considering multiple stressors in experimental designs. We used the extreme values measured in the bay to parameterize our experiments, to represent local conditions. The temperatures and DO values measured on the reef were occasionally more extreme than our experimental values, but neither the site from which we collected the animals nor the well-exposed long-term monitoring site nearby experienced pH as low as our experimental treatment. Such low pH values were, however, measured at sites within 5 km away, and given the correlation between the variables seen in the long-term monitoring dataset, and the higher temperature and low DO measured on the reef, it may not be unreasonable to assume a pH of 7.60 may occur at Hospital Point in the near future.

Our experiments were conducted in a year that appeared to be "normal" with respect to environmental conditions. Heatwaves are increasing in frequency in the Caribbean, and very warm years have been recently reported in 2010–2011, 2015, and 2017 (Muñiz-Castillo et al., 2019). The timing of these high temperatures coincided with two extreme hypoxic events at depth in Almirante Bay in 2010 and 2017, supporting the idea that episodic hypoxia and heat waves may also be correlated. If *E. lucunter* experiences reduced performance on some days during normal years, as demonstrated by our experiments, it is likely that their performance would be more significantly reduced in these extremely warm years. It should be noted that for tropical animals where normal temperatures may be within only a degree or two of the critical thermal maximum, smaller changes in temperature may be significantly more impactful than changes of a similar magnitude in temperate systems (Tewksbury et al., 2008). As *E. lucunter* is thought to live for at least 10 years (Ebert et al., 2008), most animals would now be expected to experience significantly stressful seasons several times during their lifetimes. This will likely be exacerbated by globally accelerating climate changes (Melzner et al., 2013).

CONCLUSION

Many studies of environmental stressors either fail to report the natural conditions which their study organisms normally experience and/or use conditions predicted to reflect stressful future conditions. Here we found the lowest lows of oxygen and pH occurred at night on a well-mixed Caribbean reef, and that these scaled with the increasing temperatures. We also show that oxygen, temperature, and pH co-vary along a coastal gradient from protected to well-flushed reefs. Of these three parameters, hypoxia had the largest negative impact on the performance of a key reef herbivore under realistic 2-h exposures. Warming was also detrimental, but to a lesser extent. Our study indicates that current-day environmental stressors may be pushing the physiological limits of marine organisms in coastal environments, and that in this tropical system, temperature and DO but not pH are key to adult performance and survival.

DATA AVAILABILITY STATEMENT

The original contributions presented in the study are included in the article/**Supplementary Material**, further inquiries can be directed to the corresponding author/s.

AUTHOR CONTRIBUTIONS

NL designed the experiment and collected the field data. NL and EH collected the animals and conducted the experiments. NL and RC analyzed the data and prepared the manuscript. All authors contributed to the article and approved the submitted version.

FUNDING

This work would not have been possible without the logistic support of the staff of the Bocas del Toro Research Station, permission to conduct research granted by the government of Panama (MiAmbiente permit # SE/APHBO-2-18) and financial support from the Smithsonian Tropical Research Institute (STRI). NL was supported by an STRI postdoctoral fellowship, and EH by an STRI short-term fellowship. This is contribution 66 from the Smithsonian's MarineGEO and Tennenbaum Marine Observatories Network.

ACKNOWLEDGMENTS

We thank C. Cesar for conducting the alkalinity titrations, M. Johnson for field loggers, J. Paulus for field assistance, and A. Herwig for help with the experiments.

SUPPLEMENTARY MATERIAL

The Supplementary Material for this article can be found online at: https://www.frontiersin.org/articles/10.3389/fmars.2020.588764/full#supplementary-material

REFERENCES

Almén, A.-K., Vehmaa, A., Brutemark, A., and Engström-Ost, J. (2014). Coping with climate change? Copepods experience drastic variations in their physicochemical environment on a diurnal basis. *J. Exp. Mar. Biol. Ecol.* 460, 120–128. doi: 10.1016/j.jembe.2014.07.001

Altieri, A. H., Harrison, S. B., Seemann, J., Collin, R., Diaz, R. J., and Knowlton, N. (2017). Tropical dead zones and mass mortalities on coral reefs. *Proc. Natl. Acad. Sci. U.S.A.* 114, 3660–3665. doi: 10.1073/pnas.1621517114

Angilletta, M. (2009). *Thermal Adaptation: a Theoretical and Empirical Synthesis*. Oxford: Oxford University Press.

Barry, J. P., Lovera, C., Buck, K. R., Peltzer, E. T., Taylor, J. R., Walz, P., et al. (2014). Use of a free ocean CO2 enrichment (FOCE) system to evaluate the effects of ocean acidification on the foraging behavior of a deep-sea urchin. *Environ. Sci. Technol.* 48, 9890–9897. doi: 10.1021/es501603r

Baumann, H., and Smith, E. M. (2017). Quantifying metabolically driven pH and oxygen fluctuations in US nearshore habitats at diel to interannual time scales. *Estuaries Coast.* 41, 1102–1117. doi: 10.1007/s12237-017-0321-3

Baumann, H., Wallace, R. B., Tagliaferri, T., and Gobler, C. J. (2014). Large natural pH, CO2 and O2 fluctuations in a temperate tidal salt marsh on diel, seasonal, and interannual time scales. *Estuaries Coast.* 38, 220–231. doi: 10.1007/s12237-014-9800-y

Bopp, L., Resplandy, L., Orr, J. C., Doney, S. C., Dunne, J. P., Gehlen, M., et al. (2013). Multiple stressors of ocean ecosystems in the 21st century: projections with CMIP5 models. *Biogeosciences* 10, 6225–6245. doi: 10.5194/bg-10-6225-2013

Botero, C. A., Weissing, F. J., Wright, J., and Rubenstein, D. R. (2015). Evolutionary tipping points in the capacity to adapt to environmental change. *Proc. Natl. Acad. Sci. U.S.A.* 112, 184–189. doi: 10.1073/pnas.1408589111

Boyd, P. W., Cornwall, C. E., and Davison, A. (2016). Biological responses to environmental heterogeneity under future ocean conditions. *Glob. Chang. Biol.* 22, 2633–2650. doi: 10.1111/gcb.13287

Breitburg, D., Levin, L. A., Oschlies, A., Grégoire, M., Chavez, F. P., Conley, D. J., et al. (2018). Declining oxygen in the global ocean and coastal waters. *Science* 359:eaam7240. doi: 10.1126/science.aam7240

Breitburg, D., Salisbury, J., Bernhard, J. M., Cai, W. J., Dupont, S., Doney, S. C., et al. (2015). And on top of all that coping with Ocean Acidification in the midst of many stressors. *Oceanography* 28, 48–61. doi: 10.5670/oceanog.2015.31

Brothers, C. J., and McClintock, J. B. (2015). The effects of climate-induced elevated seawater temperature on the covering behavior, righting response, and Aristotle' s lantern reflex of the sea urchin *Lytechinus variegatus*. *J. Exp. Mar. Biol. Ecol.* 467, 33–38. doi: 10.1016/j.jembe.2015.02.019

Calosi, P., Rastrick, S. P. S., Graziano, M., Thomas, S. C., Baggini, C., Carter, H. A., et al. (2013). Distribution of sea urchins living near shallow water CO2 vents is dependent upon species acid-base and ion-regulatory abilities. *Mar. Pollut. Bull.* 73, 470–484. doi: 10.1016/j.marpolbul.2012.11.040

Campanati, C., Yip, S., Lane, A., and Thiyagarajan, V. (2015). Combined effects of low pH and low oxygen on the early-life stages of the barnacle *Balanus amphitrite*. *ICES J. Mar. Sci.* 73, 791–802. doi: 10.1093/icesjms/fsv221

Challener, R. C., and McClintock, J. B. (2017). *In situ* measurements of righting behavior in the common sea urchin *Lytechinus variegatus*: the importance of body size, substrate type, and covering material. *Aquat. Biol.* 26, 33–40. doi: 10.3354/ab00669

Cheng, L., Abraham, J., Hausfather, Z., and Trenberth, K. E. (2019). How fast are the oceans warming? *Science* 363, 128–129. doi: 10.1126/science.aav7619

Claireaux, G., and Chabot, D. (2016). Responses by fishes to environmental hypoxia: integration through Fry's concept of aerobic metabolic scope. *J. Fish Biol.* 88, 232–251. doi: 10.1111/jfb.12833

Collin, R., Rendina, F., Goodwin, V., and Mccabe, S. (2018). Do tropical specialist sea urchins have higher thermal tolerances and optimal temperatures than their more widely distributed relatives? *Mar. Ecol. Prog. Ser.* 589, 157–170.

Courtney, T., Westfield, I., and Ries, J. B. (2013). CO2-induced ocean acidification impairs calcification in the tropical urchin *Echinometra viridis*. *J. Exp. Biol. Ecol.* 440, 169–175. doi: 10.1016/j.jembe.2012.11.013

Crawley, M. J. (2012). *The R Book*. Weinheim: Wiley.

Cyronak, T., Takeshita, Y., Courtney, T. A., Decarlo, E. H., Eyre, B. D., Kline, D. I., et al. (2019). Diel temperature and pH variability scale with depth across diverse coral reef habitats. *Limnol. Oceanogr. Lett.* 5, 193–203. doi: 10.1002/lol2.10129

Diaz, R. J. (2001). Overview of hypoxia around the world. *J. Environ. Qual.* 30, 275–281. doi: 10.2134/jeq2001.302275x

Díaz-Asencio, L., Helguera, Y., Fernández-Garcés, R., and Gómez-Batista, M. (2015). Two-year temporal response of benthic macrofauna and sediments to hypoxia in a tropical semi-enclosed bay (Cienfuegos, Cuba). *Rev. Biol. Trop.* 64, 177–188. doi: 10.15517/rbt.v64i1.18519

Doney, S. C., Fabry, V. J., Feely, R. A., and Kleypas, J. A. (2009). Ocean acidification: the other CO2 problem. *Ann. Rev. Mar. Sci.* 1, 169–192. doi: 10.1146/annurev.marine.010908.163834

Duarte, C. M., Hendriks, I. E., Moore, T. S., Olsen, Y. S., Steckbauer, A., Ramajo, L., et al. (2013). Is Ocean acidification an open-ocean syndrome? Understanding anthropogenic impacts on seawater pH. *Estuaries Coast.* 36, 221–236. doi: 10.1007/s12237-013-9594-3

Ebert, T. A., Russell, M. P., Gamba, G., and Bodnar, A. (2008). Growth, survival, and longevity estimates for the rock-boring growth, survival, and longevity estimates for the rock-boring sea urchin *Echinometra lucunter* (Echinodermata, Echinoidea) in Bermuda. *Bull. Mar. Sci.* 82, 381–403.

Farmanfarmaian, A., and Giese, A. C. (1963). Thermal tolerance and acclimation in the western purple sea urchin, *Strongylocentrotus purpuratus*. *Physiol. Zool.* 36, 237–243. doi: 10.1086/physzool.36.3.30152309

Farrell, A. P., Hinch, S. G., Cooke, S. J., Patterson, D. A., Crossin, G. T., and Mathes, M. T. (2008). Pacific salmon in hot water: applying aerobic scope models and biotelemetry to predict the success of spawning migrations Pacific salmon. *Comp. Biol.* 81, 697–708. doi: 10.1086/592057

Fry, F. E. J. (1971). "The effect of environmental factors on the physiology of fish," in *Environmental Relations and Behavior*, eds W. S. Hoar and D. J. Randall (London: Academic Press), 1–98. doi: 10.1016/s1546-5098(08)60146-6

Gedan, K. B., Altieri, A. H., Feller, I., Burrell, R., and Breitburg, D. (2017). Community composition in mangrove ponds with pulsed hypoxic and acidified conditions. *Ecosphere* 8:e02053. doi: 10.1002/ecs2.2053

Gobler, C. J., and Baumann, H. (2016). Hypoxia and acidification in ocean ecosystems: coupled dynamics and effects on marine life. *Biol. Lett.* 12:20150976. doi: 10.1098/rsbl.2015.0976

Gruber, N. (2011). Warming up, turning sour, losing breath: ocean biogeochemistry under global change. *Philos. Trans. R. Soc. A Math. Phys. Eng. Sci.* 369, 1980–1996. doi: 10.1098/rsta.2011.0003

Guadayol, O., Silbiger, N. J., Donahue, M. J., and Thomas, F. I. M. (2014). Patterns in temporal variability of temperature, oxygen and pH along an environmental gradient in a coral reef. *PLoS One* 9:e85213. doi: 10.1371/journal.pone.0085213

Gunderson, A. R., Armstrong, E. J., and Stillman, J. H. (2016). Multiple stressors in a changing world: the need for an improved perspective on physiological responses to the dynamic marine environment. *Ann. Rev. Mar. Sci.* 8, 357–378. doi: 10.1146/annurev-marine-122414-033953

Hannan, K. D., Miller, G. M., Rummer, J. L., Fabricius, K., and Munday, P. L. (2020). Diel pCO2 variation among coral reefs and microhabitats at Lizard Island, Great Barrier Reef. *Coral Reefs* 39, 1391–1406. doi: 10.1007/s00338-020-01973-z

Hazan, Y., Wangensteen, O. S., and Fine, M. (2014). Tough as a rock-boring urchin: adult *Echinometra* sp. from the Red Sea show high resistance to ocean acidification over long-term exposures. *Mar. Biol.* 161, 2531–2545. doi: 10.1007/s00227-014-2525-4

Huey, R. B., Kearney, M. R., Krockenberger, A., Holtum, J. A. M., Jess, M., and Williams, S. E. (2012). Predicting organismal vulnerability to climate warming: roles of behaviour, physiology and adaptation. *Philos. Trans. R. Soc. B Biol. Sci.* 367, 1665–1679. doi: 10.1098/rstb.2012.0005

Hughes, D. J., Alderdice, R., Cooney, C., Kühl, M., Pernice, M., Voolstra, C. R., et al. (2020). Coral reef survival under accelerating ocean deoxygenation. *Nat. Clim. Chang.* 10, 296–307. doi: 10.1038/s41558-020-0737-9

Humphreys, M. P. (2017). Climate sensitivity and the rate of ocean acidification: future impacts, and implications for experimental design. *ICES J. Mar. Sci.* 74, 934–940. doi: 10.1093/icesjms/fsw189

IPCC (2019). *The Ocean and Cryosphere in a Changing Climate*. Geneva: IPCC.

Johnson, M. D., Rodriguez, L. M., and Altieri, A. H. (2018). Shallow-water hypoxia and mass mortality on a Caribbean coral reef. *Bull. Mar. Sci.* 94, 143–144. doi: 10.5343/https

Keeling, R. E., Körtzinger, A., and Gruber, N. (2010). Ocean deoxygenation in a warming world. *Ann. Rev. Mar. Sci.* 2, 199–229. doi: 10.1146/annurev.marine.010908.163855

Keppel, A. G., Breitburg, D. L., and Burrell, R. B. (2016). Effects of co-varying diel-cycling hypoxia and pH on growth in the juvenile eastern oyster, *Crassostrea virginica*. *PLoS One* 11:e0161088. doi: 10.1371/journal.pone.0161088

Kim, T. W., Barry, J. P., and Micheli, F. (2013). The effects of intermittent exposure to low-pH and low-oxygen conditions on survival and growth of juvenile red abalone. *Biogeosciences* 10, 7255–7262. doi: 10.5194/bg-10-7255-2013

Kleitman, N. (1941). The effect of temperature on the righting of echinoderms. *Biol. Bull.* 80, 292–298. doi: 10.2307/1537716

Knutson, T. R., McBride, J. L., Chan, J., Emanuel, K., Holland, G., Landsea, C., et al. (2010). Tropical cyclones and climate change. *Nat. Geosci.* 3, 157–163.

Kroeker, K. J., Kordas, R. L., Crim, R. N., and Singh, G. G. (2010). Meta-analysis reveals negative yet variable effects of ocean acidification on marine organisms. *Ecol. Lett.* 13, 1419–1434. doi: 10.1111/j.1461-0248.2010.01518.x

Laboy-Nieves, E. N., Klein, E., Conde, J. E., Losada, F., Cruz, J. J., and Bone, D. (2001). Mass mortality of tropical marine communities in Morrocoy, Venezuela. *Bull. Mar. Sci.* 68, 163–179.

Lawrence, J. M., and Cowell, B. C. (1996). The righting response as an indication of stress in *Stichaster striatus* (Echinodermata, Asteroidea). *Mar. Freshw. Behav. Physiol.* 27, 239–248. doi: 10.1080/10236249609378969

Le Quéré, C., Raupach, M. R., Canadell, J. G., and Marland, G. (2009). Trends in the sources and sinks of carbon dioxide. *Nat. Geosci.* 2, 831–836. doi: 10.1038/ngeo689

Lonholdt, J. (ed.). (2005). *(Water) and Wastewater Management in the Tropics*. London: IWA Publishing.

Lucey, N. M., Collins, M., and Collin, R. (2020). Oxygen-mediated plasticity confers hypoxia tolerance in a corallivorous polychaete. *Ecol. Evol.* 10, 1145–1157. doi: 10.1002/ece3.5929

McLean, R. F. (1967). Erosion of burrows in Beachrock by the tropical sea urchin, *Echinometra lucunter*. *Can. J. Zool.* 45, 586–588. doi: 10.1139/z67-072

McPherson, B. F. (1965). Studies on the biology of the tropical sea urchins, *Echinometra lucunter* and *Echinometra viridis*. *Bull. Mar. Sci.* 19, 194–213.

Melzner, F., Thomsen, J., Koeve, W., Oschlies, A., Gutowska, M. A., Bange, H. W., et al. (2013). Future ocean acidification will be amplified by hypoxia in coastal habitats. *Mar. Biol.* 160, 1875–1888. doi: 10.1007/s00227-012-1954-1

Montgomery, D. W., Simpson, S. D., Engelhard, G. H., Birchenough, S. N. R., and Wilson, R. W. (2019). Rising CO2 enhances hypoxia tolerance in a marine fish. *Sci. Rep.* 9:15152.

Moulin, L., Grosjean, P., Leblud, J., Batigny, A., Collard, M., and Dubois, P. (2015). Long-term mesocosms study of the effects of ocean acidification on growth and physiology of the sea urchin *Echinometra mathaei*. *Mar. Environ. Res.* 103, 103–114. doi: 10.1016/j.marenvres.2014.11.009

Moulin, L., Grosjean, P., Leblud, J., Batigny, A., and Dubois, P. (2014). Impact of elevated pCO2 on acid – base regulation of the sea urchin *Echinometra mathaei* and its relation to resistance to ocean acidification: a study in mesocosms. *J. Exp. Mar. Biol. Ecol.* 457, 97–104. doi: 10.1016/j.jembe.2014.04.007

Muñiz-Castillo, A. I., Rivera-Sosa, A., Chollett, I., Eakin, C. M., Andrade-Gómez, L., Mcfield, M., et al. (2019). Three decades of heat stress exposure in Caribbean coral reefs: a new regional delineation to enhance conservation. *Sci. Rep.* 9:11013.

Nelson, H. R., and Altieri, A. H. (2019). Oxygen: the universal currency on coral reefs. *Coral Reefs* 38, 177–198. doi: 10.1007/s00338-019-01765-0

Ng, C. A., and Micheli, F. (2020). Short-term effects of hypoxia are more important than effects of ocean acidification on grazing interactions with juvenile giant kelp (*Macrocystis pyrifera*). *Sci. Rep.* 10:5403.

Perricone, V., and Collin, R. (2019). Larvae of Caribbean echinoids have small warming tolerances for chronic stress in Panama. *Biol. Bull.* 236, 115–129. doi: 10.1086/701666

Pörtner, H. O. (2010). Oxygen- and capacity-limitation of thermal tolerance: a matrix for integrating climate-related stressor effects in marine ecosystems. *J. Exp. Biol.* 213, 881–893. doi: 10.1242/jeb.037523

Pörtner, H. O., and Farrell, A. P. (2008). Physiology and climate change. *Science* 322, 690–692. doi: 10.1126/science.1163156

Pörtner, H. O., and Peck, M. A. (2010). Climate change effects on fishes and fisheries: towards a cause-and-effect understanding. *J. Fish Biol.* 77, 1745–1779. doi: 10.1111/j.1095-8649.2010.02783.x

R Core Team (2020). *R: A Language and Environment for Statistical Computing*. Vienna: R Foundation for Statistical Computing.

Reum, J. C. P., Alin, S. R., Harvey, C. J., Bednarsek, N., Evans, W., Feely, R. A., et al. (2016). Interpretation and design of ocean acidification experiments in upwelling systems in the context of carbonate chemistry co-variation with temperature and oxygen. *ICES J. Mar. Sci.* 73, 582–595. doi: 10.1093/icesjms/fsu231

Saderne, V., Baldry, K., Anton, A., Agusti, S., and Duarte, C. M. (2019). Characterization of the CO2 system in a coral reef, a seagrass meadow and a mangrove forest in the central Red Sea. *J. Geophys. Res.* 124, 7513–7528. doi: 10.1029/2019JC015266

Sangil, C., and Guzman, H. M. (2016). Assessing the herbivore role of the sea-urchin *Echinometra viridis*: keys to determine the structure of communities in disturbed coral reefs. *Mar. Environ. Res.* 120, 202–213. doi: 10.1016/j.marenvres.2016.08.008

Schmidtko, S., Stramma, L., and Visbeck, M. (2017). Decline in global oceanic oxygen content during the past five decades. *Nature* 542, 335–351. doi: 10.1038/nature21399

Schoppe, S., and Werding, B. (1996). The boreholes of the sea urchin genus *Echinoidea*: *Echinometridae* as a microhabitat in tropical South America. *Mar. Ecol.* 17, 181–186. doi: 10.1111/j.1439-0485.1996.tb00499.x

Shang, Y., Wang, X., Deng, Y., Wang, S., Gu, H., Wang, T., et al. (2020). Diel-cycling seawater acidification and hypoxia impair the physiological and growth performance of marine mussels. *Sci. Total Environ.* 722:138001. doi: 10.1016/j.scitotenv.2020.138001

Shirayama, Y., and Thornton, H. (2005). Effect of increased atmospheric CO2 on shallow water marine benthos. *J. Geophys. Res.* 110:C09S08. doi: 10.1029/2004JC002618

Spicer, J. I. (1995). Oxygen and acid-base status of the sea urchin *Psammechinus miliaris* during environmental hypoxia. *Mar. Biol.* 124, 71–76. doi: 10.1007/bf00349148

Steneck, R. S. (2020). *Regular Sea Urchins as Drivers of Shallow Benthic Marine Community Structure*, 4th Edn. Amsterdam: Elsevier B.V. doi: 10.1016/B978-0-12-819570-3.00015-9

Stillman, J. H. (2003). Acclimation capacity underlies susceptibility to climate change. *Science* 301:65. doi: 10.1126/science.1083073

Stumpp, M., Trübenbach, K., Brennecke, D., Hu, M. Y., and Melzner, F. (2012). Resource allocation and extracellular acid – base status in the sea urchin *Strongylocentrotus droebachiensis* in response to CO2 induced seawater acidification. *Aquat. Toxicol.* 111, 194–207. doi: 10.1016/j.aquatox.2011.12.020

Suckling, C. C., Clark, M. S., Richard, J., Morley, S. A., Thorne, M. A. S., Harper, E. M., et al. (2015). Adult acclimation to combined temperature and pH stressors significantly enhances reproductive outcomes compared to short-term exposures. *J. Anim. Ecol.* 84, 773–784. doi: 10.1111/1365-2656.12316

Tewksbury, J. J., Huey, R. B., and Deutsch, C. A. (2008). Ecology. Putting the heat on tropical animals. *Science* 320, 1296–1297. doi: 10.1126/science.1159328

Todgham, A. E., and Stillman, J. H. (2013). Physiological responses to shifts in multiple environmental stressors: relevance in a changing world. *Integr. Comp. Biol.* 53, 539–544. doi: 10.1093/icb/ict086

Tyler, R. M., Brady, D. C., and Targett, T. E. (2009). Temporal and spatial dynamics of diel-cycling hypoxia in estuarine tributaries. *Estuaries Coast.* 32, 123–145. doi: 10.1007/s12237-008-9108-x

Uthicke, S., Ebert, T., Liddy, M., and Johansson, C. (2016). *Echinometra* sea urchins acclimatized to elevated pCO2 at volcanic vents outperform those under present-day pCO2 conditions. *Glob. Chang. Biol.* 22, 2451–2461. doi: 10.1111/gcb.13223

van Tussenbroek, B. I., Hernández, H. A., Rodríguez-Martínez, R. E., Espinoza-Avalos, J., Canizales-Flores, H. M., González-Godoy, C. E., et al. (2017). Severe impacts of brown tides caused by *Sargassum* spp. on near-shore Caribbean seagrass communities. *Mar. Pollut. Bull.* 122, 272–281. doi: 10.1016/j.marpolbul.2017.06.057

Verberk, W. C. E. P., Overgaard, J., Ern, R., Bayley, M., Wang, T., Boardman, L., et al. (2016). Does oxygen limit thermal tolerance in arthropods? A critical

review of current evidence. *Comp. Biochem. Physiol. A Mol. Integr. Physiol.* 192, 64–78. doi: 10.1016/j.cbpa.2015.10.020

Yao, C. L., and Somero, G. N. (2014). The impact of ocean warming on marine organisms. *Chin. Sci. Bull.* 59, 468–479. doi: 10.1007/s11434-014-0113-0

Zablocki, J. A., Andersson, A. J., and Bates, N. R. (2011). Diel aquatic CO2 system dynamics of a Bermudian mangrove environment. *Aquat. Biol.* 17, 841–859. doi: 10.1007/s10498-011-9142-3

Zuur, A. F., Ieno, E. N., and Elphick, C. S. (2010). A protocol for data exploration to avoid common statistical problems. *Stat. Methods Evol. Ecol.* 1, 3–14. doi: 10.1111/j.2041-210X.2009.00001.x

Conflict of Interest: The authors declare that the research was conducted in the absence of any commercial or financial relationships that could be construed as a potential conflict of interest.

Copyright © 2020 Lucey, Haskett and Collin. This is an open-access article distributed under the terms of the Creative Commons Attribution License (CC BY). The use, distribution or reproduction in other forums is permitted, provided the original author(s) and the copyright owner(s) are credited and that the original publication in this journal is cited, in accordance with accepted academic practice. No use, distribution or reproduction is permitted which does not comply with these terms.

frontiers in Marine Science

ORIGINAL RESEARCH
published: 15 December 2020
doi: 10.3389/fmars.2020.590258

Marine Heatwaves, Sewage and Eutrophication Combine to Trigger Deoxygenation and Biodiversity Loss: A SW Atlantic Case Study

Kalina M. Brauko[1,2†], Alex Cabral[2,3*†], Natasha V. Costa[2], Juliana Hayden[4], Carlos E. P. Dias[5], Edilene S. Leite[6], Renan D. Westphal[4], Carolina M. Mueller[5], Jason M. Hall-Spencer[7,8], Regina R. Rodrigues[2,4], Leonardo R. Rörig[2,5], Paulo R. Pagliosa[1,2,4], Alessandra L. Fonseca[2,4], Orestes E. Alarcon[6] and Paulo A. Horta[1,2,5]*

[1] Graduate Program in Ecology, Federal University of Santa Catarina, Florianópolis, Brazil, [2] Graduate Program in Oceanography, Federal University of Santa Catarina, Florianópolis, Brazil, [3] Department of Marine Sciences, University of Gothenburg, Gothenburg, Sweden, [4] Department of Oceanography, Federal University of Santa Catarina, Florianópolis, Brazil, [5] Department of Botany, Federal University of Santa Catarina, Florianópolis, Brazil, [6] Department of Mechanical Engineering, Federal University of Santa Catarina, Florianópolis, Brazil, [7] School of Biological and Marine Sciences, University of Plymouth, Plymouth, United Kingdom, [8] Shimoda Marine Research Center, University of Tsukuba, Tsukuba, Japan

OPEN ACCESS

Edited by:
Richard Alan Feely,
Pacific Marine Environmental Laboratory (NOAA), United States

Reviewed by:
Laura Carrillo,
The South Border College (ECOSUR), Mexico
Alvise Finotello,
Ca' Foscari University of Venice, Italy

***Correspondence:**
Kalina M. Brauko
kalinabio@gmail.com
Alex Cabral
alex.cabral@gu.se

†These authors share first authorship

Specialty section:
This article was submitted to Coastal Ocean Processes, a section of the journal Frontiers in Marine Science

Received: 31 July 2020
Accepted: 09 November 2020
Published: 15 December 2020

Citation:
Brauko KM, Cabral A, Costa NV, Hayden J, Dias CEP, Leite ES, Westphal RD, Mueller CM, Hall-Spencer JM, Rodrigues RR, Rörig LR, Pagliosa PR, Fonseca AL, Alarcon OE and Horta PA (2020) Marine Heatwaves, Sewage and Eutrophication Combine to Trigger Deoxygenation and Biodiversity Loss: A SW Atlantic Case Study. Front. Mar. Sci. 7:590258. doi: 10.3389/fmars.2020.590258

Marine heatwaves (MHWs) are a major concern worldwide due to their increasing impacts in recent years, and these extreme events may trigger deoxygenation of coastal waters affected by sewage and eutrophication. Here we investigate the combined effects of MHWs and nutrient enrichment on the water quality and biodiversity of the Bay of Santa Catarina Island (Brazil). We used historical (1994–2020) sea surface temperature data from satellites and *in situ* physical, chemical and biological parameters to assess temporal trends. Oxygen levels have been decreasing whilst phosphorus levels have been increasing in the bay. During the austral summer of 2020 a regional sea surface heatwave was detected by satellite, lasting for 9 days and coinciding with our research cruise. During this period, seawater temperatures reached 29.8°C and anoxia was detected for the first time in the bay. A decrease in macrobenthic and phytoplankton community richness correlated with decreases in oxygen both through time and towards more urbanized areas. Overall, poor wastewater treatment is a key stressor that combined with MHWs to degrade coastal waters. Mitigation strategies are needed to minimize the impact of MHWs, including improved sewage treatment, restoration and conservation of wetlands and the use of nature-based technologies to promote coastal ecosystem recovery.

Keywords: benthos, Brazil, climate change, coastal management, dead zones, extreme events

INTRODUCTION

Much attention has been given to climate change and ocean warming projections for the end of this century (Bestion et al., 2020). However, marine heatwaves (MHWs) are already causing major biodiversity loss and are having socio-environmental consequences worldwide. These events can be defined as when sea surface temperature (SST) exceeds a threshold for more than five consecutive days (Hobday et al., 2016). On a global scale, MHW intensity, duration and frequency are increasing

(Frölicher et al., 2018; Oliver et al., 2019; Rodrigues et al., 2019; Smale et al., 2019). Some of the consequences are well known, such as widespread mortality of marine organisms, shifts in species distributions, increases in biological invasions, coral bleaching, and the loss of blue carbon storage (Garrabou et al., 2009; Cavole et al., 2016; Arias-Ortiz et al., 2018; Smale et al., 2019). In the South West Atlantic, MHWs have started to occur due to atmospheric blocking and droughts during summer (Rodrigues et al., 2019), but their effects on marine life had not previously been studied.

Organic enrichment and eutrophication are major environmental problems worldwide, especially in South America due to an exponential increase in urbanization of coastlines (Scherner et al., 2013) and inadequate sewage treatment (Barletta et al., 2019). Nutrient inputs often boost algal blooms in systems with long water residence time, such as lagoons and bays (Bricker et al., 2008). In South Brazil, harmful algal blooms, deoxygenation and human diseases (e.g., gastroenteritis, mycosis, conjunctivitis) have frequently been associated with sewage pollution and nutrient enrichment from agricultural land run-off (Silva and Fonseca, 2016; Alves and Mafra, 2018; Cabral and Fonseca, 2019). One of the few studies about the interactive effects of eutrophication and high temperatures in Brazil showed a major decline in the physiological performance of a macroalga, indicating that individuals inhabiting densely urbanized areas are more susceptible to warm water episodes (Gouvêa et al., 2017). Here, we present the first field study of the interaction between MHWs and the pollution caused by organic enrichment and eutrophication.

Hypoxic and anoxic events are defined as when the dissolved oxygen (DO) is less than 2.0 mg L^{-1} and equal to 0 mg L^{-1}, respectively, and are symptomatic of organic enrichment and eutrophication (Bricker et al., 2008). Global warming and high organic matter loads are the primary cause of deoxygenation, altering biogeochemical cycles and lowering marine species diversity (Breitburg et al., 2018). Coastal hypoxia has exponentially increased "dead zones" worldwide since the 1960s, mainly as a result of human activities (Diaz and Rosenberg, 2008). In South America, seasonal and permanent dead zones in several estuaries are linked to human population growth and lack of basic sanitation (Barletta et al., 2019). The cumulative effects of dead zones and MHWs is likely to reduce environmental resilience and biodiversity (Scherner et al., 2013) although our knowledge of this is limited due to a lack of temporal and spatial *in situ* data.

Temperature is a key driver that effects the physiology, behavior and ecology of marine fauna and flora. Initially, temperature increases usually increase metabolism and energy consumption but can eventually kill marine organisms. Shallow water species tolerate a much wider temperature range than the stenothermal inhabitants of the deep-sea. However, an increase of 2–3°C above normal peak temperature quickly compromises the physiology of coastal organisms, and can be lethal (Peck et al., 2009; Nguyen et al., 2011). For this reason, the distribution of benthic organisms is shifting in response to ocean warming, causing marine community reconfigurations worldwide (Wernberg et al., 2013; Sanford et al., 2019). Experimental tests suggest that *Anomalocardia flexuosa,* a socio-economically important bivalve in South America, is overly sensitive to temperature increases (Carneiro et al., 2020). In Brazil, higher temperatures and pollution can be expected to change the community structure and productivity of benthic marine species (Bernardino et al., 2015), although the effects of MHWs remain a key knowledge gap (Intergovernmental Panel on Climate Change, 2019).

Improving urban planning and sanitation in South America would build resilience to the cumulative effects of global stressors, helping to achieve the UN Sustainable Development Goals (Jacobi and Sulaiman, 2016). Sustainable Development Goal 14 advocates for reductions in marine pollution from all sources, including sewage, although empirical evidence of the benefits of mitigation and management actions is often lacking. Santa Catarina Island is an area of exceptionally high socioeconomic importance in South Brazil, but it suffers from multiple anthropogenic pressures, including poor wastewater treatment (Pagliosa et al., 2006; Garbossa et al., 2017; Cabral et al., 2019). This region has experienced an increase in MHW frequency, intensity and duration (Rodrigues et al., 2019). However, there are no studies addressing the interactive effects of poor water quality and MHWs. Here, we assess the long-term relationships between the physicochemical properties of the water column and phytoplanktonic and benthic communities. We hypothesize that effects of MHWs on oxygen levels are made worse by organic and inorganic enrichment degrading ecosystem state, decreasing water quality and causing biodiversity loss. We hope that the results described here will guide better management of wastewater treatment in the region, for the benefit of all.

MATERIALS AND METHODS

Study Area

Santa Catarina Island, south Brazil, has a 50-km long microtidal embayment (**Figure 1**) with a surface area of 430 km^2 and an average depth of 3 m (Bonetti et al., 2007). The water residence time is around 18 days during summer (Cabral et al., 2020) mixing with the open Atlantic at the North and the South ends of the bay and with low circulation in the central region (Garbossa et al., 2014). The semi-diurnal tides have daily amplitudes of less than 2 m (Garbossa et al., 2014). The adjacent watersheds cover an area of 1875 km^2, where around 1 million people reside permanently. The main economic activities in the region are summer tourism (1.5 million people/year) and mollusc aquaculture (70% of the Brazilian bivalve production) (Garbossa et al., 2017). The system is moderately urbanized and only ∼30% of the wastewater is treated (Garbossa et al., 2017).

Sampling and Laboratory Procedures

In situ data were collected in January 2020 at four sampling stations: Station 1 (near the island's bridge at 27.59°S 48.56°W), Station 2 (Santo Antônio de Lisboa at 27.51°S 48.52°W), Station 3 (Armação da Piedade at 27.38°S 48.54°W), and Station 4 (Ilha do Francês at 27.42°S 48.48°W) (**Figure 1**). Temperature and DO were measured using a YSI Pro 2030 probe. Water samples

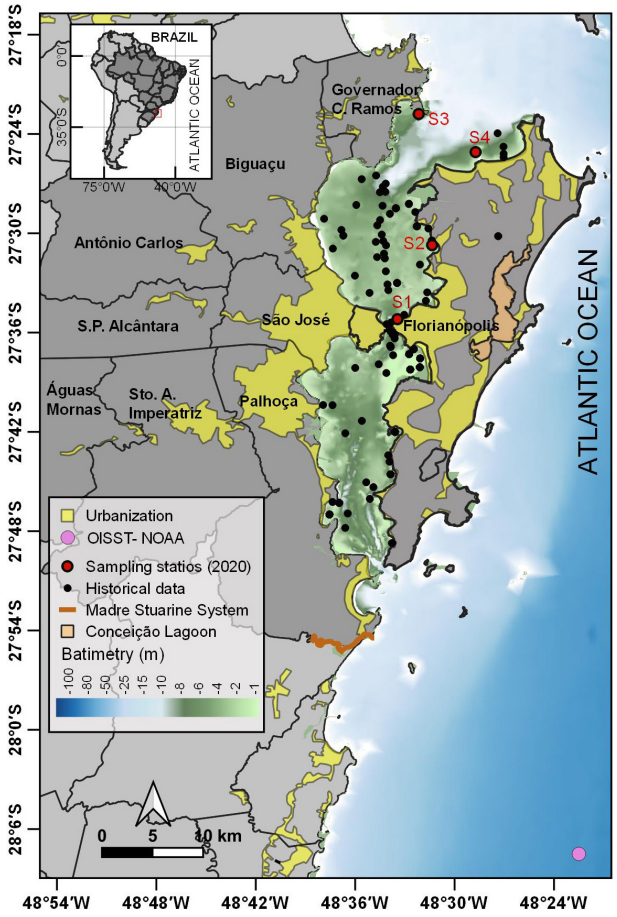


FIGURE 1 | Bay of Santa Catarina Island off Brazil showing coastal water sampling points (black and red circles) and urbanized areas (yellow). The pink circle represents NOAA–OISST: the Optimum Interpolation Sea Surface Temperature from the National Oceanic and Atmospheric Administration.

were collected and filtered to determine the dissolved inorganic phosphorus (DIP) concentration, following the colorimetric method (described in Grasshoff et al., 1999). Data from 1994 to 2019 on water temperature (°C), DO (mg L-), and DIP (μM) were obtained from Cabral et al. (2020) for the Austral summer (December, January, February, and March) (see **Figure 1** for sampling details).

To assess the MHW event in this study, we used SST data obtained from the National Oceanic and Atmospheric Administration, the Optimum Interpolation Sea Surface Temperature V2.1 (OISST) for 1982–2020, which provided better temporal coverage compared to the *in situ* data available for the study area (Reynolds et al., 2007). We calculated the climatology for a pixel at 28.13°S 48.38°W (**Figure 1**). A MHW event occurs when the SST exceeds the 90th percentile for 5 or more days (Hobday et al., 2016). Time series of MHW frequency, maximum intensity, and cumulative intensity were obtained for the whole period. Frequency is the number of MHW days per summer (December–March), maximum intensity is the maximum SST anomaly for all MHW days per summer, and cumulative intensity is the cumulative sum of the intensity for all MHW days within the summer. Number of inhabitants of the nine municipalities around the bays (Água Mornas, Antônio Carlos, Biguaçu, Florianópolis, Governador Celso Ramos, Palhoça, Santa Amaro da Imperatriz, São José, and São Pedro de Alcântara) were retrieved from the Brazilian Institute of Geography and Statistics website (Instituto Brasileiro de Geografia e Estatística – IBGE) for the period of 1994–2019.

Benthic fauna was sampled in triplicate at all stations by scuba-divers using a PVC core of 15 cm diameter and 10 cm high (0.018 m^{-2}). Samples were then washed using a 0.5 mm granulometric sieve and fixed in 70% alcohol for subsequent identification. In the laboratory, the benthic fauna was identified to the lowest possible taxonomic level under a stereoscopic microscope. Historical data of the benthos sampled during summer (December–March) were selected based on the proximity to the stations and the use of the same field and laboratory procedures. Our search returned data from summer 2001, 2006 (available in Souza, 2008) and from 2014 to 2017, corresponding to a total of 22 stations (**Supplementary Table 2**). For phytoplankton analysis, sampling was carried out at two stations (S1 and S4), using a 20 μm net towed at ∼1 m s^{-1}. Samples were fixed in 4% formaldehyde and then identified using keys (Tomas, 1997; Tenenbaum et al., 2004; Tenenbaum and Gomes, 2006).

Statistical Analyses

The significance of trends in temperature, oxygen, DIP and macrobenthic taxonomic richness were obtained using the non-parametric test of Mann–Kendall (MK; $p < 0.05$) (Harding et al., 2019). The test is calculated by paired comparisons of each data value with the previous one, determining the number of increases, decreases and draws (Gilbert, 1987). Mann–Kendall are shown by the strength of association ($-1 < \tau < 1$), where positive values indicate significant increases over the years and negative values a decrease. Kruskal–Wallis (KW) test was applied to verify significant univariate differences among groups ($p < 0.05$). When KW was significant, the Dunn's post-hoc test was used to obtain pairwise comparison results. Pearson linear regression was applied to find significant correlations ($p < 0.05$). To test which variables (DO, *in situ* temperature, DIP, MHWs frequency, maximum intensity, and cumulative intensity) better explained the temporal variations in the benthic richness of the Bays, we used individual Generalized Linear Models (GLM) under negative binomial distribution (Zuur et al., 2009), that is known to address overdispersion (which was the case for our data sets). All analyses were performed in the "R" software using packages "wq" (Jassby and Cloern, 2017), "ggplot2" (Wickham, 2016) and "MASS" (Venables and Ripley, 2013).

RESULTS

Physical and Chemical Long-Term Variability

The average SST detected by satellite was 25.6 ± 1.1 for the period of 1982–2020, ranging from a minimum of 21.5°C in

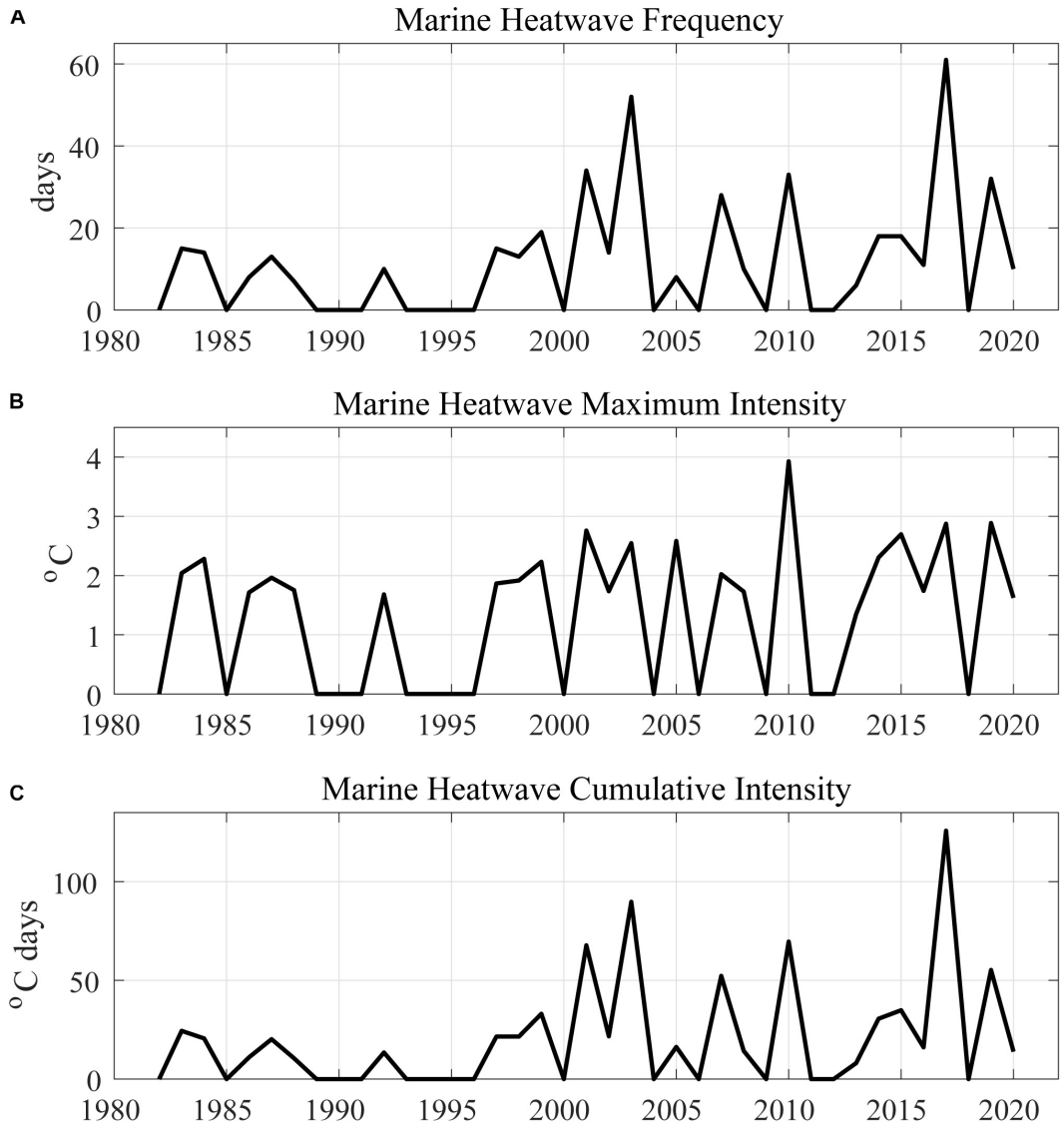


FIGURE 2 | Time series with marine heatwave metrics detected at 28.125°S 48.375°W for the Austral summer months (December–March). **(A)** Frequency in days per summer; **(B)** Maximum intensity in °C per summer; and **(C)** Cumulative intensity in °C Days per summer.

December 1984 to a maximum of 29.5°C in January 2019. The average for the *in situ* data was 26.2 ± 2.3 and ranged widely from 17.0°C in March 2008 to 34.1°C in March 2007. There was a statistically significant positive trend (τ = 0.10, $p < 0.0001$) for the OISST data time series but not for *in situ* data. Marine heatwaves frequency, intensity, and cumulative intensity have progressively increased since the 2000's (**Figure 2**). These trends are respectively 0.4, 0.025, and 0.8°C days per summer each year. Rodrigues et al. (2019) showed that the trends are statistically significant considering a large area adjacent to Santa Catarina Island. Our survey coincided with the 7th day of a MHW event, which lasted 9 days and reached a maximum SST of 26.4°C. The maximum intensity was 1.6°C and cumulative intensity was 12.7°C-Days. In the bays (*in situ* data), water temperature (29.3 ± 0.5°C) was 3°C higher than the values found in the shelf (OISST) during the MHW event. Overall, water temperature was significantly higher ($p < 0.05$) in the bays than in the shelf (OISST) in 8 of the 13 comparable years (**Figure 3A**). Temperatures were similar ($p > 0.05$) between these two data sets in the summer of 2000, 2008, 2014, 2015, and 2018.

Dissolved oxygen concentration in seawater (mean 6.4 ± 1.3 mg L^{-1}) varied from 0.0 to 10.7 mg L^{-1}. The lowest values were observed during the summer of 2020 (mean 4.0 ± 2.3 mg L^{-1}), considering all the summer season time-series (**Figure 3B**). The MK test (τ = -0.51, $p < 0.01$) also showed that DO is decreasing over the years. Dissolved inorganic phosphorus (0.5 ± 0.4 μM) ranged from 0.1 to 4.4 μM. The MK test (τ = 0.33, $p < 0.05$) indicated that DIP is increasing over the time series (**Figure 3D**), from 0.1 ± 0.1 μM in the 1990's to 0.7 ± 0.2 in

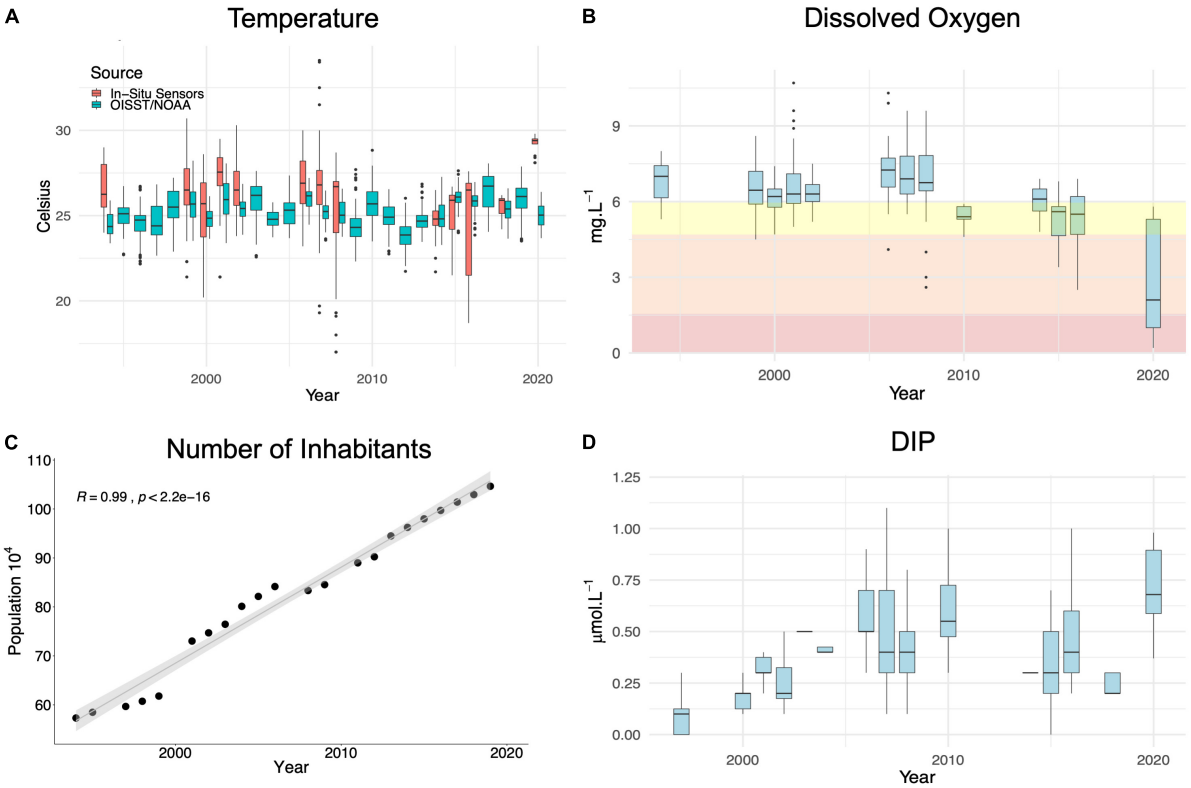


FIGURE 3 | Interannual variability (1994–2020) of **(A)** temperature (*in situ* and OISST), **(B)** dissolved oxygen (DO), **(C)** number of inhabitants, and **(D)** dissolved inorganic phosphorus (DIP) in the Bay of Santa Catarina Island during the summer seasons. The number of human inhabitants per year **(C)** was calculated considering all nine municipalities around the bay. In the DO graph, red shows hypoxia (DO < 2.0 mg L^{-1}, Breitburg et al., 2018), orange indicates biological stress conditions (DO < 5.0 mg L^{-1}, Devlin et al., 2011) and yellow indicates a warning boundary considering the benthic and phytoplanktonic richness losses found in this study.

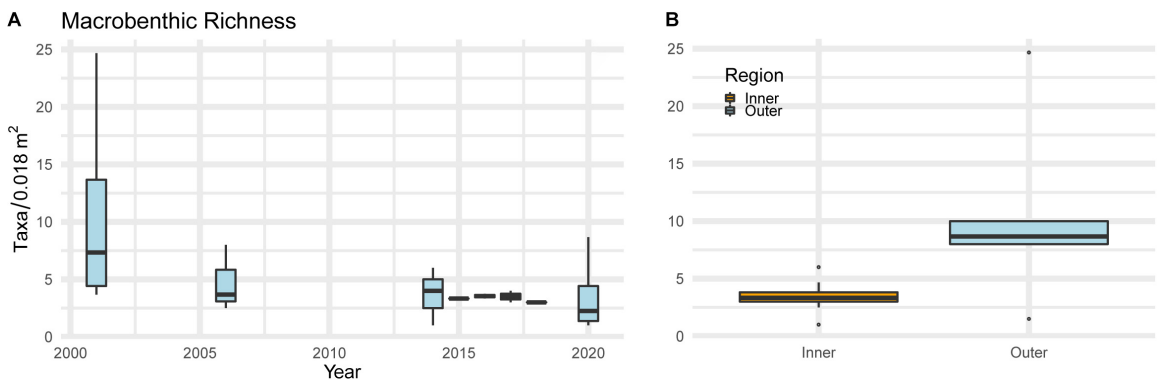


FIGURE 4 | Interannual variability (2001–2020) of macrobenthic species richness **(A)** and within inner and outer areas **(B)** of the Bay of Santa Catarina Island during the summer seasons.

2020. Demographic data show that the human population has continuously increased in the nine municipalities around the bay (**Figure 3C**).

Biological Long-Term Variability

Species richness of the benthic community has declined significantly over the years (MK test; $\tau = -0.62$, $p < 0.05$) (**Figure 4A**). There was a 67% loss, from an average of 10 ($\pm$ 9.69 taxa/0.018 m^{-2}) species in summer 2001 to the lowest average of 3.5 ($\pm$ 3.52 taxa/0.018 m^{-2}) species in summer 2020. In general, spatial patterns of richness were lower in the innermost parts of the bay, increasing to the outer reaches of the bay throughout the time series (**Figure 4B**).

General linear model results showed that variations in the richness of the macrobenthic communities were significantly affected by DO, DIP, and MHW maximum intensity between 2001 and 2020 (**Table 1**). *In situ* temperature, MHW frequency and cumulative intensity showed no influence on the benthic communities within this period. Data were adequately represented by the negative binomial models, with estimates of dispersion parameters generally close to one (range: 0.97 – 1.16).

Qualitative analysis of phyto- and protozooplankton showed differences between station 2 and 4 (**Supplementary Table 1**). In station 2, which is shallower and located inside the Bay of Santa Catarina Island, the taxon richness was lower, with 42 units, 81% of Bacillariophyceae, 7% of Dinophyceae, 10% of ciliate (protozooplankton) and 2% of other phytoplankton groups. In station 4, deeper and located outside the bay, the taxon richness was greater, with 58 units, 72% of which were Bacillariophyceae, 21% of Dinophyceae, 3.5% of ciliate and 3.5% of other phytoplankton groups. Station 2 also showed a greater number of organisms of benthic (or ticopelagic) origin, with 24% against 13% in station 4. In both stations potentially toxic taxa such as *Pseudo-nitzschia* spp., *Trichodesmium* sp. and the dinoflagellate *Dinophysis acuminata* were found.

DISCUSSION

Marine Heatwaves and Eutrophication

Our data show that MHW events are increasing both in frequency and intensity in South Brazil, as described by Rodrigues et al. (2019) for a wider area of the South Atlantic. We did not find an increasing temperature trend in the inshore waters of Santa Catarina Island due to the temporal sparseness of the *in situ* data. However, in 63% of simultaneous measurements of OISST/NOAA satellite data and *in situ* temperatures ($N = 128$), the inshore area had significantly higher temperatures than the shelf waters, indicating that heatwave events impacts are likely to be stronger in coastal regions, as observed by Schlegel et al. (2017). During a MHW in summer 2020, the inshore waters were up to 3°C warmer than offshore, and this occurred at the same time as tourism and sewage discharge peaked in the region (Silva et al., 2016). In addition, extreme rainfall events have become more frequent during summer (Ávila et al., 2016), boosting nutrient and organic matter input from the rivers and triggering eutrophication. The water residence time of the bays in the summer (∼18 days) is the lowest among all seasons (∼83 days during winter), due to high rainfall and the offshore transport of coastal waters by the northerly winds, and yet we found elevated nutrient concentrations and hypoxia in the summer as this coastal system is unable to process current sewage loads (Cabral et al., 2020).

TABLE 1 | GLM results for the Bay of Santa Catarina Island between 2001 and 2020.

	Estimate	Std Error	z value	p value
Intercept	0.3915	0.5705	0.686	0.493
DO	0.2335	0.0918	2.544	*0.011**
Intercept	3.475	2.569	1.353	0.176
Temperature	−0.0640	0.0961	−0.667	0.505
Intercept	3.336	0.3982	8.379	*<0.001****
DIP	−2.9960	0.7577	−3.954	*<0.001****
Intercept	1.736	0.1846	9.403	*<0.001****
MHW Frequency	−0.0221	0.0159	−1.391	0.164
Intercept	1.852	0.1924	9.630	*<0.001****
MHW Maximum Intensity	−0,307	0.1423	−2.157	*0.031**
Intercept	1.715	0.1867	9.184	*<0.001****
MHW Cumulative Intensity	−0,007	0.0062	−1.142	0.253

Macrobenthic richness was the dependent variable and dissolved oxygen (DO), water temperature (in situ), dissolved inorganic phosphorus (DIP), and marine heatwaves (MHW) frequency, maximum intensity and cumulative intensity were the predictors. Z value and approximate significance levels (p value). Negative Z values indicate negative relationships. Significant p values are in italic.

The watershed of our study area is now experiencing ∼60% human population growth, two times Brazil's average (IBGE, 2020). At the same time, sewage treatment is inadequate throughout the region, resulting in high organic matter and nutrient loads (Garbossa et al., 2017; Cabral et al., 2019). We show that DIP has been increasing over the years, probably related to human population increase and inadequate wastewater treatment. The pressure on sewage systems increases in summer, when the number of inhabitants triples in some watersheds because of mass tourism (Silva et al., 2016). Moreover, only 30% of the urban population in the region is serviced by sewerage; most households use cesspits or dump the sewage *in natura*, polluting the coastal zone. Human adenoviruses have been detected in streams that drain to the bays (Rigotto et al., 2010), and this is directly correlated to the elevated trophic status of its waters (Silva and Fonseca, 2016). Santa Catarina Island bays have moderate to high eutrophication pressure (Cabral et al., 2020). The combination of organic enrichment and eutrophication (Bricker et al., 2008) can cause low oxygen levels in the rivers (Pagliosa et al., 2006) and harmful algal blooms in marine shelf waters (Alves and Mafra, 2018).

Our plankton analyses showed ecological differences between the inner and outer areas of the bay. The highest proportion of diatoms was found inside the bay, indicating that the system is enriched with nutrients and affected by continuous resuspension of sediments. Previous studies also showed that the relative importance of diatoms in the bays increased during dredging in the late 1990's, leading to more sediment resuspension and, possibly, nutrients and pollutants turnover (Rörig et al., 2010, 2011). Our data show that DIP concentrations after (2001) dredging (1994) were significantly ($p < 0.05$) higher, never returning to the same levels again (**Figure 3**). This suggests that, besides sewage inputs, P fluxes from the sediment might contribute to eutrophication, especially during hypoxic events due to P desorption, as already shown for the estuaries that drain to the bay (Pagliosa et al., 2005). The greater taxon richness outside the bay, also with greater relative importance of dinoflagellates (Dinophyceae), shows a less restrictive environment, with more diversity of ecological niches. Moreover, some studies have also shown an increase in harmful algal blooms in the region, possibly related to the degradation

of water quality and anomalous meteo-oceanographic events (Proença et al., 2017; Rörig et al., 2018).

Dead Zones and Loss of Biodiversity

Dead zones are spreading worldwide mainly because of increased wastewater discharge from untreated sewage and effluents from agriculture (Diaz and Rosenberg, 2008; Breitburg et al., 2018). The interactive effects of this pollution and MHWs may generate multiple impacts in coastal ecosystems. Ocean warming can contribute to the spread of dead zones, especially in estuaries and bays, where proximity to urban areas and higher water residence times contribute to elevated water temperature and organic matter mineralization rates (Altieri and Gedan, 2014). Our data show that the shallow bays inshore of Santa Catarina Island experience these processes; DO levels in this enclosed system have been decreasing for years, at the same time as sewage and nutrient inputs have been increasing, and MHWs have become more frequent and intense. Monitoring data from 1994 to 2020 show that the first recorded episode of hypoxia and anoxia during summer occurred in 2020, concomitant with a MHW. Monitoring programs and solutions are needed in the Bay of Santa Catarina Island since the interaction of local and climate stressors might also threaten important economic activities around the region, such as aquaculture, fisheries and tourism.

A lack of monitoring data in the coastal ecosystems of the South Atlantic makes it hard to assess and control the deoxygenation problem. Two systems close to the bays have periodic dead zones due to sewage discharge (Conceição lagoon) and agricultural runoff (Madre estuarine system) (Fontes et al., 2011; Barros et al., 2017; Cabral and Fonseca, 2019). These dead zones were developed due to strong vertical stratification (saline or/and thermal) that prevents reoxygenation of the benthos. Water in the Bay of Santa Catarina Island is not stratified as it is tidal and shallow (<3 m depth) and yet we observed hypoxia and anoxia during the MHW event of 2020. Also, sediment in the northern bay is mostly mud enriched with organic matter boosting benthic respiration and deoxygenation (Bonetti et al., 2007). Limited oxygen influx into sediments during hypoxic and anoxic events decreases denitrification and stimulates P desorption from ferric complex, releasing nutrients to the water column and enhancing eutrophication in a positive feedback (Fennel and Testa, 2019).

Biological stress from low DO (< 5.0 mg L^{-1}) was first reported in 2007 and 2008 as outliers. However, concentrations below this threshold started to increase in 2015 and, in summer 2020, dead zones (<2.0 mg L^{-1}) were found. Following long-term (2001–2020) DO reductions and water temperature increases, the benthic communities also lost richness. The innermost region and most urbanized area of the bay was particularly adversely affected. The faunal responses show overlapping effects of high temperatures and low DO linked to the increase of sewage discharges. Our results reinforce the perspective that the biological stress threshold for benthic communities could be 6.0 mg L^{-1}, 1.0 mg L^{-1} more than the threshold generally used in the literature (Vaquer-Sunyer and Duarte, 2008; Devlin et al., 2011). This highlights that new coastal water quality standards should be pursued in mitigation and restoration programs.

The richness of the macrobenthos in the most urbanized areas around Santa Catarina Island have long been poor, with a more recent deterioration in the outer reaches of the bay between 2001 and 2020. Evidence of macrofaunal negative responses to higher contents of trace metals (copper and lead), suspended particulate matter, nitrogen and phosphorus have been previously found in urbanized estuaries that drain to the bay (Pagliosa et al., 2006; Netto et al., 2018). Richness, abundance, and productivity decrease in virtue of bottom hypoxia, hampering larval settlement, and community recovery (Kodama and Horiguchi, 2011; Sturdivant et al., 2014). The outer areas of the bay have higher exchange with shelf waters (Garbossa et al., 2014), promoting dilution of contaminants. Although these areas had higher macrobenthic richness than the inner bay, their decline between 2001 and 2020 suggests that even the well flushed outer bay is polluted. Carbon and nutrient content over the past 100 years have constantly increased in the bay with population growth (Lamego et al., 2017), likely affecting the benthos.

Local pressures frequently exacerbate global stressors, such as ocean warming (Todgham and Stillman, 2013), increasing the chances of damage to local ecosystem functions. Extreme summer temperatures in the Bay of Santa Catarina Island, such as observed in 2007 (34.1°C) and 2020 (29.8°C), can negatively impact the macrobenthic fauna (Bernardino et al., 2015) since DO levels fall as water temperature increases. The effects of a MHW are superimposed upon the effects of other existing stressors, such as deoxygenation and nutrient enrichment. For example, many polychaete species, the dominant faunal group in our dataset, have declined in abundance in outer parts of the bay over the years. Assemblages subjected to sewage and low DO become dominated by a few tolerant and opportunistic species (Souza et al., 2013; Brauko et al., 2016; Weis et al., 2017). Benthic productivity mediates both biogeophysical and biogeochemical feedbacks to climate change via degradation of organic matter, trophic transfer, denitrification and nutrient remineralization (Bernardino et al., 2015). Long-term monitoring efforts allied to experimental evidence are still needed for a better comprehension of their threshold limits and future scenarios aiming to maintain ecosystem functions.

Local Solutions to Mitigate Local and Global Stressors in Coastal Areas

The increase of remote techniques and studies of coastal regions have revealed spreading degradation of natural ecosystems in the last decade, associated with an increasing human population and deficient wastewater treatment. Transdisciplinary solutions are needed to address this problem, working on regional solutions to global stressors. Islands have scarce water resources for sewage treatment and frequently use crude submarine outfalls. However, given the sensitivity of coastal environments, often within nature conservation and multiple-use zones, oceanic disposal requires tertiary treatment, i.e., nutrient, pathogen and micropollutant removal. Conventional tertiary treatment technologies are costly to implement and maintain (Mota and Von Sperling, 2009),

so nature-based technologies are gaining prominence, as they integrate relatively low costs with sustainability. Examples include constructed wetlands (mainly based on aquatic plants) and phycoremediation systems (based on algae).

Wetlands and coastal vegetation can help to improve water quality, by reducing pathogen and nutrient concentrations and increasing oxygen availability (Zedler, 2000; Duarte et al., 2017). Restoration of these systems is a good option to improve effluent treatment in coastal areas. In addition, artificial wetlands can also help water quality restoration. Wetland parks, which combine treatment units in a multifunctional setting (Haron and Feisal, 2020) can be built at the land-water interface, reducing pollution

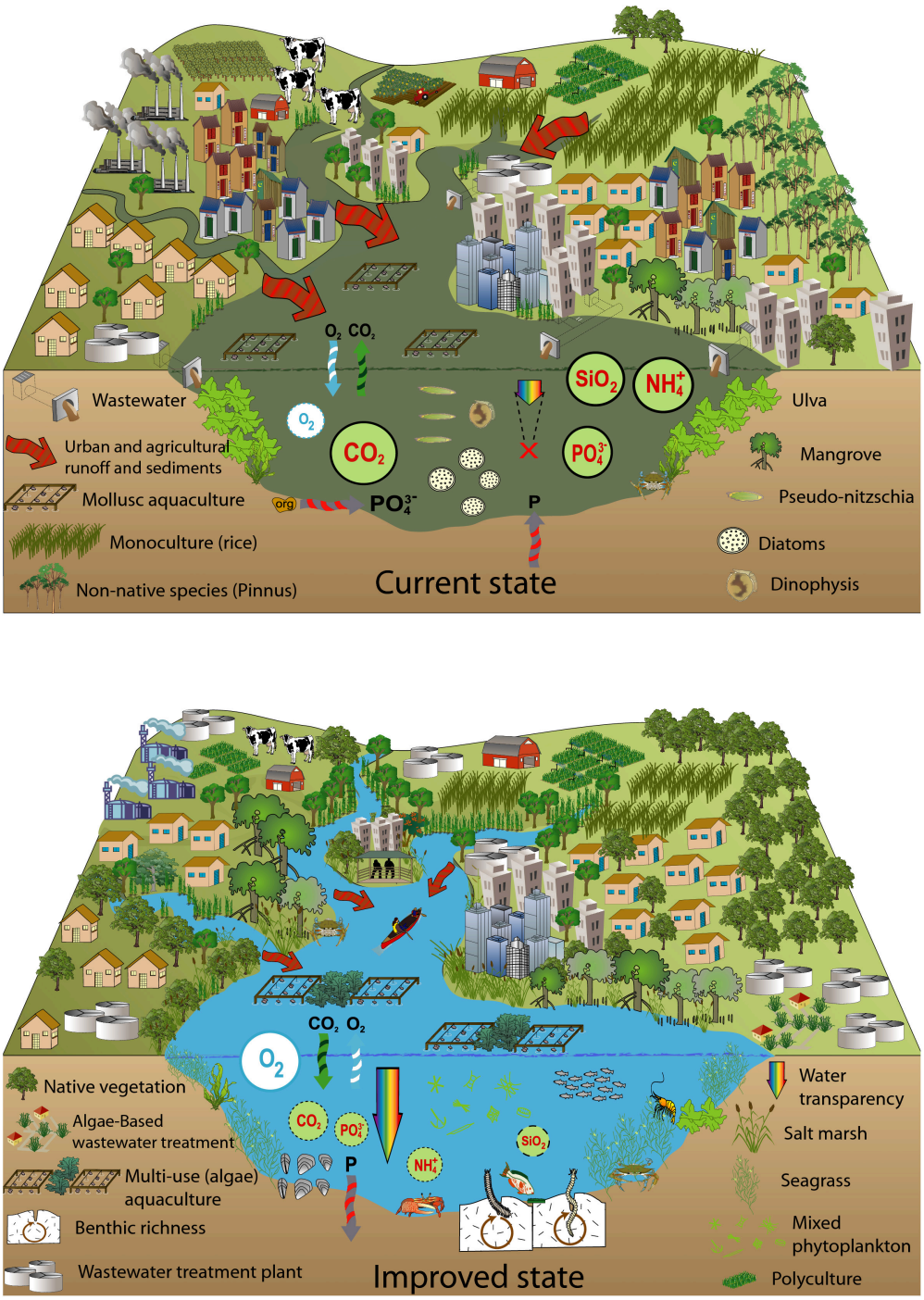


FIGURE 5 | Current state of the Bay of Santa Catarina Island, polluted by organic and inorganic enrichment, and a future scenario after improved long-term wastewater treatment and wetlands restoration.

and stimulating recovery of ecological functions. Another option is to use algal-based solutions (Young et al., 2017), such as High-Rate Algal Ponds that generate intense algal growth. Although this technology requires lot of space, it can be an alternative to manage macroalgae growth and to increase nutrient removal and biomass growth. Algal Turf Scrubbers have algal communities growing on screens, with effluent pumped into the system and released with lower nutrient and higher oxygen concentrations (Adey and Loveland, 2007). In Santa Catarina Island, this technology could be useful since the sewage treatment goes up to just the secondary phase and it is not efficient to control eutrophication (Cabral et al., 2019).

Perhaps the greatest challenge to reduce pollution in the coastal zone is not technological, given the sustainable options available. There is a major difficulty in convincing authorities and economic sectors that managing wastewater is an affordable priority (Chrispim et al., 2019) to build resilience to extreme events. Conservation and restoration of coastal wetlands and blue carbon stores, such as mangroves and salt marshes, also enhance CO_2 sequestration capacity and biodiversity recovery (Serrano et al., 2019). We propose a conceptual model considering the current scenario of the bays and an improved perspective, where some of the local solutions discussed were applied (**Figure 5**). The aim of the mitigation strategies is to build resilience against eutrophication and oxygen depletion due to MHWs. Moreover, those measures could help to recover biodiversity, aquaculture and fisheries damaged by MHW events (Carneiro et al., 2020).

CONCLUSION

We show an increase in frequency and intensity of MHWs in southern Brazil and recorded temperatures much higher than those registered using satellites in a socioeconomically important enclosed water body off Santa Catarina Island. Marine heatwaves are more intense in coastal systems with limited water exchange and this emphasizes the importance of monitoring coastal waters. The watersheds of the region are under great pressure due to the combined effect of a recent 60% increase in human population and inadequate sewage systems. This is especially problematic in the summer when the temperatures are high and the number of inhabitants triples due to tourism. Increasing phosphorus concentrations and dominance by diatoms show that the enclosed water body is eutrophic. Dissolved oxygen levels have been decreasing in this enclosed system for years, causing dead zones to appear for the first time, during a MHW in 2020. Spatio-temporal losses in the richness of benthic communities suggest overlapping effects of high temperatures and low oxygen linked to sewage discharge. Currently used thresholds of coastal pollution and related hypoxia are not conservative enough to avoid losses of biodiversity and ecosystems goods and services. Levels of permitted organic and inorganic compounds need to take ocean warming into consideration. We highlight the potential benefits of restoration efforts and relatively low-cost nature-based wastewater treatment technologies. Marine management and mitigation options are also discussed to build local resilience to global-scale warming events.

DATA AVAILABILITY STATEMENT

Macrobenthic richness data can be found in the **Supplementary Material**. Physical and chemical *in situ* datasets are available at http://dx.doi.org/10.17632/458xcpxwbh.1. Sea surface temperature were obtained from the National Oceanic and Atmospheric Administration at https://www.ncdc.noaa.gov/oisst/optimum-interpolation-sea-surface-temperature-oisst-v21.

AUTHOR CONTRIBUTIONS

KB and AC: conception of the work, data analysis and interpretation, and wrote and reviewed the article. NC: conception of the work, data collection, and heatwave analysis and recommendations. JH: phytoplankton analysis and interpretation. CD, EL, RW, and CM: conception of the work and data collection and interpretation. JH-S: conception of the work, data collection and interpretation, and article review. RR: heatwave analysis and article review. LR: data analysis and interpretation and article review. PP: benthic analysis and interpretation and article review. AF: provided historical chemical data and article review. OA: conception of the work and data collection. PH: conception of the work, data collection, and article review. All authors contributed to the article and approved the submitted version.

FUNDING

This study was funded by grants from CAPES (Higher Education Personnel Improvement Coordination) – CAPES Senior Visitor, CAPES PrInt 310793/2018-01; CNPq (National Council for Scientific and Technological Development) – CNPq PVE 407365/2013-3, CNPq Universal 426215/2016-8 and CNPq PQ 308537/2019-0; ICNT-TMCOcean 573.601/2008-9); FINEP (Brazilian Innovation Agency); the Boticario Foundation; and FAPESC – Foundation for Support of Research and Innovation, Santa Catarina.

ACKNOWLEDGMENTS

PH and KB thank CAPES – Senior Visitor, CAPES-PrInt 310793/2018-01, CNPq-PVE 407365/2013-3, CNPq-Universal 426215/2016-8, and CNPq-PQ- 308537/2019-0. OA thanks FINEP for Veleiro ECO funding. All authors thank J.C. Simonassi for the assistance with chemical analyses.

SUPPLEMENTARY MATERIAL

The Supplementary Material for this article can be found online at: https://www.frontiersin.org/articles/10.3389/fmars.2020.590258/full#supplementary-material

REFERENCES

Adey, W. H., and Loveland, K. (2007). *Dynamic Aquaria: Building Living Ecosystems*, 3rd Edn. New York: Academic Press.

Altieri, A. H., and Gedan, K. B. (2014). Climate change and dead zones. *Glob. Change Biol.* 21, 1395–1406. doi: 10.1111/gcb.12754

Alves, T. P., and Mafra, L. L. (2018). Diel variations in cell abundance and trophic transfer of diarrheic toxins during a massive dinophysis bloom in Southern Brazil. *Toxins* 10:232. doi: 10.3390/toxins10060232

Arias-Ortiz, A., Serrano, O., Masqué, P., Lavery, P. S., Mueller, U., Kendrick, G. A., et al. (2018). A marine heatwave drives massive losses from the world's largest seagrass carbon stocks. *Nat. Clim. Change* 8:338. doi: 10.1038/s41558-018-0096-y

Ávila, A., Justino, F., Wilson, A., Bromwich, D., and Amorim, M. (2016). Recent precipitation trends, flash floods and landslides in southern Brazil. *Environ. Res. Lett.* 11:114029. doi: 10.1088/1748-9326/11/11/114029

Barletta, M., Lima, A. R. A., and Costa, M. F. (2019). Distribution, sources and consequences of nutrients, persistent organic pollutants, metals and microplastics in South American estuaries. *Sci. Total Environ.* 651, 1199–1218. doi: 10.1016/j.scitotenv.2018.09.276

Barros, G. D., Fonseca, A. L. D. O., Santos, A. C. D., Fontes, M. L. S., Varela, A. R. D., and Franco, D. (2017). Nutrient distribution in a shallow subtropical lagoon, south Brazil, subjected to seasonal hypoxic and anoxic events. *Braz. J. Oceanogr.* 65, 116–127. doi: 10.1590/s1679-87592017101206502

Bernardino, A. F., Netto, S. A., Pagliosa, P. R., Barros, F., Christofoletti, R. A., Rosa Filho, J. S., et al. (2015). Predicting ecological changes on benthic estuarine assemblages through decadal climate trends along Brazilian Marine Ecoregions. *Estuar. Coast. Shelf Sci.* 166, 74–82. doi: 10.1016/j.ecss.2015.05.021

Bestion, E., Barton, S., García, F. C., Warfield, R., and Yvon−Durocher, G. (2020). Abrupt declines in marine phytoplankton production driven by warming and biodiversity loss in a microcosm experiment. *Ecol. Lett.* 23, 457–466. doi: 10.1111/ele.13444

Bonetti, C., Bonetti, J., and Barcelos, R. L. (2007). "Caracterização sedimentar e geoquímica de sistemas costeiros com ênfase na avaliação da influência de sítios de cultivo de moluscos," in *Sistemas de Cultivos Aquícolas Costeiros no Brasil: Recursos, Tecnologias e Aspectos Ambientais e Sócio-Econômicos*, eds G. F. Barroso, L. H. S. Poersch, R. O. Cavalli, and A. O. Galvez (Rio de Janeiro: Museu Nacional), 139–149.

Brauko, K. M., Muniz, P., Martins, C. C., and Lana, P. C. (2016). Assessing the suitability of five benthic indices for environmental health assessment in a large subtropical South American estuary. *Ecol. Indicators* 64, 258–265. doi: 10.1016/j.ecolind.2016.01.008

Breitburg, D., Levin, L. A., Oschlies, A., Gregoire, M., Chavez, F. P., Conley, D. J., et al. (2018). Declining oxygen in the global ocean and coastal waters. *Science* 359, 46–57.

Bricker, S. B., Longstaff, B., Dennison, W., Jones, A., Boicourt, K., Wicks, C., et al. (2008). Effects of nutrient enrichment in the nation's estuaries: a decade of change. *Harmful Algae* 8, 21–32. doi: 10.1016/j.hal.2008.08.028

Cabral, A., Bercovich, M. V., and Fonseca, A. (2019). Implications of poor-regulated wastewater treatment systems in the water quality and nutrient fluxes of a subtropical coastal lagoon. *Region. Stud. Mar. Sci.* 29:100672. doi: 10.1016/j.rsma.2019.100672

Cabral, A., Bonetti, C., Garbossa, L., Pereira-Filho, J., Besen, K., and Fonseca, A. (2020). Water masses seasonality and meteorological patterns drive the biogeochemical processes of a subtropical and urbanized watershed-bay-shelf continuum. *Sci. Total Environ.* 749:141553. doi: 10.1016/j.scitotenv.2020.141553

Cabral, A., and Fonseca, A. (2019). Coupled effects of anthropogenic nutrient sources and meteo-oceanographic events in the trophic state of a subtropical estuarine system. *Estuar. Coast. Shelf Sci.* 225:106228. doi: 10.1016/j.ecss.2019.05.010

Carneiro, A. P., Soares, C. H. L., Manso, P. R. J., and Pagliosa, P. R. (2020). Impact of marine heat waves and cold spell events on the bivalve *Anomalocardia flexuosa*: a seasonal comparison. *Mar. Environ. Res.* 156:104898. doi: 10.1016/j.marenvres.2020.104898

Cavole, L. M., Demko, A. M., Diner, R. E., Giddings, A., Koester, I., Pagniello, C. M., et al. (2016). Biological impacts of the 2013–2015 warm-water anomaly in the Northeast Pacific: winners, losers, and the future. *Oceanography* 29, 273–285.

Chrispim, M. C., Scholz, M., and Nolasco, M. A. (2019). Phosphorus recovery from municipal wastewater treatment: Critical review of challenges and opportunities for developing countries. *J. Environ. Manag.* 248, 109268. doi: 10.1016/j.jenvman.2019.109268

Devlin, M., Bricker, S., and Painting, S. (2011). Comparison of five methods for assessing impacts of nutrient enrichment using estuarine case studies. *Biogeochemistry* 106, 177–205. doi: 10.1007/s10533-011-9588-9

Diaz, R. J., and Rosenberg, R. (2008). Spreading dead zones and consequences for marine ecosystems. *Science* 321, 926–929. doi: 10.1126/science.1156401

Duarte, I. D., Silva, N. H. V. F., da Costa Souza, I., de Oliveira, L. B., Rocha, L. D., Morozesk, M., et al. (2017). Water quality of a coastal lagoon (ES, Brazil): abiotic aspects, cytogenetic damage, and phytoplankton dynamics. *Environ. Sci. Pollut. Res.* 24, 10855–10868. doi: 10.1007/s11356-017-8721-2

Fennel, K., and Testa, J. M. (2019). Biogeochemical controls on coastal hypoxia. *Annu. Rev. Mar. Sci.* 11, 105–130. doi: 10.1146/annurev-marine-010318-095138

Fontes, M. L. S., Suzuki, M. T., Cottrell, M. T., and Abreu, P. C. (2011). Primary production in a subtropical stratified coastal lagoon—contribution of anoxygenic phototrophic bacteria. *Microb. Ecol.* 61, 223–237. doi: 10.1007/s00248-010-9739-x

Frölicher, T. L., Fischer, E. M., and Gruber, N. (2018). Marine heatwaves under global warming. *Nature* 560, 360–364. doi: 10.1038/s41586-018-0383-9

Garbossa, L. H. P., Souza, R. V., Campos, C. J. A., Vanz, A., Vianna, L. F. N., and Rupp, G. S. (2017). Thermotolerant coliform loadings to coastal areas of Santa Catarina (Brazil) evidence the effect of growing urbanization and insufficient provision of sewerage infrastructure. *Environ. Monit. Assess.* 189:27.

Garbossa, L. H. P., Vanz, A., Fernandes, L. D. F., Souza, R. V. D., Vianna, L. F., and Rupp, G. S. (2014). "Modelling and validation of the Santa Catarina Island Bays hydrodynamics based on astronomical tides and measured tides," in *Proceedings of the 11th International Conference on Hydroinformatics HIC 2014*, (New York. NY: Curran Associates, Inc).

Garrabou, J., Coma, R., Bensoussan, N., Bally, M., Chevaldonné, P., Cigliano, M., et al. (2009). Mass mortality in Northwestern Mediterranean rocky benthic communities: effects of the 2003 heat wave. *Glob. Change Biol.* 15, 1090–1103. doi: 10.1111/j.1365-2486.2008.01823.x

Gilbert, R. O. (1987). *Statistical Methods for Environmental Pollution Monitoring*. Hoboken, NJ: John Wiley & Sons.

Gouvêa, L. P., Schubert, N., Martins, C. D. L., Sissini, M., Ramlov, F., Rodrigues, E. R. O., et al. (2017). Interactive effects of marine heatwaves and eutrophication on the ecophysiology of a widespread and ecologically important macroalga. *Limnol. Oceanogr.* 62, 2056–2075. doi: 10.1002/lno.10551

Grasshoff, K., Kremling, K., and Ehrhardt, M. (1999). *Methods of Seawater Analysis, Methods of Seawater Analysis: Third, Completely Revised and Extended Edition*. Hoboken, NJ: Wiley.

Harding, L. W., Mallonee, M. E., Perry, E. S., Miller, W. D., Adolf, J. E., Gallegos, C. L., et al. (2019). Long-term trends, current status, and transitions of water quality in Chesapeake Bay. *Sci. Rep.* 9, 1–19.

Haron, A., and Feisal, Z. (2020). Constructed wetland parks: a pathway to sustainability for Cairo. *J. Urban Res.* 36, 61–81.

Hobday, A. J., Alexander, L. V., Perkins, S. E., Smale, D. A., Straub, S. C., Oliver, E. C. J., et al. (2016). A hierarchical approach to defining marine heatwaves. *Prog. Oceanogr.* 141, 227–238. doi: 10.1016/j.pocean.2015.12.014

IBGE (2020). *Instituto Brasileiro de Geografia e Estatística*. Available online at: https://www.ibge.gov.br/ (accessed July, 2020)

Intergovernmental Panel on Climate Change (2019). *Special Report on the Ocean and Cryosphere in a Changing Climate*. Geneva: IPCC.

Jacobi, P. R., and Sulaiman, S. N. (2016). Governança ambiental urbana em face das mudanças climáticas. *Revist. USP* 109, 133–142. doi: 10.11606/issn.2316-9036.v0i109p133-142

Jassby, A. D., and Cloern, J. E. (2017). *wq: Some Tools for Exploring Water Quality Monitoring Data. R Package Version 0.4.8*. Available online at: https://cran.r-project.org/package=wq (accessed October 17, 2020).

Kodama, K., and Horiguchi, T. (2011). Effects of hypoxia on benthic organisms in Tokyo Bay, Japan: a review. *Mar. Pollut. Bull.* 63, 215–220. doi: 10.1016/j.marpolbul.2011.04.022

Lamego, F., da Silva, A. L. G., Simonassi, J. C., and Nepomuceno, A. (2017). Reconstructing recent land–ocean changes in the Brazilian Southern Coast

using sedimentary proxies and tracking airborne 210 Pb. *J. Radioanal. Nuclear Chem.* 314, 2281–2299. doi: 10.1007/s10967-017-5623-1

Mota, S., and Von Sperling, M. (2009). *Nutrientes de Esgoto Sanitário: Utilização e Remoção*, Vol. 1. Rio de Janeiro: FINEP, 430.

Netto, S. A., Pagliosa, P. R., Colling, A., Fonseca, A. L., and Brauko, K. M. (2018). "Benthic estuarine assemblages from the Southern Brazilian marine ecoregion," in *Brazilian Estuaries. Brazilian Marine Biodiversity*, eds P. Lana and A. Bernardino (Cham: Springer).

Nguyen, K. D. T., Morley, S. A., Lai, C.-H., Clark, M. S., Tan, K. S., Bates, A. E., et al. (2011). Upper temperature limits of tropical marine ectotherms: global warming implications. *PLoS One* 6:e29340. doi: 10.1371/journal.pone.0029340

Oliver, E. C. J., Burrows, M. T., Donat, M. G., Sen Gupta, A., Alexander, L. V., Perkins-Kirkpatrick, S. E., et al. (2019). Projected marine heatwaves in the 21st century and the potential for ecological impact. *Front. Mar. Sci.* 6:734. doi: 10.3389/fmars.2019.00734

Pagliosa, P. R., Fonseca, A., Barbosa, F. A. R., and Braga, E. (2006). Urbanization impact on subtropical estuaries: a comparative study of water properties in urban areas and in protected areas. *J. Coast. Res.* 39, 731–735.

Pagliosa, P. R., Fonseca, A., Bosquilha, G. E., Braga, E. S., and Barbosa, F. A. R. (2005). Phosphorus dynamics in water and sediments in urbanized and non-urbanized rivers in Southern Brazil. *Mar. Pollut. Bull.* 50, 965–974. doi: 10.1016/j.marpolbul.2005.04.005

Peck, L., Massey, A., Thorne, M., and Clark, M. (2009). Lack of acclimation in Ophionotus victoriae: brittle stars are not fish. *Polar Biol.* 32, 399–402. doi: 10.1007/s00300-008-0532-y

Proença, L. A. O., Schramm, M. A., Alves, T. P., and Piola, A. R. (2017). "The extraordinary 2016 autumn DSP outbreak in Santa Catarina, Southern Brazil, explained by large-scale oceanographic processes," in *Marine and Fresh-Water Harmful Algae. Proceedings of the 17th International Conference on Harmful Algae*, eds L. A. O. Proença and G. M. Hallegraeff (Washington, DC: International Society for the Study of Harmful Algae), 42–45.

Reynolds, R. W., Smith, T. M., Liu, C., Chelton, D. B., Casey, K. S., and Schlax, M. G. (2007). Daily high-resolution-blended analyses for sea surface temperature. *J. Clim.* 20, 5473–5496. doi: 10.1175/2007jcli1824.1

Rigotto, C., Victoria, M., Moresco, V., Kolesnikovas, C. K., Corrêa, A. A., Souza, D. S. M., et al. (2010). Assessment of adenovirus, hepatitis A virus and rotavirus presence in environmental samples in Florianopolis, South Brazil. *J. Appl. Microbiol.* 109, 1979–1987. doi: 10.1111/j.1365-2672.2010.04827.x

Rodrigues, R. R., Taschetto, A. S., Gupta, A. S., and Foltz, G. R. (2019). Common cause for severe droughts in South America and marine heatwaves in the South Atlantic. *Nat. Geosci.* 12, 620–626. doi: 10.1038/s41561-019-0393-8

Rörig, L. R., Pereira Filho, J., and Almeida, T. C. M. (2010). "O fitoplâncton no diagnóstico de mudanças ambientais: O Caso da Baía Sul - Florianópolis, SC," in *III Congresso Brasileiro de Oceanografia, 2010*, (Rio Grande, RS: CBO).

Rörig, L. R., Pereira Filho, J., Silva, R. L., Horta, P. A., and Almeida, T. C. M. (2011). "O fitoplâncton no diagnóstico de mudanças ambientais: O Caso da Baía Sul - Florianópolis," in *Proceedings of the XIV Congresso Latino-Americano de Ciências do Mar - XIV COLACMAR*, (Balneário Camboriú: COLACMAR).

Rörig, L. R., Tamanaha, M. S., Persich, G. R., Schettini, C. A. F., and Truccolo, E. C. (2018). "Phytoplankton patterns and processes in a tropical-subtropical transition region: Santa Catarina Coast, Southern Brazil," in *Plankton Ecology of the Southwestern Atlantic*, eds M. S. Hoffmeyer, M. E. Sabatini, F. P. Brandini, D. L. Calliari, and N. H. Santinelli (Cham: Springer International), 269–287. doi: 10.1007/978-3-319-77869-3_13

Sanford, E., Sones, J. L., García-Reyes, M., Goddard, J. H., and Largier, J. L. (2019). Widespread shifts in the coastal biota of northern California during the 2014–2016 marine heatwaves. *Sci. Rep.* 9, 1–14.

Scherner, F., Horta, P. A., Oliveira, E. C., Simonassi, J. C., Hall Spencer, J. M., Chow, F., et al. (2013). Coastal urbanization leads to remarkable seaweed species loss and community shifts along the SW Atlantic. *Mar. Pollut. Bull.* 76, 106–115. doi: 10.1016/j.marpolbul.2013.09.019

Schlegel, R. W., Oliver, E. C., Wernberg, T., and Smit, A. J. (2017). Nearshore and offshore co-occurrence of marine heatwaves and cold-spells. *Prog. Oceanogr.* 151, 189–205. doi: 10.1016/j.pocean.2017.01.004

Serrano, O., Kelleway, J. J., Lovelock, C., and Lavery, P. S. (2019). "Conservation of blue carbon ecosystems for climate change mitigation and adaptation," in *Coastal Wetlands*, eds G. M. E. Perillo, E. Wolanski, D. R. Cahoon, and C. S. Hopkinson (Amsterdam: Elsevier), 965–996. doi: 10.1016/b978-0-444-63893-9.00028-9

Silva, A. R., and Fonseca, A. L. D. (2016). Eutrofização dos recursos hídricos como ferramenta para a compreensão das doenças de vinculação hídrica. *Geosul* 31:247. doi: 10.5007/2177-5230.2016v31n62p247

Silva, A. R., Fonseca, A. L. D., Rodrigues, C. J., and Beltrame, A. V. (2016). Application of ecological indicators in coastal watershed under high pressure during summer period. *RBRH* 21, 537–548. doi: 10.1590/2318-0331.011615106

Smale, D. A., Wernberg, T., Oliver, E. C., Thomsen, M., Harvey, B. P., Straub, S. C., et al. (2019). Marine heatwaves threaten global biodiversity and the provision of ecosystem services. *Nat. Clim. Change* 9, 306–312. doi: 10.1038/s41558-019-0412-1

Souza, F. M., Brauko, K. M., Lana, P. C., Muniz, P., and Camargo, M. G. (2013). The effect of urban sewage on benthic macrofauna: a multiple spatial scale approach. *Mar. Pollut. Bull.* 67, 234–240. doi: 10.1016/j.marpolbul.2012.10.021

Souza, R. S. D. (2008). *Efeitos dos Cultivos de Bivalves (Mollusca, Bivalvia) sobre as associações bênticas macrofaunais na baía da ilha de Santa Catarina (SC), Brasil*. Ph. D. Dissertation, Universidade Federal do Paraná, Curitiba.

Sturdivant, S. K., Díaz, R. J., Llansó, R., and Dauer, D. M. (2014). Relationship between hypoxia and macrobenthic production in Chesapeake Bay. *Estuar. Coasts* 37, 1219–1232. doi: 10.1007/s12237-013-9763-4

Tenenbaum, D. R., and Gomes, E. A. T. (2006). *Dinoflagelados e Tintinídeos da Região Central da Zona Econômica Exclusiva Brasileira: Guia de Identificação*. Rio de Janeiro: Museu Nacional Rio de Janeiro.

Tenenbaum, D. R., Villac, M. C., Viana, S. C., Matos, M., Lima, I. V., and Menezes, M. (2004). *Phytoplankton Atlas of Sepetiba Bay, Rio de Janeiro, Brasil*. London: Global Ballast Water Management Programme.

Todgham, A. E., and Stillman, J. H. (2013). Physiological responses to shifts in multiple environmental stressors: relevance in a changing world. *Integr. Comp. Biol.* 53, 539–544. doi: 10.1093/icb/ict086

Tomas, C. R. (1997). *Identifying Marine Phytoplankton*. San Diego, CA: Academic Press.

Vaquer-Sunyer, R., and Duarte, C. M. (2008). Thresholds of hypoxia for marine biodiversity. *Proc. Natl. Acad. Sci. U.S.A.* 105, 15452–15457. doi: 10.1073/pnas.0803833105

Venables, W. N., and Ripley, B. D. (2013). *Modern Applied Statistics with S-PLUS*. Berlin: Springer Science & Business Media.

Weis, W. A., Soares, C. H. L., de Quadros, D. P. C., Scheneider, M., and Pagliosa, P. R. (2017). Urbanization effects on different biological organization levels of an estuarine polychaete tolerant to pollution. *Ecol. Indic.* 73, 698–707. doi: 10.1016/j.ecolind.2016.10.029

Wernberg, T., Smale, D. A., Tuya, F., Thomsen, M. S., Langlois, T. J., De Bettignies, T., et al. (2013). An extreme climatic event alters marine ecosystem structure in a global biodiversity hotspot. *Nat. Clim. Change* 3, 78–82. doi: 10.1038/nclimate1627

Wickham, H. (2016). *ggplot2: Elegant Graphics for Data Analysis*. New York, NY: Springer-Verlag.

Young, P., Taylor, M., and Fallowfield, H. J. (2017). Mini-review: high rate algal ponds, flexible systems for sustainable wastewater treatment. *World J. Microbiol. Biotechnol.* 33:117.

Zedler, J. B. (2000). *Handbook for Restoring Tidal Wetlands*. Washington, DC: CRC Press.

Zuur, A., Ieno, E. N., Walker, N., Saveliev, A. A., and Smith, G. M. (2009). *Mixed Effects Models and Extensions in Ecology with R*. Berlin: Springer Science & Business Media.

Conflict of Interest: The authors declare that the research was conducted in the absence of any commercial or financial relationships that could be construed as a potential conflict of interest.

Copyright © 2020 Brauko, Cabral, Costa, Hayden, Dias, Leite, Westphal, Mueller, Hall-Spencer, Rodrigues, Rörig, Pagliosa, Fonseca, Alarcon and Horta. This is an open-access article distributed under the terms of the Creative Commons Attribution License (CC BY). The use, distribution or reproduction in other forums is permitted, provided the original author(s) and the copyright owner(s) are credited and that the original publication in this journal is cited, in accordance with accepted academic practice. No use, distribution or reproduction is permitted which does not comply with these terms.

frontiers in Marine Science

ORIGINAL RESEARCH
published: 07 July 2021
doi: 10.3389/fmars.2021.596644

Ocean Acidification Amplifies Multi-Stressor Impacts on Global Marine Invertebrate Fisheries

Travis C. Tai[1], U. Rashid Sumaila[1,2] and William W. L. Cheung[1]*

[1] *Institute for the Oceans and Fisheries, University of British Columbia, Vancouver, BC, Canada,* [2] *School of Public Policy and Global Affairs, University of British Columbia, Vancouver, BC, Canada*

Elevated atmospheric carbon dioxide (CO_2) is causing global ocean changes and drives changes in organism physiology, life-history traits, and population dynamics of natural marine resources. However, our knowledge of the mechanisms and consequences of ocean acidification (OA) – in combination with other climatic drivers (i.e., warming, deoxygenation) – on organisms and downstream effects on marine fisheries is limited. Here, we explored how the direct effects of multiple changes in ocean conditions on organism aerobic performance scales up to spatial impacts on fisheries catch of 210 commercially exploited marine invertebrates, known to be susceptible to OA. Under the highest CO_2 trajectory, we show that global fisheries catch potential declines by as much as 12% by the year 2100 relative to present, of which 3.4% was attributed to OA. Moreover, OA effects are exacerbated in regions with greater changes in pH (e.g., West Arctic basin), but are reduced in tropical areas where the effects of ocean warming and deoxygenation are more pronounced (e.g., Indo-Pacific). Our results enhance our knowledge on multi-stressor effects on marine resources and how they can be scaled from physiology to population dynamics. Furthermore, it underscores variability of responses to OA and identifies vulnerable regions and species.

Keywords: multi-stressor, range shift, climate change, shellfish, fisheries catch, future scenarios, modelling, interdisciplinary primary research article

OPEN ACCESS

Edited by:
Nina Bednarsek, Southern California Coastal Water Research Project, United States

Reviewed by:
Lester Kwiatkowski, UMR 8539 Laboratoire de Météorologie Dynamique (LMD), France
Kirk N. Sato, University of Washington, United States
Victor M. Aguilera, Universidad Católica del Norte, Chile

****Correspondence:***
Travis C. Tai
ttai2@alumni.uwo.ca

Specialty section:
This article was submitted to Coastal Ocean Processes, a section of the journal Frontiers in Marine Science

Received: *19 August 2020*
Accepted: *10 June 2021*
Published: *07 July 2021*

Citation:
Tai TC, Sumaila UR and Cheung WWL (2021) Ocean Acidification Amplifies Multi-Stressor Impacts on Global Marine Invertebrate Fisheries. Front. Mar. Sci. 8:596644. doi: 10.3389/fmars.2021.596644

INTRODUCTION

A direct consequence of elevated atmospheric CO_2 concentrations is the rapid rate of ocean acidification (OA) (IPCC, 2013), causing changes to the biogeochemical composition of our world's oceans and affecting marine ecosystem goods and services. Global sea surface pH has already decreased by 0.1 U since the Industrial R evolution, and is projected to decrease by up to 0.3 U by the year 2100 (Bindoff et al., 2019), a 10.0% increase in acidity (hydrogen concentration). Organism responses will vary across populations, taxonomic groups, and ecosystem types (Kroeker et al., 2013; Nagelkerken and Connell, 2015). Particularly, calcareous species (e.g., mussels, oysters, coccolithophore plankton, corals) are particularly vulnerable to OA as CO_2 interferes with ocean pH and the saturation state of aragonite, affecting the formation of calcium carbonate ($CaCO_3$) structures (Fabry et al., 2008; Ries et al., 2009). While less understood, OA also affects various

physiological processes such as acid-base regulation, metabolism, and aerobic scope, as well as sensory abilities, reproduction, and development (Le Quesne and Pinnegar, 2012). These effects can lead to changes in population dynamics such as growth, survival, and fecundity, and ultimately affect marine ecosystem resources (Kroeker et al., 2013).

Interactions between OA and other concurrent climate change drivers (e.g., ocean warming, ocean deoxygenation) could exacerbate their impacts on marine species and ecosystems. In ectotherms, oxygen demand increases with temperature to maintain basal metabolic rates (Pörtner and Lannig, 2009). This reduces the aerobic scope (the capacity to increase aerobic metabolic rate above maintenance levels) and the relative supply of oxygen put toward other aerobic processes such as growth (**Figure 1A**). We see similar effects on aerobic scope with a reduction in dissolved oxygen concentration (Pörtner and Lannig, 2009). OA is proposed to operate in a similar manner, reducing the overall aerobic scope profile (Pörtner and Farrell, 2008; **Figure 1A**). Reducing aerobic scope can then have effects on life-history traits (Pauly and Cheung, 2017) (e.g., growth rate, maximum body size) and affect large-scale population dynamics (Cheung et al., 2011; **Figure 1**). However, this process is not ubiquitous and is not true for all organisms (e.g., Clark and Sandblom, 2013; Lefevre et al., 2017; Jutfelt et al., 2018); simpler alternative mechanisms for scaling physiological effects to life-history traits have yet to be proposed or identified. Studies that examined the effects of changes in multiple environmental variables on marine organisms are mostly limited to laboratory or small-scale field-based mesocosm experiments and are limited to a small number of species and ecosystems (Fabry et al., 2008; Ries et al., 2009; Alguero-Muniz et al., 2017; Doney et al., 2020), the number of environmental variables that could be controlled for as well as the limited representation of the full scope of environmental variabilities (Wahl et al., 2016). There is a call for the need to upscale the available experimental findings from OA-related experiments in terms of the number of environmental variables, species, and ecosystems (Wahl et al., 2016). Thus, it is extremely useful to use available experimental findings to inform projection models (Koenigstein et al., 2016; Furukawa et al., 2018).

Understanding the implications of the potential multi-stressor interactions for biological communities and fisheries resources at regional and global scales is important for informing climate change mitigation and adaptation policies. Here, we used a dynamic bioclimatic envelope model to project direct physiological impacts of changes in pH, temperature, and oxygen content on the spatial distribution of commercially exploited marine invertebrate populations (i.e., molluscs and crustaceans) (Pörtner and Lannig, 2009; Cheung et al., 2011; Pauly and Cheung, 2017) – the group known to be particularly sensitive to OA. Our model integrates the oxygen- and capacity-limited thermal tolerance model (Pörtner and Lannig, 2009; Deutsch et al., 2015) and the gill-oxygen limitation model (Pauly and Cheung, 2017) to determine biological responses to environmental drivers and the downstream effects on fisheries catch potential (Cheung et al., 2011, 2016c; **Figure 1**). Using these models, we expect that OA will affect aerobic scope and translate to changes in growth and fisheries catch, and vary depending on climate change scenario. We focus on using these specific hypotheses for how OA may interact with other drivers in impacting marine organisms – other potential mechanisms are outlined in the discussion.

MATERIALS AND METHODS

Dynamic Bioclimatic Envelope Model

Changes in catch potential (described below) of commercially exploited species were estimated using a dynamic bioclimatic envelope model (DBEM) (Cheung et al., 2008b, 2011, 2016b). The DBEM predicts how species abundance will change in space (on a 0.5° longitude by 0.5° latitude grid) and time (annual time steps) using an integrative approach by linking species distribution models (Jones et al., 2012), growth models (Pauly, 1980), physiological models (Pauly, 1981), population dynamics models (Pauly, 1980; Hilborn and Walters, 1992; O'Connor et al., 2007), and macroecological models (Cheung et al., 2008a). Changes in species abundance and catch potential are driven by environmental conditions (e.g., temperature, dissolved oxygen concentration, pH) and habitat (e.g., substrate) (see Cheung et al., 2008a). We used environmental data from Earth system model projections (Dunne et al., 2013) as inputs to drive changes in species abundance. We describe the necessary components of the DBEM below; for a thorough description of the model, see Cheung et al. (2008a, 2011, 2016c).

Initial species distributions were obtained from the Sea Around Us database (Close et al., 2006; Jones et al., 2012; Pauly and Zeller, 2015). Their methods use a sequence of criteria to identify and restrict the habitat of each species on a 0.5° longitude by 0.5° latitude geospatial grid (for a detailed description[1]). First, species habitats were restricted based on recorded presences in Food and Agriculture Organization of the United Nations (FAO) area(s). Next species habitats were restricted to a north–south latitudinal range within the FAO area(s). An expert reviewed range-limiting polygon was overlaid over the map generated from the previous step. Finally, species-specific parameters [primarily collected from SeaLifeBase (Palomares and Pauly, 2017)] including depth range, habitat preference, and equatorial submergence were used to determine the final distribution map.

Species-specific habitat suitability was characterized by overlaying environmental variables including temperature, salinity, depth, sea-ice, primary production, and dissolved oxygen concentration over the initial species distribution maps. Relative changes in these environmental parameters from initial conditions (i.e., start of the simulation) resulted in changes in habitat suitability. Species were assigned to two depth categories – pelagic or demersal – and environmental conditions were assigned accordingly (sea surface and sea bottom, respectively). Habitat preference was also incorporated to characterize a bioclimatic envelope and habitat preference profile for each species (Cheung et al., 2008b). Carrying capacity – the maximum possible biomass in a spatial cell – is

[1]http://www.seaaroundus.org/

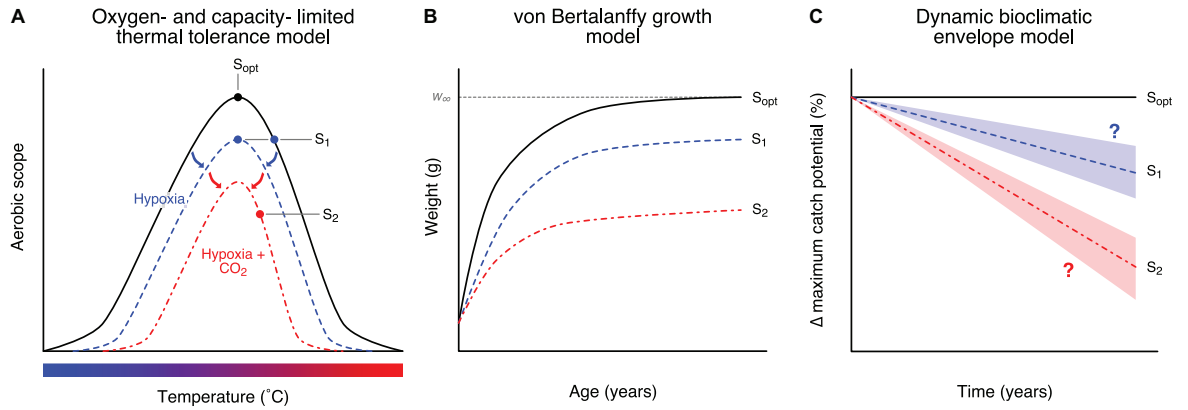


FIGURE 1 | Modelling the pathway of the impacts of ocean acidification from organism to population level in a multi-stressor framework. OA impacts were modelled as **(A)** physiological impacts (Pörtner and Lannig, 2009), then translated to **(B)** impacts on growth (Cheung et al., 2011), and **(C)** impacts on fisheries catch potential (Cheung et al., 2016c). S_{opt} is the optimal temperature at which aerobic scope is at maximum. Deviations in temperature or other stressors such as hypoxia shrink the overall performance curve (blue curve) and reduce the overall aerobic scope (S_1) **(A)**, leading to reductions in growth rate and maximum attainable size (w_∞) **(B)**, as well as potential decreases in fisheries catch **(C)**. Multi-stressor impacts of temperature, hypoxia, and elevated acidity will exacerbate physiological limitations and impacts on fisheries catch (red curve; S_2).

determined using the initial species distribution and is positively correlated with habitat suitability (Cheung et al., 2008b, 2016b). A major assumption of the DBEM is that each cell from the initial species distribution is at carrying capacity. As habitat within each cell changes and becomes more (less) suitable, the carrying capacity will increase (decrease).

Individual growth in the model is represented by the von Bertalanffy growth model with species-specific parameters and is constrained by ecophysiological conditions, specifically oxygen and temperature (Cheung et al., 2011). Populations grow using the logistic growth function (Hilborn and Walters, 1992) and population mortality rates are calculated from an empirical equation from Pauly (1980).

Movement of the organisms at different life stages were represented in the DBEM. Larval dispersal is simulated disperse using advection-diffusion models (Sibert et al., 1999; Cheung et al., 2008b), while net adult diffusion rate is determined by a fuzzy logic model (Cheung et al., 2008b). Animals actively move based on the distance between two geographic cells and their relative dispersal rate (e.g., quicker for large-bodied pelagic species, and slower for small reef-dwelling demersal species). Emigration rates are greater if neighbouring cells have a more favourable habitat, while immigration rates are greater if the present cell is preferable to surrounding neighbour cells.

Annual fisheries maximum catch potential (MCP) for each species was estimated by summing the maximum sustainable yield for each occupied spatial cell. Maximum sustainable yield is assumed to be equal to $rKC_i/4$, where r is the intrinsic rate of population growth and KC_i is the carrying capacity (biomass) of a spatial cell i.

Modelling Ocean Acidification Impacts in a Multi-Stressor Framework

We modelled the impacts of OA on species abundance in a multi-stressor framework through somatic growth and mortality rates by combining the oxygen- and capacity-limited tolerance and the gill-oxygen limitation hypothesis (Tai et al., 2018). First, we modelled growth rate dB/dt as a function of oxygen supply (anabolism) and oxygen demand for maintenance metabolism (catabolism) (Cheung et al., 2011):

$$\frac{dB}{dt} = HW^d - kW^b \quad (1)$$

where B is species biomass, and H and k represent the coefficients for anabolism and catabolism, respectively. Anabolism scales with body weight (W) to the exponent $d < 1$, while catabolism scales linearly with (W), i.e., $b = 1$. Values of d typically range from 0.5 to 0.95 across species (Pauly, 1981; Pauly and Cheung, 2017; Tai et al., 2018), but we assume a mid-range value of $d = 0.7$. Higher values of d lead to increased sensitivity of growth to temperature, while lower values lead to marginal decreases in sensitivity (Pauly and Cheung, 2017; Tai et al., 2018). Therefore, $d = 0.7$ is a conservative measure to use as a scaling coefficient across all species.

Effects of environmental drivers (i.e., temperature, oxygen concentration, and pH) are modelled to affect both growth rate parameters H and k. First, temperature affects both oxygen supply and demand for metabolism (Pauly and Cheung, 2017) following the Arhennius equation ($e^{-j/T}$). Next, oxygen availability affects overall aerobic scope, while other physiological drivers (e.g., acidification) affects maintenance metabolism (Cheung et al., 2011):

$$H = g[o_2]e^{\frac{-j_1}{T}} \quad (2)$$

and

$$k = h[H^+]e^{\frac{-j_2}{T}} \quad (3)$$

The Arhennius equation constants j_1 and j_2 (for anabolism and catabolism, respectively) are equal to E_a/R, where E_a and R

are the activation energy and Boltzmann constant, respectively. T is the absolute temperature (in Kelvin). Relative changes in oxygen [O_2] and hydrogen ion [H^+] concentration thus change H and k, respectively. These impacts on growth rate can first be depicted as impacts to aerobic scope (**Figure 1A**). Coefficients g and h were derived for each species from the maximum weight, von Bertalanffy growth rate parameter, and average environmental temperature reported in the literature (Cheung et al., 2011; Palomares and Pauly, 2017).

With changes in aerobic scope due to environmental stressors, our model predicts changes in life-history parameters including asymptotic weight (W_∞) and the von Bertalanffy growth rate parameter K (**Figure 1B**):

$$w_\infty = \left(\frac{H}{K}\right)^{1/(1-d)} \tag{4}$$

and

$$K = k(1-d) \tag{5}$$

Environmentally driven changes in life-history growth parameters will affect the size distribution of the population. We used a size transition matrix to model the probability of growing from one size class to the next, as a function of maximum body size W_∞ and the von Bertalanffy growth parameter K (Quinn and Deriso, 1999; Cheung et al., 2008b).

Pauly's (1980) empirical model was used to estimate natural population mortality rates (M):

$$M = -0.4851 - 0.0824 log\ (W_\infty) + 0.6757 log(K) + 0.4687\ log(T') \tag{6}$$

using maximum body size, growth rate, and the average water temperature of a species range in degrees Celsius (T'). This model was chosen as it is widely used and life-history data is readily available for all of the invertebrate species tested here (Tai et al., 2018). Mortality is then incorporated into the population dynamics logistic growth model, where population abundance (A) decreases (M × A) as a function of the mortality rate.

We modelled OA impacts on survival rates using a correlative approach for both larvae and adults. We measure changes in acidity and its impacts on growth and survival rates as hydrogen ion concentration [H^+]. We model changes in life-history traits based on the model:

$$Surv_t = Surv_{init} * \left[1 + \left(Per * \left(\frac{[H^+]_t}{[H^+]_{init}} - 1\right)^w\right)\right] \tag{7}$$

Surv is the survival rate per year and used here as an example but is also applied to growth. Survival rate in year t is equal to the initial (*init*) survival rate and the relative change in [H^+] between year t and initial [H^+] conditions. We define *Per* as the value of the OA effect size (from Kroeker et al., 2013) for the percent change in survival rate with a doubling of [H^+] (**Supplementary Table 1**). We assume a linear relationship because it is the most parsimonious assumption considering the highly variable responses across species (Ries et al., 2009; Tai et al., 2018). We assume that sensitivities of the organisms reported in Kroeker et al. (2013) represents the mean responses of the studied species in our model's time-step (annual). OA effect sizes for both growth and survival were assigned based on taxonomic groups for crustaceans and molluscs (**Supplementary Table 1**). Thus, environmental changes will lead to changes in growth rate, maximum body size, and survival rates. We used the DBEM to scale up and determine how the physiological responses to OA and other environmental drivers affect species distributions and fisheries catch potential (**Figure 1**).

Modelled Species

We modelled the impacts of OA and climate change on 210 commercially exploited marine invertebrate species. Invertebrate species tend to be more sensitive to OA and changes in pH (Kroeker et al., 2013), while the effects on finfish species are generally less sensitive and show greater variation. We included species from the major shellfish fisheries groups including crabs, lobsters, shrimp and prawns, oysters, scallops, and squid. Most species are distributed throughout coastal waters.

Projections of Ocean Conditions

Projections of changing ocean conditions that drived the biological responses represented by the DBEM from 1950 to 2100 were obtained from Earth system models available from the Coupled Model Intercomparison Project Phase 5 (CMIP5). Specifically, we used outputs from three Earth system models: NOAA's Geophysical Fluid Dynamics Laboratory 2M (GFDL-ESM); Max Planck Institute for Meteorology ESM-MR (MPI-ESM); and Institute Pierre Simon Laplace Climate Modelling Centre ESM-CM5-MR (IPSL-ESM). We make use of one single realization of each model. All model data were re-gridded onto a 1° × 1° grid, and subsequently interpolated onto 0.5° × 0.5° grid of the world ocean using bilinear interpolation method. Ocean condition variables that were used in the DBEM simulations included sea surface and bottom temperature, pH, oxygen level, salinity as well as sea ice extent, and surface advection. We used annual means for environmental data with 24 time steps per year. Our simulations assume that pelagic and demersal species were exposed to sea surface and bottom conditions, respectively.

Model Uncertainties

We quantified the sensitivity of our DBEM results (Cheung et al., 2016a) to three levels of uncertainty: parameter, structural, and scenario uncertainty. Sensitivity to parameter uncertainty was examined by using the upper and lower 95% confidence limits for OA effect sizes on growth and survival rates. Structural uncertainty is defined here as the variance across different earth system models used as input environmental data. We present results from three earth system models that use various socioeconomic scenarios resulting in various levels of atmospheric greenhouse gas concentrations, known as representative concentration pathways (RCPs) to develop scenarios of environmental change. In our analysis, we use a low (RCP 2.6) and a high (RCP 8.5) carbon emissions scenario for DBEM simulations (van Vuuren et al., 2011). The numbers

represent radiative forcing values in the year 2100 relative to pre-industrial periods. The low emissions scenario assumes carbon emissions are strongly mitigated and annual global greenhouse gas emissions peaks within a decade but are then substantially reduced. This trajectory is the closest RCP scenario that aligns with targets set with the 2015 "Paris Agreement" from the United Nations Framework Convention on Climate Change Conference of the Parties. The high emissions scenario is our current pathway, where carbon emissions are not curbed and the burning of fossil fuels continues to be the primary source of energy for the industrial sector. With this scenario, minimal efforts are made to reduce carbon emissions or develop green energy sources. We did not assess the scenario uncertainty of the historical period (2005 and prior).

Analysis

Changes to species abundance were calculated as percent changes between initial and final conditions:

$$\%\ \text{change in abundance} = \frac{(\overline{A}_{\text{fin}} - \overline{A}_{\text{init}})}{\overline{A}_{\text{init}}} \tag{8}$$

where $\underline{A}$ is the mean abundance of a 10 year period. Change in MCP was also calculated using this formula.

Latitudinal centroid *LC* for each species was calculated by multiplying the abundance of each occupied cell by the latitude *Lat* of each cell:

$$LC = \frac{\sum_{i=1}^{n} Lat_i * A_i}{\sum_{i=1}^{n} A_i} \tag{9}$$

The rate of species distribution latitudinal shift was estimated by finding the slope of a linear regression of the latitudinal centroid for each year. The rate of latitudinal shift was converted to kilometers by multiplying the estimated slope by $\frac{\pi r}{180}$ where $r = 6378.2$, the approximate radius of the earth. This rate was then converted to decadal shifts. This measures the decadal rate at which species are shifting poleward to cooler waters and the "tropicalization" of marine ecosystems.

Species range size for each year was calculated by summing the product of each occupied spatial cell with its average area. Projected percent changes in range size were calculated using the same formulation as Eq. (8), providing a measure of range size contraction or expansion. Correlations between projected changes in range size and abundance of the modelled invertebrates were examined using Pearson Correlation test.

Effects of OA were isolated from effects of other global change drivers by finding the difference in the outputs between simulations run with modelled effects of OA and without OA [change in hydrogen ion concentration is set to zero in Eq. (3)]. OA is expected to amplify responses in aerobic scope and subsequent life-histories, and these effects were isolated to illustrate the separate and additive effects of OA with other critical global change stressors (i.e., ocean warming, decreased oxygen content) (Cheung et al., 2016c). The projected MCP across pelagic and demersal invertebrates were summed and their changes by year 2100 relative to the average of 1951–1960 were reported.

RESULTS

Intermediary non-spatially explicit results show that modelled impacts of ocean warming and acidification show synergistic effects on aerobic scope, reducing aerobic scope by as much as 75% under the high CO_2 scenario by the end of the century (**Figure 2A**). Continuing with this scenario, maximum body size was projected to decrease by as much as 66% (**Figure 2B**). Ocean acidification had substantial effects, accounting for over 60% of the reduction in aerobic scope and 32% of the decrease in maximum body size. Global invertebrate MCP was projected to decrease by about 12% in the high CO_2 scenario due to physiological (e.g., ocean warming and acidification), and habitat constraints (e.g., primary production, habitat suitability), of which ocean acidification accounts for over 3% of this decrease (**Figure 2C**). Impacts under the low CO_2 scenario are considerably lower, where aerobic scope and maximum body size were projected to decrease by 15 and 23%, respectively, while the change in MCP was negligible (**Figure 2**).

Impacts of global change on the MCP of marine invertebrate fisheries shows regional variation where tropical regions will generally see a loss in catch while northern regions will see an increase if we continue on the "business-as-usual" high CO_2 trajectory relative to the strong mitigation low CO_2 trajectory (**Figure 3**). Increases in catch at higher latitudinal regions are largely driven by warming oceans that result in species distribution shifts and increased species turnover (Cheung et al., 2016c). Regions around the coral triangle such as the Indonesian Sea are projected to lose the most (Cheung et al., 2016c), and our models project decreases of >30% for invertebrate catch potential.

Ocean acidification is projected to decrease annual global invertebrate fisheries MCP by 0.75% for each 0.1 U decrease in surface pH, and 3.4% by the end of the century (**Figures 2C**, **4A**), although this is highly variable across regions. West Arctic large marine ecosystems – including North Bering, Chukchi Sea, Beaufort Sea, Queen Elizabeth Islands archipelago, Canadian high Arctic, and North Greenland – are likely to be most susceptible to OA as pH is projected to decrease by up to 0.5 U and fisheries catch potential to decrease more than 20% by the end of the century in a high CO_2 scenario (**Figure 4B**). While catch potential is projected to increase overall in Arctic regions, OA will largely reduce gains in potential catches for species sensitive to OA (Lam et al., 2014). Our projections show that these impacts due to OA are exacerbated with greater changes in surface temperature and oxygen concentration (i.e., IPSL earth system model) (**Figure 4B** and **Supplementary Figures 1**, **2**). Currently, there are only a few commercial marine fisheries in the West Arctic (Zeller et al., 2011) – largely restricted by national and international agreements such as commercial fishing bans in the Beaufort Sea and central Arctic – due to our limited

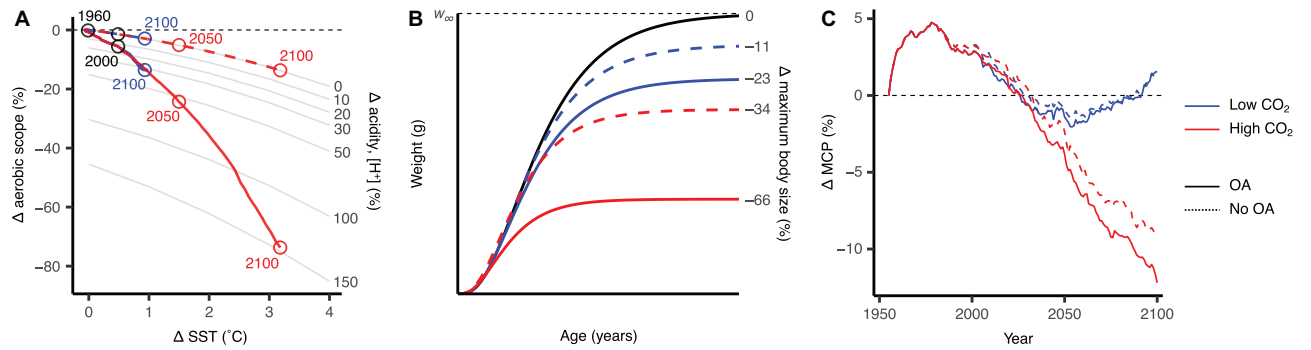


FIGURE 2 | Scaling the multi-stressor responses from the organism level to fisheries catch under the low CO_2 and high CO_2 climate change scenarios (blue and red, respectively), averaged across all modelled species (N = 210). Differences between projections with and without the modelled effects of ocean acidification (OA) are shown with solid and dashed lines, respectively. **(A)** Effects of projected ocean warming and acidification on aerobic scope for growth. **(B)** Change in the von Bertalanffy growth curve and maximum body size in the 2091–2100 period. **(C)** Changes in global maximum catch potential (MCP) projected by the dynamic bioclimatic envelope model. Results shown are relative to the 1951–1960 period and are multimodel averages from the three earth system models used in this study.

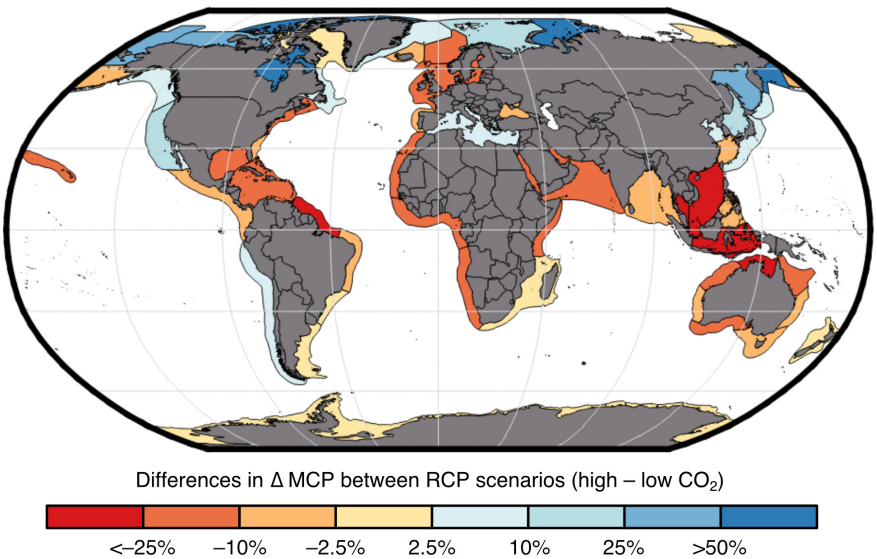


FIGURE 3 | Projected impacts by considering multiple changes in environmental conditions on maximum catch potential (MCP) of marine invertebrates across large marine ecosystems. Results shown are for the 2091–2100 period (relative to 1951–1960) in high CO_2 (RCP 8.5) relative to low CO_2 scenario (RCP 2.6).

knowledge of the baseline state and the sustainability of fisheries exploitation across these regions (e.g., Cobb et al., 2008).

Large marine ecosystems of the Northeast Pacific Ocean show decreases in MCP of up to 6% annually by year 2100 under the high CO_2 scenario (**Figure 4C**). This region includes the highly productive fishing regions of the East Bering Sea, Gulf of Alaska, and California Current large marine ecosystems. Across this region, there are highly valuable capture fisheries including Alaskan king crab and Dungeness crab fisheries, as well as open-system mariculture fisheries such as Pacific oyster and geoduck fisheries (Tai et al., 2017). Other studies using ecosystem models of the Northeast Pacific also found amplified negative impacts on species abundance with multiple global change drivers (Ainsworth et al., 2011). Similarly, projections of OA impacts on the California Current ecosystem showed negative direct impacts on epibenthic invertebrates and downstream indirect impacts on higher trophic level species assemblages (Marshall et al., 2017).

Impacts of OA on fisheries catch potential in the Central Indo-Pacific region (i.e., Gulf of Thailand, South China Sea, Sulu-Celebes Sea, Indonesian Sea) were much less significant, where MCP decreases an additional 2% by year 2100 in the high emissions scenario (**Figure 4D**). Overall, catch potential across tropical regions is projected to substantially decrease overall due to global change (Cheung et al., 2016c), and while the impacts of OA are negative, they may be overshadowed by temperature-driven changes (McNeil and Sasse, 2016). However, OA effects on critical habitat forming species (e.g., corals, mussels) or key intermediate trophic-level species (e.g., seastars) could lead to substantial ecosystem changes (Hoegh-Guldberg et al., 2007; Sunday et al., 2017).

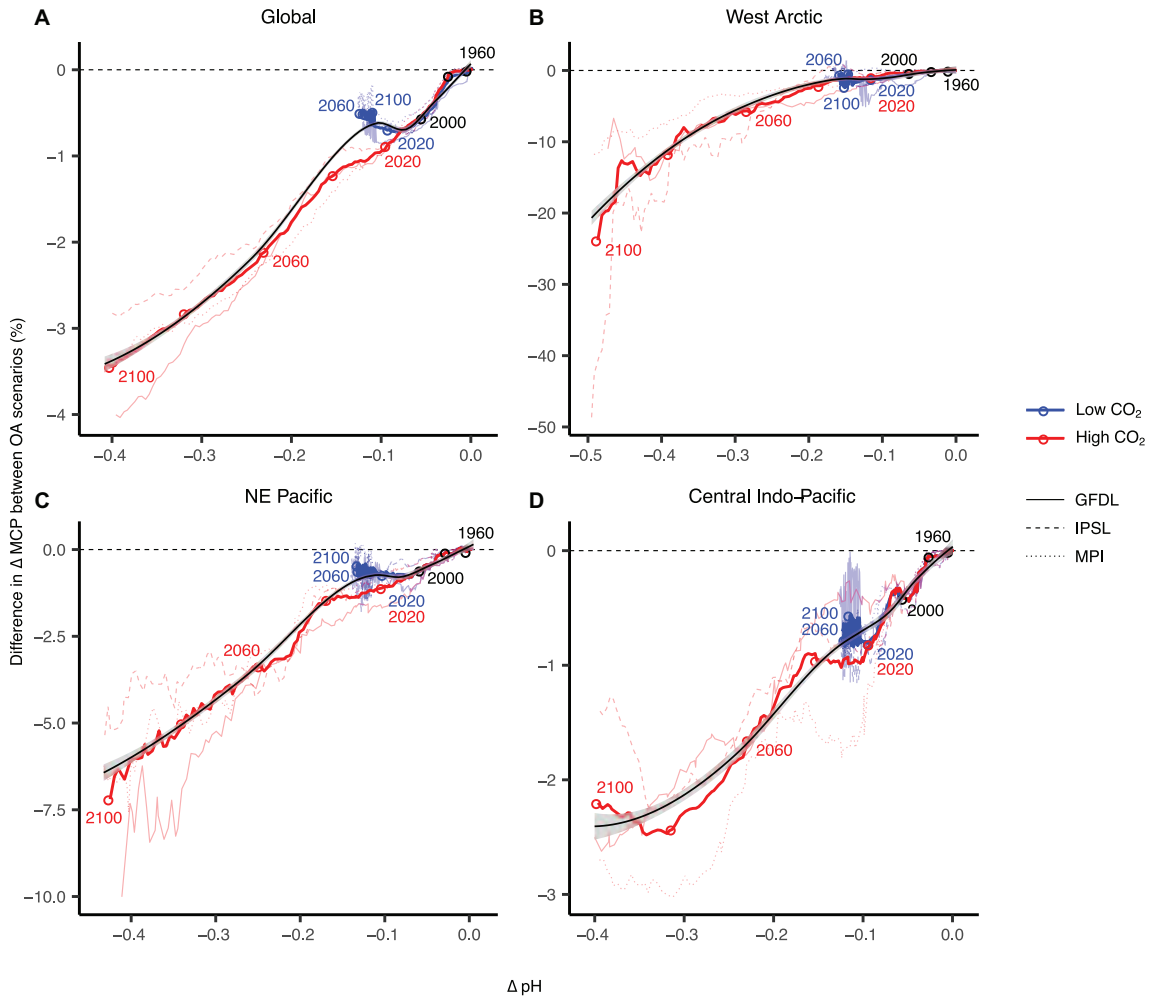


FIGURE 4 | Projected ocean acidification (OA) impacts on maximum catch potential (MCP) of marine invertebrates in addition to other climate change stressors for global **(A)** and other major regions **(B–D)**. Surface pH is used here to show the relationship between acidity and MCP. Thicker coloured lines are multi-model means and thinner lines are simulations with the different earth system models: GFDL-ESM2M; MPI-ESM-MR; IPSL-CM5A-MR. Black lines and grey bands are selected smoothed regressions and 95% confidence limits. MCP data are smoothed by a 10-year running mean and relative to 1951–1960.

Biogeographical changes of range size showed a positive correlation (r = 0.78; **Supplementary Table 2**) with changes in abundance (**Figure 5A**), while absolute changes in range sizes were positively correlated with increased rates of latitudinal centroid shift (r = 0.52; **Supplementary Table 2**). For most species, OA had negative impacts on abundance and range size, as well as decreased rates of latitudinal shift (**Figure 5B**). Species that had large decreases in abundance and range size, quicker rates of latitudinal shift, and exacerbated effects due to OA are likely to be at greatest risk to global change (e.g., banded carpet shell, Atlantic bay scallop) (**Figure 5**). Such species may also face substantially elevated risk of extinction as population viability is generally positively correlated to range size (Purvis et al., 2000). Some species such as the northern quahog showed positive responses (i.e., range expansion, abundance increase) to global non-OA environmental changes (**Figure 5A**) and negative responses to OA, likely due to an increase in suitable habitat but limited by the sensitivity to OA. Mollusc species, particularly scallops, mussels and oysters, showed greater losses in catch potential in the high CO_2 scenarios when compared with crustacean species (**Supplementary Figure 3**), explained by the greater effect size for the parameters used for molluscs than crustaceans (**Supplementary Table 1**). However, changes in catch potential for molluscs showed more variability to the effects of OA, suggesting that the interaction effects of OA and other environmental drivers in our model are not consistent across mollusc species within the same group. Conversely, crustaceans appear to be more robust to OA than molluscs (Ries et al., 2009; Whiteley, 2011; Wittmann and Pörtner, 2013; Kroeker et al., 2013) as they are generally more mobile and thus have the ability to more quickly shift their geographic range.

Sensitivity analyses showed that our model results of OA impacts are most sensitive to parameter uncertainty. Parameter uncertainty (OA effect size) accounted for most of the uncertainty (50–90%) in the first half of the model simulations, and decreased to ∼60% in later years (**Figure 6**). Therefore, it is imperative

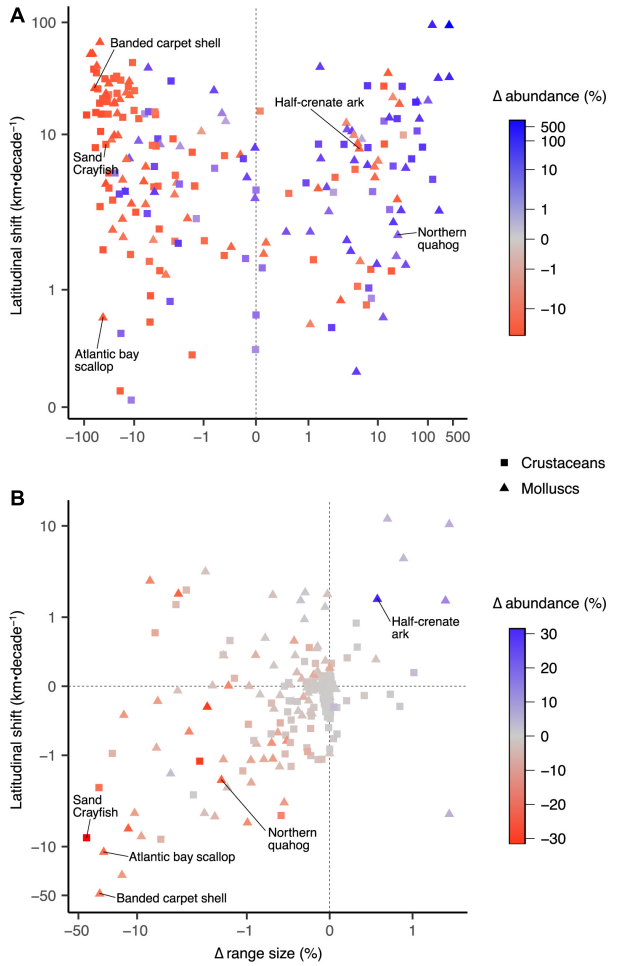


FIGURE 5 | Biogeographical changes in range size, abundance, and distributional shift of latitudinal centroids for 210 invertebrate fisheries species in the high CO_2 scenario. **(A)** Responses to global change drivers excluding ocean acidification, and **(B)** responses to ocean acidification separated from other stressors. Values shown are multi-model means for 2091–2100 period relative to 1951–1960. Correlations between variables are shown in **Supplementary Table 1**. Note log scales.

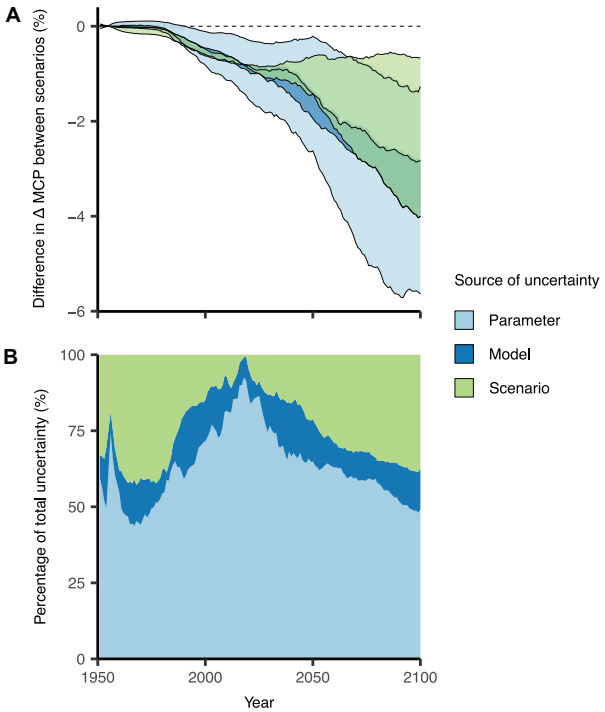


FIGURE 6 | Testing model variability for the projected impacts on maximum catch potential (MCP) due to ocean acidification (OA). **(A)** Projected changes using the upper and lower bounds of parameter, model, and scenario uncertainty; and **(B)** the proportion of total uncertainty allocated to each source of uncertainty. Default conditions held constant when testing each source of uncertainty were: (1) parameter = mean OA effect size; (2) model = GFDL-ESM2M; and (3) scenario = RCP 8.5. Results are smoothed by 10-year running means and relative to the 1951–1960 average.

to obtain accurate empirical data for parameter effect size of OA responses in order to accurately project species responses to global change. This is especially important for more localized and species-specific analyses; our results summarize effects of OA across large spatial extents and many species, therefore we used mean effect sizes across taxonomic groups. Furthermore, the proportion of total uncertainty was smallest for model uncertainty, suggesting our results are robust to the different structures of Earth system models at the global scale. Scenario uncertainty initially accounted for >25% of total uncertainty but its absolute uncertainty was negligible during this early part of the simulation. Scenario uncertainty increased from the year (∼2010) where environmental conditions diverged (**Supplementary Figure 2**) between low and high CO_2 scenarios to account for >30% of the uncertainty by the end of the simulations (**Figure 6**).

One component of uncertainty not specifically tested here is the various models of mechanistic physiological responses to environmental stressors. The models used here are much less complex than the alternatives (e.g., Then et al., 2015), which generally require a more thorough understanding of the mechanisms involved (Lefevre et al., 2017) and life-history parameters that are not readily available for all species tested. Previous studies have highlighted that the chosen models are not universally applicable (Lefevre et al., 2017; Pörtner et al., 2018), yet the oxygen- and capacity-limited thermal tolerance model provides a connection between physiological constraints and higher ecological phenomena (see response to Jutfelt et al., 2018). Thus, by combining empirical physiological and life-history models, we are able to link environmentally driven changes in aerobic scope to trade-offs with life-history parameters (Tai et al., 2018) – e.g., growth, survival – which then scale to population dynamics.

DISCUSSION

Our current understanding indicates that marine invertebrates are at most risk to the direct effects of OA (Kroeker et al., 2013), although these effects will likely differ across regions (**Figure 3**).

OA effects on marine invertebrate fisheries will have major implications for food security, livelihoods, and the global economy. At over 50 billion USD annually, invertebrate fisheries account for over 1/3 of the value of internationally traded seafood (FAO, 2014). Invertebrates support many valuable fisheries, especially in developing countries where over 50% of internationally traded seafood is caught (FAO, 2014). Developing tropical areas are already projected to be most susceptible to global change (Cheung et al., 2016c) and OA could exacerbate food and income insecurities currently faced in these regions. For example, in areas across the Fijian Islands invertebrates comprise over 70% of artisanal and 50% of subsistence harvests (Teh et al., 2009). Most of the non-subsistence catch in Fiji is exported with the largest invertebrate fisheries valued at $8.4 million FJD (∼$3.8 million USD) in 2003 (Teh et al., 2009). Additionally, small-island developing nations such as the Pacific Islands are highly dependent on invertebrates for both additional income sources and subsistence (Kronen et al., 2010). Ease of access and the minimal gear requirements for invertebrate fishing has facilitated women and even children to participate in subsistence harvesting and remains a source of easily attainable "backup" protein when fishing at sea is unsuccessful (Harper et al., 2013; Codding et al., 2014).

Regionally, invertebrates in the Arctic were projected to be most at risk to ocean acidification, potentially altering the trends in catch potential driven by warming. Previous studies using DBEM projected that ocean warming, reduction in sea ice and increases in primary production increase exploited fishes and invertebrates catch potential in the high latitude regions, although uncertainties of such projections are high partly because of the complexity of changing ocean biogeochemical conditions in the Arctic that were not fully represented in the Earth system models and DBEM (Cheung et al., 2016c). Here, we highlighted that the relatively larger decrease in pH in the Arctic Ocean and its impacts on invertebrates catch potential add to such uncertainties.

For some larger fishing nations invertebrate fisheries make substantial economic contributions. In Canada, lobster fisheries were valued at over $1.1 billion CAD in 2015 and its exports contributed over $2 billion CAD to the Canadian economy (DFO, 2015). Similarly, sea scallops in the United States had dockside revenues estimated at $559 million USD in 2012 (Cooley et al., 2015). Fisheries catch in regions at higher latitudes are projected to increase with global change (Cheung et al., 2016c), but this may not equate to benefits to fishers and the economy. Decreases in highly valuable species (e.g., shellfish) may outweigh any increases in catch of less valuable species, potentially resulting in lost revenues (Lam et al., 2016). If OA has largely negative effects on organism function, this could further reduce overall catch and amplify any losses in fisheries catch. Modelling of OA effects on marine fisheries resources has largely suggested negative impacts to fisheries resources (Ainsworth et al., 2011; Cheung et al., 2011; Lam et al., 2014).

Projection models such as these provide valuable insight for possible future scenarios to identify regions and species that may be most sensitive to global change, and where to concentrate adaptation and mitigation efforts. However, the extent of OA impacts remains uncertain. Impacts of OA on fisheries has been widely discussed and resulted in qualitative and quantitative modelling efforts (Cooley and Doney, 2009; Ainsworth et al., 2011; Ekstrom et al., 2015). These studies are informative and provide a baseline understanding of the potential OA impacts on species and possible downstream effects on fisheries resources. Our spatially explicit, multi-stressor model provides a step toward better understanding how the distribution and abundance of fisheries resources will change at a global scale. Such large-scale models highlight regions that are most susceptible to OA and global change, such as the Arctic (AMAP, 2013), and areas where OA may be overshadowed by other drivers, such as temperature in the tropics (Cheung et al., 2016c). Variability in responses to the different environmental conditions across regions and species indicate which environmental variables are of most concern. Moreover, the global-scale gridded modelled historical environmental conditions that our modelling used do not fully match with local conditions at specific sites as revealed from observations (Bopp et al., 2013). Future studies may apply our modelling framework to local-scale particularly in areas where site-specific data are available. Furthermore, the projected ocean acidification by the Earth system models are more representative of the open ocean where variations in pH are strongly driven by changes in atmospheric carbon dioxide level. However, many exploited invertebrates inhabit coastal areas where ocean acidification is influenced by other non-atmospheric CO2 drivers such as freshwater and nutrient inputs. Future studies could use environmental drivers projected from regional-scale high resolution biogeochemical models which could resolve some of these complexities in factors affecting ocean acidification in coastal waters and their impacts on invertebrates. This could include the incorporation of population-specific estimations of biological sensitivity, if the information is available, to provide finer-grained representations. Then, the capacity of fisheries to adapt and mitigate global change impacts can be evaluated together with biological models to better inform management decisions and conservation efforts. Our study supports previous findings that strong mitigation of CO_2 emissions lead to benefits in fisheries catch potential (Cheung et al., 2016c), and that these benefits are further extended due to the minimization of OA. In addition, while our study focuses on the long-term mean trends in the responses of invertebrates to ocean acidification and other environmental drivers, our modelling framework could be applied to study the effects of compounded extremes or environmental variabilities (e.g., marine heatwaves and acidification extremes) on marine species (Cheung and Frölicher, 2020; Ainsworth et al., 2020; Burger et al., 2020).

Accurate projections of OA and global change impacts on marine fisheries require interdisciplinary integration to determine how multiple environmental drivers interact to affect species at various levels of biological organization. Also, previous modelling studies show that ocean warming, deoxygenation and changes in net primary production are important global change drivers on the catch potential and biogeography of marine species with regional variations in their relative importance. Here, we show that adding ocean acidification to these ocean variables further increases the complexity of responses of

marine species to multiple environmental drivers under climate change. Thus, development of multi-stressor models requires collaboration between physiologists, biologists, oceanographers, and modellers. The development of modelling impacts of multiple drivers on marine resources is relatively new, yet numerous advances have been made to facilitate efforts and develop a thorough understanding of multi-stressor impacts (Haigh et al., 2015; Koenigstein et al., 2016). Our study contributes to the development of modelling efforts for global change, as well as to better understanding potential interactions of multiple stressors on the spatial distribution of marine fisheries resources.

DATA AVAILABILITY STATEMENT

The raw data supporting the conclusion of this article will be made available by the authors, without undue reservation.

AUTHOR CONTRIBUTIONS

TT designed and conducted the study. Original model code was written by WC and revised by TT. TT wrote the manuscript with significant contributions from US and WC. All authors reviewed and approved the manuscript.

FUNDING

This contribution is supported by the Social Sciences and Humanities Research Council (SSHRC) and the Natural Sciences and Engineering Research Council (NSERC) of Canada through partnerships with the *OceanCanada* partnership and the Marine Environmental Observation Prediction And Response (MEOPAR) Network.

ACKNOWLEDGMENTS

WC would also like to acknowledge support from the Nippon Foundation–The University of British Columbia Nereus Program. The content of this manuscript has been published in part as part of the thesis of TT (Tai, 2019).

SUPPLEMENTARY MATERIAL

The Supplementary Material for this article can be found online at: https://www.frontiersin.org/articles/10.3389/fmars.2021.596644/full#supplementary-material

REFERENCES

Ainsworth, C. H., Samhouri, J. F., Busch, D. S., Cheung, W. W. L., Dunne, J., and Okey, T. A. (2011). Potential impacts of climate change on Northeast Pacific marine foodwebs and fisheries. *ICES J. Mar. Sci.* 68, 1217–1229. doi: 10.1093/icesjms/fsr043

Ainsworth, T. D., Hurd, C. L., Gates, R. D., and Boyd, P. W. (2020). How do we overcome abrupt degradation of marine ecosystems and meet the challenge of heat waves and climate extremes? *Glob. Chang. Biol.* 26, 343–354. doi: 10.1111/gcb.14901

Alguero-Muniz, M., Alvarez-Fernandez, S., Thor, P., Bach, L. T., Esposito, M., Horn, H. G., et al. (2017). Ocean acidification effects on mesozooplankton community development: results from a long-term mesocosm experiment. *PLoS One* 12:e0175851. doi: 10.1371/journal.pone.0175851

AMAP (2013). *AMAP Assessment 2013: Arctic Ocean Acidification*. Oslo: AMAP.

Bindoff, N. L., Cheung, W. W. L., Kairo, J. G., Arístegui, J., Guinder, V. A., Hallberg, R., et al. (2019). "Changing ocean, marine ecosystems, and dependent communities," in *IPCC Special Report on the Ocean and Cryosphere in a Changing Climate*, eds H. O. Pörtner, D. C. Roberts, V. Masson-Delmotte, P. Zhai, M. Tignor, E. Poloczanska, et al. (Geneva: IPCC).

Bopp, L., Resplandy, L., Orr, J. C., Doney, S. C., Dunne, J. P., Gehlen, M., et al. (2013). Multiple stressors of ocean ecosystems in the 21st century: projections with CMIP5 models. *Biogeosciences* 10, 6225–6245. doi: 10.5194/bg-10-6225-2013

Burger, F. A., John, J. G., and Frölicher, T. L. (2020). Increase in ocean acidity variability and extremes under increasing atmospheric CO 2. *Biogeosciences* 17, 4633–4662. doi: 10.5194/bg-17-4633-2020

Cheung, W. W., Close, C., Lam, V., Watson, R., and Pauly, D. (2008a). Application of macroecological theory to predict effects of climate change on global fisheries potential. *Mar. Ecol. Prog. Ser.* 365, 187–197. doi: 10.3354/meps07414

Cheung, W. W., and Frölicher, T. L. (2020). Marine heatwaves exacerbate climate change impacts for fisheries in the northeast Pacific. *Sci. Rep.* 10:6678.

Cheung, W. W. L., Dunne, J., Sarmiento, J. L., and Pauly, D. (2011). Integrating ecophysiology and plankton dynamics into projected maximum fisheries catch potential under climate change in the Northeast Atlantic. *ICES J. Mar. Sci.* 68, 1008–1018. doi: 10.1093/icesjms/fsr012

Cheung, W. W. L., Frolicher, T. L., Asch, R. G., Jones, M. C., Pinsky, M. L., Reygondeau, G., et al. (2016a). Building confidence in projections of the responses of living marine resources to climate change. *ICES J. Mar. Sci.* 73, 1283–1296. doi: 10.1093/icesjms/fsv250

Cheung, W. W. L., Jones, M. C., Reygondeau, G., Stock, C. A., Lam, V. W. Y., and Froelicher, T. (2016b). Structural uncertainty in projecting global fisheries catches under climate change. *Ecol. Modell.* 325, 57–66. doi: 10.1016/j.ecolmodel.2015.12.018

Cheung, W. W. L., Lam, V. W. Y., and Pauly, D. (2008b). Modelling present and climate-shifted distribution of marine fishes and invertebrates. *Fish. Cent. Res. Reports* 16:76.

Cheung, W. W. L., Reygondeau, G., and Frölicher, T. L. (2016c). Large benefits to marine fisheries of meeting the 1.5°C global warming target. *Science* 6319, 1591–1594. doi: 10.1126/science.aag2331

Clark, T. D., and Sandblom, E. (2013). Aerobic scope measurements of fishes in an era of climate change: respirometry, relevance and recommendations. *J. Exp. Biol.* 216, 2771–2782. doi: 10.1242/jeb.084251

Close, C., Cheung, W., Hodgson, S., Lam, V., Watson, R., and Pauly, D. (2006). Distribution ranges of commercial fishes and invertebrates. *Fishes Databases Ecosyst. Fish. Cent. Res. Rep.* 14, 27–37.

Cobb, D., Fast, H., Papst, M. H., Rosenberg, D., Rutherford, R., and Sareault, J. E. (2008). *Beaufort Sea Large Ocean Management Area: Ecosystem Overview and Assessment Report*. Winnipeg, Manitoba.

Codding, B. F., Whitaker, A. R., and Bird, D. W. (2014). global patterns in the exploitation of shellfish global patterns in the. *J. Isl. Coast. Archaeol.* 9, 145–149. doi: 10.1080/15564894.2014.881939

Cooley, S. R., and Doney, S. C. (2009). Anticipating ocean acidification's economic consequences for commercial fisheries. *Environ. Res. Lett.* 4:024007. doi: 10.1088/1748-9326/4/2/024007

Cooley, S. R., Rheuban, J. E., Hart, D. R., Luu, V., Glover, D. M., Hare, J. A., et al. (2015). An integrated assessment model for helping the united states sea scallop (*Placopecten magellanicus*) fishery plan ahead for ocean acidification and warming. *PLoS One* 10:e0124145. doi: 10.1371/journal.pone.0124145

Deutsch, C., Ferrel, A., Seibel, B., Pörtner, H. O., and Huey, R. B. (2015). Climate change tightens a metabolic constraint on marine habitats. *Science* 348, 1132–1135. doi: 10.1126/science.aaa1605

DFO (2015). *Fisheries and Oceans Canada National Fisheries Statistics*. Available online at: http://www.dfo-mpo.gc.ca/stats/stats-eng.htm (accessed August 28, 2017).

Doney, S. C., Busch, D. S., Cooley, S. R., and Kroeker, K. J. (2020). The impacts of ocean acidification on marine ecosystems and reliant human communities. *Annu. Rev. Environ. Resour.* 45, 83–112. doi: 10.1146/annurev-environ-012320-083019

Dunne, J. P., John, J. G., Shevliakova, S., Stouffer, R. J., Krasting, J. P., Malyshev, S. L., et al. (2013). GFDL's ESM2 global coupled climate-carbon earth system models. Part II: Carbon system formulation and baseline simulation characteristics. *Am. Meteorol. Soc.* 26, 2247–2267. doi: 10.1175/JCLI-D-12-00150.1

Ekstrom, J. A., Suatoni, L., Cooley, S. R., Pendleton, L. H., Waldbusser, G. G., Cinner, J. E., et al. (2015). Vulnerability and adaptation of US shellfisheries to ocean acidification. *Nat. Clim. Chang.* 5, 207–214. doi: 10.1038/nclimate2508

Fabry, V. J., Seibel, B. A., Feely, R. A., and Orr, J. C. (2008). Impacts of ocean acidification on marine fauna and ecosystem processes. *ICES J. Mar. Sci.* 65, 414–432. doi: 10.1093/icesjms/fsn048

FAO (2014). *State of World Fisheries and Aquaculture: Opportunities and Challenges*. Rome: FAO.

Furukawa, M., Sato, T., Suzuki, Y., Casareto, B. E., and Hirabayashi, S. (2018). Numerical modelling of physiological and ecological impacts of ocean acidification on coccolithophores. *J. Mar. Syst.* 182, 12–30. doi: 10.1016/j.jmarsys.2018.02.008

Haigh, R., Ianson, D., Holt, C. A., Neate, H. E., and Edwards, A. M. (2015). Effects of ocean acidification on temperate coastal marine ecosystems and fisheries in the northeast pacific. *PLoS One* 10:e0117533. doi: 10.1371/journal.pone.0117533

Harper, S., Zeller, D., Hauzer, M., Pauly, D., and Sumaila, U. R. (2013). Women and fisheries: contribution to food security and local economies. *Mar. Policy* 39, 56–63. doi: 10.1016/j.marpol.2012.10.018

Hilborn, R., and Walters, C. J. (1992). *Quantitative Fisheries Stock Assessment*. Boston, MA: Springer US, doi: 10.1007/978-1-4615-3598-0

Hoegh-Guldberg, O., Mumby, J., Hooten, J., Steneck, S., Greenfield, P., Gomes, E., et al. (2007). Coral reefs under rapid climate change and ocean acidification. *Science* 318:1737.

IPCC (2013). in *Climate Change 2013: The Physical Science Basis. Contribution of Working Group I to the Fifth Assessment Report of the Intergovernmental Panel on Climate Change*, eds T. F. Stocker, D. Qin, G.-K. Plattner, M. Tignor, S. K. Allen, J. Boschung, et al. (Cambridge: Cambridge University Press), doi: 10.1017/CBO9781107415324

Jones, M. C., Dye, S. R., Pinnegar, J. K., Warren, R., and Cheung, W. W. L. (2012). Modelling commercial fish distributions: prediction and assessment using different approaches. *Ecol. Modell.* 225, 133–145. doi: 10.1016/j.ecolmodel.2011.11.003

Jutfelt, F., Norin, T., Ern, R., Overgaard, J., Wang, T., McKenzie, D. J., et al. (2018). Oxygen- and capacity-limited thermal tolerance: blurring ecology and physiology. *J. Exp. Biol.* 221:jeb169615. doi: 10.1242/jeb.169615

Koenigstein, S., Mark, F. C., Gößling-Reisemann, S., Reuter, H., and Poertner, H. O. (2016). Modelling climate change impacts on marine fish populations: process-based integration of ocean warming, acidification and other environmental drivers. *Fish Fish.* 17, 972–1004. doi: 10.1111/faf.12155

Kroeker, K. J., Kordas, R. L., Crim, R., Hendriks, I. E., Ramajo, L., Singh, G. S., et al. (2013). Impacts of ocean acidification on marine organisms: quantifying sensitivities and interaction with warming. *Glob. Chang. Biol.* 19, 1884–1896. doi: 10.1111/gcb.12179

Kronen, M., Vunisea, A., Magron, F., and McArdle, B. (2010). Socio-economic drivers and indicators for artisanal coastal fisheries in Pacific island countries and territories and their use for fisheries management strategies. *Mar. Policy* 34, 1135–1143. doi: 10.1016/j.marpol.2010.03.013

Lam, V. W. Y., Cheung, W. W. L., Reygondeau, G., and Sumaila, U. R. (2016). Projected change in global fisheries revenues under climate change. *Sci. Rep.* 6:32607. doi: 10.1038/srep32607

Lam, V. W. Y., Cheung, W. W. L., and Sumaila, U. R. (2014). Marine capture fisheries in the Arctic: winners or losers under climate change and ocean acidification? *Fish Fish.* 17, 335–357. doi: 10.1111/faf.12106

Le Quesne, W. J. F., and Pinnegar, J. K. (2012). The potential impacts of ocean acidification: scaling from physiology to fisheries*. *Fish Fish.* 13, 333–344. doi: 10.1111/j.1467-2979.2011.00423.x

Lefevre, S., Mckenzie, D. J., and Nilsson, G. E. (2017). Models projecting the fate of fish populations under climate change need to be based on valid physiological mechanisms. *Glob. Chang. Biol.* 23, 3449–3459. doi: 10.1111/gcb.13652

Marshall, K. N., Kaplan, I. C., Hodgson, E. E., Hermann, A., Busch, D. S., McElhany, P., et al. (2017). Risks of ocean acidification in the California Current food web and fisheries: ecosystem model projections. *Glob. Chang. Biol.* 23, 1525–1539. doi: 10.1111/gcb.13594

McNeil, B. I., and Sasse, T. P. (2016). Future ocean hypercapnia driven by anthropogenic amplification of the natural CO2 cycle. *Nature* 529, 383–386. doi: 10.1038/nature16156

Nagelkerken, I., and Connell, S. D. (2015). Global alteration of ocean ecosystem functioning due to increasing human CO2 emissions. *Proc. Natl. Acad. Sci.U.S.A.* 112, 13272–13277. doi: 10.1073/pnas.1510856112

O'Connor, M. I., Bruno, J. F., Gaines, S. D., Halpern, B. S., Lester, S. E., Kinlan, B. P., et al. (2007). Temperature control of larval dispersal and the implications for marine ecology, evolution, and conservation. *Proc. Natl. Acad. Sci. U.S.A.* 104, 1266–1271. doi: 10.1073/pnas.0603422104

Palomares, M. L. D., and Pauly, D. (2017). *SeaLifeBase. World Wide Web Electron. Publ., Version (06/2017)*. Available online at: www.sealifebase.org (accessed January 1, 2017).

Pauly, D. (1980). On the interrelationships between natural mortality, growth parameters, and mean environmental temperatuer in 175 fish stocks. *ICES J. Mar. Sci.* 39, 175–192. doi: 10.1093/icesjms/39.2.175

Pauly, D. (1981). The relationship between gill surface area and growth performance in fish: a generalization of von Bertalanffy's theory of growth. *Berichte Dtsch. Wissenschaftlichen Kommission für Meeresforsch.* 28, 251–282.

Pauly, D., and Cheung, W. W. L. (2017). Sound physiological knowledge and principles in modeling shrinking of fishes under climate change. *Glob. Chang. Biol.* 24, e15–e26. doi: 10.1111/gcb.13831

Pauly, D., and Zeller, D. (2015). *Sea Around Us Concepts, Design and Data*. (seaaroundus.org).

Pörtner, H. O., and Farrell, A. P. (2008). Physiology and climate change. *Science* 322, 690–692. doi: 10.1126/science.1163156

Pörtner, H. O., and Lannig, G. (2009). "Oxygen and capacity limited thermal tolerance," in *Fish Physiology*, eds J. G. Richards, A. P. Farrell, and C. J. Brauner (Burlington: Elsevier Inc), 143–191. doi: 10.1016/S1546-5098(08)00004-6

Pörtner, H.-O., Bock, C., and Mark, F. C. (2018). Oxygen- and capacity-limited thermal tolerance: blurring ecology and physiology. *J. Exp. Biol.* 221, jeb169615. doi: 10.1242/jeb.169615

Purvis, A., Gittleman, J. L., Cowlishaw, G., and Mace, G. M. (2000). Predicting extinction risk in declining species. *Proc. R. Soc. B Biol. Sci.* 267, 1947–1952. doi: 10.1098/rspb.2000.1234

Quinn, T. J. II, and Deriso, R. B. (1999). *Quantitative Fish Dynamics*. (New York, NY: Oxford University Press). doi: 10.1007/s13398-014-0173-7.2.

Ries, J. B., Cohen, A. L., and Mccorkle, D. C. (2009). Marine calcifiers exhibit mixed responses to CO2-induced ocean acidification. *Geology* 37, 1131–1134. doi: 10.1130/G30210A.1

Sibert, J. R., Hampton, J., Fournier, D. A., and Bills, P. J. (1999). An advection-diffusion-reaction model for the estimation of fish movement par. *Can. J. Fish. Aquat. Sci.* 56, 925–938. doi: 10.1139/f99-017

Sunday, J. M., Fabricius, K. E., Kroeker, K. J., Anderson, K. M., Brown, N. E., Barry, J. P., et al. (2017). Ocean acidification can mediate biodiversity shifts by changing biogenic habitat. *Nat. Clim. Chang.* 1, 81–85. doi: 10.1038/nclimate3161

Tai, T. C. (2019). *Building Tools to Model the Effects of Ocean Acidification and How it Scales From Physiology to Fisheries.* Ph.D. Thesis. Vancouver CA: University of British Columbia, 226.

Tai, T. C., Cashion, T., Lam, V. W. Y., Swartz, W., and Sumaila, U. R. (2017). Ex-vessel fish price database: disaggregating prices for low-priced species

from reduction fisheries. *Front. Mar. Sci.* 4:363. doi: 10.3389/fmars.2017.00363

Tai, T. C., Harley, C. D. G., and Cheung, W. W. L. (2018). Comparing model parameterizations of the biophysical impacts of ocean acidification to identify limitations and uncertainties. *Ecol. Modell.* 385, 1–11. doi: 10.1016/j.ecolmodel.2018.07.007

Teh, L. C. L., Teh, L. S. L., Starkhouse, B., and Rashid Sumaila, U. (2009). An overview of socio-economic and ecological perspectives of Fiji's inshore reef fisheries. *Mar. Policy* 33, 807–817. doi: 10.1016/j.marpol.2009.03.001

Then, A. Y., Hoenig, J. M., Hall, N. G., and Hewitt, D. A. (2015). Evaluating the predictive performance of empirical estimators of natural mortality rate using information on over 200 fish species. *ICES J. Mar. Sci.* 72, 82–92. doi: 10.1093/icesjms/fsu136

van Vuuren, D. P., Edmonds, J., Kainuma, M., Riahi, K., Thomson, A., Hibbard, K., et al. (2011). The representative concentration pathways: an overview. *Clim. Change* 109, 5–31. doi: 10.1007/s10584-011-0148-z

Wahl, M., Saderne, V., and Sawall, Y. (2016). How good are we at assessing the impact of ocean acidification in coastal systems? Limitations, omissions and strengths of commonly used experimental approaches with special emphasis on the neglected role of fluctuations. *Mar. Freshwater Res.* 67, 25–36. doi: 10.1071/mf14154

Whiteley, N. M. (2011). Physiological and ecological responses of crustaceans to ocean acidification. *Mar. Ecol. Prog. Ser.* 430, 257–271. doi: 10.3354/meps09185

Wittmann, A. C., and Pörtner, H. O. (2013). Sensitivities of extant animal taxa to ocean acidification. *Nat. Clim. Chang.* 3, 995–1001. doi: 10.1038/nclimate1982

Zeller, D., Booth, S., Pakhomov, E., Swartz, W., and Pauly, D. (2011). Arctic fisheries catches in Russia, USA, and Canada: baselines for neglected ecosystems. *Polar Biol.* 34, 955–973. doi: 10.1007/s00300-010-0952-3

Conflict of Interest: The authors declare that the research was conducted in the absence of any commercial or financial relationships that could be construed as a potential conflict of interest.

The reviewer LK declared a past co-authorship with one of the author WC to the handling editor.

Copyright © 2021 Tai, Sumaila and Cheung. This is an open-access article distributed under the terms of the Creative Commons Attribution License (CC BY). The use, distribution or reproduction in other forums is permitted, provided the original author(s) and the copyright owner(s) are credited and that the original publication in this journal is cited, in accordance with accepted academic practice. No use, distribution or reproduction is permitted which does not comply with these terms.

frontiers in Marine Science

ORIGINAL RESEARCH
published: 19 May 2021
doi: 10.3389/fmars.2021.602601

Synthesis of Thresholds of Ocean Acidification Impacts on Echinoderms

Nina Bednaršek[1,2], Piero Calosi[3], Richard A. Feely[4], Richard Ambrose[5], Maria Byrne[6], Kit Yu Karen Chan[7], Sam Dupont[8], Jacqueline L. Padilla-Gamiño[9], John I. Spicer[10], Faycal Kessouri[1], Miranda Roethler[1], Martha Sutula[1] and Stephen B. Weisberg[1]*

[1] Southern California Coastal Water Research Project, Costa Mesa, CA, United States, [2] National Institute of Biology, Ljubljana, Slovenia, [3] Département de Biologie, Chimie et Géographie, Université du Québec à Rimouski, Rimouski, QC, Canada, [4] NOAA Pacific Marine Environmental Laboratory, Seattle, WA, United States, [5] Department of Environmental Health Sciences, University of California, Los Angeles, Los Angeles, CA, United States, [6] School of Life and Environmental Sciences, The University of Sydney, Sydney, NSW, Australia, [7] Biology Department, Swarthmore College, Swarthmore, PA, United States, [8] Department of Biological and Environmental Sciences, University of Gothenburg, Gothenburg, Sweden, [9] School of Aquatic and Fishery Sciences, University of Washington, Seattle, WA, United States, [10] Marine Biology and Ecology Research Centre, School of Biological and Marine Sciences, University of Plymouth, Plymouth, United Kingdom

OPEN ACCESS

Edited by:
Punyasloke Bhadury, Indian Institute of Science Education and Research Kolkata, India

Reviewed by:
Kelig Mahe, Institut Français de Recherche pour l'Exploitation de la Mer (IFREMER), France
Marian Hu, Christian-Albrechts-Universität zu Kiel, Germany

***Correspondence:**
Nina Bednaršek
ninab@sccwrp.org

Specialty section:
This article was submitted to Marine Biology, a section of the journal Frontiers in Marine Science

Received: *03 September 2020*
Accepted: *01 March 2021*
Published: *19 May 2021*

Citation:
Bednaršek N, Calosi P, Feely RA, Ambrose R, Byrne M, Chan KYK, Dupont S, Padilla-Gamiño JL, Spicer JI, Kessouri F, Roethler M, Sutula M and Weisberg SB (2021) Synthesis of Thresholds of Ocean Acidification Impacts on Echinoderms. Front. Mar. Sci. 8:602601. doi: 10.3389/fmars.2021.602601

Assessing the vulnerability of marine invertebrates to ocean acidification (OA) requires an understanding of critical thresholds at which developmental, physiological, and behavioral traits are affected. To identify relevant thresholds for echinoderms, we undertook a three-step data synthesis, focused on California Current Ecosystem (CCE) species. First, literature characterizing echinoderm responses to OA was compiled, creating a dataset comprised of >12,000 datapoints from 41 studies. Analysis of this data set demonstrated responses related to physiology, behavior, growth and development, and increased mortality in the larval and adult stages to low pH exposure. Second, statistical analyses were conducted on selected pathways to identify OA thresholds specific to duration, taxa, and depth-related life stage. Exposure to reduced pH led to impaired responses across a range of physiology, behavior, growth and development, and mortality endpoints for both larval and adult stages. Third, through discussions and synthesis, the expert panel identified a set of eight duration-dependent, life stage, and habitat-dependent pH thresholds and assigned each a confidence score based on quantity and agreement of evidence. The thresholds for these effects ranged within pH from 7.20 to 7.74 and duration from 7 to 30 days, all of which were characterized with either medium or low confidence. These thresholds yielded a risk range from early warning to lethal impacts, providing the foundation for consistent interpretation of OA monitoring data or numerical ocean model simulations to support climate change marine vulnerability assessments and evaluation of ocean management strategies. As a demonstration, two echinoderm thresholds were applied to simulations of a CCE numerical model to visualize the effects of current state of pH conditions on potential habitat.

Keywords: ocean acidification, biological threshold, echinoderms, expert consensus, biological, quality, synthesis, calcifiers

INTRODUCTION

Climate change is accelerating the oceanic uptake of anthropogenic CO_2, causing a decline in pH and the availability of calcium carbonate minerals, a process termed ocean acidification (OA). Intensification of OA conditions directly contributes to the decline in suitable habitats for many marine invertebrates, such as mollusks, echinoderms, crustaceans, and pteropods (Kroeker et al., 2013; Fabricius et al., 2014; Przeslawski et al., 2015; Bednaršek et al., 2019, 2020), potentially altering their population abundances, causing local extirpation, shifts in species' geographical ranges and, at worst, global extinction. Many studies have described pathways related to OA vulnerability, but only a few that have identified the thresholds where those effects occur. Taxon-specific syntheses are lacking on the critical thresholds at which OA impacts a range of developmental, physiological, biomineralization, growth and behavioral, and lethal endpoints. These thresholds are critical to the development of management strategies, as they provide an understanding of the priority species and geographic areas and a means with which to evaluate preventative or ameliorative strategies.

Ocean acidification thresholds have been previously described for pteropods (Bednaršek et al., 2019) and decapods (Bednaršek et al., in review). Thresholds have yet to be comprehensive described for echinoderms, despite their known sensitivity (e.g., Dupont et al., 2008; Wood et al., 2008; Spicer et al., 2011; Byrne et al., 2013; Kroeker et al., 2013; Stumpp et al., 2013; Byrne and Fitzer, 2019; Byrne and Hernández, 2020), though only a few thresholds have been reported (Dorey et al., 2013; Jager et al., 2016; Lee et al., 2019). Echinodermata is one the most abundant and ecologically successful phyla of marine animals and have been successful in colonizing a range of habitats, including shallow coastal, neritic (0–200 m), down to upper (0.2–1 km), and lower bathyal (>2000 m) zones (Micael et al., 2009; Lawrence, 2013, 2020; Byrne and O'Hara, 2017). Echinoderm classes including the Crinoidea (e.g., feather stars), Ophiuroidea (e.g., brittle stars) and Asteroidea (e.g., sea stars), Echinoidea (sea urchins), and Holothuroidea (sea cucumbers) are ecologically important as ecosystem engineers in rocky reef ecosystems, serving as macroalgal grazers and keystone predators where their grazing and predation play a key role in structuring benthic communities (Paine, 1966; Lawrence, 2013, 2020; Filbee-Dexter and Scheibling, 2014). They also have important functions in benthic-pelagic coupling as bioturbators and remineralizers (Ambrose et al., 2001) and as a food source for crustaceans, fish, mammals, and sea birds (Baden et al., 1990; Mattson, 1990; Wolfe et al., 2018). Economically, sea urchins' gonads and cucumber based beche-de-mer products contribute to a multi-million-dollar industry for international food markets (Conand and Byrne, 1993; Eriksson and Byrne, 2015; O'Hara and Byrne, 2017; Teck et al., 2018).

Echinoderms represent an ideal animal model for understanding the balance between the sensitivity and tolerance mechanisms to OA conditions, due to their diverse habitat preferences and associated local and regional carbonate chemistry exposure regime (Wolfe et al., 2020) that structures their acclimatization and adaptation strategies (Barry et al., 2010; Yu et al., 2011; Calosi et al., 2013b, 2017; Kelly et al., 2013; Sunday et al., 2014; Vargas et al., 2017), The sensitivity of echinoderms to OA occurs *via* multiple pathways that are also life stage specific. Common pathways of OA sensitivity include reduced ability for homeostasis, skeletogenesis and growth rate, increased mortality, impaired reproduction; alterations to the chemosensory behavior; and reduced feeding efficiency (Wood et al., 2008, 2011; Byrne et al., 2010, 2013; Spicer et al., 2011; Barry et al., 2014; Taylor et al., 2014). pH effects on larvae occur through various pathways (Politi et al., 2004; Byrne and Przeslawski, 2013; Byrne et al., 2013; Padilla-Gamiño et al., 2013), such as the allocation of metabolic energy for protein synthesis and ion transport (Pan et al., 2015), with the acid-base and osmo-ionic regulatory reaching their capacity threshold (Dupont and Thorndyke, 2012; Stumpp et al., 2012b; Byrne et al., 2013; Dubois, 2014; Smith et al., 2016; Byrne and Fitzer, 2019) and resulting in reduced scope for growth and metabolic requirements, and ultimately also negatively impacted organismal performance and survival. Given greater larval echinoderm OA sensitivity and the control of larval recruitment on population abundance and distribution, the larval OA thresholds define a key point of vulnerability by which the ecological and economic role of echinoderms within coastal marine ecosystems could be heavily compromised in the future.

This study presents a comprehensive literature review and a synthesis of published studies related to the experimental and *in situ* OA exposure that were published through October 2018 for echinoderm taxa of California Current Ecosystem (CCE), an eastern boundary upwelling system on the Pacific Coast of North America. From ∼12,000 compiled data points, statistical analyses were conducted to identify duration-dependent pH thresholds specific to the life stage and their habitat (pelagic, benthic). Through the expert discussion, deliberation and consensus, eight representative pH thresholds were selected ranging from duration-dependent early warning to lethal impacts. The experts also provide recommendations on how to apply these thresholds to monitoring data and model output, here demonstrated as an example application to a CCE numerical model to illustrate the importance of life history in determining species sensitivity. Finally, further research is recommended to improve the understanding of echinoderm responses to OA and to support the implementation of OA thresholds to various management applications, from climate change to local pollution impact assessments.

MATERIALS AND METHODS

The synthesis was conducted in three steps. First, a review of literature was conducted on the effects of OA on echinoderm species present in the CCE to compile information on the species-specific experimental or observational responses to OA stress, including the treatment duration, life stage, and geographic region. When limited information was available for a CCE species, a geographically expanded data search was conducted on phylogenetically closely related species. Second, statistical

analyses were used to identify thresholds of OA for each of the impairment pathways. Finally, a panel of decapod experts provided their professional judgment to evaluate the quality of studies, weigh (or remove) them based on that data quality assessment, assign a duration-dependent threshold and associated confidence score, which was based on the data quality and consistency of findings for the studies (**Table 1**). The experts also scored them for regional importance in the CCE (**Table 1**). To illustrate how these thresholds could be applied, two thresholds applied to simulations of a regional biogeochemical model to visualize potential habitat constraints.

Literature Review and Compilation of Raw Experimental or Field Observation Data

The literature search was conducted by searching Google Scholar and Web of Science, as well as the reference lists of the identified studies for analysis until October 1, 2018. The search terms used included "ocean acidification" or "climate change" with "echinoderm." The literature search and review identified 40 experimental studies and one observational study that met the minimum criterion of: (1) experimental studies with data on a minimum of four treatment levels or (2) field stress-response studies conducted across a range of pH values. It is important to note that not each study needs at least four treatments levels, but all the studies combined that have contributed to the generation of one specific thresholds need to have at least four experimental treatment levels.

This search yielded a review database of 13 species: six sea urchins/sand dollars (*Dendraster excentricus, Lytechinus pictus, Mesocentrotus franciscanus, Strongylocentrotus droebachiensis, Strongylocentrotus fragilis,* and *Strongylocentrotus purpuratus*), four brittle stars (*Amphiura filiformis, Ophiocten sericeum, Ophionereis schayeri,* and *Ophiura ophiura*). Approximately 55% of the data came from CCE-specific studies. No data suitable to generate pH thresholds were available for holothuroids and crinoids, so these groups were excluded from the review. Data were extracted presented from **Supplementary Material** associated with the articles or from the article's figures using WebPlotDigitizer version 4.3[1]. A range of covariates were recorded including the life stage, taxonomic information, location, and treatment duration (days). A total of ∼12,000 datapoints were extracted from the raw experimental data in published literature or from authors with unpublished data. Data from multi-generation studies were excluded.

An explicit step in the review involved standardizing the specific response metric and/or the OA measure, specifically related to the individual body size with growth rate and feeding rate. If needed, metabolic parameters were transformed so that the units were comparable among studies. A variety of OA exposure metrics were used across studies, but the majority used pH as the primary measure; as such, all data were placed in the context of this single parameter. When another carbonate system parameter was utilized but the paper contained the necessary water chemistry values, it was converted to pH using the R Seacarb package (Gattuso et al., 2019), using Equation 1. Program preferences were set to use carbonate system solubility products from Lueker et al. (2000), $KHSO_4$ dissociation constants from Dickson et al. (1990), total boron from Lee et al. (2010), and k_f from Dickson and Riley (1979) as cited in Dickson and Goyet (1994). If pH values were unavailable or not able to be generated, the study was excluded. When possible (i.e., when sufficient water chemistry data were available), pH values were converted to pH_T.

Additional categorical variables were recorded in the review database and included life stage, habitat depth, geographic origin, and duration. Egg and larval (pelagic), juvenile and adult (benthic) life stages of echinoderms are physiologically disparate and will experience fundamentally different exposure regimes. Thus, data were categorized by life stage independently. Most data (about 50%) were from studies of larval stages, while only 17% of the data came from adult life stages. Additionally, benthic organisms will experience different pH ranges depending on whether they inhabit shallow (<200 m) or deep water (>200 m depth) so species data were categorized by habitat depth. All the data came from shallow-water species, apart from one deep-water species (*S. fragilis*). A total of 237 response endpoints across various species, life stages and geographic locations were characterized into four effect categories: (1) behavior, (2) growth, (3) physiology, and (4) mortality.

Threshold Analysis

Two types of statistical analyses were used support expert decisions on thresholds (**Supplementary Figure 1**). First, a *breakpoint* was identified, defined as the point at which there is a significant change in echinoderm responses (*Y*-axis) as a result of the incremental change in the environmental stressor (*x*-axis, e.g., pH pH_T). Piecewise regression analysis was used to identify the breakpoint in slopes in the response measures over the gradient in OA stress (package "segmented"; version 2.15.1, Muggeo, 2008; R Development Core Team, 2020). A Davies test was used to determine the significance of the breakpoint. Second, the data were fitted to least squares regression (LSR). When the LSR was significant at p value < 0.05 and data followed a linear trend, the panel (see below) considered what were meaningful changes in the response parameters and used that information to support their threshold decisions. **Table 1** provides the LSR-predicted percent change from the mean of the control treatments in the dataset that final pH threshold represents, based on expert consensus. Data were analyzed in R (Version 3.5.0). Only analyses that were significant at $p < 0.05$ are reported in the text (**Table 1**). After running the threshold analyses for all studies, the thresholds were grouped by response metric, life stage, habitat depth, duration, and species.

Expert Consensus on Thresholds and Exposure Duration and Assessment of Uncertainty

We employed a formal, structured process to obtain the expert evaluation and synthesis of OA effects on selected decapod parameters, including: (1) evaluation of study data and threshold analyses; (2) assembly of expert panel members based on their expertise; (3) expert discussion through the consensus-based

[1]https://automeris.io/WebPlotDigitizer

TABLE 1 | Compilation of the magnitude and duration of the expert derived thresholds of echinoderm pH thresholds for effect pathways by life stage and habitat, life function (response parameter and unit), direction of response, and species used in study.

Effect	Life Stage	Habitat	Life function	Units	Direction response	Species	Threshold ref. No.	pH threshold, expert consensus	Duration (days)	LSR predicted change from the mean of the control (selected by the experts)	Breakpoint pH threshold	CCE relevance	Confidence	Data Source
Behavior	Larvae	Pelagic	Behavior, swimming speed	mm/s	+	*Dendraster excentricus, Strongylocentrotus purpuratus*	1	7.70	7	43%	N.S.	2.5	low evidence	Chan et al., 2011, 2016
	Adult	Benthic, deep	Behavior, righting time	seconds	+	*Strongylocentrotus fragilis*	2	7.20	30	40%	7.25	3.0	low evidence	Taylor et al., 2014
Physiology	Larvae	Pelagic	Physiology, respiration	pmol/ind./ hour/day	+	*Strongylocentrotus droebachiensis*	3	7.74	7	25%	N.S.	2.0	low evidence	Dorey et al., 2013
	Adult	Benthic, shallow	Physiology, coelomic fluid pH	NA	–	*Strongylocentrotus fragilis, Strongylocentrotus droebachiensis*	4	7.60	7	42%	7.40	3.0	low evidence	Spicer et al., 2011; Taylor et al., 2014
			Physiology respiration (normalized)	NA	+	*Amphiura filiformis, Ophiura ophiura, Ophionereis schayeri, Ophiocten sericeum*	5	7.75	7	35%	N.S.	1.0	medium evidence, medium-high agreement	Wood et al., 2008, 2010, 2011; Christensen et al., 2011
		Benthic, deep	Physiology, Feeding rate	mg kelp/g wet wt./day	–	*Strongylocentrotus fragilis*	6	7.38	30	25%	N.S.	3.0	low evidence	Taylor et al., 2014
Growth	Larvae	Pelagic	Growth rate at midline	mm/day	–	*Strongylocentrotus droebachiensis*	7a	7.49	7	35%	7.25	2.0	low evidence	Dorey et al., 2013; Runcie et al., 2016
			Growth, total Length	um	–	*Strongylocentrotus purpuratus*	7b	7.68	7	46%	7.74	2.5	medium evidence; medium-high agreement	Yu et al., 2011; Matson et al., 2012; Kelly et al., 2013; Padilla-Gamiño et al., 2013; Pespeni et al., 2013
			Growth, Symmetry Index	NA	–	*Strongylocentrotus droebachiensis*	7c	7.64	14	35%	N.S.	2.5	low evidence	Dorey et al., 2013
			Composite growth and development (based on threshold number 7a-c)				7	7.62	7	–	–	2.5	high evidence; medium-high agreement	Yu et al., 2011; Matson et al., 2012; Dorey et al., 2013; Kelly et al., 2013; Padilla-Gamiño et al., 2013; Pespeni et al., 2013; Pan et al., 2015; Chan et al., 2016
Mortality	Larvae	Pelagic	Mortality	%/day	Positive	*Strongylocentrotus droebachiensis*	8	7.23	7	50%	7.23	2.0	low evidence	Dorey et al., 2013; Chan et al., 2015

The next set of column gives the final the expert consensus pH and associated duration (days), then, for reference, what percent change that expert derived thresholds represents from the mean experimental control value (in percentage) when the least squares regression (LSR) was significant (p-value < 0.05), and, when significant, the statistical breakpoint pH. The expert certainty rating is specified based on degree of evidence and degree of agreement among studies considered (ranging from high to low). CCE relevance is specified as "1" indicating low relevance is the species is not found in the CCE, and the study was not conducted on organisms from the CCE; with "2" indicating medium relevance (the species is found in the CCE but the study was conducted on organisms that were not from the CCE); and "3" indicating high relevance (the species is found in the CCE and the study was conducted on organisms from the CCE). When "2.5" is specified, it means that the mix of studies evaluated were a range of CCE relevance of 2 to 3. Finally, source of data used to derive the thresholds is given.

approach to select the final set of thresholds and associated confidence scores.

The expert panel were recruited based on the following criteria related to the required expertise: (1) echinoderm ecophysiology; (2) echinoderm taxonomy and morphology, biomechanics, biomineralization; (3) echinoderm ecology and community ecology; and (4) OA biogeochemistry and observations. The candidates were ultimately selected based on a qualitative evaluation of the quality and depth of the publication record and the availability of the candidates to attend a 3-day workshop. OA expertise was highly regarded, but not strictly required if the expert provided a unique expertise.

Our process required that the experts considered and discussed the statistical threshold analyses and the underlying study data, applied their individual expertise, communicated relevant information, and made recommendations or challenged the conclusions to ultimately generate a set of consolidated thresholds. The experts excluded studies with data quality limitations or interpretability issues, refined interpretation of the analytical outcomes based on their knowledge of the studies and how data should be weighted for unbiased results. In one case (swimming speed), they pulled in Chan et al. (2011), which had only two treatments because they decided to combine it with Chan et al. (2016) because of the compatible response measures and experimental procedures. After discussion of these data and their interpretation, each of the nine experts and now listed in the co-author contribution section, voted on the numeric value as well as the confidence score for each specific threshold, providing a rationale for their choice as needed, particularly if it deviated from the majority opinion. The experts identified the most appropriate time frame (duration) over which the thresholds should be applied. Experts could abstain from voting if they did not feel confident that there was sufficient evidence that the threshold existed for a given metric. In cases where the experts disagreed with the statistical result and/or were divided in their opinions, the threshold value with the most votes was chosen; if there was no clear majority on the value and the uncertainty, the value was discussed until consensus was reached.

Experts were asked to score their confidence in the final threshold into one of nine categories based on the scoring metric developed by the IPCC (**Supplementary Figure 1**). The matrix has two components, the agreement and evidence. The agreement indicates the consistency of results among studies, while evidence encompasses the quantity and quality of studies used to establish the threshold. For agreement, a study comprising a single experiment had low level of agreement by default, though a single paper could contribute to a high level of agreement if multiple experiments were done on multiple species. The group identified 1–3 studies as a low evidence, 3–10 studies as a medium evidence, and 10 or more studies as a robust evidence. These were guidelines rather than strict rules because individual studies contained different amounts of data. Agreement referred to agreement amongst experiments on the specific parameter being considered (e.g., swimming speed) as opposed to the general category as a whole (e.g., behavior).

Scoring for Regional Relevance

Echinoderms have diverse habitat preferences and exposure related to the natural variability of the local and regional carbonate chemistry (Wolfe et al., 2020) that structures their acclimatization and adaptation strategies (Barry et al., 2010; Yu et al., 2011; Calosi et al., 2013b, 2017; Kelly et al., 2013; Sunday et al., 2014; Vargas et al., 2017). Thresholds were designated with a CCE regional relevance score, acknowledging this issue of local acclimatization and adaptation. A score of #1 indicated low relevance (species that are not present in the CCE, and study not conducted on specimens from the CCE); #2 indicated medium relevance (species that are found in the CCE but study conducted on specimens from outside of the CCE); and #3 indicated high relevance (species that are found in the CCE and study conducted on specimens from the CCE) (see **Tables 1**, **2**). All data from urchin were only from the CCE species whereas brittle stars were from species not found in the CCE.

Applying Thresholds to Numerical Ocean Biogeochemical Model Simulations

Experts recommended use of measures such as: intensity (magnitude deviation from threshold), duration (number of days below threshold), frequency (the number of events below the pH threshold for events longer than the duration threshold), severity (duration times intensity of departure from the thresholds), and recovery (average number of days between adverse events; Hauri et al., 2013). Application of OA thresholds to either monitoring data or numerical model simulations considered available data on relevant demographics parameters. This included habitat-specific life history, vertical dimensions of habitat of different life stages and their seasonal occurrence, an appropriate spatial and vertical aggregation, duration of exposure and adaptation traits.

These measures were applied for a set of OA thresholds applied to a set of model simulations from the Regional Ocean Modeling System (ROMS; Shchepetkin and McWilliams, 2005, 2009), with biogeochemical elements (Biogeochemical Elemental Cycling; BEC, Moore et al., 2004) that has been developed for the CCE, the Pacific Coast of North America. The ROMS-BEC model provides a realistic three-dimensional representation of the physical circulation (Renault et al., 2020) and the biogeochemical cycles of nutrients, oxygen, inorganic and organic carbon species, and several plankton functional groups (Deutsch et al., in review). The simulation analyzed here is at 1 km spatial resolution southern CCE horizontal resolution domain of the ROMS-BEC, a geographic region synonymous with California coast (Deutsch et al., 2020; Renault et al., 2020). Daily pH values at specific water depths that were life- and species- specific were used together with the duration of exposure associated with a specific threshold over the 10-year simulation from 1996 to 2007. Two case studies focused on thresholds applicable to two different life stages. A respiratory effects threshold (pH = 7.75; 1-week duration) was applied year-around for the adult sea urchin species (e.g., *S. fragilis*, *S. droebachiensis,* etc.) to represent their habitat found along the 0–500 m shelf of the Californian coast. A larval behavioral response threshold (impaired swimming speed; pH = 7.7; 1-week duration) was applied to pelagic

TABLE 2 | Description of all the responses for which the thresholds were determined with accompanied biological (life stage, habitat, function) and threshold parameters (LR, breakpoint point, relevance in CCE, confidence score).

Effect	Life Stage	Habitat	Life function	Units	Sign of Response	Species	Threshold Ref. No.	pH Threshold, Expert Consensus	Duration (days)	LR Predicted Change from the mean of the Control (as seleted by the Expert)	Breakpoint pH Threshold	CCE Relevance	Confidence Score	Data Source
Behavior	Larvae	Pelagic	Swimming speed	mm/s	Positive	*Dendraster excentricus, Strongylocentrotus purpuratus*	1	7.70	7	43%	N.R.	2.5	low evidence	Chan et al., 2011, 2016
	Adult	Benthic, deep	Righting time	seconds	Positive	*Strongylocentrotus fragilis*	2	7.20	30	40%	7.25	3.0	low evidence	Taylor et al., 2014
Physiology	Larvae	Pelagic	Respiration	pmol/ ind./ hour/day	Positive	Strongylocentrotus droebachiensis	3	7.74	7	25%	N.S.	2.0	low evidence	Dorey et al., 2013
	Adult	Benthic, shallow	Coelomic fluid pH	NA	Negative	Strongylocentrotus fragilis, Strongylocentrotus droebachiensis	4	7.60	7	42%	7.40	3.0	low evidence	Spicer et al., 2011; Taylor et al., 2014
			Respiration (normalized)	NA	Positive	Amphiura filiformis, Ophiura ophiura, Ophionereis schayeri, Ophiocten sericeum	5	7.75	7	35%	N.S.	1.0	medium evidence, medium-high agreement	Christensen et al., 2011; Wood et al., 2008, 2010, 2011
		Benthic, deep	Feeding rate	mg kelp/g wet wt./day	Negative	Strongylocentrotus fragilis	6	7.38	30	25%	N.S.	3.0	low evidence	Taylor et al., 2014
Growth	Larvae	Pelagic	Growth rate at midline	mm/day	Negative	Strongylocentrotus droebachiensis	7	7.49	7	35%	7.25	2.0	low evidence	Dorey et al., 2013; Runcie et al., 2016
			Total Length	um	Negative	Strongylocentrotus purpuratus	9	7.68	7	46%	7.74	2.5	medium evidence; medium-high agreement	Yu et al., 2011; Matson et al., 2012; Kelly et al., 2013; Padilla-Gamiño et al., 2013; Pespeni et al., 2013
			Symmetry Index	NA	Negative	Strongylocentrotus droebachiensis	10	7.64	14	35%	N.S.	2.5	low evidence	Dorey et al., 2013
			Composite growth and development (based on threshold number 7, 9, and 10)				11	7.62		–	–	2.5	high evidence; medium-high agreement	Yu et al., 2011; Matson et al., 2012; Dorey et al., 2013; Kelly et al., 2013; Padilla-Gamiño et al., 2013; Pespeni et al., 2013; Pan et al., 2015; Chan et al., 2016
Mortality	Larvae	Pelagic	Mortality	%/day	Positive	*Strongylocentrotus droebachiensis*	12	7.23	7	50%	7.23	2.0	low evidence	Dorey et al., 2013; Chan et al., 2015

habitat for echinoderm species including *S. purpuratus* and *D. excentricus* over April–July period (Kenner and Lares, 1991; Basch and Tegner, 2007; Hammond and Hofmann, 2010).

RESULTS OF EXPERT CONSENSUS

pH as the Measure to Define OA-Related Stress Level

The expert panel recommended pH as a measure to describe the stress levels in echinoderms because the majority or studies frequency reported pH as a variable (12 out of 16), as well as because most of the synthesis and meta-analyses literature up to date used pH as a comparable response. Based on the studies selected, pH response in experimental treatments spanned a range of pH conditions of 6.44–8.31 (**Figure 1**), with exposure duration varying from 1 day to 5 months, but predominantly <50 days.

Synthesis of Thresholds by Endpoints

The expert synthesis produced eight thresholds across multiple physiological, growth and development, behavioral, and survival endpoints (**Table 1** and **Figure 2**), scored by expert confidence certainty (**Figure 3** and **Table 1**) and CCE relevance (**Table 1**) and the implication for the echinoderm group.

Behavior: Larvae

The larval behavior threshold was based on larvae swimming speed data from two papers on the sand dollar *D. excentricus* and *S. purpuratus* (Chan et al., 2011, 2016). Swimming speed increased with decreasing pH. The panel placed the threshold at pH = 7.70 (7-day duration), corresponding a LSR predicted 35% reduction from the experimental control (p = 0.023, R^2 = 0.12, F = 5.22, DF = 40). The threshold was rated as low evidence and agreement (two studies, **Table 1**). The observed change in swimming behaviors could be a result of coordinated morphological changes (*D. excentricus*), which has biomechanical implications for larvae to maintain directed movement (stability) in moving water and imply settling at a smaller size and elevate risk of juvenile mortality (Chan et al., 2015, 2016).

Behavior: Adults

The threshold for behavior of adults living in the deep-water below 200 m was determined based on a single study of *S. fragilis* related to the time of righting (Taylor et al., 2014). The righting time (after being flipped over) as a measure of muscular function could indicate an indirect measure of the exposure to physiologically stressful conditions and increased with decreasing pH. The breakpoint analysis detected a significant breakpoint at pH = 7.25 (p = 0.034) which the panel adjusted down 7.20 (30-day duration), with low evidence confidence rating (single study). In general, the panel considered behavioral category to be not only data deficient but also highly variable, making it difficult to generalize this threshold across wide range of behavior patterns. Only deep-water data were available for this threshold; there is no equivalent shallow-water threshold that could be synthesized.

Physiology: Larvae

Respiration rate was considered a proxy for aerobic metabolism and was derived from Dorey et al. (2013) and Stumpp et al. (2013). At the chosen threshold of 7.74 (14-day

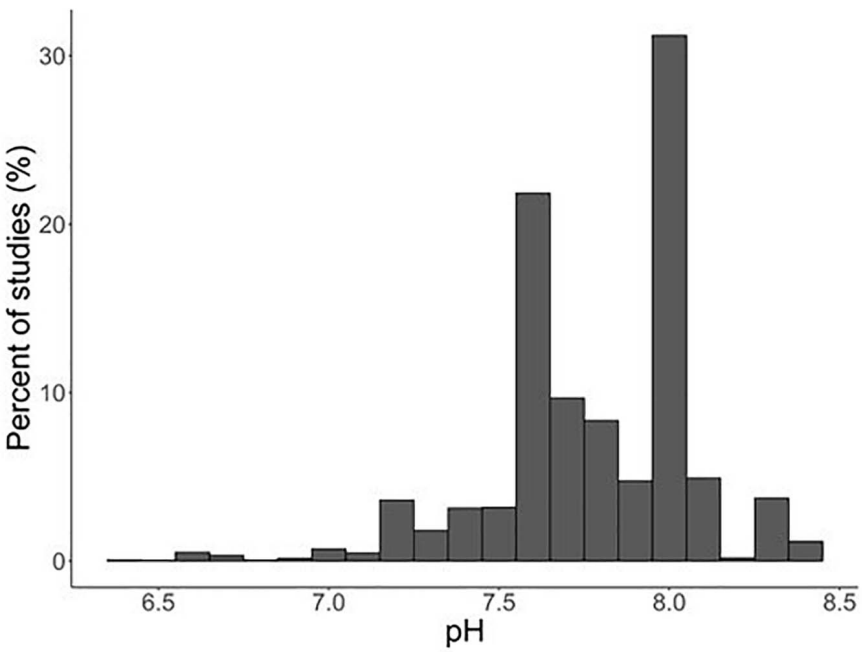


FIGURE 1 | Summary of the number of experimental studies with respect to pH levels used.

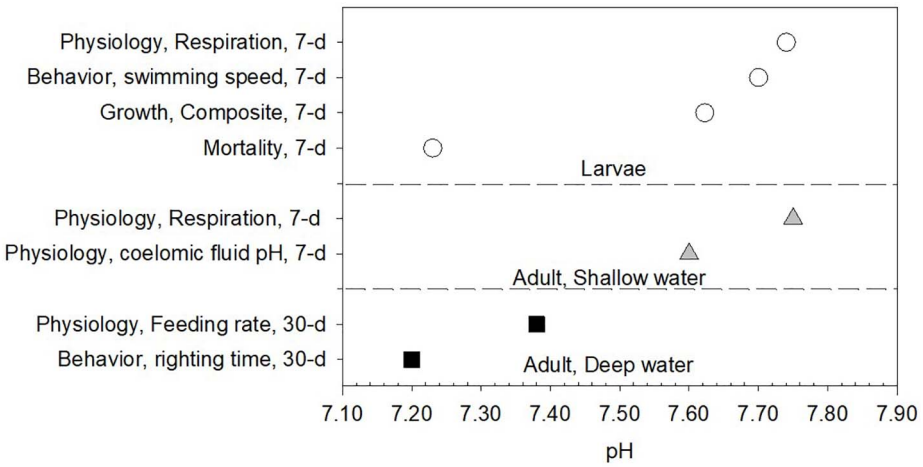


FIGURE 2 | Synthesis of thresholds for echinoderms related to eight different endpoints, separately by depth and life stage. The magnitude (pH) and duration of exposure of the endpoints are provided. Thresholds were determined based on experimental data using breakpoint analyses, linear regressions, and expert consensus.

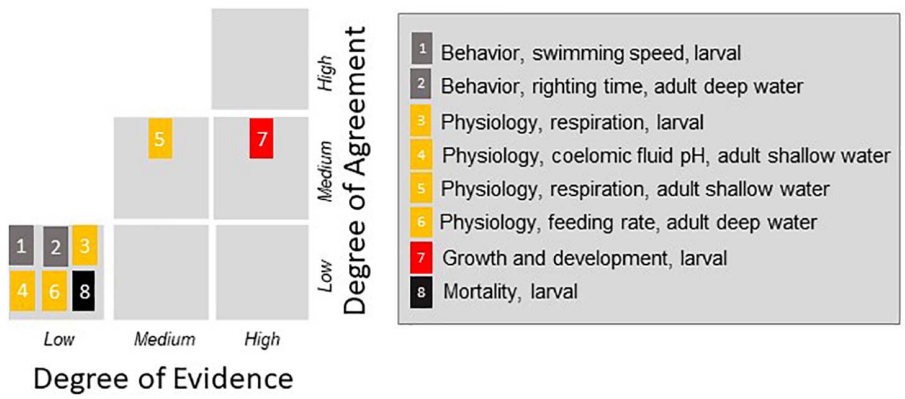


FIGURE 3 | Confidence score based on the combination of degree of volume and quality of evidence and degree of agreement among studies for the eight different endpoints identified as determined by the expert consensus. Figure adapted from IPCC 2014 report.

duration), respiration was an LSR-predicted 25% higher than the experimental control value (p = 0.04, R^2 = 0.04, F = 0.74, DF = 16), a value with low evidence (two studies). Larval respiration increased with reduced pH levels, an effect that could be attributed to increased basal metabolic demand (Dorey et al., 2013) and a reduction in gastric pH and intracellular pH (Stumpp et al., 2012a, Stumpp et al., 2013). This is indicative of increased cost to maintain the cellular and digestive system acid-base balance and resulted in increased compensatory feeding.

Physiology: Shallow-Water Adults

Two metrics, extracellular fluid pH and respiration rate, were combined into the category of physiological threshold for adults of shallow species (Wood et al., 2008, 2010, 2011; Christensen et al., 2011; Spicer et al., 2011; Taylor et al., 2014). Despite some initial evidence of compensation or intracellular buffering capacity (Spicer et al., 2011; Stumpp et al., 2012b; Moulin et al., 2014; Stumpp and Hu, 2017), reduced seawater pH led to an overall linear decrease in extracellular fluid pH. Given this reason, and the fact that the response was strongly linear (LSR $p < 0.001$, R^2 = 0.81, F = 167, DF = 40), the panel placed the extracellular fluid pH threshold at a lower pH = 7.60 (7-day duration), an LSR-predicted value 42% below the experimental control (**Table 1**) and low evidence. The panel noted that the buffering capacity is highly species-specific (Calosi et al., 2013a), varying among individuals within a species (Guscelli et al., 2019) and can take up to 6–12 months for a species to regain its initial acid-base status (Spicer, unpubl.).

Data on rates of aerobic metabolism came from four studies (**Table 2**) of brittle stars (*A. filiformis, O. ophiura, O. schayeri, and O. sericeum*), and were normalized using control values to facilitate study comparisons (Wood et al., 2008, 2010, 2011; Christensen et al., 2011). The panel set respiration threshold was set at pH = 7.75 (7-day duration) based on consistent changes after a week of exposure in all species, a value representing a LSR-predicted 35% increase from the experimental control

(p = 0.004, R^2 = 0.55, F = 13.22, DF = 11). The expert panel gave this threshold medium evidence and medium-to-high agreement. Respiration rate initially increased with decreasing pH, indicating increased energetic demand for vital biological processes, such as calcification (Wood et al., 2008) or mucus production (Christensen et al., 2011), as well as a likely plastic metabolic response that buffers against the temporary increase in energetic demand. Brittle stars have the capacity to withstand a certain degree of physiological stress due to acclimatization and/or adaptation to local conditions (as seen in echinoderms – Pespeni et al., 2013 – and other phyla, see Calosi et al., 2013b, 2017; Lardies et al., 2014; Vargas et al., 2017). However, ultimately the respiration rates decreased, and the respiratory threshold identified here refers to the loss of compensation capacity.

Physiology: Deep-Water Adults

The feeding rate threshold for the adults of deep-water species was determined from a single study investigating the feeding rate of *S. fragilis*, a species that, while adapted to the lower pH conditions typical of depths >200 m, exhibits poor ability to regulate acid-base balance (Taylor et al., 2014). To utilize this study, the panel adjusted the control pH in the experimental treatments from 7.92 to 7.64 to reflect naturally occurring low pH conditions. Feeding rate decreased linearly and a final threshold of pH = 7.38 was a value roughly equivalent to an LSR-predicted 25% reduction from the control treatment ($p < 0.001$, R^2 = 0.47, F = 45.23, DF = 52). With only a single study, it was rated low in confidence (**Table 1**). The implication of this threshold is important toward understanding how the shifts in grazing rates, competition, and other biological interactions, can restructure communities in deep-sea benthic ecosystems (Barry et al., 2014). Reduced foraging efficiency could lead to food limitation and potential decline in an individual's growth, survival and ultimately, negatively affect population dynamics.

Growth and Development: Larvae

The thresholds for larval growth rate (expressed as $\mu m\ d^{-1}$) were developed from three different metrics and 10 studies (see **Table 1**). The three metrics were: growth rate along the midline for *S. purpuratus*, total body length and symmetry index, for *S. droebachiensis* and *S. purpuratus*, respectively. The growth rate for *S. purpuratus* was calculated by fitting a logarithmic regression on the size data over the first week of the experiment when growth is mostly linear (Stumpp et al., 2011; Dorey et al., 2013). Only papers that found a significant treatment-related difference in growth rate were included (Stumpp et al., 2011; Pespeni et al., 2013; Pan et al., 2015; Chan et al., 2016). The panel positioned the growth rate threshold for *S. droebachiensis* at pH = 7.49 (7-day duration) based on a 35% LSR-predicted reduction of the experimental control ($p < 0.001$, R^2 = 0.61, F = 42.38, DF = 27). The total body length threshold, based on six studies of *S. purpuratus* (Yu et al., 2011; Matson et al., 2012; Kelly et al., 2013; Padilla-Gamiño et al., 2013; Pespeni et al., 2013) was placed at pH = 7.67 (7-day duration), 46% below the experimental control value, and below the statistical breakpoint of 7.74 (p = 0.025). The final threshold considered was based on a single study on *S. droebachiensis* (Dorey et al., 2013) of a symmetry index of the right and left postoral arms, with asymmetry indicating abnormal morphological development. The panel set the threshold at pH = 7.64 (14-day duration), a value corresponding to LSR-predicted 35% linear reduction from the experimental control (p = 0.0018, R^2 = 0.36, F = 12.63, DF = 22).

The panel thought it useful to provide a single mean threshold for larval growth and development based on the three thresholds. The panel judged two of these thresholds were of higher quality (larval growth rate, total body length) and were given twice as much weight as the symmetry index that was fair quality. This yielded a final pH = 7.62 (7-day duration set conservatively) with high level of evidence and medium-to-high agreement between studies for larval growth and development. The implication of this thresholds related to the fact reduced larval growth and development thresholds signal important changes in the organismal energy budget. Also, they can alter larval movement and clearance rates (Chan, 2012), prolong duration in the pelagic larval stage, delay settlement, and significantly reduce the number of settlers due to high mortality in the plankton (Chan et al., 2016).

Growth and Regeneration: Adults

The panel considered establishing a growth and regeneration thresholds for shallow water adults, based on a single study examining arm regeneration rate in *O. ophiura* (Wood et al., 2010). Arm regeneration rate increased with decreasing pH and a threshold was considered at pH = 7.63 (30-day duration), consistent with a LSR 35% = 7.63 (p = 0.004, F = 13.7, DF = 10). However, the study only had three treatments and finally, the panel deferred because of data quantity and consistency with other thresholds and chose not to set a threshold. Likewise, no equivalent dataset exists from which to derive a threshold for deep-water species.

Mortality: Larvae

Larval mortality signals the potential number of recruits to the population and increases with declining pH. The mortality threshold was based on mortality data from two studies on *S. droebachiensis* that tracked mortality over time and mortality occurred after 1 week of exposure (Dorey et al., 2013; Chan et al., 2015). The panel set the threshold at pH = 7.23 (7-day duration) a value consistent with breakpoint analyses ($p < 0.001$).

No adult mortality threshold could be produced from the synthesized studies, an artifact of limitations of the lower range of experimental pH conditions tested, which are often constructed with the aim to investigate future experimental conditions of the surface open water, largely deviating from the current benthic pH conditions (e.g., as seen for intertidal habitats, Wolfe et al., 2020). In this case, insufficient experimental data could be partially complemented by evidence from the spatially limited field studies around the marine vents. In these environments, echinoderms have been observed at pH = 7.1 but not at pH of 6.8 (Calosi et al., 2013a; Foo et al., 2018; González-Delgado and Hernández, 2018), positioning the local threshold below 7.1. The panel declined to advance this threshold into the selected set of all the thresholds.

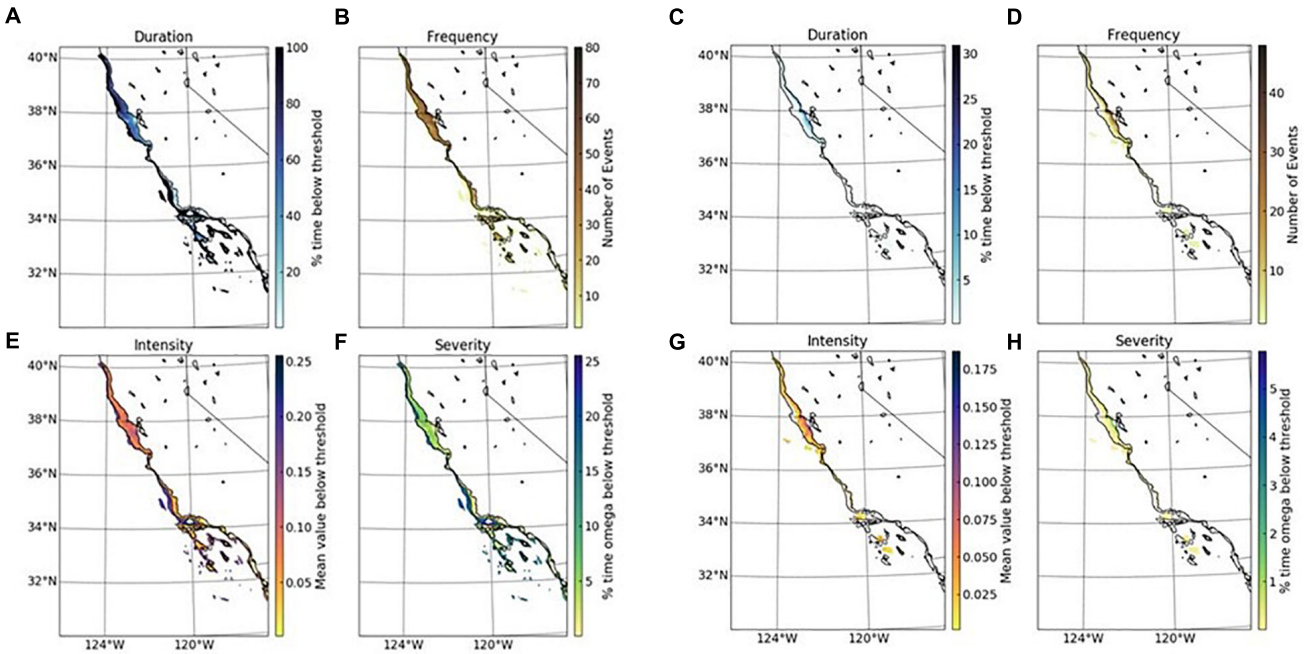


FIGURE 4 | Examples of threshold applications to modeled estimates of pH for adults and larvae at the bottom (topographic 0–500 m) and surface, respectively, along the California coast. Duration (upper left), frequency (upper right), intensity (lower left), and severity (lower right) were calculated for two thresholds, respectively: **(A–D)** Physiology (respiration)threshold for adult echinoderms threshold in the over the upper 0–500 m benthic habitat (5 m above the depth) (pH = 7.75; applied for 7 days over the entire year period); **(E–H)** Physiology (behavior) threshold for larval echinoderm stages (pH = 7.70 applied for 7 days in the upper surface waters over the entire year for details see section "Materials and Methods").

Demonstration of Threshold Application to Southern CCE Model Numerical Simulations

Application of the exposure metrics (duration, intensity, frequency, and severity of departure of the thresholds) and thresholds of larval behavioral and adult physiological impairments to ROMS-BEC numerical simulations illustrate key points in echinoderm application (**Figure 4**). First, these exposure metrics indicate that declining habitat suitability is more severe for benthic (adults) than for pelagic (larval) life stages. The conditions that characterize the exposure (maximum) with pH below the thresholds for the adult physiology occur for 60–100 days (**Figure 4A**), with 30–50 such events (**Figure 4B**) occurring in the coastal regions on the annual basis, and with 0.15–0.25 pH units below the threshold (**Figures 4C,D**). Comparatively, the percent time below the larval thresholds is shorter (5–15%; **Figure 4E**) and the events are less frequent (**Figure 4F**) and less intense (**Figures 4G,H**). Second, there is a consistent pattern of increasing magnitude, duration, and severity from offshore to onshore (**Figure 4**); on average, the greatest magnitude and duration of exposure to low pH conditions that could result in impaired physiological or behavioral responses of adults or larvae, respectively, is in the CA coastal regions where both life stages are most abundant and ecologically important. Thus, increased OA-related exposure can occur frequently and might carry the risks related to the cross-generational carryover effects through adults' exposure (Byrne et al., 2020).

DISCUSSION

Synthesis of the Effects of OA on Echinoderms: Synthesis and Limitation

This synthesis, represented in a form of eight thresholds, shows a high level of confidence that OA negatively affects a variety of biological processes (behavior, physiology, growth and development, survival) and represent a potential risk for echinoderm population's demography and survival. It demonstrates robust evidence from the primary literature that indicates echinoderm sensitivity to OA. Compared with the pH thresholds for pteropods (Bednaršek et al., 2019), decapods (Bednaršek et al., in review), and bivalves (Barton et al., 2012; Gimenez et al., 2018), the pH thresholds across all life stages of the echinoderm are significantly lower.

Our conclusion of lesser pH sensitivity of echinoderms contrasts with the results of several reviews of invertebrate groups that indicated that echinoderms are more sensitive to acidification (Byrne and Przeslawski, 2013; Kroeker et al., 2013; Wittmann and Pörtner, 2013; Przeslawski et al., 2015). However, it is consistent with the Dupont et al. (2010) who found that echinoderms appear to be robust to future 2100

conditions (RCP 8.5). Five of the eight thresholds occur in the narrow pH range of 7.60–7.75, indicating that multiple pathways will be affected simultaneously and impact organismal fitness. The magnitude and duration of exposure required to trigger this effect was highly variable amongst endpoints and life stages; the duration that triggered larval and shallow-water adult thresholds (7 days) was comparable to that for pteropods (2–14 days, Bednaršek et al., 2019), but adult deep-water species (>200 m) required prolonged OA conditions >30 days in order to trigger this effect. Lower pH thresholds were associated with less sensitive stages and processes (like lethality) in adults, while higher pH thresholds are characteristic for the early life stages. This is indicative of higher susceptibility in the early life stages compared to adults and a potential bottleneck for species/population responses and agree with previous studies (Kroeker et al., 2013; Przeslawski et al., 2015). Work by Lee et al. (2019), which was published after our working group's deliberations determined sensitivity thresholds of larval *S. purpuratus* based on midgut pH, metabolic rate and expression of acid-base transporters, suggested a physiological tipping point of pH = 7.20. Similarly, Hu et al. (2017) showed that pH regulation in the larval gut was strongly correlated with the larval sensitivity to OA. In addition, the outcome for these larvae, however, appears to be strongly influenced by carryover effects that depend on the pH environment of their parents. Overall, robust evidence from the primary literature and agreement on echinoderm biological responses across reduced pH levels in the experimental conditions (Sato et al., 2018) lend a strong support for a potential role of echinoderm thresholds as a useful tool to interpret monitoring data and biogeochemical model simulations.

Echinoderm OA thresholds are habitat dependent, underscoring that processes of acclimatization and adaptation to small-scale variability environmental conditions and multiple stressors can structure species sensitivity in the regional OA hotspots. The processes of acclimatization and adaptation to local environmental conditions can structure species sensitivity across the small-scale spatial, temporal, and vertical variability in the regional OA hotspots. The adults of the single deep-water habitat species can tolerate inherently lower pH conditions due to their exposure and adaptation to naturally low pH conditions and variability, ultimately resulting in lower OA thresholds (e.g., Calosi et al., 2013b; Dorey et al., 2013; Chakravarti et al., 2016; Vargas et al., 2017; Byrne et al., 2020). In contrast, shallow water species tend to live at higher pH levels, which are reflected in their higher pH threshold values. These processes can influence the larval sensitivity through the carryover effects that depend on the pH environment of their parents. For instance, *S. purpuratus* larvae generated from parents living in the CCE upwelling zone are more resilient to low pH compared to larvae by parents from higher ambient pH conditions (Yu et al., 2011; Byrne et al., 2013; Kelly et al., 2013). How the greater resilience of CCE echinoid larvae to OA applies to the other regions and taxonomic groups is not known. For instance, the larvae of the North Atlantic ophiuroid *Ophiothrix fragilis* are extremely sensitive to OA (Dupont et al., 2008) demonstrating that a cross-life stage impacts might appear sooner than predicted only based on a single pathway. This emphasizes the fact that echinoderm OA thresholds are OA-habitat exposure dependent and need to be considered on the regional scale.

Threshold Application to Observations or Numerical Modeling Simulations

Application of thresholds to numerical model simulations and observations can visualize the magnitude, duration, severity of OA exposure (Hauri et al., 2013), and potential for biological effects, a critical step to marine resource and water quality management (Bednaršek et al., 2020). However, the management applications of these investments cannot be fully realized without practical guidance on how to consistently apply them (Weisberg et al., 2016). Such guidance should take all relevant demographics parameters, including habitat specific life history, an appropriate horizontal and vertical aggregation, duration of exposure and adaptation traits, into account. Here, we demonstrated the application of echinoderm thresholds to biogeochemical model output based on insights from the current knowledge of the echinoderm ecology. The model output show that larval echinoderms are already being exposed to pH conditions along the California coast to the extent to cause negative sub-lethal response (**Figure 4**). Late autumn and winter conditions indicate relaxation of low pH conditions for pelagic stages, but exposure to low pH in the benthic habitats for the juvenile/adults. Based on the determined thresholds, prolonged benthic adult exposure to low pH can lead to reduced fitness and survival (Morley et al., 2009; Steckbauer et al., 2015), however, this could be offset through a species plasticity or adaptation capacity. This is particularly the case in the CCE with its known mosaic pattern in upwelling and pH variability (Chan et al., 2017) that can differentially structure vulnerability of the spatially distant adult populations. As such, the information on the adaptation scope should be included into the model input when available. Finally, one issue in accurate model interpretation of the larval OA exposure is the lack of understanding of their vertical distribution, which is considered a "black box" of echinoderm ecology (Chan et al., 2018), yet paramount to appropriately understanding their temporal and spatial distribution with respect to particular life stage and critical habitats of impact.

Limits of Synthesis and Priority Research Recommendations

On several occasions, experts did not support assigning the thresholds to a specific process, or thresholds had high uncertainty because they were based on a single study. These instances were due to insufficient or poorly curated data (which were removed from consideration); disparity in response measures or equivocal responses with poor signal to noise ratio; data gaps that did not allow for the extrapolation across spatial scales or life stages, insufficient evidence (shallow and deep-water adult growth and mortality and shallow water behavior); for and the number of experimental treatments (more than three); and because the studies did not realistically capture *in situ* pH variability the defines species exposure in the field (e.g., Frieder et al., 2014; Kapsenberg et al., 2018; Hoshijima and Hofmann, 2019; Chan and Tong, 2020).

Beyond the expert scoring of confidence based on amount and agreement of evidence, other sources of uncertainty exist in the echinoderm pH thresholds. First, information was pooled across species from different localities in order to increase applicability of thresholds across taxa, as well as augment the statistical power and confidence for several endpoints. An important caveat to pooling is that it assumes that different locations can be treated comparatively despite potentially reducing the signal based on the OA related pre-exposure history re to OA conditions. Second, experimental data used in this synthesis measured effects based on chronic, static pH conditions, which does not realistically capture the natural variability species experience in the field, including press (long term perturbations), and pulse events [extreme events, discrete variability (e.g., Frieder et al., 2014; Kapsenberg et al., 2018; Hoshijima and Hofmann, 2019; Chan and Tong, 2020)], fluctuating conditions or "relaxation period" to test the duration of the exposure needed for the organisms to recover. Third, potentially the largest knowledge gap, relates to the need to consideration of OA with other stressors, that can potentially act as modulators for OA thresholds. Sufficient evidence exists to show that combinations of multiple stressors can change the magnitude and the direction of single, univariate stressors (Christensen et al., 2011; Wood et al., 2011; Guscelli et al., 2019). However, there is still a considerable lack of experimental data that included treatments of OA with variable temperature and DO, which precluded consideration of how to incorporate multiple stressors into the OA thresholds. Currently, only five studies have been identified that have dual stressor effect using the same species and response measures were identified. Furthermore, no studies exist examining the effects of pH and low dissolved oxygen on the physiology of the echinoderm species found in the CCE.

Additional field and experimental data can refine these thresholds over time, particularly if conducted in a way to extract or identify thresholds rather than simply document OA adverse effects. These kinds of integrated analyses provide an opportunity for identifying information gaps; here we identified five areas where future research investments would substantially improve our ability to define OA thresholds. To overcome the limitations of synthetizing the data from the experiments that are not intended for threshold extraction, the experimental designs should increase the number of treatments and scale the appropriate range of OA stress in order to optimize threshold derivation (see for example Christen et al., 2013; Dorey et al., 2013). The application of thresholds can also be improved if a critical understanding of the relationship between exposure duration and recovery time is acquired. Experimental evidence also needs to be validated in the field, supported by the co-location of the biological and chemical monitoring and development of geochemical proxies. Studies focusing on the role of local acclimatization and adaptation vs. short-term plasticity are needed, such as latitudinal experiments with genetically different populations differing to track genetic changes and variation in time and space, as well as laboratory breeding and natural selection experiments. Ultimately, for a more accurate future projections with incorporated ecological complexities, studies with multiple stressors and trophic levels and supported with demographic and ecosystem models are urgently needed.

DATA AVAILABILITY STATEMENT

The raw data supporting the conclusions of this article will be made available upon the request, without undue reservation.

AUTHOR CONTRIBUTIONS

NB designed and led the study and led the manuscript writing with the input from all the co-authors. MR and NB conducted the literature review. MR conducted the threshold analyses, revised by NB, and expert panel. FK conducted the analyses of numerical model simulations. NB, RA, MB, SD, PC, KC, RF, JS, and JP-G are expert panelists. MS and SW facilitated the expert panel process. All authors contributed to the article and approved the submitted version.

FUNDING

This research was supported by the California Ocean Protection Council, grant number C0302500. This is PMEL contribution number 5124.

SUPPLEMENTARY MATERIAL

The Supplementary Material for this article can be found online at: https://www.frontiersin.org/articles/10.3389/fmars.2021.602601/full#supplementary-material

REFERENCES

Ambrose, W. G. Jr., Clough, L. M., Tilney, P. R., and Beer, L. (2001). Role of echinoderms in benthic remineralization in the Chukchi Sea. *Mar. Biol.* 139, 937–949. doi: 10.1007/s002270100652

Baden, S., Pihl, L., and Rosenberg, R. (1990). Effects of oxygen depletion on the ecology, blood physiology and fishery of the Norway lobster *Nephrops norvegicus*. *Mar. Ecol. Prog. Ser.* 67, 141–155. doi: 10.3354/meps067141

Barry, J. P., Hall-Spencer, J. M., and Tyrrell, T. (2010). "In situ perturbation experiments: natural venting sites, spatial/temporal gradients in ocean pH, manipulative in situ $p(CO_2)$ perturbations," in *Guide to Best Practices for Ocean Acidification Research and Data Reporting*, eds U. Riebesell, V. J. Fabry, L. Hansson, and J. P. Gattuso (Luxembourg: Publications Office of the European Union).

Barry, J. P., Lovera, C., Buck, K. R., Peltzer, E. T., Taylor, J. R., Walz, P., et al. (2014). Use of a free ocean CO2 enrichment (FOCE) system to evaluate the effects of ocean acidification on the foraging behavior of a deep-sea urchin. *Environ. Sci. Technol.* 48, 9890–9897. doi: 10.1021/es501603r

Barton, A., Hales, B., Waldbusser, G. G., Langdon, C., and Feely, R. A. (2012). The Pacific oyster, *Crassostrea gigas*, shows negative correlation to naturally elevated

carbon dioxide levels: implications for near-term ocean acidification effects. *Limnol. Oceanogr.* 57, 698–710. doi: 10.4319/lo.2012.57.3.0698

Basch, L. V., and Tegner, M. J. (2007). Reproductive responses of purple sea urchin (*Strongylocentrotus purpuratus*) populations to environmental conditions across a coastal depth gradient. *Bull. Mar. Sci.* 81, 255–282.

Bednaršek, N., Feely, R. A., Beck, M. W., Alin, S. R., Siedlecki, S. A., Calosi, P., et al. (2020). Exoskeleton dissolution with mechanoreceptor damage in larval Dungeness crab related to severity of present-day ocean acidification vertical gradients. *Sci. Total Environ.* 716:136610. doi: 10.1016/j.scitotenv.2020.136610

Bednaršek, N., Feely, R. A., Howes, E. L., Hunt, B., Kessouri, F., and León, P. (2019). Systematic review and meta-analysis towards synthesis of thresholds of ocean acidification impacts on calcifying pteropods and interactions with warming. *Front. Mar. Sci.* 6:227. doi: 10.3389/fmars.2019.00227

Byrne, M., and Fitzer, S. (2019). The impact of environmental acidification on the microstructure and mechanical integrity of marine invertebrate skeletons. *Conserv. Physiol.* 7:coz062.

Byrne, M., Foo, A. S., Ross, P. M., and Putnam, H. M. (2020). Limitations to cross- and multigenerational plasticity for marine invertebrates faced with global climate change. *Glob. Chang. Biol.* 26, 80–102. doi: 10.1111/gcb.14882

Byrne, M., and Hernández, J. C. (2020). "Sea urchins in a high CO_2 world: impacts of climate warming and ocean acidification across life history stages," in *Sea Urchins: Biology and Ecology*, 4th Edn, ed. J. M. Lawrence (Amsterdam: Elsevier B.V), 281–297. doi: 10.1016/b978-0-12-819570-3.00016-0

Byrne, M., Ho, M. A., Koleits, L., Price, C., King, C. K., Virtue, P., et al. (2013). Vulnerability of the calcifying larval stage of the Antarctic sea urchin *Sterechinus neumayeri* to near-future ocean acidification and warming. *Glob. Chang. Biol.* 19, 2264–2275. doi: 10.1111/gcb.12190

Byrne, M., and O'Hara, T. D. (eds) (2017). *Australian Echinoderms: Biology Ecology and Evolution*. Clayton South, VIC: CSIRO Press.

Byrne, M., and Przeslawski, R. (2013). Multistressor impacts of warming and acidification of the ocean on marine invertebrates' life histories. *Integr. Comp. Biol.* 53, 582–596. doi: 10.1093/icb/ict049

Byrne, M., Soars, N. A., Ho, M. A., Wong, E., McElroy, D., Selvakumaraswamy, P., et al. (2010). Fertilization in a suite of coastal marine invertebrates from SE Australia is robust to near-future ocean warming and acidification. *Mar. Biol.* 157, 2061–2069. doi: 10.1007/s00227-010-1474-9

Calosi, P., Melatunan, S., Turner, L. M., Artioli, Y., and Davidson, R. L. (2017). Regional adaptation defines sensitivity to ocean acidification. *Nat. Commun.* 8:13994.

Calosi, P., Rastrick, S. P. S., Graziano, M., Thomas, S. C., Baggini, C., Carter, H. A., et al. (2013a). Distribution of sea urchins living near shallow water CO2 vents is dependent upon species acid–base and ion-regulatory abilities. *Mar. Pollut. Bull.* 73, 470–484. doi: 10.1016/j.marpolbul.2012.11.040

Calosi, P., Rastrick, S. P. S., Lombardini, C., de Guzman, H. J., and Davidson, L. (2013b). Adaptation and acclimatization to ocean acidification in marine ectotherms: an in-situ transplant. *Philos. Trans. R. Soc. B Biol. Sci.* 368:20120444. doi: 10.1098/rstb.2012.0444

Chakravarti, L. J., Jarrold, M. D., Gibbin, E. M., Christen, F., Massamba-N'Siala, G., Blier, P. U., et al. (2016). Can trans-generational experiments be used to enhance species resilience to ocean warming and acidification? *Evol. Appl.* 9, 1133–1146. doi: 10.1111/eva.12391

Chan, F., Barth, J. A., Blanchette, C. A., Byrne, R. H., Chavez, F., Cheriton, O., et al. (2017). Persistent spatial structuring of coastal ocean acidification in the California current system. *Sci. Rep.* 7:2526. doi: 10.1038/s41598-017-02777-y

Chan, K. Y. K. (2012). Biomechanics of larval morphology affect swimming: insights from the sand dollars *Dendraster excentricus*. *Integr. Comp. Biol.* 52, 458–469. doi: 10.1093/icb/ics092

Chan, K. Y. K., García, E., and Dupont, S. (2015). Acidification reduced growth rate but not swimming speed of larval sea urchins. *Sci. Rep.* 5:9764. doi: 10.1038/srep09764

Chan, K. Y. K., Grünbaum, D., Arnberg, M., and Dupont, S. (2016). Impacts of ocean acidification on survival, growth, and swimming behaviours differ between larval urchins and brittlestars. *ICES J. Mar. Sci.* 73, 951–961. doi: 10.1093/icesjms/fsv073

Chan, K. Y. K., Grunbaum, D., and O'Donnell, M. J. (2011). Effects of ocean-acidification-induced morphological changes on larval swimming and feeding. *J. Exp. Biol.* 214, 3857–3867. doi: 10.1242/jeb.054809

Chan, K. Y. K., Sewell, M. A., and Byrne, M. (2018). Revisiting the larval dispersal black box in the Anthropocene. *ICES J. Mar. Sci.* 75, 1841–1848. doi: 10.1093/icesjms/fsy097

Chan, K. Y. K., and Tong, C. S. D. (2020). Temporal variability modulates pH impact on larval sea urchin development: themed issue article: biomechanics and climate change. *Conserv. Physiol.* 8:coaa008.

Christen, N., Calosi, P., and McNeill, C. L. (2013). Structural and functional vulnerability to elevated pCO_2 in marine benthic communities. *Mar. Biol.* 160, 2113–2128. doi: 10.1007/s00227-012-2097-0

Christensen, A. B., Nguyen, H. D., and Byrne, M. (2011). Thermotolerance and the effects of hypercapnia on the metabolic rate of the ophiuroid *Ophionereis schayeri*: inferences for survivorship in a changing ocean. *J. Exp. Mar. Biol. Ecol.* 403, 31–38. doi: 10.1016/j.jembe.2011.04.002

Conand, C., and Byrne, M. (1993). Recent developments in the beche-de-mer fishery in the Indo-Pacific. *Mar. Fish. Rev.* 55, 1–13.

Deutsch, C. A., Frenzel, H., McWilliams, J. C., Renault, L., Kessouri, F., Howard, E. M., et al. (2020). Biogeochemical variability in the California Current System. *bioRxiv* [Preprint]

Dickson, A. G., and Goyet, C. (1994). Handbook of Methods for the Analysis of the Various Parameters of the Carbon Dioxide System in Sea Water. Version 2, Report no:ORNL/CDIAC-74. U.S. Department of Energy (accessed May 17, 2018).

Dickson, A. G., and Riley, J. P. (1979). The estimation of acid dissociation constants in sea-water media from potentiometric titrations with strong base. II. The dissociation of phosphoric acid. *Mar. Chem.* 7, 101–109. doi: 10.1016/0304-4203(79)90002-1

Dickson, A. G., Wesolowski, D. J., Palmer, D. A., and Mesmer, R. E. (1990). Dissociation constant of bisulfate ion in aqueous sodium chloride solutions to 250. degree. C. *J. Phys. Chem.* 94, 7978–7985. doi: 10.1021/j100383a042

Dorey, N., Lançon, P., Thorndyke, M., and Dupont, S. (2013). Assessing physiological tipping point of sea urchin larvae exposed to a broad range of pH. *Glob. Chang. Biol.* 19, 3355–3367.

Dubois, P. (2014). The skeleton of postmetamorphic echniderms in a changing world. *Biol. Bull.* 226, 223–236. doi: 10.1086/bblv226n3p223

Dupont, S., Havenhand, J., Thorndyke, W., Peck, L., and Thorndyke, M. (2008). Near-future level of CO_2-driven ocean acidification radically affects larval survival and development in the brittlestar *Ophiothrix fragilis*. *Mar. Ecol. Progr. Ser.* 373, 285–294. doi: 10.3354/meps07800

Dupont, S., Lundve, B., and Thorndyke, M. (2010). Near future ocean acidification increases growth rate of the lecithotrophic larvae and juveniles of the sea star *Crossaster papposus*. *J. Exp. Zool. B Mol. Dev. Evol.* 314, 382–389. doi: 10.1002/jez.b.21342

Dupont, S., and Thorndyke, M. (2012). Relationship between CO_2-driven changes in extracellular acid–base balance and cellular immune response in two polar echinoderm species. *J. Exp. Mar. Biol. Ecol.* 42, 32–37. doi: 10.1016/j.jembe.2012.05.007

Eriksson, A., and Byrne, M. (2015). The sea cucumber fishery in Australia's Great Barrier Reef Marine Park follows global patterns of serial exploitation. *Fish Fish.* 16, 329–341. doi: 10.1111/faf.12059

Fabricius, K. E., De'ath, G., Noonan, S., and Uthicke, S. (2014). Ecological effects of ocean acidification and habitat complexity on reef-associated macroinvertebrate communities. *Proc. R. Soc. B Biol. Sci.* 281:20132479. doi: 10.1098/rspb.2013.2479

Filbee-Dexter, K., and Scheibling, R. E. (2014). Sea urchin barrens as alternative stable states of collapsed kelp ecosystems. *Mar. Ecol. Progr. Ser.* 495, 1–25. doi: 10.3354/meps10573

Foo, S. A., Byrne, M., Ricevuto, E., and Gambi, M. C. (2018). The carbon dioxide vents of Ischia, Italy, a natural laboratory to assess impacts of ocean acidification on marine ecosystems: an overview of research and comparisons with other vent systems. *Oceanogr. Mar. Biol. Ann. Rev.* 56, 237–310. doi: 10.1201/9780429454455-4

Frieder, C. A., Gonzalez, J. P., Bockmon, E. E., Navarro, M. O., and Levin, L. A. (2014). Can variable pH and low oxygen moderate ocean acidification outcomes for mussel larvae? *Glob. Chang. Biol.* 20, 754–764. doi: 10.1111/gcb.12485

Gattuso, J., Epitalon, J., Lavigne, H., and Orr, J. (2019). *Seacarb: Seawater Carbonate Chemistry. R package version 3.2.12.*

Gimenez, I., Waldbusser, G. G., and Hales, B. (2018). Ocean acidification stress index for shellfish (OASIS): linking Pacific oyster larval survival and exposure to variable carbonate chemistry regimes. *Elem. Sci. Anthropocene* 6:51.

González-Delgado, S., and Hernández, J. C. (2018). The importance of natural acidified systems in the study of ocean acidification: what have we learned? *Adv. Mar. Biol.* 80, 57–99. doi: 10.1016/bs.amb.2018.08.001

Guscelli, E., Spicer, J. I., and Calosi, P. (2019). The importance of inter-individual variation in predicting species' responses to global change drivers. *Ecol. Evol.* 9, 4327–4339. doi: 10.1002/ece3.4810

Hammond, L. M., and Hofmann, G. E. (2010). Thermal tolerance of *Strongylocentrotus purpuratus* early life history stages: mortality, stress-induced gene expression and biogeographic patterns. *Mar. Biol.* 157, 2677–2687. doi: 10.1007/s00227-010-1528-z

Hauri, C., Gruber, N., McDonnell, A. M. P., and Vogt, M. (2013). The intensity, duration, and severity of low aragonite saturation state events on the California continental shelf. *Geophys. Res. Lett.* 40, 3424–3428. doi: 10.1002/grl.50618

Hoshijima, U., and Hofmann, G. E. (2019). Variability of seawater chemistry in a kelp forest environment is linked to *in situ* transgenerational effects in the purple sea urchin, *Strongylocentrotus purpuratus*. *Front. Mar. Sci.* 6:62. doi: 10.3389/fmars.2019.00062

Hu, M., Tseng, Y. C., Su, Y. H., Lein, E., Lee, H. G., Lee, J. R., et al. (2017). Variability in larval gut pH regulation defines sensitivity to ocean acidification in six species of the Ambulacraria superphylum. *Proc. R. Soc. B Biol. Sci.* 284:20171066. doi: 10.1098/rspb.2017.1066

Jager, T., Ravagnan, E., and Dupont, S. (2016). Near-future ocean acidification impacts maintenance costs in sea-urchin larvae: identification of stress factors and tipping points using a DEB modelling approach. *J. Exp. Mar. Biol. Ecol.* 474, 11–17. doi: 10.1016/j.jembe.2015.09.016

Kapsenberg, L., Miglioli, A., Bitter, M. C., Tambutte, E., Dumollard, R., and Gattuso, J. P. (2018). Ocean pH fluctuations affect mussel larvae at key developmental transitions. *Proc. R. Soc. B Biol. Sci.* 285:20182381. doi: 10.1098/rspb.2018.2381

Kelly, M. W., Padilla-Gamiño, J. L., and Hofmann, G. E. (2013). Natural variation and the capacity to adapt to ocean acidification in the keystone sea urchin *Strongylocentrotus purpuratus*. *Glob. Chang. Biol.* 19, 2536–2546. doi: 10.1111/gcb.12251

Kenner, M. C., and Lares, M. T. (1991). Size at first reproduction of the sea urchin *Strongylocentrotus purpuratus* in a central California kelp forest. *Mar. Ecol. Prog. Ser.* 76, 303–306. doi: 10.3354/meps076303

Kroeker, K. J., Kordas, R. L., Crim, R., Hendriks, I. E., Ramajo, L., and Singh, G. S. (2013). Impacts of ocean acidification on marine organisms: quantifying sensitivities and interaction with warming. *Glob. Chang. Biol.* 19, 1884–1896. doi: 10.1111/gcb.12179

Lardies, M. A., Arias, M. B., Poupin, M. J., Manrıquez, P. H., and Torres, R. (2014). Differential response to ocean acidification in physiological traits of *Concholepas concholepas* populations. *J. Sea Res.* 90, 127–134. doi: 10.1016/j.seares.2014.03.010

Lawrence, J. M. (ed.) (2020). *Sea Urchins: Biology and Ecology*, 4th Edn. Amsterdam: Elsevier B.V, 281–297.

Lawrence, J. M. (ed) (2013). *Starfish: Biology and Ecology of the Asteroidea*. Baltimore, MD: John Hopkins Press.

Lee, H. G., Stumpp, M., Yan, J. J., Tseng, Y. C., Heinzel, S., and Hu, M. Y. A. (2019). Tipping points of gastric pH regulation and energetics in the sea urchin larva exposed to CO2-induced seawater acidification. *Comp. Biochem. Physiol. A Mol. Int. Physiol.* 234, 87–97. doi: 10.1016/j.cbpa.2019.04.018

Lee, K., Kim, T. W., Byrne, R. H., Millero, F. J., Feely, R. A., and Liu, Y. M. (2010). The universal ratio of boron to chlorinity for the North Pacific and North Atlantic oceans. *Geochim. Cosmochim. Acta* 74, 1801–1811. doi: 10.1016/j.gca.2009.12.027

Lueker, T. J., Dickson, A. G., and Keeling, C. D. (2000). Ocean pCO2 calculated from dissolved inorganic carbon, alkalinity, and equations for K1 and K2: validation based on laboratory measurements of CO2 in gas and seawater at equilibrium. *Mar. Chem.* 70, 105–119. doi: 10.1016/s0304-4203(00)00022-0

Mastrandrea, M. D., Field, C. B., Stocker, T. F., Edenhofer, O., Ebi, K. L., Frame, D. J., et al. (2010). *Guidance Note for Lead Authors of the IPCC Fifth Assessment Report on Consistent Treatment of Uncertainties*. Geneva: Intergovernmental Panel on Climate Change (IPCC).

Matson, P. G., Yu, P. C., Sewell, M. A., and Hofmann, G. E. (2012). Development under elevated pCO_2 conditions does not affect lipid utilization and protein content in early life-history stages of the purple sea urchin. *Strongylocentrotus purpuratus*. *Biol. Bull.* 223, 312–327. doi: 10.1086/bblv223n3p312

Mattson, S. (1990). Food and feeding habits of fish species over a soft sublittoral bottom in the northeast atlantic: 1. COD (GADUS MORHUA L.) (GADIDAE). *Sarsia* 75, 247–267. doi: 10.1080/00364827.1990.10413454

Micael, J., Alves, M. J., Costa, A. C., and Jones, M. B. (2009). Exploitation and conversation of echinoderms. *Oceanogr. Mar. Biol. Ann. Rev.* 47, 191–208. doi: 10.1201/9781420094220.ch4

Moore, A. M., Arango, H. G., Di Lorenzo, E., Cornuelle, B. D., Miller, A. J., and Neilson, D. J. (2004). A comprehensive ocean prediction and analysis system based on the tangent linear and adjoint of a regional ocean model. *Ocean Model.* 7, 227–258. doi: 10.1016/j.ocemod.2003.11.001

Morley, S. A., Lurman, G. J., Skepper, J. N., Pörtner, H.-O., and Peck, L. S. (2009). Thermal plasticity of mitochondria: a latitudinal comparison between Southern Ocean molluscs. *Comp. Biochem. Physiol. A Mol. Integr. Physiol.* 152, 423–430. doi: 10.1016/j.cbpa.2008.11.015

Moulin, L., Grosjean, P., Leblud, J., Batigny, A., and Dubois, P. (2014). Impact of elevated pCO_2 on acid–base regulation of the sea urchin *Echinometra mathaei* and its relation to resistance to ocean acidification: a study in mesocosms. *J. Exp. Mar. Biol. Ecol.* 457, 97–104. doi: 10.1016/j.jembe.2014.04.007

Muggeo, V. M. R. (2008). Segmented: an R package to fit regression models with broken-line relationships. *R News* 8/1, 20–25.

O'Hara, T. D., and Byrne, M. (eds) (2017). "Management: fisheries, ferals and conservation," in *Australian Echinoderms: Biology Ecology and Evolution* (Clayton South, VIC: CSIRO PUBLISHING).

Padilla-Gamiño, J. L., Kelly, M. W., Evans, T. G., and Hofmann, G. E. (2013). Temperature and CO_2 additively regulate physiology, morphology, and genomic responses of larval sea urchins, *Strongylocentrotus purpuratus*. *Proc. R. Soc. B Biol. Sci.* 280:20130155. doi: 10.1098/rspb.2013.0155

Paine, R. T. (1966). Food web complexity and species diversity. *Am. Nat.* 100, 65–75. doi: 10.1086/282400

Pan, T. C. F., Applebaum, S. L., and Manahan, D. T. (2015). Experimental ocean acidification alters the allocation of metabolic energy. *Proc. Nat. Acad. Sci. U.S.A.* 112, 4696–4701. doi: 10.1073/pnas.1416967112

Pespeni, M. H., Sanford, E., Gaylord, B., Hill, T. M., Hosfelt, J. D., Jaris, H. K., et al. (2013). Evolutionary change during experimental ocean acidification. *Proc. Nat. Acad. Sci. U.S.A.* 110, 6937–6942. doi: 10.1073/pnas.1220673110

Politi, Y., Arad, T., Klein, E., Weiner, S., and Addadi, L. (2004). Sea urchin spine calcite forms via a transient amorphous calcium carbonate phase. *Science (New York, N.Y.)* 306, 1161–1164. doi: 10.1126/science.1102289

Przeslawski, R., Byrne, M., and Mellin, C. (2015). A review and meta-analysis of the effects of multiple abiotic stressors on marine embryos and larvae. *Glob. Chang. Biol.* 21, 2122–2140. doi: 10.1111/gcb.12833

R Development Core Team (2020). *R: A Language and Environment for Statistical Computing, v4.2.0*. Vienna: R Foundation for Statistical Computing.

Renault, L., McWilliams, J. C., Jousse, A., Deutsch, C., Frenzel, H., Kessouri, F., et al. (2020). The physical structure and behavior of the California Current System. *bioRxiv* [Preprint] doi: 10.1101/2020.02.10.942730

Runcie, D. E., Dorey, N., Garfield, D. A., Stumpp, M., Dupont, S., and Wray, G. A. (2016). Genomic characterization of the evolutionary potential of the sea urchin *Strongylocentrotus droebachiensis* facing ocean acidification. *Genome Biol. Evol.* 8, 3672–3684.

Sato, K. N., Andersson, A. J., Day, J. M. D., Taylor, J. R. A., Frank, M. B., Jung, J. Y., et al. (2018). Response of sea urchin fitness traits to environmental gradients across the southern California oxygen minimum zone. *Front. Mar. Sci.* 5:258. doi: 10.3389/fmars.2018.00258

Shchepetkin, A. F., and McWilliams, J. C. (2005). The regional oceanic modeling system (ROMS): a split-explicit, free-surface, topography-following-coordinate oceanic model. *Ocean Model.* 9, 347–404. doi: 10.1016/j.ocemod.2004.08.002

Shchepetkin, A. F., and McWilliams, J. C. (2009). Correction and commentary for "Ocean forecasting in terrain-following coordinates: formulation and skill assessment of the regional ocean modeling system" by Haidvogel et al., J. Comp. Phys. 227, pp. 3595–3624. *J. Comput. Phys.* 228, 8985–9000. doi: 10.1016/j.jcp.2009.09.002

Smith, A. M., Byrne, M., Clark, D. E., Lamare, M. D., and Winter, D. J. (2016). Risk and resilience: variations in magnesium in echinoid skeletal calcite. *Mar. Ecol. Prog. Ser.* 561, 1–16. doi: 10.3354/meps11908

Spicer, J. I., Widdicombe, S., Needham, H. R., and Berge, J. A. (2011). Impact of CO_2-acidified seawater on the extracellular acid–base balance of the northern sea urchin *Strongylocentrotus dröebachiensis*. *J. Exp. Mar. Biol. Ecol.* 407, 19–25. doi: 10.1016/j.jembe.2011.07.003

Steckbauer, A., Ramajo, L., Hendriks, I. E., Fernandez, M., Lagos, N., Prado, L., et al. (2015). Synergistic effects of hypoxia and increasing CO_2 on benthic invertebrates of the central Chilean coast. *Front. Mar. Sci.* 2:49. doi: 10.3389/fmars.2015.00049

Stumpp, M., Dupont, S., Thorndyke, M. C., and Melzner, F. (2011). CO_2 induced seawater acidification impacts sea urchin larval development II: gene expression patterns in pluteus larvae. *Comp. Biochem. Physiol. A Mol. Integr. Physiol.* 160, 320–330. doi: 10.1016/j.cbpa.2011.06.023

Stumpp, M., Hu, M., Casties, I., Saborowski, R., Bleich, M., Melzner, F., et al. (2013). Digestion in sea urchin larvae impaired under ocean acidification. *Nat. Clim. Chang.* 3, 1044–1049. doi: 10.1038/nclimate2028

Stumpp, M., and Hu, M. Y. (2017). "pH regulation and excretion in echinoderms," in *Acid-Base Balance and Nitrogen Excretion in Invertebrates*, eds D. Weihrauch and M. O'Donnell (Cham: Springer,), 261–273. doi: 10.1007/978-3-319-39617-0_10

Stumpp, M., Hu, M. Y., Melzner, F., Gutowska, M. A., Dorey, N., Himmerkus, N., et al. (2012a). Acidified seawater impacts sea urchin larvae pH regulatory systems relevant for calcification. *Proc. Nat. Acad. Sci. U. S. A.* 109, 18192–18197. doi: 10.1073/pnas.1209174109

Stumpp, M., Trübenbach, K., Brennecke, D., Hu, M. Y., and Melzner, F. (2012b). Resource allocation and extracellular acid–base status in the sea urchin *Strongylocentrotus droebachiensis* in response to CO2 induced seawater acidification. *Aquat. Toxicol.* 11, 194–207. doi: 10.1016/j.aquatox.2011.12.020

Sunday, J. M., Calosi, P., Dupont, S., Munday, P. L., Stillman, J. H., and Reusch, T. B. H. (2014). Evolution in an acidifying ocean. *Trends Ecol.Evol.* 29, 117–125. doi: 10.1016/j.tree.2013.11.001

Taylor, J. R., Lovera, C., Whaling, P. J., Buck, K. R., Pane, E. F., and Barry, J. P. (2014). Physiological effects of environmental acidification in the deep-sea urchin *Strongylocentrotus fragilis*. *Biogeosciences* 11, 1413–1423. doi: 10.5194/bg-11-1413-2014

Teck, S. J., Lorda, J., Shears, N. T., Ben-Horin, T., Toseland, R. E., Rathbone, S. T., et al. (2018). Quality of a fished resource: assessing spatial and temporal dynamics. *PLoS One* 13:e0196864. doi: 10.1371/journal.pone.0196864

Vargas, C. A., Lagos, N. A., Lardies, M. A., Duarte, C., Manríquez, P. H., Aguilera, V. M., et al. (2017). Species-specific responses to ocean acidification should account for local adaptation and adaptive plasticity. *Nat. Ecol. Evol.* 1:84. doi: 10.1038/s41559-017-0084

Weisberg, S. B., Bednaršek, N., Feely, R. A., Chan, F., Boehm, A. B., Sutula, M., et al. (2016). Water quality criteria for an acidifying ocean: challenges and opportunities for improvement. *Ocean Coast. Manag.* 126, 31–41. doi: 10.1016/j.ocecoaman.2016.03.010

Wittmann, A. C., and Pörtner, H.-O. (2013). Sensitivities of extant animal taxa to ocean acidification. *Nat. Clim. Chang.* 3, 995–1001. doi: 10.1038/nclimate1982

Wolfe, K., Nguyen, H. D., Davey, M., and Byrne, M. (2020). Characterizing biogeochemical fluctuations in a world of extremes: a synthesis for temperate intertidal habitats in the face of global change. *Glob. Chang. Biol.* 26, 3858–3879. doi: 10.1111/gcb.15103

Wolfe, K., Vidal-Ramirez, F., Dove, S., Deaker, D., and Byrne, M. (2018). Altered sediment biota and lagoon habitat carbonate dynamics due to sea cucumber bioturbation in a high-pCO_2 environment. *Glob. Chang. Biol.* 24, 465–480. doi: 10.1111/gcb.13826

Wood, H. L., Spicer, J. I., Kendall, M. A., Lowe, D. M., and Widdicombe, S. (2011). Ocean warming and acidification; implications for the Arctic brittlestar *Ophiocten sericeum*. *Polar Biol.* 34, 1033–1044. doi: 10.1007/s00300-011-0963-8

Wood, H. L., Spicer, J. I., Lowe, D. M., and Widdicombe, S. (2010). Interaction of ocean acidification and temperature; the high cost of survival in the brittlestar *Ophiura ophiura*. *Mar. Biol.* 157, 2001–2013. doi: 10.1007/s00227-010-1469-6

Wood, H. L., Spicer, J. I., and Widdicombe, S. (2008). Ocean acidification may increase calcification rates, but at a cost. *Proc. R. Soc. B Biol. Sci.* 275, 1767–1773. doi: 10.1098/rspb.2008.0343

Yu, P. C., Matson, P. G., Martz, T. R., and Hofmann, G. E. (2011). The ocean acidification seascape and its relationship to the performance of calcifying marine invertebrates: laboratory experiments on the development of urchin larvae framed by environmentally relevant pCO_2/pH. *J. Exp. Mar. Biol. Ecol.* 400, 288–295. doi: 10.1016/j.jembe.2011.02.016

Conflict of Interest: The authors declare that the research was conducted in the absence of any commercial or financial relationships that could be construed as a potential conflict of interest.

Copyright © 2021 Bednaršek, Calosi, Feely, Ambrose, Byrne, Chan, Dupont, Padilla-Gamiño, Spicer, Kessouri, Roethler, Sutula and Weisberg. This is an open-access article distributed under the terms of the Creative Commons Attribution License (CC BY). The use, distribution or reproduction in other forums is permitted, provided the original author(s) and the copyright owner(s) are credited and that the original publication in this journal is cited, in accordance with accepted academic practice. No use, distribution or reproduction is permitted which does not comply with these terms.

frontiers in Marine Science

ORIGINAL RESEARCH
published: 01 December 2020
doi: 10.3389/fmars.2020.604411

Molecular Biomarkers of the Mitochondrial Quality Control Are Differently Affected by Hypoxia-Reoxygenation Stress in Marine Bivalves *Crassostrea gigas* and *Mytilus edulis*

Jennifer B. M. Steffen[1], Halina I. Falfushynska[2], Helen Piontkivska[3] and Inna M. Sokolova[1,4]*

[1] Department of Marine Biology, Institute of Biological Sciences, University of Rostock, Rostock, Germany, [2] Department of Orthopedagogy and Physical Therapy, Ternopil V. Hnatiuk National Pedagogical University, Ternopil, Ukraine, [3] Department of Biological Sciences, Kent State University, Kent, OH, United States, [4] Department of Maritime Systems, Interdisciplinary Faculty, University of Rostock, Rostock, Germany

OPEN ACCESS

Edited by:
Nina Bednarsek, Southern California Coastal Water Research Project, United States

Reviewed by:
Anwesha Ghosh, Indian Institute of Science Education and Research Kolkata, India
Danielle Ferraz Mello, Duke University, United States
Katherine Silliman, Auburn University, United States

***Correspondence:**
Inna M. Sokolova
inna.sokolova@uni-rostock.de

Specialty section:
This article was submitted to Marine Biology, a section of the journal Frontiers in Marine Science

Received: *09 September 2020*
Accepted: *11 November 2020*
Published: *01 December 2020*

Citation:
Steffen JBM, Falfushynska HI, Piontkivska H and Sokolova IM (2020) Molecular Biomarkers of the Mitochondrial Quality Control Are Differently Affected by Hypoxia-Reoxygenation Stress in Marine Bivalves Crassostrea gigas and Mytilus edulis. Front. Mar. Sci. 7:604411. doi: 10.3389/fmars.2020.604411

Coastal environments commonly experience strong oxygen fluctuations. Resulting hypoxia/reoxygenation stress can negatively affect mitochondrial functions, since oxygen deficiency impairs ATP generation, whereas a surge of oxygen causes mitochondrial damage by oxidative stress. Marine intertidal bivalves are adapted to fluctuating oxygen conditions, yet the underlying molecular mechanisms that sustain mitochondrial integrity and function during oxygen fluctuations are not yet well understood. We used targeted mRNA expression analysis to determine the potential involvement of the mitochondrial quality control mechanisms in responses to short-term hypoxia (24 h at <0.01% O_2) and subsequent reoxygenation (1.5 h at 21% O_2) in two hypoxia-tolerant marine bivalves, the Pacific oysters *Crassostrea gigas* and the blue mussels *Mytilus edulis*. We hypothesized that the genes involved in the mitochondrial quality control will be upregulated during hypoxia, and the less hypoxia-tolerant of the two studied species (*M. edulis*) will show a stronger dependence on transcriptional upregulation of these pathways than *C. gigas*. To test these hypotheses, mRNA expression of 17 (*C. gigas*) and 11 (*M. edulis*) marker genes involved in mitochondrial fusion, fission, proteolysis and mitophagy was analyzed in the digestive gland of *M. edulis* and *C. gigas* in normoxia and during hypoxia-reoxygenation (H/R) stress. In the mussels, the mRNA expression of the transcripts related to mitochondrial dynamics and quality control was strongly altered during H/R stress showing a shift toward fission, suppression of fusion, an increase in mitochondrial proteolysis and onset of mitophagy. These changes indicate that H/R stress induces mitochondrial injury in *M. edulis* requiring upregulation of the protective mechanisms to segregate the dysfunctional mitochondria by fission and degrade the oxidative damaged proteins

and/or organelles. Unlike mussels, the transcript levels of all studied genes in the oysters remained at the baseline (normoxic) levels during H/R stress. This muted transcriptional response of *C. gigas* is in agreement with earlier findings showing better ability to maintain cellular homeostasis and higher resistance to apoptosis during H/R stress in the oysters compared with the mussels. The revealed species-specific differences in the expression of the mitochondrial quality control pathways shed light on the potentially important mechanisms of mitochondrial protection against H/R-induced damage that might contribute to hypoxia tolerance in marine bivalves.

Keywords: mitochondrial fusion and fission, quantitative real time PCR (qPCR), mRNA expression, mollusca, proteolysis, mitophagy

INTRODUCTION

Deoxygenation driven by nutrient pollution and warming is a major stressor in estuarine and coastal oceans worldwide (Breitburg et al., 2018, 2019). The deficiency (hypoxia) or lack (anoxia) of oxygen occurs in the estuarine and coastal habitats where oxygen depletion due to respiration outstrips the oxygen influx from diffusion, water mixing and photosynthesis. As a result, these habitats can experience hypoxic periods from a few hours (such as in a diel cycling hypoxia) to several weeks or months in the case of seasonal hypoxia (Diaz and Rosenberg, 1995, 2008). Most benthic metazoans including important ecosystem engineers and keystone species of bivalves, crustaceans and fish require oxygen to survive and complete their life cycles, and oxygen deficiency can lead to a decrease in growth, performance and survival of marine benthos thereby threatening coastal marine ecosystems (Diaz and Rosenberg, 1995). Low motility of benthic marine invertebrates such as bivalves limits their ability to escape local hypoxia, making them reliant on physiological and biochemical adaptations to survive oxygen deficiency (Grieshaber et al., 1994). Metabolic regulation is at the crux of such adaptations due to the direct dependence of the mitochondria (generating >90% of the cellular ATP) on oxygen availability and the key role of these organelles in the energetic and redox balance of the cell. Investigation of mitochondrial responses to fluctuating oxygen conditions is thus important for understanding the fundamental physiological mechanisms setting limits of hypoxic tolerance in marine organisms.

In benthic invertebrates, severe hypoxia (<4% O_2) and anoxia results in transition to a metabolically suppressed state, where ATP production and consumption are downregulated and anaerobic pathways are engaged to compensate for insufficient aerobic ATP generation (Hochachka et al., 1996; Hochachka and Lutz, 2001; Storey, 2002). Under these conditions, the mitochondrial respiration strongly declines or ceases (Zwaan et al., 1991; van den Thillart et al., 1992). In hypoxia-sensitive organisms such as terrestrial mammals, mitochondria become depolarized and eventually damaged during hypoxia due to the ATP depletion, acidosis and Ca^{2+} overload (Piper et al., 2003; Chen et al., 2007; Solaini et al., 2010). Post-hypoxic reoxygenation restores the aerobic ATP synthesis in mammalian mitochondria but may come at a cost due to a surge of the mitochondrial production of reactive oxygen species (ROS) that can damage the cellular proteins, lipids and DNA (Cadenas and Davies, 2000; Paradis et al., 2016). Similar patterns of mitochondrial responses during hypoxia-reoxygenation (H/R) stress involving oxidative damage, collapse of the mitochondrial membrane potential and loss of the OXPHOS capacity has been reported in hypoxia-sensitive marine mollusks such as the bay scallops (Ivanina and Sokolova, 2016; Ivanina et al., 2016). In hypoxia-tolerant organisms such as freshwater turtles, fish and marine intertidal mollusks, mitochondrial respiration, OXPHOS capacity and membrane potential are preserved and the oxidative damage is mitigated during the H/R stress (Galli and Richards, 2014; Sokolova, 2018; Sokolova et al., 2019). These findings imply that maintenance of the mitochondrial integrity through mitochondrial damage sensing and quality control mechanisms might play an important role in mitochondrial tolerance to H/R stress (Berlett and Stadtman, 1997; Cabiscol et al., 2000; Zorov et al., 2014). However, the mitochondrial quality control mechanisms remain poorly understood in hypoxia-tolerant organisms including benthic marine bivalves and require further investigations.

The mitochondrial quality control is well studied in hypoxia-sensitive terrestrial mammals (such as rodents) and encompasses a complex protective network of proteins regulating mitochondrial dynamics (fission and fusion), as well as proteases and mitophagic pathways degrading oxidatively damaged proteins and defective mitochondria (Eisner et al., 2018; Li and Liu, 2018). Under normal conditions, mitochondria tend to form mitochondrial networks by mitochondrial fusion. Fusion of the outer mitochondrial membrane (OMM) is mediated by mitofusins 1 and 2 (Mfn1 and 2), while dynamin-related GTPase OPA1 induces fusion of the inner mitochondrial membrane (IMM) (Chen et al., 2003; Song et al., 2009). Under stress, membrane depolarization activates the metalloendopeptidase OMA1, which degrades OPA1 (Baker et al., 2014; Xiao et al., 2014) and induces mitochondrial fission through interactions of dynamin-related protein DRP1 and its adaptor proteins (the mitochondrial fission factor Mff and fission protein 1 Fis1) (Otera et al., 2010; Losón et al., 2013). Mitochondrial fission removes the damaged mitochondria and facilitates apoptosis under extreme cellular stress (Youle and van der Bliek, 2012), while the hypoxia upregulated protein (HYOU1) supports the mitochondrial repair by suppressing premature hypoxia-induced cell death (Ozawa et al., 1999).

Mechanisms involved in the degradation of the damaged proteins and organelles play an important role in the cellular responses to hypoxia in mammalian models. Protein quality surveillance in the mitochondria is supported by multiple ATP-dependent and –independent proteases including Lon protease and paraplegin (both selectively degrading oxidatively damaged proteins) (Atorino et al., 2003; Venkatesh et al., 2012; Kuo et al., 2015; Pinti et al., 2015; Shanmughapriya et al., 2015; Sepuri et al., 2017), the IMM protease ATP23, and the caseinolytic matrix peptidase chaperone (Osman et al., 2007; Doyle and Wickner, 2008). On DNA level, the helicase Twinkle is responsible for mtDNA maintenance and replication (Spelbrink et al., 2001). Cells can also degrade complete damaged mitochondria through mitophagy to prevent joining of dysfunctional mitochondria to the network. These pathways involve the PTEN-induced kinase 1 (PINK1) which accumulates under the hypoxia and recruits Parkin to tag damaged mitochondria for degradation (Eiyama and Okamoto, 2015). Mitophagic mediators in the PINK1-Parkin pathway are regulated via reversible phosphorylation by a serine/threonine-protein phosphatase PGAM5 (Chen et al., 2016). Additional to the PINK1-Parkin pathway, an alternative mitophagic pathway degrading unhealthy mitochondria is mediated by the mitochondrial eating protein (MIEAP) (Kitamura et al., 2011; Nakamura and Arakawa, 2017).

The important role of mitochondrial quality control mechanisms (involving the regulation of the mitochondrial fission and fusion, proteolysis and mitophagy) in the responses to H/R stress is well established in the hypoxia-sensitive mammalian models such as rodents (Kulek et al., 2020; Wang and Zhou, 2020). Earlier studies also indicate that high activity and upregulated mRNA expression of mitochondrial proteases correlates with elevated hypoxia tolerance in marine bivalves (Ivanina and Sokolova, 2016; Ivanina et al., 2016). However, involvement of the pathways regulating mitochondrial dynamics and quality control in the response to H/R stress have not been extensively studied in hypoxia-tolerant organisms including bivalves. Here, we explored the molecular mechanisms underlying the mitochondrial responses to H/R stress by measuring the mRNA expression of key marker genes in the mitochondrial quality control pathways in the Pacific oyster *Crassostrea gigas* and the blue mussel *Mytilus edulis*. The two studied species are commonly exposed to fluctuating oxygen conditions in intertidal, coastal and estuarine habitats and are therefore good models to study the mitochondrial adaptations to hypoxia and reoxygenation stress (Sokolova et al., 2019).

Earlier studies found that the Pacific oyster is more tolerant to abiotic stressors (including hypoxia) than the blue mussel (David et al., 2005; Le Moullac et al., 2007; Sokolov et al., 2019). At the cellular level, higher hypoxia tolerance of *C. gigas* was associated with the resistance to apoptosis and muted inflammation response indicating less pronounced mitochondrial and cellular damage during the H/R stress in oysters compared with the mussels (Falfushynska et al., 2020a,b). Therefore, we hypothesized that the less hypoxia-tolerant of the two studied species (*M. edulis*) will more strongly rely on the regulation of the mitochondrial quality control mechanisms to counteract the H/R-induced cellular damage compared with the more tolerant *C. gigas* that experiences less cellular injury (Falfushynska et al., 2020b) and thus might require less protection from the inducible mitochondrial quality control mechanisms. To test this hypothesis, mRNA expression of 17 *(C. gigas)* and 11 (*M. edulis*) key genes in the mitochondrial fusion, fission, proteolysis and mitophagy pathways were analyzed by quantitative RT-PCR in the digestive gland of the two studied species of bivalves exposed to hypoxia and reoxygenation relative to the normoxic controls. We focused on the transcript levels of the following marker genes: for mitochondrial fission and fusion - *mfn*2 (encoding mitofusin 2), *opa*1 (mitochondrial dynamin-like 120 kDa protein), *dnm1l* (dynamin-1-like protein), *mff* (mitochondrial fission factor), *fis*1 (mitochondrial fission protein 1); for protein and DNA quality control - *tsfm* (encoding mitochondrial translation elongation factor Ts), *lonp*1 (mitochondrial Lon protease), *spg*7 (paraplegin), *oma*1 (mitochondrial metalloendopeptidase OMA1), *clpB* (mitochondrial caseinolytic matrix peptidase chaperone subunit B), *atp*23 (mitochondrial inner membrane protease ATP23), *twnk* (mitochondrial twinkle mtDNA helicase); and for mitophagy - *mieap* (encoding mitochondrial eating protein), *hyou*1 (hypoxia upregulated protein 1), *prkn* (parkin), *pink*1 (PTEN-induced kinase 1), and *pgam*5 (mitochondrial serine/threonine protein phosphatase PGAM5).

MATERIALS AND METHODS

Animal Maintenance

Adult oysters [mean shell length ± the standard deviation (SD): 99.3 ± 13.1 mm] were obtained from the low intertidal zone of the German Wadden Sea near List/Sylt (55°01′42″N 8°26′04″E) and transported within 48 h of collection to the University of Rostock, Germany. Adult blue mussels (mean shell length ± SD: 52.5 ± 3.22 mm) were collected at Warnemünde marina "Mittelmole" (54°10′49.4″N 12°05′19.9″E) and brought to the University of Rostock within an hour of collection. All bivalves were transported in coolers lined with seawater-soaked paper towels, and the shells were cleaned from epibionts upon arrival. Two weeks prior to experiments, oysters and mussels were acclimated in recirculated temperature-controlled aquarium systems (Kunststoff-Spranger GmbH, Plauen, Germany) with aerated artificial seawater (ASW) (Tropic Marin®, Wartenberg, Germany) at salinity 33 ± 1 (*C. gigas*) and 15 ± 1 (*M. edulis*), respectively, and temperature 15 ± 0.5°C. These salinity and temperature were within natural range of the respective oysters' and mussels' habitat conditions. Bivalves were fed *ad libitum* by continuous addition of a commercial live algal blend (DTs Premium Blend Live Marine Phytoplankton, Coralsands, Mainz Kastel, Germany) according to the manufacturer's instructions (0.01 ml g^{-1} fresh mass per day) using an automatic aquarium feeder.

Experimental Exposures

Bivalves (three oysters or six mussels in 2 l of ASW) were exposed to 24 h of severe hypoxia (<0.1% O_2) by bubbling the ASW with pure nitrogen (Westfalen AG, Münster, Germany) in

air-tight chambers at 15 ± 0.5°C and respective salinity. Oxygen concentration was monitored with an Intellical™ LDO101 Laboratory Luminescent/Optical Dissolved Oxygen (DO) Sensor (HACH, Loveland, CO, United States). During exposure, bivalves were not fed to prevent bacterial growth in the chambers. It is worth noting that oysters and mussels spontaneously close their shells and cease feeding during hypoxic exposures regardless of the presence of algae in surrounding water. After hypoxia exposure, a subset of bivalves was allowed to recover in normoxic ASW (21% O_2) for 1.5 h. The H/R incubation times were chosen based on tidal and diurnal cycles of oxygen fluctuations and previous findings that show that strongest mitochondrial response to reoxygenation occurs within the first hours of recovery (Kurochkin et al., 2009; Richards, 2011; Ivanina and Sokolova, 2016; Andrienko et al., 2017). The control group was maintained in normoxia (21% O_2) in recirculated temperature-controlled aquarium systems (10 oysters or 30 mussels per 30 l of seawater) with continuous feeding as described in section "Animal Maintenance."

Hepatopancreas tissue was sampled on ice after hypoxia, reoxygenation and in normoxic control, immediately shock-frozen in liquid nitrogen and stored at −80°C until further analysis. We have chosen hepatopancreas because it is one of the largest metabolically active organs in bivalves involved in digestion, energy storage and maintenance of energy homeostasis (Gosling, 1992; Kennedy, 1996). Furthermore, earlier studies in bivalves showed strong hypoxia-induced shifts in the hepatopancreas metabolome (Haider et al., 2020) and induction of apoptotic and inflammatory responses in this tissue during H/R stress (Falfushynska et al., 2020a). This makes hepatopancreas a useful tissue to investigate the pathways that maintain the mitochondrial integrity during H/R exposure. Samples sizes were 10 and 6 per treatment group for oysters and mussels, respectively.

Quantitative Real-Time PCR (qRT-PCR)

RNA extraction and cDNA synthesis was conducted as described elsewhere (Falfushynska et al., 2020a). Briefly, 20 to 50 mg hepatopancreas tissue were extracted in RNA Extracol (EURX Ltd.–molecular biology products, Gdansk, Poland) according to manufacturer's instructions using an automatic homogenizer for 40 s at 6.0 m s^{-1} (FastPrep-24 MP Biomedicals, Valiant Co. Ltd., Yantai, Shandong, China). To avoid potential cross-reaction with residual DNA, RNA extracts were treated with DNase using the TURBO DNA-free kit (ThemoFisher Scientific, Waltham, MA, United States). RNA with a 280/260 absorbance ratio > 2.0 assessed by NanoVue Plus™ spectrophotometer (GE Healthcare, Chicago, IL, United States) was used for further processing. cDNA was synthesized from 2 μg of total RNA using RevertAid RT Kit (Thermo Fischer Scientific, Waltham, MA, United States). Expression levels were quantified by quantitative PCR (qPCR) using the StepOnePlus Realtime-PCR System instrument (Applied Biosystems, Thermo Fisher Scientific Corp., Foster City, CA, United States) and Biozym Blue S'Green qPCR BlueMix Separate ROX kit (Biozym Scientific GmbH, Hessisch Oldendorf, Germany). Each reaction comprised of 10 μl 2x qPCR master mix with ROX additive, 6.4 μl DNase/RNase-free water, 1.6 μl gene-specific reverse and forward primer mix (each to a final concentration of 0.4 μM) and 2 μl cDNA. For the genes where species-specific annotated transcript sequences were available, gene-specific primers were designed using published gene sequences of *M. edulis* and *C. gigas* in the NCBI/GenBank database. This was the case for all *C. gigas* target genes (except *lonp*1, *opa*1, *hyou*1 and *fis*1) and for the housekeeping genes from *M. edulis*. For those *Mytilus* sequences where no annotated transcripts were found in the NCBI/GenBank, we have used a transcriptome from a closely related species *Mytilus galloprovincialis* that belongs to the *Mytilus edulis* species complex (Varvio et al., 1988; Gaitán-Espitia et al., 2016). *M. edulis* and *M. galloprovincialis* are closely related, genetically similar and characterized by a high degree of hybridization and introgression in the nature (Gosling and Wilkins, 1981; Varvio et al., 1988; Gardner, 1996; Daguin et al., 2001; Gaitán-Espitia et al., 2016). To identify the candidate regions for primer design in *Mytilus*, we have aligned *M. galloprovincialis* sequences with available homologous sequences from multiple molluscan species, including *Crassostrea*. The regions with the high degree of nucleotide sequence conservation were chosen for primer design, and the qPCR was conducted under stringent conditions to avoid non-specific priming. The relevant fragments of sequence alignments between *Crassostrea* and *M. galloprovincialis* are provided in **Supplementary Table S1**. For *lonp1*, *opa*1, *hyou*1 and *fis*1 genes, for which no transcript from *C. gigas* were publicly available at the time of this study, primers were designed using a sequence from a closely related species, *Crassostrea virginica* (**Supplementary Table S2**). The identified sequence segments were then used to design gene-specific primers (**Table 1**). For primer check, the fragments were amplified using the following cycling parameters: 2 min at 95°C for polymerase activation, 40 cycles of 15 s at 95°C and 30 s at 60°C. Only the primers that produced a single product of expected length were used in the following analyses. All 17 target genes were successfully amplified from *C. gigas*. Six out of 17 target genes (including *tsfm*, *clpB, mieap*, *atp23, hyou1*, and *twnk*) could not be amplified from *Mytilus* due to the low quality or insufficient length of the respective transcript sequences available in the NCBI/GenBank.

To measure mRNA levels of the target and housekeeping genes, the following cycling parameters were used: 2 min at 95°C for polymerase activation, 40 cycles of 15 s at 95°C, 15 s at 57°C (annealing), 20 s at 72°C (extension) and 30 s at a primer specific reading temperature (for acquiring the product signal). For quality control, the melt curve analysis was conducted at the end of each run. To determine the apparent amplification efficiency of the primers and to correct for the possible plate-to-plate variation, a standard dilution series of a single pooled cDNA sample was run on each plate. All measurements were conducted in duplicates. Expression levels of the target samples relative to the reference genes were conducted using the relative standard curve method (Dorak, 2006). Reference genes were chosen as described elsewhere (Falfushynska et al., 2020a). In pilot experiments, we tested five potential housekeeping genes (encoding eukaryotic elongation factor 1, α-tubulin, β-actin,

TABLE 1 | Primers used for qRT-PCR for genes of mitochondrial quality control in *C. gigas* and *M. edulis*.

Gene	Forward primer (5′–3′)	Reverse primer (5′–3′)	NCBI accession No. of targeted sequence
Crassostrea			
mfn2	GCTGGCGGATCATTGCTGTC	ACGACCTCTCCTTGGCCTTG	XM_011450871.2
opa1	CCAGGAGTGCAGGAAAGGATTC	ACTTGTTGTCGGAGAGCGTTAC	XM_022486900.1
dnm1l	GCCCACAGTGTTAAAGGGGT	AGGCGCTCAATGACATCACA	XM_011429781.2
mff	CTTTCCTACCTGGCGACTCC	AGCTTGGCTACTGCGTTTCT	XM_011416039.2
fis1	GGTTGGCTCATCTGAAAGCTCAC	AGGTTGAGGAGGACTGGCTGAG	XM_022482332.1
tsfm	GTTGGGCCAAAGCAGACAAG	CTCCTGCTCTGGACTGCAAA	XM_011429054.2
lonp1	GACAGGAAGTGGCCATGACA	TCCTTGAGTCCACCAATGGC	XM_022478813.1
spg7	GCTGTGGTTTCGTGGTTGAC	GGAGATCCCTCTCCGGCTTA	XM_011448210.2
oma1	CCTCCAGAACTGGTCCTGAATA	GATCGATCGGAGAGCTGCAA	XM_011440234.2
clpB	AGCTGACGGAGTGCCCAAAC	ACCTCACTGGCAAGGTTAGAGG	XM_020071562.1
mieap	GGAACATGAGTGCTCTGGCT	TGGTTCACAAGTGGTGCTGT	LOC105320964
atp23	GCACGGAACATTACGGAGGA	CTGTGACTCGAATGGAGCGA	XM_011425806.2
hyou1	GGCCATGGTGCTGGAAAAAG	TGATCCCCACCATTTCTGCC	LOC111125576
twnk	ACAGAACATTGACCATGTGTAGAGA	GTGTATGTGCACGATTCAGGT	XM_011427422.2
prkn	CTCGGGGTTGGGAACCATAC	TGATCGTGAGTTGGTGGCTC	XM_011439893.2
pink1	ATCGTGCTGCTTTGGGATGTTTAC	GCTTCTTTCACCCTCCTGGCATAAG	XM_011426001.2
pgam5	AACAGGCGGACTACTGTGGAAAG	ACGGCTCTGGTCATTGTAGAAG	XM_020067497.1
*bAct**	TCCGGAATCCATGAAACATCA	TCCTTTTGCATACGGTCAGC	NM_001308859.1
Mytilus			
mfn2	TGACCAATTCTGTCTGGATGCT	ATCGGGAGCTCACTTTGTGG	SRR1598987
opa1	AGGAGACCAGAGTTCTGGGAA	CGCCTGATCCTCTGGGAAAT	SRR1598987
dnm1l	CACAGCAAGAGATGCTCCGA	ACCATTGTGTTAGTTGGAGGT	SRR1598987
mff	GCATCATACCTGAACATAACTCG	AAATCAGCATGATAAATTGTCCCA	SRR1598987
fis1	GAATTTGCAGGCGACATGGG	ATGATTTCCCCACGAAGTGTT	SRR1598987
lonp1	AGAGGTGTTGGAAGAAGACCA	AGCTGGCTTACTGCTATAAATTCAA	SRR1598987
spg7	ACAAGAAGAAGAACAACAGCATTCA	TTTCCCACATCCTGGTCCAC	SRR1598987
oma1	ACAACTGTTTGATGTGTTTGGT	GGAACCGTTCTGGAGGTAGC	SRR1598987
prkn	ACTTTTGTAACTATCTCGATTGCCA	TGCTTCTACGCTTCTTATATTGTTG	SRR1598987
pink1	GAAGAGCCATATTGTTTGGTAATGA	TGATAGCAAGGAGCATCTCG	SRR1598987
pgam5	CAACTTCGCACTCTCGCATC	CTATGGTGTTCCGATGGGGC	SRR1598987
*tsfm**	CAGATCCCAAGTTTGTCGAGT	TTCTGCCATCTTCTCACAGAAT	HQ690240.1

ubiquitin and 18S rRNA) as potential reference genes. Only one out of five tested genes (eukaryotic elongation factor 1 in mussels and actin in oysters) showed no significant change in expression ($p > 0.05$) with ≤1 difference in mean CT values between different experimental treatments. Therefore, target mRNA expression was normalized to the expression of a reference gene (β-actin β*Act* for *C. gigas* and the eukaryotic elongation factor 1 eEF1 *tsfm* for *M. edulis*) and the mean CT of the normoxic group as described elsewhere (Dorak, 2006)

Statistics

Data were tested for normal distribution in IBM® SPSS® Statistics v. 25 (IBM Corp., Armonk, NY, United States) using the Shapiro-Wilk test and for homogeneity of variances by the Brown-Forsythe test in SigmaPlot 13 (v. 13.0.0.83, Systat Software Inc., San Jose, CA, United States). Outliers were removed using box-whisker plots in IBM® SPSS® Statistics. Non-normally distributed data were transformed via Box-Cox transformation by Minitab 19 (Minitab LLC., State College, PA, United States). Significant differences between exposures were tested by a one-way ANOVA within each species using SigmaPlot 13. Oxygen regime was used as a fixed factor with three levels (normoxic control, 1 day hypoxia, reoxygenation). Significant differences between the pairs of means were determined using a Tukey's Honest Significant Differences (HSD) *post hoc* test. Pearson correlation analysis was carried out by RStudio's packages "mixOmics" and "factoextra" [v. 1.2.5033 and R v. 3.6.3 (R Core Team, 2020)] with cut off $R = 0.6$. To reduce the dimensionality of the data, the principal component analysis (PCA) was conducted on transformed data with outliers replaced by group means. PCA and graphs were designed in RStudio. All effects were considered significant at $p < 0.05$.

RESULTS

Mitochondrial Dynamics: Fusion and Fission

In *M. edulis*, severe hypoxia suppressed mRNA levels of *mfn2* encoding mitofusin-2, which were rapidly

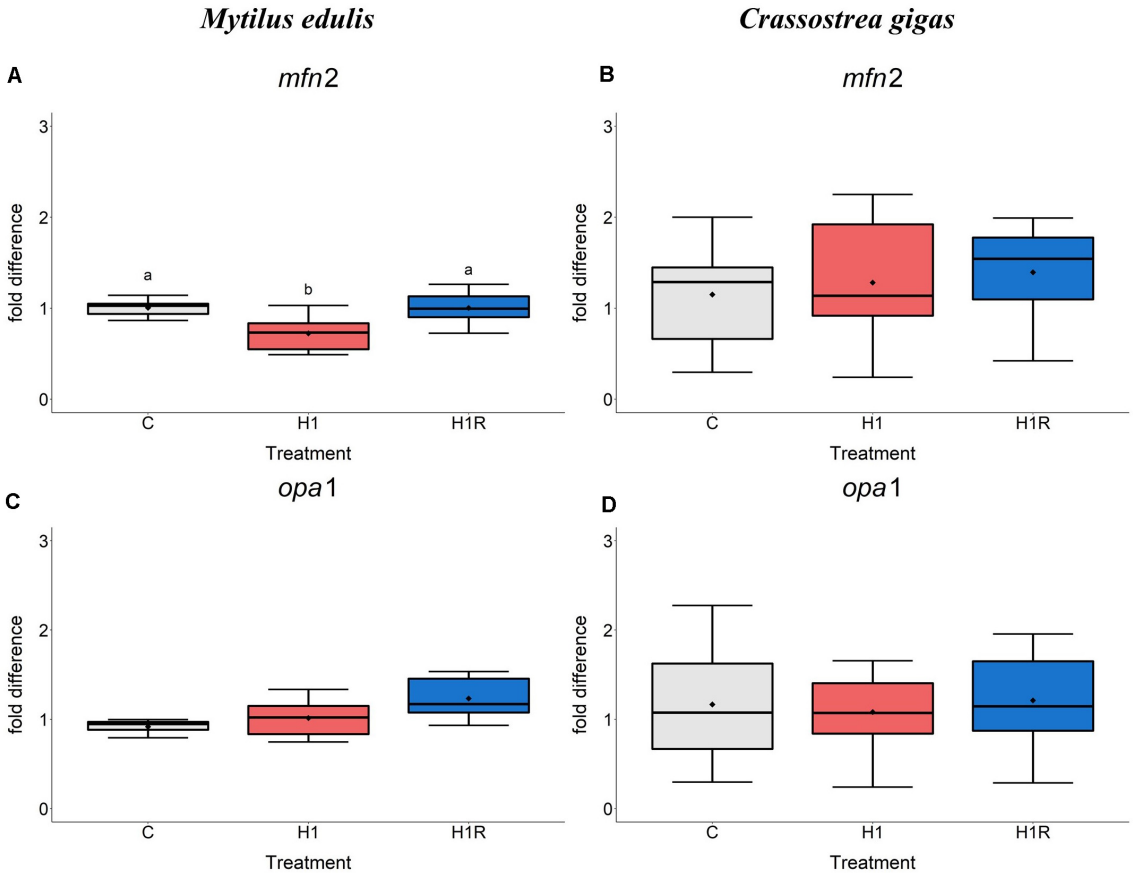


FIGURE 1 | mRNA expression of mitochondrial fusion proteins in *M. edulis* and *C. gigas* hepatopancreas in response to H/R stress. **(A,C)** *M. edulis*; **(B,D)** *C. gigas*; **(A,B)** *mfn*1 mRNA; **(C,D)** *opa*1 mRNA. Experimental groups: C, control; H1, short-term (1 day) severe hypoxia; H1R, short-term (1 day) severe hypoxia and subsequent 1.5 h reoxygenation. Means are depicted as points within corresponding Box-Whisker-plot. Outliers are shown as asterisk (*). Different letters above plots represent values that are statistical significantly different from each other ($p < 0.05$). Plots sharing a letter are not significantly different ($p > 0.05$). $N = 6–10$.

restored during reoxygenation (**Figure 1A**). Transcript levels of *opa*1 encoding dynamin-like 120 kDa protein did not change during H/R exposure in the mussels (**Figure 1C**). In *C. gigas*, tissue levels of *mfn*2 and *opa*1 mRNA did not change in response to H/R stress (**Figures 1B,D**).

Transcript levels of mitochondrial fission mediators *dnm*1*l*, *mff* and *fis*1 were significantly higher in the hepatopancreas of the mussels exposed to hypoxia than the control group (**Figures 2A,C,F**). Reoxygenation led to a further significant increase in the mRNA expression levels of these genes. Levels of *mff* mRNA were ∼4-fold and 6-fold elevated in hypoxia and reoxygenation, respectively, compared to control. Expression of *fis*1 mRNA was ∼2.5- to 3-fold increased in hypoxia and reoxygenation compared to normoxia. The *dnm*1*l* gene was ∼1.5- to 2-fold elevated by hypoxia and reoxygenation in the mussels compared to normoxic control. In *C. gigas*, transcript levels of the mitochondrial fission factors *dnm*1*l*, *mff*, *tsfm* and *fis*1 were not significantly affected by hypoxia and reoxygenation (**Figures 2B,D,E,G**).

Mitochondrial Protein and DNA Quality Control

Transcript levels of the genes encoding mitochondrial proteases involved in the protein quality control including *lonp*1 and *spg*7 were not affected by hypoxia and reoxygenation in *M. edulis* (**Figures 3A,C**). In contrast, transcript levels of metalloendopeptidase OMA1 (*oma*1) increased during hypoxia and reoxygenation by ∼1.5-fold and ∼1.7-fold, respectively, compared to the normoxic controls (**Figure 3E**).

In *C. gigas*, the mRNA level of the genes involved in mitochondrial protein quality control including *lonp*1, *spg*7, *oma*1 (**Figures 3B,D,F**) as well as four additional genes (not measured in *M. edulis* due to the lack of specific primers) including *clp*B, *mieap*, *atp*23 and *hyou*1 did not change in response to H/R stress (**Figures 4A–D**). Transcript levels of the mitochondrial helicase TWINKLE (*twnk*) responsible for mtDNA maintenance, remained unchanged in *C. gigas* throughout experimental exposures (**Figure 4E**) (no data are available for *M. edulis* due to the lack of specific primers).

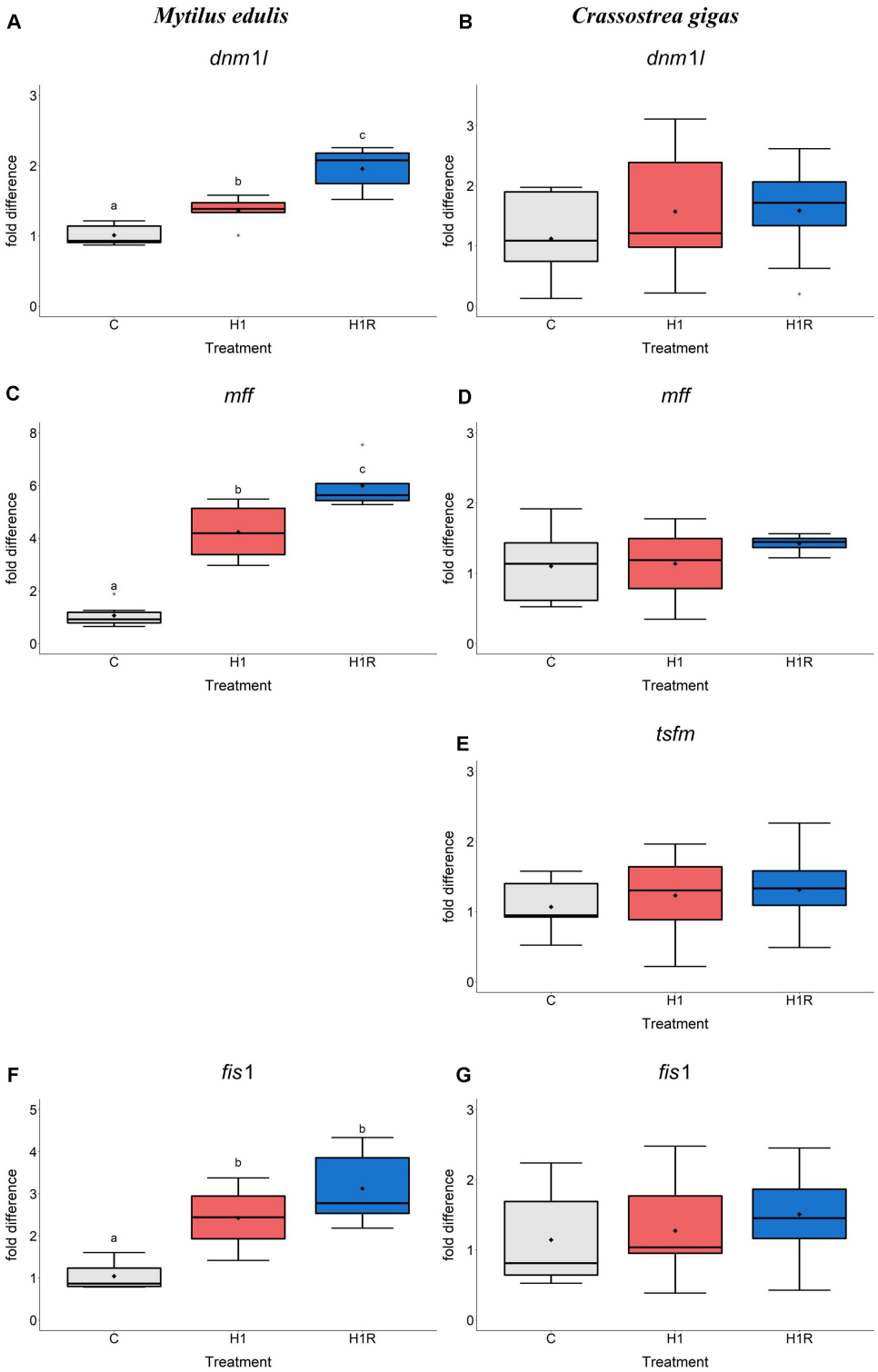


FIGURE 2 | mRNA expression of mitochondrial fission proteins in *M. edulis* and *C. gigas* hepatopancreas in response to H/R stress. **(A,C,F)** *M. edulis*; **(B,D,E,G)** *C. gigas*; **(A,B)** *dnm1l* mRNA; **(C,D)** *mff* mRNA; **(E)** *tsfm* mRNA; **(F,G)** *fis1* mRNA. Experimental groups: C, control; H1, short-term (1 day) severe hypoxia; H1R, short-term (1 day) severe hypoxia and subsequent 1.5 h reoxygenation. Means are depicted as points within corresponding Box-Whisker-plot. Outliers are shown as asterisk (*). Different letters above plots represent values that are statistical significantly different from each other ($p < 0.05$). Plots sharing a letter are not significantly different ($p > 0.05$). $N = 6–10$.

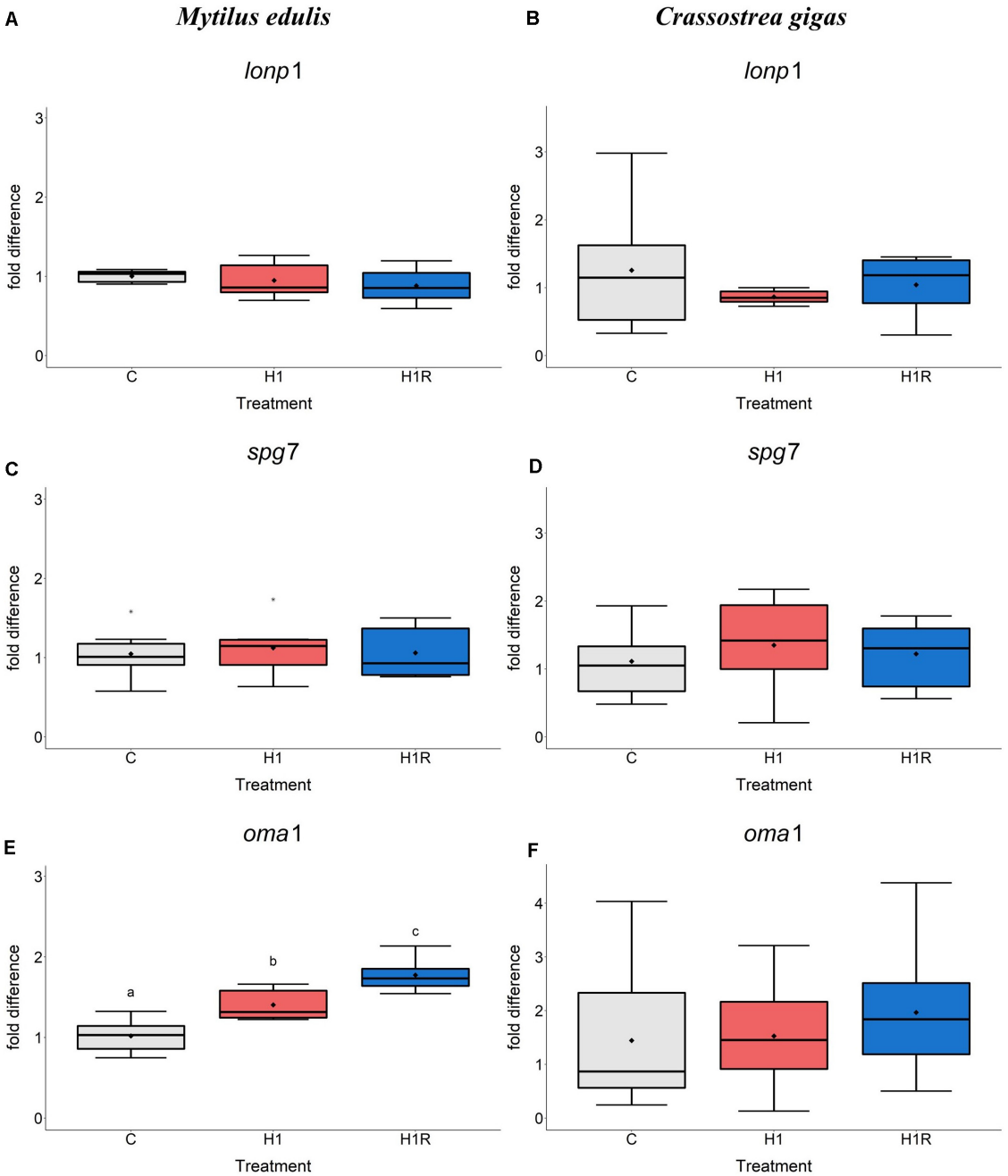


FIGURE 3 | mRNA expression of mitochondrial protein quality control and proteolysis proteins in *M. edulis* and *C. gigas* hepatopancreas in response to H/R stress. **(A,C,E)** *M. edulis*; **(B,D,F)** *C. gigas*; **(A,B)** *lonp*1 mRNA; **(C,D)** *spg*7 mRNA, **(E,F)** *oma*1 mRNA. Experimental groups: C, control; H1, short-term (1 day) severe hypoxia; H1R, short-term (1 day) severe hypoxia and subsequent 1.5 h reoxygenation. Means are depicted as points within corresponding Box-Whisker-plot. Outliers are shown as asterisk (*). Different letters above plots represent values that are statistical significantly different from each other ($p < 0.05$). Plots sharing a letter are not significantly different ($p > 0.05$). $N = 6–10$.

Mitophagy

In *M. edulis*, hypoxia induced a ∼2-fold higher expression of *prkn* mRNA (encoding a mitophagy mediator Parkin) compared to normoxic condition (**Figure 5A**). The levels of *prkn* remained elevated during reoxygenation in the mussels (**Figure 5A**). Expression of its co-mediator *pink*1 did not change with hypoxia, while reoxygenation led to a ∼2.5-fold increase of *pink*1 expression compared to normoxic controls (**Figure 5C**). Transcript levels of the protein phosphatase PGAM5 showed a decreasing trend with hypoxia, followed by a significant increase during reoxygenation (**Figure 5E**). In *C. gigas*, the expression

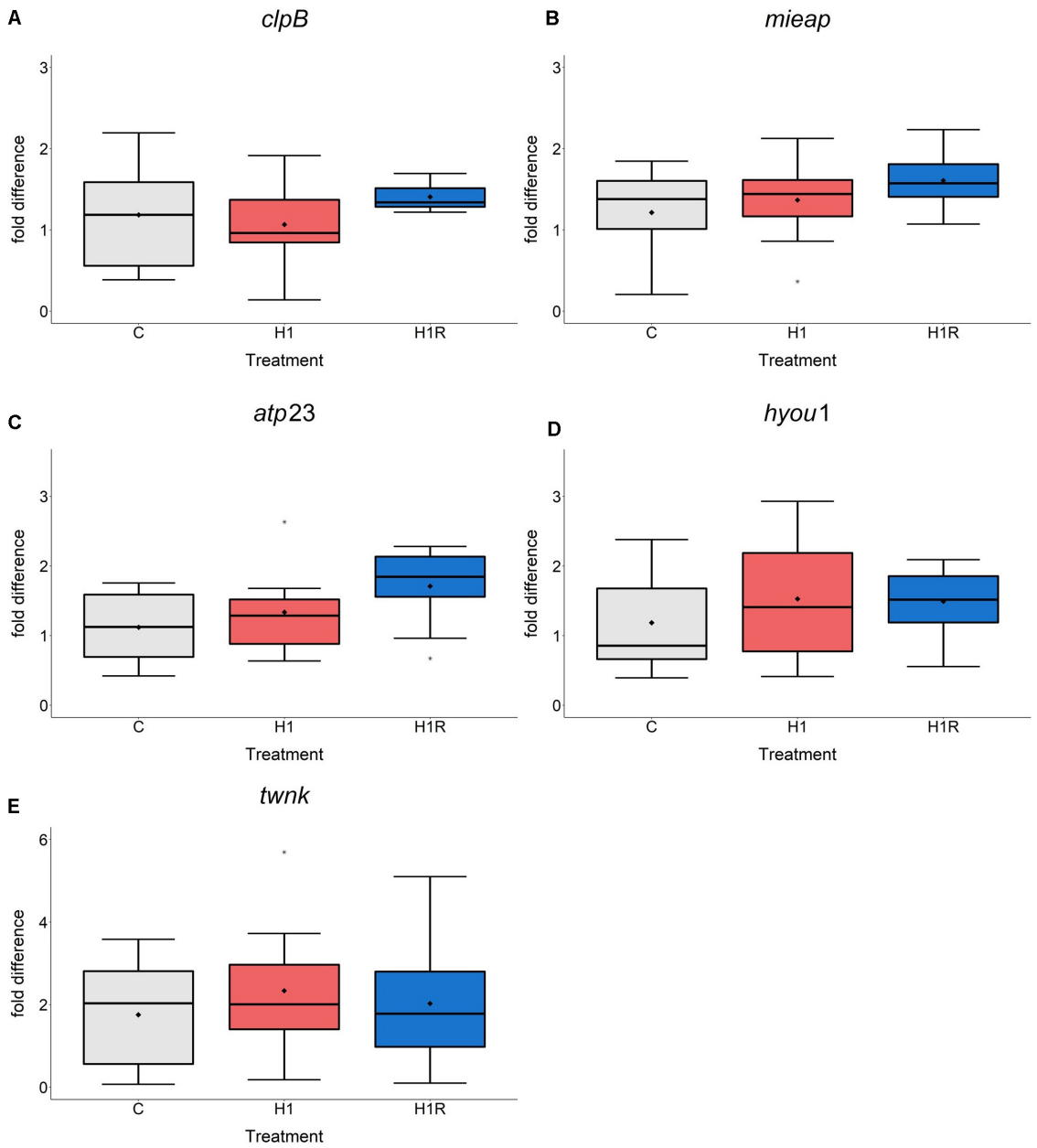


FIGURE 4 | mRNA expression of mitochondrial quality control proteolysis and mtDNA maintenance in *C. gigas* hepatopancreas in response to H/R stress. **(A–D)** *C. gigas*; **(A)** *clpB* mRNA; **(B)** *mieap* mRNA; **(C)** *atp*23 mRNA; **(D)** *hyou*1 mRNA; **(E)** *twnk* mRNA. Experimental groups: C, control; H1, short-term (1 day) severe hypoxia; H1R, short-term (1 day) severe hypoxia and subsequent 1.5 h reoxygenation. Means are depicted as points within corresponding Box-Whisker-plot. Outliers are shown as asterisk (*). Different letters above plots represent values that are statistical significantly different from each other ($p < 0.05$). Plots sharing a letter are not significantly different ($p > 0.05$). $N = 6–10$.

pattern of the studied mitophagy genes did not show pronounced effects of hypoxia and subsequent reoxygenation (**Figures 5B,D,F**).

Data Integration

The principal component analysis in *M. edulis* hepatopancreas revealed two principal components explaining 47.2% (PC1) and 19.1% (PC2) of the data variation (**Figure 6C** and **Supplementary Table S3**). The 1st component showed high positive loadings for genes of mitochondrial fission (*dnm1l*, *mff*, *fis*1) and fusion (*opa1*) and mitophagy (*prkn*, *pink*1) (**Figure 6D** and **Supplementary Table S4**). The 2nd principal component had high positive loadings of genes of mitochondrial quality control (*spg*7, *lonp*1) and a strong negative loading of *mfn*2, mediator of mitochondrial fusion.

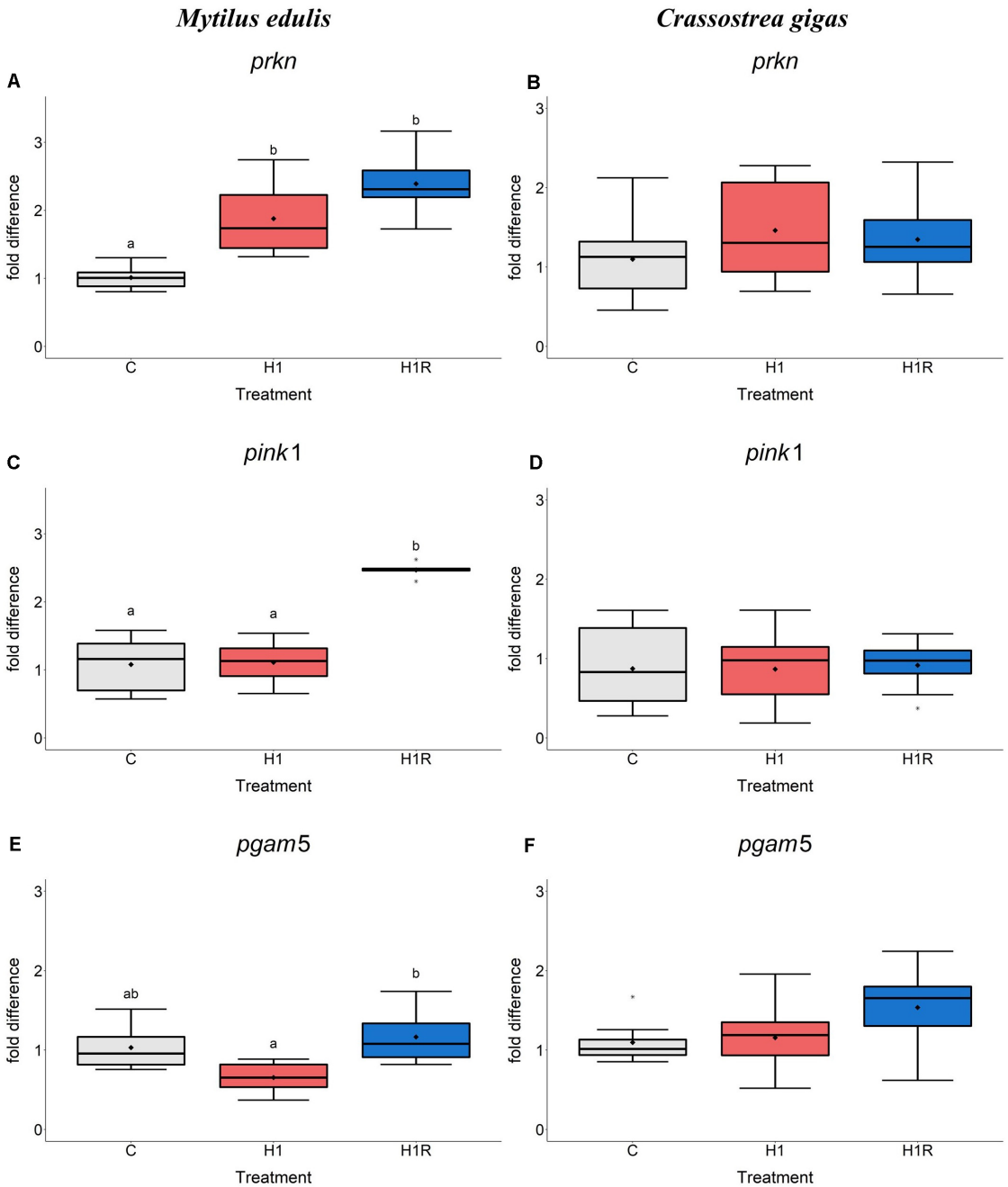


FIGURE 5 | mRNA expression of mitophagy proteins in *M. edulis* and *C. gigas* hepatopancreas in response to H/R stress. **(A,C,E)** *M. edulis*; **(B,D,F)** *C. gigas*; **(A,B)** *pink*1 mRNA; **(C,D)** *prkn* mRNA, **(E,F)** *pgam*5 mRNA. Experimental groups: C, control; H1, short-term (1 day) severe hypoxia; H1R, short-term (1 day) severe hypoxia and subsequent 1.5 h reoxygenation. Means are depicted as points within corresponding Box-Whisker-plot. Outliers are shown as asterisk (*). Different letters above plots represent values that are statistical significantly different from each other ($p < 0.05$). Plots sharing a letter are not significantly different ($p > 0.05$). $N = 6–10$.

In *M. edulis,* control and reoxygenation group were clearly separated along the 1st principal component (**Figure 6C**). Hypoxia and to greater degree reoxygenation induced a shift toward more positive values of the 1st principal component compared to the normoxic control reflecting upregulation of fission genes *mff, fis*1 and *dnm1l* and a gene encoding a mitochondrial protease *oma*1. All experimental treatment groups showed a high variance along the 2nd principal component axis.

Pearson correlation on mRNA expression of *M. edulis* showed a tight connection between the fission mediators *fis*1, *mff* and *dnm1l*, fusion mediator *opa1,* mitophagic inducing genes

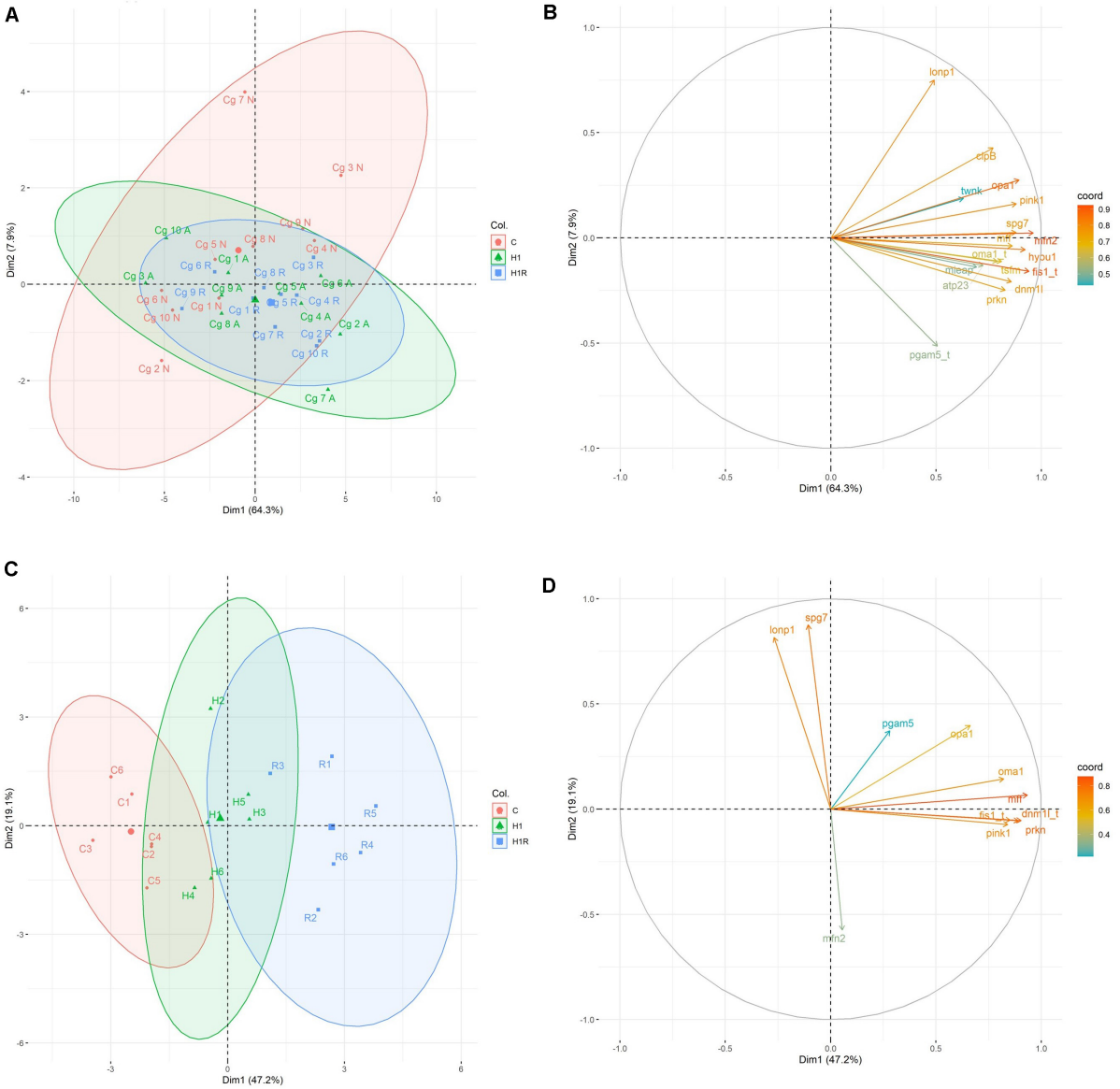


FIGURE 6 | PCA score plots and variable loading plots based on the studied biomarkers from *M. edulis* and *C. gigas* during H/R stress. **(A,B)** *C. gigas*; **(C,D)** *M. edulis*; **(A,C)** PCA score plot, position of the individual measurements from different experimental group within a coordinate system of first and second principal component. Horizontal axis depicts PC1 and vertical axis PC2. Colored ellipse includes all samples within 95% confidence interval. **(B,D)** Variable loading plot, visualization of weight distribution of different biomarkers on first and second principal component based on correlations between variables and dimensions. Close vectors define positive correlation between corresponding biomarkers. Coloring of vectors visualize coordinates. Horizontal axis depicts PC1 and vertical axis PC2. Gene name with appended "t" depicts transformed data to ensure normal distribution. Experimental groups: C, control, red; H1, short-term (1 day) severe hypoxia, green; H1R, short-term (1 day) severe hypoxia and subsequent 1.5 h reoxygenation, blue. Gene abbreviations: *mfn*2, mitofusin 2; *opa*1, mitochondrial dynamin-like 120 kDa protein; *dnm*1*l*, dynamin-1-like protein; *mff*, mitochondrial fission factor; *fis*1, mitochondrial fission protein; *tsfm*, mitochondrial translation elongation factor Ts; *lonp*1, mitochondrial Lon protease; *spg*7, paraplegin; *oma*1, mitochondrial metalloendopeptidase OMA1; *clpB*, mitochondrial caseinolytic matrix peptidase chaperone subunit B protein homolog; *mieap*, mitochondrial eating protein; *atp*23, mitochondrial inner membrane protease ATP23; *hyou*1, hypoxia upregulated protein 1; *twnk*, mitochondrial twinkle mtDNA helicase; *prkn*, E3 ubiquitin-protein ligase parkin; *pink*1, PTEN-induced kinase 1; *pgam*5, mitochondrial serine/threonine protein phosphatase PGAM5; β*Act*, beta Actin

prkn and *pink*1 and mitochondrial dynamics regulator *oma*1 (**Figures 7C,D**).

In *C. gigas*, the 1st and 2nd principal component explained 64.3% and 7.9% of variance, respectively (**Figure 6A** and **Supplementary Table S5**). All genes analyzed in this study had high positive loadings on the 1st principal component (>0.05) (**Figure 6B** and **Supplementary Table S6**).

Gene transcription of *C. gigas* from all three experimental treatments showed considerable overlap in the plane of the

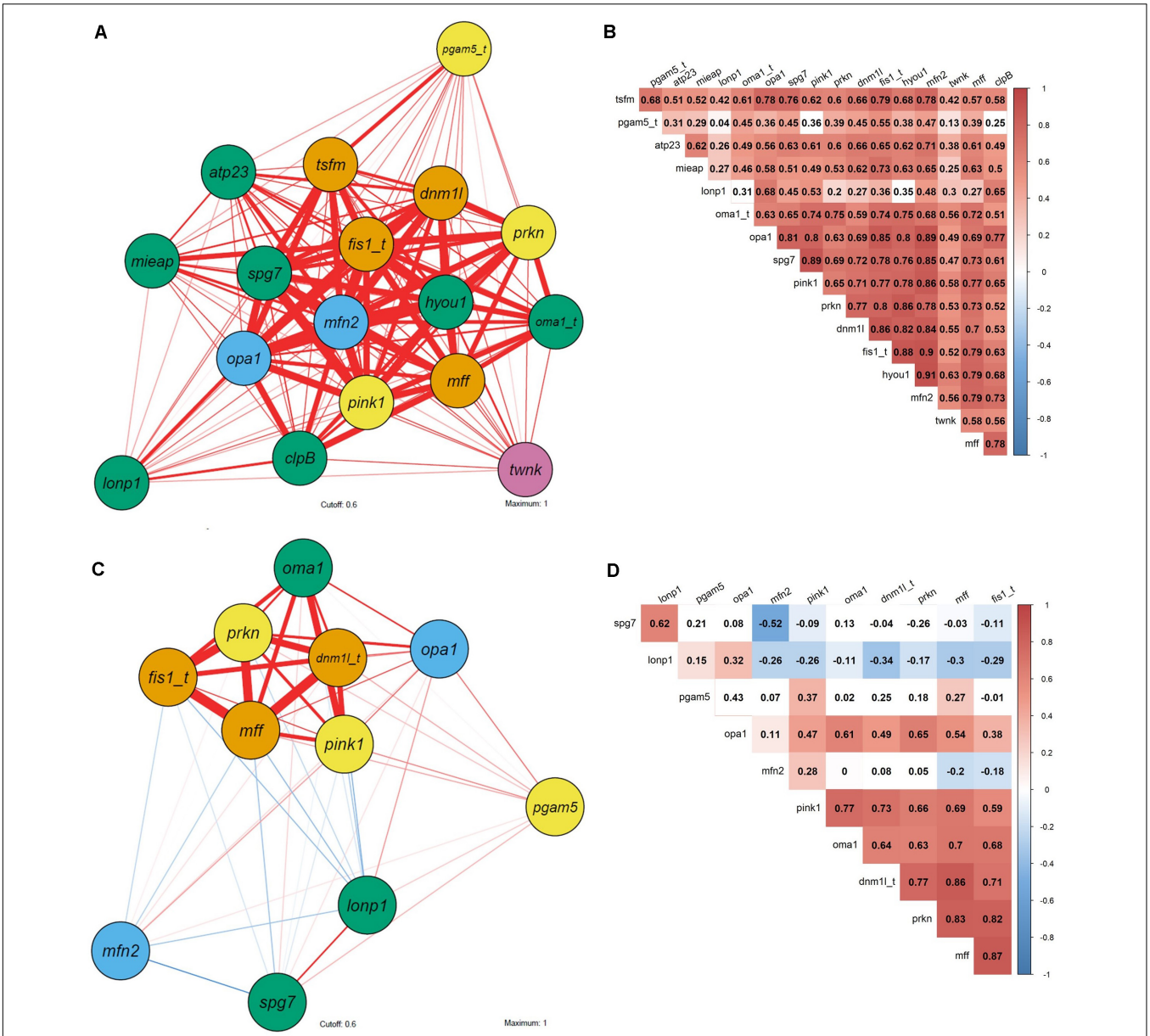


FIGURE 7 | Correlation network and corresponding heatmap of biomarker expression in *C. gigas* and *M. edulis* in response to H/R stress. **(A,B)** *C. gigas*; **(C,D)** *M. edulis*; **(A,C)** correlation network; **(B,D)** heatmap. Functional gene groups: orange, mitochondrial fission; light blue, mitochondrial fusion; green, mitochondrial quality control and proteolysis; yellow, mitophagy; pink, mtDNA maintenance. Pearson correlation coefficient: red, positive correlation; blue, negative correlation. Correlation networks are based on Pearson's correlation with a cutoff of 0.6 and maximum of 1. Non-colored fields of heatmaps and thin shaped correlation network represent non-statistical significant correlations. Thickness of lines represent statistically significant correlations ($p < 0.05$). Underlying Pearson correlation coefficient are depicted in associated heatmap. Gene name with appended "t" depicts transformed data to ensure normal distribution.

two first principal components consistent with the lack of change in the mRNA expression profiles of the studied genes in response to the H/R stress. In *C. gigas*, no apparent correlated gene clusters were found with the tight correlation across all studied genes (**Figures 7A,B**). These data indicate that the observed variability and correlations in the mRNA expression profiles of *C. gigas* mostly reflects individual differences between bivalves rather than the effects of the oxygen regime.

DISCUSSION

Short-term severe hypoxia and subsequent reoxygenation had different effects on mRNA expression of mitochondrial quality control in *C. gigas* and *M. edulis* (**Table 2**). In *C. gigas*, transcript levels were not affected by H/R stress indicating that the mitochondrial injury thresholds needed to induce the protective quality control mechanisms might not have been reached in this hypoxia-tolerant species. In *M. edulis,* mRNA expression of the

TABLE 2 | Summary of the observed changes in mRNA expression patterns of the mitochondrial quality control genes in *Crassostrea gigas* and *Mytilus edulis*.

Gene	*Crassostrea gigas*			*Mytilus edulis*		
	C	H1	H1R	C	H1	H1R
mfn2		↔	↔		↓	↔
opa1		↔	↔		↔	↔
dnm1l		↔	↔		↑	↑
mff		↔	↔		↑	↑
fis1		↔	↔		↑	↑
lonp1		↔	↔		↔	↔
spg7		↔	↔		↔	↔
oma1		↔	↔		↑	↑
clpB		↔	↔	/	/	/
mieap		↔	↔	/	/	/
atp23		↔	↔	/	/	/
hyou1		↔	↔	/	/	/
twnk		↔	↔	/	/	/
prkn		↔	↔		↑	↑
pink1		↔	↔		↔	↑
pgam5		↔	↔		↔	↑

Red fields with upward arrows show upregulated mRNA expression, while blue fields with downward arrows show downregulated mRNA expression (compared to the normoxic baseline). Horizontal arrows – no change. Gray diagonally crossed fields – no data available. Exposure groups: C, normoxia (21% O_2); H1, 24 h hypoxia (<0.01% O_2); and H1R, 24 h hypoxia with subsequent 1.5 h reoxygenation (<0.01% to 21% O_2). Gene abbreviations: mfn2, mitofusin 2; opa1, mitochondrial dynamin-like 120 kDa protein; dnm1l, dynamin-1-like protein; mff, mitochondrial fission factor; fis1, mitochondrial fission protein; tsfm, mitochondrial translation elongation factor Ts; lonp1, mitochondrial Lon protease; spg7, paraplegin; oma1, mitochondrial metalloendopeptidase OMA1; clpB, mitochondrial caseinolytic matrix peptidase chaperone subunit B protein homolog; mieap, mitochondrial eating protein; atp23, mitochondrial inner membrane protease ATP23; hyou1, hypoxia upregulated protein 1; twnk, mitochondrial twinkle mtDNA helicase; prkn, E3 ubiquitin-protein ligase parkin; pink1, PTEN-induced kinase 1; pgam5, mitochondrial serine/threonine protein phosphatase PGAM5.

transcripts related to mitochondrial dynamics and quality control was strongly regulated during H/R stress showing a shift toward the predominance of mitochondrial fission over fusion and an onset of mitophagy.

Effects of H/R Stress on Transcriptional Regulation of Mitochondrial Quality Control in the Mussels

Mitochondrial dynamics (in particular fission and fusion) plays a critical role in maintaining functional mitochondria during stress exposures in animals (Youle and van der Bliek, 2012). In mammalian models, ischemia-reperfusion (I/R) stress regulates transcription and post-translational modifications of fusion and fission proteins reflecting the important role of the mitochondrial dynamics in adjustments to interrupted oxygen supply (Li and Liu, 2018). Cellular stress commonly shifts mitochondrial dynamics toward mitochondrial fission to allow degradation of damaged mitochondria and avoid re-joining of non-functional mitochondria into the mitochondrial network (Chen et al., 2016; Eisner et al., 2018; Sokolova et al., 2019). The GTPase Drp1/Dnm1l mediates mitochondrial fission in response to cellular stress signals such as increase of Ca^{2+} concentration, ROS production or depolarized mitochondrial membrane as shown during H/R (I/R) stress in mammalian models (Yu et al., 2016; Tian et al., 2017; Yang et al., 2017; Li and Liu, 2018). Drp1/Dnm1l binds to the OMM with the help of the adaptor proteins Mff and Fis1 and initializes division of the membrane (Mears et al., 2011; van der Bliek et al., 2013; Osellame et al., 2016). Drp1/Dnm1l is a transcriptional target of p53 and, in rats, it is regulated at the transcriptional level (Li et al., 2010). The finding of transcriptional upregulation of *dnm1l* and its two adapter proteins *mff* and *fis*1 during H/R stress in *M. edulis* is consistent with upregulation of the fission pathways possibly as a mechanism to protect mitochondrial integrity by segregation of dysfunctional mitochondria (Twig et al., 2008; Anzell et al., 2018). mRNA expression of the fission-related proteins remained elevated during reoxygenation indicating that 1.5 h reoxygenation might not be sufficient for the full recovery of the mitochondrial fusion-fission balance in *M. edulis*.

Fusion is an effective strategy to protect against the stress-induced DNA damage, as the damaged mitochondria fuse with the healthy ones and replace the damaged mitochondrial DNA through complementation (Youle and van der Bliek, 2012). In our present study, mRNA levels of a key fusion mediator *mfn*2 (encoding the mitochondrial Mfn 2 protein) were suppressed during hypoxia in *M. edulis* indicating downregulation of the mitochondrial fusion pathways. This lack of induction of *mfn2* might indicate that mitochondrial DNA damage is not critically involved in the H/R stress responses of the blue mussels. An earlier study in the eastern oysters *C. virginica* showed an increase in the levels of DNA damage during exposure to 6 days of hypoxia and subsequent reoxygenation in the oysters exposed to a toxic metal cadmium, but not in their counterparts exposed to H/R stress only (Kurochkin et al., 2009). In the mussels *M. edulis,* hypoxia caused by emersion (72 h) had no effect on the DNA damage assessed by the Comet assay (Singh and Hartl, 2012). In the brown mussels *Perna perna,* 24 h of emersion-induced hypoxia led to the elevated oxidative DNA damage in the gills but not in the digestive gland (Almeida et al., 2005). In these studies, the oxidative lesions were assessed in the total rather than the mitochondrial DNA. To the best of our knowledge, the effects of H/R stress on the mitochondrial DNA damage have not been studied in marine bivalves. It is worth noting that mitofusin 2 requires energy in the form of GTP to mediate the mitochondrial fusion (Filadi et al., 2018), so that the downregulation of *mfn*2 in hypoxia-exposed mussels might be a consequence of the metabolic rate depression, a common energy-saving strategy to survive the oxygen deficiency in hypoxia-tolerant mollusks (Hochachka, 1993; Storey, 1998; Storey and Storey, 2004). During reoxygenation mRNA expression of *mfn*2 returned to the normoxic (baseline) levels in the mussels, which indicates a rapid re-balancing of mitochondrial fusion during post-hypoxic recovery.

The transcript levels of *opa*1 (encoding the mitochondrial dynamin-like GTPase OPA1) were not affected by H/R stress in *M. edulis*. The mitochondrial OPA1 is involved in the regulation of the mitochondrial fusion and the cross-talk between fusion and fission (Cipolat et al., 2004). In mammals, OPA1 activity is

regulated transcriptionally (Ryu et al., 2015; Zheng et al., 2019) as well as post-translationally through proteolytic cleavage by the mitochondrial metalloprotease OMA1 (Chen et al., 2016). Mitochondrial stress such as a decrease in the mitochondrial membrane potential or ATP deficiency stimulates the proteolytic processing of OPA1 generating short isoforms unable to support mitochondrial fusion (Anand et al., 2014; Chen et al., 2016; Ali and McStay, 2018). The posttranslational regulation of OPA1 allows for rapid suppression of mitochondrial fusion and mitochondrial fragmentation but might not be reflected in the changes in mRNA expression (Ali and McStay, 2018). Nevertheless, *opa1* was observed to be transcriptionally regulated during formation of immune cells in mice (Ryu et al., 2015), while disorders related to impaired mitochondrial functions were associated with transcriptional regulation of *opa*1 (Zheng et al., 2019). The observed stability of *opa1* mRNA in the mussels might indicate the lack of involvement of OPA1 in the mitochondrial response to the H/R stress in *M. edulis*. Alternatively, if post-translational regulation plays a predominant role in the OPA1 activation in the mussels, activation of OPA1 might not be reflected at the transcript level. Further studies are needed to distinguish between these alternative explanations.

In *M. edulis*, H/R stress led to a strong upregulation of *oma*1 mRNA encoding the mitochondrial metalloprotease OMA1. As discussed above, OMA1 mediates the proteolytic cleavage of fusion mediator OPA1 during stress thereby suppressing mitochondrial fusion (Anand et al., 2014). OMA1-dependent degradation of OPA1 is thus essential for the selective removal of defective mitochondrial fragments and prevention of incorporation of those into the mitochondrial network (Head et al., 2009; Baker et al., 2014). Consequently, elevated *oma1* expression during hypoxia and subsequent reoxygenation in the mussels might reflect the overall shift in the mitochondrial fusion-fission dynamics toward the predominance of fission (Ali and McStay, 2018) and is consistent with the transcriptional upregulation of the fission regulating proteins *dnm*1*l, mff* and *fis*1 and suppressed expression of a fusion regulator *mfn*2 in *M. edulis* during the H/R stress. Furthermore, OMA1 mediates an ATP-independent proteolytic breakdown of misfolded inner membrane proteins and is complementary to the action of m-AAA proteases (Käser et al., 2003). OMA1 activity is strongly upregulated in response to various stresses in metazoans, plants and yeast (Bohovych et al., 2014; Rainbolt et al., 2015; Migdal et al., 2017) and is required for stabilization of the mitochondrial respiratory supercomplexes and maintenance of the mitochondrial respiration (Bohovych et al., 2015; Richter et al., 2015). Therefore, transcriptional upregulation of *oma*1 during H/R stress in the mussels might assist in the degradation of the damaged mitochondrial proteins and protection of the mitochondrial integrity and function.

Our study shows that unlike *oma*1, two other studied mitochondrial proteases (including the mitochondrial Lon protease and paraplegin, encoded by *lonp*1 and *spg*7, respectively) are not transcriptionally upregulated during H/R stress in *M. edulis*. Lon protease is highly conserved throughout organisms and essential for mitochondrial proteostasis (Pinti et al., 2015). It is activated by ROS, protein carbonylation and lipid peroxidation (Kuo et al., 2015) and specifically targets the oxidatively damaged proteins for ATP dependent degradation (Bota and Davies, 2002; Bayot et al., 2010). Lon protease activity is regulated transcriptionally and post-translationally suggesting a fine tuning by several mechanisms, although stronger regulatory patterns are commonly seen at the protein level (Pinti et al., 2015). Earlier studies in bivalves showed that Lon protease mRNA expression was upregulated during H/R stress in the hypoxia-sensitive scallops *Argopecten irradians* but not in the hypoxia-tolerant hard shell clams *Mercenaria mercenaria* (Ivanina et al., 2016). Upregulation of *lonp1* transcripts in the scallops was associated with accumulation of oxidative lesions (i.e., lipid and protein peroxidation products) in the mitochondria, whereas in the hard shell clams the mitochondrial oxidative stress markers remained at the baseline (normoxic) levels (Ivanina et al., 2016). Upregulation of *lonp1* mRNA expression was also found in the Eastern oyster *C. virginica* during simultaneous exposure to high temperature and a toxic metal cadmium (Sanni et al., 2008), a combination of stressors known to cause strong oxidative stress in oysters (Bagwe et al., 2015). Taken together, these findings indicate that transcriptional upregulation of *lonp1* in bivalves might occur when the oxidative stress reaches a species-specific threshold in the mitochondria, and the lack of transcriptional upregulation of *lonp*1 mRNA levels during H/R stress in *M. edulis* might indicate that this threshold has not been reached under the conditions of our present study. Similar to *lonp1*, transcript levels of *spg*7 gene encoding a mitochondrial metalloprotease paraplegin did not change during H/R stress in the mussels. To the best of our knowledge, expression of *spg*7 has not been studied in other marine bivalves. In model organisms including mammals and yeast, paraplegin is regulated by mitochondrial stress signals such as Ca^{2+} accumulation and elevated ROS levels (Ishihara et al., 2006; Shanmughapriya et al., 2015). If similar ROS-dependent mechanisms exist in bivalves, the lack of *spg*7 (as well as *lonp1*) transcriptional responses to H/R stress might be explained by the relatively low levels of oxidative stress insufficient to trigger transcriptional upregulation of these proteases. Further studies of the ROS production, oxidative injury and expression of mitochondrial proteases in bivalve mitochondria during exposures to different stressors are required to test this hypothesis and shed light on the thresholds of mitochondrial injury required for induction of these protective mechanisms.

Mitophagy is a selective form of autophagy to degrade damaged mitochondria (Pickles et al., 2018). Based on the studies in the model organisms, the PINK1-Parkin pathways plays a key role in the stress-induced mitophagy (Jin et al., 2010). In healthy mitochondria, the constitutively expressed PINK1 is translocated to mitochondria in a membrane-potential-dependent manner, cleaved by proteases and released to cytosol for further degradation. Membrane depolarization in dysfunctional mitochondria causes stabilization and dimerization of PINK1 on mitochondrial surface (Ding and Yin, 2012). Bound PINK1 recruits and phosphorylates parkin (Dagda et al., 2009; Eiyama and Okamoto, 2015), which tags damaged mitochondria for further degradation by mitophagy (Narendra and Youle, 2011).

Activity of the protein phosphatase PGAM5 also contributes to the activation of mitophagy (Chen et al., 2014; Wu et al., 2014) and promotes the mitochondrial fission by activating the Drp1/Dnm1l protein (Wang et al., 2012). In our present study, hypoxia exposure induced elevated mRNA expression of *prkn* in *M. edulis*, while the transcript levels of the associated key genes *pink*1 and *pgam*5 rose during reoxygenation mitochondria. This expression pattern indicates an onset of mitophagy during reoxygenation as the PINK1-parkin pathway is increasingly required to tag dysfunctional mitochondria caused by oxidative stress. Transcriptional upregulation of PGAM5 also indicates activation of the cell death pathways (Wang et al., 2012) during reoxygenation in *M. edulis*, consistent with the earlier findings of upregulated apoptosis in this species during H/R stress (Falfushynska et al., 2020a).

The correlation network analysis showed strong correlation of mRNA expression of all three fission mediators, the PINK1-parkin pathway regulators and *oma*1, underpinning the common regulatory mechanism for these pathways. This is also reflected by the clear separation of mRNA expression profiles of the mussels exposed to hypoxia and (especially) reoxygenation from the normoxic control groups along the 1st principal component axis in the PCA associated with the high loadings of the fission-mitophagy-related transcripts. An earlier study showed a similar major shift of the mRNA expression profiles of the pro-apoptotic and pro-inflammatory genes in *M. edulis* exposed to the short-term H/R stress (Falfushynska et al., 2020a). The metabolic profiling in a related study showed onset of anaerobiosis, downregulation of gluconeogenesis and a shifted balance between protein synthesis and breakdown in *M. edulis* indicating early onset of severe stress response during H/R exposure (Haider et al., 2020).

Muted Transcriptional Response of the Mitochondrial Dynamics and Quality Control Genes During H/R Stress in *C. gigas*

Unlike *M. edulis*, *C. gigas* did not change its mRNA expression in any of the 17 studied genes in response to 24 h hypoxia and subsequent 1.5 h reoxygenation. Furthermore, the overlap of gene transcription found by PCA and the apparent tight correlation across all studied genes supports a conclusion of the lack of a transcriptional shift in the studied pathways during H/R stress in the Pacific oyster. A similar transcriptional stability was found for *lonp1* expression after 6 days of hypoxia and 1–12 h of reoxygenation in the eastern oyster *C. virginica* (Ivanina et al., 2010). Previously, metabolic and mRNA expression profiling on apoptotic and pro-inflammatory genes in *C. gigas* revealed no changes in response to short-term hypoxia (Falfushynska et al., 2020a; Haider et al., 2020). Only 6 days exposure to hypoxia led to a small shift in metabolite profiles indicating metabolic rate depression, maintenance of balanced FAA/metabolite pool and effective detoxification by urea and purine cycles. Furthermore, maintenance of steady activity levels of mitoproteases during the H/R stress was earlier reported in *C. gigas* (Ivanina and Sokolova, 2016). Together with the muted mRNA expression regulation of mitochondrial quality control genes and mitochondrial dynamics, these findings indicate that 24 h of severe hypoxia might not be sufficient to induce strong stress markers in *C. gigas*. However, short-term hypoxia (24 h, <1% O_2) and subsequent reoxygenation affected a reversible phosphorylation pattern of mitochondrial quality control proteins such as PGAM5 in *C. gigas* (Sokolov et al., 2019). This indicates that despite the lack of a strong transcriptional induction of the key genes in the mitochondrial quality control pathways, the activity of these pathways might be modulated by posttranslational protein modifications (PTM) in *C. gigas*. This hypothesis requires further investigation as the role of the PTM in the regulation of the mitochondrial function of marine bivalves has not been extensively studied (Sokolov et al., 2019; Falfushynska et al., 2020b). Notably, a muted transcriptional response to short-term hypoxia and subsequent reoxygenation has been earlier shown for other important pathways involved in cellular bioenergetics of the oysters. Thus, hypoxia induced genes (especially respiratory chain genes) were regulated in *C. gigas* only after 7 days of exposure to 30% O_2 saturation, with no apparent changes at the earlier exposures (David et al., 2005). In the eastern oyster *C. virginica*, key marker genes in the mitochondrial electron chain and Krebs' cycle, as well as the cytosolic glycolytic genes showed stable expression during 6 days of severe hypoxia (< 1% O_2) and subsequent reoxygenation (Ivanina et al., 2010). Like other hypoxia-tolerant mollusks, the Eastern and Pacific oyster rely on metabolic rate depression to cope with oxygen deficiency (Storey and Storey, 2004) and use a reversible global transcription repression to arrest energy consuming transcription (Larade and Storey, 2002). Only specific transcription factors seem to be upregulated to allow transcription of certain hypoxic genes (David et al., 2005). These factors might contribute to the muted transcriptional response during H/R stress in the oysters. Overall, the hypoxia tolerant Pacific oyster seems to maintain its mitochondrial integrity and functions by reversible enzyme regulations sufficient for fast recovery in reoxygenation, which might contribute to the high stress tolerance of this species adapted to the habitat conditions of daily immersion and emersion (Sussarellu et al., 2013). Further investigations in a broader comparative framework (involving multiple species of bivalves with different levels of hypoxia tolerance) are needed to determine whether the hypoxia-tolerant mitochondrial phenotypes generally correlate with the transcriptional stability and stronger dependence on post-translational regulatory mechanisms during H/R stress in marine bivalves.

CONCLUSION

Our study showed that differential transcriptional regulation of the mitochondrial quality control pathways is involved in the molecular response to H/R stress in the blue mussels *M. edulis* but not in the oysters *C. gigas*. In the mussels, the H/R stress induced the pathways related to the mitochondrial fission,

mitophagy and ATP-independent mitochondrial proteolysis. Interestingly, the transcripts of the proteins encoding ATP-dependent mitochondrial quality control proteins (such as mitofusin 2, Lon protease and paraplegin) remained stable or downregulated during hypoxia, possibly as a consequence of the metabolic rate depression and an associated decrease in the ATP turnover rates. In *C. gigas*, no clear transcriptional response of the mitochondrial quality control pathways was found during H/R stress, with all studied transcripts maintained at control (normoxic) levels. This might indicate that unlike *M. edulis*, other mechanisms (such as post-transcriptional and post-translational regulation of the respective pathways) are involved in the regulation of the mitochondrial integrity in oysters. Alternatively, it is possible that the level of the mitochondrial damage in oysters did not reach the threshold required to trigger the respective transcriptional activation of the mitochondrial quality control pathways. The latter explanation appears plausible, given the relative stability of the metabolomics profile and the transcript levels of other stress genes (such as those involved in apoptosis and inflammation) during H/R stress in oysters compared with the mussels (Falfushynska et al., 2020a; Haider et al., 2020). Our present study and earlier published research (Falfushynska et al., 2020a; Haider et al., 2020) also indicate that the mRNA expression of the stress-related genes may not be a good biomarker of hypoxia-induced stress in an extremely tolerant species such as *C. gigas*. It is worth noting that the natural habitat conditions differ with regard to salinity (ocean vs. brackish, respectively) and the tidal height (intertidal vs. subtidal, respectively) between the two studied populations of the oysters and the mussels. Further studies are needed to determine whether the established links between the mRNA expression profiles of the stress-related mitochondrial genes and hypoxia tolerance reflect the species-specific differences between the oysters and the mussels, or some other aspects of the local adaptation to the divergent habitats in which these organisms were collected.

DATA AVAILABILITY STATEMENT

The datasets presented in this study can be found in online repositories. The names of the repository/repositories and accession number(s) can be found below: Zenodo: doi: 10.5281/zenodo.4266408.

AUTHOR CONTRIBUTIONS

JS and HF conducted the experimental exposures and tissue collections with *C. gigas*, and *M. edulis*, respectively. mRNA extraction, cDNA synthesis and quantitative real-time PCR were done by JS and HF, and statistical analysis and data integration was done by JS. HF and JS designed primers according to transcripts provided by bioinformatical analysis from HP. JS, IS, and HP wrote the first draft of the manuscript, and all author contributed to the data interpretation and revisions of the manuscript. All authors contributed to the article and approved the submitted version.

FUNDING

This study was funded by the Deutsche Forschungsgemeinschaft within the project "MitoBOX: the mitochondrial basis of hypoxia tolerance in marine mollusks" (grant number 415984732). HP was supported by the NIH grant R21AG064479-01 and a Brain Health Research Institute Pilot Award from Kent State University.

ACKNOWLEDGMENTS

We thank Mathias Wegner of the Alfred-Wegener-Institute List/Sylt, Germany, for supply and shipping of oysters. We also thank Eugene Sokolov for training and helpful advice in molecular methods. The metadata of the project have been uploaded to an open repository Zenodo (doi: 10.5281/zenodo.4266408).

SUPPLEMENTARY MATERIAL

The Supplementary Material for this article can be found online at: https://www.frontiersin.org/articles/10.3389/fmars.2020.604411/full#supplementary-material

REFERENCES

Ali, S., and McStay, G. P. (2018). Regulation of mitochondrial dynamics by proteolytic processing and protein turnover. *Antioxidants* 7, 1–15. doi: 10.3390/antiox7010015

Almeida, E. A., Bainy, A. C. D., Dafre, A. L., Gomes, O. F., Medeiros, M. H. G., and Di Mascio, P. (2005). Oxidative stress in digestive gland and gill of the brown mussel (*Perna perna*) exposed to air and re-submersed. *J. Exp. Mar. Biol. Ecol.* 318, 21–30. doi: 10.1016/j.jembe.2004.12.007

Anand, R., Wai, T., Baker, M. J., Kladt, N., Schauss, A. C., Rugarli, E., et al. (2014). The i-AAA protease YME1L and OMA1 cleave OPA1 to balance mitochondrial fusion and fission. *J. Cell Biol.* 204, 919–929. doi: 10.1083/jcb.201308006

Andrienko, T. N., Pasdois, P., Pereira, G. C., Ovens, M. J., and Halestrap, A. P. (2017). The role of succinate and ROS in reperfusion injury - A critical appraisal. *J. Mol. Cell Cardiol.* 110, 1–14. doi: 10.1016/j.yjmcc.2017.06.016

Anzell, A. R., Maizy, R., Przyklenk, K., and Sanderson, T. H. (2018). Mitochondrial quality control and disease: insights into ischemia-reperfusion injury. *Mol. Neurobiol.* 55, 2547–2564. doi: 10.1007/s12035-017-0503-9

Atorino, L., Silvestri, L., Koppen, M., Cassina, L., Ballabio, A., Marconi, R., et al. (2003). Loss of m-AAA protease in mitochondria causes complex I deficiency and increased sensitivity to oxidative stress in hereditary spastic paraplegia. *J. Cell Biol.* 163, 777–787. doi: 10.1083/jcb.200304112

Bagwe, R., Beniash, E., and Sokolova, I. M. (2015). Effects of cadmium exposure on critical temperatures of aerobic metabolism in eastern oysters *Crassostrea virginica* (Gmelin, 1791). *Aquat. Toxicol.* 167, 77–89. doi: 10.1016/j.aquatox.2015.07.012

Baker, M. J., Lampe, P. A., Stojanovski, D., Korwitz, A., Anand, R., Tatsuta, T., et al. (2014). Stress-induced OMA1 activation and autocatalytic turnover regulate OPA1-dependent mitochondrial dynamics. *EMBO J.* 33, 578–593. doi: 10.1002/embj.201386474

Bayot, A., Gareil, M., Rogowska-Wrzesinska, A., Roepstorff, P., Friguet, B., and Bulteau, A. -L. (2010). Identification of novel oxidized protein substrates and physiological partners of the mitochondrial ATP-dependent Lon-like Protease Pim1. *J. Biol. Chem.* 285, 11445–11457. doi: 10.1074/jbc.M109.065425

Berlett, B. S., and Stadtman, E. R. (1997). Protein oxidation in aging, disease, and oxidative stress. *J. Biol. Chem.* 272, 20313–20316. doi: 10.1074/jbc.272.33.20313

Bohovych, I., Donaldson, G., Christianson, S., Zahayko, N., and Khalimonchuk, O. (2014). Stress-triggered activation of the metalloprotease Oma1 involves Its C-terminal region and is important for mitochondrial stress protection in Yeast. *J. Biol. Chem.* 289, 13259–13272. doi: 10.1074/jbc.M113.542910

Bohovych, I., Fernandez, M. R., Rahn, J. J., Stackley, K. D., Bestman, J. E., Anandhan, A., et al. (2015). Metalloprotease OMA1 fine-tunes mitochondrial bioenergetic function and respiratory supercomplex stability. *Sci. Rep.* 5:13989. doi: 10.1038/srep13989

Bota, D. A., and Davies, K. J. A. (2002). Lon protease preferentially degrades oxidized mitochondrial aconitase by an ATP-stimulated mechanism. *Nat. Cell Biol.* 4, 674–680. doi: 10.1038/ncb836

Breitburg, D., Baumann, H., Sokolova, I., and Frieder, C. (2019). "6. Multiple stressors -forces that combine to worsen deoxygenation and its effects," in *Ocean Deoxygenation: Everyone's Problem. Causes, Impacts, Consequences and Solutions*, eds. D. D. A. Laffoley, and J. M. Baxter (Gland: IUCN), 225–247.

Breitburg, D., Levin, L. A., Oschlies, A., Grégoire, M., Chavez, F. P., Conley, D. J., et al. (2018). Declining oxygen in the global ocean and coastal waters. *Science* 359, 1–11. doi: 10.1126/science.aam7240

Cabiscol, E., Piulats, E., Echave, P., Herrero, E., and Ros, J. (2000). Oxidative stress promotes specific protein damage in *Saccharomyces cerevisiae*. *J. Biol. Chem.* 275, 27393–27398. doi: 10.1074/jbc.M003140200

Cadenas, E., and Davies, K. J. A. (2000). Mitochondrial free radical generation, oxidative stress, and aging. *Free Radic. Biol. Med.* 29, 222–230.

Chen, G., Han, Z., Feng, D., Chen, Y., Chen, L., Wu, H., et al. (2014). A regulatory signaling loop comprising the PGAM5 phosphatase and CK2 controls receptor-mediated mitophagy. *Mol. Cell* 54, 362–377. doi: 10.1016/j.molcel.2014.02.034

Chen, H., Detmer, S. A., Ewald, A. J., Griffin, E. E., Fraser, S. E., and Chan, D. C. (2003). Mitofusins Mfn1 and Mfn2 coordinately regulate mitochondrial fusion and are essential for embryonic development. *J. Cell Biol.* 160, 189–200. doi: 10.1083/jcb.200211046

Chen, M., Chen, Z., Wang, Y., Tan, Z., Zhu, C., Li, Y., et al. (2016). Mitophagy receptor FUNDC1 regulates mitochondrial dynamics and mitophagy. *Autophagy* 12, 689–702. doi: 10.1080/15548627.2016.1151580

Chen, Q., Camara, A. K. S., Stowe, D. F., Hoppel, C. L., and Lesnefsky, E. J. (2007). Modulation of electron transport protects cardiac mitochondria and decreases myocardial injury during ischemia and reperfusion. *Am. J. Physiol. Cell Physiol.* 292, C137-C147. doi: 10.1152/ajpcell.00270.2006

Cipolat, S., Brito, O. M. de, Dal Zilio, B., and Scorrano, L. (2004). OPA1 requires mitofusin 1 to promote mitochondrial fusion. *Proc. Natl. Acad. Sci. U.S.A.* 101, 15927–15932. doi: 10.1073/pnas.0407043101

Dagda, R. K., Cherra S. J. III., Kulich, S. M., Tandon, A., Park, D., and Chu, C. T. (2009). Loss of PINK1 function promotes mitophagy through effects on oxidative stress and mitochondrial fission. *J. Biol. Chem.* 284, 13843–13855. doi: 10.1074/jbc.M808515200

Daguin, C., Bonhomme, F., and Borsa, P. (2001). The zone of sympatry and hybridization of *Mytilus edulis* and *M. galloprovincialis*, as described by intron length polymorphism at locus mac-1. *Heredity* 86, 342–354. doi: 10.1046/j.1365-2540.2001.00832.x

David, E., Tanguy, A., Pichavant, K., and Moraga, D. (2005). Response of the Pacific oyster *Crassostrea gigas* to hypoxia exposure under experimental conditions. *FEBS J.* 272, 5635–5652. doi: 10.1111/j.1742-4658.2005.04960.x

Diaz, R. J., and Rosenberg, R. (1995). Marine benthic hypoxia: a review of its ecological effects and the behavioural responses of benthic macrofauna. *Oceanogr. Mar. Biol.* 33, 245–303.

Diaz, R. J., and Rosenberg, R. (2008). Spreading dead zones and consequences for marine Ecosystems. *Science* 321, 926–929. doi: 10.1126/science.1156401

Ding, W. -X., and Yin, X. -M. (2012). Mitophagy: mechanisms, pathophysiological roles, and analysis. *Biol. Chem.* 393, 547–564. doi: 10.1515/hsz-2012-0119

Dorak, M. T. (2006). *Real-time PCR*. New York, NY: Taylor & Francis Group.

Doyle, S. M., and Wickner, S. (2008). Hsp104 and ClpB: protein disaggregating machines. *Trends Biochem. Sci.* 34, 40–48. doi: 10.1016/j.tibs.2008.09.010

Eisner, V., Picard, M., and Hajnóczky, G. (2018). Mitochondrial dynamics in adaptive and maladaptive cellular stress responses. *Nat. Cell Biol.* 20, 755–765. doi: 10.1038/s41556-018-0133-0

Eiyama, A., and Okamoto, K. (2015). PINK1/Parkin-mediated mitophagy in mammalian cells. *Curr. Opin. Cell Biol.* 33, 95–101. doi: 10.1016/j.ceb.2015.01.002

Falfushynska, H. I., Piontkivska, H., and Sokolova, I. M. (2020a). Effects of intermittent hypoxia on cell survival and inflammatory responses in the intertidal marine bivalves *Mytilus edulis* and *Crassostrea gigas*. *J. Exp. Biol.* 223:jeb217026. doi: 10.1242/jeb.217026

Falfushynska, H. I., Sokolov, E., Piontkivska, H., and Sokolova, I. M. (2020b). The role of reversible protein phosphorylation in regulation of the mitochondrial electron transport system during hypoxia and reoxygenation stress in marine bivalves. *Front. Mar. Sci*.7:467. doi: 10.3389/fmars.2020.00467

Filadi, R., Pendin, D., and Pizzo, P. (2018). Mitofusin 2: from functions to disease. *Cell Death Dis.* 9, 1–13. doi: 10.1038/s41419-017-0023-6

Gaitán-Espitia, J. D., Quintero-Galvis, J. F., Mesas, A., and D'Elía, G. (2016). Mitogenomics of southern hemisphere blue mussels (Bivalvia: Pteriomorphia): insights into the evolutionary characteristics of the *Mytilus edulis* complex. *Sci. Rep.* 6:26853. doi: 10.1038/srep26853

Galli, G. L. J., and Richards, J. G. (2014). Mitochondria from anoxia-tolerant animals reveal common strategies to survive without oxygen. *J. Comp. Physiol. B* 184, 285–302. doi: 10.1007/s00360-014-0806-3

Gardner, J. P. A. (1996). The *Mytilus edulis* species complex in southwest England: effects of hybridization and introgression upon interlocus associations and morphometric variation. *Mar. Biol.* 125, 385–399. doi: 10.1007/bf00346319

Gosling, E., (ed.) (1992). *The Mussel Mytilus: Ecology, Physiology, Genetics and Culture*. Amsterdam: Elsevier.

Gosling, E. M., and Wilkins, N. P. (1981). Ecological genetics of the mussels *Mytilus edulis* and *M. galloprovincialis* on irish coasts. *Mar. Ecol. Prog. Ser.* 4, 221–227. doi: 10.3354/meps004221

Grieshaber, M. K., Hardewig, I., Kreutzer, U., and Pörtner, H. -O. (1994). Physiological and metabolic responses to hypoxia in invertebrates. *Rev. Physiol. Biochem. Pharmacol.* 125, 43–147. doi: 10.1007/bfb0030909

Haider, F., Falfushynska, H. I., Timm, S., and Sokolova, I. M. (2020). Effects of hypoxia and reoxygenation on intermediary metabolite homeostasis of marine bivalves *Mytilus edulis* and *Crassostrea gigas*. *Comp. Biochem. Phys. A Mol. Integr. Physiol.* 242:110657. doi: 10.1016/j.cbpa.2020.110657

Head, B., Griparic, L., Amiri, M., Gandre-Babbe, S., and van der Bliek, A. M. (2009). Inducible proteolytic inactivation of OPA1 mediated by the OMA1 protease in mammalian cells. *J. Cell Biol.* 187, 959–966. doi: 10.1083/jcb.200906083

Hochachka, P. W. (1993). *Surviving Hypoxia: Mechanisms of Control and Adaptation*. Boca Raton, FL: CRC Press.

Hochachka, P. W., Buck, L. T., Doll, C. J., and Land, S. C. (1996). Unifying theroy of hypoxia tolerance: molecular/metabolic defense and rescue mechanisms for surviving oxygen lack. *Proc. Natl. Acad. Sci. U.S.A.* 93, 9493–9498. doi: 10.1073/pnas.93.18.9493

Hochachka, P. W., and Lutz, P. L. (2001). Mechanism, origin, and evolution of anoxia tolerance in animals. *Comp. Biochem. Phys. B* 130, 435–459. doi: 10.1016/s1096-4959(01)00408-0

Ishihara, N., Fujita, Y., Oka, T., and Mihara, K. (2006). Regulation of mitochondrial morphology through proteolytic cleavage of OPA1. *EMBO J.* 25, 2966–2977. doi: 10.1038/sj.emboj.7601184

Ivanina, A. V., Nesmelova, I., Leamy, L., Sokolov, E. P., and Sokolova, I. M. (2016). Intermittent hypoxia leads to functional reorganization of mitochondria and affects cellular bioenergetics in marine molluscs. *J. Exp. Biol.* 219, 1659–1674. doi: 10.1242/jeb.134700

Ivanina, A. V., Sokolov, E. P., and Sokolova, I. M. (2010). Effects of cadmium on anaerobic energy metabolism and mRNA expression during air exposure and recovery of an intertidal mollusk *Crassostrea virginica*. *Aquat. Toxicol.* 99, 330–342. doi: 10.1016/j.aquatox.2010.05.013

Ivanina, A. V., and Sokolova, I. M. (2016). Effects of intermittent hypoxia on oxidative stress and protein degradation in molluscan mitochondria. *J. Exp. Biol.* 219, 3794–3802. doi: 10.1242/jeb.146209

Jin, S. M., Lazarou, M., Wang, C., Kane, L. A., Narendra, D. P., and Youle, R. J. (2010). Mitochondrial membrane potential regulates PINK1 import and proteolytic destabilization by PARL. *J. Cell Biol.* 191, 933–942. doi: 10.1083/jcb.201008084

Käser, M., Kambacheld, M., Kisters-Woike, B., and Langer, T. (2003). Oma1, a Novel Membrane-bound Metallopeptidase in Mitochondria with Activities Overlapping with the *m*-AAA Protease. *J. Biol. Chem.* 278, 46414–46423. doi: 10.1074/jbc.M305584200

Kennedy, V. S. (1996). *The Eastern Oyster: Crassostrea virginica*. College Park, MD: Maryland Sea Grant College.

Kitamura, N., Nakamura, Y., Miyamoto, Y., Miyamoto, T., Kabu, K., Yoshida, M., et al. (2011). Mieap, a p53-inducible protein, controls mitochondrial quality by repairing or eliminating unhealthy mitochondria. *PLoS One* 6:e16060. doi: 10.1371/journal.pone.0016060

Kulek, A. R., Anzell, A. R., Wider, J. M., Sanderson, T. H., and Przyklenk, K. (2020). Mitochondrial quality control: role in cardiac models of lethal ischemia-reperfusion injury. *Cells* 9:214. doi: 10.3390/cells9010214

Kuo, C. -Y., Chiu, Y. -C., Lee, A. Y.-L., and Hwang, T. -L. (2015). Mitochondrial Lon protease controls ROS-dependent apoptosis in cardiomyocyte under hypoxia. *Mitochondrion* 23, 7–16. doi: 10.1016/j.mito.2015.04.004

Kurochkin, I. O., Ivanina, A. V., Eilers, S., Downs, C. A., May, L. A., and Sokolova, I. M. (2009). Cadmium affects metabolic responses to prolonged anoxia and reoxygenation in eastern oysters (*Crassostrea virginica*). *Am. J. Physiol. Regul. Integr. Comp. Physiol.* 297, R1262-R1272. doi: 10.1152/ajpregu.00324.2009

Larade, K., and Storey, K. B. (2002). "A Profile of the Metabolic Responses to Anoxia in Marine Invertebrates," in *Sensing, Signaling and Cell Adaptation*, eds K. B. Storey, and J. M. Storey (Amsterdam: Elsevier Science), 27–46. doi: 10.1016/s1568-1254(02)80005-5

Le Moullac, G., Quéau, I., Le Souchu, P., Pouvreau, S., Moal, J., Le René Coz, J., et al. (2007). Metabolic adjustments in the oyster *Crassostrea gigas* according to oxygen level and temperature. *Mar. Biol. Res.* 3, 357–366. doi: 10.1080/17451000701635128

Li, J., Donath, S., Li, Y., Qin, D., Prabhakar, B. S., and Li, P. (2010). miR-30 regulates mitochondrial fission through targeting p53 and the dynamin-related protein-1 pathway. *PLoS Genet.* 6:e1000795. doi: 10.1371/journal.pgen.1000795

Li, Y., and Liu, X. (2018). Novel insights into the role of mitochondrial fusion and fission in cardiomyocyte apoptosis induced by ischemia/reperfusion. *J. Cell Physiol.* 233, 5589–5597. doi: 10.1002/jcp.26522

Losón, O. C., Song, Z., Chen, H., and Chan, D. C. (2013). Fis1, Mff, MiD49, and MiD51 mediate Drp1 recruitment in mitochondrial fission. *Mol. Biol. Cell* 24, 659–667. doi: 10.1091/mbc.E12-10-0721

Mears, J. A., Lackner, L. L., Fang, S., Ingerman, E., Nunnari, J., and Hinshaw, J. E. (2011). Conformational changes in Dnm1 support a contractile mechanism for mitochondrial fission. *Nat. Struct. Mol. Biol.* 18, 20–26. doi: 10.1038/nsmb.1949

Migdal, I., Skibior-Blaszczyk, R., Heidorn-Czarna, M., Kolodziejczak, M., Garbiec, A., and Janska, H. (2017). AtOMA1 affects the OXPHOS system and plant growth in contrast to other newly identified ATP-independent proteases in Arabidopsis mitochondria. *Front. Plant Sci.* 8:1543. doi: 10.3389/fpls.2017.01543

Nakamura, Y., and Arakawa, H. (2017). Discovery of Mieap-regulated mitochondrial quality control as a new function of tumor suppressor p53. *Cancer Sci.* 108, 809–817. doi: 10.1111/cas.13208

Narendra, D. P., and Youle, R. J. (2011). Targeting mitochondrial dysfunction: role for PINK1 and Parkin in mitochondrial quality control. *Antioxid Redox. Signal.* 14, 1929–1938. doi: 10.1089/ars.2010.3799

Osellame, L. D., Singh, A. P., Stroud, D. A., Palmer, C. S., Stojanovski, D., Ramachandran, R., et al. (2016). Cooperative and independent roles of the Drp1 adaptors Mff, MiD49 and MiD51 in mitochondrial fission. *J. Cell Sci.* 129, 2170–2181. doi: 10.1242/jcs.185165

Osman, C., Wilmes, C., Tatsuta, T., and Langer, T. (2007). Prohibitins interact genetically with Atp23, a novel processing peptidase and chaperone for the F1Fo-ATP synthase. *Mol. Biol. Cell* 18, 627–635. doi: 10.1091/mbc.e06-09-0839

Otera, H., Wang, C., Cleland, M. M., Setoguchi, K., Yokota, S., Youle, R. J., et al. (2010). Mff is an essential factor for mitochondrial recruitment of Drp1 during mitochondrial fission in mammalian cells. *J. Cell Biol.* 191, 1141–1158. doi: 10.1083/jcb.201007152

Ozawa, K., Kuwabara, K., Tamatani, M., Takatsuji, K., Tsukamoto, Y., Kaneda, S., et al. (1999). 150-kDa Oxygen-regulated protein (ORP150) suppresses hypoxia-induced Apoptotic Cell Death*. *J. Biol. Chem.* 274, 6397–6404. doi: 10.1074/jbc.274.10.6397

Paradis, S., Charles, A. -L., Meyer, A., Lejay, A., Scholey, J. W., Chakfé, N., et al. (2016). Chronology of mitochondrial and cellular events during skeletal muscle ischemia-reperfusion. *Am. J. Physiol. Cell Physiol.* 310, C968-C982. doi: 10.1152/ajpcell.00356.2015

Pickles, S., Vigié, P., and Youle, R. J. (2018). Mitophagy and quality control mechanisms in mitochondrial maintenance. *Curr. Biol.* 28, R170-R185. doi: 10.1016/j.cub.2018.01.004

Pinti, M., Gibellini, L., Liu, Y., Xu, S., Lu, B., and Cossarizza, A. (2015). Mitochondrial Lon protease at the crossroads of oxidative stress, ageing and cancer. *Cell Mol. Life Sci.* 72, 4807–4824. doi: 10.1007/s00018-015-2039-3

Piper, H. M., Meuter, K., and Schäfer, C. (2003). Cellular mechanisms of ischemia-reperfusion injury. *Ann. Thorac. Surg.* 75, S644-S648. doi: 10.1016/S0003-4975(02)04686-6

R Core Team (2020). *R: A Language and Environment for Statistical Computing*. Vienna: R Foundation for Statistical Computing.

Rainbolt, T. K., Saunders, J. M., and Wiseman, R. L. (2015). YME1L degradation reduces mitochondrial proteolytic capacity during oxidative stress. *EMBO Rep.* 16, 97–106. doi: 10.15252/embr.201438976

Richards, J. G. (2011). Physiological, behavioral and biochemical adaptations of intertidal fishes to hypoxia. *J. Exp. Biol.* 214, 191–199. doi: 10.1242/jeb.047951

Richter, V., Singh, A. P., Kvansakul, M., Ryan, M. T., and Osellame, L. D. (2015). Splitting up the powerhouse: structural insights into the mechanism of mitochondrial fission. *Cell Mol. Life Sci.* 72, 3695–3707. doi: 10.1007/s00018-015-1950-y

Ryu, S. -W., Han, E. C., Yoon, J., and Choi, C. (2015). The mitochondrial fusion-related proteins Mfn2 and OPA1 are transcriptionally induced during differentiation of bone marrow progenitors to immature dendritic cells. *Mol. Cells* 38, 89–94. doi: 10.14348/molcells.2015.2285

Sanni, B., Williams, K., Sokolov, E. P., and Sokolova, I. M. (2008). Effects of acclimation temperature and cadmium exposure on mitochondrial aconitase and LON protease from a model marine ectotherm, *Crassostrea virginica*. *Comp. Biochem. Phys. C Toxicol. Pharmacol.* 147, 101–112. doi: 10.1016/j.cbpc.2007.08.005

Sepuri, N. B. V., Angireddy, R., Srinivasan, S., Guha, M., Spear, J., Lu, B., et al. (2017). Mitochondrial LON protease-dependent degradation of cytochrome c oxidase subunits under hypoxia and myocardial ischemia. *Biochim. Biophys. Acta Bioenerg.* 1858, 519–528. doi: 10.1016/j.bbabio.2017.04.003

Shanmughapriya, S., Rajan, S., Hoffman, N. E., Higgins, A. M., Tomar, D., Nemani, N., et al. (2015). SPG7 is an essential and conserved component of the mitochondrial permeability transition pore. *Mol. Cell* 60, 47–62. doi: 10.1016/j.molcel.2015.08.009

Singh, R., and Hartl, M. G. (2012). Fluctuating estuarine conditions are not confounding factors for the Comet assay assessment of DNA damage in the mussel *Mytilus edulis*. *Ecotoxicology* 21, 1998–2003. doi: 10.1007/s10646-012-0934-z

Sokolov, E. P., Markert, S., Hinzke, T., Hirschfeld, C., Becher, D., Ponsuksili, S., et al. (2019). Effects of hypoxia-reoxygenation stress on mitochondrial proteome and bioenergetics of the hypoxia-tolerant marine bivalve *Crassostrea gigas*. *J. Prot.* 194, 99–111. doi: 10.1016/j.jprot.2018.12.009

Sokolova, I. M. (2018). Mitochondrial adaptations to variable environments and their role in animals' stress tolerance. *Integr. Comp. Biol.* 58, 519–531. doi: 10.1093/icb/icy017

Sokolova, I. M., Sokolov, E. P., and Haider, F. (2019). Mitochondrial mechanisms underlying tolerance to fluctuating oxygen conditions: lessons from hypoxia-tolerant organisms. *Integr. Comp. Biol.* 59, 938–952. doi: 10.1093/icb/icz047

Solaini, G., Baracca, A., Lenaz, G., and Sgarbi, G. (2010). Hypoxia and mitochondrial oxidative metabolism. *Biochim. Biophys. Acta* 1797, 1171–1177. doi: 10.1016/j.bbabio.2010.02.011

Song, Z., Ghochani, M., McCaffery, J. M., Frey, T. G., and Chan, D. C. (2009). Mitofusins and OPA1 mediate sequential steps in mitochondrial membrane fusion. *Mol. Biol. Cell* 20, 3525–3532. doi: 10.1091/mbc.e09-03-0252

Spelbrink, J. N., Li, F. Y., Tiranti, V., Nikali, K., Yuan, Q. P., Tariq, M., et al. (2001). Human mitochondrial DNA deletions associated with mutations in the gene encoding Twinkle, a phage T7 gene 4-like protein localized in mitochondria. *Nat. Genet.* 28, 223–231. doi: 10.1038/90058

Storey, K. B. (1998). Survival under stress: molecular mechanisms of metabolic rate depression in animals. *South Afr. J. Zool.* 33, 55–64. doi: 10.1080/02541858.1998.11448454

Storey, K. B. (2002). Life in the slow lane: molecular mechanisms of estivation. *Comp. Biochem. Phys. A Mol. Integr. Physiol.* 133, 733–754. doi: 10.1016/S1095-6433(02)00206-4

Storey, K. B., and Storey, J. M. (2004). Metabolic rate depression in animals: transcriptional and translational controls. *Biol. Rev. Camp Philos. Soc.* 79, 207–233. doi: 10.1017/s1464793103006195

Sussarellu, R., Dudognon, T., Fabioux, C., Soudant, P., Moraga, D., and Kraffe, E. (2013). Rapid mitochondrial adjustments in response to short-term hypoxia and re-oxygenation in the Pacific oyster, *Crassostrea gigas*. *J. Exp. Biol.* 216, 1561–1569. doi: 10.1242/jeb.075879

Tian, L., Neuber-Hess, M., Mewburn, J., Dasgupta, A., Dunham-Snary, K., Wu, D., et al. (2017). Ischemia-induced Drp1 and Fis1-mediated mitochondrial fission and right ventricular dysfunction in pulmonary hypertension. *J. Mol. Med.* 95, 381–393. doi: 10.1007/s00109-017-1522-8

Twig, G., Elorza, A., Molina, A. J. A., Mohamed, H., Wikstrom, J. D., Walzer, G., et al. (2008). Fission and selective fusion govern mitochondrial segregation and elimination by autophagy. *EMBO J.* 27, 433–446. doi: 10.1038/sj.emboj.7601963

van den Thillart, G., van Lieshout, G., Storey, K., Cortesi, P., and Zwaan, A. de (1992). Influence of long-term hypoxia on the energy metabolism of the haemoglobin-containing bivalve *Scapharca inaequivalvis*: critical O2 levels for metabolic depression. *J. Comp. Physiol. B* 162, 297–304. doi: 10.1007/bf00260756

van der Bliek, A. M., Shen, Q., and Kawajiri, S. (2013). Mechanisms of mitochondrial fission and fusion. *Cold Spring Harb. Perspect. Biol.* 5:a011072. doi: 10.1101/cshperspect.a011072

Varvio, S. -L., Koehn, R. K., and Väinölä, R. (1988). Evolutionary genetics of the *Mytilus edulis* complex in the North Atlantic region. *Mar. Biol.* 98, 51–60. doi: 10.1007/BF00392658

Venkatesh, S., Lee, J., Singh, K., Lee, I., and Suzuki, C. K. (2012). Multitasking in the mitochondrion by the ATP-dependent Lon protease. *Biochim. Biophys. Acta* 1823, 56–66. doi: 10.1016/j.bbamcr.2011.11.003

Wang, J., and Zhou, H. (2020). Mitochondrial quality control mechanisms as molecular targets in cardiac ischemia–reperfusion injury. *Acta Pharm. Sin. B* 10, 1866–1879. doi: 10.1016/j.apsb.2020.03.004

Wang, Z., Jiang, H., Chen, S., Du, F., and Wang, X. (2012). The mitochondrial phosphatase PGAM5 functions at the convergence point of multiple necrotic death pathways. *Cell* 148, 228–243. doi: 10.1016/j.cell.2011.11.030

Wu, H., Xue, D., Chen, G., Han, Z., Huang, L., Zhu, C., et al. (2014). The BCL2L1 and PGAM5 axis defines hypoxia-induced receptor-mediated mitophagy. *Autophagy* 10, 1712–1725. doi: 10.4161/auto.29568

Xiao, X., Hu, Y., Quirós, P. M., Wei, Q., López-Otín, C., and Dong, Z. (2014). OMA1 mediates OPA1 proteolysis and mitochondrial fragmentation in experimental models of ischemic kidney injury. *Am. J. Physiol. Renal Physiol.* 306, F1318-F1326. doi: 10.1152/ajprenal.00036.2014

Yang, Y., Zhao, L., and Ma, J. (2017). Penehyclidine hydrochloride preconditioning provides cardiac protection in a rat model of myocardial ischemia/reperfusion injury via the mechanism of mitochondrial dynamics mechanism. *Eur. J. Pharmacol.* 813, 130–139. doi: 10.1016/j.ejphar.2017.07.031

Youle, R. J., and van der Bliek, A. M. (2012). Mitochondrial fission, fusion, and stress. *Science* 337, 1062–1065. doi: 10.1126/science.1219855

Yu, J., Wu, J., Xie, P., Maimaitili, Y., Wang, J., Xia, Z., et al. (2016). Sevoflurane postconditioning attenuates cardiomyocyte hypoxia/reoxygenation injury via restoring mitochondrial morphology. *PeerJ.* 4:e2659. doi: 10.7717/peerj.2659

Zheng, J., Croteau, D. L., Bohr, V. A., and Akbari, M. (2019). Diminished OPA1 expression and impaired mitochondrial morphology and homeostasis in Aprataxin-deficient cells. *Nucl. Acids Res.* 47, 4086–4110. doi: 10.1093/nar/gkz083

Zorov, D. B., Juhaszova, M., and Sollott, S. J. (2014). Mitochondrial reactive oxygen species (ROS) and ROS-induced ROS release. *Physiol. Rev.* 94, 909–950. doi: 10.1152/physrev.00026.2013

Zwaan, A. de, Cortesi, P., van den Thillart, G., Roos, J., and Storey, K. B. (1991). Differential sensitivities to hypoxia by two anoxia-tolerant marine molluscs: a biochemical analysis. *Mar. Biol.* 111, 343–351. doi: 10.1007/bf01319405

Conflict of Interest: The authors declare that the research was conducted in the absence of any commercial or financial relationships that could be construed as a potential conflict of interest.

Copyright © 2020 Steffen, Falfushynska, Piontkivska and Sokolova. This is an open-access article distributed under the terms of the Creative Commons Attribution License (CC BY). The use, distribution or reproduction in other forums is permitted, provided the original author(s) and the copyright owner(s) are credited and that the original publication in this journal is cited, in accordance with accepted academic practice. No use, distribution or reproduction is permitted which does not comply with these terms.

frontiers in Marine Science

ORIGINAL RESEARCH
published: 11 March 2021
doi: 10.3389/fmars.2021.600184

Biological Impact of Ocean Acidification in the Canadian Arctic: Widespread Severe Pteropod Shell Dissolution in Amundsen Gulf

Andrea Niemi[1], Nina Bednaršek[2,3], Christine Michel[1], Richard A. Feely[4], William Williams[5], Kumiko Azetsu-Scott[6], Wojciech Walkusz[1] and James D. Reist[1]*

[1] Fisheries and Oceans Canada, Freshwater Institute, Winnipeg, MB, Canada, [2] Southern California Coastal Water Research Project, Costa Mesa, CA, United States, [3] National Institute of Biology, Ljubljana, Slovenia, [4] NOAA Pacific Marine Environmental Laboratory, Seattle, WA, United States, [5] Fisheries and Oceans Canada, Institute of Ocean Sciences, Sidney, BC, Canada, [6] Fisheries and Oceans Canada, Bedford Institute of Oceanography, Dartmouth, NS, Canada

OPEN ACCESS

Edited by:
Xinping Hu, Texas A&M University Corpus Christi, United States

Reviewed by:
Elizabeth H. Shadwick, Oceans and Atmosphere (CSIRO), Australia
Silke Lischka, GEOMAR Helmholtz Centre for Ocean Research Kiel, Germany

***Correspondence:**
Andrea Niemi
Andrea.Niemi@dfo-mpo.gc.ca

Specialty section:
This article was submitted to Marine Biogeochemistry, a section of the journal Frontiers in Marine Science

Received: *28 September 2020*
Accepted: *19 February 2021*
Published: *11 March 2021*

Citation:
Niemi A, Bednaršek N, Michel C, Feely RA, Williams W, Azetsu-Scott K, Walkusz W and Reist JD (2021) Biological Impact of Ocean Acidification in the Canadian Arctic: Widespread Severe Pteropod Shell Dissolution in Amundsen Gulf. Front. Mar. Sci. 8:600184. doi: 10.3389/fmars.2021.600184

Increasing atmospheric CO_2, cold water temperatures, respiration, and freshwater inputs all contribute to enhanced acidification in Arctic waters. However, ecosystem effects of ocean acidification (derived from anthropogenic and/or natural sources) in the Arctic Ocean are highly uncertain. Zooplankton samples and oceanographic data were collected in August 2012–2014 and again in August 2017 to investigate the pelagic sea snail, *Limacina helicina*, a biological indicator of the presence and potential impact of acidified waters in the Canadian Beaufort Sea. Between 2012 and 2014 *L. helicina* abundance ranged from <1 to 1942 Ind. m^{-2}, with highest abundances occurring at stations on the Canadian Beaufort Shelf in 2012. The majority of individuals (66%) were located between 25 and 100 m depth, corresponding to upper halocline water of Pacific origin. In both 2014 and 2017, $>85\%$ of *L. helicina* assessed ($n = 134$) from the Amundsen Gulf region displayed shell dissolution and advanced levels of dissolution occurred at all stations. The severity of dissolution was not significantly different between 2014 and 2017 despite the presence of larger individuals that are less prone to dissolution, and higher food availability that can provide some physiological benefits in 2014. Corrosive water conditions were not widespread in the Amundsen Gulf at the time of sampling in 2017, and aragonite undersaturation ($\Omega_{ar} < 1$) occurred primarily at depths >150 m. The majority of dissolution was observed on the first whorl of the shells strongly indicating that damage was initiated during the larval stage of growth in May or early June when sea ice is still present. Evidence of shell modification was present in 2014, likely supported by abundant food availability in 2014 relative to 2017. The proportion of damaged *L. helicina* collected from coastal embayments and offshore stations is higher than in other Arctic and temperate locations indicating that exposure to corrosive waters is spatially widespread in the Amundsen Gulf region, and periods of exposure are extreme enough to impact the majority of the population.

Keywords: arctic, pteropods, *Limacina helicina*, ocean acidification, life history, sea ice

INTRODUCTION

The intrusion of CO_2 into the oceans is supporting the acidification of waters in regions around the Arctic (AMAP, 2018). Reduced summer sea ice provides a positive feedback to CO_2 uptake as ocean-air gas exchange is enhanced by the larger areas and longer periods of open water (Cross et al., 2018; Zhang et al., 2020). Additional factors, including water mass transport, low water temperatures, upwelling, riverine inflow, sea ice meltwater, and respiration, contribute to the acidification process and create regional differences in the extent and duration of low pH waters (Feely et al., 2008, 2016; Azetsu-Scott et al., 2010, 2014; Robbins et al., 2013; Qi et al., 2017). Biological effects of Arctic ocean acidification, derived from anthropogenic and/or natural sources (IPCC, 2011), are highly uncertain at individual to ecosystem scales.

With increasing acidity, the saturation state of calcium carbonate ($CaCO_3$) minerals (e.g., aragonite, calcite) decreases creating suboptimal conditions for the formation and maintenance of shells. The $CaCO_3$ saturation state (Ω) is the product of calcium and carbonate ion concentrations divided by the apparent stoichiometric solubility product for either aragonite or calcite (Feely et al., 2008). The calcium ion concentration is estimated from the salinity, and the carbonate ion concentration is calculated from measurements of the dissolved inorganic carbon (DIC) and total alkalinity (TA). With increased exposure to undersaturated conditions, physical damage (e.g., shell dissolution) as well as physiological costs, may impact feeding, growth or reproduction (Kroeker et al., 2013; Bednaršek et al., 2017a) of a variety of benthic and pelagic calcifying species and fish of high-latitudinal habitats, such as red king and Tanner crabs (Long et al., 2013), bivalves (Klok et al., 2014), and salmon (Ou et al., 2015; Williams et al., 2019).

The planktonic sea snail, *Limacina helicina*, is the most common shelled pteropod in arctic waters. This genus is found in all oceans, and is particularly abundant at high-latitudes (Bednaršek et al., 2012a). It produces an external aragonite shell (Bednaršek et al., 2012a). Aragonite is a metastable polymorph of calcium carbonate that is 1.5 times more soluble in seawater than are shells secreted from calcite (Fabry et al., 2008). Consequently, *L. helicina* is sensitive to dissolution under corrosive conditions and is a sensitive indicator of the presence and impacts of acidified water. In corrosive waters ($\Omega_{ar} < 1 \sim 1.5$ for pteropods; Bednaršek et al., 2019), *L. helicina* can be affected by varying degrees of shell dissolution (Bednaršek et al., 2012b) with concurrent declines in calcification (Comeau et al., 2010), decreases in growth (Lischka et al., 2011; Gardner et al., 2018) and, increased mortality (Busch et al., 2014; Bednaršek et al., 2017a).

Limacina helicina is known to occur on the Canadian Beaufort Shelf and in the Amundsen Gulf during the open-water period (Darnis et al., 2008; Walkusz et al., 2013). In this study *L. helicina* was selected as a biological indicator of ocean acidification in the Canadian Beaufort Sea. This region has relatively low Ω_{ar} compared to other ocean regions due to colder water temperatures and regional circulation patterns, especially the inflow of naturally corrosive, undersaturated Pacific halocline waters (Fabry et al., 2009; Mathis et al., 2015; Qi et al., 2017; Cross et al., 2018; Mol et al., 2018). Reductions in saturation state of halocline waters is occurring off (i.e., Canada Basin) and on the shelf (i.e., upper halocline) (Miller et al., 2014; Qi et al., 2017; AMAP, 2018; Cross et al., 2018; Mol et al., 2018) and increases in upwelling are expected to enhance localized and periodic undersaturation events as the halocline waters mix with and displace supersaturated surface waters (Mathis et al., 2012, 2015; Qi et al., 2017; Mol et al., 2018).

Given the current state of ocean acidification in Arctic waters, and expected declines in aragonite saturation, the objectives of this study were to, (1) identify the distribution of *L. helicina*, in offshore habitats of the Canadian Beaufort Sea and in coastal embayments of the Amundsen Gulf not previously assessed and, (2) evaluate the presence and extent of *L. helicina* shell dissolution in years with contrasting sea-ice opening (2014 and 2017) to identify potential environmental drivers of the observed dissolution. Earlier opening of the sea ice could affect multiple factors relevant to pteropod status including mixing of saturated and undersaturated waters, as well changes in the timing and availability of food. This study provides an initial assessment of the biological impact of acidified waters in the Canadian Beaufort Sea, comparing effects among different habitats of the Amundsen Gulf. We hypothesized that highest shell dissolution would be associated with areas of known upwelling, specifically Cape Bathurst and Cape Parry in the Anguniaqvia niqiqyuam Marine Protected Area, because of exposure to low Ω_{ar}.

MATERIALS AND METHODS

Study Area

Sampling locations varied between years due to sea-ice conditions and program priorities. Sampling on the Canadian Beaufort Shelf extended to slope waters in 2012 and to the west side of Banks Island in 2014 (**Figure 1**). In the Amundsen Gulf, sampling extended eastward to Dolphin and Union Strait and five different embayments were sampled (Franklin, Darnley, Wise and Walker bays, and Minto Inlet). Water depth in embayments (i.e., Minto Inlet and Franklin Bay) approaches 300 m in deep channels whereas water depth reaches over 600 m in the central basin of the Amundsen Gulf (**Figure 1**). The water column of the study area is stratified and dominated by three main layers depending on station location. Generally, at the time of the study, the nutrient-depleted surface Polar mixed layer (Salinity < 31.6; ca. 0–50 m depth) lays over the nutrient rich Pacific halocline ($32.4 <$ Salinity > 33.1; ca. 50–200 m), and the warm Atlantic layer (Salinity > 34) is located at depths >200 m (Carmack and MacDonald, 2002). The water layers are influenced by dynamic physical oceanographic processes including cross-shelf and localized upwelling and eddies (Williams and Carmack, 2008; Sévigny et al., 2015; Kirillov et al., 2016) as well as seasonally variable inflow of the Mackenzie River.

Shell dissolution results are compared among three areas (**Figure 1**) with different oceanographic conditions, (1) the recurrent upwelling areas of Cape Bathurst (CPB transect) and Cape Parry (CPY transect), (2) Dolphin and Union Strait (DOL

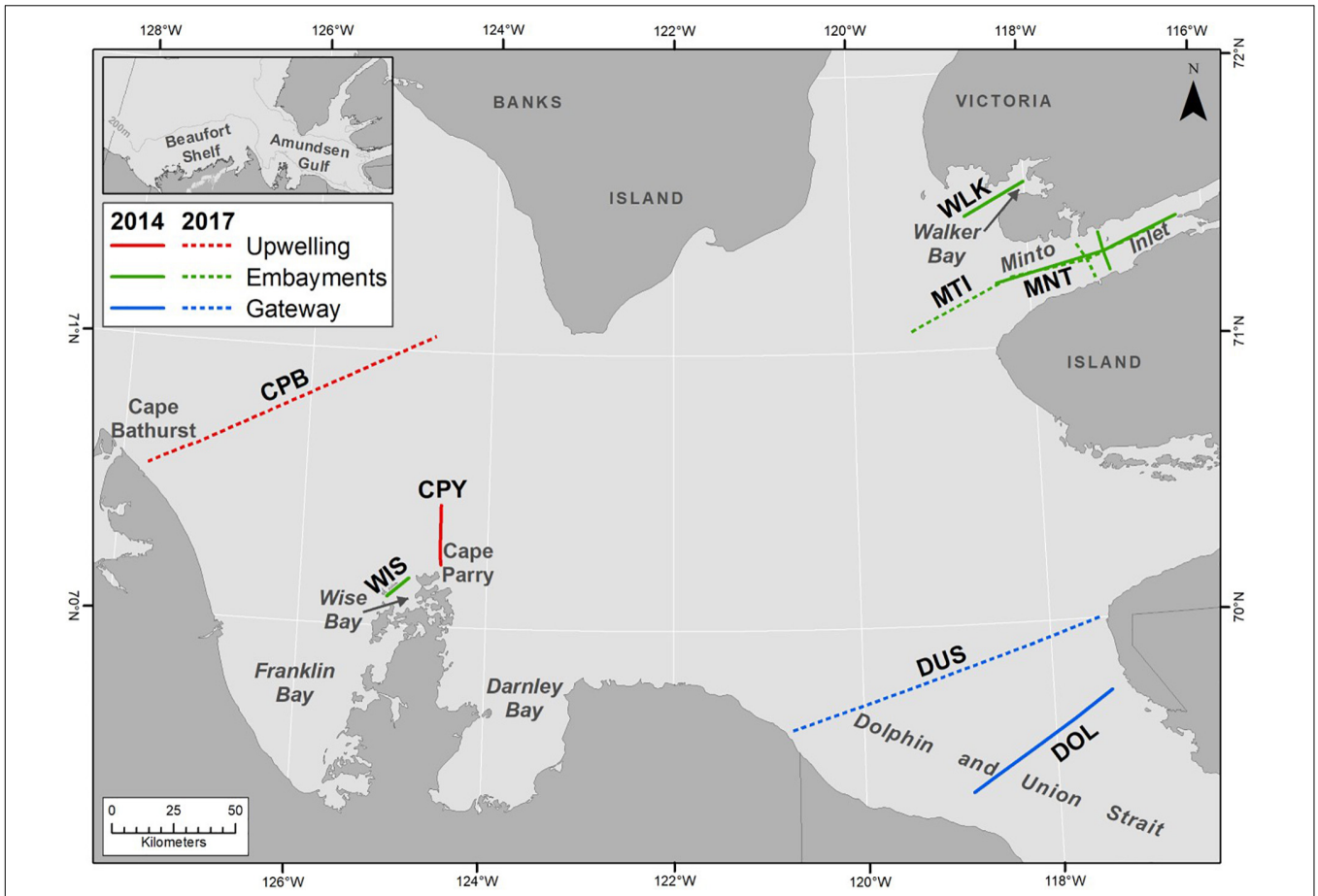


FIGURE 1 | Upwelling, embayment and gateway transects sampled in 2014 and 2017 to assess pteropod shell dissolution in the Amundsen Gulf.

and DUS transects), an oceanographic gateway between the Amundsen Gulf and the Coronation Gulf of the Kitikmeot region, and, (3) small embayments of Amundsen Gulf (Wise (WIS transect) and Walker Bay (WLK transect), and Minto Inlet (MNT and MTI transects) that have a semi-distinct circulation relative to the central gulf. During the ice-covered period, the upwelling and gateway areas are generally covered with seasonal pack ice whereas the small embayments are covered with seasonal land-fast ice.

Sampling and Analyses

From 2012 to 2014 sampling was conducted as part of the Beaufort Regional Environmental Assessment Marine Fishes program (BREA-MFP) and in 2017 work continued as part of the Canadian Beaufort Sea-Marine Ecosystem Assessment (CBS-MEA) program. In all years sampling occurred between the first week of August and mid-September. During this period there is no polar night (complete darkness). Twilight illumination increases at the end of August with daylight decreasing to ca. 13 h by mid-September.

Zooplankton sampling and CTD casts were conducted in all years along transects that ranged in depth from 20 m to a maximum of 1020 m on the lower slope of the Beaufort Shelf. At each station, physical oceanographic data (salinity, temperature, and dissolved oxygen) were collected with a rosette-mounted Seabird SBE-25 CTD and averaged over 1 m intervals. Herein we provide chlorophyll *a* (chl *a*) concentrations from 2014 to 2017, corresponding to the years of shell dissolution analyses. Total chl *a* was determined from discrete water samples collected with the rosette. Duplicate chl *a* subsamples were filtered onto 25-mm Whatman GF/F filters and extracted for 24 h in 90% acetone at 4°C in the dark, for fluorometric determination (10AU Turner Designs fluorometer), according to Parsons et al. (1984).

Sampling for DIC and TA occurred in 2017 only. DIC and TA samples were collected from the rosette in 250 ml borosilicate glass bottles and preserved with mercuric chloride following the best practices (Dickson et al., 2007). The DIC was determined using gas extraction and a coulometric titration with photometric endpoint detection (Johnson et al., 1985). The TA was measured by open-cell potentiometric titration with a full curve Gran end-point determination (Haradsson et al., 1997). All measurements were calibrated using Certified Reference Material supplied by A. Dickson, Scripps Institute of Oceanography. Precision of measurements for DIC and TA was better than 0.1 and 0.2%, respectively. The saturation state of seawater with respect to aragonite was calculated from the DIC and TA measurements

with the CO2SYS program (Lewis and Wallace, 1998) using the dissociation constants of Lueker et al. (2000) and the boron constant of Lee et al. (2010).

The vertical distribution of *L. helicina* was determined from zooplankton taxonomy samples (2012–2014, 2017) collected with a HYDRO-BIOS MultiNet, type Midi (0.25 m^2 aperture, 150 μm mesh) deployed to within 10 m of the bottom. All zooplankton sampling was conducted during the daytime hours, ca. 7 am to 6 pm local time. The net was hauled vertically and programmed to collect stratified samples from a maximum of five depth strata. Targeted strata were generally 0–25 m, 25–50 m, 50–100 m, 100–200 m, and >200 m. Samples from each depth stratum were preserved in a 4% buffered formaldehyde solution in seawater. Samples processed in the lab were split using a Folsom splitter (2012, Fisheries and Oceans Canada, Freshwater Institute) or beaker method (2013, 2014, Van Guelpen et al., 1982, Huntsman Marine Institute). *L. helicina* was identified from splits containing ca. 300 individuals or from larger fractions when rare. From the 2017 CBS-MEA zooplankton samples, only select stations from CPB, MTI and DUS transects were analyzed to inform the three oceanographic areas identified for shell dissolution comparisons (**Figure 1**). Abundances presented as Ind. m^{-2} have been integrated over the entire water column, to the maximum sampling depth at each station.

In 2014 and 2017, *L. helicina* was opportunistically collected from MultiNet or oblique Bongo net (500 μm mesh) tows at stations within the three focal areas. Individual specimens were carefully picked, without magnification, from fresh samples for dissolution analyses. The individual *L. helicina* were rinsed with fresh water to remove salts and stored frozen at −80°C until analysis. Such preservation eliminated any potential of shell dissolution during the storage.

Limacina helicina shell dissolution was assessed by scanning electron microscopy (SEM). Shells were prepared for SEM analysis by, (i) removal of abiogenic crystals from the shell surface, (ii) dehydration, (iii) mounting on the SEM stub, (iv) removal of the organic layer, and (v) sputter coating. Detailed procedures are provided in Bednaršek et al. (2012b), noting that a longer period (ca. 25 min versus 15–20 min) was needed to remove the organic layer from the larger individuals collected in the Amundsen Gulf. SEM images of shell microstructure were taken across the entire shell and a stage of dissolution [no dissolution, Type I, II, or III (**Table 1**)] was assigned to each individual based on the extent of pitting, cracks, and/or areas where aragonite crystals were absent, porous or dissolved. Shell size and the distribution of shell damage were recorded. Descriptions of each dissolution category and associated saturation condition from other studies are summarized in **Table 1**.

RESULTS

Environmental Conditions

There was at most a 1-month time difference in the start of sea-ice opening during the years when shell dissolution was assessed (2014 and 2017). In 2014 the day of sea-ice opening [DOO, last day sea-ice concentration drops below 80% before the first summer minimum (Peng et al., 2018); data from the Canadian Ice Service] occurred during the week following June 2nd and July 7th at Cape Bathurst and Minto Inlet, respectively. In 2017 the DOO was earlier relative to 2014, occurring during the week following May 8th and June 26th at the same respective locations. The sea-ice loss period occurs over a period of weeks in the Dolphin and Union Strait area, with bands of fractured ice persisting in the area. In contrast to Cape Bathurst and Minto Inlet, the DOO was slighter earlier in 2014 relative to 2017, estimated for the week following May 19 and May 29, respectively.

The water masses in Amundsen Gulf, that set the general physical and geochemical conditions, mostly originate from outside the gulf. The three dominant water masses (polar mixed layer, Pacific halocline and Atlantic layer) were present in each of the three areas where shell dissolution was assessed, and the water column structure was generally similar in 2014 and 2017 (**Figure 2**). Deeper waters flow in to the gulf, and extend into the embayments, from the Beaufort continental slope, and from the offshore Beaufort Gyre. The Atlantic-origin bottom waters transitioned to Pacific-origin water (**Figure 2**) around 200 m depth. The Pacific-origin waters included Pacific Winter Water, identified by the temperature minimum (∼−1.3°C) at ∼150 m deep (see **Figure 2** at salinity ∼33), and Pacific Summer Water, identified by the temperature maximum (∼−0.2°C) at ∼50 m deep (see **Figure 2** at salinity ∼31).

As is expected for the Arctic Ocean, surface waters in the three areas were generally freshened due to a combination of factors including river water input, ice melt, and the advection and mixing of lower salinity waters. In the Amundsen Gulf, the direct river inputs are from the relatively small rivers, such as the Hornaday River that flows into Darnley Bay. The large inflow from the Mackenzie River can also have a direct influence when summertime downwelling favorable winds occur on the shelf, pushing Mackenzie River water to the coast where it rapidly flows into the Amundsen Gulf in a boundary current. In 2017 surface water freshening is especially evident at Cape Bathurst (salinity as low as 26) where Mackenzie River plume waters are more frequently observed.

In 2017, aragonite saturation in the Amundsen Gulf ranged from 0.95 to 3.43 (average 1.47) in the surface mixed layer (0–50 m), 0.69–2.15 (average 1.09) in the Pacific halocline (50–200 m), and 0.72–1.40 (average 1.10) in waters deeper than 200 m (**Figure 3**), similar to summer measurements in Shadwick et al. (2011). Aragonite undersaturation occurred at upwelling, embayment and gateway stations, with 98% of undersaturated samples occurring between 100 and 600 m. Aragonite saturation state, over the entire water column, was correlated to dissolved oxygen concentrations at Cape Bathurst, Minto Inlet, and Dolphin and Union Strait ($r = 0.50, p < 0.01$).

Chlorophyll *a* integrated concentrations over the euphotic zone were, on average, four times higher in 2014 than 2017 at the stations in the Amundsen Gulf. In the three areas assessed for dissolution, integrated euphotic zone (maximum 100 m depth) chl *a* concentrations averaged 54.1 ± 35.5 mg m^{-2} and 14.1 ± 2.2 mg m^{-2} in 2014 and 2017, respectively. In 2014,

TABLE 1 | Descriptive features of pteropod shell dissolution stages and associated saturation conditions as described in Bednaršek et al. (2012b).

Dissolution Type	Shell Dissolution Features	Saturation Conditions
Type I	• First indices of slightly increased porosity • Aragonite crystals within the upper-prismatic layer affected by dissolution. 'Cauliflower heads' present	• In a small extent present in the natural environment • Widespread at decreased Ω_{ar} supersaturation
Type II	• Increased porosity • Dissolved patches more extensive and numerous • Prismatic layer partially or completely dissolved; crossed-lamellar layer exposed	• In small extent present at transitional saturation states; more common in undersaturated conditions
Type III	• Less compact crystal structure with compromised shell integrity and extreme frailness • Dissolution within crossed-lamellar layer with crystals thicker and chunkier	• At transitional Ω_{ar} conditions; larger, more extensive patches in Ω_{ar} undersaturated conditions, particularly with increased time of exposure

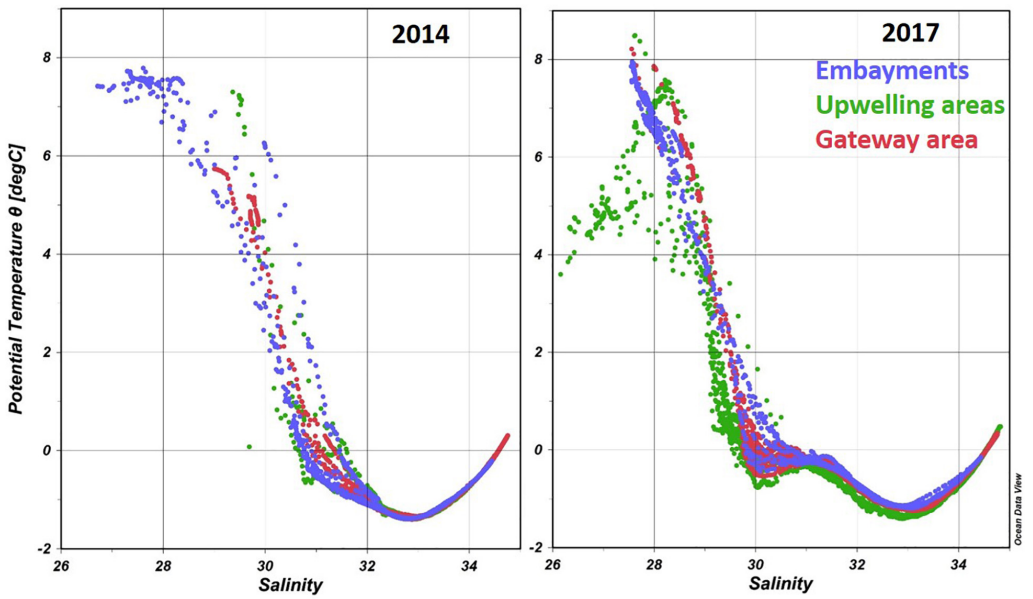


FIGURE 2 | Temperature-salinity plots for pteropod shell dissolution focal areas in the Amundsen Gulf in 2014 and 2017. Embayments include Wise and Walker bays, and Minto Inlet in 2014 and Minto Inlet in 2017.

the highest chl *a* concentrations occurred in the embayments, reaching 144.5 mg m^{-2} in Wise Bay. Primary production contributed to the observed Ω_{ar} supersaturation in the surface waters at the time of sampling and given that maximum values of Ω_{ar} correspond with peak summer open-water phytoplankton concentrations in Amundsen Gulf (Shadwick et al., 2013), it is expected that euphotic zone Ω_{ar} would have been higher in August/September 2014 than measured in August/September 2017 (**Figure 3**).

Limacina helicina Distribution

The abundance and distribution of *L. helicina* varied spatially and between years (2012–2014) on the Beaufort Shelf and in the Amundsen Gulf (**Figure 4**). These pteropods were found in all small embayments, i.e., Wise and Walker bays and Minto Inlet, sampled for the first time, indicating that this species is widely distributed in near-shore as well as offshore areas of the Canadian Beaufort Sea. Shelf waters contained the highest number of individuals in 2012 (water column integrated abundance, maximum 1942 Ind. m^{-2}). However, they were not found or occurred at abundances $\leq$5 Ind. m^{-2} during repeat sampling on the shelf in 2014. In the Amundsen Gulf, *L. helicina* was found primarily in surface waters (86% of individuals in 0–25 m strata) of offshore stations in 2013, whereas they were more broadly distributed in 2014 (**Figure 4**). In 2017, *L. helicina* abundance ranged from 0 to 625 Ind. m^{-2} at select stations from the Cape Bathurst, Minto Inlet and Dolphin and Union Strait transects (**Figure 3**), with the majority of individuals distributed between the 50–100 m (52 $\pm$ 35%) and the 100–200 m (32 $\pm$ 22%) depth strata. The abundance of *L. helicina* in 2017 was not correlated to Ω_{ar} but was weakly correlated to dissolved oxygen concentrations (Kendall's $\tau = 0.37$, $p = 0.01$).

Shell Size and Growth Pattern

The diameter of individuals assessed for shell dissolution averaged 932.2 $\pm$ 469.8 μm in 2014 and 732.1 $\pm$ 357.7 μm

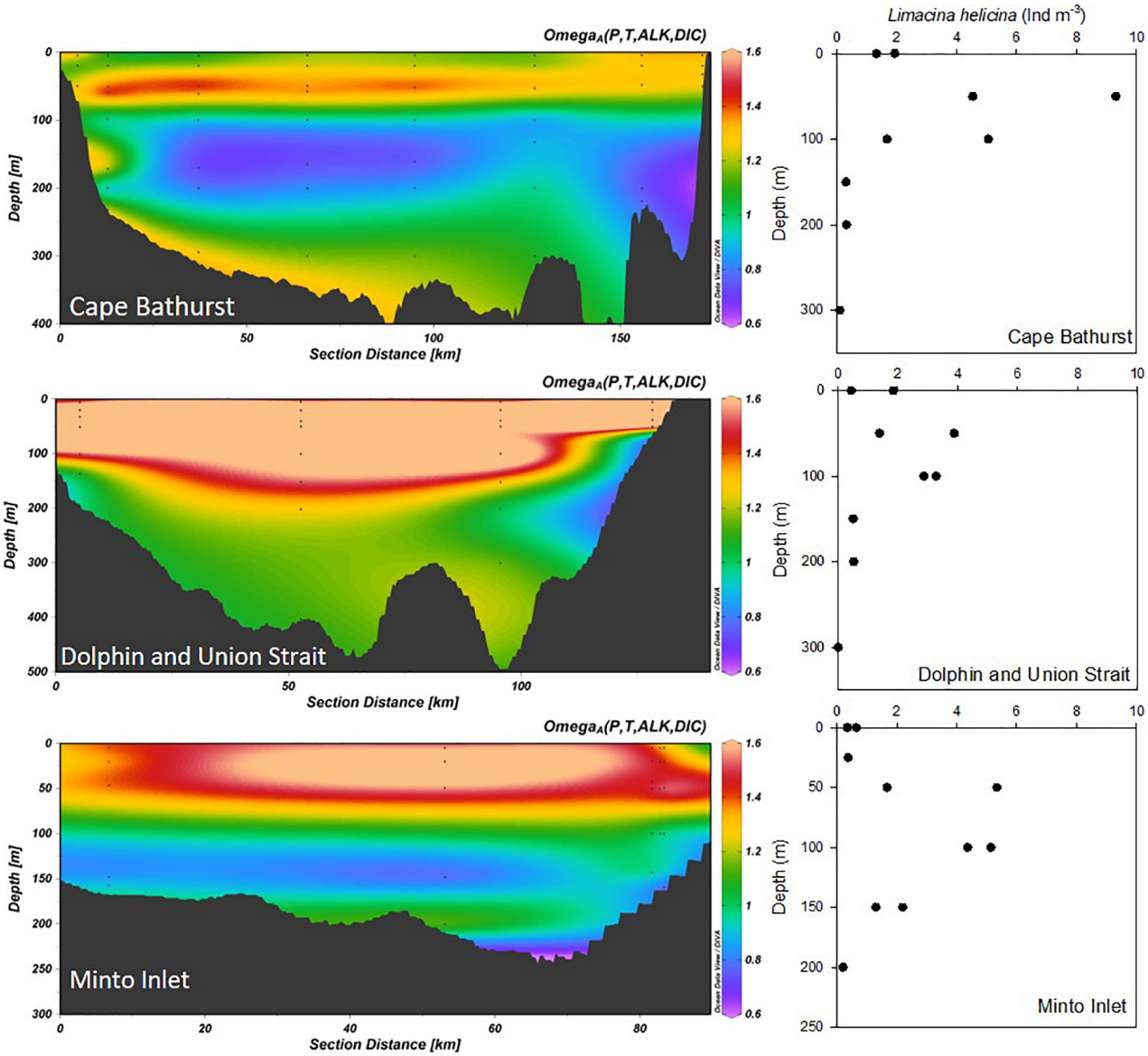


FIGURE 3 | Aragonite saturation (Omega) and *Limacina helicina* abundance (Ind. m^{-3}) at Cape Bathurst (CPB), Dolphin and Union Strait (DUS), and Minto Inlet (MTI) in 2017. Sections correspond to 2017 transects in **Figure 1**, running from the SW to NE.

in 2017. There was no significant difference in the size of individuals collected in August versus September suggesting limited growth during the study period (**Figure 5**). Among the individuals assessed for shell dissolution, there were two size classes present. Firstly, the majority of individuals was between 500 and 700 μm in size and can be considered juveniles, and secondly, adult individuals ≥1000 μm that were present in small numbers compared to the juveniles. The low numbers of adults present (<10% of examined individuals) during the August to September sampling period in 2014 and 2017, indicates that the peak of adults was probably earlier in the spring with spawning occurring in May–June, just prior to or at the time of sea-ice melt/break-up. A May/June spawning is consistent with larvae developing into the juveniles that were found in the August–September period.

Shell Dissolution

In both years, every individual assessed displayed some level of shell dissolution indicative of decreased supersaturation or undersaturated Ω_{ar} conditions. Levels of dissolution (**Table 1**) were similar in 2014 (Type I 17%, Type II 13%, Type III 70%) and 2017 (Type I 10.5%, Type II 18.5%, Type III 71%) (**Figure 6**). There were no individuals detected without shell dissolution but the shells were not entirely covered with dissolution damage; rather spots of the various Type I–III dissolutions were observed in discrete locations on the shells

Mean (SE) (%)	2012	2013	2014
0-25 m	23(6)	98(48)	50(17)
25-50 m	44(9)	0	47(22)
50-100 m	28(9)	0	1.4(1.3)
100-200 m	5(0.9)	0	0
>200 m	0.2(0.1)	2(1.8)	0.8(0.8)

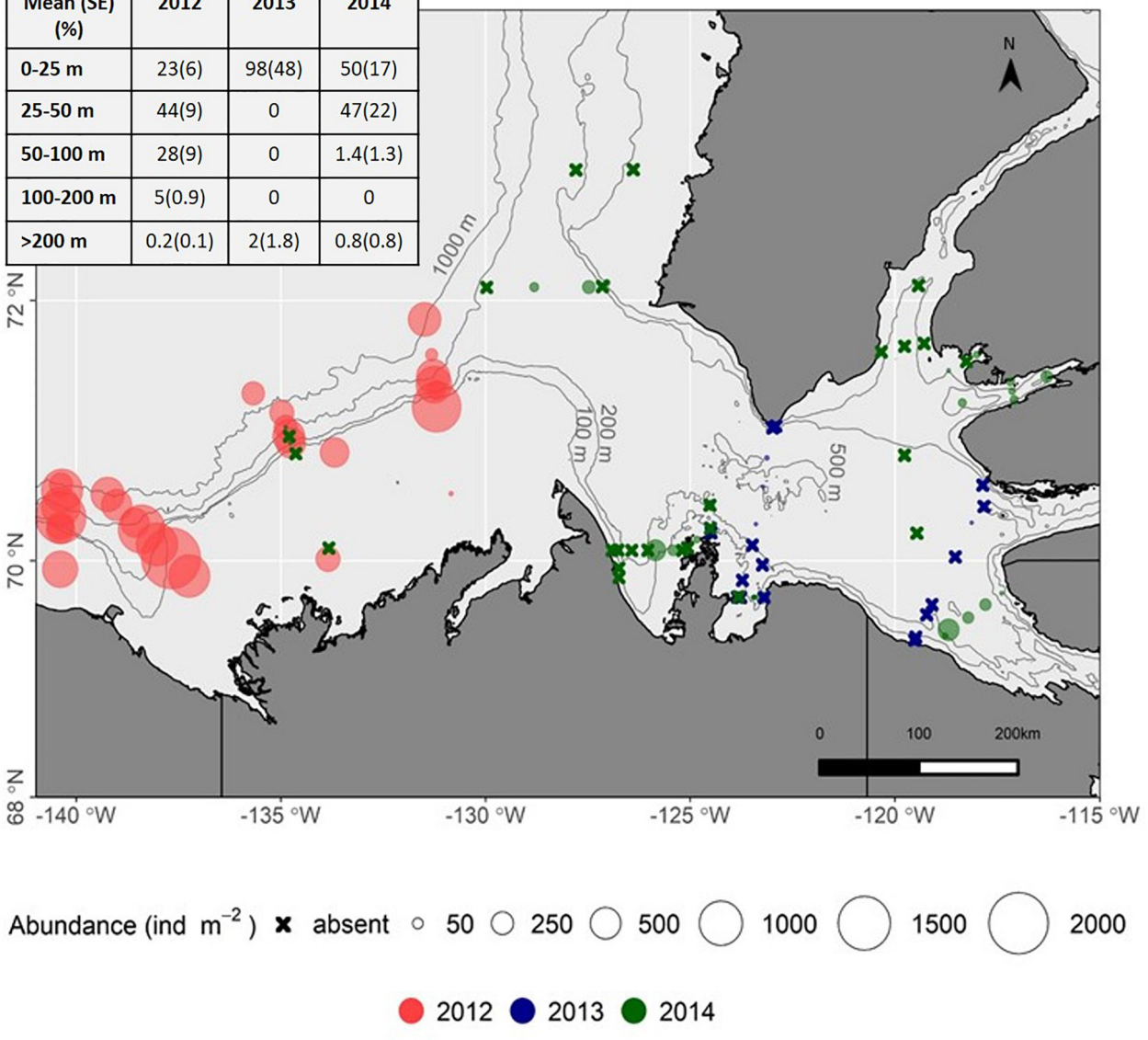


FIGURE 4 | Distribution of *Limacina helicina* on the Beaufort shelf and in the Amundsen Gulf, 2012–2014 (sampling depth integrated abundance indicated by circles, Ind m^{-2}). Inset table shows the distribution (%) of *Limacina helicina* present in sampled depth strata, all stations combined within a year.

(**Figure 7**). The high percentage of Type III dissolution indicates a very high incidence of the most severe dissolution present. The ratio of shells with dissolution linked to undersaturated ($\Omega_{ar} < 1$) conditions (i.e., Type II + Type III) was not significantly different between years (Wilcoxon, $p = 0.4$) and the extent of shell dissolution did not significantly vary between the upwelling ($n = 41$), embayment ($n = 60$), or Dolphin and Union Strait gateway ($n = 33$) areas (Kruskal–Wallis, $p = 0.4$–0.7; **Figure 8**). The ratio of individuals with Type II or Type III dissolution was not significantly correlated to Ω_{ar} measured at the time of sampling but the occurrence of Type II and Type III dissolution did increase with increasing average salinity (Kendall's $\tau = 0.40$, $p = 0.02$). Higher average salinity was found in the Pacific and Atlantic layers, relative to the surface polar mixed layer, corresponding to the seasonal occurrence of undersaturated Ω_{ar} conditions in the deeper layers.

For the 2014 sampling period, the majority of the most intense shell dissolution (Type III) occurred in Walker Bay (93% of individuals) followed by similar dissolution rates in Minto Inlet (80% of individuals) and Dolphin and Union Strait (83% of individuals), whereas only 40% of individuals from Cape Parry showed Type III dissolution. In 2014 the most severe dissolution occurred for samples collected between 25 and 80 m depth, and several individuals from Minto Inlet and Dolphin and Union Strait, collected from >150 m, also exhibited Type III dissolution.

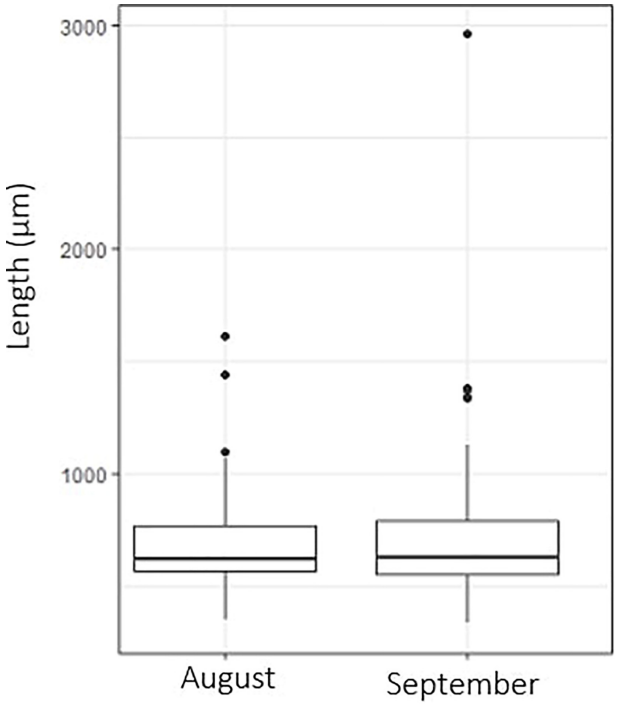


FIGURE 5 | *Limacina helicina* size range of individuals collected during August (n = 40) and September (n = 98) sampling dates. 2014 and 2017 samples are combined.

In 2017 the highest occurrence of Type III dissolution (93% of individuals) was found at stations along the Cape Bathurst transect, followed by Dolphin and Union Strait (63% of individuals) and Minto Inlet (70% individuals) stations. General trends for Type II and Type III dissolution seem to indicate more dissolved shells in the inlets/nearshore areas, with a gradual decrease in dissolution intensity with increasing distance from shore. Similar to 2014, water depths ca. 25–50 m had the highest occurrence of Type II and Type III dissolution although stations along the Dolphin and Union Strait transect had the majority (12 of 18 individuals) of Type III dissolution at depths >100 m.

Distribution of Shell Dissolution

The most significant extent of shell dissolution damage occurred on the first whorl (**Figure 7**) across stations and individuals, although smaller extents of dissolution were also scattered around the shell, in particular at the growing edge. The extent of overall shell dissolution is likely linked to the various degrees of Ω_{ar} throughout the pteropod life history, with the growing edge dissolution linked to the most recent $\Omega_{ar} < 1$ conditions. The most intense shell dissolution on the first whorl most likely relates to when Ω_{ar} conditions were lower during the period of sea-ice melt when early life stages were present. Given that the timing of sea-ice melt likely coincides with the spawning event, the low Ω_{ar} conditions at the time of spawning would explain the most extensive dissolution on the larval shell around the first whorl.

In 2014 there was evidence of shell structural modification in the adults, but not in juveniles (**Figure 9**). Shell modification was focused around the first whorl, and was evident as a crystalline regrowth overlaid on surface areas of dissolution. This structural modification in the shape of crystalline regrowth was unstructured and homogenous, and in this, distinctively different than the typical prismatic and underlying cross-lamellar microstructure of pteropod shells (Sato-Okoshi et al., 2010). Shell modification was evident on few individuals, in particular where the shell dissolution was most severe, and not across all the adults. In 2017, there was no or extremely limited evidence of shell modification, again only in the adult group, indicating some plastic responses in adults, but not in the juveniles.

DISCUSSION

Abundance and Growth of the Pteropod *Limacina helicina*

Limacina helicina was widely distributed across the study area including coastal embayments. Although the occurrence of dissolution was severe and consistent in 2014 and 2017, *L. helicina* abundance was variable between years (**Figure 4**). Highest abundance was observed on the Beaufort shelf (1948 Ind. m^{-2}) within the range previously observed during cross-shelf transects in the same region (0 to >10,000 Ind. m^{-2}, Walkusz et al., 2010; Smoot and Hopcroft, 2017). Abundances measured in the Amundsen Gulf were similar to later season (September/October) sampling reported by Darnis et al. (2008). Abundances recorded on the Beaufort shelf are among the highest recorded since the 1950s (Bednaršek et al., 2012a), identifying the Beaufort Sea as an important pteropod hotspot across all ocean regions. Despite the sensitivity of polar waters to ocean acidification, dense populations of *Limacina* spp. also occur in Antarctic waters (e.g., Bednaršek et al., 2012c; Nishizawa et al., 2016) and it is evident that *L. helicina* life history is well adapted to the short productive season on Arctic shelves.

Limacina helicina abundance was not correlated with aragonite saturation (Ω_{ar}) at the time of sampling in 2017, and further comparative studies are needed to adequately assess population level responses to annual acidification conditions in the Beaufort Sea. Hypoxia or oxygen minimum zones (dissolved oxygen < 3.5 ml l^{-1}) have not been detected in the study area suggesting that the positive correlation between *L. helicina* abundance and dissolved oxygen may be a result of food web linkages between zooplankton and primary producers. During the study period, *L. helicina* was distributed primarily in the upper 50 m of the water column (**Figure 4**) where a subsurface chl *a* maximum is usually located shortly after ice break up, and persists at lower concentrations under post-bloom conditions (Martin et al., 2010). Chlorophyll *a* integrated concentrations over the euphotic zone were, on average, four-times higher in 2014 than 2017 at the stations in the Amundsen Gulf. Oceanographic and sea-ice conditions, and shelf upwelling can drive interannual variations in primary production of this order of magnitude in the Canadian Beaufort Sea, with cascading impacts on

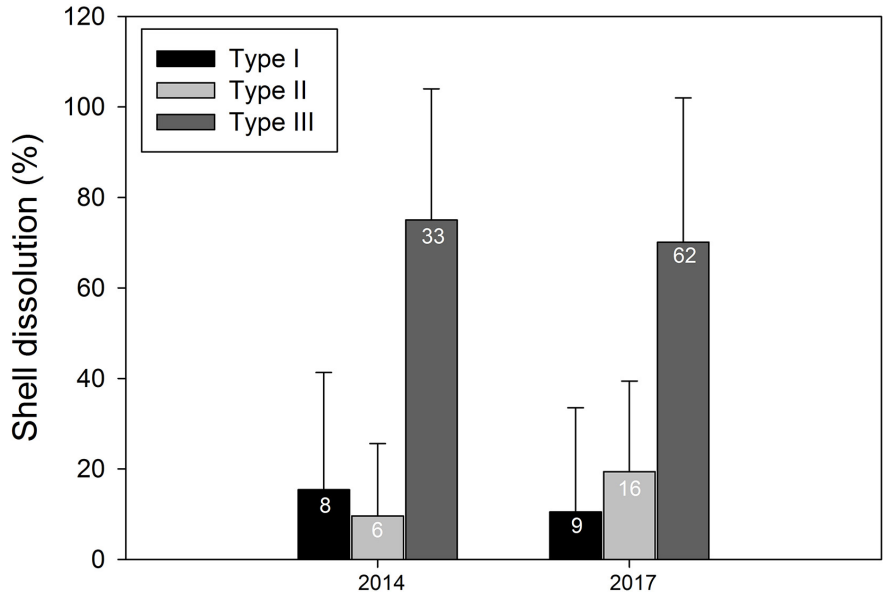


FIGURE 6 | *Limacina helicina* dissolution severity in 2014 and 2017. Sample size (n) indicated on each bar.

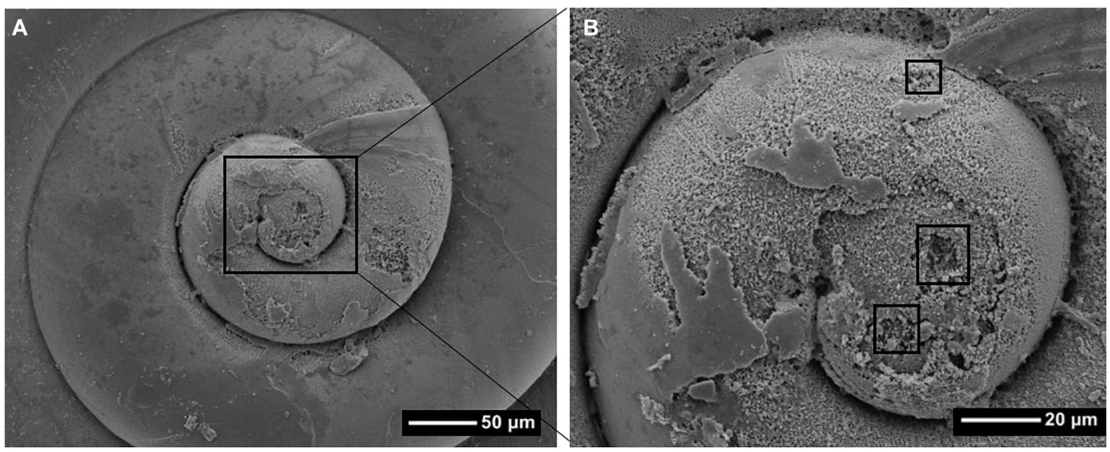


FIGURE 7 | Scanning Electron Microscope (SEM) image **(A)** showing the distribution of dissolution on a *Limacina helicina* shell collected near Cape Bathurst in 2017. In panel **(B)**, damage on the first whorl is shown in greater detail with the squares indicating deeper-protruding Type III dissolution.

food availability to zooplankton grazers (Tremblay et al., 2011). Despite the higher summer chl *a* concentrations in 2014, *L. helicina* abundance was ca. four times lower in 2014 than the 2017 stations assessed (**Figure 3**). However, individuals were on average larger in 2014 suggesting that the additional summer resources supported enhanced growth but the later ice opening in 2014 may have impeded recruitment, possibly due to a timing mismatch between critical life stages and needed resources.

Growth estimates suggest that *L. helicina* in Amundsen Gulf likely spawned in May or June, coinciding with the sea-ice algal bloom (Riedel et al., 2008; Różańska et al., 2009) and possible onset of an under-ice or ice-edge phytoplankton bloom in June (Mundy et al., 2009), or early phytoplankton bloom as observed in years of early sea ice retreat (Sallon et al., 2011). The sea-ice algal bloom provides abundant and critical food (Michel et al., 1996; Kohlbach et al., 2016) to support high growth rates following spawning in surface waters. The consumption of ice algae specifically by pteropods has been identified through food web studies in the high Arctic and in Antarctica (Kohlbach et al., 2016, 2018). Pteropods are reported to feed opportunistically, switching from phytoplankton to mobile prey post-bloom (Gilmer and Harbison, 1991; Pasternak et al., 2017). Open-water isotopic signatures of *L. helicina* from the Beaufort Shelf and Amundsen Gulf indicate pelagic feeding closely linked to phytoplankton ($\delta^{13}C$ −25.5 ± 0.79 ‰, $\delta^{15}N$ 9.09 ± 0.8 ‰; Stasko et al., 2017; A. Ehrman unpublished data), in agreement with evidence of an efficient transfer from primary producers to pelagic grazers in this region (Forest et al., 2011; Sallon et al., 2011). Around Cape

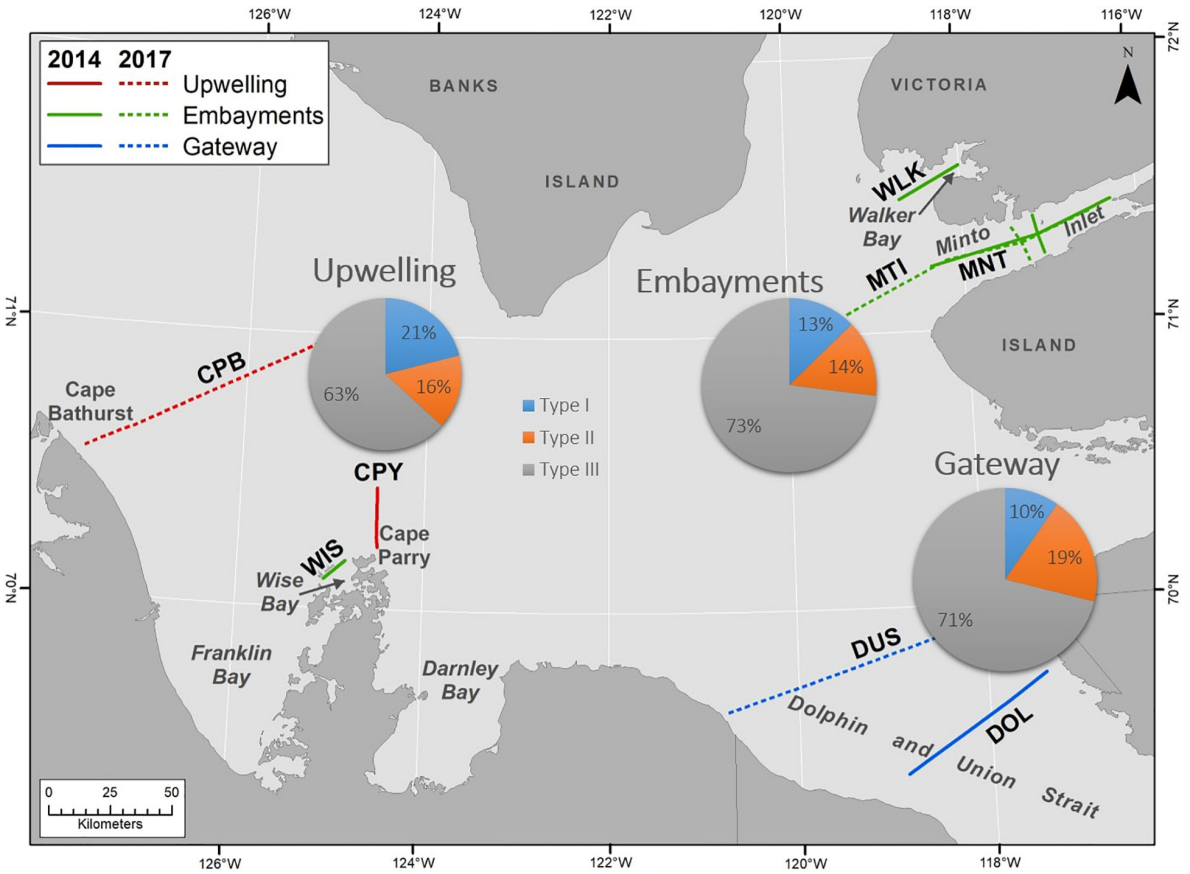


FIGURE 8 | Distribution and extent of *Limacina helicina* shell dissolution (Type I, II, or III) in the Amundsen Gulf. 2014 and 2017 data are combined for upwelling, embayment and gateway areas.

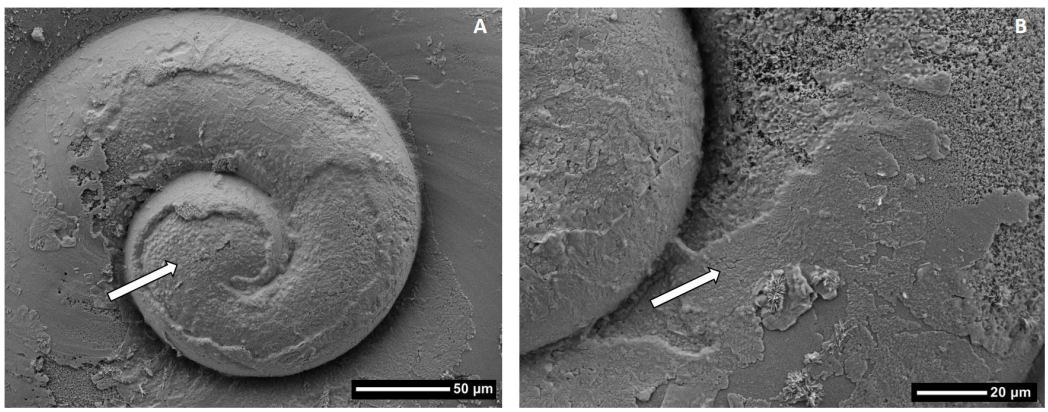


FIGURE 9 | Shell modification on adult *Limacina helicina* collected from Minto Inlet in 2014, **(A)** observed on recessed area of shell with severe underlying dissolution of the surface shell layer, **(B)** the modification on the shell is of crystalline origin, yet it appears unstructured relative to typical pteropod shell microstructure. The white arrow points to the recessed area **(A)** and shell modification layer **(B)**.

Parry, *L. helicina* was trophically positioned more closely to phytoplankton than the key zooplankton grazer, *Calanus hyperboreus* (Niemi et al., 2020). It is likely that herbivory provides the highest quality diet to support *L. helicina* energy requirements and consequently, tolerance to less favorable ($\Omega_{ar} < 1$) conditions.

The low number and size of adults observed in August indicates a potential mass adult mortality event after spring

spawning. In the study years, the population may have been comprised of a single cohort that overwinters and has a longevity of a single year. The life span of *L. helicina* is location dependent and has been reported to range from one to over 3 years (Kobayashi, 1974; Gannefors et al., 2005; Bednaršek et al., 2012c; Wang et al., 2017). Reliance on the sea-ice algal and spring phytoplankton blooms, in the oligotrophic Beaufort Sea, may only support a single cohort which increases the susceptibility of the population to the effects of ocean acidification. Contingent on key factors such as stratification and mixing which shape the response of primary producers to on-going changes (Ardyna et al., 2011; Blais et al., 2017), the lengthening of the open-water period due to sea-ice loss and potential increased occurrence of fall phytoplankton blooms (Ardyna et al., 2014) may benefit cohort recruitment and population resilience.

Exposure

Spawning in May or June indicates that larval and juvenile stages are primarily exposed to spring and summer Ω_{ar} conditions whereas adults are more exposed to Ω_{ar} conditions at overwintering depths and under the sea ice. In the Amundsen Gulf, *L. helicina* occurred primarily in the top 50 m (**Figure 4**) comprised of corrosive waters of Pacific origin and Arctic surface waters freshened by sea-ice melt and Mackenzie River inflow. This water column habitat is thus susceptible to seasonal and episodic $\Omega_{ar} < 1$ conditions as well as enhanced acidification (i.e., lower aragonite undersaturation) from the intrusion of anthropogenic CO_2 via air-sea exchange and lateral transport. We hypothesized that dissolution would be highest in areas of upwelling, a known source of undersaturated waters for shelf environments (Feely et al., 2008; Schulz et al., 2019). However, the extent of dissolution was not significantly different between the upwelling, embayment and gateway areas (**Figure 8**), with 83% (2014) and 89.5% (2017) of individuals assessed displaying advanced (Type II or III) shell dissolution. Severe dissolution occurred at every station, indicating that Ω_{ar} dissolution thresholds were surpassed across the entire region. The prevalence of dissolution in the Amundsen Gulf is the highest reported from the natural environment including all the high-latitudinal habitats reported so far (Bednaršek et al., 2012c, 2014). The proportion of individuals affected by $\Omega_{ar} < 1$ conditions in the Amundsen Gulf is significantly higher than in the Gulf of Alaska or the Bering Sea (Bednaršek et al., submitted). Amundsen Gulf *Limacina* is also more impacted than those in regions of known change. For example, in the California Current ecosystem it is estimated that the incidence of severe shell dissolution due to anthropogenic ocean acidification has doubled in near shore habitats since pre-industrial times yet, on average, only 53% of onshore individuals and 24% of offshore individuals were found to have severe dissolution damage (Bednaršek et al., 2014).

The extent of dissolution was positively correlated with salinity, supporting the notion that Pacific-origin waters are a stronger driver of dissolution than the freshened surface water with reduced buffering capacity (Yamamoto-Kawai et al., 2009; Qi et al., 2017; Zhang et al., 2020). Water conditions near the surface and around the coast (i.e., in embayments) of Amundsen Gulf are variable due to wind forcing of the ocean. Upwelling and downwelling is particularly evident at Cape Bathurst where it is topographically amplified (Williams and Carmack, 2008), and undersaturated Pacific-origin water can reach the surface during upwelling events. Due to the large response of the coastal ocean to wind forcing, synoptic, seasonal and inter-annual variation in the winds over Amundsen Gulf and the adjacent Beaufort Shelf and Slope will be strong drivers of coastal conditions, including salinity, dissolved nutrients and aragonite saturation state.

Flow along the coast, continental shelf and slope has the potential to move water from far away to the gulf. For example, surface drifters during a downwelling favorable autumn storm traveled along the coast from the Canadian Beaufort Shelf to Darnley Bay in a few days (B. Williams unpublished data). Therefore, pteropods sampled in Amundsen Gulf could have been brought to the gulf by surface oceanic flows and thus conditions experienced on the Beaufort Shelf or slope may have also contributed to their shell dissolution. Exposure to Ω_{ar} undersaturated conditions may also be affected by tidal mixing which has the potential to mix the low-omega, high-nutrient Pacific-origin water with surface waters in shallow regions where tidal flows are amplified. In the study area, regions of potential tidal mixing include the continental shelves on either side of the mouth of Amundsen Gulf, including Cape Bathurst, as well as Dolphin and Union Strait (McLaughlin et al., 2004; Hannah et al., 2009).

Ocean acidification impacts are related to both the magnitude and duration of $\Omega_{ar} < 1$ exposure in natural environments. Pteropod responses are likely based on recurring patterns of exposure, and experimental work suggests that natural populations can exist near their physiological tolerance limit (Bednaršek et al., 2017b). From the 1970s to 2010, the aragonite saturation state has been variable and declining in the upper halocline and deep waters of the Canada Basin and Beaufort Sea (Miller et al., 2014; Zhang et al., 2020). Within this period of decline, an annual (2007–2008) study found that the upper halocline waters of the Amundsen Gulf, between 50 and 150 m depth, had $\Omega_{ar} < 1$ conditions for the entire year except for a short reprieve during June/July (Shadwick et al., 2011). This seasonal persistence of $\Omega_{ar} < 1$ conditions in the halocline is similar to seasonal estimates from the Pacific Arctic region (Cross et al., 2018). In this study, Ω_{ar} conditions (**Figure 3**) were similarly distributed as Shadwick et al. (2011), with saturated conditions occurring in waters <50 m and $\Omega_{ar} < 1$ occurring in the halocline and Atlantic water masses. This indicates that Ω_{ar} undersaturated conditions continue to be a persistent characteristic of the Pacific layer in the Amundsen Gulf and are the result of both natural and anthropogenic sources for the increased CO_2 and lower aragonite saturation state (Ko and Quay, 2020; Zhang et al., 2020). Ongoing monitoring is needed to identify how the saturation state is changing over time and how susceptible species and life stages in the Amundsen Gulf will be affected, with respect to physical damage, physiological impairments, or mortality, by both the magnitude of $\Omega_{ar} < 1$ exposure, and the rate at which Ω_{ar} decreases in coming years.

Although *L. helicina* was located primarily above 50 m at the time of sampling (94–98%, **Figure 4**), it is expected that

L. helicina undergoes diel migrations (Lalli and Gilmer, 1989), suggesting $\Omega_{ar} < 1$ exposure in the Pacific layer on a daily basis. This regular exposure could explain dissolution at the growing edge. The surface mixed layer represents an important portion of habitat without undersaturated conditions. However, the surface mixed layer can be below or near $\Omega_{ar} = 1$ for periods of weeks, in the study area, as biological processes lower Ω_{ar} by up to 0.3 in the spring and fall (Chierici et al., 2011) and wind events bring undersaturated waters to the surface episodically. In the central Arctic Ocean, widespread Ω_{ar} undersaturation of surface waters is projected within the next decade due to elevated atmospheric CO_2 (Steinacher et al., 2009) and a similar response to elevated atmospheric CO_2 is projected for the Amundsen Gulf given seasonal warming and freshening as well as lower alkalinity which limits the region's capacity to buffer saturation decreases (Shadwick et al., 2013). Consequently, the surface mixed layer habitat will likely become increasingly corrosive with respect to the magnitude and duration of $\Omega_{ar} < 1$, thereby increasing pteropod exposure over daily and annual cycles.

Severe dissolution on the first whirl (**Figure 7B**) indicates that larval pteropods are vulnerable to dissolution, and $\Omega_{ar} < 1$ conditions due to the remineralization of organic matter can occur when larvae are present in the Amundsen Gulf (Shadwick et al., 2011). Pteropods may over winter at depths >50 m, similar to key copepod species in the Amundsen Gulf (Darnis and Fortier, 2014). Consequently, hatching and metamorphosis to the juvenile stage could all occur within the undersaturated Pacific halocline where the corrosive Pacific Winter Water resides (Qi et al., 2017; Zhang et al., 2020). Recent under-ice sampling in Darnley Bay, an Amundsen Gulf embayment, measured $\Omega_{ar} < 1$ near 100 m depth in April, with values 3 m below the sea ice averaging only 1.2 (B. Williams, unpublished data). A dissolution threshold of $\Omega_{ar} = 1.2$ has been identified for pteropods from other ocean regions (Bednaršek et al., 2019). Although dissolution thresholds have not been experimentally determined for the Amundsen Gulf, it is possible that the larval shell with a thinner or incompletely formed organic layer, is vulnerable to $\Omega_{ar} > 1$ conditions such that seasonal or even short-term exposure of larvae while at depth, or feeding near the ice, may affect pteropod recruitment and thus interannual variability in *L. helicina* abundance. Annual measurements of Ω_{ar} in the Pacific halocline and surface mixed layer are needed from the study area to advance our understanding of seasonal and episodic occurrences of $\Omega_{ar} < 1$ conditions.

Shell Modification

This study provides evidence of shell modification in adult individuals sampled in 2014. A homogenous yet unstructured crystalline layer was deposited in patches over damaged areas on the surface of only the first whorl (**Figure 9**). The shell modification occurred at locations with the most severe dissolution suggesting that the pteropods may have initiated such a process to build a more mechanically durable shell by reducing the porosity or increasing its thickness. Beaufort Sea pteropods naturally build thinner shells in comparison to those from other high latitude habitats (Bednaršek et al., submitted), that could become even thinner under severe dissolution as observed in this study. More detailed study of the crystalline layer is required to describe the modifications at the nano- or micro-scale of shell building. The unstructured and homogenous layer deposited on the pteropod shells may be similar to reduced crystallographic control of shell formation observed for mussels grown under acidification conditions (Fitzer et al., 2016).

Shell modification as a repair mechanism has been previously documented for *L. helicina* in Arctic waters, characterized as a thickening of the shell caused by the deposition of newly formed aragonite on the inside of the shell (Lischka et al., 2011; Peck et al., 2016, 2018). In this study it is not possible to determine the seasonal timing of the shell modification. It could have occurred during the growth of early life stages, in which case the structurally homogenous crystalline deposition represents a plastic repair response to unfavorable conditions (i.e., lower Ω_{ar} in the spring). Alternatively, it could have deposited under more favorable conditions later in the summer, in which case the unstructured layer would qualify as shell regrowth.

The observed shell modification in 2014, and not in 2017, implies that such deposition is not always feasible and is likely dependent on suitable environmental conditions (Seibel et al., 2012). In 2014, summer phytoplankton concentrations may have provided an adequate, accessible energy source to support shell modification in the absence of other metabolic costs such as reproduction. The absence of the unstructured layer on juvenile shells suggests that energy may have been allocated to growth rather than repair. The shell modification may confer some resilience for damaged adults, and as such potentially allows for higher fitness and better reproductive success.

The shell modification appears to be more of a plastic response to the external environmental conditions, rather than an adaptive response. It is evident that the observed depositions on the first whorl do not constitute a process that would have entirely eliminated the shell dissolution apparent at the individual or population level. Given that the shell modification process was only observed in a few adult individuals at spatially limited locations (e.g., Minto Inlet), regrowth could be an energetically expensive process that organisms will not initiate unless the severity of dissolution is at a critical stage. Nevertheless, under future conditions with lower aragonite undersaturation, it is possible that energy devotion to shell modifications may become more common, or necessary, for survival. If shell modifications are not possible in juveniles, future decreases in aragonite undersaturation may lead to death in early life stages with population and ecosystem consequences.

Ecosystem Linkages

In the Amundsen Gulf, the prevalence and location of dissolution on shells identifies *Limacina* spp. as a sensitive biological indicator of $\Omega_{ar} < 1$ exposure on a seasonal basis, as proposed for other ocean regions (Bednaršek et al., 2012b, 2017b). Longer periods of monitoring are required to use *Limacina* spp. as a population-level indicator of anthropogenic ocean acidification (IPCC, 2011) given that variability in abundance and distribution is likely related to multiple factors, including the timing of sea-ice opening. Due to ongoing anthropogenic contributions of atmospheric CO_2, it is predicted that Arctic *L. helicina* will

be unable to form shells by the end of the century (IPCC SRES A2 scenario; Comeau et al., 2012). Tolerances to current rapid rates of change and cumulative perturbation of marine ecosystems are not well known such that the future survival of *Limacina* spp. is uncertain despite apparent resilience to perturbations in the Earth's carbon cycle over evolutionary timescales (Peijnenburg et al., 2019).

Pteropods contribute significantly to marine biogeochemical cycling (Pasternak et al., 2017; Buitenhuis et al., 2019) and are components of zooplankton, fish and seabird diets. On the Canadian Beaufort Shelf, *L. helicina* was found to be a small component of demersal Arctic Cod diets (Majewski et al., 2016), specifically age one fish (Walkusz et al., 2013). *L. helicina* can be a significant part of Pacific Salmon diets, with *L. helicina* abundance explaining 30% of the variability of pink salmon survival in Prince William Sound (Doubleday and Hopcroft, 2015). Dense populations of pteropods in nearshore waters may provide critical energy for juvenile fish. Recent nearshore fish collections in Darnley Bay (2018 and 2019) and near Sachs Harbour (Banks Island, 2018) found *Limacina* sp. in the stomachs of Arctic Char (n = 4; <1–13% of diet items), Starry Flounder (n = 2; 30–93% of diet items) and Greenland Cod (n = 1; 98% of diet items) (D. McNicholl, unpublished data). These results provide evidence that that *L. helicina* are used by Arctic nearshore fishes with different life histories and feeding strategies. The high numbers in some stomachs (100–160 individuals) suggest that *Limacina* sp. may be available in dense populations for nearshore fishes in coastal areas of Amundsen Gulf and are consumed, at minimum, opportunistically. Further studies are needed to assess nearshore distributions of *L. helicina*, e.g., the occurrence of swarms, and the accessibility of pteropods to key life stages of fishes and other predators.

Limacina helicina, as a model indicator, provides direct evidence of combined effects of anthropogenic ocean acidification and other natural processes on aragonite saturation state in the Amundsen Gulf that surpasses other ocean regions. An understanding of food web and other ecosystem consequences (e.g., carbon cycling) requires regional, inter-annual assessments to determine, among other things, pteropod recruitment success relative to the aragonite saturation state over annual cycles. In addition, *L. helicina* provides a warning for other biota with life stages and structures sensitive to calcium carbonate dissolution. Of particular concern is the direct effect of ocean acidification on larval otoliths of near and off-shore fishes in the study area, especially Arctic Cod. *L. helicina*, when treated as a biological indicator, can be an important component of monitoring, and modeling wider ecosystem change related to anthropogenic CO_2 intrusion or cumulative effects of changing atmospheric-ice-ocean interactions.

CONCLUSION

The prevalence of dissolution observed in this study indicates the presence of $\Omega_{ar} < 1$ conditions under the sea ice when larval *L. helicina* were present, as well as during open-water periods when dissolution occurred along the growing edge of shells. The timing of sea-ice opening may be a key driver of the interannual variability in *L. helicina* abundance. However, sea ice and resource variability did not appear to affect the wide spread occurrence and observed severity of dissolution. The seasonal persistence of $\Omega_{ar} < 1$ in the Pacific layer suggests that this *L. helicina* habitat in the Amundsen Gulf is largely corrosive and populations possibly function near their tolerance level such that some adult individuals can initiate shell modifications upon the most severe dissolution conditions if resources are adequate and available. The energetic balance between shell modification and growth needs to be better understood to determine the response of *L. helicina* populations to variable environmental conditions, and the follow-on consequences for the ecosystem.

Past occurrence and recent trends in shell dissolution are not currently known for the Beaufort Shelf or the Amundsen Gulf. It is expected that dissolution has been augmented by enhanced acidification over the last 20 years. Changes in Pacific winter waters are currently driving the rapid expansion (i.e., area and depth) of ocean acidification in the western Arctic Ocean (Qi et al., 2017) and the Canadian Beaufort shelf remains vulnerable to changes in the volume and freshwater content of Pacific waters, upwelling of undersaturated waters, as well as the intrusion of atmospheric CO_2 over a lengthening open-water period. Given the ecological importance of *L. helicina* in the Canadian Arctic, the inclusion of *L. helicina* as an indicator species in offshore and coastal programs will inform the severity of biological responses to ongoing ocean acidification. The severe occurrence of dissolution indicates that other vulnerable species and life stages should also be assessed.

DATA AVAILABILITY STATEMENT

The raw data supporting the conclusions of this article will be made available by the authors, without undue reservation.

AUTHOR CONTRIBUTIONS

AN conducted the field work and drafted the manuscript. AN and WWa contributed the zooplankton data. NB contributed the SEM analyses. WWi contributed the oceanographic data. CM and KA-S contributed the chemistry data. JR was the BREA program lead and RF led program collaborations, both provided expert input. All authors participated in the writing of the manuscript and approved the submitted version.

FUNDING

AN, CM, and KA-S were supported by the Aquatic Climate Change Adaptation Services Program, Fisheries and Oceans Canada. RF was supported by the NOAA Ocean Acidification Program and the Pacific Marine Environmental Laboratory. This is contribution number 5128 from the NOAA Pacific Marine Environmental Laboratory. Financial support for the

BREA-MFP and CBS-MEA programs was provided by Fisheries and Oceans Canada (Rotational Fund, Northern Contaminants Program, Marine Conservation Targets, International Governance Strategy), Environmental Studies Research Fund (NRCan), the Beaufort Regional Environmental Assessment (AANDC), and the Beaufort Regional Strategic Environmental Assessment (CIRNAC).

ACKNOWLEDGMENTS

We acknowledge the excellent support of the captains and crew of the *FV Frosti* and the staff at Frosti Fishing Inc. We appreciate the leadership of all the chief scientists during the BREA-MFP and CBS-MEA. Field collections were supported by J. Eert, H. Maclean, S. Zimmerman, M. Dempsey, G. Meisterhans, R. Hussherr, S. MacPhee, A. Sastri, K. Young, and A. Timmerman. Coastal fish collection was supported by community monitors from Paulatuk and Sachs Harbour NT. A. Burt processed the 2017 pteropod taxonomy samples, S. Punshon performed DIC and TA analyses and J. Charette prepared the omega database. E. Ipsen, A. Ehrman, and M. Ouellette provided manuscript support. We are grateful to the Inuvialuit Game Council for supporting this project and for providing valuable input to the study design and logistics.

REFERENCES

AMAP (2018). *AMAP Assessment 2018: Arctic Ocean Acidification*. Tromsø: Arctic Monitoring and Assessment Programme (AMAP), vi+187.

Ardyna, M., Babin, M., Gosselin, M., Devred, E., Rainville, L., and Tremblay, J. −É (2014). Recent Arctic Ocean sea ice loss triggers novel fall phytoplankton blooms. *Geophys. Res. Lett*. 41, 6207–6212. doi: 10.1002/2014GL061047

Ardyna, M., Gosselin, M., Michel, C., Poulin, M., and Tremblay, J. -É (2011). Environmental forcing of phytoplankton community structure and function in the Canadian High Arctic: contrasting oligotrophic and eutrophic regions. *Mar. Ecol. Prog. Ser*. 442, 37–47. doi: 10.3354/meps09378

Azetsu-Scott, K., Clarke, A., Falkner, K., Hamilton, J., Jones, E. P., Lee, C., et al. (2010). Calcium carbonate saturation states in the waters of the Canadian Arctic Archipelago and the Labrador Sea. *J. Geophys. Res*. 115:C11021. doi: 10.1029/2009JC005917

Azetsu-Scott, K., Starr, M., Mei, Z.-P., and Granskog, M. (2014). Low calcium carbonate saturation state in an Arctic inland sea having large and varying fluvial inputs: the Hudson Bay system. *J. Geophys. Res. Oceans* 119, 6210–6220. doi: 10.1002/2014JC009948

Bednaršek, N., Feely, R. A., Howes, E. L., Hunt, B. P. V., Kessouri, F., León, P., et al. (2019). Systematic review and meta-analysis toward synthesis of thresholds of ocean acidification impacts on calcifying pteropods and interactions with warming. *Front. Mar. Sci.* 6:227. doi: 10.3389/fmars.2019.00227

Bednaršek, N., Feely, R. A., Reum, J. C. P., Peterson, B., Menkel, J., Alin, S., et al. (2014). *Limacina helicina* shell dissolution as an indicator of declining habitat suitability owing to ocean acidification in the California Current Ecosystem. *Proc. R. Soc. B Biol. Sci*. 281:20140123. doi: 10.1098/rspb.2014.0123

Bednaršek, N., Feely, R. A., Tolimieri, N., Hermann, A. J., Siedlecki, S. A., Waldbusser, G. G., et al. (2017a). Exposure history determines pteropod vulnerability to ocean acidification along the US West Coast. *Sci. Rep*. 7:4526. doi: 10.1038/s41598-017-03934-z

Bednaršek, N., Klinger, T., Harvey, C. J., Weisberg, S., McCabe, R. M., Feely, R. A., et al. (2017b). New ocean, new needs: application of pteropod shell dissolution as a biological indicator for marine resource management. *Ecol. Indic*. 76, 240–244. doi: 10.1016/j.ecolind.2017.01.025

Bednaršek, N., MoŽina, J., Vogt, M., O'Brien, C., and Tarling, G. A. (2012a). The global distribution of pteropods and their contribution to carbonate and carbon biomass in the modern ocean. *Earth Syst. Sci. Data* 4, 167–186. doi: 10.5194/essd-4-167-2012

Bednaršek, N., Naish, K., Feely, R. A., Hauri, C., Kimoto, K., Hermann, A. J., et al. (submitted). Integrated assessment of the risks to ocean acidification in the Northern high latitudes: regional comparison of exposure, sensitivity and adaptive capacity of pelagic calcifiers. *Front. Mar. Sci.*

Bednaršek, N., Tarling, G. A., Bakker, D. C. E., Fielding, S., Cohen, A., Kuzirian, A., et al. (2012b). Description and quantification of pteropod shell dissolution: a sensitive bioindicator of ocean acidification. *Glob. Change Biol.* 18, 2378–2388. doi: 10.1111/j.1365-2486.2012.02668.x

Bednaršek, N., Tarling, G. A., Fielding, S., and Baker, D. C. E. (2012c). Population dynamics and biogeochemical significance of *Limacina helicina Antarctica* in the Scotia sea (Southern Ocean). *Deep Sea Res. II* 59–60, 105–116. doi: 10.1016/j.dsr2.2011.08.003

Blais, M., Ardyna, M., Gosselin, M., Dumont, D., Bélanger, S., Éric, J., et al. (2017). Contrasting interannual changes in phytoplankton productivity and community structure in the coastal Canadian Arctic Ocean. *Limnol. Oceanogr*. 62, 2480–2497. doi: 10.1002/lno.1058

Buitenhuis, E. T., Le Quéré, C., Bednaršek, N., and Schiebel, R. (2019). Large contribution of pteropods to shallow $CaCO_3$ export. *Global Biogeochem. Cycles* 33, 458–468. doi: 10.1029/2018GB006110

Busch, D. S., Maher, M., Thibodeau, P., and McElhany, P. (2014). Shell condition and survival of Puget Sound pteropods are impaired by ocean acidification conditions. *PLoS One* 9:e105884. doi: 10.1371/journal.pone.0105884

Carmack, E. C., and MacDonald, R. W. (2002). Oceanography of the Canadian shelf of the Beaufort Sea: a setting for marine life. *Arctic* 55, 29–45.

Chierici, M., Fransson, A., Lansard, B., Miller, L. A., Mucci, A., Shadwick, E., et al. (2011). The impact of biogeochemical processes and environmental factors on the calcium carbonate saturation state in the circumpolar flaw lead in the Amundsen Gulf, Arctic Ocean. *J. Geophys. Res*. 116:C00G09. doi: 10.1029/2011JC007184

Comeau, S., Gattuso, J.-P., Nisumaa, A.-M., and Orr, J. (2012). Impact of aragonite saturation state changes on migratory pteropods. *Proc. R. Soc. B* 279, 732–738. doi: 10.1098/rspb.2011.0910

Comeau, S., Jefferee, R., Teyssié, J.-L., and Gattuso, J.-P. (2010). Response of the Arctic pteropod *Limacina helicina* to projected future environmental conditions. *PLoS One* 5:e11362. doi: 10.1371/journal.pone.0011362

Cross, J. N., Mathis, J. T., Pickart, R. S., and Bates, N. R. (2018). Formation and transport of corrosive water in the Pacific Arctic region. *Deep Sea Res.* 152, 67–81. doi: 10.1016/j.dsr2.2018.05.020

Darnis, G., Barber, D. G., and Fortier, L. (2008). Sea ice and the onshore-offshore gradient in pre-winter zooplankton assemblages in southeastern Beaufort Sea. *J. Mar. Syst*. 74, 994–1011. doi: 10.1016/j.jmarsys.2007.09.003

Darnis, G., and Fortier, L. (2014). Temperature, food and the seasonal vertical migration of key arctic copepods in the thermally stratified Amundsen Gulf (Beaufort Sea. Arctic Ocean). *J. Plankton Res.* 36, 1092–1108. doi: 10.1093/plankt/fbu035

Dickson, A. G., Sabine, C. L., and Christian, J. R. (eds). (2007). *Guide to Best Practices for Ocean CO2 Measurements*. PICES Special Publication. Sidney, NSW: North Pacific Marine Science Organization, Vol. 3, 191.

Doubleday, A. J., and Hopcroft, R. R. (2015). Interannual patterns during spring and late summer of larvaceans and pteropods in the coastal Gulf of Alaska, and their relationship to pink salmon survival. *J. Plankton Res*. 37, 134–150. doi: 10.1093/plankt/fbu092

Fabry, V. J., McClintock, J. B., Mathis, J. T., and Grebmeier, J. M. (2009). Ocean acidification at high latitudes: the bellwether. *Oceanography* 22, 160–171. doi: 10.5670/oceanog.2009.105

Fabry, V. J., Seibel, B. A., Feely, R. A., and Orr, J. C. (2008). Impacts of ocean acidification on marine fauna and ecosystem processes. *ICES J. Mar. Sci*. 65, 414–432. doi: 10.1093/icesjms/fsn048

Feely, R. A., Alin, S., Carter, B., Bednaršek, N., Hales, B., Chan, F., et al. (2016). Chemical and biological impacts of ocean acidification along the west coast of North America. *Estuar. Coast. Shelf Sci.* 183, 260–270. doi: 10.1016/j.ecss.2016.08.043

Feely, R. A., Sabine, C. L., Hernandez-Ayon, J. M., Ianson, D., and Hales, B. (2008). Evidence for upwelling of corrosive "acidified" water onto the continental shelf. *Science* 320, 1490–1492. doi: 10.1126/science.1155676

Fitzer, S., Chung, P., Maccherozzi, F., Dhesi, S. S., Kamenos, N. A., Phoenix, V. R., et al. (2016). Biomineral shell formation under ocean acidification: a shift from order to chaos. *Sci. Rep.* 6:21076. doi: 10.1038/srep21076

Forest, A., Tremblay, J. -É, Gratton, Y., Martin, J., Gagnon, J., Darnis, G., et al. (2011). Biogenic carbon flow pathways in the planktonic food web of the Amundsen Gulf (Arctic Ocean): a synthesis of field measurements and inverse modeling analyses. *Prog. Oceanogr.* 91, 410–436. doi: 10.1016/j.pocean.2011.05.002

Gannefors, C., Böer, M., Kattner, G., Graeve, M., Eiane, K., Gulliksen, B., et al. (2005). The Arctic sea butterfly *Limacina helicina*: lipids and life strategy. *Mar. Biol.* 147, 169–177. doi: 10.1007/s00227-004-1544-y

Gardner, J., Manno, C., Bakker, D. C. E., Peck, V. L., and Tarling, G. A. (2018). Southern Ocean pteropods at risk from ocean warming and acidification. *Mar. Biol.* 165:8. doi: 10.1007/s00227-017-3261-3

Gilmer, R. W., and Harbison, G. R. (1991). Diet of *Limacina helicina* (Gastropoda: thecosomata) in Arctic waters in midsummer. *Mar. Ecol. Prog. Ser.* 77, 125–134.

Hannah, C. G., Dupont, F., and Dunphy, M. (2009). Polynyas and tidal currents in the Canadian Arctic Archipelago. *Arctic* 62, 83–95.

Haradsson, C., Anderson, L. G., Hassellöv, M., Hulth, S., and Olsson, K. (1997). Rapid high-precision potentiometric titration of alkalinity in ocean and sediment pore waters. *Deep Sea Res. Part I* 44, 2031–2044.

IPCC (2011). "Workshop report of the intergovernmental panel on climate change workshop on impacts of ocean acidification on marine biology and ecosystems," in *IPCC Working Group II Technical Support Unit*, eds C. B. Field, V. Barros, T. F. Stocker, D. Qin, K. J. Mach, G.-K. Plattner, et al. (Stanford, CA: Carnegie Institution), 164.

Johnson, K. M., King, A. E., and Mc Sieburth, M. (1985). Coulometric TCO_2 analyses for marine studies: an introduction. *Mar. Chem.* 16, 61–82.

Kirillov, S., Dmitrenko, I., Tremblay, B., Gratton, Y., Barber, D., and Rysgaard, S. (2016). Upwelling of Atlantic water along the Canadian Beaufort Sea continental slope: favorable atmospheric conditions and seasonal and interannual variations. *J. Clim.* 29, 4509–4523. doi: 10.1175/jcli-d-15-0804.1

Klok, C., Wijsman, J. W. M., Kaag, K., and Foekema, E. (2014). Effects of CO_2 enrichment on cockle shell growth interpreted with a dynamic energy budget model. *J. Sea Res.* 94, 111–116. doi: 10.1016/j.seares.2014.01.011

Ko, Y., and Quay, P. (2020). Origin and accumulation of an anthropogenic CO_2 and ^{13}C Suess effect in the Arctic Ocean. *Global Biogeochem. Cycle* 34:e2019GB006423. doi: 10.1029/2019GB006423

Kobayashi, H. A. (1974). Growth cycle and related vertical distribution of the thecosomatous pteropod *Spiratella ("Limacina") helicina* in the central Arctic Ocean. *Mar. Biol.* 26, 295–301. doi: 10.1007/BF00391513

Kohlbach, D., Graeve, M., Lange, B., David, C., Peeken, I., and Flores, H. (2016). The importance of ice algae-produced carbon in the central Arctic Ocean ecosystem: food web relationships revealed by lipid and stable isotope analyses. *Limnol. Oceanogr.* 61, 2027–2044. doi: 10.1002/lno.10351

Kohlbach, D., Graeve, M., Lange, B., David, C., Schaafsma, F. L., van Franeker, J. A., et al. (2018). Dependency of Antarctic zooplankton species on ice algae-produced carbon suggests a sea ice-driven pelagic ecosystem during winter. *Glob. Change Biol.* 24, 4667–4681. doi: 10.1111/gcb.14392

Kroeker, K. J., Kordas, R. L., Crim, R., Hendriks, I. E., Ramajo, L., Singh, G. S., et al. (2013). Impacts of ocean acidification on marine organisms: quantifying sensitivities and interaction with warming. *Glob. Change Biol.* 19, 1884–1896. doi: 10.1111/gcb.12179

Lalli, C. M., and Gilmer, R. W. (1989). *Pelagic Snails: The Biology of Holoplanktonic Gastropod Mollusks*. Stanford, CA: Stanford University Press.

Lee, K., Kim, T. −W., Byrne, R. H., Millero, F. J., Feely, R. A., and Liu, Y. −M. (2010). The universal ratio of boron to chlorinity for the North Pacific and North Atlantic oceans. *Geochim. Cosmochim. Acta* 74, 1801–1811. doi: 10.1016/j.gca.2009.12.027

Lewis, E., and Wallace, D. W. R. (1998). *Program Developed for CO_2 Systems Calculations, ORNL/CDIAC-105, Carbon Dioxide Info. Anal. Cent.* Oak Ridge, TN: Oak Ridge National Laboratory.

Lischka, S., Büdenbender, J., Boxhammer, T., and Riebesell, U. (2011). Impact of ocean acidification and elevated temperatures on early juveniles of the polar shelled pteropod *Limacina helicina*: mortality, shell degradation, and shell growth. *Biogeosciences* 8, 919–932. doi: 10.5194/bg-8-919-2011

Long, W. C., Swiney, K. M., Harris, C., Page, H. N., and Foy, R. J. (2013). Effects of Ocean Acidification on Juvenile Red King Crab (*Paralithodes camtschaticus*) and Tanner Crab (*Chionoecetes bairdi*) Growth, Condition, Calcification, and Survival. *PLoS One* 8:e60959. doi: 10.1371/journal.pone.0060959

Lueker, T. J., Dickson, A. G., and Keeling, C. D. (2000). Ocean pCO_2 calculated from dissolved inorganic carbon, alkalinity, and equations for K1 and K2: validation based on laboratory measurements of CO_2 in gas and seawater at equilibrium. *Mar. Chem.* 70, 105–119. doi: 10.1016/S0304-4203(00)00022-0

Majewski, A. R., Walkusz, W., Lynn, B. R., Atchison, S., Eert, J., and Reist, J. D. (2016). Distribution and diet of demersal Arctic Cod, *Boreogadus saida*, in relation to habitat characteristics in the Canadian Beaufort Sea. *Polar Biol.* 39, 1087–1098. doi: 10.1007/s00300-015-1857-y

Martin, J., Tremblay, J. E., Gagnon, J., Tremblay, G., Lapoussiere, A., Jose, C., et al. (2010). Prevalence, structure and properties of subsurface chlorophyll maxima in Canadian Arctic waters. *Mar. Ecol. Prog. Ser.* 412, 69–84. doi: 10.3354/meps08666

Mathis, J. T., Byrne, R. H., McNeil, C. L., Pickart, R. P., Juranek, L., Moore, G. W. K., et al. (2012). Storm-induced upwelling of high pCO_2 waters onto the continental shelf of the western Arctic Ocean and implications for carbonate mineral saturation states. *Geophys. Res. Lett.* 39:L07606. doi: 10.1029/2012GL051574

Mathis, J. T., Cross, J. N., Evans, W., and Doney, S. C. (2015). Ocean acidification in the surface waters of the Pacific-Arctic boundary regions. *Oceanography* 28, 122–135. doi: 10.5670/oceanog.2015.36

McLaughlin, F. A., Carmack, E. C., Ingram, R. G., Williams, W. J., and Michel, C. (2004). "Oceanography of the northwest passage," in *The Sea: The Global Coastal Ocean*, Vol. 14B, eds R. Robinson and K. H. Brink (Cambridge, MA: Harvard University Press), 1211–1236.

Michel, C., Legendre, L., Ingram, R. G., Gosselin, M., and Levasseur, M. (1996). Carbon budget of ice algae under first-year ice: evidence of a significant transfer to zooplankton grazers. *J. Geophys. Res.* 101, 18345–18360. doi: 10.1029/96JC00045

Miller, L. A., Macdonald, R. W., McLaughlin, F., Mucci, A., Yamamoto-Kawai, M., Giesbrecht, K. E., et al. (2014). Changes in the marine carbonate system of the western Arctic: patterns in a rescued data set. *Polar Res.* 33:20577. doi: 10.3402/polar.v33.20577

Mol, J., Thomas, H., Myers, P. G., Hu, X., and Mucci, A. (2018). Inorganic carbon fluxes on the Mackenzie Shelf of the Beaufort Sea. *Biogeosciences* 15, 1011–1027. doi: 10.5194/bg-15-1011-2018

Mundy, C. J., Gosselin, M., Ehn, J., Gratton, Y., Rossnagel, A., Barber, D. G., et al. (2009). Contribution of under-ice primary production to an ice-edge upwelling phytoplankton bloom in the Canadian Beaufort Sea. *Geophys. Res. Lett.* 36:L17601. doi: 10.1029/2009gl038837

Niemi, A., Majewski, A., Archambault, P., Atchison, S., Cypihot, V., Eert, J., et al. (2020). *Data from the BREA-MFP and CBS-MEA Research Programs Describing the Anguniaqvia niqiqyuam Marine Protected Area (ANMPA) Ecosystem.* Canadian Data Report of Fisheries and Aquatic Sciences 1316, ix + 91. Ottawa: Fisheries and Oceans Canada

Nishizawa, Y., Sasaki, H., and Takahashi, K. (2016). Interannual variability in shelled pteropods (*Limacina* spp.) in the Indian sector of the Southern Ocean during austral summer. *Antarct. Rec.* 60, 35–48. doi: 10.15094/00012672

Ou, M., Hamilton, T. J., Eom, J., Lyall, E. M., Gallup, J., Jiang, A., et al. (2015). Responses of pink salmon to CO_2−induced aquatic acidification. *Nat. Clim. Change* 5, 950–955. doi: 10.1038/nclimate2694

Parsons, T. R., Maita, Y., and Lalli, C. M. (1984). *A Manual of Chemical and Biological Methods for Seawater Analysis*. Oxford: Pergamon Press.

Pasternak, A. F., Drits, A. V., and Flint, M. V. (2017). Feeding, egg production, and respiration rate of pteropods Limacina in Arctic seas. *Oceanology* 57, 122–129. doi: 10.1134/s000143701701012x

Peck, V. L., Oakes, R. L., Harper, E. M., Manno, C., and Tarling, G. A. (2018). Pteropods counter mechanical damage and dissolution through extensive shell repair. *Nat. Commun*. 9:264. doi: 10.1038/s41467-017-02692-w

Peck, V. L., Tarling, G. A., Manno, C., Harper, E. M., and Tynan, E. (2016). Outer organic layer and internal repair mechanism protects pteropod *Limacina helicina* from ocean acidification. *Deep Sea Res.* 127, 41–52. doi: 10.1016/j.dsr2.2015.12.005

Peijnenburg, K. T. C. A., Janssen, A. W., Wall-Palmer, D., Goetze, E., Maas, A., Jonathan, A. D., et al. (2019). The origin and diversification of pteropods predate past perturbations in the Earth's carbon cycle. *bioRxiv* [preprint] doi: 10.1101/813386

Peng, G., Steele, M., Bliss, A. C., Meier, W. N., and Dickinson, S. (2018). Temporal means and variability of arctic sea ice melt and freeze season climate indicators using a satellite climate data record. *Remote Sens*. 10:1328. doi: 10.3390/rs10091328

Qi, D., Chen, L., Chen, B., Gao, A., Zhong, W., Feely, R. A., Anderson, L. G., et al. (2017). Increase in acidifying water in the western Arctic Ocean. *Nat. Clim. Change* 7, 195–199. doi: 10.1038/nclimate3228

Riedel, A., Michel, C., Gosselin, M., and LeBlanc, B. (2008). Winter-spring dynamics in sea-ice carbon cycling in the coastal Arctic Ocean. *J. Mar. Syst.* 74, 918–932. doi: 10.1016/j.jmarsys.2008.01.003

Robbins, L. L., Wynn, J. G., Lisle, J. T., Yates, K. K., Knorr, P. O., Byrne, R. H., et al. (2013). Baseline monitoring of the western Arctic Ocean estimates 20% of Canadian Basin surface waters are undersaturated with respect to aragonite. *PLoS One* 8:e73796. doi: 10.1371/journal.pone.0073796

Różańska, M., Gosselin, M., Poulin, M., Wiktor, J. M., and Michel, C. (2009). Influence of environmental factors on the development of bottom landfast ice protists in the Canadian Beaufort Sea during the winter-spring transition. *Mar. Ecol. Prog. Ser*. 386, 43–59. doi: 10.3354/meps08092

Sallon, A., Michel, C., and Gosselin, M. (2011). Summertime primary production and carbon export in the southeastern Beaufort Sea during the low ice year of 2008. *Polar Biol.* 34, 1989–2005. doi: 10.1007/s00300-011-1055-5

Sato-Okoshi, W., Okoshi, K., Sasaki, H., and Akiha, F. (2010). Shell structure of two polar pelagic molluscs, Arctic *Limacina helicina* and Antarctic *Limacina helicina antarctica* forma *antarctica*. *Polar Biol.* 33, 1577–1583. doi: 10.1007/s00300-010-0849-1

Schulz, K. G., Hartley, S., and Eyre, B. (2019). Upwelling amplifies ocean acidification on the east australian shelf: implications for marine ecosystems. *Front. Mar. Sci.* 6:636. doi: 10.3389/fmars.2019.00636

Seibel, B. A., Maas, A. E., and Dierssen, H. M. (2012). Energetic plasticity underlies a variable response to ocean acidification in the pteropod, *Limacina helicina antarctica*. *PLoS One* 7:e30464. doi: 10.1371/journal.pone.0030464

Sévigny, C., Gratton, Y., and Galbraith, P. S. (2015). Frontal structures associated with coastal upwelling and ice-edge subduction events in southern Beaufort Sea during the Canadian Arctic Shelf exchange study. *J. Geophys. Res. Oceans* 120, 2523–2539. doi: 10.1002/2014jc010641

Shadwick, E. H., Thomas, H., Chierici, M., Else, B., Fransson, A., Michel, C., et al. (2011). Seasonal variability of the inorganic carbon system in the Amundsen Gulf region of the southeastern Beaufort Sea. *Limnol. Oceanogr.* 56, 303–322. doi: 10.4319/lo.2011.56.1.0303

Shadwick, E. H., Trull, T. W., Thomas, H., and Gibson, J. A. E. (2013). Vulnerability of polar oceans to anthropogenic acidification: comparison of Arctic and Antarctic seasonal cycles. *Sci. Rep*. 3:2339.

Smoot, C. A., and Hopcroft, R. R. (2017). Cross-shelf gradients of epipelagic zooplankton communities of the Beaufort Sea and the influence of localized hydrographic features. *J. Plankton Res*. 39, 65–78. doi: 10.1093/plankt/fbw080

Stasko, A., Swanson, H., Atchison, S., MacPhee, S., Majewski, A., de Montety, L., et al. (2017). *Stable Isotope Data (δ15N, δ13C) for Marine Fishes and Invertebrates from the Beaufort Regional Environmental Assessment Marine Fishes Project, August-September 2012 and 2013*. Canadian Data Report of Fisheries and Aquatic Sciences 1270, vi + 63. Ottawa: Fisheries and Oceans Canada

Steinacher, M., Joos, F., Frölicher, T. L., Plattner, G. K., and Doney, S. C. (2009). Imminent ocean acidification in the Arctic projected with the NCAR global coupled carbon cycle-climate model. *Biogeosciences* 6, 515–533. doi: 10.5194/bg-6-515-2009

Tremblay, J. -É, Bélanger, S., Barber, D. G., Asplin, M., Martin, J., Darnis, G., et al. (2011). Climate forcing multiplies biological productivity in the coastal Arctic Ocean. *Geophys. Res. Lett*. 38:L18604. doi: 10.1029/2011GL048825

Van Guelpen, L., Markle, D. F., and Duggan, D. J. (1982). An evaluation of accuracy, precision, and speed of several zooplankton sub-sampling techniques. *J. Cons. Int. Explor. Mer*. 40, 226–236.

Walkusz, W., Paulić, J. E., Kwaśniewski, S., Williams, W. J., Wong, S., and Papst, M. H. (2010). Distribution, diversity and biomass of summer zooplankton from the coastal Canadian Beaufort Sea. *Polar Biol.* 33, 321–335. doi: 10.1007/s00300-009-0708-0

Walkusz, W., Williams, W. J., and Kwasniewski, S. (2013). Vertical distribution of mesozooplankton in the coastal Canadian Beaufort Sea in summer. *J. Mar. Syst*. 127, 26–35. doi: 10.1016/j.jmarsys.2012.01.001

Wang, K., Hunt, B. P. V., Liang, C., Pauly, D., Pakhomov, E. A. (2017). Reassessment of the life cycle of the pteropod *Limacina helicina* from a high resolution interannual time series in the temperate North Pacific. *ICES J. Mar. Sci.* 74, 1906–1920. doi: 10.1093/icesjms/fsx014

Williams, C. R., Dittman, A. H., McElhany, P., Busch, D. S., Maher, M. T., Bammler, T. K., et al. (2019). Elevated CO_2 impairs olfactory−mediated neural and behavioral responses and gene expression in ocean−phase coho salmon (*Oncorhynchus kisutch*). *Glob Change Biol.* 25, 963–977. doi: 10.1111/gcb.14532

Williams, W. J., and Carmack, E. C. (2008). Combined effect of wind-forcing and isobath divergence on upwelling at Cape Bathurst. *Beaufort Sea. J. Mar. Res.* 66, 645–663. doi: 10.1357/002224008787536808

Yamamoto-Kawai, M., McLaughlin, F. A., Carmack, E. C., Nishino, S., and Shimada, K. (2009). Aragonite undersaturation in the Arctic Ocean: effects of ocean acidification and sea ice melt. *Science* 326, 1098–1100. doi: 10.1126/science.1174190

Zhang, Y., Yamamoto-Kawai, M., and Williams, W. J. (2020). Two decades of ocean acidification in the surface waters of the Beaufort Gyre, Arctic Ocean: effects of sea ice melt and retreat from 1997-2016. *Geophys. Res. Lett*. 47:e60119. doi: 10.1029/2019GL086421

Conflict of Interest: The authors declare that the research was conducted in the absence of any commercial or financial relationships that could be construed as a potential conflict of interest.

Copyright © 2021 Niemi, Bednaršek, Michel, Feely, Williams, Azetsu-Scott, Walkusz and Reist. This is an open-access article distributed under the terms of the Creative Commons Attribution License (CC BY). The use, distribution or reproduction in other forums is permitted, provided the original author(s) and the copyright owner(s) are credited and that the original publication in this journal is cited, in accordance with accepted academic practice. No use, distribution or reproduction is permitted which does not comply with these terms.

frontiers in Marine Science

PERSPECTIVE
published: 13 May 2021
doi: 10.3389/fmars.2021.613778

Comparative Sensitivities of Zooplankton to Ocean Acidification Conditions in Experimental and Natural Settings

Katherine E. Keil[1], Terrie Klinger[1], Julie E. Keister[2] and Anna K. McLaskey[2,3,4]*

[1] School of Marine and Environmental Affairs, University of Washington, Seattle, WA, United States, [2] School of Oceanography, University of Washington, Seattle, WA, United States, [3] Institute for the Oceans and Fisheries, The University of British Columbia, Vancouver, BC, Canada, [4] Hakai Institute, Campbell River, BC, Canada

OPEN ACCESS

Edited by:
Nina Bednarsek, Southern California Coastal Water Research Project, United States

Reviewed by:
Silke Lischka, GEOMAR Helmholtz Center for Ocean Research Kiel, Germany
Vladimir G. Dvoretsky, Murmansk Marine Biological Institute, Russia
Grace Saba, Rutgers, The State University of New Jersey, United States
Ella Louise Howes, Centre for Environment, Fisheries and Aquaculture Science (CEFAS), United Kingdom

***Correspondence:**
Terrie Klinger
tklinger@uw.edu

Specialty section:
This article was submitted to Coastal Ocean Processes, a section of the journal Frontiers in Marine Science

Received: *03 October 2020*
Accepted: *16 April 2021*
Published: *13 May 2021*

Citation:
Keil KE, Klinger T, Keister JE and McLaskey AK (2021) Comparative Sensitivities of Zooplankton to Ocean Acidification Conditions in Experimental and Natural Settings. Front. Mar. Sci. 8:613778. doi: 10.3389/fmars.2021.613778

Zooplankton can serve as indicators of ecosystem health, water quality, food web structure, and environmental change, including those associated with climate change and ocean acidification (OA). Laboratory studies demonstrate that low pH and high pCO_2 associated with OA can significantly affect the physiology and survival of zooplankton, with differential responses among taxa. While laboratory studies can be indicative of zooplankton response to OA, *in situ* responses will ultimately determine the fate of populations and ecosystems. In this *perspective*, we compare expectations from experimental studies with observations made in Puget Sound (Washington, United States), a highly dynamic estuary with known vulnerabilities to low pH and high pCO_2. We found little association between empirical measures of *in situ* pH and the abundance of sensitive taxa as revealed by meta-analysis, calling into question the coherence between experimental studies and field observations. The apparent mismatch between laboratory and field studies has important ramifications for the design of long-term monitoring programs and interpretation and use of the data produced. Important work remains to be done to connect traits that are sensitive to OA with those that are ecologically relevant and reliably observable in the field.

Keywords: ocean acidification, zooplankton, Puget Sound, meta-analysis, pteropods, calcification, pH

INTRODUCTION

Zooplankton are excellent indicators of ecosystem health, food web function, and water quality (Beaugrand, 2005) because their short life cycles allow them to respond to seasonal variations and abrupt changes in environmental conditions. While the response of zooplankton to ocean acidification (OA) is understudied compared with that of many benthic species, the critical importance of zooplankton to marine food webs underscores the need to better understand their sensitivities to changing seawater carbonate chemistry. Laboratory studies show that low pH and high pCO_2 associated with OA can significantly affect the survival, growth, calcification, development, and reproduction of planktonic organisms (Kroeker et al., 2013; Busch et al., 2014; Cripps et al., 2014; Busch and McElhany, 2016; McLaskey et al., 2016; Tills et al., 2016; Bednaršek et al., 2017; Lischka and Riebesell, 2017), and that sensitivity to current and projected levels of pH

and pCO_2 can vary substantially among zooplankton taxa. Understanding the ecological context in which these responses occur is important, given the co-occurring environmental stressors (e.g., increasing temperature and oxygen stress) to which zooplankton are exposed.

Here, we present the results of an exploratory study to assess the level of correspondence between the results of experimental studies and field observations of zooplankton abundance in a natural setting. Specifically, we asked whether relative sensitivities to pCO_2 as reported in the literature and revealed through meta-analysis could explain a significant proportion of the variation in zooplankton abundance at two time points, across six stations, in Puget Sound, Washington. We focused on Puget Sound because pH and pCO_2 are known to vary substantially across short spatial and temporal scales, often reaching values that are more extreme than in open-ocean environments (Feely et al., 2010; Bianucci et al., 2018; Pelletier et al., 2018), and because the fate of zooplankton in nearshore environments such as this imposes critical controls on food webs and fisheries in coastal environments. We interpret our results in the context of long-term monitoring studies and their utility in detecting biological response to ocean change.

EVIDENCE FROM CONTROLLED EXPERIMENTS

To better understand zooplankton sensitivities to OA conditions in Puget Sound, we performed a meta-analysis of experimental studies reporting responses of seasonally abundant, holoplanktonic taxa known to occur in Washington State's marine waters. Meroplanktonic larvae of shellfish, including crabs, were also included due to their regional economic and ecological importance. Studies published in peer-reviewed journals over the 10-year period from January 2009 to February 2019 were included. We modified the approach of Wittmann and Pörtner (2013) to determine the effect of increasing pCO_2 on major taxonomic groups and to compare sensitivity across groups. The coarse nature of our taxonomic groupings was necessitated by the relative scarcity of published results and was similar to the broad taxonomic levels used by Wittmann and Pörtner (2013). For each species, we interpolated and extrapolated data to help compensate for missing values and cleaned the dataset to eliminate duplicative response categories. For example, because weight and diameter are both measures associated with growth, only one was used in the meta-analysis, thereby reducing the likelihood of over-representation of response categories by including only one experiment per response category per study. Thirty-six studies met our criteria for inclusion in the meta-analysis, representing 17 species and eight taxonomic groups.

Negative responses increased with increasing levels of pCO_2 across taxonomic groups, with the exception of shrimp and larvaceans (**Figure 1**). Pteropods emerged as the taxon most sensitive to OA, showing negative effects at pCO_2 levels as low as 530 μatm. Copepods were the second-most sensitive group, with reproduction and survival negatively affected at pCO_2 levels as low as 824 μatm. Larval bivalve calcification, growth, development, reproduction, and survival were negatively affected, with calcification affected at pCO_2 levels as low as 545 μatm. Shrimp were the only taxon to show positive response to OA conditions, but this was not consistent across studies. Krill development, growth, metabolism, and survival were all negatively affected at pCO_2 levels as low as 956 μatm, while crab larvae showed tolerance up to pCO_2 levels of 1,361 μatm. Jellyfish growth was affected at pCO_2 levels above 1,000 μatm, but other response categories showed no effect. Larvaceans showed the least sensitivity, with no significant response to the levels of pCO_2 tested. We note, however, that our meta-analysis included only one study of larvaceans.

Pooling data across all taxa revealed that calcification was the response category most sensitive to increasing pCO_2, followed by development, growth, reproduction, survival, and metabolism, in that order.

MATCHING EXPERIMENTAL DATA WITH FIELD OBSERVATIONS

To compare results of the meta-analysis with field observations, we collected zooplankton via vertical tows and used standard techniques to characterize water chemistry at six stations in Puget Sound in 2017 from June 23 to 30 and again from August 25 to September 01 (hereafter referred to as June and August). The sampling stations and dates were chosen to cover a range of physical and chemical conditions, targeting stations where high pCO_2 or low pH had been previously reported (Feely et al., 2010; McLaskey et al., 2016; Pelletier et al., 2018). We chose abundance as our response variable because abundance or its co-variate, biomass, is the most commonly measured variable in long-term monitoring studies, including those that have been used to detect changes due to ocean condition (e.g., Hays et al., 2005; Mackas and Beaugrand, 2010; McKinstry and Campbell, 2018). Moreover, abundance has been used to detect response to change in short-term studies of marine microbes (Currie et al., 2017; Rahlff et al., 2021).

Twenty-five taxonomic groups of zooplankton were represented in our samples. Copepods were abundant across stations, accounting for 70% of total abundance across all samples, while larvaceans were abundant at two stations in August, accounting for 15% across all samples.

To compare sensitivities between experimental and field settings, we used the taxon-specific sensitivities revealed by the meta-analysis to infer a hierarchical range of susceptibilities to pCO_2. We grouped taxa into four categories, with pteropods (and all other gastropods), copepods, and bivalve larvae designated as "most susceptible"; shrimp and krill as "susceptible"; crab larvae, jellyfish, and larvaceans as "least susceptible"; and all other taxa as "insufficient data." The distribution of differentially susceptible taxa varied across stations and sampling points (**Figure 2**), but overall we detected no clear association between zooplankton abundance and sensitivity as inferred from meta-analysis.

The BIOENV function (R package "vegan": Clarke and Ainsworth, 1993) was used to estimate the combination

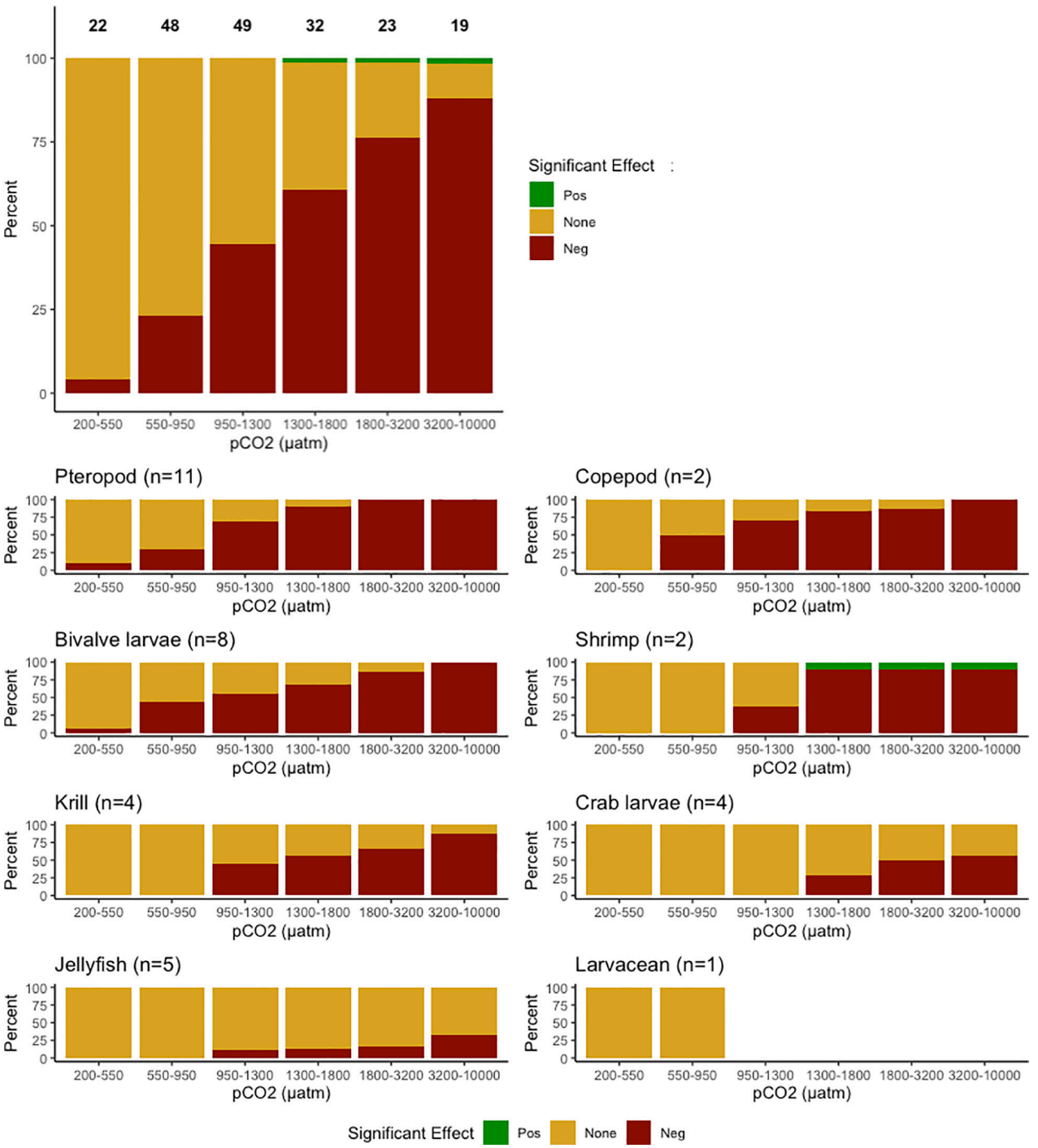


FIGURE 1 | Top panel: Percent (%) of representative experiments across all taxonomic groups (pteropod, copepod, bivalve larvae, shrimp, krill, crab larvae, jellyfish, and larvacean) exhibiting positive (green), negative (red), or no significant response (yellow) to elevated levels of pCO_2 (µatm). The number above each bar indicates the number of experiments analyzed for each level of pCO_2, not including interpolated or extrapolated data. Bottom panels: Responses to varying levels of pCO_2 by taxonomic group, with *n* representing the number of studies included in the analysis.

of environmental variables most highly correlated with the biological matrix. The best fit model did not include pCO_2 or its covariate, pH, but instead included a combination of minimum temperature, maximum dissolved oxygen, and minimum fluorescence. Research indicates that zooplankton are negatively affected by pCO_2 conditions that currently occur in Puget Sound, including conditions that were observed in this study (Barton et al., 2012; McLaskey et al., 2016;

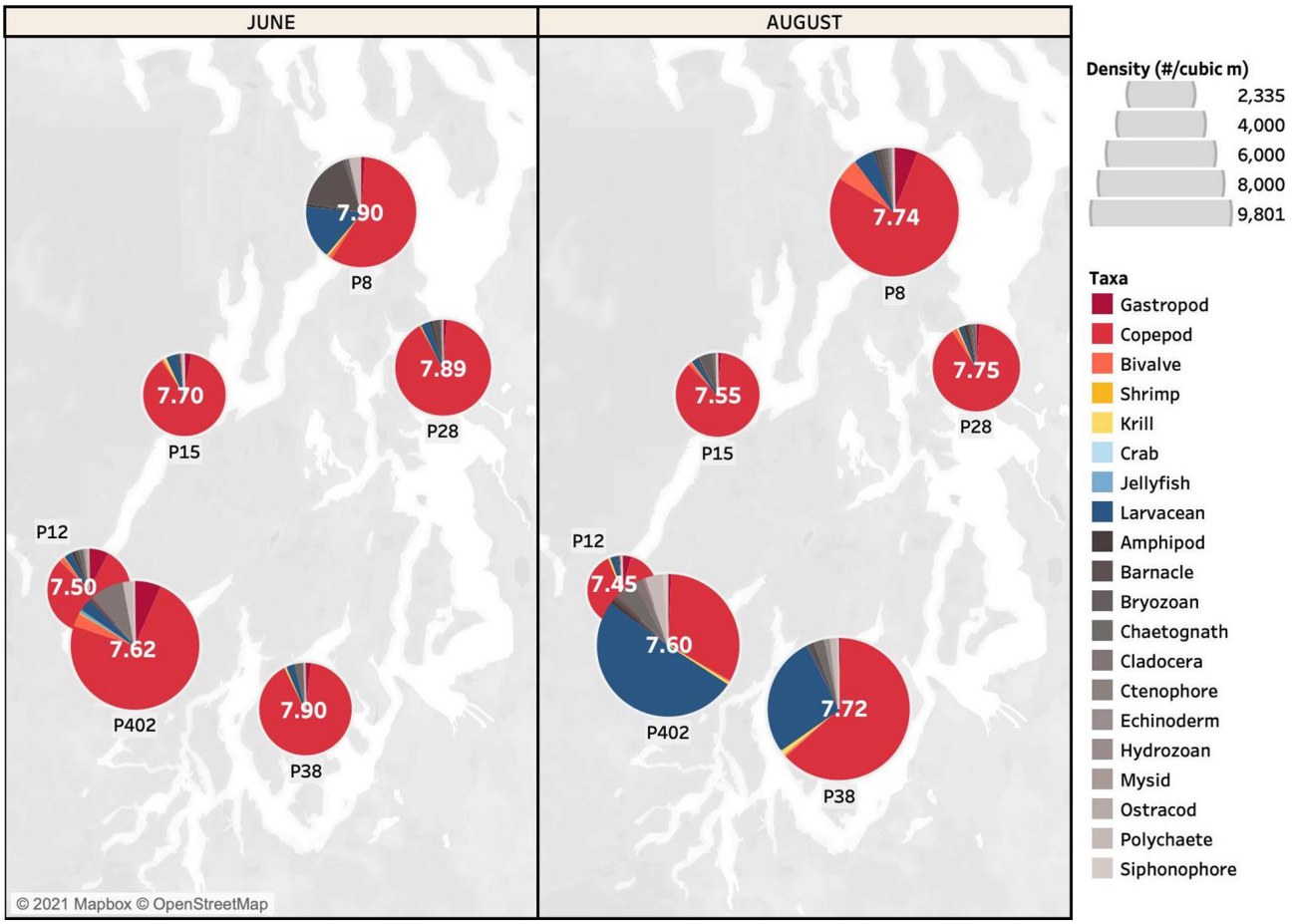


FIGURE 2 | Total abundance of zooplankton (individuals/m^3) by broad taxonomic grouping at six stations established by the Puget Sound Regional Synthesis Model program (P8, P12, P15, P28, P38, and P402) sampled in Puget Sound, WA, United States in June and August 2017. Isopods and arachnids were recorded three or fewer times and were omitted. The color of each taxon is based on estimated levels of susceptibility to ocean acidification derived from the meta-analysis: red taxa are most susceptible, yellow taxa are susceptible, blue taxa are least susceptible, and gray taxa have insufficient data. The mean pH for each station is recorded in white in the center of each pie.

Bednaršek et al., 2017, 2020c). Our results, however, did not suggest that zooplankton abundance was responsive to low pH or waters undersaturated with respect to Ω_{ar}; if effects were present, they were not detectable by our methodology. The mean values of pH observed across stations ranged from 7.45 to 7.90; for comparison, the pH predicted for the surface ocean by the end of this century is 7.75 (IPCC, 2014).

DISCUSSION

Zooplankton abundance as measured in the field did not reflect evidence from laboratory studies regarding organismal response to low pH/high pCO_2. Taxa reported to be most susceptible to low pH in the laboratory reached high abundances at stations with pH as low as 7.45. Our analysis revealed that temperature, dissolved oxygen, and fluorescence, but not pH, were leading environmental variables influencing zooplankton abundance at the locations and dates sampled.

Zooplankton abundance tends to be positively associated with primary production (or its correlate, chlorophyll fluorescence), and our observations confirm the importance of primary production to zooplankton abundance in Puget Sound. This strong positive relationship is consistent with evidence that food availability can mediate organismal response to OA (Thomsen et al., 2013; Pansch et al., 2014; Ramajo et al., 2016). We note, however, that this is not always the case: for example, Brown et al. (2018, 2020) found that food sufficiency exacerbated the negative effects of low pH on organismal performance. Given our limited dataset, the relationship between food availability and zooplankton abundance in our study should be interpreted with caution with respect to zooplankton response to OA.

Although several of our stations were similar in the physical and chemical properties we measured, their zooplankton communities differed, especially in our samples from August. Notably, the stations differ in depth, but according to our analyses, depth did not appear as a significant explanatory factor. Factors that we did not measure, such as life-cycle

timing, competition and predation, and physical factors such as advection, could contribute to differences in community composition. Moreover, while all species considered in this study inhabit Washington waters, most studies included in the meta-analysis used specimens collected from outside of our study area. Consequently, we cannot evaluate the potential influence of local adaptation, including changes in gene expression that can act on short timescales. Accounting for local adaptation will be important in any study that strives to make inferences about the response of local populations to OA conditions, but the difficulties of measuring local adaptation at meaningful scales remain considerable.

The expression of behavioral traits likely plays important but unstudied roles in determining differential sensitivity to OA in natural habitats. Some zooplankton species exhibit behaviors that can influence their ability to tolerate or avoid stressful conditions. Copepods, for example, have been shown to actively adjust their position or motility in response to a variety of stimuli, including turbulent flow (Michalec et al., 2017), light (Martynova and Gordeeva, 2010), pollutants (Michalec et al., 2013), and hypoxia (Keister and Tuttle, 2013), while echinoderm larvae can alter their swimming behavior to avoid low pH (Maboloc et al., 2020). Our data collection methods almost certainly obscured any behavioral responses that might have occurred.

Moreover, we cannot estimate the duration of individual exposure to specific levels of pH or other stressors. While seawater pH varies seasonally in Puget Sound (Feely et al., 2010; Pelletier et al., 2018), variation also occurs over diel cycles and short-term changes in circulation (Murray et al., 2015). Variation in the duration of exposure could partially explain why the meta-analysis revealed copepods to have high sensitivity to OA but our field observations did not. Zooplankton species and life stages with stronger vertical migration capabilities have been associated with higher tolerance to low pH because they experience a wide range of pH daily (Lewis et al., 2013). Our decision to identify samples to higher-order taxonomic levels (i.e., not to genus or species) allowed broad assessment across taxa, but constrained our ability to detect species-specific differences in response to environmental conditions, including those caused by differences in behavior.

Copepods dominated nearly every station we sampled, and much of the mismatch we observed between experimental and field observations could be attributable to our categorization of copepods as "most susceptible." A more detailed look conceivably would reveal differential responses among species and life stages of copepods, not all of which are likely to be highly susceptible to OA. Our analysis failed to capture variation at this level, and in assigning all copepods to the same category, we could have overestimated the abundance of highly susceptible taxa. This observation suggests that, for monitoring programs, sampling to the lowest possible taxonomic level is advisable. It also cautions against the use of coarse taxonomic data to infer ecological response or for use as input to numerical models.

New research that has been published since the completion of our meta-analysis suggests that our results could over- or underestimate susceptibility among the taxa we included. One such study demonstrates that early life stages of a common copepod in Puget Sound—a taxon in the most susceptible category according to our meta-analysis—are generally tolerant of short-term direct effects of OA (McLaskey et al., 2019). Another study found that larval crabs—a taxon in the least susceptible category—may be more sensitive than indicated by prior laboratory studies (Bednaršek et al., 2020a). These apparent discrepancies likely result from a combination of factors, including a relatively small but growing literature, differential responses among life-history stages, and the short duration of our field sampling.

Over the course of this study, zooplankton at the stations sampled were exposed to a wide range of environmental conditions, including pH as low as 7.30 and Ω_{ar} as low as 0.32, conditions that could be expected to elicit responses among susceptible taxa. According to our meta-analysis, survival is among the least sensitive response categories, suggesting that changes in abundance due to differential survival could take time to grow to detectable levels. Sub-lethal effects may emerge more readily, but our data indicate that sublethal effects, if operative in these populations, were not of sufficient magnitude or duration to cause measurable declines in population abundance over the period sampled. Despite the limited temporal duration of our observations, we expected that such effects may have emerged across sites because the large spatial differences in seawater conditions that we sampled across are generally consistent year after year (Feely et al., 2010; McLaskey et al., 2016; Pelletier et al., 2018). This observation is important in the context of long-term monitoring programs that use measures of zooplankton abundance as indicators of environmental conditions. The strength of inferences made possible by monitoring data is likely to be dependent on the strength of the relationship(s) between OA conditions and the abundance of specific taxa. It is important that the scale of the response variable is adequate to reveal effects over the temporal and spatial scales sampled.

Even so, abundance is a logical first factor to examine zooplankton response to OA based on the expectation that significant effects of low pH or high pCO_2 on development, reproduction, and other traits that influence individual fitness ultimately will be reflected in measures of population abundance. Moreover, changes in abundance *can* serve as an indicator of zooplankton response to OA. For example, Smith et al. (2016) used natural gradients in CO_2 to show significant reductions in zooplankton biomass and abundance under high CO_2 conditions. Other taxa have shown similar declines in abundance in response to increasing pCO_2 or acidity (Hall-Spencer et al., 2008; Cigliano et al., 2010; Kroeker et al., 2011). Measures of abundance are commonly used for zooplankton observations in time series, and relative shifts in species abundances have been used extensively to examine zooplankton responses to climate (e.g., Mackas et al., 2007; Mackas and Beaugrand, 2010; Peterson et al., 2017) and as input to models of food web and ecosystem response to OA (Busch et al., 2013; Marshall et al., 2017). Abundance data can also capture shifts in a species' center of abundance, indicating the directionality and magnitude of responses to climate change (Chivers et al., 2017). Hence, understanding the utility and limitations of abundance measures to broader environmental and ecological inquiries is

essential to interpretation of empirical studies and to natural resource management. Importantly, the results of our study suggest that the relationship between measures of zooplankton abundance and seawater pH is not simple, emphasizing the utility of intensive sampling over longer time periods to elucidate underlying relationships. Longer time series that pair chemical and biological observations and distinguish the effects of seawater carbonate chemistry from factors such as temperature and dissolved oxygen will improve attribution of biological effects among co-occurring stressors (Doo et al., 2020). Our results underscore the importance of long-term monitoring of species abundance to determine the direction and magnitude of change associated with climate and OA.

Low statistical power is common among small datasets, and interpretation of our results is further limited by the existing literature. Many zooplankton monitoring efforts lack long-term and consistent data even though it is increasingly recognized that decades-long time series will be needed to confidently identify the effects of OA on zooplankton abundance. Our findings corroborate this by demonstrating that snapshots of zooplankton abundance in relation to seawater pH can fail to detect effects of pH on abundance and community composition, even when spatial gradients in pH are relatively steep and conditions differ sharply among sampling locations.

Although abundance is more easily and frequently measured in field settings, other variables could be more informative. Measuring calcification is a clear choice because of its known sensitivity to low values of Ω_{ar} and the relative wealth of relevant laboratory studies concerning the ability of organisms to create calcium carbonate structures under OA conditions. Recent research studying *in situ* impacts on calcification found reduced calcification in pteropods collected in the California Current Ecosystem (Mekkes et al., 2021) and severe dissolution in pteropods in our study area (Bednaršek et al., 2020b). Importantly, some measures of calcification can be made on preserved samples, potentially alleviating constraints of some monitoring programs. However, calcification is important to only a subset of key zooplankton taxa, and even for calcifiers, is only one of many processes affected by OA. Where possible, adding biological measures in addition to abundance may provide key insights into sensitivity and add substantial value to monitoring programs. Ultimately, including mechanistic studies that can reveal cause-and-effect relationships between OA conditions and biological response will be more informative than correlation-based studies alone.

Overall, we found that observations of zooplankton abundance and community composition in response to pH and pCO_2 did not match experimental evidence from the literature. We propose that this mismatch could be explained by a number of factors, including response to co-occurring physical factors such as temperature and dissolved oxygen, data limitations, and biological and ecological factors, including food availability, competition and predation, local adaptation, life history stage, and the taxonomic level at which data are aggregated. Accounting for such factors in monitoring studies should improve our ability to attribute change to specific causes. Finally, and perhaps most importantly, our results underscore the importance of testing evidence from laboratory studies against the response of natural populations in defined settings. Context clearly matters, and assumptions to the contrary are likely to lead to equivocal or even misleading findings.

DATA AVAILABILITY STATEMENT

The raw data supporting the conclusions of this article will be made available by the authors, without undue reservation.

AUTHOR CONTRIBUTIONS

KK co-designed the research, performed the meta-analysis and field sampling, analyzed results, and led preparation of the manuscript. TK co-designed and supervised the research. JK contributed to the research design and supported laboratory analysis. AM supported the research cruises, collaborated on collection of the field data, and processed environmental samples. All authors contributed to preparation of the manuscript and approved the version submitted.

FUNDING

TK, AM, and JK were partially supported by funding provided by the Washington Ocean Acidification Center. JK was partially supported by the Washington Sea Grant. AM was partially supported by an NSF GRFP fellowship.

ACKNOWLEDGMENTS

This work represents research performed in partial fulfillment of the Master's degree of KK (Keil, 2021). We thank R. P. Kelly and R. Gallego for analytical assistance and A. Winans and B. Herrmann for laboratory assistance. We gratefully acknowledge the outstanding support of the crew of the R/V Clifford A. Barnes.

REFERENCES

Barton, A., Hales, B., Waldbusser, G. G., Langdon, C., and Feely, R. A. (2012). The Pacific oyster, *Crassostrea gigas*, shows negative correlation to naturally elevated carbon dioxide levels: implications for near-term ocean acidification effects. *Limnol. Oceanogr.* 57, 698–710. doi: 10.4319/lo.2012.57.3.0698

Beaugrand, G. (2005). Monitoring pelagic ecosystems using plankton indicators. *ICES J. Mar. Sci.* 62, 333–338. doi: 10.1016/j.icesjms.2005.01.002

Bednaršek, N., Feely, R. A., Beck, M. W., Alin, S. R., Siedlecki, S. A., Calosi, P., et al. (2020a). Exoskeleton dissolution with mechanoreceptor damage in larval *Dungeness crab* related to severity of present-day ocean acidification vertical gradients. *Sci. Total Environ.* 716:136610. doi: 10.1016/j.scitotenv.2020.136610

Bednaršek, N., Feely, R. A., Tolimieri, N., Hermann, A. J., Siedlecki, S. A., Waldbusser, G. G., et al. (2017). Exposure history determines pteropod vulnerability to ocean acidification along the US West Coast. *Sci. Rep.* 7:4526. doi: 10.1038/s41598-017-03934-z

Bednaršek, N., Newton, J. A., Beck, M. W., Alin, S. R., Feely, R. A., Christman, N. R., et al. (2020b). Severe biological effects under present-day estuarine acidification in the seasonally variable Salish Sea. *Sci. Total Environ.* 765:142689. doi: 10.1016/j.scitotenv.2020.142689

Bednaršek, N., Pelletier, G., Ahmed, A., and Feely, R. A. (2020c). Chemical exposure due to anthropogenic ocean acidification increases risks for estuarine calcifiers in the Salish sea: biogeochemical model scenarios. *Front. Mar. Sci.* 7:580. doi: 10.3389/fmars.2020.00580

Bianucci, L., Long, W., Khangaonkar, T., Pelletier, G., Ahmed, A., Mohamedali, T., et al. (2018). Sensitivity of the regional ocean acidification and carbonate system in Puget Sound to ocean and freshwater inputs. *Elem. Sci. Anth.* 6:22. doi: 10.1525/elementa.151

Brown, N. E. M., Bernhardt, J. R., Anderson, K. M., and Harley, C. D. G. (2018). Increased food supply mitigates ocean acidification effects on calcification but exacerbates effects on growth. *Sci. Rep.* 8:9800. doi: 10.1038/s41598-018-28012-w

Brown, N. E. M., Bernhardt, J. R., and Harley, C. D. G. (2020). Energetic context determines species and community responses to ocean acidification. *Ecology* 101:e03073. doi: 10.1002/ecy.3073

Busch, D. S., Harvey, C. J., and McElhany, P. (2013). Potential impacts of ocean acidification on the puget sound food web. *ICES J. Mar. Sci.* 70, 823–833. doi: 10.1093/icesjms/fst061

Busch, D. S., Maher, M., Thibodeau, P., and McElhany, P. (2014). Shell condition and survival of puget sound pteropods are impaired by ocean acidification conditions. *PLoS One* 9:e105884. doi: 10.1371/journal.pone.0105884

Busch, D. S., and McElhany, P. (2016). Estimates of the Direct Effect of Seawater pH on the Survival Rate of Species Groups in the California Current Ecosystem. *PLoS One* 11:e0160669. doi: 10.1371/journal.pone.0160669

Chivers, W. J., Walne, A. W., and Hays, G. C. (2017). Mismatch between marine plankton range movements and the velocity of climate change. *Nat. Commun.* 8:14434. doi: 10.1038/ncomms14434

Cigliano, M., Gambi, M. C., Rodolfo-Metalpa, R., Patti, F. P., and Hall-Spencer, J. M. (2010). Effects of ocean acidification on invertebrate settlement at volcanic CO2 vents. *Mar. Biol.* 157, 2489–2502. doi: 10.1007/s00227-010-1513-6

Clarke, K. R., and Ainsworth, M. (1993). A method of linking multivariate community structure to environmental variables. *Mar. Ecol. Progr.Ser.* 92, 205–219. doi: 10.3354/meps092205

Cripps, G., Lindeque, P., and Flynn, K. J. (2014). Have we been underestimating the effects of ocean acidification in zooplankton? *Glob. Chang. Biol.* 20, 3377–3385. doi: 10.1111/gcb.12582

Currie, A. R., Tait, K., Parry, H., de Francisco-Mora, B., Hicks, N., Osborn, A. M., et al. (2017). Marine microbial gene abundance and community composition in response to ocean acidification and elevated temperature in two contrasting coastal marine sediments. *Front. Microbiol.* 8:1599. doi: 10.3389/fmicb.2017.01599

Doo, S. S., Kealoha, A., Andersson, A., Cohen, A. L., Hicks, T. L., Johnson, Z. I., et al. (2020). The challenges of detecting and attributing ocean acidification impacts on marine ecosystems. *ICES J. Mar. Sci.* 77, 2411–2422. doi: 10.1093/icesjms/fsaa094

Feely, R. A., Alin, S. R., Newton, J., Sabine, C. L., Warner, M., Devol, A., et al. (2010). The combined effects of ocean acidification, mixing, and respiration on pH and carbonate saturation in an urbanized estuary. *Estuarine, Coastal Shelf Sci.* 88, 442–449. doi: 10.1016/j.ecss.2010.05.004

Hall-Spencer, J. M., Rodolfo-Metalpa, R., Martin, S., Ransome, E., Fine, M., Turner, S. M., et al. (2008). Volcanic carbon dioxide vents show ecosystem effects of ocean acidification. *Nature* 454, 96–99. doi: 10.1038/nature07051

Hays, G. C., Richardson, A. J., and Robinson, C. (2005). Climate change and marine plankton. *Trends Ecol. Evol.* 20, 337–344. doi: 10.1016/j.tree.2005.03.004

IPCC, (2014). "Climate change 2014: synthesis report," in *Contribution of Working Groups I, II and III to the Fifth Assessment Report of the Intergovernmental Panel on Climate Change*, eds Core Writing Team, R. K. Pachauri, and L. A. Meyer, (Geneva: IPCC), 151.

Keil, K. E. (2021). *Estimating Relative Sensitivities of Zooplankton to Ocean Acidification and Comparing to Observations in situ.* Master's Thesis. Seattle (WA): University of Washington.

Keister, J. E., and Tuttle, L. B. (2013). Effects of bottom-layer hypoxia on spatial distributions and community structure of mesozooplankton in a sub-estuary of puget sound, Washington, U.S.A. *Limnol. Oceanogr.* 58, 667–680. doi: 10.4319/lo.2013.58.2.0667

Kroeker, K. J., Kordas, R. L., Crim, R., Hendriks, I. E., Ramajo, L., Singh, G. S., et al. (2013). Impacts of ocean acidification on marine organisms: quantifying sensitivities and interaction with warming. *Glob. Chang. Biol.* 19, 1884–1896. doi: 10.1111/gcb.12179

Kroeker, K. J., Micheli, F., Gambi, M. C., and Martz, T. R. (2011). Divergent ecosystem responses within a benthic marine community to ocean acidification. *PNAS* 108, 14515–14520. doi: 10.1073/pnas.1107789108

Lewis, C. N., Brown, K. A., Edwards, L. A., Cooper, G., and Findlay, H. S. (2013). Sensitivity to ocean acidification parallels natural pCO2 gradients experienced by Arctic copepods under winter sea ice. *PNAS* 110, E4960–E4967. doi: 10.1073/pnas.1315162110

Lischka, S., and Riebesell, U. (2017). Metabolic response of Arctic pteropods to ocean acidification and warming during the polar night/twilight phase in Kongsfjord (Spitsbergen). *Polar Biol.* 40, 1211–1227. doi: 10.1007/s00300-016-2044-5

Maboloc, E., Batzel, G., Grünbaum, D., and Chan, K. (2020). Vertical distribution of echinoid larvae in pH stratified water columns. *Mar. Biol.* 167:13. doi: 10.1007/s00227-019-3629-7

Mackas, D. L., Batten, S., and Trudel, M. (2007). Effects on zooplankton of a warmer ocean: recent evidence from the Northeast Pacific. *Progr. Oceanogr.* 75, 223–252. doi: 10.1016/j.pocean.2007.08.010

Mackas, D. L., and Beaugrand, G. (2010). Comparisons of zooplankton time series. *J. Mar. Syst.* 79, 286–304. doi: 10.1016/j.jmarsys.2008.11.030

Marshall, K. N., Kaplan, I. C., Hodgson, E. E., Hermann, A., Busch, D. S., McElhany, P., et al. (2017). Risks of ocean acidification in the California current food web and fisheries: ecosystem model projections. *Glob. Chang. Biol.* 23, 1525–1539. doi: 10.1111/gcb.13594

Martynova, D. M., and Gordeeva, A. V. (2010). Light-dependent behavior of abundant zooplankton species in the White Sea. *J. Plankton Res.* 32, 441–456. doi: 10.1093/plankt/fbp144

McKinstry, C. A. E., and Campbell, R. W. (2018). Seasonal variation of zooplankton abundance and community structure in Prince William Sound, Alaska, 2009–2016. *Deep Sea Res. Part II Topical Stud. Oceanogr.* 147, 69–78. doi: 10.1016/j.dsr2.2017.08.016

McLaskey, A. K., Keister, J. E., McElhany, P., Olson, M. B., Busch, D. S., Maher, M., et al. (2016). Development of Euphausia pacifica (krill) larvae is impaired under pCO2 levels currently observed in the Northeast Pacific. *Mar. Ecol. Progr. Ser.* 555, 65–78. doi: 10.3354/meps11839

McLaskey, A. K., McElhany, P., Busch, D. S., Maher, M., Winans, A. K., and Keister, J. E. (2019). Early life stages of Calanus pacificus are neither exposed nor sensitive to low pH waters. *J. Plankton Res.* 41, 893–896. doi: 10.1093/plankt/fbz059

Mekkes, L., Renema, W., Bednaršek, N., Alin, S. R., Feely, R. A., Huisman, J., et al. (2021). Pteropods make thinner shells in the upwelling region of the California current ecosystem. *Sci. Rep.* 11:1731. doi: 10.1038/s41598-021-81131-9

Michalec, F.-G., Fouxon, I., Souissi, S., and Holzner, M. (2017). Zooplankton can actively adjust their motility to turbulent flow. *PNAS* 114, E11199–E11207. doi: 10.1073/pnas.1708888114

Michalec, F.-G., Holzner, M., Menu, D., Hwang, J.-S., and Souissi, S. (2013). Behavioral responses of the estuarine calanoid copepod *Eurytemora affinis* to sub-lethal concentrations of waterborne pollutants. *Aquat. Toxicol.* 138–139, 129–138. doi: 10.1016/j.aquatox.2013.05.007

Murray, J. W., Roberts, E., Howard, E., O'Donnell, M., Bantam, C., Carrington, E., et al. (2015). An inland sea high nitrate-low chlorophyll (HNLC) region with naturally high pCO2. *Limnol. Oceanogr.* 60, 957–966. doi: 10.1002/lno.10062

Pansch, C., Schaub, I., Havenhand, J., and Wahl, M. (2014). Habitat traits and food availability determine the response of marine invertebrates to ocean acidification. *Glob. Chang. Biol.* 20, 765–777. doi: 10.1111/gcb.12478

Pelletier, G., Roberts, M., Keyzers, M., and Alin, S. R. (2018). Seasonal variation in aragonite saturation in surface waters of Puget Sound – a pilot study. *Elem. Sci. Anth.* 6:5. doi: 10.1525/elementa.270

Peterson, W. T., Fisher, J. L., Strub, P. T., Du, X., Risien, C., Peterson, J., et al. (2017). The pelagic ecosystem in the Northern California Current off Oregon during the 2014–2016 warm anomalies within the context of the past 20 years. *J. Geophys. Res.* 122, 7267–7290. doi: 10.1002/2017JC012952

Rahlff, J., Khodami, S., Voskuhl, L., Humphreys, M. P., Stolle, C., Arbizu, P. M., et al. (2021). Short-term responses to ocean acidification: effects on relative abundance of eukaryotic plankton from the tropical Timor Sea. *Mar. Ecol. Progr. Ser.* 658, 59–74. doi: 10.3354/meps13561

Ramajo, L., Pérez-León, E., Hendriks, I. E., Marbà, N., Krause-Jensen, D., Sejr, M. K., et al. (2016). Food supply confers calcifiers resistance to ocean acidification. *Sci. Rep.* 6:19374. doi: 10.1038/srep19374

Smith, J. N., De'ath, G., Richter, C., Cornils, A., Hall-Spencer, J. M., and Fabricius, K. E. (2016). Ocean acidification reduces demersal zooplankton that reside in tropical coral reefs. *Nat. Clim. Chang.* 6, 1124–1129. doi: 10.1038/nclimate 3122

Thomsen, J., Casties, I., Pansch, C., Körtzinger, A., and Melzner, F. (2013). Food availability outweighs ocean acidification effects in juvenile *Mytilus edulis*: laboratory and field experiments. *Glob. Chang. Biol.* 19, 1017–1027. doi: 10. 1111/gcb.12109

Tills, O., Sun, X., Rundle, S. D., Heimbach, T., Gibson, T., Cartwright, A., et al. (2016). Reduced pH affects pulsing behaviour and body size in ephyrae of the moon jellyfish, *Aurelia aurita*. *J. Exp. Mar. Biol. Ecol.* 480, 54–61. doi: 10.1016/j.jembe.2016.03.014

Wittmann, A. C., and Pörtner, H.-O. (2013). Sensitivities of extant animal taxa to ocean acidification. *Nat. Clim. Chang.* 3, 995–1001. doi: 10.1038/nclimate1982

Conflict of Interest: The authors declare that the research was conducted in the absence of any commercial or financial relationships that could be construed as a potential conflict of interest.

The handling editor declared a past co-authorship with one of the authors, AM.

Copyright © 2021 Keil, Klinger, Keister and McLaskey. This is an open-access article distributed under the terms of the Creative Commons Attribution License (CC BY). The use, distribution or reproduction in other forums is permitted, provided the original author(s) and the copyright owner(s) are credited and that the original publication in this journal is cited, in accordance with accepted academic practice. No use, distribution or reproduction is permitted which does not comply with these terms.

frontiers in Marine Science

ORIGINAL RESEARCH
published: 10 September 2021
doi: 10.3389/fmars.2021.671497

Integrated Assessment of Ocean Acidification Risks to Pteropods in the Northern High Latitudes: Regional Comparison of Exposure, Sensitivity and Adaptive Capacity

Nina Bednaršek[1,2], Kerry-Ann Naish[3], Richard A. Feely[4], Claudine Hauri[5], Katsunori Kimoto[6], Albert J. Hermann[7], Christine Michel[8], Andrea Niemi[8] and Darren Pilcher[7]*

[1] Southern California Coastal Water Research Project, Costa Mesa, CA, United States, [2] National Institute of Biology, Marine Biological Station, Piran, Slovenia, [3] School of Aquatic and Fishery Sciences, University of Washington, Seattle, WA, United States, [4] NOAA Pacific Marine Environmental Laboratory, Seattle, WA, United States, [5] International Arctic Research Center, University of Alaska Fairbanks, Fairbanks, AK, United States, [6] Research Institute for Global Change (RIGC), JAMSTEC, Yokosuka, Japan, [7] Joint Institute for the Study of the Atmosphere and Ocean, University of Washington, Seattle, WA, United States, [8] Fisheries and Oceans Canada, Freshwater Institute, University Crescent, Winnipeg, MB, Canada

OPEN ACCESS

Edited by:
Anas Ghadouani, University of Western Australia, Australia

Reviewed by:
Silke Lischka, GEOMAR Helmholtz Center for Ocean Research Kiel, Germany
Kristen Marie Krumhardt, National Center for Atmospheric Research (UCAR), United States

***Correspondence:**
Nina Bednaršek
nina.bednarsek@gmail.com;
ninab@sccwrp.org

Specialty section:
This article was submitted to Coastal Ocean Processes, a section of the journal Frontiers in Marine Science

Received: *23 February 2021*
Accepted: *18 August 2021*
Published: *10 September 2021*

Citation:
Bednaršek N, Naish K-A, Feely RA, Hauri C, Kimoto K, Hermann AJ, Michel C, Niemi A and Pilcher D (2021) Integrated Assessment of Ocean Acidification Risks to Pteropods in the Northern High Latitudes: Regional Comparison of Exposure, Sensitivity and Adaptive Capacity. Front. Mar. Sci. 8:671497. doi: 10.3389/fmars.2021.671497

Exposure to the impact of ocean acidification (OA) is increasing in high-latitudinal productive habitats. Pelagic calcifying snails (pteropods), a significant component of the diet of economically important fish, are found in high abundance in these regions. Pteropods have thin shells that readily dissolve at low aragonite saturation state (Ω_{ar}), making them susceptible to OA. Here, we conducted a first integrated risk assessment for pteropods in the Eastern Pacific subpolar gyre, the Gulf of Alaska (GoA), Bering Sea, and Amundsen Gulf. We determined the risk for pteropod populations by integrating measures of OA exposure, biological sensitivity, and resilience. Exposure was based on physical-chemical hydrographic observations and regional biogeochemical model outputs, delineating seasonal and decadal changes in carbonate chemistry conditions. Biological sensitivity was based on pteropod morphometrics and shell-building processes, including shell dissolution, density and thickness. Resilience and adaptive capacity were based on species diversity and spatial connectivity, derived from the particle tracking modeling. Extensive shell dissolution was found in the central and western part of the subpolar gyre, parts of the Bering Sea, and Amundsen Gulf. We identified two distinct morphotypes: *L. helicina helicina* and *L. helicina pacifica*, with high-spired and flatter shells, respectively. Despite the presence of different morphotypes, genetic analyses based on mitochondrial haplotypes identified a single species, without differentiation between the morphological forms, coinciding with evidence of widespread spatial connectivity. We found that shell morphometric characteristics depends on omega saturation state (Ω_{ar}); under Ω_{ar} decline, pteropods build flatter and thicker shells, which is indicative of a certain level of phenotypic plasticity. An integrated risk evaluation based on multiple approaches assumes a high risk for pteropod population persistence with intensification of OA in the high latitude eastern North Pacific because of their known vulnerability, along with limited evidence of

species diversity despite their connectivity and our current lack of sufficient knowledge of their adaptive capacity. Such a comprehensive understanding would permit improved prediction of ecosystem change relevant to effective fisheries resource management, as well as a more robust foundation for monitoring ecosystem health and investigating OA impacts in high-latitudinal habitats.

Keywords: Gulf of Alaska, Bering Sea, Amundsen Gulf, ocean acidification, pteropod morphotype shell dissolution, genetic structure, spatial connectivity, vulnerability assessment

INTRODUCTION

The pervasiveness of global climate change threatens biodiversity, habitat suitability, ecosystem function, structure and services (Bindoff et al., 2019). Such changes are especially pertinent in high-latitudinal habitats across the eastern North Pacific Ocean, including the Gulf of Alaska (GoA) and its subpolar gyre, the polar waters of the Bering Sea, one of the most productive seas on the planet (Brown et al., 2011), and the Amundsen Gulf of the Canadian Beaufort Sea. Yet, the subpolar and polar seas are sensitive to ocean acidification (OA) due to naturally low buffering capacity, coupled with multiple climate-change and related physical-chemical drivers, such as increasing freshwater input from glacial runoff, rivers, sea ice melt, and increasing temperature (Mathis et al., 2011; Evans et al., 2013; Cross et al., 2013, Hauri et al., 2020). Substantial changes in carbonate chemistry conditions have already been detected, demonstrating increasing corrosiveness in high-latitudinal North Pacific regions (IPCC, 2014, 2019; Carter et al., 2017, 2019; Bindoff et al., 2019; Hauri et al., 2021). These changes coincide spatially and temporally with the habitats of important commercial and subsistence fisheries (Mathis et al., 2014), underscoring the need for a detailed understanding of the species tolerances and their habitats that will most likely be at risk. Currently, experimental data from the Pacific subpolar gyre, GoA, and Bering Sea show that economically important crab species (Long et al., 2013, 2016) and coho salmon (Williams et al., 2019) are sensitive to OA. However, very limited information exists from field measurements on the current impacts of OA on the most sensitive marine calcifying zooplankton (Cai et al., 2020), such as pteropods, with direct or indirect importance for the fisheries. Pteropods are a key species within the high-latitudinal ecosystems (Kobayashi, 1974; Fabry, 1989; Bednaršek et al., 2012a) that demonstrate severe sensitivity to OA. Multiple biological pathways of this species are impacted by OA conditions, compromising their growth, fecundity, and ultimately their survival (Comeau et al., 2009; 2010; Lischka et al., 2011; Bednaršek et al., 2014, 2019; Feely et al., 2016; Manno et al., 2016). As a result of such OA-related sensitivity, pteropods rank in the top quartile of ecological integrity indicators and are used to identify early warning signs and habitats of concern related to OA (Bednaršek et al., 2017).

Pteropods have a wide-ranging, year-around distribution in the subpolar gyre (Mackas and Galbraith, 2012), offshore and coastal habitats of the GoA (Tsurumi et al., 2005; Doubleday and Hopcroft, 2015), and Bering Sea (Eisner et al., 2014, 2017; Janssen et al., 2019), and the Amundsen Gulf (Darnis et al., 2008; Walkusz et al., 2013; Niemi et al., 2021). Pteropods in the GoA are commonly found in the diets of various life stages of Pacific Salmon species, such as pink, sockeye and chum salmon (Auburn and Ignell, 2000; Daly et al., 2019), that rely upon pteropods to support somatic growth and lipid reserves, especially during the critical summer and autumn growth periods (Auburn and Ignell, 2000; Armstrong et al., 2005; Beauchamp et al., 2007; Zavolokin et al., 2014; Doubleday and Hopcroft, 2015; Daly et al., 2019). They can also play a role in the diet of various fish in the Bering Sea, where high pteropod abundance occurs in the southern part of the basin, predominantly during the autumn (Eisner et al., 2014, 2017, 2017), making them one of the most dominant components of the diet of various salmon species (Zavolokin et al., 2007). In the Amundsen Gulf, pteropods comprise a small component of demersal Arctic cod diets (Majewski et al., 2016) and can be found at high numbers in the stomachs of coastal fish, including Arctic char (Niemi et al., 2021). In addition, given that pteropods in these regions have one of the highest abundances and biomass on the global scale, they also significantly contribute to the biological pump, especially to the carbonate flux (Bednaršek et al., 2012a). The most abundant species is *Limacina helicina*, which is present in two forms that are morphologically distinct from each other in the adult stage; one designated as *L. helicina helicina*, distinguished by an extended spire with striated surface, and the other as *L. helicina pacifica*, with a depressed (flat) spire and no striae present (McGowan, 1963; Janssen et al., 2019).

Assessing OA risks requires explicit linkages between three components (*sensu* Williams et al., 2008): (1) regional and local *exposure* to OA (e.g., changes in habitat suitability, spatial and temporal habitat change); (2) species' *sensitivity* governed by intrinsic metabolic and ecological traits, such as climatic preferences, reproductive outputs, habitat use, and biotic and abiotic interactions; and (3) *resilience and adaptive capacity* (e.g., genetic and phylogenetic diversity, phenotypic plasticity, life history traits, dispersal potential, spatial connectivity). Emerging literature illustrates the species' sensitivity under increasing OA exposure, but little is known about a vital component of the risk assessment: their distinct ecological, phenotypic or evolutionary specialization to changing conditions (e.g., Williams et al., 2008; Burridge et al., 2015).

Given the key role of pteropods in high-latitude ecosystems, there is an urgent need for an integrated assessment of OA risks for pteropod population viability in the high-latitudinal habitats, including the eastern part of the North Pacific, GoA,

Bearing and Amundsen Gulf. Following Williams et al. (2008), we delineated pteropod OA risk assessment as a combination of exposure, sensitivity, and adaptive capacity. First, OA *exposure* was estimated using hydrographic observations and regional ocean biogeochemical models; we used model outputs to define short-term, seasonal OA exposure, as well as longer-term OA trends with the interannual and decadal changes that characterize a gradual OA intensification in the species' exposure. These metrics of change offer tools to delineate the location of OA hotspots and habitat suitability with respect to OA, as well as temporal windows during which the biological exposure will be most significant.

Second, *sensitivity* was determined by observing early and well-defined negative effects of OA on pteropods, starting at aragonite saturation state (Ω_{ar}) values below 1.3 (Bednaršek et al., 2019), which is related to the shell biomineralization processes (dissolution and calcification). Such sensitivity was explored with respect to various morphotypes and matched with Ω_{ar} observations of the pteropods' place of origin. Another important aspect of sensitivity is life history, specifically that of exposure severity as it co-occurs with varying levels of vulnerability over pteropod life stages.

Third, potential *resilience* was related to adaptive capacity, or phenotypic plasticity, genetic population structure, and population (spatial) connectivity. Genetic-based analyses can be used to identify cryptic species and their distribution and connectivity across all regions. Given limited knowledge about pteropod cryptic diversity (on the level of *Limacina spp.*) in the region, we focus our initial efforts on characterizing diversity at the species, subspecies, and morphotype levels (Maas et al., 2013; Gasca and Janssen, 2014; Sromek et al., 2015a,b; Shimizu et al., 2018, 2021). OA-induced exposure would not necessarily result in local vulnerability if individuals were replaceable. Evidence of co-occurring cryptic species or subspecies with differential response to OA might buffer changes in abundance. Similarly, large-scale spatial connectivity between geographic areas may promote replacement from unaffected areas.

Here, we conduct a comprehensive assessment of OA risks for the pteropod population in the eastern North Pacific Ocean and identify the areas of potential concern with respect to OA in the North Pacific subpolar gyre, GoA, Bering Sea, and Amundsen Gulf. We used a combination of high-resolution models, chemical observations, particle tracking and genetic surveys of species morphometrics to determine exposure, biological responses related to sensitivity, and resilience or adaptive capacity of pteropods to OA.

METHODS

Physical-Chemical Seawater Characterization

Water samples for physical and chemical parameters were collected on the GO-SHIP P16N cruise (**Figure 1A**), the Dyson cruise in the Bering Sea (**Figure 1B**) and in the Amundsen Gulf (Canadian Beaufort Sea-Marine Ecosystem Assessment, or CBS-MEA; **Figure 1C**). Water was collected with a CTD/rosette package equipped with sensors for temperature (°C), salinity (PSU), and oxygen (μmol kg^{-1}), and a rosette of Niskin bottles for collecting discrete water samples throughout the water column. Dissolved oxygen was measured using titrations. Dissolved inorganic carbon (DIC) and total alkalinity (TA) samples were collected at discrete depths throughout the water column. In the Bering Sea, TA and DIC lab analyses were conducted on the water samples where pteropods were present. DIC and TA samples were collected in 250 ml borosilicate glass bottles and preserved with mercuric chloride following Dickson et al. (2007). DIC was measured using gas extraction and colorimetric titration with photometric endpoint detection (Johnson et al., 1998). TA was determined using open-cell potentiometric titration with a full curve Gran end-point determination (Haradsson et al., 1997). Certified Reference Materials (CRMs) were analyzed with both the DIC and TA samples as an independent verification of instrument calibrations (Dickson et al., 2007; Feely et al., 2016). Precision of measurements for DIC and TA was better than 0.1 % and 0.2 %, respectively. The saturation state of seawater with respect to aragonite was calculated from the DIC and TA measurements with the CO2SYS program (Lewis and Wallace, 1998) using the dissociation constants of Lueker et al. (2000) and the boron constant of Lee et al. (2010). Based on the uncertainties in the DIC and TA measurements and the thermodynamic constants, the uncertainty in the calculated Ω_{ar} was approximately 0.02. The Ω_{ar} observed values were correlated with the pteropod shell parameters (dissolution, density, thickness).

Pteropod Sampling

The list of stations where pteropods were collected, along with the data on abundance (reported in individuals per m^2), shell morphological and genetic characteristics across all the investigated stations (North Pacific subpolar gyre, GoA, Bering Sea, Amundsen Gulf) are presented in **Figure 1** and **Table 1**. Pteropods were sampled at 12 stations ranging from 48° to 56°N in the Gulf of Alaska and North Pacific subpolar gyre on the GO-SHIP P16N cruise in May and June 2015. Pteropods were collected using 202 and 335 μm mesh Bongo nets that were obliquely trawled for 20 min across the upper 100 m of the water column at night. Pteropod samples from the Bering Sea were obtained during an oceanographic survey by NOAA Alaska Fisheries Science Center (DY17-04 and DY17-08) in spring and summer (April and August) 2017. Samples were collected using 505 μm mesh net at six different stations. All pteropods were preserved in 100% buffered ethanol. Such sampling method does not accurately represent pteropod abundances or their life stages, and thus, abundance data was not reported for the Bering Sea. During the 2018, pteropods in the Amundsen Gulf were collected using a 500 μm mesh Bongo net that was obliquely trawled for up to 15 min across five different depth strata: 0–25 m, 25–50 m, 50–100 m, 100–200 m, and > 200 m. All sampling was conducted during daylight hours and pteropods were handpicked and frozen (−80°C) for genetic and shell analyses. From the 2018 CBS-MEA sampling stations, pteropods were selected from stations at CPB, MTI

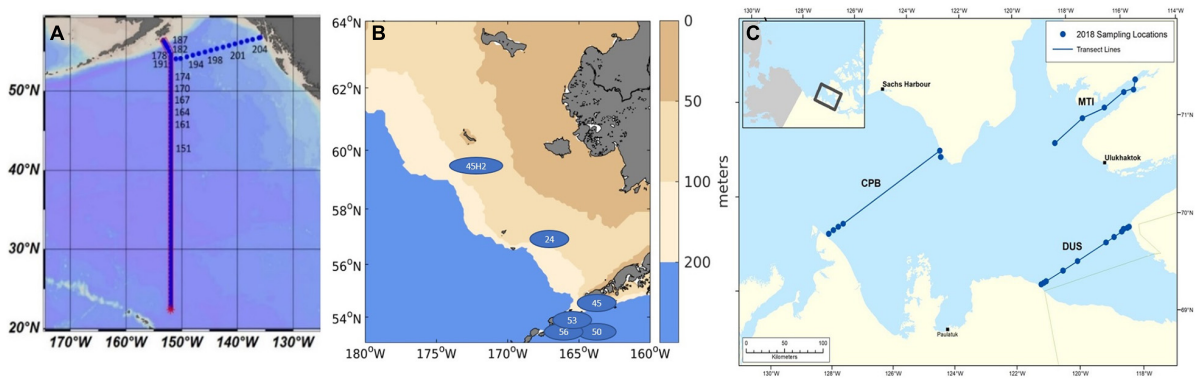


FIGURE 1 | Biological samples taken in the Eastern pacific subpolar gyre and the GoA (**A**; samples analyzed from stations 164 to 204), and the Bering Sea (**B**; blue ellipses) and Amundsen Gulf **(C)** with three indicated transects related to the pteropod origin (Cape Bathurst (CPB), Dolphin and Union Strait (DUS), and Minto Inlet (MTI; see Niemi et al., 2021).

and DUS transects to be analyzed for shell morphometrics, density, and thickness.

Exposure to OA in the GoA Based on the GoA-COBALT Model

To estimate seasonal, decadal, and long-term exposure to OA in the GoA, we used model output from a hindcast simulation conducted with the GoA-COBALT (Carbon, Ocean Biogeochemistry and Lower Trophic) model (Hauri et al., 2020). This model is based on the three-dimensional physical Regional Oceanic Model System (ROMS, Shchepetkin and McWilliams, 2005), the modified version of the COBALT (3PS-COBALT, Stock et al., 2014; van Oostende et al., 2018) model, and the moderately high-resolution terrestrial hydrological model by Beamer et al. (2016). Physical initial and boundary conditions were taken from the Simple Ocean Data assimilation ocean/sea ice reanalysis 3.3.1 (SODA; Carton et al., 2018). Dissolved inorganic carbon (DIC) and total alkalinity (TA) initial conditions were taken from the mapped version 2 of the Global Ocean Data Analysis Project (GLODAPv2.2016b; Lauvset et al., 2016) data set. DIC was adjusted to the corresponding hindcast year using regional anthropogenic CO_2 estimates by Carter et al. (2017). Nitrate, phosphate, oxygen, and silicate initial conditions were extracted from the World Ocean Atlas 2013 (Garcia et al., 2013). All other variables were initialized based on a climatology from a GFDL-COBALT simulation (1988– 2007), as described in Stock et al. (2014). The model was run from 1980 to 2013 and was forced with atmospheric pCO_2 observations from the Mauna Loa CO_2 record ([1]last accessed 22 January 2018). Winds, surface air temperature, pressure, humidity, and radiation were forced with data from the Japanese 55-year Reanalysis (JRA55-do) 1.3 project (Tsujino et al., 2018). Modeled freshwater was brought in from numerous rivers and tidewater glaciers at a 1 km resolution and daily timestep with point-source river input via exchange of mass, momentum, and tracers through the coastal wall at all depths (Beamer et al., 2016; Danielson et al., 2020). Nutrient, DIC, and TA concentrations in the freshwater were based on available observations (Stackpoole et al., 2016, 2017). The reader is referred to Hauri et al. (2020) for more information on the model and a detailed model evaluation.

Exposure to OA in the Bering Sea

Ocean acidification (OA) exposure in the Bering Sea was estimated with model results from a 10 km horizontal resolution implementation of the Regional Ocean Modeling System (ROMS; Shchepetkin and McWilliams, 2005; Danielson et al., 2011) denoted as "Bering10K", coupled to the BEST-NPZ ecosystem model (Gibson and Spitz, 2011). Atmospheric forcing of air temperature, winds, specific humidity, rainfall, and shortwave and longwave radiation come from The Climate Forecast System Reanalysis (CFSR; Saha et al., 2010) and CVSv2 operational analysis (Saha et al., 2014). Tidal mixing and ice dynamics were also included. The BEST-NPZ ecosystem model recently underwent a substantial code revision aimed at improving model simulation of biological variables, namely primary productivity, through revisions to the ecosystem light and nutrient equations and by increasing the number of vertical layers from 10 to 30 (Kearney et al., 2020). This ecosystem model includes two phytoplankton groups (large and small), microzooplankton, large and small copepods, and euphausiids. Phytoplankton productivity consumes nutrients (nitrate, ammonium, iron) which are transferred to zooplankton biomass via grazing, or to detritus via mortality. Carbonate chemistry has also been added to model ocean acidity and elucidate underlying mechanisms of inorganic carbon cycling within different shelf regions (Pilcher et al., 2019). Boundary and initial conditions for DIC and TA were calculated from empirically derived fits with salinity using ship-based data collected during the Bering Sea Ecosystem Study (BEST) and Bering Sea Integrated Research Project (BSIERP). Freshwater runoff was modified to contain seasonally varying concentrations of DIC and TA representative of outflow from the mouth of the Yukon River. Atmospheric CO_2 varied seasonally following output from the NOAA Earth System

[1]https://www.esrl.noaa.gov/gmd/ccgg/trends/data.html

TABLE 1 | Collected samples with indication for all the additionally conducted measurements on shell morphology, genetics, and dissolution estimates from the Eastern Pacific subpolar gyre and GoA on the GOSHIP P16N cruise; Dyson CBS-MEA in the Bering Sea cruise; and in the Amundsen Gulf.

Stations number	Depth (m)	Temp (°C) at 50 m	Lat	Long	Measurements conducted	Abund (ind per m^2)	Dissolution Type	Aragonite Saturation State (Ω_{ar}) at 50 m	Sample size for genetics
Stations in the North Pacific subpolar gyre and the Gulf of Alaska from the GO-SHIP P16N cruise									
151	50		41.301	152.001	genetics	NA	NA	NA	5
161	50	7.1	46.300	151.599	genetics	NA	NA	NA	6
164	50	6.9	48.001	152.598	SEM, μCT, H/D, genetics	100	Type I (73%), intact (27%)	1.83	11
167	50	6.5	49.230	152.000	SEM, H/D, genetics	102	Type I (53%), intact (47%)	1.73	17
170	50	6.0	51.000	152.000	SEM, H/D, genetics	42	Type II (70%), intact (30%)	1.68	9
174	50	5.6	52.599	151.598	SEM, μCT, H/D, genetics	91	Type II (92%) intact (8%)	1.48	12
178	50	6.7	54.396	151.597	SEM, H/D, genetics	69	Type II (60%), Type III (40%)	1.69	9
182	50	6.2	55.466	152.504	SEM, μCT, H/D, genetics	123	Type I (80%), Type II (20%)	1.62	10
187	50	6.4	56.144	153.111	SEM, H/D, genetics	307	Type I (70%) Type II (30%)	1.51	11
191	50	5.6	54.043	151.067	SEM, H/D, genetics	332	Type II (100%)	1.46	10
194	50	5.9	54.330	148.034	SEM, μCT, H/D, genetics	423	Type II (83%), intact (17%)	1.57	6
198	50	7.2	56.218	143.434	SEM, H/D, genetics	149	Type I (55%), intact (45%)	1.83	6
201	50	8.2	55.581	140.297	SEM, H/D, genetics	88	Type I (67%), intact (33%)	1.78	6
204	50	8.1	56.330	137.183	SEM, H/D, genetics	87	Type I (36%), intact (64%)	1.68	6
Stations in the Bering Sea from the Dyson CBS-MEA cruise									
24	50	0.7	57.520	163.601	SEM, H/D, genetics	NA	Type II (40%), Type III (60%)	1.27	5
45	50	3.2	55.056	165.087	SEM, μCT, H/D, genetics	NA	Type I (55%), intact (45%)	1.48	7
50	50	3.9	54.426	165.146	SEM, H/D, genetics	NA	Type I (35%), intact (65%)	1.82	7
53	50	4.2	54.360	165.916	SEM, μCT, H/D, genetics	NA	Intact (100%)	1.11	8
56	50	4.6	54.711	165.202	SEM, H/D, genetics	NA	Type I (45%), intact (55%)	1.45	5
45H2	50	NA	60.573	173.644	H/D, genetics	NA	N/A	1.12	7
Stations in the Amundsen Gulf (Canadian Beaufort Sea-Marine Ecosystem Assessment)									
MTI 06	50	NA	71.405	116.536	μCT, H/D	NA	MTI: Type III (70%),	MTI: 1.30	NA
MTI 04	50	NA	71.296	117.346	μCT, H/D	NA	Type II (16%)		NA
DUS 04	50	NA	63.727	119.954	μCT, H/D	NA	Type I (14%)		NA
BPT03	50	NA	69.699	123.439	genetics	NA	DUS: Type III (63%),	DUS: 1.61	4
CPB03	50	NA	70.605	127.397	genetics	NA	Type II (21%),		6
DUS03	50	NA	69.652	120.575	genetics	NA	Type I (16%)		6
FKN05	50	NA	70.002	125.966	genetics	NA	CPB: Type III (93%),	CPB: 1.10	4
MTI03	50	NA	71.368	117.482	genetics	NA	Type II 7%		2
MTI05	50	NA	71.235	117.278	genetics	NA			2
FEXHC3	50	NA	70.297	126.383	genetics	NA			2

Research Laboratory's CarbonTracker 2016 Product (CT2016; Peters et al., 2007).

Estimating Spatial Connectivity Using Particle Tracking Model

To examine spatial connectivity in the GoA, we used hydrodynamic output from the model hindcasts described in Coyle et al. (2019). Atmospheric forcing of air temperature, winds, specific humidity, rainfall, and shortwave and longwave radiation were interpolated from the CFSR (Saha et al., 2010) and CVSv2 operational analysis (Saha et al., 2014). These hindcasts include coastal runoff (Beamer et al., 2016) as well as explicit tidal dynamics (and associated mixing). Tidally filtered weekly averaged velocities from this ROMS-based, 3-km resolution model were re-gridded to regular latitude-longitude-depth coordinates, and these values were subsequently interpolated to track particles forward in time, using a daily time step, at a constant 200 m depth.

The literature suggests that, due to prevalent currents, pteropods from the eastern North Pacific Gyre are advected (McGowan, 1963) into the GoA via northwards transport. As such, we initiated particle tracking in the offshore regions at 53°N in April for the following reasons: first, the prevalence of the northward advection that can carry pteropods from the offshore eastern Pacific subpolar gyre toward the GoA within the duration of their life cycle; second, the known offshore regional presence of pteropods and their spring spawning (e.g.,

Mackas and Galbraith, 2012; Doubleday and Hopcroft, 2015); third, southernmost boundary in the model domain where the initiation was feasible. The duration of particle tracking for 8 or 12 months was used to correspond to the pteropod life history, delineated by the completion of their early life stage into subadults or adults (Fabry, 1989). The particle tracking location with the shortest duration of initiation was thus used as an indicator of the early, most sensitive life stages, while the location of particles with the longest duration indicated the presence of the adults.

To examine spatial connectivity in the Bering Sea, a similar procedure was employed using output from the ROMS-based, 10-km resolution model described in Kearney et al. (2020). The physical structure and forcing of this model was identical to the version used for the Bering Sea OA exposure methods, as described above for the ROMS Bering 10K model. Regularly gridded, weekly averaged velocities from this model hindcast were interpolated to track particles backward in time using 60°N, 173°W as an ending location (on April 15, 2017) in a daily time step at a constant 50 m depth, which is an average depth distribution for *L. helicina*.

Morphometrics of Pteropod Morphotypes

Individuals of two different morphotypes of species *Limacina helicina*, recognized as *L. helicina helicina* and *L. helicina pacifica*, were selected from the samples to conduct the analyses at the morphotype level. The samples did not include morphotype characterization for individuals smaller than 0.5 mm in diameter. Individual pteropod height and width were measured with the Amscope software (Irvine, CA, United States) to subsequently determine specific morphotype. Separation of different morphotypes is possible only among the adults (McGowan, 1963; Janssen et al., 2019); thus, we only analyzed the adult life stages. Separation of the adults was first based on the presence or absence of striation (Janssen et al., 2019) and the shape of the shell (high spired shape vs flattened). The shape was reported as a height-diameter ratio (H/D) ratio (McGowan, 1963). Lower H/D ratios (flat shells) with no striation identified adult *L. helicina pacifica*, while higher H/D (with extended shell spire) and striation presence identified the adults of *L. helicina helicina* (**Figure 2**). When H/D ratios were plotted against the diameter of the shell, the shell proportions were fairly constant throughout the size range of the individuals collected, allowing subsequent separation of the two morphotypes (McGowan, 1963). Altogether, 98 individuals were analyzed for the morphometric analyses: 56 from the Eastern Pacific subpolar gyre, including the GoA, 17 from the Bering Sea, and 25 from the Amundsen Gulf. However, the sampling approach was not adequate to quantitatively determine spatial distribution of different morphotypes. We used both morphotypes for genetic analyses and shell dissolution analyses, while only *L. helicina pacifica* was used for investigating shell dissolution in combination with bulk shell density and thickness, due to insufficient sample numbers for *L. helicina helicina*.

Bulk Shell Density and Thickness Using Microcomputer Tomography (μXCT)

For measures of pteropod shell deposition processes, an average of 10 organisms of *L. helicina pacifica* per station were analyzed for bulk shell density and thickness using micro-computed tomography (μXCT; **Figure 2**). Only the adult animals with greater than 4 whorls were analyzed, so that shell deposition patterns could be related to a single life stage, thus excluding the early life stages that could potentially introduce life-stage bias. We differentiated two morphotypes based on their H/D ratio (McGowan, 1963; Janssen et al., 2018), as well as the absence of striation. Therefore, density and thickness measurements were morphotype-specific (only on *L. helicina pacifica)*. A total of 83 air-dried individuals were analyzed, 41 from the Eastern subpolar gyre with the GoA, 16 from the Bering Sea and 25 from the Amundsen Gulf. After overnight drying, a μXCT ScanXmate–D160TSS105 (Comscantecno Co., Ltd., Yokohama, Japan) was used to apply X-rays to the sample stage. This system can rotate through 360 degrees, with high-resolution settings (X-ray focus spot diameter, 0.8 μm; X-ray tube voltage, 80 kV; detector array size, 1024 × 1024; 1800 projections/360°, four-times averaging). This X-ray analysis focused on the aragonite shell; therefore, the soft tissue inside the shells was not considered and was numerically removed from the 3D images. Spatial resolution of the scanned image was from 1.0 to 1.2 μm, depending on the size of the shell. Reconstruction of 3D tomography was obtained by the convolution back projection (CBP) method used the ConeCTexpress (Comscantecno Co., Ltd., Yokohama, Japan). Calculation of shell thickness and density was performed by Molcer Plus imaging software (White Rabbit Corp., Inc., Tokyo, Japan).

To evaluate the bulk density of shell, we used the CT number. The CT number is a relative number of mean grayscale value with respect to the standard material of known density. When the object is constituted by a single substance, the CT number is proportional to the bulk density. In this study, we used a limestone grain (calcite crystal, calcite standard NIST RM8544 (NBS19)) with a 300 μm diameter as the standard material, which has the same composition of the target material. This limestone particle was used on individual pteropod shells for all analysis and the calculation of the CT number. Pteropod bulk shell density was evaluated by 16-bit grayscale contrasts (65,536 gray level gradations) of a transparent image achieved by μXCT. We used the CT number of the pteropod shell which is represented by equation 1:

$$CT\ number = [(\mu_shell - \mu_air)/(\mu_calciteSTD - \mu_air)] \times 1000 \quad (1)$$

where μ_{shell}, μ_{air}, and $\mu_{calciteSTD}$ were the X-ray attenuation coefficients of the sample, calcite, and air, respectively. The bulk shell density for an entire test was evaluated with equation 2:

$$Mean\ CT\ number = \frac{1}{T}\sum_{n=230}^{1000} nT_n \quad (2)$$

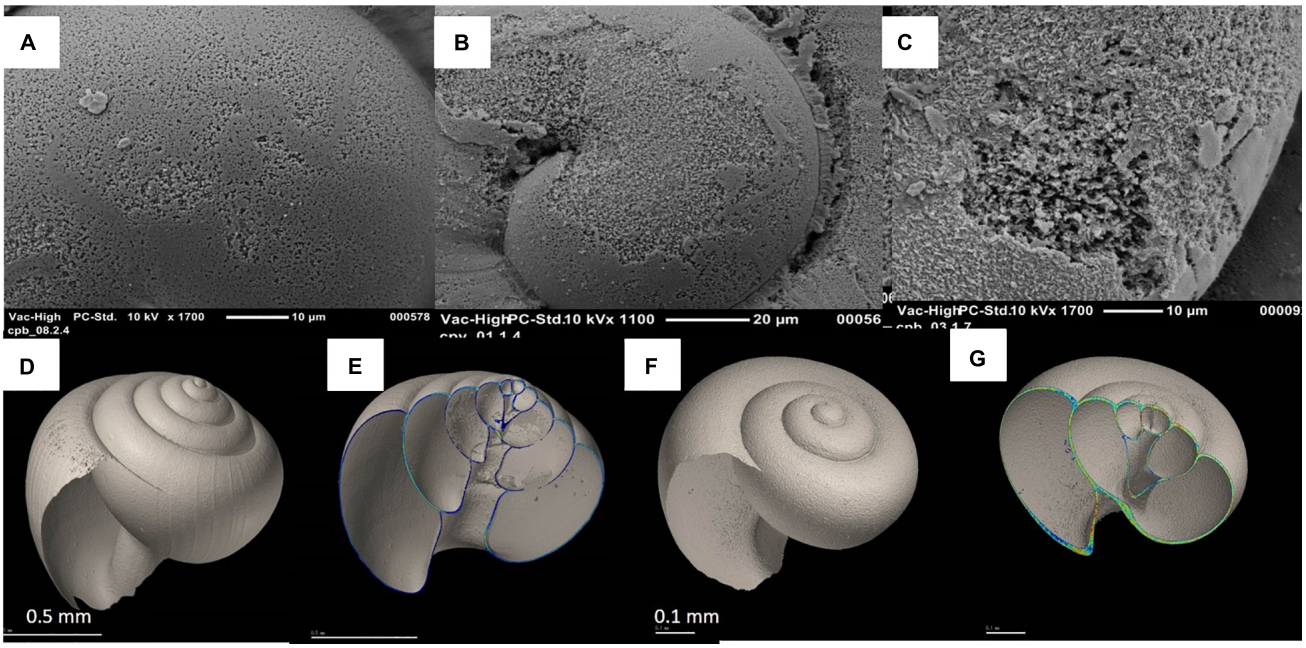


FIGURE 2 | Various degrees of pteropod shell dissolution from the GoA and the Bering Sea, progressing from increased porosity, moderate to the most severe dissolution; Type I **(A,B)**, Type II **(B,C)**, and Type III **(C)**. Two different Morphotypes of *Limacina helicina*: *Limacina h. helicina* **(D)** and *Limacina h. pacifica* **(F)** with respective images of their shell thickness for *Limacina h. helicina* **(E)** *and for Limacina h. pacifica* **(G)**. Color bar indicates the CT number as a shell density from 380 (lowest density) to 1000 (highest density).

where n was the CT number, T_n was the total number of voxels with a specific CT number (n), and T was the total number of voxels in the whole shell. The highest density was 1000 and the lowest density was 230, being represented by the boundary between the pteropod shell and the surrounding air. The mean CT number indicated the mean density of an individual test as normalized per shell length, which we refer to as 'normalized shell thickness' or 'normalized bulk shell density' in the text below.

Bulk shell density (g per cm^{-3}) was calculated from the mean CT number as following:

$$Bulk\ shell\ density\ =\ (CT\ number - 49.04)/350.47 \quad (3)$$

Shell morphometrics (H/D ratio), thickness, and density data were compared with the observational data related to Ω_{ar} to investigate the impact of carbonate chemistry on shell-building processes over the depth of the water column inhabited by the pteropods (*sensu* Bednaršek et al., 2014). In addition, shell density and thickness were statistically correlated to the H/D ratio across all the investigated basins using either linear or polynomial regression (**Supplementary Figure 1**).

Shell Dissolution

We identified the incidence of different types of shell dissolution across individuals (**Table 1** and **Supplementary Figure 2**) collected along carbonate chemistry gradients and compared shell dissolution across different regions of the subpolar gyre, GoA and Bering Sea. While evaluating shell dissolution, it is important to have as unbiased process as possible. Thus, while we randomly selected the individuals for shell dissolution not to introduce any bias in the shell examination process, we also made sure we had a sufficient number of organisms present to determine any difference in the shell dissolution between two different morphotypes. When the number of organisms allowed for this, we aimed to equally split the analyzed subsample between two different morphotypes (in the North Pacific subpolar gyre and the GoA); however, when this was not possible due to insufficient amount of pteropod individuals (such as in the Bering Sea), then we analyzed whatever morphotypes were present. The occurrence of pteropod shell dissolution in the Amundsen Gulf, as relevant to this study, has been described by Niemi et al. (2021) and here only discussed briefly. Shell dissolution was assessed for each individual and an average value was calculated per station (**Table 1** and **Supplementary Figure 2**). We analyzed 10-15 individuals from each of 12 stations from the subpolar gyre, including the GoA, and 6 stations from the Bering Sea.

We prepared each individual by removing the organic layer using a combination of protocols (Bednaršek et al., 2012b, 2016a). Briefly, pteropods were transferred from 100% to 70% and 50% ethanol in gradual steps, rinsed thoroughly with DI water, exposed to diluted bleach (5% sodium hypochlorite) for a treatment of approximately 30 min that was subsequently rinsed with DI water for 2-3 times to clean the shell surface, and subsequent air-dried for 12 h. Mounted samples were coated with a combination of Au-Pd for 120 s at 35A before being examined under the scanning electron microscopy (SEM).

For measures of shell dissolution severity, the presence of three categories of dissolution was assessed following Bednaršek et al. (2012b). Type I indicated a shallow, upper-prismatic level of dissolution, followed by Type II with modest dissolution protruding deeper into the cross-lamella layer, and Type III indicating the most severe dissolution protruding deeper into the crystalline layers (**Supplementary Figure 2**). The percentage dissolution type occurrence was assessed per each individual and correlated with the observational cruise data related to Ω_{ar} in the subpolar gyre, the GoA and the Bering Sea.

GENETIC-BASED ANALYSES

Sample Collection

Between five and 17 individuals per station were sampled from the Bering Sea and Gulf of Alaska cruises (**Table 1**). Sampling was opportunistic and depended on frequency and condition of individuals collected at each station. An additional 13 individuals were sampled from the Amundsen Gulf to act as "outlier" samples to determine species or subspecies distribution across broader oceanographic basins (**Table 1**). Individuals were photographed prior to DNA extraction and their morphotypes were recorded using the methods described above.

DNA Extraction, PCR, and Sequencing

DNA from each individual was extracted using the QIAGEN DNeasy tissue extraction kit (Hilden, Germany). An approximately 600 base pair region of Cytochrome c oxidase I (COI) unit was amplified using universal primers for marine invertebrates (Forward: GGTCAACAAATCATAAAGATATTGG, Reverse: TAAACTTCAGGGTGACCAAAAAATCA; Folmer et al., 1994; Geller et al., 2013; Sromek et al., 2015b). Polymerase chain reactions comprised 10–15 ng of template DNA, 4.0 mM $MgCl_2$ and GoTaq G2 Master Mix (Promega, United States), using an initial cycle at 98°C for 3 min, 30 cycles of 10 s at 98°C, 30 s at 55°C and 30 s at 72°C, and 5 min at 72°C. PCR products were Sanger sequenced in both directions at a commercial facility (Molecular Cloning Laboratories, San Francisco, CA, United States). Consensus haplotype sequences for each individual were created using the COI forward and reverse sequences obtained.

To determine whether there was evidence for cryptic species within the regions we sampled, we examined genetic distances between individual haplotypes and visualized the data using phylogenetic trees. The haplotype distribution across the two morphotypes was explicitly examined. To determine whether there was evidence for population structure, genetic distances were calculated within and between haplotypes at each geographic station. Finally, the sequences generated as part of the current study were compared to previously published sequences (**Supplementary Tables 1**, **2**), to determine whether there was any evidence for species or population differentiation across the range of *L. helicina*.

In all analyses, sequences were aligned between individuals using the *Muscle* algorithm (Edgar, 2004). Pairwise distances (p-distance) between haplotypes and populations were estimated in MEGA V7.0 (Kumar et al., 2016), and standard error estimates were derived using 500 bootstrap replicates (**Supplementary Tables 3**, **4**). Phylogenies between haplotypes were determined using a Minimum-spanning network (Bandelt et al., 1999), calculated in PopART (Leigh and Bryant, 2015).

RESULTS

Habitats of Concern in the Subpolar Gyre and GoA as Related to OA

The P16N cruise data (from 2015) in the subpolar gyre and GoA shows that the dissolution-inducive corrosive waters (threshold for severe dissolution $\Omega_{ar} < 1.2$; Bednaršek et al., 2019) are shallowest at about 53°N, 152°W (**Figure 3**), with the isolines of $\Omega_{ar} < 1.2$ deepening both to the south in the southern subpolar region and to the north on the GoA continental shelf. The corrosive waters are characterized by "low" temperature (< 6°C), high DIC (> 2180 μmol kg−1), and $\Omega_{ar} < 1.2$ (**Figures 3A–F**).

GoA-COBALT model output (Hauri et al., 2020) of the time series of Ω_{ar} at 54°N, 152°W and at 57°N, 152°W indicate that the Ω_{ar} shoaling into the upper 50 – 100 m of the water column occurs during winter and early spring, partially extending into summer (**Figure 4**). At depths greater than 100 m, most of the deeper waters across the GoA and shelf region are undersaturated with respect to aragonite ($\Omega_{ar} < 1$). In the GoA model outputs from 2013, there is a west-to-east deepening of Ω_{ar} in the upper 100 m of the water column, with the minimum Ω_{ar} occurring at about 51-55°N, 152°W, in the subpolar gyre (**Figures 3**, **5**). Accordingly, the depth of the Ω_{ar} saturation horizon (where $\Omega_{ar} = 1$) is shallowest in the western part of the study region (< 100 m) and deepens toward the eastern side of the subpolar gyre to approximately 110-130 m (**Figure 6**). The highest saturation state and deepest aragonite saturation horizon occur in the summer and autumn months, and significantly lower saturation states and shallower Ω_{ar} horizon occur during winter and early spring months (**Figure 4**). Summertime subsurface Ω_{ar} (spatially averaged across 50 to 100 m depth, and temporally averaged across June, July, and August) is generally < 1.3 across the region, especially in the near-shore regions of the northern and eastern GoA. From Kodiak (57°N/150°W) southward, wintertime (temporally averaged across December, January, and February) subsurface Ω_{ar} increases to levels > 1.3 along the shelf, while off the shelf, a large area stays undersaturated with respect to Ω_{ar} (**Figure 4A**). In the central region of the subpolar gyre and the GoA, Ω_{ar} saturation horizon is located near 50 m throughout the year (**Figure 5A**), while seasonal changes in the Ω_{ar} saturation horizon in the eastern part of the GoA cause shorter periods of exposure to low Ω_{ar} conditions (**Figures 5A,B**).

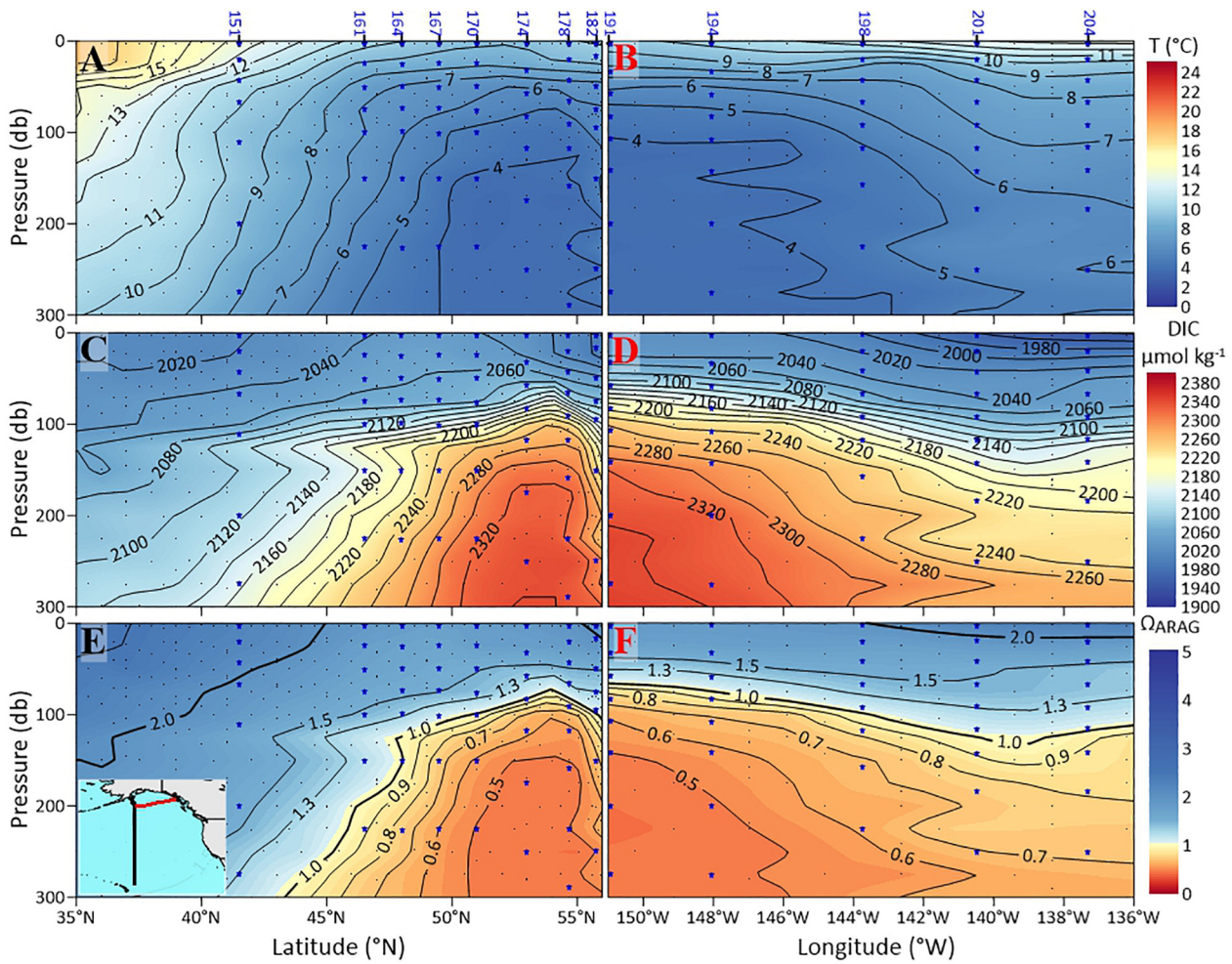


FIGURE 3 | Plots of observational data from the P16N cruise (Eastern Pacific subpolar gyre and the GoA) sections of: potential temperature °C **(A,B)**; dissolved inorganic carbon (DIC) in µmol kg^{-1} **(C,D)**; and aragonite saturation state, Ω_{ar} **(E,F)**. The sections on the left are from the south to north transect (black-colored contour on the small map), and the sections on the right (red colored contour on the small map) are from the west to east transect (see insert map in **E**). The pteropod station numbers are at the top. Indicated are the two solid black contour lines showing Ω_{ar} of 1 and 1.3.

Decadal Changes in OA Habitats in the GoA Over the 34-Year Period

In evaluating long-term change in the subpolar gyre and GoA since the 1980s, the model output suggests significant decline of Ω_{ar} in the upper 100 m of the water column (**Figure 4**). The area of undersaturated water over the 50 to 100 m depth range more than doubled between 1980 and 2013 at the location of the model output (**Figure 4A**). Such modelling results are consistent with large-scale field observations (Carter et al., 2017). While some subsurface waters are already undersaturated with respect to aragonite in 1980, areas of $\Omega_{ar} < 1$ are now much more widespread across the GoA. Furthermore, in 1980, Ω_{ar} frequently reach levels < 1.2 in waters deeper than 50 m, while in more recent years, Ω_{ar} also frequently reaches levels < 1.2 in the upper 50 m of the water column in both on- and off-shelf areas on a seasonal basis (**Figure 6**). In particular, the subpolar gyre is significantly lower in Ω_{ar} in the winter months. While Ω_{ar} conditions in the subpolar gyre in the 1980s ranged from $0.8 < \Omega_{ar} < 1.2$, current ranges are from $0.5 < \Omega_{ar} < 0.8$. Overall, the center of the subpolar gyre is currently the most vulnerable to the effects of increasing OA (Hauri et al., 2021). Although the eastern part of the GoA has seen a similar magnitude of change, the current OA conditions are less severe.

Current Habitats of Concern With Respect to OA in the Bering Sea

The Bering Sea 10K model output suggests that in the subsurface water between 50 and 100 m Ω_{ar} is < 1.3 across nearly all of the Bering Sea shelf, and $\Omega_{ar} < 1$ for large portions of the northwestern shelf for both winter (December-February) and summer (June-August) months (**Figure 7**). In **Figure 7**, regions with a depth < 50 m, which are representative of the inner-shelf domain, are excluded. Subsurface Ω_{ar} values are generally lower in summer months compared to winter months, except for a

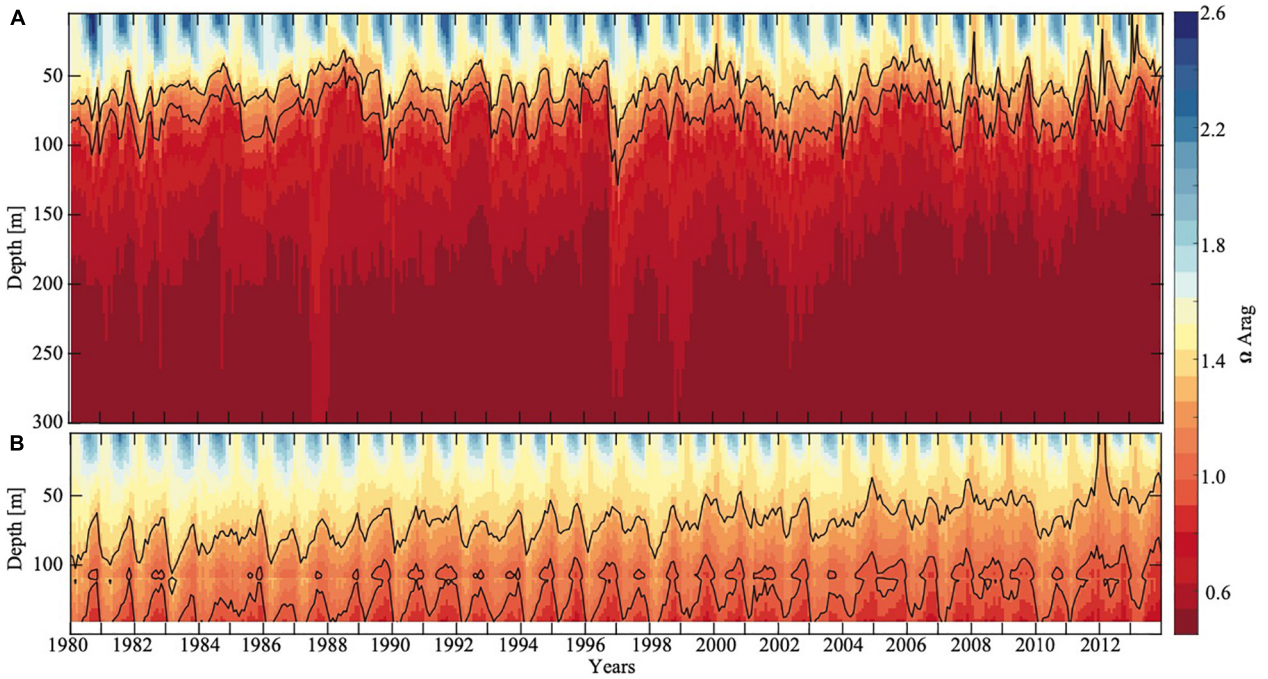


FIGURE 4 | Modeled aragonite saturation state of the Eastern Pacific subpolar gyre and the GoA as a function of depth and time (years) at station 191 (**A**, 54°N and 152°W) and at a random location on the shelf (**B**, 57°N and 152°W). Solid black contour lines show Ω_{ar} equal to 1 and 1.3. On the shelf, the seafloor is located at around 140 m depth (white area). Model output is from the GoA -COBALT hindcast simulation described by Hauri et al. (2020).

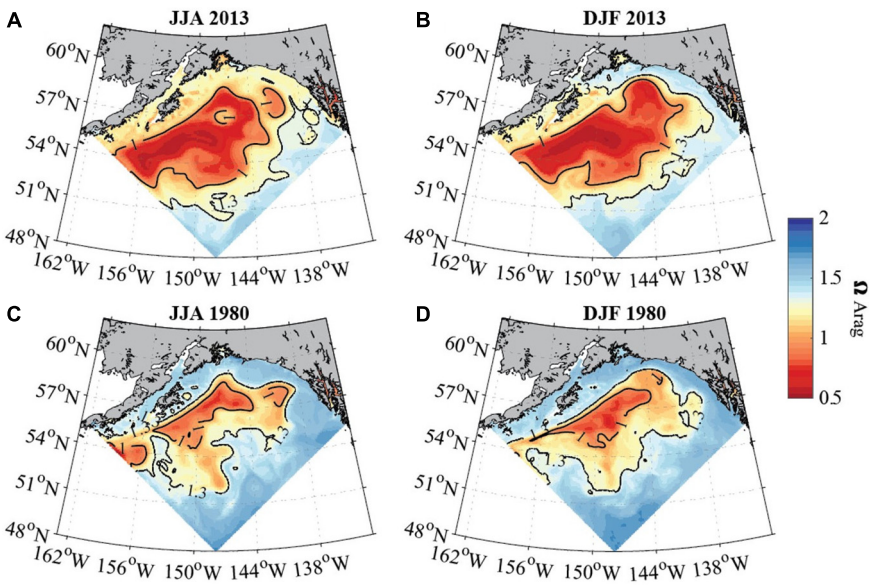


FIGURE 5 | Average seasonal aragonite saturation state (modeled data) across the upper 50 to 100 m in the GoA for June to August (**A,C**; left column) and December to February (**B,D**; right column) for 2013 (top row) and 1980 (bottom row). Solid black contour lines depict aragonite saturation state equal to 1 and 1.3. White areas show locations where the topography is shallower than 50 m. Model output is from the GOA-COBALT hindcast simulation described by Hauri et al. (2020).

relatively small region of buffered waters within Bristol Bay. The most corrosive waters are located in the northwestern Bering Sea. Panels A and B in **Figure 8** illustrate a depth profile of model output for Ω_{ar} along the midnorth (MN) shelf transect (denoted by the magenta line in **Figure 7**). Phytoplankton productivity in surface waters and respiration at depth generate a very strong

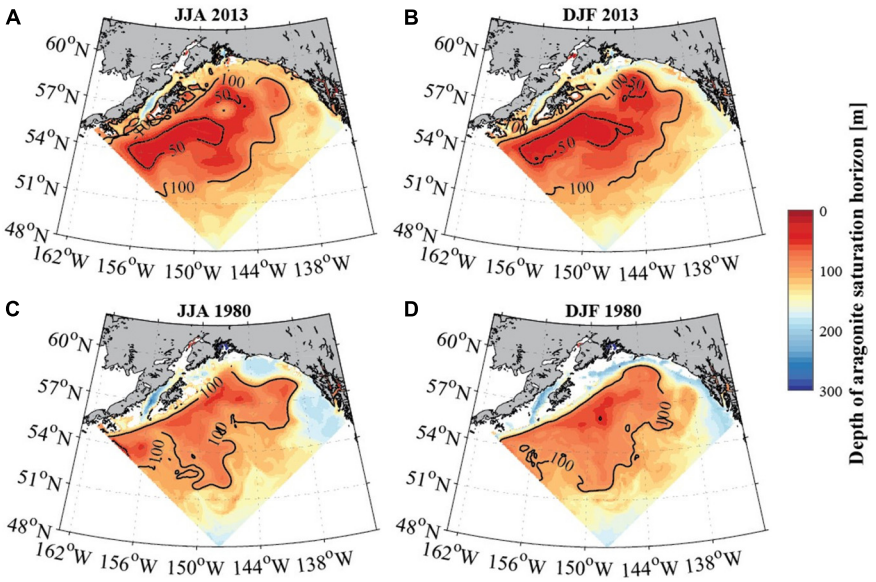


FIGURE 6 | Average seasonal depth of the aragonite saturation horizon [m] in the GoA for June to August (**A,C**; left column) and December to February (**B,D**; right column) for 2013 (top row) and 1980 (bottom row). Solid black contour lines depict depth of the aragonite saturation horizon at 50 and 100 m (modeled data). White areas show locations where the aragonite saturation (Ω_{ar}) horizon is deeper than the topography, indicating the absence of undersaturated waters. Model output is from the GOA-COBALT hindcast simulation described by Hauri et al. (2020).

vertical gradient in Ω_{ar} during summer, compared to a relatively weak vertical gradient in winter. Surface Ω_{ar} values are greater than 2 during the summer, but less than 1.3 during the winter. Panel C in **Figure 8** shows the modeled vertical profile of Ω_{ar} at an outer shelf location over the entire 2003–2012 period. This figure illustrates the seasonal cycle of low winter surface values, followed by higher surface Ω_{ar} values in spring-summer, and a subsequent subsurface drawdown in autumn due to respiration. Such intense seasonal changes in the spatial and vertical Ω_{ar} conditions define the exposure time of less favorable conditions ($\Omega_{ar} < 1.3$) on a seasonal basis. The subsurface values of Ω_{ar} tend to decrease by ∼0.1 over the 2003-2012 timeframe, coinciding with a shift in physical variability from a warm temperature period to a cold temperature period. This temperature shift in the colder years due to increased vertical mixing and nutrient resupply in the euphotic layer (Pilcher et al., 2019) generates an increase in primary productivity and anthropogenic carbon uptake, with subsequent increase in respiration that exacerbates the expected OA trend over this timeframe. The surface trends of 0.025–0.04 units/year are significant for the inner and middle shelf domains (Pilcher et al., 2019).

Current Conditions in the Amundsen Gulf

Generally, in the Canadian sector of the Amundsen Sea, the supersaturated conditions occurred in surface waters, while undersaturated conditions ($\Omega_{ar} < 1$) occurred across the Gulf in the Pacific halocline layer (50–200 m). Some smaller-scale variation in the Ω_{ar} is possible, depending on the transects sampled (**Figures 9A–C**), with such conditions described in more detail by Niemi et al. (2021). In the areas where pteropods were collected, Ω_{ar} in the Pacific layer ranged from 0.76 to 1.3, and averaged around 0.88, indicating that the pteropods' main habitat is largely corrosive in summer (**Figure 9**).

Sensitivity-Related Biological Parameters

Morphotype Distribution

Pteropods were present across all of our study regions in high abundances, especially from 55 °N (**Table 1**). Based on the presence of striations, as well as H/D ratios, two adult morphotypes were detected: *L. helicina helicina* with an inflated spire and striated whorls (**Figure 2D**), and *L. helicina pacifica* with a depressed flat spire and no striation (**Figure 2F**). The H/D ratios plotted against the diameter of the shell showed a relatively constant ratio, regardless of the size range of the adults (**Supplementary Figure 1A**). The ranges of H/D values for the two morphotypes were similar to those previously reported by McGowan (1963). The H/D range for *L. h. pacifica* was between 0.8 to 1, while H/D range for *L. h. helicina* was higher than 1. All morphotypes were found in all three basins (**Supplementary Figure 1B**).

Shell Thickness and Density Related to the Shell Morphometrics

The distribution of H/D ratios in two morphotypes was also related to a specific range of normalized shell thickness and density (**Supplementary Figures 1C,D**). Normalized bulk shell thickness showed an inverted bell curve shape relationship with the H/D ratio; its decrease was correlated with declining H/D ratios to a value of approximately 0.9 to 1. Below this ratio, normalized shell thickness started to increase (polynomial fit with $R^2 = 0.17$, p-value = 8.622E-05). These results indicate that the

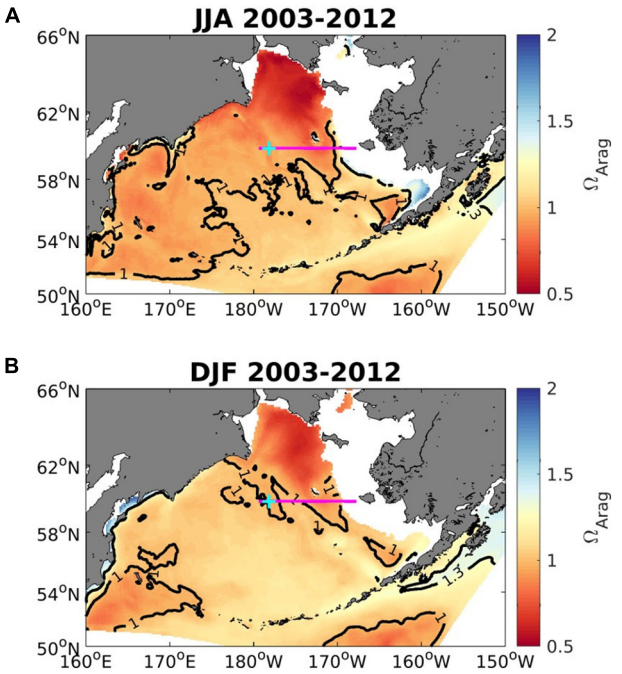


FIGURE 7 | Average seasonal aragonite saturation state (Ω_{ar}) across the upper 50 to 100 m in the Bering Sea for June to August (**A**; upper) and December to February (**B**; lower), averaged over 2003-2012 (modeled data). Solid black contour lines depict aragonite saturation state equals 1 and 1.3. White areas show locations shallower than 50 m. Magenta line shows the midnorth (MN) shelf transect, and cyan plus-sign denotes the MN18 station location. Model output is from the Bering10K hindcast simulation described by Pilcher et al. (2019).

organisms with lower spire (lower H/D range) built thicker shells compared to those on the upper range that built thinner shells (**Supplementary Figure 1C**). The density was not dependent on the H/D ratio, with similar densities across the range ($R^2 = 0.052$; $p = 0.0155$; **Supplementary Figure 1D**).

Environmental Control on Shell Building Processes

The impact of Ω_{ar} on the processes of pteropod morphometrics and shell characteristics (H/D ratio, normalized bulk shell density and thickness) across all investigated ocean regions (GoA, Bering, Amundsen) was examined in one morphotype, *L. h. pacifica* only. The H/D ratio of adult individuals was significantly correlated with Ω_{ar}. Linear regressions showed the best fit of H/D ratio to be correlated with the $\Omega_{ar,}$ at 50 m ($\Omega_{ar,50}$) representing an average depth of daily pteropod vertical migration (**Figure 10A**; $R^2 = 0.6966$, $p = 8.074E\text{-}16$). Linking shell morphometrics with the $\Omega_{ar,}$ adult individuals with higher H/D ratios (extended shell with higher spire) were observed at higher Ω_{ar}, while the organisms with lower H/D (flatter shell with lower spire) were present at lower $\Omega_{ar.}$ We fitted normalized bulk shell thickness against Ω_{ar} averaged over 100m depth ($\Omega_{ar,avg100}$). The best linear fit shows the shell thickness to significantly increase with a declining $\Omega_{ar,avg100}$ (**Figure 10B**; $R^2 = 0.31$, p-value = 0.028). At higher values of $\Omega_{ar,}$ adult pteropods built shells with higher H/D ratios and lower shell thicknesses (**Figures 10A,B**; **Supplementary Figure 1**). We also fitted shell thickness against the Ω_{ar} at 100 m; the best fit found was polynomial one, where shell thickness increased up to a Ω_{ar} of 1.1, upon which it started to decrease ($R^2 = 0.623$; p-value = 2.581E-07; **Figure 10C**). This value could be considered an inflection point (threshold), below which the shell building processes start to decline. Such patterns were observable when combining the data of *L. helicina pacifica* across investigated ocean regions. However, on the regional basis, the lack of sufficient data or limited $\Omega_{ar,avg100}$ condition gradients prevented us from making conclusions for each region separately, especially for the Bering Sea region with its narrow range of $\Omega_{ar,avg100}$ conditions. Normalized bulk shell density was not significantly correlated with $\Omega_{ar,avg100}$ ($R^2 = 0.027$, p-value = 0.273; **Figure 10D**). These results imply that only the processes influencing shell thickness, and not density, were impacted by the carbonate chemistry conditions.

Pteropod Shell Dissolution Across the Regions

High resolution observations of pteropod shell surface under SEM demonstrated a range of dissolution values, depending on observed Ω_{ar} conditions at the specific sample locations (**Figure 2**). The samples collected during spring-summer in the subpolar gyre and the GoA were characterized by a notable difference in the shell dissolution, with the stations across the central and western side of the study region (stations 178-191, **Figure 11**) showing the greatest severity of dissolution (**Table 1**). The areas of dissolution spatially coincide with the regions characterized by a shallower Ω_{ar} depth horizon, depicted in both the observational data and model outputs (**Figure 5**). In comparison, shell dissolution declined toward the east, with complete disappearance of any dissolution patterns east of 139°W. In addition, the more inshore locations (Station 187) had less severe dissolution compared to the offshore samples. This result again coincides with the GoA-COBALT model output of higher Ω_{ar} onshore and lower Ω_{ar} and shallower Ω_{ar} saturation horizon offshore (**Figures 5**, **11**).

Out of the six collected samples in the Bering Sea during spring-summer, various dissolution ranges were observable (**Table 1**), mostly characterized by Type I and II dissolution, with only station 24 having more severe (Type III) dissolution present. Because there was insufficient data from the cruise to interpolate across the stations, we could not correlate shell dissolution with the oceanographic gradients as in the GoA, so we used the model output instead (**Figures 7**, **8**). The stations with the most severe dissolution were distributed over the central part of the eastern Bering Sea shelf. This coincides with the model outputs of the observed shallow Ω_{ar} horizon and $\Omega_{ar} < 1$ around 50 m depth during this period, which is also in the Bering 10k model output. Intact organisms were present in the southern part of the Bering Sea and around the Aleutian Islands, with the Ω_{ar} horizon positioned at depth ranges below 100 m.

Shell dissolution in the Amundsen Gulf was described in detail by Niemi et al. (2021). In short, shell dissolution was widespread, occurring at coastal and offshore locations as well as in small embayments. In an initial assessment of 134 samples of *L. helicina*, greater than 85% of individuals exhibited severe

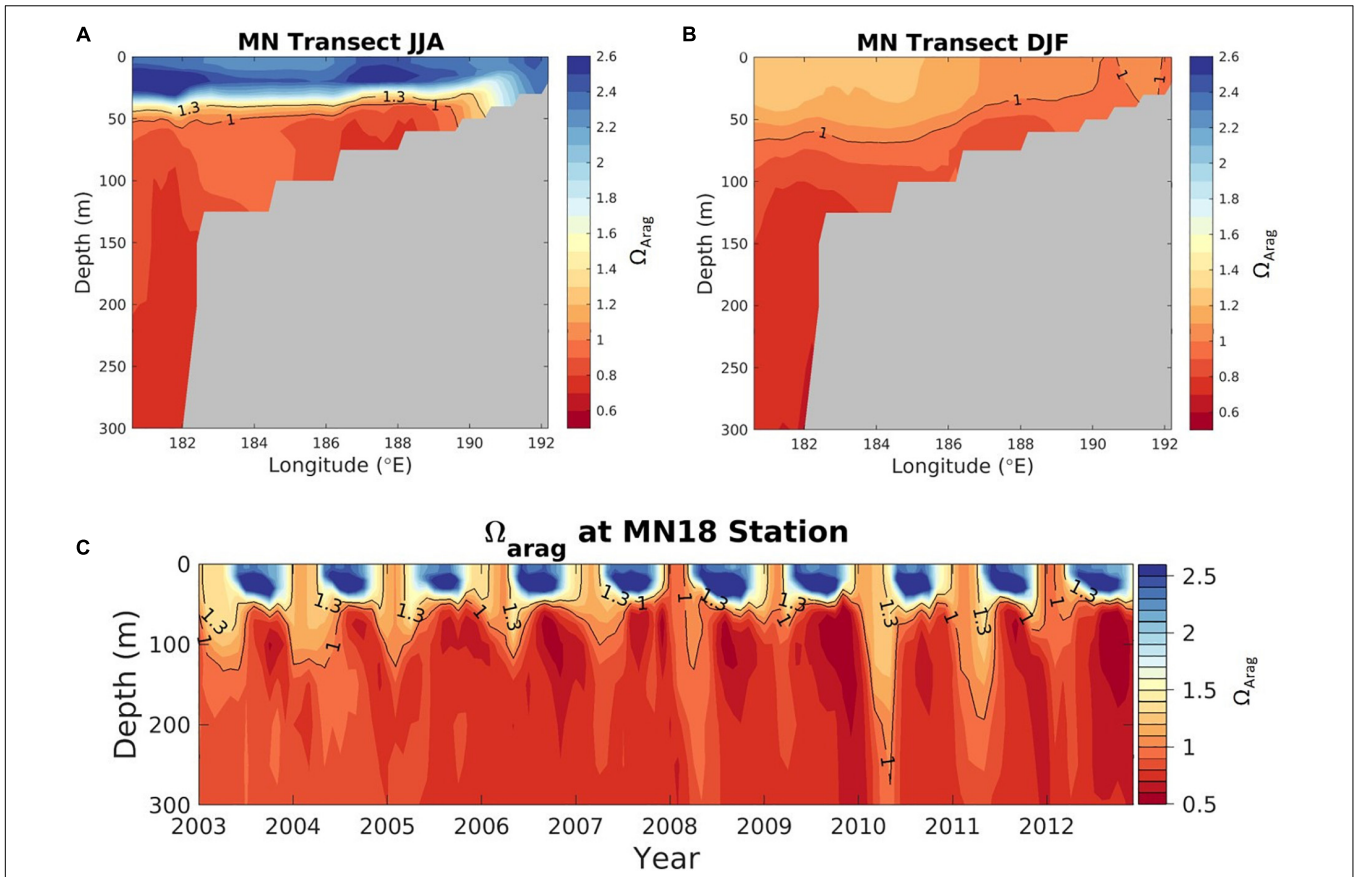


FIGURE 8 | Transect plots of aragonite saturation state (Ω_{ar}) in the Bering Sea, along the midnorth (MN) shelf transect line, denoted by the magenta line in **Figure 7**, for **(A)** June July August (JJA) and **(B)** December, January, February (DJF), averaged over 2003-2012 (modeled data). **(C)** Aragonite saturation state at station MN18 (cyan plus-sign, **Figure 7**) as a function of depth (*y*-axis), and time (*x*-axis). Model output is from the Bering10K hindcast simulation described by Pilcher et al. (2019).

dissolution. The majority of shell damage occurred on the first whorl, indicating that damage likely occurred in early life stages during the spring period (May/June) when sea ice may still be present in the Amundsen Gulf. Overall, we found no observable difference in shell dissolution between two different morphotypes across any of the high latitude regions, indicating that shell dissolution is not a trait that would be morphotype-specific.

Biological Parameters Related to Resilience and Adaptive Capacity

Genetic Analyses

A total of 176 individuals were sequenced at cytochrome c oxidase I (COI) across 21 stations (**Supplementary Tables 1**, **2**). Of these, 130 represented the *L. helicina helicina* phenotype and 38 represented the *L. helicina pacifica* phenotype. The phenotype of eight sequences were not determined due to sample deterioration. After alignment, 544bp were shared across all individuals, representing 20 unique COI haplotypes across the entire dataset.

Haplotype diversity was low (**Supplementary Table 3**): overall nucleotide diversity was 0.005 (SE 0.001). Pairwise distances between individual haplotypes varied between 0.002 and 0.009. These values were lower than accepted for species definition at the CO1 locus (Hebert et al., 2003). The samples were dominated by three haplotypes (**Figure 12A**): Haplotype 1 was found in 118 individuals, Haplotype 2 in 34 individuals, and Haplotype 3 in 5 individuals. The remaining haplotypes were found in two individuals (Haplotype 4 and 5) or in one individual only (Haplotypes 6-20).

The minimum spanning network described a star phylogeny for CO1 haplotypes (**Figure 12A**); that is, several short branches connected by a common haplotype. Such phylogenies are often interpreted to represent an evolutionarily recent founder event, followed by population expansion. There was no evidence for genetic differentiation between *L. helicina* morphotypes (**Figure 12A**). Both morphotypes were represented within three most frequent haplotypes.

Visualization of the frequency distributions of the three most common haplotypes (1-3) suggests that sequence diversity decreases in the northernmost populations, particularly in the Bering Sea and Amundsen Gulf (**Figure 12B**). However, formal analysis of haplotype diversity between stations sampled revealed no significant differences between populations (**Supplementary Table 4**). Divergence of haplotype frequencies

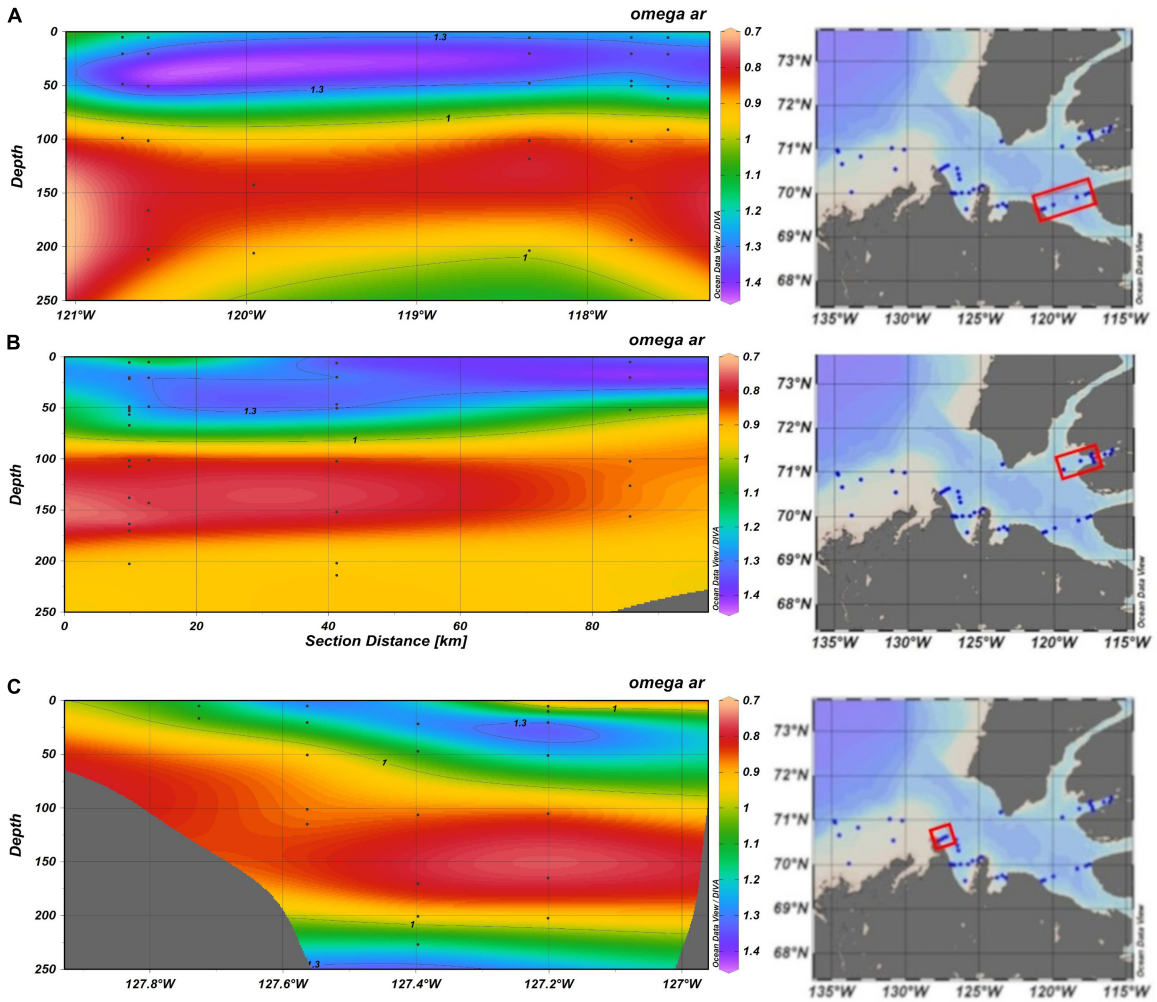


FIGURE 9 | Transect plots of aragonite saturation state (Ω_{ar}; based on the observational data) in the Amundsen Gulf in the Canadian Arctic sampled in August 2018. Transects extend across Dolphin and Union Strait **(A)**; Minto Inlet **(B)** and across the mouth of the Gulf from Cape Bathurst **(C)**. Red boxes on the transect maps include the biological stations investigated for pteropod shell dissolution (previously published in Niemi et al., 2021).

between populations varied between 0.001 and 0.002, with standard errors falling in the same order of magnitude. The power of this analysis may be affected by sample sizes, which varied between 5 and 17 individuals per station. However, given the high frequency of the most common haplotype, as well as the close relationship between these haplotypes, large sample sizes per station would be required to detect putative differences.

A total of 259 published COI sequences (**Supplementary Table 2**) were combined with the 179 sequences derived from this study and were grouped into nine broad geographic regions: Amundsen Gulf, Bering Sea, subpolar gyre, Greenland, Kara Sea, Hudson Bay (Northern Canada), Western North Pacific, Svalbard and White Sea. Global haplotype divergence was small, with most haplotypes differing from each other by a few mutations (**Supplementary Figure 3**). However, two previously described haplogroups (Abyzova et al., 2018; Shimizu et al., 2018) described the data, with evidence of a unique haplogroup limited to Svalbard and the Kara Sea, and dominance of the second haplogroup in the Bering Sea, Amundsen Gulf and North Pacific Seas. While the haplogroups differ by only a few mutations, these data suggests separate colonization and divergence events and broad-scale population structure. However, pairwise tests for divergence (**Supplementary Table 5**) revealed small pairwise distances between geographic regions.

Spatial Connectivity Based on Particle Tracking Model Outputs

Particle tracking models were used to investigate pteropod spatial connectivity over the subpolar gyre in the GoA. These were based on the assumption of a northward juvenile pteropod advection from the eastern North Pacific and life duration of approximately eight months to a year, during which pteropods would reach adulthood. The results indicate that pteropods were dispersed throughout the entire area

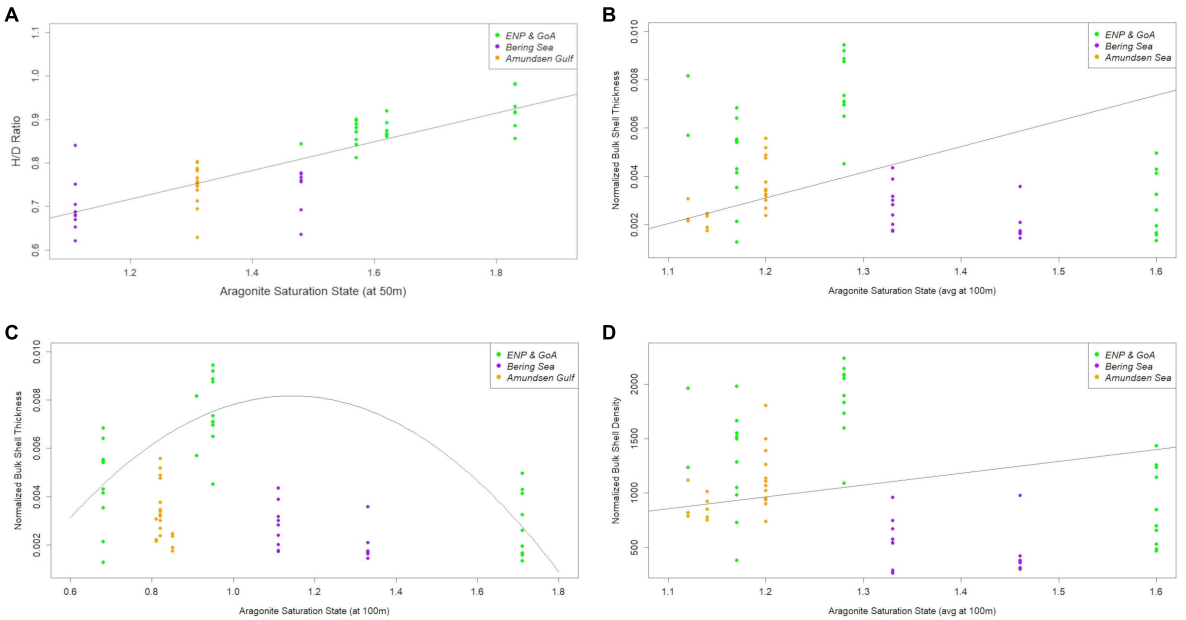


FIGURE 10 | Height-diameter (H/D) ratio distribution **(A)**, normalized bulk shell thickness with linear fit **(B)**, normalized bulk shell thickness with polynomial fit **(C)**, and normalized bulk shell density **(D)** along the omega saturation state (*ar*) in three basins (based on the observational data) in *Limacina helicina* pacifica. The equations for correlation with omega saturation state (Ω_{ar}) or the combination of temperature and Ω_{ar} are following: Shell morphology (H/D; **Figure 10A**) = 0.32095+0.33014* Ω_{ar}; Normalized Shell Thickness (linear; **Figure 10B**) = 0.001459+0.001895* Ω_{ar}; Normalized Shell Thickness (polynomial, **Figure 10C**) = 0.005569−0.0010466* Ω_{ar} −0.0004721* Ω_{ar}^2; Normalized Shell Thickness (f (T and Ω_{ar})) = 6.803*10^{-3}−3.984*10^{-5}*T-2.364*10^{-3}* Ω_{ar}; Normalized Shell Density (**Figure 10D**) = −182.5+294.3* T −234.9* Ω_{ar}.

during this period, irrespective of location origin (**Figure 13**), with high abundances present (**Table 1**). On the other hand, shorter durations of particle tracking indicated the locations of the early life stages, which are dependent on the location of their spawning.

Northward advection dominates in the first three months after the typical spawning period in late spring. In the following 4–8 months, flow of the GoA waters occurs westward along the Aleutian Islands (**Figure 13A**). If initiation is assumed to occur in the offshore subpolar gyre, the early life stages can thus reach the GoA in the summer, while the subadults and adults would be distributed in the GoA's coastal and shelf region and advected westward in the winter. The dispersal of the particles over long distances demonstrates large-scale biogeographic distribution with no apparent species boundaries across the entire area.

Extensive spatial connectivity was also observed in the Bering Sea (**Figure 13B**), where we tracked particles backward in time for a full year from a mid-shelf location on the northwestern shelf. This ending location was chosen based on observational results. Particles reaching this destination all originated from the south, primarily from the Gulf of Alaska (passing through Unimak Pass), but also from the deep basin to the north of the Western Aleutian Islands. From either starting location the particles travel along the shelf break to the north of the Aleutian Islands during an approximately 8-month period, subsequent to their initial release in April. In general a smaller spread of particles was observed for the Bering Sea than was the case in the GOA. Note these results are not strictly comparable, as we tracked particles forward in time in the GOA case, and backwards in the Bering Sea case. It is further possible that more dispersion would have been obtained with a different ending location in the Bering Sea. Fundamentally, however, the smaller spread of the Bering Sea tracks reflects the presence of vigorous 200-km scale eddies in the deep GOA, as compared to the relatively quiescent conditions on the shallow Bering Sea shelf.

DISCUSSION

This interdisciplinary study provides an integrated OA risk assessment for high-latitudinal pteropod populations of the subpolar gyre, GoA, Bering Sea and Amundsen Gulf. Here, we synthetize multi-faceted components of the risk assessment, as defined by OA exposure, species and morphotype sensitivity, and resilience through genetic structure and spatial connectivity.

Model output comparisons between the two regions (the GoA and the Bering Sea) revealed the differences in the magnitude of Ω_{ar} conditions, both in the context of the vertical gradients and seasonal cycles related to Ω_{ar}. Overall, the model outputs as well as data based on P16N cruise observations (**Figure 1**), suggest that Ω_{ar} is lower in the North Pacific subpolar gyre, while the habitats in the eastern part of the GoA seem to be less OA-compressed, providing more favorable conditions for pteropod populations. The Bering Sea, in comparison, has

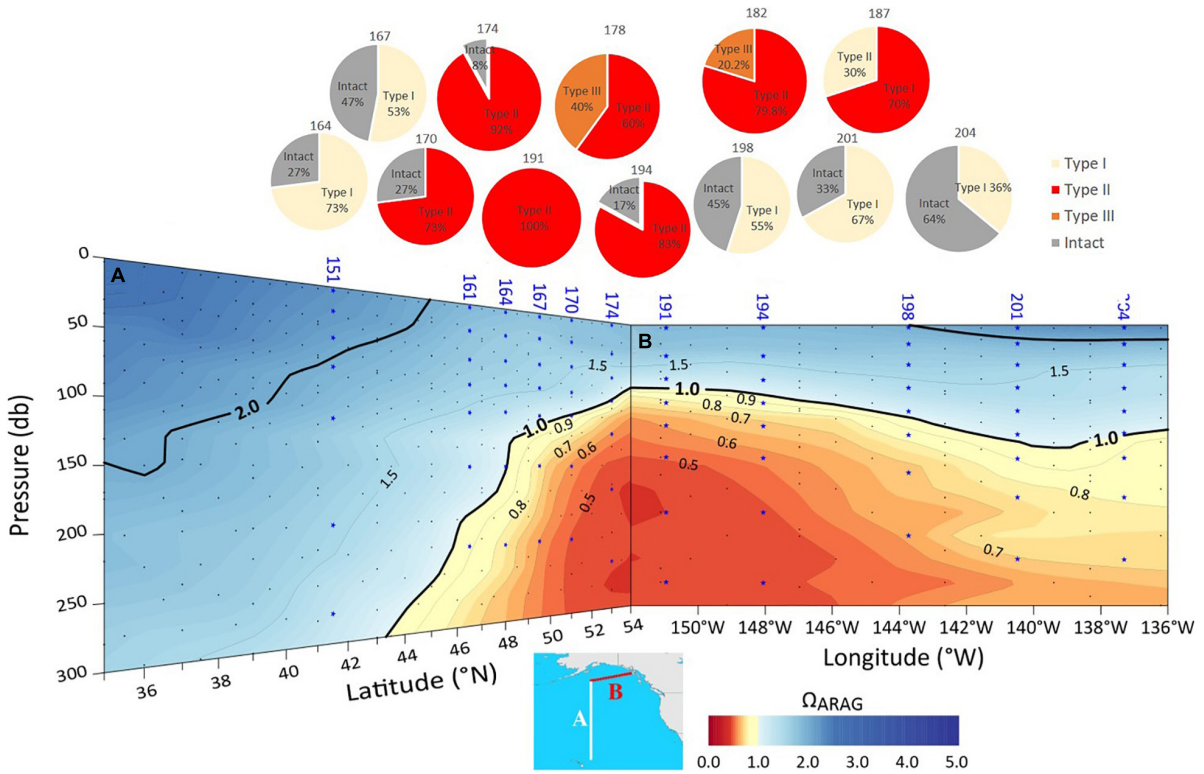


FIGURE 11 | The depth of the aragonite saturation state (Ω_{ar}; based on observational data) along two sections conducted on P16N cruise in the Eastern P16N cruise in the Eastern Pacific subpolar gyre **(A)** and GoA **(B)**. with corresponding proportions of different types of pteropod shell dissolution. Pteropod samples were analyzed from stations 164 to 204.

somewhat lower values of Ω_{ar} and a shallower Ω_{ar} horizon than the subpolar gyre/GoA. This observation is consistent with decreasing Ω_{ar} towards the poles in North-Pacific-Arctic waters (Mathis et al., 2015), indicating that this region may have experienced more severe biological impacts corresponding with the changes, especially in the last two to three decades (Carter et al., 2017). Seasonality is an important parameter to consider, because it defines the duration of exposure to less favorable conditions. In the GoA, the subsurface conditions are less favorable in the summer, while the subsurface conditions in the Bering Sea are less favorable in the winter (**Figures 5–8**). As illustrated by the Bering Sea model, vertical habitat suitability is reduced in the summertime, showing persistent subsurface $\Omega_{ar} < 1.2$ conditions despite high surface Ω_{ar} conditions that are buffered by substantial primary productivity. There is a clear exception in the subpolar gyre, where unfavorable conditions appear to persist throughout the year. Still, while surface waters of the subarctic Pacific are projected to become $\Omega_{ar} < 1$ (Bindoff et al., 2019), global model simulations suggest that surface waters of the Bering Sea will remain supersaturated even under the RCP 8.5 scenario. Hence, the upper surface waters represent suitable habitat for sensitive pelagic calcifiers. However, it remains uncertain if the vertical migrators, such as pteropods, could only occupy surface waters given their ecological dependence on deeper depths (Lalli and Gilmer, 1989).

With respect to the trend observed over the last 34 years, the GoA-COBALT model output of the subpolar gyre and the GoA suggests a declining trend of Ω_{ar} and shoaling of the Ω_{ar} saturation horizon. This indicates that pteropod populations have been experiencing an increase in exposure to lower Ω_{ar} in their habitats over decadal time scales. While we do not have biological data over the same time period as the model output, we assume that it is very likely that the severity of pteropod shell dissolution described here is a consequence of rapid, multiple human-related impacts in the region, and not a natural change in the region (Mathis et al., 2015; Carter et al., 2017; Hauri et al., 2021). The lack of a hindcast simulation in the Bering Sea does not allow such biological risk assessment over a longer time period.

Insights into the seasonal carbonate chemistry variability is important to infer the impacts of exposure within the *L. helicina* life history. The life cycle of northern high-latitude pteropods is regionally specific, lasting between 1 and 2 years (Kobayashi, 1974; Fabry, 1989; Gannefors et al., 2005), and is characterized by late spring-summer spawning, with subsequent presence of subadults and adults during the winter periods of the corresponding years. Successful recruitment depends mostly on survivorship during two key periods: the early life stages that have higher sensitivity to OA, and the adult stages that are responsible for successful spawning and recruitment (Bednaršek et al., 2016b). Model outputs during the spring-summer period

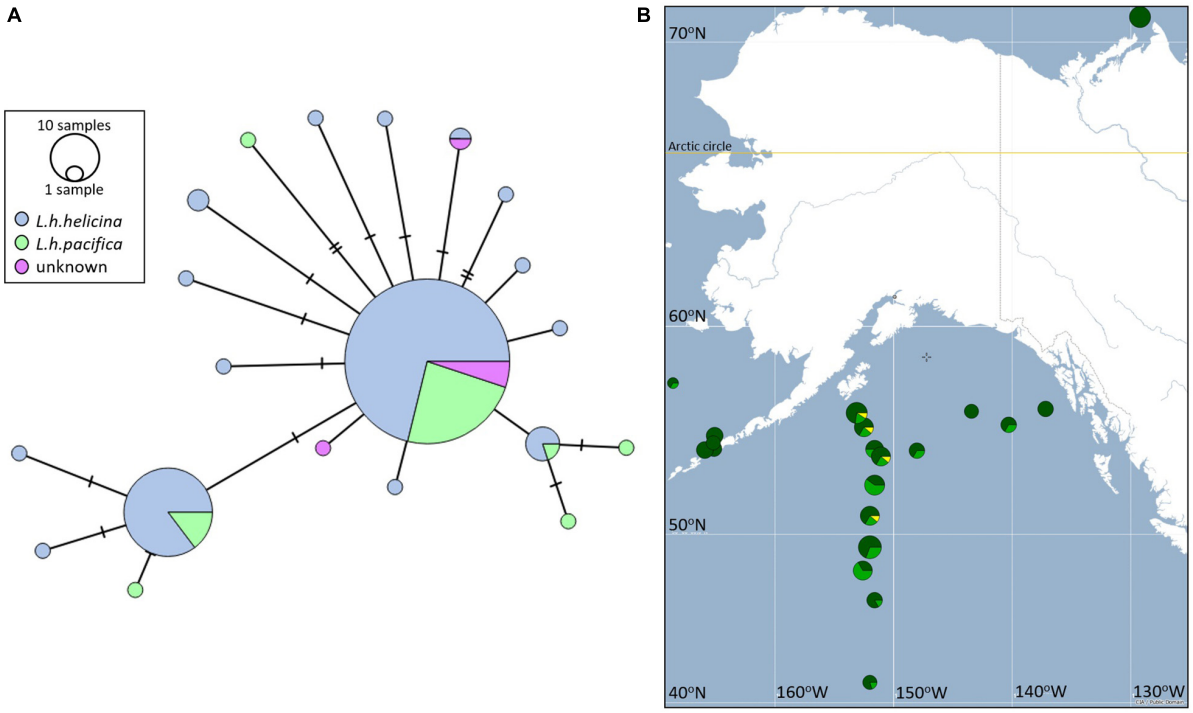


FIGURE 12 | (A) Minimum spanning network between 20 CO1 Haplotypes sequenced across 176 *L. helicina* morphotypes, sampled from the eastern North Pacific, GoA, Bering Sea and Amundsen Gulf. Haplotypes are joined by number of mutations (horizontal lines), circle sizes represent number of individuals representing each haplotype. The two morphotypes are represented in blue (*L.helicina helicina*) and green (*L. helicina pacifica*). Samples in purple could not be phenotyped. **(B)** Distribution of the three most common COI haplotypes across sampling stations in the Eastern Pacific subpolar gyre, GoA, Bering Sea and the Amundsen Gulf.

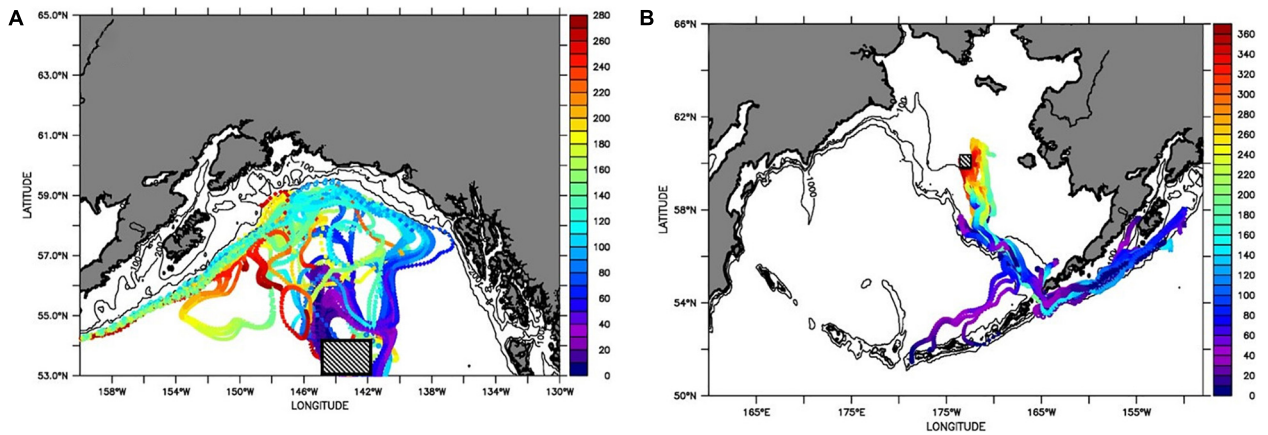


FIGURE 13 | Particle tracking at **(A)** 200 m depth in the Eastern Pacific subpolar gyre for a time period of 8 months (280 days), and **(B)** at 50 m depth in the Bering Sea for the time period of 12 months (365 days). Vertical scale bar indicates **(A)** number of days in the forward tracked particles since their release near 53°N, 143°W on April 15, 2012; and for **(B)** days of the backward tracked particles using 60°N, 173°W as ending location on April 15, 2017 (with initial release in April 15, 2016). Blue colors indicate shorter, and red color indicate longer time intervals since release. Initial release is indicted by a square. The hydrodynamic output from the model hindcasts is described by Coyle et al. (2019) and Kearney et al. (2020).

can be used to characterize exposure of the early life stages (larval and juveniles) to OA, while the model outputs integrated over the upper 50–100 m of the water column for the winter months can serve as an approximation of the adult exposure (Bednaršek et al., 2019). The summer conditions in the GoA are more favorable, thus early life stages will be less impacted relative to the adults that experience lower Ω_{ar} wintertime exposure. In contrast, the Bering Sea has opposite seasonality, characterized by the summer reduction of the suitable Ω_{ar} conditions, with adults being less impacted compared to the early life stages. It is

also important to note that regionally specific conditions, like the year-round unfavorable conditions in the subpolar gyre, might impact both early and adult life stages, delineating this region of the highest OA concern.

Observations of adult pteropod shell dissolution during spring-summer surveys in both basins spatially correlate with the spring spatial carbonate chemistry patterns, as delineated by the P16N cruise observations and biogeochemical models in the GoA and subpolar gyre (**Figures 1**, **11**). In the GoA, there was more severe dissolution in the western part of the study area, coinciding with the highest pteropod abundances, and less severe dissolution in the onshore waters. In the Bering Sea, severe dissolution occurred in the north-central part, where the model outputs projected lower Ω_{ar} compared to the higher Ω_{ar} in the south. The GoA is more likely to experience severe spring and summertime dissolution of pteropod shells compared to the same period in the Bering Sea. Our data show that thinner shells, along with dissolution uniformly distributed around the shell surface, are evidence of an impact related to lower Ω_{ar} cumulative exposure (Bednaršek et al., 2016a). This is opposite to the conclusion from Peck et al. (2016); namely that dissolution only occurs if the periostracum is damaged or if imposed through predation pressure. More severe dissolution in the Amundsen Gulf likely occurs because of the dominance of undersaturated Pacific waters within the pteropod habitat, where prolonged low Ω_{ar} exposure could represent higher risks, characteristic of the polar habitats of the Northern Hemisphere. Given that our genetic analyses show that the Amundsen Gulf pteropods share the same species distribution as the GoA and the Bering Sea individuals, there is no reason to believe that another more resilient species or subspecies will replace the current populations (Niemi et al., 2021).

There are additional parameters that can impact shell processes (Bednaršek et al., 2018; Oakes and Sessa, 2020), including regional parameters that can reverse the shell patterns observed in this study (Mekkes et al., 2021), making it important to compare the differences always among the same morphotypes. Seasonal patterns of high primary production in the Bering Sea could potentially offset some of the negative effects (*sensu* Bednaršek et al., 2018), with temperature and oxygen also playing a role in the shell building processes (Mekkes et al., 2021). Both the GoA and the Bering Sea pteropods have substantially less severe dissolution compared to that reported in the Arctic regions, such as the Amundsen Gulf. Limited extent of shell repair in the form of crystalline regrowth was reported in the presence of abundant food availability only in a few adult organisms (Niemi et al., 2021). Against a general pattern of thinner shells with only a few individuals displaying limited shell repair, this data shows high risk for pteropod population. Our findings therefore do not support the observation of pteropod resilience to OA by Peck et al. (2018).

Sensitivity and adaptation capacity were evaluated by examining the shell morphometric characteristics. Flatter and thicker (lower H/D) individuals were found in habitats associated with more severe Ω_{ar}, while high-spire, less thick (high H/D) individuals were present at higher Ω_{ar}. This distribution likely indicates that pteropods can build thicker shells and display some plastic responses, thus indicating a phenotypic response in the less favorable conditions that protects them against intense shell dissolution. A divergent range of plastic responses in the two distinct phenotypic morphotypes could be differential acclimation to Ω_{ar} exposure. The extended height over the same diameter results in higher surface shell area of *L. helicina helicina*, pointing towards the fact that a larger extent of shell surface can be exposed to the surrounding waters compared to *L. helicina pacifica* with lower surface area. As such, we postulate that different morphotypes might develop in the native habitats characterized by the intensity of Ω_{ar} exposure. By inhabiting more intense OA conditions, *L. helicina pacifica* may form flatter and thicker shells to protect the shell against more severe exposure to lower Ω_{ar}. Flatter shells with lower surface exposure is intended to reduce the exposure to low Ω_{ar}, while thicker shells can potentially tolerate more extensive dissolution better at lower Ω_{ar}. On the other hand, *L. helicina helicina* inhabits the habitat with less severe, low Ω_{ar} exposure and does not need such protecting mechanisms; greater shell surface and thinner shells can be sustained at less intense OA condition.

Pteropod morphotype distribution data over much larger spatial scales in the North Pacific clearly demonstrates the eastward occurrence of *L. helicina pacifica*, while *L. helicina helicina* is dominant westwards (McGowan, 1963). In combination with the carbonate chemistry data over the examined area that shows a progressing shoaling of carbonate chemistry eastwards (Carter et al., 2017; Cai et al., 2020), there is a spatial pattern of *L. helicina helicina* inhabiting the westward region with higher Ω_{ar} and *L. helicina pacifica* present in the lower Ω_{ar} eastward region, to which they seem to be more adapted to via their morphometric characteristics. However, given the presences of both morphotypes across the stations of the investigated area of the subpolar gyre and the GoA, our study is likely not spatially extensive enough to be able to demonstrate differential morphotype occurrence over Ω_{ar} scales.

In terms of shell building processes, pteropods continue building their shells even under lower Ω_{ar} conditions (*sensu* Comeau et al., 2010) but at reduced growth rates, presumably due to the trade-offs in the compensatory processes. However, it seems that the conditions of around $1.1 < \Omega_{ar} > 1.3$ (**Figures 10B,C**) could be delineated as a threshold below which the shell building process becomes energetically more expensive, and thus, shell processes start to decline. A similar Ω_{ar} biomineralization threshold was previously reported by Bednaršek et al. (2019). Interestingly, shell density seems to be an independent process not driven by Ω_{ar}, likely pointing towards the fact that building a shell with consistent density is an important process for the organisms and is thus more tightly regulated than processes governing shell thickness. While the differences across the eastern-western area in aragonite saturation state were substantially different, we note minimal differences in temperature across the same area, with only 1-2°C difference (**Figures 3A,B**), suggesting a relatively homogenous habitat temperature wise (*sensu* McGowan, 1963). As Ω_{ar} and temperature are highly colinear in both basins, it makes it impossible to differentiate which parameter is a major driver

behind the biological responses. In addition, the lack of data on other potentially important parameters, such as food availability (*sensu* Bednaršek et al., 2018) is currently not allowing for a more accurate interpretation and prediction of the drivers and mechanisms behind the biomineralization processes and population-level outcomes under future OA intensification.

Beside a direct impact of OA on reproduction (*sensu* Manno et al., 2016), there could be indirect implications of energetic expenditure related to reproductive outputs. The assumption is that higher Ω_{ar} conditions would allow individuals to potentially invest more energy into growth, resulting in larger shells with greater tissue mass. Building shells under low Ω_{ar} conditions (below 1.1) would require greater energetic investment, which may be indirectly reflected in smaller-sized organisms. Since the reproductive efforts of the individuals are inherently linked to tissue weight (Lalli and Gilmer, 1989), smaller-sized organisms with lower gamete production might have a lower reproductive effort under future OA intensification.

Examining the parameters related to the adaptation capacity (genetic structure, cryptic species, and spatial connectivity) is also important to potentially determine the morphotype-level risks on pteropod population level. For example, OA-induced exposure would not necessarily result in local vulnerability if individuals were replaceable or if spatial connectivity may bring new flux of organism from less impacted areas, while the presence of genetically differentiated subspecies with differential response to OA might buffer changes in distribution and abundance. Despite morphological differences, genetic analyses reveal that there was no basis for differentiation between these two forms at the species level, because both share mitochondrial DNA haplotypes. In addition, particle tracking modeling indicates that the organisms are well mixed over the investigated area, supporting genetic uniformity of the investigated pteropods. Therefore, we suggest that the differences in morphotypes might reflect phenotypic plasticity related to the differential exposure to prevailing OA-related environmental conditions, but likely not limited to Ω_{ar} only. Alternatively, such differences may arise through fine- scale population structure and local adaptation; this explanation cannot be ascertained with our available data. We conclude that there is no evidence for cryptic species or subspecies across the geographic ranges sampled, based on tests for divergence at the mitochondrial DNA cytochrome oxidase I locus. It is unlikely that hidden species diversity may account for differential morphotype responses to low Ω_{ar}. It is possible that there is within-species diversity that should be examined using nuclear DNA markers. Our results reveal a possible reduction in haplotype diversity in northern populations, which may point toward population differentiation. However, this result was not significant. On a species-wide range, the previously reported differentiation between unique haplogroups in the Arctic Ocean north of mainland Europe (Kara Sea and Svalbard), the Western North Pacific (Shimizu et al., 2018), and the Okhotsk Sea (Shimizu et al., 2021) was supported here by the addition of further samples from the subpolar gyre, the Bering Sea, and Amundsen Gulf. While the differences between the two haplogroups were small, the results suggest population structure at the species-wide scale, explained by separate colonization events with subsequent divergence over broad geographic ranges. These results are intriguing, given that the single molecular marker used has relatively little power to differentiate between populations.

Investigations based on particle analyses and prevailing advective patterns suggest extensive spatial connectivity. These analyses further support the result of a single cosmopolitan species of *L. helicina,* revealed by the mitochondrial DNA analyses. Given the time trajectories of the particles modeled here, the results suggest a continuous process of repopulation and intermixing of pteropods in the GoA region in the spatial context of the North Pacific subpolar gyre. High connectivity might alleviate localized negative impacts, especially if different morphotypes are constantly repopulating this region, therefore providing resilience. However, poor survival at different life history stages may affect recruitment throughout the region. For example, the early life stages encounter exposure to low Ω_{ar} conditions between 53 and 56°N through northward advection. It is also unknown to what degree adaptive capacity at the population level may buffer recruitment variation. Overall, high risk for pteropod population persistence with intensification of OA has to be assumed because of their known vulnerability, along with low evidence for species diversity and the progressive severity of OA exposure, despite their wide connectivity across the considered habitats and our insufficient knowledge on their adaptive capacity in the high latitudes.

Corresponding with pteropod high risk related to OA in the high latitudinal habitats are also high-risk repercussion for the commercially important fisheries and high trophic levels marine vertebrates. Considering the magnitude of OA change in this region coupled with a high pteropod biomass (Bednaršek et al., 2012a; Doubleday and Hopcroft, 2015), negative pteropod population implications could ultimately have an impact for the fisheries dependent on pteropods as a food source, most explicitly for the various salmon species, cod and char, during the fall time in the absence of the other food sources essential for successful fish development. Moreover, given the changes in pteropod shell building processes, i.e. reduced calcification and shell thickness and lower H/D ratio, along with increased dissolution, these high latitudinal regions' with one of the highest pteropod abundances on a global scale (**Table 1**; Bednaršek et al., 2012a) might also experience potentially significant biogeochemical effects related to the biological pump, resulting in the lower carbonate export fluxes over time (Carter et al., 2021; Lee and Feely, 2021; Sulpis et al., 2021). The results of this study suggest that an important component of the alkalinity change in the North Pacific may be the result of changes in pteropod production and dissolution. Moving forward into the future, the ecological and biogeochemical implications of these long-term changes will depend on multiple interacting processes, including the morphotype distribution, net shell calcification and dissolution, changes in the morphometrics, their abundance and phenology.

Given the dominance of pteropods in the subpolar gyre and the GoA, long-term observations should be strategically

positioned along the W-E gradients where the differences in OA are most pronounced. Understanding of biological vulnerability on the regional scales provides an opportunity to prioritize monitoring to manage, and thus potentially reduce, the realized impact on the fisheries and ecosystems in the high-latitudinal ecosystems under predicted climate change scenarios.

DATA AVAILABILITY STATEMENT

All sequence data are available in Genbank under accession numbers MZ502688–MZ502863 and in the Supplementary Material. The GoA-COBALT model output is publicly available (https://doi.org/10.24431/rw1k43t, Hauri et al., 2020). Carbonate chemistry data from the hydrographic cruise P16N are archived in the NCEI database: https://www.ncei.noaa.gov/data/oceans/ncei/ocads/metadata/0163182.html. The carbonate chemistry data from the Amundsen Gulf (2018) are publicly available in the Ocean Carbon Data System (OCADS), NCEI Accession number 0238161 (https://www.ncei.noaa.gov/data/oceans/ncei/ocads/metadata/0238161.html). The Bering10K model output fields and particle tracking output for the Bering Sea and Gulf of Alaska used in this analysis are available online from the Zenodo library (https://doi.org/10.5281/zenodo.5117852). Model source code for the Bering10K ROMS model is available here (https://github.com/beringnpz/roms-bering-sea). Pteropod abundance data from the GoA and the Bering regions are archived in the NCEI database, along with the hydrographic P16N data; data from the Amundsen Gulf are currently available upon request (Niemi) and will be submitted into the NCEI after the manuscript acceptance. Pteropod shell dissolution data and shell morphometrics and properties are available upon request (Niemi, Bednaršek; pers. communications), followed by the submission into the NCEI database after the manuscript acceptance.

AUTHOR CONTRIBUTIONS

NB wrote the manuscript with contributions from all coauthors. NB and K-AN conceived the research, analyzed the data, and provided visualizations. CH, DP, and AH provided model outputs. NB directed the zooplankton fieldwork. AN provided biological data from the Amundsen Gulf. RF and CM provided carbonate chemistry data. KK analyzed pteropod shell density and thickness and contributed to the findings about the relevance of environmental data. All authors contributed to the article and approved the submitted version.

FUNDING

This work was funded by the North Pacific Research Board (NPRB; project number 1615: Pteropods as indicators in the high latitudinal environment) awarded to NB and K-AN. CH acknowledges funding from the National Science Foundation (NSF; Grant Nos. OCE-1459834 and 1656070). RF acknowledges support from the NOAA GOMO Program.

ACKNOWLEDGMENTS

We thank Isadora Jimenez-Hidalgo for her technical expertise and Lorenz Hauser and Ana Ramón-Laca for their advice in genetic analyses. We also thank AFSC team, Phyllis Stabeno and Janet Duffy-Anderson. We are grateful to Colleen Harpold and Nissa Ferm to conduct pteropod sampling in the Bering Sea, as well as Peter Proctor for collecting samples for carbonate chemistry in the Bering Sea, and to Shaun Bell to help assist analyses of physical-chemical parameters from Bering Sea cruises. Carbonate chemistry analyses in Beaufort shelf was done in the lab of Kumiko Azetsu-Scott at BIO, funded by ACCASP. Special thank you goes to Jesse Turner who collected pteropod samples on P16, Brendan Carter to collect carbonate chemistry samples, also to Alison MacDonald for making pteropod sampling on P16 feasible. We also thank S. Punshon and J. Charette for carbonate chemistry sample and data analysis for the Amundsen Gulf. We are grateful Arie Janssen with help on distinguishing different pteropod morphotypes.

SUPPLEMENTARY MATERIAL

The Supplementary Material for this article can be found online at: https://www.frontiersin.org/articles/10.3389/fmars.2021.671497/full#supplementary-material

Supplementary Figure 1 | The distribution of two different morphotypes based on the H/D ratios (*L. helicina helicina* and *L. helicina pacifica*) **(A)**, and as separated per different ocean basins **(B)**. The H/D ratio was correlated with the normalized shell thickness **(C)** and the density **(D)** from the individuals across the three ocean basins.

Supplementary Figure 2 | Depiction of three different types of dissolution (each column representing Type I, II or Type III) found on the pteropod shells collected across different basins (gyre, GoA, Bering, and Amundsen Gulf). Types and the extent of dissolution are linked with the sample location and additional analyses conducted on the samples (**Table 1**). Each photo depicts the type of shell dissolution of the individual organism from a different sampled location, with the scale bar indicating the size.

Supplementary Figure 3 | Minimum spanning network between CO1 Haplotypes sequenced across 427 individual *L. helicina*, sampled from the Amundsen Gulf (abbr. BeauSea), Bering Sea (abbr. BerngSea), Eastern North Pacific (abbr. ENPac), Greenland (abbr. Grnld), Kara Sea (abbr. Kara), Hudson Bay (abbr. NCanada), Western North Pacific (abbr. WNPac), Svalbard (abbr. Svbd) and White Sea. Haplotypes are joined by number of mutations (horizontal lines), circle sizes represent number of individuals representing each haplotype.

Supplementary Table 1 | COI gene sequences for both morphotypes of *L. helicina* across all the investigated regions (subpolar gyre, GoA, Bering, Bering Sea, Amundsen Gulf).

Supplementary Table 2 | Referenced studies, locations, and accession numbers of the previously published COI gene sequences for *Limacina helicina*.

Supplementary Table 3 | Estimates of Evolutionary Divergence (p-distance) between COI haplotype sequences 1-20 (in bold), genotyped in *L. helicina* collected from the North Pacific, Bering Sea and Amundsen Gulf. Below the diagonal: number of base pair differences per site calculated between haplotypes. Standard error estimate(s) derived from 500 bootstrap replicates are above the diagonal.

Supplementary Table 4 | Estimates of Evolutionary Divergence (p-distance) between Stations, based on COI haplotype sequences sampled at each station. The number of base differences per site from averaging over all sequence pairs

between groups below the diagonal, standard error estimate(s) derived from 500 bootstrap replicates are above the diagonal.

Supplementary Table 5 | Estimates of Evolutionary Divergence (p-distance) between regions. The number of base differences per site from averaging over all sequence pairs between groups below the diagonal, standard error estimate(s) derived from 500 bootstrap replicates are above the diagonal. The samples originate from the North Pacific (abbr. ENPac), Greenland (abbr. Grnld), Kara Sea (abbr. Kara), Hudson Bay (abbr. NCanada), Western North Pacific (abbr. WNPac), Svalbard (abbr. Svbd) and White Sea.

REFERENCES

Abyzova, G. A., Nikitin, M. A., Popova, O. V., and Pasternak, A. F. (2018). Genetic population structure of the pelagic mollusk *Limacina helicina* in the Kara Sea. *PeerJ* 6:e5709.

Armstrong, J. L., Boldt, J. L., Cross, A. D., Moss, J. H., Davis, N. D., Myers, K. W., et al. (2005). Distribution, size, and interannual, seasonal and diel food habits of northern Gulf of Alaska juvenile pink salmon, *Oncorhynchus gorbuscha*. *Deep Sea Res. Part II* 52, 247–265. doi: 10.1016/j.dsr2.2004.09.019

Auburn, M. E., and Ignell, S. E. (2000). Food habits of juvenile salmon in the Gulf of Alaska July–August 1996. *N. Pac. Anadr. Fish. Comm. Bull.* 2, 89–97.

Bandelt, H. J., Forster, P., and Röhl, A. (1999). Median-joining networks for inferring intraspecific phylogenies. *Mol. Biol. Evol.* 16, 37–48.

Beamer, J. P., Hill, D. F., Arendt, A., and Liston, G. E. (2016). High-resolution modeling of coastal freshwater discharge and glacier mass balance in the Gulf of Alaska watershed. *Water Resour. Res.* 52, 3888–3909. doi: 10.1002/2015wr018457

Beauchamp, D. A., Cross, A. D., Armstrong, J. L., Myers, K. W., Moss, J. H., Boldt, J. L., et al. (2007). Bioenergetic responses by Pacific salmon to climate and ecosystem variation. *N. Pac. Anadr. Fish. Comm. Bull.* 4, 257–269.

Bednaršek, N., Možina, J., Vogt, M., O'Brien, C., and Tarling, G. A. (2012a). The global distribution of pteropods and their contribution to carbonate and carbon biomass in the modern ocean. *Earth Syst. Sci. Data* 4, 167–186. doi: 10.5194/essd-4-167-2012

Bednaršek, N., Tarling, G. A., Bakker, D. C., Fielding, S., Cohen, A., Kuzirian, A., et al. (2012b). Description and quantification of pteropod shell dissolution: a sensitive bioindicator of ocean acidification. *Glob. Chang. Biol.* 18, 2378–2388. doi: 10.1111/j.1365-2486.2012.02668.x

Bednaršek, N., Johnson, J., and Feely, R. A. (2016a). Comment on Peck et al: vulnerability of pteropod (*Limacina helicina*) to ocean acidification: shell dissolution occurs despite an intact organic layer. *DSRII* 127, 53–56. doi: 10.1016/j.dsr2.2016.03.006

Bednaršek, N., Feely, R. A., Reum, J. C. P., Peterson, B., Menkel, J., Alin, S. R., et al. (2014). Limacina helicina shell dissolution as an indicator of declining habitat suitability owing to ocean acidification in the California Current Ecosystem. *Proc. R. Soc. B Biol. Sci.* 281:20140123. doi: 10.1098/rspb.2014.0123

Bednaršek, N., Harvey, C. J., Kaplan, I. C., Feely, R. A., and Možina, J. (2016b). Pteropods on the edge: cumulative effects of ocean acidification, warming, and deoxygenation. *Prog. Oceanogr.* 145, 1–24. doi: 10.1016/j.pocean.2016.04.002

Bednaršek, N., Feely, R. A., Tolimieri, N., Hermann, A. J., Siedlecki, S. A., Waldbusser, G. G., et al. (2017). Exposure history determines pteropod vulnerability to ocean acidification along the US West Coast. *Sci. Rep.* 7:4526. doi: 10.1038/s41598-017-03934-z

Bednaršek, N., Feely, R. A., Beck, M. W., Glippa, O., Kanerva, M., and Engström-Öst, J. (2018). El Niño-related thermal stress coupled with upwelling-related ocean acidification negatively impacts cellular to population-level responses in pteropods along the California current system with implications for increased bioenergetic costs. *Front. Mar. Sci.* 5:486. doi: 10.3389/fmars.2018.00486

Bednaršek, N., Feely, R. A., Howes, E. L., Hunt, B. P. V., Kessouri, F., León, P., et al. (2019). systematic review and meta-analysis toward synthesis of thresholds of ocean acidification impacts on calcifying pteropods and interactions with warming. *Front. Mar. Sci.* 6:227. doi: 10.3389/fmars.2019.00227

Bindoff, N. L., Cheung, W. W. L., Kairo, J. G., Arístegui, J., Guinder, V. A., Hallberg, R., et al. (2019). "Changing ocean, marine ecosystems, and dependent communities," in *IPCC Special Report on the Ocean and Cryosphere in a Changing Climate*, eds H.-O. Pörtner, D. C. Roberts, V. Masson-Delmotte, P. Zhai, M. Tignor, and E. Poloczanska (Geneva: IPCC).

Brown, Z. W., van Dijken, G. L., and Arrigo, K. R. (2011). A reassessment of primary production and environmental change in the Bering Sea. *J. Geophys. Res. Oceans* 116, doi: 10.1029/2010JC006766

Burridge, A. K., Goetze, E., Raes, N., Huisman, J., and Peijnenburg, K. T. C. A. (2015). Global biogeography and evolution of *Cuvierina pteropods*. *BMC Evol. Biol.* 15:39. doi: 10.1186/s12862-015-0310-8

Cai, W.-J., Xu, Y.-Y., Feely, R. A., Wanninkhof, R., Jönsson, B., Alin, S. R., et al. (2020). Controls on surface water carbonate chemistry along North American ocean margins. *Nat. Commun.* 11:2691. doi: 10.1038/s41467-020-16530-z

Carter, B. R., Feely, R. A., Wanninkhof, R., Kouketsu, S., Sonnerup, R. E., Pardo, P. C., et al. (2019). Pacific anthropogenic carbon between 1991 and 2017. *Global Biogeochem. Cycles* 33, 597–617. doi: 10.1029/2018gb006154

Carter, B. R., Feely, R. A., Lauvset, S. K., Olsen, A., DeVries, T., and Sonnerup, R. (2021). Preformed properties for marine organic matter and carbonate mineral cycling quantification. *Global Biogeochem. Cycles* 35:e2020GB006623. doi: 10.1029/2020GB006623

Carter, B. R., Feely, R. A., Mecking, S., Cross, J. N., Macdonald, A. M., Siedlecki, S. A., et al. (2017). Two decades of Pacific anthropogenic carbon storage and ocean acidification along Global Ocean Ship-based Hydrographic Investigations Program sections P16 and P02. *Global Biogeochem. Cycles* 31, 306–327. doi: 10.1002/2016GB005485

Carton, J. A., Chepurin, G. A., and Chen, L. (2018). SODA3: a new ocean climate reanalysis. *J. Clim.* 31, 6967–6983. doi: 10.1175/JCLI-D-18-0149.1

Comeau, S., Gorsky, G., Jeffree, R., Teyssié, J.-L., and Gattuso, J.-P. (2009). Impact of ocean acidification on a key Arctic pelagic mollusc (*Limacina helicina*). *Biogeosciences* 6, 1877–1882. doi: 10.5194/bg-6-1877-2009

Comeau, S., Gorsky, G., Alliouane, S., and Gattuso, J. P. (2010). Larvae of the pteropod *Cavolinia* inflexa exposed to aragonite undersaturation are viable but shell-less. *Mar. Biol.* 157, 2341–2345. doi: 10.1007/s00227-010-1493-6

Coyle, K. O., Hermann, A. J., and Hopcroft, R. R. (2019). Modeled spatial-temporal distribution of productivity, chlorophyll, iron and nitrate on the northern Gulf of Alaska shelf relative to field observations. *Deep Sea Res. Part II* 165, 163–191. doi: 10.1016/j.dsr2.2019.05.006

Cross, J. N., Mathis, J. T., Bates, N. R., and Byrne, R. H. (2013). Conservative and non-conservative variations of total alkalinity on the southeastern Bering Sea shelf. *Mar. Chem.* 154, 100–112. doi: 10.1016/j.marchem.2013.05.012

Daly, E. A., Moss, J. H., Fergusson, E., and Debenham, C. (2019). Feeding ecology of salmon in eastern and central Gulf of Alaska. *Deep Sea Res. Part II* 165, 329–339. doi: 10.1016/j.dsr2.2019.06.006

Danielson, S., Curchitser, E., Hedstrom, K., Weingartner, T., and Stabeno, P. (2011). On ocean and sea ice modes of variability in the Bering Sea. *J. Geophys. Res. Oceans* 116:C12034. doi: 10.1029/2011JC007389

Danielson, S. L., Hill, D. F., Hedstrom, K. S., Beamer, J., and Curchitser, E. (2020). Demonstrating a high-resolution Gulf of Alaska ocean circulation model forced across the coastal interface by high-resolution terrestrial hydrological models. *J. Geophys. Res. Oceans* 125:e2019JC015724. doi: 10.1029/2019JC015724

Darnis, G., Barber, D. G., and Fortier, L. (2008). Sea ice and the onshore-offshore gradient in pre-winter zooplankton assemblages in southeastern Beaufort Sea. *J. Mar. Syst.* 74, 994–1011. doi: 10.1016/j.jmarsys.2007.09.003

Dickson, A. G., Sabine, C. L., and Christian, J. R. (2007). *Guide to Best Practices for Ocean CO2 Measurements*. Sidney BC: North Pacific Marine Science Organization.

Doubleday, A. J., and Hopcroft, R. R. (2015). Interannual patterns during spring and late summer of larvaceans and pteropods in the coastal Gulf of Alaska, and their relationship to pink salmon survival. *J. Plankton Res.* 37, 134–150. doi: 10.1093/plankt/fbu092

Eisner, L. B., Napp, J. M., Mier, K. L., Pinchuk, A. I., and Andrews, A. G. III (2014). Climate-mediated changes in zooplankton community structure for the eastern Bering Sea. *Deep Sea Res. Part II Top. Stud. Oceanogr.* 109, 157–171.

Eisner, L. B., Pinchuk, A. I., Kimmel, D. G., Mier, K. L., Harpold, C. E., and Siddon, E. C. (2017). Seasonal, interannual, and spatial patterns of community composition over the eastern Bering Sea shelf in cold years. Part I: zooplankton. *ICES J. Mar. Sci.* 75, 72–86. doi: 10.1093/icesjms/fsx156

Edgar, R. C. (2004). MUSCLE: multiple sequence alignment with high accuracy and high throughput. *Nucleic Acids Res.* 32, 1792–1797. doi: 10.1093/nar/gkh340

Evans, W., Mathis, J. T., Winsor, P., Statscewich, H., and Whitledge, T. E. (2013). A regression modeling approach for studying carbonate system variability in the northern Gulf of Alaska. *J. Geophys. Res. Oceans* 118, 476–489. doi: 10.1029/2012JC008246

Fabry, V. J. (1989). Aragonite production by pteropod molluscs in the subarctic Pacific. *Deep Sea Res. Part A Oceanogr. Res. Pap.* 36, 1735–1751. doi: 10.1016/0198-0149(89)90069-1

Feely, R. A., Alin, S. R., Carter, B., Bednaršek, N., Hales, B., Chan, F., et al. (2016). Chemical and biological impacts of ocean acidification along the west coast of North America. *Estuar. Coast. Shelf Sci.* 183, 260–270. doi: 10.1016/j.ecss.2016.08.043

Folmer, O., Black, M., Hoeh, W., Lutz, R., and Vrijenhoek, R. (1994). DNA primers for amplification of mitochondrial cytochrome c oxidase subunit I from diverse metazoan invertebrates. *Mol. Mar. Biol. Biotechnol.* 3, 294–299.

Gannefors, C., Böer, M., Kattner, G., Graeve, M., Eiane, K., Gulliksen, B., et al. (2005). The Arctic sea butterfly *Limacina helicina*: lipids and life strategy. *Mar. Biol.* 147, 169–177. doi: 10.1007/s00227-004-1544-y

Garcia, H. E., Locarnini, R. A., Boyer, T. P., Antonov, J. I., Baranova, O. K., Zweng, M. M., et al. (2013). in *World Ocean Atlas 2013, Volume 4: Dissolved Inorganic Nutrients (Phosphate, Nitrate, Silicate)*, Vol. 76, eds S. Levitus and A. Mishonov (Washington DC: NOAA Atlas NESDIS), 25.

Gasca, R., and Janssen, A. W. (2014). Taxonomic review, molecular data and key to the species of Creseidae from the Atlantic Ocean. *J. Molluscan Stud.* 80, 35–42. doi: 10.1093/mollus/eyt038

Geller, J., Meyer, C., Parker, M., and Hawk, H. (2013). Redesign of PCR primers for mitochondrial cytochrome c oxidase subunit I for marine invertebrates and application in all-taxa biotic surveys. *Mol. Ecol. Resour.* 13, 851–861. doi: 10.1111/1755-0998.12138

Gibson, G. A., and Spitz, Y. H. (2011). Impacts of biological parameterization, initial conditions, and environmental forcing on parameter sensitivity and uncertainty in a marine ecosystem model for the Bering Sea. *J. Mar. Syst.* 88, 214–231. doi: 10.1016/j.jmarsys.2011.04.008

Haradsson, C., Anderson, L. G., Hassellöv, M., Hulth, S., and Olsson, K. (1997). Rapid high-precision potentiometric titration of alkalinity in ocean and sediment pore waters. *Deep Sea Res. Part I* 44, 2031–2044. doi: 10.1016/s0967-0637(97)00088-5

Hauri, C., Pagès, R., McDonnell, A. M. P., Stuecker, M. F., Danielson, S. L., Hedstrom, K., et al. (2021). Modulation of ocean acidification by decadal climate variability in the Gulf of Alaska. *Nat. Commun. Earth Environ. (in press)*. doi: 10.1038/s43247-021-00254-

Hauri, C., Schultz, C., Hedstrom, K., Danielson, S., Irving, B., Doney, S. C., et al. (2020). A regional hindcast model simulating ecosystem dynamics, inorganic carbon chemistry, and ocean acidification in the Gulf of Alaska. *Biogeosciences* 17, 3837–3857. doi: 10.5194/bg-17-3837-2020

Hebert, P. D., Ratnasingham, S., and De Waard, J. R. (2003). Barcoding animal life: cytochrome c oxidase subunit 1 divergences among closely related species. *Proc. R. Soc. Lond.* 270(Suppl. 1), S96–S99.

IPCC (2014). in *Climate Change 2014: Synthesis Report. Contribution of Working Groups I, II and III to the Fifth Assessment Report of the Intergovernmental Panel on Climate Change*, eds Core Writing Team, R. K. Pachauri, and L. A. Meyer (Geneva: IPCC), 151.

IPCC (2019). in *IPCC Special Report on the Ocean and Cryosphere in a Changing Climate*, eds H.-O. Pörtner, D. C. Roberts, V. Masson-Delmotte, P. Zhai, M. Tignor, E. Poloczanska, et al. (Geneva: IPCC).

Janssen, A. W., Burridge, A. K., Mekkes, L., and Peijnenburg, K. T. C. A. (2018). History of the Clio pyramidata-complex (Mollusca, Gastropoda, Euthecosomata, Cliidae) in the northern and central Atlantic Ocean, Caribbean and Mediterranean, restoring its original concept. *Basteria* 82, 83–102.

Janssen, A. W., Bush, S. L., and Bednaršek, N. (2019). The shelled pteropods of the northeast Pacific Ocean (Mollusca: Heterobranchia, Pteropoda). *Zoosymposia* 13, 305–346. doi: 10.11646/zoosymposia.13.1.22

Johnson, K. M., Andrew, G. D., Eischeid, G., Catherine, G., Guenther, P., Key, R. M., et al. (1998). Coulometric total carbon dioxide analysis for marine studies: assessment of the quality of total inorganic carbon measurements made during the US Indian Ocean CO2 Survey 1994–1996. *Mar. Chem.* 63, 21–37.

Kearney, K., Hermann, A., Cheng, W., Ortiz, I., and Aydin, K. (2020). A coupled pelagic–benthic–sympagic biogeochemical model for the Bering Sea: documentation and validation of the BESTNPZ model (v2019.08.23) within a high-resolution regional ocean model. *Geosci. Model Dev.* 13, 597–650. doi: 10.5194/gmd-13-597-2020

Kobayashi, H. A. (1974). Growth cycle and related vertical distribution of the thecosomatous pteropod Spiratella ("Limacina") helicina in the central Arctic Ocean. *Mar. Biol.* 26, 295–301. doi: 10.1007/BF00391513

Kumar, S., Stecher, G., and Tamura, K. (2016). MEGA7: molecular evolutionary genetics analysis version 7.0 for bigger datasets. *Mol. Biol. Evol.* 33, 1870–1874. doi: 10.1093/molbev/msw054

Lalli, C. M., and Gilmer, R. W. (1989). *Pelagic Snails: The Biology of Holoplanktonic Gastropod Mollusks*. Palo Alto CA: Stanford University Press.

Lauvset, S. K., Key, R. M., Olsen, A., Van Heuven, S., Velo, A., Lin, X., et al. (2016). A new global interior ocean mapped climatology: The 1× 1 GLODAP version 2. *Earth Syst. Sci. Data* 8, 325–340.

Lee, K., and Feely, R. A. (2021). News and views: dissolution resolution. *Nat. Geosci.* 14, 356–358. doi: 10.1038/s41561-021-00765-6

Lee, K., Kim, T. W., Byrne, R. H., Millero, F. J., Feely, R. A., and Liu, Y. M. (2010). The universal ratio of boron to chlorinity for the North Pacific and North Atlantic oceans. *Geochim. Cosmochim. Acta* 74, 1801–1811.

Leigh, J. W., and Bryant, D. (2015). popart: full-feature software for haplotype network construction. *Methods Ecol Evol* 6, 1110–1116. doi: 10.1111/2041-210X.12410

Lewis, E., and Wallace, D. W. R. (1998). Program Developed for CO2 System Calculations, ORNL/CDIAC-105, Carbon Dioxide Inf. Anal. Cent., Oak Ridge Natl. Lab., Oak Ridge, Tenn. 38. https://salish-sea.pnnl.gov/media/ORNL-CDIAC-105.pdf (accessed January 2019).

Lischka, S., Büdenbender, J., Boxhammer, T., and Riebesell, U. (2011). Impact of ocean acidification and elevated temperatures on early juveniles of the polar shelled pteropod *Limacina helicina*: mortality, shell degradation, and shell growth. *Biogeosciences (BG)* 8, 919–932. doi: 10.5194/bg-8-919-2011

Long, W. C., Swiney, K. M., Harris, C., Page, H. N., and Foy, R. J. (2013). Effects of Ocean Acidification on Juvenile Red King Crab (*Paralithodes camtschaticus*) and Tanner Crab (*Chionoecetes bairdi*) Growth, Condition, Calcification, and Survival. *PLoS One* 8:e60959. doi: 10.1371/journal.pone.0060959

Long, W. C., Swiney, K. M., and Foy, R. J. (2016). Effects of high pCO2 on Tanner crab reproduction and early life history, Part II: carryover effects on larvae from oogenesis and embryogenesis are stronger than direct effects. *ICES J. Mar. Sci.* 73, 836–848. doi: 10.1093/icesjms/fsv251

Lueker, T. J., Dickson, A. G., and Keeling, C. D. (2000). Ocean pCO2 calculated from dissolved inorganic carbon, alkalinity, and equations for K1 and K2: validation based on laboratory measurements of CO2 in gas and seawater at equilibrium. *Mar. Chem.* 70, 105–119. doi: 10.1016/s0304-4203(00)00022-0

Maas, A. E., Blanco-Bercial, L., and Lawson, G. L. (2013). Reexamination of the species assignment of diacavolinia pteropods Using DNA barcoding. *PLoS One* 8:e53889. doi: 10.1371/journal.pone.0053889

Mackas, D. L., and Galbraith, M. D. (2012). Pteropod time-series from the NE Pacific. *ICES J. Mar. Sci.* 69, 448–459. doi: 10.1093/icesjms/fsr163

Majewski, A. R., Walkusz, W., Lynn, B. R., Atchison, S., Eert J. (2016). Distribution and diet of demersal Arctic Cod, Boreogadus saida, in relation to habitat characteristics in the Canadian Beaufort Sea. *Polar Biol.* 39, 1087–1098. doi: 10.1007/s00300-015-1857-y

Manno, C., Peck, V. L., and Tarling, G. A. (2016). Pteropod eggs released at high pCO 2 lack resilience to ocean acidification. *Sci. Rep.* 6:25752. doi: 10.1038/srep25752

Mathis, J. T., Cross, J. N., and Bates, N. R. (2011). Coupling primary production and terrestrial runoff to ocean acidification and carbonate mineral suppression in the eastern Bering Sea. *J. Geophys. Res. Oceans* 116, doi: 10.1029/2010JC006453

Mathis, J. T., Cross, J. N., Monacci, N., Feely, R. A., and Stabeno, P. (2014). Evidence of prolonged aragonite undersaturations in the bottom waters of the southern Bering Sea shelf from autonomous sensors. *Deep Sea Res. Part II Top. Stud. Oceanogr.* 109, 125–133. doi: 10.1016/j.dsr2.2013.07.019

Mathis, J. T., Cross, J. N., Evans, W., and Doney, S. C. (2015). Ocean acidification in the surface waters of the Pacific-Arctic boundary regions. *Oceanography* 28, 122–135. doi: 10.5670/oceanog.2015.36

McGowan, J. A. (1963). "Geographical variation in *Limacina helicina* in the North Pacific," in *Speciation in the Sea*, eds J. P. Harding and N. Tebble (London: Publications of the Systematics Association), 109–128.

Mekkes, L., Renema, W., Bednaršek, N., Alin, S. R., Feely, R. A., Huisman, J., et al. (2021). Pteropods make thinner shells in the upwelling region of the California current ecosystem. *Sci. Rep.* 11:1731.

Niemi, A., Bednaršek, N., Michel, C., Feely, R. A., Williams, W., and Azetsu-Scott, K. (2021). Widespread severe pteropod shell dissolution in Amundsen Gulf. *Front. Mar. Sci.* 8:600184. doi: 10.3389/fmars.2021.600184

Oakes, R. L., and Sessa, J. A. (2020). Determining how biotic and abiotic variables affect the shell condition and parameters of *Heliconoides inflatus* pteropods from a sediment trap in the Cariaco Basin. *Biogeosciences* 17, 1975–1990. doi: 10.5194/bg-17-1975-2020

Peck, V. L., Tarling, G. A., Manno, C., Harper, E. M., and Tynan, E. (2016). Outer organic layer and internal repair mechanism protects pteropod *Limacina helicina* from ocean acidification. *Deep Sea Res. Part II Top. Stud. Oceanogr.* 127, 41–52. doi: 10.1016/j.dsr2.2015.12.005

Peck, V. L., Oakes, R. L., Harper, E. M., Manno, C., and Tarling, G. A. (2018). Pteropods counter mechanical damage and dissolution through extensive shell repair. *Nat. Commun.* 9:264.

Peters, W., Jacobson, A. R., Sweeney, C., Andrews, A. E., Conway, T. J., Masarie, K., et al. (2007). An atmospheric perspective on North American carbon dioxide exchange: carbontracker. *Proc. Natl. Acad. Sci.U.S.A.* 104, 18925–18930. doi: 10.1073/pnas.0708986104

Pilcher, D. J., Naiman, D. M., Cross, J. N., Hermann, A. J., Siedlecki, S. A., Gibson, G. A., et al. (2019). Modeled effect of coastal biogeochemical processes, climate variability, and ocean acidification on aragonite saturation state in the Bering Sea. *Front. Mar. Sci.* 5:508. doi: 10.3389/fmars.2018.00508

Saha, S., Moorthi, S., Pan, H. L., Wu, X., Wang, J., Nadiga, S., et al. (2010). The NCEP climate forecast system reanalysis. *Bull. Am. Meteorol. Soc.* 91, 1015–1057. doi: 10.1175/2010BAMS3001.1

Saha, S., Moorthi, S., Wu, X., Wang, J., Nadiga, S., Tripp, P., et al. (2014). The NCEP climate forecast system version 2. *J. Clim.* 27, 2185–2208. doi: 10.1175/JCLI-D-12-00823.1

Shchepetkin, A. F., and McWilliams, J. C. (2005). The regional oceanic modeling system (ROMS): a split explicit, free-surface, topography-following-coordinate oceanic model. *Ocean Modell.* 9, 347–404. doi: 10.1016/j.ocemod.2004.08.002

Shimizu, K., Kimoto, K., Noshita, K., Wakita, M., Fujiki, T., and Sasaki, T. (2018). Phylogeography of the pelagic snail *Limacina helicina* (*Gastropoda: Thecosomata*) in the subarctic western North Pacific. *J. Molluscan Stud.* 84, 30–37. doi: 10.1093/mollus/eyx040

Shimizu, K., Noshita, K., Kimoto, K., and Sasaki, T. (2021). Phylogeography and shell morphology of the pelagic snail *Limacina helicina* in the Okhotsk Sea and western North Pacific. *Mar. Biodivers.* 51:22.

Sromek, L., Lasota, R., Szymelfenig, M., and Wolowicz, M. (2015a). Genetic evidence for the existence of two species of the "Bipolar" Pelagic Mollusk *Clione limacina*. *Am. Malacol. Bull.* 33, 118–120. doi: 10.4003/006.033.0108

Sromek, L., Lasota, R., and Wolowicz, M. (2015b). Impact of glaciations on genetic diversity of pelagic mollusks: antarctic *Limacina antarctica* and Arctic *Limacina helicina*. *Mar. Ecol. Prog. Ser.* 525, 143–152. doi: 10.3354/meps11237

Stackpoole, S., Butman, D., Clow, D., Verdin, K., Gaglioti, B., and Striegl, R. (2016). "Chapter 8. carbon burial, transport, and emission from inland aquatic ecosystems in Alaska," in *Baseline and Projected Future Carbon Storage and Greenhouse-Gas Fluxes in Ecosystems of Alaska*, eds Z. Zhu, A. David, and Guire Mc (Reston VA: U.S. Geological Survey).

Stackpoole, S. M., Butman, D. E., Clow, D. W., Verdin, K. L., Gaglioti, B. V., Genet, H., et al. (2017). Inland waters and their role in the carbon cycle of Alaska. *Ecol. Appl.* 27, 1403–1420. doi: 10.1002/eap.1552

Stock, C. A., Dunne, J. P., and John, J. G. (2014). Global-scale carbon and energy flows through the marine planktonic food web: an analysis with a coupled physical–biological model. *Prog. Oceanogr.* 120, 1–28. doi: 10.1016/j.pocean.2013.07.001

Sulpis, O., Jeansson, E., Dinauer, A., Lauvset S. K., Middelburg J. J. (2021). Calcium carbonate dissolution patterns in the ocean. *Nat. Geosci.* 14, 423–428. doi: 10.1038/s41561-021-00743-y

Tsujino, H., Urakawa, S., Nakano, H., Small, R. J., Kim, W. M., Yeager, S. G., et al. (2018). JRA-55 based surface dataset for driving ocean–sea-ice models (JRA55-do). *Ocean Modell.* 130, 79–139. doi: 10.1016/j.ocemod.2018.07.002

Tsurumi, M., Mackas, D. L., Whitney, F. A., DiBacco, C., Galbraith, M. D., and Wong, C. S. (2005). Pteropods, eddies, carbon flux, and climate variability in the Alaska gyre. *Deep Sea Res. Part II Top. Stud. Oceanogr.* 52, 1037–1053. doi: 10.1016/j.dsr2.2005.02.005

van Oostende, N., Dussin, R., Stock, C. A., Barton, A. D., Curchitser, E., Dunne, J. P., et al. (2018). Simulating the ocean's chlorophyll dynamic range from coastal upwelling to oligotrophy. *Prog. Oceanogr.* 168, 232–247. doi: 10.1016/j.pocean.2018.10.009

Walkusz, W., Williams, W. J., and Kwasniewski, S. (2013). Vertical distribution of mesozooplankton in the coastal Canadian Beaufort Sea in summer. *J. Mar. Syst.* 127, 26–35. doi: 10.1016/j.jmarsys.2012.01.001

Williams, C. R., Dittman, A. H., McElhany, P., Busch, D. S., Maher, M. T., Bammler, T. K., et al. (2019). Elevated CO2 impairs olfactory-mediated neural and behavioral responses and gene expression in ocean-phase coho salmon (*Oncorhynchus kisutch*). *Global Chang. Biol.* 25, 963–977. doi: 10.1111/gcb.14532

Williams, S. E., Shoo, L. P., Isaac, J. L., Hoffmann, A. A., and Langham, G. (2008). Towards an integrated framework for assessing the vulnerability of species to climate change. *PLoS Biol.* 6:2621–2626. doi: 10.1371/journal.pbio.0060325

Zavolokin, A. V., Efimkin, A. Y., Slabinskiy, A. M., and Kosenok, N. S. (2007). Food supply and trophic relationships of Pacific salmon (*Oncorhynchus* spp.) and Atka mackerel (*Pleurogrammus monopterygius*) in the western Bering Sea in fall 2002–2004. *N. Pac. Anadr. Fish. Comm. Bull.* 4, 127–131.

Zavolokin, A. V., Kulik, V. V., and Zavarina, L. O. (2014). The food supply of the Pacific salmon of the genus *Oncorhynchus* in the northwestern Pacific Ocean. 2. comparative characterization and general state. *Russ. J. Mar. Biol.* 40, 199–207. doi: 10.1134/S1063074014030092

Conflict of Interest: The authors declare that the research was conducted in the absence of any commercial or financial relationships that could be construed as a potential conflict of interest.

Publisher's Note: All claims expressed in this article are solely those of the authors and do not necessarily represent those of their affiliated organizations, or those of the publisher, the editors and the reviewers. Any product that may be evaluated in this article, or claim that may be made by its manufacturer, is not guaranteed or endorsed by the publisher.

Copyright © 2021 Bednaršek, Naish, Feely, Hauri, Kimoto, Hermann, Michel, Niemi and Pilcher. This is an open-access article distributed under the terms of the Creative Commons Attribution License (CC BY). The use, distribution or reproduction in other forums is permitted, provided the original author(s) and the copyright owner(s) are credited and that the original publication in this journal is cited, in accordance with accepted academic practice. No use, distribution or reproduction is permitted which does not comply with these terms.

frontiers in Marine Science

ORIGINAL RESEARCH
published: 02 August 2021
doi: 10.3389/fmars.2021.685955

Distribution and Activity of Ammonia-Oxidizers on the Size-Fractionated Particles in the Pearl River Estuary

*Li Ma[1,2], Shangjin Tan[3,4], Hongbin Liu[3,4], Shuh-Ji Kao[1], Minhan Dai[1] and Jin-Yu Terence Yang[1]**

[1] State Key Laboratory of Marine Environmental Science, College of Ocean and Earth Sciences, Xiamen University, Xiamen, China, [2] Department of Chemical Engineering, Chengde Petroleum College, Chengde, China, [3] Department of Ocean Science, The Hong Kong University of Science and Technology, Hong Kong SAR, China, [4] Hong Kong Branch of the Southern Marine Science and Engineering Guangdong Laboratory (Guangzhou), The Hong Kong University of Science and Technology, Hong Kong SAR, China

To distinguish between the distribution and activity of ammonia-oxidizing bacteria (AOB) and ammonia-oxidizing archaea (AOA) in the Pearl River estuary (PRE), we investigated the DNA- and cDNA-based β-proteobacterial and archaeal *amo*A genes on three size-fractionated particles of >3.0 μm, 0.45–3.0 μm, and 0.22–0.45 μm. Results showed that AOB were more abundant in the freshwater with high concentrations of ammonium (NH_4^+) and low dissolved oxygen, whereas AOA were dominant in the NH_4^+-depleted seawater and sensitive to temperature. Obvious shifts in ammonia-oxidizing communities were found along the salinity gradient in the PRE. AOB clearly presented a particle-associated nature, as evidenced by higher relative abundance of *amo*A genes attached to the large particles (>3.0 μm) and their transcripts exclusively detected on this fraction. Moreover, higher transcriptional activity (indicated by the cDNA/DNA ratio) of AOB on the large particles, suggesting AOB were actively involved in ammonia oxidation despite their lower abundance in the mid- and lower estuarine regions. In contrast, AOA exhibited higher transcriptional activity on the 0.45–3.0 μm and 0.22–0.45 μm particles, implying the free-living strategy of these microbes. Together, these findings from field observations provide useful information on the ecological strategies of ammonia-oxidizing communities in response to different environmental conditions.

Keywords: ammonia-oxidizing bacteria, ammonia-oxidizing archaea, size-fractionated particles, Pearl River estuary, environmental factors

OPEN ACCESS

Edited by:
Arnaud Laurent, Dalhousie University, Canada

Reviewed by:
Chris Sedlacek, University of Vienna, Austria
Jiapeng Wu, Guangzhou University, China
Haitao Wang, Nankai University, China

****Correspondence:***
Jin-Yu Terence Yang
jyyang@xmu.edu.cn

Specialty section:
This article was submitted to Marine Biogeochemistry, a section of the journal Frontiers in Marine Science

Received: *26 March 2021*
Accepted: *12 July 2021*
Published: *02 August 2021*

Citation:
Ma L, Tan S, Liu H, Kao S-J, Dai M and Yang J-YT (2021) Distribution and Activity of Ammonia-Oxidizers on the Size-Fractionated Particles in the Pearl River Estuary. Front. Mar. Sci. 8:685955. doi: 10.3389/fmars.2021.685955

INTRODUCTION

Nitrification is an important process in the marine nitrogen cycle, which determines the distribution of oxidized and reduced nitrogen components in the ocean (Ward, 2008). It is an oxygen- and alkalinity-consuming process, contributing to hypoxia development and the enhancement of ocean acidification especially in coastal waters (Hu and Cai, 2011). The produced greenhouse gas nitrous oxide (N_2O) through nitrification pathway highlights its importance in the global climate change (Santoro et al., 2011; Stein, 2011; Löscher et al., 2012; Frame et al., 2017).

Ammonia oxidation is the first and rate-limiting step of nitrification, which is microbially mediated oxidation of ammonia (NH_3) to nitrite (NO_2^-). Ammonia-oxidizing bacteria (AOB), including a few genera of β- and γ-Proteobacteria, and ammonia-oxidizing archaea (AOA) belonging to *Thaumarchaeota* are the two major types of microorganisms that catalyze ammonia oxidation and N_2O production in the estuarine and marine ecosystems (Ward, 2008; Santoro et al., 2011; Stein, 2011; Löscher et al., 2012; Frame et al., 2017).

Estuaries, which are highly affected by coastal nutrients and eutrophication due to anthropogenic activity, have been found to occur high rates of nitrification at the land-ocean interface (Bricker et al., 2008; Damashek et al., 2016). Estuaries are also recognized as the hot-spot regions for N_2O production and emission (Seitzinger and Kroeze, 1998; Mortazavi et al., 2000; Usui et al., 2001; Kroeze et al., 2010; Allen et al., 2011; Lin et al., 2016). In estuarine regions, the distribution of AOB and AOA generally presents a complex picture; for example, the ratio of AOB to AOA varies extensively and exhibits an inconsistent pattern along a salinity gradient (Caffrey et al., 2007; Mosier and Francis, 2008; Sahan and Muyzer, 2008; Santoro et al., 2008; Bernhard et al., 2010). On the other hand, it is well-established that AOB are in general larger in size than AOA (Holt et al., 1994; Könneke et al., 2005; De La Torre et al., 2008; Hatzenpichler et al., 2008; Jung et al., 2011; Lehtovirta-Morley et al., 2011; Tourna et al., 2011). Related studies in estuaries showed that AOB more clearly attached to particles (>3.0 μm) in the high-turbidity freshwater (Zhang et al., 2014; Hou et al., 2018), whereas the free-living (<3.0 μm) AOA appeared to be more abundant in a low-particle and saline environment (Hou et al., 2018). However, the activity of AOB *versus* AOA in estuarine systems and their relationship with different size-fractionated particles, are still currently lacking.

The Pearl River estuary (PRE) is one of the complex estuarine systems, which is a funnel-shaped sub-estuary with a surface area of 1,180 km^2 (Dai et al., 2014). The low-salinity waters in the upper PRE are characterized by low concentrations of O_2 and they are rich in nutrients from anthropogenic sources. NH_4^+ is the dominant species of inorganic nitrogen with extremely high concentrations of ∼300–800 μmol L^{-1} in this region, and NO_3^- becomes more important seaward (Dai et al., 2008). A year-round pattern of dramatic decrease in NH_4^+ and increase in NO_3^- is found in the upper estuary. This feature suggests an elevated level of nitrification (Dai et al., 2006, 2008; He et al., 2014), which corresponds to a high concentration of N_2O in the water column (Lin et al., 2016; Ma et al., 2019). Moreover, the remineralization of organic matter leads to the formation of hypoxic zones both at the head of the estuary and in the downstream bottom waters, which may enhance the nitrification rates performed by nitrifying microorganisms (He et al., 2014; Su et al., 2017; Qian et al., 2018; Zhao et al., 2020). The hydrological and chemical parameters of the waters in the mid- and lower estuarine regions are primarily controlled by the intermixing of freshwater and seawater (Harrison et al., 2008). The complicated biogeochemical settings of PRE provide an ideal ecosystem for elucidating the distribution patterns of AOB and AOA in response to the environments (Hou et al., 2018; Ma et al., 2019).

To better understand the activity of AOB and AOA and their relationship to the environmental parameters in the PRE, we investigated the abundance and transcripts of AOB and AOA *amo*A genes on different size-fractionated particles. According to the shapes and sizes of AOB and AOA cells reported in the coastal and estuarine waters (**Supplementary Table 1**), we found the diameter of AOA cells generally less than 0.3 μm and relatively larger size for AOB cells. Filters of three pore sizes (3.0 μm, 0.45 μm, and 0.22 μm) were applied to fractionate particles in the PRE.

MATERIALS AND METHODS

Study Sites and Sampling

Our study was based on a summer research cruise that was conducted along the mainstream of the PRE in July 2014 (**Figure 1**). According to its geographical characteristics, the PRE is divided into an upper region, which is upstream of the Humen outlet, and mid- and lower regions, called Lingdingyang (**Figure 1**). Surveys of the waters in the mid- and lower estuarine region (Lingdingyang) were conducted during July 19–22 (Section "A"), whereas those conducted in the upper estuary from Humen to Guangzhou (Section "P") took place during July 28–29. Water samples were taken from the surface (0.5 m) and bottom (2.0–15.0 m) layers of each site by using a conductivity-temperature-depth (CTD) rosette sampling system (SBE 25, Sea-Bird Co., United States) fitted with 4 L Niskin bottles (General Oceanics). Samples for total suspended matter (TSM) were collected by filtering 1–2 L of water onto pre-combusted and pre-weighed GF/F membranes (Whatman), and then stored at −20°C. Samples collected for the determination of inorganic nutrients were filtered with 0.45 μm cellulose acetate membranes and frozen at −20°C until analysis. The exception was NH_4^+, which was analyzed on board immediately after collection. Samples for N_2O were collected into 125 mL headspace glass bottles, to which 100 μL of saturated $HgCl_2$ was added. The bottles were immediately closed with rubber stoppers and aluminum crimp caps, and then stored in the dark at 4°C until analysis.

Analysis of Biogeochemical Parameters

The temperature and salinity were determined using the CTD system. Dissolved oxygen (DO) was measured using the Winkler titration method (Carpenter, 1965). The TSM on the filters were lyophilized and then weighed. The increase in weight of the filters represents the content of TSM. NH_4^+ was analyzed using the indophenol blue spectrophotometric method (Pai et al., 2001). Nitrate (NO_3^-), and nitrite (NO_2^-) were measured by an automatic analysis system (Bran-Lube, GmbH) (Han et al., 2012). N_2O was determined at 25°C using a purge and trap system (Tekmar Velocity XPT, United States) coupled with a gas chromatograph (Agilent 6890, United States) equipped with a μECD detector (Lin et al., 2016; Ma et al., 2019).

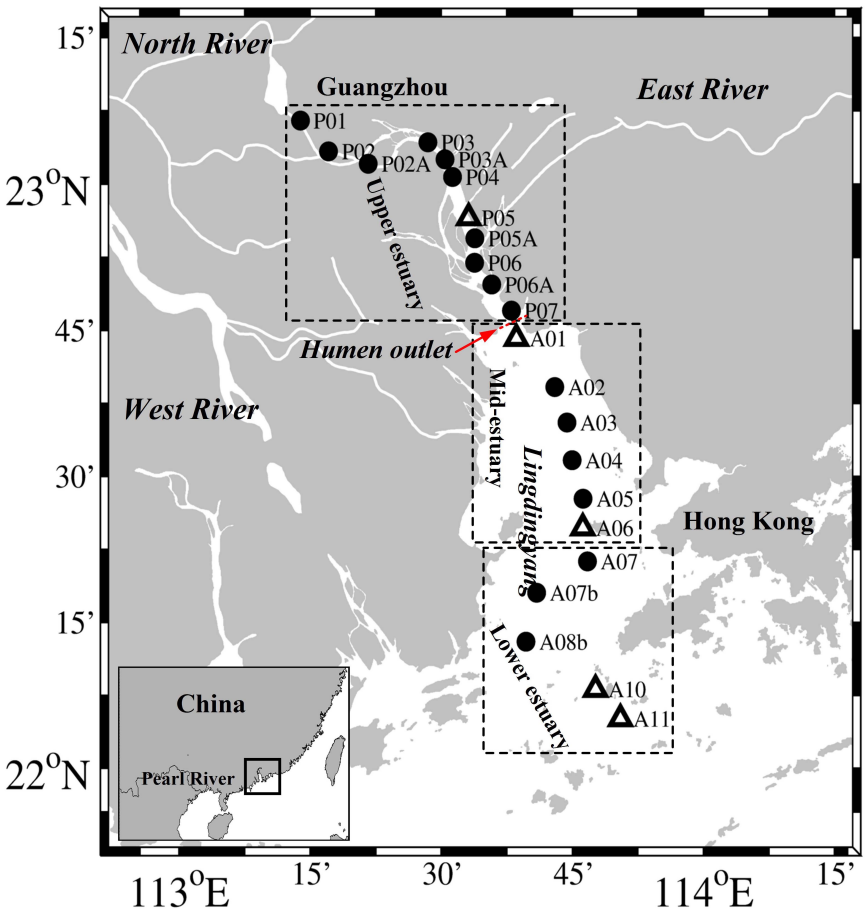


FIGURE 1 | Map of the Pearl River estuary and the sampling sites in July 2014. The dotted boxes separate the study sites into the upper, mid, and lower estuarine regions. The open triangles represent the sites (P05, A01, A06, A10, and A11) where we conducted size fractionation experiments.

Size Fractionation Experiments

Experimental Design

Size fractionation experiments were conducted at site P05, which is located in the upper estuary, sites A01 and A06, which are located in the mid-estuary, and sites A10 and A11, which are located in the lower estuary (**Figure 1**). For the gene analysis, water samples of 500–1000 mL were sequentially filtered through 3.0 μm, 0.45 μm, and 0.22 μm polycarbonate membranes (47 mm diameters, Millipore, Isopore^{TM}, United States) within ∼2 h at a pressure <0.03 MPa to retain the size fractionated communities (>3.0 μm, 0.45–3.0 μm, and 0.22–0.45 μm). To avoid the aperture of membrane filters blocked, we carefully monitored the filtration rates and changed the membrane filters when each 250–500 mL of water was filtered. RNAlater solution (Ambion, Austin, TX, United States) was immediately added to the samples to prevent RNA degradation. The filters were then immediately frozen in liquid nitrogen and stored at −80°C until further analyses.

Nucleic Acid Extraction and qPCR Analysis

DNA was extracted using a modified enzyme-phenol/chloroform protocol (Xia et al., 2015). According to Tan et al. (2019), RNA was extracted using the TRIzol reagent (Ambion, Austin, TX, United States) in combination with the PureLink^{TM} RNA Mini kit (Ambion, Austin, TX, United States), eluted with 50 μL RNase-free water and stored at −80°C. cDNA was obtained by reverse transcribing RNA using the First-Strand cDNA Synthesis kit (Invitrogen, Austin, TX, United States).

The Bact1369F/Prok1541R (Suzuki et al., 2000), 340F/1000R (Gantner et al., 2011), Arch-*amo*AF/Arch-*amo*AR (Francis et al., 2005), and *amo*A-1F/*amo*A-2R (Rotthauwe et al., 1997) primers were used for qPCR of the bacterial 16S rRNA, archaeal 16S rRNA, AOA-*amo*A and β-AOB-*amo*A genes, respectively. qPCR was performed using a LightCycler 480 Instrument II (Roche, Basel, Switzerland). All the samples were measured in triplicate, each in a total volume of 10 μL, comprising 0.5 μL of the template, 5 μL of 2 × SYBR Green Master Mix (Takara, Otsu, Japan), 0.5 μL of each primer, and 0.2 μL of ROX II. Details of the qPCR assays and primer sets are provided in the **Supplementary Tables 2, 3**. The presence and abundance of γ-AOB-*amo*A gene were also checked using two primer sets A189-F/A682-R and amoA3F/amoA4R (Holmes et al., 1995; Lam et al., 2009). However, the obtained results may be inaccurate due to its extremely low abundance. This is consistent with the previous

study conducted in the PRE that found no trace of γ-AOB sequences in *amo*A clone libraries (Jin et al., 2011). Therefore, the data of γ-AOB-*amo*A gene was not included in the present study.

Statistical Analyses

The parametric ANOVA test or non-parametric Mann–Whitney *U* test was applied for comparing two variables, depending on the normality of the data set. The bivariate correlations between environmental factors and *amo*A genes were described by Pearson correlation coefficients (**Table 1**), using SPSS 18.0 (SPSS Inc., Chicago, IL, United States). False discovery rate (FDR)-based multiple comparison procedures were applied to evaluate the significance of multiple hypotheses and identify truly significant results (FDR-adjusted *P* value) (Pike, 2011). **Table 1** shows the environmental parameters correlated significantly ($P < 0.05$) with at least one of the total abundances of DNA-based and cDNA-based *amo*A genes of β-AOB and AOA on the three size-fractionated particles. In addition, detrended correspondence analyses (DCA) were conducted based on the environmental parameter datasets and qPCR-based abundance of *amo*A genes. The maximum gradient length of DCA was >4.0, thus a canonical correspondence analysis (CCA) was used to analyze the variations in the AOB *versus* AOA distributions on different size-fractionated particles under different environmental constraints using R (version 3.4.4; vegan 2.5-3). The value of variance inflation factor (VIF) was used to check the multicollinearity of correlating variables, and here we used environmental parameters without multicollinearity (i.e., VIF < 10) in CCA (Sadyś et al., 2014). The qPCR-based relative abundances and environmental parameters were normalized via Z transformation (Magalhães et al., 2008). Hypothesis testing was performed using a Monte Carlo analysis (999 permutations).

RESULTS

Hydrochemistry and Biogeochemical Characteristics

In this investigation, we covered 22 sites in the PRE, including the upper (P01–P07), mid (A01–A06), and lower (A07–A11) estuarine regions (**Figure 1**). Most sites in the upper estuary were characterized by freshwater such that the salinity was close to 0, except for site P07 at which the salinity in the surface and bottom waters was 0.3 and 0.9, respectively. The salinity in the mid and lower estuarine regions increased seaward from 0.7 at site A01 to 16.5 at site A11 in the surface waters and from 1.6 at site A02 to 33.8 at site A11 in the bottom waters (**Figure 2A**). In general, the concentrations of TSM decreased seaward from the upper estuary. In the surface waters, the highest TSM concentration of 79.9 mg L^{-1} was found at site P01 and the lowest concentration of 8.2 mg L^{-1} was detected at site A11. The TSM concentrations were relatively higher in the bottom waters, with highest value of 124.4 mg L^{-1} at site P01 and lowest value of 16.5 mg L^{-1} at site A07 (**Figure 2B**). The total concentrations of $NO_3^- + NO_2^-$ increased from 83.4 μmol L^{-1} at site P01 to >150 μmol L^{-1} at sites P06 and P07 in the upper estuary, and then decreased seaward to 3.2 μmol L^{-1} in the bottom water at site A11 (**Figure 2C**). The NH_4^+ concentration in the upper estuary was highest 308–314.6 μmol L^{-1} at site P01 and decreased dramatically to 1–2 μmol L^{-1} at site P06. Lower concentrations of NH_4^+ were found in the mid- and lower estuarine regions, ranging from 9.9 μmol L^{-1} at site A05 to below the detection limit at site A11 (**Figure 2D**).

As shown in **Figure 2E**, the DO concentration varied from 24.6 to 139.4 μmol L^{-1} in the upper estuary with the lowest value in the bottom water at site P05, and it was relatively higher in the mid- and lower estuarine regions, ranging from 69.8 to 224.7 μmol L^{-1}. In addition, the N_2O concentration was higher in the upper region, ranging from 32.6 to 157.7 nmol L^{-1}, and decreased seaward in the mid- and lower estuarine regions (20.2 to 5.2 nmol L^{-1}) (**Figure 2F**). The highest N_2O concentration was observed in the bottom water at site P05, corresponding to the lowest DO concentration therein. The concentrations of DO and N_2O in the surface and bottom waters had significant negative linear correlations (**Supplementary Figure 1**). However, the DO concentrations did not significantly correlate with NH_4^+ concentrations in the surface and bottom waters (**Supplementary Figure 1**).

TABLE 1 | The Pearson correlations between environmental parameters and total abundances of DNA-based and cDNA-based *amo*A genes of AOB and AOA on the three size-fractionated particles.

Environmental parameter	DNA-based *amo*A gene		cDNA-based *amo*A gene	
	AOB (*n* = 9)	AOA (*n* = 9)	AOB (*n* = 7)	AOA (*n* = 7)
Salinity	−0.720*	0.641	−0.288	0.618
Temperature	0.776*	−0.863*	−0.016	−0.795*
NH_4^+	0.630	−0.550	0.844*	−0.432
NO_2^-	0.700*	−0.570	0.786*	−0.293

The cDNA-based amoA genes of AOB were only detected on the particles of >3.0 μm. The environmental parameters without significant correlation to any of DNA-based and cDNA-based amoA genes of AOB and AOA are not included.
**False discovery rate (FDR)-adjusted P < 0.05.*

Distributions and Transcripts of *amoA* Genes on the Different Size Fractions

The abundances of the β-AOB and AOA *amo*A genes were measured on three size-fractionated samples, collected from five sites representing the upper estuary (P05, with surface salinity of ∼0), mid-estuary (A01 and A06, with surface salinity of 0.6–3.3), and lower estuary (A10 and A11, with surface salinity of ∼16.5), respectively. We defined the three size fractions as the large (>3.0 μm), medium (0.45–3.0 μm), and small (0.22–0.45 μm) particles.

The total abundance of the DNA-based β-AOB *amo*A gene on the three size fractions varied from $1.11 \pm 0.20 \times 10^4$ to $1.61 \pm 0.31 \times 10^5$ copies L^{-1}, with higher abundance in the upper estuarine waters and lower abundance in the mid- and lower estuarine waters (**Figure 3A**). In contrast, the total abundance of the DNA-based AOA *amo*A gene on the three size fractions increased seaward, varying from $4.72 \pm 0.63 \times 10^3$

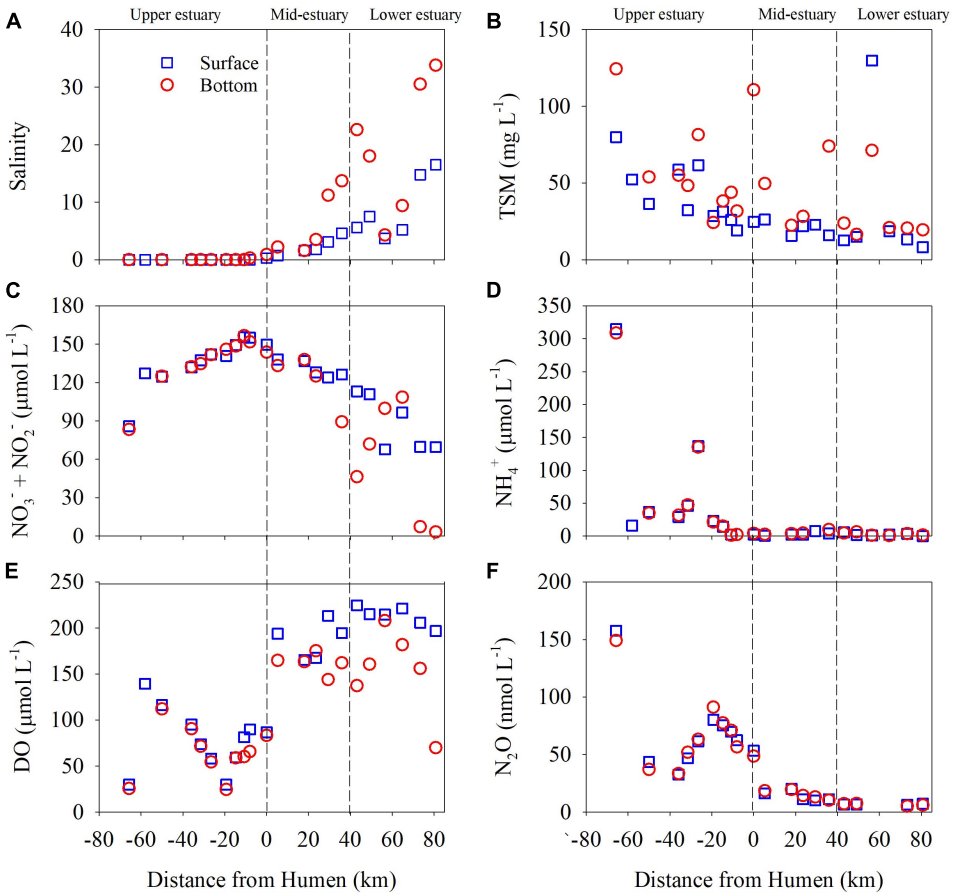


FIGURE 2 | The distributions of salinity **(A)**, total suspended matter (TSM) **(B)**, nitrate (NO_3^-) + nitrite (NO_2^-) **(C)**, ammonium (NH_4^+) **(D)**, dissolved oxygen (DO) **(E)**, and nitrous oxide (N_2O) **(F)** in the Pearl River estuary in July 2014. The dotted vertical lines separate the study sites into the upper, mid, and lower estuarine regions. The salinity and DO datasets in the mid and lower regions (Lingdingyang) were reported previously by Su et al. (2017). The blue open squares and red open dots represent samples collected in the surface and bottom waters, respectively. Humen Outlet is represented here at 0 km. Negative distance values represent sites in the upper estuary, and positive distance values represent sites in the mid- and lower estuary.

copies L^{-1} in the upper estuarine waters to 7.57 ± 0.48 × 10^6 copies L^{-1} in the lower estuarine waters (**Figure 3B**). The ratios of β-AOB/AOA for DNA-based *amo*A gene varied from 0.002 to 30.1 along the salinity gradient in the PRE (**Supplementary Figure 2**). Overall, the DNA-based β-AOB *amo*A genes had higher abundance than AOA only in the freshwater at site P05, whereas the abundance of the DNA-based AOA *amo*A genes were approximately 1–3 orders of magnitude higher than AOB in the saltwater (non-parametric Mann–Whitney *U* test, $P < 0.01$). Such distribution patterns were consistent on the different size fractionated particles (**Supplementary Figure 2**).

In general, the AOB had higher abundance on the large particles. Their relative abundance (when compared with the total amounts of β-AOB *amo*A genes) on this size-fraction varied from 33.5 to 93.2%, with higher values in the mid-estuary (**Figure 4A** and **Supplementary Table 4**). The relative abundances of DNA-based AOA *amo*A gene were 0.0–82.4% on the large particles, 16.7–70.0% on the medium particles, and 0.9–58.5% on the small particles, respectively (**Figure 4B** and **Supplementary Table 4**). Compared with AOB, the AOA were not dominated in any size fractionated particles. In addition, no clear trends in their relative abundances were found on the three size fractions (**Figure 4B**).

Notably, β-AOB *amo*A gene transcripts were only detected on the large samples, where the cDNA-based gene abundances varied from 7.76 ± 0.41 × 10^3 to 2.70 ± 0.11 × 10^4 copies L^{-1} (**Figure 3A**). In contrast, AOA *amo*A gene transcripts were detected on all three of the size fractions with the total cDNA-based genes varying from 2.41 ± 0.84 × 10^3 to 7.96 ± 0.22 × 10^5 copies L^{-1} (**Figure 3B**). The cDNA-based AOA *amo*A genes on the large particles ranging from 47 ± 57 to 7.74 ± 0.26 × 10^4 copies L^{-1} (**Figure 3B**) accounted for a minor contribution to the total abundances (0.5–35.1%), whereas higher contributions were found on the smaller size fractions of 0.22–0.45 and 0.45–3.0 μm (**Figure 4C**). Unfortunately, we did not obtain cDNA from the samples collected from site P05 in the upper estuary because these samples were stored without RNAlater. Thus, an accurate comparison of the P05 samples with the samples from the other sites, which were stored with RNAlater, was not possible.

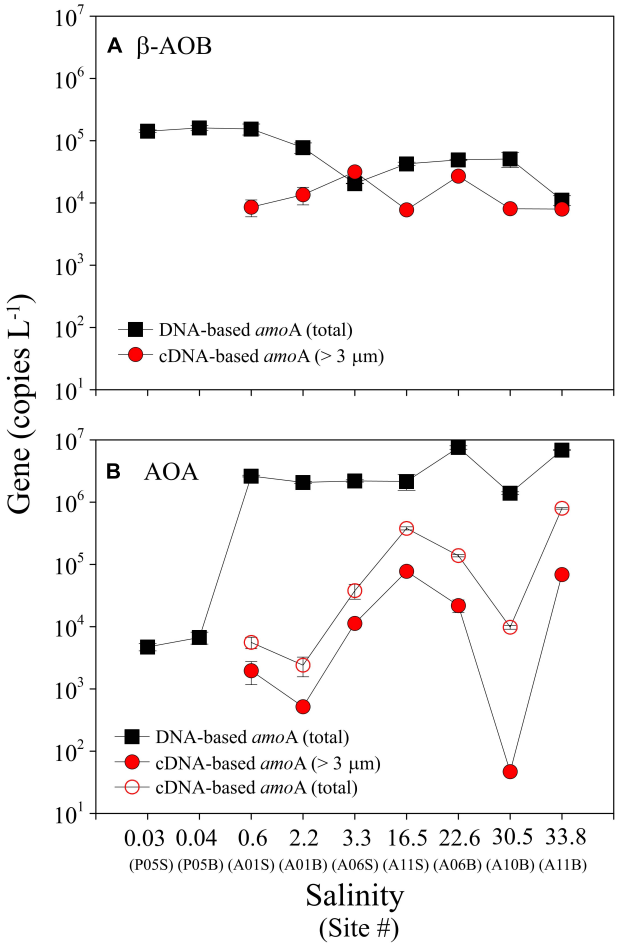


FIGURE 3 | Total abundance of the DNA-based and cDNA-based *amo*A genes of β-AOB **(A)** and AOA **(B)** on three size-fractioned particles (>3.0 μm, 0.45–3.0 μm, and 0.22–0.45 μm) along the salinity gradient in the PRE. Note that the cDNA-based β-AOB *amo*A genes were only detected on particles of >3.0 μm (red solid circle). cDNA at site P05 was not studied because these samples were not stored with RNAlater (see text). The suffixes "S" and "B" of site information represent the surface and bottom samples at each site, respectively.

Correlations Between the Abundance of the *amo*A Genes and Environmental Parameters

The bivariate correlations between environmental parameters and total abundances of the *amo*A genes on the three size-fractionated particles in the PRE were described by Pearson correlation coefficients (R value, see **Table 1**). The DNA-based β-AOB *amo*A genes on the three size fractions were significantly correlated ($P < 0.05$) with temperature ($R = 0.776$), NO_2^- ($R = 0.700$), and salinity ($R = -0.720$), while the cDNA-based β-AOB *amo*A genes that were only detected on the large particles were positively correlated ($P < 0.05$) with NH_4^+ ($R = 0.844$) and NO_2^- ($R = 0.786$). Unlike to AOB, both DNA-based and cDNA-based AOA *amo*A genes on the three size fractions were negatively correlated with temperature ($P < 0.05$-0.01). The correlation between AOA *amo*A genes and NH_4^+ concentrations ($R = -0.550$, $P = 0.13$) was not significant.

The CCA was further conducted to identify variations in the distributions of the ammonia oxidizers on the large, medium, and small particles under different environmental constraints. As shown in **Figure 5**, the first two CCA axes explained 93.5% of the variations in the AOB and AOA *amo*A genes on the different size fractions under the environmental parameters in the PRE. NH_4^+, DO, temperature, and salinity were the significant variables that determined the distributions of different size-fractionated ammonia oxidizers in the PRE ($P < 0.05$-0.01), whereas the TSM may play a minor role. It is worth noting that DO was not significantly correlated with the total abundances of DNA- and cDNA-based AOB and AOA *amo*A genes during the study period. Overall, the AOB-related samples were consistently distributed in the upper estuary. The AOB on all three size fractions were positively correlated with NH_4^+ and temperature, whereas negatively correlated with DO and salinity. Conversely, the AOA-related samples distributed in the mid- and lower estuarine regions (Lingdingyang), with reverse correlations with the environmental parameters. In addition, the AOA on the small particles, and on both the large and medium particles were divided by the positive and negative half of CCA2 axis.

DISCUSSION

Distribution of AOB Versus AOA in Response to Environmental Factors in the PRE

In estuaries characterized by strong gradients in salinity, TSM and nutrients, the AOB and AOA often display disparate patterns in response to environmental features (Leininger et al., 2006; Wuchter et al., 2006; Santoro et al., 2008; Zhang et al., 2014). In this study conducted in the PRE, the abundance of AOB exceeded that of AOA in the freshwaters. The numbers of AOB decreased with an increase in salinity, whereas the AOA were more abundant in the high-salinity waters of the lower estuary. Similar distribution patterns of AOB and AOA have been reported in Chesapeake Bay (Ward et al., 2007) and Westerschelde estuary (Sahan and Muyzer, 2008). However, other studies showed different distribution patterns of AOB and AOA along the salinity gradients. For example, in San Francisco Bay (Mosier and Francis, 2008) and Weeks Bay (Caffrey et al., 2007) AOB were found to outnumber AOA as the salinity increased. In addition, in Plum Island Sound estuary, the ratios of AOA to AOB generally decreased with increasing salinity, but AOA were more abundant than AOB (Bernhard et al., 2010). The abundances and distribution patterns of AOB and AOA in the estuarine system are not solely regulated by the salinity effect. Our results based on the CCA and Pearson correlation revealed that the distribution patterns of ammonia-oxidizers in the PRE were likely controlled by a combination of temperature, salinity, substrate (NH_4^+ and NO_2), and DO (**Table 1** and **Figure 5**).

The β-AOB *amo*A genes decreased along the salinity gradient, while the AOA *amo*A genes increased considerably at sites with salinity higher than 0.5 (**Figure 3**). The corresponding ratios of

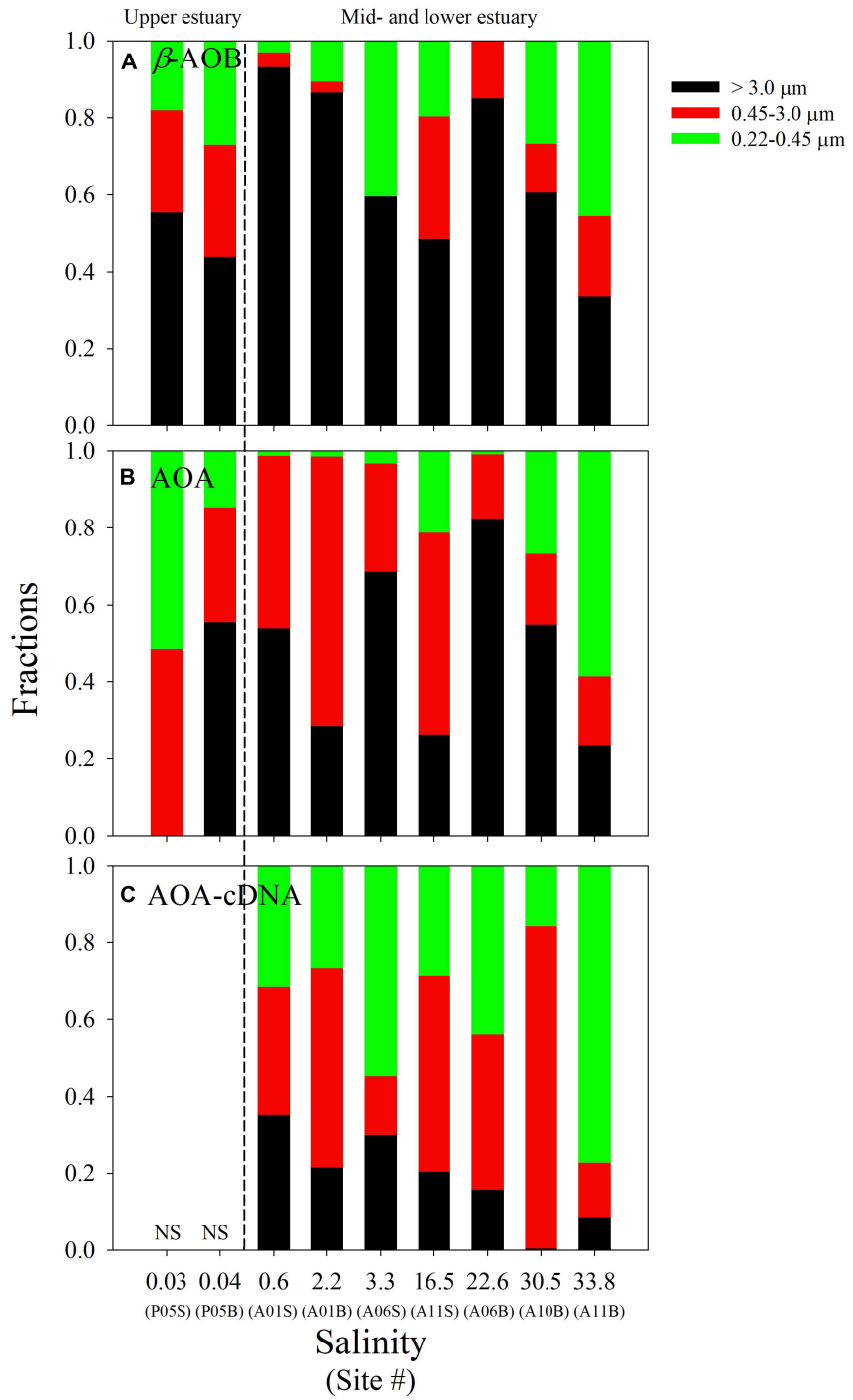


FIGURE 4 | Relative abundance of the DNA-based *amo*A genes of β-AOB **(A)** and AOA **(B)** on the different size fractions along the salinity gradient in the PRE. In addition, the relative abundance of the cDNA-based *amo*A genes of AOA **(C)** on the different size fractions are also shown. The dashed line separates the study sites into the upper estuarine region, and the mid- and lower estuarine regions. The suffixes "S" and "B" of site information represent the surface and bottom samples at each site, respectively. The detailed data are presented in **Supplementary Table 4**.

β-AOB to AOA *amo*A genes changed from >30 in the freshwater to 0.002 in the seawater. This result indicates obvious shifts in ammonia-oxidizing communities in the PRE. The disparate distribution patterns of AOB and AOA also reflect differences in their adaptation to the various environmental gradients of the PRE. The β-AOB *amo*A genes were more abundant in the upper estuary than those in the lower estuarine regions. This finding is consistent with a previous study, which similarly found that AOB had a higher abundance than AOA along the Dongjiang tributary in the upper reach of the PRE (Sun et al., 2014). Low

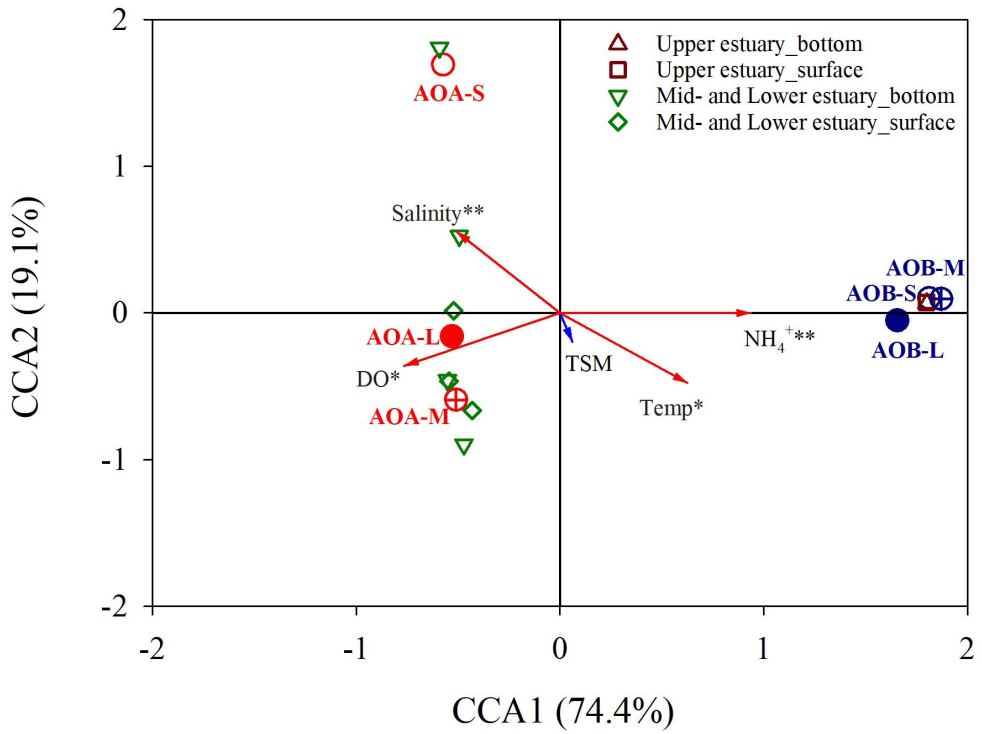


FIGURE 5 | Constrained ordinations of the DNA-based AOB and AOA *amo*A genes on the large (L; >3.0 μm; solid circle), medium (M; 0.45–3.0 μm; crossed circle), and small (S; 0.22–0.45 μm; open circle) size-fractionated particles with environmental factors by canonical correspondence analysis (CCA). Samples in the surface and bottom waters from the upper estuary (n = 2) and the Lingdingyang (the mid- and lower estuary, n = 7) are also shown. The vectors represent the environmental variables. These variables that have statistically significant influence on the distribution of size-fractionated ammonia oxidizers are marked with asterisk and revealed by the red arrows. Temp stands for temperature.

DO (<30 μmol L^{-1}) and enriched NH_4^+ substrate (25–30 μmol L^{-1}) in the upper estuary (**Figure 2**) may stimulate the growth and activity of AOB on the large particles, as we found that the abundance and transcripts of β-AOB *amo*A gene on the large particles were positively correlated with DO and NH_4^+ (**Table 1** and **Figure 5**). This is supported by the previous studies that indicated higher abundance of DNA-based AOB *amo*A genes associated with increased potential nitrification rates in the upper PRE (Sun et al., 2014; Hou et al., 2018). Our observation suggests that AOB *amo*A genes might be more active in rich substrate and oxygen-depleted conditions.

In contrast, AOA were generally more abundant than AOB in the mid- and lower estuarine regions that are characterized by the low concentrations of NH_4^+, due to mixing with oligotrophic seawater (**Figures 2**, **3**). Recent studies have proposed that the AOA have evolved their substrate-transport mechanisms to thrive in conditions of low NH_4^+, and they thus have a higher affinity to oligotrophic environments (Martens-Habbena et al., 2009; Kits et al., 2017). Archaea of Marine Group I are generally the abundant archaeaplankton members of the coastal and open ocean (Karner et al., 2001; Könneke et al., 2005). Indeed, the *Nitrosopumilus maritimus* SCM1 has been recently found as the dominated *amo*A genotype AOA in the PRE (Zou et al., 2019). In addition, it is reasonable that changes in salinity due to the physical mixing has more effect on the distribution of the AOA on the small particles (**Figure 5**). Notably, we observed that temperature (27.7–31.5°C) was negatively correlated with AOA *amo*A gene transcripts and the abundances of AOA *amo*A gene on the different size fractions in the present study (**Table 1** and **Figure 5**), which supports the finding that increasing temperature (24–34°C) would suppress ammonia oxidation in the oligotrophic offshore where AOA dominate in the ammonia oxidizers (Zheng et al., 2020). Together, these results reveal the AOA are sensitive to temperature and adapt to the NH_4^+-depleted environment.

Niche Differences of AOB Versus AOA on Size Fractionated Particles

The size-fractionated results clearly showed that in the PRE, the AOB prefer to attach to large particles as evidenced by the highest relative abundance of DNA-based β-AOB *amo*A gene on the large particles at most sites (33.5–93.2% with an average of 62.8%; **Figure 4A** and **Supplementary Table 4**). In contrast, the AOA appear not to be dominated on any size-fractionated particle. This finding is consistent with a previous study by Hou et al. (2018), in which a two-size fraction design (>3.0 μm and 0.22–3.0 μm) and different primer sets for amplifying β-proteobacterial *amo*A were applied. Moreover, cDNA-based β-AOB *amo*A genes were exclusively detected on the large particles. In this regard, the β-AOB *amo*A

gene on the medium and small particles that accounted for ∼37.2% of total abundances may be inactive. These results suggest the particle-associated nature of AOB. Conversely, more of the cDNA-based AOA *amo*A genes were detected on the medium and small particles, suggesting the free-living strategy of these microbes. We further compared the transcriptional activity (indicated by the cDNA/DNA ratio) of AOB *versus* AOA on the large particles. The cDNA/DNA ratios of AOB are significantly higher than those of AOA (**Figure 6**), suggesting that the AOB community is more metabolically active than the AOA community on the large particles. These findings indicate that the AOB attached to the large particles might be more actively involved in ammonia oxidation than AOA, despite their lower abundance in the mid- and lower estuarine regions.

In addition, it is possible that the recently discovered complete ammonia-oxidizing (comammox) microorganisms may play a role in ammonia oxidation especially in the mid- to lower estuary. This is because that ammonia affinities of comammox bacteria are higher than those of AOB and most species of AOA, except for *Nitrosopumilus* species (Kits et al., 2017; Zhang et al., 2020). The presence of comammox bacteria has been reported in sediments of some coastal systems (Yu et al., 2018; Sun et al., 2020; Bernhard et al., 2021). However, recent evidence indicates no comammox bacteria found on suspended particles of 0.22–3 μm in the PRE (close to site A11 in this study) (Zou et al., 2019). The contribution of comammox bacteria attached to the large particles could not be ruled out. In order to fully understand the potential importance of comammox bacteria in the estuary, further studies on their distribution and transcriptional activity on different size-fractionated particles should be considered in future field studies.

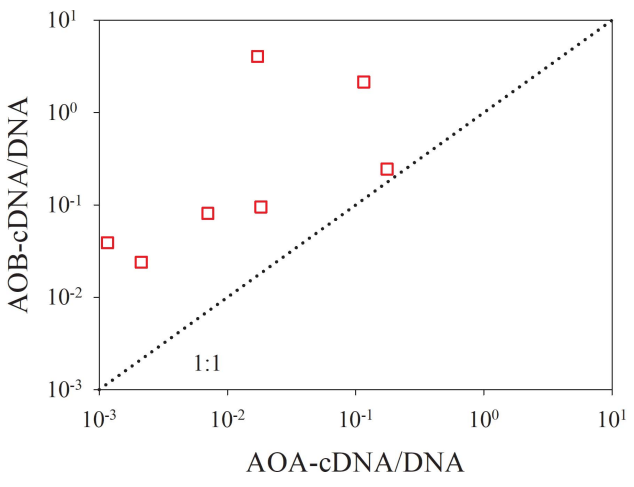


FIGURE 6 | The transcriptional activity of AOB versus AOA on the >3.0 μm size fraction. The ratio of cDNA-based to DNA-based *amo*A gene (cDNA/DNA) is defined as the transcriptional activity. The dotted line is the 1:1 line.

DATA AVAILABILITY STATEMENT

The original contributions presented in the study are included in the article/**Supplementary Material**, further inquiries can be directed to the corresponding author. The datasets presented in this study can also be found in the PANGAEA Data Archiving and Publication.

AUTHOR CONTRIBUTIONS

MD and HL conceived and designed the experiments. LM and ST performed the experiments and analyzed the data. LM, ST, and J-YY wrote the manuscript. All authors contributed to the interpretation of results and critical revision.

FUNDING

This work was supported by the National Key Scientific Research Project sponsored by the Ministry of Science and Technology of the People's Republic of China (Grant #2015CB954000) and the Strategic Priority Research Program of Chinese Academy of Sciences (Grant #XDB42000000). This study was also supported by the National Natural Science Foundation of China (Grants #41730533, #41721005, #91851209, #92058204, and #41890804), the Fundamental Research Funds for the Central University (Grants #20720190092 and #20720212005), State Key Laboratory of Marine Resource Utilization in South China Sea (Hainan University) (Grant #MRUKF2021018), and partially supported by a grant from the Research Grants Council of the Hong Kong Special Administrative Region, China (Project N_HKUST609/16 and T21-602/16R).

ACKNOWLEDGMENTS

We thank Baiyun Wang, Wenbin Zou, Li Tian, Yangyang Lu, and Qing Li for assisting with the on-deck ammonium measurements, Jianzhong Su for measuring dissolved oxygen, Tao Huang and Lifang Wang for providing the cruise measurements of nitrate and nitrite, Liguo Guo for helping with the DIC data and Huade Zhao for making the site map. We sincerely thank Xiuli Yan, Xiaomin Xia, and Sarah E. Ho for comments on the manuscript. We also thank the editor and three reviewers for their insightful comments.

SUPPLEMENTARY MATERIAL

The Supplementary Material for this article can be found online at: https://www.frontiersin.org/articles/10.3389/fmars.2021.685955/full#supplementary-material

Supplementary Figure 1 | Scatter plots of DO vs. N_2O **(A)** and NH_4^+ **(B)** for the surface and bottom waters in the study area.

Supplementary Figure 2 | Ratios of β-AOB/AOA for DNA-based *amo*A gene on the >3.0 μm **(A)**, 0.45–3.0 μm **(B)**, and 0.22–0.45 μm **(C)** particles, and on all three size fractionated particles **(D)**. N.D. denotes the β-AOB or AOA undetected on that size fraction.

REFERENCES

Allen, D., Dalal, R. C., Rennenberg, H., and Schmidt, S. (2011). Seasonal variation in nitrous oxide and methane emissions from subtropical estuary and coastal mangrove sediments, Australia. *Plant Biol.* 13, 126–133. doi: 10.1111/j.1438-8677.2010.00331.x

Bernhard, A. E., Beltz, J., Giblin, A. E., and Robert, B. J. (2021). Biogeography of ammonia oxidizers in New England and Gulf of Mexico salt marshes and the potential importance of comammox. *ISME Commun.* 1:9. doi: 10.1038/s43705-021-00008-0

Bernhard, A. E., Landry, Z. C., Blevins, A., De La Torre, J. R., Giblin, A. E., and Stahl, D. A. (2010). Abundance of ammonia-oxidizing archaea and bacteria along an estuarine salinity gradient in relation to potential nitrification rates. *Appl. Environ. Microbiol.* 76, 1285–1289. doi: 10.1128/AEM.02018-09

Bricker, S. B., Longstaff, B., Dennison, W., Jones, A., Boicourt, K., Wicks, C., et al. (2008). Effects of nutrient enrichment in the nation's estuaries: a decade of change. *Harmful Algae* 8, 21–32. doi: 10.1016/j.hal.2008.08.028

Caffrey, J. M., Bano, N., Kalanetra, K., and Hollibaugh, J. T. (2007). Ammonia oxidation and ammonia-oxidizing bacteria and archaea from estuaries with differing histories of hypoxia. *ISME J.* 1, 660–662. doi: 10.1038/ismej.2007.79

Carpenter, J. H. (1965). The Chesapeake Bay Institute technique for the Winkler dissolved oxygen method. *Limnol. Oceanogr.* 10, 141–143. doi: 10.4319/lo.1965.10.1.0141

Dai, M., Gan, J., Han, A., Kung, H. S., and Yin, Z. (2014). "Physical dynamics and biogeochemistry of the Pearl River plume," in *Biogeochemical dynamics at major river-coastal interfaces, Linkages with Global Change*, eds T. Bianchi, M. Allison, and W.-J. Cai (Cambridge, NY: Cambridge University), 321–352. doi: 10.1017/cbo9781139136853.017

Dai, M., Guo, X., Zhai, W., Yuan, L., Wang, B., Wang, L., et al. (2006). Oxygen depletion in the upper reach of the Pearl River estuary during a winter drought. *Mar. Chem.* 102, 159–169. doi: 10.1016/j.marchem.2005.09.020

Dai, M., Wang, L., Guo, X., Zhai, W., Li, Q., He, B., et al. (2008). Nitrification and inorganic nitrogen distribution in a large perturbed river/estuarine system: the Pearl River Estuary. *China. Biogeosci.* 5, 1227–1244. doi: 10.5194/bg-5-1227-2008

Damashek, J., Casciotti, K. L., and Francis, C. A. (2016). Variable Nitrification Rates Across Environmental Gradients in Turbid, Nutrient-Rich Estuary Waters of San Francisco Bay. *Estuar. Coasts* 39, 1050–1071. doi: 10.1007/s12237-016-0071-7

De La Torre, J. R., Walker, C. B., Ingalls, A. E., Könneke, M., and Stahl, D. A. (2008). Cultivation of a thermophilic ammonia oxidizing archaeon synthesizing crenarchaeol. *Environ. Microbiol.* 10, 810–818. doi: 10.1111/j.1462-2920.2007.01506.x

Frame, C. H., Lau, E., Joseph Nolan, E. IV, Goepfert, T. J., and Lehmann, M. F. (2017). Acidification Enhances Hybrid N_2O Production Associated with Aquatic Ammonia-Oxidizing Microorganisms. *Front. Microbiol.* 7:104. doi: 10.3389/fmicb.2016.02104

Francis, C. A., Roberts, K. J., Beman, J. M., Santoro, A. E., and Oakley, B. B. (2005). Ubiquity and diversity of ammonia-oxidizing archaea in water columns and sediments of the ocean. *Proc. Natl. Acad. Sci. U.S.A.* 102, 14683–14688. doi: 10.1073/pnas.0506625102

Gantner, S., Andersson, A. F., Alonso-Sáez, L., and Bertilsson, S. (2011). Novel primers for 16S rRNA-based archaeal community analyses in environmental samples. *J. Microbiol. Methods* 84, 12–18. doi: 10.1016/j.mimet.2010.10.001

Han, A., Dai, M., Kao, S.-J., Gan, J., Li, Q., Wang, L., et al. (2012). Nutrient dynamics and biological consumption in a large continental shelf system under the influence of both a river plume and coastal upwelling. *Limnol. Oceanogr.* 57, 486–502. doi: 10.4319/lo.2012.57.2.0486

Harrison, P. J., Yin, K., Lee, J. H. W., Gan, J., and Liu, H. (2008). Physical–biological coupling in the Pearl River estuary. *Continent. Shelf Res.* 28, 1405–1415. doi: 10.1016/j.csr.2007.02.011

Hatzenpichler, R., Lebedeva, E. V., Spieck, E., Stoecker, K., Richter, A., Daims, H., et al. (2008). A moderately thermophilic ammonia-oxidizing crenarchaeote from a hot spring. *Proc. Natl. Acad. Sci. U.S.A.* 105, 2134–2139. doi: 10.1073/pnas.0708857105

He, B., Dai, M., Zhai, W., Guo, X., and Wang, L. (2014). Hypoxia in the upper reaches of the Pearl River Estuary and its maintenance mechanisms: A synthesis based on multiple year observations during 2000-2008. *Mar. Chem.* 167, 13–24. doi: 10.1016/j marchem.2014.07.003

Holmes, A. J., Costello, A., Lidstrom, M. E., and Murrell, J. C. (1995). Evidence that particulate methane monooxygenase and ammonia monooxygenase may be evolutionarily related. *FEMS Microbiol. Lett.* 132, 203–208. doi: 10.1111/j.1574-6968.1995.tb07834.x

Holt, J. G., Krieg, N. R., Sneath, P. H. A., Staley, J. T., and Williams, S. T. (eds) (1994). *Bergey's manual of determinative bacteriology*, 9th Edn. Maryland: Williams and Wilkins.

Hou, L., Xie, X., Wan, X., Kao, S. J., Jiao, N., and Zhang, Y. (2018). Niche differentiation of ammonia and nitrite oxidizers along a salinity gradient from the Pearl River estuary to the South China Sea. *Biogeosciences* 15, 5169–5187. doi: 10.5194/bg-2018-189

Hu, X. P., and Cai, W. J. (2011). An assessment of ocean margin anaerobic processes on oceanic alkalinity budget. *Glob. Biogeochem. Cycles* 25:GB3003. doi: 10.1029/2.10GB003859

Jin, T., Zhang, T., Ye, L., Lee, O. O., Wong, Y. H., and Qian, P. Y. (2011). Diversity and quantity of ammonia-oxidizing archaea and bacteria in sediment of the Pearl River Estuary. *China. Appl. Microbiol. Biotechnol.* 90, 1137–1145. doi: 10.1007/s00253-011-3107-8

Jung, M.-Y., Park, S.-J., Min, D., Kim, J.-S., Rijpstra, W. I. C., Sinninghe Damsté, J. S., et al. (2011). Enrichment and Characterization of an Autotrophic Ammonia-Oxidizing Archaeon of Mesophilic Crenarchaeal Group I.1a from an Agricultural Soil. *Appl. Environ. Microbiol.* 77, 8635–8647. doi: 10.1128/AEM.05787-11

Karner, M. B., DeLong, E. F., and Karl, D. M. (2001). Archaeal dominance in the mesopelagic zone of the Pacific Ocean. *Nature* 409, 507–510. doi: 10.1038/35054051

Kits, K. D., Sedlacek, C. J., Lebedeva, E. V., Han, P., Bulaev, A., Pjevac, P., et al. (2017). Kinetic analysis of a complete nitrifier reveals an oligotrophic lifestyle. *Nature* 549, 269–272. doi: 10.1038/nature23679

Könneke, M., Bernhard, A. E., de la Torre, J. R., Walker, C. B., Waterbury, J. B., and Stahl, D. A. (2005). Isolation of an autotrophic ammonia-oxidizing marine archaeon. *Nature* 437, 543–546. doi: 10.1038/nature03911

Kroeze, C., Dumont, E., and Seitzinger, S. (2010). Future trends in emissions of N_2O from rivers and estuaries. *J. Integr. Environ. Sci.* 7, 71–78. doi: 10.1080/1943815X.2010.496789

Lam, P., Lavik, G., Jensen, M. M., van de Vossenberg, J., Schmid, M., Woebken, D., et al. (2009). Revising the nitrogen cycle in the Peruvian oxygen minimum zone. *Proc. Natl. Acad. Sci. U.S.A.* 106, 4752–4757. doi: 10.1073/pnas.0812444106

Lehtovirta-Morley, L. E., Stoecker, K., Vilcinskas, A., Prossera, J. I., and Nicol, G. W. (2011). Cultivation of an obligate acidophilic ammonia oxidizer from a nitrifying acid soil. *Proc. Natl. Acad. Sci. U.S.A.* 108, 15892–15897. doi: 10.1073/pnas.1107196108

Leininger, S., Urich, T., Schloter, M., Schwark, L., Qi, J., Nicol, G. W., et al. (2006). Archaea predominate among ammonia-oxidizing prokaryotes in Soils. *Nature* 442, 806–809. doi: 10.1038/nature04983

Lin, H., Dai, M., Kao, S.-J., Wang, L., Roberts, E., Yang, J.-Y. T., et al. (2016). Spatiotemporal variability of nitrous oxide in a large eutrophic estuarine system: The Pearl River Estuary, China. *Mar. Chem.* 182, 14–24. doi: 10.1016/j.marchem.2016.03.005

Löscher, C. R., Kock, A., Könneke, M., LaRoche, J., Bange, H. W., and Schmitz, R. A. (2012). Production of oceanic nitrous oxide by ammonia-oxidizing archaea. *Biogeosciences* 9, 2419–2429. doi: 10.5194/bg-9-2419-2012

Ma, L., Lin, H., Xie, X., Dai, M., and Zhang, Y. (2019). Major role of ammonia oxidizing bacteria in N_2O production in the Pearl River estuary. *Biogeosciences* 16, 4765–4781. doi: 10.5194/bg-16-4765-2019

Magalhães, C., Bano, N., Wiebe, W. J., Bordalo, A. A., and Hollibaugh, J. T. (2008). Dynamics of nitrous oxide reductase genes (*nosZ*) in intertidal rocky biofilms and sediments of the Douro River Estuary (Portugal), and their relation to N-biogeochemistry. *Microbial. Ecol.* 55, 259–269. doi: 10.1007/s00248-007-9273-7

Martens-Habbena, W., Berube, P. M., Urakawa, H., de la Torre, J. R., and Stahl, D. A. (2009). Ammonia oxidation kinetics determine niche separation of nitrifying Archaea and Bacteria. *Nature* 461, 976–979. doi: 10.1038/nature08465

Mortazavi, B., Iverson, R. L., Huang, W., Graham Lewis, F., and Caffrey, J. M. (2000). Nitrogen budget of Apalachicola Bay, a bar-built estuary in the

northeastern Gulf of Mexico. *Mar. Ecol. Progr. Ser.* 195, 1–14. doi: 10.3354/meps195001

Mosier, A. C., and Francis, C. A. (2008). Relative abundance and diversity of ammoniaoxidizing archaea and bacteria in the San Francisco Bay estuary. *Environ. Microbiol.* 10, 3002–3016. doi: 10.1111/j.1462-2920.2008.01764.x

Pai, S.-C., Tsau, Y.-J., and Yang, T.-I. (2001). pH and buffering capacity problems involved in the determination of ammonia in saline water using the indophenol blue spectrophotometric method. *Analyt. Chim. Acta* 434, 209–216. doi: 10.1016/S0003-2670(01)00851-0

Pike, N. (2011). Using false discovery rates for multiple comparisons in ecology and evolution. *Methods Ecol. Evolut.* 2, 278–282. doi: 10.1111/j.2041-210X.2010.00061.x

Qian, W., Gan, J., Liu, J., He, B., Lu, Z., Guo, X., et al. (2018). Current status of emerging hypoxia in a eutrophic estuary: The lower reach of the Pearl River Estuary, China. *Estuarine* 205, 58–67. doi: 10.1016/j.ecss.2018.03.004

Rotthauwe, J. H., Witzel, K. P., and Liesack, W. (1997). The ammonia monooxygenase structural gene *amo*A as a functional marker: Molecular fine-scale analysis of natural ammonia-oxidizing populations. *Appl. Environ. Microbiol.* 63, 4704–4712. doi: 10.1128/aem.63.12.4704-4712.1997

Sadyś, M., Strzelczak, A., Grinn-Gofroń, A., Kennedy, and Roy. (2014). Application of redundancy analysis for aerobiological data. *Int. J. Biometeorol.* 59, 25–36. doi: 10.1007/s00484-014-0818-4

Sahan, E., and Muyzer, G. (2008). Diversity and spatio-temporal distribution of ammoniaoxidizing archaea and bacteria in sediments of the Westerschelde estuary. *FEMS Microbiol. Ecol.* 64, 175–186. doi: 10.1111/j.1574-6941.2008.00462.x

Santoro, A. E., Buchwald, C., McIlvin, M. R., and Casciotti, K. L. (2011). Isotopic Signature of N_2O Produced by Marine Ammonia-Oxidizing Archaea. *Science* 333, 1282–1285. doi: 10.1126/science.1208239

Santoro, A. E., Francis, C. A., de Sieyes, N. R., and Boehm, A. B. (2008). Shifts in the relative abundance of ammonia-oxidizing bacteria and archaea across physicochemical gradients in a subterranean estuary. *Environ. Microbiol.* 10, 1068–1079. doi: 10.1111/j.1462-2920.2007.01547.x

Seitzinger, S. P., and Kroeze, C. (1998). Global distribution of nitrous oxide production and N inputs in freshwater and coastal marine ecosystems. *Global Biogeochem. Cycles* 12, 93–113. doi: 10.1029/97GB03657

Stein, L. Y. (2011). Surveying N_2O-Producing Pathways in Bacteria. *Methods Enzymol.* 486, 131–152. doi: 10.1016/B978-0-12-381294-0.00006-7

Su, J., Dai, M., He, B., Wang, L., Gan, J., Guo, X., et al. (2017). Tracing the origin of the oxygen-consuming organic matter in the hypoxic zone in a large eutrophic estuary: the lower reach of the Pearl River Estuary. *China. Biogeosci.* 14, 4085–4099. doi: 10.5194/bg-14-4085-2017

Sun, D., Tang, X., Zhao, M., Zhang, Z., Hou, L., Liu, M., et al. (2020). Distribution and diversity of comammox *Nitrospira* in coastal wetlands of China. *Front. Microbiol.* 11:589268. doi: 10.3389/fmicb.2020.589268

Sun, W., Xia, C., Xu, M., Guo, J., Sun, G., and Wang, A. (2014). Community structure and distribution of planktonic ammonia-oxidizing archaea and bacteria in the Dongjiang River. *China. Res. Microbiol.* 165, 657–670. doi: 10.1016/j.resmic.2014.08.003

Suzuki, M. T., Taylor, L. T., and DeLong, E. F. (2000). Quantitative Analysis of Small-Subunit rRNA Genes in Mixed Microbial Populations via 5'-Nuclease Assays. *Appl. Environ. Microbiol.* 66, 4605–4614. doi: 10.1128/AEM.66.11.4605-4614.2000

Tan, S., Cheung, S., Ho, T. Y., and Liu, H. B. (2019). Metatranscriptomics of the bacterial community in response to atmospheric deposition in the Western North Pacific Ocean. *Mar. Genom.* 45, 57–63. doi: 10.1016/j.margen.2019.01.008

Tourna, M., Stieglmeier, M., Spang, A., Könneke, M., Schintlmeister, A., Urich, T., et al. (2011). *Nitrososphaera viennensis*, an ammonia oxidizing archaeon from soil. *Proc. Natl. Acad. Sci. U.S.A.* 108, 8420–8425. doi: 10.2307/25830066

Usui, T., Koike, I., and Ogura, N. (2001). N_2O production, nitrification and denitrification in an estuarine sediment. *Estuarine* 52, 769–781. doi: 10.1006/ecss.2000.0765

Ward, B. B. (2008). "Nitrification in marine systems," in *Nitrogen in the Marine Environment*, 2nd Edn, eds D. G. Capone, D. A. Bronk, M. R. Mulholl, and E. J. Carpenter (Burlington: Academic Press), 199–261. doi: 10.1016/b978-0-12-372522-6.00005-0

Ward, B. B., Eveillard, D., Kirshtein, J. D., Nelson, J. D., Voytek, M. A., and Jackson, G. A. (2007). Ammonia-oxidizing bacterial community composition in estuarine and oceanic environments assessed using a functional gene microarray. *Environ. Microbiol.* 9, 2522–2538. doi: 10.1111/j.1462-2920.2007.01371.x

Wuchter, C., Abbas, B., Coolen, M. J. L., Herfort, L., van Bleijswijk, J., Timmers, P., et al. (2006). Archaeal nitrification in the ocean. *Proc. Natl. Acad. Sci. U.S.A.* 103, 12317–12322. doi: 10.1073/pnas.0600756103

Xia, X., Guo, W., and Liu, H. (2015). Dynamics of the bacterial and archaeal communities in the Northern South China Sea revealed by 454 pyrosequencing of the 16S rRNA gene. *Top. Stud. Oceanogr.* 117, 97–107. doi: 10.1016/j.dsr2.2015.05.016

Yu, C., Hou, L., Zheng, Y., Liu, M., Yin, G., Gao, J., et al. (2018). Evidence for complete nitrification in enrichment culture of tidal sediments and diversity analysis of clade a comammox *Nitrospira* in natural environments. *Appl. Microbiol. Biotechnol.* 102, 9363–9377. doi: 10.1007/s00253-018-9274-0

Zhang, Y., Qin, W., Hou, L., Zakem, E. J., Wan, X., Zhao, Z., et al. (2020). Nitrifier adaptation to low energy flux controls inventory of reduced nitrogen in the dark ocean. *Proc. Natl. Acad. Sci. U.S.A.* 117, 4823–4830. doi: 10.1073/pnas.1912367117

Zhang, Y., Xie, X., Jiao, N., Hsiao, S. S.-Y., and Kao, S.-J. (2014). Diversity and distribution of *amo*A-type nitrifying and *nir*S-type denitrifying microbial communities in the Yangtze River estuary. *Biogeosciences* 11, 2131–2145. doi: 10.5194/bg-11-2131-2014

Zhao, Y., Liu, J., Uthaipan, K., Song, X., Xu, Y., He, B., et al. (2020). Dynamics of inorganic carbon and pH in a large subtropical continental shelf system: Interaction between eutrophication, hypoxia, and ocean acidification. *Limnol. Oceanogr.* 65, 1359–1379. doi: 10.1002/lno.11393

Zheng, Z. Z., Zheng, L. W., Xu, M. N., Tan, E., Hutchins, D. A., Deng, W., et al. (2020). Substrate regulation leads to differential responses of microbial ammonia-oxidizing communities to ocean warming. *Nat. Commun.* 11:3511. doi: 10.1038/s41467-020-17366-3

Zou, D., Li, Y., Kao, S. J., Liu, H., and Li, M. (2019). Genomic adaptation to eutrophication of ammonia oxidizing archaea in the Pearl River estuary. *Environ. Microbiol.* 21, 2320–2332. doi: 10.1111/1462-2920.14613

Conflict of Interest: The authors declare that the research was conducted in the absence of any commercial or financial relationships that could be construed as a potential conflict of interest.

Publisher's Note: All claims expressed in this article are solely those of the authors and do not necessarily represent those of their affiliated organizations, or those of the publisher, the editors and the reviewers. Any product that may be evaluated in this article, or claim that may be made by its manufacturer, is not guaranteed or endorsed by the publisher.

Copyright © 2021 Ma, Tan, Liu, Kao, Dai and Yang. This is an open-access article distributed under the terms of the Creative Commons Attribution License (CC BY). The use, distribution or reproduction in other forums is permitted, provided the original author(s) and the copyright owner(s) are credited and that the original publication in this journal is cited, in accordance with accepted academic practice. No use, distribution or reproduction is permitted which does not comply with these terms.

frontiers in Marine Science

ORIGINAL RESEARCH
published: 25 February 2021
doi: 10.3389/fmars.2021.624322

Deoxygenation in Marginal Seas of the Indian Ocean

S. Wajih A. Naqvi†*

Council of Scientific & Industrial Research, New Delhi, India

This article describes oxygen distributions and recent deoxygenation trends in three marginal seas – Persian Gulf and Red Sea in the Northwestern Indian Ocean (NWIO) and Andaman Sea in the Northeastern Indian Ocean (NEIO). Vertically mixed water column in the shallow Persian Gulf is generally well-oxygenated, especially in winter. Biogeochemistry and ecosystems of Persian Gulf are being subjected to enormous anthropogenic stresses including large loading of nutrients and organic matter, enhancing oxygen demand and causing hypoxia (oxygen < 1.4 ml l^{-1}) in central and southern Gulf in summer. The larger and deeper Red Sea is relatively less affected by human activities. Despite its deep water having remarkably uniform thermohaline characteristics, the central and southern Red Sea has a well-developed perennial oxygen minimum at mid-depths. The available data point to ongoing deoxygenation in the northern Red Sea. Model simulations show that an amplified warming in the marginal seas of the NWIO may cause an intensification of the Arabian Sea oxygen minimum zone (OMZ). Increases in particulate organic carbon and decreases in oxygen contents of the outflows may also have a similar effect. In the Andaman Sea, waters above the sill depth (∼1.4 km) have characteristics similar to those in the Bay of Bengal, including an intense OMZ. As in the case of the Bay of Bengal, oxygen concentrations within the Andaman Sea OMZ appear to have declined slightly but significantly between early 1960s and 1995. The exceedingly isothermal and isohaline water that fills the deep Andaman Basin is also remarkably homogenous in terms of its oxygen content. A very slight but statistically significant decrease in oxygen content of this water also seems to have occurred over three decades preceding 1995. New information is badly needed to assess the extent of further change that may have occurred over the past 25 years. There have been some reports of coastal "dead zones" having developed in the Indian Ocean marginal seas, but they are probably under-reported and the effects of hypoxia on the rich and diverse tropical ecosystems – coral reefs, seagrasses, and mangroves – in these seas remain to be investigated.

Keywords: deoxygenation, Indian Ocean, Red Sea, Persian Gulf, Andaman Sea, marginal seas

OPEN ACCESS

Edited by:
Xianghui Guo,
Xiamen University, China

Reviewed by:
Tim Rixen,
Leibniz Centre for Tropical Marine Research (LG), Germany
Birgit Gaye,
University of Hamburg, Germany

***Correspondence:**
S. Wajih A. Naqvi
wnaqvi@iitk.ac.in

†*Present address:*
S. Wajih A. Naqvi,
Department of Earth Sciences, Indian Institute of Technology, Kanpur, India

Specialty section:
This article was submitted to Marine Biogeochemistry, a section of the journal Frontiers in Marine Science

Received: *31 October 2020*
Accepted: *21 January 2021*
Published: *25 February 2021*

Citation:
Naqvi SWA (2021) Deoxygenation in Marginal Seas of the Indian Ocean. Front. Mar. Sci. 8:624322. doi: 10.3389/fmars.2021.624322

INTRODUCTION

The northern Indian Ocean is distinguished by several unusual oceanographic processes arising from its unique geographical setting. The presence of landmass that limits the Indian Ocean at rather low latitudes (∼25°N) has a profound impact on its climate in the form of seasonally reversing winds – the monsoons. Regional geomorphology dominantly controls climate dynamics,

particularly the distribution of monsoonal energy and rainfall, and the resultant variability of oceanographic processes. The contribution of orography (especially the presence of the Himalayas, Western Ghats, and East African Highlands) is crucial in this regard (e.g., Chakraborty et al., 2002). Also important is the eastward sloping of the Deccan Peninsula and the Ganges Basin (east of the Delhi Ridge) as a result of which most South Asian rivers flow into the Bay of Bengal (the Northeastern Indian Ocean, NEIO) and not into the Arabian Sea (the Northwestern Indian Ocean, NWIO). This creates a fresher, warmer surface layer and a very strong thermohaline stratification in the NEIO (Naqvi et al., 2006). Moreover, winds are generally weaker in the NEIO than in the NWIO, which in conjunction with the strong stratification prevents large-scale upwelling of cold subsurface waters, even along the eastern boundary (e.g., off Myanmar – Naqvi et al., 2006). Together these processes create favorable conditions for large-scale deep convection in the atmosphere, providing positive feedback to rainfall (Shenoi et al., 2002), which is quite high in the NEIO. Consequently, the NEIO is a region of highly positive water balance (large excess of precipitation and runoff over evaporation). The situation is quite different in most of the NWIO, where strong southwesterly winds drive intense and large-scale upwelling (Naqvi et al., 2006), resulting in low sea surface temperatures (SSTs) during summer in the western Arabian Sea, greatly contributing to regional aridity. The freshwater runoff is very modest and the rainfall is scanty except along the west coast of India. As a result, except for a narrow belt in the eastern Arabian Sea, evaporation far exceeds precipitation and runoff (Prasad, 2004). The contrasting climatic and hydrographic conditions in the NWEO and NWIO are also reflected in oceanographic characteristics of the marginal seas, as described below.

Of the three marginal seas of the Indian Ocean, two (the Red Sea and Persian Gulf) are connected to the NWIO, while the third (the Andaman Sea) forms a part of the NEIO (**Figure 1**). The Mediterranean-type marginal seas of the NWIO have been fairly well investigated (Morcos, 1970; Grasshoff, 1975, 1976; Brewer and Dyrssen, 1985; Yao et al., 2014a,b; Al-Yamani and Naqvi, 2019). In comparison, oceanographic processes of the Andaman Sea are not so well known (Sen Gupta et al., 1981; Sarma and Narvekar, 2001; Jithin and Francis, 2020). All three marginal seas are connected to open ocean basins having some of the most intense mesopelagic oxygen minimum zones (OMZs) of the world oceans, although the redox status of these OMZs are quite different (Rao et al., 1994; Naqvi et al., 2006; Bristow et al., 2017). Utilizing historical and the most recent data available in public domain (**Table 1**), the present study investigates distributions of dissolved oxygen and current trends of deoxygenation in these basins.

STUDY AREAS

Geological and Geographical Settings

The marginal seas of the NWIO were formed as a result of tectonic movement of the Arabian Plate. The Arabian Plate began separating from the African Plate during the late Oligocene, ∼25 million years before present (Ma) (Stern and Johnson, 2010), creating the Red Sea, and as the Arabian Plate collided with the Eurasian Plate, the Persian Gulf was formed during the early Miocene (23–16 Ma) (Allen et al., 2004). The two basins are quite different in terms of the geomorphology. The Red Sea is ∼1,930 km long, extending in the SSE-NNW direction from the Strait of Bab-el-Mandeb (latitude 12.58°N, longitude 43.33°E) up to latitude ∼28°N, where it bifurcates into the Gulf of Suez and the Gulf of Aqaba. It is on an average ∼280 km wide, and measures ∼438,000 km^2 in area (Morcos, 1970). Much of the Red Sea is comprised of shallow shelves, but the central axial trough is quite deep, reaching a maximum depth of ∼3,000 m; the average depth is 491 m (Morcos, 1970). The Red Sea is a silled basin connected to the Gulf of Aden through the Strait of Bab-el-Mandeb where the maximum depth is 160 m according to Sofianos and Johns (2007) and 137 m according to Lambeck et al. (2011).

Like the Red Sea, the Persian Gulf is also almost completely land-locked, having only a narrow connection to the Arabian Sea through the Gulf of Oman at the Hormuz Strait (latitude 26.6°N, longitude 56.25°E); however, unlike the Bab-el-Mandeb the Hormuz Strait does not have a sill. The Persian Gulf is bounded in the northwest by the Tigris-Euphrates Delta at ∼30°N latitude, in the east by Iran and in the west by the Arabian Peninsula. The Persian Gulf basin is wedge-shaped. It is about 1,000 km long, but with a maximum width of 336 km, the total area of the Persian Gulf is only 251,000 km^2 (Sheppard et al., 2010). With reference to the main axis the bottom topography of the Persian Gulf is highly asymmetrical with a steep slope on the Iranian side and a very gentle slope on the Arabian side. Thus, the deepest part of the Persian Gulf is off the Iranian coast, but even here the water depth does not exceed ∼90 m. The average depth of the Persian Gulf is only 36 m, and so, in spite of a fairly large area, the total volume of the Persian Gulf is only ∼8,600 km^3 (Sheppard et al., 2010) about 1/27 of the volume of the Red Sea (∼233,000 km^3) (Morcos, 1970).

The Andaman Sea extends ∼1,250 km from Myanmar to Sumatra (Indonesia). This basin was formed by the oblique converging boundaries of the Indian Oceanic Plate and South East Asian Plate, a process that started in the early Cretaceous and is still ongoing (Scaife et al., 2010). The Andaman-Nicobar island arc created during this process bounds the basin in the west. Due to the complex tectonics the bottom topography is quite rugged (Cochran, 2010). The East Basin is the largest and deepest basin of the Andaman Sea where the maximum depth exceeds 4,200 m. To the north and east of this basin lies the broad continental shelf of Myanmar and Thailand, with the Irrawaddy Delta in the north being another prominent geographical feature. The average depth of the Andaman Sea is 1,096 m.[1] However, the connection with the Bay of Bengal through the deepest saddle in the Andaman-Nicobar Ridge is only ∼1,400 m deep at the Great Passage (as determined by the divergence of vertical

[1] http://bse.sci-lib.com/article057639.html

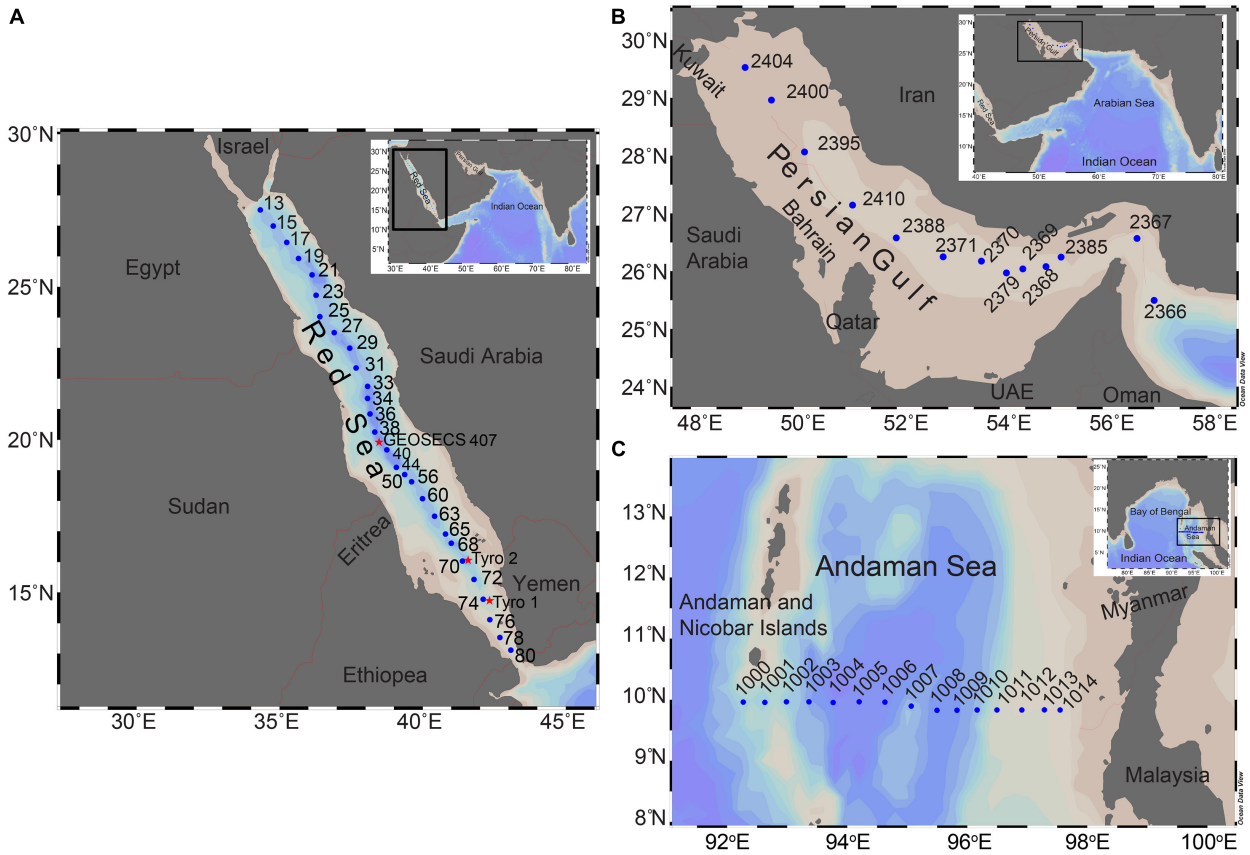


FIGURE 1 | The marginal seas of the Indian Ocean and locations of stations constituting vertical sections presented in **Figures 2**, **4**, **5**: **(A)** Red Sea, R.V. *Sagar Kanya* cruise in May 1983 (black symbols); **(B)** Persian Gulf, R.V. *Atlantis II* cruise in February 1977; and **(C)** Andaman Sea, R.V. *Knorr* cruise in October 1995. The red symbols in **(A)** denote locations of GEOSECS Station 407 and the two *Tyro* stations data from which are compared with *Sagar Kanya* data in **Figure 3**.

profiles of temperature within and just outside the Andaman Basin – Naqvi et al., 1994).

Hydrography and Oxygen Distribution

As stated above, the Red Sea and the Persian Gulf on one hand and the Andaman Sea on the other are located in contrasting climatic regimes. Moreover, unlike the Andaman Sea, the Red Sea, and the Persian Gulf are almost land locked. Evaporation rates in both basins are exceedingly high (>2 m year^{-1}) while rainfall is negligible (Sofianos et al., 2002; Sheppard et al., 2010). While the Red Sea does not receive any river runoff, some freshwater flow does occur into the Persian Gulf, although it is quite modest (35–133 km^3 year^{-1}) and restricted to the northwestern region, mainly from the Shatt al-Arab River which carries the combined flows from the Tigris, Euphrates, and Karun rivers (Sheppard et al., 2010). The resultant Mediterranean-type (anti-estuarine) exchanges (near surface inflow and near-bottom outflow) between the Red Sea and the Persian Gulf with the Gulf of Aden and Gulf of Oman, respectively, are primarily driven by the highly negative water balance. That is, in order to compensate for the net loss of water within these basins, there is inflow of fresher waters from the Gulf of Aden and the Gulf of Oman. However, these inflows also bring in salt, and in order to maintain the salt balance, there must also be export of more saline waters out of these basins. This mostly occurs close to the bottom by outflowing currents through the Straits of Bab-el-Mandeb and Hormuz. Estimates of respective inflows and outflows are ~12,620 km^3 year^{-1} and 11,680 km^3 year^{-1} for the Red Sea (Murray and Johns, 1997), and 7,250 km^3 year^{-1} and 6,620 km^3 year^{-1} for the Persian Gulf (Sheppard et al., 2010). Circulation in the Hormuz Strait is two layered: surface water from the Gulf of Oman flows in through the northern part of the strait, although a part of it re-circulates and flows out through the southern part, while the dense, high-salinity water exits the Persian Gulf close to the bottom throughout the year with little seasonal variability (Johns et al., 2003; Pous et al., 2015). A two-layer circulation also prevails in the Bab-el-Mandeb Strait for most parts of the year, but in the summer (June–September) northwesterly winds drive weak outflow at the surface while strong intrusion of Gulf of Aden Intermediate Water (GAIW) occurs at mid-depth above the greatly weakened outflowing current close to the bottom (Maillard and Soliman, 1986; Murray and Johns, 1997; Sofianos et al., 2002; Sofianos and Johns, 2007; Yao et al., 2014a). The outflows from the Red Sea and the Persian Gulf, easily distinguished by prominent salinity maxima, spread widely across the NWIO with their cores located around 27.2 and

TABLE 1 | Sources of data.

Red Sea

Vessel/platform, project/program	Period	Data availability URL	Remarks/reference
R.V. *Melville* GEOSECS Indian Ocean Leg 4	December 1977	https://epic.awi.de/id/eprint/34721/1/indian-exped_geosces.pdf	Weiss et al., 1983
R.V. *Sagar Kanya* Test Trial III Cruise	May 1983	https://did.nio.org/	Sections unpublished, but data used by Naqvi et al. (1986)
R.V. *Tyro* Cruises 43 and 52 Netherlands Indian Ocean Program	May 1992, February 1993	National Centers for Environmental Information, National Oceanic and Atmospheric Administration (NOAA) https://www.nodc.noaa.gov	
Argo floats #6901573 #6901577 EURO-ARGO	September 29, 2015–February 19, 2017 September 30, 2015–December 29, 2016	http://www.ifremer.fr/co-argoFloats/float?ptfCode=6901573&lang=en\penalty-\@M http://www.ifremer.fr/co-argoFloats/float?ptfCode=6901577&lang=en	

Persian Gulf

Vessel, project/program	Period	Data availability URL	Remarks/reference
R.V. *Lesnoye* Cruise 188	September 1968	https://www.nodc.noaa.gov	Al-Said et al., 2018
R.V. *Atlantis II* Cruise 2968	February 1977	https://www.nodc.noaa.gov	Brewer et al., 1978; Brewer and Dyrssen, 1985
R.V. *Mukhtabar al-Bahr*	September–October 2000 February–March 2001		Read from: Al-Ansari et al., 2015
KISR's research boats	July 19, 2011, April 30, 2017		Al-Yamani et al., 2020; raw data provided by Faiza Al-Yamani

Andaman Sea

Vessel project/program	Period	Data availability URL	Remarks/reference
R.V. *Vityaz* Cruise 9506 International Indian Ocean Expedition (IIOE)	March 1961	https://www.nodc.noaa.gov	
U.S.S. *Serrano* Cruise 545 IIOE	November–December 1961	https://www.nodc.noaa.gov	Cast 55 data suspect; not included
U.S.S. *Serrano* Cruise 90 IIOE	March 1963	https://www.nodc.noaa.gov	
I.N.S. *Kistna* Cruise 414 IIOE	September 1963	https://www.nodc.noaa.gov	Only Cast 212 data included
R.V. *Kushi Maru* Cruise 30184 IIOE	November 1963	https://www.nodc.noaa.gov	
R.V. *Pioneer* Cruise 201 IIOE	April 1964	https://www.nodc.noaa.gov	
I.N.S. *Kistna* Cruise 409 IIOE	August 1964	https://www.nodc.noaa.gov	Only Cast 309 data included
R.V. *Knorr* Cruise 14517 World Ocean Circulation Experiment (WOCE)	October 1995	https://www.nodc.noaa.gov	Talley, 2013

26.5 σ_θ surfaces (Wyrtki, 1971). They play an important role in mesoplelagic water mass structure and biogeochemical cycling in the NWIO (Naqvi et al., 2006). Dense waters within the two seas, from which these outflows originate, are formed through cooling of high-salinity waters in winter. In the Red Sea this happens in the northern extreme of the Red Sea proper and in the Gulf of Suez and Gulf of Aqaba (Wyrtki, 1974). While the upper deep water (above ∼300 m), which is the source of the

outflow, is formed in the northern Red Sea (Cember, 1988; Yao et al., 2014b), the deeper waters are supplied by the two gulfs (Woelk and Quadfasel, 1996; Plahn et al., 2002).

Despite the very similar geographical and climatic settings there are three important depth-related hydrographic differences between the Red Sea and the Persian Gulf: (1) The Persian Gulf is far more rapidly ventilated (renewal time ∼1.2 year – Al-Said et al., 2018) than the Red Sea (renewal time 36 years according to Cember (1988), and 40–90 years according to Woelk and Quadfasel (1996); (2) water column in the Persian Gulf is, in general, vertically well mixed; and (3) seasonality is far more pronounced throughout the Persian Gulf as reflected by the very wide SST range (∼12–35°C – Al-Yamani et al., 2004; Al-Said et al., 2018).

Distributions of temperature, salinity and dissolved oxygen along the main axes of the Red Sea and the Persian Gulf are presented in **Figures 2**, **4**, respectively. While the data from the Red Sea were collected by the author on board R.V. *Sagar Kanya* in May 1983, those from the Persian Gulf were generated during a cruise of R.V. *Atlantis II* in February 1977 (Brewer et al., 1978; Brewer and Dyrssen, 1985). Despite marked seasonal changes that are known to occur, especially in the Persian Gulf, these data adequately describe main features of hydrography and spatial oxygen variability in the two seas, and highlight their depth-dependent differences.

As the *Sagar Kanya* observations were made in early summer, the effect of winter cooling could still be seen in lower SSTs and relatively weaker thermocline near the northern end of the transect, close to the formation zones of deep waters. The isothermal and isohaline character of deep water is evident from the temperature and salinity panels (**Figure 2**). The mean values (±SD) for temperature and salinity at depths ≥400 m at and south of Station 25 are 21.709 ± 0.035 and 40.569 ± 0.019°C, respectively, with a σ_θ value of ∼28.59. In fact, the deep water in the Red Sea is warmer and more saline than in any other marine basin (WOA-18[2]). Despite the remarkably uniform thermohaline characteristics, oxygen concentrations are not uniformly distributed within this layer. Instead, the Red Sea exhibits a typical mid-depth oxygen minimum observed in most other parts of the ocean (**Figure 2**). The oxygen distribution pattern is similar to that reported by Sofianos and Johns (2007), except that the minimum associated with the intruding GAIW with its core around 75 m, reported by these authors, is not seen in the *Sagar Kanya* data. This is consistent with the observations of Murray and Johns (1997) in terms of the timing of initiation of the GAIW intrusion. Subsurface oxygen concentrations generally decrease southward from the source regions of deep water, but the distribution is somewhat patchy, arising from the complex balance between supply and consumption. One would expect respiration, fuelled by organic matter exported from the euphotic zone, to be important in controlling the intensity of the oxygen minimum. Going by the chlorophyll distribution, the southern extreme of the Red Sea is more productive than the central and northern parts (Brewin et al., 2015), and as it is also most downstream of the deep water flow, the oxygen minimum is expected to be the most intense in the southern Red Sea. Such is not exactly the case. However, it must be pointed out that the deep central axis of the Red Sea is a relatively narrow and elongated feature (**Figure 1A**). In such a system benthic processes are expected to substantially influence water column characteristics through lateral exchanges/mixing, and this might contribute to the observed slight deviation of oxygen distribution from the expected trend. Moreover, the presence of eddies (Sofianos and Johns, 2003, 2007; Yao et al., 2014b) might also cause the observed patchiness.

In order to check the representativeness of the *Sagar Kanya* data, oxygen profiles from three selected *Sagar Kanya* stations are compared in **Figure 3** with those from nearby sites sampled on other cruises (SK Station 40 with GEOSECS 407, sampled on board R.V. *Melville* on December 22, 1977; SK Stations 70 and 74 with two stations sampled on board R.V. *Tyro* during the Netherlands Indian Ocean Program on February 03, 1993 and May 27, 1992, respectively). Although sampled over 5 years apart and in different seasons, the GEOSECS 407 and SK Station 40 profiles are remarkably similar. The *Sagar Kanya* data also compare well with the *Tyro* data collected 9 years later, indicating that oxygen distribution seen in **Figure 2** is typical of the Red Sea.

Observations in the Persian Gulf (**Figure 4**) show weak or no thermal stratification. This is because of low atmospheric temperatures and shallow depths ensure vertical mixing throughout the water column. However, the density does increase with depth. As the Persian Gulf basin is not separated by a sill, the Gulf Deep Water formed along the coasts of Kuwait and UAE is not topographically confined. The highest densities (σ_θ reaching up to 29.856) occurred off UAE on this cruise. In comparison the maximum σ_θ value off Kuwait was 29.36 (winter-time density has increased greatly off Kuwait in recent years – Al-Said et al., 2018). The highest density in the deepest part of the Persian Gulf in the south was slightly lower (σ_θ 29.159 at 76 m at Station 2368), but the near-bottom densities were quite variable (σ_θ 28.388–29.36 north of Station 2385) along the transect. However, as in the case of the Red Sea Outflow, the density of water that flows out of the Persian Gulf and spreads into the Gulf of Aden and then in the Arabian Sea is much lower (σ_θ 26.5 – Wyrtki, 1971), reflecting modification of this watermass through mixing in the Hormuz Strait region (Swift and Bower, 2003). Considering the above-mentioned estimates of the volumes of water within the Persian Gulf and of the outflows and inflows, the flushing time of Persian Gulf is just over 1 year (Al-Said et al., 2018), and this is reflected by the well-oxygenated conditions prevailing in the water column. There is one other data set with basin-wide oxygen measurements made on a cruise of F.S. *Meteor* in the Persian Gulf slightly later in the year (March–April 1965), that shows similar distribution pattern (Grasshoff, 1976). Oxygen concentrations below 70% saturation at mid depths in the southern Gulf were observed on this occasion. At one station located in the central Gulf off Iran, however, a single near-bottom sample had 1.84 ml l^{-1} O_2 (82.11 μM), ∼36% of the saturation value; at two other nearby stations the observed oxygen depletion was more moderate (<80%). Later, in September 1986, minimum oxygen concentrations ranging between 1.2 and 2.0 ml l^{-1} (53.55–89.25 μM) were measured

[2]https://www.nodc.noaa.gov/OC5/woa18/

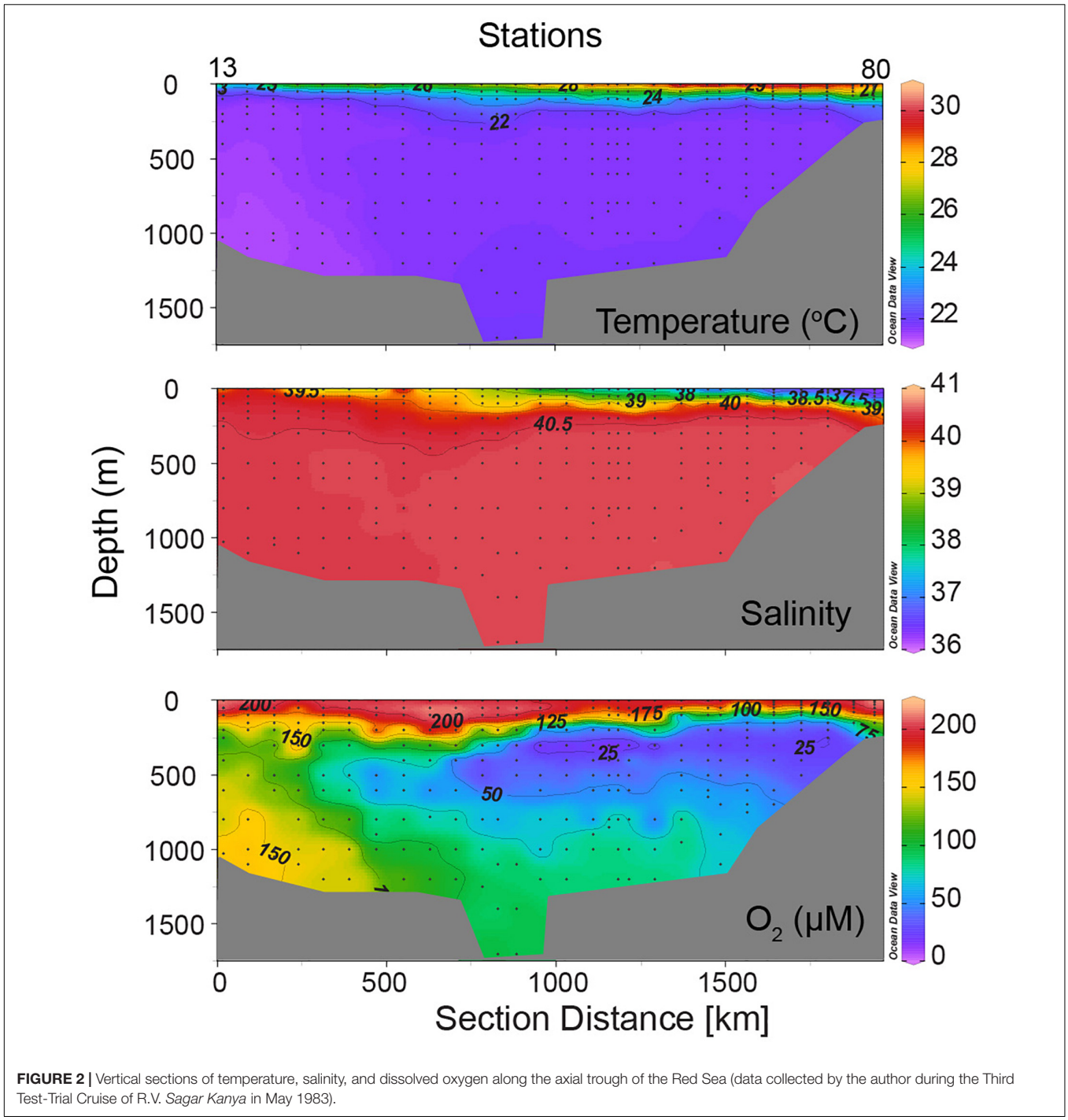


FIGURE 2 | Vertical sections of temperature, salinity, and dissolved oxygen along the axial trough of the Red Sea (data collected by the author during the Third Test-Trial Cruise of R.V. *Sagar Kanya* in May 1983).

during a cruise of R.V. *Mukhtabar al-Bahr* in the southeastern Gulf (El Samra and El Gindy, 1990), and Hashimoto et al. (1998) found even lower oxygen concentrations during the cruise of R.V. *Umitaka-Maru* – 1.12 ml l^{-1} (49.98 µM) in December 1993 and 1.00 ml l^{-1} (44.62 µM) – in December 1994. Unfortunately, other than the observations to be described later that were made on board the Russian Research Vessel *Lesnoye* in the summer of 1968, there are no basin-wide oxygen data in the global data base from the Persian Gulf for peak summer.

The hydrography of the Andaman Sea is greatly influenced by (a) large runoff from the Irrawaddy River that, like other parts of the NEIO, creates a low-salinity surface layer resulting in strong thermohaline stratification (Naqvi et al., 2006), and (b) the isolation of deep waters by the Andaman-Nicobar Ridge below the sill depth (~1,400 m). As a result, the deep and bottom waters cannot flow into the Andaman Basin, and the water throughout the basin below the sill depth is derived from the Bay of Bengal from the sill depth, and so the thermohaline characteristics of

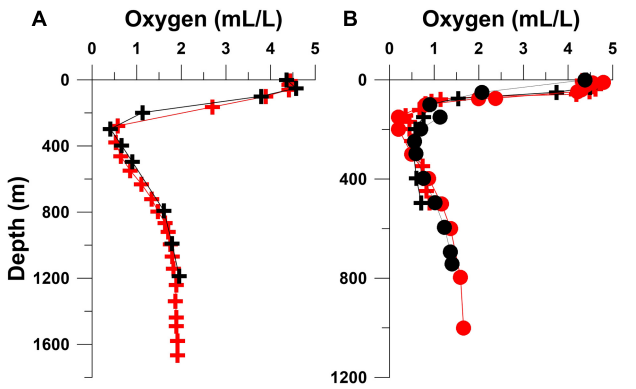


FIGURE 3 | Comparison of oxygen profiles from selected *Sagar Kanya* (SK) stations with those from nearby stations occupied during other cruises: **(A)** SK Station 40 (black crosses) sampled on May 24, 1983 with GEOSECS Station 407 (red crosses) sampled on December 22, 1977; **(B)** SK Station 70 (black circles) sampled on May 29, 1983 with *Tyro* Station 1 (red circles) sampled on May 27, 1992, and SK Station 74 sampled on May 29, 1983 (black crosses) with *Tyro* Station 2 (red crosses) sampled on February 03, 1993. See **Figure 1** for station locations.

water at depths exceeding 2 km are extraordinarily homogenous. Observations along a zonal (∼10°N) transect in the Andaman Sea made during a cruise of R.V. *Knorr* in October 1995 (**Figure 5**) show a potential temperature range of 4.693–4.761 (mean ± SD = 4.73 ± 0.014), and a salinity range of 34.854–34.861 (mean ± SD = 34.860 ± 0.001) with a highly invariable σ_θ of 27.595 ± 0.001. Just outside the Andaman Sea in the Bay of Bengal this density surface is found at ∼1.4 km, and so this should be the sill depth at the Great Passage.

It has been proposed recently that the rate of tide-induced vertical mixing in deep waters of the Andaman Sea is about two-orders of magnitude higher than that in the Bay of Bengal and that this may contribute to downward diffusion of heat in the Andaman Sea, in part accounting for the high deep-water temperature (Jithin and Francis, 2020). However, it must be pointed out that the greatly enhanced vertical mixing is by itself a consequence of the lack of vertical stratification below the sill depth in the Andaman Sea, thereby making the proposed mechanism secondary.

The strong thermohaline stratification resulting from freshwater runoff by the Irrawaddy is seen in **Figure 5**, which also shows the absence of upwelling over the shelf in the eastern Andaman Sea, typical of the eastern boundaries of the Pacific and Atlantic Oceans at comparable latitudes. The regional OMZ of the NEIO is present below the pycnocline, but unlike the eastern boundaries of the North and South Pacific and South Atlantic where oxygen concentrations within the OMZ often fall below the detection limit of even the highly sensitive STOX oxygen sensors accompanied by the accumulation of nitrite indicating microbial reduction of nitrate (e.g., Thamdrup et al., 2012), such "functional anoxia" does not occur in the Andaman Sea. In fact, the minimum recorded oxygen concentration was slightly lower (15.6 μM O_2 at 149 m, Station 1000) at the eastern end of the transect (close to the Ten-Degree Channel) than that measured over the Myanmar-Thailand shelf (22.9 μM at 217 m, Station 1013). What prevents the OMZ of the NEIO from turning fully anoxic (supporting vigorous reductive loss of combined nitrogen) is still not fully understood (Rao et al., 1994; Bristow et al., 2017). One possible explanation is that ballast provided by the terrigenous mineral particles rapidly removes particulate organic matter from the water column to the seafloor with little pelagic degradation (Ittekkot et al., 1992; Rao et al., 1994; Naqvi et al., 1996; Rixen et al., 2019). Anomalous near-bottom anomalies in oxygen and nutrients in the Bay of Bengal (Broecker et al., 1980; Mantyla and Reid, 1995) have been taken as a proof of relatively fresh organic matter reaching the seafloor in the NEIO. Consequently, one should expect significant oxygen depletion in the deep Andaman Basin. Clearly, such is not the case. The remarkably uniform oxygen concentrations (77.9–80.67 μM, mean ± SD = 79.06 ± 0.69 at depths >2 km along the *Knorr* section) are intriguing. These are consistent with the observations of Naqvi et al. (1994) who reported the apparent oxygen utilization (AOU) at depths >1.3 km in the Andaman Sea (239 ± 2 μM) to be the same as the AOU at 1.3 km just outside the Andaman Sea in the Bay of Bengal, leading them to conclude that the renewal of deep waters in the Andaman Sea is rapid, with minimal chemical changes occurring during the residence of water below the sill depth.

RECENT DEOXYGENATION TRENDS IN OFFSHORE WATERS

In this section, the most recent oxygen data from the three marginal seas are compared with reliable historical data available in the global data base to extract trends of the ongoing deoxygenation. All but one of the data sets used here were generated following the classical Winkler procedure, the principle of which has remained essentially unchanged since its introduction in the late 19th century (Winkler, 1888). Modified applications of this technique for seawater dissolved oxygen measurements since the 1960s claim an accuracy of 0.1% (Carpenter, 1965). While earlier Winkler titrations involved manual titrations with visual end-point detection using starch as the indicator, automated titrations are increasingly being used in recent times. The two techniques give very similar results except when oxygen levels approach zero, and manual titrations yield somewhat higher values (by ∼0.04 ml l^{-1}, 1.8 μM – Banse et al., 2014). Only one data set used here, viz. from the 1995 *Knorr* cruise in the Andaman Sea was obtained with the automated measurements. The Argo float data, used in the case of Red Sea, are relatively less accurate, but with the existing protocol for oxygen optode calibration and correction of any drift the accuracy of float data is still within 1% (Bettig and Körtzinger, 2015). The shifts in oxygen levels being reported here are well beyond these uncertainties.

Red Sea

There is a dearth of recent information from the Red Sea in the available global databases to assess the ongoing deoxygenation trends in the region, except for the high-density profiles

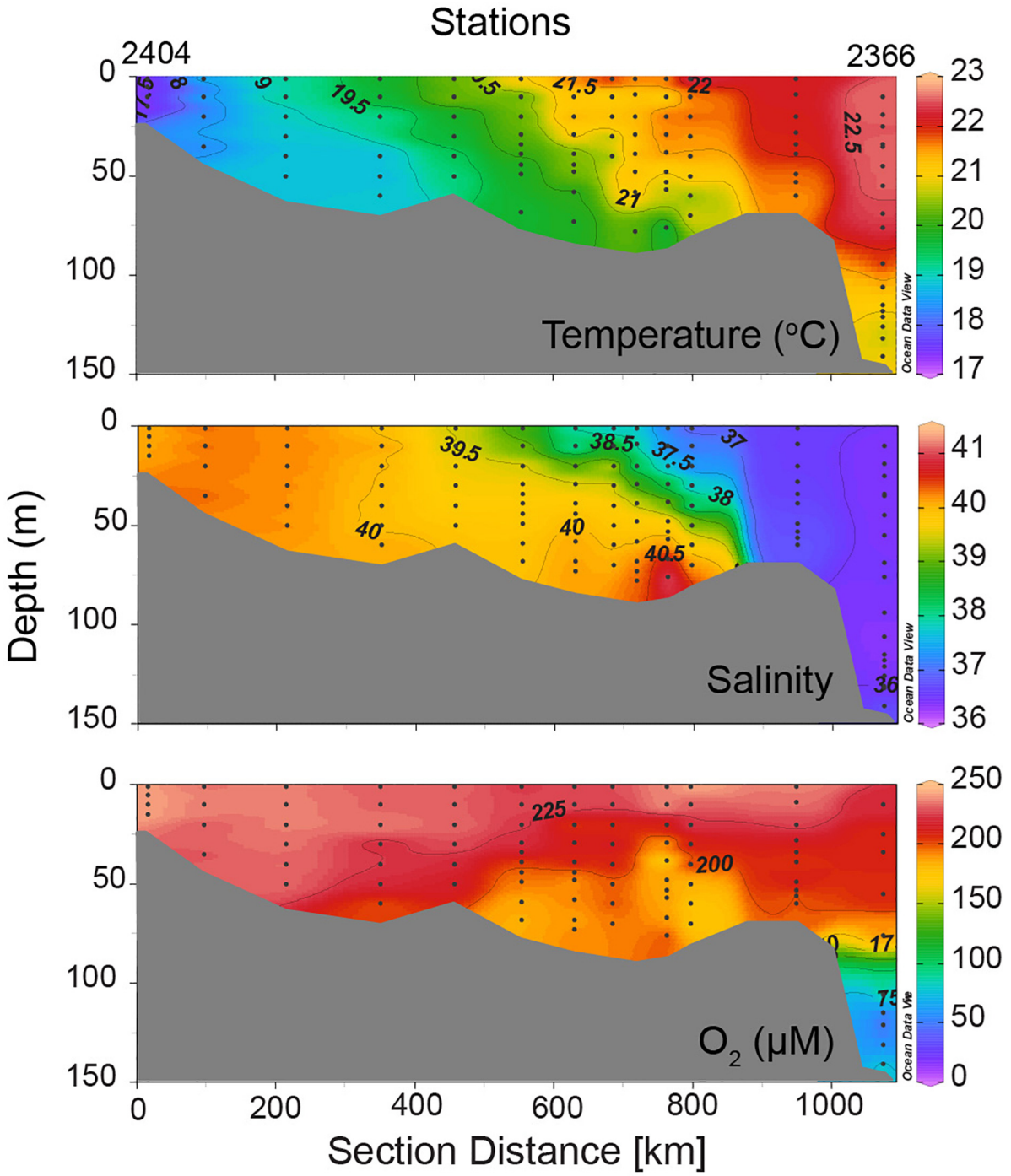


FIGURE 4 | Vertical sections of temperature, salinity, and dissolved oxygen along the main axis of the Persian Sea constructed using data collected during the R.V. *Atlantis II* cruise in February 1977 (Brewer et al., 1978). Salinity and oxygen sections are redrawn from Brewer and Dyrssen (1985).

generated by two Argo floats north of ∼23°N latitude (**Table 1**). While one of these floats operated from September 29, 2015 to February 19, 2017, the other was active from September 30, 2015 to December 29, 2016. A comparison of the data from these floats with those generated north of 23°N latitude during the above-mentioned cruise of R.V. *Sagar Kanya* (up to Station 29 – **Figure 2**) is made in **Figure 6** (modified from Naqvi, 2019). While the *Sagar Kanya* data provide a snapshot of the conditions prevailing at the time of the cruise, the float data covered a period well beyond an annual cycle at a very high resolution. Despite the seasonal cooling in the northern Red Sea and in the Gulfs of Aqaba and Suez, which lead to convection and

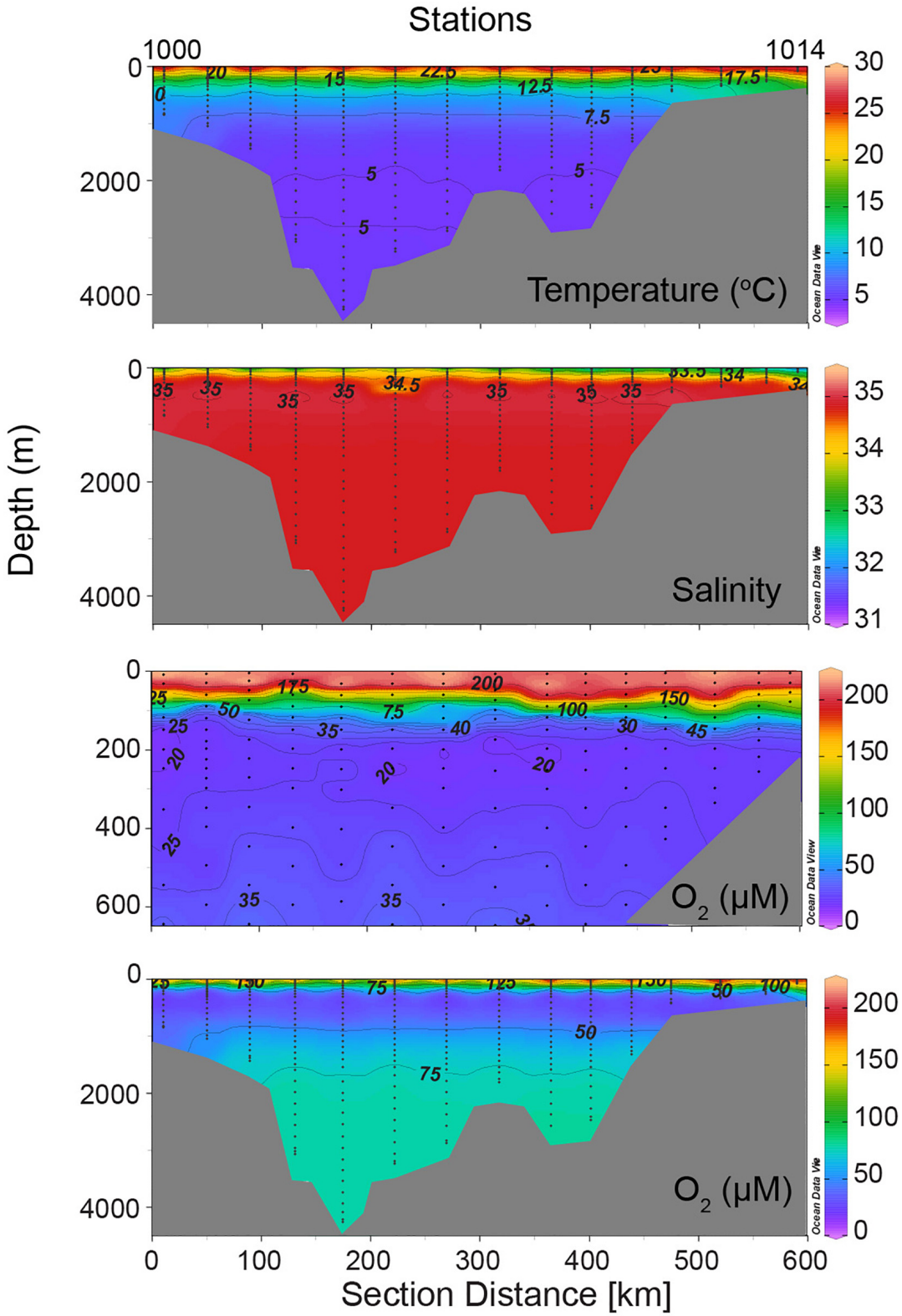


FIGURE 5 | Vertical sections of temperature, salinity, and dissolved oxygen along ~10°N (part of WOCE I01 Line) in the Andaman Sea constructed using data collected during the R.V. *Knorr* cruise in October 1995. These data form a subset of those presented in the WOCE Indian Ocean Atlas (Talley, 2013; http://whp-atlas.ucsd.edu/indian_index.htm).

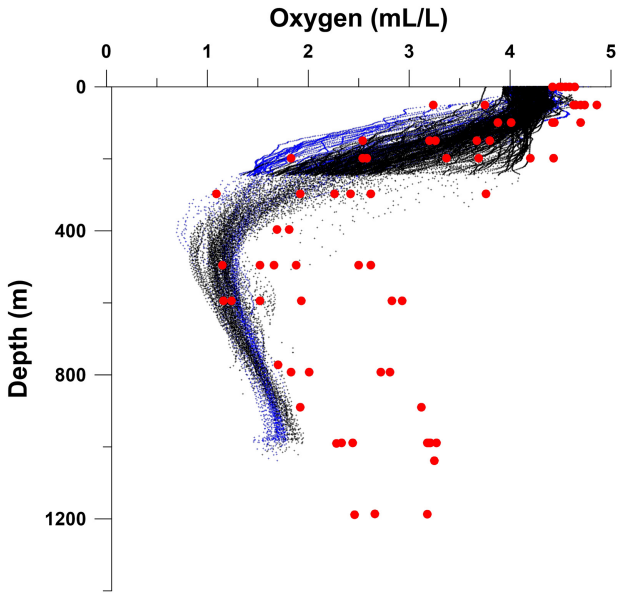


FIGURE 6 | Comparison of oxygen profiles generated by two Argo floats deployed in the Red Sea north of ~23°N latitude: #6901573 from September 29, 2015 to February 19, 2017 (black symbols) and #6901577 from September 30, 2015 to December 29, 2016 (blue symbols) with the Winkler oxygen data (red circles) collected during the May 1983 cruise of R.V. *Sagar Kanya* (**Figures 1A**, **2**).

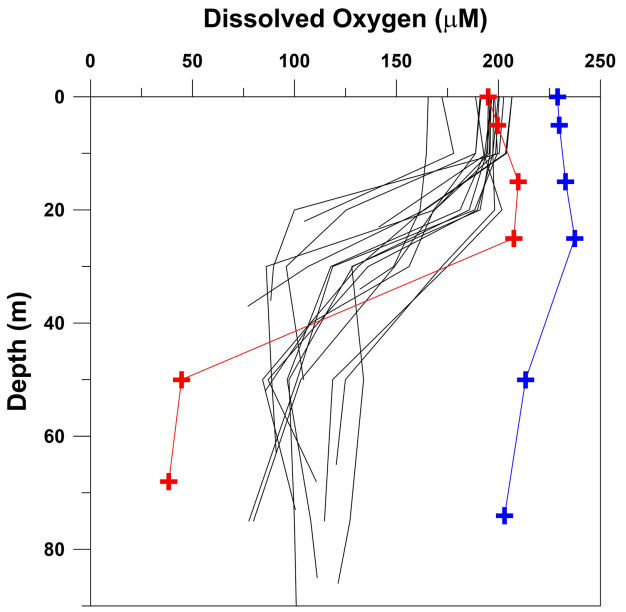


FIGURE 7 | Comparison of oxygen data in the Persian Gulf collected east of longitude 51.77°E during a cruise of R.V. *Lesnoye* in September 1968 (black profiles) with measurements made north of the Qatar peninsula during cruises of R.V. *Mukhtabar al-Bahr* in September–October 2000 (red symbols) and February–March 2001 (blue symbols).

deep water formation, the float data are fairly tightly clustered, with good overlapping of values from the two floats. In addition to the seasonal change, geographical variability – southward decrease in oxygen seen in **Figure 2** – would also contribute to the spread seen in **Figure 6**. Even considering this scatter, oxygen concentrations recorded by the floats during 2015–2017 were generally much lower than those measured on the *Sagar Kanya* cruise, especially in deeper water (below 400 m). As the concentration shift, most pronounced at the northern stations, far exceeds any potential error in the float data it may be concluded that substantial deoxygenation has occurred the Red Sea over the past three decades.

Persian Gulf

Substantial seasonal changes in oxygen distribution are expected to occur in the Persian Gulf due to wide temperature range. Results of Grasshoff (1976) and Brewer and Dyrssen (1985) (**Figure 4**) showed that the water column is vertically well-mixed and well-oxygenated during winter almost everywhere. However, an oxycline may develop in the deeper parts of the central and southern Gulf during summer due to warming of surface waters. This is evident from the contrasting profiles (**Figure 7**) at a station located close to the northern edge of the Qatar's EEZ that was sampled in late summer (September–October, 2000) and winter (February–March, 2001) (Al-Ansari et al., 2015). While the bottom-water oxygen concentration was ~90% of the saturation value in winter, the saturation level fell to ~18% in summer with the lowest recorded concentration of 0.86 ml l^{-1} (38.38 μM). In order to resolve the seasonality from the decadal scale shift, oxygen profiles at a number of stations sampled by the R.V. *Lesnoye* in September 1968 in the southern Gulf (**Table 1**) have also been included in **Figure 7**. The *Lesnoye* data set is the only historical data set generated in summer from this region. It is clear that summer-time oxygen depletion in the central Gulf also occurred in the 1960s, but not to the extent observed by Al-Ansari et al. (2015). At the same time near-surface oxygen values in the summer of 2000 were higher than most values in 1968, a tell-tale sign of eutrophication. Extrapolating their highly limited data, Al-Ansari et al. (2015) estimated the area of the "hypoxic" zone to exceed 7,000 km^2. Obviously, this estimate suffers from large uncertainty; nevertheless, in all likelihood the emergence of hypoxia in Qatari EEZ appears to be linked to human activities. If so, it is expected that further declines in oxygen should have occurred over the past two decades, underlining the urgent need for generation of new data from the southern Gulf, especially in summer.

Andaman Sea

A large number of oxygen profiles were generated from the Andaman Sea during the International Indian Ocean Expedition (IIOE), which can be used as the baseline for detecting and quantifying changes, if any, that have occurred in the region since then. These data, extracted from the WOD-NOAA database for the period 1961–1964 (**Table 1**), were compared with the latest publicly available data. Unfortunately, as the entire Andaman Sea falls within the EEZs of surrounding countries, it is not easily accessible for international exploration. The *Knorr* cruise that sampled WOCE I01 Line was an exception. Not only are there no

more recent bottle data from this region in the global data base, there have also not been any BIOARGO floats deployments in the Andaman Sea so far.

While the *Knorr* data came from a zonal transect, the IIOE stations were located over a wide latitudinal range. While this would not make a difference for the data below the sill depth (~1.4 km) since the deep water is exceedingly homogenous throughout the basin, it would matter for shallower depths because oxygen concentrations below the surface mixed layer and above the sill depth decrease steadily northward (Wyrtki, 1971). This is reflected in the larger scatter of oxygen concentrations at shallower depths, especially close to the oxygen minimum, in **Figure 8**, where all IIOE data are plotted along with the *Knorr* data. It must also be pointed out that the IIOE observations covered different seasons (**Table 1**). However, as stated earlier, one of the most distinguishing features of the NEIO, including the Andaman Sea, is the extremely strong stratification in the upper water column arising from the large river runoff and local precipitation. The moderate winter cooling is unable to overcome this barrier, and so in contrast with the NWIO, subsurface layers in the NEIO are not affected by seasonal mixing and are not ventilated by locally formed water masses (Naqvi et al., 2006). The isolation of waters below the pycnocline, including the OMZ, is reflected by low penetration of anthropogenic tracers like tritium and chlorofluorocarbons (Rao et al., 1994; Talley, 2013). Therefore, while no seasonal changes are expected to occur in deep waters, such changes are also most probably negligible within the OMZ. In general, oxygen concentrations measured on the *Knorr* cruise are slightly lower than those recorded in the early 1960s. At depths >1.5 km the mean ± SD of *Knorr* oxygen data is 78.40 ± 1.37 μM (1.76 ± 0.03 ml l^{-1}) as compared to 79.73 ± 2.77 μM (1.79 ± 0.06 ml l^{-1}) for the IIOE data. The difference, although small, is statistically significant (2-tailed Student *t*-test, $p = 0.000564$). A similar comparison was also made for data from the OMZ, but only within the depth range 150–350 m and from stations located between latitudes 9°N and 11°N. The mean ± SD values for the *Knorr* data – 22.52 ± 2.51 μM (0.50 ± 0.06 ml l^{-1}) – were even more significantly lower (two-tailed Student *t*-test, $p < 0.00001$) than those for the IIOE data – 28.88 ± 3.80 μM (0.65 ± 0.09 ml l^{-1}). However, it may be pointed out that while on the IIOE cruises Winkler titrations were carried out manually with visual end point detection, an automated procedure involving photometric end-point detection was followed on the *Knorr*. It has been pointed out earlier that at oxygen concentrations approaching zero, automated titrations yield consistently lower values (by ~0.04 ml l^{-1}, 1.79 μM) than manual titrations (Banse et al., 2014). However, even after considering this potential offset (i.e., subtracting it from each value for the IIOE data), the *Knorr* values would still be significantly lower ($p < 0.00001$). Thus, it appears that the core of the Andaman Sea OMZ had already lost small but significant amount of oxygen by the mid-1990s. Accordingly, mean water column oxygen inventory, computed to a constant depth of 3,000 m for the deepest part of the Andaman Basin, decreased from 206.9 mol m^{-2} ($n = 5$) during 1961–1964 to 199.9 mol m^{-2} ($n = 2$) in 1995.

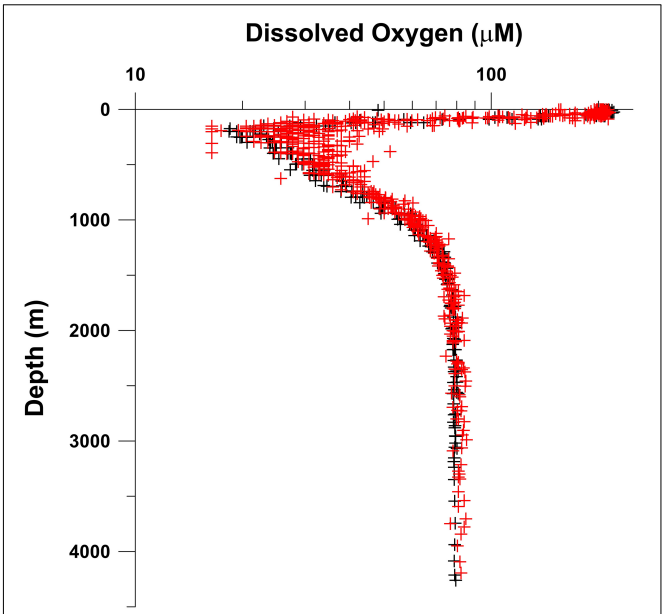


FIGURE 8 | Comparison of oxygen data from the Andaman Sea collected during the International Indian Ocean Expedition (1961–1964) (red symbols) with those taken on a cruise of R.V. *Knorr* (black symbols) in October 1995.

Coastal "Dead Zones"

Among the hundreds of hypoxic "dead zones" that are known to have developed globally in coastal waters over the past few decades due to human activities, mainly eutrophication (Diaz and Rosenberg, 2008), there are only two confirmed cases from the Indian Ocean's marginal seas (Breitburg et al., 2018). The most severe oxygen depletion in this category has been reported from the vicinity of Jeddah, the largest city along the Red Sea shores having a population of around 3 million. Three coastal lagoons in this area – Al-Shabab, Al-Arbaeen and Al-Salam – receive large quantities of treated or untreated sewage discharge from Jeddah City, which in conjunction with restricted flushing creates low oxygen conditions. Hypoxic/anoxic conditions in the Al-Shabab and Al-Arbaeen lagoons have been described in detail by Orif et al. (2017). Although similar data from the water column are not available from the Al-Salam lagoon, considering the sedimentary characteristics described by Abu-Zied and Orif (2019) together with the waste-water runoff and organic matter/nutrients loadings, hypoxia probably affects this lagoon as well. Oxygen concentrations have been observed to fall to hypoxic level of 63 μM in Al-Shahab lagoon, and water in the Arbaeen lagoon turns fully anoxic below 0.5 m with large build-up of H_2S (up to 55.5 μM). Substantial loss of fixed nitrogen also appears to occur in these lagoons along with huge production of methane, probably in sediments (Orif et al., 2017). In fact, bottom water methane levels in the Al-Arbaeen lagoon (maximum 13.2 μM) are comparable to those recorded in the deep anoxic basins of Black Sea and Cariaco Basin (Naqvi et al., 2010).

Shorter-lived episodes of deoxygenation have also been reported from coastal waters of Kuwait that receive huge quantities of anthropogenic nutrients and organic matter from

land. The group of semi-enclosed bays (Kuwait Bay along with the embedded Sulaibikhat Bay and Doha Bay) located at the northwestern extreme of the Persian Gulf receive enormous quantities of sewage and other effluents from Kuwait City and nearby industrial establishments. The region has extensive mudflats that are highly important from the ecological and biogeochemical points of view (Al-Yamani et al., 2004). The conditions within these sediments are strongly reducing (Dr. Turki Al-Said, personal communication). The tidal amplitude is fairly high (∼4 m), and periodic inundation of reducing intertidal sediments probably causes substantial depletion of oxygen in the overlying waters. An analysis of data collected during January 2009–November 2011 at a number of monitoring stations in this area revealed low oxygen saturation (minimum < 39%) off Kuwait City, extending from Sulaibikhat Bay to Doha Bay (Al-Mutairi et al., 2015). However, further away from the coast in the center of the Kuwait Bay, monthly sampling at a fixed station (K6, latitude 29.45°N, longitude 47.967°E, depth 12 m) being carried out since 2004 revealed that bottom water oxygen content has almost always been above 4 mg l^{-1} (2.8 ml l^{-1}, 125 μM), the nominal threshold for mild hypoxia (Dr. Faiza Al-Yamani, personal communication). However, eutrophication has led to a marked increase in the frequency of algal blooms, including harmful blooms, in Kuwait's waters in recent years (Al-Yamani et al., 2012; Al-Yamani and Naqvi, 2019). There have been instances of fish mortality in Kuwait waters associated with hypoxia as described by Al-Yamani et al. (2020). In one such incident mass mortality of sardines (*Sardinella fimbriata*) occurred in Ras Al-Adrdh Marina, Salimya, Kuwait on August 10, 2005. As the oxygen content was low throughout the water column [1.26 ml l^{-1} (56.23 μM), 1.19 ml l^{-1} (53.10 μM) and 0.70 ml l^{-1} (31.24 μM) O_2 at the surface, mid-depth, and bottom, respectively], hypoxia was considered to be a possible cause of the observed mortality. A similar but more extended mortality episode involving the same fish in the same area took place again in June–July, 2011, during which oxygen concentrations were also quite low (**Figure 9A**). Fish kills also occurred around the same time further to the south in the Messila Marina where the oxygen level in the upper 1 m fell to 0.14 ml l^{-1} (6.25 μM). Water discoloration by a bloom of the dinoflagellate *Gonyaulax verior* was conspicuously seen here. An even more widespread mortality event involving two catfish species, *Netuma thalassina* and *Plicofollis tenuspinus*, took place in Kuwait waters – especially in Kuwait Bay – in April–May, 2017. This was also associated with water discoloration due to blooms of potentially harmful raphidophycean flagellate *Heterosigma akashiwo* and dinoflagellate *Karenia papilionacea* (known to produce Brevetoxin, a neurotoxin). Oxygen measurements made during this period revealed generally well-oxygenated water column, except in one case where the vertical profile in Shuwaikh Port (**Figure 9B**) showed almost complete oxygen removal close to the bottom (∼10.5 m) (Al-Yamani et al., 2020). Thus, while oxygen-deficiency may or may not be the cause of the observed fish mortality, it is clearly one of the effects of episodic, excessive phytoplankton production (evident from very high oxygen concentration at the surface in **Figure 9B**) resulting from nutrient-over enrichment in coastal waters of the Persian Gulf.

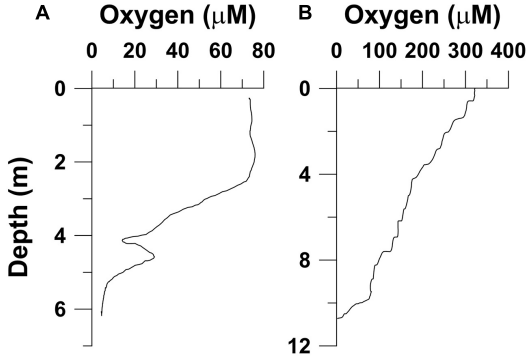


FIGURE 9 | Oxygen profiles at Rescue Station Marina in Salmiya, Kuwait (latitude 29.34°N, longitude 48.10°E) during a fish kill incident on July 19, 2011 **(A)**, and in Shuwaikh Port (latitude 29.36°N, longitude 47.93°E) on April 30, 2017 **(B)**. Redrawn from Al-Yamani et al. (2020).

DISCUSSION

The results presented above show declining trends in oxygen levels in all three basins. Before discussing their significance it is necessary to address a few issues that have important bearings on the inferences being drawn. First and foremost is the concern about compatibility of oxygen data used. As already discussed, the magnitudes of observed shifts are well beyond potential errors of measurements. The second issue relates to seasonality in oxygen distribution. Again, as pointed out above, seasonality is probably not very pronounced in the deep basins – the Red Sea and the Andaman Sea – below the surface layer. Moreover, in the case of the Red Sea the Argo float data cover all seasons and the range of values recorded by the floats is well below oxygen concentrations measured in 1983. On the other hand, seasonal changes are expected to be quite large in the Persian Gulf. This is, in fact, apparent from the data from the Qatari EEZ in the central Gulf taken during two consecutive summer and winter periods in 2000–2001, with the subsurface water being expectedly more oxygen depleted in summer (**Figure 7**). However, for the same month (September), bottom water oxygen concentrations were much lower in 2000 as compared to those in 1968. Thus, after taking into account the seasonality, the results strongly indicate increasing summer-time deoxygenation in the Persian Gulf. The third issue pertains to shifting baselines. That is, it is not known to what extent the data used as reference (collected in May 1983 in the case of Red Sea, in September 1968 in the case of the Persian Gulf. and during 1961–1964 in the case of the Andaman Sea) had already been anthropogenically impacted. Such an impact is expected to have been largest in the Persian Gulf that is quite shallow and small in size and has been subjected to human activities for a long time, especially after the discovery of oil and the wealth and "development" it brought to the region around the middle of the last century. However, even if the data used as reference might not represent "pristine" conditions, the comparisons with more recent measurements still yield reliable *trends* of change.

It is also not clear if or to what extent the observed deoxygenation trends are contributed by long-term natural variability, an inherent problem with any two-point comparison, but one that unfortunately cannot be addressed with the available data. It may be pointed out that there is evidence for existence of such variability in the Red Sea on the decadal scale. Satellite remote-sensed SST data have revealed a warming trend with values ranging from 0.17 to 0.45°C decade^{-1} across the Red Sea basin for the period 1982–2015 (Chaidez et al., 2017). However, the analysis of available water column data for the period 1958–2017 showed a more complex pattern – a steady decrease in SST from the 1960s up to the mid-1980s and an increasing trend thereafter (Agulles et al., 2020). It has been suggested that the long-term SST oscillations may be associated with the Atlantic Multidecadal Oscillation (AMO) and that the above-mentioned high warming rates over the past three decades or so are probably a combined effect of global warming and a positive phase of natural SST oscillations (Krokos et al., 2019). According to Krokos et al. (2019) the cooling AMO phase may offset the global warming related SST increase in the Red Sea in the future. What is really intriguing is that the temporal trends in subsurface water temperatures appear to be decoupled to the SST trend, showing an overall cooling trend in deep waters during 1958–2017 (Agulles et al., 2020). The data compiled by Agulles et al. (2020) show that since the time of the *Sagar Kanya* cruise the 100–500 m layer cooled up to mid 1990s and has been warming thereafter; the deeper waters showed a similar pattern, except that the minimum occurred a little later (in the late 1990s) and the subsequent warming has been more subdued. It is hard to reconcile the observed deoxygenation in deep waters of the Red Sea with these temperature variations, but it is clear that the oxygen decrease cannot be simply attributed to decreased solubility in warmer water.

Interannual and decadal-scale variability in oxygen forced by regional climate modes (e.g., the Indian Ocean Dipole) has been reported to control the intensity of seasonal anoxia over the western Indian shelf (Vallivattathillam et al., 2017). Such a variability may also occur in the off shore OMZs of the northern Indian Ocean (Rixen et al., 2020), but convincing evidence for this is lacking so far. Nevertheless, even though it is unlikely, one cannot completely rule out such a variability to account for a part of the oxygen declines being reported here.

Deoxygenation in the Mediterranean-type marginal seas is of special significance because of their unusual hydrography and the potential for its impact extending beyond the marginal seas themselves. For example, it has been pointed out by Seibel et al. (2016), who studied the metabolism and hypoxia tolerance of the Euphausiid species *Euphausia diomedeae* in the Red Sea, that owing to the higher water temperature and consequently elevated oxygen demand even moderate hypoxia may be physiologically more challenging to organisms than more severe hypoxia in colder water. These authors postulated that *E. diomedeae* in the Red Sea reached the limits of adaptation even though P_{crit}, the partial pressure of oxygen (PO_2) below which oxygen consumption rate becomes independent of PO_2, occurs deeper (∼270 m) in the water column as compared to the California Current and the eastern tropical Pacific, where waters with more intense oxygen minima are cooler. Changes in oxygen content and temperature will combine to determine the extent of habitat compression of marine organisms in all areas, more so in the Red Sea (Seibel et al., 2016).

Besides impacting local biogeochemistry and ecology, deoxygenation in the Persian Gulf and Red Sea is also expected to affect the intensity and volume of the Arabian Sea OMZ, which is uniquely ventilated by outflows from these regional seas (Naqvi, 2019). These outflows are strongly affected by the climate and local hydrography, particularly temperature (Lachkar et al., 2019). Changes in water temperature in the Red Sea have been discussed above. In the Persian Gulf, analysis of time series data from Kuwait's coastal waters has revealed a long-term warming rate of 0.38°C decade^{-1} (Al-Yamani et al., 2017), which is more than thrice the average warming rate (0.11°C decade) in the ocean (Rhein et al., 2013). Given the smaller size of the Persian Gulf, and the associated short renewal time, effects of warming of this magnitude are expected to be far more rapidly manifested than in the case of the Red Sea. Model simulations have shown that warming of the Persian Gulf has a particularly strong impact on the volume and intensity of the OMZ as the Persian Gulf Outflow advects right into the core of the OMZ (Codispoti et al., 2001; Lachkar et al., 2019). Warming will make the outflow lighter, thereby causing intensification of the OMZ and the associated denitrification process. However, this response is projected to be non linear as under strong warming (e.g., by 4°C), loss of nitrate in the upper layer caused by denitrification is expected to provide a negative feedback to deoxygenation. The model simulations also suggested a relatively weaker effect of increase in salinity in the Persian Gulf on the Arabian Sea OMZ (Lachkar et al., 2019). Warming of the Red Sea is also projected to lead to intensification of the OMZ, but to a smaller extent and at greater depths; as a result of the latter, the response to temperature increase is also more linear than in the case of the Persian Gulf Outflow. However, as discussed above, there does not seem to be consistent trend of warming in the Red Sea at depths from which the outflow is drawn. A more direct effect of the ongoing deoxygenation in the Persian Gulf and the Red Sea on the Arabian Sea OMZ would be through depression of preformed oxygen contents of the outflowing waters. This is expected to be caused both by a lower solubility of oxygen in warmer and more saline waters and an increase in oxygen demand as a consequence of increased productivity fuelled by anthropogenically supplied nutrients. Recent intensification of OMZ in the Gulf of Oman, which directly receives the outflow from the Persian Gulf, has been reported by Queste et al. (2018). It may be noted that salinity in the northern Persian Gulf has increased, especially during the crucial winter months when the dense water is formed, by as much as 10 (Al-Yamani et al., 2017; Al-Said et al., 2018). The total organic carbon (TOC) content of these waters is quite high (101.0–318.4, mean 161.2 μM – Al-Said et al., 2018). Even higher TOC values (336.7–543.3 μM) were measured in Kuwait Bay in April 2017 during the phytoplankton bloom mentioned above. Al-Said et al. (2018) proposed that the high oxygen demand arising from elevated TOC may be the principal driver of the emerging hypoxia in the Persian Gulf. They also speculated that the semi-labile portion of the TOC

that escapes degradation in the water column may be exported to the Arabian Sea by the outflow, potentially contributing further to the intensification of the Arabian Sea OMZ. To what extent similar processes also operate in the Red Sea, where the magnitude of human perturbation is much smaller, still remains to be investigated.

The observed deoxygenation trend within the oxygen minimum in the Andaman Sea is comparable to that reported by Naqvi (2019) for the northern Bay of Bengal, even though in the latter case the most recent data used for the comparison with the IIOE observations came from April 2007. This provides support to the view that the rate of oxygen decline in the Indian Ocean, in general, and in the NEIO, in particular, is smaller than in the OMZs of the Pacific Ocean (Stramma et al., 2008; Schmidtko et al., 2017). The present analysis shows that the trend also extends down to the depth in the NEIO (1.4 km) from where water in the deep Andaman Basin is derived. The extent to which the modest shift being reported here is caused by warming-related changes in oxygen solubility or circulation, or even increases in oxygen consumption cannot be evaluated with the present data. According to Oschlies (2019) the contribution of lower O_2 solubility in seawater arising from global warming to the observed decrease in oceanic O_2 inventory is relatively small (15%), but it could be as much as 50% in the upper kilometer of the water column. He attributed the majority of the change in deep waters to altered water circulation. The role of warming-induced increase in respiration also appears to be small (<15%). However, since the Andaman Sea receives large runoff from Irrawaddy River, and is also a part of a region with some of highest deposition rates of nitrogen from the atmosphere (Duce et al., 2008), an increase in primary productivity and associated organic matter export from the surface as an important contributing factor to the observed change cannot be ruled out. It must be pointed out that the current state-of-the-art models underestimate the extent of ocean deoxygenation as compared to what is inferred from observations (Oschlies et al., 2017), underlining the lack of our understanding of controlling processes.

One important common feature of all three marginal seas is they all contain sensitive tropical ecosystems viz. coral reefs, seagrasses and mangroves. Both naturally- and anthropogenically caused hypoxia may occur in some of these ecosystems. One such instance has been reported by Roik et al. (2016) based on an year-long monitoring of physico-chemical variables, which also involved oxygen measurements with a sensor, at 7.5–9 m in three reefs along a cross-shelf gradient off the Saudi Arabian coast in the central Red Sea. Their results showed considerable onshore-offshore and temporal (diurnal to seasonal) variations with an overall oxygen concentration range of 0.05–6.21 ml l^{-1} (2.2–277.2 μM). The very low values, occurring more often in, but not confined to, summer and in the nearshore reef (the lowest value was recorded in the offshore reef in winter, however, probably arising from community respiration at night), indicate high vulnerability of such ecosystems to human-induced deoxygenation. As compared to temperate ecosystems, occurrence of such deoxygenation from tropical ecosystems is probably greatly under-reported globally, and according to one estimate 13% of all coral ecosystems might have already turned into "dead zones" (Altieri et al., 2017, 2019). The ecosystems of Indian Ocean's marginal seas probably also suffer from such under-reporting. As exemplified by the above mentioned reports from the relatively well-studied coastal waters of Kuwait, this may particularly apply to the entire Persian Gulf, which is one of anthropogenically most impacted marine areas in the world (Sheppard et al., 2010), as well as to the poorly investigated shores of the Andaman Sea. The need for capacity building to adequately address this deficiency cannot be over-emphasized.

DATA AVAILABILITY STATEMENT

Publicly available datasets were analyzed in this study. Data sources are listed in **Table 1**.

AUTHOR CONTRIBUTIONS

The author confirms being the sole contributor of this work and has approved it for publication.

FUNDING

Salary support provided by CSIR.

ACKNOWLEDGMENTS

The author expresses his gratitude to Shekhar Mande, Director General, Council of Scientific & Industrial Research (India) for his support and encouragement. He is grateful to Amit Sarkar for drafting **Figures 1**, **2**, **4**, **5**, and to Akshay Hegde for extracting the data. Thanks are also due to Faiza Al-Yamani of KISR for making available oxygen data plotted in **Figure 9**. Bob Diaz and Denise Breitburg kindly allowed access to the global data base on hypoxic zones. This work forms a part of the activities of the Global Ocean Oxygen Network (GO_2NE) of the Intergovernmental Oceanographic Commission of UNESCO.

REFERENCES

Abu-Zied, R. H., and Orif, M. I. (2019). Recent environmental changes of Al-Salam Lagoon as inferred from core sediment geochemistry and benthic foraminifera, Jeddah City, Saudi Arabia. *Environ. Earth Sci.* 78, 60.

Agulles, M., Jordà, G., Jones, B., Agusti, S., and Duarte, C. M. (2020). Temporal evolution of temperatures in the Red Sea and the Gulf of Aden based on in situ observations (1958–2017). *Ocean Sci.* 16, 149–166. doi: 10.5194/os-16-149-2020

Al-Ansari, E. M. A. S., Rowe, G., Abdel-Moati, M. A. R., Yigiterhan, O., Al-Masalmani, I., Al-Yafei, M. A., et al. (2015). Hypoxia in the central Arabian Gulf exclusive economic zone of Qatar during summer season. *Estuar. Coast. Shelf Sci.* 159, 60–68. doi: 10.1016/j.ecss.2015.03.022

Allen, M., Jackson, J., and Walker, R. (2004). Late Cenozoic reorganization of the Arabia-Eurasia collision and the comparison of short-term and long-term deformation rates. *Tectonics* 23, TC2008. doi: 10.1029/2003TC001530

Al-Mutairi, N., AbaHussain, A., and El-Battay, A. (2015). Spatial assessment of monitoring network in coastal waters: a case study of Kuwait Bay. *Environ. Monit. Assess.* 187, 621.

Al-Said, T., Naqvi, S. W. A., Al-Yamani, F., Goncharov, A., and Fernandes, L. (2018). High total organic carbon in surface waters of the northern Arabian Gulf: implications for the oxygen minimum zone of the Arabian Sea. *Mar. Poll. Bull.* 129, 35–42. doi: 10.1016/j.marpolbul.2018.02.013

Altieri, A. H., Harrison, S. B., Seemann, J., Collin, R., Diaz, R. J., and Knowlton, N. (2017). Tropical dead zones and mass mortalities on coral reefs. *Proc. Natl. Acad. Sci. U.S.A.* 114, 3660–3665. doi: 10.1073/pnas.1621517114

Altieri, A. H., Nelson, H. R., and Gedan, K. B. (2019). "The significance of ocean deoxygenation for tropical ecosystems – corals, seagrasses and mangroves," in *Ocean Deoxygenation: Everyone's Problem. Causes, Impacts, Consequences and Solutions*, eds D. Laffoley and J. M. Baxter (Gland: International Union for Conservation of Nature), 401–429.

Al-Yamani, F., and Naqvi, S. W. A. (2019). Chemical oceanography of the Arabian Gulf. *Deep Sea Res. II* 161, 72–80. doi: 10.1016/j.dsr2.2018.10.003

Al-Yamani, F., Saburova, M., and Polikarpov, I. (2012). A preliminary assessment of harmful algal blooms in Kuwait's marine environment. *Aquat. Ecosyst. Health Manag.* 15(Suppl. 1), S64–S72.

Al-Yamani, F., Yamamoto, T., Al-Said, T., and Alghunaim, A. (2017). Dynamic hydrographic variations in Northwestern Arabian Gulf over the past three decades: temporal shifts and trends derived from long-term monitoring data. *Mar. Poll. Bull.* 122, 488–499. doi: 10.1016/j.marpolbul.2017.06.056

Al-Yamani, F. Y., Bishop, J. M., Ramadhan, E., Al-Husaini, M., and Al-Ghadban, A. N. (2004). *Oceanographic Atlas of Kuwait's Waters*. Kuwait City: Kuwait Institute for Scientific Research.

Al-Yamani, F. Y., Polikarpov, I., and Saburova, M. (2020). Marine life mortalities and Harmful Algal Blooms in the northern Arabian Gulf. *Aquat. Ecosyst. Health Manag.* 23, 196–209. doi: 10.1080/14634988.2020.1798157

Banse, K., Naqvi, S. W. A., Narvekar, P. V., Postel, J. R., and Jayakumar, D. A. (2014). Oxygen minimum zone of the open Arabian Sea: variability of oxygen and nitrite from daily to decadal timescales. *Biogeosciences* 11, 2237–2261. doi: 10.5194/bg-11-2237-2014

Bettig, H., and Körtzinger, H. (2015). Tackling oxygen optode drift: Near-surface and in-air oxygen optode measurements on a float provide an accurate in situ reference. *J. Atmos. Oceanic Technol.* 32, 1536–1543. doi: 10.1175/jtech-d-14-00162.1

Breitburg, D., Conley, D. J., Levin, L. A., Oschlies, A., Oschlies, A., Chavez, F. P., et al. (2018). Declining oxygen in the global ocean and coastal waters. *Science* 359, eaam7240.

Brewer, P. G., and Dyrssen, D. (1985). Chemical oceanography of the Persian Gulf. *Prog. Oceanogr.* 14, 41–55. doi: 10.1016/0079-6611(85)90004-7

Brewer, P. G., Fleer, A. P., Kadar, S., Shafer, D. K., and Smith, C. L. (1978). Chemical oceanographic data from the Persian Gulf and Gulf of Oman. *Woods Hole Oceanogr. Inst. Tech. Rep.* 105, 78–37.

Brewin, R. J. W., Raitsos, D. E., Dall'Olmo, G., Zarokanellos, N., Jackson, T., Racault, M.-F., et al. (2015). Regional ocean-colour chlorophyll algorithms for the Red Sea. *Rem. Sens. Environ.* 165, 64–85. doi: 10.1016/j.rse.2015.04.024

Bristow, L. A., Callbeck, C. M., Larsen, M., Altabet, M. A., Dekaezemacker, J., Forth, M., et al. (2017). N_2 production rates limited by nitrite availability in the Bay of Bengal oxygen minimum zone. *Nat. Geosci.* 10, 24–29. doi: 10.1038/ngeo2847

Broecker, W. S., Toggweiler, J. R., and Takahashi, T. (1980). The Bay of Bengal – A major nutrient source for the deep Indian Ocean. *Earth Planet. Sci. Lett.* 49, 506–512. doi: 10.1016/0012-821x(80)90091-6

Carpenter, J. (1965). The accuracy of the Winkler method for dissolved oxygen analysis. *Limnol. Oceanogr.* 10, 135–140. doi: 10.4319/lo.1965.10.1.0135

Cember, R. P. (1988). On the sources, formation, and circulation of Red Sea deep water. *J. Geophys. Res.* 93, 8175–8191. doi: 10.1029/jc093ic07p08175

Chaidez, V., Dreano, D., Agusti, S., Duarte, C. M., and Hoteit, I. (2017). Decadal trends in Red Sea maximum surface temperature. *Sci. Rep.* 7, 1–8.

Chakraborty, A., Nanjundiah, R. S., and Srinivasan, J. (2002). Role of Asian and African orography in Indian summer monsoon. *Geophys. Res. Lett.* 29, 50.1–50.4. doi: 10.1029/2002GL015522

Cochran, J. R. (2010). Morphology and tectonics of the Andaman Forearc, northeastern Indian Ocean. *Geophys. J. Int.* 182, 631–651. doi: 10.1111/j.1365-246X.2010.04663.x

Codispoti, L. A., Brandes, J. A., Christensen, J. P., Devol, A. H., Naqvi, S. W. A., Paerl, H. W., et al. (2001). The oceanic fixed nitrogen and nitrous oxide budgets: moving targets as we enter the anthropocene. *Sci. Mar.* 65 (Suppl. 2), 85–105. doi: 10.3989/scimar.2001.65s285

Diaz, R. J., and Rosenberg, R. (2008). Spreading dead zones and consequences for marine ecosystems. *Science* 321, 926–929. doi: 10.1126/science.1156401

Duce, R. A., LaRoche, J., Altieri, K., Arrigo, K. R., Baker, A. R., Capone, D. G., et al. (2008). Impacts of atmospheric anthropogenic nitrogen on the open ocean. *Science* 320, 893–897.

El Samra, M. I., and El Gindy, A. A. H. (1990). Vertical distribution and inter-relations of oxygen and nutrients in the Arabian Gulf and the Gulf of Oman in summer. *Qatar Univ. Sci. Bull.* 10, 445–464.

Grasshoff, K. (1975). "The hydrochemistry of landlocked basins and fjords," in *Chemical Oceanography*, Vol. 2, eds J. P. Riley and G. Skirrow (London: Academic Press), 455–597.

Grasshoff, K. (1976). *Review of Hydrographical and Productivity Conditions in the Gulf Region, Marne Sciences in the Gulf Area*, Vol. 26. Paris: UNESCO Technical Papers in Marine Science, 39–62.

Hashimoto, S., Tsujimoto, R., Maeda, M., Ishimaru, T., Yoshida, J., Takasu, Y., et al. (1998). "Distribution of nutrient, nitrous oxide and chlorophyll a of RSA: extremely high ratios of nitrite to nitrate in whole water column," in *Offshore Environment of the ROPME Sea Area After the War-Related Oil Spill: Results of the 1993 – 94 Umitaka-Maru Cruises*, (Tokyo: Terra Science), 99–124.

Ittekkot, V., Haake, B., Bartsch, M., Nair, R. R., and Ramaswamy, V. (1992). "Organic carbon removal in the sea: the continental connection," in *Upwelling Systems: Evolution Since the Early Miocene*, Vol. 64, eds C. P. Summerhayes, W. L. Prell, and K.-C. Emeis (London: Geological Society of London), 167–176. doi: 10.1144/gsl.sp.1992.064.01.11

Jithin, A. K., and Francis, P. A. (2020). Role of internal tide mixing in keeping the deep Andaman Sea warmer than the Bay of Bengal. *Sci. Rep.* 10:11982. doi: 10.1038/s41598-020-68708-6

Johns, W. E., Yao, F., Olson, D. B., Josey, S. A., Grist, J. P., and Smeed, D. A. (2003). Observations of seasonal exchange through the Straits of Hormuz and the inferred heat and freshwater budgets of the Persian Gulf. *J. Geophys. Res.* 108, 3391. doi: 10.1029/2003JC001881

Krokos, G., Papadopoulos, V. P., Sofianos, S. S., Ombao, H., Dybczak, P., and Hoteit, I. (2019). Natural climate oscillations may counteract Red Sea warming over the coming decades. *Geophys. Res. Lett.* 46, 3454–3461. doi: 10.1029/2018gl081397

Lachkar, Z., Levy, M., and Smith, K. S. (2019). Strong intensification of the Arabian Sea oxygen minimum zone in response to Arabian Gulf warming. *Geophys. Res. Lett.* 46, 5420–5429. doi: 10.1029/2018gl081631

Lambeck, K., Purcell, A., Flemming, N. C., Vita-Finzi, C., Alsharekh, A. M., and Bailey, G. N. (2011). Sea level and shoreline reconstructions for the Red Sea: Isostatic and tectonic considerations and implications for hominin migration out of Africa. *Quat. Sci. Rev.* 30, 3542–3574. doi: 10.1016/j.quascirev.2011.08.008

Maillard, C., and Soliman, G. (1986). Hydrography of the Red Sea and exchanges with the Indian Ocean in summer. *Oceanol. Acta* 9, 249–269.

Mantyla, A. W., and Reid, J. L. (1995). On the origins of deep and bottom waters of the Indian Ocean. *J. Geophys. Res.* 100, 2417–2439. doi: 10.1029/94jc02564

Morcos, S. A. (1970). Physical and chemical oceanography of the Red Sea. *Oceanogr. Mar. Biol. Ann. Rev.* 8, 73–202.

Murray, S. P., and Johns, W. (1997). Direct observations of seasonal exchange through the Bab el Mandab Strait. *Geophys. Res. Lett.* 24, 2557–2560. doi: 10.1029/97gl02741

Naqvi, S. W. A. (2019). "Evidence for ocean deoxygenation and its patterns: Indian Ocean," in *Ocean Deoxygenation: Everyone's Problem. Causes, Impacts, Consequences and Solutions*, eds D. Laffoley and J. M. Baxter (Gland: International Union for Conservation of Nature), 51–71.

Naqvi, S. W. A., Bange, H. W., Farias, L., Monteiro, P. M. S., Scranton, M. I., and Zhang, J. (2010). Marine hypoxia/anoxia as a source of CH_4 and N_2O. *Biogeosciences* 7, 2159–2190.

Naqvi, S. W. A., Charles, C. D., and Fairbanks, R. G. (1994). Carbon and oxygen isotopic records in benthic foraminifera from the Northeast Indian Ocean:

implications on glacial interglacial atmospheric CO_2 changes. *Earth Planet. Sci. Lett.* 121, 110.

Naqvi, S. W. A., Hansen, H. P., and Kureishy, T. W. (1986). Nutrient uptake and regeneration ratios in the Red Sea with reference to the nutrient budgets. *Oceanolog. Acta* 9, 271–275.

Naqvi, S. W. A., Narvekar, P. V., and Desa, E. (2006). "Coastal biogeochemical processes in the North Indian Ocean (14, SW)," in *The Sea*, Vol. 14, eds A. Robinson and K. Brink (Cambridge, MA: Harvard University Press), 723–780.

Naqvi, S. W. A., Shailaja, M. S., Kumar, M. D., and Sen Gupta, R. (1996). Respiration rates in subsurface waters of the northern Indian Ocean: evidence for low decomposition rates of organic matter within the water column in the Bay of Bengal. *Deep Sea Res. II* 43, 73–81. doi: 10.1016/0967-0645(95)00080-1

Orif, M. I., Kavil, Y. N., Kelassanthodi, R., Al-Farawati, R., and Al Zobidi, M. I. (2017). Dissolved methane and oxygen depletion in the two coastal lagoons, Red Sea. *Indian J. Geo-Mar. Sci.* 46, 1287–1297.

Oschlies, A. (2019). "Ocean deoxygenation from climate change," in *Ocean Deoxygenation: Everyone's Problem. Causes, Impacts, Consequences and Solutions*, eds D. Laffoley and J. M. Baxter (Gland: International Union for Conservation of Nature), 105–116.

Oschlies, A., Duteil, O., Getzlaff, J., Koeve, W., Landolfi, A., and Schmidtko, S. (2017). Patterns of deoxygenation: sensitivity to natural and anthropogenic drivers. *Philos. Trans. R. Soc. A* 375, 2102.

Plahn, O., Baschek, B., Badewien, T. H., Walter, M., and Rhein, M. (2002). Importance of the Gulf of Aqaba for the formation of bottom water in the Red Sea. *J. Geophys. Res.* 107, 22-1-22-18. doi: 10.1029/2000jc000342

Pous, S., Pascal, L., and Xavier, C. (2015). A model of the general circulation in the Persian Gulf and in the Strait of Hormuz: interseasonal to interannual variability. *Cont. Shelf. Res.* 94, 55–90. doi: 10.1016/j.csr.2014.12.008

Prasad, T. G. (2004). A comparison of mixed-layer dynamics between the Arabian Sea and Bay of Bengal: One-dimensional model results. *J. Geophys. Res.* 109, C03035. doi: 10.1029/2003JC002000

Queste, B. Y., Vic, C., Heywood, K. J., and Piontkovski, S. A. (2018). Physical controls on oxygen distribution and denitrification potential in the North West Arabian Sea. *Geophys. Res. Lett.* 45, 4143–4152. doi: 10.1029/2017gl076666

Rao, C. K., Naqvi, S. W. A., Kumar, M. D., Varaprasad, S. J. D., Jayakumar, D. A., George, M. D., et al. (1994). Hydrochemistry of the Bay of Bengal: possible reasons for a different water column cycling of carbon and nitrogen from the Arabian Sea. *Mar. Chem.* 47, 290.

Rhein, M., Qin, D., Plattner, G. K., Tignor, M. M. B., Allen, S. K., Boschung, J., et al. (2013). "Observations: Ocean," in *Climate Change 2013: The Physical Science Basis. Contribution of Working Group I to the Fifth Assessment Report of the Intergovernmental Panel on Climate Change*, ed. T. F. Stocker (Cambridge: Cambridge University Press), 255–315.

Rixen, T., Cowie, G., Gaye, B., Goes, J., do Rosário Gomes, H., Hood, R. R., et al. (2020). Reviews and syntheses: present, past, and future of the oxygen minimum zone in the northern Indian Ocean. *Biogeosciences* 17, 6051–6080. doi: 10.5194/bg-17-6051-2020

Rixen, T., Gaye, B., Emeis, K.-C., and Ramaswamy, V. (2019). The ballast effect of lithogenic matter and its influences on the carbon fluxes in the Indian Ocean. *Biogeosciences* 16, 485–503. doi: 10.5194/bg-16-485-2019

Roik, A., Röthig, T., Roder, C., Ziegler, M., Kremb, S. G., and Voolstra, C. R. (2016). Year-long monitoring of physico-chemical and biological variables provide a comparative baseline of coral reef functioning in the Central Red Sea. *PLoS One* 11:e0163939. doi: 10.1371/journal.pone.0163939

Sarma, V. V. S. S., and Narvekar, P. V. (2001). A study on inorganic carbon components in the Andaman Sea during the post monsoon season. *Oceanol. Acta* 24, 125–134. doi: 10.1016/s0399-1784(00)01133-6

Scaife, G., Spectrum, and Billings, A. (2010). *Andaman Basin*. Available online at: tGEOEXPRO, 7, https://www.geoexpro.com/articles/2010/05/andaman-basin (accessed October 20, 2020)

Schmidtko, S., Stramma, L., and Visbeck, M. (2017). Decline in global oceanic oxygen content during the past five decades. *Nature* 542, 335. doi: 10.1038/nature21399

Seibel, B. A., Schneider, J. L., Kaartvedt, S., Wishner, H. F., and Daly, K. L. (2016). Hypoxia tolerance and metabolic suppression in oxygen minimum zone Euphausiids: implications for ocean deoxygenation and biogeochemical cycles. *Integr. Comp. Biol.* 56, 510–523. doi: 10.1093/icb/icw091

Sen Gupta, R., Moraes, C., George, M. D., Kureishy, T. W., Noronha, R. J., and Fondekar, S. P. (1981). Chemistry and hydrography of the Andaman Sea. *Indian J. Mar. Sci.* 10, 228–233.

Shenoi, S. S. C., Shetye, S. R., and Shankar, D. (2002). Differences in heat budgets of the near−surface Arabian Sea and Bay of Bengal: Implications for the summer monsoon. *J. Geophys. Res* 107, 5-1-5-14. doi: 10.1029/2000JC000679

Sheppard, C. R. C., Al-Husiani, M., Al-Jamali, F., Al-Yamani, F., Baldwin, R., Bishop, J., et al. (2010). The Gulf: a young sea in decline. *Mar. Pollut. Bull.* 60, 13–38.

Sofianos, S. S., and Johns, W. E. (2002). An Oceanic general circulation model (OGCM) investigation of the Red Sea circulation. 1. Exchange between the Red Sea and the Indian Ocean. *J. Geophys. Res* 107, 3196. doi: 10.1029/2001JC001185

Sofianos, S. S., and Johns, W. E. (2003). An Oceanic General Circulation Model (OGCM) investigation of the Red Sea circulation: 2. Three dimensional circulation in the Red Sea. *J. Geophys. Res* 108, 3066.

Sofianos, S. S., and Johns, W. E. (2007). Observations of the summer Red Sea circulation. *J. Geophys. Res* 112, C06025. doi: 10.1029/2006JC003886

Sofianos, S. S., Johns, W. E., and Murray, S. P. (2002). Heat and freshwater budgets in the Red Sea from direct observations at Bab el Mandeb. *Deep-Sea Res. II* 49, 1323–1340. doi: 10.1016/s0967-0645(01)00164-3

Stern, R. J., and Johnson, P. (2010). Continental lithosphere of the Arabian Plate: a geologic, petrologic, and geophysical synthesis. *Earth Sci. Rev.* 101, 29–67. doi: 10.1016/j.earscirev.2010.01.002

Stramma, L., Johnson, G. C., Sprintall, J., and Mohrholz, V. (2008). Expanding oxygen-minimum zones in the tropical oceans. *Science* 320, 655–658. doi: 10.1126/science.1153847

Swift, S. A., and Bower, A. S. (2003). Formation and circulation of dense water in the Persian/Arabian Gulf. *J. Geophys. Res.* 108, 3004. doi: 10.1029/2002JC001360

Talley, L. D. (2013). *Hydrographic Atlas of the World Ocean Circulation Experiment (WOCE)* Vol. 4: Indian Ocean, eds M. Sparrow, P. Chapman, and J. Gould (Southampton: International WOCE Project Office). doi: 10.21976/C61595

Thamdrup, B., Dalsgaard, T., and Revsbech, N. P. (2012). Widespread functional anoxia in the oxygen minimum zone of the Eastern South Pacific. *Deep Sea Res. I* 65, 36–45. doi: 10.1016/j.dsr.2012.03.001

Vallivattathillam, P., Iyyappan, S., Lengaigne, M., Ethé, C., Vialard, J., Levy, M., et al. (2017). Positive Indian Ocean Dipole events prevent anoxia off the west coast of India. *Biogeosciences* 14, 1541–1559. doi: 10.5194/bg-14-1541-2017

Weiss, R. F., Broecker, W. S., Craig, H., and Spencer, D. (1983). *GEOSECS Indian Ocean Expedition, vol. 5, Hydrographic Data*. Washington, DC: National Science Foundation, 48.

Winkler, L. W. (1888). Die bestimmung des in Wasser gelösten sauerstoffes. *Ber. Dtsch. Chem. Ges.* 21, 2843–2854. doi: 10.1002/cber.188802102122

Woelk, S., and Quadfasel, D. (1996). Renewal of deep water in the Red Sea during 1982–1987. *J. Geophys. Res.* 101, 18155–18165. doi: 10.1029/96jc01148

Wyrtki, K. (1971). *Oceanographic Atlas of the International Indian Ocean Expedition*. Washington, DC: National Science Foundation, 531.

Wyrtki, K. (1974). "On the Deep Circulation of the Red Sea" in *L'oceanographie Physique de la Mer Rouge*. Paris: Centre national pour l'Exploitation des Oceans, 135–163.

Yao, F., Hoteit, I., Pratt, L. J., Bower, A. S., Köhl, A., Gopalakrishnan, G., et al. (2014b). Seasonal overturning circulation in the Red Sea: 2. Winter circulation. *J. Geophys. Res.* 119, 2263–2289. doi: 10.1002/2013jc009331

Yao, F., Hoteit, I., Pratt, L. J., Bower, A. S., Zhai, P., Köhl, A., et al. (2014a). Seasonal overturning circulation in the Red Sea: 1. Model validation and summer circulation. *J. Geophys. Res.* 119, 2238–2262. doi: 10.1002/2013jc009004

Conflict of Interest: The author declares that the research was conducted in the absence of any commercial or financial relationships that could be construed as a potential conflict of interest.

Copyright © 2021 Naqvi. This is an open-access article distributed under the terms of the Creative Commons Attribution License (CC BY). The use, distribution or reproduction in other forums is permitted, provided the original author(s) and the copyright owner(s) are credited and that the original publication in this journal is cited, in accordance with accepted academic practice. No use, distribution or reproduction is permitted which does not comply with these terms.

frontiers in Marine Science

ORIGINAL RESEARCH
published: 14 July 2021
doi: 10.3389/fmars.2021.688008

Decadal Dynamics of the CO_2 System and Associated Ocean Acidification in Coastal Ecosystems of the North East Atlantic Ocean

*Jean-Philippe Gac[1], Pierre Marrec[2], Thierry Cariou[1], Emilie Grosstefan[3], Éric Macé[1], Peggy Rimmelin-Maury[3], Marc Vernet[1] and Yann Bozec[1]**

[1] Sorbonne Université, CNRS, UMR 7144 AD2M, Station Biologique de Roscoff, Roscoff, France, [2] Graduate School of Oceanography, University of Rhode Island, Narragansett, RI, United States, [3] IUEM, UMS 3113, Service d'Observation, Technopôle Brest-Iroise, Plouzané, France

Weekly and bi-monthly carbonate system parameters and ancillary data were collected from 2008 to 2020 in three coastal ecosystems of the southern Western English Channel (sWEC) (SOMLIT-pier and SOMLIT-offshore) and Bay of Brest (SOMLIT-Brest) located in the North East Atlantic Ocean. The main drivers of seasonal and interannual partial pressure of CO_2 (pCO_2) and dissolved inorganic carbon (DIC) variabilities were the net ecosystem production (NEP) and thermodynamics. Differences were observed between stations, with a higher biological influence on pCO_2 and DIC in the near-shore ecosystems, driven by both benthic and pelagic communities. The impact of riverine inputs on DIC dynamics was more pronounced at SOMLIT-Brest (7%) than at SOMLIT-pier (3%) and SOMLIT-offshore (<1%). These three ecosystems acted as a weak source of CO_2 to the atmosphere of 0.18 ± 0.10, 0.11 ± 0.12, and 0.39 ± 0.08 mol m^{-2} $year^{-1}$, respectively. Interannually, air-sea CO_2 fluxes (FCO_2) variability was low at SOMLIT-offshore and SOMLIT-pier, whereas SOMLIT-Brest occasionally switched to weak annual sinks of atmospheric CO_2, driven by enhanced spring NEP compared to annual means. Over the 2008–2018 period, monthly total alkalinity (TA) and DIC anomalies were characterized by significant positive trends (*p*-values < 0.001), from 0.49 ± 0.20 to 2.21 ± 0.39 μmol kg^{-1} $year^{-1}$ for TA, and from 1.93 ± 0.28 to 2.98 ± 0.39 μmol kg^{-1} $year^{-1}$ for DIC. These trends were associated with significant increases of calculated seawater pCO_2, ranging from +2.95 ± 1.04 to 3.52 ± 0.47 μatm $year^{-1}$, and strong reductions of calculated $pH_{in\ situ}$, with a mean $pH_{in\ situ}$ decrease of 0.0028 $year^{-1}$. This ocean acidification (OA) was driven by atmospheric CO_2 forcing (57–66%), Sea surface temperature (SST) increase (31–37%), and changes in salinity (2–5%). Additional $pH_{in\ situ}$ data extended these observed trends to the 2008–2020 period and indicated an acceleration of OA, reflected by a mean $pH_{in\ situ}$ decrease of 0.0046 $year^{-1}$ in the sWEC for that period. Further observations over the 1998–2020 period revealed that the climatic indices North Atlantic Oscillation (NAO) and Atlantic Multidecadal Variability (AMV) were linked to trends of SST, with cooling during 1998–2010 and warming during 2010–2020, which might have

OPEN ACCESS

Edited by:
Hongjie Wang, National Oceanic and Atmospheric Administration (NOAA), United States

Reviewed by:
Emily Osborne, National Oceanic and Atmospheric Administration (NOAA), United States
Wei-dong Zhai, Shandong University (Qingdao), China

***Correspondence:**
Yann Bozec
bozec@sb-roscoff.fr

Specialty section:
This article was submitted to Marine Biogeochemistry, a section of the journal Frontiers in Marine Science

Received: *30 March 2021*
Accepted: *28 May 2021*
Published: *14 July 2021*

Citation:
Gac J-P, Marrec P, Cariou T, Grosstefan E, Macé É, Rimmelin-Maury P, Vernet M and Bozec Y (2021) Decadal Dynamics of the CO_2 System and Associated Ocean Acidification in Coastal Ecosystems of the North East Atlantic Ocean. Front. Mar. Sci. 8:688008. doi: 10.3389/fmars.2021.688008

impacted OA trends at our coastal stations. These results suggested large temporal variability of OA in coastal ecosystems of the sWEC and underlined the necessity to maintain high-resolution and long-term observations of carbonate parameters in coastal ecosystems.

Keywords: ocean acidification, coastal ecosystem, long-term monitoring, NE Atlantic, carbonate system dynamics

INTRODUCTION

Coastal ecosystems are often associated with important and variable inputs of nutrients (phosphates, nitrates, nitrites, and silicates) *via* river discharge, which induce large seasonal and interannual variability of the carbonate system (Gypens et al., 2009, 2011). High nutrient concentrations increase carbon absorption by promoting biological production (Elser et al., 2007). Up to 30% of primary production [and organic matter (OM) remineralization] is concentrated in coastal shelf zones (Walsh et al., 1988; de Haas et al., 2002; Bauer et al., 2013), leading to high uptake (and release) of dissolved inorganic carbon (DIC) and partial pressure of CO_2 (pCO_2) (Thomas et al., 2005). In addition, natural riverine carbon originating from the lithosphere and organic matter of the terrestrial biosphere (Ludwig et al., 1998) are partly exported to coastal ecosystems (Hartmann et al., 2014). Finally, depending on the nature of the soil, weathering processes can either increase or decrease DIC and total alkalinity (TA) (Hartmann et al., 2009; McGrath et al., 2019) in surface waters. All of these intricate interactions make it difficult to assess the drivers of the carbonate system in the diverse coastal ecosystems.

Continental margins represent only 4.5% of the global ocean uptake of anthropogenic carbon (Bourgeois et al., 2016), estimated at 2.6 ± 0.3 PgC $year^{-1}$ of CO_2 (31 ± 4% of anthropogenic CO_2 emissions) (Gruber et al., 2019), yet they are particularly vulnerable to anthropogenic forcing, such as urban development, atmospheric deposition, from fossil fuel combustion and agricultural activities. All of these anthropogenic stressors can have compensatory or additive effects on the CO_2 system (Doney, 2010; Sunda and Cai, 2012; Da et al., 2018), and consequently on potential coastal seawater acidification (Borges et al., 2010; Borges and Gypsens, 2010; Wallace et al., 2014; Carstensen and Duarte, 2019). Ocean acidification (OA) has been ongoing over the last 250 years, with a pH decrease of 0.11 units in the global ocean, equivalent to a hydrogen ion concentration increase of 28% (Gattuso et al., 2015). Coastal acidification can be far more dramatic relative to the open ocean as a result of multiple stressor interactions (Duarte et al., 2013; Osborne et al., 2020). OA has major consequences, particularly for organisms with shells or skeletons composed of calcium carbonate ($CaCO_3$) (Doney et al., 2020). Coastal ecosystems can experience extreme OA hotspots due to the intrusion of acidified water with low aragonite saturation states (Ω_{Arag}, Feely et al., 2010, 2016; Chan et al., 2017; Fennel et al., 2019) or conversely constitute refuges with more stable pH (Chan et al., 2017). Carbon and pH variability affect algal physiology, impacting phytoplankton inorganic carbon fixation (Raven et al., 2017), and may contribute to increased harmful algal blooms (Fu et al., 2012; Flynn et al., 2015; Raven et al., 2020).

Monitoring of physical and biogeochemical processes in seawater is essential to understand the evolution of oceans, especially in the context of increasing temperature and atmospheric CO_2 (IPCC, 2013). Recent decades have seen the emergence of a large number of CO_2 monitoring programs in the open ocean (Bates et al., 2014; Sutton et al., 2017). Monitoring stations are distributed around the Pacific (e.g., Munida, Currie et al., 2011; Bates et al., 2014; WHOTS, ALOHA, Sutton et al., 2017) and the Atlantic (e.g., ESTOC, González-Dávila et al., 2010; BATS, Bates et al., 2014), and cover a wide range of latitudes, from sub-polar waters (Iceland/Iriminger seas, Olafsson et al., 2009, 2010; Bates et al., 2014) to tropical waters (CARIACO, Caribbean Sea, Astor et al., 2013; Taylor et al., 2012; Bates et al., 2014; Muller-Karger et al., 2019). The SOOP-CO_2 provided pCO_2 data acquired from ships of opportunity[1], while the growing BGC-Argo array (Claustre et al., 2020) will provide open ocean pH observations, in addition to salinity-derived TA. SOCAT (Bakker et al., 2016) and LDEO Global Surface Database (Takahashi et al., 2020) contribute to these international efforts by compiling quality CO_2 observations from the scientific community, while GLODAP (Lauvset et al., 2016) and OceanSODA-ETHZ (Gregor and Gruber, 2021) databases provide global gridded data of the open ocean carbonate system. The limited CO_2 system variability in the oceanic environment, compared to coastal ecosystems, favors observations of the alterations associated to climate change such as carbon accumulation or OA. Global estimates of OA in the open ocean were estimated at −0.0018 ± 0.0004 $year^{-1}$ for the period 1991–2011 (Lauvset et al., 2015) and relate to pCO_2 increase of 1.2 ± 0.5 μatm $year^{-1}$ to 2.1 ± 0.5 μatm $year^{-1}$ in different ocean basins (Takahashi et al., 2009, 2014). These trends are highly linked to the studied periods and can vary regionally and seasonally (Leseurre et al., 2020). Long-term monitoring in nearshore ecosystems is particularly relevant since these ecosystems host large stocks of shellfish species sensitive to ongoing OA (Doney et al., 2020), yet remain scarce. Coastal margins present additional challenges because of the intense daily, seasonal, and interannual variability associated to these environments (riverine inputs, climatic, and anthropogenic drivers), which make it more challenging to observe trends related to climate change (Kapsenberg et al., 2017; Reimer et al., 2017a; Chen and Hu, 2019).

In the North East Atlantic Ocean, a recent initiative by the Global Ocean Acidification Network (GOA-ON[2]) has aimed to

[1]https://www.aoml.noaa.gov/ocd/ocdweb/occ_soop.html

[2]http://goa-on.org

coordinate, encourage, and maintain long-term observations of the CO_2 system at local and national scales. In this context, we report on three time series of carbonate parameters in the southern Western English Channel off Roscoff (SOMLIT-pier and SOMLIT-offshore) and in the Bay of Brest (SOMLIT-Brest), initiated within the French network for the monitoring of coastal environments (SOMLIT[3]). From 2008 to 2020, we performed weekly to bimonthly observations of carbonate system and ancillary physical and biogeochemical parameters at these northeast Atlantic Ocean coastal stations. The present study, which builds on the work of Salt et al. (2016) and Gac et al. (2020), aims to decipher, for the first time, trends and drivers of OA in NE Atlantic coastal waters based on long-term time series. In light of the relatively long duration of the study, we attempt to identify the main factors influencing the variability of the carbonate system from local [rivers, Net Ecosystem Production (NEP)] to large-scale [North Atlantic Oscillation (NAO) and Atlantic Multidecadal Variability (AMV)] processes.

STUDY AREA

This study focused on coastal waters of the English Channel and the Iroise Sea, located in one of the world's largest temperate continental margins, the North West European shelf. As part of SOMLIT, two sites (Roscoff and Brest, **Figure 1**) are sampled bimonthly since 2008 to monitor physical, chemical, and biological parameters, including carbonate system parameters. The region is characterized by low temperature ranges between winter and summer, by sustained wind throughout the year with frequent storms from fall to spring, and by heavy rainfall, with a maximum monthly mean rainfall during December (140 mm at Brest and 125 mm at Roscoff), causing significant discharges of fresh water from many rivers and estuaries (Tréguer et al., 2014). Large-scale hydro-climatic indices such as the NAO (Hurrell, 1995) and the AMV can significantly influence the climate regimes in the area. AMV has been linked for example with decadal variations in temperature and rainfall patterns (Sutton et al., 2018). The NAO produces large changes in surface air temperatures, storm-track position, and precipitation over the North Atlantic and is strongly related to changes in sea surface temperature (SST) at the Brest and Roscoff sites (Tréguer et al., 2014 and reference therein). Freshwater inputs release important nutrient stocks into the aquatic environment (Meybeck et al., 2006; Dürr et al., 2011; Tréguer and De La Rocha, 2013), fueling phytoplankton blooms (e.g., Del Amo et al., 1997; Beucher et al., 2004). In these ecosystems, nutrient inputs maintain sustained phytoplankton biomass during the summer.

SOMLIT-Brest is located in the Bay of Brest, a macrotidal estuary located in a semi-enclosed bay covering 180 km^2. The hydrology is controlled by exchanges of high salinity and relatively warm waters from the Atlantic Ocean and freshwater inputs from two main estuaries: the Aulne (annual mean discharge during the study period of $Q_{mean} = 24.0 \pm 24.4\ m^3\ s^{-1}$) and the Elorn ($Q_{mean} = 5.9 \pm 5.0\ m^3\ s^{-1}$). Samples were taken at a station near the coast (48°21′32″N; 4°33′07″W) characterized by a shallow water column (∼10 m), not sufficient to observe seasonal stratification due to intense semi-diurnal tidal streams, with a maximum tidal amplitude of 8 m.

The Roscoff stations are located about 55 km north east of Brest in the south of the Western English Channel (WEC), which is a pathway between the North Atlantic Drift and the North Sea. Two stations (a near-shore station SOMLIT-pier, 48°43′59″N; 3°58′58″W, and an offshore station SOMLIT-offshore, 48°46′49″N; 3°58′14″W) were sampled along the coastal gradient in the Roscoff area, which has freshwater inputs from two small rivers, the Penzé ($Q_{mean} = 2.8 \pm 2.7\ m^3\ s^{-1}$) and the Morlaix river ($Q_{mean} = 4.3 \pm 3.9\ m^3\ s^{-1}$). SOMLIT-pier is located near the coast (∼500 m) with a shallow water column (∼10 m), influenced by continental freshwater inputs and by a strong semi-diurnal tidal cycle, with a maximum tidal amplitude of 8 m. SOMLIT-offshore has a deeper water column (∼60 m), representative of the permanently well-mixed waters of the south of the WEC (Pingree and Griffiths, 1978). The distance between this station and the coast (3.5 km) limits the impact of rainwater and river inflow compared to the SOMLIT-pier station.

MATERIALS AND METHODS

Weekly and Bimonthly Measurements of the Long-Term Time Series

Environmental data were collected from 1998 to 2020, whereas carbonate parameters were sampled from July 2008 to December 2020 (see details below). At SOMLIT-Brest (January 1998–2020), sampling took place on a weekly basis at high tide slack. The two Roscoff stations, SOMLIT-offshore (January 1998–2020) and SOMLIT-pier (January 2000–2020), were sampled bimonthly during neap tides and at high tide slack. Sampling in Brest was carried out from the observation pier of Sainte-Anne-du-Portzic, while sampling in Roscoff took place aboard the *R/V Neomysis* research vessel. During each sampling event, SST measurements were obtained using a Seabird SBE19+, with a temperature accuracy of 0.005°C. Surface seawater (2 m depth at the Brest station and 1 m depth at the Roscoff station) was sampled using a 10-L Niskin bottle. Discrete sea surface salinity (SSS) was measured by storing seawater samples in glass bottles with a rubber seal with analysis conducted in the following months in a temperature-regulated room with a portasal Guidline Salinometer at the SHOM (Service Hydrologique et Océanographique de la Marine) with a precision of 0.002. Samples for dissolved oxygen (DO) measurements were stored in 280-ml brown glass bottles, analyzed after addition of 1.7 ml of Winkler reagent I and II, and kept in the dark in a water bath. DO concentrations were determined by the Winkler method using a potentiometric end-point determination with a Metrohm titrator. The estimated accuracy of this method is 0.2 μM (Carpenter, 1965). To evaluate the impact of non-thermodynamic processes on DO variations, the dissolved oxygen saturation (DO%) was calculated using the equations of Garcia and Gordon (1992) from SST, SSS, and DO values. Chlorophyll-*a* (Chl *a*) concentrations were obtained by filtration

[3]https://www.somlit.fr/

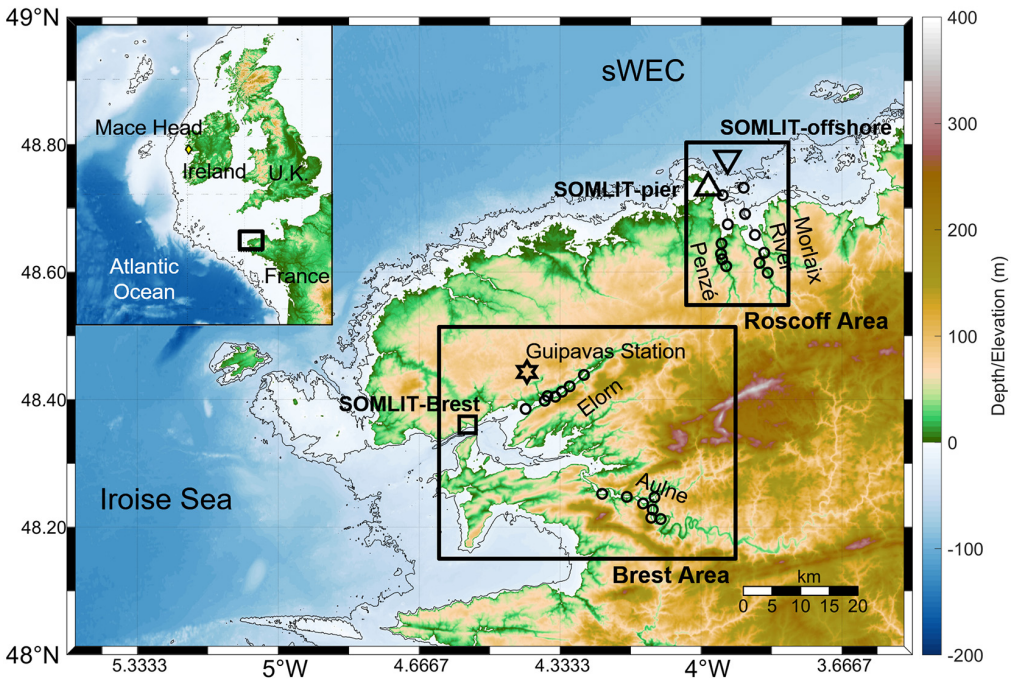


FIGURE 1 | Map, bathymetry, and topography of the study area in the southern Western English Channel (sWEC), with the two regions of study: the Brest region, with the SOMLIT-Brest station (black square), the Aulne and Elorn rivers; and the Roscoff region, with SOMLIT-pier (upward black triangle) and SOMLIT-offshore (downward black triangle) stations and the Penzé and Morlaix rivers. Black circles indicate the locations of sampling in the rivers and the black star the location of the Meteo France station ("Guipavas station") for wind speed data. Bathymetry contours show 20 and 50-m isobaths. (Top left) Map and bathymetry (200-m isobath) of the North Atlantic Ocean with the location of the Mace Head atmospheric station (yellow diamond); the black frame represents the zoom on the study area. Note that the color map (–6000 to 2000 m) is different from the main map.

of 500 ml of seawater through glass-fiber filters (Whatman GF/F) under 0.2 bar vacuum. After storage in plastic tubes at −20°C, Chl *a* was extracted using the EPA method (1997) with a 90% acetone solution for a few hours at 4°C. Chl *a* concentrations were determined using a Turner AU10 fluorometer. Nitrate, nitrite, dissolved silicate (DSi), and soluble reactive phosphate (SRP) concentrations were determined following the method of Aminot and Kérouel (2007) using an AA3 auto-analyzer (AXEFLOW) with accuracies of 0.05 μmol L^{-1} for nitrate and DSi and 0.01 μmol L^{-1} for SRP and nitrite concentrations.

For carbonate system parameters, TA and DIC measurements were performed from July 2008 to December 2017 at SOMLIT-Brest, from May 2009 to December 2017 at SOMLIT-offshore, and from July 2010 to December 2017 at SOMLIT-pier. Water samples were immediately poisoned with 50 μl of saturated $HgCl_2$. TA and DIC were determined at the SNAPO (Service National d'Analyse des Paramètres Océaniques) using potentiometric analysis following the method of Edmond (1970) and DOE (1994) with accuracies of 2.5 μmol kg^{-1} for both parameters (see Marrec et al., 2013 for details). A total of 412, 162, and 189 measurements of each parameter were obtained from samples from SOMLIT-Brest, SOMLIT-pier, and SOMLIT-offshore, respectively.

Dissolved inorganic carbon data for 2018–2020 were excluded since unexplained noise appeared among replicates, potentially linked to an extended period of conservations of the samples prior to analysis. Consequently, the SOMLIT-Brest dataset was completed with 72 weekly measurements of $pH_{in\ situ}$ performed from July 2019 to December 2020. The SOMLIT-pier and SOMLIT-offshore datasets were completed from January 2018 to December 2019 with 48 bi-monthly measurements of TA combined with 72 bi-monthly measurements of $pH_{in\ situ}$ from January 2018 to December 2020. For these specific periods, TA and pH were collected in 500-ml borosilicate glass bottles and poisoned with 50 μl of saturated $HgCl_2$. TA at SOMLIT-offshore was determined from approximately 51 g of weighed sample at 25°C using a potentiometric titration with 0.1 M HCl using a Titrino 847 plus Metrohm. The balance point was determined by the Gran method (Gran, 1952) according to the method of Haraldsson et al. (1997). The accuracy of this method is ± 2.1 μmol kg^{-1} (Millero, 2007) and was verified by Certified Reference Material (CRM 131) provided by A. Dickson (Scripps Institute of Oceanography, University of South California, San Diego, United States). pH was determined with an accuracy of 0.002 by spectrophotometry (Perin-Elmer Lambda 11) at a controlled temperature of 25°C with the method of Clayton and Byrne (1993) and corrected by Chierici et al. (1999), using the sulfonephthaleindiprotic indicator meta-CresolPurple (mCP).

The combination of SST, SSS, DIC, TA, DSi, and SRP was used as input parameters for the CO_2 chemical speciation model in the CO_{2sys} program (Matlab version by van Heuven et al., 2011,

based on calculation of Lewis and Wallace, 1998) to calculate the carbonate system before 2018. For calculation after 2018, SST, SSS, pH, and TA were used as input parameters. K1 and K2 constants were defined based on the last calculations of Waters et al. (2014) on the total pH scale, and the KSO_4 dissociation constant was based on Dickson (1990) and Uppstrom (1974). The calculated uncertainties were estimated at 0.6% for pH, 0.5% for DIC, and 14% for aragonite (Millero et al., 2007; McLaughlin et al., 2015). The average of pCO_2 uncertainties was close to the uncertainties estimated in Gac et al. (2020), with 18 µatm based on TA/DIC and 11 µatm based on TA/pH. In 2017, three carbonate parameters (pH, DIC, and TA) were collected at the same time at SOMLIT-offshore. Computed pCO_2(DIC/TA) and pCO_2(TA/pH) showed a robust relationship (1:1 slope, $r^2 = 0.90$; $n = 14$; $p < < 0.001$, RMSE = 8). Similarly, $pH_{in\ situ}$ and pH(TA/DIC) showed robust consistency (1:1 slope; $r^2 = 0.89$, $n = 14$; $p < < 0.001$, RMSE = 0.008) during that period, which would indicate that the time-series trends (Section "Analysis of Trends") were not affected by the change in variables.

Seasonal Measurements in Adjacent Rivers

Four seasonal cruises were performed in the Brest rivers (Aulne and Elorn) in February 2009 (winter), May 2009 (spring), July 2009 (summer), and November 2010 (winter). Surface seawater was sampled using a 10-L Niskin bottle, and SST, SSS, nutrient concentration, TA, and DIC were measured using the methods outlined above and detailed in Bozec et al. (2011). The Roscoff rivers (Penzé and Morlaix river) were sampled from the *R/V Neomysis* and *R/V Aurelia* on a monthly basis from February 2011 to November 2011 in the Penzé, completed with seven monthly cruises in the Penzé and Morlaix rivers from January 2019 to July 2019, and from two cruises in January and February 2020, using the same analytical methods. Six stations were sampled along the salinity gradient in the Morlaix and Penzé rivers, and seven stations were sampled in the Aulne and Elorn rivers (**Figure 1**). The upper stations in the Roscoff estuary presented salinity values below 5, and down to 0 in the Brest rivers. A total of 55 and 230 measurements of each parameter were obtained from Brest and Roscoff rivers, respectively.

Air–Sea CO_2 Exchanges

Atmospheric pCO_2 (pCO_2^{air}) was calculated from the atmospheric molar fraction of CO_2 (xCO_2) recorded at the Mace Head site (53°33′N 9°00′W, southern Ireland) of the RAMCES network (Observatory Network for Greenhouse gasses) and from the water vapor pressure (pH_2O) using the equations of Weiss and Price (1980). Atmospheric pressure and wind data were obtained from the Guipavas meteorological station (48°26′36′N, 4°24′42″W, Météo France) and fitted to the dataset using the monthly averages. Air–sea CO_2 fluxes (FCO_2, in mmol C m^{-2} day^{-1}, Equation 1) were determined from the difference of pCO_2 between surface seawater and air ($\delta pCO_2 = pCO_2 - pCO_2^{air}$), SST, SSS, wind speed, and atmospheric pressure.

$$FCO_2 = k \times \alpha \times \delta pCO_2 \quad (1)$$

Where k represents the gas transfer velocity (m s^{-1}) and α represents the solubility coefficient of CO_2 (mol atm^{-1} m^{-3}) calculated as in Weiss (1970). The exchange coefficient k (Equation 2) was calculated from the wind speeds with the updated algorithm of Wanninkhof (2014) appropriate for both regional and global flux estimates:

$$k = 0.251 \times u_{10}^2 \times \left(\frac{Sc}{660}\right)^{-0.5} \quad (2)$$

Where u_{10} represents the wind speed at 10 m height (m s^{-1}) and Sc denotes the Schmidt number at *in situ* SST.

Computation of the Thermal vs. Non-thermal Drivers of the pCO_2 Signal

The variability of sea surface pCO_2 induced by thermal and non-thermal processes was estimated using the equations of Takahashi et al. (1993, 2002), based on the well-constrained temperature dependence of pCO_2 (4.23% °C^{-1}) (Takahashi et al., 1993; Millero, 1995). The thermal (pCO_2^{therm}) and non-thermal ($pCO_2^{non-therm}$) influence on pCO_2 was determined as:

$$pCO_2^{therm} = pCO_{2,mean} \times e^{0.0423 \times (T_{obs} - T_{mean})} \quad (3a)$$

$$pCO_2^{non-therm} = pCO_{2,obs} \times e^{0.0423 \times (T_{mean} - T_{obs})} \quad (3b)$$

with annual mean values calculated from January 2008 to December 2017 at SOMLIT-Brest (T_{mean} = 13.3 ± 2.9°C, n = 493; $pCO_{2,mean}$ = 400 ± 56 µatm, n = 412), SOMLIT-pier (T_{mean} = 13.0 ± 2.45 °C, n = 245; $pCO_{2,mean}$ = 390 ± 68 µatm, n = 162), and SOMLIT-offshore (T_{mean} = 12.9 ± 2.2°C, n = 245; $pCO_{2,mean}$ = 412 ± 39 µatm, n = 189).

Determination of Processes Controlling DIC/pCO_2 Based on a 1-D Mass Budget Model

The influence of temperature, air–sea exchange, mixing, and biological activity on carbonate parameters was investigated based on the calculations developed in Xue et al. (2016) and adapted to our data as described in detail below. The calculations were based on the difference of SST, SSS, TA, DIC, pCO_2, SRP, and DSi at time n and time $n + 1$ during 8 annual cycles from January 2010 to December 2017 with a time increment at all sites based on monthly averages. The total pCO_2 and DIC changes from time n and $n + 1$ were induced by the combination of different processes explained in Equations 6, 7, and 8 and developed in the following subsections.

$$\triangle pCO_2 = (pCO_2)_{n+1} - (pCO_2)_n \quad (4)$$

$$\triangle pCO_2 = \triangle pCO_2^{therm} + \triangle pCO_2^{gas} + \triangle pCO_2^{mix} + \triangle pCO_2^{bio} + \triangle pCO_2^{non} \quad (5)$$

$$\triangle DIC = \triangle DIC^{gas} + \triangle DIC^{mix} + \triangle DIC^{bio} \quad (6)$$

Temperature Changes

The variability induced by thermal processes was estimated using the coefficient proposed by Takahashi et al. (1993) and verified by Millero (1995).

$$\triangle pCO_2^{them} = (pCO_2)_n \times e^{0.0423\times(SST_{(n+1)}-SST_n)} - (pCO_2)_n \quad (7)$$

Air–Sea Exchange

The effect of air–sea CO_2 (gas) exchange was first estimated on DIC, and subsequently on pCO_2 from DIC, TA, SSS, SST, SRP, and DSi using the CO_2SYS program (Section "Weekly and Bimonthly Measurements of the Long-term Time-Series"):

$$\triangle DIC^{gas} = -FCO_2 \times (t_{(n+1)} - t_n)/(\rho \times d) \quad (8a)$$

$$(DIC)^{gas}_{(n+1)} = (DIC)_n + \triangle DIC^{gas} \quad (8b)$$

$$\triangle pCO_2^{gas} = f\Big((DIC)^{gas}_{(n+1)}, TA_n, SSS_n, SST_n, (SRP)_n, (DSi)_n\Big)_{pCO_2(CO_2SYS)} - (pCO_2)_n \quad (8c)$$

where FCO_2 is the air–sea CO_2 flux (see Section "Air-sea CO2 exchanges"), $t_{(n+1)} - t_n$ is the number of days between two measurements, ρ is the seawater density (kg m^{-3}) calculated from the TEOS-10 calculations (McDougall et al., 2012), and d is the depth fixed at 10 m for comparable computations at the three stations.

Mixing

Mixing was attributed to the horizontal mixing (or lateral advection) induced by river inputs and Atlantic Ocean waters, while other processes such as evaporation and precipitation were neglected. The effect of mixing on TA and DIC was estimated based on the relationship between DIC and SSS, and between TA and SSS from the seasonal sampling in Brest and Roscoff rivers and coastal stations (**Figure 2**). These seasonal samplings were performed during typical years in terms of freshwater inputs and then SSS variability (**Figure 3**). The following equations were used to compute ΔDIC^{mix} and ΔTA^{mix} and then $(DIC)^{mix}_{(n+1)}$ and $(TA)^{mix}_{(n+1)}$, the predicted DIC and TA values at time $n+1$ due to the mixing:

$$\triangle DIC^{mix} = Slope_{DIC/SSS} \times (SSS_{(n+1)} - SSS_n) \quad (9a)$$

$$(DIC)^{mix}_{(n+1)} = (DIC)_n + \triangle DIC^{mix} \quad (9b)$$

$$\triangle TA^{mix} = Slope_{TA/SSS} \times (SSS_{(n+1)} - SSS_n) \quad (9c)$$

$$(TA)^{mix}_{(n+1)} = (TA)_n + \triangle TA^{mix} \quad (9d)$$

$Slope_{DIC/SSS}$ was estimated from the linear regression (r^2 = 0.99, n = 585 for Brest rivers and r^2 = 0.96, n = 683 for Roscoff rivers) between DIC and SSS (**Figure 2A**, 46.8 μmol kg^{-1} $uSSS^{-1}$ for Brest rivers and 41.3 μmol kg^{-1} $uSSS^{-1}$ for Roscoff rivers). $Slope_{TA/SSS}$ was estimated from the linear regression (r^2 = 0.98, n = 660 for Brest rivers and r^2 = 0.98, n = 660 for Roscoff rivers) between DIC and SSS (**Figure 2B**, 55.3 μmol kg^{-1} $uSSS^{-1}$ for Brest rivers and 49.5 μmol kg^{-1} $uSSS^{-1}$ for Roscoff rivers).

Based on these values, the effect of mixing on pCO_2 was computed using the following equation:

$$\triangle pCO_2^{mix} = f\Big((DIC)^{mix}_{(n+1)}, TA^{mix}_{(n+1)}, SSS_{(n+1)}, SST_n, (SRP)_n, (DSi)_n\Big)_{pCO_2(CO_2SYS)} - (pCO_2)_n \quad (9e)$$

The mixing term at SOMLIT-offshore was considered negligible because sampling always occurred at high tide slack when the influence of rivers did not modify SSS throughout the year.

Biological Processes

The remainder of DIC changes were assigned to biological processes, such as the effect of photosynthesis, respiration, degradation of organic matter, or calcification/dissolution of $CaCO_3$.

$$\triangle DIC^{bio} = \triangle DIC - (\triangle DIC^{gas} - \triangle DIC^{mix}) \quad (10a)$$

$$(DIC)^{bio}_{(n+1)} = (DIC)_n + \triangle DIC^{bio} \quad (10b)$$

$$\triangle pCO_2^{bio} = f\Big((DIC)^{bio}_{(n+1)}, TA_n, SSS_n, SST_n, (SRP)_n, (DSi)_n\Big)_{pCO_2(CO_2SYS)} - (pCO_2)_n \quad (10c)$$

Non-linear Term

$\triangle pCO_2^{non}$ is a non-linear term calculated from the difference between ΔpCO_2 and the sum of pCO_2 due to each process detailed above, considering that pCO_2 responses to SST or DIC changes were not linear [see Xue et al. (2016) for more details].

Net Ecosystem Production (NEP)

Net ecosystem production represents the difference between gross primary production (GPP) and ecosystem respiration (R). Positive NEP values indicate that the ecosystem is predominantly autotrophic; i.e., the production of organic matter is larger than its consumption. Negative NEP values indicate that the ecosystem is heterotrophic, with higher organic matter remineralization than production. NEP calculations are derived from the biological effect on ΔDIC following the equation:

$$NEP = -\triangle DIC^{bio} \times \rho \times d/(t_{(n+1)} - t_n) \quad (11)$$

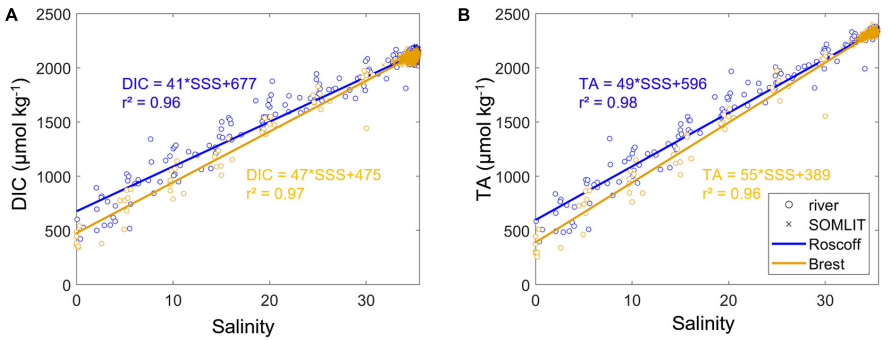


FIGURE 2 | Linear regressions between **(A)** dissolved inorganic carbon concentration (DIC, µmol kg^{-1}) and sea surface salinity (SSS), and **(B)** total alkalinity (TA, µmol kg^{-1}) vs. SSS based on the data collected at Penze/Morlaix rivers (blue circles) in 2010–2011 and 2019–2020 and Roscoff stations (SOMLIT-pier and SOMLIT-offshore, blue asterisks) from 2008 to 2019 and Elorn and Aulne rivers (orange circles) in 2009–2010 and SOMLIT-Brest (orange asterisks) from 2008 to 2019.

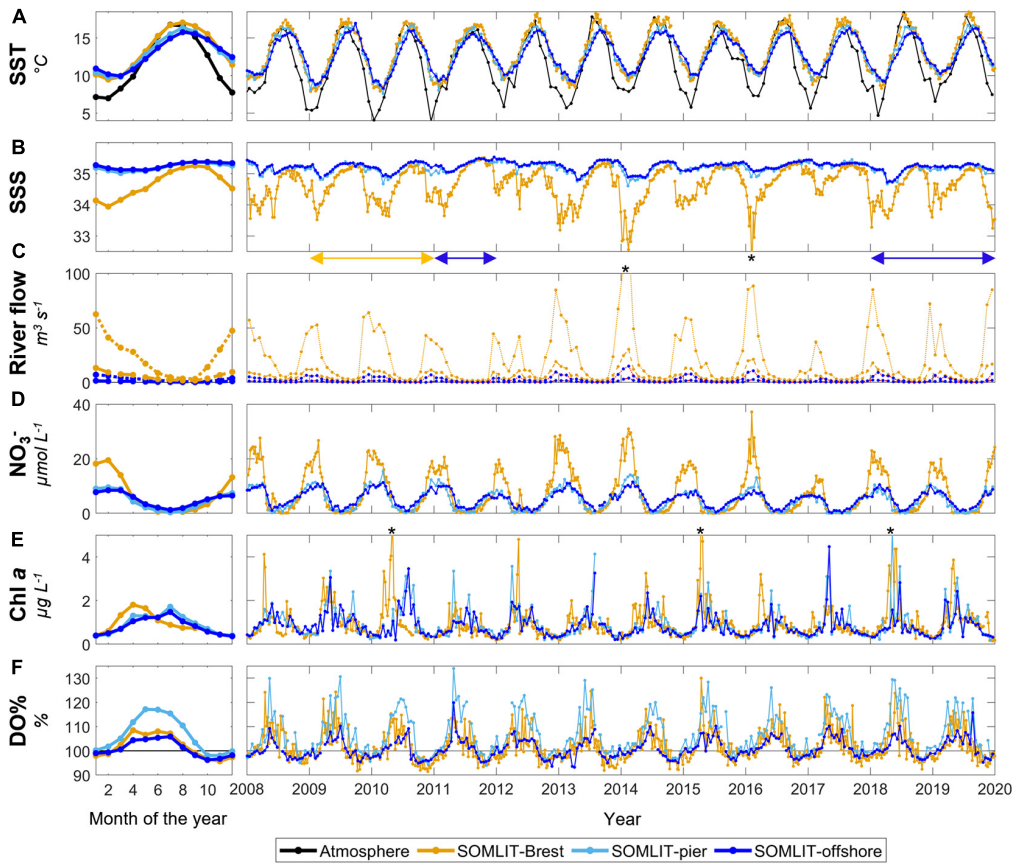


FIGURE 3 | Monthly mean climatology for **(A)** sea surface temperature (SST, °C), **(B)** sea surface salinity (SSS), **(C)** river flow (m^3 s^{-1}), **(D)** nitrate (µmol L^{-1}), **(E)** Chl *a* (µg L^{-1}), and **(F)** oxygen saturation (DO%, %) at SOMLIT-Brest (orange), SOMLIT-pier (light blue), and SOMLIT-offshore (dark blue), from January 2010 to December 2017, and the associated time series of weekly/bimonthly data from January 2008 to January 2020. **(C)** Brest river flow is shown in orange and Roscoff river flow is shown in blue. The black line represents the atmospheric temperature (°C). The monthly mean climatologies were computed based on complete years acquired from January 2010 to December 2017. Salinity values down to 32.5 and 31.7 (out of the figure range and indicated by black asterisks) were observed in February 2014 and February 2016, respectively. In February 2014, river flow values up to 130 m^3 s^{-1} were observed in the Aulne river (indicated by a black asterisk). Chl *a* concentrations of 5.9, 6.3, and 5.2 µg L^{-1} were observed in May 2010, April 2015, and May 2018 (indicated by a black asterisk), respectively. Blue double-arrows below the SSS plot represent the period of sampling in the Roscoff rivers, and the orange double-arrow represents the period of sampling of the Brest rivers.

Analysis of Trends

Climatologies were computed based on monthly means over the entire period of study. Data were detrended for seasonality by subtracting the respective monthly mean climatology computed for the study period to the time series (hereafter "monthly means"). The resulting residuals were analyzed using linear regressions to compute anomaly trends, called "monthly anomaly trend." This approach follows methods from Niu (2013) applied on seawater parameters by Tréguer et al. (2014) and Bates et al. (2014) to allow for comparisons of trends observed at different time-series stations. All analyses were performed with Matlab 2020a.

Deconvolution of $pH_{in\ situ}$ and pCO_2

The relative contributions of various drivers on carbonate system trends at Brest and Roscoff were identified based on the deconvolution of $pH_{in\ situ}$ and pCO_2 time series following the methods described in García-Ibáñez et al. (2016) and applied by Kapsenberg et al. (2017) on coastal time series. Equations 12 and 13 represent the changes in pH and pCO_2 linked to SST, SSS, TA, and DIC over time (t).

$$\frac{\mathrm{dpH}_{in-situ}}{\mathrm{dt}} = \frac{\partial \mathrm{pH}_{in-situ}}{\partial \mathrm{SST}}\frac{\mathrm{dSST}}{\mathrm{dt}} + \frac{\partial \mathrm{pH}_{in-situ}}{\partial \mathrm{SSS}}\frac{\mathrm{dSSS}}{\mathrm{dt}} + \frac{\partial \mathrm{pH}_{in-situ}}{\partial \mathrm{TA}}\frac{\mathrm{dTA}}{\mathrm{dt}} + \frac{\partial \mathrm{pH}_{in-situ}}{\partial \mathrm{DIC}}\frac{\mathrm{dDIC}}{\mathrm{dt}} \quad (12)$$

$$\frac{\mathrm{dpCO}_2}{\mathrm{dt}} = \frac{\partial \mathrm{pCO}_2}{\partial \mathrm{SST}}\frac{\mathrm{dSST}}{\mathrm{dt}} + \frac{\partial \mathrm{pCO}_2}{\partial \mathrm{SSS}}\frac{\mathrm{dSSS}}{\mathrm{dt}} + \frac{\partial \mathrm{pCO}_2}{\partial \mathrm{TA}}\frac{\mathrm{dTA}}{\mathrm{dt}} + \frac{\partial \mathrm{pCO}_2}{\partial \mathrm{DIC}}\frac{\mathrm{dDIC}}{\mathrm{dt}} \quad (13)$$

Here, $\frac{\partial \mathrm{pH}_{in-situ}}{\partial variable}\frac{\mathrm{d}variable}{\mathrm{dt}}$ and $\frac{\partial \mathrm{pCO}_2}{\partial variable}\frac{\mathrm{d}variable}{\mathrm{dt}}$ represent the slope contribution of a changing "*variable*" to the estimated change in $pH_{in-situ}$ or pCO_2, respectively. The contribution of each "*variable*" corresponding to SST, SSS, TA, and DIC. The sensitivity of $pH_{in-situ}$ and pCO_2 to "*variable*" ($\frac{\partial \mathrm{pH}_{in-situ}}{\partial variable}$ and $\frac{\partial \mathrm{pCO}_2}{\partial variable}$) was estimated by calculating $pH_{in-situ}$ and pCO_2 using true values of the "*variable*" and holding the other three variables constant (mean values of the 2008–2017 time series) and regressing to the "*variable*." Sensitivities ($\frac{\partial \mathrm{pH}_{in-situ}}{\partial variable}$ and $\frac{\partial \mathrm{pCO}_2}{\partial variable}$) were then multiplied by the monthly anomaly trend of the "*variable*."

Hydroclimatic Indices

The impact of two main large-scale hydroclimatic indices, the NAO and AMV, on environmental parameters recorded in the study area was investigated to evaluate the climatic context of our observations.

The NAO was calculated by and retrieved from the National Weather Service (NOAA[4]). NAO is defined as the distribution of atmospheric mass between the Arctic and the subtropical Atlantic and swings from positive (NAO+) to negative (NAO−), producing large changes in surface air temperatures, storm-track position, and precipitation over the North Atlantic and western Europe. Seasonal variations of NAO are controlled by non-linear processes: wave-mean flux intensities and air–sea interactions (Peng et al., 2003). In this study, we compared the winter period to the measured parameters (December–January–February, called here wNAO), when the amplitude was the highest.

The AMV, also known as the Atlantic Multidecadal Oscillation (AMO), was calculated by and retrieved from the Physical Science Laboratory (NOAA[5]). The AMV describes the pattern of SST in the North Atlantic (Kerr, 2000; Enfield et al., 2001), which can either represent decades of warm or cool anomalies at the basin scale, relative to the global mean.

RESULTS

Hydrographical Properties

Sea surface temperature seasonality at the three sampling sites was characterized by a limited amplitude between winter minimum and summer maximum values (**Figure 3A**), a typical feature for temperate oceanic regions. The seasonal SST signal was more pronounced in Brest (7.8°C) than in Roscoff (6–6.6°C), with mean minimum values of 9.5°C in Brest and 9.8°C in Roscoff in winter, and mean maximum values in summer of 17.1°C, 16.4°C, and 15.8°C, in SOMLIT-Brest, SOMLIT-pier, and SOMLIT-offshore, respectively. SST increased from February in Brest, one month earlier than in Roscoff. A similar pattern was observed for SST lowering in late summer, with an earlier decrease observed in Brest than in Roscoff. Mean temperatures at SOMLIT-pier were slightly lower during winter than at SOMLIT-offshore and slightly higher during summer.

The seasonal variability of SSS was much more pronounced in Brest than in Roscoff (**Figure 3B**), highlighting the stronger influence of freshwater inputs in the Bay of Brest than in the coastal sWEC. The lowest SSS values (down to 33.1) were observed in winter in Brest, while in Roscoff, SSS reached minimum values (<35.1) in spring. The highest SSS values were observed in summer at both sites, with mean values of 34.9 in Brest and 35.2 in Roscoff. Salinity at SOMLIT-pier was 0.1 lower than at SOMLIT-offshore along the year because of the proximity of the SOMLIT-pier station to the coast. The impact of riverine freshwater inputs on SSS was evident for Aulne and Elorn river flows (**Figure 3C**). During the winters of 2013/2014 and 2015/2016, Aulne and Elorn river flows were particularly high, with values > 80 $m^3\ s^{-1}$ and > 20 $m^3\ s^{-1}$, when the lowest SSS values were recorded at the Brest site. In Roscoff, the two major rivers flowing into the area were characterized by much lower flows (<15 $m^3\ s^{-1}$), with limited effects on SSS.

Biogeochemical Seasonality

The higher influence of riverine freshwater inputs in Brest than in Roscoff led to higher maximum winter values of nitrate concentration. Winter nitrate concentrations in Brest reached

[4]https://www.cpc.ncep.noaa.gov/products/precip/CWlink/pna/nao.shtml

[5]https://psl.noaa.gov/data/timeseries/AMO/

values higher than 20 μmol L^{-1}, two times higher than in Roscoff (**Figure 3D**). Nitrate concentrations started to decrease from February in Brest, 1 month earlier than in Roscoff. Most of the winter nitrate stock was consumed from April in Brest, characterized by a sharp decrease. From April to August, nitrate concentrations remained below 3 μmol L^{-1} and were depleted in summer in the Bay of Brest. Slightly higher nitrate concentrations were observed at SOMLIT-pier than at SOMLIT-offshore during winter. In Roscoff, the winter stock of nitrate decreased more slowly than in Brest, and surface waters were never nitrate depleted during summer at SOMLIT-offshore. Undetectable nitrate concentration were recorded at SOMLIT-pier in some years.

Brest and Roscoff were characterized by a different seasonality in terms of phytoplankton production, as represented by Chl *a* concentrations (**Figure 3E**). Spring phytoplankton blooms occurred in April in Brest, with mean Chl *a* concentration $>$ 1.5 μg L^{-1}. In Roscoff, Chl *a* concentrations started to increase in spring and reached their highest values ($\sim$1.5 μg L^{-1}) from May to July. In fall and winter, Chl *a* concentrations remained $<$ 0.4 μg L^{-1}. Chl *a* concentrations at SOMLIT-pier and SOMLIT-offshore followed a similar dynamic with similar values. Important interannual variability in terms of bloom timing and intensity was observed at both sites. In 2010, an intense spring phytoplankton bloom (Chl *a* up to 6 μg L^{-1}) was observed in early spring in Brest, but not in Roscoff, where Chl *a* concentrations remained abnormally high ($>$2 μg L^{-1}) all summer in that year. On the contrary, intense spring blooms were observed at both Brest and Roscoff in 2015, with values $>$ 2.0 μg L^{-1} during most of the productive period.

Surface waters were oversaturated in O_2 from March to August–September at all study sites (**Figure 3F**), while O_2 undersaturation down to 95% was observed in fall. Winter values were close to atmospheric equilibrium. The highest DO% values (up to 120%) were recorded at SOMLIT-pier. The spring increase of DO% was observed from March in Brest and at SOMLIT-pier, while at SOMLIT-offshore, DO% increased 1 month after with lower maximum DO% values. The end of summer decrease in DO% occurred in August in Brest and at SOMLIT-offshore. At SOMLIT-pier, DO% values $>$ 100% were recorded up to September. Chl *a* concentrations and DO% followed similar trends for SOMILT-Brest and SOMLIT-offshore. The overall seasonal variability in terms of Chl *a* concentrations was similar at SOMLIT-offshore and SOMLIT-pier, but the signal in terms of DO% was different, with higher DO% and longer DO% values $>$ 100% at SOMLIT-pier than at SOMLIT-offshore.

Seasonality of the Carbonate System

Total alkalinity did not exhibit marked seasonality at the Roscoff stations, remaining constant all year at around 2335 μmol kg^{-1} (**Figure 4A**). At SOMLIT-Brest, TA was $<$ 2300 μmol kg^{-1} during the winter and was in a similar range to the Roscoff values during the summer. The lowest TA values in Brest were observed during the winters of 2013/2014 and 2015/2016, periods characterized by high riverine freshwater input and low SSS. As shown on **Figure 2B**, the rivers flowing in the vicinity of the study sites were characterized by low TA end-member values (400–600 μmol kg^{-1}). The lower TA values observed in Brest than in Roscoff were related to the stronger influence of riverine freshwater inputs, which was confirmed by the SSS-normalization of TA (**Figure 4E**).

Dissolved inorganic carbon concentrations showed a clear seasonality at the three stations (**Figure 4B**) with maximum values observed in fall in Brest ($>$2100 μmol kg^{-1}) and in winter in Roscoff ($>$2150 μmol kg^{-1}). In Brest, minimum DIC values down to 2050 μmol kg^{-1} were observed during spring, while DIC reached minimum values during summer in Roscoff. DIC values at SOMLIT-offshore and SOMLIT-pier were in a similar range during winter. From early spring to the end of summer, lower DIC concentrations were recorded at SOMLIT-pier than at SOMLIT-offshore. As for TA, the rivers in the study area were characterized by low DIC values (**Figure 2A**). The stronger influence of riverine inputs in Brest than in Roscoff might be the cause of low winter DIC values observed in Brest, which were confirmed when the effect of SSS on DIC was accounted for (**Figure 4F**).

The seasonal variability of pH was more pronounced at SOMLIT-pier and SOMLIT-Brest, with amplitudes $>$ 0.15, than at SOMLIT-offshore, where the pH amplitude was $<$ 0.10 (**Figure 4C**). Maximum pH values were observed during the spring ($>$8.10), while values $<$ 8.00 were recorded during winter. Like for Chl *a* concentrations, pH values reached their maximum spring values 1 month earlier in Brest than in Roscoff. Maximum pH values were attained in April in Brest and in May in Roscoff. After reaching their spring maxima, pH values decreased during the summer down to their minimum fall values for each site. $pH_{25°C}$ was $<$ 0.2 units (**Figure 4D**) compared to the $pH_{in\ situ}$. $pH_{25°C}$ followed a different seasonality close to that of SST, with values $>$ 7.9 during summer and close to 7.8 during winter.

Ω_{Cal} and Ω_{Arag} were always $>$ 1 and followed a pronounced seasonal variability with higher values during spring and summer than during fall and winter (**Figure 4G**). In spring, the maximum values of Ω_{Cal} at SOMLIT-Brest and SOMLIT-pier were $>$ 4, and $\sim$3.8 in SOMLIT-offshore. Maximum Ω_{Arag} values observed in SOMLIT-Brest and SOMLIT-pier were $>$ 2.5 and $\sim$2.5 in SOMLIT-offshore. The Ω_{Cal} and Ω_{Arag} were $\sim$3.2 and $\sim$2 during the winter for each station.

Seasonality of pCO_2 and FCO_2

The seasonal pCO_2 signal in the near-shore stations SOMLIT-Brest and SOMLIT-pier were characterized by a similar mean amplitude of $\sim$170 μatm (**Figure 4H**). Seasonality was less pronounced at SOMLIT-offshore, where, on an annual scale, the mean pCO_2 signal varied from 350 to 480 μatm. Maximum pCO_2 values were observed during fall, in October in Brest and in November in Roscoff. During winter, surface water pCO_2 decreased down to the atmospheric equilibrium, from January in Brest and in March–April in Roscoff. pCO_2 values were minimal in April in Brest ($\sim$310 μatm), in May at SOMLIT-offshore ($\sim$360 μatm), and in June at SOMLIT-pier ($\sim$310 μatm). Sea surface pCO_2 remained below the atmospheric equilibrium for 6 months at SOMLIT-pier (up to August), 5 months in Brest (up to June), and only 4 months at SOMLIT-offshore (up to July). On

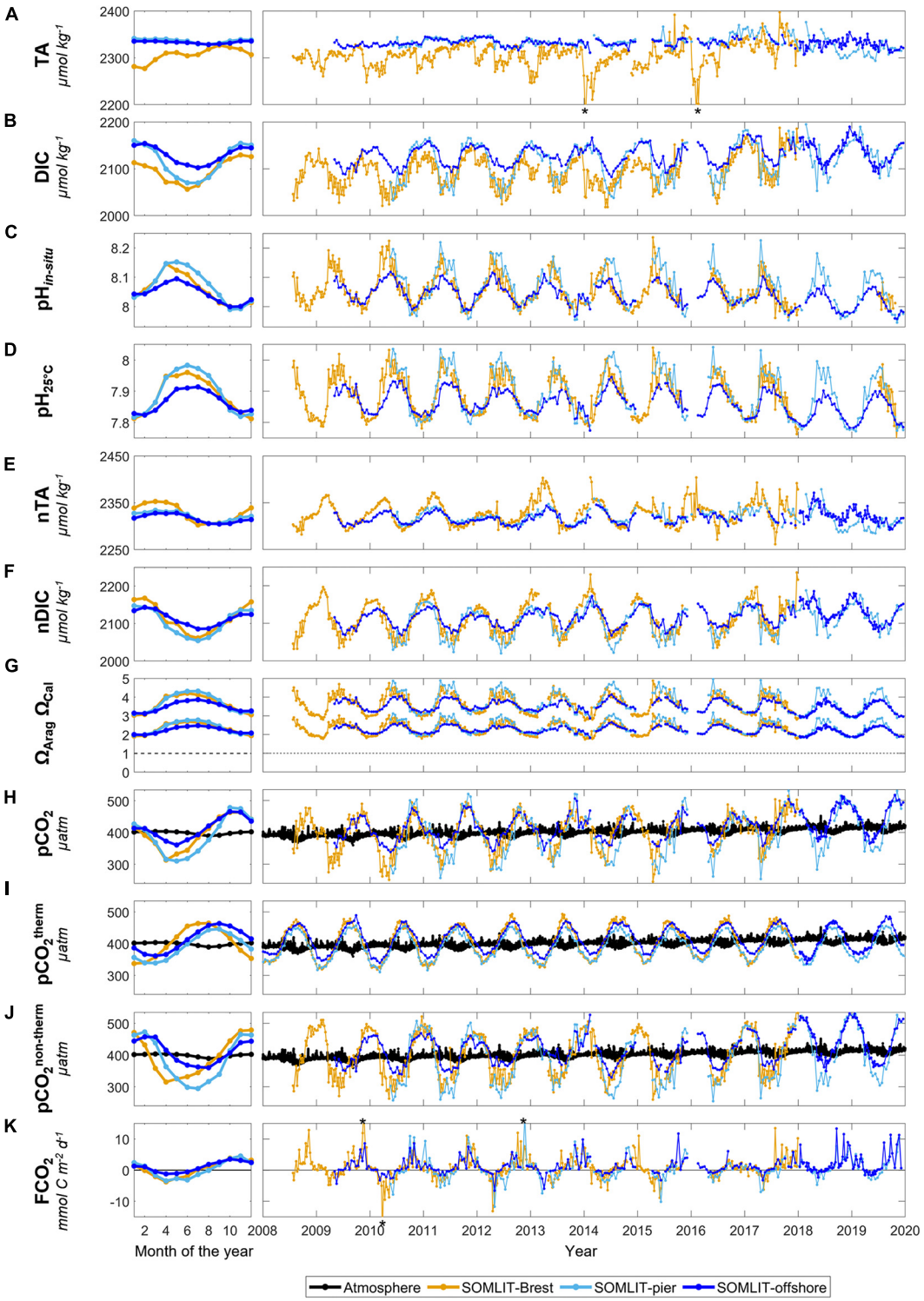


FIGURE 4 | Monthly mean climatology for **(A)** total alkalinity (TA, µmol kg^{-1}), **(B)** dissolved inorganic carbon (DIC, µmol kg^{-1}), **(C)** $pH_{in\ situ}$, **(D)** $pH_{25°C}$, **(E)** SSS normalized TA (nTA, µmol kg^{-1}), **(F)** SSS normalized DIC (nDIC, µmol kg^{-1}), **(G)** Ω_{Arag} and Ω_{Cal}, **(H)** pCO_2 (µatm), **(I)** pCO_2^{therm} (µatm), **(J)** $pCO_2^{non-therm}$ (µatm), and **(K)** FCO_2 (mmol C m^{-2} day^{-1}) at SOMLIT-Brest (orange), SOMLIT-pier (light blue), and SOMLIT-offshore (dark blue), from January 2010 to December 2017, and the associated time series of weekly/bimonthly data from January 2008 to January 2020. The black line represents atmospheric pCO_2 (µatm). TA values down to 2194 and 2181 µmol kg^{-1} (out of figure range and indicated by black asterisks) were observed in January 2014 and February 2016, respectively. FCO_2 values of 18.9, –20.82, and 17.3 mmol C m^{-2} day^{-1} were recorded in November 2009, March 2010, and November 2012 (indicated by a black asterisk), respectively. nTA and nDIC computations were based on Friis et al. (2003) and the SSS vs. TA/DIC relationships from **Figure 2**.

a seasonal scale, pCO_2 and pH exhibited clear opposite trends at each site, in terms of both timing and intensity.

The influence of the SST on pCO_2 variability is represented by the pCO_2^{therm} signal (**Figure 4I**). Minimum pCO_2^{therm} values were observed during winter when low SST favored CO_2 solubility in surface waters. Lower pCO_2^{therm} values were observed in the nearshore stations at SOMLIT-Brest and at SOMLIT-pier, than at SOMLIT-offshore. The seasonality of the pCO_2^{therm} signal was similar between sites in terms of timing, with pCO_2^{therm} values below the atmospheric equilibrium from January to April, and above the atmospheric equilibrium from May to November.

The influence of non-thermodynamic processes on pCO_2 variability is represented by the $pCO_2^{non-therm}$ signal (**Figure 4J**). $pCO_2^{non-therm}$ values were high and above atmospheric pCO_2 during fall and winter, with higher values at SOMLIT-Brest and SOMLIT-pier than at SOMLIT-offshore. The seasonal variability was similar at SOMLIT-Brest and SOMLIT-pier, with a higher amplitude ($\sim$200 µatm) than at SOMLIT-offshore ($<$100 µatm). The seasonality of $pCO_2^{non-therm}$ followed an opposite dynamic to DO% and Chl *a*, with low values observed during the biologically productive period (spring and summer) when DO% and Chl *a* were high. The overall features of pCO_2^{therm} and $pCO_2^{non-term}$ seasonality indicated that non-thermal processes counteracted the effect of thermal processes on surface water pCO_2 during winter and summer.

The seasonal dynamic of FCO_2 at the three sites was characterized by a net sink of atmospheric CO_2 in spring and a net source of CO_2 to the atmosphere in fall (**Figure 4J**). FCO_2 varied between -20 mmol C m^{-2} day^{-1} and $+18$ mmol C m^{-2} day^{-1} during the year. SOMLIT-Brest acted as a sink of atmospheric CO_2 from February, while in Roscoff, negative FCO_2 values were observed 1 month later. The average seasonal amplitudes were similar at SOMLIT-Brest and SOMLIT-pier, but lower at SOMLIT-offshore due to less pronounced atmospheric CO_2 sinks during spring. SOMLIT-offshore acted as a sink of atmospheric CO_2 for 4 months (March–June), SOMLIT-Brest was an atmospheric CO_2 sink for 5 months (February–June), and at SOMLIT-pier surface waters were a sink of CO_2 for 6 months (March–August). Annually, all sites were weak sources of CO_2 to the atmosphere except for 2010 and 2015 at SOMLIT-Brest (**Table 1**) (see Section "Comparison Between Ecosystems of the Processes Controlling the Carbonate System" for details).

Trends Over the 2008–2017 Period

Trends were studied over the 2008–2017 period during which time the DIC/TA and ancillary datasets were robust enough to separate the main drivers of pCO_2 and pH. From the first day of sampling to December 2017, SST increased significantly (p-values < 0.001) with observed positive trends of $+0.08 \pm 0.01$°C $year^{-1}$ at SOMLIT-Brest, $+0.06 \pm 0.02$°C $year^{-1}$ at SOMLIT-pier, and $+0.07 \pm 0.01$°C $year^{-1}$ at SOMLIT-offshore (**Figures 5A**, **6**). SST increased at a similar rate as the atmospheric temperature ($+0.07 \pm 0.04$°C $year^{-1}$, p-value < 0.05). No significant trends were observed for SSS (**Figures 5B**, **6**) or for river flow (data not shown).

Significant reductions in nitrate concentration were recorded at all sites with rates of -0.19 ± 0.04, -0.21 ± 0.03, and -0.32 ± 0.06 µmol L^{-1} $year^{-1}$ at SOMLIT-pier, SOMLIT-offshore, and SOMLIT-Brest, respectively (**Figures 5C**, **6**). Monthly Chl *a* anomalies remained stable over these 10 years (**Figures 5D**, **6**). DO% significantly (p-values < 0.01) increased (0.18 ± 0.05 % $year^{-1}$) at SOMLIT-offshore, but not at SOMLIT-pier and SOMLIT-Brest (**Figure 6**).

Monthly TA and DIC anomalies were characterized by significant positive trends (p-values < 0.001). TA increased by 0.49 ± 0.20 and 1.64 ± 0.32 µmol kg^{-1} $year^{-1}$ at SOMLIT-offshore and at SOMLIT-pier, respectively, and by 2.21 ± 0.39 µmol kg^{-1} $year^{-1}$ at SOMLIT-Brest (**Figures 5E**, **6**). DIC increased by 1.93 ± 0.28 and 2.61 ± 0.62 µmol kg^{-1} $year^{-1}$ at SOMLIT-offshore and at SOMLIT-pier, respectively, and by 2.98 ± 0.39 µmol kg^{-1} $year^{-1}$ at SOMLIT-Brest (**Figures 5F**, **6**). Positive TA and DIC trends were associated with significant increases (p-values < 0.001) of seawater pCO_2 ranging from $+2.95 \pm 1.04$ to $+3.52 \pm 0.7$ µatm $year^{-1}$ (**Figures 5G**, **6**), higher than the rise of atmospheric pCO_2 ($+2.27 \pm 0.08$ µatm $year^{-1}$). The highest pCO_2 positive trend was observed in Brest. pCO_2^{therm} increased at all stations with values similar at SOMLIT-Brest and at SOMLIT-offshore (1.21 µatm $year^{-1}$) and 0.96 ± 0.26 µatm $year^{-1}$ at SOMLIT-pier. Reduction of surface seawater pH was observed at all three sites with significant pH decrease of 0.0029 ± 0.0005, 0.0028 ± 0.0010, and 0.0027 ± 0.0004 $year^{-1}$ (p-values < 0.001) at SOMLIT-Brest, SOMLIT-Pier, and SOMLIT-offshore (**Figures 5H**, **6**).

DISCUSSION

Comparison Between Ecosystems of the Processes Controlling the Carbonate System

The seasonal patterns of pCO_2 and air–sea CO_2 fluxes in the WEC have been extensively investigated (Borges and Frankignoulle, 2003; Padin et al., 2007; Dumousseaud et al., 2010; Litt et al., 2010; Kitidis et al., 2012; Marrec et al., 2013, 2014) but never based on large carbonate system datasets such as in the present study, with almost a decade of discrete DIC/TA data at three contrasted coastal sites. The seasonal pCO_2 signal has conventionally been divided into "thermal" (pCO_2^{therm}) and "non-thermal" ($pCO_2^{non-therm}$) signals to disentangle thermal from biological (OM production/remineralization) processes impacting the pCO_2 seasonal dynamics in the WEC (Marrec et al., 2013, 2014, Gac et al., 2020) or in the Bay of Brest (Bozec et al., 2011). However, in such nearshore ecosystems, the carbonate system can be affected by various other processes, such as estuarine inputs, mixing, air–sea CO_2 fluxes, calcification/dissolution of $CaCO_3$, or pelagic/benthic coupling (Salt et al., 2016; Chen and Hu, 2019; **Figure 7**). The unprecedented TA/DIC dataset collected in this study over a relatively long period, and concomitantly at three different sites, allowed further evaluation of the drivers of spatial and interannual variability of the carbonate system. A simple

TABLE 1 | Seasonal and annual means ± standard error (SE) of FCO_2 and NEP (in mol C m^{-2} $year^{-1}$) at SOMLIT-Brest, SOMLIT-pier, and SOMLIT-offshore from 2009 to 2017.

		Season	2009			2010			2011			2012			2013			2014			2015			2016			2017			2010–2017		
			Mean	±	***SE***	***Mean***	±	***SE***	***Mean***	±	***SE***	***Mean***	±	***SE***	***Mean***	±	***SE***	***Mean***	±	***SE***	***Mean***	±	***SE***	***Mean***	±	***SE***	***Mean***	±	***SE***	***Mean***	±	***SE***
FCO_2 (mol m^{-2} $year^{-1}$)	SOMLIT-Brest	Winter	0.53	±	0.25	0.02	±	0.20	0.78	±	0.51	0.37	±	0.27	0.78	±	0.42	0.90	±	0.59	0.62	±	0.55	0.28	±	0.00	0.62	±	0.55	0.57	±	0.14
		Spring	*−0.67*	±	*0.11*	*−2.08*	±	*0.38*	*−0.79*	±	*0.06*	*−1.37*	±	*0.66*	*−1.23*	±	*0.00*	*−0.62*	±	*0.30*	*−0.79*	±	*0.34*	*−0.44*	±	*0.00*	*−0.41*	±	*0.36*	*−0.99*	±	*0.16*
		Summer	0.30	±	0.35	*−0.25*	±	*0.33*	*−0.06*	±	*0.14*	0.18	±	0.32	*−0.05*	±	*0.38*	*−0.13*	±	*0.39*	*−0.57*	±	*0.81*	*−0.24*	±	*0.27*	0.49	±	0.43	*−0.08*	±	*0.14*
		Fall	2.23	±	0.95	1.28	±	0.34	1.46	±	0.35	1.56	±	0.53	1.03	±	0.20	0.85	±	0.24	0.48	±	0.16	0.60	±	0.12	1.25	±	0.13	1.06	±	0.11
		Annual	**0.60**	±	**0.39**	***−0.26***	±	***0.39***	**0.35**	±	**0.29**	**0.19**	±	**0.37**	**0.40**	±	**0.26**	**0.25**	±	**0.26**	***−0.13***	±	***0.29***	**0.11**	±	**0.15**	**0.49**	±	**0.25**	**0.18**	±	**0.10**
	SOMLIT-pier	Winter		-			-		1.13	±	0.23	0.44	±	0.30	0.85	±	0.53	0.87	±	0.26	1.93	±	0.00	0.44	±	0.00	0.62	±	0.17	0.79	±	0.12
		Spring		-			-		*−0.97*	±	*0.28*	*−1.10*	±	*0.50*	*−1.21*	±	*0.54*	*−0.63*	±	*0.32*	*−0.78*	±	*0.14*	*−0.87*	±	*0.05*	*−0.85*	±	*0.52*	*−0.96*	±	*0.12*
		Summer		-		*−0.67*	±	*0.47*	*−0.43*	±	*0.26*	*−0.71*	±	*0.58*	*−0.57*	±	*0.39*	*−0.76*	±	*0.21*	*−0.77*	±	*0.70*	*−0.30*	±	*0.27*	*−0.20*	±	*0.07*	*−0.55*	±	*0.13*
		Fall		-		1.28	±	0.83	1.46	±	0.73	1.56	±	0.84	1.03	±	0.41	0.85	±	0.57	0.48	±	0.55	0.60	±	0.15	1.25	±	0.06	1.06	±	0.19
		Annual		-			-		**0.42**	±	**0.40**	**0.05**	±	**0.40**	**0.04**	±	**0.35**	**0.14**	±	**0.30**	**0.04**	±	**0.37**	***−0.08***	±	***0.18***	**0.18**	±	**0.26**	**0.11**	±	**0.12**
	SOMLIT-offshore	Winter		-		0.05	±	0.02	0.55	±	0.10	0.39	±	0.19	0.93	±	0.65	0.97	±	0.34	1.44	±	0.00	0.78	±	0.00	0.49	±	0.21	0.63	±	0.12
		Spring		-		*−0.67*	±	*0.07*	*−0.22*	±	*0.11*	*−0.46*	±	*0.31*	*−0.68*	±	*0.33*	*−0.24*	±	*0.13*	*−0.27*	±	*0.04*	0.04	±	0.17	*−0.12*	±	*0.31*	*−0.33*	±	*0.08*
		Summer	0.32	±	0.16	0.08	±	0.37	0.10	±	0.15	0.73	±	0.29	0.18	±	0.13	0.01	±	0.25	*−0.15*	±	0.56	0.05	±	0.15	0.34	±	0.28	0.17	±	0.10
		Fall	1.43	±	0.39	1.04	±	0.58	1.59	±	0.46	0.93	±	0.48	1.49	±	0.72	0.86	±	0.32	1.35	±	0.43	1.00	±	0.60	1.06	±	0.15	1.18	±	0.16
		Annual		-		**0.12**	±	**0.23**	**0.50**	±	**0.23**	**0.35**	±	**0.21**	**0.48**	±	**0.33**	**0.40**	±	**0.20**	**0.50**	±	**0.30**	**0.44**	±	**0.20**	**0.38**	±	**0.16**	**0.39**	±	**0.08**
NEP (mol m^{-2} $year^{-1}$)	SOMLIT-Brest	Winter	*−0.51*	±	*1.68*	1.84	±	1.91	*−0.71*	±	*1.34*	0.07	±	1.20	*−1.17*	±	*0.32*	*−0.75*	±	*1.85*	0.70	±	0.34	*−2.86*	±	*0.00*	*−1.40*	±	*1.02*	*−0.33*	±	*0.46*
		Spring	4.39	±	0.70	4.20	±	0.39	3.91	±	1.66	3.44	±	1.11	5.64	±	0.00	4.17	±	0.05	4.06	±	2.42	5.31	±	0.00	4.19	±	1.96	4.14	±	0.44
		Summer	*−1.65*	±	*0.88*	*−1.02*	±	*1.07*	*−0.75*	±	*1.32*	*−1.56*	±	*1.89*	0.00	±	2.24	*−0.81*	±	*0.09*	*−1.45*	±	*1.11*	*−1.70*	±	*0.21*	*−2.83*	±	*2.36*	*−1.27*	±	*0.48*
		Fall	*−4.50*	±	*0.49*	*−3.98*	±	*0.17*	*−3.09*	±	*0.78*	*−3.47*	±	*0.26*	*−3.54*	±	*0.94*	*−3.76*	±	*1.09*	*−3.57*	±	*3.89*	*−2.40*	±	*0.09*	*−2.68*	±	*1.13*	*−3.30*	±	*0.38*
		Annual	***−0.57***	±	***0.00***	**0.26**	±	**1.18**	***−0.16***	±	***1.06***	***−0.38***	±	***0.99***	***−0.81***	±	***0.93***	***−0.29***	±	***1.09***	**0.21**	±	**1.05**	***−1.23***	±	***0.78***	***−0.68***	±	***0.92***	***−0.35***	±	***0.34***
	SOMLIT-pier	Winter		-			-		0.38	±	1.37	0.35	±	1.10	*−0.88*	±	*2.22*	*−1.72*	±	*0.36*		-		*−2.54*	±	*0.00*	*−0.21*	±	*1.08*	*−0.56*	±	*0.43*
		Spring		-			-		3.59	±	1.86	3.88	±	1.27	3.05	±	1.90	4.73	±	1.05	0.59	±	2.75	1.57	±	1.54	3.49	±	1.67	3.33	±	0.56
		Summer		-		*−1.02*	±	*1.64*	*−1.76*	±	*2.72*	*−0.91*	±	*1.39*	*−0.16*	±	*1.04*	*−0.13*	±	*2.09*	1.13	±	1.38	*−0.98*	±	*2.06*	*−0.79*	±	*1.45*	*−0.58*	±	*0.55*
		Fall		-		*−4.42*	±	*1.68*	*−2.70*	±	*0.53*	*−3.91*	±	*1.18*	*−2.32*	±	*1.24*	*−3.80*	±	*0.76*	*−3.72*	±	*1.75*	*−2.21*	±	*0.94*	*−2.32*	±	*1.89*	*−3.17*	±	*0.43*
		Annual		-			-		***−0.12***	±	***1.06***	***−0.15***	±	***0.99***	***−0.08***	±	***0.93***	***−0.23***	±	***1.09***	***−0.82***	±	***1.05***	***−0.99***	±	***0.78***	**0.04**	±	**0.92**	***−0.39***	±	***0.34***
	SOMLIT-offshore	Winter		-		0.07	±	0.02	*−0.14*	±	*0.10*	0.00	±	0.19	*−1.09*	±	*0.65*	*−1.51*	±	*0.34*		-		*−1.21*	±	*0.00*	*−0.37*	±	*0.21*	*−0.58*	±	*0.12*
		Spring		-		2.14	±	0.07	1.93	±	0.11	1.96	±	0.31	1.41	±	0.33	2.21	±	0.13	0.55	±	0.04	1.85	±	0.17	1.82	±	0.31	1.78	±	0.08
		Summer	0.05	±	0.16	*−0.71*	±	*0.37*	*−1.12*	±	*0.15*	*−1.06*	±	*0.29*	*−0.12*	±	*0.13*	*−0.91*	±	*0.25*	0.41	±	0.56	*−1.02*	±	*0.15*	*−1.12*	±	*0.28*	*−0.71*	±	*0.10*
		Fall	*−2.84*	±	*0.39*	*−2.49*	±	*0.58*	*−2.24*	±	*0.46*	*−2.75*	±	*0.48*	*−2.21*	±	*0.72*	*−1.78*	±	*0.32*	*−2.45*	±	*0.43*	*−2.29*	±	*0.60*	*−0.29*	±	*0.15*	*−2.11*	±	*0.16*
		Annual		-		***−0.25***	±	***0.60***	***−0.39***	±	***0.59***	***−0.26***	±	***0.57***	***−0.50***	±	***0.53***	***−0.50***	±	***0.61***	***−0.63***	±	***0.84***	***−0.62***	±	***0.58***	**0.04**	±	**0.65**	***−0.38***	±	***0.21***

Annual means are represented in bold, negative means are in italic.

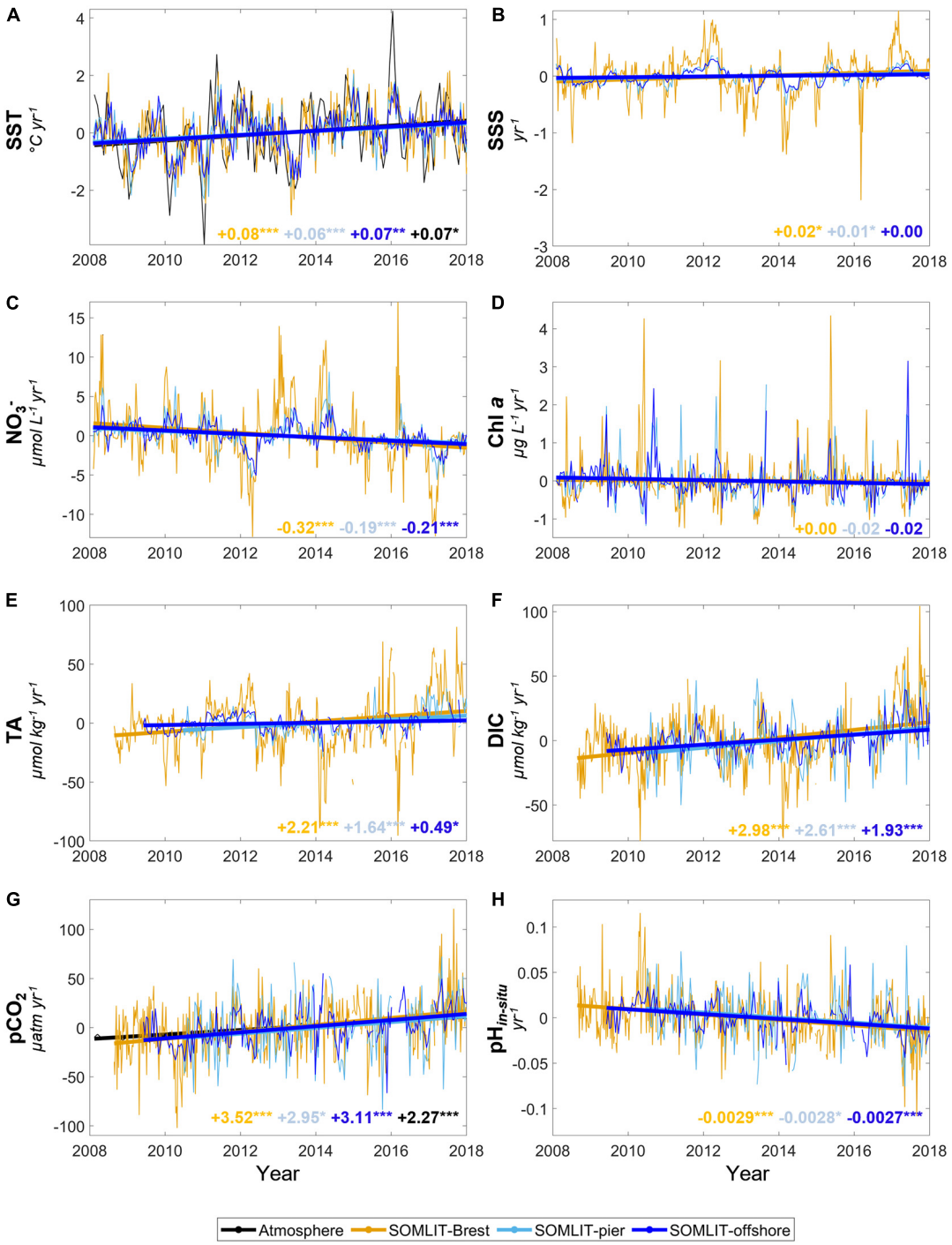


FIGURE 5 | Trends of monthly anomalies of **(A)** SST (°C year^{-1}), **(B)** SSS (year^{-1}), **(C)** nitrate (µmol L^{-1} year^{-1}), **(D)** Chl *a* (µg L^{-1} year^{-1}), **(E)** TA (µmol kg^{-1} year^{-1}), **(F)** DIC (µmol kg^{-1} year^{-1}), **(G)** pCO_2 (µatm year^{-1}), and **(H)** $pH_{in\ situ}$ (year^{-1}) at SOMLIT-Brest (orange), SOMLIT-pier (light blue), and SOMLIT-offshore (dark blue) for January 2008 to December 2017 (see Section "Weekly and Bimonthly Measurements of the Long-term Time-Series" for details on starting dates of sampling). The black lines **(A,G)** represent the monthly anomaly of atmospheric temperature (°C year^{-1}) and pCO_2^{atm} (µatm year^{-1}). The asterisks represent the *p*-values: ****p*-value < 0.001, ***p*-value < 0.01, **p*-value < 0.05, and no asterisk indicates non-significant trends.

comparison of the DIC/TA relationship at the three sites over the 2010–2017 period revealed a high heterogeneity of the carbonate system between nearshore and offshore waters within a limited geographical region (**Figure 7**). These background concentrations condition the control on FCO_2 (Humphreys et al., 2018) and the response or buffering of the ecosystem to various

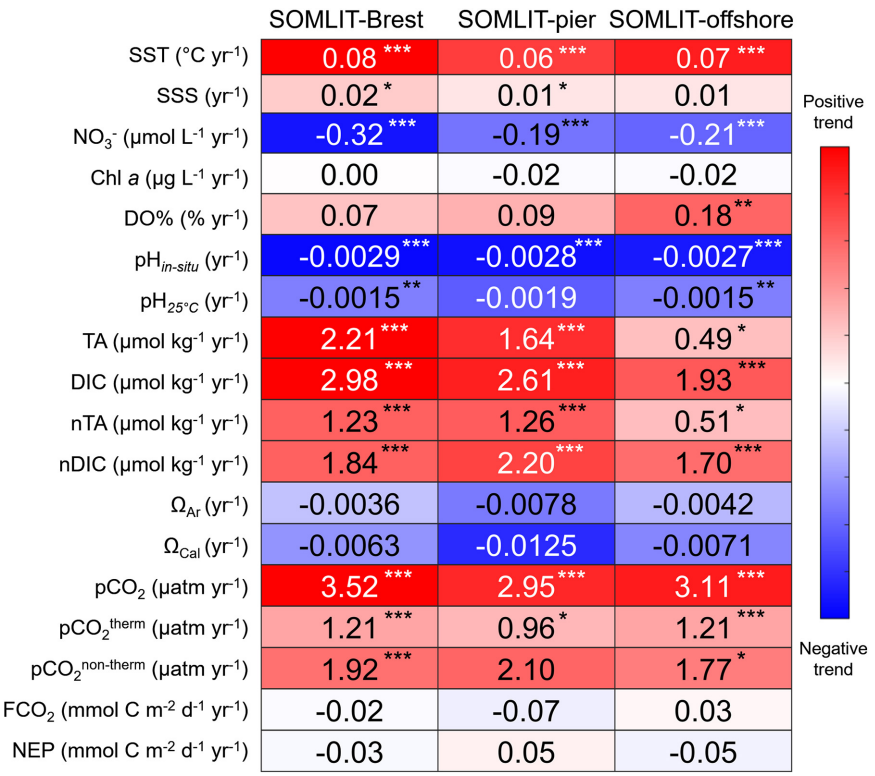


FIGURE 6 | Heatmap of the trends of monthly anomalies of the parameters collected at the three SOMLIT stations for the January 2008 to December 2017 period (see Section "Weekly and Bimonthly Measurements of the Long-term Time-Series" for details on sampling dates). Red represents a positive trend, blue denotes a negative trend, and white indicates no trend, with the maximum and minimum attributed based on the maximum and the minimum of the trends of each parameter. The color bar values of $pH_{25°C}$, nTA, nDIC, pCO_2^{therm}, and $pCO_2^{non-therm}$ were attributed by the color bar of $pH_{in\ situ}$, TA, DIC, and pCO_2, respectively. Asterisks represent *p*-values: ***p-value < 0.001, **p-value < 0.01, *p-value < 0.05, and missing asterisk indicates non-significant trends.

biogeochemical processes (Middelburg et al., 2020). **Figure 7** also shows the influence of the dominant drivers and stoichiometry on DIC and TA, indicating complex interactions in these coastal ecosystems. A straightforward SSS-normalization of DIC and TA (**Figures 4**, **7**) revealed a stronger impact of mixing on DIC and TA in the Bay of Brest than in WEC ecosystems. We adapted the study of Xue et al. (2016) (Section "Determination of Processes Controlling DIC/pCO_2 Based on a 1-D Mass Budget Model") to construct a 1-D DIC/pCO_2 model to quantify the physical (mixing, air–sea exchange) and biological (NEP) drivers of the carbonate system. This model is well suited for considering freshwater inputs in addition to thermal and non-thermal drivers. Factors driving monthly DIC and pCO_2 variability at the three study sites are represented in **Figure 8**. While the conclusions derived from the 1-D model are in general agreement with those derived from the simple $pCO_2^{therm}/pCO_2^{non-therm}$ separation, they also illustrate how various processes enhance or cancel each other out. Note that the impact of each factor is represented by monthly ΔDIC and ΔpCO_2.

Over a full annual cycle, mixing processes had a relatively larger contribution in the Bay of Brest compared to SOMLIT-pier and SOMLIT-offshore. Riverine inputs were characteristic of non-limestone watersheds, with low DIC and low TA end-members, as also observed in coastal and shelf waters around Ireland (McGrath et al., 2016) and in Liverpool Bay (Hydes and Hartman, 2012). These riverine inputs induced decreases of DIC and pCO_2 in fall and winter with maxima of 19 µmol kg^{-1} and 5 µatm, respectively, at SOMLIT-Brest. As mentioned in Sections "Hydrographical Properties" and "Seasonality of the Carbonate System," the winters of 2013/2014 and 2015/2016 were characterized by large freshwater input responsible for large drawdowns of TA in the bay. Computation based on our model estimated that the contribution of the mixing term on DIC was three to four times higher in November 2013 compared to the annual average, highlighting the strong interannual variability driven by freshwater inputs. It is worth noting that for the same period, the mixing term on DIC at SOMLIT-pier was also four times stronger, reaching −14 µmol kg^{-1} compared to the standard mean of −3 µmol kg^{-1} observed over the period (data not shown). Mixing effects were still substantial in the Bay of Brest during early spring, with increased DIC/TA due to the larger contribution of Atlantic surface waters with higher DIC/TA and reduced riverine inputs. Similar observations were made at SOMLIT-pier and SOMLIT-offshore with increasing SSS during spring.

During spring, biological processes controlled the DIC/pCO_2 signal at all three sites as previously observed (Marrec, 2014; Salt et al., 2016; Gac et al., 2020). This period was characterized

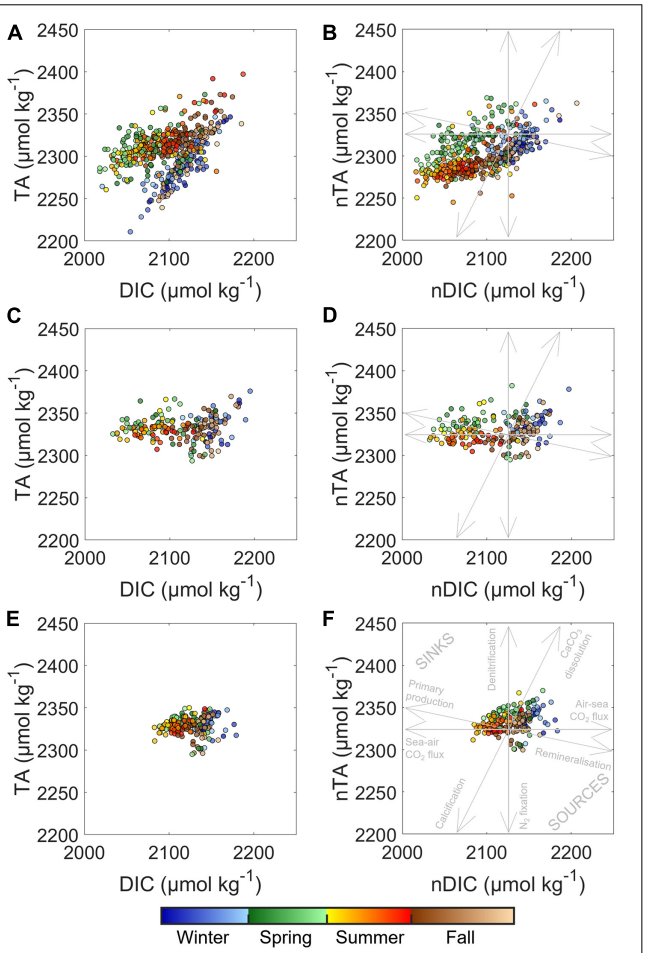


FIGURE 7 | DIC (µmol kg^{-1}) vs. TA (µmol kg^{-1}) and nDIC (µmol kg^{-1}) vs. nTA (µmol kg^{-1}) at **(A,B)** SOMLIT-Brest, **(C,D)** SOMLIT-pier, and **(E,F)** SOMLIT-offshore with the **(F)** dominant annual processes affecting the carbonate system and their stoichiometric influence on nDIC and nTA.

by DO% > 100%, high Chl *a* (**Figure 3E**), and DIC/TA ratios following the OM production stoichiometric ratio (**Figure 7**). We estimated mean DIC uptakes of 30–45 µmol kg^{-1} in nearshore ecosystems and 15–20 µmol kg^{-1} offshore with concomitant uptake of pCO_2 of 60–80 and 36 µatm, respectively. This biological uptake was counterbalanced by mixing in the Bay of Brest, but more significantly by air-to-sea fluxes for DIC/pCO_2 and thermodynamic effect for pCO_2 at all three sites. In March 2010 and 2015, exceptional phytoplankton blooms were responsible for an extra DIC uptake 20% to 25% higher than mean annual uptake rates. The competing importance of biological vs. thermodynamics on pCO_2 continued during early summer with both signals representing 40% of the variability, while air-to-sea fluxes closed the budget (**Figure 8**). Starting in July, OM remineralization overtook OM production processes, as revealed by the increase of DIC and $pCO_2^{non-therm}$ at all three sites, while DO% decreased. At the same time, thermodynamic effects (for pCO_2) and sea-to-air fluxes (for DIC and pCO_2) tended to compensate the release of inorganic carbon due to OM remineralization, representing 20% to 30% of the pCO_2 signal, respectively (**Figure 8**).

An enhanced contribution of mixing occurred in early fall in the bay of Brest as mentioned above. Freshwater inputs with low DIC, combined with sea-to-air CO_2 fluxes and cooling of surface seawater, all acted to decrease pCO_2 in the same proportion as the pCO_2 and DIC releases by OM remineralization processes. Similar observations for the fall period were made in the Roscoff ecosystems and continued in early winter, with January marking the transition to another annual cycle. Full characterization and quantification of processes controlling the carbonate system in highly dynamic and contrasted coastal ecosystems relies on long-term time series (Borges et al., 2008; Bauer et al., 2013; Fennel et al., 2019). Without taking into consideration the inherent interannual variability at each site, such characterization can be incomplete (Borges et al., 2008). Extreme values recorded in this study, together with the long duration, strengthen our understanding of the physical and biogeochemical processes driving the carbonate system at these coastal sites.

As mentioned in Section "Study Area," the water column was well-mixed throughout the year at the three coastal stations with an average depth of 10 m for SOMLIT-pier and SOMLIT-Brest and 60 m for SOMLIT-offshore. For the latter, the relatively deep water column and the limited amount of light reaching the seafloor might limit the contribution of the benthic compartment to the pelagic signal observed at the surface. Conversely, in the two shallow nearshore ecosystems, the benthic compartment may exert a strong control on the carbonate signal with high OM production/remineralization and/or $CaCO_3$ dissolution/precipitation characteristic of benthic communities in various coastal environments (Hammond et al., 1999; Cai et al., 2000; Forja et al., 2004; Martin et al., 2007; Waldbusser and Salisbury, 2014; Oliveira et al., 2018). These two nearshore stations were characterized by different benthic communities with maerl (coralline red algae) beds in the bay of Brest (e.g., Martin et al., 2007; Longphuirt et al., 2007; Lejart and Hily, 2011) and seagrass and macroalgae beds at SOMLIT-pier (Ouisse et al., 2011; Bordeyne et al., 2017). The latter sustained large production/remineralization of OM (Migné et al., 2005; Golléty et al., 2008) with a limited impact of calcification processes, whereas Martin et al. (2006, 2007) showed that intense benthic calcification occurred in the bay of Brest during spring and summer, with dissolution the rest of the year, which exert a control on the carbonate system. Our model did not take into account the impact of the $CaCO_3$ precipitation/dissolution. Salt et al. (2016) estimated that 10% of DIC/TA signals during spring and fall were due to $CaCO_3$ precipitation and dissolution, respectively. During summer, OM production is sufficiently high to mask the effect of calcification, while during winter, sustained freshwater input with low DIC/TA tend to mask dissolution of $CaCO_3$ (Salt et al., 2016). Our model potentially resulted in a minor overestimation of DIC uptake by OM production in spring and an underestimation of the contribution of OM degradation during fall. However, the 1-D model remained robust for identifying the main drivers throughout the year. At SOMLIT-pier, the production/dissolution of $CaCO_3$ was

likely negligible, with biological signals on DIC/pCO_2 most likely due to the combined effect of benthic and pelagic OM production/remineralization (Gac et al., 2020), both of which are included in the model.

Seasonal and annual NEP (**Table 1** and **Figure 9**) estimates were computed based on modeled DIC budgets with FCO_2 correction, providing reliable estimates of the metabolic rates of ecosystems (Borges et al., 2008; Staeher et al., 2012). In the nearshore ecosystems, both benthic and pelagic compartments contributed to NEP estimates, while pelagic processes can reasonably be considered as the major NEP drivers at the SOMLIT-offshore station. Over the study period, the amplitude of NEP per surface area was two times higher in nearshore shallow waters (10 mol C m^{-2} $year^{-1}$) than in offshore deeper waters (5 mol C m^{-2} $year^{-1}$) (**Figure 9**) as previously observed in estuarine plumes (Borges et al., 2008) or tidal wetlands (Herrmann et al., 2015; Najiar et al., 2018) vs. shelf waters. From summer to winter, all of the study sites were characterized by negative NEP values; i.e., the ecosystems were heterotrophic. During early spring, positive NEP values indicate that all ecosystems were autotrophic. NEP mirrored monthly FCO_2 (**Figure 9**), except during the transition from spring to summer in nearshore ecosystems when OM remineralization in the benthic compartment could overturn the system to heterotrophic, while pCO_2 values of the water column were still below CO_2 atmospheric equilibrium (Salt et al., 2016). This transition occurred 1 month earlier in the Bay of Brest than at SOMLIT-Pier. At SOMLIT-offshore, the seasonal trophic state of the ecosystem correlated with the direction of the fluxes. **Table 1** shows that all three ecosystems were very close to trophic and atmospheric equilibrium on an annual scale, which led to interannual variability in terms of ecosystem trophic status and sink/source of CO_2 from year to year.

On an annual scale, SOMLIT-Brest waters could either be weakly heterotrophic or autotrophic depending on the year. The close relationship found between NEP and FCO_2 (**Figure 9D**) suggested that amid the numerous drivers of the carbonate system described above, NEP, and more particularly spring NEP, controlled the direction of FCO_2. The massive blooms recorded in spring 2010 and 2015, characterized by high Chl *a* values (**Figure 3**), were sufficient to turn the ecosystem into an annual sink of atmospheric CO_2 (-0.26 and -0.13 mol C m^{-2} $year^{-1}$, respectively) compared to the average value of $+0.18 \pm 0.10$ mol C m^{-2} $year^{-1}$ over the 2010–2017 period. The latter estimate was similar to recent estimations for the 2008–2015 period of $+0.14 \pm 0.2$ mol C m^{-2} $year^{-1}$ (Salt et al., 2016). Similar interannual variability in carbonate system dynamics and FCO_2 directions was observed in the South Atlantic Bight (SAB) by Reimer et al. (2017a) and amplified by continental and riverine inputs in the Gulf of Maine (Vandemark et al., 2011) or off the coast of Georgia, United States (Xue et al., 2016).

More pronounced and constant heterotrophic features were observed at SOMLIT-pier and SOMLIT-offshore with mean negative (or close to zero) NEP values with an average value of -0.39 mol C m^{-2} $year^{-1}$ from 2010 to 2017. As suggested by the significant correlation ($r^2 = 0.66$, p-value $<< 0.05$, $n = 36$ at SOMLIT-Brest; $r^2 = 0.57$, p-value $<< 0.05$, $n = 29$ at SOMLIT-pier; and $r^2 = 0.73$ p-value $<< 0.05$, $n = 33$ at SOMLIT-offshore, based on the seasonal means of **Table 1**) between NEP and FCO_2, SOMLIT-pier and SOMLIT-offshore were weak sources of CO_2 to the atmosphere of $+0.11 \pm 0.12$ mol m^{-2} $year^{-1}$ and of $+0.40 \pm 0.08$ mol m^{-2} $year^{-1}$ over the 8-year period, respectively. These FCO_2 estimations confirmed the nearshore/offshore gradient observed for the 2015–2019 period with values of $+0.37$ mol C m^{-2} $year^{-1}$ and $+0.65$ mol C m^{-2} $year^{-1}$ based on HF data (Gac et al., 2020) and were within the range of larger scale estimations for the sWEC of $+0.53$ mol C m^{-2} $year^{-1}$ (Marrec, 2014).

Deconvolution of Carbonate System Trends During the 2008–2017 Period

Long-term time series of carbonate parameters in coastal ecosystems remain scarce but are essential to assess their evolution under climate change. Time-series based on at least two parameters of the carbonate system are essential to fully understand the processes driving the observed trends. In this study, the DIC/TA dataset revealed a significant increase in DIC concomitant with a somewhat unexpected increase of TA at the two nearshore stations and relatively stable TA at SOMLIT-offshore during the study period (**Figure 5**). Recent observations based on similar DIC/TA datasets also revealed an increase in TA for the 2007–2015 period, albeit in very different ecosystems at the coastal Point B site in the Mediterranean Sea (Kapsenberg et al., 2017) and in the North Atlantic Subpolar Gyre (Leseurre et al., 2020). In our study, similarly, to the observations made at point B and contrary to the North Atlantic Subpolar Gyre, the increase in TA was concomitant with a significant increase in pCO_2 of 3.52 ± 0.47, 2.95 ± 1.04, and 3.11 ± 0.49 µatm $year^{-1}$ and decrease in pH of -0.0029 ± 0.0005, -0.0028 ± 0.0010, and -0.0027 ± 0.0004 $year^{-1}$ at SOMLIT-Brest, SOMLIT-pier, and SOMLIT-offshore, respectively (**Figure 5**).

The deconvolution model (Section "Analysis of Trends") made it possible to approximate the effect of increasing atmospheric temperature, as well as the increase in DIC exerted by the forcing of atmospheric CO_2, on pCO_2/pH trends. The observed variations in DIC/TA were associated with sea surface warming of 0.08 ± 0.01°C $year^{-1}$, 0.06 ± 0.02°C $year^{-1}$, and 0.07 ± 0.01°C $year^{-1}$ at SOMLIT-Brest, SOMLIT-pier, and SOMLIT-offshore, respectively. Based on the theoretical relationship between SST and pCO_2 of 0.0423% $°C^{-1}$ (Takahashi et al., 1993), these SST increases resulted in a pCO_2 increase of 1.21 ± 0.21, 0.96 ± 0.26, and 1.21 ± 0.24 µatm $year^{-1}$ over the study period, respectively (**Figure 6**). These pCO_2^{therm} trends were consistent with the slopes related to SST obtained from the deconvolution model for these three stations (**Table 2**). Similarly, the differences between the trends of $pH_{in\ situ}$ and $pH_{25°C}$ (**Figure 6**) were close to the values obtained for the contribution of SST to $pH_{in\ situ}$ trends based on the deconvolution model. These observations confirmed that the deconvolution model correctly estimated the impact of warming surface waters on the increase of pCO_2 and the decrease of $pH_{in\ situ}$ observed during the study period. The contributions of SST to the observed trends of both pCO_2 and $pH_{in\ situ}$ varied from 26 to 31% at

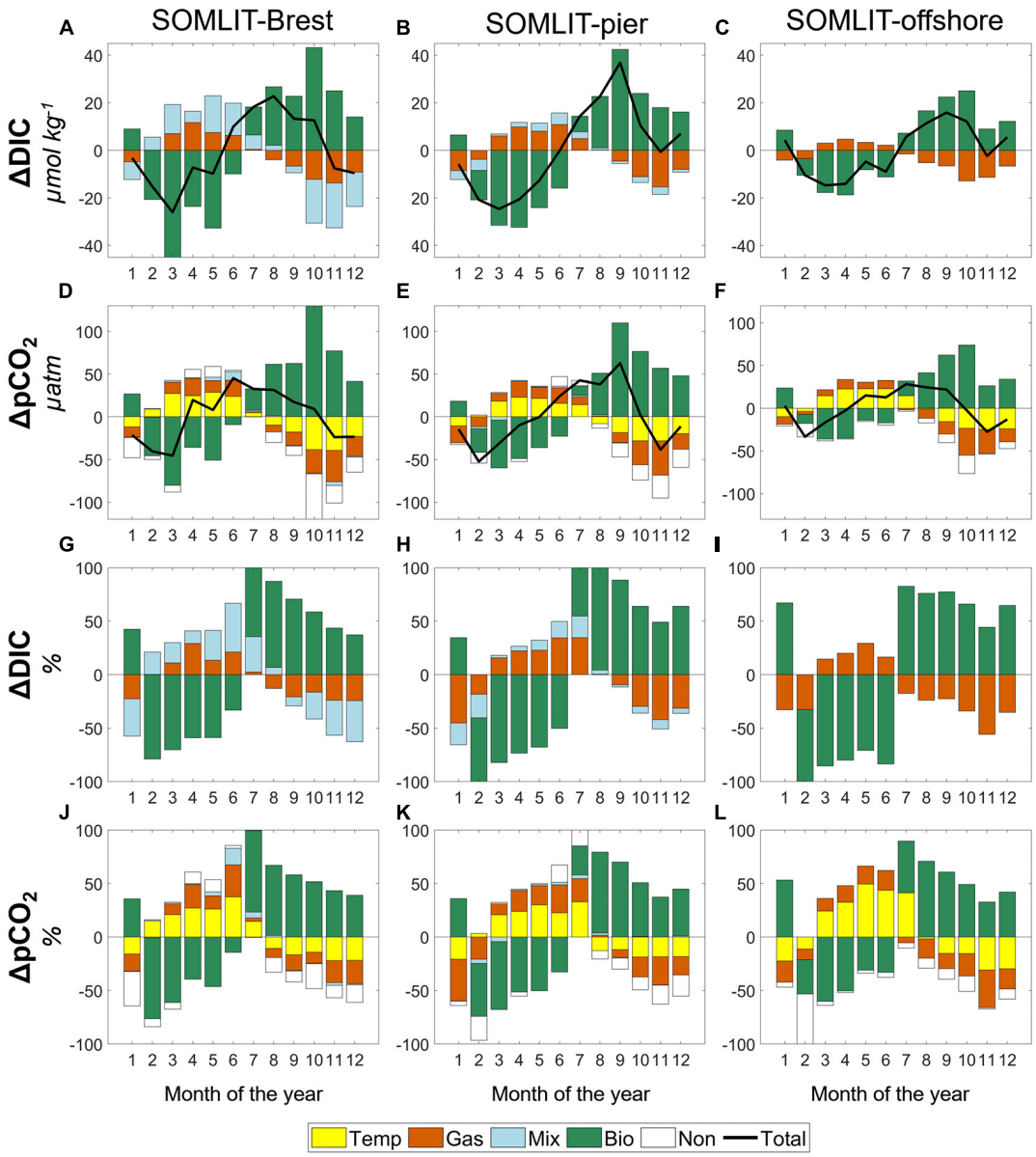


FIGURE 8 | (Top) Monthly means and (bottom) relative importance (%) of DIC (μmol kg^{-1}) and pCO_2 (μatm) changes due to thermodynamics (Δx^{tem}, in yellow), air–sea exchanges (Δx^{gas}, in vermillion), mixing (Δx^{mix}, in light blue), and biological activity (Δx^{bio}, in sea green) at **(A,D,G,J)** SOMLIT-Brest, **(B,E,H,K)** SOMLIT-pier, and **(C,F,I,L)** SOMLIT-offshore. Δx is the difference of pCO_2 or DIC between two consecutive months over the January 2010 to December 2017 period. Positive (or negative) values denote the increase (or decrease) between two consecutive months (see Section "Determination of Processes Controlling DIC/pCO_2 Based on a 1-D Mass Budget Model" for details on calculations).

the Roscoff stations and was 35%–37% at SOMLIT-Brest. These contributions related to the increase in temperature were similar to the observations made by Kapsenberg et al. (2017) in the Mediterranean Sea for pCO_2^{therm} (+1.19 μatm $year^{-1}$ for surface waters) with similar trends of SST (+0.07°C $year^{-1}$, period 2007–2015).

The sum of the contributions of SST, SSS, TA, and DIC to the trends of pCO_2 and $pH_{in\ situ}$ based on the deconvolution model was similar to the observed trends of these parameters at the nearshore stations, which further confirmed the robustness of the method for these stations (**Table 2**). At SOMLIT-offshore, the aggregated trends were slightly overestimated but still near the range of error of the method. The increase in DIC exerted by the forcing of atmospheric CO_2 was partly compensated by the increase in TA (which has a buffering effect on OA and is not directly impacted by addition of anthropogenic CO_2 to seawater). Using the pCO_2 deconvolution model, we can sum the contribution of TA and DIC to pCO_2 to assess the relative contribution of ΔDIC to ΔpCO_2 that is unrelated to changes in DIC due to TA increase (Kapsenberg et al., 2017). The

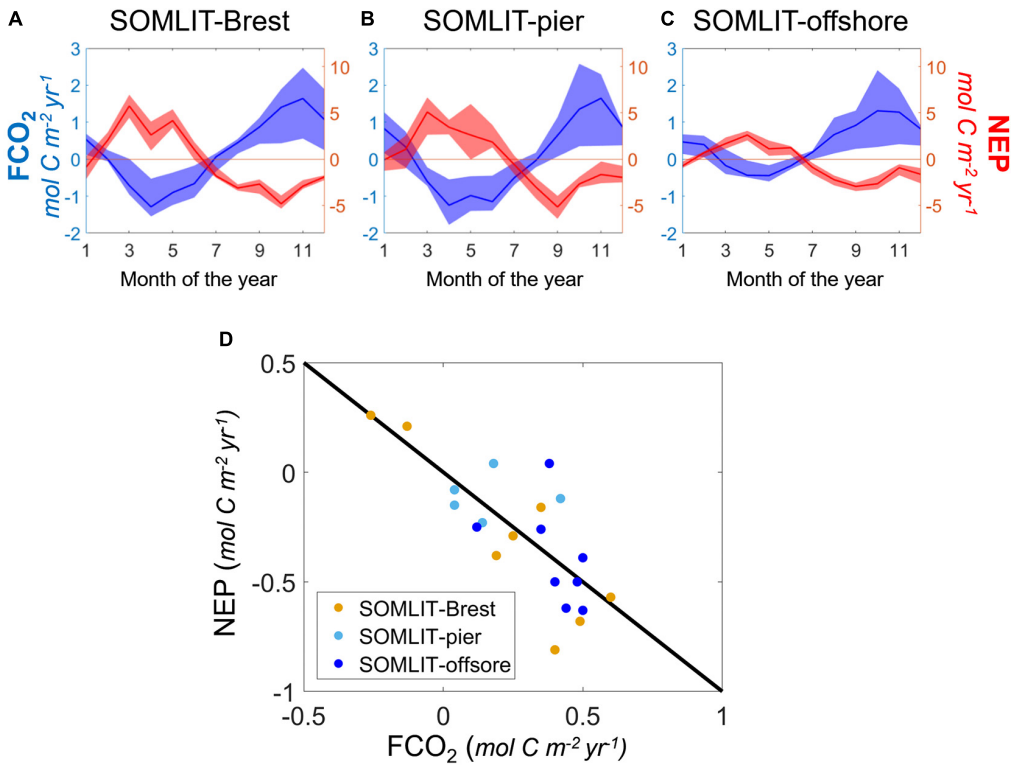


FIGURE 9 | Monthly average of FCO_2 (blue, mol C m^{-2} $year^{-1}$) and NEP (red, mol C m^{-2} $year^{-1}$) at **(A)** SOMLIT-Brest, **(B)** SOMLIT-pier, and **(C)** SOMLIT-offshore. Shaded areas represent the quartiles of the annual means. **(D)** NEP vs. FCO_2 annual means at SOMLIT-Brest (orange), SOMLIT-pier (light blue), and SOMLIT-offshore (dark blue), from January 2010 to December 2017. The black line represents the 1:1 relationship.

remaining increase of 2.11 and 2.57 µatm pCO_2 $year^{-1}$ due to increasing DIC at the nearshore stations closely matched the magnitude of atmospheric pCO_2 increase during the observation period (2.27 µatm $year^{-1}$ at Mace Head, Ireland). Since surface waters at the nearshore stations were a weak source of CO_2 over annual cycles (Section "Comparison Between Ecosystems of the Processes Controlling the Carbonate System"), we can assume that OA in these coastal sites was mainly driven by this atmospheric CO_2 increase. Applying this simple model to $pH_{in\ situ}$, assuming changes in DIC are due to both increasing TA (a neutralizing effect) and atmospheric CO_2 forcing, the surface OA trend at SOMLIT-Brest can be attributed primarily to atmospheric CO_2 forcing (57%), secondarily to warming (37%) and finally to changes in SSS (7%). At SOMLIT-pier, OA can be attributed primarily to atmospheric CO_2 forcing (66%), secondarily to warming (31%) and finally to changes in SSS (3%). At SOMLIT-offshore, the model was not as robust as for the other sites, possibly due to limited SSS and/or TA variations. In addition, the annual emission of CO_2 to the atmosphere was higher than at nearshore sites, which might have induced a bias in the computation. The OA trend nevertheless seemed to be primarily driven by atmospheric CO_2 forcing (71%) and secondarily by warming (27%).

While the trends in atmospheric CO_2 and temperature were the main drivers of OA at all three sites, the increase in TA and DIC, beyond what can be attributed to changes in atmospheric CO_2, were unexpected. Considering the variability associated with the deconvolution of pCO_2 due to DIC increase at the three sites, the atmospheric CO_2 increase should represent 33%–49% of the total DIC contribution to $dpCO_2/dt$ (**Table 2**). This leaves 51%–67% of the total DIC contribution to pCO_2 trends unaccounted for. The buffering effect of TA partly compensated this DIC contribution in the model for the two nearshore ecosystems. Estimating the additional source of DIC and TA to the surface waters of these ecosystems would require several hypotheses. Assuming that the same processes were responsible for both the increase in DIC and TA, numerous drivers can modify the buffering capacity of the ecosystem (Middelburg et al., 2020). For a complete consideration of each process, we refer to Wolf-Gladrow et al. (2007), and simply consider here the dominant processes driving the carbonate systems described in Section "Comparison Between Ecosystems of the Processes Controlling the Carbonate System" (**Figure 7**). A decrease in NEP (i.e., increase in OM remineralization) based on DIC^{bio} corrected from FCO_2 (Section "Determination of Processes Controlling DIC/pCO2 Based on a 1-D Mass Budget Model") could increase both DIC and TA, but neither NEP nor DO% showed significant trends during the study period (**Figures 5**, **6**). An increase in $CaCO_3$ dissolution in the benthic compartment at both nearshore sites could also result in simultaneous increase in DIC and TA. As mentioned in Section "Comparison Between Ecosystems of the Processes Controlling the Carbonate System," SOMLIT-Brest

TABLE 2 | Deconvolution of $pH_{in\ situ}$ anomalies ($\frac{dpH_{in\ situ}}{dt}$, year^{-1}) and pCO_2 anomalies ($\frac{dpCO_2}{dt}$, μatm year^{-1}) at SOMLIT-Brest, SOMLIT-pier, and SOMLIT-offshore.

$pH_{in\ situ}$

Location	Variable	Sensitivity ± SE			Deconvolution ± RMSE			Contribution (%)	Total trend	Trend Figure 6
SOMLIT-Brest	SST (°C)	−0.0150	±	< 0.0001	−0.0011	±	0.0002	37	−0.0030	−0.0029
	SSS	−0.0126	±	< 0.0001	−0.0002	±	0.0001	7		
	TA (μmol kg^{-1})	0.0021	±	< 0.0001	0.0046	±	0.0008	−153		
	DIC (μmol kg^{-1})	−0.0021	±	< 0.0001	−0.0063	±	0.0008	210		
SOMLIT-pier	SST (°C)	−0.0150	±	< 0.0001	−0.001	±	0.0002	31	−0.0032	−0.0028
	SSS	−0.0126	±	< 0.0001	−0.0001	±	< 0.0001	3		
	TA (μmol kg^{-1})	0.0019	±	< 0.0001	0.0031	±	0.0006	−97		
	DIC (μmol kg^{-1})	−0.0020	±	< 0.0001	−0.0052	±	0.0012	163		
SOMLIT-offshore	SST (°C)	−0.0150	±	< 0.0001	−0.0011	±	0.0002	27	−0.0041	−0.0027
	SSS	−0.0125	±	< 0.0001	−0.0001	±	< 0.0001	2		
	TA (μmol kg^{-1})	0.0020	±	< 0.0001	0.001	±	0.0004	−24		
	DIC (μmol kg^{-1})	−0.0021	±	< 0.0001	−0.0039	±	0.0006	95		

pCO_2

Location	Variable	Sensitivity ± SE			Deconvolution ± RMSE			Contribution (%)	Total trend	Trend Figure 6
SOMLIT-Brest	SST (°C)	16.1,	±	0.03	1.21	±	0.20	35	3.52	3.52
	SSS	10.30	±	0.01	0.19	±	0.06	5		
	TA (μmol kg^{-1})	−2.16	±	0.03	−4.77	±	0.84	−136		
	DIC (μmol kg^{-1})	2.31	±	0.02	6.88	±	0.89	196		
SOMLIT-pier	SST (°C)	15.67	±	0.04	1.01	±	0.25	28	3.68	2.95
	SSS	10.13	±	< 0.00	0.09	±	0.03	3		
	TA (μmol kg^{-1})	−1.74	±	0.01	−2.85	±	0.56	−77		
	DIC (μmol kg^{-1})	2.08	±	0.02	5.42	±	1.29	147		
SOMLIT-offshore	SST (°C)	17.02	±	0.04	1.26	±	0.23	26	4.93	3.11
	SSS	10.9	±	< 0.00	0.07	±	0.02	1		
	TA (μmol kg^{-1})	−2.04	±	0.01	−1,00	±	0.42	−20		
	DIC (μmol kg^{-1})	2.39	±	0.01	4.60	±	0.68	93		

*Sensitivities of $pH_{in\ situ}$ and pCO_2 with respect to variables ($\frac{\partial pH_{in\ situ}}{\partial variable}$ and $\frac{\partial pCO_2}{\partial variable}$), where the variables sea surface temperature (SST), sea surface salinity (SSS), total alkalinity (TA), and dissolved inorganic carbon (DIC) were multiplied by the anomaly of the variable ($\frac{dvariable}{dt}$, **Figure 6**). SE is the standard error and RMSE the root mean square error. Trends illustrated in **Figure 6** were added to the table for comparison.*

and SOMLIT-pier have very different benthic populations with non-calcifying species dominating at SOMLIT-pier. Given the simultaneous increase in DIC/TA at both sites, it is unlikely that $CaCO_3$ dissolution was the additional source of DIC/TA. Long-term variability in river discharge has been linked to intensified drought in Europe (Caloiero et al., 2018) and/or to AMV fluctuations (Tréguer et al., 2014; Sutton et al., 2018). Variations in river discharge can modify both DIC and TA in nearshore ecosystems, but SSS did not exhibit any significant trends during the study period (**Figure 5**). Increasing TA of the freshwater end-member could be a conceivable mechanism causing the unexpected TA and DIC trends. Positive trends in river TA have been documented in North America and occur *via* various processes. Stets et al. (2014) observed TA increases in North American rivers together with decrease in nitrate due to modified agricultural practice. Similar modifications in agricultural practice have been encouraged in Brittany and confirmed by the decreasing trends in nitrate concentration in nearshore ecosystems for the past two decades (**Figures 3**, **10** and Section "Comparison of OA Trends and Climatic Context Over the 1997–2020 Period" below). Changes in end-member DIC/TA could be linked to limestone addition used to enhance agricultural soil pH to counteract acidifying effects of fertilizer usage and nitrogen-fixing plants (Oh and Raymond, 2006; Hamilton et al., 2007). However, given the complexity of TA/DIC control in these agricultural watersheds, this hypothesis cannot be confirmed and would require further evaluation. Maintaining time series of at least two carbonate system parameters in coastal ecosystem is challenging but provides key information on the potential drivers of OA. Given the complexity of these ecosystems, combining these time series with additional regular sampling in adjacent rivers and estuaries might improve our understanding of interacting anthropogenic drivers.

Comparison of OA Trends and Climatic Context Over the 1997–2020 Period

In this study, the additional pH data collected (Section "Weekly and Bimonthly Measurements of the Long-term Time-Series") at the three sites allowed us to extend the pH trends until December 2020 and to consider the trends previously established for the 2008–2017 period in a larger climatic context covering the period

1997–2020 (**Figure 10**). With additional $pH_{in\ situ}$ measurements, we extended the $pH_{in\ situ}$ trends at SOMLIT-Brest, SOMLIT-pier, and SOMLIT-offshore from 9.5, 8.5, and 7.5 years to 12.5, 11.5, and 10.5 years, respectively. Trends were established with missing data in the time series: The trend at SOMLIT-Brest was established without data in 2018, whereas at the two other sites, sampling was interrupted for the first time in 20 years due to the COVID-19 pandemic from March to June 2020. The OA trends extended until December 2020 remained relatively constant at -0.0026 ± 0.0004 year^{-1} at SOMLIT-Brest, whereas OA was -0.0046 ± 0.0006 and -0.0045 ± 0.0003 year^{-1} at SOMLIT-pier and SOMLIT-offshore, respectively. It is worth noticing that the seasonal amplitudes of pH were > 0.15 at the nearshore stations and > 0.10 at the SOMLIT-offshore station and that daily pH variability, linked to the diel biological cycle in the Bay of Brest (Bozec et al., 2011) and to the tidal cycle in Roscoff (Gac et al., 2020), was in the same order of magnitude as seasonal variability. These daily and seasonal amplitudes represented 6 to 10 times the regional OA trend over a decade, respectively. The superimposition of decadal, seasonal, and daily dynamics in coastal ecosystems represents a challenge to quantify pH trends in coastal ecosystems. Keller et al. (2014) estimated time of emergence (ToE), that is, the point in time when a signal finally emerges from the background noise of natural variability, around 12 years for pCO_2 and pH and between 10 and 30 years for DIC depending on the study sites. Based on a more recent study by Turk et al. (2019), we estimated a ToE of 11 to 20 years from our dataset. Our study period corresponds to the minimal time period allowing long-term climate trends to emerge from coastal variability and maintaining such time series will be critical to confirm these observed trends.

Previous studies in coastal seas of NW Europe estimated OA either based on seasonal cruises or on voluntary observing ship surveys (Clargo et al., 2015; Ostle et al., 2016; Omar et al., 2019). OA in North Sea surface waters ranged from -0.0022 year^{-1} (period 2001–2011; Clargo et al., 2015) to -0.0035 year^{-1} (period 1984–2014; Ostle et al., 2016), with a recent estimate of -0.0024 year^{-1} in the northern North Sea (Omar et al., 2019). The 2008–2017 trends observed in this study were of the same order of magnitude as those reported in these surrounding coastal margins. These trends were also close to values previously reported at several coastal observatories, such as in the Irminger Sea (-0.0026 ± 0.0006 year^{-1}), in the Cariaco Basin (-0.0025 ± 0.0004 year^{-1}) (see review of Bates et al., 2014), or in the Mediterranean Sea at Point B (-0.0028 ± 0.0003 year^{-1}) (Kapsenberg et al., 2017), although care must be taken when comparing such diverse ecosystems. The North Atlantic trends ranged from -0.0013 ± 0.0009 year^{-1} (period 1995–2013, Kitidis et al., 2017) to -0.0017 year^{-1} (period 1993–2017, Leseurre et al., 2020). In open ocean regions of the northern hemisphere, pH trends have been observed concomitantly with sea surface pCO_2 increases close to the atmospheric CO_2 forcing (Kitidis et al., 2017; Wang et al., 2017; Leseurre et al., 2020). Deviations from these atmospheric trends have been reported for specific periods or regions and may reflect local changes in oceanic buffering capacity as discussed in Section "Deconvolution of Carbonate System Trends During the 2008–2017 Period" and elsewhere (Lauvset and Gruber, 2014; Lauvset et al., 2015; Leseurre et al., 2020). These deviations can be even more significant in coastal margins, as reported in the Mediterranean Sea (Kapsenberg et al., 2017) or in the SAB, with decrease in pH reaching 0.004 year^{-1} based on multidecadal observations (Reimer et al., 2017b). Our results indicated similar deviations, but these remained relatively limited over the long term, especially for such dynamic coastal ecosystems. As mentioned above, adding 3 years of data increased the trends at SOMLIT-Pier and SOMLIT-offshore to values similar to those observed in the SAB (Reimer et al., 2017b). It is worth noting that independent high-frequency measurement of pCO_2 combined with discrete TA sampling at the adjacent ASTAN cardinal buoy (Gac et al., 2020) confirmed a higher increase in pCO_2 associated with decrease in $pH_{in\ situ}$ over the 2017–2020 period. This period was too short to establish any significant trends, but confirmed that for carbonate parameters, especially in coastal ecosystems, values can vary significantly. Decadal-scale observations, which facilitate the understanding of the changes occurring in these ecosystems, remain rather limited.

To further evaluate in which climatic context our observations took place, we relied on concomitant data collected since 1997/2000 at the three sites. Tréguer et al. (2014) reported a decrease of SST of -0.01°C year^{-1} at SOMLIT-Brest and SOMLIT-pier, and -0.02°C year^{-1} at SOMLIT-offshore, for the 1997–2013 period. Recently, Charria et al. (2020) extended the 15-year study of Tréguer et al. (2014) to a 20-year period concomitant with our observation of carbonate parameters. During the 1998–2018 period, Charria et al. (2020) reported an increase in SST ($+0.008$°C year^{-1} at SOMLIT-Brest and $+0.003$°C year^{-1} at SOMLIT-pier). Only a slope break in terms of slope directions could explain such contrasting values between these studies. We applied a seasonal-trend decomposition procedure based on Loess (STL, Cleveland et al., 1990) on the SST time series over the 1997–2020 period. A slope break in the SST time-series clearly appeared around 2009–2011. The STL applied to the SSS time series showed a slope break during the same period (**Figure 10**). We therefore established trends for these parameters for the 1997–2013 period as in Tréguer et al. (2014), and after the slope break for the 2010–2020 period. We obtained significant SST trends of -0.02°C year^{-1}, p-value < 0.05 and $+0.05$°C year^{-1}, p-value < 0.001, as well as significant SSS trends around $+0.02$ year^{-1}, p-value < 0.001 and -0.01 year^{-1}, p-value < 0.001 for the first and second periods at SOMLIT-Brest and SOMLIT-pier, respectively.

Previous studies have shown a significant connection between hydro-climatic indices such as AMV/NAO and SST/SSS variations in the coastal waters of NW Europe (Tréguer et al., 2014; Sutton et al., 2018). A slope break around 2009/2011 (**Figure 10D**) clearly appeared when the STL was applied to the wNAO. The wNAO ($+0.08 \pm 0.05$ year^{-1}, $n = 721$, $r = 0.48$, $p < 0.05$) increased during 2010–2020 and was related to warming in European surface waters (Sutton et al., 2018; Charria et al., 2020; **Figure 10**), which, on a longer time scale, was correlated with positive AMV (Sutton et al., 2018). At the SOMLIT stations, as previously reported by Tréguer et al. (2014), regressions between SST and wNAO showed significant

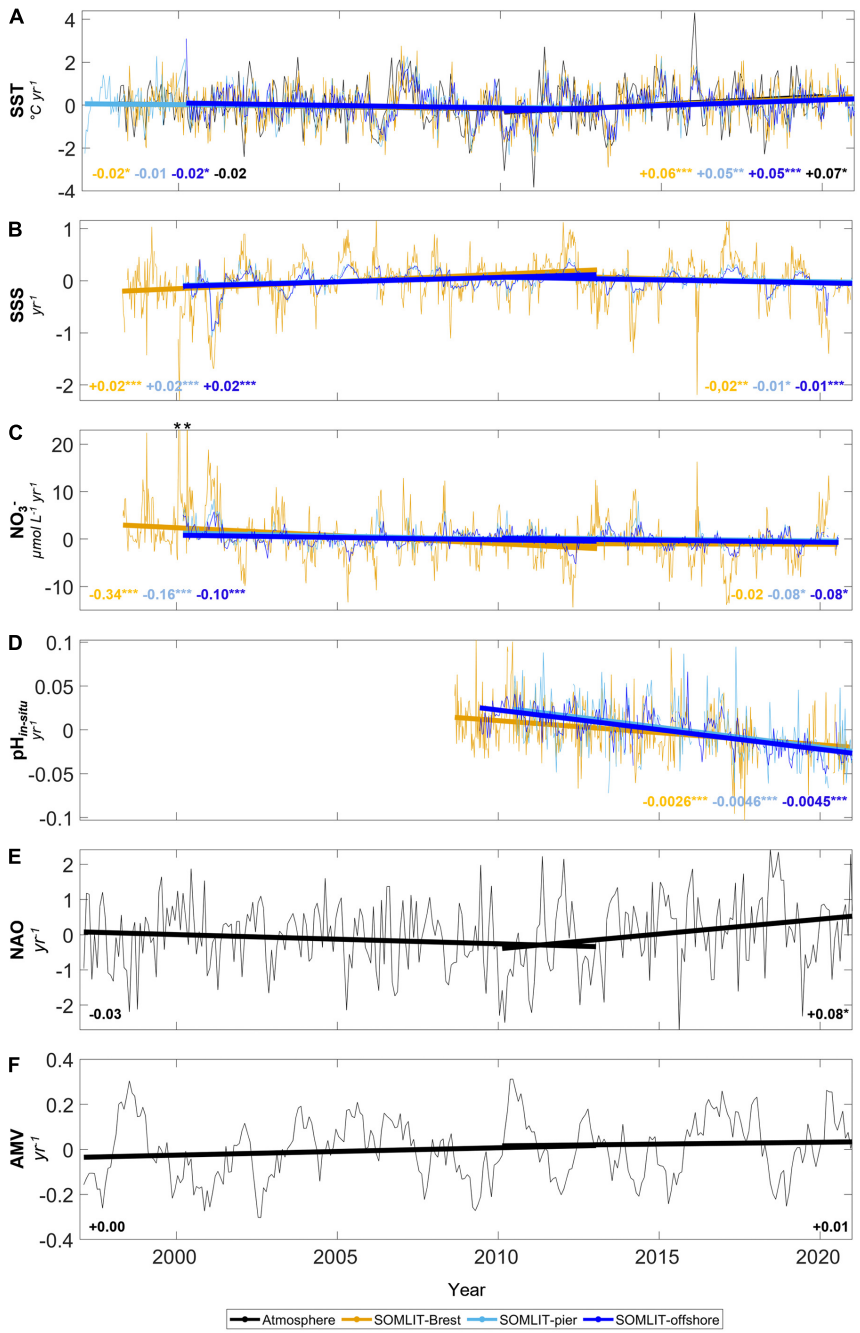


FIGURE 10 | Trends of monthly anomalies of **(A)** SST (°C year^{-1}), **(B)** SSS (year^{-1}), **(C)** nitrate (µmol L^{-1} year^{-1}), and **(D)** $pH_{in\ situ}$ (year^{-1}) at (orange) SOMLIT-Brest, (light blue) SOMLIT-pier, and (dark blue) SOMLIT-offshore, and monthly values of **(E)** NAO and **(F)** AMV climatic indices. Trends were divided into two periods separated by the slope break detected around 2009–2011 with the STL (Cleveland et al., 1990) applied to the SST time series over the 1998–2020 period (see Section "Comparison of OA Trends and Climatic Context Over the 1997–2020 Period" for details). Asterisks represent *p*-values: ***p-value < 0.001, **p-value < 0.01, *p-value < 0.05, and no asterisk indicates non-significant trends.

correlations ($r = 0.59$, p-value < 0.01 at SOMLIT-Brest; $r = 0.64$, p-value < 0.001 at SOMLIT-pier; and $r = 0.56$, p-value < 0.01 at SOMLIT-offshore, **Table 3**). Several studies have previously linked the NAO and AMV to pCO_2 variability during short study periods (Breeden and McKinley, 2016; Landschützer et al., 2019). Recently, a 100-year time series of proxy-reconstructed carbonate chemistry noted a significant modulation and relationship between OA and climate modes; both positive and negative forcing on the state of the carbonate system were observed (Osborne et al., 2020). Here, the impact of wNAO on SST was

TABLE 3 | Coefficient of determination (*r*) of the Pierson correlations between the monthly anomalies of the winter North Atlantic Oscillation (wNAO) and the Atlantic Multidecadal Variability (AMV), and monthly anomalies of SST (°C), SSS, pCO_2, pCO_2^{therm}, and $pCO_2^{non-therm}$ (all in μatm) from 2008 to 2017 at SOMLIT-Brest, SOMLIT-pier, and SOMLIT-offshore.

	SOMLIT-Brest		SOMLIT-pier		SOMLIT-offshore	
Variable	**wNAO**	**AMV**	**wNAO**	**AMV**	**wNAO**	**AMV**
SST (°C)	0.59**	0.50***	0.64***	0.50***	0.56**	0.48***
SSS	0.02	0.46***	0.20	0.28**	0.09	0.22*
pCO_2 (μatm)	0.34	0.15	0.00	0.05	0.30	0.19
pCO_2^{therm} (μatm)	0.59**	0.50***	0.53*	0.56***	0.56**	0.49***
$pCO_2^{non-term}$ (μatm)	−0.12	−0.27**	−0.28	−0.23*	−0.57**	−0.27**
SST (°C)	0.59**	0.50***	0.64***	0.50***	0.56**	0.48***
SSS	0.02	0.46***	0.20	0.28**	0.09	0.22*
pCO_2 (μatm)	0.34	0.15	0.00	0.05	0.30	0.19
pCO_2^{therm} (μatm)	0.59**	0.50***	0.53*	0.56***	0.56**	0.49***
$pCO_2^{non-term}$ (μatm)	−0.12	−0.27**	−0.28	−0.23*	−0.57**	−0.27**

*Asterisks represent p-values: ***p-value < 0.001, **p-value < 0.01, *p-value < 0.05, and no asterisk indicates non-significant trends.*

apparent on pCO_2^{therm}, with a Pearson correlation *r* value of 0.56, but was not correlated with $pCO_2^{non-therm}$ at these coastal stations. Similar significant trends were observed year-round between the AMV index and SST ($r \sim 0.50$) and pCO_2^{therm} ($r \sim 0.55$) (**Table 3**). These observations indicate a certain link between the AMV index and pCO_2^{therm}. As mentioned in Section "Deconvolution of Carbonate System Trends During the 2008–2017 Period," the increase in SST was responsible for 25%–30% of the pCO_2 increase driving OA in our coastal ecosystems. Since no significant warming trend was recorded for the 1997–2013 period, which was associated with a different NAO regime, the pCO_2 and pH trends might differ from those observed in this study. Datasets covering periods over 20–30 years are necessary to define trends of OA and to make the distinction between local and global drivers. Different, even opposite, trends have been observed on limited spatial and temporal scales, which highlights that necessity to operate and maintain as dense as possible a network of observation sites to assess the intensity and impact of OA on the coastal environment.

CONCLUSION AND PERSPECTIVES

Based on data collected from 2008 to 2020 in three coastal ecosystems located in the North East Atlantic Ocean, this study provides for the first time a decadal overview of the interannual dynamics of the carbonate system chemistry in three nearshore ecosystems. We demonstrated that interannual variability can reverse the metabolic state and regional air–sea CO_2 fluxes of a given ecosystem, which emphasized the importance of long-term monitoring. We showed that OA has potentially been ongoing at all three coastal sites for the past decade, primarily driven by atmospheric CO_2 forcing, secondarily by warming, and additionally by changes in salinity. This is particularly relevant since nearshore ecosystems are not included in current global climate models and host large stocks of calcifying shellfish species sensitive to OA. Further observations over the 1998–2020 period revealed that the climatic indices NAO and AMV were linked to trends of SST, with cooling during 1998–2010 and warming during 2010–2020, which might have impacted OA trends at our coastal stations.

Our study period corresponded to the minimal time period allowing long-term climate trends to emerge from coastal variability, but demonstrated that different trends can be observed on limited spatial and temporal scales. Maintaining time series of at least two carbonate system parameters in coastal ecosystem is challenging but will provide key information on the potential drivers of OA and will be critical to confirm the observed trends over extended time periods.

DATA AVAILABILITY STATEMENT

Raw data supporting the conclusion of this article are available at https://www.somlit.fr/en/.

AUTHOR CONTRIBUTIONS

J-PG collected, analyzed, processed, and interpreted the data and wrote the first version of the manuscript. PM provided scientific discussion and new ideas on interpretation of the results and contributed to writing the manuscript. TC, EG, PR-M, ÉM, and MV collected all data in the field, analyzed discrete samples in the laboratory, processed the data, and implemented the databases. YB designed and led the study, managed the project, and wrote the manuscript. All authors contributed to the article and approved the submitted version.

FUNDING

This work was funded by the CNRS through INSU [SOMLIT, project CHANNEL (LEFE/CYBER)] and INEE, by the "Conseil Général du Finistère" (CD29), and by the "Region Bretagne" (program ARED, project Hi-Tech). Part of this work

was supported by the JERICO-NEXT project from the European Union's Horizon 2020 Research and Innovation Program under grant agreement no. 654410 and by the ANR CO2COAST 2021–2025. YB is PI of the CHANNEL and Hi-Tech projects and associate researcher (CRCN) at the CNRS. J-PG holds a Ph.D. grant from the Region Bretagne and Sorbonne University (ED129).

ACKNOWLEDGMENTS

We thank the successive teams from the "Service Mer" of the SBR and IUEM for their long-term and valuable support during sampling at sea in all kinds of weather conditions. We also thank all of the technicians, engineers, master's students, and researchers who helped to collect, analyze, and qualify the data over more than 20 years within the SOMLIT (Service d'Obervation du Milieu LIToral) network. We are grateful to the SNAPOCO2 for DIC/TA analysis and M. Ramonet for providing the atmospheric CO_2 data from the RAMCES network (Observatory Network for Greenhouse gasses). We thank A. Durand and E. Collin for their help during field campaigns in the Penzé river. We are grateful to the Menden-Deuer Lab (URI-GSO), A. C. Baudoux, and I. Probert for constructive collaboration, scientific discussions, and correction during finalization of the manuscript. We also thank both reviewers for their constructive comments on a previous version of the manuscript.

REFERENCES

Aminot, A., and Kérouel, R. (2007). *Dosage Automatique des Nutriments Dans Les Eaux Marines: Méthodes en Flux Continu*. Brest: Ifremer.

Astor, Y. M., Lorenzoni, L., Thunell, R., Varela, R., Muller-Karger, F., Troccoli, L., et al. (2013). Interannual variability in sea surface temperature and fCO2 changes in the Cariaco Basin. *Deep Sea Res. Part II Top. Stud. Oceanogr.* 93, 33–43. doi: 10.1016/j.dsr2.2013.01.002

Bakker, D. C., Pfeil, B., Landa, C. S., Metzl, N., O'brien, K. M., Olsen, A., et al. (2016). A multi-decade record of high-quality fCO_2 data in version 3 of the Surface Ocean CO_2 Atlas (SOCAT). *Earth Syst. Sci. Data* 8, 383–413. doi: 10.5194/essd-8-383-2016

Bates, N. R., Astor, Y. M., Church, M. J., Currie, K., Dore, J. E., González-Dávila, M., et al. (2014). A time-series view of changing surface ocean chemistry due to ocean uptake of anthropogenic CO2 and ocean acidification. *Oceanography* 27, 126–141. doi: 10.5670/oceanog.2014.16

Bauer, J. E., Cai, W. J., Raymond, P. A., Bianchi, T. S., Hopkinson, C. S., and Regnier, P. A. (2013). The changing carbon cycle of the coastal ocean. *Nature* 504, 61–70. doi: 10.1038/nature12857

Beucher, C., Treguer, P., Corvaisier, R., Hapette, A. M., and Elskens, M. (2004). Production and dissolution of biosilica, and changing microphytoplankton dominance in the Bay of Brest (France). *Mar. Ecol. Prog. Ser.* 267, 57–69. doi: 10.3354/meps267057

Bordeyne, F., Migné, A., and Davoult, D. (2017). Variation of fucoid community metabolism during the tidal cycle: insights from in situ measurements of seasonal carbon fluxes during emersion and immersion. *Limnol. Oceanogr.* 62, 2418–2430. doi: 10.1002/lno.10574

Borges, A. V., Alin, S. R., Chavez, F. P., Vlahos, P., Johnson, K. S., Holt, J. T., et al. (2010). "A global sea surface carbon observing system: inorganic and organic carbon dynamics in coastal oceans," in *Proceedings of the OceanObs'09: Sustained Ocean Observations and Information for Society*, Vol. 2, (Paris: European Space Agency), 67–88. doi: 10.5270/OceanObs09.cwp.07

Borges, A. V., and Frankignoulle, M. (2003). Distribution of surface carbon dioxide and air sea exchange in the english channel and adjacent areas. *J. Geophys. Res. Oceans* 108:3140. doi: 10.1029/2000JC000571

Borges, A. V., and Gypsens, N. (2010). Carbonate chemistry in the coastal zone responds more strongly to eutrophication than ocean acidification. *Limnol. Oceanogr.* 55, 346–353. doi: 10.4319/lo.2010.55.1.0346

Borges, A. V., Ruddick, K., Schiettecatte, L.-S., and Delille, B. (2008). Net ecosystem production and carbon dioxide fluxes in the Scheldt estuarine plume. *BMC Ecol.* 8:15. doi: 10.1186/1472-6785-8-15

Bourgeois, T., Orr, J. C., Resplandy, L., Terhaar, J., Ethé, C., Gehlen, M., et al. (2016). Coastal-ocean uptake of anthropogenic carbon. *Biogeosciences* 13, 4167–4185. doi: 10.5194/bg-13-4167-2016

Bozec, Y., Merlivat, L., Baudoux, A. C., Beaumont, L., Blain, S., Bucciarelli, E., et al. (2011). Diurnal to inter-annual dynamics of pCO2 recorded by a CARIOCA sensor in a temperate coastal ecosystem (2003–2009). *Mar. Chem.* 126, 13–26. doi: 10.1016/j.marchem.2011.03.003

Breeden, M. L., and McKinley, G. A. (2016). Climate impacts on multidecadal pCO2 variability in the North Atlantic: 1948–2009. *Biogeosciences* 13:3387. doi: 10.5194/bg-13-3387-2016

Cai, W. J., Wiebe, W. J., Wang, Y., and Sheldon, J. E. (2000). Intertidal marsh as a source of dissolved inorganic carbon and a sink of nitrate in the Satilla River-estuarine complex in the southeastern US. *Limnol. Oceanogr.* 45, 1743–1752. doi: 10.4319/lo.2000.45.8.1743

Caloiero, T., Veltri, S., Caloiero, P., and Frustaci, F. (2018). Drought analysis in Europe and in the Mediterranean basin using the standardized precipitation index. *Water* 10:1043. doi: 10.3390/w10081043

Carpenter, J. H. (1965). The accuracy of the winkler method for dissolved oxygen analyisis. *Limnol. Oceanogr.* 10, 135–140.

Carstensen, J., and Duarte, C. M. (2019). Drivers of pH variability in coastal ecosystems. *Environ. Sci. Technol.* 53, 4020–4029. doi: 10.1021/acs.est.8b03655

Chan, F., Barth, J. A., Blanchette, C. A., Byrne, R. H., Chavez, F., Cheriton, O., et al. (2017). Persistent spatial structuring of coastal ocean acidification in the California Current System. *Sci. Rep.* 7:2526. doi: 10.1038/s41598-017-02777-y

Charria, G., Rimmelin-Maury, P., Goberville, E., L'Helguen, S., Barrier, N., David-Beausire, C., et al. (2020). "Temperature and salinity changes in coastal waters of western europe: variability, trends and extreme events," in *Evolution of Marine Coastal Ecosystems under the Pressure of Global Changes*, eds H. J. Ceccaldi, Y. Hénocque, T. Komatsu, P. Prouzet, B. Sautour, and J. Yoshida (Cham: Springer), 207–226. doi: 10.1007/978-3-030-43484-7_15

Chen, S., and Hu, C. (2019). Environmental controls of surface water pCO2 in different coastal environments: observations from marine buoys. *Continental Shelf Res.* 183, 73–86. doi: 10.1016/j.csr.2019.06.007

Chierici, M., Fransson, A., and Anderson, L. G. (1999). Influence of m-cresol purple indicator additions on the pH of seawater samples: correction factors evaluated from a chemical speciation model. *Mar. Chem.* 65, 281–290. doi: 10.1016/S0304-4203(99)00020-1

Clargo, N. M., Salt, L. A., Thomas, H., and de Baar, H. J. (2015). Rapid increase of observed DIC and pCO2 in the surface waters of the North Sea in the 2001-2011 decade ascribed to climate change superimposed by biological processes. *Mari. Chem.* 177, 566–581.1.

Claustre, H., Johnson, K. S., and Takeshita, Y. (2020). Observing the global ocean with biogeochemical-Argo. *Ann. Rev. Mari. Sci.* 12, 23–48. doi: 10.1146/annurev-marine-010419-010956

Clayton, T. D., and Byrne, R. H. (1993). Spectrophotometric seawater pH measurements: total hydrogen ion concentration scale calibration of m-cresol purple and at-sea results. *Deep Sea Res. Part I Oceanogr. Res. Pap.* 40, 2115–2129. doi: 10.1016/0967-0637(93)90048-8

Cleveland, R. B., Cleveland, W. S., McRae, J. E., and Terpenning, I. (1990). STL: a seasonal-trend decomposition. *J. Offi. Statist.* 6, 3–73.

Currie, K. I., Reid, M. R., and Hunter, K. A. (2011). Interannual variability of carbon dioxide drawdown by subantarctic surface water near New Zealand. *Biogeochemistry* 104, 23–34. doi: 10.1007/s10533-009-9355-3

Da, F., Friedrichs, M. A. M., and St-Laurent, P. (2018). Impacts of atmospheric nitrogen deposition and coastal nitrogen fluxes on oxygen concentrations in Chesapeake Bay. *J. Geophys. Res. Oceans* 123, 5004–5025. doi: 10.1029/2018JC014009

de Haas, H., van Weering, T. C., and de Stigter, H. (2002). Organic carbon in shelf seas: sinks or sources, processes and products. *Continental Shelf Res.* 22, 691–717. doi: 10.1016/S0278-4343(01)00093-0

Del Amo, Y., Quéguiner, B., Tréguer, P., Breton, H., and Lampert, L. (1997). Impacts of high-nitrate freshwater inputs on macrotidal ecosystems. II. specific role of the silicic acid pump in the year-round dominance of diatoms in the bay of brest (France). *Mar. Ecol. Prog. Ser.* 161, 225–237. doi: 10.3354/meps161225

Dickson, A. G. (1990). Standard potential of the reaction: AgCl (s)+ 12H2 (g)= Ag (s)+ HCl (aq), and the standard acidity constant of the ion HSO4- in synthetic sea water from 273.15 to 318.15 K. *J. Chem. Thermody.* 22, 113–127.

DOE (1994). *Handbook of Methods for Analysis of the Various Parameters of the Carbon Dioxide System in Sea Water, Version 2*. Available online at: https://core.ac.uk/download/pdf/98639593.pdf (accessed July 17, 2020).

Doney, S. C. (2010). The growing human footprint on coastal and open-ocean biogeochemistry. *Science* 328, 1512–1516. doi: 10.1126/science.1185198

Doney, S. C., Busch, D. S., Cooley, S. R., and Kroeker, K. J. (2020). The impacts of ocean acidification on marine ecosystems and reliant human communities. *Ann. Rev. Environ. Res.* 45, 83–112. doi: 10.1146/annurev-environ-012320-083019

Duarte, C. M., Hendriks, I. E., Moore, T. S., Olsen, Y. S., Steckbauer, A., Ramajo, L., et al. (2013). Is ocean acidification an open-ocean syndrome? Understanding anthropogenic impacts on seawater pH. *Estuar. Coasts* 36, 221–236. doi: 10.1007/s12237-013-9594-3

Dumousseaud, C., Achterberg, E. P., Tyrrell, T., Charalampopoulou, A., Schuster, U., Hartman, M., et al. (2010). Contrasting effects of temperature and winter mixing on the seasonal and inter-annual variability of the carbonate system in the Northeast Atlantic Ocean. *Biogeosciences (BG)* 7, 1481–1492. doi: 10.5194/bg-7-1481-2010

Dürr, H. H., Meybeck, M., Hartmann, J., Laruelle, G. G., and Roubeix, V. (2011). Global spatial distribution of natural riverine silica inputs to the coastal zone. *Biogeosciences* 8, 597–620. doi: 10.5194/bg-8-597-2011

Edmond, J. M. (1970). High precision determination of titration alkalinity and total carbon dioxide content of sea water by potentiometric titration. *Deep Sea Res. Oceanogr. Abstr.* 17, 737–750. doi: 10.1016/0011-7471(70)90038-0

Elser, J. J., Bracken, M. E., Cleland, E. E., Gruner, D. S., Harpole, W. S., Hillebrand, H., et al. (2007). Global analysis of nitrogen and phosphorus limitation of primary producers in freshwater, marine and terrestrial ecosystems. *Ecol. Lett.* 10, 1135–1142. doi: 10.1111/j.1461-0248.2007.01113.x

Enfield, D. B., Mestas-Nuñez, A. M., and Trimble, P. J. (2001). The Atlantic multidecadal oscillation and its relation to rainfall and river flows in the continental US. *Geophy. Res. Lett.* 28, 2077–2080. doi: 10.1029/2000GL012745

Feely, R. A., Alin, S. R., Newton, J., Sabine, C. L., Warner, M., Devol, A., et al. (2010). The combined effects of ocean acidification, mixing, and respiration on pH and carbonate saturation in an urbanized estuary. *Estuar. Coast. Shelf Sci.* 88, 442–449. doi: 10.1016/j.ecss.2010.05.004

Feely, R. A., Alin, S., Carter, B., Bednaršek, N., Hales, B., Chan, F., et al. (2016). Chemical and biological impacts of ocean acidification along the west coast of North America. *Estuar. Coast. Shelf Sci.* 183, 260–270. doi: 10.1016/j.ecss.2016.08.043

Fennel, K., Alin, S., Barbero, L., Evans, W., Bourgeois, T., Cooley, S., et al. (2019). Carbon cycling in the North American coastal ocean: a synthesis. *Biogeosciences* 16, 1281–1304. doi: 10.5194/bg-16-1281-2019

Flynn, K. J., Clark, D. R., Mitra, A., Fabian, H., Hansen, P. J., Glibert, P. M., et al. (2015). Ocean acidification with (de) eutrophication will alter future phytoplankton growth and succession. *Proc. R. Soc. B Biol. Sci.* 282:20142604. doi: 10.1098/rspb.2014.2604

Forja, J. M., Ortega, T., DelValls, T. A., and Gómez-Parra, A. (2004). Benthic fluxes of inorganic carbon in shallow coastal ecosystems of the Iberian Peninsula. *Mar. Chem.* 85, 141–156. doi: 10.1016/j.marchem.2003.09.007

Friis, K., Körtzinger, A., and Wallace, D. W. (2003). The salinity normalization of marine inorganic carbon chemistry data. *Geophys. Res. Lett.* 30:57. doi: 10.1029/2002GL015898

Fu, F. X., Tatters, A. O., and Hutchins, D. A. (2012). Global change and the future of harmful algal blooms in the ocean. *Mari. Ecol. Progr. Series* 470, 207–233. doi: 10.3354/meps10047

Gac, J. P., Marrec, P., Cariou, T., Guillerm, C., Macé, É, Vernet, M., et al. (2020). Cardinal buoys: an opportunity for the study of air-sea CO2 fluxes in coastal ecosystems. *Front. Mari. Sci.* 9:20153. doi: 10.3389/fmars.2020.00712

Garcia, H. E., and Gordon, L. I. (1992). Oxygen solubility in seawater: better fitting equations. *Limnol. Oceanogr.* 37, 1307–1312.

García-Ibáñez, M. I., Zunino, P., Fröb, F., Carracedo, L. I., Ríos, A. F., Mercier, H., et al. (2016). Ocean acidification in the subpolar North Atlantic: rates and mechanisms controlling pH changes. *Biogeosciences* 13, 3701–3715. doi: 10.5194/bg-13-3701-2016

Gattuso, J. P., Magnan, A., Billé, R., Cheung, W. W., Howes, E. L., Joos, F., et al. (2015). OCEANOGRAPHY Contrasting futures for ocean and society from different anthropogenic CO2 emissions scenarios. *Science* 349:aac4722. doi: 10.1126/science.aac4722

Golléty, C., Migne, A., and Davoult, D. (2008). Benthic metabolism on a sheltered rocky shore: role of the canopy in the carbon budget. *J. Phycol.* 44, 1146–1153. doi: 10.1111/j.1529-8817.2008.00569.x

González-Dávila, M., Santana-Casiano, J. M., Rueda, M. J., and Llinás, O. (2010). The water column distribution of carbonate system variables at the ESTOC site from 1995 to 2004. *Biogeosciences* 7, 3067–3081. doi: 10.5194/bg-7-3067-2010

Gran, G. (1952). Determination of the equivalence point in potentiometric titrations. *Part II. Anal.* 77, 661–671.

Gregor, L., and Gruber, N. (2021). OceanSODA-ETHZ: a global gridded data set of the surface ocean carbonate system for seasonal to decadal studies of ocean acidification. *Earth Syst. Sci. Data* 13, 777–808. doi: 10.5194/essd-13-777-2021

Gruber, N., Clement, D., Carter, B. R., Feely, R. A., Van Heuven, S., Hoppema, M., et al. (2019). The oceanic sink for anthropogenic CO2 from 1994 to 2007. *Science* 363, 1193–1199. doi: 10.1126/science.aau5153

Gypens, N., Borges, A. V., and Lancelot, C. (2009). Effect of eutrophication on air–sea CO2 fluxes in the coastal Southern North sea: a model study of the past 50 years. *Global Chan. Biol.* 15, 1040–1056. doi: 10.1111/j.1365-2486.2008.01773.x

Gypens, N., Lacroix, G., Lancelot, C., and Borges, A. V. (2011). Seasonal and inter-annual variability of air–sea CO2 fluxes and seawater carbonate chemistry in the Southern North sea. *Progr. Oceanogr.* 88, 59–77. doi: 10.1016/j.pocean.2010.11.004

Hamilton, S. K., Kurzman, A. L., Arango, C., Jin, L., and Robertson, G. P. (2007). Evidence for carbon sequestration by agricultural liming. *Global Biogeochem. Cycl.* 21. doi: 10.1029/2006GB002738

Hammond, D. E., Giordani, P., Berelson, W. M., and Poletti, R. (1999). Diagenesis of carbon and nutrients and benthic exchange in sediments of the Northern Adriatic sea. *Mar. Chem.* 66, 53–79. doi: 10.1016/S0304-4203(99)00024-9

Haraldsson, C., Anderson, L. G., Hassellöv, M., Hulth, S., and Olsson, K. (1997). Rapid, high-precision potentiometric titration of alkalinity in ocean and sediment pore waters. *Deep Sea Res. Part I Oceanogr. Res. Pap.* 44, 2031–2044. doi: 10.1016/S0967-0637(97)00088-5

Hartmann, J., Jansen, N., Dürr, H. H., Kempe, S., and Köhler, P. (2009). Global CO2-consumption by chemical weathering: what is the contribution of highly active weathering regions? *Glob. Planet. Change* 69, 185–194. doi: 10.1016/j.gloplacha.2009.07.007

Hartmann, J., Moosdorf, N., Lauerwald, R., Hinderer, M., and West, A. J. (2014). Global chemical weathering and associated P-releasethe role of lithology, temperature and soil properties. *Chem. Geol.* 363, 145–163. doi: 10.1016/j.chemgeo.2013.10.025

Herrmann, M., Najjar, R. G., Kemp, W. M., Alexander, R. B., Boyer, E. W., Cai, W. J., et al. (2015). Net ecosystem production and organic carbon balance of US East Coast estuaries: a synthesis approach. *Global Biogeochem. Cycl.* 29, 96–111. doi: 10.1002/2013GB004736

Humphreys, M. P., Daniels, C. J., Wolf-Gladrow, D. A., Tyrrell, T., and Achterberg, E. P. (2018). On the influence of marine biogeochemical processes over CO2 exchange between the atmosphere and ocean. *Mari. Chem.* 199, 1–11. doi: 10.1016/j.marchem.2017.12.006

Hurrell, J. W. (1995). Decadal trends in the North Atlantic Oscillation: regional temperatures and precipitation. *Science* 269, 676–679.

Hydes, D. J., and Hartman, S. E. (2012). Seasonal and inter-annual variability in alkalinity in Liverpool Bay (53.5 N, 3.5 W) and in major river inputs to the North sea. *Ocean Dynam.* 62, 321–333. doi: 10.1007/s10236-011-0503-7

IPCC. (2013). "Carbon and other biogeochemical cycles," in *Climate Change 2013 – The Physical Science Basis: Working Group I Contribution to the Fifth Assessment Report of the Intergovernmental Panel on Climate Change*, (Cambridge: Cambridge University Press), 465–570.

Kapsenberg, L., Alliouane, S., Gazeau, F., Mousseau, L., and Gattuso, J.-P. (2017). Coastal ocean acidification and increasing total alkalinity in the northwestern Mediterranean sea. *Ocean Sci.* 13, 411–426. doi: 10.5194/os-13-411-2017

Keller, K. M., Joos, F., and Raible, C. C. (2014). Time of emergence of trends in ocean biogeochemistry. *Biogeosciences* 11, 3647–3659. doi: 10.5194/bg-11-3647-2014

Kerr, R. A. (2000). A North atlantic climate pacemaker for the centuries. *Science* 288, 1984–1985. doi: 10.1126/science.288.5473.1984

Kitidis, V., Brown, I., Hardman-Mountford, N., and Lefèvre, N. (2017). Surface ocean carbon dioxide during the Atlantic Meridional Transect (1995–2013); evidence of ocean acidification. *Prog. Oceanogr.* 158, 65–75. doi: 10.1016/j.pocean.2016.08.005

Kitidis, V., Hardman-Mountford, N. J., Litt, E., Brown, I., Cummings, D., Hartman, S., et al. (2012). Seasonal dynamics of the carbonate system in the Western English Channel. *Cont. Shelf Res.* 42, 30–40. doi: 10.1016/j.csr.2012.04.012

Landschützer, P., Ilyina, T., and Lovenduski, N. S. (2019). Detecting regional modes of variability in observation−based surface ocean pCO2. *Geophys. Res. Lett.* 46, 2670–2679. doi: 10.1029/2018GL081756

Lauvset, S. K., and Gruber, N. (2014). Long-term trends in surface ocean pH in the North Atlantic. *Mari. Chem.* 162, 71–76. doi: 10.1016/j.marchem.2014.03.009

Lauvset, S. K., Gruber, N., Landschützer, P., Olsen, A., and Tjiputra, J. F. (2015). Trends and drivers in global surface ocean pH over the past 3 decades. *Biogeosciences* 12, 1285–1298. doi: 10.5194/bg-12-1285-2015

Lauvset, S. K., Key, R. M., Olsen, A., Heuven, S. V., Velo, A., Lin, X., et al. (2016). A new global interior ocean mapped climatology: The 1× 1 GLODAP version 2. *Earth Syst. Sci. Data* 8, 325–340. doi: 10.5194/essd-8-325-2016

Lejart, M., and Hily, C. (2011). Differential response of benthic macrofauna to the formation of novel oyster reefs (*Crassostrea gigas*, Thunberg) on soft and rocky substrate in the intertidal of the Bay of Brest, France. *J. Sea Res.* 65, 84–93. doi: 10.1016/j.seares.2010.07.004

Leseurre, C., Monaco, C. L., Reverdin, G., Metzl, N., Fin, J., Olafsdottir, S., et al. (2020). Ocean carbonate system variability in the North Atlantic Subpolar surface water (1993-2017). *Biogeosciences* 17, 2553–2577. doi: 10.5194/bg-17-2553-2020

Lewis, E. R., and Wallace, D. W. R. (1998). Program developed for CO2 system calculations (No. cdiac: CDIAC-105). *Environ. Syst. Sci. Data Infrastr. Virt. Ecosyst*. doi: 10.15485/1464255

Litt, E. J., Hardman-Mountford, N. J., Blackford, J. C., Mitchelson-Jacob, G., Goodman, A., Moore, G. F., et al. (2010). Biological control of pCO2 at station L4 in the Western english channel over 3 years. *J. Plankton Res.* 32, 621–629. doi: 10.1093/plankt/fbp133

Longphuirt, S. N., Clavier, J., Grall, J., Chauvaud, L., Le Loc'h, F., Le Berre, I., et al. (2007). Primary production and spatial distribution of subtidal microphytobenthos in a temperate coastal system, the Bay of Brest, France. *Estuar. Coastal Shelf Sci.* 74, 367–380. doi: 10.1016/j.ecss.2007.04.025

Ludwig, W., Amiotte Suchet, P., Munhoven, G., and Probst, J.-L. (1998). Atmospheric CO2 consumption by continental erosion: presentday controls and implications for the last glacial maximum, Glob. *Planet. Change* 16/17, 107–120.

Marrec, P. (2014). *Dynamics of the Carbonate System and Air-Sea CO2 Fluxes in Western European Shelf Waters: A Multi-Scale Approach*. Paris: Sorbonnes Université.

Marrec, P., Cariou, T., Collin, E., Durand, A., Latimier, M., Macé, E., et al. (2013). Seasonal and latitudinal variability of the CO2 system in the Western english channel based on voluntary observing ship (VOS) measurements. *Mar. Chem.* 155, 29–41. doi: 10.1016/j.marchem.2013.05.014

Marrec, P., Cariou, T., Latimier, M., Macé, E., Morin, P., Vernet, M., et al. (2014). Spatio-temporal dynamics of biogeochemical processes and air–sea CO2 fluxes in the Western english channel based on two years of ferry box deployment. *J. Mar. Syst.* 140, 26–38. doi: 10.1016/j.jmarsys.2014.05.010

Martin, S., Thouzeau, G., Chauvaud, L., Jean, F., Guérin, L., and Clavier, J. (2006). Respiration, calcification, and excretion of the invasive slipper limpet, *Crepidula fornicata* L.: implications for carbon, carbonate, and nitrogen fluxes in affected areas. *Limnol. Oceanogr.* 51, 1996–2007. doi: 10.4319/lo.2006.51.5.1996

Martin, S., Thouzeau, G., Richard, M., Chauvaud, L., Jean, F., and Clavier, J. (2007). Benthic community respiration in areas impacted by the invasive mollusk *Crepidula fornicata*. *Mari. Ecol. Progr. Series* 347, 51–60. doi: 10.3354/meps07000

McDougall, T. J., Jackett, D. R., Millero, F. J., Pawlowicz, R., and Barker, P. M. (2012). A global algorithm for estimating Absolute Salinity. *Ocean Sci.* 8, 1123–1134. doi: 10.5194/os-8-1123-2012

McGrath, T., McGovern, E., Cave, R. R., and Kivimäe, C. (2016). The inorganic carbon chemistry in coastal and shelf waters around Ireland. *Estuar. Coasts* 39, 27–39. doi: 10.1007/s12237-015-9950-6

McGrath, T., McGovern, E., Gregory, C., and Cave, R. R. (2019). Local drivers of the seasonal carbonate cycle across four contrasting coastal systems. *Reg. Stud. Mar. Sci.* 30:100733. doi: 10.1016/j.rsma.2019.100733

McLaughlin, K., Weisberg, S. B., Dickson, A. G., Hofmann, G. E., Newton, J. A., Aseltine-Neilson, D., et al. (2015). Core principles of the California current acidification network: linking chemistry, physics, and ecological effects. *Oceanography* 28, 160–169.

Meybeck, M., Dürr, H. H., and Vörösmarty, C. J. (2006). Global coastal segmentation and its river catchment contributors: a new look at land-ocean linkage. *Glob. Biogeochem. Cycles* 20:W07517. doi: 10.1029/2005GB002540

Middelburg, J. J., Soetaert, K., and Hagens, M. (2020). Ocean alkalinity, buffering and biogeochemical processes. *Rev. Geophys.* 58:e2019RG000681. doi: 10.1029/2019RG000681

Migné, A., Davoult, D., Bourrand, J. J., and Boucher, G. (2005). Benthic primary production, respiration and remineralisation: in situ measurements in the soft-bottom Abra alba community of the western English Channel (North Brittany). *J. Sea Res.* 53, 223–229. doi: 10.1016/j.seares.2004.12.002

Millero, F. J. (1995). Thermodynamics of the carbon dioxide in the oceans. *Geochimica et Cosmochimica Acta* 59, 661–677. doi: 10.1016/0016-7037(94)00354-O

Millero, F. J. (2007). The marine inorganic carbon cycle. *Chem. Rev.* 107, 308–341. doi: 10.1021/cr0503557

Muller-Karger, F. E., Astor, Y. M., Benitez-Nelson, C. R., Buck, K. N., Fanning, K. A., Lorenzoni, L., et al. (2019). The scientific legacy of the CARIACO ocean time-series program. *Ann. Rev. Mari. Sci.* 11, 413–437. doi: 10.1146/annurev-marine-010318-095150

Najiar, R. G., Herrmann, M., Alexander, R., Boyer, E. W., Burdige, D. J., Butman, D., et al. (2018). Carbon budget of tidal wetlands, estuaries, and shelf waters of eastern North America. *Global Biogeochem. Cycl.* 32, 389–416. doi: 10.1002/2017GB005790

Niu, J. (2013). Precipitation in the pearl river basin, South China: scaling, regional patterns, and influence of large-scale climate anomalies. *Stochastic Environ. Res. Risk Assess.* 27, 1253–1268. doi: 10.1007/s00477-012-0661-2

Oh, N. H., and Raymond, P. A. (2006). Contribution of agricultural liming to riverine bicarbonate export and CO2 sequestration in the Ohio River basin. *Global Biogeochem. Cycl.* 20:3. doi: 10.1029/2005GB002565

Olafsson, J., Olafsdottir, S. R., Benoit-Cattin, A., and Takahashi, T. (2010). The irminger sea and the iceland sea time series measurements of sea water carbon and nutrient chemistry 1983-2008. *Earth Syst. Sci. Data* 2:99. doi: 10.5194/essd-2-99-2010

Olafsson, J., Olafsdottir, S. R., Benoit-Cattin, A., Danielsen, M., Arnarson, T. S., and Takahashi, T. (2009). Rate of iceland sea acidification from time series measurements. *Biogeosciences* 6, 2661–2668. doi: 10.5194/bg-6-2661-2009

Oliveira, A. P., Pilar-Fonseca, T., Cabeçadas, G., and Mateus, M. (2018). Local variability of CO2 partial pressure in a mid-latitude mesotidal estuarine system (Tagus Estuary, Portugal). *Geosciences* 8:460. doi: 10.3390/geosciences8120460

Omar, A. M., Thomas, H., Olsen, A., Becker, M., Skjelvan, I., and Reverdin, G. (2019). Trends of ocean acidification and pCO2 in the northern North Sea, 2003–2015. *J. Geophys. Res. Biogeosci.* 124, 3088–3103. doi: 10.1029/2018JG004992

Osborne, E. B., Thunell, R. C., Gruber, N., Feely, R. A., and Benitez-Nelson, C. R. (2020). Decadal variability in twentieth-century ocean acidification in the California current ecosystem. *Nat. Geosci.* 13, 43–49. doi: 10.1038/s41561-019-0499-z

Ostle, C., Willliamson, P., Artioli, Y., Bakker, D. C., Birchenough, S. N. R., Davis, C. E., et al. (2016). *Carbon Dioxide and Ocean Acidification Observations in UK Waters: Synthesis Report With a Focus On 2010–2015*. Available online at: www.researchgate.net/publication/304324178_Carbon_dioxide_and_ocean_acidification_observations_in_UK_waters_Synthesis_report_with_a_focus_on_2010_-_2015?channel=doiandlinkId=576be75d08aead4e3add04a1andshow Fulltext=true (accessed July 17, 2020)

Ouisse, V., Migné, A., and Davoult, D. (2011). Community-level carbon flux variability over a tidal cycle in Zostera marina and Z. noltii beds. *Mari. Ecol. Progr. Series* 437, 79–87. doi: 10.3354/meps09274

Padin, X. A., Vázquez-Rodríquez, M., Ríos, A. F., and Pérez, F. F. (2007). Surface CO2 measurements in the english channel and southern bight of North Sea

using voluntary observing ships. *J. Mar. Syst.* 66, 297–308. doi: 10.1016/j.jmarsys.2006.05.011

Peng, S., Robinson, W. A., and Li, S. (2003). Mechanisms for the NAO responses to the North Atlantic SST tripole. *J. Clim.* 16, 1987–2004. doi: 10.1175/1520-04422003016<1987:MFTNRT<2.0.CO;2

Pingree, R. D., and Griffiths, D. K. (1978). Tidal fronts on the shelf seas around the British Isles. *J. Geophys. Res. Oceans* 83, 4615–4622. doi: 10.1029/JC083iC09p04615

Raven, J. A., Beardall, J., and Sánchez-Baracaldo, P. (2017). The possible evolution and future of CO2-concentrating mechanisms. *J. Exp. Bot.* 68, 3701–3716. doi: 10.1093/jxb/erx110

Raven, J. A., Gobler, C. J., and Hansen, P. J. (2020). Dynamic CO2 and pH levels in coastal, estuarine, and inland waters: theoretical and observed effects on harmful algal blooms. *Harmful Algae* 91:101594. doi: 10.1016/j.hal.2019.03.012

Reimer, J. J., Cai, W.-J., Xue, L., Vargas, R., Noakes, S., Hu, X., et al. (2017a). Time series pCO2 at a coastal mooring: internal consistency, seasonal cycles, and interannual variability. *Cont. Shelf Res.* 145, 95–108. doi: 10.1016/j.csr.2017.06.022

Reimer, J. J., Wang, H., Vargas, R., and Cai, W.-J. (2017b). Multidecadal fCO2 increase along the United States southeast coastal margin. *J. Geophys. Res. Oceans* 122, 10,061–10,072. doi: 10 1002/2017JC013170

Salt, L. A., Beaumont, L., Blain, S., Bucciarelli, E., Grossteffan, E., Guillot, A., et al. (2016). The annual and seasonal variability of the carbonate system in the bay of brest (Northwest Atlantic Shelf, 2008–2014). *Mar. Chem.* 187, 1–15. doi: 10.1016/j.marchem.2016.09.003

Staeher, P. A., Baastrup-Spohr, L., Sand-Jensen, K., and Stedmon, C. (2012). Lake metabolism scales with lake morphometry and catchment conditions. *Aquatic Sci.* 74, 155–169. doi: 10.1007/s00027-011-0207-6

Stets, E. G., Kelly, V. J., and Crawford, C. G. (2014). Long-term trends in alkalinity in large rivers of the conterminous US in relation to acidification, agriculture, and hydrologic modification. *Sci. Total Environ.* 488, 280–289. doi: 10.1016/j.scitotenv.2014.04.054

Sunda, W. G., and Cai, W. J. (2012). Eutrophication induced CO2-acidification of subsurface coastal Waters: interactive effects of temperature, salinity, and atmospheric pCO2. *Environ. Sci. Technol.* 46, 10651–10659. doi: 10.1021/es300626f

Sutton, A. J., Wanninkhof, R., Sabine, C. L., Feely, R. A., Cronin, M. F., and Weller, R. A. (2017). Variability and trends in surface seawater pCO2 and CO2 flux in the Pacific Ocean. *Geophys. Res. Lett.* 44, 5627–5636. doi: 10.1002/2017GL073814

Sutton, R. T., McCarthy, G. D., Robson, J., Sinha, B., Archibald, A. T., and Gray, L. J. (2018). Atlantic multidecadal variability and the UK ACSIS program. *Bull. Am. Meteorol. Soc.* 99, 415–425. doi: 10.1175/BAMS-D-16-0266.1

Takahashi, T., Olafsson, J., Goddard, J. G., Chipman, D. W., and Sutherland, S. C. (1993). Seasonal variation of CO2 and nutrients in the high-latitude surface oceans: a comparative study. *Glob. Biogeochem. Cycles* 7, 843–878. doi: 10.1029/93GB02263

Takahashi, T., Sutherland, S. C., and Kozyr, A. (2020). *Global Ocean Surface Water Partial Pressure of CO2 Database: Measurements Performed During 1957-2019 (LDEO Database Version 2019) (NCEI Accession 0160492). Version 9.9*. doi: 10.3334/CDIAC/OTG.NDP088(V2015.

Takahashi, T., Sutherland, S. C., Chipman, D. W., Goddard, J. G., Ho, C., Newberger, T., et al. (2014). Climatological distributions of pH, pCO2, total CO2, alkalinity, and CaCO3 saturation in the global surface ocean, and temporal changes at selected locations. *Mari. Chem.* 164, 95–125. doi: 10.1016/j.marchem.2014.06.004

Takahashi, T., Sutherland, S. C., Sweeney, C., Poisson, A., Metzl, N., Tilbrook, B., et al. (2002). Global sea–air CO2 flux based on climatological surface ocean pCO2, and seasonal biological and temperature effects. *Deep Sea Res. Part II Top. Stud. Oceanogr.* 49, 1601–1622. doi: 10.1016/S0967-0645(02)00003-6

Takahashi, T., Sutherland, S. C., Wanninkhof, R., Sweeney, C., Feely, R. A., Chipman, D. W., et al. (2009). Climatological mean and decadal change in surface ocean pCO2, and net sea–air CO2 flux over the global oceans. *Deep Sea Res. Part II Top. Stud. Oceanogr.* 56, 554–577. doi: 10.1016/j.dsr2.2008.12.009

Taylor, G. T., Muller-Karger, F. E., Thunell, R. C., Scranton, M. I., Astor, Y., Varela, R., et al. (2012). Ecosystem responses in the southern Caribbean Sea to global climate change. *Proc. Natl. Acad. Sci.* 109, 19315–19320. doi: 10.1073/pnas.1207514109

Thomas, H., Bozec, Y., de Baar, H. J., Borges, A., and Schiettecatte, L. S. (2005). Controls of the surface water partial pressure of CO2 in the North Sea. *Biogeosciences* 2, 323–334. doi: 10.5194/bg-2-323-2005

Tréguer, P. J., and De La Rocha, C. L. (2013). The world ocean silica cycle. *Annu. Rev. Mar. Sci.* 5, 477–501. doi: 10.1146/annurev-marine-121211-172346

Tréguer, P., Goberville, E., Barrier, N., l' Helguen, S., Morin, P., Bozec, Y., et al. (2014). Large and local-scale influences on physical and chemical characteristics of coastal waters of Western Europe during winter. *J. Mar. Syst.* 139, 79–90. doi: 10.1016/j.jmarsys.2014.05.019

Turk, D., Wang, H., Hu, X., Gledhill, D. K., Wang, Z. A., Jiang, L., et al. (2019). Time of emergence of surface ocean carbon dioxide trends in the North American coastal margins in support of ocean acidification observing system design. *Front. Mari. Sci.* 6:91. doi: 10.3389/fmars.2019.00091

Uppstrom, L. R. (1974). The boron/chlorinity ratio of deep-sea water from the Pacific Ocean. *Deep Sea Res.* 21, 161–162.

van Heuven, S. M. A. C., Pierrot, D., Rae, J. W. B., Lewis, E., and Wallace, D. W. R. (2011). *MATLAB Program Developed for CO2 System Calculations. ORNL/CDIAC-105b*. Tennessee: Oak Ridge National Laboratory, US Department of Energy, 530.

Vandemark, D., Salisbury, J. E., Hunt, C. W., Shellito, S. M., Irish, J. D., McGillis, W. R., et al. (2011). Temporal and spatial dynamics of CO2 air−sea flux in the gulf of maine. *J. Geophys. Res. Oceans* 116. doi: 10.1029/2010JC006408

Waldbusser, G. G., and Salisbury, J. E. (2014). Ocean acidification in the coastal zone from an organism's perspective: multiple system parameters, frequency domains, and habitats. *Annu. Rev. Mar. Sci.* 6, 221–247. doi: 10.1146/annurev-marine-121211-172238

Wallace, R. B., Baumann, H., Grear, J. S., Aller, R. C., and Gobler, C. J. (2014). Coastal ocean acidification: the other eutrophication problem. *Estuar. Coastal Shelf Sci.* 148, 1–13. doi: 10.1016/j.ecss.2014.05.027

Walsh, J. J., Biscaye, P. E., and Csanady, G. T. (1988). The 1983–1984 shelf edge exchange processes (SEEP)I experiment: hypotheses and highlights. *Cont. Shelf Res.* 8, 435–456. doi: 10.1016/0278-4343(88)90063-5

Wang, H., Hu, X., Cai, W. −J., and Sterba−Boatwright, B. (2017). Decadal fCO2 trends in global ocean margins and adjacent boundary current−influenced areas. *Geophys. Res. Lett.* 44, 8962–8970. doi: 10.1002/2017GL074724

Wanninkhof, R. (2014). Relationship between wind speed and gas exchange over the ocean revisited. *Limnol. Oceanogr. Methods* 12, 351–362. doi: 10.4319/lom.2014.12.351

Waters, J., Millero, F. J., and Woosley, R. J. (2014). Corrigendum to "the free proton concentration scale for seawater pH",[MARCHE: 149 (2013) 8-22]. *Mari. Chem.* 165, 66–67. doi: 10.1016/j.marchem.2014.07.004

Weiss, R. F. (1970). The solubility of nitrogen, oxygen and argon in water and seawater. *Deep Sea Res. Oceanogr. Abstr.* 17, 721–735. doi: 10.1016/0011-7471(70)90037-9

Weiss, R. F., and Price, B. A. (1980). Nitrous oxide solubility in water and seawater. *Mar. Chem.* 8, 347–359. doi: 10.1016/0304-4203(80)90024-9

Wolf-Gladrow, D. A., Zeebe, R. E., Klaas, C., Körtzinger, A., and Dickson, A. G. (2007). Total alkalinity: the explicit conservative expression and its application to biogeochemical proÎsses. *Mari. Chem.* 106, 287–300. doi: 10.1016/j.marchem.2007.01.006

Xue, L., Cai, W.-J., Hu, X., Sabine, C., Jones, S., Sutton, A. J., et al. (2016). Sea surface carbon dioxide at the georgia time series site (2006–2007): air–sea flux and controlling processes. *Prog. Oceanogr.* 140, 14–26.

Conflict of Interest: The authors declare that the research was conducted in the absence of any commercial or financial relationships that could be construed as a potential conflict of interest.

Copyright © 2021 Gac, Marrec, Cariou, Grosstefan, Macé, Rimmelin-Maury, Vernet and Bozec. This is an open-access article distributed under the terms of the Creative Commons Attribution License (CC BY). The use, distribution or reproduction in other forums is permitted, provided the original author(s) and the copyright owner(s) are credited and that the original publication in this journal is cited, in accordance with accepted academic practice. No use, distribution or reproduction is permitted which does not comply with these terms.

frontiers in Marine Science

ORIGINAL RESEARCH
published: 10 February 2021
doi: 10.3389/fmars.2021.634184

Climate and Human-Driven Variability of Summer Hypoxia on a Large River-Dominated Shelf as Revealed by a Hypoxia Index

Kui Wang[1,2], Wei-Jun Cai[3], Jianfang Chen[2], David Kirchman[3], Bin Wang[2], Wei Fan[1] and Daji Huang[2,4]*

[1] Ocean College, Zhejiang University, Zhoushan, China, [2] Key Laboratory of Marine Ecosystem Dynamics, Second Institute of Oceanography, Ministry of Natural Resources, Hangzhou, China, [3] School of Marine Science and Policy, University of Delaware, Newark, DE, United States, [4] Fourth Institute of Oceanography, Ministry of Natural Resources, Beihai, China

Coastal hypoxia has become common especially in large river dominated coastal ecosystems. To better quantify the severity of hypoxia and the contribution of hypoxia drivers, we applied principal component analysis (PCA) on observable properties from eight summer hypoxia events in the East China Sea and defined the first principal component as the hypoxia index (HI). Multiple linear regression showed that the HI significantly correlated with three direct hypoxia drivers including water column stratification, subsurface water residence time, and respiration rates, which accounted for 5.7, 55.3, and 34.5%, respectively, of the total variance of PCA derived HI. We further reconstructed the HI over the past 60 years using available long-term data of stratification, model-derived residence times and respiration rates. The results show that summer hypoxia has become more severe since the 1960s. ENSO and global warming may have exacerbated hypoxia by affecting the river discharge, resulting in freshening in the plume-impacted shelf area, while anthropogenic activities may have exacerbated hypoxia by elevating fluvial nutrient concentrations, resulting in higher respiration rates. In addition, warming of the bottom water from the Kuroshio Current accounts for an additional increasing rate for HI, which made hypoxia more severe by means of decreasing oxygen solubility. Overall, our results indicate that stratification, water residence and oxygen solubility resulting from climate change can explain about 80% while higher respiration resulting from higher nutrient inputs can explain about 20% of the variation in the severity of hypoxia during the past half century.

Keywords: coastal hypoxia, hypoxia index, East China Sea, respiration, stratification, residence time

OPEN ACCESS

Edited by:
Xianghui Guo,
Xiamen University, China

Reviewed by:
Yingxu Wu,
State Oceanic Administration, China
Tianqi Xiong,
Shandong University, China
Zhiming Yu,
Institute of Oceanology (CAS), China

****Correspondence:***
Jianfang Chen
jfchen@sio.org.cn

Specialty section:
This article was submitted to Marine Biogeochemistry, a section of the journal Frontiers in Marine Science

Received: *27 November 2020*
Accepted: *18 January 2021*
Published: *10 February 2021*

Citation:
Wang K, Cai W-J, Chen J, Kirchman D, Wang B, Fan W and Huang D (2021) Climate and Human-Driven Variability of Summer Hypoxia on a Large River-Dominated Shelf as Revealed by a Hypoxia Index. Front. Mar. Sci. 8:634184. doi: 10.3389/fmars.2021.634184

INTRODUCTION

Coastal hypoxia has become common especially in large river dominated coastal ecosystems, where a substantial amount of oxygen is consumed in subsurface waters via oxidation of organic matter coming from either external sources or internal primary production (Breitburg et al., 2018). Recent studies show hypoxia has become more wide-spread or severe in the last two decades; the number of

reported global "dead zones" is increasing (Breitburg et al., 2018), the area of hypoxia is expanding, and the minimum values of dissolved oxygen (DO) concentration are decreasing, even approaching anoxia. However, using a single property, such as hypoxic area, may be biased and insufficient to elucidate the severity of hypoxia. Other properties, such as thickness and minimum and average oxygen concentrations, are also crucial for exploring the severity of the hypoxia problem (Matli et al., 2018; Scavia et al., 2018).

Climate change and human activities influence coastal hypoxia via immediate or direct drivers and peripheral or indirect drivers. By immediate or direct drivers, we mean those factors that consume O_2 or limit the supply of O_2 to the bottom water (Fennel and Testa, 2018). The former includes water column and benthic organic carbon respiration (Resplandy, 2018), while the latter includes vertical advection and diffusion (Zhu et al., 2016; Markus Meier et al., 2018) (as characterized by water column stratification), lateral advection (Fennel and Testa, 2018) [as characterized by subsurface water residence time (τ)], and oxygen solubility (Lui et al., 2014). By peripheral or indirect factors, we mean those that lead to the direct factors. For example, eutrophication or high primary production in surface waters can lead to high respiration and thus hypoxia in bottom waters, and temperature and/or salinity gradients can lead to water column stratification. Most of the research on the coastal hypoxia mechanisms has focused on indirect factors, such as eutrophication driven by human activity (Rabalais et al., 2014; Wang et al., 2016) and ensuing enhancement of primary production and organic matter input (Chen et al., 2007; Li et al., 2018), or temperature and non-temperature effects driven by climate change (Altieri and Gedan, 2015; Li et al., 2016a). We argue that the relative contribution of each of these factors is still not clear. Because these indirect factors influence hypoxia via direct pathways, we must disentangle the contributions of the direct drivers in order to quantify the contributions of climate change and human activities and to delineate the pathways impacting the long-term variation of coastal hypoxia.

The relative contributions of direct drivers controlling long-term hypoxia also vary due to location and climatological regimes of local marine ecosystems. In this study, we have developed a hypoxia index (HI) as defined by the first component of principal component analysis (PCA), using data of observable properties from eight cruises in the Changjiang plume-impacted shelf area in the East China Sea (ECS). We then use a regression analysis of the derived HI and three direct hypoxia drivers (stratification, τ, and biological respiration) to quantify their relative contributions to hypoxia severity. As these direct factors were not available for long-term trend analysis, we used long-term observed data and model results, to reconstruct the HI and to explore the contribution of climate change (associated with stratification, τ, and oxygen solubility) and human activities (associated with biological respiration) to variation in hypoxia over the past 60 years. This study also has implications for understanding hypoxia in estuaries and bays affected by substantial nutrient runoff and climate change.

MATERIAL, MODEL, AND METHODS

Study Area and Sampling Collection

Changjiang River (also Yangtze River) is the largest river in the Euro-Asian continent, freshening the area continuously (Park et al., 2011) with its annual discharge of 924.8×10^9 m^3 yr^{-1} (Liu et al., 2016). Changjiang plume-impacted shelf area is one of the most productive continental shelf sea in the world due to the mixing of nutrient-laden Changjiang River plume and Kuroshio Current. Summer hypoxia occurs with strong stratification and prolonged residence time for subsurface water (Zhang et al., 2019), and also fueled by marine organic matter exporting from the surface (Wang et al., 2016). Hypoxia has been recorded since 1950s, and has become more severe recently with DO minimum decreasing and hypoxic area expanding (Zhu et al., 2011; Wei et al., 2017).

We visited the 31°N transect in the ECS eight times in August 2006, August 2009, September 2010, August 2011, August 2013, August 2014, August 2016, and August 2017 (**Supplementary Figure 1**). For this study, we focused on an area between 30.5°N and 32°N, 122.5°E and 125°E, and assembled oceanographic data over the past 60 years. This is the only transect in the region where long-term data are available.

At each station, temperature and salinity were measured with a Sea Bird model 911 conductivity-temperature depth (CTD) recorder. Water samples for measuring concentrations of nutrients, chlorophyll *a* (Chl *a*), and DO were collected with Niskin bottles attached to the CTD rosette.

Chemical Analysis

Concentrations of nutrients (NO_3^-, NO_2^-, NH_4^+, PO_4^{3-}, and SiO_3^{2-}) were determined with colorimetric methods, and DO was measured by Winkler titration method (Grasshoff et al., 1999). Chl *a* was measured using a Turner Designs 10-AU fluorometer (Holm-Hansen et al., 1965).

Conceptual Model

Observable Properties for Extended Definition of Hypoxia Severity

Since the status of hypoxia is not merely reflected by the area or oxygen concentration, it is necessary to find an index to express the hypoxia severity more comprehensively. In this study, we derive the index based on a PCA of six observable properties (**Supplementary Table 1**): sectional area, mean thickness, the longitude span of the hypoxia area (**Figure 1**), DO minimum, mean bottom DO, and mean DO concentration when saturation (DO%) was below 100%. Since the conventional hypoxia threshold of 2 mg L^{-1} is below the empirical sublethal and lethal DO thresholds for many organisms (Vaquer-Sunyer and Duarte, 2008), we defined hypoxia area as the vertical sectional area surrounded by the 94 μmol L^{-1} (3 mg L^{-1}) contour along the 31° N transect, the same threshold for hypoxia as previous reports defined (Chen et al., 2007; Levin et al., 2009; Zhou et al., 2017). The mean thickness of the hypoxia area (D_{hy}, m) is the averaged vertical distance between the 94 μmol L^{-1} contour and the bottom of the stations. The longitude span of the hypoxia

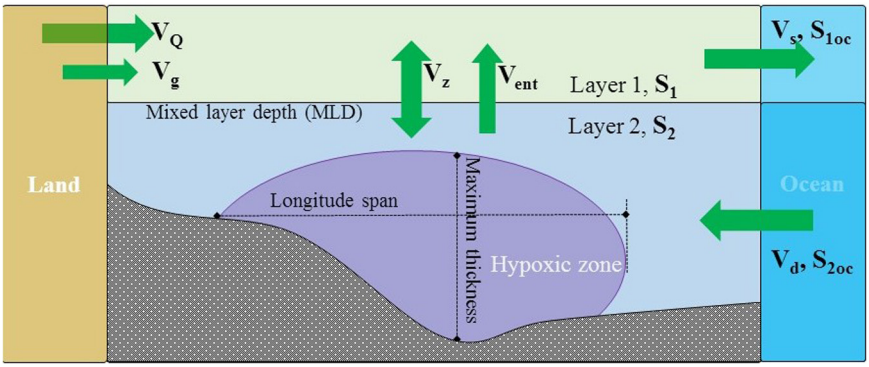


FIGURE 1 | A conceptual model for the dimension of sectional hypoxia area and water and salt budget. V_Q, volume of Changjiang River runoff; V_g, volume of groundwater runoff; V_z, vertical exchange volume between layer 1 and 2; V_{ent}, volume of advection-induced entrainment; V_s, surface advective outflow volume from layer 1; V_d, deep advective inflow volume to the layer 2; S_1, salinity of layer 1; S_2, salinity of layer 2; S_{1oc} and S_{2oc}, are oceanic endmember salinities of layer 1 and 2, respectively.

area is the maximum distance of the 94 μmol L^{-1} contour along 31°N transect.

Calculating the Direct Drivers Using the LOICZ Model

In order to quantify the contributions of the direct drivers in regulating hypoxia, we calculated τ and respiration rates during each cruise, using a two-layer river dominated LOICZ (Land-Ocean Interactions in the Coastal Zone) model (**Figure 1**), which was based on water and salt balances within each layer at steady state (Gordon et al., 1996). Layers 1 and 2 were divided by the mixed layer depth (MLD). We assumed the Changjiang River and the Kuroshio Current are the two major water masses mixing in the studied system. As groundwater data is very limited and the distribution is patchy, we assumed fresh groundwater only contribute to the layer 1 and a constant flux (V_g) of 0.02 m^3 m^{-2} d^{-1} (Guo et al., 2020) with average salinity (S_g) of 5 and phosphate of 3.3 μmol L^{-1} (Wang et al., 2018). Thus, water and salt balances in the entire system are:

$$V_s\,(\text{output}) = V_Q + V_g + V_d\,(\text{inputs}) \quad (1)$$

$$V_s \times S_1\,(\text{output}) = V_d \times S_{2oc} + V_Q \times S_Q + V_g \times S_g\,(\text{inputs}). \quad (2)$$

The salt contributed by Changjiang River water and groundwater were far less than deep advective inflow (V_d) [salinity of Changjiang River water (S_Q) at the Xuliujing station (**Supplementary Figure 1**) was usually <0.15 (unpublished data)] and the total discharge of Changjiang River water and groundwater was far less than V_d, then the last two items ($V_Q \times S_{2Q} + V_g \times S_{2g}$) of Eq. 2 could be ignored.

A combination of Eqs1 and 2 gives:

$$V_d = (V_Q + V_g) \times S_1 / (S_{2oc} - S_1) \quad (3)$$

For the bottom layer, the salt balance is:

$$V_d \times S_{2oc} = V_{ent} \times S_2. \quad (4)$$

The variables are defined in **Figure 1**.

Stratification (Δσ) was defined as the average difference in the density anomaly between bottom and surface (0–2 m depth) at stations along the transect. We used the simple linear equation of seawater state (Intergovernmental Oceanographic Commission [IOC], 2010) to estimate the density difference between bottom and surface seawater,

$$\Delta\sigma = \rho_b\,(S_b, T_b, p_b) - \rho_s\,(S_s, T_s, p_s) \quad (5)$$

where T_s and T_b are surface and bottom temperature (°C), S_s and S_b are surface and bottom absolute salinity, and p_s and p_b are surface and bottom pressure (dbar), respectively. For reducing the observational errors of S_s and S_b, we used historical data from the Japan Meteorological Agency, Oceanographic Data Center (JODC), the Korea Oceanographic Data Center (KODC), and the World Ocean Atlas (WOA), which were averaged in the specified box (122.5°E–125°E, 30.5°N–32°N, **Supplementary Figure 1**), besides of our own data. MLD is defined as the depth at which the density differs by 0.125 from the surface value (Huang and Russell, 1994).

Average water residence time is typically expressed as the ratio of system volume to the average rate of outflow through the system (Gordon et al., 1996). For layer 2, there are two types of water mixing; one is the vertical exchange with layer 1 including diffusion and advection (including entrainment) (V_z), and the other is layer 2 water exchange with the offshore subsurface water (V_d). The latter often accounts for most of the water mixing. If so, then τ is the total volume of subsurface water divided by the water inputs (outputs) or V_2/V_d, can be simply presented by combining Eq. (3) for canceling out V_d:

$$\tau = V_2/V_d = V_2 \times (S_{2oc}/S_1 - 1)\,/(V_Q + V_g). \quad (6)$$

The long-term τ can be calculated based on Eq. 6, V_2 was obtained by multiplying the depth below MLD and assuming a fixed study area of 1.8×10^{10} m^3 along the transect (122°E–124°E, 30.5°N–31.5°N).

The last direct driver is the respiration rates in the water (R_h, mmol C m^{-2} d^{-1}), which we derive from the difference

between NPP (net primary production) and NEP (net ecosystem production), as NPP = GPP−R_a and NEP = GPP−(R_a + R_h). GPP is gross primary production, and R_a is autotrophic respiration rates. NPP data were acquired from the Marine Satellite Data Online Analysis Platform ($SatCO_2$)[1], including monthly SeaWiFS VGPM NPP from 1997 to 2007 and MODIS Aqua VGPM NPP from 2002 to 2016. These NPP products were corrected by euphotic layer depth including the effect of colored dissolved organic matter absorption (He et al., 2017). NEP was calculated using the LOICZ model, as the net biological uptake or release of carbon calculated from phosphate stoichiometrically (C/P = 106) (Gordon et al., 1996) within each layer.

Thus, we have,

$$R_h = NPP - NEP \quad (7)$$

R_h of 37.0 mmol C m^{-2} d^{-1} from *in situ* incubation was applied for 2014 due to too much cloud for deriving satellite NPP in the study area. The mean values and uncertainties (standard deviation) of satellite NPP and LOICZ model derived NEP are 68.8 ± 7.9 and 28.2 ± 68.9 mmol C m^{-2} d^{-1}, respectively, based on the eight cruises with an error propagation method (Taylor, 1997). The mean value and uncertainty of R_h is estimated to be 44.7 ± 70.2 mmol C m^{-2} d^{-1}. The volumetric respiration rates (mmol C m^{-3} d^{-1}) was assumed constant over the whole water column in the hypoxia area. This approach is verified and deemed acceptable based on our results during 2011 cruise at five stations of 24 h-incubation for respiration along the transect in Changjiang plume-impacted shelf area (averaged 30.1 ± 24.8, 35.5 ± 19.2, and 26.4 ± 21.5 for 2 m, 10 m, and bottom waters, respectively). The integrated respiration rates in the hypoxia area (R_{hy}, mmol C m^{-2} d^{-1}) depends on the thickness of the hypoxia area and the water depth (D, m) over longitudes (L) spanning the sampling stations from west (Lw) to east (Le):

$$R_{hy} = R_h \int_{Lw}^{Le} (D_{hy}/D) dL. \quad (8)$$

The contribution of sediment to R_{hy} was assumed to be 50% (Zhou et al., 2017) and an average 8.43 mmol O_2 m^{-2} d^{-1} of sediment oxygen consumption (Song et al., 2016) compare to our 16.26 mmol O_2 m^{-2} d^{-1} of R_{hy} in 2011. Redox-mediated phosphorus desorption from inorganic particles were assumed to be very limited due to adsorption-desorption equilibrium at mineral surfaces (Meng and Yao, 2014) and very high phosphorus burial efficiency (Liu et al., 2016) in the study area.

Long-Term Data

Changjiang River discharge (Q) data were downloaded from the website of the Ministry of Water Resources of the People's Republic of China.[2] The discharges were measured at the hydrological gauge station, Datong, which has no tidal influence and is 624 km upstream from the river mouth.

Dissolved inorganic nitrogen (DIN) and dissolved inorganic phosphate (DIP) fluxes in August were calculated as the product of Changjiang River discharge in August and nutrient concentrations at Datong gage station or Xuliujing station (**Supplementary Figure 1**) in historical records (Gu, 1980; Quan et al., 2005; Wang, 2006; Li et al., 2007, 2016b; Dai et al., 2011; Gao et al., 2012) and *in situ* observations during summers of 2009, 2010, 2011, 2013, 2014, and 2016 at Xuliujing station.

Multivariate ENSO index (MEI) was obtained from https://www.esrl.noaa.gov/psd/enso/mei/ (Wolter and Timlin, 1998).

Sea surface temperature (SST) in August along the 31°N transect was provided by the NOAA-ESRL Physical Sciences Division, Boulder Colorado from their website at https://www.esrl.noaa.gov/psd/, named as COBE SST2.

In situ observations of long-term temperature and salinity in August within the study box were from JODC,[3] KODC,[4] and WOA version 2013.[5]

Wind speed data were acquired from the International Comprehensive Ocean-Atmosphere Data Set (ICOADS) with 2-degree spatial resolution at the website of the Royal Netherlands Meteorological Institute (KNMI[6]).

Data Analysis

To quantify the hypoxia severity, we applied PCA to the six observable properties. PCA is a useful technique for reducing the dimensionality of large datasets, increasing interpretability but at the same time minimizing information loss. Numerous variables including those correlated with each other can be synthesized to create new uncorrelated variables (as principal components), for successively maximizing the variance of datasets (Jolliffe and Cadima, 2016). Briefly, a data matrix of six observable properties for eight cruises (**Supplementary Table 1**) was standardized by substracting the mean and dividing their standard deviation to give a new data matrix, which then was multiplied by the eigenvector to give the variances matrix of six properties for 8 years. We then summed the variances for each year to give the first component. The differences in order of magnitudes of the six properties will not affect the first principal component. The first principal component accounted for 74% of the total variance of the observable properties, and was significantly positively correlated with sectional area (**Supplementary Table 1**), mean thickness and the longitude span of the hypoxia area, but significantly negatively correlated with DO minimum, mean bottom DO, and mean DO concentration when DO < 100%, representing the status of the "severity" of the hypoxia. Therefore, we use the first principal component as a HI to indicate the severity of hypoxia along the transect. The larger the index, the more severe the hypoxia is.

To estimate the contribution of the direct controlling factors to the HI, multiple regression was applied to generate coefficients of the individual variables, which were then standardized by multiplying by the ratio of the standard deviation of each independent variable to the standard deviation of the dependent variable in order to compare them. We

[1]http://www.satco2.com

[2]http://www.hydroinfo.gov.cn

[3]http://www.jodc.go.jp/jodcweb/

[4]http://www.nifs.go.kr/kodc/index.kodc

[5]https://www.nodc.noaa.gov/OC5/woa13/woa13data.html

[6]http://climexp.knmi.nl

used SPSS® v.13 software for PCA and multiple regression, as well as the outlier identification based on a boxplot procedure (Sim et al., 2005).

RESULTS

DO and Nutrients

The core of the under-saturated water was usually located between 122.5°E and 123.25°E (**Supplementary Figure 2**). The area where DO < 42% (~3 mg L^{-1} in DO concentration) varied in shape over the 8 years, and the largest area was in summer of 2016. The lowest DO saturation of 12% was found in 2017 in the bottom water of station B8 (unpublished data).

Dissolved inorganic nitrogen along the 31°N transect was high in the west and low in the east (**Supplementary Figure 3**), due to high concentrations in the Changjiang River plume. The highest concentration was 105 μmol L^{-1} at station G9 in the summer of 2009. DIN was below 1 μmol L^{-1} in the outer shelf surface water in the summers of 2006 and 2013.

There were usually two areas of high PO_4^{3-} (**Supplementary Figure 4**). One is in Changjiang plume-impacted shelf area, and the other is in the bottom water coming from the outer shelf deep water or Kuroshio subsurface water. The highest concentration of PO_4^{3-} was 2.1 μmol L^{-1} at station M4-1 during the summer of 2011, while P from the upwelling was up to 1.1 μmol L^{-1} at the bottom layer of station M4-8 in 2006.

Observable Properties of Hypoxia and the Hypoxia Index

The DO minimum was 69.5 μmol L^{-1} in 2006 and 42.19 μmol L^{-1} in 2010, then it jumped to the highest value of 73.44 μmol L^{-1} in 2013. It then decreased to 26.88 μmol L^{-1} in 2017 (**Figure 2A**).

The hypoxia area along the 31°N transect increased from 0.315 km^2 in 2006 to more than 10 times larger in 2014 and in 2016. The mean thickness also increased from 5.97 m in 2006 to a maximum of 21.9 m in the summer of 2016. The longitude span of the hypoxia area expanded from 2006 to 2016, from less than 95 km to up to 190 km (**Figure 2B**).

The HI showed that hypoxia has been becoming more severe (**Figure 2C**) in terms of decreasing DO concentration and increasing area, thickness and longitude span from 2006 to 2014, but alleviated a bit after 2014.

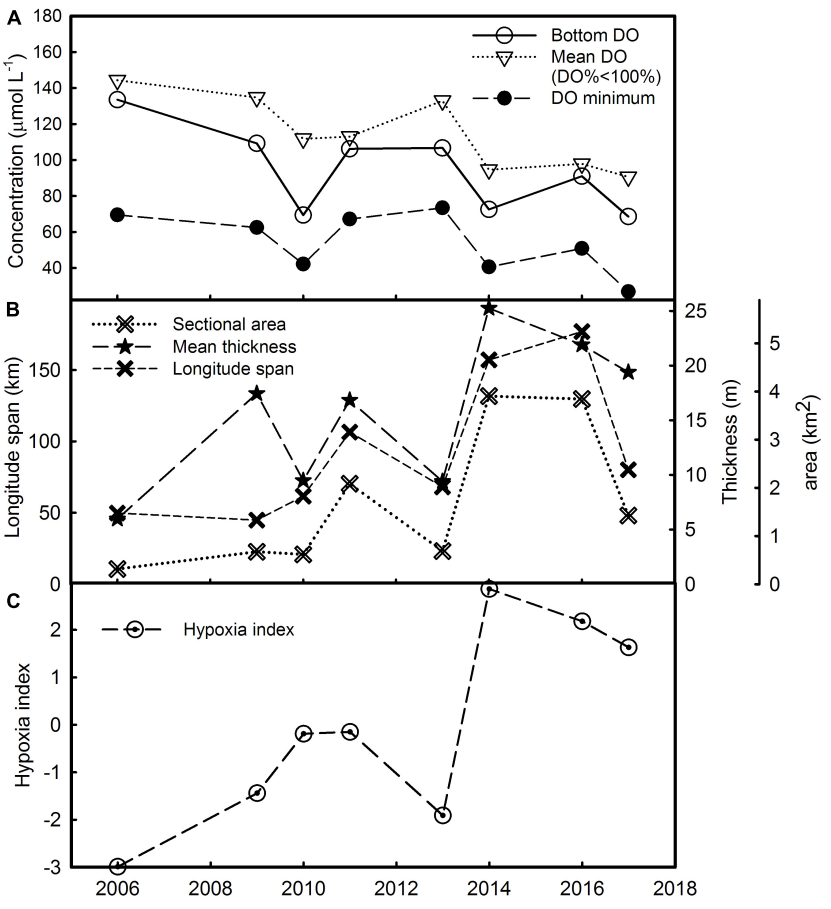


FIGURE 2 | Observable properties of hypoxia including **(A)** bottom DO, mean DO concentration when DO < 100% and DO minimum, and **(B)** sectional area, mean thickness and longitude span used to derive **(C)** the hypoxia index (HI) during 8 years.

Direct Drivers of Hypoxia

Seawater density anomaly of the 8 years showed strong stratification along the 31°N transect (**Supplementary Figure 5**). The density anomaly difference between bottom and surface ($\Delta\sigma$) indicated that strong stratification usually occurred between 122.5°E and 124°E. The highest was 13.06 kg m^{-3}, at 122.65°E in summer 2009, while the lowest value of 3.68 kg m^{-3} was from the summer 2006.

τ was the lowest in the 2006, and maximal in 2016 (**Supplementary Table 2**). Surface NEP in 2013 was the highest and subsurface NEP was the lowest among the eight cruises, indicating a high export production and respiration rates. Temperature associated with oxygen solubility changed little so we did not present it for the eight cruises.

DISCUSSION

Direct Driver Contribution to Hypoxia Severity

Stratification of the water column plays an important role in hypoxia development (Zhu et al., 2016). Over the 8 years, the bottom DO was significantly negatively correlated with the density difference ($\Delta\sigma$) between bottom and surface ($r = -0.66$, $p < 0.01$, $n = 47$) (**Figure 3A**), indicating the stronger stratification the lower bottom DO. HI was significantly correlated with averaged $\Delta\sigma$ between 122.3 and 124°E ($r = 0.82$, $p < 0.01$, $n = 8$) (**Figure 3B**), demonstrating an important role of stratification in regulating hypoxia.

Hypoxia index also significantly correlated with τ ($r = 0.83$, $p < 0.01$, $n = 8$) (**Figure 3C**), indicating the longer the water stayed under the MLD, the more severe the hypoxia became, due to insufficient oxygen supply from deep water or the upper mixed layer (Fennel and Testa, 2018). This is consistent with previous studies on river-dominated ocean margins (Rabouille et al., 2008).

In R_{hy} and HI dataset, an outlier (R_{hy} for 2014) was identified. After removing the outlier, the significant correlation between R_{hy} and HI (**Figure 3D**) ($r = 0.82$, $p < 0.03$, $n = 7$) showed that community respiration of organic matter by microorganisms such as bacteria (Chen et al., 2006) was a direct crucial factor that controls the extent of hypoxia. Biogenic particles from the euphotic zone dominated the organic matter as a substrate respired in the aphotic layer in the Changjiang plume-impacted shelf area (Wang et al., 2016).

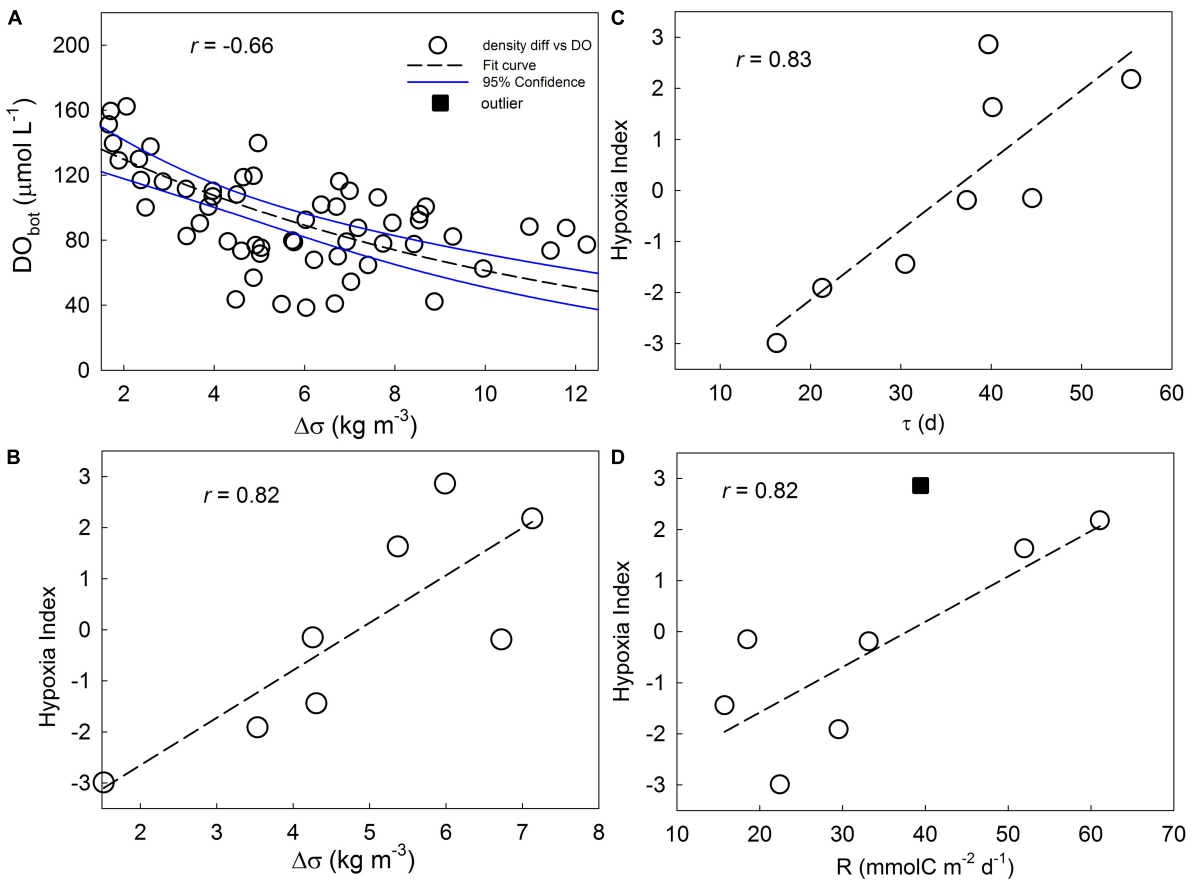


FIGURE 3 | Correlations between **(A)** bottom DO and $\Delta\sigma$ of stations between 122.3–124°E during summers of the 8 years along the transect, **(B)** HI and mean $\Delta\sigma$ of all stations, **(C)** HI and residence time (τ) under mixed layer depth (MLD), and **(D)** hypoxia index (HI) and R in hypoxia area (R_{hy}) for 8 years.

In addition, temperature may play a role in determining the respiration rates (Hopkinson and Smith, 2005), but there was no significant correlation between R_{hy} and bottom temperature, perhaps because temperature changed little in the bottom waters over the eight summers (21.29 ± 0.91°C). If we use the relationship between pelagic respiration and temperature derived by Hopkinson and Smith (2005), respiration would be 391.9 ± 12.9 mmol C m^{-2} d^{-1} which varied less than 3% over this narrow temperature range. In fact, respiration may not follow temperature in some estuaries (Jensen et al., 1990; Satta et al., 1996), especially when there is substantial input of external organic matter (Iriarte et al., 1997). While temperature plays an important role in regulating seasonal respiration rates variation, its influence cannot be distinguished during warm summer periods.

According to a multiple regression analysis, Δσ, τ, and R_{hy} together explained 95.6% of the total variance of HI (r = 0.98, p = 0.02, n = 7). Area and DO_{min} are the most common observable properties used to characterize hypoxic zones. The correlation coefficients between the drivers and area or DO_{min} were lower than for the drivers and HI. The correlations for area and DO_{min} are 0.79 (p = 0.23, n = 8) and 0.75 (p = 0.30, n = 8), respectively, suggesting HI was more robust in describing the severity of hypoxia. The regression equation linking HI to the direct drivers is:

$$\begin{aligned} HI = {} & (0.06 \pm 0.23) \times \Delta s + (0.09 \pm 0.03) \times \tau \\ & + (0.04 \pm 0.02) \times R_{hy} - (5.24 \pm 0.64)\,. \end{aligned} \quad (9)$$

The standardized coefficients were 0.06, 0.57, and 0.35, for Δσ, τ, and R_{hy}, respectively. Based on these coefficients, the three factors contributed 5.7, 55.3, and 34.5%, respectively, to the total variance of HI. If we consider Δσ and τ as two related physical parameters and combine them into one category, then, we could argue that physical stability of the bottom water contributes more than does respiration in forming hypoxia (61.0 versus 34.5%).

Reconstruction of Hypoxia Index for the Past Six Decades

In this section, we reconstruct the HI during the past 60 years, using Eq. 9 and data about direct drivers from field observations and/or correlations between direct and indirect parameters.

To calculate Δσ over the long-term, we used averaged salinity and temperature of surface and bottom layers in the study area based on historical data from JODC, KODC, and WOA. Δσ showed an increase at a rate of 0.025 kg m^{-3} yr^{-1} during 1961–1996. After a slight decrease during 1997–2002 it rose after 2003 at a higher rate of 0.047 kg m^{-3} yr^{-1}. Δσ was consistent with the variation of Changjiang River discharge during 1957–2017 (r = 0.32, p < 0.05, n = 55) (**Figure 4A**), which freshening the sea surface continuously. Previous studies also suggested a long-term freshening in the northern ECS (Siswanto et al., 2008; Park et al., 2011). Although the August discharge temporarily decreased by ∼10% at June 2003 when the Three Gorges Dam began to impound water (Chai et al., 2009), it has been increasing before and after 2003 (**Figure 4A**). The more stratified conditions allow more severe hypoxia in the study area (Wei et al., 2007; Zhu et al., 2016).

The long-term τ has been increasing at a rate of 0.11 d yr^{-1} during 1961–1996, and increased at a much higher rate of 2.52 d yr^{-1} during 2003–2017 (**Figure 4B**). This is also associated with the discharge but more closely associated with salinity of the upper mixed layer (**Figure 4B**) according to Eq. 6. The fresher the sea surface is, the less water exchange, which allows for longer time for decomposition of organic matter and more consumption of oxygen.

Because respiration data in the hypoxia area are lacking for this long time period, we used NPP based on the significant correlation between NPP and R_{hy} during the 8-year record. As previous studies have found, R_h significantly correlated with NPP (Hopkinson and Smith, 2005), so we can use NPP to estimate R_{hy} assuming a fixed averaged hypoxic water thickness over longitude to water depth ratio (0.52) derived from the eight cruises, and assuming 50% contribution of sediment to hypoxia:

$$\begin{aligned} R_{hy} = {} & (1 + 0.5) \times 0.52 \times R_h = 1.5 \times 0.52 \times ((1.60 \pm 0.72) \\ & \times NPP - (59.81 \pm 48.20)). \end{aligned} \quad (10)$$

High NPP was due to higher river DIN flux in recent decades (Gong et al., 2006). While summer discharge varied relatively little during the past 60 years (p > 0.05; **Figure 4A**), nutrient concentrations have increased most of the period (**Figures 4C,D**) due to anthropogenic activity such as agricultural use of fertilizers and industrial and household pollution (Wang, 2006; Li et al., 2007, 2016b; Dai et al., 2011). After 2010, both DIN and DIP concentrations and fluxes decreased. Together DIN and DIP fluxes accounted for 56.9% of the variation of NPP, whereas individually DIN and DIP contributed 33.3 and 23.6%, respectively. We can build a relationship between NPP and DIN and DIP fluxes (p < 0.05, n = 12):

$$\begin{aligned} NPP = {} & \left(4.59 \times 10^{-8} \pm 1.85 \times 10^{-8}\right) \times F_{DIN} \\ & + \left(1.27 \times 10^{-6} \pm 7.25 \times 10^{-7}\right) \\ & \times F_{DIP} + (36.83 \pm 7.96)\,. \end{aligned} \quad (11)$$

Then the long-term R_{hy} (**Figure 4E**) can be calculated by incorporating Eq. 11 into Eq. 10. Finally the long-term HI variation can be reconstructed with long-term Δσ, τ, and R_{hy} using Eq. 9. The reconstructed HI varied between −4.42 and 2.68 (**Figure 4F**), and the standard deviation was from ±1.95 to ±3.58. The highly significant correlation between the reconstructed HI values and PCA-derived HI values (2006–2017) verifies the HI reconstructing model (r = 0.89, p < 0.01, n = 8). The reconstructed HI was highest in 2016 while PCA-derived HI was highest in 2014 (**Figure 4F**). This difference could be from the uncertainty of reconstructed HI or the limited sampling locations and periods, suggesting we should be careful when comparing hypoxia severity between specific years, and more historical field data are needed for the verification of HI. However, in summer of 2016 DO was nearly zero north of the 31°N transect during the same cruise, indicating hypoxia was most severe in 2016, consistent with our reconstructed HI. Therefore, we use reconstructed HI for trend analysis.

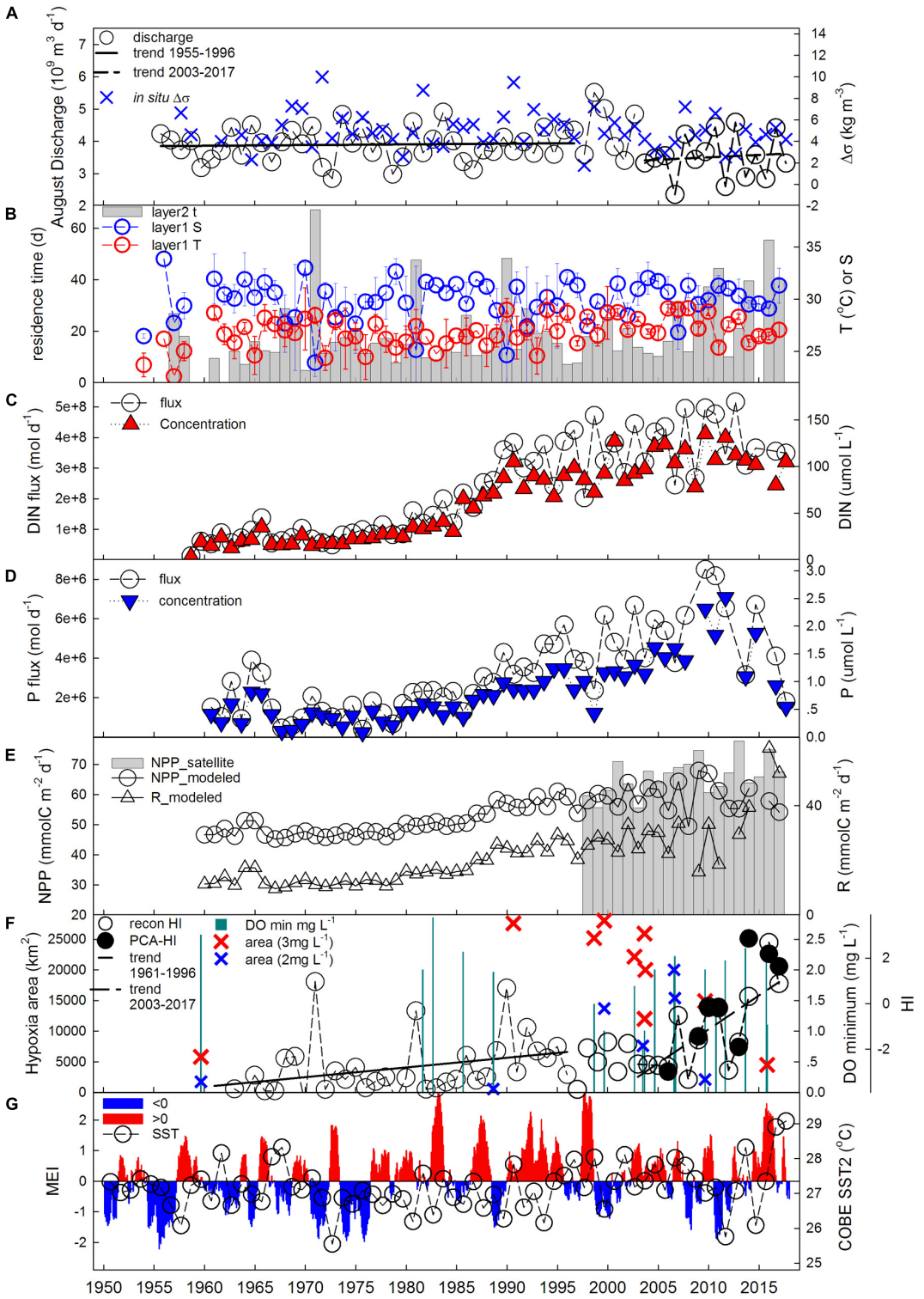


FIGURE 4 | Long-term variation of **(A)** Changjiang River discharge in August and averaged density difference between bottom and surface ($\Delta\sigma$); **(B)** averaged temperature (T) and salinity (S) in layer 1 using historical data and water residence time in layer 2 derived from LOICZ model. **(C)** DIN (DIN = NO_3^- + NO_2^- + NH_4^+) concentration and flux and **(D)** DIP concentration and flux in the fresh water endmember in Changjiang River; **(E)** averaged NPP derived from satellite along 31°N transect using the $SatCO_2$ platform, modeled NPP based on Eq. 11, and modeled respiration in the hypoxia area (R_{hy}); **(F)** plane area of bottom hypoxia region (<3 and <2 mg L^{-1}) and DO concentration minimum in historical records (Gu, 1980; Tian et al., 1993; Li et al., 2002; Quan et al., 2005; Wei et al., 2007; Pei et al., 2009; Li et al., 2018), compared with reconstructed (recon) and PCA-derived hypoxia index (HI); **(G)** MEI (multivariate ENSO index) and averaged August SST (COBE-SST2 from NOAA) at 31°N transect in Changjiang plume-impacted shelf area.

The hypoxia index showed an overall increase over time accelerating in the last two decades (**Figure 4F**). Specifically, HI increased slowly during 1961–1996 (with the rate of 0.042 yr^{-1}), then it increased during 1997–2002 and during 2003–2017 at higher rates (0.222 and 0.298 yr^{-1}, respectively). Long-term variation of HI is consistent with the general trends of $\Delta\sigma$, τ, and R_{hy} (**Figures 2E,F**, **4B**), suggesting all three direct drivers also regulate the long-term HI variation.

Climate Change and Human Activities Effects on Inter-Annual Variation of Hypoxia

ENSO and global warming contributed to long-term variation of hypoxia in terms of fluvial discharge freshening Changjiang plume-impacted shelf area, resulting in stronger stratification and longer residence time in the study area (**Figure 5**). Indeed, the average salinity in layer 1, were significantly negatively correlated with $\Delta\sigma$ ($r = -0.90$, $p < 0.01$, $n = 53$) and residence time ($r = -0.697$, $p < 0.01$, $n = 53$). The influence of ENSO on the Asian summer monsoon propagates from winter until early summer (Yang et al., 2018). Warm and cold ENSO phases were represented by MEI, consistent with the surface temperature along the 31°N transect (**Figure 4G**). The warm phase (El Niño events) will elevate freshwater discharge of Changjiang River, through affecting precipitation and evaporation in the Changjiang River drainage area during the summer monsoon (Gong and Ho, 2002). This is supported by the significant positive correlation between MEI (November-December) and August discharge of the next year for Changjiang River during 1955–2017 (**Supplementary Figure 6**), similar to the results of Bai et al. (2014). Meltwater from glaciers in the Qinghai-Tibetan Plateau in western China, which has increased due to global warming, is another probable freshwater source contributing to the runoff increase (Ding et al., 2006; Siswanto et al., 2008).

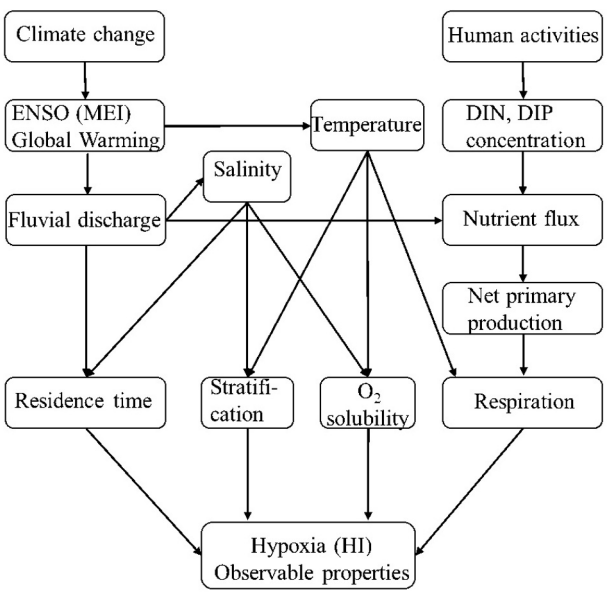


FIGURE 5 | Schematic diagram of factors controlling estuarine hypoxia. Climate change and anthropogenic activities affect coastal hypoxia by direct drivers through many pathways.

Surface warming would also play a role in regulating stratification in Changjiang plume-impacted shelf area (Park et al., 2011); the correlation between SST in layer 1 and $\Delta\sigma$ was significant ($r = 0.39$, $p < 0.01$, $n = 53$), suggesting that global warming and ENSO also contributed to the change in stratification in terms of temperature over the past 60 years (**Figure 5**). Water masses such as Taiwan Warm Current (Pei et al., 2009), the Kuroshio Current and Ekman transport could also play a role in regulating the long-term variation in stratification (Siswanto et al., 2008), but this needs more data and further exploration.

Moreover, the fourth direct driver—oxygen solubility, was closely associated with subsurface water temperature, and rapid warming in the ECS (Belkin, 2009) will decrease oxygen solubility. Although salinity also affects oxygen solubility, we ignored its effect due to very little variation during the past 60 years (∼0.007 yr^{-1}) and ∼1/3 less significant impact on oxygen solubility in seawater than temperature when they change to the same extent. Our analysis showed bottom water has been warmed up by 4.44°C from 1961 to 2017 [(0.078°C yr^{-1}, much faster than SST increasing at a rate of 0.026°C yr^{-1} for the whole ECS (Belkin, 2009) and 0.011°C yr^{-1} of Kuroshio Current (Wu et al., 2012)]. Since the bottom water mainly comes from Kuroshio Current and will be cooled down and oxygenated each winter, we infer the warming of Kuroshio Current not the bottom water *per se* contributes to the long-term oxygen solubility decrease. Warming rate of 0.011°C yr^{-1} corresponds to oxygen solubility decrease rate of 0.317 μmol L^{-1} yr^{-1} at salinity of 34, then increasing rate of HI will be higher by an additional 0.022 yr^{-1} (based on the correlation between HI and average bottom DO); namely, warming will make hypoxia ∼34% (∼10%) more severe by means of decreasing oxygen solubility during 1961–1996 (1997–2017) in the study area.

If we use multiple linear regression again between the long-term reconstructed HI and the three direct drivers, we can differentiate the contribution of $\Delta\sigma$, τ, and R_{hy} to the total variance of HI, as 6.1, 63.6, and 30.2%, respectively. Considering the oxygen solubility as the fourth direct driver, the contribution of four direct drivers would be 4.0, 41.8, 19.8, and 34.4% (5.5, 56.9, 27.0, and 10.6%) during 1961–1996 (1997–2017). Although many studies focus on stratification (Zhu et al., 2016; Zhang et al., 2018) or organic matter-induced respiration (Chen et al., 2007; Zhu et al., 2011; Wang et al., 2016) based on short time observations, τ played a more important role than the other three drivers in controlling HI variation in Changjiang plume-impacted shelf area during the past decades. This can be attributed to both advection rate and low DO context of Taiwan Warm Current (Qian et al., 2017) or Kuroshio Intermediate Water (Lui et al., 2014). Other studies also addressed the water residence time as a dominant driver of hypoxia, e.g., in Bellingham Bay (Wang and Yang, 2015), Gulf of St. Lawrence (Fennel and Testa, 2018), and comparison study between ECS and Gulf of Mexico (Rabouille et al., 2008), but few quantified its importance.

Wind plays a less important role in regulating interannual stratification, although eastward Ekman transport, forced by the prevailed southerly or southwesterly wind, may contribute to the eastward extension of the Changjiang River plume (Siswanto et al., 2008). If we use the wind mixing parameter h/W^3 (h is the water depth, W is the wind speed) with a value of 0.056 m^{-2} s^3 (Xuan et al., 2012) and a highest (mean) wind speed of 5.33 (3.41 ± 0.86) m s^{-1} from 1961 to 2017 along the transect during summer, the MLD is estimated to be 8.47 (2.26 ± 0.035) m. This calculation indicates that wind may influence only the very surface, which is consistent with our 8 years of observations. On the other hand, a typhoon will break the hypoxia, but it would not last long compared with the time scale of weeks to months for hypoxia. Moreover, local hypoxia would persist and even be exacerbated after a typhoon as biological production is enhanced by bring nutrients from bottom to surface water due to the storm mixing (Ni et al., 2016).

Enhanced respiration was mainly caused by anthropogenic activities releasing nutrients to Changjiang plume-impacted shelf area, resulting in elevated NPP (**Figures 4F**, **5**). This is consistent with results from the northern Gulf of Mexico (Rabalais et al., 2014), Chesapeake Bay (Li et al., 2016a), and other eutrophic coastal waters (Breitburg et al., 2018). Increasing temperatures may also lead to higher NPP (Altieri and Gedan, 2015; Li et al., 2016b), but there was no significant correlation between MEI and satellite NPP during 1997–2017, nor was there a significant correlation between SST and NPP. Unlike the eight cruises, the long-term variability in respiration was associated with warming to some extent, as demonstrated by a weak correlation between bottom R_{hy} and temperature ($r = 0.376$, $p < 0.01$, $n = 53$).

CONCLUSION

Overall, in coastal waters or shelf seas, hypoxia severity in the subsurface water is directly regulated by $\Delta\sigma$, τ, R_{hy}, and oxygen solubility. The year-to-year variation in reconstructed HI indicates that summer hypoxia has become more severe since 1960s, because fluvial nutrients concentrations have increased due to increases in anthropogenic activities, and stratification has been stronger and water residence time longer than before. ENSO and global warming may have indirect affects through regulating the fluvial discharge and altering the stratification and residence time by freshening and warming the surface sea, as well as reducing oxygen solubility in the subsurface water. In addition, higher nutrients inputs, as one of the most significant human activities, will enhance primary production and eventually the respiration rates in the subsurface waters; these nutrient fluxes will also be enhanced by elevated discharge. In conclusion, our analyses suggest that climate change accounts for about 80% of the forces regulating hypoxia in the Changjiang river-impacted shelf while human activity accounts for the remaining 20%.

DATA AVAILABILITY STATEMENT

The original contributions presented in the study are included in the article/**Supplementary Material**, further inquiries can be directed to the corresponding author/s.

AUTHOR CONTRIBUTIONS

KW, JC, and W-JC conceived the study. KW, DH, BW, and WF conducted the field studies. W-JC and DK polished the manuscript. KW processed the data. All authors prepared the manuscript.

FUNDING

This study was funded by National Natural Science Foundation of China (Nos. U1709201, U1609201, 41976154 and 41706120), Long-term Observation and Research Plan in the Changjiang Estuary and East China Sea Project (LORCE). The Scientific Research Fund of the Second Institute of Oceanography, Ministry of Natural Resources, China (No. JT1603). MNR Pilot Project of Early Warning Monitoring of Hypoxia and Ocean Acidification in the Changjiang Estuary (2020–2022).

ACKNOWLEDGMENTS

We sincerely thank Maotian Li in East China Normal University for long-term nutrients data at Datong hydrographic station, and Xianqiang He, Feng Zhou, Yan Bai, Qiang Hao, Ping Du, Tao Lian, Xiaobo Ni, Jiliang Xuan, and Dewang Li in Second Institute of Oceanography, Ministry of Nature Resource of China, Willard Moore in University of South Carolina for their helpful comments. We also thank the crews of R/V "Haijian49," R/V "Beidou," and R/V "Runjiang" for their help on sampling.

SUPPLEMENTARY MATERIAL

The Supplementary Material for this article can be found online at: https://www.frontiersin.org/articles/10.3389/fmars.2021.634184/full#supplementary-material

REFERENCES

Altieri, A. H., and Gedan, K. B. (2015). Climate change and dead zones. *Global Change Biol.* 21, 1395–1406. doi: 10.1111/gcb.12754

Bai, Y., He, X., Pan, D., Chen, C. T. A., and Kang, Y. (2014). Summertime Changjiang River plume variation during 1998–2010. *J. Geophys. Res. (C Oceans)* 119, 6238–6257. doi: 10.1002/2014jc009866

Belkin, I. M. (2009). Rapid warming of large marine ecosystems. *Prog. Oceanogr.* 81, 207–213. doi: 10.1016/j.pocean.2009.04.011

Breitburg, D., Levin, L. A., Oschlies, A., Grégoire, M., Chavez, F. P., and Conley, D. J. (2018). Declining oxygen in the global ocean and coastal waters. *Science* 359:eaam7240.

Chai, C., Yu, Z., Shen, Z., Song, X., Cao, X., and Yao, Y. (2009). Nutrient characteristics in the Yangtze River Estuary and the adjacent East China Sea

before and after impoundment of the Three Gorges Dam. *Sci. Total Environ.* 407, 4687–4695. doi: 10.1016/j.scitotenv.2009.05.011

Chen, C. C., Chiang, K. P., Gong, G. C., Shiah, F. K., Tseng, C. M., and Liu, K. K. (2006). Importance of planktonic community respiration on the carbon balance of the East China Sea in summer. *Global Biogeochem. Cycles* 20, 1–14.

Chen, C. C., Gong, G. C., and Shiah, F. K. (2007). Hypoxia in the East China Sea: one of the largest coastal low -oxygen areas in the world. *Mar. Environ. Res.* 64, 399–408. doi: 10.1016/j.marenvres.2007.01.007

Dai, Z., Du, J., Zhang, X., Su, N., and Li, J. (2011). Variation of riverine material loads and environmental consequences on the Changjiang (Yangtze) Estuary in recent decades (1955-2008). *Environ. Sci. Technol.* 45, 223–227. doi: 10.1021/es103026a

Ding, Y., Liu, S., Li, J., and Shangguan, D. (2006). The retreat of glaciers in response to recent climate warming in western China. *Annal. Glaciol.* 43, 97–105. doi: 10.3189/172756406781812005

Fennel, K., and Testa, J. M. (2018). Biogeochemical controls on coastal hypoxia. *Ann. Rev. Mar. Sci.* 11, 105–130. doi: 10.1146/annurev-marine-010318-095138

Gao, L., Li, D., and Zhang, Y. (2012). Nutrients and particulate organic matter discharged by the Changjiang (Yangtze River): seasonal variations and temporal trends. *J. Geophys. Res. Biogeosci.* 117:G04001.

Gong, D. Y., and Ho, C. H. (2002). Shift in the summer rainfall over the Yangtze River valley in the late 1970s. *Geophys. Res. Lett.* 29:78-1.

Gong, G. C., Chang, J., Chiang, K. P., Hsiung, T. M., and Hung, C. C. (2006). Reduction of primary production and changing of nutrient ratio in the East China Sea: effect of the three gorges dam? *Geophys. Res. Lett.* 33:L07610.

Gordon, D. C., Boudreau, P. R., Mann, K. H., Ong, J.-E., Silvert, W. L., and Smith, S. V. (1996). *LOICZ Biogeochemical Modelling Guidelines*. Netherlands: LOICZ Core Project.

Grasshoff, K., Kremling, K., and Manfred, E. (1999). eds *Methods of Seawater Analysis*. Weinheim: WILEY-VCH.

Gu, H. (1980). The maximum value of dissolved oxygen in its vertical distribution in yellow sea. *Acta Oceanologica Sinica* 2, 70–80.

Guo, X., Xu, B., Burnett, W. C., Wei, Q., Nan, H., and Zhou, S. (2020). Does submarine groundwater discharge contribute to summer hypoxia in the Changjiang (Yangtze) River Estuary? *Sci. Total Environ.* 719:137450. doi: 10.1016/j.scitotenv.2020.137450

He, X., Pan, D., Bai, Y., Wang, T., Chen, C. T. A., and Zhu, Q. (2017). Recent changes of global ocean transparency observed by SeaWiFS. *Cont. Shelf Res.* 143, 159–166. doi: 10.1016/j.csr.2016.09.011

Holm-Hansen, O., Lorenzen, C. J., Holmes, R. W., and Strickland, J. D. H. (1965). Fluorometric determination of chlorophyll. *ICES J. Mar. Sci.* 30, 3–15. doi: 10.1093/icesjms/30.1.3

Hopkinson, C., and Smith, E. M. (2005). "Estuarine respiration: an overview of benthic, pelagic, and whole system respiration," in *Respiration in Aquatic Ecosystems*, eds P. A. D. Giorgio and P. J. L. B. Williams (Oxford: Oxford University Press), 122–146. doi: 10.1093/acprof:oso/9780198527084.003.0008

Huang, R. X., and Russell, S. (1994). Ventilation of the subtropical North Pacific. *J. Phys. Oceanogr.* 24, 2589–2605. doi: 10.1175/1520-0485(1994)024<2589:votsnp>2.0.co;2

Intergovernmental Oceanographic Commission [IOC] (2010). *IAPSO: The International Thermodynamic Equation of Seawater–2010: Calculation and use of Thermodynamic Properties, Intergovernmental Oceanographic Commission, Manuals and Guides No. 56*. New Delhi: IOC.

Iriarte, A., de Madariaga, I., Diez-Garagarza, F., Revilla, M., and Orive, E. (1997). Primary plankton production, respiration and nitrification in a shallow temperate estuary during summer. *J. Exp. Mar. Biol. Ecol.* 208, 127–151. doi: 10.1016/s0022-0981(96)02672-x

Jensen, L. M., Sand-Jensen, K., Marcher, S., and Hansen, M. (1990). Plankton community respiration along a nutrient gradient in a shallow Danish estuary. *Mar. Ecol. Prog. Ser. Oldendorf* 61, 75–85. doi: 10.3354/meps061075

Jolliffe, I. T., and Cadima, J. (2016). Principal component analysis: a review and recent developments. *Phil. Trans. R. Soc. A Mathemat. Phys. Eng. Sci.* 374:20150202. doi: 10.1098/rsta.2015.0202

Levin, L. A., Ekau, W., Gooday, A. J., Jorissen, F., Middelburg, J. J., and Naqvi, W. (2009). Effects of natural and human-induced hypoxia on coastal benthos. *Biogeosciences* 6, 2063–2098. doi: 10.5194/bg-6-2063-2009

Li, D., Zhang, J., Huang, D., Wu, Y., and Liang, J. (2002). the Oxygen deficit in the Changjiang Estuary. *Sci. China Series D* 32, 686–694.

Li, M., Lee, Y. J., Testa, J. M., Li, Y., Ni, W., and Kemp, W. M. (2016a). What drives interannual variability of hypoxia in Chesapeake Bay: climate forcing versus nutrient loading? *Geophys. Res. Lett.* 43, 2127–2134. doi: 10.1002/2015gl067334

Li, M., Wang, H., Li, Y., Ai, W., Hou, L., and Chen, Z. (2016b). Sedimentary BSi and TOC quantifies the degradation of the Changjiang Estuary, China, from river basin alteration and warming SST. *Estuarine Coastal Shelf Sci.* 183, 392–401. doi: 10.1016/j.ecss.2016.08.001

Li, M. T., Xu, K. Q., Watanabe, M., and Chen, Z. Y. (2007). Long-term variations in dissolved silicate, nitrogen, and phosphorus flux from the Yangtze River into the East China Sea and impacts on estuarine ecosysem. *Estuar. Coast. Shelf Sci.* 71, 3–12. doi: 10.1016/j.ecss.2006.08.013

Li, Z., Song, S., Li, C., and Yu, Z. (2018). The sinking of the phytoplankton community and its contribution to seasonal hypoxia in the Changjiang (Yangtze River) estuary and its adjacent waters. *Estuarine Coast. Shelf Sci.* 208, 170–179. doi: 10.1016/j.ecss.2018.05.007

Liu, S. M., Qi, X. H., Li, X., Ye, H. R., Wu, Y., and Ren, J. L. (2016). Nutrient dynamics from the Changjiang (Yangtze River) estuary to the East China Sea. *J. Mar. Syst.* 154, 15–27. doi: 10.1016/j.jmarsys.2015.05.010

Lui, H.-K., Chen, C.-T. A., Lee, J., Bai, Y., and He, X. (2014). Looming hypoxia on outer shelves caused by reduced ventilation in the open oceans: case study of the East China Sea. *Estuar. Coast. Shelf Sci.* 151, 355–360. doi: 10.1016/j.ecss.2014.08.010

Markus Meier, H. E., Väli, G., Naumann, M., Eilola, K., and Frauen, C. (2018). Recently accelerated oxygen consumption rates amplify deoxygenation in the Baltic Sea. *J. Geophys. Res. Oceans* 123, 3227–3240. doi: 10.1029/2017jc013686

Matli, V. R. R., Fang, S., Guinness, J., Rabalais, N. N., Craig, J. K., and Obenour, D. R. (2018). Space-Time geostatistical assessment of hypoxia in the Northern Gulf of Mexico. *Environ. Sci. Technol.* 52, 12484–12493. doi: 10.1021/acs.est.8b03474

Meng, J., and Yao, P. (2014). Speciation, bioavailability and preservation of phosphorus in surface sediments of the Changjiang Estuary and adjacent East China Sea inner shelf. *Estuar. Coast. Shelf Sci.* 144, 27–38. doi: 10.1016/j.ecss.2014.04.015

Ni, X., Huang, D., Zeng, D., Zhang, T., Li, H., and Chen, J. (2016). The impact of wind mixing on the variation of bottom dissolved oxygen off the Changjiang Estuary during summer. *J. Mar. Syst.* 154, 122–130. doi: 10.1016/j.jmarsys.2014.11.010

Park, T., Jang, C. J., Jungclaus, J. H., Haak, H., and Park, W. (2011). Effects of the Changjiang river discharge on sea surface warming in the Yellow and East China Seas in summer. *Cont. Shelf Res.* 31, 15–22. doi: 10.1016/j.csr.2010.10.012

Pei, S., Shen, Z., and Laws, E. A. (2009). Nutrient dynamics in the upwelling area of Changjiang (Yangtze River) Estuary. *J. Coast. Res.* 25, 569–580. doi: 10.2112/07-0948.1

Qian, W., Dai, M., Xu, M., Kao, S. J., Chuanjun, D., and Liu, J. (2017). Non-local drivers of the summer hypoxia in the East China Sea off the Changjiang Estuary. *Estuar. Coast. Shelf Sci.* 198, 393–399. doi: 10.1016/j.ecss.2016.08.032

Quan, W. M., Shen, X. Q., Han, J. D., and Chen, Y. Q. (2005). Analysis and assessment on eutrophication status and developing trend in Changjiang Estuary and adjacent sea. *Mar. Environ. Sci.* 24, 13–16.

Rabalais, N. N., Cai, W. J., Carstensen, J., Conley, D. J., Fry, B., and Hu, X. (2014). Eutrophication-driven deoxygenation in the coastal ocean. *Oceanography* 27, 172–183. doi: 10.5670/oceanog.2014.21

Rabouille, C., Conley, D. J., Dai, M., Cai, W. J., Chen, C. T. A., and Lansard, B. (2008). Comparison of hypoxia among four river-dominated ocean margins: the Changjiang(Yangtze). Mississippi, Pearl, and Rhone rivers. *Cont. Shelf Res.* 28, 1527–1537. doi: 10.1016/j.csr.2008.01.020

Resplandy, L. (2018). *Will Ocean zones With Low Oxygen Levels Expand or Shrink?* Berlin: Nature Publishing Group.

Satta, M. P., Agustí, S., Mura, M. P., Vaqué, D., and Duarte, C. M. (1996). Microplankton respiration and net community metabolism on the NW Mediterranean coast. *Aquat. Microb. Ecol.* 10, 165–172. doi: 10.3354/ame010165

Scavia, D., Justic, D., Obenour, D. R., Craig, K., and Wang, L. (2018). Hypoxic volume is more responsive than hypoxic area to nutrient load reductions in the northern Gulf of Mexico–and it matters to fish and fisheries. *Environ. Res. Lett.* 14:024012. doi: 10.1088/1748-9326/aaf938

Sim, C. H., Gan, F. F., and Chang, T. C. (2005). Outlier labeling with boxplot procedures. *J. Am. Statist. Assoc.* 100, 642–652. doi: 10.1198/016214504000001466

Siswanto, E., Nakata, H., Matsuoka, Y., Tanaka, K., Kiyomoto, Y., and Okamura, K. (2008). The long-term freshening and nutrient increases in summer surface water in the northern East China Sea in relation to Changjiang discharge variation. *J. Geophys. Res. Oceans* 113:C10.

Song, G., Liu, S., Zhu, Z., Zhai, W., Zhu, C., and Zhang, J. (2016). Sediment oxygen consumption and benthic organic carbon mineralization on the continental shelves of the East China Sea and the Yellow Sea. *Deep Sea Res. Part II: Top. Stud. Oceanography* 124, 53–63. doi: 10.1016/j.dsr2.2015.04.012

Taylor, J. R. (1997). (Ed). *An Introduction to Error Analysis*. Mill Valley, CA: University Science Books.

Tian, R. C., Hu, F. X., and Martin, J. M. (1993). Summer nutrient fronts in the Changjiang (Yangtze River) Estuary. *Estuar. Coast. Shelf Sci.* 37, 27–41. doi: 10.1006/ecss.1993.1039

Vaquer-Sunyer, R., and Duarte, C. M. (2008). Thresholds of hypoxia for marine biodiversity. *Proc. Natl. Acad. Sci. U S A.* 105, 15452–15457. doi: 10.1073/pnas.0803833105

Wang, B. D. (2006). Cultural eutrophication in the Changjiang (Yangtze River) plume: history and perspective. *Estuar. Coast. Shelf Sci.* 69, 471–477. doi: 10.1016/j.ecss.2006.05.010

Wang, H., Dai, M., Liu, J., Kao, S. J., Zhang, C., Cai, W. J., et al. (2016). Eutrophication-driven hypoxia in the East China Sea off the Changjiang Estuary. *Environ. Sci. Technol.* 50, 2255–2263. doi: 10.1021/acs.est.5b06211

Wang, T., and Yang, Z. (2015). Understanding the flushing capability of Bellingham Bay and its implication on bottom water hypoxia. *Estuar. Coast. Shelf Sci.* 165, 279–290. doi: 10.1016/j.ecss.2015.04.010

Wang, X., Baskaran, M., Su, K., and Du, J. (2018). The important role of submarine groundwater discharge (SGD) to derive nutrient fluxes into River dominated Ocean Margins–The East China Sea. *Mar. Chem.* 204, 121–132. doi: 10.1016/j.marchem.2018.05.010

Wei, H., He, Y., Li, Q., Liu, Z., and Wang, H. (2007). Summer hypoxia adjacent to the Changjiang Estuary. *J. Mar. Syst.* 67, 292–303. doi: 10.1016/j.jmarsys.2006.04.014

Wei, Q., Wang, B., Yu, Z., Chen, J., and Xue, L. (2017). Mechanisms leading to the frequent occurrences of hypoxia and a preliminary analysis of the associated acidification off the Changjiang estuary in summer. *Sci. China Earth Sci.* 60, 360–381. doi: 10.1007/s11430-015-5542-8

Wolter, K., and Timlin, M. S. (1998). Measuring the strength of ENSO events: how does 1997/98 rank? *Weather* 53, 315–324. doi: 10.1002/j.1477-8696.1998.tb06408.x

Wu, L., Cai, W., Zhang, L., Nakamura, H., Timmermann, A., and Joyce, T. (2012). Enhanced warming over the global subtropical western boundary currents. *Nat. Climate Change* 2, 161–166. doi: 10.1038/nclimate1353

Xuan, J. L., Huang, D., Zhou, F., Zhu, X. H., and Fan, X. (2012). The role of wind on the detachment of low salinity water in the Changjiang Estuary in summer. *J. Geophys. Res. Oceans* 117:C10004.

Yang, Z., Chen, J., Chen, M., Ran, L., Li, H., and Lin, P. (2018). Sources and transformations of nitrogen in the South China Sea: insights from nitrogen isotopes. *J. Oceanogr.* 74, 101–113. doi: 10.1007/s10872-017-0443-z

Zhang, W., Wu, H., Hetland, R. D., and Zhu, Z. (2019). On mechanisms controlling the seasonal hypoxia hot spots off the Changjiang River Estuary. *J. Geophys. Res. Oceans* 124, 8683–8700. doi: 10.1029/2019jc015322

Zhang, W., Wu, H., and Zhu, Z. (2018). Transient hypoxia extent off changjiang river estuary due to mobile Changjiang River Plume. *J. Geophys. Res. Oceans* 123, 9196–9211. doi: 10.1029/2018jc014596

Zhou, F., Chai, F., Huang, D., Xue, H., Chen, J., and Xiu, P. (2017). Investigation of hypoxia off the Changjiang Estuary using a coupled model of ROMS-CoSiNE. *Prog. Oceanogr.* 159, 237–254. doi: 10.1016/j.pocean.2017.10.008

Zhu, J., Zhu, Z., Lin, J., Wu, H., and Zhang, J. (2016). Distribution of hypoxia and pycnocline off the Changjiang Estuary. *China. J. Mar. Syst.* 154, 28–40. doi: 10.1016/j.jmarsys.2015.05.002

Zhu, Z. Y., Zhang, J., Wu, Y., Zhang, Y. Y., Lin, J., and Liu, S. M. (2011). Hypoxia off the Changjiang (Yangtze River) Estuary: oxygen depletion and organic matter decomposition. *Mar. Chem.* 125, 108–116. doi: 10.1016/j.marchem.2011.03.005

Conflict of Interest: The authors declare that the research was conducted in the absence of any commercial or financial relationships that could be construed as a potential conflict of interest.

Copyright © 2021 Wang, Cai, Chen, Kirchman, Wang, Fan and Huang. This is an open-access article distributed under the terms of the Creative Commons Attribution License (CC BY). The use, distribution or reproduction in other forums is permitted, provided the original author(s) and the copyright owner(s) are credited and that the original publication in this journal is cited, in accordance with accepted academic practice. No use, distribution or reproduction is permitted which does not comply with these terms.

Advantages of publishing in Frontiers

OPEN ACCESS
Articles are free to read for greatest visibility and readership

FAST PUBLICATION
Around 90 days from submission to decision

HIGH QUALITY PEER-REVIEW
Rigorous, collaborative, and constructive peer-review

TRANSPARENT PEER-REVIEW
Editors and reviewers acknowledged by name on published articles

Frontiers
Avenue du Tribunal-Fédéral 34
1005 Lausanne | Switzerland

Visit us: www.frontiersin.org
Contact us: frontiersin.org/about/contact

REPRODUCIBILITY OF RESEARCH
Support open data and methods to enhance research reproducibility

DIGITAL PUBLISHING
Articles designed for optimal readership across devices

FOLLOW US
@frontiersin

IMPACT METRICS
Advanced article metrics track visibility across digital media

EXTENSIVE PROMOTION
Marketing and promotion of impactful research

LOOP RESEARCH NETWORK
Our network increases your article's readership